PROCEEDINGS OF

The First SIMS EUROSIM Conference on Simulation and Modelling SIMS EUROSIM 2021

The 62nd SIMS Conference on Simulation and Modelling SIMS 2021

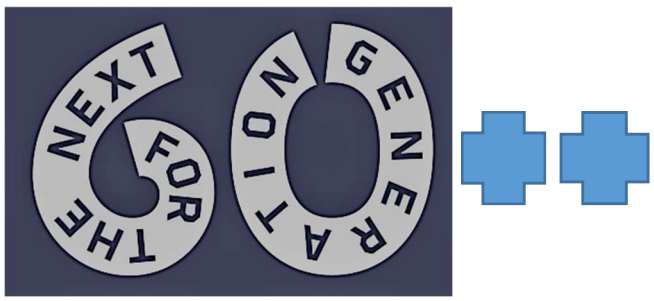

Editors: Esko Juuso, Bernt Lie, Erik Dahlquist, and Jari Ruuska

Organized by University of Oulu
Finnish Simulation Forum (FinSim)
and
Finnish Society of Automation

Proceedings of
The First SIMS EUROSIM Conference on Simulation and Modelling
SIMS EUROSIM 2021

The 62nd SIMS Conference on Simulation and Modelling
SIMS 2021

Virtual Conference, Finland, 21-23 September 2021

Editors:
Esko Juuso, Bernt Lie, Erik Dahlquist, and Jari Ruuska

Published by:
Scandinavian Simulation Society and Linköping University Electronic Press
ISBN: 978-91-7929-219-5
Series: Linköping Electronic Conference Proceedings, No. 185
ISSN: 1650-3686
eISSN: 1650-3740
DOI: https://doi.org/ecp21185

Organized by:
University of Oulu
Finnish Simulation Forum (FinSim)
and
Finnish Society of Automation

in cooperation with:
Scandinavian Simulation Society (SIMS)

Preface

The first SIMS EUROSIM conference on Simulation and Modelling (SIMS EUROSIM 2021) and 62nd SIMS conference on Simulation and Modelling (SIMS 2021) were organized as a joint virtual conference. Originally, this conference was planned to be organized in Oulu, Finland. The COVID-19 pandemic presented tremendous challenges for the global research community and for the entire world. The organizers were first postponing the deadlines and keeping the plan of organizing the conference in person. Since the pandemic was continuing strongly, the plans were changed: the conference was decided to organize as a virtual conference in September 2021.

The Scandinavian Simulation Society consists of members from five Nordic countries: Denmark, Finland, Norway, Sweden, and Iceland. The goal of SIMS is to further develop the science and practice of modelling and simulation in all application areas and to be a forum for information interchange between professionals and non-professionals in the Nordic countries. SIMS is a member society of The Federation of European Simulation Societies (EUROSIM) was set up in 1989. The purpose of EUROSIM is to provide a European forum for regional and national simulation societies to promote the advancement of modelling and simulation in industry, research and development. EUROSIM consists of 17 European Simulation Societies. The Scandinavian simulation society (SIMS) had Board and Annual Meetings during the conference.

The conference program consisted of three keynote presentations, 68 regular presentations and a panel discussion. The proceedings include 67 full papers. The keynotes are included as abstracts. The call for papers resulted in 83 submissions prepared by 152 authors from nine countries. The reviews of all submissions were done by four chairs, 19 IPC members and 37 international reviewers. Full papers were selected on the grounds of academic merit and relevance to the conference theme. Each submission had 2-4 reviews and the acceptance rate was 83% for the full papers published in the proceedings.

The SIMS 61 conference covered broad aspects of simulation, modeling and optimization in engineering applications, including many papers on multivariate data analysis, machine learning, control, diagnostics, decision making, power plants, energy storage, oil and gas industry, CO_2 capture, computational fluid dynamic, wastewater treatment, biosystems and epidemiological models.

Panel discussions were organized on modelling and simulation in tackling challenges of the climate change. The discussion focused on three areas: biofuels, renewable energy sources and quality of measurements. The audience asked about next generation nuclear systems, biogas and CO_2 emissions. The virtual conference did not include technical tours. Industrial and environmental applications, development of modelling and simulation tools and strong support for PhD students continue for stimulating process development model-based automation.

We would like to express our sincere thanks to the keynote speakers, authors, session chairs, members of the program committee and additional reviewers who made this conference such an outstanding success. Finally, we hope that you will find the proceedings to be a valuable resource in your professional, research, and educational activities whether you are a student, academic, researcher, or a practicing professional.

Esko Juuso, Bernt Lie, Erik Dahlquist, and Jari Ruuska

Table of Contents

Conferences location

The conference was organized as a virtual event.

Opening, 21 September 2021

Opening of The First SIMS EUROSIM Conference on Simulation and Modelling SIMS EUROSIM 2021

The 62nd International Conference of Scandinavian Simulation Society (SIMS):

- SIMS President, Prof. Bernt Lie, University of South-Eastern Norway, Norway
- Adj. prof. Esko Juuso, Conference Chair, University of Oulu, Finland

Keynote presentations

How process automation is making the world more resource and energy efficient – future trends
Digital Lead Martin Björnmalm, Hub North Europe, Process Industries Division. ABB, Sweden

How to lead the process industry to a safe and sustainable future?
Head of Product Management Jyri Lindholm, NAPCON, Neste Engineering Solutions Oy, Finland

The Road to SMARTER and not BIGGER on Data problems in Transportation
Assoc. prof. Miguel Mujica-Mota, Eurosim President, Aviation Academy, Amsterdam University of Applied Sciences, The Netherland

Conference topics

The Proceedings includes 68 articles in five tracks including ten topics:

Panel discussion on Future challenges and possibilities for simulation, 23 September 2021

Chair: Adj. prof. Jari Ruuska, University of Oulu, Finland

Panelists:

Hub Manager Björn Jonsson, ABB, Sweden
Head of Product Management, Jyri Lindholm, Neste Engineering Solutions Oy, Finland
Assoc. prof. Miguel Mujica-Mota, Eurosim President, Amsterdam University of Applied Sciences, The Netherlands
Prof. Bernt Lie, University of South-Eastern Norway, Norway
Senior prof. Erik Dahlquist, Mälardalen University, Sweden
Adj. prof. Esko Juuso, University of Oulu, Finland

Conference program

Each conference day started with a keynote and continued with three parallel sessions. The Annual SIMS meeting was in the end of the first day. The third day ended with the panel discussion. More information is available at SIMS website (https://www.scansims.org/).

Conference General Chair

Adjuct prof. Esko Juuso, University of Oulu, Finland

International Program Committee

Prof. Bernt Lie, University of South-Eastern Norway, Norway, Chair

Adj. prof. Esko Juuso, University of Oulu, Finland, Co-Chair

Prof. Erik Dahlquist, Malardalen University, Sweden, Co-Chair

Adj. prof. Jari Ruuska, University of Oulu, Finland, Co-Chair

Prof. Felix Breitenecker, Vienna University of Technology, Austria

Prof. Lars Eriksson, Linköping University, Sweden

Dr. David Hästbacka, Tampere University, Finland

Prof. Tiina Komulainen, Oslo Metropolitan University, Norway

Dr. Andreas Körner, Vienna University of Technology, Austria

Prof. Juan Ignacio Latorre-Biel, Public University of Navarre, Spain

Prof. Kauko Leiviskä, University of Oulu, Finland

Prof. Miguel Mujica-Mota, Amsterdam University of Applied Sciences, The Netherlands

Adj. prof. Esa Muurinen, University of Oulu, Finland

Dr. Markku Ohenoja, University of Oulu, Finland

Prof. Kim Sörensen, Alborg University, Denmark

Dr. Satu Tamminen, University of Oulu, Finland

Adj. prof. Kai Zenger, Aalto University, Finland

Prof. Borut Zupančič, University of Ljubljana, Slovenia

Prof. Lars Erik Øi, University of South-Eastern Norway, Norway

National Organizing Committee

Adj. prof. Jari Ruuska, University of Oulu, Finland, Chair

Adj. prof. Esko Juuso, University of Oulu, Finland, Co-Chair

Ms. Anu Randén-Siippainen, Finnish Automation Society, Finland

Mr. Marko Vuorio, Finnish Automation Society, Finland

International Reviewers

Title	Givenname	Surname	Affiliation	Country
Dr.	Sailesh	Abburu	SINTEF	Norway
Assoc. prof.	W.K. Hiromi	Ariyaratne	University of South-Eastern Norway	Norway
Assoc. prof.	Wenche Hennie	Bergland	University of South-Eastern Norway	Norway
Dr.	Ole Magnus	Brastein	BEDCO AS	Norway
Assoc. prof.	Carlos	Dinamarca	University of South-Eastern Norway	Norway
Prof.	Jo	Eidsvik	NTNU	Norway
Assoc. prof.	André Vagner	Gaathaug	University of South-Eastern Norway	Norway
Prof.	Maths	Halstensen	University of South-Eastern Norway	Norway
M.Sc.	Petri	Hietaharju	University of Oulu	Finland
Prof.	Yrjö	Hiltunen	University of Eastern Finland	Finland
M.Sc.	Heikki	Hyyti	Aalto University	Finland
M.Sc.	Esin	Iplik	Mälardalen University	Sweden
M.Sc.	Antti	Koistinen	University of Oulu	Finland
Prof.	Juho	Könnö	University of Oulu	Finland
Prof.	Hailong	Li	Mälardalen University	Sweden
Dr.	Toni	Liedes	University of Oulu	Finland
Dr.	Jean-Nicolas	Louis	University of Oulu	Finland
Assoc. prof.	Joachim	Lundberg	University of South-Eastern Norway	Norway
M.Sc.	Heidi	Marais	Mälardalen University	Sweden
M.Sc.	Madeleine	Martinsen	ABB Service	Sweden
Prof.	Britt	Moldestad	University of South-Eastern Norway	Norway
M.Sc.	Riku-Pekka	Nikula	University of Oulu	Finland
Dr.	Wathsala	Perera	CEMIT Group	Norway
Prof.	Carlos	Pfeiffer	University of South-Eastern Norway	Norway
M.Sc.	Jari	Pulkkinen	University of Oulu	Finland
M.Sc.	Achref	Rabhi	Mälardalen University	Sweden
Prof.	Mika	Ruusunen	University of Oulu	Finland
Prof.	Nils-Olav	Skeie	University of South-Eastern Norway	Norway
M.Sc.	Jerol	Soibam	Mälardalen University	Sweden
Dr.	Aki	Sorsa	University of Oulu	Finland
Prof.	Eva	Thorin	Mälardalen University	Sweden
Assoc. prof.	Kristian	Thorsen	University of Stavanger	Norway
Dr.	Jani	Tomperi	University of Oulu	Finland
Dr.	Cansu	Uluseker	University of Stavanger	Norway
Dr.	Stavros	Vouros	Mälardalen University	Sweden
Dr.	Ari	Vuokila	University of Oulu	Finland
Dr.	Petri	Österberg	University of Oulu	Finland

How process automation is making the world more resource and energy efficient – future trends

Martin Bjornmalm

Digital Lead, Northern Europe, Process Industries, Process Automation
ABB, Sweden

Abstract

The world is facing major challenges in coping with the supply of food and other necessities to all people, while ensuring a sustainable and environmentally friendly future. To improve industry processes, meet the increasing efficiency, safety and quality demands, new digital technology and advanced automation are the most effective means. With relatively small investments, great effects can be achieved.

Today, the collection of data from the entire plant can be done faster and more accurately, while in the same time it is processed using various algorithms, advanced control systems or cloud services. It provides decision support to operators and predicted maintenance. It enables production planning based on customer orders from raw materials, overall production steps to distribution of the product and model-based control and optimization of not only individually processes, but entire factories or even entire corporations via Collaborative Operation Centers by the supplier's experts around the world 365/24.

Biography

Education

2015	Master of Science in Engineering Physics, Royal Institute of Technology, Stockholm, Sweden

Professional Experience

2020 to date	Digital Lead Process Industries – Process Industries, Northern Europe, ABB
2020 to date	Head of Advanced Services – Process Industries, Sweden
2019 - 2020	Digital Solutions Manager – Process Industries, Sweden
2018 - 2019	Sales and Business Development Digital Operations – ABB, Sweden
2017 - 2019	Business Development & Digital Lead – Country Service Organisation ABB, Sweden
2016 - 2017	Graduate Trainee – ABB, Sweden

DOI: 10.3384/ecp21185

How to lead the process industry to a safe and sustainable future?

Jyri Lindholm
Head of Product Management
NAPCON, Neste Engineering Solutions Oy, Finland

Abstract

Process safety is an integral part of sustainable business. Operating a process plant is high demanding work and mostly teamwork. This means that cooperation and communication between people throughout the shift is a key part of safety. How can we improve this with training? Using an integrated training environment where high fidelity dynamic training simulator and Reality Capture technology is integrated to the one training environment enables the panel and field operators to train together in one session. This kind of environment enables development of communication and cooperation between operators. One other added value is that there may be the situation that practices and procedures are poorly documented for the field operators so this kind of environment is a useful tool also for developing those.

Training environments are normally used to improve process safety. The training usually covers the handling of a wide range of abnormal situations, equipment maintenance procedures, such as the replacement of the pump and compressor with spare pumps, the replacement of the heat exchanger during the cleaning period. From the other hand there should be high motivation to invest in the training environments also from the environmental aspect. How about the emission during the hazards? Plant operators are the pilots who control the plant operations and it's obvious that there is a direct link between operators actions and emissions. It is really important that the operator also takes this environmental aspect into account in normal use. By minimizing malfunctions and hazards, emissions are also reduced. Naturally, minimizing flaring and driving as economically as possible will also reduce emissions. These aspects bring new challenges to building comprehensive training programs to meet environmental considerations.

Important questions are how individuals learn best and how they want to learn and where or when they have time to train. Gamification increases motivation and fun factor of learning. However the comprehensive operator training simulator (OTS) environments are difficult to gamificate and on the other hand, the training environment needs to be very realistic for the experienced operators. Anyhow, educational games fit very well for beginners and students. Referring to other questions, companies are international and have production facilities in several countries and experts around the world, so the demand for location-independent training is growing. Nowadays Technology allows us to build a fully functional multi user cloud OTS environment where several operators and specialists can train simultaneously from different locations.

How to make better operators - would it be possible to increase human capabilities with Artificial Intelligence? Would it be possible to develop one new safety layer which is powered by AI? One solution was presented where an AI solution helps operators to run plants as optimally as possible. The implementation is for distillation columns used in oil refining. The solution supports operators and production engineers to maximize the yield of most valuable products.

High fidelity Unit OTS data and scenarios were used for developing the ML model in the first steps. The challenge for the future is whether the high fidelity simulators can be used to train ML models to detect different kinds of process anomalies and abnormal behaviours which are very rare in real life. In addition,would it be possible to use OTS data to build AI models that provide guidance to operators on how to run more energy efficiencently and how to minimize emissions?

Biography

Jyri Lindholm has extensive experience in managing the performance, resources, training, development and innovation of Neste Engineering uSolution Automation Technology. He has more than 15 years of experience in various management ositions. Jyri has long experience in cooperating with relevant engineering partners and universities. He is currently responsible for NAPCON product management in the NAPCON business unit. He is responsible for looking at the overall picture of the NAPCON product range and leading Product Lines to create and implement a winning development plan that secures and enables both commercial success and high customer satisfaction for NAPCON and related services. Jyri Lindholm has more than 20 years of work experience from advanced industrial process control engineering, especially in training simulator environments. He has been responsible for projects' cost stimation, project management, definition, design, engineering, integration, commissioning and model development in multiple Training Simulator Systems for oil refining, biorefining, and polymer plant sites. Also he has been responsible for control application design of distributed Control Systems applications and act as a Project Manager of the Process Computer System implementation in several petrochemical units.

NAPCON leads the process industry to a safe and sustainable future. We offer a wide range of innovative solutions to enhance your production spanning from operational intelligence and advanced process optimization solutions to boosting your competence through simulators and games. As part of Neste Engineering Solutions that offers engineering, procurement, construction and project management services for the Oil & Gas, Petrochemicals and Bio-industries, we apply our extensive process know-how on modern software engineering to fulfil your needs in the areas of availability, production optimization, sustainability and safety. In addition to our head office in Porvoo, Finland, we operate in international Neste locations such as Singapore and Rotterdam. Altogether we employ over 800 engineering professionals. For more information, please visit: www.napconsuite.com

Education

M. Sc., Process Engineering, automation and information technology University of Oulu, 1996. Thesis on Fitting of a dynamic simulator to process measurement and development of a real time estimator.

Employment History

2017	Head of Product Management of NAPCON and Member of NAPCON Supervisory Board, Neste Engineering Solution Oy, Porvoo, Finland
2015 - 2017	Product Manager of NAPCON Suite product family. Neste Jacobs Oy, NAPCON Business Unit, Porvoo, Finland
2013 - 2015	Head of Automation Technology, Neste Jacobs Oy, Competence Center of Technology and Process, Porvoo, Finland
2011 - 2013	Manager, Dynamic Simulation and Real Time Optimization, Neste Jacobs Oy, Competence Center of Technology and Process, Porvoo, Finland
2010 - 2011	Manager, Automation Technology, Neste Jacobs Oy, Automation and Electrical Engineering, Porvoo, Finland
2006 - 2010	Section Manager, Application Engineering, Neste Jacobs Oy, Automation Engineering, Porvoo, Finland
1996 - 2006	Process Control Engineer, Neste Engineering Oy, Automation Engineering, Porvoo, Finland

Trophy

Viva Automation Recognition Prize awarded to a team from Neste Jacobs. Finnish Society of Automation 2011.

Fields of Competence

Product Management, Business Management, Line Management, Project Management, Resource Management, Development Management, Application Engineering, Training Simulator Systems, On-line Process Calculations

Technology

Automation Technology, NAPCON Technology

Techniques

Dynamic Simulation, Real Time Optimization, Training Simulator System, On-line process calculations, Process Computer System, Multivariable Process Control, Distributed Control System

The Road to SMARTER and not BIGGER on Data problems in Transportation

Miguel Mujica Mota

Eurosim President, Assoc. prof., Aviation Academy,
Amsterdam University of Applied Sciences, The Netherlands

Abstract

In This talk, I will discuss the role of M&S in the new ecosystem of techniques for data analysis; the audience will get some light on how I consider the different techniques should be coupled to solve current real problems in different transport modalities ranging from Road to Aviation. This talk will give also direction to young professionals on what are the key areas to put focus on if they want to pursue a successful career in the future using current techniques like AI, Big Data, Process and Data Mining, optimization, Statistical analysis and of course simulation.

Biography

Associate Professor, Simulation/optimization (Aviation Academy, Amsterdam U. of Applied Sciences | School of Technology)

Visiting Professor at University of Aviation in Queretaro (UNAQ), 2016

Visiting Professor at The National University of Mexico

Visiting Professor at the Ecole National De L'Aviation Civile, Tolouse France

Work experience

2013 -	Associate Professor, Aviation Academy, Amsterdam University of Applied Sciences
2011 - 2013	Post-Doc Researcher, Sub-director of the Aeronautical Management studies, Universitat Autònoma de Barcelona, Spain
2005 - 2011	Master/PhD Student, Teaching Assistant, Sub-director of the Aeronautical Management studies, Universitat Autònoma de Barcelona, Spain
2000 - 2004	Master Production Planner and Scheduler (Supply Chain Department), Avon Cosmetics Mexico, Celaya, Guanajuato, Mexico
2003	Lecturer, Universidad Nacional Autónoma de México; Ciudad Universitaria, Mexico

Education and training

2013	Accredited Evaluator of the Iberoamerican Database of Evaluators: Sector Engineering and Industry
2012	Professional Certification (ACTIVE)
2008 - 2011	PhD Industrial Informatics, Thesis Title: “Systems Optimization based on the Exploration of Timed Coloured Petri Nets State Space”, research that contribute to the simulation/optimization approach, Universitat Autònoma de Barcelona, Spain
2004 - 2011	PhD Operations Research, graduated with Honours, Universidad Nacional Autónoma de México, Mexico
2005 - 2008	MSc in Industrial Informatics/Advanced Studies Diploma, graduated with Honours, Thesis: “Optimization of a Coloured Petri Net Simulator”, Universitat Autònoma de Barcelona, Spain
1996 - 1998	MSc in Operations Research, Thesis: “Simulation as an Analysis and Optimization Tool in Manufacture Processes”, Universidad Nacional Autónoma de México, Mexico
1992 - 1996	Chemical Engineering, Thesis: “Development of a Photo catalytic Reactor of fluidized bed for Decomposition of pollutants in Waste Water Treatment”, Universidad Autónoma Metropolitana, México

Panel discussion: Modelling and simulation in tackling challenges of the climate change

Chair: Adj. prof. Jari Ruuska, University of Oulu, Finland
Panelists:
Hub Manager Björn Jonsson, ABB, Sweden
Head of Product Management, Jyri Lindholm, Neste Engineering Solutions Oy, Finland
Prof. Bernt Lie, University of South-Eastern Norway, Norway
Senior prof. Erik Dahlquist, Mälardalen University, Sweden
Adj. prof. Esko Juuso, University of Oulu, Finland

The panel discussion was the last part the conference. The panelist were the keynote presenters, the current and two past presidents of SIMS, including the chair of the conference, who is also the past president of Eurosim. The chair of the national organizing committee was the chair of the panel. The discussion focused on five questions: simulation, energy systems, big data, environment and simulation toolboxes. The questions were presented by the panel chair.

1 Can we get enough biofuels and how could we use them as efficiently as possible?

Björn: Extremely interesting topic. It is very clear that people can change behavior when absolutely needed but it is not enough. Largest impact comes from companies and industry. Industry together with universities can create great initiatives to tackle climate change e.g., LKAB sustainable underground mining and transition to hydrogen-based production in green steel making. Many initiatives in papermaking and other areas as well. Simulation and modeling capabilities are important in developing these new important technologies.

Erik: What resources do we have and how we can utilize them more efficiently. LKAB Hydrogen production example where hydrogen is then used to reduce ion oxide to metallic ion. We are producing lots of electrical vehicles now. If you replace one carbon molecule in steel reduction you have to put in roughly 2.5 times more energy but if you like to replace one carbon molecule in electrical vehicle you only need 30% of energy compared to fossil alternative. How can you utilize limited resources in long run and increasing demand when looking from overall perspective? We as researchers can help politicians and society to do some prioritization.

Esko: We have lots of possibilities what we can do. First step is that we must assess whether we can do it; E. g. in steel industry we have areas where hydrogen does not work. Then as a second step we need to assess how fast we can do it as there is always some dynamics that needs to be accounted. Third step after that is that we need to think about the life cycle since we have already solutions, and we need to consider whether it is reasonable to move into new solutions. Simulations and modeling can help decision making.

Bernt: There is a connection between my Covid related presentation. In Norway there are approximately 400 thousand people that are refusing vaccinations. Even among in well-educated people there are ones that deny covid. It is very difficult to convince them as denial is so strong that even facts will not help. It is very hard to convince large fraction of people and that is the challenge.

Jyri: There is an increasing race to find new kind of feedstocks. Recycling materials are important in future to make sure do not outrun resources. Economic and logistics modeling helps in finding reasonable solutions for their utilization.

Erik: There has been a lot of discussion about meat and that we should eat less of it. Livestock produces methane which creates 5 – 10% of global warming equivalents. You can extract almost all the methane using activated carbon when indoors. Methane production of livestock correlates with 1100 TWh of heating power annually. This could be possibility to create a good solution.

Bernt: One of the concerns in fossil fuels is that you introduce a new carbon source into atmosphere.

When it comes to cows, they are not a fossil source but recirculation of biomass. Interesting question is that will we have the same problem if we use biomass for fuel? If you harvest wood early in life, they grow faster. Increasing cycle of biomass generates more CO2 into atmosphere. Better economic system controls population number which affects climate change. Better health system and economy correlates with fewer children for some reason. This is very ethical question.

Jari: Resource sharing evenly globally is politically impossible but ethically right.

Esko: Living environment of people has great impact on climate change. We need to think where specific resources are produced and how they are transported. How the food is produced, what livestock is eating and how food is transported. Organizing this optimally is important. We need to think the whole system instead some isolated part of it.

Erik: The lack of measurements makes simulating difficult. We should work together to make good measurement structures and identify how we can measure important variables to make modeling possible.

Bernt: Convincing general population is easier when you can show measurements to support your claims. Yara uses satellite data to help local farmers in optimal watering and fertilizer use. Successful circular economy puts huge demand for the models and simulations because systems will interact in a way that is impossible for person to predict.

Jari: Measurements are needed but most important measurements are usually quite challenging to get.

Björn: Affecting on individual people is important as they select the decision makers who make the overall decisions. Everything is interconnected and it is important to get people understand this. E.g. we cannot have electrical vehicles without mining. It is important to get everybody to understand this connection between things. New innovations and technologies that we develop here in north have great impact when we transfer them to other places globally. It is important to build strong foundation for investments in industry and development activities.

2 Jari: How we can get enough renewable energy sources?

Bernt: In corona virus case, people say that fewer have died than in normal influenza and that lock-down and other precautions are pointless. It is very hard to make people understand that mortality rate is low because of these precautions. Corona virus is an unstable system that is being controlled using lock down. Without lock down Norway could have had ten times higher mortality rate. It is hard to convince people that has certain view and are refusing to change it. Same thing with climate that it is very hard to convince people that something has to be done.

Erik: Hydrogen system total efficiency is 50% (from electricity produced to mechanical output) today which is too inefficient compared to batteries which has 90% efficiency. On the other hand, production of batteries takes lots of energy. Cost of using some technology can be totally separated from the efficiency. There is a competition between different technologies and where certain technology should be used. E.g., Volvo ab thinks hydrogen cells should be used in heavy vehicles and Scania relies on batteries. The price will be the final driving factor.

Esko: Fair competition and where we are going to use each technology. Green electricity has lots of fluctuations. In hydrogen production this might not be too big of a problem. Optimization is needed to balance production according to some variable.

Bernt: Batteries use rare earth metals found in specific location which is a challenging problem. Fast charging 3000 vehicles simultaneously would require all the energy produced by Hoover Dam in US, so it is not realistic. Lifecycle of great number of batteries creates new challenges as well. In Norway there was an initiative where they used windmill for producing hydrogen. People fear that hydrogen cells can have leakages which are dangerous. Oil is not good in long term, but it is still needed now and in transition period. Future of energy will be a mixture of many technologies.

Björn: Agree with Bernt. There will be hydrogen, oil, batteries together. Technologies are involving. As all these technologies are involving, this is very interesting simulation task for universities – price point, sources coming in, technology development, scaling, … What technology to use and when?

3 Jari: What kind of measurements we are la*cking in order to get good data?*

Erik: We had a train case where battery needed to be operated between 30 to 70% capacity. How to do a good prediction model for this case. We need to have good measurements from environment and system to model how we can go from A to B without stopping and to minimize the battery. Simulation models are important for this kind of case.

Jyri: Future is in mixture of different fuels. Some of fuels can be used in near future and some can be left for future.

Jari: Does anybody in audience have any questions?

Esko: We do not have to find global optimum. We have local differences e.g., in airplane usage like distances and support. We need to think about what we are doing. Electric car is very good if you are do not need to drive long distances and have easy access to electricity for loading batteries. We need to consider attributes of specific areas.

Bernt: What is a measurement? Most people accept the temperature as a measurement. Thermometer can have length of a mercury column which has a correlation with temperature. Combining several classical measurements creates new measurements. We can use indirect measurements like smart sensors or soft sensors with some sort of a model. When we have evermore intelligent sensors in future, will people develop distrust towards their data or information?

Erik: We had a diploma thesis worker in Skellefteå working on how you can utilize power more efficiently considering transporting of batteries, degradation, etc... AI systems could be used for optimizing this soft of operations and systems.

Esko: I had a discussion about what is a measurements and indirect measurement where somebody said that you should not use indirect measurements but real measurements. Is temperature a real measurement? If you can reliably calculate value from another then it can be considered as a measurement.

4 Question from the audience 1: Very interesting discussion! What are your thoughts on next generation nuclear as a solution both to produce green energy and to burn the nuclear waste already produced?

Erik: In nuclear system you want to extract unwanted things and increase uranium to wanted level. Principally great solution but needs a lot of wet chemistry with very active components and therefore it is difficult because you cannot have any corrosion or leakages. Maintenance and upkeep are very difficult in this process.

Bernt: Norway has only two small nuclear reactors for research purposes. Norway is skeptical towards nuclear energy. One proposition is to produce Ethanol in nuclear reactors, but you might need to use all the fresh water in the world to make it work. We need to have mixture of several energy sources including solar energy which have improved a lot lately. With intermittent energy like solar and wind you have variations in production, and you might need to develop some new operational developments.

5 Question from the audience 2: Why does biogas get so little attention, even though there have been cars using it for a couple of decades already and you can produce it quite efficiently from biowaste from communities and farms?

Erik: I have a biogas car myself and I wonder also why we do not use more of it. We do not have strong drivers for biogas as for the energy forms. In Germany the biogas is used in heating and power, and you get paid for what you have produced.

6 Question from the audience 3: How can we best approach CO2 emissions globally? (China 28%, USA 15%, India 7%). We should focus on where we can make the most difference?

Björn: What we do here does have impact all around the world since we introduce new technologies and prove their reliability here and those are then adapted in other parts of the world, and this has a massive impact. We have project with company doing recycling of clothes and site which can be replicated globally to make massive impact. Focus on Nordics and export technology.

Esko: Electricity is just a part of the possible energy sources. Direct heat sources like solar and geothermal should be utilized better. This frees energy capacity as well..

7 Jari: Short comment from everybody on what is in your opinion the best way to use modeling and simulation to tackle climate change?

Jari: We should be able to build global models with accurate enough sub-models that tell us what parts we should concentrate on. In Eurosim society we could then showcase how to make difference.

Erik: Most important thing is to try to optimize processes so that you can utilize resources as efficiently as possible. Simulation can be used to present possibilities for the society what we can do, and we need to assess reliability of measurements to understand how reliable our predictions are.

Jyri: Old or existing way to use simulations to simulate processes to make processes as efficient as possible is very important. Global things are important but optimal driving of existing processes is very important.

Esko: Main thing of modeling and simulation is to develop ways to compare alternative and then comes optimization which can be done in several levels.

Bernt: 700-year-old paper was optimistic in predicting future which is very interesting. There is a fight in the society that we do not understand of believe in science anymore. Models should be made familiar to young people to increase understanding in modeling and simulation. Transparency and honesty is important to increase general trust in modeling. Short term predictions are more important than what is going to happen in 100 years. Modeling and simulation use for energy planning and usage is interesting and new sensors makes new models possible through Big Data. Modeling and simulation is very important topic and groups like SIMS will be needed in future.

Björn: It is important to continue increasing collaboration between people from academic and industry people.

Jari: closing words.

8 Conclusions

The discussion covered well the modelling and simulation in tackling challenges of the climate change. The panel was a highly valuable conclusion for the conference in linking the keynotes and topics of the regular papers with the history and the future of the simulation.

Acknowledgements

The chair and the panelists thank doctoral student Antti Koistinen for collecting efficiently the answers of the panelists during the panel discussion.

Author index

List of Papers

1. Multivariate data analysis and modelling

2. Machine learning

3. Control, diagnostics and decision making

4. Power plants and energy storage

5. Oil and gas industry

6. CO2 capture and use

7. Computational Fluid Dynamic (CFD)

8. Wastewater treatment

9. Biosystems

10. Epidemiological models

Development of a Surrogate-model Based Energy Efficiency Estimator for a Multi-step Chemical Process

Markku Ohenoja Tero Vuolio Teemu Pätsi Petri Österberg Mika Ruusunen

Environmental and Chemical Engineering Research Unit, Control Engineering, University of Oulu, Finland,
{forename.surname}@oulu.fi

Abstract

Energy efficiency is increasingly being considered as a critical measure of process performance due to its importance both in production costs and in environmental footprint. In this work, an indirect energy efficiency estimator was developed for the Tennessee Eastman (TE) benchmark process for the first time. The TE model was first modified to provide the reference values of energy efficiency. A sophisticated model selection scheme was then applied to build the surrogate-model. The results indicate reasonable model performance with mean absolute prediction error around 1.7%. The results also highlight the limitations present in the training set, which are, together with other practical implementation issues, discussed in this work.

Keywords: Chemical Process Engineering, Tennessee Eastman, Energy Efficiency, PLSR models, Model adaptation

1 Introduction

Energy efficiency is an important factor to consider in modern chemical process engineering; the efficiencies often are concentrated to reducing energy costs per product. Higher energy prices strongly contribute to increasing operating and manufacturing costs. Additionally, inefficiencies in energy usage also contribute to higher greenhouse gas emissions and environmental footprint. It has been concluded that the improvements in energy efficiency require pragmatic and holistic approaches (Drumm *et al.*, 2012).

The increased computational resources have enabled energy efficiency estimation and monitoring using large data sets collected from process plants. The dynamic losses (difference between the current energy consumption and the historical or theoretical energy consumption) can be estimated from the process data and visualized to the plant operators (Drumm *et al.*, 2012). The predictive soft sensors could also assist in the selection of process paths at least with a suboptimal energy efficiency (Nikula *et al.*, 2016). However, with large and complex data sets, the development of soft sensors is not straightforward. It should be also mentioned that regardless of the suboptimality, typically large energy savings can be realized in the chemical industry because of the high production volumes (Saygin *et al.*, 2011).

This study demonstrates the development of a real-time data-driven energy efficiency estimator using an artificial data set. For this aim, a multivariate simulation study with the Tennessee Eastman (TE) process benchmark is carried out. The TE process is a multi-step chemical process with relatively slow dynamics and consequently large delays. After introducing a step change, the settling time is approximately 24–48 hours, severely complicating the analysis (Downs and Fogel, 1993). The TE process has five main unit comprising an exothermic reactor, a condenser, a compressor, a separator, and a stripper. The operating cost of the TE process is related to the loss of product and reactants (in purge and product streams), steam utilization and the compressor work (Konge *et al.*, 2020).

Being an open-loop unstable process, the TE process has been extensively used to develop and test plant-wide control strategies (e.g. Larsson *et al.*, 2001; Jämsä, 2018). The scenarios embedded to the benchmark model have also resulted as numerous studied aimed for fault detection and diagnosis (e.g. Kulkarni *et al.*, 2005; Xie and Bai, 2015; Zou *et al.*, 2018). In addition, the plant-wide, nonlinear nature of the TE process has gained attention for developing surrogate models; For example, Tran and Georgakis (2018) used Net-elastic regularization and D-optimal designs to reach steady-state surrogate models with reduced complexity. Sheta *et al.* (2019) developed dynamic NNARX models with interpretable structures for four TE outputs. Recently, Konge *et al.* (2020) proposed several machine learning based regression modeling techniques for building lower dimensional subsystems and performing process operability analysis to the TE process.

However, the energy efficiency estimation of the TE process is still an unexplored topic. The energy balances for the reactor, the product separator, the stripper and the mixing zone were introduced by Jockenlhövel *et al.* (2003).

2 Material and methods

2.1 Energy efficiency

Energy efficiency is here defined as the energy consumed by the process divided by the amount of

product produced. Hence, the value should be minimized in order to minimize the energy usage per produced tons. Both terms should also involve possible losses related to production and energy utilization, having negative effect to the energy efficiency, namely increasing the value. In TE process model, the product losses are negligible (less than 0.7%) and the model does not account for the energy losses. Therefore, the simplified definition of the instantaneous energy efficiency for the product component *n* at time instant *k* is calculated as in Eq. (1):

$$\eta_n(k) = \frac{P(k)}{m_n(k)} \quad (1)$$

Where η_n is the energy efficiency with respect to component *n* at time instance *k*, *P* [MJ/h] is the energy consumed per hour by the compressor and reboiler, and m_n [ton/h] is the amount of produced component *n* per hour. In TE process, the components of interest are the liquid products *G* and *H*.

In order to extract the instantaneous, real value of the energy efficiency from the TE model, a set of modifications to the simulation were required:

1. The average liquid densities of the product streams were calculated based on the measured molar fractions, and component liquid densities given in Downs and Vogel (1993),
2. The product mass flows were calculated from the average liquid densities and the measured product volumetric flows,
3. The reboiler energy was calculated from the measured steam mass flow according to Jockenhövel *et al.* (2003).

The product stream's molar fractions were the delay and disturbance free model outputs, while the other measurements consisted of the default delays and noise levels of TE benchmark. The energy efficiency described above represents the reference (target) signal for the surrogate model.

2.2 Simulation scenario

In TE process, gaseous reactants *A, C, D* and *E* are converted into liquid products *G* and *H*, and byproduct *F* (Downs and Vogel, 1993). TE model by Balthelt *et al.* (2015) is used in this study to generate the simulated process data. In the simulation, the base case operational mode of the TE process is considered, where the target product mass ratio of *G* and *H* is set to 50/50. The simulation was run with disturbance flags disabled and using the decentralized control strategy included in the TE simulator.

First, a subset of manipulated variables was selected using first order finite difference-based sensitivity analysis of the inputs with respect to η_G and η_H (energy efficiency of components *G* and *H*). The ranges for the selected variables were determined based on simulations and earlier findings from the literature. It is well known that the ranges of inputs need to be reduced as the number of inputs is increased (Konge *et al.*, 2020; Tran and Georgakis, 2018). Table 1 lists the selected variables and their feasible ranges applied to this study.

Next, a Monte Carlo type simulation scenario is formulated. There, the TE process is simulated for two months (60 days, 1440 h) to mimic a typical set of routine process data. The set points of the manipulated and operational variables are changed pseudo randomly to illustrate the effect of sudden changes in the production and on the energy consumption.

The simulation was performed in a following way; Firstly, a random number generator was initialized. Secondly, a random time instant between 24 and 48 hours was selected from an even distribution. Then, one to four manipulated variables are randomly selected to the adjusted time step. Finally, their values are randomly chosen from an even distribution and previously adjusted variables are changed back to nominal values to keep the process within control range.

The time spans for the set points changes were chosen to occur between 24 and 48 hours after the previous change in order to ensure robust process behavior and following the recommendations in original TE model (Downs and Vogel, 1993). Using a step size of five seconds, the resulting data matrix consist of 1,036,801 rows (time instants) and 43 columns (simulated process variables).

Table 1. Setpoints of the manipulated variables and their range in TE simulation.

Manipulated variable	*Nominal value*	*Lower bound*	*Upper bound*
Production rate [m^3/h]	22.9	20.5	24.0
Stripper level (%)	50.0	40.0	60.0
Component G in product (mole-%)	53.7	51.0	57.0
Component A in reactor feed (mole-%)	55.0	49.5	65.9
Components A&C in reactor feed (mole-%)	58.6	52.7	64.4
Reactor temperature [°C]	120.0	118.0	125

2.3 Data preprocessing

The simulated data had a substantial start-up transient. Hence, the first 1000 data points (1.39 h) were excluded from the training set prior to modeling.

The data matrix was then down-sampled to reduce the effect of delays and measurement noise present in the simulated process measurements. The down-sampling was performed with 6-minute averaging, resulting as a data matrix with 14,400 x 43 (41 inputs, 2 reference

outputs). Then, each of the input variables were delay-compensated using a discrete time shift with a maximum lag of 30 minutes (*i.e.*, 5 different time shifts with a 6-minute sampling time). Consequently, before filtering there were 41 x 5 = 205 input variable candidates.

Prior to model selection the down-sampled data set was divided into training and testing sets. The division was simply made with respect to simulation time, reserving the latter 30% for testing.

2.4 Model selection and validation

In the second phase, a dynamic surrogate model for the operational mode one is constructed based on the training data (70% of the whole set) to estimate the energy efficiency. Prior to model selection, the input data space was normalized such that $X = \{0,1\}$ using the min-max-scaling.

The model structure here is based on the partial least-squares (PLS) regression. The estimator is selected based on a sufficiently representative training set of 40 days and tested with an independent time series of 20 days. The delay analysis and input variable selection are carried out using out signal correlation-based filtering, using linear correlation with the desired output and the time compensated signals as the filtering metric. In filter-based variable selection, the rule for variable inclusion or exclusion is given as

$$i = \begin{cases} 1, & R \geq T \\ 0, & R < T \end{cases}, \tag{2}$$

where i is the logical iterator, R is the linear Pearson product-moment correlation coefficient and T is the manually selected threshold. In this study, the threshold was set heuristically to $T = 0.25$. Consequently, the filtered estimator is

$$\hat{y} = \mathrm{X}b_{\mathrm{PLS}} + \varepsilon, \tag{3}$$

where b_{PLS} is the estimated parameter vector with the PLS algorithm, X is the input data matrix, $\hat{y}$ is the estimated output and the ε is the residual term with $\mathrm{N}(0, \sigma^2)$. The PLS parameter estimation is performed for the filtered matrix, i.e. $X[i{=}1]$ with the algorithm presented in de Jong (1993). The number of PLS components was selected using a grid search with cross-validation, consequently resulting as 4 and 3 selected components for the models of η_G and η_H, respectively. The objective function in selection was based on k-fold sequential cross-validation. After testing different values of the k-fold, a 3-fold cross-validation was selected.

The model performance was evaluated with the following figures of merit including R, RMSE (root mean squared error) and MAPE (mean absolute prediction error).

3 Results and discussion

3.1 Model Selection

Using the presented model selection procedure, a feasible model was identified. The figures of merit for the model training and testing results for the two energy efficiencies are shown in Table 2. For the η_G, the figures of merit for the out of sample data set (test set) can be considered sufficient for process control purposes. The predictions can be considered to be within ±0.0028 MJ/ton (2.8 kJ/ton) with 95.4% confidence. Similarly, for the final product component H, the model performance is comparable to the previous model with slightly higher correlation coefficient. The 95.4% confidence interval for energy efficiency model for component H was ±0.0032 MJ/ton (3.2 kJ/ton). In addition, it can be seen that the model's testing set performance metrics are quite optimistic for the component H, which can be seen as a higher correlation coefficient and lower error values compared to the training set.

Table 2. Figures of merit for the identified PLSR models.

Criteria	*Training*		*Testing*	
Product	*G*	*H*	*G*	*H*
R	0.86	0.88	0.85	0.89
RMSE, kJ/ton	1.6	1.6	1.6	1.6
MAPE, %	1.7	1.7	1.7	1.6

3.2 Model applicability

The test set estimations using the selected models for η_G and η_H are presented in Figure 1 and Figure 2, respectively, with corresponding confidence intervals of the selected estimators.

According to Figures 1 and 2, the testing set shows decreased performance, and for some regions the output value seems to interpolate poorly. In data-driven modeling, this often could indicate overfitting the model during the training phase, which means that the model parameters are biased because of estimating the noise in the system rather than the true dependencies. Utilization of an overly complex model as the estimator is a common cause of this behavior. (Hastie *et al.*, 2009)

In the modeling case of this study, the lack of fit in the test set seems to be at least partially explained with the non-similar distributions of the training and testing input data sets, often referred as the covariate shift (Moreno-Torres *et al.*, 2012). This issue is discussed in the following.

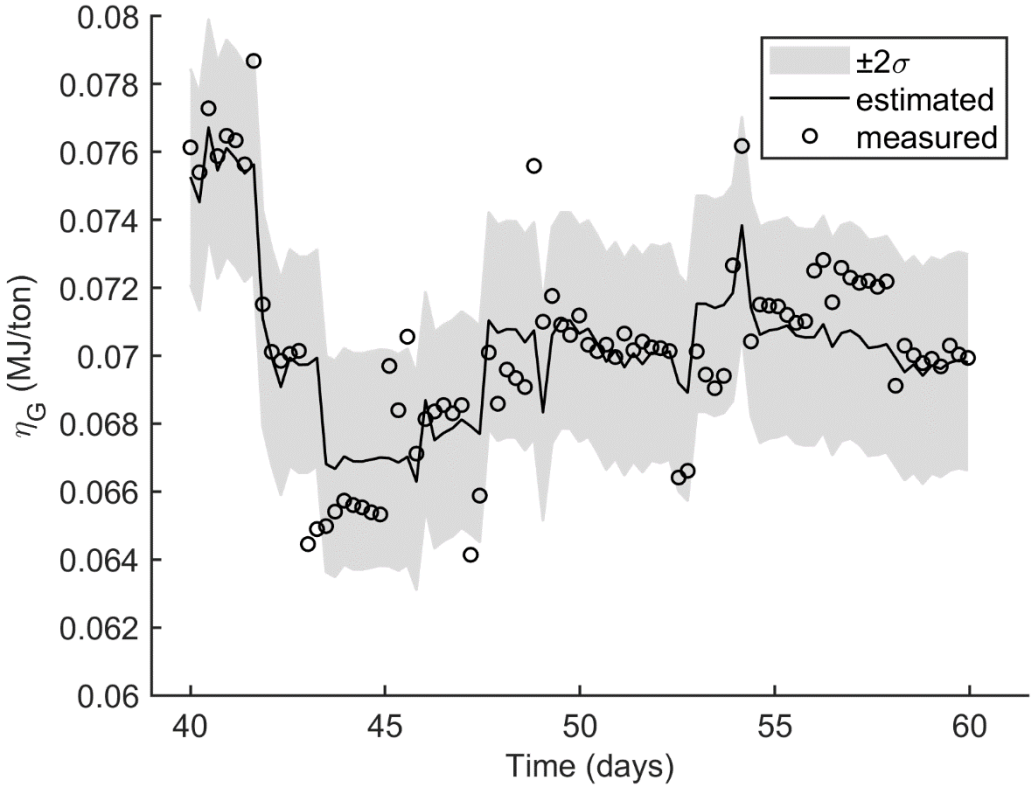

Figure 1. Measured and estimated energy efficiency for component *G* with corresponding confidence intervals. Only every 50 sample is plotted for the sake of clarity.

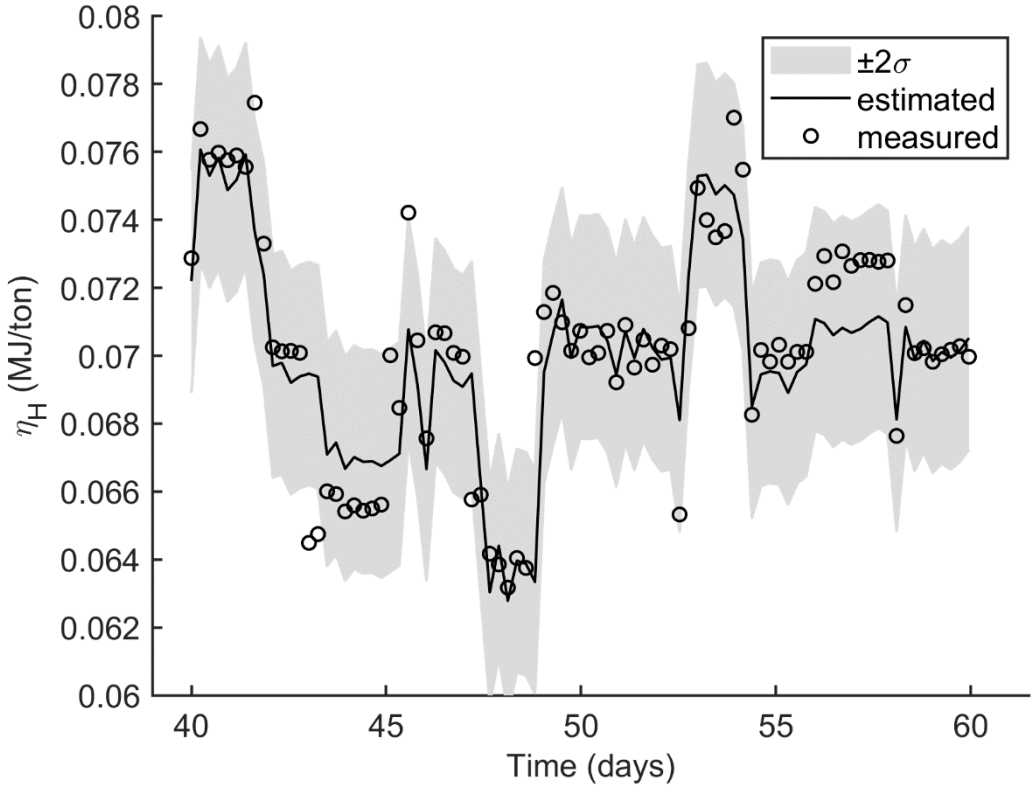

Figure 2. Measured and estimated energy efficiency for component *H* with corresponding confidence intervals. Only every 50 sample is plotted for the sake of clarity.

The difference between the training and test sets was further analyzed using Euclidean histogram distance (Ma *et al.*, 2010) and histogram intersection similarity (Swain and Ballard, 1991) and Kullback-Leibler (KL) divergence (Mathiassen *et al.*, 2002) in sliding windows for each *m* inputs used in the PLSR model. Using these, a novel metric is presented and denoted as the I_α. The I_α is given here as

$$I_\alpha = \sum_{j=1}^{m} b_{\mathrm{PLS},j}\left(\alpha D_j - s_j\right), \qquad (4)$$

where $D_j = D_j(X_{train}, X_{test})$ is the Euclidean distance between the training and test set histograms for input j and $s_j = s_j(X_{train}, X_{test})$ is the similarity between the train and test set histograms for input j. It was found that the KL divergence provided practically the same information as the presented distance metric, thus it was intentionally left out from the definition of the index. However, the KL divergence was found also to give a qualitative indication of the data drift. The α_j for an input variable is defined as the fraction of samples out of range in a test set window. The global parameter α is the maximum of all α_j's. It can be seen from the Eq. (4) that the proposed metric highlights the variables with more significant effect on the input. In addition, the α thresholds the Euclidean histogram distance, and the s_j acts as a penalty if the train and the test set have non-similar histograms. It should be noted that the higher index values I_α indicate a higher covariate shift, and thus higher histogram similarity needs to decrease the value of the proposed index.

The applied metrics are illustrated together with the RMSE for component *G* in Figure 3. The visual inspection in the Figure 3 shows that in fact that the training set might not be representative, as some of the model inputs diverge from the training data set. It can be seen from the Figure 3 that it is apparent that the covariate shift correlates well with the observed modelling error with testing data. Thus, monitoring the input space could be at least partially used to aid in the decision-making concerning the need of soft sensor maintenance. De facto, in actual use this issue would have to be fixed with model adaptation (or model re-training) to a more comprehensive training set. However, the recognition and tackling not only the covariate shift, but also the other type of dataset shifts such as the prior probability shift and the contextual shift (Moreno-Torres *et al.*, 2012) in real-time demands further studies on model adaptation. From these, the prior probability shift is the most of obvious to be dealt with, especially in the case of models with single output.

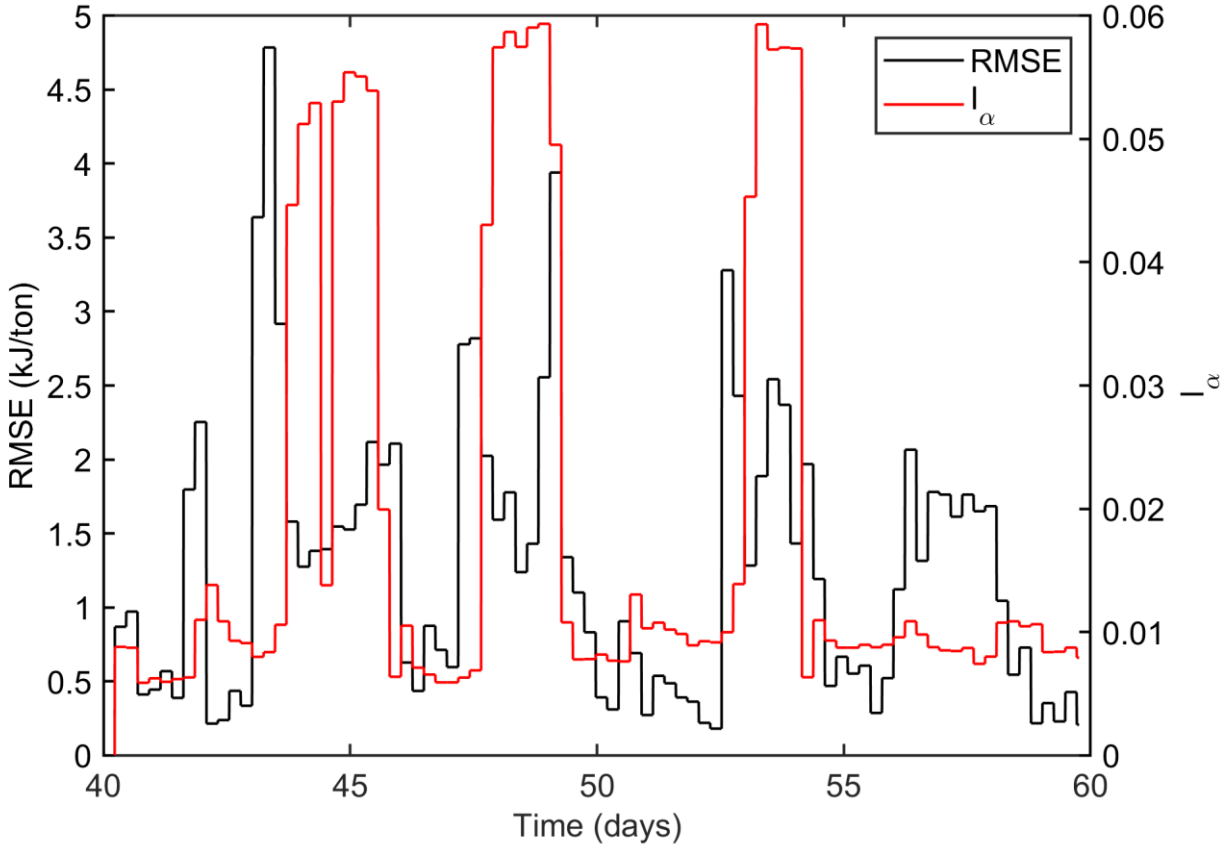

Figure 3. Illustration on the possibility of monitoring the soft sensor's covariate shift (I_α, red line) and its effect on the RMSE with testing data (black line). The illustration is computed with the sliding window size of 50 samples for the component *G*.

3.3 Practical Implications

The results of the study give guidelines to soft sensor selection in monitoring of energy intensive production processes with large input delays. Monitoring of the energy efficiency provide basis for real-time optimization of the processes also with respect to energy consumption. Hence, the study contributes to life-cycle analysis theme of the multi-step chemical processes, and by that demonstrates how the soft sensors could be utilized to lower the carbon footprint of an industrial process. In order to comprehend the analysis from the process engineering point of view, some further considerations related to practical implementation to TE process are required.

First of all, the surrogate model developed here utilizes a rather simple approach. Although a more sophisticated variable construction, delay estimation and variable selection methods may enhance the estimator performance, in industrial applications it is often beneficial to have a model structure in a representable format. In case of PLSR model, and with limited number of projections, this requirement can be met.

Additionally, it is important to give insight on the explanatory variables used in the model. In the case presented, after the correlation-based filtering the subset of 18 and 14 variables for the two surrogate models were used in PLS model estimation. From these, the most important ones were found to be:

- Component *F*, *G* and *H* mol-% in product stream,
- Component *D* mol-% in purge stream,
- Reactor temperature (°C),
- Product separator underflow (m^3/h),
- Stripper underflow (m^3/h),
- Compressor power (W),
- Condenser cooling water outlet temperature (°C).

Based on the presented list, the liquid molar fraction measurements of the final product components (*G*, *H*) in the product stream, together with the by-product *F* are needed. In TE model, these are sampled with relative high frequency of 0.25 h and 0.25 h delay. The soft sensor approach utilized in this paper considered a maximum lag of 0.5 h, suggesting that the indirect energy efficiency estimation is strongly based to recent analysis results from the product composition. Similarly, the purge stream molar fraction of reactant *D* is assumed to be measured with interval of 0.1 h and delay of 0.1 h in TE model. These assumptions set high requirements for the online gas and liquid analyzers.

As indicated by Konge *et al.* (2020), the steam cost in overall cost-efficiency of the TE process is relatively small. On the other hand, it might have more important effect to the energy efficiency. This cannot be directly seen from the most important variables selected to the energy efficiency model. However, the product separator underflow is used as an explanatory variable and this liquid stream is directed to the stripper, having impact to required steam consumption. Utilization of temperature measurements from several process points and the compressor work as explanatory variables also have natural connection to process energy efficiency. Finally, the surrogate model also uses the production rate (stripper underflow) as an input. Thus, the model incorporates most of the variables affecting to the energy efficiency by definition given in Eq. (1).

Finally, it was highlighted in this work, and also in previous studies related to surrogate modeling of TE process (e.g. Sheta *et al.*, 2019), that the selection of the training data deserves attention. Sheta *et al.* (2019) suggest approaches such as peak shaving and smoothing of intensive changes as pre-processing methods to avoid overfitting problems. However, as indicated in Section 3.2, the implementations in real systems typically need to include also efficient model adaptation as all the process points are seldom available in the training data.

Development of ensemble models can also help to reduce the estimator uncertainties and to overcome the challenges related to unseen process points (Hastie *et al.*, 2009). In addition, gradual changes due to fouling and wear of equipment, or even process design changes (which could be expected if the training set is extended over very long time period) set challenges to any surrogate models. Hence, maintenance of the soft sensor to ensure its performance over time is in fact a very interesting and important topic to study.

4 Conclusions

In this work, an indirect energy efficiency estimator was developed for the Tennessee Eastman (TE) benchmark. For this aim, the TE benchmark was modified to be suited for generating the necessary data with a realistic simulation scheme. Based on the simulated data, a surrogate-model was selected using a sophisticated model selection scheme. The final model structure was the Partial Least-Squares (PLS) regression. With these, a reasonable model performance was obtained. By monitoring the histogram similarity metrics along with the test set estimation error, it was found that the applicability of the estimator could be partially limited because of the covariate shift. All and all, the data drift was identified to be an important factor that plausibly could complicate the use of soft sensors in industrial applications. In this simulation study, this was attributed to multivariable nature of the process and motivate the future research towards selection and maintenance of soft sensors.

Acknowledgements

This work was partially funded by Business Finland via project ‘Operational eXcellence by Integrating Learned information into AcTionable Expertise (OXILATE)’, under the ITEA3 Programme and project ‘Autonomous

Processes Facilitated by Artificial Sensing Intelligence (APASSI)'.

References

A. Bakdi and A. Kouadri. An improved plant-wide fault detection scheme based on PCA and adaptive threshold for reliable process monitoring: Application on the new revised model of Tennessee Eastman process. *Journal of Chemometrics*, 32(5), 2018. doi: 10.1002/cem.2978

A. Bathelt, N. Ricker, and M. Jelali. Revision of the Tennessee Eastman Process Model. *IFAC-PapersOnLine*, 48(8):309– 314, 2015. doi: 10.1016/j.ifacol.2015.08.199S.

S. de Jong. SIMPLS: An Alternative Approach to Partial Least Squares Regression. *Chemometrics and Intelligent Laboratory Systems*, 18(3):251–263, 1993. doi: 10.1016/0169-7439(93)85002-X

J. Downs and E. Vogel. A plant-wide industrial process control problem. *Computers & Chemical Engineering*, 17(3):245-255, 1993. doi: 10.1016/0098-1354(93)80018-I

C. Drumm, J. Busch, W. Dietrich, J. Eickmans, and A. Jupke. STRUCTese® – Energy efficiency management for the process industry. *Chemical Engineering and Processing – Process Intensification*, 67:99–110. doi: 10.1016/j.cep.2012.09.009

T. Hastie, R. Tibshirani, and J. Friedman. *The elements of statistical learning: data mining, inference, and prediction*. 2009. Springer Science & Business Media.

T. Jockenhövel, L. Biegler, and A. Wächter. Dynamic optimization of the Tennessee Eastman process using the OptControlCentre. *Computers & Chemical Engineering*. 27:1513–1531, 2003. doi: 10.1016/S0098-1354(03)00113-3

N. Jämsä. *Model predictive control for the Tennessee Eastman process*, M.Sc. Thesis, Aalto University, 2018.

U. Konge, A. Baikadi, J. Mondi, and S. Subramanian. Data-Driven Model Based Computation and Analysis of Operability Sets Using High-Dimensional Continuation: A Plant-Wide Case Study. *Industrial & Engineering Chemistry Research*, 59(21):10043—10060, 2020. doi: 10.1021/acs.iecr.9b07087

A. Kulkarni, V. Jayaraman, and B. Kulkarni. Knowledge incorporated support vector machines to detect faults in Tennessee Eastman Process. *Computers & Chemical Engineering*, 29(10):2128-2133, 2005. doi: 10.1016/j.compchemeng.2005.06.006

T. Larsson, K. Hestetun, E. Hovland, and S. Skogestad. Self-Optimizing Control of a Large-Scale Plant: The Tennessee Eastman Process. *Industrial & Engineering Chemistry Research*, 40:4889–4901, 2001. doi: 10.1021/ie000586y

Y. Ma, X. Gu, and Y. Wang. Histogram similarity measure using variable bin size distance. *Computer Vision and Image Understanding*, 114(8):981–989, 2010. doi: 10.1016/j.cviu.2010.03.006

J. Mathiassen, A. Skavhaug, and K. Bø. Texture similarity measure using Kullback-Leibler divergence between gamma distributions. In *Proceedings – 7th European Conference on Computer Vision, ECCV 2002, 28-31 May, 2002, Copenhagen, Denmark*, pages 133–147, 2002. doi: 10.1007/3-540-47977-5_9

J. Moreno-Torres, T. Raeder, R. Alaiz-Rodríguez, N. Chawla and F. Herrera. A unifying view on dataset shift in classification. *Pattern Recognition*, 45(1):521-530, 2012. doi: 10.1016/j.patcog.2011.06.019

R. Nikula, M. Resonant, and K. Leiviskä. Data-driven framework for boiler performance monitoring. *Applied Energy*, 183:1374-1388, 2016. doi: 10.1016/j.apenergy.2016.09.072

N. Ricker. Tennessee Eastman Challenge Archive, 2015, https://depts.washington.edu/control/LARRY/TE/download.html#Basic_TE_Code.

D. Saygin, M. Patel, E. Worrell, C. Tam, and D. Gielen. Potential of best practice technology to improve energy efficiency in the global chemical and petrochemical sector. *Energy*, 36(9):5779-5790, 2011. doi: 10.1016/j.energy.2011.05.019

A. Sheta, M. Braik and H. Al-Hiary. Modeling the Tennessee Eastman chemical process reactor using bio-inspired feedforward neural network (BI-FF-NN). *The International Journal of Advanced Manufacturing Technology*, 103:1359–1380, 2019. doi: 10.1007/s00170-019-03621-5

M. Swain and H. Ballard. Color indexing. *International Journal of Computer Vision*, *7*(1):11-32, 1991. doi: 10.1007/BF00130487

A. Tran and C. Georgakis. On the estimation of high-dimensional surrogate models of steady-state of plant-wide processes characteristics. *Computers & Chemical Engineering*, 116:56–68, 2018. doi: 10.1016/j.compchemeng.2018.02.014

D. Xie and L. Bai. A hierarchical deep neural network for fault diagnosis on Tennessee-Eastman process. In *Proceedings - 2015 IEEE 14th International Conference on Machine Learning and Applications (ICMLA), 9-11 December, 2015, Miami, FL, USA*, pages 745–748, 2015. doi: 10.1109/ICMLA.2015.208

W. Zou, Y. Xia, and H. Li. Fault diagnosis of Tennessee-Eastman process using orthogonal incremental extreme learning machine based on driving amount. *IEEE Transactions on Cybernetics*, 48(12):3403–3410, 2018. doi: 10.1109/TCYB.2018.28

Modelling and Simulation of Detection Rates of Emergent Behaviours in System Integration Test Regimes

Rune André Haugen[1,2] Ali Ghaderi[3]

[1]Department of Science and Industry Systems, University of South-Eastern Norway, rune.a.haugen@usn.no
[2]Kongsberg Defence and Aerospace AS, Norway, rune.andre.haugen@kongsberg.com
[3]Department of Mathematics and Science Education, University of South-Eastern Norway, ali.ghaderi@usn.no

Abstract

System level testing generally lacks coverage due to cost of performing realistic tests on the "system as a whole". This lack in test coverage gives rise to seemingly emergent behaviour at system level. The interactions between multiple sub-systems lead to "the whole being greater than the sum of its parts", which is a famous saying dated back to the time of the Greek philosopher Aristotle. Either we should test more extensively at system level, or we should test smarter. The company needs to validate its current test regime to see if the current way of testing detects the emergent behaviours in question. We seek to validate the company's system integration test regime to see if it can detect a given set of emergent behaviours. This paper aims to find the probabilities of detecting specified types of emergent behaviour in the way the company performs system integration testing today and compare that to alternative test regimes. A model is set-up to find the probabilities of the emergent behaviour types in the different test regimes, and to simulate the corresponding detection rates and related uncertainties. The results show that the company could benefit from changing to an alternative test regime, which has higher probability of detecting a given set of unwanted behaviours emerging through system integration testing.

Keywords: Bayes' theorem, emergent behaviour, experimental design, statistical inference, system integration testing.

1 Introduction

System level testing generally lacks coverage due to cost of performing realistic tests on the "system as a whole". This lack in test coverage gives rise to seemingly emergent behaviour at system level. The interactions between multiple sub-systems lead to "the whole being greater than the sum of its parts", which is a famous saying dated back to the time of the Greek philosopher Aristotle. Either we should test more extensively at system level, or we should test smarter. The company needs to validate its current test regime to see if the current way of testing detects the emergent behaviours in question.

This paper looks at how well the system-level test regime detects unwanted behaviours for an autonomous underwater vehicle (AUV) that uses a camera to capture images of the current seabed.

We seek to validate the company's system integration test regime's ability to detect a given set of emergent behaviours. This paper aims to find the probabilities of detecting specified types of emergent behaviour in the way the company performs system integration testing today and compare that to alternative test regimes.

1.1 Problem Statement

The company performs system integration testing based on manual operations, which is a bottleneck for them to ensure mature and robust products (Haugen and Mansouri, 2020).

Analysts in the company do not have enough time to analyse all available test results from performed test executions / simulations. Roughly, system domain experts analyse 10% of test results on average. About 80% of tests analysed contain no errors. Around 20% of tests with errors detected include behaviour-related errors (Kjeldaas et al., 2021). Illustration in Figure 1.

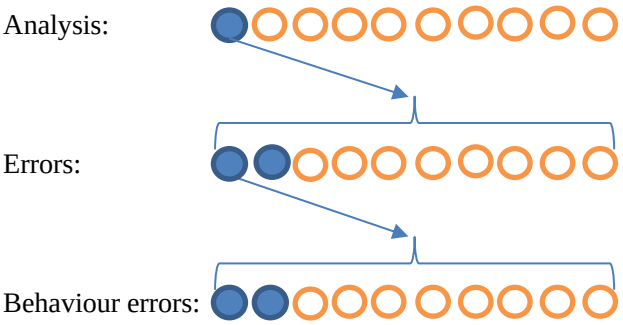

Figure 1. Portion of tests with detected behaviour related errors.

We believe the company tests too many "sunny day" scenarios compared to "rainy day" scenarios. This test strategy fails to trigger the system's inherent emergent behaviours to the extent that we can collect enough data on them through testing to perform effective analyses of these behaviour issues.

The AUV uses available map data to plan missions. The map data varies in quality, which may give problems for the accuracy of the planning functionality. Map areas lacking data works as tripwires for the

planning system and could cause the planning to fail if it is not possible to avoid these areas, ref. Figure 2.

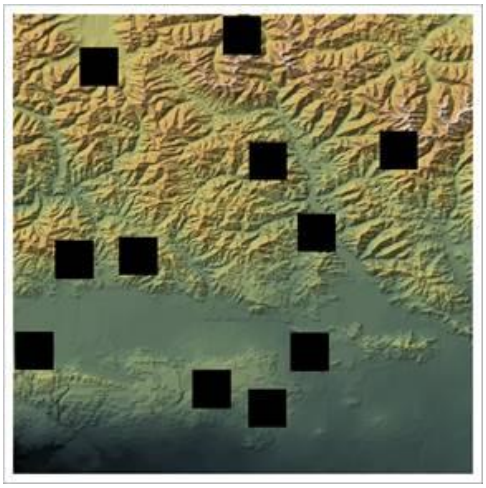

Figure 2. Principle sketch of issue with lacking (black areas) map data.

The AUV plans route segments within available fuel limit, including departure from -and arrival to the mothership. Complex ocean currents yield large fuel calculation error margins. Reaching fuel point of no return forces the AUV to abandon mission and return to mothership, ref. Figure 3.

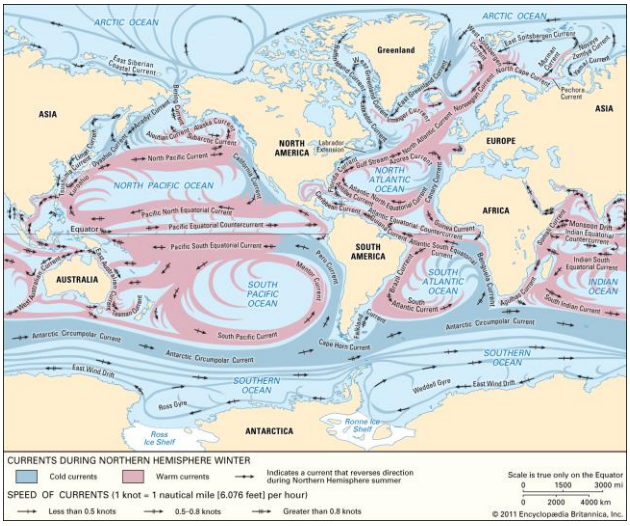

Figure 3. Principle sketch of issue with complex ocean currents (Cenedese and Gordon, 2021).

The height information available of the seabed have varying uncertainty, which is a critical factor for the AUV's ability to capture seabed images of sufficient quality. To ensure desired quality in the photograph of a given area, the AUV needs a minimum number of pictures of the same area. If the slope of a ridge is too steep, the AUV does not have time to photograph the slope with sufficient quality, or photograph it at all, without special considerations in planning the route, ref. Figure 4.

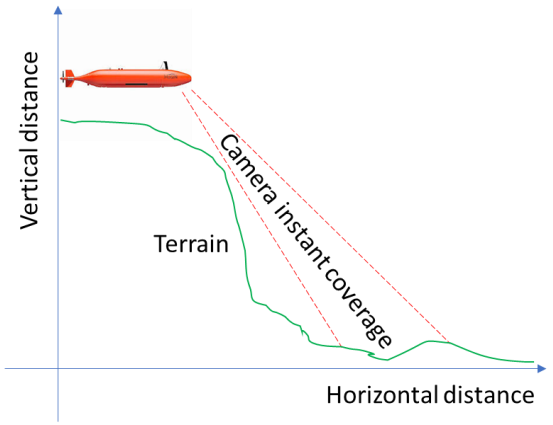

Figure 4. Principle sketch of issue with steep ridges.

The AUV uses an acoustic positioning system (APS) to keep on track with the planned route. If the AUV APS information is lost due to some interferences, the AUV drifts from its planned route depending on the inertial navigation system (INS) and terrain correlation, ref. Figure 5.

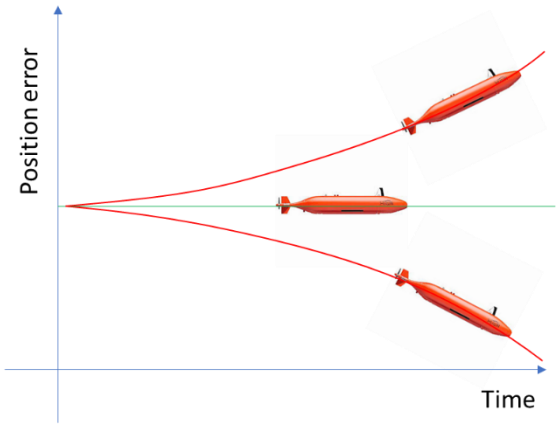

Figure 5. Principle sketch of issue with navigation drift.

The company assumes the AUV system is complicated and even complex. Complex systems are understood only in retrospect and do not usually repeat, while complicated systems can be understood by reductionism and detailed analysis. The company assumes that the AUV system exhibits weak emergence, and potentially strong emergence. Strong emergence is unpredictable and inconsistent in simulations, while weak emergence is predictable and consistently reproducible in simulations (Mittal et al., 2018).

1.2 Methods

The company uses the *Changing One Single Thing at a time* (COST) or *Only one Factor At a Time* (OFAT) model (Montgomery, 2017). We use the COST/OFAT principle for the first test regime in this paper.

For the second test regime, we use a *two-level full factorial design* (Dunn, 2021) and (Montgomery, 2017).

For the third test regime, we use an optimum design for maximizing the probability of detecting the emergent behaviours in question.
We seek to answer the following research questions:

- How well is the company able to detect a given set of emergent behaviours?
- What is the probability of the company detecting a given set of emergent behaviours in the current company test regime?
- How much can the company increase the detection of a given set of emergent behaviours in an alternative test regime?

1.3 Literature Review

The *Only one Factor At a Time* (OFAT) method consists of selecting a starting point, or baseline set of levels, for each factor, and then successively varying each factor over its range with the other factors held constant at the baseline level (Montgomery, 2017).

For a *two-level full factorial design*, we run the complete set of 2^k experiments, where k is the number of factors and 2 is the number of levels for each factor. The results of the experiments we use to quantify the importance of each factor. Indeed, for this purpose, linear regression models, considering both the single factor and two-factor effects are used in this paper. For example, in the case of two factor model, the following fitted regression model can be used to determine the importance of each factor (Dunn, 2021).

$$y = \beta_0 + \beta_A x_A + \beta_B x_B + \beta_{AB} x_{AB} \quad (1)$$

In the following, the total probability is calculated based on the inclusion-exclusion principle when the different emergent behaviours are independent but not disjoint events. We calculate the total probability by formulas regarding different number of factors (Allenby and Slomson, 2010):

$$P(A+B) = P(A) + P(B) - P(A,B) \quad (2)$$

$$P(A+B+C) = P(A) + P(B) + P(C) - P(A,B) - P(A,C) - P(B,C) + P(A,B,C) \quad (3)$$

$$P(A_1 + A_2 \ldots + A_n) = \sum_{i=1}^{n} P(A_i) - \sum_{i<j} P(A_i, A_j) + \sum_{i<j<k} P(A_i, A_j, A_k) + \cdots + (-1)^{n-1} \sum_{i<\cdots<n} P(A_1, A_2 \ldots, A_n) \quad (4)$$

The union of a four-factor probability is illustrated in Figure 6.

The Bayes' theorem is expressed as

$$P(X|Y,I) = \frac{P(Y|X,I)\,P(X|I)}{P(Y|I)} \quad (5)$$

where X is our hypothesis, Y is our data, and I is relevant available information. The various terms in Bayes' theorem have formal names. The quantity on the far right, $P(X|I)$, is called the prior probability; it represents our state of knowledge (or ignorance) about the truth of the hypothesis before we have analysed the current data. This is modified by the experimental measurements through the likelihood function, or $P(Y|X,I)$, and yields the posterior probability, $P(X|Y,I)$, representing our state of knowledge about the truth of the hypothesis in the light of the data. In a sense, Bayes' theorem encapsulates the process of learning. The denominator is often simply a normalization constant (not depending explicitly on the hypothesis). In some situations, like in model selection, this term plays a crucial role. For that reason, it is sometimes given the special name of evidence (Sivia and Skilling, 2006).

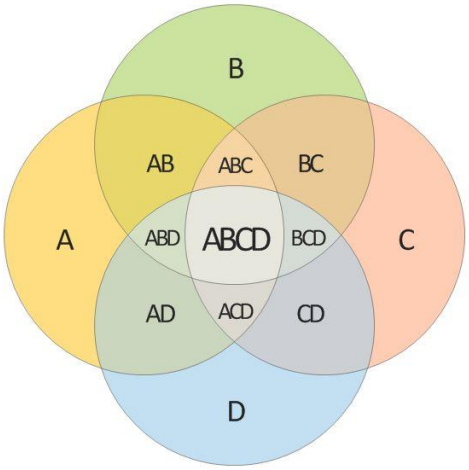

Figure 6. Inclusion-exclusion illustrated by a Venn diagram for four sets (Concept Draw, 2021).

2 Design of Experiment

This paper explores the probabilities and detections of a given set of emergent behaviours in different test regimes, the current company test regime and two other alternatives.

2.1 Data

We select a set of emergent behaviour types for study in this paper. The emergent behaviour types are:

- F1: Planning failure [0...1]
- F2: Fuel exceeded [0...1]
- F3: Photo quality degradation [0...1]
- F4: Photo coverage deviation [0...1]
- G: Any emergent behaviour [0…1]

For the purpose of this study, we have focused our efforts on a set of four dichotomous variables, which can take only two possible values (low and high). These are:

- A: Navigation quality [Low, High]
- B: Map delta height [Low, High]
- C: Real world environmental delta [Low, High]
- D: Map quality [Low, High]

Further, based on previous experience with comparable systems, we have selected a set of probabilities for this study. Accordingly, based on expert knowledge within the company, the probabilities of the emergent behaviours are assumed to be [%]:

- $P(F1) = 0.15$
- $P(F2) = 1.25$
- $P(F3) = 1.88$
- $P(F4) = 0.31$
- $P(G) = 3.59$

Moreover, based on the available data in the company's database, we will assume the following [%]:

- $P(D|F1) = 10$
- $P(D'|F1) = 90$
- $P(C|F2) = 55$
- $P(BD|F3) = 25$
- $P(BD'|F3) = 75$
- $P(A'|F4) = 100$
- $P(D) = 98$
- $P(D') = 2$
- $P(C) = 10$
- $P(BD) = 18$
- $P(BD') = 2$
- $P(A') = 1$

In general, we are interested in the probabilities for the different emergent behaviours at different factor levels. For example, we are interested in probability of planning failure (F1) under the condition that the map quality is high (D). That is, we are interested in $P(F1|D)$. This probability can be calculated using the Bayes' theorem (5),

$$P(F1|D) = \frac{P(D|F1)P(F1)}{P(D)} = \frac{10 * 0.15}{98} = 1.5 * 10^{-2}$$

The probabilities [%] of other emergent behaviours can similarly be calculated

- $P(F1|D') = 6.75$
- $P(F2|C) = 6.88$
- $P(F3|BD) = 2.6$
- $P(F3|BD') = 70.31$
- $P(F4|A') = 31.25$

2.2 Test Regime 1

The test regime 1 is the current company test regime and is the baseline for comparison with the other alternative test regimes. There are 16 possible combinations, using two values for 4 parameters. However, the company does not test all 16 cases. The principle is to start with a reference case and add cases with level-change in only one factor at a time as compared to the reference. This COST/OFAT principle makes it easier to analyse the effect of the level-change in one factor. Table 1 shows the company's selected test case types. Test case type 1 is the reference experiment type, and to reduce the number of test set-ups the company re-uses this as much as possible to verify system requirements. The company uses the test case types 2-5 to analyse the impact of the factors C, B, BD, and A, respectively.

Table 1. Scenario factor levels for test regime 1.

Test Case Type	A	B	C	D	# Runs
1	+	-	-	+	245
2	+	-	+	+	6
3	+	+	-	+	60
4	+	+	-	-	6
5	-	-	-	+	3

2.3 Test Regime 2

The test regime 2 is the first alternative test regime, which is also known as two-level full factorial experiment. The two-level full factorial design has four factors with two levels, which gives 2^4 = 16 experiments. Table 2 shows the experiment set-up for test regime 2 with the yield for each test case type based on expert opinion that we choose for this study. The yield is the total number of emergent behaviour detections in 20 runs per test case type. Further, in the test regime 2, each test case is run equal number of times. For the purpose of comparison, we choose the total number of runs to be the same for both test regime 1 and 2.

Table 2. Scenario factor levels for test regime 2, full factorial design.

Test Case Type	A	B	C	D	Yield	# Runs
1	-	-	-	-	8	20
2	+	-	-	-	1	20
3	-	+	-	-	22	20
4	+	+	-	-	15	20
5	-	-	+	-	9	20
6	+	-	+	-	3	20
7	-	+	+	-	23	20
8	+	+	+	-	17	20
9	-	-	-	+	6	20
10	+	-	-	+	0	20
11	-	+	-	+	7	20
12	+	+	-	+	1	20
13	-	-	+	+	8	20
14	+	-	+	+	1	20
15	-	+	+	+	8	20
16	+	+	+	+	2	20

2.3.1 Effect of Experiment Factors

One way to find the effect of each factor on yield is by conducting a regression analysis based on the test results. In the case of the test regime 2, the Equation (1) has 16 parameters. The first coefficient being the average of all the yield values, while the other coefficients represent the effects of the different factors and factor interactions. Estimating the parameters with respect to the observed yield, results in the following relation with only six non-zero coefficients,

$$y = 8.14 - 3.13x_A + 3.65x_B + 0.69x_C - 4.06x_D - 3.39x_{BD}$$

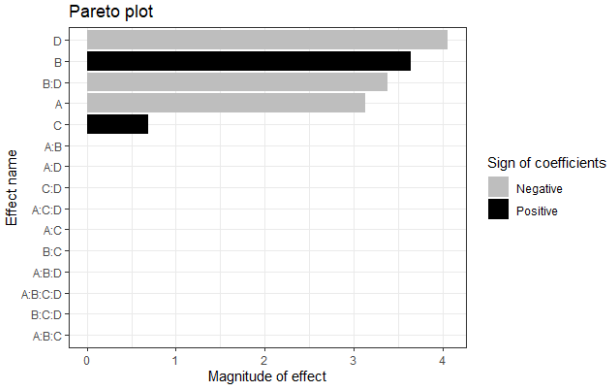

Figure 7. Magnitude of the effect of the factors.

The coefficient $-3.13x_A$ of factor A means that A at high level has a negative effect on the detection of the emergent behaviour. The coefficients are calculated for one step, but the regression model uses two steps from low to high. Therefore, the test regime 2 gives on average 6.25 more detections of any emergent behaviour type on a test case run 20 times with factor A at low level compared to high level. We can see the calculated factor coefficients in a Pareto plot (see Figure 7). Factor D has the highest impact on the detection of emergent behaviour among the main factors, while factor C has the lowest impact. The only active two-factor interaction is BD.

2.4 Test Regime 3

The test regime 3 is the second alternative test regime and is designed to optimize the detection of the given emergent behaviour types. The optimum way of detecting the emergent behaviours in question is to run the test case type(s) which have the highest probability of detecting the different emergent behaviour types. The probabilities for the different emergent behaviours were calculated based on Bayes' theorem in Section 2.1.

From Table 3 we see that test case type number 7 is the optimal test case type for triggering all emergent behaviour types. In the test regime 3, one runs only the case type number 7. However, the number of replicates is the same as the total number of tests run in other test regimes.

Table 3. Scenario factor levels and probabilities [%] for test regime 3, optimizing test design.

Test Case Type	A	B	C	D	F1	F2	F3	F4
1	-	-	-	-	6.75	0	0	31.25
2	+	-	-	-	6.75	0	0	0
3	-	+	-	-	6.75	0	70.31	31.25
4	+	+	-	-	6.75	0	70.31	0
5	-	-	+	-	6.75	6.88	0	31.25
6	+	-	+	-	6.75	6.88	0	0
7	-	+	+	-	6.75	6.88	70.31	31.25
8	+	+	+	-	6.75	6.88	70.31	0
9	-	-	-	+	0.015	0	0	31.25
10	+	-	-	+	0.015	0	0	0
11	-	+	-	+	0.015	0	2.6	31.25
12	+	+	-	+	0.015	0	2.6	0
13	-	-	+	+	0.015	6.88	0	31.25
14	+	-	+	+	0.015	6.88	0	0
15	-	+	+	+	0.015	6.88	2.6	31.25
16	+	+	+	+	0.015	6.88	2.6	0

3 Results

In this section the capability of the different test regimes in detecting any given emergent behaviour types is evaluated. The emergent behaviour type F1 has a single factor dependency in D. The formula for finding the probability of emergent behaviour type F1 in test regime 1, follows from the application of the marginalisation and product rule of the probability theory (Sivia and Skilling, 2006):

$$\begin{aligned} P(F1|T1) &= P(F1, D|T1) + P(F1, D'|T1) \\ &= P(F1|D, T1)P(D|T1) \\ &\quad + P(F1|D', T1)P(D'|T1) \end{aligned} \tag{6}$$

Further note that

$$P(D'|T1) = 1 - P(D|T1) \tag{7}$$

thus

$$\begin{aligned} P(F1|T1) &= P(F1|D', T1) \\ &\quad + \big(P(F1|D, T1)P(D|T1) \\ &\quad - P(F1|D', T1)\big)P(D|T1) \end{aligned} \tag{8}$$

and hence

$$\frac{P(F1|T1)}{P(F1|D',T1)} = 1 - \left(1 - \frac{P(F1|D,T1)}{P(F1|D',T1)}\right)P(D|T1) \quad (9)$$

Since the detection of the emergent behaviours depends only on the factors, then $P(F1|D',T1) = P(F1|D')$. The specific probabilities like $P(F1|D')$ are determined based on the abovementioned method in Section 2.1. We can then use a more general formula where we can separate the physical processes that we cannot control from the test set-up that we can control. The formula for finding the probability of emergent behaviour type F1 in test regime 1 is then:

$$\frac{P(F1|T1)}{P(F1|D')} = 1 - \left(1 - \frac{P(F1|D)}{P(F1|D')}\right)P(D|T1) \quad (10)$$

Using the results in Section 2.1 we get:

$$P(F1|T1) = \left(1 - \left(1 - \frac{0.015}{6.75}\right) * 98\right) * 6.75 = 0.15$$

Note that we have a generalized formula where we can replace T1 with T2 or T3. Indeed, on the right-hand side of the Equation (10), the choice of test regime only changes $P(D|T1)$. On the left-hand side, the denominator is fixed, which means that the change on the right-hand side can only affect $P(F1|T1)$. Consequently, we can then calculate the lower and upper bounds for detecting the emergent behaviour types by setting $P(D|T1) = 0$ and $P(D|T1) = 1$, ref. Table 5. The same principle applies to all emergent behaviour types with a single factor dependency (F1 and D, F2 and C, F4 and A) in the different test regimes (T1, T2, and T3).

The emergent behaviour type F3 has a two-factor dependency in BD. Although the final formula is different, it is also derived from the sum and product rule of the probabilities. Indeed, the formula for the probability of emergent behaviour type F3 in test regime 1 is:

$$P(F3|T1) = P(F3, BD|T1) + P(F3, BD'|T1) + P(F3, B'D|T1) + P(F3, B'D'|T1) \quad (11)$$

Further note that:

$$P(F3, BD|T1) = P(F3|BD, T1)P(BD|T1) \quad (12)$$

$$P(F3, BD'|T1) = P(F3|BD', T1)P(BD'|T1) \quad (13)$$

$$P(F3, B'D|T1) = P(F3|B'D, T1)P(B'D|T1) \quad (14)$$

$$P(F3, B'^{D'}|T1) = P(F3|B'^{D'}, T1)P(B'^{D'}|T1) \quad (15)$$

thus

$$\frac{P(F3|T1)}{P(F3|BD',T1) + P(F3|B'D',T1)} = \frac{P(F3|BD,T1)}{P(F3|BD',T1) + P(F3|B'D',T1)}P(BD|T1) + \frac{P(F3|BD',T1)}{P(F3|BD',T1) + P(F3|B'D',T)}P(BD'|T1) + \frac{P(F3|B'D,T1)}{P(F3|BD',T1) + P(F3|B'D',T1)}P(B'D|T1) + \frac{P(F3|B'D',T1)}{P(F3|BD',T1) + P(F3|B'D',T1)}P(B'D'|T1) \quad (16)$$

Given the information:

$$P(F3|B'D,T1) = P(F3|B'D',T1) = P(B'D|T1) = P(B'D'|T1) = 0$$

Furthermore, using the results in Section 2.1 we get:

$$P(F3|T1) = \left(\frac{2.6}{70.31} * 18 + 2\right) * 70.31 = 1.87$$

The same principle applies to all other test regimes (T2, and T3). See Table 4 for the complete set of probabilities from the model.

Table 4. Calculated probabilities [%] for emergent behaviour types.

	TR1	**TR2**	**TR3**
F1	0.15	3.38	6.75
F2	0.69	3.44	6.88
F3	1.87	18.29	70.31
F4	0.31	15.62	31.25
G	3	36.84	89.17

We see from Table 4 and Table 5 that test regime 3 is at the upper bound and are the optimum way of testing to maximize detection of the emergent behaviour types. The total (G) is calculated using the inclusion-exclusion principle for the probability (Allenby and Slomson, 2010). The optimum test regime for detecting the given set of emergent behaviours has a probability of ~89% of detecting any given emergent behaviour, while the current test regime has only probability of ~3%. The test regime 3 can be used as the baseline in order to evaluate the capabilities of the other test regimes (see Table 5). Test regime 2 is detecting about half of the given emergent behaviours compared to Test Regime 3, while the test regime 1 is barely detecting any emergent behaviours at all.

Table 5. Calculated lower and upper bounds and relative frequencies for emergent behaviour types.

%	**Lower bound**	**Upper bound**	**TR1**	**TR2**	**TR3**
F1	0.15	6.75	2.22	50.1	100
F2	0	6.88	10	50	100
F3	0	70.31	2.67	26.01	100

%	Lower bound	Upper bound	TR1	TR2	TR3
F4	0	31.25	1	50	100
G	0.15	89.17	3.37	41.31	100

The probabilities in Table 4 can be used to answer many questions related to emergent behaviours. For example, if one chooses a test regime consisting of n runs, how many emergent failures of different types are expected to be detected? For each run, the probability of detecting a failure, say F1 in test regime 1, is $P(F1|T1)$. In each run, one either detects F1 or not. Moreover, since the runs are independent, then the probability of detecting k failures of type F1, follows a binomial distribution (n, p), for which $P = P(F1|T1)$. In Figure 8, we have simulated the probabilities for the detections of the different failures for the aforementioned three test regimes in 320 runs to find the detection rates of the emergent behaviours and the related uncertainties.

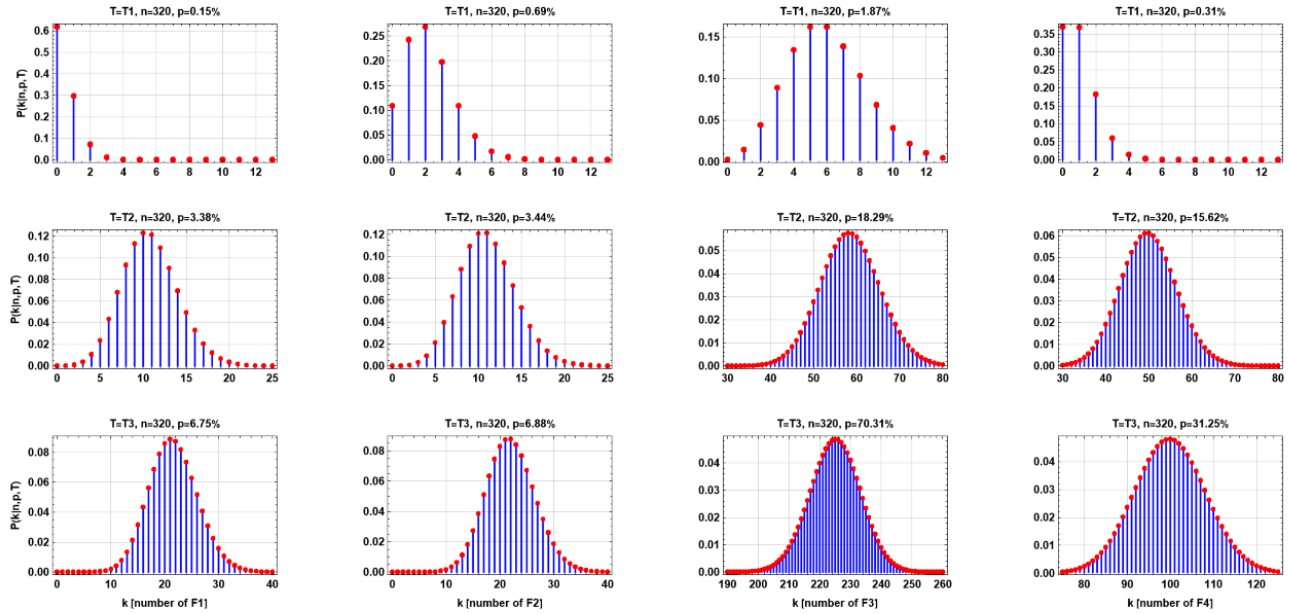

Figure 8. The probabilities of detections of emergent behaviours in different test regimes. Each row, from top to bottom, corresponds to a given test regime, T1, T2 and T3, respectively. Each column corresponds to a given failure type. In the present case the total number of simulated runs is 320.

4 Discussion

The company should increase the test analysis coverage at system level in their projects. The current test analysis coverage is in-sufficient to detect all emergent behaviour types of the system under test. The company cannot increase the test analysis coverage without automating the test result analysis. The test result analysis is the main bottleneck of the test system, and it is therefore crucial to make the analysis work more efficient.

For the company to stay competitive in the future underwater industry market they need to be able to run projects faster and run more projects in parallel. The automation of test result analysis is necessary to make the transition from the current test system to the desired future test system.

For the company not to have latent undesired emergent behaviour in their products, the test analysis needs to detect these with high enough probabilities. The test regime needs to change in the direction of triggering more of the emergent behaviour types of the system and trigger them with higher probabilities. The company will have better data to perform analysis of the emergent behaviours if the test regime triggers all emergent behaviour types of the system sufficient times in different scenarios. The company can get more insight into why the emergent behaviour types are triggered through deductive logic (Sivia and Skilling, 2006), and decide if they can do something to prevent or reduce the unwanted behaviours or the unwanted effects.

A combination of the different test regimes analysed in this paper may be the best approach for the company to deal with this problem of emergent behaviours. Test regime 3 triggers most emergent behaviours but does not see the effect of different settings. Test regime 3 satisfies the need to detect emergent behaviours by triggering emergent behaviours in about 89% of the tests. Test regime 2 sees the effect of different settings but does not trigger as much emergent behaviours as test regime 3. Test regime 2 also satisfies the need to detect emergent behaviours by triggering emergent behaviours in about 37% of the tests. Test regime 1 only sees the effect of a limited set of different settings and does not trigger as much emergent behaviours as either of the

other two alternatives. We consider Test regime 1 not satisfactory for detection of the emergent behaviours in question. Since it is only capable of detecting emergent behaviours in about 3% of the tests.

If we are to select only a few "rainy day" scenarios to complement "sunny day" verification testing, we should choose test cases with factor C at high level to ensure the test regime will detect the emergent behaviour type F2. This is the least probable behaviour to detect, based on the effect of factors found in Section 2.3.1. We should further include some test cases with factor B at high level, factor A at low level, and factor D at low level.

In all statistical inference, we use an idealized model to approximate a real-world process that interests us (Lambert, 2018). The model for exploring probabilities in this paper is no exception, leaving some residual risk for the operational phase of the product.

5 Conclusion

The results show that the company could benefit from changing to an alternative test regime, which has higher probability of detecting a given set of unwanted behaviours emerging through system integration testing. The current test regime does not sufficiently trigger the emergent behaviours explored in this paper, but an alternative test regime indicates that the company should be able to sufficiently detect the given set of emergent behaviours.

6 Further Work

The company must perform further analysis to find the optimum test regime to meet all the requirements considering the different needs from integration, verification, and validation testing.

Acknowledgements

We would like to thank Kent Aleksander Kjeldaas for data input to make the paper relevant to company specific problems.

Notations

Table 6. Nomenclature.

Notation	Description
[0…1]	Not present (0) or present (1)
A	Factor A at high level [+]
A'	Factor A at low level [-]
β_A	Coefficient of factor A
F1	Emergent behaviour type 1
G	Any emergent behaviour type
P(A)	Probability of factor A at high level
P(A')	Probability of factor A at low level
P(AB)	Probability of both factor A and B at high level
P(F1)	Probability of emergent behaviour type 1
T1	Test regime 1

References

R. Allenby and A. Slomson. *How to count: An introduction to combinatorics*. CRC Press. 2010.

C. Cenedese and A. L. Gordon. *Ocean Current*. Encyclopedia Britannica. 2021. https://www.britannica.com/science/ocean-current.

Concept Draw. 2021. https://www.conceptdraw.com/a2059c3/p3/preview/640/pict--4-set-venn-diagram-vector-stencils-library.

K. Dunn. Process Improvements Using Data. 2021. https://learnche.org/pid.

R. A. Haugen and M. Mansouri. Applying Systems Thinking to Frame and Explore a Test System for Product Verification; a Case Study in Large Defence Projects. In *Proceedings – 30th INCOSE International Symposium, INCOSE IS 2020, 20-22 July, 2020, virtual*, pages 78-93, 2020. doi:10.1002/j.2334-5837.2020.00709.x

K. A. Kjeldaas, R. A. Haugen, and E. Syverud. Challenges in Detecting Emergent Behavior in System Testing. In *Proceedings – 31st INCOSE International Symposium, INCOSE IS 2021, 17-22 July, 2021, virtual*, pages 1211-1228, 2021. doi: 10.1002/j.2334-5837.2021.00896.x

B. Lambert. *A Student's Guide to Bayesian Statistics, 1st ed*. SAGE Publications Ltd. 2018.

S. Mittal, S. Diallo, and A. Tolk. *Emergent Behavior in Complex Systems Engineering: A Modelling and Simulation Approach*. Wiley. 2018.

D. C. Montgomery. *Design and Analysis of Experiments, 8th ed*. Wiley. 2017.

D. S. Sivia and J. Skilling. *Data Analysis: A Bayesian tutorial, 2nd ed*. Oxford Science Publications. 2006.

Application of multivariate data analysis of Raman Spectroscopy spectra of 2-oxazolidinone

Federico Mereu[1,2] Jayangi D. Wagaarachchige[3] Klaus-J. Jens[2] Zulkifli Idris[2,*]

[1]Department of Civil and Environmental Engineering, Politecnico di Milano, Piazza Leonardo da Vinci 32, 20133 Milano, Italy
[2]Department of Process, Energy and Environmental Technology, University of South-Eastern Norway, Kjølnes Ring 56, 3918 Porsgrunn, Norway
[3]Department of Electrical, IT and Cybernatics, University of South-Eastern Norway, Kjølnes Ring 56, 3918 Porsgrunn, Norway
[*]corresponding author: zulkifli.idris@usn.no

Abstract

Chemical absorption of carbon dioxide (CO_2) using amine solution is considered as the readiest technology available for capturing CO_2 gas from industrial processes. The well-known amine for this process is 2-aminoethanol (MEA) which is normally mixed with water to a typical concentration of 30 wt%. MEA degrades over time producing non-reactive chemicals such as 2-oxazolidinone (OZD) due to exposure to impurities and high process temperature. It is thus important to find a suitable method for OZD qualification and quantification. In this work, we approach this challenge by means of Raman spectroscopy and multivariate data analysis. We started by collecting Raman spectra of 40 OZD samples and applying Principal Component Analysis to study these samples.

Keywords: multivariate data analysis, MEA, Raman spectroscopy, CO_2 capture, degradation

1 Introduction

Due to the economic development and the subsequent increase in world population, the global demand for energy will continue to rise in the following decades. The dependence on fossil fuels, the primary source of energy, emitting copious amount of CO_2, is the main cause of global warming. Even if large investments are underway to decarbonise the world energy production, renewable electricity may not be suitable for certain applications, such as the cement, iron and steel, and chemical sectors.

Carbon capture and storage (CCS) and its ability to avoid CO_2 emissions at their source, represents a solution in the fight against climate change. Among all the different alternatives, post-combustion capture by using amine-based solvent is considered to be the most advanced technology (Sexton and Rochelle, 2011). This process relies on the ability of the amine solution to chemically reacts with CO_2 in the flue gas. The best absorbents are the ones with high net cyclic capacity, fast reaction with CO_2, low heat of reaction, high chemical stability, low vapor pressure and minimally corrosive (Hartono et al., 2017). Of the many solvents tested, 2-aminoethanol (MEA) is the most used due to its good operational properties and relatively low price. The solvent used in operating plants simply consists of water and amines, whose concentration is usually made based on operating experience (typical concentration range values goes from 12% wt to a maximum of 32% wt (Kohl and Nielsen, 1997)).

A typical chemical absorption process for CO_2 capture plant is shown in Figure 1.

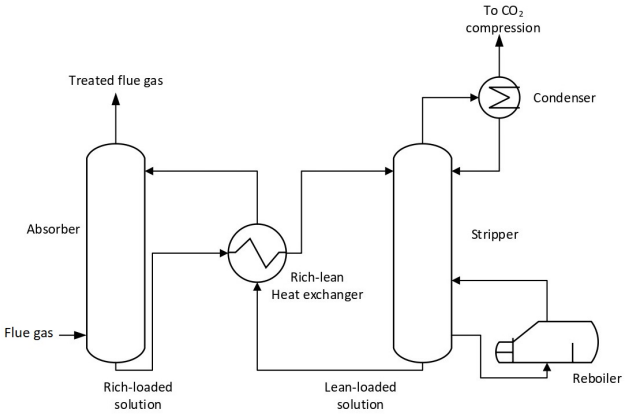

Figure 1. Schematic of a chemical absorption process for CO_2 capture.

After a preliminary purification from NO_X, SO_X, and particulate matter, the flue gas enters the absorber. Through contact with MEA solvent, part of CO_2 in the flue gas is absorbed into amine solution, forming a weakly bonded and quite stable compound, carbamate. The scrubbed gas is then washed with water to remove the solvent and discharged into the atmosphere. Then, the rich-loading solvent (with absorbed CO_2) passed through a cross-heat exchanger and pumped up to the head of the stripper. In the stripper, the high temperature and pressure generated by a reboiler cause the carbamate to dissociate back to MEA and CO_2. The obtained product stream with high CO_2 purity is conveyed to compression for trans-

portation to storage sites. At the bottom of the stripper, the high temperature lean-loading is conveyed to a heat exchanger to decrease the temperature of the lean-loading solution before entering the absorber again.

The entire process chemistry is complex, and the two main reactions taking place in the absorber and the stripper are:

CO_2 absorption: $2\,R-NH_2 + CO_2 \longrightarrow R-NH_3^+ + R-NH-COO^-$

MEA regeneration: $R-NH-COO^- + R-NH_3^+ \xrightarrow{Heat} CO_2 + 2\,R-NH_2$

For simplicity, MEA is expressed by R-NH_2, where R stands for OH-CH_2-CH_2. The first reaction shows that only half a mole of CO_2 is absorbed per mole of MEA, leading to the formation of carbamate. In the second equation, under the application of heat, the carbamate dissociates to give back CO_2 and amine sorbent.

However, there is a main problem associated with this process, which is degradation of the solvent caused by heat exposure and impurities in the exhaust gas. This leads to foaming, fouling, increased viscosity, corrosion and formation of different degradation compounds that are unreactive towards CO_2. In the case of MEA, one of the main degradation products is 2-oxazolidinone (OZD), a heterocyclic five-membered ring organic compound, which formation pathway is shown in Figure 2.

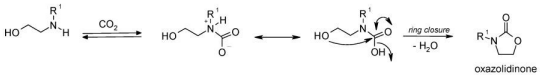

Figure 2. Oxazolidinones formation (R^1, R^2: H, alkyle) (Lepaumier et al., 2009).

The formation of OZD starts with a reaction between MEA and CO_2, which leads to the formation of carbamate complex, as shown in the first equation above. Elimination of a water molecule from the carbamate complex during a ring closure reaction yields an OZD molecule. The formation of OZD is a problem because it is unstable and will react giving other degradation products (namely HEEDA, HEIA, AEHEIA, BHEI (Gouedard et al., 2012)) that must be purged from the system to prevent their build-up.

For this purpose, it is essential to find a procedure for the conversion of the molecule to its precursor amine. This requires a preliminary identification and quantification step.

Raman spectroscopy is a valuable technique for qualitative and quantitative analyses, since there is a relationship between intensity of the Raman band, chemical information and the concentration of a sample being analyzed (Larkin, 2011). Raman spectrums are generally plotted as intensity against Raman Shift (or wavenumber). Vibrations of functional groups of a molecule appear in a Raman spectrum at characteristic Raman shift, which is similar for all molecules containing the same functional group.

Chemometric multivariate analysis is an advanced statistical method that can be used to extract this huge information by building specific model for specific chemical species.

The approach in this paper started with the analysis of OZD samples at different concentrations using Raman spectrometer. Principal component analysis (PCA) was then performed on these samples to check for any outliers, relevant peaks for OZD, and monitor changes in the OZD at different concentrations.

2 Materials & Methods

2.1 Sample preparation and Raman analysis

The first big part of this work consisted of sample preparation. Stock solution of OZD was prepared dissolving 2-Oxazolidinone (Sigma-Aldrich, purity 98%) in Milli-Q® water (18.2 MΩ ·cm at 25°C). Samples of increasing concentration from 5 to 815 mM were then prepared by diluting the stock solution in ditilled water.

The amount of OZD and water needed were weighted using a Mettler-Toledo MS 105 balance.

The Raman scans were taken using a Kaiser Raman Rxn2 analyzer of 785 nm laser wavelength, 400 mW laser power and 150-3425 cm^{-1} spectral range. In a typical experiment, a vial containing OZD solution was placed inside a black sample holder to avoid light disturbance and the top part of the sample holder was also covered with aluminum foil to further reduce any possible disturbance from fluorescence of external light sources. A fiber-optic immersion probe (optic of ¼ inch) from Kaiser Optical Systems Inc. was used for the measurement. To avoid contamination, the probe was first washed with deionized water followed by acetone before each measurement to remove any possible impurities/leftovers on the probe tip. The Raman probe was kept at the same depth and same temperature (20 °C) for all the measurements to ensure consistency and to avoid changes of acquisition background. In order to improve sample sensitivity for offline analysis of each measurement, maximum laser power (400 W) was used with exposure time of 30 seconds and an average of six scans. iC Raman software from Kaiser Optical Systems Inc. was used for the acquisition of the spectra.

2.2 Principal Component Analysis (PCA)

PCA is a data simplification technique used in multivariate statistics. The aim of the technique is to reduce the high number of variables describing a set of data to a smaller number of compressed variables, called Principal Components, PCs, which describe the variation and structure of the data. The PCs can then be plotted to visualize the relationship between samples and variables through the use of scores (which describe the relationship between observations) and loading plots (which show the relationship of the variables) (Wold et al., 1987).

The data is seen as a matrix, called data matrix or *X*

matrix, composed by n objects (samples) and p variables (the measurement for each object) (Esbensen, 2012). This data matrix can be represented in a Cartesian co-ordinate system of dimension p. Considering the first variable, $X1$, its entries can be plotted along a 1-dimensional axis. This approach can be extended considering the next variable, $X2$, resulting in a 2-dimensional plot and so on, until all p variables are covered. This p-dimensional co-ordinate system is the variable space.

To better understand, it is assumed an X matrix with n objects and 3 variables. Its variable space will be composed by 3 axes: one for each variable. And for each object in the variable space, its x-value will be plotted, meaning that all the objects can be as a point in the variable space. When all the points are plotted, the result is a swarm of points. It is then possible to recognize a linear behaviour, which can be described by a line that lies along the direction of maximum variance in the data set, called the first Principal Component, PC1. Further PCs can be plotted; the second principal component will lie along the direction of the second largest variance, and it will be orthogonal to the first PC. The third PC will be orthogonal to both PC1 and PC2, lying along the direction of the third largest variance and so on for the subsequent PCs. This PCs system will constitute a new coordinate system, where each PC will represent successively smaller and smaller variances. The PCs are uncorrelated with each other since they are mutually orthogonal.

There are two main parameters used in PCA: loadings and scores. The loadings are coefficient of linear combination for each PC, namely p_{ka}, where k is the index for p variables and a is the index for principal component direction coefficients. All the loadings constitute a matrix, P, which expresses the transformation between the initial variable space and the new space formed by the PCs. These loading vectors, namely the columns in P, are orthogonal. In synthesis, loadings describe the relationship between the initial p variables and the PCs.

The score is the distance between the object and its projection into the PC, and it is called score for object i, t_{i1}, if it refers to PC1. The projection of object i onto PC2 will give the score t_{i2}, and so on. The projected object i will correspond to a point in the new co-ordinate system, an A-dimensional surface. Each object will thus have its own set of scores in this dimensionality-reduced subspace. The NIPALS (Nonlinear Iterative Partial Least Squares) algorithm (Wold, 1966) is one of the several methods used to find the score and loading vectors. In this study, NIPALS algorithm was applied when using PLS toolbox with MATLAB ® software.

3 Results & Discussion

3.1 Pre-processing of raw spectra

Raw spectra from 40 different OZD samples in water at different concentration are shown in Figure 3.

The raw spectra contain important information on chemical fingerprints of the samples but also noise from background and instrument. Pre-processing of the raw spectra can be applied to extract useful information and to remove offset and irrelevant signals.

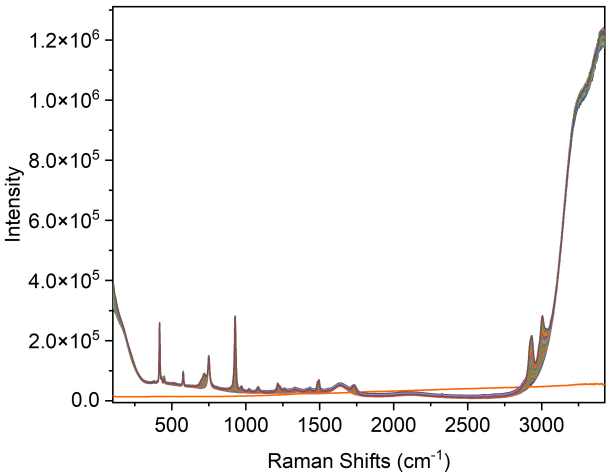

Figure 3. Raman raw data of the 40 analysed samples.

The raw spectra were subjected to a baseline correction technique by applying Automatic Whittaker filter with lambda equals to 100 and P equals to 0.001. The Whittaker filter used is an extended version of Eilers, 2003, available in the PLS toolbox in MATLAB, where a weighted least square method was applied to remove baseline variations and background noise. The factor lambda controls the curvature allowed for the baseline, while the P factor governs the extent of asymmetry required of the fit (Eilers, 2003).

Baseline corrected spectra of OZD samples are shown in Figure 4. As can be seen, as the concentration of OZD increases, the intensity values of some peaks also increase, suggesting that OZD concentration is proportional to the peak intensity, according to the Beer-Lambert law.

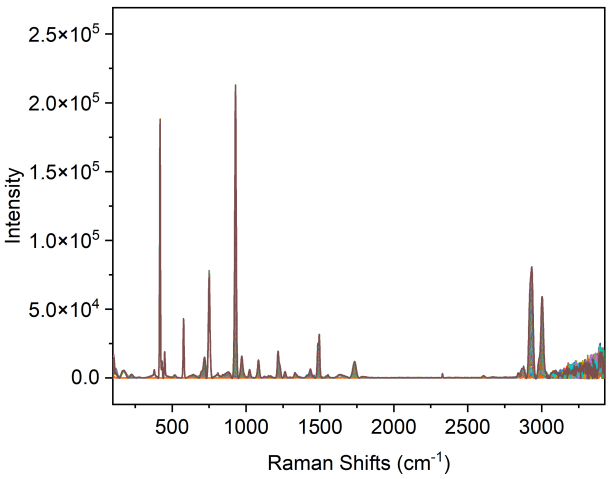

Figure 4. Baseline corrected Raman spectra of the 40 analysed samples.

The peaks that change according to changes in the OZD

concentration are now easily identified and their signals and band assignments are listed in Table 1.

Observed frequency [cm^{-1}]	Vibrational mode
719	C-C stretch
928	C-C stretch
1083	C-H_2 rock
1216	C-H_2 twist
1333, 1261	C-H_2 wag
1436	C-H_2 scissor
1495	C'-N stretch; C=O stretch
1733	C=O stretch
2932	C-H_2 symetric stretch
3003	C-H_2 asymetric stretch

Table 1. Vibrational assignments of OZD (McDermott, 1986) (C'= carbonyl carbon).

All the band assignments were referenced to earlier work from McDermott (1986) from the spectra of γ-butyrolactone and 2-pyrrolidinones, which are cyclic esters, like 2-oxazolidinone.

There are also strong peaks at wavelengths 418, 577, and 750 cm^{-1} that do not change according to the changes in OZD concentration and these peaks can be assigned to the noise from the Raman instrument. These peaks were also seen previously in earlier publication from Jinadasa (2019).

Concerning water, its characteristic peaks are cut off from the range of interest, since it usually shows bands below 300 cm^{-1} corresponding to the hydrogen bond bending and stretching motions and strong bands above 3000 cm^{-1} typical of the O-H stretching region; the low intensity peak at 1650 cm^{-1} arises from the intramolecular bending motion (Franks, 1972).

3.2 Initial PCA Analysis

Using the whole spectra as a starting point, the preprocessed OZD spectra were then subjected to initial PCA analysis. Figure 5 illustrates the cumulative variance of the PCA model. PC1 is defined as the first principal component which relates to the maximum variance of the data, while PC2 is the second principal component which corresponds to the second largest variance. The number of PCs corresponds to the number of orthogonal variables in the spectral data set. As can be seen, PC1 explains 92.58% of the total variance, while PC2 describes an additional 6.88%. These two PCs make up 99.46% of the variation in the model, suggesting that they are probably sufficient to determine the most important variables for the description of OZD samples.

In Figure 6, a score plot of PC1 versus PC2 for the preprocessed OZD spectra is shown. The dotted circle represents a 95% confidence level. As can be seen, one of the samples is outside the area of interest meaning that this sample is most likely an outlier. By checking the raw spectra of OZD samples, this sample is confirmed to be an outlier and it is probably coming from an error when using the Raman instrument. The outlier was thus removed.

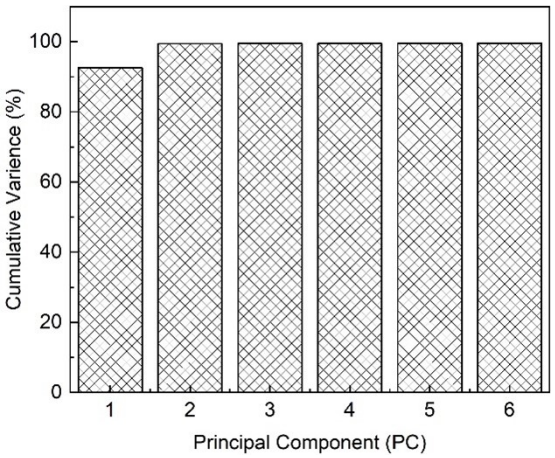

Figure 5. Cumulated percentage variation explained.

The pre-processed OZD spectra as shown in Figure 4 also show some noise in the region of >3000 cm^{-1} Raman shift and this region was also removed in the next PCA analysis.

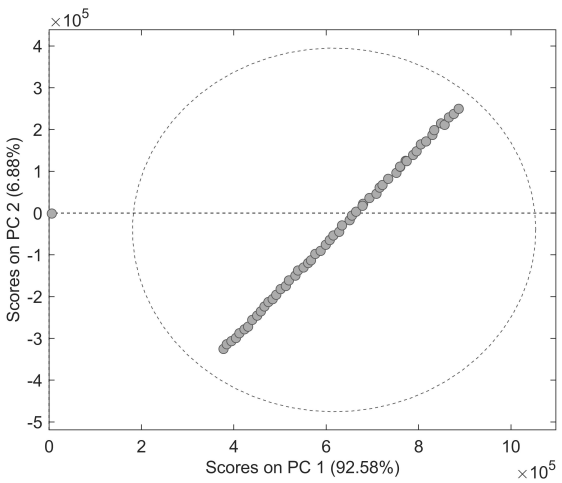

Figure 6. PCA analysis for preprocessed Raman data, first score plot of PC1 vs PC2.

The loading plot for PC 1 for the PCA model is shown in Figure 7. As mentioned by Wold et al. (1987), loading plots define what a principal component represents. The higher the loading value, the higher the contribution of the variable to the PC. In the case of this work, these plots will represent OZD concentrations in the samples. Figure 7 indicates that significant contribution comes from peaks at 418, 577, and 750 cm^{-1}. These peaks however do not correspond to OZD or water, and thus most likely coming from the instrument. The fact that these peaks have higher loading values even though they do not really represent the actual components in the samples necessitates further correction to the PCA model. These peaks were therefore excluded from the model.

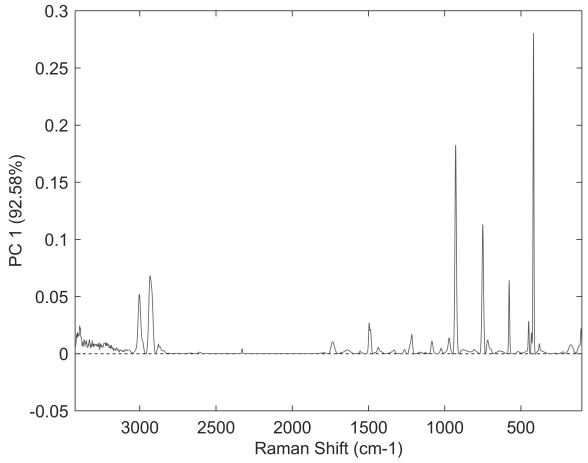

Figure 7. Loading plot for PC1.

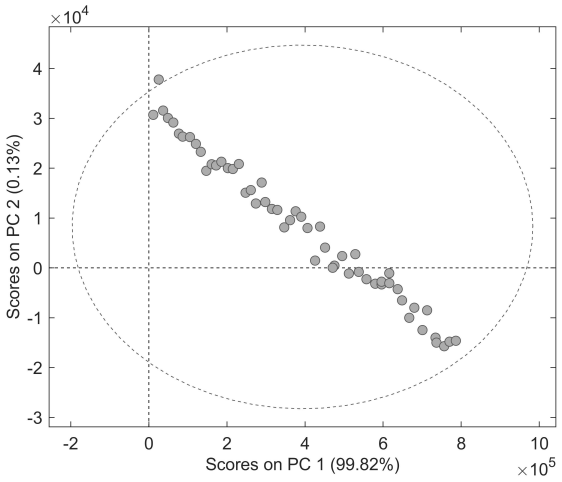

Figure 9. PCA analysis for preprocessed Raman data, score plot of PC1 vs PC2 after removal of variables below 650 cm^{-1}.

3.3 Optimized PCA with Variable Selection

Based on earlier considerations, the PCA model was recalibrated, and Figure 8 displays the new cumulative variance of the model. PCA model was recalibrated by selecting the variable range of OZD to optimize the PC1, which mainly describes the OZD concentration variation.

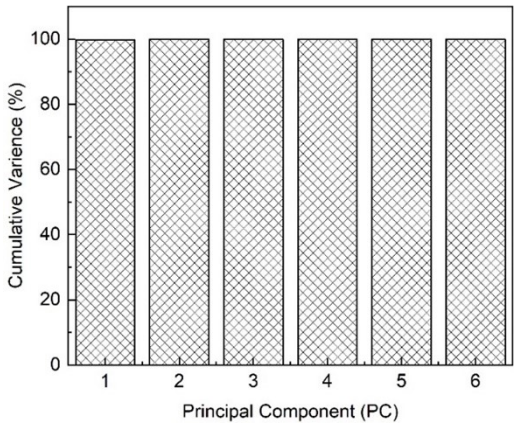

Figure 8. Cumulated percentage variation for different principal components.

The new score plot is shown in Figure 9. Based on the figure, PC1 and PC2 account for 99.78 and 0.17% of the model variance, respectively. These two principal components already make up 99.95% of the cumulative variance for the model suggesting that it is very likely that the OZD changes are sufficiently described by PC1.

With the elimination of outliers, all samples are now at 95% confidence level. Values of PC1 are always positive, whilst values of PC2 change from positive to negative for all the samples. The samples also show a linear trend suggesting that there is a linear trend between Raman intensity and OZD concentration and that the PCA model can be used to classify OZD.

The loading plot for PC1 is illustrated in Figure 10. According to the plot, the sharp OZD peak at 928 cm^{-1} gives the highest contribution to PC1. This indicates that this peak can be used as an indicator for the presence or changes in OZD concentration in a sample. Other peaks that positively contribute to PC1 loading plot include 3003, 2933, 1736, 1496, and 720 cm^{-1} and these peaks are observed as relevant functional group peaks for OZD, as shown in Table 1.

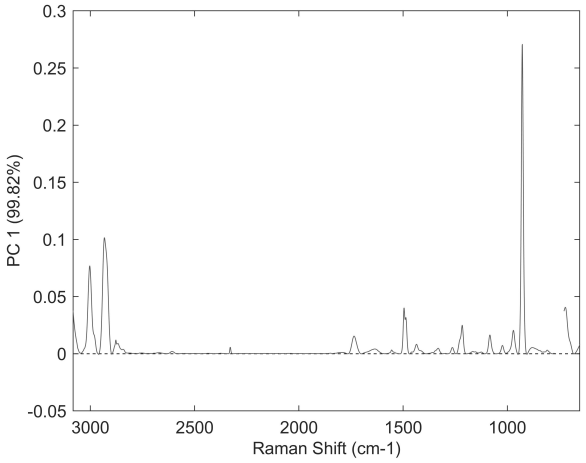

Figure 10. Loading plot for PC1 with variable selection.

4 Conclusion

This paper aims to analyze Raman spectra of 2-oxazolidinone samples by using Principal Component Analysis to detect relevant peaks, monitor changes in the samples at different concentrations and remove outliers.

After spectra acquisition and a preliminary baseline correction, the data were subjected to PCA analysis. The first two PCs, which made up 99.46% of the variation in the model, were considered for the analysis. After that, outlier removal was performed and the PCA model was recalibrated by selecting relevant variable range of OZD

to optimize PC1, which describes the OZD concentration variation. With these considerations, the two PCs made up 99.95% of the cumulative variance, an increase of 0.49 percentage point.

Finally, according to the loading plot for PC1, it was found out that the sharp OZD peak at 928 cm^{-1} gave the highest contribution to PC1, indicating that this peak can be used as an indicator for the presence or changes in OZD concentration in a sample.

By using PCA, we have shown in this work that we can systematically identify with precision any outliers, relevant peaks for OZD, and monitor changes in the OZD at different concentrations.

References

Paul H. C. Eilers. A perfect smoother. *Analytical Chemistry*, 75(14):3631–3636, 2003. doi:10.1021/ac034173t. PMID: 14570219.

K. H. Esbensen. *Multivariate data analysis in practice: an introduction to multivariate data analysis and experimental design*. 5th ed. edition, 2012. ISBN 978-8299333030.

Felix Franks. *The Physics and Physical Chemistry of Water*. Springer New York, 1972. ISBN 978-1-4684-8336-9 978-1-4684-8334-5. doi:10.1007/978-1-4684-8334-5.

C. Gouedard, D. Picq, F. Launay, and P.L. Carrette. Amine degradation in CO_2 capture. i. a review. *International Journal of Greenhouse Gas Control*, 10:244–270, 2012. doi:https://doi.org/10.1016/j.ijggc.2012.06.015.

Ardi Hartono, Solrun Vevelstad, Arlinda Ciftja, and Hanna Knuutila. Screening of strong bicarbonate forming solvents for CO_2 capture. *International Journal of Greenhouse Gas Control*, 58:201–211, 2017. doi:https://doi.org/10.1016/j.ijggc.2016.12.018.

M.H. Wathsala N. Jinadasa. *Process analytical technology for real-time quantitative speciation of aqueous phase CO_2 capture solvents*. PhD thesis, University of South-Eastern Norway, 2019.

Arthur L. Kohl and Richard B. Nielsen. *Gas Purification*. Gulf Professional Publishing, fifth edition, 1997. ISBN 978-0-88415-220-0. doi:https://doi.org/10.1016/B978-088415220-0/50002-1.

Peter Larkin. *Infrared and Raman Spectroscopy*. Elsevier, 2011. ISBN 978-0-12-386984-5. doi:10.1016/B978-0-12-386984-5.10001-1.

Helene Lepaumier, Dominique Picq, and Pierre-Louis Carrette. New amines for CO_2 capture. i. mechanisms of amine degradation in the presence of CO_2. *Industrial & Engineering Chemistry Research*, 48(20):9061–9067, 2009. doi:10.1021/ie900472x.

Dana P. McDermott. Vibrational assignments and normal-coordinate analyses of γ-butyrolactone and 2-pyrrolidinones. *The Journal of Physical Chemistry*, 90(12):2569–2574, 1986. doi:10.1021/j100403a006.

Andrew J. Sexton and Gary T. Rochelle. Reaction products from the oxidative degradation of monoethanolamine. *Industrial & Engineering Chemistry Research*, 50(2):667–673, 2011. doi:10.1021/ie901053s.

H. Wold. Estimation of principal components and related models by iterative least squares. *Multivariate analysis*, pages 391–420, 1966.

Svante Wold, Kim Esbensen, and Paul Geladi. Principal component analysis. *Chemometrics and Intelligent Laboratory Systems*, 2:37–52, 1987. doi:https://doi.org/10.1016/0169-7439(87)80084-9.

Characterization of the Flow (Breakup) Regimes in a Twin-Fluid Atomizer based on Nozzle Vibrations and Multivariate Analysis

Raghav Sikka[1] Maths Halstensen[2] Joachim Lundberg[1]

[1] Department of Process, Energy and Environmental Technology, University of South-Eastern Norway, Norway, Raghav.sikka@usn.no

[2] Department of Electrical Engineering, IT and Cybernetics, University of South-Eastern Norway, Norway, Maths.Halstensen@usn.no

Abstract

In the study, a new non-intrusive approach based on acoustic chemometrics, which includes vibration signal collection using glued-on accelerometers, was assessed for the classification of the different flow (breakup) regimes spanning a whole range of fluids (water and air) flow rates in this twin-fluid atomizer *(one-analyte system)*. This study aims to determine the flow regimes based on the dimensionless number (B), whose unique values correspond to different flow (breakup) regimes. The principal component analysis (PCA) was employed to visually classify the breakup regimes through cluster formation using score plots. The model prediction performance was studied using PLS-R, RMSEP values show error ranges within acceptable limit when tested on independent data. The present acoustic study can serve as a good alternative to the imaging methods employed for flow classification.

Keywords: Multivariate Regression, Acoustic Chemometrics, Principal Component Analysis, Flow Regimes

1 Introduction

Twin-fluid atomizers have been widely used atomizers in various applications such as the aerospace industry, internal combustion engines, process industry, spray drying, etc. Classification of the flow regimes using a high-speed imaging setup is quite common, as mentioned in different twin-fluid studies (Choi, 1997; Leboucher et al., 2010). While it is a fairly convenient way to categorize flow regimes for a laboratory-scale test setup using imaging setup (Adzic et al., 2001; Li et al., 1999), it can be a greater concern for industrial-scale atomizers due to the significantly larger fluid flow rates. Acoustic chemometrics, thoroughly applied (Esbensen et al., 1999; Halstensen et al., 2000) lately has proved to be a decent approach for tackling fluid-related problems. The applications for acoustic chemometrics are multitude, ranging from qualitative analysis to process monitoring. The ambit of acoustic analysis lies in the fact that all flow processes comprise some form of energy output emission in the form of signals that can be tapped and analyzed. The flow in the nozzles gives rise to certain vibrations for a particular set of fluid flow rates. By recording those signals through a data acquisition device using sensors (accelerometers) and performing signal analysis, useful qualitative information can be extracted by multivariate analysis.

To suffice the currently used imaging methods for flow regimes classification, an experimental setup, including novel twin-fluid atomizers, is investigated with real-time monitoring of the acoustic signal data. This study aims to assess the feasibility of the acoustic chemometrics approach for this air-assisted spray atomizer problem. The main objective is to determine the flow regimes based on the dimensionless number B, whose unique set of values corresponds to different flow (breakup) regimes. This analysis will further cater to whether the acoustics chemometrics approach, including both unsupervised learning technique (PCA) and supervised learning technique (PLS-R), is suitable for extracting valuable information through recorded vibration signals.

2 Materials and Methods

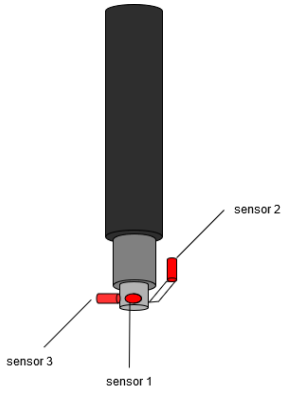

Figure 1. Schematic of the novel atomizer attached at the end of the lance, along with the accelerometers (in red).

2.1 Experimental Method

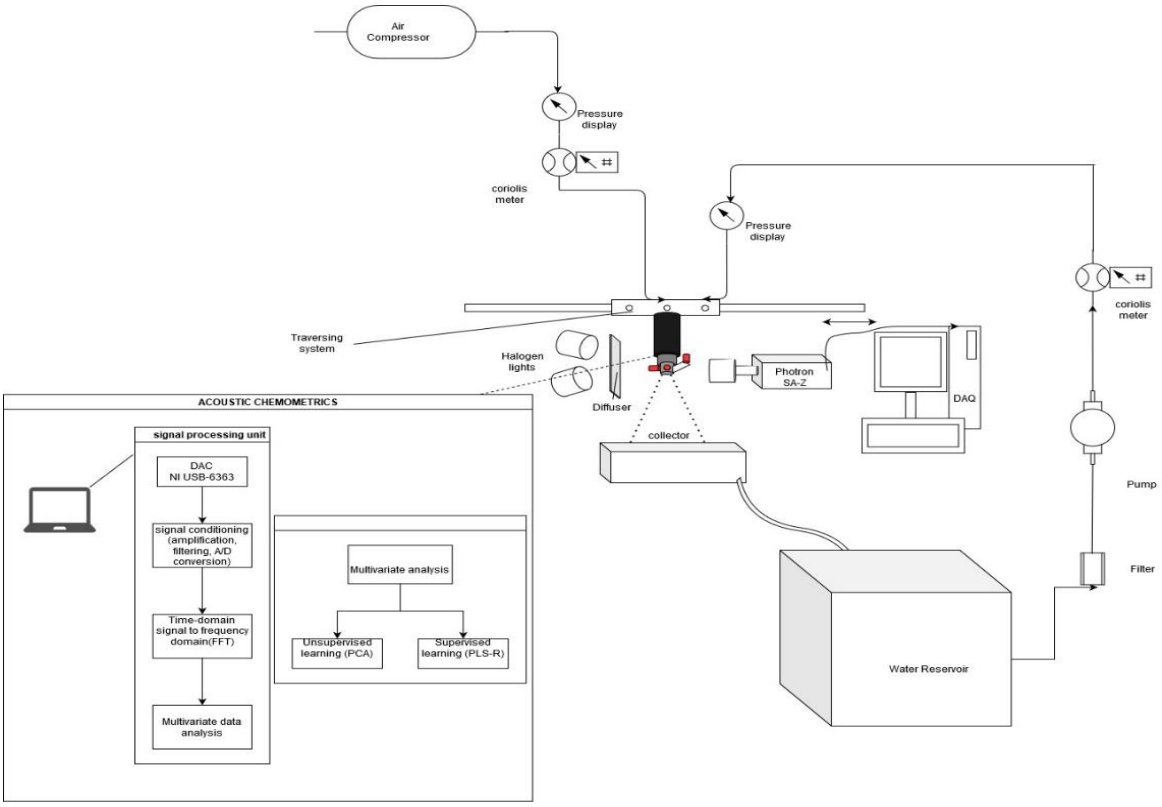

Figure 2. Schematic of the experimental setup along with the acoustic chemometrics flow chart (in box).

The experiments were carried out in a laboratory-scale experimental test rig in the process energy laboratory at the USN. The test rig consists of the lance, which is mounted at the traversing system, at whose end a twin-fluid atomizer (Figure 1) with 3.0 mm orifice (throat) diameter for core air was attached. The sensors in the three-axis (x, y, and z) were glued onto the atomizer. The liquid (water) was flowing in an annular manner through a slit of 280 µm along with the high-speed air core with the aid of hoses and pipes attached to the lance (Figure 2).

The high-speed imaging performed using the CMOS Photron camera SA-Z and two 250 W each Halogen lights from Dedocool Dedolight renders the different flow regimes visible at certain different fluid flow rates (Figure 3). Certain breakup regimes or modes were found at specific air-to-liquid mass ratios (ALR) and Weber number (We) based on liquid sheet velocity. ALR is defined as:

$$ALR = \frac{m_{air}}{m_{liquid}} \quad (1)$$

where mass flow rate in kg/hr.

Weber number is defined as:

$$We = \frac{\rho U^2 t}{\sigma} \quad (2)$$

Where ρ is liquid density (1000 kg/m^3), U is sheet velocity calculated through mass flow rate, σ is surface tension, and t is sheet thickness (280 µm).

A new dimensionless number (B) (depicted in Table 1) was employed, which is defined as:

$$B = We \cdot ALR \quad (3)$$

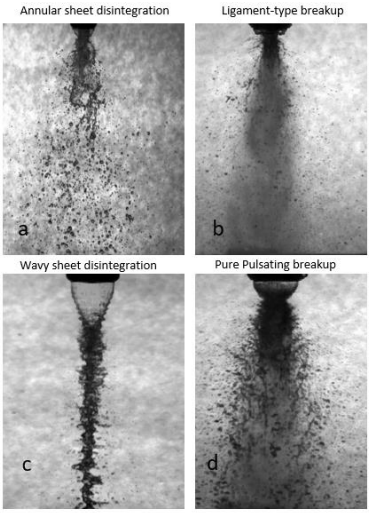

Figure 3. Different breakup regimes based on different fluid mass flow rates.

Table 1. Breakup regimes and the corresponding non-dimensional number values

Breakup Regimes	***B***	***ALR***	***We***
Annular sheet disintegration	2.586	0.150	17.24
Ligament type breakup	6.035	0.350	17.24
Wavy sheet breakup	9.052	0.0428	211.2
Pure-pulsating breakup	21.12	0.10	211.2

Both fluid flow rates were measured and monitored using Coriolis flowmeters. Two air flow rates (15 kg/hr and 35 kg/hr) were employed as per the visualization study and manually operated through the pressure regulator. 100 kg/hr corresponds to Weber number (We) of 17.24, whereas 350 kg/hr corresponds to Weber number (We) value of 211.2. The liquid (water) flow rates taken were low flow rate (100 kg/hr) and high flow rate (350 kg/hr), which were altered through a frequency-based flow rate controller. The air-to-liquid ratio varied from 0.0428 to 0.35, depending on the combination of fluid flow rates as depicted in Table 1. At lower flow rates, annular sheet disintegration was visualized, whereas it reached pure-pulsating breakup mode at higher flow rates for both air and water. Ligament type breakup corresponds to high airflow rates & low liquid flow rates, whereas wavy sheet breakup corresponds to high airflow rates & low liquid flow rates, as mentioned in Figure 3.

2.2 Acoustic chemometrics

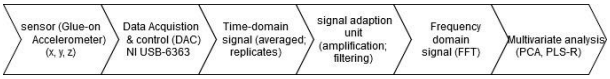

Figure 4. Block diagram of the acoustic analysis in-flow process from the vibration data collection.

The name acoustic chemometrics (Esbensen et al., 1998) implies that the information extraction from the data recorded in vibrational energy is measured using some acoustic sensors (say, accelerometers). Some inherent advantages related to acoustic chemometrics are:

- Non-intrusive technology system
- Real-time monitoring of signals
- Easy sensor deployment (glued-on)
- Relatively inexpensive technology
- Prediction of several parameters from the same acoustic spectrum

The acoustic measurements in this study were taken using sensors (accelerometer, which is a piezoelectric type 4518) from Bruel & Kjær, Denmark. Three sensors are utilized in the test experiments to tap the noise/vibration data from all three axes (x, y, and z), as depicted in Figure 1. The fluid flow ejected out of the atomizer outlet forces the atomizer a sudden backward blow, recorded in an electrical signal proportional to the vibration acceleration. A signal amplification unit, a data acquisition device (NI USB-6363) from National Instruments and a personal laptop were employed. NI USB-6363 data acquisition device (DAQ) was utilized to acquire the signal, where the signal converted from analog to digital. A digital signal is required for the signal amplification unit for further processing. The frequency range used for this study is (0 - 200 kHz).

For the acoustic chemometrics signal collection and signal conditioning, the LabVIEW-based in-house created interface (Halstensen et al., 2019) was used. The signal processing was carried out in few steps. Firstly, time series of 4096 samples were recorded from the sensor. The time-series signal was multiplied by a window (Blackman Harris), which cancels the end of the series to avoid spectral leakage in the acoustic spectrum. This signal is finally transformed into the frequency domain using Discrete Fourier Transform (DFT). The Discrete Fourier Transform transforms a sequence of N complex numbers $\{x_n\}:= x_0,x_1,...,x_{n-1}$ into another sequence of complex numbers, $\{X_k\}:= X_0,X_1,...,X_{N-1}$, which is defined by equation:

$$X_k = \sum_{n=0}^{n-1} x_n \, e^{-i2\pi kn/N} \;\; k = 0, \dots, N-1 \qquad (4)$$

A more advanced and efficient form of the DFT is the Fast Fourier Transform (FFT) (Ifeachor et al., 1993), which was implemented in the LabVIEW interface for fast real-time calculation. The whole in-flow acoustic analysis process from signal conditioning to domain transformation from time to frequency and then supervised (PLS-R) and unsupervised (PCA) multivariate analysis techniques are mentioned in a block diagram (Figure 4).

2.3 Principal Component Analysis (PCA)

Principal component analysis (PCA) analyses multivariate data by examining the common variances. Large multivariate data sets can be noisy and difficult to interpret. PCA projects mean-centred data (X) consisting of variables (columns) and samples (rows) onto a new plane. The new plane is represented by scores (T) and loadings (P). E is the notation of the data not explained by the model, the residuals, given by the equation:

$$X = T\,P^T + E \tag{5}$$

PCA uses an orthogonal transformation to convert correlated variables into few linearly uncorrelated variables called principal components. The method is called the unsupervised method due to no guidance to the singular value decomposition from the data. The nonlinear Iterative Partial Least Squares (NIPALS) algorithm developed earlier (Wold et al., 1987) was used because of its many advantages. It works on matrices with moderate amounts of randomly distributed missing observations. The other advantage of NIPALS is that it is less time-consuming than Singular value decomposition (SVD), as the former allows defining the number of components to calculate.

2.4 Partial Least Squares Regression

Partial least squares regression (PLS-R) is a supervised method used for calibrating the predicting models, which is well explained in (Geladi et al., 1986).

PLS-R is a good alternative to other regression techniques due to its robustness. The model parameters do not change much even when new calibration samples are taken from the population. It relies on representing training data for two-variable blocks X and Y, respectively. In the present work, the X data matrix contains the acoustic frequency spectra, and Y is a vector containing the non-dimensional number B values that define the breakup regimes.

The NIPALS algorithm is the most widely used in the PLS regression technique. In this algorithm, PLS-R allows modelling both the X and Y simultaneously, which might raise orthogonality issues. For low precision data, PLS-R gives more accurate results than other regression methods. A simplified version of the NIPALS algorithm is presented in earlier studies (Ergon et al., 2001), where A is an optimal number of components. A step-wise NIPALS algorithm is described in some detail (Halstensen, 2020).

In evaluating the regression model, the root mean squared error of prediction RMSEP offset, slope and correlation coefficient are commonly used. Besides these, visual evaluation of the relevant T-U score plots, loading weights plots, explained variance plots also provide useful information for calibrating and developing the prediction model. The root mean square is given by:

$$\text{RMSEP} = \frac{\sqrt{\Sigma_{i=1}^{n}\left(\hat{y}_{i,predicted} - y_{i,reference}\right)^2}}{n} \tag{6}$$

Where, i = sample index number
n = total number of samples
RMSEP = Root Mean Squared Error of Prediction.

3 Results and Discussion

3.1 PCA results

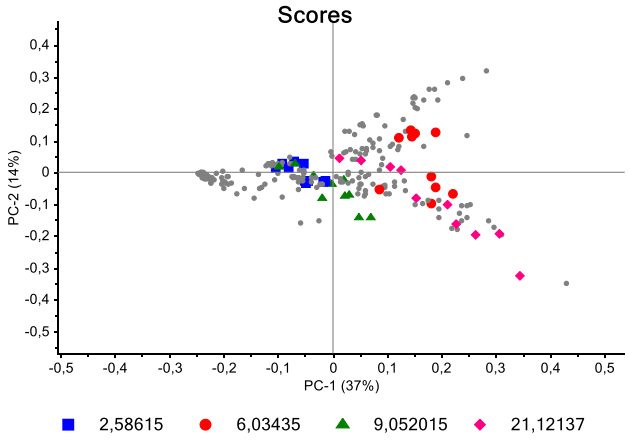

Figure 5. Score plot t1-t2 for both atomizer.

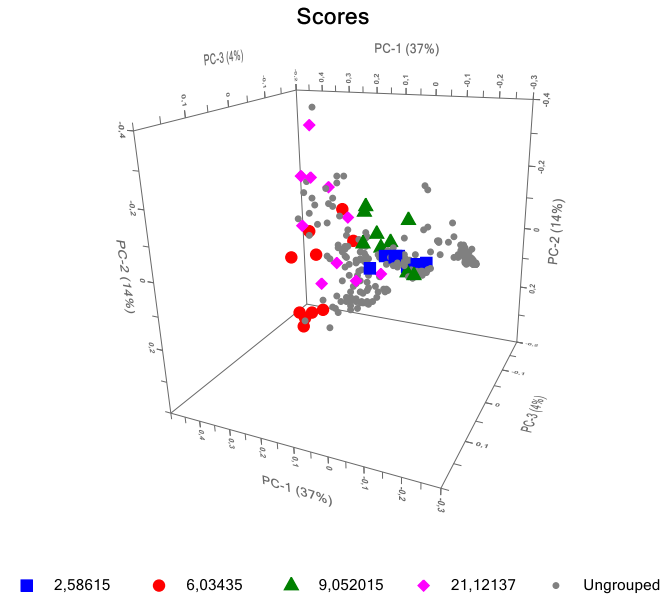

Figure 6. 3-D Score plot t1-t2 for both atomizers.

PCA score-plots depicts how the acoustic spectrum and different breakup regimes are correlated based on the tests carried out at various flow rates. A colour indicates each breakup regime in the data-centred score plot. The score plots show a cluster of points for a particular type of breakup regime/mode for principal component 1. The score plot shows a trend in the data from low airflow rates on the left side (blue) to the high air flow rates on the right side (pink).

The score plots were obtained with the whole frequency spectrum for all three sensors deployed. The score plots depicting two different atomizer type-converging and converging-diverging (CD) atomizer. To avoid repeatability, both converging and converging-diverging (CD) atomizer are shown in a single score plot as a 2-D plot (Figure 5) and for better visualization as in a 3-D plot (Figure 6). The loading plot (Figure 7) shows that the information based on the frequencies recorded from sensor 2 is different from the other two sensors, provided that sensor 2 is located opposite to the fluid flow direction, which is relevant in this case.

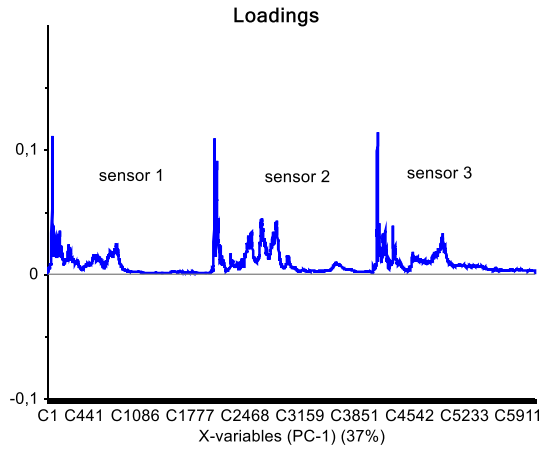

Figure 7. Loadings plot for all three sensors.

3.2 PLS-R prediction for the breakup regimes

PLS-R was employed to do model prediction based on the acquired acoustic spectra. The non-dimensional number (B) values were used as the reference values (Figure 8). The acoustic spectra used to calibrate the PLS-R model was a 240x2048 matrix containing 240 frequency spectra for each sensor. The test set validation was performed for alternate data matrix values, 50 % (120) of the total column set. Each spectrum consisted of 2048 frequencies ranging from 0 to 200 kHz. The statistical parameters that evaluate the model prediction are slope and RMSEP. Both slope and RMSEP define the model's quality fitting the reference data; in this case, their value is reasonably within permissible limits.

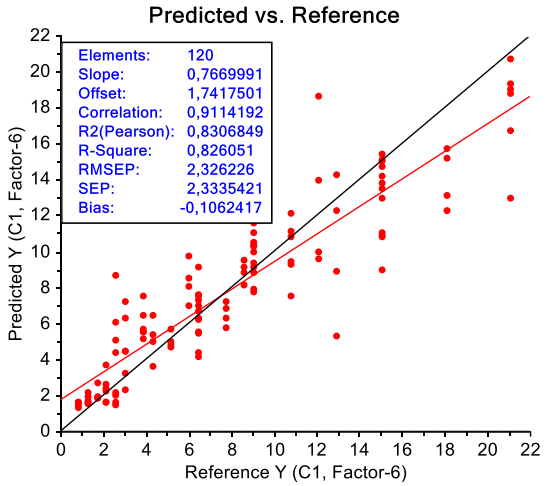

Figure 8. Predicted Vs. Reference (B) value. The target line (black) and regression line (red) are indicated.

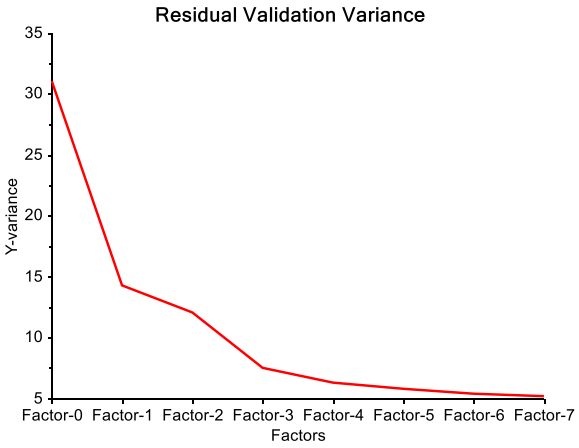

Figure 9. Residual validation variance plot.

Based on the residual validation variance plot (Figure 9), six components can be fixed as optimal for model prediction. The same results can be plotted as samples taken in time (Figure 10). The green line is the reference line for non-dimensional number (B), and the blue line is the prediction line.

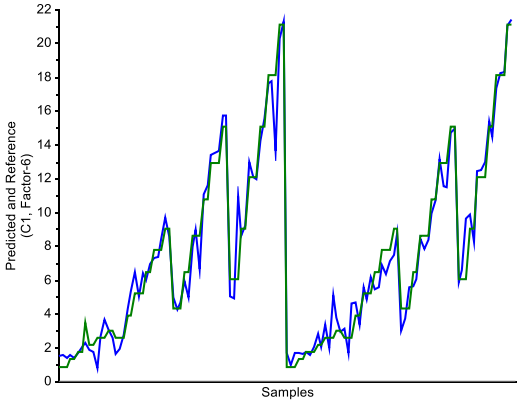

Figure 10. Predicted and Reference (B) values for samples taken in time.

4 Conclusions

To corroborate the visualization study performed for breakup regimes identification, the non-invasive acoustic/vibrations study incorporating sensors (accelerometer) with an appropriate signal processing system was performed, allowing the estimation of the flow breakup modes. The feasibility of this approach for fluid flow classification is the main objective of this study, rendering relevant information about the flow breakup regimes for various fluid flow rates. The acoustic measurements provide valuable insight into the regime classification based on a derived dimensionless number (B) from other fluid-based non-dimensional numbers. The pattern study using principal component analysis provides relevant information through the clusters formed for each breakup regime. The chemometric method provided sufficiently good model prediction with slope and RMSEP values within acceptability limits. The main advantage of this non-invasive acoustic method is that it renders the visualization study for different breakup modes optional for industrial-scale atomizers for flow regime prediction which can be implemented on the industrial-scale setup.

References

M. Adzic, I. S.Carvalho, and M. V. Heitor. Visualization of the disintegration of an annular liquid sheet in a coaxial air-blast injector at low atomizing air velocities. *Optical Diagnostics in Engineering*, *5*(1), 27–38, 2001.

C. J. Choi. Disintegration of Annular Liquid Sheet with Core Air Flow -Mode Classification. *International Journal of Fluid Mechanics Research*, *24*(1–3), 399–406, 1997.

R. Ergon, and K. H. Esbensen. A didactically motivated PLS prediction algorithm. *Modeling, Identification and Control*, *22*(3), 131–139, 2001. doi: 10.4173/mic.2001.3.1

K. H. Esbensen, M. Halstensen, T. Tønnesen Lied, Saudland Arild, J. Svalestuen, S. De Silva and Hope, B. Acoustic chemometrics - From noise to information. *Chemometrics and Intelligent Laboratory Systems*, *44*(1–2), 61–76, 1998. doi: 10.1016/S0169-7439(98)00114-2

K. H. Esbensen, B. Hope, T. T. Lied, M. Halstensen, T. Gravermoen and K. Sundberg. Acoustic chemometrics for fluid flow quantifications - II: A small constriction will go a long way. *Journal of Chemometrics*, *13*(3–4), 209–236, 1999. doi: 10.1002/(sici)1099-128x(199905/08)13:3/4<209::aid-cem553>3.0.co;2-5

P.Geladi, and B. R. Kowalski. PARTIAL LEAST-SQUARES REGRESSION: A TUTORIAL. *Analytica Chimica Acta*, *185*, 1–17, 1986.

M. Halstensen. *Classification of Gases and Estimation of Gas Flow Rate Based on Unsupervised and Supervised Learning Respectively*.*September*,22–24,2020. doi: 10.3384/ecp20176451

M. Halstensen and K. Esbensen. New developments in acoustic chemometric prediction of particle size distribution - "The problem is the solution." *Journal of Chemometrics*, *14*(5–6), 463–481, 2000. doi: 10.1002/1099-128X(200009/12)14:5/6<463::AID-CEM628>3.0.CO;2-Y

M. Halstensen, J. Lundberg, P. I. Januschas and H. P. Halvorsen. On-line Monitoring of Viscous Properties of Anti-icing Fluid Based. *Proceedings of The 60th SIMS Conference on Simulation and Modelling SIMS 2019, August 12-16, Västerås, Sweden*, *170*, 26–31, 2019. doi: 10.3384/ecp2017026

E. C. Ifeachor and B. W. Jervis,. *Digital signal Processing*, 1993.

N. Leboucher, F. Roger and J. L. Carreau. Disintegration process of an annular liquid sheet assisted by coaxial gaseous coflow(S). In *Atomization and Sprays* (Vol. 20, Issue10,847–862,2010. doi:10.1615/AtomizSpr.v20.i10.20

X. Li and J. Shen. Experimental study of sprays from annular liquid jet breakup. *Journal of Propulsion and Power*, *15*(1), 103–110, 1999. doi: 10.2514/2.5397

S. Wold, K. Esbensen and P. Geladi. Principal Component Analysis. *Chemometrics and Intelligent Laboratory Systems*,*2*(1–3),37–52,1987. http://files.isec.pt/DOCUMENTOS/SERVICOS/BIBLIO/ Documentos de acesso remoto/Principal components analysis.pdf

RESOURCE SIMULATOR - a tool for scenario studies on limited resources

Erik Dahlquist

Mälardalen University, Västerås, Sweden erik.dahlquist@mdh.se

Abstract

In this paper global resources have been gathered from different sources. From these resources scenarios have been made to get an overview of what resources will last at the present annual usage, as well as if we assume all individual would utilize the same amount or the difference between regions and populations. The most critical metal is according to this Zn, while also Cu, U, Co and Mn are relatively limited with reserves lasting in the range of 100 years. Some elements like P is not limited as such, but there is always a trade-off between total amount and at what concentration the extraction is made. For biomass and food we have enough resources if used efficiently. Wind, sun and hydropower are in reality unlimited resources for electricity production. We also have huge amounts of biomass. A question is what biomass should be used for. First it can be as a building material, then for chemical production and paper/packaging and last as energy source seems reasonable.

Keywords: resources, simulation, predictions

1 Introduction

There is a limited amount of resources available at Earth. Some of these are fossil, others renewable. Most resources utilized can be reused or recycled to a greater or smaller extent. The situation with respect to resources varies from country to country but can principally be grouped with respect to UN´s World Bank Statistics (2020) where data for each country (total 213) is collected but also grouped into "low income countries", "middle income countries" and "high income countries". We also look at regions of the world. Data from this is used in this paper for the resource simulation with respect to energy and environmental emissions. Other data from many different sources are complemented, and more detailed specification for specific factors described more in detail. The author has collected data during many years and published in books and papers. References are made to these as the data has been refined compared to original sources. These are then used for extrapolation to cover use today and possible scenarios for the future for countries in the three income groups. The simulations are made where the structure is set, but the use of resources varied.

2 Overview different resources

The most important input factors are Primary Energy sources, crops and raw materials (inorganics like metals). These are then utilized for heating, electricity production, transportation, food production and industrial use. In this section the resources are calculated and extrapolated into the UN grouping after income.

2.1 Energy

Primary energy is from Oil, Coal, Natural gas, Biomass, Waste, Sun, Wind, Hydropower and Geothermal energy. These resources are converted (Tomas-Aparicio et al., 2020) into useful forms like electricity, heat, cooling, transport work, industrial production, food production, building houses and other infrastructure. For these uses we also have input energy to manufacture wind power towers, PV-cell systems, thermal power plants, hydro power plants etc (Tomas-Aparicio et al., 2020). For transportation we can utilize fossil fuels and diesel or benzine vehicles, but also electric vehicles are coming fast (Irena, 2019; MacDicken et al., 2016). For the future we also see both more efficient engines as well as new energy conversion techniques like Fuel Cells utilizing Hydrogen as fuel. Biofuels can replace fossil fuels, but also replace use of oil or other fossil fuels for all kind of applications like production of plastics, chemicals, building materials etc. (Chaudhary et al., 2019; Larsson et al., 2018).

2.2 Other resources:

Recycling of materials is affecting the true input of both materials and energy. We have limited resources of metals and other inorganic materials as well as Phosphorous, while Nitrogen is a non-limited resource (Martinsen et al., 2020). On the other hand, conversion of Nitrous gas (N_2) to ammonia (NH_3) for e.g. use as fertilizer as well as "destruction" of ammonium compounds in waste water treatment plants consume huge amounts of electric energy.

In Table 1, we see the available resources as reserves, the annual use globally as well as the per capita use of important materials. We also see how much energy is used for production per kg related to virgin material or recycled material at typical recovery rates today in OECD countries.

Table 1. Important resources – annual extraction, reserves, and energy for processing.

Material	Prod Mt/y	Reserv Mt	Recycled Harvest %	kg/c,y world	Energy f p kWh/kg virgin	Energy f p kWh/kg recycled	GHG emis kgCO2/kg virgin	Reserves last years
Si								
Al	63	336786	75	8,2	63	3,15		5346
Ca	125	164286		16,3	0,33			1314
Cu	21,3	1600	80	2,8	18	2,7	2-4	75
Fe	1869	230000	88	243,6	3,7	0,444	1,9	123
Zn	12,9	232	35	1,7	14,5	3,48	2,6	18
Co	0,14	15		0,018				107
Li	0,082	20		0,011				244
Mn	0,1	11,8		0,013				118
RE								
U	0,065	5,7-20						88
V	17			2,2				
N	170			22,2	12,7			
P	33	112000		4,3	8,5			3394
plastic	299			39,0	25		2,4	
paper &cardboard	420		65	54,7	2,9	1,015		
pulp	180			23,5	4			
e-waste	41,8			5,4				
steel (50% recycled	1869		0,5	243,6	3,7	1,85	1,9	
cement	4100			534,3	0,11		1,25	
Tot cereals	2700			351,9				

Table 2. Annual crop production; use of fertilizers and energy; GDP per capita and population in different regions and income groups.

	2017,0	2016		2015	2014	2014	2019	2019
Function	ton cereal,	fertilizer	El fr	% fossil of	el	energ us	GDP	population
Region	per ha	kg/ha	fossil %	all energy %	kWh/cap	koe/cap	US$/cap	
world	4,1	140,5	65,2	79,7	3132	1922	11442	7673534
East asia & pacific	5,1	331	74,6	87,9	3678	2135	11530	2340629
Europé & central asia	3,9	80,7	49	71,6	5377	3162	24744	921141
Latin america & caribian	4,7	140,2	43,8	87,9	2158	1360	8869	646431
Middle east & N Africa	2,5	94,8	88,9	97,9	2896	1490	7991	456707
Subsaharan Africa	1,5	16,1	64,1	39,8	487	687	1596	1106957
South Asia	3,2	160,3	80	71,5	705	574	1957	1835777
North America	7,4	127,2	60,8	81,5	13257	6889	63344	365893
High income	6,0	136,6	59,3	79,1	8929	4606	44618	1235852
Middle income	3,9	158,1	71,1	89	2045	1390	5573	5769226
Low income	1,4	10,4	22,2	23,4			810	668455

The most critical metal is according to this Zn, while also Cu, U, Co and Mn are relatively limited with reserves lasting in the range of 100 years at present consumption level. Some elements like P are not limited as such, but there is always a trade-off between total amount and what concentrations there are where the extraction is made. With more efficient separation methods, the available amounts are increasing. Still, we should know the estimates of available resources of different elements are built on a limited number of measurements, especially for the rarer elements.

2.3 Emissions

Conversion of fossil fuels release CO_2 that has been bound in earth for millions of years. When released we get a greenhouse effect. For biomass we have a release of CO_2 as well, but this CO_2 is bound back into new crops through photo synthesis. It is then interesting to evaluate how much biomass we have as a "storage" globally, and what happens if we take out biomass or just let it degrade in nature. There are voices saying that we should let the forests stand to store CO_2 long term.

In a few decades perspective this is correct, but long term the trees stop growing and will not absorb more

CO_2. When the trees finally dies, they are degraded by microorganisms and fungi while releasing both CO_2 and CH_4. CH_4 is approximately 25 times stronger as greenhouse gas than CO_2. Also, N_2O may be released simultaneously, especially if there is a deficiency of oxygen. If we take out a certain amount of wood and let the forest reproduce itself continuously, we will get material for use in many ways. In Table 2, we can see that cereal productivity varies a lot between regions and this correlates to climate differences and use of fertilizers generally. GDP/capita is dramatically different, but the differences are reduced by time. In Table 3, we see that renewable energy is dominating in low-income countries and especially in Africa south of Sahara. We can also see that electricity from fossil fuels is highest in middle income countries. High income countries have reduced the fossil part significantly, while low-income countries use a lot of especially hydro power, aside of biomass.

From this we can see that there is a huge potential to increase productivity in low income countries but also that CO_2 emissions are many times higher in high income countries than low income countries. The challenge will be to reduce CO_2 emissions in high income countries and increase yields in low-income countries without increasing CO_2 emissions.

Table 3. Distribution of REN (PV and wind), Hydro + Nuclear power respectively fossil fuels and CO_2 emission per capita in different regions and income groups.

Function	CO2emiss	Energ Use	El fr	El fr oil,NG	Hydro+
Region	ton/capita	fr REN %	REN %	Coal %	Nuclear %
world	4,6	18,1	22,9	65,2	11,9
East asia & pacific	6,1	13,9	20,4	74,6	5
Europé & central asia	6,9	13,1	28	49	23
Latin america & caribian	2,9	27,6	51,7	43,8	4,5
Middle east & N Africa	6	1,56	2,7	88,9	8,4
Subsaharan Africa	0,8	70,1	26,6	64,1	9,3
South Asia	1,5	38,3	16,9	80	3,1
North America	15,5	10,2	20	60,8	19,2
High income	10,4	11,3	21,3	59,3	19,4
Middle income	3,7	21,2	23,9	71,1	5
Low income	0,3	76,2	66,4	22,2	11,4

3 Scenarios for the future development – Results and Discussions

What would happen if we replace all fossil fuels with biomass? Will there be enough biomass to cover all demands?

In Worldbank database we can find the area in different countries and regions given in km2 or ha. This is for Agricultural land, arable land and forests, as well as more detailed data on how many ha are used for production of different cereals, which is the major food for humans. We can see a very strong development in cereal production last 60 years. This is depending on increased use of fertilizers, irrigation, and better crop species. In Table 4, we can see such balances for Europe where we have assumed 5 ton DS cereal grain/ha,y, but also assume some additional (2.5-) 5 ton DS/y as straw and root system. 5.4 MWh/ton DS for the heating value has been used.

The production can be significantly higher, but also in more arid areas lower. For forests in northern boreal areas the production is in the range 2 ton DS/ha,y as "productive biomass", with an additional 1 ton DS/ha,y at least as roots, bark and leaves. In sub-tropical and tropical areas these values are normally higher, and for some species significantly higher like up to 10 ton DS/ha,y for Salix, Eucalyptus, Acacia and similar. Probably the production in Russia is significantly lower than the average due to colder climate.

The annual forest growth is calculated to be 121 miljoner m3sk/y if only logs are included. If we include also roots and branches this corresponds to 93-million-ton DS. 84 million m3 are taken out by harvest and another 12 degraded in the forest. This means that the annual storage volume is increasing with 25 million m3/y corresponding to 25-million-ton CO_2. This can be compared to the total emissions of CO_2 in Sweden of 53-million-ton CO_2 according to Skogforsk (2019). We have a similar situation in most boreal forests, where the biomass storage is increasing.

For subtropic and tropical forests though the outtake of biomass is often larger than the growth rate. The IPCC report (2019) presents the global balance for CO_2 for year 2005: Emission to air due to change of land use is estimated to be 1.6 Gton C/y, while increase of

biomass in forests 2.6 Gton C/y. This can be compared to annual emissions through combustion of fossil fuels, 6.4 Gton C/y. From 2005 to 2014, the sum of the national GHG inventories net emission is estimated to be 0.1 ± 1.0 GtCO2/y, while the mean of two global bookkeeping models is 5.2 ± 2.6 $GtCO_2$/y (likely range). Global net removals is estimated to be 11.2 ± 2.6 $GtCO_2$/y (likely range) during 2007– 2016. The sum of the net removals due to this response and the AFOLU net emissions gives a total net land-atmosphere flux that removed 6.0 ± 3.7 $GtCO_2$/y during 2007–2016 (likely range) (IPCC, 2019).

Table 4. Balance between energy use and crop production in Northern Europe as TWh/year.

2008/2009	Cereal Inc.	Other Agro	Forestry	Energy	Prod-Use
	Straw	than cere		use	
	TWh	TWh	TWh	TWh	TWh
Austria	56	204	63	332	-10
Belgium	36	103	11	586	-436
Denmark	110	196	9	190	125
Esthonia	9	60	36	54	51
Finland	46	188	359	353	240
Germany	537	1207	179	3353	-1429
Netherland	22	153	6	797	-617
Norway	10	86	163	297	-37
Ireland	22	275	12	150	159
Latvia	18	135	54	45	162
Lithuania	41	189	35	92	173
Poland	322	1108	151	979	602
Sweden	57	258	457	496	275
Switzerland	11	100	20	267	-136
UK	240	1128	47	2085	-669
Russian Fed	1027	16249	13107	6868	23515
Belarus	88	661	140	281	607

If we look at a scenario where productivity in forests would be globally as in Sweden we can see that today harvested forests globally is 2997 Mt/y (see Table 5) with an annual growth of 0.8 m3/ha,y and a harvested production of 260 kg Wood/capita,y. In Sweden the annual growth is 1300 kg/capita,y and 4 m3/ha,y, that is five times higher. With the same growth rate at average globally it would mean 14 985 Mt/y. With a heating value of 5.4 MWh per tDS wood this corresponds to 16 183 TWh with today´s harvests but 80 919 TWh/y if we could reach Sweden´s average. The reported value today in World bank data base is 21 800 TWh/y for biomass plus waste. If we summarize the probable production (annual growth) from all crops today we come to approximately 250 000 TWh/y assuming 5.4 MWh/ton DS.

This is more than the approximately 160 000 TWh energy we use annually, from which approximately 80-85 % is coming from fossil fuels, and only 10% from biomass in official statistics.

As can be seen the potential for increasing biomass production is significant if we would optimize with respect to optimal amount of water, fertilizer and light, as well as temperature and suitable species. This gives a huge potential for production also indoor in buildings like in the cellars and at roof tops. This also would be needed as a lot of productive land has been destroyed by buildings and road systems.

How will different technologies like wind and PV affect the system?

Sun is the major energy resource. It is driving weather systems like wind and hydro power, as well as PV systems. The only other source we have is nuclear reactions directly in the ground or after refinement in nuclear reactors. Neither sun nor nuclear are renewables, but both can be considered as being it as the time perspective is very long. The fossil fuels were produced from biomass more than 100 million years ago

and due to this is affecting the climate due to greenhouse effects when burned, and thus should be avoided. The biomass is emitting CO_2 but is incorporated back into crops continuously, and thus do not give increased temperature long term (range 100 years), at a balance point. If we look at the energy resources we use today it looks like in Table 6.

Table 5. Annual global production, harvest and stock of crops totally (Mton/y) and as per capita and year.

Material	Prod Mt/y	Reserv Mt	Recycled	kg/c,y	Energy f p	Energy f p	GHG emis	Reserves
			Harvest	world	kWh/kg	kWh/kg	kgCO2/kg	last years
			%		virgin	recycled	virgin	
sugar cane	1910			248,9				
rape seed	27,3			3,6				
palm oil	72,3			9,4				
corn	1090			142,0				
wheat	765			99,7	0,24			
rice	496			64,6				
soybean	349			45,5				
Crops	4709,6			613,7				
Tot cereal	2700			351,9				
Cow	78,6			10,2			22,6	
Pig	117,3			15,3			3,5	
hen	112,9			14,7			1,6	
sheep	15,9			2,1				
Meet	340			41,0				
Milk	800			83,0				
peas	19,9			2,6				
cheese								
fruit				29-78				
vegetables				75-385				
fruit+vegetables				200				
sugar				25				
cereals				332	0,24			
roots&tubers				71				
veg oils				14				
sea food				10				
wood		531000	2997	260	5,4		1/2as fuel	177

We can see that 82-83% of the primary energy (totally 167 588 TWh/y) is with fossil fuels. For electricity production (totally 25 418 TWh/y) the figure is 65 % from fossil fuels. What is remarkable is that wind power and solar power is increasing so dramatically fast. Today (2021) the installed capacity for solar power (629 GW) and wind power (651 GW) is together in the same range as hydro power (1308 GW). If we add all non-fossil power production capacities, we get 2978 GW while for fossil fuels we have approximately 3900 GW. This means 44 % installed capacity from non-fossil technologies. It is true that the capacity factor is lower for the non-fossil techniques, but this is increasing a lot due to much higher wind power towers taking wind from where it is stronger. Also, PV cells becomes more efficient, almost twice as high per m2 as 15 years ago. With high power transmission lines, it should be possible to balance demand to wind and sunshine over larger regions in the future. The capacity factor is in the same range for offshore wind power at the North Sea as for coal fueled power plants, around 50 %! Concerning biomass only 10% of the total primary energy demand is used globally, although the production could principally cover all demands. There will be significant increase in electricity demand when going from internal combustion engines to electric motors in vehicles, but also significantly less primary energy use as electric engines are so efficient. If electricity is stored in batteries or as fuel (H_2) and used in fuel cells both alternatives will be complementary.

Table 6. Global power generation and installed capacity by different methods.

	Installed	Total elect	Total el
	electric pow	Energy	Energy
	GW	TWh/y	%
	2019	2019	2019
Fossil	3857	16546	65,1
Ren + nucl	2978	8872	34,9
Nuclear	390	2500	9,8
Hydro	1308	4222	16,6
PV	629	720	2,8
Wind	651	1430	5,6
Total TWh/y		25418	167588

3.1 Use of resources

In Table 7, we see the distribution of different resources for Sweden per capita as MWh/y,c.

All materials together amount to approximately 7 MWh out of 43, which means 16%. The electricity is also including power for industry and will increase further as electric power will replace fossil fuels, while the heat will go down due to more heat efficient buildings. As we get more electric vehicles the energy for transportation will also go down.

What are limiting resources and how could these be recycled long term – Phosphorous, Nitrogen, rare metals, other materials?

Table 7. Energy use per capita and year for the average Swede, MWh/capita,year.

Energy use split as MWh per ca	MWh/c,y
Food and drink	2
extra for production	1
Paper & paper products	0,89
Plastics & chemicals	1,2
Metals	2,3
Total materials	7,39
Electricity	12,7
Heat	13,9
Transport	9,2
Total all	43,2

Phosphorous (P) and Nitrogen (N) are key elements in all biological bodies and crops, aside of primarily C, H and O. This means that all crops we grow to produce food demand a certain amount of P and N per kg product. Today we recirculate manure from animals, but also a lot of additional P is coming from mineral resources from e.g. Spanish Sahara/Morocco. Available resources have been gatherd in (Dahlquist, 2013; Dahlquist and Hellstrand, 2017; Sigson and Dahlquist 2017). There are also large amounts available in other minerals like Thomas Phosphate in iron ores in e.g. Northern Sweden. Still, the available amount is a limiting factor for crop production, and we should recycle as much as possible. This demands recovery from wastewater treatment plants, organic residues in sludges etc. It would also be interesting to recover Nitrogen in wastewater treatment plants (Caballero et al., 2012). The energy to produce ammonia is approximately 13 kWh/kg, while the electricity needed for degrading NH4 to N2 in activated sludge processes is also approximately 13 kWh/kg. If we could reuse N instead of destroying NH_4/NO_3 and recycle back sludge to farmland we thus could save 2*13= 26 kWh/kg principally!! Still, today there are no efficient processes for this, but the Anamox process at least reduces the energy demand for the destruction to half. But by using selected species of microorganisms, it should be possible, to reach at least much further than today. Here advanced control and learning systems will be very interesting in the future (Dahlquist et al., 2021).

Other limited elements are e.g. rare earth metals and similar. A problem here is that these are not equally distributed in the ground and a few countries control production which may cause political problems in the future. In Table 1, we see how long known reserves of different elements would last at today´s extraction rates. For Cobolt, Niob and Zink we have quite limited resources, but also for Iron because it is used in such large volumes. This concerning mines with relatively high concentration of iron.

3.2 Industrial use and possibilities

We are using 39 kg/capita,y of plastics at average globally. Will there be enough wood to replace fossil fuels for plastic and chemical products production?

We have 260 kg Wood/capita,y available, so principally there should be no problem. The Swedish consumption of plastics and chemicals is 1.2 MWh/capita,y which corresponds to 48 kg plastic and chemicals. To produce this from wood we would need some 75-100 kg wood/capita,y.

Can we replace coal with hydrogen in steel production?

The global steel production today is 1869 Mton/y with use of 3,7 kWh/kg for virgin iron production and 0,44 kWh/kg if recycled assuming recycling rate of 88%. It would be 1,85 kWh/kg if the recycling rate was 50% instead. This means 1869 Mt/y *3.7 MWh/ton iron or 6915 TWh/y. With 0.44 MWh/t it would be 822 TWh/y. Today almost only fossil fuels, especially coal, are used giving huge fossil CO_2 emissions. Approximately 1.9 t CO_2 is emitted per ton steel at average. The total emission then is 1869 Mt/y*1.9 tCO_2/t = 3 551 Mt CO_2/y. The global anthropogeny CO_2 emission is estimated to be 36 000 Mt/y and thus approximately 10% is coming from steel production if all is from virgin iron. If we instead could utilize

Hydrogen for the reduction, we principally need 1 kg H2 to replace 3 kg C (2 H2 +O2 – 2H2O compared to 1 C+ O_2 – 1 CO_2, but 2 H_2 has molar weight 4 while 1 C has molar weight 12. Ratio 12/4=3). 1 kg H_2 demand 58 kWh electricity for the electrolysis today. 3 kg C as coal contain 3*7 kWh/kg = 21 kWh. This means 58/21 = 2.76 times more energy. For virgin iron it would mean 19086 TWh/y but 2270 TWh/y if we use 88% recycled iron. The total annual wind power production is 1430 TWh and thus the energy demand would be 13 times the total annual production of wind assuming only virgin iron, but with 88% recycled iron 1.6 times more than total production. Still, this shows that replacing fossil fuels in steel reduction is less rewarding than replacing fossil fuels in vehicles.

Can use biomass instead, or as a complement for reduction of iron oxide?

For reduction of iron ore (oxides) an alternative is to gasify biomass. Also raw material for bio-diesel and chemicals could be produced from pyrolysis of biomass combined with gasification in CHP plants. Here we then can utilize the reaction heat for district heating/cooling and produce electricity as a balancing production when there is little wind and sun. We probably need at least twice as much biomass for the production, although the rest also will be utilized. This means some 15 500 TWh/y. If we look at the potential biomass production with same productivity as Swedish forests, it means 80900 TWh/y. This means that there should be a good potential to do this also in reality.

What would the impact be on material use and energy demand for transportation if we go for electric vehicles with batteries compared to replacing fossil fuels with biofuels/renewables (including Hydrogen) ?

For transport sector we today have almost all fuels being fossil, 30 200 TWh/y globally. The electric engines are much more efficient so to replace the fossil fuels we demand approximately 25-30% of that energy only. This means that we need 30 200 TWh/y *0,25 = 7 550 TWh electricity to replace the fossil fuels. Here the replacement of fossil fuels with electricity makes much sense! For use of Hydrogen we will need less kWh/km if we use fuel cells with high efficiency. We can expect up to 80% efficiency in the future, but significantly lower today. Even the compression of the hydrogen consumes some 15-20 % of the heating value. So here batteries look better from a system perspective if all materials are recycled at end of life. (Ottorino editor, 2017).

How much resources are we utilizing per capita and what would happen if everyone would have access to same amount of resources as the one spending most, average or least?

Some metals are very common in the earth crust, like iron and aluminum. These are very important for production of machinery, vehicles, and buildings. For others like Cobolt, Niob and Litium we have limited resources. These are important for production of high efficiency motors in wind power plants and for production of Litium ion batteries. When we want to scale up the production of new technologies, we will see either increased price due to limited supply or a transfer to use of other materials or combination of materials. Probably we will se a combination of these.

What is the impact if everything is produced locally compared to a free market where a lot of goods is transported longer or shorter distances?

If we produce most products locally, we will reduce the amount of fossil fuels used for transportation. At the same time the competition will be lowered and thus the prizes higher. This can be seen clearly in Sweden. Before joining EU Sweden was producing most food like meet in Sweden. After joining EU the price on meat was lowered to roughly and thus the import became important and is now approximately 50% of what is consumed (SCB, 2020). For some product like fish fingers long chains are seen, where fish can be taken up in the North Sea. Filets are made in France. These are sent to China where they are cut and covered by bread crisp. After this back again to Europe for packaging and distribution to end customers. It is difficult to claim that one alternative is better than the other generally, but we should act in a rational way. Then different regulations on energy and resources might be a way to direct how we should act.

How would food production look like if we produce much more in our cellars or at the roof in aquatic systems without soil compared to only at farmland? Can insect larvae produced from waste be a new food?

There are several projects going on in many parts of the world to produce vegetables and spices in buildings. One example is Swegreen, who produce vegetables for shops in Stockholm in the cellar of a sky scraper and recently inside a shop in Gothenburg (Swegreen, 2020). Other examples are roof top plantations in New York, Gothenburg, Stockholm and other cities. In Eskilstuna food waste is converted into larvae of Black Soldier Flies. A yield of 30-36 % from waste to larvae has been achieved with high content of protein (40%) and fat (30%) (Lalander et al., 2020). The plan is to use as fish fodder at first, but later also for other animals and possibly also for humans.

To produce meat, consume a lot of fodder for the animals. The Lancet commission (Willet et al., 2019) has concluded that we should reduce the intake of especially red meat significantly, both for health reasons, and to enhance the efficiency from crop to humane use. One kg of beef may consume 19.8 kg of fodder (Lesschen et al., 2011). At the same time cows emit a lot methane, some 135 kg CH_4/cow,y. There are approximately 1000 million cows (Statista, 2020), which means 135 million tons CH_4/y. The global impact then would be 3 375 million CO_2 eq. By absorbing most of this, 85 %, in active coal filters could then reduce emissions by 2 870 million ton CO_2eq/y. At the same time the heating value of the recovered CH_4 would be approximately 1150 TWh/y, all non-fossil biogas!

What is the potential to make more efficient buildings and more efficient industrial processes.

Sun has been utilized to heat buildings since long, but due to poor design there is a much wider potential. By having large windows heating can be achieved during spring and autumn but shaded off during summer to avoid overheating. In the EU project PLEEC, planning of energy efficient cities, good examples of both technologies, behavior changes and also organization of work in cities was reviewed go find best possible methodology for different type of cities (Dahlquist et al, 2015; Kullman et al, 2016). Concerning more efficient industries EU SPIRE program has had several projects on this, where Fudipo can be mentioned. The potential savings for EU process industries is in the range of 300- 500 TWh/y (Dahlquist et al., 2021).

How can we make energy balances where no fossil fuel is used on different levels from regions to countries and globally?

In several articles we have made energy balances for regions, countries and globally. They are presented in e.g. (Dahlquist et al., 2012). The general conclusion is that there are enough resources, but we need to use these in a fair and knowledgeable way. This means use methods guaranteeing biodiversity and a fair distribution of the resources to all humans, but also give animals and crops reasonable conditions for the future.

4 Results an discussion

How can the simulator be used?

In Tables 1-7, we find a lot of basic information: Table 1 shows annual consumption vs total resources for important materials, and in Table 5 consumption of food species. In Table 2, we have key data on population and use per capita for energy use, income and crop production per capita. Table 3 and 4 are energy conversion related while Table 7 shows distribution between different human needs in a high-income country. With the simulator you principally multiply per capita use (X_c) with number of people (Pi) in a region or income group (i). Consumption per capita (Ci) is assumed to be proportional to income in an income group to high income group (Ch). Total consumption for a group (X_t) then is calculated as:

$$Xt = Xc * Pi * Ci/Ch \quad (1)$$

With Y% recycling of materials we can get a net consumption of virgin materials and resources (Xt,r) as:

$$Xt,r = Xt * (1-Y) \quad (2)$$

The global consumption (Xg) then will be for all regions or all income groups (i):

$$Xg = \sum n\ Xt, r, ii \quad (3)$$

What could be mechanisms to drive a society in one direction or the other?

Different economic incentives and regulation, CO_2 tax and similar is one way. Information campaigns and showing good examples another. How different mechanisms have been successful or not can be discussed from a historical perspective. Freons and Montreal protocol was successful, while Kyoto protocol not so successful. In the first case there was principally only one supplier of Freons, Dupont. Then it was easy to push this company. The Kyoto protocol should reduce the use of fossil fuels, where countries like China, the US, Poland and Germany all have strong interests in domestic resources. Then national interests stand against global ones. Sulphur tax versus emission rights on a regional level have both been successful, but in different time scales. Carbon tax in Sweden has been very successful to move over from oil to biomass and a governmental drive for nuclear power replaced half of the major primary energy source oil from 1970 to 1990. This is showing that it is possible to make changes, but it is tough to get everyone “on-board”.

Concerning information campaigns and similar it has not been so successful to really achieve long-lasting changes, although it paves the road for the other regulatory mechanisms, which is important! If good examples can be demonstrated and regulations give the incentive, we can get fast changes like the introduction of wind power and solar power on a large scale last 20 years!

5 Conclusions

There are huge possibilities to make the globe sustainable. In this paper it is shown how different actions could be used. There are mostly several different technical solutions giving the same result and thus it is

best if we can develop several different technologies in parallel and have mechanisms driving towards the primary goal to reduce global warming more general. International regulations and agreements are important. Information and mass-media has an impact, but mostly to give the politicians incentives to "make the right decisions". The simulations in this paper are not strict mathematical but more discussions around different scenarios. It should be noticed that this is an alternative type of simulation that could be utilized more.

References

Chaudhary Awais Salman, Eva Thorin, Konstantinos Kyprianidis, and Anders Avelin. Future directions for CHP plants using biomass and waste – adding production of vehicle fuel and other chemicals SUPEHR19 SUstainable PolyEnergy generation and HaRvesting Volume 1, Savona, Italy, Edited by Sorce, A.; Tucker, D.; Sayma, A.; E3S Web of Conferences, Volume 113, id.01006. Pub Date: September 2019. DOI: 10.1051/e3sconf/201911301006. Bibcode: 2019E3SWC.11301006A

Veneri Ottorino (editor). Technologies and Applications for Smart Charging of Electric and Plug-in Hybrid Vehicles; ISBN 978-3-319-43651-7, by, Springer Verlag, 2017.

E. Dahlquist (editor). Biomass as Energy source: Resources, Systems and Applications. sustainable energy book series, ISSN 2164-0645; 3. P 278. 2013. ISBN 978-0-415-62087-1.

E. Dahlquist and S. Hellstrand. Natural resources available today and in the future: How to perform change management for achieving a sustainable world (pp. 1-304). Springer International Publishing, 2017. https://doi.org/10.1007/978-3-319-54263-8

E. Dahlquist. Nonorganic and fossil resources: Known and estimated resources. In Natural Resources Available Today and in the Future: How to Perform Change Management for Achieving a Sustainable World, pp. 181-205. Springer International Publishing, 2017. https://doi.org/10.1007/978-3-319-54263-8_6

Erik Dahlquist, Javier Campillo, Iana Vassileva, and Lukas Lundström. - Energy efficiency improvements by renovation actions : in Lagersberg and Råbergstorp, Stoke on Trent and Allingsås, 2015. ISBN: 978-91-7485-243-1

Erik Dahlquist, Iana Vassileva, Eva Thorin, and Fredrik Wallin. How to save energy to reach a balance between production and consumption of heat, electricity and fuels for vehicles. Journal Energy (ISSN 0360-5442) 46 (1): 16-20. 2012.

Global number of cows, https://www.statista.com/statistics/263979/global-cattle-population-since-1990/

IPCC Report on Global Climate 2019. https://www.ipcc.ch/site/assets/uploads/2019/11/SRCCL-Full-Report-Compiled-191128.pdf

IRENA. BIOENERGY FROM BOREAL FORESTS Swedish approach to sustainable wood use. https://www.irena.org/-/media/Files/IRENA/Agency/Publication/2019/Mar/IRENA_Swedish_forest_bioenergy_2019.pdf

M. Kullman, J. Campillo, E. Dahlquist, C. Fertner, R. Giffinger, J. Grosse, and J. Haselberger. Note: The PLEEC project-planning for energy efficient cities. Journal of Settlements and Spatial Planning 5: 89-92, 2016. https://doi.org/10.19188/09JSSPSI052016.

C. Lalander, E. Ermolaev, V. Wiklicky, and B. Vinnerås.| Process efficiency and ventilation requirement in black soldier fly larvae composting of substrates with high water content. Science of The Total Environment, 729:138968, 2020. https://doi.org/10.1016/j.scitotenv.2020.138968

A. Larsson, I. Gunnarsson, and F. Tengberg. The GoBiGas Project Demonstration of the production of Biomethane from Biomass via Gasification. Göteborg Energi, 2018. 10.13140/RG.2.2.27352.55043.

J. P. Lesschen, M. van den Berg, H. J. Westhoek, ,H. P. Witzke, and O. Oenemaa: Greenhouse gas emission profiles of European livestock sectors. Animal Feed Science and Technology Volumes 166–167, 23 June 2011, Pages 16-28.

K. MacDicken, Ö. Jonsson, L. Piña, L. Marklund, S. Maulo, V. Contessa, Y. Adikari, M. Garzuglia, E. Lindquist, G. Reams, and R. D'Annunzio. Global Forest Resources Assessment 2015 How are the world's forests changing? FOOD AND AGRICULTURE ORGANIZATION OF THE UNITED NATIONS Rome. Second edition. ISBN 978-92-5-109283-5. 2016.

Madeleiene Martinsen, Erik Dahlquist, and Jinyue Yan: Augmented Reality reducing energy uses and CO_2 emissions. International Conference on Applied Energy 2020. Dec. 1 - Dec. 10, 2020, Bangkok / Virtual Paper ID: 695.

Rodriguez Caballero, Adrian ,Hallin, S , C. Påhlson, and Monica Odlare. Ammonia oxidizing bacterial community composition relates to process performance in wastewater treatment plants under low temperature conditions. Water Science and Technology (ISSN 0273-1223). 65(2): 197-204, 2012.

SCB, Sweden National Statistics https://www.statistikdatabasen.scb.se/pxweb/sv/ssd/ (February 2021)

Skogforsk. https://www.skogforsk.se/cd_20190523090341/contentassets/4b4b423402784d658204a7784723637b/det-svenska-skogsbrukets-klimatpaverkan.pdf, 2019. ISBN: 978-91-88277-08-04.

Swegreen signes agreement with ICA in Gothenburg about local production of crops.

https://www.mynewsdesk.com/se/swegreen-ab/pressreleases/swegreens-odlingstjaenst-tar-plats-paa-ica-focus-i-goeteborg-3026538

Elena Tomas-Aparicio Elena, Jinyue Yan, Konstantinos Kyprianidis, and Bertil Moritz. Comparison between different renewable energy solutions from a materials and CO_2 perspective International Conference on Applied Energy 2020, Dec. 1 - Dec. 10, 2020, Bangkok / Virtual Paper ID: 518.

UN Worldbank database https://data.worldbank.org/indicator, 2021.

Walter Willett, Johan Rockström, Brent Loken, Marco Springmann, Tim Lang, Sonja Vermeulen, Tara Garnett, David Tilman, Fabrice DeClerck, Amanda Wood, Malin Jonell, Michael Clark, Line J Gordon, Jessica Fanzo, Corinna Hawkes, Rami Zurayk, Juan A Rivera, Wim De Vries, Lindiwe Majele Sibanda, Ashkan Afshin, AbhishekChaudhary, Mario Herrero, Rina Agustina, Francesco Branca, Anna Lartey, Shenggen Fan, Beatrice Crona, Elizabeth Fox, Victoria Bignet, Max Troell, Therese Lindahl, Sudhvir Singh, Sarah E Cornell, K Srinath Reddy, Sunita Narain, Sania Nishtar, Christopher J L MurrayFood in the Anthropocene: the EAT–Lancet Commission on healthy diets from sustainable food systems. ww.thelancet.com. Vol 393, February 2, 2019.

Variable selection and grouping for large-scale data-driven modelling

Esko K. Juuso

Control Engineering, Environmental and Chemical Engineering, Faculty of Technology,
University of Oulu,Finland
esko.juuso@oulu.fi

Abstract

For large-scale systems, the number of possible variable combinations becomes very large. Variable grouping means finding feasible groups of variables for modelling. Systems can be divided into subsystems but even then the number of available variables is often impractically high to be used with the data-based methods. Interactive variable selection and grouping by comparing the performance of the model alternatives is a good solution if there are not too many variables. This paper describes possibilities of variable selection in large-scale industrial systems. It classifies the variable selection and grouping into four categories: knowledge-based grouping, grouping with data analysis, decomposition, and model-based grouping and selection. The data analysis part consists of correlation analysis and handling of high dimension data with principal components. These originally linear methodologies were extended to nonlinear systems by using the nonlinear scaling approach. Decomposition can be realised with various clustering methods or learning with case-based reasoning. The multimodel systems are handled with fuzzy set systems. Numerous studies based on linear multivariate statistical modelling have been reported in literature. The methodologies approaches have been tested in several applications: bioprocesses, continuous brewing, condition monitoring, web break sensitivity analysis and wastewater treatment. Industrial process data, a pilot system and a test rig were used in the analysis. Uncertainty handling is a part of the analysis method: uncertainty is represented with the degrees of membership.

Keywords: variable selection and grouping, data analysis, intelligent methods, data-driven modelling

1 Introduction

Data-driven modelling always requires variable grouping and selection. In small systems, expert knowledge gives a clear basis for the variable selection since possible interactions and causal effects are known fairly well. For these cases, few modelling alternatives can be compared interactively. Variable selection becomes important when the number of variables increases, especially when normal process data is used. In large-scale systems, the number of possible variable combinations becomes easily very large (Figure 1), This rapidly increasing number of combinations, known as the combinatorial explosion (Pyle, 1999), can easily defeat even powerful computers.

In big data processing, the analysis is even more challenging (Hashem et al., 2015). The amount of different types of data generated from different sources is increasing fast. Discovering hidden values from these large heterogeneous datasets requires versatile methodologies (Juuso, 2020a). Neural deep learning methods provide highly complex structures (Schmidhuber, 2015) but because of a huge set of parameters they are not easy to assess with expert knowledge.

The model assessment becomes easier through the better process insight provided by the modules based on analyzed variable groups. Already, the development and tuning require that the models should not include too many variables. In practical cases, variable selection is necessary either because it is computationally infeasible to use all available variables, or when limited data samples have numerous variables. Finding feasible groups and combinations of variables for modelling is closely connected with data clustering since the interactions can depend on the operating area. Variable selection, also known as subset selection or feature selection, is a process commonly used in machine learning, wherein a subset of the features available from the data are selected for application of a learning algorithm.

Systems can be divided into subsystems but even the number of available variables is often impractically high to be used with the data-based methods. Interactive variable selection and grouping by comparing the performance of the model alternatives is a good solution if there are not too many variables. This approach can be extended to a wider set of variables by evolutionary computation. As the number of variables becomes too big even for these methods, the number of alternatives must be reduced before model development.

There is a lot of literature on both the model and data-based techniques. Spectroscopic data, multi-sensor systems, multivariate analysis and modelling of large-scale systems seem to require efficient methods for variable selection. A large number of different methods have also been used in process monitoring (Venkatasubramanian et al., 2003). Commonly used data-based monitoring methods are reviewed in (Vermasvuori, 2006). Partitioning-based clustering algorithms are compared in

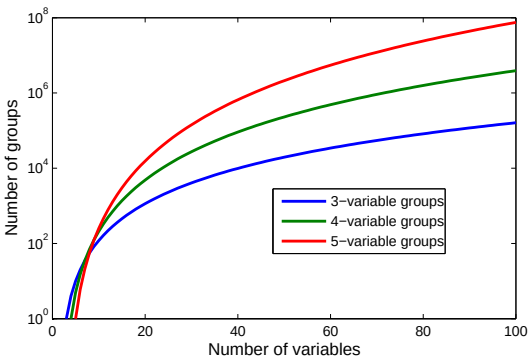

Figure 1. Variable combinations (Juuso and Ahola, 2008).

(Äyrämö and Kärkkäinen, 2006). A literature review of inference and decision making methods in fault diagnosis is presented in (Cheng, 2006).

The final selection and grouping step is based on modelling. Multivariate statistical modelling and structural relationships are widely used. In linguistic equation (LE) models, nonlinear scaling is used together with one or more linear equations (Juuso, 2004). Equations can be generated for all the combinations, e.g. three-variable combinations, or selected combinations. Selected combinations can be constructed also for several groups of variables by generating all the combinations within each variable group. The set of variable groups may also contain groups with different number of variables. For small systems, these groups can be defined manually. Non-informative groups can be removed manually but the variable selection need to be partially automated for large-scale systems.

This paper focuses on the methodologies of variable selection for large-scale modelling. The analysis starts with knowledge-based methods (Section 2) before going to data-based grouping (Section 3). Decomposition is needed for more complex structures (Section 4). The selection and grouping are finalized with modelling (Section 5). Several applications are discussed in Section 6. The classification of methodologies is discussed in Section 7. Conclusions and future studies are presented in Section 8.

2 Knowledge-based variable grouping

Knowledge-based information is essential for all types of variable selection and grouping. For small systems, only expert knowledge is needed. In large-scale systems, expertise is used for selecting variable combinations which should be avoided, e.g. calculated variables should not be used together with the variables used in calculating them. This is important if indirect measurements are used. A group containing a controlled variable and its set point is not usually appropriate. These problems are avoided by defining the inappropriate groups as non-groups, i.e. as variable groups which should not be a part of any acceptable variable group.

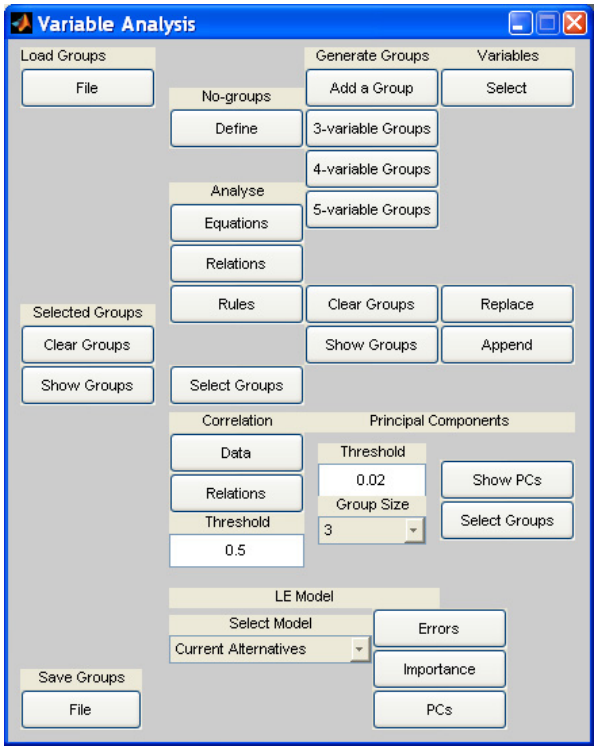

Figure 2. Variable selection (Juuso et al., 2008).

Too few variables mean that models cannot capture the phenomena. Too many variables may cause overfitting and models which are difficult to understand and evaluate. This is especially important for frequency range analysis. Redundancy, i.e. practically the same measurement is obtained by several sensors, the measurements can be combined as a weighted sum. However, sensor failures must be taken into account in real-time applications.

Knowledge-based information can effect in many ways on the variable grouping, which reduces strongly the variable combinations. For large-scale systems, some variables are suitable for the system decomposition and some for developing specialized models. The working point variables, which are used for defining different operating areas, are not necessarily in the corresponding specialized models. The specialized models can be totally different in different operating conditions.

Each equation has normally from three to five variables, and the FuzzEqu Toolbox (Juuso, 2000) is designed for analyzing these variable groups (Figure 2). The generation of the alternatives is based on three variable groups: one variable is selected to be in all four variable groups, and two variables are selected to be in all five variable groups.

The interactive variable grouping shown in Figure 2 can be used as a tool in learning the system. Three variable groups are the basic elements. The subsets of the variables and the important variables in the four and five variable groups can be based on process knowledge. This analysis already reduces the number of alternatives with 70 percent (Juuso et al., 2008).

3 Grouping with data analysis

Correlation analysis provides methods for pruning variables. Principal component analysis (PCA) is a well-known method for variable selection in large data sets. PCA explains variations within one data set.

3.1 Correlation analysis

Correlation coefficients are indicators of the strength of the linear relationship between two variables. The most common coefficient is called Pearson's product-moment correlation coefficient (Ranta et al., 1999; Karttunen, 1994). Statistical correlations are not indications of real causal interactions. Statistical reasoning based on correlation coefficients presumes bivariate normal distribution between variables (Ranta et al., 1999). This assumption is fairly seldom true in process data.

Binary correlations and their combinations are used for pruning the set of acceptable groups defined by domain expertise (Section 2). For forecasting models, input variables should have high correlation to the output variable but low correlation between each other. For case detection, this requirement is not necessary (Section 3.3).

Low correlation may be caused by noise and observation errors. The result is improved by using appropriate filtering and correct time delays between the variables. Moving averages, medians or value ranges have time delays which depend on the calculation window and the applied methodology.

3.2 Correlations in nonlinear systems

For the nonlinear systems, basic correlation analysis and rank correlation methods like Spearman rank correlation coefficients and Kendall rank correlation coefficient do not give reliable results although Spearman correlation coefficient can sometimes identify also nonlinear interaction between variables (Ranta et al., 1999).

There are extensions of the analysis to nonlinear systems (Juuso et al., 2008). A nonlinear correlation of a binary relationship can be implemented for example by using time sequential joint transfer correlation (JTC), morphological correlation (MC) and sliced orthogonal nonlinear generalized decomposition (SONG) (Oton et al., 2005). A weighted SONG (WSONG) correlation has been presented in (Garcia-Martinez et al., 2002). The WSONG correlation is based on the sum of many linear correlations between binary images.

The nonlinear scaling brings measurements and features to the same scale by using monotonously increasing scaling functions $x_j = f(X_j)$ where x_j is the variable and X_j the corresponding scaled variable. The function $f()$ consist of two second order polynomials, one for the negative values of X_j and one for the positive values, respectively. The corresponding inverse functions $X_j = f^{-1}(x_j)$ based on square root functions are used for scaling to the range [-2, 2], denoted as linguistification. The monotonous functions allow scaling back to the real values by using the function $f()$. (Juuso, 2004)

The nonlinear scaling functions are developed by using central tendencies, statistical dispersion and shape of the data distribution. The data-based method for developing the scaling functions is presented in (Juuso and Lahdelma, 2010). Nonlinear models can be developed by using these scaled values and linear relationships. This approach extends the correlation analysis for curvilinear relationships.

3.3 Correlations in variable groups

For the multivariable correlation, Kendall's coefficient of concordance is a measure of agreement among raters is often used (Ranta et al., 1999). It is based on the rank values of observations. In variable group correlation analysis, the scaled values of variables are used and the evaluation of interaction is based on multivariate regression.

Combinations of the binary correlation coefficients are used in the FuzzEqu Toolbox. The methodology depends on the model type. For forecasting models, the correlations between the input variables should be low, and each input variable and the output variable should have high correlation. For detecting operating conditions, there are not necessarily any output variable, i.e. also groups where several variables have high correlation between each other are acceptable. Both alternative approaches are used for variable grouping for the detection of operating conditions.

3.4 High-dimensional data

Principal component analysis (PCA) is a data reduction method using mathematical techniques to identify patterns in a data matrix. The principal components are a small set of new orthogonal, i.e. non-correlated, variables derived from a linear combination of the original variables. They do not necessarily have any meaning as they are combinations of initial variables. However, these new axes provide the angles to see the data by representing the directions of the data which explain a maximal amount of variance.

The main element of this approach consists of the construction of PCAs which compres the data by reducing the number of dimensions with minor losses of information. Each principal component is a linear combination of the original variables.

The full set is as large as the original set of variables but it is common that the sum of the variances of the first few principal components to exceed 80 percent of the total variance of the original data. All the principal components are orthogonal to each other so there is no redundant information. The plots of these new variables help to understand the driving forces of the system.

Principal components can be used In data-based process monitoring by tracking how well the data points are explained with the PCA model (Vermasvuori, 2006).

Testing of loadings and their estimated standard uncertainties are used to calculate significance on each variable for each component (Westad et al., 2003). Variable selection can also mean identifying a k-subset of a set of

original variables that is optimal for a given criterion that adequately approximates the whole data set (Cadima et al., 2004).

The static PCA can be extended to dynamic systems by using several past measurements. The number of the lagged variables is selected in tuning (Ku et al., 1995; Li and Qin, 2001; Vanhatalo et al., 2017). Another variant is moving PCA developed by (Kano et al., 2001) for detecting changes in operating conditions. A special multiway approach has been developed for analyzing variations from the normal trajectories in batch processes (Nomikos and MacGregor, 1994). Multiscale PCA combines PCA with wavelet decompositions (Bakshi, 1998; Aminghafari and Cheze, 2006).

PCA is a linear method, which does not produce accurate results for nonlinear processes. Linguistic principal component analysis (LPC) extends the linear combinations for nonlinear systems by combining the nonlinear scaling with PCA. In the FuzzEqu Toolbox, the scaling functions can be used also for the normal principal components.

4 Decomposition

A modelling problem can be divided into smaller parts by developing separate models for independent subprocesses. In addition to spatial or logical blocks decomposed modelling can be based on different frequency ranges. Different operating conditions can be detected with cluster analysis, model-based reasoning, rule-based reasoning, or learned with case-based reasoning. Fuzzy set systems provide feasible techniques for handling the resulting partially overlapping models.

4.1 Clustering

Clustering consists of partitioning a data set into subsets (clusters), so that the data in each subset share common similarities or proximities for some defined distance measures. Cluster analysis, also called segmentation analysis or taxonomy analysis, is a way to create groups of objects, or clusters, in such a way that the profiles of objects in the same cluster are very similar and the profiles of objects in different clusters are quite distinct. Similarity criteria (distance based, associative, correlative, probabilistic) among the several clusters facilitate the recognition of patterns and reveal otherwise hidden structures.

- Hierarchical clustering groups data, simultaneously over a variety of scales, by creating a cluster tree. The tree is not a single set of clusters, but rather a multi-level hierarchy, where clusters at one level are joined as clusters at the next higher level. Hierarchical clustering produce a set of solutions with different numbers of clusters. The level or scale of clustering is chosen according to the application.

- Partitioning-based clustering algorithms minimize a given clustering criterion by iteratively relocating data points between clusters until a (locally) optimal partition is attained. In a basic iterative algorithm, such as K-means- or K-medoids, convergence is local and the globally optimal solution can not be guaranteed. (Äyrämö and Kärkkäinen, 2006) The fuzzy c-means algorithm imposes a spherical shape on the clusters, regardless of the actual data distribution (Babuška, 1998).

- Fuzzy clustering -based clustering algorithms minimize a given clustering criterion by iteratively relocating data points between clusters until a (locally) optimal partition is attained (Bezdek, 1981). In a basic iterative algorithm, such as K-means- or K-medoids, convergence is local and the globally optimal solution can not be guaranteed. (Äyrämö and Kärkkäinen, 2006)

- Neural computing can be used for clustering. Self-organising maps (SOM) (Kohonen, 1995) can be used for finding operating conditions or simply for clustering. Also radial basis networks (Chen et al., 1991) combine clustering with models.

- Nonlinear clustering is aimed to detect clusters of different geometrical shapes. (Gustafson and Kessel, 1979) extended the standard fuzzy c-means algorithm for this. The nonlinear scaling extends the clustering methods to different shapes.

- Robust clustering uses spatial medians to reduce effects of erroneous and missing values (Äyrämö and Kärkkäinen, 2006).

4.2 Reasoning

Decision making between different operating conditions is based on different types of reasoning. These methods can also be considered as inference fault diagnosis methods (Cheng, 2006).

Model-based reasoning. Causal directed graphs represent physical cause-effect relations between variables. Fault tree analysis provides graphical models of the pathways within a system that interconnect the basic cause events and conditions using standard symbols, and lead to a foreseeable, critical event. Bayesian networks represents probability relations among random variables as a graphical model to be used in probability inference.

Rule-based reasoning. Rule-based systems use IF-THEN rules representing domain expertise. Inference methods are data-driven forward chaining and goal-driven backward chaining. Conflict resolution is applied to select one rule out of the active ones. Preferences and priorities may be utilized in the conflict resolution. Fuzzy logic provides feasible solutions for resolving the conflicts and handling the uncertainty.

Case-based reasoning. Case-based reasoning (CBR) is a problem solving paradigm for finding out the solution to a new problem by remembering previous similar situations and by reusing information and knowledge of that situation (Aamodt and Plaza, 1994). The solutions are maintained in carefully indexed memory. The case base containing the previous cases with possible general knowledge of the problem area and the problem solving starts with the identification of the current problem situation (Figure 3). With information on new cases, the most similar case is retrieved from the case base. The retrieved case is reused to solve the current problem. During the revise step the suggested solution is evaluated to get the confirmed solution. Finally, the useful solutions with related case information are retained as new learned cases to the case base.

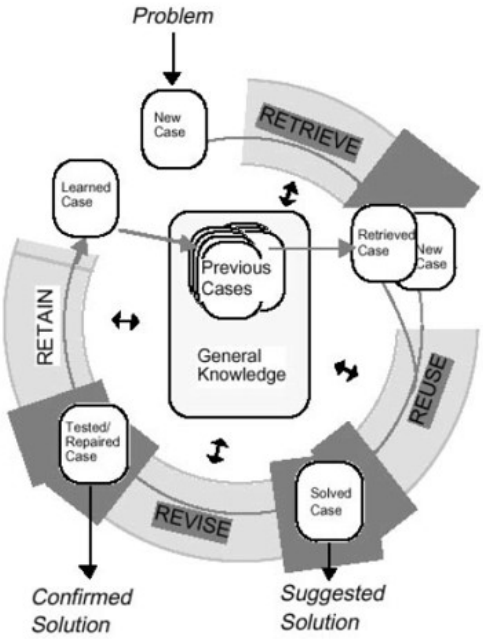

Figure 3. Case-based reasoning (CBR) (Aamodt and Plaza, 1994).

5 Model-based selection and grouping

Multivariate statistical tools are used for analyzing data matrices with regression and/or pattern recognition techniques. These methodologies are primarily linear. Nonlinear systems can be handled with fuzzy set systems, artificial neural networks or their combinations. In LE models, linear methodologies are combined with the nonlinear scaling discussed in Section 3.2.

Multivariate statistical modelling. The application of principal component regression (PCR) to the trajectories of the process variables (block-wise PCR) has given straightforward results without requiring a deep knowledge of the process (Zarzo and Ferrer, 2004). Partial least squares (PLS), also known as projection to latent structures, is a robust multivariate generalized regression method using projections to summarize multitudes of potentially collinear variables (Gerlach et al., 1979).

Fuzzy set systems. Different types of fuzzy set systems have been compared in (Juuso, 2004). Prior knowledge can be used in constructing rule-based fuzzy models: qualitative knowledge can be incorporated in linguistic fuzzy models (Driankov et al., 1993), or in fuzzy relational models if there are several alternative rules (Pedrycz, 1984); locally valid linear models can be collected by Takagi-Sugeno (TS) fuzzy models (Takagi and Sugeno, 1985).

Artificial neural networks. Artificial neural networks (ANNs) are commonly used in modelling of large scale systems. ANNs are nonlinear and aimed for strongly nonlinear systems. Multilayer perceptrons (MLPs) are supervised feedforward networks, which are mainly used for approximating nonlinear behaviour. Another popular network, the self-organising map (SOM) (Kohonen, 1995) based on unsupervised competitive learning, can be considered as a clustering method (Section 4.1). Radial basis networks (Chen et al., 1991) provide an interesting alternative as they can be used both as a clustering tool and a modelling tool.

Neurofuzzy methods. Neurofuzzy methods provide various techniques for generating fuzzy set systems, e.g. ANFIS method (Adaptive-Network-based Fuzzy Inference Systems) is a well-known neurofuzzy method which is suitable for tuning of membership functions (Jang, 1993). Partitioning clustering is used in this tuning (Section 4.1).

Linguistic equations. The nonlinear scaling transforms the nonlinear problem to a linear one. A LE model with several equations is represented as a matrix equation

$$AX + B = 0, \tag{1}$$

where the interaction matrix A contains all coefficients A_{ij} and the bias vector B all bias terms B_i. Each equation has from two to five variables.

6 Application cases

The variable selection and grouping methods described above have been tested in several applications.

Bioprocesses. Batch bioprocesses are difficult to model due to strong nonlinearities, dynamic behaviour, lack of complete understanding and unpredictable disturbances. The fed-batch fermentation model has three growth phases, each including three interactive models.A decision system based on fuzzy logic to provide smooth gradual changes between phases. (Juuso, 2019)

Continuous brewing. Brewing is based on ethanol fermentation but the most important aim is a balanced flavour

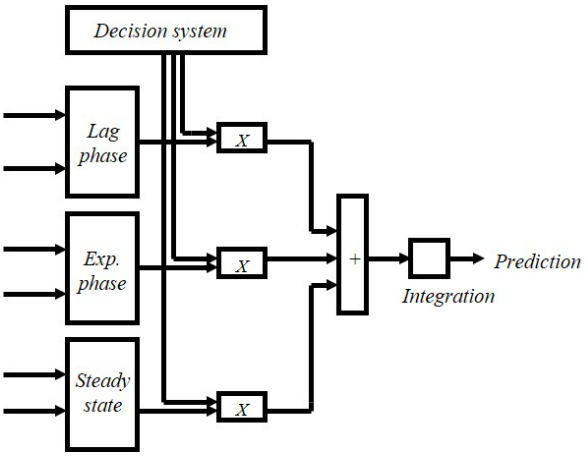

Figure 4. Subprocesses with interactions (Juuso, 2008).

not the highest possible ethanol yield. The desired traditional flavour is based on a balance of numerous compounds. Experiments with immobilized yeast were carried out in a pilot scale. The LE models were generated for five variable groups, each group contains two of the three control variables (air, CO_2 and flow) and three flavour compounds or attenuation. Fluctuations from the normal operation are detected to warn process operators. (Juuso and Kronlöf, 2005).

Condition monitoring. Reliability of operation, high quality, safety and environmental issues are increasingly important and machine condition monitoring enables reliable and economical way of action. Overhaul before a breakdown is in many cases more effective than run to failure. The earlier model-based approach discussed in (Juuso et al., 2008) was an interesting case for variable selection and grouping. New features and indicators have completely changed in this application. The methodologies have been tested in test rigs and industrial processes. (Juuso, 2017).

Paper machine. The ambition to increase the production of paper has made the paper machine runnability important. The paper web breaks when the strain on it is greater than the strength of paper. The machine can be run at the desired speed with the least possible number of breaks if the runnability is good. The web break sensitivity indicator was developed as a CBR application which combines LE models and fuzzy logic (Juuso et al., 1998; Ahola et al., 2003). The analyses are based on the online process data. There are several runnability categories, each including several case models defined by several equations based on up to five scaled variables. The final selection of the active cases, corresponding categories and the value of the break sensitivity are obtained by fuzzy logic (Juuso and Ahola, 2008).

Wastewater treatment. In the biological wastewater treatment, the model consists of three interactive models (Figure 5): the biomass quality obtained in Model B has a

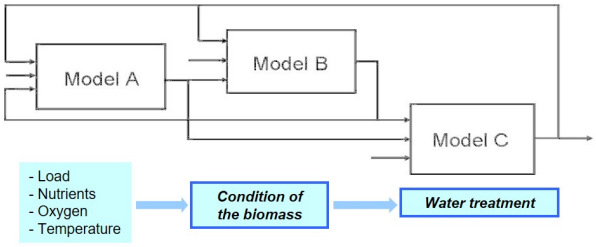

Figure 5. Subprocesses with interactions (Juuso, 2009).

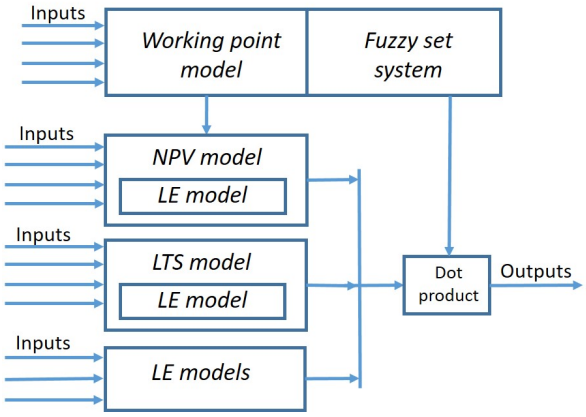

Figure 6. Multimodel LE system with a fuzzy decision module (Juuso, 2020b).

strong effect on the treatment (Model C). In Model A, the effects of the incoming wastewater and return sludge are combined. The chemical oxygen demand (COD) and suspended solids are used in the calculations. Nutrients, oxygen and temperature effect on both the biomass (Model B) and operating conditions Model C. The condition of the biomass has a key effect on the treatment performance (Juuso, 2009). Long periods of high load reduce the biomass quality which deteriorates the treatment performance and it takes time to get the good performance back.

7 Discussion

Variable selection was in all cases started with manual methods, continued with data analysis, and the final variable selection is based on generated alternative interactions assessed with domain expertise. The automatic analysis has several phases and alternative approaches. Correlation analysis is used for selecting interesting groups from the acceptable groups and principal components extend this analysis to the high dimensional systems. Several clustering methods are used for dividing the data sets into different operating areas. The nonlinear scaling provides new possibilities for these analysis methods as an essential part of the model-based analysis of interactions.

In these cases, the submodels are based on LE models Smooth operation and high quality products are the main goals of all these applications, and this can be achieved

by combining the LE models with fuzzy logic. Parametric LE models can make the model structure very compact (Figure 6). For diagnostics, the degree of membership calculated for the normal operation is a good indicator. This was used for the brewing case. The memberships of different faults are used in the condition monitoring. In the paper machine case, the case structure is highly complicated.

The data-based grouping provide high performance solutions but the phases, cases and interactions between models reduce the automatic analysis to the submodels. Also, the indirect measurements based on a set of measurements needs to be analyzed separately. New indicators can combine several measurements and several new features can be developed from individual signals. These case types which require decomposition are challenging for machine learning.

8 Conclusions and future studies

Variable selection and grouping are an essential part in the developing model-based applications. Domain expertise is used for removing useless combinations of variables. Data-based methods are divided into three classes: data analysis, decomposition and modelling. The model-based analysis is the final step. The originally linear methodologies were extended to nonlinear systems by using the nonlinear scaling approach. Applications are based on integrated approaches which combine all the techniques. The presented classification of methodologies was successfully used in the case studies.

Future studies are needed for applying these methodologies iteratively for the expanding heterogeneous data available in big data.

References

A. Aamodt and E. Plaza. Case-based reasoning: Foundational issues, methodological variations and system approaches. *AICom - Artifical Intelligence Communications*, 7(1):39–59, 1994.

T. Ahola, H. Kumpula, and E. Juuso. Case based prediction of paper web break sensitivity. In *Proceedings of Eunite 2003 - European Symposium on Intelligent Technologies, Hybrid Systems and their implementation on Smart Adaptive Systems, July 10-11, 2003, Oulu, Finland*, pages 161–167. Wissenschaftsverlag Mainz, Aachen, 2003.

Mina Aminghafari and Nathalie Cheze. Multivariate denoising using wavelets and principal component analysis. *Computational Statistics & Data Analysis*, 50:2381–2398, 2006.

S. Äyrämö and T. Kärkkäinen. Introduction to partitioning-based clustering methods with a robust example. Reports of the Department of Mathematical Information Technology Series C. University of Jyväskylä, Software and Computational Engineering No. C. 1/2006. Jyväskylä, 2006.

R. Babuška. *Fuzzy Modeling and Identification*. Kluwer Academic Publisher, Boston, 1998.

B. Bakshi. Multiscale PCA with application to multivariate statistical process monitoring. *AIChE Journal*, 44:1596–1610, 1998.

J. C. Bezdek. *Pattern Recognition with Fuzzy Objective Function*. Plenum Press, New York, 1981.

J. Cadima, J. Orestes Cerdeira, and M. Minhoto. Computational aspects of algorithms for variable selection in the context of principal components. *Computational Statistics & Data Analysis*, 47(2):225–236, 2004.

S. Chen, C.F.N. Cowan, and P. M. Grant. Orthogonal least squares learning algorithm for radial basis function networks. *IEEE Transactions on Neural Networks*, 2(2):302–309, 1991.

H. Cheng. Inference and decision making methods in fault diagnosis. A literature review. Helsinki University of Technology, Laboratory of Process Control and Automation. no. 9. Espoo, 2006.

D. Driankov, H. Hellendoorn, and M. Reinfrank. *An Introduction to Fuzzy Control*. Springer, Berlin, Germany, 1993.

P. Garcia-Martinez, M. Tejera, C. Ferreira, D. Lefebve, and H. H. Arsenault. Optical implementation of the weighted sliced orthogonal nonlinear generalized correlation for nonuniform illumination conditions. *Applied Optics*, 41 (32):6867–6873, 2002.

R. W. Gerlach, B. R. Kowalski, and H. O. A. Wold. Partial least squares modelling with latent variables. *Anal. Chim. Acta*, 112(4):417–421, 1979.

D. E. Gustafson and W. C. Kessel. Fuzzy clustering with a fuzzy covariance matrix. In *Proceedings of IEEE CDC, San Diego, CA, USA*, pages 761–766. IEEE Press, 1979.

I.A.T. Hashem, I. Yaqoob, N.B. Anuar, S. Mokhtar, A. Gani, and S. Ullah Khan. The rise of "big data" on cloud computing: Review and open research issues. *Information Systems*, 47: 98–115, 2015. doi:10.1016/j.is.2014.07.006.

J.-S. R. Jang. ANFIS: Adaptive-Network-based Fuzzy Inference Systems. *IEEE Transactions on Systems, Man, and Cybernetics*, 23(3):665–685, 1993.

E. Juuso and S. Lahdelma. Intelligent scaling of features in fault diagnosis. In *7th International Conference on Condition Monitoring and Machinery Failure Prevention Technologies, CM 2010 - MFPT 2010, 22-24 June 2010, Stratford-upon-Avon, UK*, volume 2, pages 1358–1372, 2010. URL `www.scopus.com`.

E. Juuso, T. Ahola, K. Oinonen, and K. Leiviskä. Web break sensitivity indicator for a paper machine. In H.-J. Zimmermann, editor, *Proceedings of the 6th European Congress on Intelligent Techniques & Soft Computing -EUFIT'98, Aachen, September 7 - 10, 1998*, volume 3, pages 1549–1553, Aachen, 1998. Mainz.

E. Juuso, T. Ahola, and K. Leiviskä. *Variable selction and grouping. Report A 36, August 2008.* Control Engineering Laboratory, University of Oulu, Oulu, 2008.

E. K. Juuso. Linguistic equations for data analysis: FuzzEqu toolbox. In L. Yliniemi and E. Juuso, editors, *Proceedings of TOOLMET 2000 Symposium - Tool Environments and Development Methods for Intelligent Systems, Oulu, April 13-14, 2000*, pages 212–226, Oulu, 2000. Oulun yliopistopaino.

E. K. Juuso. Integration of intelligent systems in development of smart adaptive systems. *International Journal of Approximate Reasoning*, 35(3):307–337, 2004. doi:10.1016/j.ijar.2003.08.008.

E. K. Juuso. Intelligent dynamic simulation of a fed-batch enzyme fermentation process. In *Tenth International Conference on Computer Modelling and Simulation, EUROSIM/UKSim, Cambridge, UK, April 13, 2008.*, pages 301–306. The Institute of Electrical and Electronics Engineers IEEE, 2008. doi:10.1109/UKSIM.2008.133.

E. K. Juuso. Hybrid models in dynamic simulation of a biological water treatment process. In J. Kunovský, P. Hanácek, F. Zboril, Al-Dabass, and A. Abraham, editors, *Proceedings First International Conference on Computational Intelligence, Modelling and Simulation, 7- 9 September 2009, Brno, Czech Republik*, pages 30–35. IEEE Computer Society, 2009. doi:10.1109/CSSim.2009.52.

E. K. Juuso. Intelligent performance analysis with a natural language interface. *Management Systems in Production Engineering*, 25(3):168–175, 2017. doi:10.1515/mspe-2017-0025.

E. K. Juuso. Intelligent dynamic simulation of fed-batch fermentation processes. In E. Dahlquist, E. Juuso, B. Lie, and L. Eriksson, editors, *Proceedings of The 60th Conference on Simulation and Modelling (SIMS 60), 13-16, 2019, Västerås, Sweden*, number 170 in Linköping Electronic Conference Proceedings, pages 132–138. Linköping University Electronic Press, Linköpings universitet, 2019. doi:10.3384/ecp20170132.

E. K. Juuso. Expertise and uncertainty processing with nonlinear scaling and fuzzy systems for automation. *Open Engineering*, 10(1):712–720, 2020a. doi:10.1515/eng-2020-0080.

E. K. Juuso. Intelligent methodologies in recursive data-based modelling. In E. Juuso, B. Lie, E. Dahlquist, and J. Ruuska, editors, *Proceedings of The 61st Conference on Simulation and Modelling (SIMS 61), 22-24, 2020, Virtual Conference, Finland*, number 176 in Linköping Electronic Conference Proceedings, pages 466–474. Linköping University Electronic Press, Linköpings universitet, 2020b. doi:10.3384/ecp20176466.

E. K. Juuso and T. Ahola. Case-based detection of operating conditions in complex nonlinear systems. *IFAC Proceedings Volumes*, 41(2):11142–11147, 2008. doi:10.3182/20080706-5-KR-1001.01888.

E. K. Juuso and J. Kronlöf. Model-based monitoring of immobilized yeast fermentation using fuzzy logic and linguistic equations. *IFAC Proceedings Volumes*, 38(1):97–102, 2005. doi:10.3182/20050703-6-CZ-1902.02220.

M. Kano, S. Hasebe, I. Hashimoto, and H. Ohno. A new multivariate statistical process monitoring method using principal component analysis. *Computers and Chemical Engineering*, 20:1103–1113, 2001.

H. Karttunen. *Datan käsittely*. CSC-Tieteellinen laskenta, Yliopistopaino, Helsinki, 1994.

T. Kohonen. *Self-Organizing Maps*. Springer, Berlin, 1995.

W. Ku, R. Storer, and C. Georgakis. Disturbance detection and isolation by dynamic principal components. *Chemometrics and Intelligent Laboratory Systems*, 30:179–196, 1995.

W. Li and S. Qin. Consistent dynamic PCA based on errors-in-variables subspace identification. *Journal of Process Control*, 11:661–678, 2001.

P. Nomikos and J. MacGregor. Monitoring batch processes using multiway principal component analysis. *AIChE Journal*, 40 (8):1361–1375, 1994.

J. Oton, P. Garcia-Martinez, I. Moreno, and J. Garcia. Phase joint transform sequential correlator for nonlinear binary correlations. *Optical Communications*, 245:113–124, 2005.

W. Pedrycz. An identification algorithm in fuzzy relational systems. *Fuzzy Sets and Systems*, 13(2):153–167, 1984.

D. Pyle. *Data preparation for data mining*. Morgan Kaufmann Publishers, San Francisco, 1999.

E. Ranta, H. Rita, and J. Kouki. *Biometria – Tilastotiedettä ekologeille*. Yliopistopaino, Helsinki, 1999.

J. Schmidhuber. Deep learning in neural networks: An overview. *Neural Networks*, 61 (Supplement C):85 – 117, 2015. ISSN 0893-6080. doi:https://doi.org/10.1016/j.neunet.2014.09.003. URL `http://www.sciencedirect.com/science/article/pii/S0893608014002135`.

T. Takagi and M. Sugeno. Fuzzy identification of systems and its applications to modeling and control. *IEEE Transactions on Systems, Man, and Cybernetics*, 15(1):116–132, 1985.

Erik Vanhatalo, Murat Kulahci, and Bjarne Bergquist. On the structure of dynamic principal component analysis used in statistical process monitoring. *Chemometrics and Intelligent Laboratory Systems*, 167:1–11, 2017. doi:10.1016/j.chemolab.2017.05.016.

V. Venkatasubramanian, R. Rengaswamy, K. Yin, and S. N. Kavuri. A review of process fault detection and diagnosis part i: Quantitative model-based methods. *Computers and Chemical Engineering*, 27:293–311, 2003.

M. Vermasvuori. Data-based methods and prior knowledge in process monitoring. A literature review. Helsinki University of Technology, Laboratory of Process Control and Automation. Report series no. 10. Espoo, 2006.

F. Westad, M. Hersleth, P. Lea, and H. Martens. Variable selection in PCA in sensory descriptive and consumer data. *Food Quality and Preference*, 14(5-6):463–472, 2003.

M. Zarzo and A Ferrer. Batch process diagnosis: PLS with variable selection versus block-wise PCR. *Chemometrics and Intelligent Laboratory Systems*, 73(1):15–27, 2004.

Dynamic Modelling and Simulation of Raw Meal Calcination for Isothermal Boundary Conditions

Lars-André Tokheim

Department of Process, Energy and Environmental Technology, University of South-Eastern Norway, Norway, {lars.a.tokheim@usn.no}@usn.no

Abstract

This article describes modelling and simulation of heating and calcination of raw meal particles. The purpose is to determine the time required to obtain a certain calcination degree for particles that are exposed to surroundings with a specified temperature. The impact of applying different reactor temperature values and different particle sizes is investigated. The aggregated calcination degree as a function of time is calculated for a typical raw meal with a specified particle size distribution and with different contents of $CaCO_3$ in different size classes. The developed model can be used as a basis for determining the required size of potential new calciner reactor types.

Keywords: Raw meal, Heat transfer, Calcination, Particle size distribution

1 Introduction

Raw meal is a finely ground mixture of solid materials used as the main feed in modern cement kilns. It usually contains 75-80 wt% calcium carbonate, $CaCO_3$. The rest is a mixture of mainly SiO_2, Al_2O_3 and Fe_2O_3 as well as some MgO, K_2O and Na_2O (Duda, 1985).

One of the key reactions occurring in the kiln system is calcination, in which the calcium carbonate decomposes into calcium oxide and carbon dioxide; $CaCO_3(s) \rightarrow CaO(s) + CO_2(g)$. This is an endothermic reaction that needs a temperature of around 900 °C to occur. After completion of calcination, further heating and partly melting of the solid material will take place. However, during the calcination process, which is the focus in this article, the other components in the meal (SiO_2, Al_2O_3, etc.) can be considered inert.

In a modern cement kiln system, the decarbonation reaction will be done in a separate calcination reactor. In the calciner, the particles are exposed to high temperature surroundings in the form of heat transfer surfaces, flames and hot combustion gases. Thermal radiation, convection and conduction all contribute in the heat transfer process.

Most calciners operate in the pneumatic conveying regime (Tokheim, 1999), i.e., the particles are vertically entrained by hot gases while being calcined. Such calciners typically have a gas residence time of 2-6 seconds, whereas the particle residence time may be several times longer due to internal recycling of particles inside the calciner. A long residence time is particularly important in cases where lumpy alternative fuels are to be utilized (Tokheim, 2006). The particle calcination process will benefit from a long residence time, meaning that a lower calcination temperature may be used.

Other types of calciners, operating in other regimes, for example bubbling fluidized bed (BFB) calciners (Samani et al., 2020) or drop tube calciners (Hills, 2017; Hodgson, 2018) may be of interest in cases where combustion gases are absent and the heat transfer is to be provided mainly through radiation from hot surfaces. Such reactors are of special relevance if the calcination process is to be electrified (Tokheim et al., 2019).

When designing new reactor types for the calcination process, it is necessary to understand the dynamic behavior of the calcining particles in order to size the reactor. The time required for calcination will largely depend on the particle size and the temperature in the reactor of interest. The size of the raw meal particles ranges from about 1 to 500 µm, and the median is typically 20-30 µm.

The purpose of this paper is to 1) develop a dynamic model of the heating and calcination of raw meal particles of difference size, and 2) combine this model with experimental data on particle size and chemical composition, in order to 3) determine the time required to obtain a certain calcination degree for an industrial raw meal exposed to a specified reactor temperature.

The contribution of this study is to provide a model that can be applied to industrial raw meal mixtures with a typical distribution of particle size and chemical composition. It will apply to systems with any CO_2 concentration in the calciner, including those operating with pure CO_2. The latter is relevant for electrically heated calciners.

2 Dynamic model of a particle being heated and calcined

In this section, the system is described, the mathematical model equations are explained, the discretized model equations are given and the model input values are listed.

2.1 System description

The heat transfer from the isothermal surroundings (e.g., a hot, temperature-controlled wall) to the particle mainly occurs through radiation. The supplied thermal energy is used for heating and calcining the particles.

The particle enters the calciner in a preheated state. When the particle is exposed to an environment with a higher temperature than the particle, it will be further heated. The environment for a particle is typically a gas surrounding the particle, a reactor wall constituting the boundary of the heat transfer domain, as well as other particles.

As the particle temperature increases, $CaCO_3$ will decompose; $CaCO_3(s) \rightarrow CaO(s) + CO_2(g)$. The higher the temperature, the faster the calcination. The calcination is endothermic, and the typical calcination temperature is around 900 °C, depending on the process conditions.

After a certain time, the calcination will be complete, and the particle is pure CaO (plus any inert components), as all CO_2 has been driven out. Any heat supplied after this, will result in further heating of the calcined particle, and the particle will gradually approach the temperature of the surroundings and hence reach a new constant level. However, in general, a calcination degree of 90-95 % is targeted, so the particle will in general not exceed the calcination temperature.

The process described above, is illustrated in Figure 1, where T_{calc} indicates the temperature at which conversion from $CaCO_3$ (blue) to CaO (red) starts.

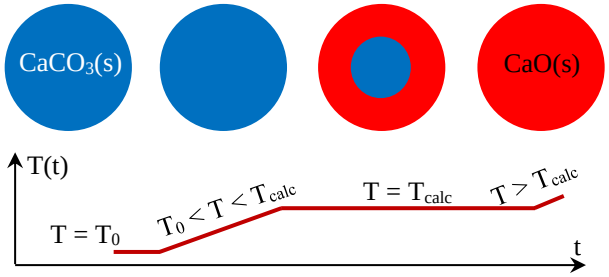

Figure 1. Heating and calcination of a $CaCO_3$ particle.

It should be noted that in an industrial process, the calcination degree (also called the degree of calcination, *DoC*) of the meal in the calciner should not exceed 90-95 %. This is because complete conversion will lead to a fast temperature increase in the reactor, and this may in turn cause unwanted sintering effects due to partial melt formation. In traditional calciner systems operating with fuel as the energy source, the *DoC* is kept in the range 90-95 % by adjusting the fuel feed rate to obtain a certain exit temperature, which by experience is found to give a suitable *DoC* value. The *DoC* value is checked regularly by sampling and laboratory analyses. A similar control concept can be applied for an electrified system, but then the electric power input is adjusted to comply with the temperature setpoint. Interlocks based on local wall temperatures should also be implemented to make sure overheating is avoided.

The uncalcined particle has a specified mass density and volume, i.e., a certain mass. During decarbonation, the particle mass will gradually decrease as CO2 is driven out. However, according to shrinking core model (Levenspiel, 1989), the volume of the particle is believed to stay approximately unchanged whereas the porosity will increase, meaning that the effective particle density will decrease.

There are many experimental studies on calcination kinetics available, typically involving the use of thermogravimetric analysis (TGA) to determine the mass loss as a function temperature and time (Ar et al., 2001; Garcia-Labiano et al., 2002; Valverde et al., 2015; Maya et al., 2018; Fedunik-Hoffman et al., 2019). Other types of furnaces are also used (Hu and Scaroni, 1996; Wang et al., 2007; Ghiasi et al., 2021). Many of these refer to Silcox et al. (1989), who developed a model to take into account decarbonation of $CaCO_3$ at the reactant-product interface, diffusion of CO_2 through the growing CaO layer and sintering of CaO. Some studies (for example, Hu and Scaroni,1996; Wang et al., 2005; Valverde et al., 2015) also apply scanning electron microscope (SEM) analyses to study how the structure of the limestone changes during the process. CaO sintering effects will reduce the porosity of the particles and thereby reduce the effective decompostion rate. The effect increases with increasing partial pressure of CO_2.

As pointed out above, different factors contribute to particle heat-up. However, in this study, only radiation heat transfer from the wall is considered. Convection and radiation heat transfer from the gas to the particle are neglected, as these contributions are believed to be quite small compared to the wall contribution, at least in the main energy-consuming phase, i.e., the calcination phase. Furthermore, radiation (and conduction) from other particles are neglected as all particles will likely have approximately the same temperature.

As the particles are small, spatial temperature gradients inside the particles are neglected, i.e., the particle temperature is assumed to depend on time only. For larger particles, the model should be used with caution.

Sintering effects, which may be significant for larger particles, are not included in this study, but may be implemented at a later stage.

In a real system, the particles will have different shapes. In this study, however, spherical particles are assumed. This makes it easy to calculate the surface area and the volume of the particle. The surface area is important because the heating is an area-specific process. The volume is required to calculate the initial mass of the particle.

2.2 Model equations

An energy balance of the particle may be given as in Equation 1, where E means energy [J], $\dot{E}$ means energy flow [W] and t is time [s]:

$$\dot{E}_{in} - \dot{E}_{out} + \dot{E}_{gen} = \frac{dE}{dt} \quad (1)$$

The inflow of energy, $\dot{E}_{in}$, can be described as the product of the heat flux, $q^{"}$ [W/m²], and the surface area of the particle, A_p [m²]:

$$\dot{E}_{in} = q^{"} A_p \quad (2)$$

Assuming that the particle is completely enclosed in large isothermal surroundings, the heat flux inflow can be expressed in terms of the radiation flux from the wall to the particle, which is a function of the wall temperature T_{wall} [K], the particle temperature (a variable input parameter), T [K], and the emissivity of the particle, ε [-]:

$$q^{"} = \varepsilon\sigma(T_{wall}^4 - T^4) \quad (3)$$

σ is the Stefan-Boltzmann constant, which has a value of $5.67 \cdot 10^{-8}$ W/(m²K⁴). The surface area is a function of the particle diameter, D_p [m] (another variable input parameter):

$$A_p = \pi D_p^2 \quad (4)$$

The outflow of energy will be zero as only heating is modelled in this study. This means that the term $\dot{E}_{out}$ in Equation 1 can be deleted.

The term $\dot{E}_{gen}$ in Equation 1 is a source term. In this case, the source term is a sink, i.e., it represents the endothermic reaction happening during calcination, and can be formulated as in equation 5, where r is the reaction rate [mol/(m²·s)], M_{CO_2} is the molecular mass of CO_2 [kg/mol] (constant) and ΔH_{calc} is the specific calcination enthalpy [J/kg] (another constant):

$$\dot{E}_{gen} = r A_p M_{CO_2} \Delta H_{calc} \quad (5)$$

The transient term (right-hand side) in Equation 1, can be re-written as:

$$\frac{dE}{dt} = \frac{d(mcT)}{dt} = Tc\frac{dm}{dt} + mc\frac{dT}{dt} \quad (6)$$

Here, c is the specific heat capacity of the particle [J/(kg·K)], whereas m is the particle mas [kg]. The specific heat capacity is a weak temperature function, but here it is taken as a constant. The temperature dependence is moderate, so this simplification should not give a big error if a representative mean temperature is applied.

The time derivative of the mass is included in Equation 6. By utilizing the mass balance of the particle, the term $\frac{dm}{dt}$ may be replaced by an algebraic expression:

$$\frac{dm}{dt} = -r A_p M_{CO_2} \quad (7)$$

By combining equations 1–6, the following first order differential equation is found:

$$\frac{dT}{dt} = \frac{A_p}{mc}\varepsilon\sigma(T_{wall}^4 - T^4) - \frac{A_p r M_{CO_2} \Delta H_{calc}}{mc} + \frac{T}{m} r A_p M_{CO_2} \quad (8)$$

The reaction rate in equation 8 may be expressed as a function of a rate constant, K_d [mol/(m²·s·Pa)], the equilibrium pressure of CO_2, $p_{CO_2,eq}$ [Pa], and the partial pressure of CO_2 in the gas surrounding the particle, p_{CO_2} [Pa] (which will be given by the process conditions):

$$r = K_d\left(p_{CO_2,eq} - p_{CO_2}\right) \quad (9)$$

The rate constant is a function of the temperature and two model constants, i.e. a frequency factor, A_d [mol/(m²·s·Pa)], an activation energy, E_d [J/mol], and the universal gas constant, R (8.314 J/(mol·K):

$$K_d = A_d e^{-\frac{E_d}{RT}} \quad (10)$$

The equilibrium pressure of CO_2 is also a function of the temperature and two model constants, A_{eq} [mol/(m²·s·Pa)] and E_{eq} [J/mol]:

$$p_{CO_2,eq} = A_{eq} e^{-\frac{E_{eq}}{RT}} \quad (11)$$

Equation 7 shows that the mass will drop if the reaction rate is positive, but will increase if the reaction rate is negative. The latter will occur if the equilibrium pressure of CO_2 is lower than the partial pressure – then carbonation ($CaO(s)+CO_2 \rightarrow CaCO_3(s)$) will happen instead of calcination. However, the mass may not have higher values than the initial (uncalcined) mass m_0 [kg] and not lower values than the minimum mass m_{min} [kg], which will be reached when all CO_2 has been expelled from the particle. These two constraints must be implemented in the model. The minimum mass may be calculated through equation 12, where M_{CaCO_3} is the molecular mass of calcium carbonate [kg/mol] and w_{CaCO_3} is the weight fraction of calcium carbonate:

$$m_{min} = m_0 \left(1 - \frac{M_{CO_2}}{M_{CaCO_3}} w_{CaCO_3}\right) \quad (12)$$

The initial mass may be calculated based on the particle volume, V_p [m³], and the initial particle density, $\rho_{p,0}$ [kg/m³]:

$$m_0 = \rho_{p,0} V_p \quad (13)$$

The particle volume is assumed constant, as a shrinking core model is assumed, and can be calculated as:

$$V_p = \frac{\pi}{6} D_p^3 \quad (14)$$

The particle density, ρ_p [kg/m³], is a function of the particle mass and the particle volume:

$$\rho_p = \frac{m}{V_p} \quad (15)$$

The degree of calcination, DoC, is a function of the initial particle mass, the minimum particle mass and the time-dependent particle mass:

$$DoC = \frac{m_0 - m}{m_0 - m_{min}} 100\% \quad (16)$$

Equation 8 shows that the temperature is impacted by three terms: i) the wall temperature term, which always gives a positive temperature contribution, ii) the calcination enthalpy term, which is negative during calcination (if $p_{CO_2,eq} > p_{CO_2}$), meaning that $r > 0$), but positive during carbonation if $p_{CO_2,eq} < p_{CO_2}$, meaning that $r < 0$); iii) the mass loss term, which gives a positive contribution during calcination, but negative during carbonation.

2.3 Discretized model equations

The first-order differential equations, Equation 7 and 8, can be discretized according to Euler's forward method (with index k):

$$\left(\frac{\Delta T}{\Delta t}\right)_k = \frac{A_p}{m_k c}\left(\varepsilon\sigma(T_{wall}^4 - T_k^4) - r_k M_{CO_2} \Delta H_{calc} + T_k r c M_{CO_2}\right) \quad (17)$$

$$T_{k+1} = T_k + \left(\frac{\Delta T}{\Delta t}\right)_k \quad (18)$$

$$\left(\frac{\Delta m}{\Delta t}\right)_k = -r_k A_p M_{CO_2} \quad (19)$$

$$m_{k+1} = m_k + \left(\frac{\Delta m}{\Delta t}\right)_k \quad (20)$$

In addition to equations 17 – 20, the algebraic equations given in equations 9 – 11 and 15 – 16 are solved for each time step, i.e., for each value of T_k.

2.4 Input values

Model constants, temperature dependent data and true constants are given in Table 1, whereas Table 2 gives input values for calculation of a base-case.

A particle size of 300 µm is within the range of the raw meal particle size distribution and is used here just as an example (other particle sizes are investigated later). A temperature of 658 °C was selected based on calculations carried out in a previous phase of the project (Tokheim et al., 2019), and this value is within the typical variation range of a modern cement kiln system. The $CaCO_3$ content of 77% is also a typical value for cement plants producing ordinary Portland cement. Finally, the partial pressure in current cement kiln systems is typically 0.2-0.3 atm in the calciner, but in this study, a value of 1 atm is used because 100 % CO_2 is the relevant case for calciners with indirect heat transfer from hot surfaces. In such cases, no combustion gases will be mixed with the CO_2 coming from the decarbonation.

Table 1. Values of model constants, thermophysical data and true constants used in the calcination model.

Symbol	Unit	Value	Remark
A_d	mol/(m²s·Pa)	$1.2 \cdot 10^{-5}$	Stanmore and Gilot (2005); Wang et al. (2007)
E_d/R	K	4 026	
A_{eq}	Pa	$4.19 \cdot 10^{12}$	
E_{eq}/R	K	20 474	
c	J/(kg K)	850	Approx. value
ε	-	0.9	Approx. value
$\rho_{p,0}$	kg/m³	2 700	Typical value
ΔH_{calc}	J/kg	$3.6 \cdot 10^6$	Typical value
M_{CO_2}	kg/mol	0.044	Constant
M_{CaCO_3}	kg/mol	0.100	Constant

Table 2. Base case input parameters in the model.

Symbol	Unit	Value
D_p	µm	300
T_{wall}	°C	1 050
T_0	°C	658
w_{CaCO_3}	wt%	77%
p_{CO_2}	atm	1
Δt	ms	20

The input variables are independent parameters that may take different values. Table 3 shows ranges to be applied in order to investigate how variations in some of these will affect the behavior of the particle.

The particle size variations reflects the variation in an industrial raw meal (cf. Section 1). A typical value for the wall temperature may be 1050°C. However, the maximum allowed value depends on the wall material, so lower and higher values are also investigated.

Table 3. Variation in input parameter values.

Symbol	Unit	Value
D_p	µm	1 – 300
T_{wall}	°C	950 – 1100

Table 4 shows that different size fractions in raw meal have different chemical compositions. The size classes were determined by manual sieving, and the weight fractions (w_i) in the raw meal as well as the $CaCO_3$ content in each size class were back calculated from XRF-measured values of CaO content in each size class.

This means that the fraction of material to calcine is different in different size classes, and this will influence the required calcination time.

Table 4. Content of $CaCO_3$ ($w_{CaCO3,i}$) in different size fractions (w_i) in raw meal.

$D_{p,i}$ [µm]	$w_{CaCO3,i}$	w_i [wt%]
16	80.5 %	54.9
48	78.9 %	26.1
77	73.0 %	9.4
108	64.0 %	4.4
163	54.6 %	3.6
600	48.4 %	1.7

3 Results and discussion

First, a base case is simulated, using the values given in Table 1 and 2. Next, selected input parameters are varied according to ranges given in Table 3. Finally, the calcination of a raw meal consisting of different particle sizes with different chemical composition is simulated for typical process conditions in an industrial calciner, as indicated in Table 4.

3.1 Base case

Figure 2 shows that the temperature first increases from the initial (inlet) temperature of 658 °C. This is due to the heat flux from the wall. As the temperature increases, the equilibrium pressure increases and reaches a stable plateau value after about 0.6 s. From then on, the temperature (and accordingly also the equilibrium pressure) stays constant at about 1005 °C until about 6.2 s. After this, the temperature rises to a new plateau, corresponding to the wall temperature, i.e. 1050 °C. The system has now reached the state of thermal equilibrium.

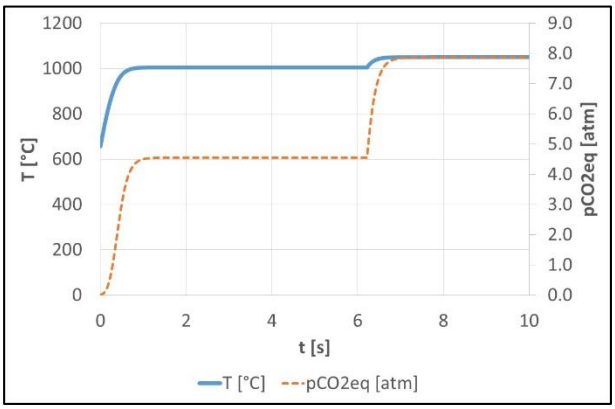

Figure 2. Temperature and equilibrium pressure as a function of time.

Figure 3 shows that the rate constant follows the same trend as the equilibrium pressure (cf. Figure 2), as the expressions given in equations 10 and 11 are both of a similar exponential nature. Moreover, the temperature gradient gradually drops and reaches a constant value, which abruptly increases for a short time when the calcination is complete. At equilibrium, it goes back to zero.

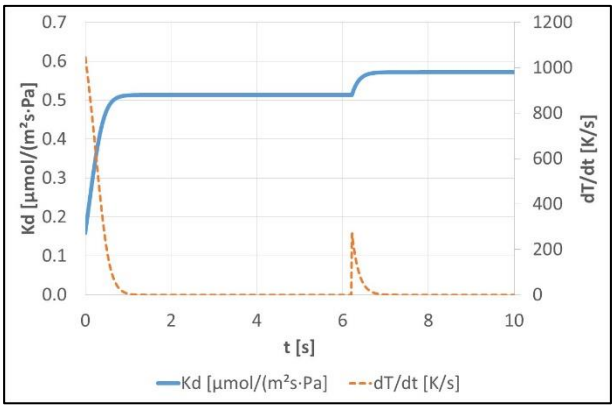

Figure 3. Rate constant and temperature gradient as a function of time.

Figure 4 shows that the particle mass is initially more or less constant for short period (about 0.1 s). This is because the reaction rate is low as the temperature is initially rather low. However, when the temperature and the reaction rate increase, the mass starts to drop. The mass reduction is linear in the period with a constant reaction rate. After about 6.2 s, the particle mass flattens out on a level corresponding to the minimum mass, as all CO_2 has been driven out of the particle, i.e. the calcination is complete. After this, the reaction rate drops to zero.

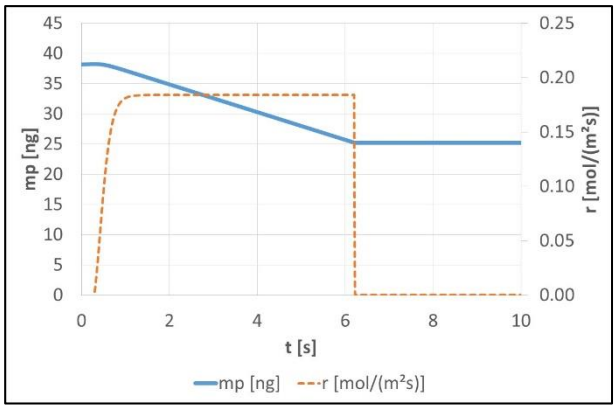

Figure 4. Particle mass and reaction rate as a function of time.

Figure 5 illustrates the co-variation of the temperature and the heat flux. Initially, the heat flux is extremely high, as there is a big difference between the wall temperature (1050 °C) and the particle temperature (658 °C). However, as the particle heats up, the flux drops quickly and reaches a constant level of about 20 kW/m² during the calcination period with a constant particle temperature. After completion of calcination, the particle temperature increases, which means that the driving force for the heat transfer drops, and eventually the flux reaches a zero value when the thermal equilibrium has been reached after about 7 s. However, as was mentioned in system description section, in a real system, the calcination process will be stopped before complete conversion occurs, so that high temperature levels and sintering effects are avoided.

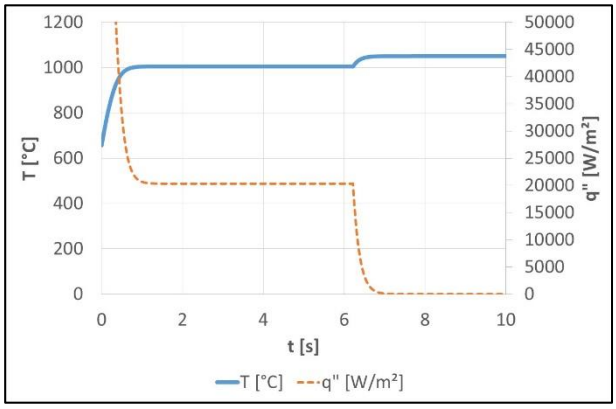

Figure 5. Heat flux and temperature as a function of time.

Figure 6 shows that the particle density drops from the initial level of 2700 kg/m³ to 1785 kg/m³ when the calcination is complete. After a very short period (about 0.6 s) with virtually no calcination, as the equilibrium pressure is lower than the partial pressure of CO_2, the calcination degree increases from 0 % to 100 %.

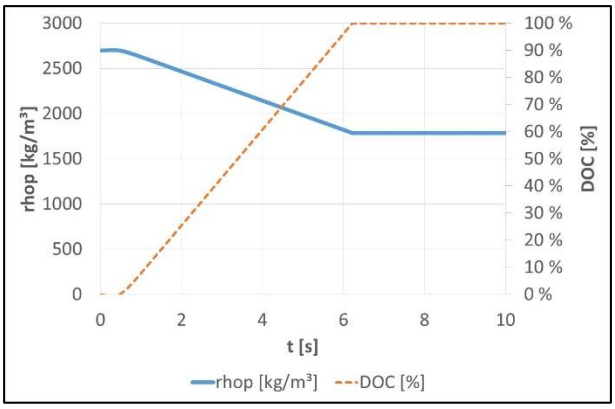

Figure 6. Particle density and calcination degree (*DoC*) as a function of time.

3.2 Variable particle size and temperature

Figure 7 shows that the reactor temperature and the particle size both have a big impact on the time required for complete calcination.

As an example, with a wall temperature of 1050 °C, a 100-µm particle needs 2.1 s to be completely calcined. If the wall temperature is 1100 °C, the required time is only 1.3 s. A very low wall temperature of 950 °C, on the other hand, increases the required conversion time to 9 s for this particle size. Similar differences are found for other particle sizes.

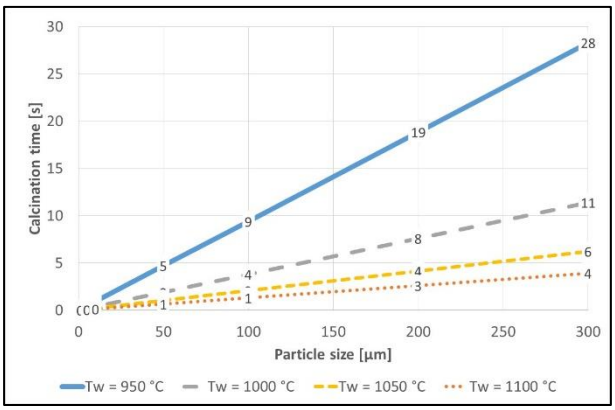

Figure 7. The impact of temperature and particle size on calcination time (T_0=658 °C, p_{CO_2}=1 atm, w_{CaCO_3}=1).

The calcination time is linearly dependent on the particle size. At a reactor temperature of 1050 °C, the calcination time increases from 2.1 s for a 100-µm particle to 6.3 s for a 300-µm particle.

3.3 Raw meal calcination

The calculated values of $CaCO_3$ content and weight fraction specified in Table 4 are used in the model to calculate the aggregated degree of calcination of the calcined meal at different residence times in the calciner.

The results are shown in Figure 8. The DoC values (calcination degree) seem to fit well with typical values in industrial calciners, in which 90-95 % conversion typically takes a few seconds (Tokheim, 1999).

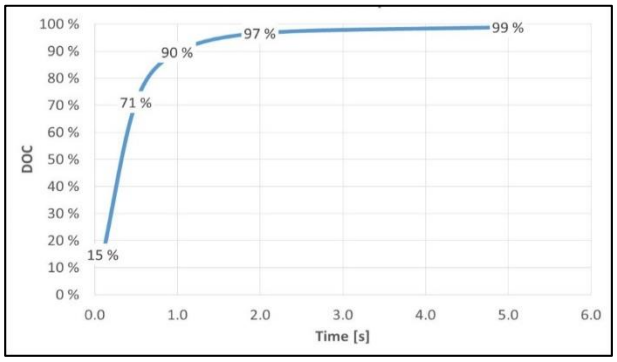

Figure 8. Raw meal calcination time (T_0=658 °C, p_{CO_2}=1 atm, T_{wall}=1050 °C, composition and particle size as given in Table 4).

4 Conclusion

The particle size and the reactor temperature are key variables controlling the calcination time for raw meal particles. A typical raw meal will be completely calcined in about 5 s when exposed to isothermal surroundings at 1050 °C. At lower temperatures, the calcination time will increase – and vice versa.

The model can be used as a basis for determining the required size of a potential new calcination reactor type, as different reactor types will operate at different temperatures. Developing a new reactor type is of particular interest in electrification of the calcination process, a concept that is currently being investigated aiming at a significant reduction in CO_2 emissions from cement plants employing electrified calcination.

Acknowledgements

This study was carried out as part of the research project "Combined calcination and CO_2 capture in cement clinker production by use of CO_2-neutral electrical energy – Phase 2". Gassnova and Norcem are greatly acknowledged for funding this project. Many thanks to Christoffer Moen, laboratory manager at Norcem, for reading and giving useful comments to the article.

References

Irfan Ar and Gülsen Dogu. Calcination Kinetics of High Purity Limestones. *Chemical Engineering Journal*, 83:131–137, 2001.

Walter H. Duda. *Cement Data Book Volume 1, 3rd edition*. Bauverlag GmbH, 1985.

Larissa Fedunik-Hofman, Alicia Bayon, and Scott W. Donne. Comparative Kinetic Analysis of $CaCO_3$/CaO Reaction System for Energy Storage and Carbon Capture. *Applied Sciences*, 9:4601, 2019. doi.org/10.3390/app9214601.

Vanessa Fierro, Juan Adánez, and Francisco García-Labiano. Effect of Pore Geometry on the Sintering of Ca-based Sorbents During Calcination at High Temperatures. *Fuel*, 83: 1733–1742, 2004. doi:10.1016/j.fuel.2004.03.011

Francisco García-Labiano, Alberto Abad, Luis F. de Diego, Pilar Gayán, and Juan Adánez. Calcination of Calcium-based Sorbents at Pressure in a Broad Range of CO_2 concentrations. *Chemical Engineering Science*, 57:2381–2393, 2002.

Meisam Ghiasi, Mahmoud Abdollahy, and Mohammadreza Khalesi. Investigating the Kinetics, Mechanism, and Activation Energy of Limestone Calcination Using Isothermal Analysis Methods. *Mining, Metallurgy & Exploration*, 38:129–140, 2021. doi.org/10.1007/s42461-020-00300-y.

Thomas P. Hills, Mark Sceats, Daniel Rennie, and Paul Fennella. LEILAC: Low Cost CO_2 Capture for the Cement and Lime Industries. *Energy Procedia*, 114:6166–6170, 2017. doi: 10.1016/j.egypro.2017.03.1753.

Phil Hodgson, Mark Sceats, Adam Vincent, Daniel Rennie, Paul Fennell, and Thomas Hills. Direct Separation Calcination Technology for Carbon Capture: Demonstrating a Low Cost Solution for the Lime and Cement Industries in the LEILAC Project. *14th International Conference on Greenhouse Gas Control Technologies (GHGT-14)*, 21st–25th October, Melbourne, Australia, 2018.

Naiyi Hu and Alan W. Scaroni. Calcination of Pulverized Limestone Particles Under Furnace Injection Conditions. *Fuel*, 75(2):177–186, 1996.

Octave Levenspiel, *The Chemical Reactor Omnibook*. OSU Book Stores, Oregon, USA, 1989.

Nastaran A. Samani, Chameera K. Jayarathna, and Lars-André Tokheim. Fluidized Bed Calcination of Cement Raw Meal: Laboratory Experiments and CPFD Simulations. *Linköping Electronic Conference Proceedings*, (61st SIMS conference, September 22–24), 399–406, 2020. doi.org/10.3384/ecp20176407.

Juan C. Maya , Farid Chejne, Carlos A. Gómez, and Suresh K. Bhatia. Effect of the CaO Sintering on the Calcination Rate of $CaCO_3$ Under Atmospheres Containing CO_2. *AIChE Journal - Reaction Engineering, Kinetics And Catalysis*, 64(10):3638–3648, 2018. doi.org/10.1002/aic.16326.

Geoffrey D. Silcox, John C. Kramlich, and David W. Pershing. A Mathematical Model for the Flash Calcination of Dispersed $CaCO_3$ and $Ca(OH)_2$ Particles. *Ind. Eng. Chem. Res.*, 28:155–160, 1989. doi:10.1016/j.fuproc.2005.01.023

Brian R. Stanmore and Patrick Gilot. Review – Calcination and Carbonation of Limestone During Thermal Cycling for CO_2 Sequestration. *Fuel Processing Technology*, 86:1707–1743, 2005.

Lars-André Tokheim. *The Impact of Staged Combustion On the Operation of a Precalciner Cement Kiln*, PhD dissertation, NTNU/TUC, 1999.

Lars-André Tokheim. Kiln System Modification for Increased Utilization of Alternative Fuels at Norcem Brevik, *Cement International*, 4:1–8, 2006.

Lars-André Tokheim, Anette Mathisen, Lars E. Øi, Chameera Jayarathna, Nils H. Eldrup, and Tor Gautestad.

Combined Calcination and CO_2 Capture in Cement Clinker Production by Use of Electrical Energy. *SINTEF Proceedings*, 4:101–109, 2019.

Jose M. Valverde, Pedro E. Sanchez-Jimenez, and Luis A. Perez-Maqueda, Limestone Calcination Nearby Equilibrium: Kinetics, CaO Crystal Structure, Sintering and Reactivity. *The Journal of Physical Chemistry*, 119:1623–1641, 2015. doi.org/10.1021/jp508745u

Yin Wang, Shiying Lin and, Yoshizo Suzuki. Study of Limestone Calcination with CO_2 Capture: Decomposition Behavior in a CO_2 Atmosphere. *Energy & Fuels*, 21:3317–3321, 2007. doi.org/10.1021/ef700318c.

Hygrothermal Simulation of Prefabricated Cold-Formed Wall Panels

Ayman R. Hamdallah Filip Fedorik Antti H. Niemi

Civil Engineering Research Unit, University of Oulu, Finland,
{ayman.hamdallah,filip.fedorik,antti.niemi}@oulu.fi

Abstract

Steel structures are light and durable, but in the building envelope they can transfer heat energy easily from the building interior to outside and hinder the energy performance of the building. In this study, we simulate the thermal performance of cold-formed steel panels that can be used as prefabricated units in building envelopes. More precisely, the thermal performance of hollow cold-formed steel elements filled with thermal insulation is studied with varying panel geometry. The focus is on stainless steel but also mild steel is briefly considered. Attention is paid especially to the thermal bridges associated to the relatively high thermal conductivity of steel materials. The influence of the width, depth and the height of the panel to thermal bridging is assessed and panel geometries with reasonable thermal performance are found. By considering also the moisture transport, the overall hygrothermal performance of the panels is then evaluated.

Keywords: cold-formed steel, hygrothermal simulation, thermal bridge, stainless steel, prefabricated elements

1 Introduction

Cold-Formed Steel (CFS) cross-sections are used extensively in the construction industry as secondary loads-carrying members, such as roof purlins and girts in framed walls. These sections are manufactured by bending flat sheets with thickness ranging typically from 0.4 mm to 6.4 mm in Europe and North America (Dubina et al., 2012; Hancock et al., 2001). Nowadays, CFS sections are employed increasingly also as primary structural elements in framing systems of single-story industrial buildings with short to intermediate spans.

Use of prefabricated wall panels provides an answer to environmental and economic demands of sustainability and quality by reducing mis-fabrication and time consumption on building sites particularly regarding the thermal insulation process in cold and humid as well as in hot and moist weather conditions. Thin cold-formed steel sheets are suitable for this purpose because they can be formed in the shape of hollow sections and transported relatively easily. When compared with traditional construction materials such as timber, or ordinary steel frames, which use mineral wool as insulation material, the cold-formed panels offer distinct benefits in construction process, quality control, cost-effectiveness as well and sustainability.

However, the high thermal conductivity of steel means that the heat flow must be carefully controlled with insulation and that attention must be paid to thermal bridges, i.e. areas where the heat flow is locally increased. If not controlled properly, the thermal bridges may lead to higher energy costs, moisture problems and thermal discomfort of the building occupants.

The earlier study by Soares et al. reviews the main features of steel-framed construction from the point of view of life cycle energy consumption (Soares et al., 2017). The overview indicates some strategies for reducing thermal bridges and improving the thermal resistance of steel structures in the building envelope. Furthermore, the effectiveness of insulation with respect to its position in the steel-framed wall with CFS elements and non-structural panels has been recently discussed in (Roque and Santos, 2017; Roque et al., 2020; Kapoor and Peterman, 2021). By comparing CFS framing and hybrid-frame construction, the authors have observed that the location of the insulation significantly affects thermal bridges and the overall thermal performance of the wall.

Hollow tubes and other shapes can be used as structural elements in lightweight steel frames. Our study is focused on prefabricated hollow CFS wall panels that

- can be easily insulated thermally and acoustically due to the core space inside
- are easily recyclable
- have high mechanical strength combined with light weight
- reduce the risk of moisture problems because of dry construction environment
- can be transported economically
- are easy and fast to assemble

We present a family of such panels where the geometry is varied parametrically and evaluate the thermal and hygrothermal performance of the building constructions in northern conditions. It should be noted that due to their large slenderness, i.e. width-to-thickness ratio, such elements are inherently susceptible to local, distortional and

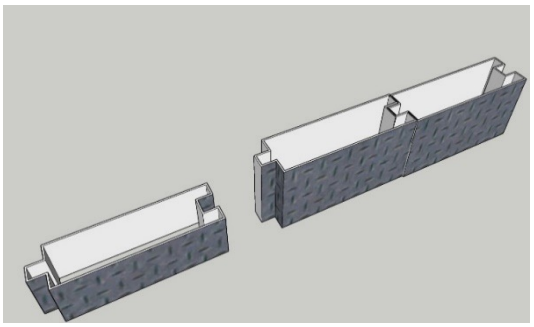

Figure 1. 3D sketch of the hollow CFS unit.

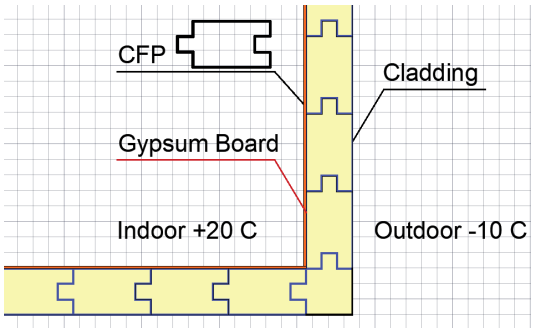

Figure 3. Conceptual model of the corner of the building made of CFS units and temperature boundary conditions.

global buckling phenomena. We do not consider the structural integrity in this study but the insulation is expected to help to prevent local buckling.

The structure of the paper is as follows. The proposed wall element is introduced in the next section. Section 3 describes the models and the numerical simulation used to analyze and optimize the thermal performance of the wall element and contains the main results of the paper. Moisture transport is then considered in Section 4 and the paper ends with conclusions and remarks in Section 5.

2 Proposed Wall Element

The prefabricated wall element that we propose and analyze consists of a hollow cold-formed section filled with insulation as shown in Figure 1. Such prefabricated panels can be easily assembled at the construction site, and they form the main core of wall. This concept could be used to substitute traditional construction techniques in heated and non-heated buildings like the one shown in Figure 2. The final assembly of such wall elements shall then include e.g. a gypsum board and a suitable weather protection or cladding on the inner and outer face of the core wall respectively as shown in Figure 3.

Based on the practical demands and dimensional recommendations of the cold-formed steel industry, we choose six different panel geometries for comparison by simulation. The interior gypsum board and the weather protection layer remain unchanged as they do not contribute significantly to the overall assessment of the wall element. The studied wall elements are labeled based on their characteristic geometric information (width, depth, and thickness) and are listed in Table 1.

Table 1. Geometric parameters of the wall assemblies.

Label	*Width* [cm]	*Depth* [cm]	*Thickness* [cm]
W100-30-0.1	100	30	0.1
W100-30-0.2	100	30	0.2
W100-30-0.3	100	30	0.3
W100-15-0.2	100	15	0.2
W050-30-0.1	50	30	0.2
W150-30-0.1	150	30	0.2

Assuming a density of 7500 kg/m^3 for steel and a density of 30 kg/m^3 for the insulation, the unit masses of the different assemblies per square meter of building envelope are shown in Table 2 to demonstrate their practicality.

Table 2. Unit masses of the wall assemblies.

Label	*Unit Mass* [kg/m^2]
W100-30-0.1	39
W100-30-0.2	58.4
W100-30-0.3	77.8
W100-15-0.2	44.2
W050-30-0.1	67.4
W150-30-0.1	55.4

Figure 2. Storage building in Oulu, Finland.

3 Heat Transfer Analysis

The thermal analysis is based on a steady-state heat transfer simulation of the selected wall assemblies using the COMSOL software. The basic model takes into account only heat conduction so that the governing partial differential equation is elliptic. Then the finite element method produces the best approximation of the exact temperature distribution on a given mesh. Two-dimensional models of the wall assembly were created near a rectangular corner which is the critical area concerning heat transfer in buildings and the finite element mesh was refined enough so

that the thin structural components of the assembly can be analyzed.

The main quantity of interest and optimization criterion in the thermal analysis is the linear thermal transmittance [W/(m^{2}K)] defined typically in the building codes as

$$\psi = L_{2D} - \sum_j U_j \cdot l_j, \quad (1)$$

where U_j is the thermal transmittance [W/(m^{2}K)], l_j is the length [m] over which U_j applies and L_{2D} is the thermal coupling coefficient [W/(m^{2}K)].

In our study, the thermal coupling coefficient L_{2D} is obtained by integrating the heat flow rate obtained from the numerical simulation over the interior surface including the corner and the thermal transmittances U_1 and U_2 are determined similarly as the average heat flow rate of the straight periodic wall segments. Because of symmetry, $U_1 = U_2 = U$ in our case.

3.1 Material Properties and Boundary Conditions

One of the key elements in the present analysis is the thermal transmittance due to the relatively high thermal conductivity of steel. However, there is a considerable difference between the thermal conductivities of stainless and mild steels. We use the value the value $15\,\mathrm{W/(mK)}$ for stainless steel and the value $50\,\mathrm{W/(mK)}$ for mild steel.

The thermal conductivities of the gypsum board and the weather protection layer are taken as $0.21\,\mathrm{W/(mK)}$ and $0.06\,\mathrm{W/(mK)}$, respectively. Furthermore, the convective heat flux boundary conditions are used on the external and internal sides of the wall by taking 1/0.04 and 1/0.13 as the external and internal heat transfer coefficients, respectively (Hopkin et al., 2011).

3.2 Results

Figure 4 shows as an example the steady-state temperature distribution and the finite element mesh for the assembly W100-30-0.2 with stainless steel. The thermal bridges at the corner as well as near the junction of two neighboring steel sections lead to slightly cooler temperatures at the interior surface of the wall.

As expected, the temperature distribution is influenced by the steel elements that have a very high thermal conductivity as compared with the insulation. The phenomenon becomes even more clear, if we look at the distribution of the heat flow rate over the interior surface of the wall assembly. Figure 5 shows the heat flow rates calculated along the interior wall surface for the wall assemblies W100-30-0.1, W150-30-0.2, and W100-15-0.2, respectively. The geometry affects somewhat significantly the heat flow rate near the corner as well as its overall distribution along the wall assembly.

The different wall element geometries are then compared in Table 3 in terms of their U-value and the thermal transmittance ψ at the corner according to Equation (1). The comparison of the assemblies shows that increasing the thickness of the steel sheet strengthens the thermal bridges between neighboring elements and hence the average U-value of the wall. Increasing the width of the wall unit reduces the U-value but it cannot be increased excessively because of practical reasons regarding economy and transport. On the other hand, the relationship between the geometric parameters and the thermal admittance at the corner is more complex and the performance assessment requires engineering judgement.

Table 3. Comparison of thermal characteristics of different wall assemblies.

Label	U [W/m^2]	ψ [W/(mK)]]
W100-30-0.1	0.18	0.03
W100-30-0.2	0.21	0.09
W100-30-0.3	0.26	0.06
W100-15-0.2	0.39	0.05
W050-30-0.2	0.30	0.03
W150-30-0.2	0.19	0.01

The influence of the specific steel type to the overall thermal characteristics of the wall assembly is addressed in Table 4 showing the thermal characteristics of the panel W100-30-0.1 made of mild steel with thermal conductivity $50\,\mathrm{W/(mK)}$. Comparing these values with the first line of Table 3 shows that the higher thermal conductivity is reflected in the average U-value of the wall assembly and especially in the thermal bridge at the corner.

Table 4. Thermal characteristics of a wall assembly made of mild steel.

Label	U [W/m^2]	ψ [W/(mk)]]
W100-30-0.1 (mild)	0.26	0.13

4 Hygrothermal Analysis

A time-dependent heat and moisture transport simulation of the wall assembly was carried out again by the COMSOL software. The outdoor boundary conditions for the temperature and the relative humidity were taken from the values recorded by the Finnish Meteorological Institute in Oulu, Finland for the year 2020. Indoor conditions were represented by temperature and relative humidity derived from the outdoor conditions according to the guidelines by the Finnish Association of Civil Engineers (Suomen Rakennusinsinöörien Liitto RIL ry, 2012). The simulation was performed for a period of two years by replicating the same boundary condition data. The reason for this is to neglect any impact of the initial conditions on the obtained results. Material properties required for coupled heat and moisture transfer analysis are thermal conductivity, heat

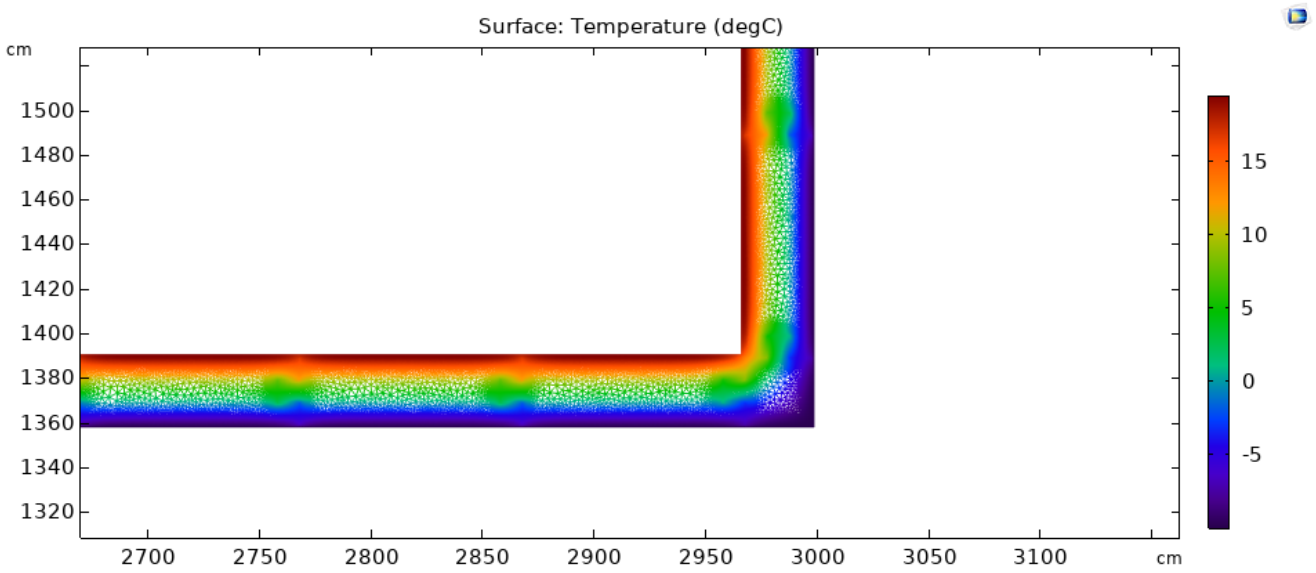

Figure 4. Temperature distribution for the assembly W100-30-0.2 with stainless steel.

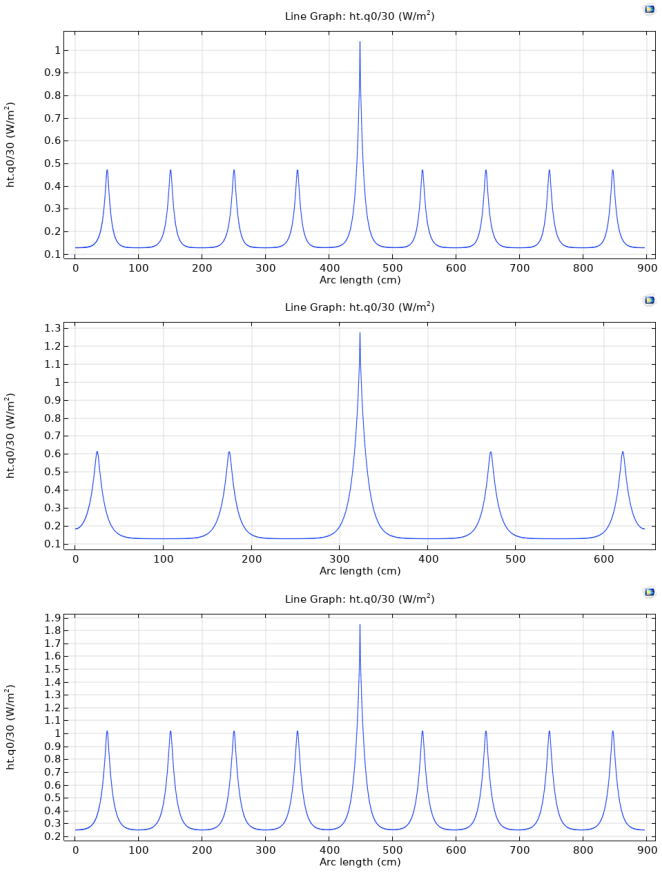

Figure 5. Temperature distribution for the assemblies W100-30-0.1 (top), W150-30-0.2 (middle), and W100-15-0.2 (bottom) with stainless steel.

capacity, density, water vapor resistance factor, and moisture isotherm. These were determined according to the ISO 14056:2007 standard (International Organization for Standardization, 2007).

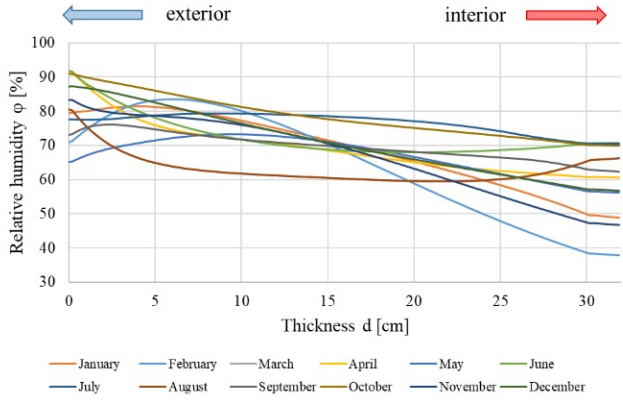

Figure 6. Distribution of the relative humidity over the wall cross section at the first day of each month.

Figure 6 shows the distribution of relative humidity computed across the cross section at the center of a wall element at the first day of each month. The relative humidity has a tendency to decrease towards the interior of the building. This is caused by diffusion that is mostly transporting humidity from inside to outside, because the indoor temperature exceeds the outdoor temperature for most of the time. The distribution of the humidity in the cross-section does not indicate humidity levels that might lead to excessive condensation. However, humidity levels around 90% are detected on the interior surface of the outside metal sheet. This is natural since the steel sheet cannot absorb moisture.

To investigate this phenomenon in more detail, we show in Figure 7 the temperature and relative humidity on the inner surface of outer metal sheet during one full year. The relative humidity remains below 90 % for most of the time so that the risk of condensation seems to be relatively small.

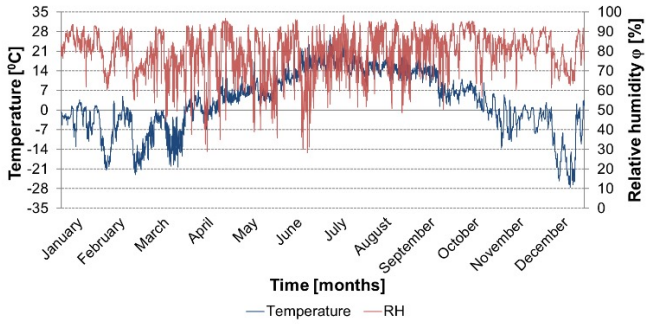

Figure 7. Temperature and relative humidity at the inner surface of the outside metal sheet during one year simulation.

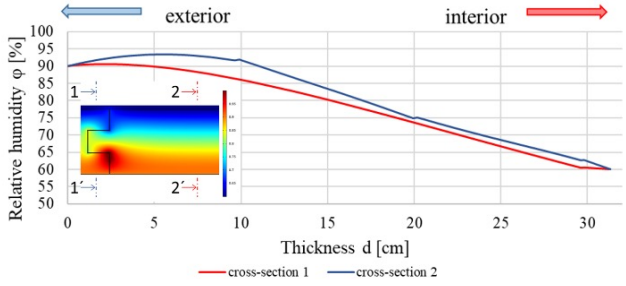

Figure 8. Relative humidity distribution in cross-section 1 (through joint between two elements) and cross-section 2 (through middle of an element).

A more detailed assessment of the hygrothermal performance of the wall was carried out by using a two-dimensional simulation model. In this case, a steady-state simulation was performed to detect whether there is a risk of excessive humidity at the joint between two elements. The boundary conditions were specified identically to the dynamic approach except that temperature and relative humidity which were set to 20°C and 50% for the inside and to 0°C and 90% for the outside, respectively.

As in the dynamic 1D case, the relative humidity does not seem to reach condensation levels under the defined conditions. However, as Figure 8 shows, higher relative humidity is found at the joint between two elements near the indoor wall. One possible reason for the humidity accumulation is the contact of permeable thermal insulation and the metal sheet. However, because the high level of relative humidity (>90%) is located near the indoor and the temperature should never drop below the freezing point there, the risk of freezing will remain small at this location.

5 Concluding Remarks

Cold-formed steel members in the building envelope can form thermal bridges that may affect the overall hygrothermal performance of the building quite considerably. We have introduced and studied a family of hollow cold-formed steel panels filled with insulation and parametrized with respect to their main structural dimensions. Thermal performance of six unique panel geometries was examined computationally by using the COMSOL software while keeping the insulation properties fixed. The heat transfer analysis was based on well-established 2D steady state finite element analysis with typical boundary conditions.

The thermal analysis revealed a clear correlation between the thickness of the hollow section and the thermal bridging at the panel intersections. On the other hand, it is more difficult to assess fairly the influence of the panel thickness, width and depth to thermal bridging at building corners because the overall performance is influenced by the internal thermal bridges. We also showed that the notable difference between the thermal conductivities of stainless and mild steels is clearly reflected in the thermal performance of the corresponding wall assemblies.

We also performed time-dependent and steady-state hygrothermal analyses of the panels based on recent meteorological data from Oulu, Finland. The results showed that the hygrothermal conditions inside the studied elements do not give raise to a significant risk for excessive humidity and/or water condensation. However, it is of high importance to avoid any surface condensation on the interior surface of the wall, especially in the vicinity of thermal bridges e.g. by providing well-ventilated indoor environment and/or by adding thermal insulation on the exterior side of the wall assembly.

Our work provides the foundations for a further parametric optimization study of the structural elements where also local and global buckling phenomena of the thin sheets are considered. Further optimization of thermal and hygrothermal performance can also be carried out by refining the parametric space and developing novel optimization algorithms.

Acknowledgements

This research has been supported by the Kolartic-CBC project KO1089 Green Arctic Building. This support is gratefully acknowledged.

References

Dan Dubina, Viorel Ungureanu, and Raffaele Landolfo. *Design of Cold-formed Steel Structures: Eurocode 3: Design of Steel Structures. Part 1-3 – Design of Cold-formed Steel Structures*. ECCS – European Convention for Constructional Steelwork, 2012.

Gregory J Hancock, Thomas Murray, and Duane S Ellifrit. *Cold-formed Steel Structures to the AISI Specification*. CRC Press, 2001.

D.J. Hopkin, J. El-Rimawi, V. Silberschmidt, and T. Lennon. An effective thermal property framework for softwood in parametric design fires: Comparison of the Eurocode 5 parametric charring approach and advanced calculation models. *Construction and Building Materials*, 25(5):2584–2595, 2011. doi:10.1016/j.conbuildmat.2010.12.002.

International Organization for Standardization. *ISO10456:2007 Building materials and products – Hygrothermal properties – Tabulated design values and procedures for determining declared and design thermal values*. International Organization for Standardization, 2007.

Divyansh R. Kapoor and Kara D. Peterman. Quantification and prediction of the thermal performance of cold-formed steel wall assemblies. *Structures*, 30:305–315, 2021. doi:10.1016/j.istruc.2020.12.060.

Eduardo Roque and Paulo Santos. The effectiveness of thermal insulation in lightweight steel-framed walls with respect to its position. *Buildings*, 7(1):13, 2017. doi:10.3390/buildings7010013.

Eduardo Roque, Rui Oliveira, Ricardo M.S.F. Almeida, Romeu Vicente, and Antonio Figueiredo. Lightweight and prefabricated construction as a path to energy efficient buildings: thermal design and execution challenges. *International Journal of Environment and Sustainable Development*, 19(1):1–32, 2020. doi:10.1504/IJESD.2020.105465.

N. Soares, P. Santos, H. Gervásio, J.J. Costa, and L. Simões Da Silva. Energy efficiency and thermal performance of lightweight steel-framed (LSF) construction: A review. *Renewable and Sustainable Energy Reviews*, 78:194–209, 2017. doi:10.1016/j.rser.2017.04.066.

Suomen Rakennusinsinöörien Liitto RIL ry. *RIL 107-2012 Rakennusten veden- ja kosteudeneristysohje (in Finnish)*. Suomen Rakennusinsinöörien Liitto RIL ry, 2012.

Modeling of Artificial Snow Production Using Annular twin-fluid nozzle

Malene Nordbø[1] Odd Ivar Lindløv[2] Joachim Lundberg[1]

[1]Department of Process, Energy and Environmental Technology, University of South-Eastern Norway, Norway, Joachim.lundberg@usn.no

[2]Nedsnødd AS, Norway

Abstract

Nedsnødd AS develops a system for generating artificial snow. The concept is to optimize snow production for geographical locations where so-called 'marginal' conditions for snow production dominate the weather picture. To produce artificial snow, liquid water in a spray is exposed to cold air and becomes an agglomerate of frozen droplets. The basic idea is to improve the atomization of water to enhance the snow production capability. This work develops a model for the cooling process of the water droplets to simulate the processes determining the capabilities for snow production equipment.

Keywords: heat transfer, mass transfer, droplets

1 Introduction

Nedsnødd AS is a company specialized in nozzles for artificial snow production in climatically marginal regions. Marginal conditions mean that the climate is close to 0°C and the humidity is high. To produce artificial snow, liquid water is discharged as a spray to cold air and becomes an agglomerate of frozen droplets.

The basic mechanism of natural snow generation is kernel growth, in contrast to artificial snow where multi-droplet agglomeration is dominant. The trajectory of natural snow is several orders of magnitude longer than artificial snow. Several factors affect the production of artificial snow: air temperature and humidity, water temperature and velocity, droplet size distribution, and possible amount of nucleation kernels to enhance growth.

Current equipment for snow production has the disadvantage of high energy consumption (Techno Alpin, 2021) and the tendency to produce too wet snow at marginal conditions. By enhancing water atomization, artificial snow is produced at reduced water and air pressures, which reduce the energy consumption and ultimately the cost of the snow.

The artificial snow production technology started in the 1940s by a mistake where Dr. Ray Ringer studied the effect of rime icing on a jet engine in Canada. In 1961, Alden Hanson designed and patented a so-called snow fan machine for the generation of artificial snow by the addition of nucleation agents. Later on, several inventors have developed snow machines based on developed technology in addition to trial-and-error tests (Bellis, 2020).

Today, artificial snowmaking products are available worldwide, but the theory behind technology and process is not well documented or published. For this study, datasheets from different vendors and experimental studies performed in the Austrian Alps (Olefs et al., 2010) and at NTNU (Berg, 2017) have been used to understand how artificial snow production technology works.

Olefs et al. (2010) investigated the maximum wet-bulb temperature for producing artificial snow in the Alps. The study's author recommends that the maximum air temperature for producing snow is -1°C with 75% relative humidity but do not specify what weather conditions resulted in the snow density of 400 kg/m^3. They also indicated that relative humidity plays an essential role in the freezing process, where the amount of cooling is directly proportional to the relative humidity. If the humidity decrease, the evaporative cooling increases which give better snowmaking conditions.

Berg (2017) investigated techniques for artificial snow production aimed at Granåsen ski resort with an altitude of 180 m in Trondheim, which is in marginal conditions. The equipment of the study is a Northwind 450 snow fan, produced by DemacLenco with a water pressure of 30 bar(g). The estimate for the production of artificial snow was 52 m^3/h of snow. The lowest snow-density was found to be 811-936 kg/m^3. The study was performed in March, but ambient relative humidity and temperature are not specified.

Current work uses a novel twin-fluid nozzle developed by Nedsnødd AS. The nozzle is applied to a lance using low pressure (<5 bar(g)) air and water. An expanding air jet is aimed onto a deflector plate where an annular water sheet meets the high-velocity air jet. The result is enhanced droplet breakup and the droplets are expected to be smaller than for traditionally flat fan sprays. The nozzle design is similar to Lundberg et al. (2019).

A model is developed to simulate the behavior of the Nedsnødd artificial snow nozzle and the outcomes are discussed. The model is supported by experimental measurements. An image of the setup for the artificial snow spray is given in Figure 1.

Figure 1. Experimental setup and artificial snow spray located in Arabygdi.

2 Materials and methods

Artificial snow consists of cold small water droplets, that stick together to make agglomerates of droplets to imitate natural snow. In this work, an annular sheet twin-fluid nozzle is used to generate the droplets (Figure 2). The nozzle utilizes compressed air to accelerate the flow through a venture-type nozzle aimed at an external deflection cone. An annular water sheet is exposed to the deflected high-velocity airflow. Due to the high velocity of the air, the water sheet breaks up into fine water droplets with a high initial velocity. Traveling from the nozzle the droplets are exposed to ambient air where both mass (evaporation) and heat (convection) transfer occur. Depending on the surrounding air temperature and relative humidity, the droplets may freeze or remain as a liquid until it reaches the ground.

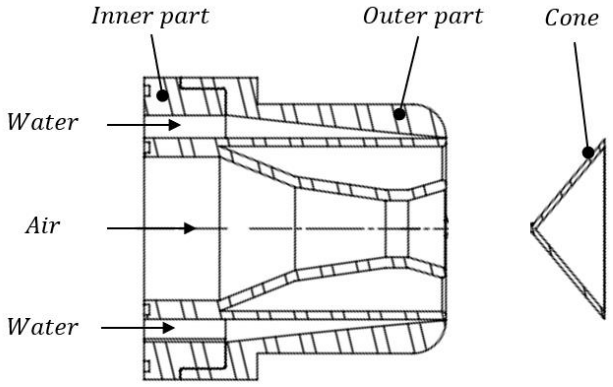

Figure 2. Split drawing of the Nedsnødd AS nozzle.

2.1 Modeling

The model is limited to single-sized droplets with ambient air at constant relative humidity, pressure, and temperature. In addition, the collision between the droplets throughout the trajectory and the interaction between other droplets are neglected. The models for atomization air from the nozzle, the water droplets, and the surrounding air are combined to output droplet behaviors like heat transfer, mass transfer, and droplet trajectory.

An important parameter in artificial snowmaking is relative humidity. It can be found by Cengel et al. (2015) using the vapor pressure of the water in the ambient air (P_v) divided by the saturation vapor pressure ($P_{v,sat@T}$) at the ambient pressure using:

$$RH\% = \frac{P_v}{P_{v,sat@T}} \quad (1)$$

The saturated vapor pressure is calculated using Buck's formula (Xu et al., 2012). It is assumed that the $RH\%$ is constant.

The velocity of the atomization air is modeled using thermodynamic relations for compressible flow (Cengel et al., 2015) as:

$$u_{a,0} = \sqrt{\gamma R_a T_{a,0}} \quad (2)$$

where γ, R_a, and $T_{a,0}$ is the heat capacity ratio, specific gas constant, and initial atomization air temperature, respectively.

The initial velocity of the water sheet is modeled using:

$$u_{sheet} = \frac{\dot{m}_w}{\rho_d A_{sheet}} \quad (3)$$

where

$$A_{sheet} = \frac{\pi}{4}\left((d_{annular} + \epsilon)^2 - d_{annular}^2\right). \quad (4)$$

$d_{annular}$ is the internal diameter of the sheet and ϵ is the sheet thickness. $\dot{m}_w$ is the mass flow of water and ρ_d is the water or droplet density.

Using Equations 2 and 3 indicates the initial droplet velocity, nevertheless the air velocity is in the order of 300 m/s and the sheet in the order of 10 m/s. The droplets are assumed to have an initial velocity of 10% of the air velocity with the directional vector:

$$u_{d,x0} = 0.1 \cdot u_{a,0}\cos(\theta) \quad (5)$$

$$u_{d,y0} = 0.1 \cdot u_{a,0}\sin(\theta) \quad (6)$$

where the angle θ is the deflection angle of the cone.

The density of surrounding air is modeled as Tracy et al. (1980) like:

$$\rho_{amb} = \frac{P}{287.04(T_{amb} + 273.15)} \quad (7)$$

where P is the atmospheric pressure and T_{amb} is the ambient temperature.

2.1.1 Motion (droplet trajectory)

An expression for the trajectory is found by applying Newton's second law on a droplet, as shown in Figure 3. Here, the drag, gravity, and buoyancy forces are included. Notice that if the drag force is equal to the gravity force, the acceleration becomes zero, gives the terminal velocity (Young & Freedman, 2014). The differential equations for calculating the acceleration of the droplet in x and y-direction are obtained, as shown in Equations 8 and 9 (Dehghani-Sanij et al., 2018).

The droplet velocity in the x-direction dx/dt and y-direction $/dt$, equals u_x and u_y, respectively. Further, the velocity of ambient air in the x and y-direction is represented by u_{rx} and u_{ry}. d represents the droplet diameter.

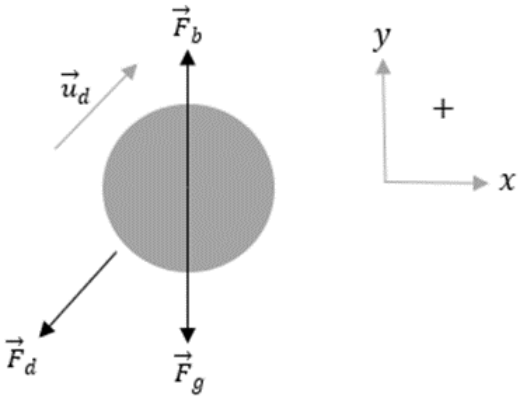

Figure 3. Free body diagram of a water droplet.

$$\frac{d^2x}{dt^2} = -\frac{3}{4}\frac{C_d}{d}\frac{\rho_{amb}}{\rho_d}\left(\frac{dx}{dt} - u_{rx}\right) \cdot \sqrt{\left(\frac{dx}{dt} - u_{rx}\right)^2 + \left(\frac{dy}{dt} - u_{ry}\right)^2} \tag{8}$$

$$\frac{d^2y}{dt^2} = g\left(\frac{\rho_{amb}}{\rho_d} - 1\right) - \frac{3}{4}\frac{C_d}{d}\frac{\rho_{amb}}{\rho_d}\left(\frac{dy}{dt} - u_{ry}\right) \cdot \sqrt{\left(\frac{dx}{dt} - u_{rx}\right)^2 + \left(\frac{dy}{dt} - u_{ry}\right)^2} \tag{9}$$

In this paper, the air represents a mixture of entrained air from the surroundings and air from the nozzle. This is simplified by adding an initial ambient air velocity. The droplet velocity is then calculated by using Equation 10 (Dehghani-Sanij et al., 2018).

$$u_d = \sqrt{{u_x}^2 + {u_y}^2} \tag{10}$$

To determine the drag coefficient C_d, which is a function of the droplet Reynolds number Re_d, the Schiller Neumann model is applied similar to Dehghani-Sanij et al. (2018):

$$C_d = \begin{cases} \frac{24}{\mathrm{Re_d}} & Re_d \leq 1 \\ \frac{24}{\mathrm{Re_d}}(1 + 0.15\mathrm{Re_d}^{0.687}) & 1 < Re_d \leq 1000 \\ 0.44 & Re_d > 1000 \end{cases} \tag{11}$$

$$Re_d = \frac{\rho_{amb} d u_{eff}}{\mu_a} \tag{12}$$

where u_{eff} is the relative motion of the droplets to the ambient air and μ_a is the dynamic viscosity of air.

2.1.2 Heat transfer

When the droplets are discharged from the nozzle, the heat transfer influences the droplet size. In this model, convection and evaporation are considered, while conduction and radiation are neglected. It is assumed that the droplet evaporated from positive centigrade until it obtains 0°C. When this temperature is reached, the droplets are considered to be frozen at 0°C.

The following expression is used to calculate the change of the droplet temperature, given in Dehghani-Sanij et al. (2018) as:

$$\frac{dT_d}{dt} = \left[\frac{6(\frac{dm_d}{dt})}{\pi \rho_d d^3}\right] T_d - \frac{6}{\rho_d c_{p,d} d}(Q_e + Q_c) \tag{13}$$

where the convective heat loss can be found in Lozowski et al. (2000) using

$$Q_c = h_c(T_d - T_{amb}). \tag{14}$$

The heat transfer coefficient h_c is modeled as

$$h_c = \frac{Nu \cdot k_a}{d} \tag{15}$$

with the Nusselt number Nu and the thermal conductivity of air k_a.

$$Nu = 2.0 + 0.6 Pr^{0.33} Re_d^{0.5} \tag{16}$$

$$k_a = 9.027 \cdot 10^{-5}\, T_{amb} + 0.0246 \tag{17}$$

The Prandtl number Pr is modeled like Bergman et al. (2011) using the dynamic viscosity of air μ_a and the thermal diffusivity α_a of air.

$$Pr = \frac{\mu_a}{\rho_{amb} \cdot \alpha_a} \tag{18}$$

$$\mu_a = \mu_0 \left[\frac{T_0 + 120}{T_{amb} + 120}\left(\frac{T_{amb}}{T_o}\right)^{1.5}\right] \tag{19}$$

$$\alpha_a = \frac{1}{57736 - 585.78\, T_{amb}} \tag{20}$$

2.1.3 Mass transfer

From Equation 13 Q_e is used. This is the heat loss due to vaporization (Bergman et al., 2011) and is modeled as:

$$Q_e = h_c \left(\frac{Pr}{Sc}\right)^{0.63} \frac{E \cdot \Delta H_{vap}}{P \cdot c_{p,amb}} P_v \tag{21}$$

where

$$Sc = \frac{\mu_a}{\rho_{amb} D_{d,amb}} \tag{22}$$

E is the ratio of molar weight, ΔH_{vap} is the heat of vaporization, and $D_{d,amb}$ is the binary diffusion coefficient of water into the air at atmospheric pressure (Incropera, 2017)

$$D_{d,amb} = 0.26x10^{-4}\left(\frac{T_{amb} + 273.15}{273.15}\right)^{.1,5} \tag{23}$$

The heat capacities for the airflow water and entrained air are assumed constant throughout the process. The change of the droplet diameter is calculated by using Equation 24.

$$\frac{d\mathrm{d}}{dt} = -\frac{(\frac{dm_d}{dt})}{\rho_d \pi d^2} \tag{24}$$

where $(\frac{dm_d}{dt})$ is calculated according to Horjen (2013) using:

$$(\frac{dm_d}{dt}) = \frac{Q_e}{\Delta H_{vap}} A_d \quad (25)$$

A_d is the surface area of the droplet.

2.1.4 Constants

The constants for the modeling are summarized in Table 1 where the reference is indicated.

Table 1. The table presents constants and initial conditions are used in the model.

	Value	Units	References
$c_{p,amb}$	1.005	[J/kg K]	Cengel et al. (2015)
$c_{p,d}$	4180	[J/kg K]	Cengel et al. (2015)
$d_{annulai}$	$1.4 \cdot 10^{-2}$	[m]	Measured
E	0.6215	[-]	(Dehghani-Sanij et al., 2018)
g	9.81	$[m/s^2]$	Cengel et al. (2015)
ΔH_{vap}	$22.6 \cdot 10^5$	$[J/kg]$	Cengel et al. (2015)
P	101325	$[Pa]$	Cengel et al. (2015)
R_a	287	[J/kg K]	Cengel et al. (2015)
$RH\%$	79	$[-]$	Measured
T_{amb}	-3	$[\,°C]$	Measured
T_o	296.16	$[\,K]$	(Dehghani-Sanij et al., 2018)
γ	1.4	[-]	Cengel et al. (2015)
ϵ	50	[µm]	Measured
μ_0	$1.8325 \cdot 10^{-5}$	$[Pa \cdot s]$	(Dehghani-Sanij et al., 2018)
ρ_d	1000	$[\,Kg/m^3]$	Cengel et al. (2015)
Initial conditions			
x_0	0	$[m]$	Defined
y_0	1.324	$[m]$	Measured
u_{rx}	1.0	[m/s]	Defined
u_{ry}	0	[m/s]	Defined
θ	50	[°]	Measured
$T_{d,0}$	1	$[°C]$	Measured
$T_{a,0}$	-37.19	$[\,°C]$	Nordbø (2021)
d_0	40,50,120,170,360	$[\mu m]$	Defined
t	6	$[s]$	Defined

2.2 Experimental setup

Nedsnødd AS is using a transportable snow-producing rig on a car trailer. In short, the rig contained two aggregates, a water tank, a pump, a compressor, an electric converter, a dryer, water, and air hoses, sensors, lance, and a nozzle. The experimental rig is described in detail in Nordbø (2021).

The experimental measurement intends to compare and adjust the model. The model demands an input on bulk flow velocity, droplet sizes, and droplet velocity distribution.

The measurements were performed using a LED-based shadow imaging technique developed in the work by Lundberg et al. (2019). Back-illuminated images were captured by a high-speed camera where the droplets were manually counted by mouse-clicking on the image. The velocity was found from the adjacent frame. The same procedure was performed for 77 droplets used in the experimental measurements. The camera settings are shown in Table 2.

Table 2. High-speed camera settings.

Fastcam – APX RS model 250K	
Frame rate	5000 fps
Shutter velocity	1/50000 sec
Resolution	512 x 1024
Recording time	0.1144 sec

3 Results and discussion

3.1 Experimental

The model developed in this work is based on three experiments (Porsgrunn, Arabygdi, and Kviteseid). The only experiment yielding snow is the Arabygdi experiment. The ambient conditions and the pressure parameters in each experiment are given in Table 3.

The experimental measurement in Arabygdi gives the droplet size distribution in Figure 4 compared to a Rosin-Rammler distribution (solid line). Figure 5 shows the quality of the fit in an ln-ln plot. The fit does not represent the largest droplets very well and can benefit from a higher number of samples. It is important to consider that this is from a single location in the flow and might be different in other locations. The location in the spray is 41 cm from the nozzle and 16 cm radially.

Table 3. Experimental parameters.

Place	*Porsgrunn*	*Arabygdi*	*Kviteseid*
Date	13.03.2021	18-19.03.21	21.03.2021
Altitude	7 m	687 m	307 m
T-Ambient	-2.6 °C	-2.5 to -4 °C	-1 to 1 °C
RH%	96%	79 %	64 %
U-wind	0-0.8 m/s	0-1.7 m/s	5 m/s
P-Water	2.66 bar(g)	4.64 bar(g)	4.64 bar(g)
T-Water	~10 °C	1 °C	2 °C
P-Air	5.38 bar(g)	1.95 bar(g)	1.95 bar(g)
T-Air	10 °C	10 °C	10 °C
T-Wet-bulb	-3.05 °C	- 4.6 °C	-3.64 °C

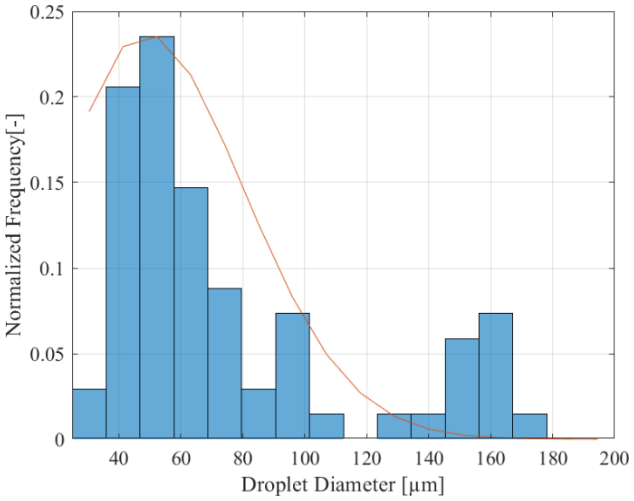

Figure 4. Droplet distribution of experiments in Arabygdi compared to an optimized Rosin-Rammler distribution.

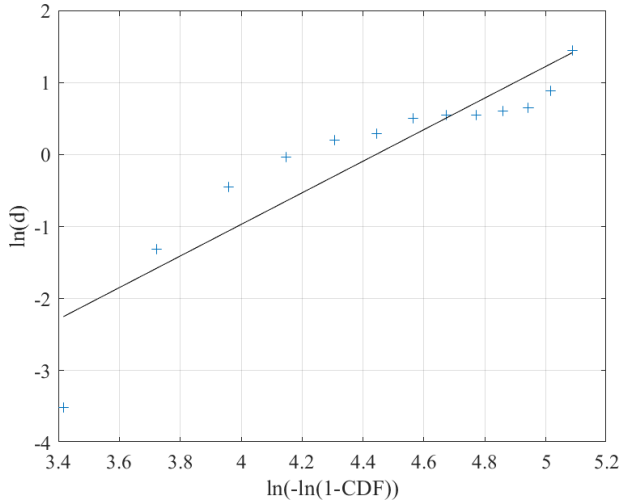

Figure 5. ln-ln plot of the quality of fit for the experiment in Arabygdi, where CDF is the cumulative distribution function.

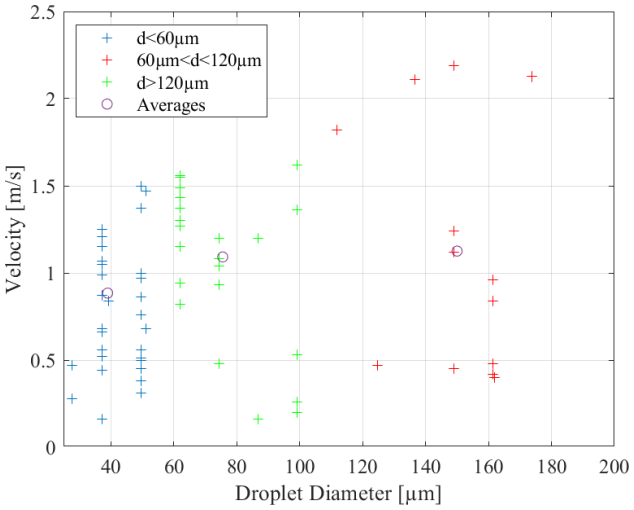

Figure 6. The velocity of the droplets from the experiment in Arabygdi.

The velocity of the droplets (Figure 6) shows a weak tendency of increased velocity with increasing diameter. Nevertheless, the measurements show that the bulk velocity is approximately constant in this region of the spray.

Visual considerations during the experiment confirmed that the nozzle produced artificial snow at given parameters. From the image shown in Figure 7, the droplets form large agglomerates according to theory.

Figure 7. Rime-shaped snow in Arabygdi.

3.2 Simulation

The trajectory, flight time, velocity- and temperature profile using the initial conditions are shown for droplets with the diameter of 40, 50, 120, 170, and 360 µm. The range of 40 – 170 µm droplet sizes is defined based on the image processing performed in Arabygdi. The 360 µm is to investigate how larger droplets influence heat and mass transfer.

The initial angle of the droplet angle is set to 50°. Also, the initial height of the droplets is defined as 1.324 m, based on the nozzle position measured during the experiment.

The droplets of 40 µm and 50 µm obtain the most significant displacement with more or less neutral gravitational force. The droplet of 360 µm shows weak affection of the entrapped air velocity following a ballistic pattern. The 360 µm droplet shows a higher influence of the gravitational force while the other droplets are drag force driven. This is shown in Figure 8 and Figure 9. The velocity profile of each droplet is shown in Figure 10.

The initial temperature of the droplets is 1 °C based on experimental measurements. The droplets are cooled down to 0 °C within microseconds due to evaporation before the temperature is further decreased. Figure 11 shows how the temperature of the droplets converges to its final temperature.

Figure 11 shows that the 360 µm droplet does not reach the same final temperature as the other droplets. All droplets, except the 360 µm droplet, cool down to a temperature just below the ambient temperature of - 3°C before hitting the ground. The droplet temperature as a function of travel length is illustrated in Figure 11.

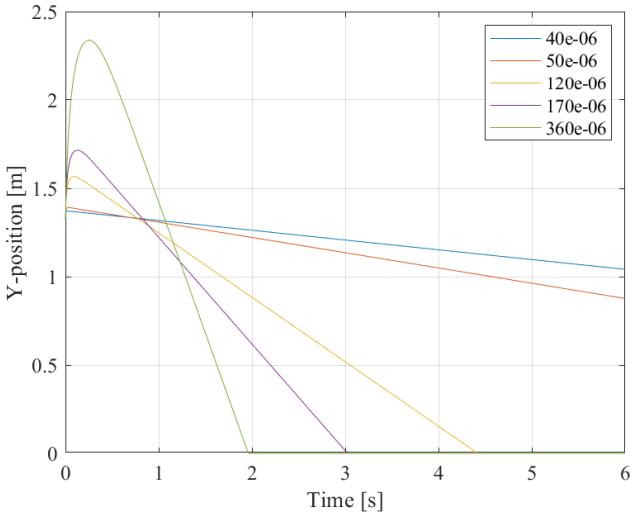

Figure 8. Predicted flight time that is obtained by the modeled droplets.

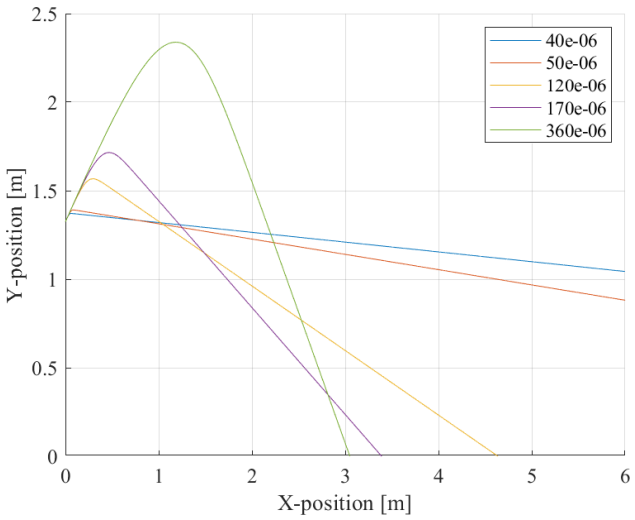

Figure 9. Position/trajectory of the modeled droplets.

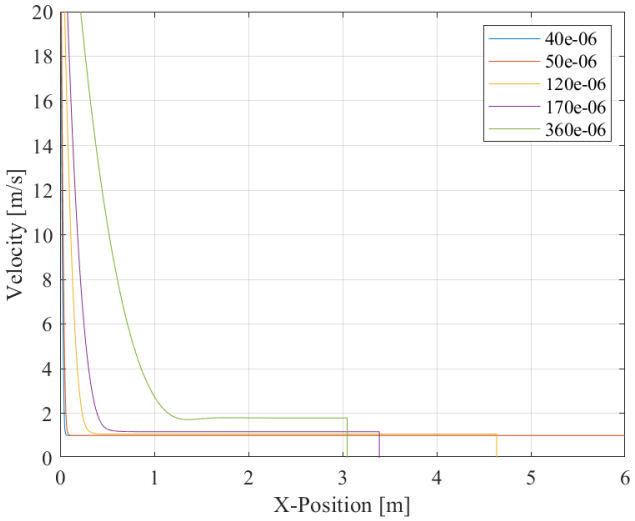

Figure 10. Velocity profile of the modeled droplets concerning the x-position of the droplets.

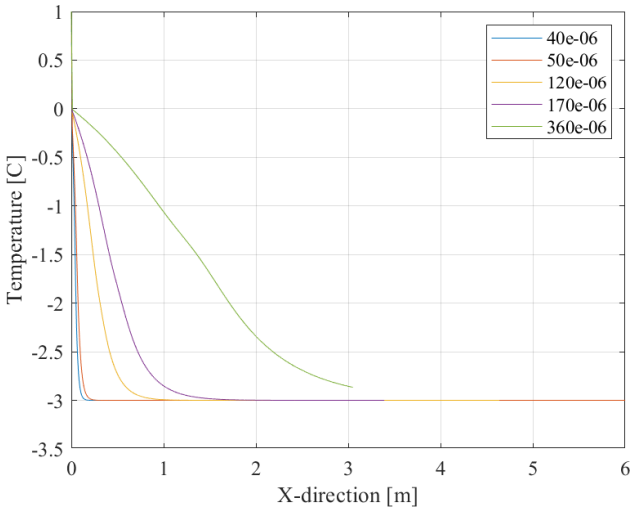

Figure 11. Temperature change concerning the motion of modeled droplets in the x-direction.

The airflow temperature inside the nozzle's throat was calculated to be -37.19 °C, assuming an isentropic process, compressible gas, and the stagnation temperature from the compressor to be 10°C. A thermographic photo captured in Arabygdi shows that the material at the nozzle tip is - 37.5°C, which indicates this to be a reasonable assumption. On the other hand, the amount of water flow was three times greater than the airflow through the nozzle, and the water was assumed to be 1 °C. The heat transfer of the water contributes more significantly to the mixture temperature of the ejected droplets.

A thermographic photograph of the discharged water sheet, 1 cm out from the nozzles exit plane in Arabygdi, indicated that the water was reduced to roughly -1.4 °C. The temperature simulation of the droplets showed that the droplets rapidly decreased at this point of the nozzle. As the thermographic camera used has an accuracy of ± 2°, the result seems reasonable. In addition, the temperature simulation showed that all droplets reached 0 °C within 150 µs and could freeze before they reached the ground. Here, the definition of evaporative heat loss comes into sight. It was defined to stop when the surface temperature of the droplets had reached 0°C. Thus, the water molecules of high internal energy would stop ejecting themselves from the droplets and thereby stabilize the temperature of the droplets. The wet-bulb temperature, measured to be –4.6 °C by using the weather conditions in Arabygdi, was thereby not reached.

Changes in the relative humidity RH% were not simulated in this work. As an effect of this, the evaporative heat transfer was expected to be larger than in the experiment. In the experiments, the humidity from the evaporation is expected to saturate the air rapidly after the atomization.

The diameter 40 and 360 droplets were reduced by 0.04 and 0.06 %, respectively. The experiment in Arabygdi gave snow density of 490 kg/m^3 in the other

locations, no snow was produced. There may have been other factors that influenced the product. The experiment in Porsgrunn was not performed within a continuous cold period like the experiment performed in Arabygdi. Thus, the ground in Porsgrunn was probably not frozen and heated the falling droplets.

The snow shape obtained in Arabygdi was photographed. From the picture, frozen droplets are stacked on each other and may be characterized as rime formation.

4 Conclusion

This work aimed to perform both literature, modeling, and experimental study of artificial snow production in marginal geographic conditions. A snow-producing rig designed by Nedsnødd AS was used during the experimental study. The innovative part of the rig was the assembled novel twin-fluid annular sheet nozzle, where a thin sheet of water was atomized into droplets by high-velocity air.

As the literature on artificial snow production was limited, the water cycle and natural snow formation were studied to understand artificial snow production. A theoretical model was developed to analyze the trajectory and heat and mass balance of a single droplet discharged from the nozzle. The snow density goal was defined to be 500 kg/m3. A high-speed camera was used to record the droplet size and velocity in the spray. The experimental measurements were further used to improve the droplet model.

Only one of the experiments performed in Arabygdi yielded snow with a density of 490 kg/m3, which satisfied the snow density goal of 500 kg/m3.

The model developed during this work can be used for general trends in artificial snow production. The model gives reasonable results for single droplets that can be further developed into a multi-droplet system.

Acknowledgments

The University of South-Eastern Norway acknowledges Nedsnødd AS for the support and experimental rig.

References

M. Bellis. Who Invented the Snowmaking Machine? ThoughtCo, Oct. 29, 2020.

O.E.H. Berg, *Optimal produksjon av snø fra flere produksjonsenheter i samme område*. Master's thesis, Department of Engineering cybernetics, Norwegian University of Science and Technology, Trondheim, 2017.

T.L. Bergman, A.S. Lavine, F.P. Incropera and D.P. DeWitt. *Introduction to Heat Transfer, 6th ed*. John Wiley & Sons, Inc, 2011.

Y. A. Cengel, M. A. Boles and M. Kanoglu. *Thermodynamics: An Engineering Approach, 8th ed*. New York: McGraw-Hill Education, 2015.

A.R. Dehghani-Sanij, Y.S. Muzychka and G.F Naterer. Droplet trajectory and thermal analysis of impinging saline spray flow on marine platforms in cold seas and ocean regions. *Ocean Engineering*, 148:538-547, 2018. doi:10.1016/j.oceaneng.2017.11.053.

I. Horjen. Numerical modeling of two-dimensional sea spray icing on vessel-mounted cylinders. *Cold Regions Science and Technology* 93:20–35, 2013. doi:10.1016/j.coldregions.2013.05.003.

F. P. Incropera, D. P. Dewitt, T.L. Bergman and A. S. Lavine. *Incroperas's principles of heat and mass transfer, 1st ed.* New York: John Wiley & Sons Inc, 2017.

E.P. Lozowski, K. Szilder and L. Makkonen. Computer simulation of marine ice accretion. *Philosophical Transactions of the Royal Society A*, 358:2811–2845, 2000. doi:10.1098/rsta.2000.0687.

J. Lundberg, K. Vaagsaether and O.I. Lindløv. Performance of a novel diesel atomization nozzle. Nordic Flame days 2019, August 28th-29th, Turku, Finland, 2019.

M. Nordbø. *Experimental investigation of artificial snow production in marginal geographic conditions*, Master's Thesis, Faculty of Technology, Natural sciences and Maritime Sciences, University of South-Eastern Norway, Norway, 2021.

M. Olefs, A. Fischer and J.Lang. Boundary Conditions for Artificial Snow Production in the Austrian Alps. *Journal of applied meteorology and climatology*, 49(6):1096-1113, 2010. doi:10.1175/2010JAMC2251.1.

Techno Alpin. TT10: Tower power. technoalpin.com (accessed online Apr. 21, 2021).

C.R. Tracy, W.R. Welch and W.P. Porter. *Properties of Air, a Manual for Use in Biophysical Ecology*. Technical report No. 1, third ed. University of Wisconsin, 1980.

J. Xu, Q. Wei, S.Peng and Y. Yu. Error of Saturation Vapor Pressure Calculated by Different Formulas and Its Effect on Calculation of Reference Evapotranspiration in High Latitude Cold Region. *Procedia Engineering*, 28:43-48, 2012. doi:10.1016/j.proeng.2012.01.680.

H. D. Young and R. A. Freedman. *Sears and Zemansky's University Physics with Modern Physics*, 13th Edition, Pearson, 2014.

Electrification of an entrainment calciner in a cement kiln system – heat transfer modelling and simulations

Ron M. Jacob Lars-Andre Tokheim

Department of Process, Energy and Environmental Technology, University of South-Eastern Norway,
{ron.jacob, Lars.A.Tokheim}@usn.no

Abstract

Carbon capture and storage may be applied to reduce the CO_2 emissions from a cement plant. However, this often results in complex CO_2 capture solutions. To simplify the capturing process, an alternative is to electrify the cement calciner. This study covers the feasibility of electrifying an existing calciner by inserting electrically heated rods in the calciner. An existing entrainment calciner in a Norwegian cement plant is used as a case study.

A model is developed to quantify the aspects concerning the feasibility of the calciner. The model first estimates the possible area of inserted rods in the available space. A mass and energy balance is then performed to estimate the heat duty of the heating rods. Further, a radiation heat transfer model is included to identify the feasibility of transferring heat from the rods to the raw meal. Finally, the model includes the design of the heating rod to estimate the required number of heating elements.

The results indicate that it is technically feasible to electrify the calciner. The total heat duty of the calciner is 77 MW, with 68 MW for meal preheating and calcining, and 9 MW for gas preheating. 2570 heating rods are required, operating at 1150 °C in the gas preheating zone and 1050 °C in the meal preheating and calcining zone. The feasible heat flux is 26-34 kW/m² for gas preheating, 35-80 kW/m² for meal preheating and 30-50 kW/m² for calcination. However, some challenges related to recuperating the heat from the gas and maintenance of the system must be studied further.

Keywords: Calcination, Electrification, Heat transfer, Resistance heating

1 Introduction

The cement industry is responsible for around 7% of the global emission of CO_2 and around 4% in the EU (IEA, 2020). The primary sources of these emissions are the combustion of fossil fuels and the decomposition of limestone ($CaCO_3 \rightarrow CaO + CO_2$). A modern cement kiln system couples these two processes, and this coupling gives a very efficient, direct-contact heat transfer.

The CO_2 emission from the system may be captured by using carbon capture and storage technologies. However, in this method, the CO_2 must be separated from other components in the flue gas, making it a complex process. A simpler solution may be to electrify the calciner. An electrified calciner will have pure CO_2 generated from the decomposition reaction, thus the need for separation from flue gas may be avoided. This method has the potential to avoid around 72 % of the CO_2 emission from the cement kiln system (Tokheim et al., 2019). However, for this to be an environmentally viable solution, the electricity must be produced from renewable sources, thereby avoiding indirect CO_2 emissions.

A suitable calciner design must be selected to electrify a calciner. Different designs may be selected, such as rotary calciners, drop tube calciners, fluidized bed calciners and tunnel calciners. The literature available on electrified calciner is sparse, and no studies of an electrified entrainment calciner have been found. The Leilac project studied a drop tube calciner with indirect heating using natural gas (Hills et. al., 2017), and this drop tube calciner may be electrified by replacing natural gas with an electrical heater (Usterud et al., 2021). A fluidized bed calciner concept using binary particles has also been studied (Samani et. al., 2020).

In this study, electrification of an existing calciner operating in the entrainment mode is used in a case study. This will provide a reference case to which other potential calciner designs may be compared when it comes to electrification.

This work aims to study the possibility of electrifying the entrainment calciner by inserting heating rods in it. Such a concept may make it easy for the cement industry to quickly transition to an electrically heated calciner without making significant changes to the existing calciner geometry. Such a study has not been published before to the best of authors' knowledge.

2 System description

An entrainment calciner operating in a Norwegian cement plant, producing 1 Mt of clinker per year, is considered for electrification in this study. A comparison of the existing calciner and an electrified version of this calciner are shown in Figure 1.

The existing calciner (cf. the left-hand side of Figure 1) has five main parts; a downdraft flash calciner with a burner, a mixing chamber, a tube calciner, a swirl chamber and gas duct connections to cyclone separators (Tokheim, 2006).

The fuel mix (coal, refused derived fuel, solid hazardous waste and animal meal) is fed into the downdraft burning-chamber where it is mixed with tertiary air and preheated meal. The fuel ignites and provides energy for calcination of the preheated meal. The meal swirls around the burner wall and protects it from too high temperature generated by the burning fuel. The meal is then transported to the mixing chamber where it mixes with high temperature kiln gas. The kiln gas provides additional energy needed for meal calcination and also enough energy to entrain the meal through the tubular calciner (the "Pyroclone") towards the swirl chamber (the "Pyrotop"), which improves the burnout of fuel particles. The mixture of gas and meal is then transported to cyclone separators, where the calcined meal is sent to the rotary kiln for further processing, whereas the gas is used for preheating of meal in cyclone preheater tower (Tokheim, 2006). The dimensions of the reference calciner used for calculations are summarized in Table 1.

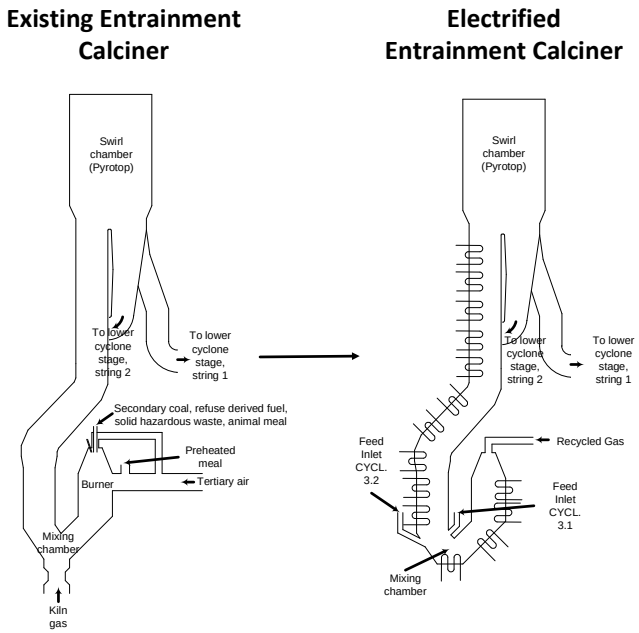

Figure 1: Existing (left) vs electrified entrainment calciner (right)

Table 1. Dimensions of the reference calciner geometry

Dimensions	Symbol	Value
Diameter of the tubular calciner [m]	D_C	3.74
Length of the gas preheater section [m]	L_{GP}	7
Length of the calciner section after meal feeding [m]	L_C	50.2

The existing calciner may be converted to an electrified calciner by making the following changes (Figure 1, right-hand side):

1. Cutting the supply of kiln gas
2. Cutting the supply of fuel, air and preheated meal in the burner
3. Moving the meal inlets to a position right above the mixing chamber
4. Feeding recycled CO_2 (required for particle entrainment) at the top of the combustion chamber
5. Inserting heating rods in the combustion chamber and the mixing chamber to provide energy for preheating of the recycled gas
6. Inserting heating rods along the tube calciner geometry to provide energy for calcination

The kiln gas and the tertiary air will bypass the electrified calciner (Figure 1, left-hand side) and will instead be mixed and lead to the preheater tower (not shown in the figure) for meal preheating, so that the rest of the kiln system is unaffected by the calciner modification.

3 Model development

The modelling combines a mass and energy balance of the calciner with a geometric model for insertion of heating rods, a model for heat transfer from the heating rods and design of an appropriate heating element. This section covers these four aspects of the modelling work.

3.1 Heating element design

Resistance heating is a relatively simple technology for electricity-based heating. The heat is produced when an electric current (I) passes though a resistor (the heating element) with a certain resistance (R). The produced heating rate ($\dot{q}_e$) may be quantified as,

$$\dot{q}_e = I^2 R = VI \qquad (1)$$

Here, V is the voltage drop over the heating element.

The resistance of the heating element (R) is further given by,

$$R = \rho_e \frac{4 l_e}{\pi {d_e}^2} \qquad (2)$$

Here, ρ_e is the resistivity of the heating element, l_e is the length of the heating element and d_e is its diameter (assuming it is a wire).

The resistivity of the heating element is dependent on the resistor material. A range of materials is available in the market. They include metallic alloys such as nichrome, Kanthal wires, and non-metallic elements such as silicon carbide and molybdenum disilicide.

Metallic alloys are generally recommended for temperature ranges of 1200-1400 °C, whereas non-metallic materials are recommended for higher temperatures, i.e. the range 1600-1900 °C (Lupi, 2017).

The calciner will operate between 900 and 1000 °C. Hence, metallic alloys are considered in this work. The maximum operating temperature of some metal alloys are shown in Figure 2, whereas the resistivity as a function of temperature is shown in Figure 3.

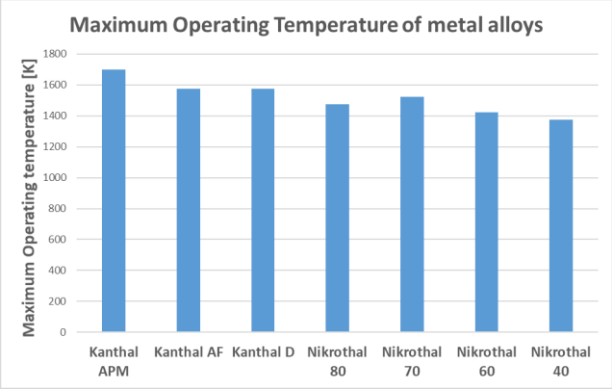

Figure 2: Maximum operating temperatures of some metal alloys used for resistance heating

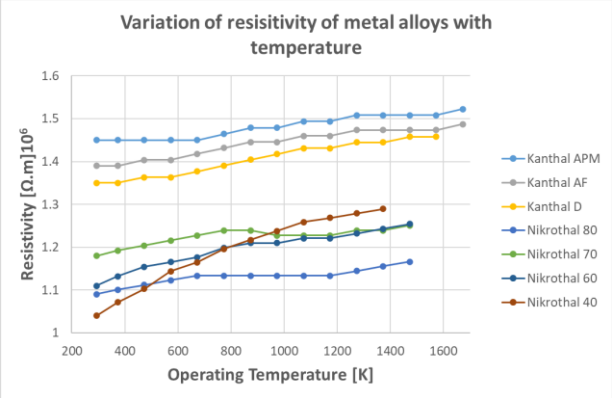

Figure 3: Variation of resistivity with temperature for some metal alloys

The heating elements may be mounted into the furnace with various support systems. In this study, spiral winding of heating elements on a ceramic tube is considered, referred to as heating rods in the study. The schematic of this system is shown in Figure 4.

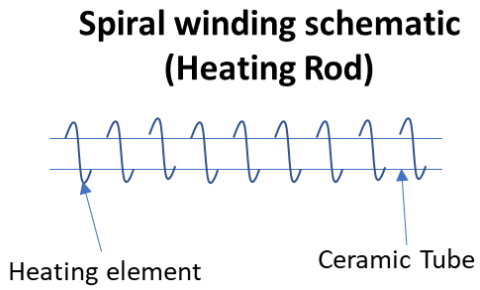

Figure 4: Spiral-winding schematic (heating rod)

The recommended value for the diameter of the heating element (d_e) is 2.0 – 6 .5 mm and that of the ceramic tube diameter (D_R) is $D_R = (12 - 14) \times d_e$ (Kanthal, 2020). In this study, the diameter of the heating element (d_e) is assumed to be 4 mm, and the ceramic tube diameter (D_R) is assumed to be 50 mm.

3.2 Heating rod insertion model

A model is developed to predict the area occupied by the inserted heating rods (A_R). In general, if this area is large, the contact between the heating surface and the meal will be large, leading to a higher heat transfer rate. However, if the area is too large, by inserting too many rods, then the space between the rods might be too small, which will affect the structural integrity of the calciner. A model is developed by assuming a defined heating rod arrangement and using the fraction of axial and radial length occupied by heating rods (f_C) and the diameter of the heating rods (D_R) as input parameters. The proposed heating rod arrangement is shown in Figure 5.

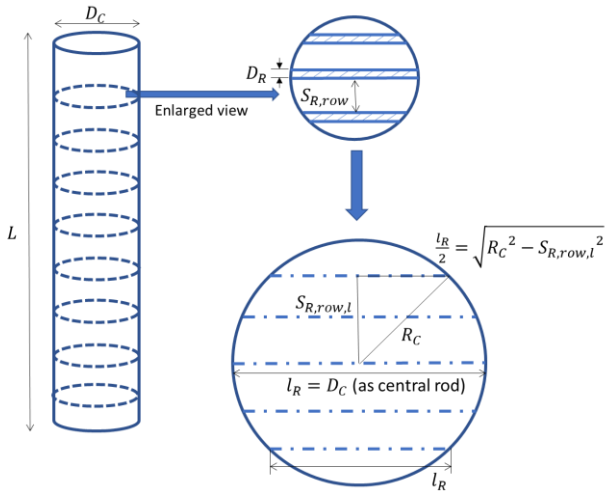

Figure 5: Heating rod design pattern

The fraction f_C is directly related to the heating rod area. Increasing this fraction will provide more space for the placement of heating rods, which in turn will increase the total area of the heating rods.

The total length occupied by the heating rods is given by,

$$f_C L = D_R N_{col} \tag{3}$$

Here, L is the length of the section, equal to L_{GP} in the gas preheating section and equal to L_C in the meal section. N_{col} is the number of columns in the axial (gas flow) direction. Rearranging the equation,

$$N_{col} = \frac{f_C L}{D_R} \tag{4}$$

To simplify calculations in the radial direction, one rod is assumed to go through the center of the calciner (the length of this rod is equal to calciner diameter, D_C), whereas the other rods are placed between the center rod and the wall in both directions, as shown in Figure 5. To

facilitate visualization, only a few rods are shown in the figure.

The number of rods in each radial direction ($N_{R,row,m}$) is given by,

$$N_{R,row,m} = \frac{f_C R_C}{D_R} \quad (5)$$

Here, R_C is the radius of calciner. The number of heating rods per rows is given by,

$$N_{R,row} = \left(2 \times N_{R,row,m}\right) + 1 \quad (6)$$

The total number of rods is further be given by,

$$N_R = N_{R,row} \times N_{col} \quad (7)$$

If the spacing between the rods in a row ($S_{R,row}$) is equal, it can be determined by,

$$S_{R,row} = \frac{R_C - \left(N_{R,row,m} \times D_R\right)}{N_{R,row,m} + 1} \quad (8)$$

The length of each rod (l_R) in the radial direction is, however, different for each rod. This length can be derived from Pythagoras' theorem as shown in Figure 5 and is given by,

$$l_R = 2 \times \sqrt{{R_C}^2 - {S_{R,row,l}}^2} \quad (9)$$

Here $S_{R,row,l}$ is the actual spacing distance of each rod from the central rod (as also shown in Figure 5).

An effective rod length ($l_{R,eff}$) is then calculated by taking the average over all possible lengths in the calciner. The total area occupied by the inserted rods (A_R) can thus be given by,

$$A_R = N_R \times \pi D_R l_{R,eff} \quad (10)$$

3.3 Heat and mass balance

To simplify the calculations, the modified calciner may be divided into three zones.

1. **Gas preheating zone:** The gas is preheated to the calcination temperature in this zone.
2. **Meal preheating zone:** The meal is preheated to the calcination temperature in this zone.
3. **Meal calcining zone:** The meal gets calcined ($CaCO_3$ → $CaO + CO_2$) in this zone.

The simplified reactor model is shown in Figure 6.

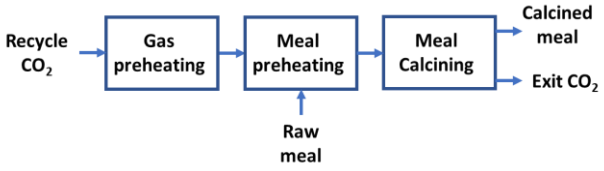

Figure 6: Different zones used in the heat and mass balance

The entrainment velocity in existing calciners may vary between 10-20 m/s (Becker et al., 2016), while in some calciners, this gas velocity may be as low as 5-7 m/s. In this study, the entrainment velocity is assumed to be 7 m/s. The impact of changing this is presented in the results. Other assumptions are summarized in Table 2.

The calcination temperature (T_{calc}) is relatively high (914 °C) compared to regular calciners. This is because the gas in the electrified calciner is pure CO_2, so a higher temperature is required to generate a CO_2 equilibrium pressure (Stanmore and Gilot, 2005) higher than the partial pressure in the calciner (~1 atm). The temperature of the recycled gas ($T_{in,g}$) is based on a previous study on CO_2 heat utilization (Jacob, 2019). The other values in the table are based on a previous calciner electrification study applying the same kiln system as a design basis (Tokheim et al., 2019).

Table 2: Assumptions for heat and mass balance

Section	Parameter	Symbol	Value
General assumptions	Entrainment velocity	v_C	7 m/s
	Calcination temperature	T_{calc}	914°C
	Weight fraction of CaCO3 in raw meal	w_{CaCO3}	0.77
Gas preheating	Inlet temperature of recycle gas	$T_{in,g}$	470°C
	Outlet temperature of recycle gas	$T_{out,g}$	914°C
Meal preheating	Mass flow rate of raw meal	$\dot{m}_{PHM}$	210 ton/hr
	Inlet temperature of raw meal	$T_{in,PHM}$	658°C
Meal calcination	Enthalpy of calcination	H_{calc}	-3.6 MJ/kgCO_2
	Enthalpy of other reactions in the calciner	$H_{calc,other}$	0.3 MJ/kgCO_2
	Calcination degree	f_{calc}	0.94

The mass flow rate of CO_2 ($\dot{m}_{CO2,C}$) inside the calciner may be calculated from entrainment velocity by,

$$\dot{m}_{CO2,C} = \rho_{CO2} A_C v_C \quad (11)$$

Here, ρ_{CO2} is the density of gas calculated from the ideal gas law, A_C is the cross-sectional area of the calciner and v_C is the velocity of gas inside the calciner (entrainment velocity). The mass flow of CO_2 ($\dot{m}_{CO2,calc}$) produced from calcination reaction is calculated by,

$$\dot{m}_{CO2,calc} = \dot{m}_{PHM} w_{CaCO3} \frac{M_{CO2}}{M_{CaCO3}} \frac{1}{f_{calc}} \quad (12)$$

Here, M_{CO2} is the molecular mass of CO_2 and M_{CaCO3} is the molecular mass of $CaCO_3$.

The mass flow rate of recycling CO2 ($\dot{m}_{CO2,recyc}$) can thus be determined by,

$$\dot{m}_{CO2,recyc} = \dot{m}_{CO2,C} - \dot{m}_{CO2,calc} \quad (13)$$

The heat required to heat the CO_2 (q_{GP}) in the gas preheater section is given by,

$$q_{GP} = \dot{m}_{CO2,recyc} C_{p,CO2} \left(T_{in,g} - T_{out,g}\right) \quad (14)$$

Here $C_{p,CO2}$ is the heat capacity of the gas given by a polynomial equation (Green, Perry, 2008),

$$C_{p,CO2} = C1 + C2\left[\frac{C3/T}{sinh\,(C3/T)}\right]^2 + C4\left[\frac{C5/T}{cosh\,(C5/T)}\right]^2 \times \frac{M_{CO2}}{1000}\, J/kg.K \quad (15)$$

Here, C1 = 29370, C2 = 34540, C3 = 1428, C4 = 26400 and C5 = 588 (units are skipped here for simplicity).

The heat required in the meal preheating section (q_{MP}) is given by,

$$q_{MP} = \dot{m}_{PHM} C_{p,PHM} \left(T_{in,PHM} - T_{calc}\right) \quad (16)$$

Here $C_{p,PHM}$ is the heat capacity of preheated meal and is equal to 1260 J/(kg·K) (Samani, 2020).

The heat required in the meal calcination (q_{MC}) is given by,

$$q_{MC} = q_{MC,out} - q_{MC,in} - q_{cal} - q_{cal,other} \quad (17)$$

Here, $q_{MC,out}$ is the outlet heat from calcination section, which is given by the sum of heat in the calcined meal and the outlet gas. $q_{MC,in}$ is the heat in the inlet raw meal after meal heating and the heat in the inlet gas. q_{cal} is the heat required to calcine the meal and $q_{cal,other}$ is the heat from other meal reactions (Samani, 2020).

3.4 Heat transfer coefficient

Convection and radiation are the main heat transfer modes in an entrainment calciner. However, at temperatures higher than 600 °C, the heat transfer by radiation is much more dominant than the heat transfer by convection (Lupi, 2017). Since heat transfer from radiation is dominant, this study covers radiation only, and a network modelling approach is applied.

A pure CO_2 environment is expected inside the calciner due to recycled CO_2 and CO_2 formed in the calcination reaction. CO_2 emits and absorbs radiation over a wide temperature range, as it is a polar gas (Incropera et. al., 2017). The radiating property of CO_2 complicates the radiation modelling as it participates in radiation heat transfer along with the particles, the calciner wall and the heating rods. This is handled by using a network modelling approach in this work, as described below.

The total radiation heat transfer (q_{rad}) from surface i to N surfaces (each surface denoted by j), and assuming the surfaces to be grey, is given by (Incropera et. al., 2017),

$$q_{rad} = \sum_{j=1}^{N} q_{ij} = \frac{E_{b,i} - J_i}{(1-\varepsilon_i)/\varepsilon_i A_i} = \sum_{j=1}^{N} \frac{J_i - J_j}{\left(A_i F_{ij}\right)^{-1}} \quad (18)$$

Here, q_{ij} is the heat transferred from surface i to another surface denoted by j subscript, $E_{b,i}$ is the total emissive power for a black surface i, J_i is the radiosity which accounts for all radiant energy leaving the surface i, ε_i is the emissivity of the surface i, A_i is the area of surface i and F_{ij} is the view factor from surface i to surface j. The formulated network equation is visualized in Figure 7.

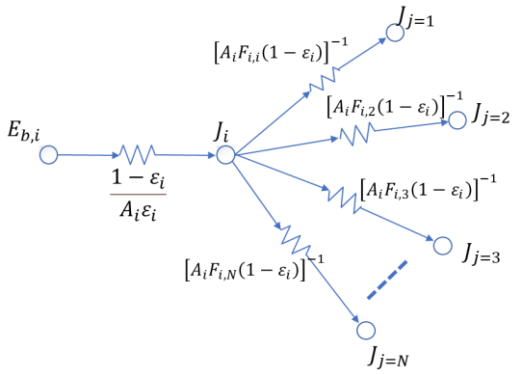

Figure 7: Schematic of a network model with total radiative heat transfer from surface i to other surfaces

3.4.1 Gas preheating

In the gas preheating section, the heat is exchanged between the gas (subscript g), the heating rods (subscript R) and the calciner wall (subscript w). The wall is well insulated, so heat loss is neglected. Then the wall can be assumed to be a re-radiating surface, i.e., it re-radiates all the incident heat. The resulting network of this system is shown in Figure 8. Approximate values of emissivities and view factors are given in Table 3.

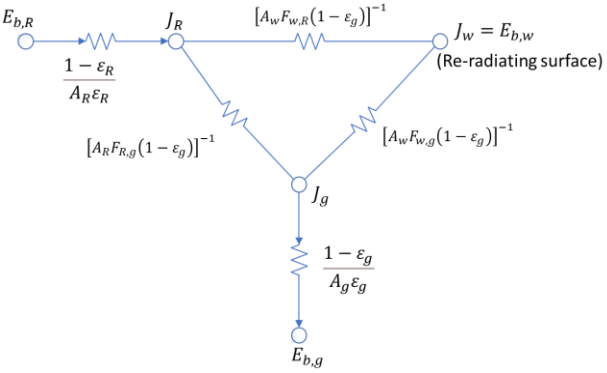

Figure 8: Network model of radiative heat transfer in the gas preheating zone

Table 3: Assumed parameters in the network model for radiation heat transfer in the gas preheating zone

Parameter	Symbol	Value
Emissivity of CO_2	ε_g	0.15
Emissivity of heating rod	ε_R	0.7
View factor from rod to wall	$F_{w,R}$	0.5
View factor from rod to gas	$F_{R,g}$	1
View factor from wall to gas	$F_{w,g}$	1

The emissivity of CO_2 (ε_g) is dependent on the partial pressure of CO_2, the mean beam length and the gas temperature (Hottel and Egbert, 1940). An approximate emissivity of CO_2 is read from Hottel's chart, which correlates these factors to the emissivity of the gas.

The emissivity of the heating rod (ε_R) was approximated based on literature (Kanthal, 2020). There are some uncertainties related to the rod-wall view factor between ($F_{R,w}$). This factor may lie between 0 and 1. An approximate value of 0.5 is chosen, and a sensitivity study on this parameter is presented in the results. The rod-gas and wall-gas view factors should be 1 as the gas is fully visible to these surfaces.

3.4.2 Meal preheating and calcining

In the preheating and calcination section, the heat is exchanged between the gas (subscript g), the heating rods (subscript R), the raw meal particles (subscript p) and the calciner wall (subscript w). The wall can be assumed to be re-radiating if no heat loss present. The gas is also assumed to be re-radiating as the gas has already been heated to the calcination temperature, and now, it is just re-radiating all the incident heat directly to the raw meal particles, the wall and the heating rods. The resulting network is shown in Figure 9.

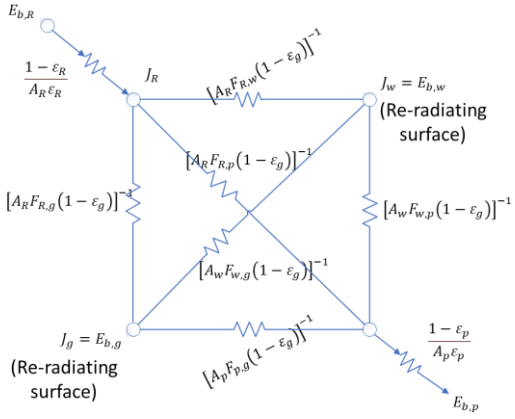

Figure 9: Network model of radiative heat transfer in meal preheating and calcining

Approximate input values are given in Table 4. There are some uncertainties related to the area of the particles and the view factors. The higher the area of particles, the higher is the heat transfer. To be on a conservative side, the smalles probable particle area is estimated qualitatively, and then a sensitivity study is done using higher values. Assuming a void fraction (ε_m) of 0.99, the bulk density (ρ_{bulk}) of the particle inside the calciner is given by,

$$\rho_{bulk} = \rho_P \times (1 - \varepsilon_m) \quad (19)$$

Here, ρ_P is the particle density and is assumed to be 2700 kg/m^3. The calciner is assumed to be a cylinder and the volume of the calciner is calculated using the calciner dimensions (Table 1). The mass of particles inside the calciner is calcuted using bulk density and the volume of calciner. The specific surface area of traditional limestone is 1 – 10 m^2/g (Stanmore and Gilot, 2005). Using the mass of particles and the specific area of a traditional limestone, the total particle area (A_p) is higher than 10^6 m^2. This value is taken as a base case, and a sensitivity study is later performed with a higher particle area. The rod-particle view factor ($F_{w,p}$) and the wall-particle view factor ($F_{w,p}$) should both be close to 1 as in case of dusty flow inside the calciner, the particles are fully visible to the rod and the wall. Due to the presence of this dust, the rod-wall view factor should be low (close to 0). Based on these arguments, approximate values are selected, and a sensitivity analysis is done on the results.

Table 4: Assumed parameters in the network model for radiation in the preheating and calcining zone

Parameter	Symbol	Value
Emissivity of CO_2	ε_g	0.15
Emissivity of heating rod	ε_R	0.7
Emissivity of particles	ε_p	0.7
Area of particles	A_p	10^6
View factor from rod to wall	$F_{R,w}$	0.1
View factor from rod to particle	$F_{R,p}$	0.8
View factor from wall to particle	$F_{w,p}$	0.8
View factor from particle to gas	$F_{p,g}$	1
View factor from rod to gas	$F_{R,g}$	1
View factor from wall to gas	$F_{w,g}$	1

4 Results and discussions

Simulations are performed with the model described in Section 3. The results from the heating rod insertion model are presented in Figure 10. The results show the boundary limits of the rod area of in the gas preheating zone ($A_{R,GP}$), the meal preheating zone ($A_{R,MP}$) and the meal calcination zone ($A_{R,MC}$). The minimum area of the rod should be at least the area of calciner geometry ($A_{GP}/A_{MP}/A_{MC}$). The maximum area is the area at which the minimum possible spacing between the heating rod is reached in each zone ($A_{GP,Smin}/A_{MP,Smin}/A_{MC,Smin}$). The minimum spacing between rods is assumed to be 2.5 times the

rod diameter. This information is used to estimate the heat transfer from radiation.

The heat transfer results from the heat and mass balance in each zone are shown in Figure 11. 8.7 MW of heat is required to preheat the recycled CO_2. This heat might be difficult to recuperate and may result in significant heat losses from the system (Jacob, 2019). If the entrainment velocity is higher than the assumed value (7 m/s), the heat loss will be even higher. A sensitivity analysis of this heat duty by varying the entrainment velocity is shown in Figure 12. The results clearly show the importance of minimizing the gas recycling.

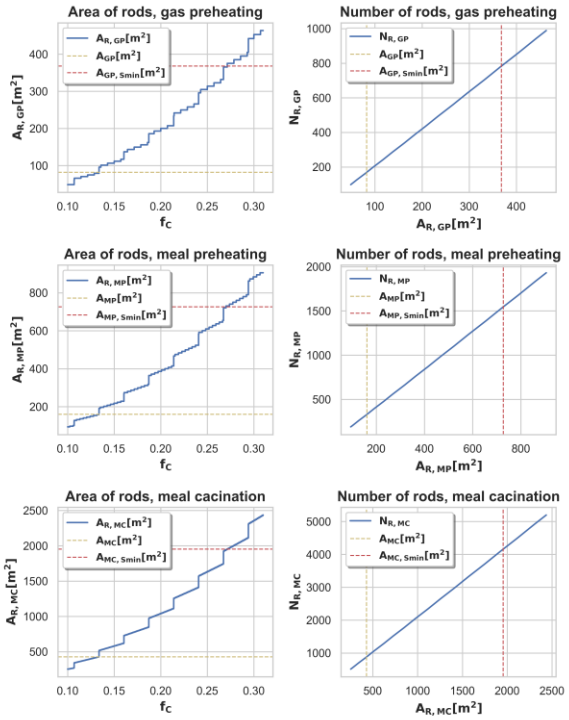

Figure 10: Result from the heating rod insertion model

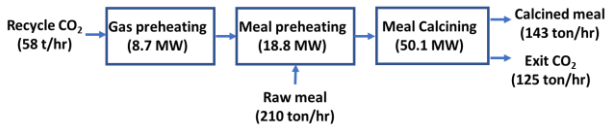

Figure 11: Results from the heat and mass balance calculations

The heat transfer results for each calciner section are shown in Figure 13. The results are plotted for three different heating rod temperatures in each case. The band represents the sensitivity to the uncertainties discussed in Section 3.4. Monte-Carlo simulations are performed on the uncertainties to find the maximum and minimum values of heat transfer given the uncertainties. The dotted line in Figure 13 represents the required heat duty in each section of the calciner calculated from the heat and mass transfer calculations (cf. Figure 11).

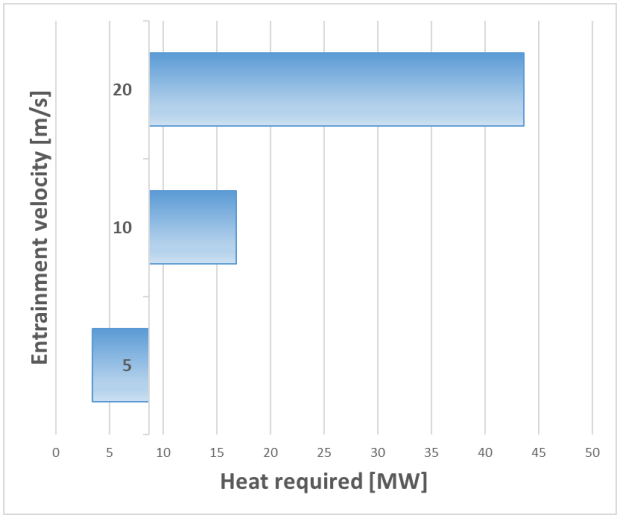

Figure 12: Sensitivity analysis on gas preheating duty (potential heat loss)

The results in Figure 13 show that it is technically feasible to transfer heat through the radiation mechanism. The total number of rods required can be read by combining Figure 10 and Figure 13. In the gas preheating section, the temperature of the rod should be 1150 °C, and the number of required heating rods required at the feasibility point will be around 450. In the meal preheating section, the heat may be transferred at 1050 °C with around 420 rods at the feasibility point. In the meal calcining section, the heat can also be transferred at 1050 °C with around 1700 heating rods at the feasibility point. The total number of required heating rods is around 2570.

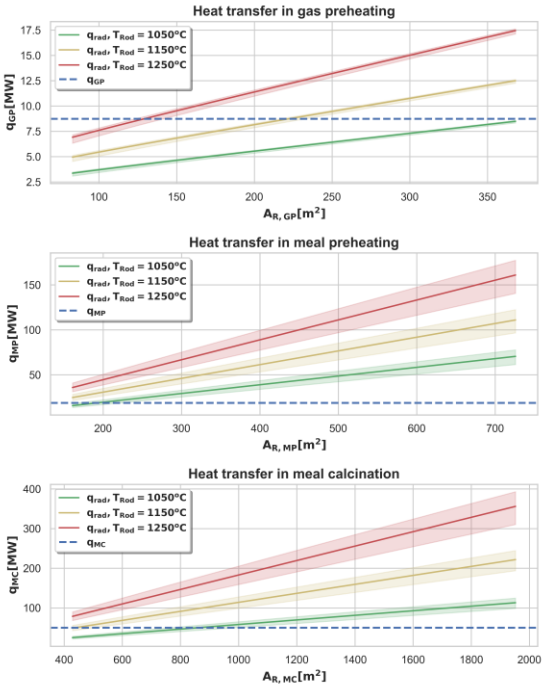

Figure 13: Heat transfer results from each calciner section

A range of feasible heat fluxes are obtained by dividing heat rate with rod area. This result is then utilized to find a heating element design and estimate the mass of the heating element required. The mass of heating elements in the feasible range of heat fluxes in different calciner zones is shown in Figure 14. The lowest mass required in the feasible range of operating calciner is found by using Kanthal APM heating elements.

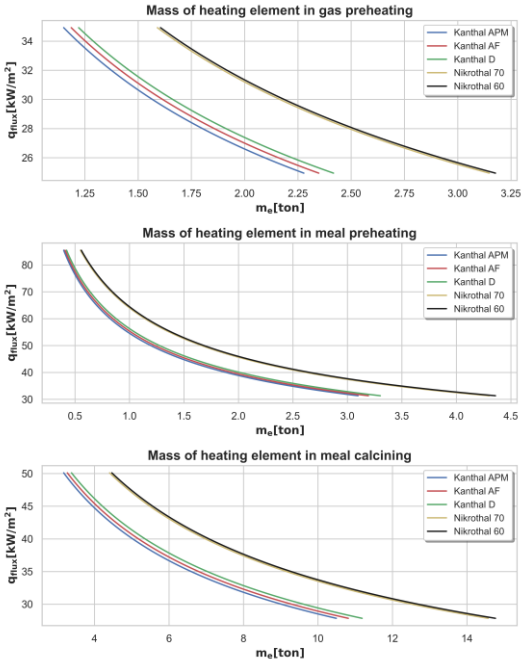

Figure 14: Mass of elements required in the feasible range of operating calciner

5 Conclusion

Electrification of the existing calciner appears to be technically feasible. There is sufficient volume available in the calciner, and there is enough calciner shell surface area available, to insert the number of heating rods that are required to provide the heat and calcine the meal, i.e., about 2570 heating elements operating with surface temperature of 1150 °C in gas preheating zone and 1050 °C in meal preheating and calcining zone.

The total heat transferred from the electrical heating elements to the meal is 69 MW and the total heat transferred is 78 MW. The gas preheating section may operate feasibly with a heat flux of 26-34 kW/m². The meal preheating section may operate feasibly with a heat flux of 35-80 kW/m², and the meal calcining section should feasibly operate with heat flux of 30-50 kW/m². At higher heat fluxes, the heat transfer from radiation will not be enough to transfer the heat to the gas or the raw meal. At lower heat fluxes, the spacing between the heating rods will be so small that it will affect the structural integrity of the calciner. Moreover, a lower heat flux also means a higher heating element cost as the mass of the elements will increase. The mass of Kanthal APM elements, which have the highest heat flux, is around 5 tons, and the mass of the elements with the lowest heat flux is around 15 tons.

The results, however, also indicate some challenges. The gas flow rate required to entrain the raw meal may lead to high flow of energy out of the calciner, and it may be a challenge to recuperate all the heat from this

One may think of adding a fan operating at high temperature to recycle the gas at 900 °C, thereby avoiding the heat exchange. However, additional studies must be performed to check the feasibility of this. The results also indicate that a large number (at least 2120) of rods and a high mass of heating elements (at least 4 are required. The particles may flow at a high velocity in this region which may cause abrasion, erosion, and element breakage. So, maintenance may become a challenge logistically due to a large number of heating rods (finding the damaged heating rod), and economically due to the high mass of heating elements (erosion of elements). Additional studies on these aspects must be performed to find detailed economic and logistic challenges.

Thus, the results indicate that electrification of an entrainment calciner is theoretically possible. However, there are some challenges to address with this concept. One way to address the challenge may be to study other calciner systems where it is easier to avoid these challenges.

Acknowledgments

This study was carried out as part of the research project Combined calcination and CO_2 capture in cement clinker production by use of CO_2-neutral electrical energy – Phase 2". Gassnova and Norcem are greatly acknowledged for funding this project. The technical recommendations from representatives of Kanthal, Cementa, IFE and SINTEF are also acknowledged.

References

Simon Becker, Robert Mathai, Kristina Fleiger, Giovanni Cinti. Status report on calciner technology. *CEMCAP*, Rev. 2, 2016.

Don W. Green, Robert H. Perry. Perry's chemical engineers' handbook, *McGraw-Hill*, Ed. 8, 2008.

H.C. Hottel, R.B. Egbert, The radiation of furnace gas. *ASME*, 1940.

Technology Roadmap - Low-Carbon Transition in the Cement Industry. 2018.

Frank P. Incropera, David P. Dewitt, Theodore L. Bergman, Adrienne S. Lavine. Principles of heat and mass transfer. *John Wiley & Sons*, Global edition, 2017.

Ron M. Jacob. Gas-to-gas heat exchanger for heat utilization in hot CO_2 from an electrically heated calcination process, *Master's thesis*, USN, 2019.

Kanthal. Resistance heating alloys and systems for industrial furnaces, *Product overview*, 2020.

Sergio Lupi. Fundamentals of Electroheat – Electrical technologies for process heating. *Springer*, 2017

Martin H. Usterud, Ron M. Jacob, Lars-Andre Tokheim. Modelling and Simulation of an electrified drop-tube calciner. Submitted to the *SIMS conference*, 2021.

Nastaran Ahmadpour Samani. Calcination in an electrically heated bubbling fluidized bed applied in calcium looping, *Master's thesis*, University of South-Eastern Norway, 2020.

Nastaran Ahmadpour Samani, Chameera K. Jayarathna, Lars-Andre Tokheim. CPFD simulation of enhanced cement raw meal fluidization through mixing with coarse inert particles, Linköping Electronic Conference Proceedings, 176:57 (Proceedings of the 61st SIMS, September 22nd - 24th, virtual conference), pp. 399–406, 2020, https://doi.org/10.3384/ecp20176399B. R. Stanmore, P. Gilot. Review – Calcination and carbonation of limestone during thermal cycling for CO_2 sequestration, *Fuel process technology*, 86, pp. 1707-1743, 2005.

Lars-André Tokheim. The impact of staged combustion on the operation of a precalciner cement kiln, *PhD dissertation*, Norwegian University of Science and Technology / Telemark University College, 1999

Lars-André Tokheim. Kiln system modification for increased utilization of alternative fuels at Norcem Brevik, *Cement International*, 4, pp. 1-8, 2006

Lars-André Tokheim, Anette Mathisen, A., Lars E. Øi, Chameera Jayarathna, Nils H. Eldrup and Tor Gautestad. Combined calcination and CO_2 capture in cement clinker production by use of electrical energy, *SINTEF proceedings*, 4, pp 101-109, 2019

Thomas P. Hills, Mark Sceats, Daniel Rennie, Paul Fennell, LEILAC: Low cost CO_2 capture for the cement and lime industries. Energy Procedia, Vol. 114, pp. 6166-6170, 2017.

Consolidating Industrial Batch Process Data for Machine Learning

Simon Mählkvist[1,2] Jesper Ejenstam[2] Konstantinos Kyprianidis[1]
[1]Future Energy Center, Mälardalen University, Sweden, simon.mahlkvist@mdh.se
[2]Kanthal, Sweden

Abstract

The paradigm change of Industry 4.0 brings attention to data-driven modeling and the incentive to apply machine learning methods in the process industry. Further, capitalizing on a great deal of data available is an adverse task. For batch processes, the dataset is in a three-way format (Batch × Sensor × Time). Depending on the process and the goal of the analysis, it might be necessary to aggregate batches together. For this reason, a campaign unfolding structure is applied. By grouping the batches under new labels relevant to the analytical goal, campaigns are created. These labels can be created from periodical occurrences, such as refurbishing the refractory lining in the case of the case study. In order to utilize the three-way batch format, it is necessary to align the batches. In order to address this, the feature-oriented approach Statistical Pattern Analysis (SPA) is applied. SPA derives statistics, e.g., mean, skewness and kurtosis from the time series, consequently aligning the batches. The SPA and the campaign approach create a dataset consisting of select statistics instead of an irregular three-way array. Functional data analysis (FDA) is used to smooth and extract first- and second-order derivative information from the sensors in which functional behavior can be observed before creating features. Principal Component Analysis (PCA) is used to examine the final dataset. Further, industrial processes are notoriously nonlinear, and even more so batch processes. Therefore, kernel-based principal component analysis (KPCA) is used to review the final dataset. The KPCA can accommodate different underlying characteristics by modifying the kernel function used.

Batch Process Analysis (BDA), Batch Preprocessing, Functional Data Analysis (FDA), Statistical Pattern Analysis (SPA), Kernel Principal Component Analysis (KPCA)

1 Introduction

Within the scope of industry 4.0, industries are determined to incorporate into their analytical framework machine learning methods. Despite the vast selection of turn-key solutions, the procedure often falls short on the neglected part of the analytical procedure: data acquisition and preprocessing. Legacy process industries suffer from the fallback of outdated infrastructure, making data-acquisition procedures cumbersome and preprocessing complex due to, e.g., lack of contextual information such as accurate timestamps.

Batch data analytics (BDA) is a field of study that focuses on analyzing industrial batch processes. A batch process produces products in a turn-based manner which repeats over the following phases: charging, operating, and discharging. Working with batch process datasets offers unique challenges. The dataset a batch process provides is a three-dimensional matrix (Batch × Sensor × Time, see Figure 1), which offers additional challenges. E.g., each batch is going to be of different lengths, leading to an uneven dataset. Also, the time interval between samples may not be uniform. To accommodate irregular sampling or uneven batches, batch synchronization or feature extraction can be applied. In this work, The Statistical Pattern Analysis (SPA) method is used to compile relevant statistics from the sensor data and create an aligned three-dimensional array. Further, there are many strategies to convert a three-dimensional array into a two-dimensional array. This procedure is commonly called unfolding. It is necessary to unfold batch data to make it suitable for a more comprehensive array of models. Also, a campaign structure is applied to understand and explain variables after several batches. In short, the campaign approach entails concatenating the batches into new batches before the feature extraction procedure.

Furthermore, industrial batch processes can be expected to be nonlinear, making them unsuitable for many conventional methods. In order to investigate the nonlinear phenomenon, the batch structured datasets are analyzed using kernel-PCA (KPCA), which can accommodate nonlinear behavior due to its variation of kernel functions. A more conventional Principal Component Analysis (PCA) supplements this analysis to investigate the linear behavior as well.

A common phenomenon in industrial process analysis is noisy data. Also, for some processes, it may be beneficial to investigate derivative information. Therefore, to smooth the sensor data and extract derivative information, functional data analysis (FDA) is utilized. FDA creates a battery of approximation functions that describe the underlying processes, allow extraction of derivative information, and, consequently, smoothing. There are many complex methods available regarding

structuring the data, smoothen and extract derivative information, and select or reduce features. This work combines several methods to see the potential for this blend. This work intends to impart a perspective towards consolidating complex industrial batch process data with machine learning methods.

The rest of the paper is organized as follows. Section 2. contains the methodology of the paper, which in turn consists of several subsections. Section 2.1 describes the process from which the dataset is constructed. Section 2.2. explains the data acquisition procedure. Section 2.3. elaborates on batch data processing and the campaign structure. Section 2.4. is on the functional data analysis. Section 2.5. on the feature-oriented approach. Section 2.6 on PCA and KPCA. Section 2.7 describes the analytical framework.

2 Methodology

2.1 Steel Converter Dataset

The data in this paper is derived from a steel converter. The purpose of a steel converter is to enable the use of low-grade resources, e.g., scrap-based or low purity, to produce high-quality steel. A converter refines steel batch-wise and is used as a secondary procedure. The raw material is melted and then fed into the converter. The converters' refractory lining interacts with the melt directly, and when the lining is exhausted, the converter is put out of commission and requires relining before it can be reinstated. The chemical composition of the melt is registered before and after the process. Also, gas inlet temperature, flow, and pressure are stored. The number of batches produced in the variable of interest is referred to as the campaign metric. The methodology aims to explore the relations between the degradation, the sensor, and chemistry.

2.2 Data Acquisition

Acquiring data in a legacy process industry is a diverse procedure. The accessible data is likely limited to a static tabular view. Due to the large size of unconstrained sensor data, such tables are usually limited in scope, i.e., duration, time-resolution, or amount of sensors. The memory of the computer or server can be a limiting factor if analyzing high-resolution data with many sensors. By dynamically detecting relevant sensors or duration in time of interest, it is helpful to systematically collect similar or more data regarding this or even connect a model directly to the system. Being able to analyze and collect data from the same development platform is beneficial. There are several parameters to consider when working on data acquisition for process data. Extracting the duration of interest may prove difficult. For each batch, identifying the duration in which the process is working with respect towards the batch is called local batch time. The accuracy of the local batch times' start and stop timestamps should be reviewed for

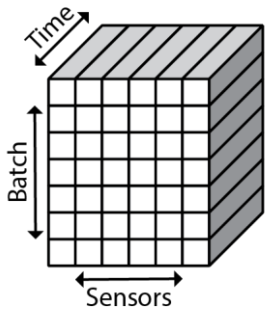

Figure 1. Aligned batch data

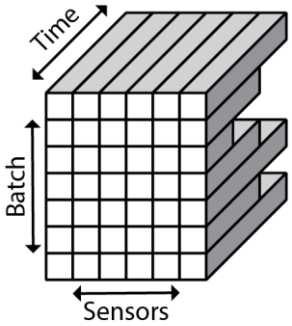

Figure 2. Uneven batch data

accuracy. The stored information about the batch may not initially be intended to be used for analytics purposes and, therefore, inaccurate. The workstation and database server has limited memory. Hence when working with multiple batches over a significant duration, it is necessary to extract the data in manageable segments.

2.3 Structuring Batch Data

Batch data is designed in a three-way array structure with I, J, and K corresponds to a number of batches, variables, and time (local batch time) respectively, see Figure 1. (Nomikos & MacGregor, 1994) This results from the distinct structure of batch processes and, as a result, inhibits the utilization of conventional method without first transforming from three- to two-dimensions array. In practice, the batch duration deviates between batches, and batch data from industrial processes have different durations, hence producing an uneven dataset, as depicted in Figure 2. The procedure of aligning batch data is called batch synchronization or batch alignment.

By employing a campaign structure along with SPA, the need for time-sensitive alignment is circumvented. A description of how to combine and restructure the three-way array with data from upstream and downstream processes follows. The batch-wise unfolding approach transforms the dataset from an uneven three-way array to an uneven two-way array by concatenating the sensor trajectories (see Figure 3).

Wu et al. (2018) introduce a campaign-based batch unfolding structure which is further advanced by Wu et al. (2019). In batch processes where the metric or variable of interest varies or resets over several batches, the

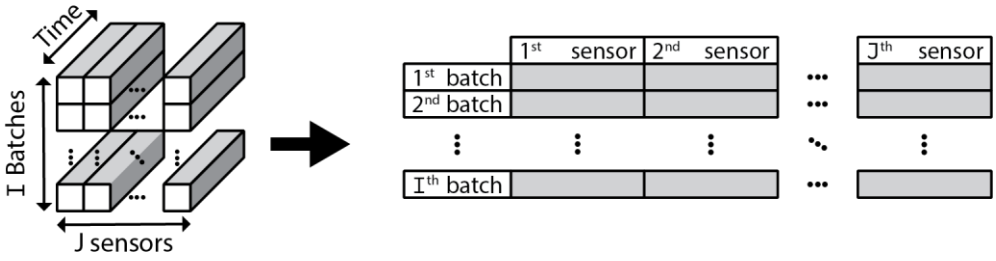

Figure 3. Batch-wise unfolding

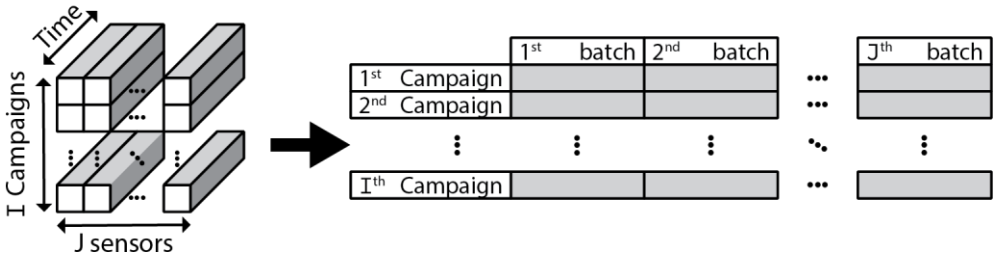

Figure 4. Campaign-wise unfolding

campaign approach coalesces metric-relevant data into a new type of batch (see Figure 4).

2.4 Functional Data Analysis

Functional data analysis (FDA), it applied in order to extract derivative information and to smooth the trajectories. FDA creates a battery of approximation functions that represents the underlying characteristic. Observing derivative information of physical variables, e.g., temperature and flow, can be beneficial since the derivative adds further information to the system. Using FDA, it is possible to interpret derivative information from time-series sensor data that show functional nature. (Ramsay & Silvermann, 1998) In Figure 5, the FDA is showcased where the original data is overlaid on top of the approximation function in subfigure (a). Further, it shows the 1st and 2nd derivatives of the approximation in subfigures (b) and (c), respectively.

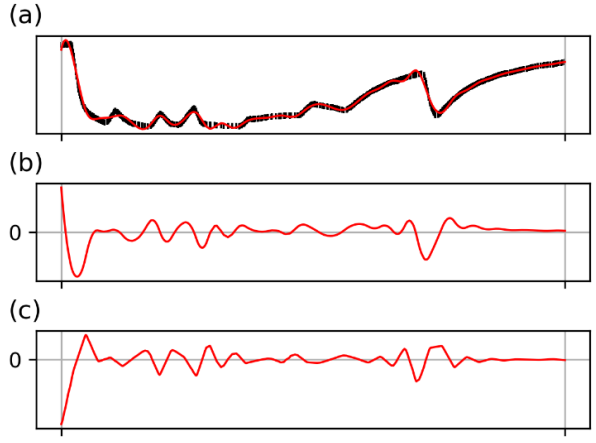

Figure 5. FDA example show smoothing and 1st and 2nd order derivative: (a) raw samples (black dots) and smoothing (red line), (b) 1st derivative, (c) 2nd derivative

Functional data representation is used in a multivariate functional kernel principal component analysis in (H. Wang & Yao, 2015). The functional local kernel principal component analysis is also in (F. He & Zhang, 2020). For more information about the FDA's fundamentals, see Ramsay et al. works on Functional Data Analysis (Ramsay & Silvermann, 1998).

2.5 Statistical Patten Analysis

The Feature-oriented method used in this approach is SPA. SPA was introduced in He and Wang (2011) as a fault detection framework and utilizes 1st, 2nd higher-order statistics derived from batch trajectories instead of the trajectories themselves to monitor the process. Like other feature-oriented methods, SPA alleviates the pre-processing step batch trajectory alignment by creating statistical metrics from the trajectories.

He and Wang (2011) monitor a semiconductor batch process and use the SPA statistics: mean, skewness, kurtosis, and covariance. Wang and He (2010) apply SPA with continuous processes and uses the following statistics: mean, variance, autocorrelation, cross-correlation, skewness, kurtosis. In this work, the mean, kurtosis, and skewness are used as statistics for pattern identification. Skewness is a measurement of distribution asymmetry. Kurtosis is a measurement of the spread of the data. In this work, SPA is used to transform a time series of data into a set of three statistics; mean, variance, kurtosis, and skewness.

For more information on feature-oriented methods for BDA, see Rendall et al. (2017) and Rendall et al. (2019). For a perspective on how the SPA framework relates to challenges purposed by smart manufacturing and other methods, see He et al. (2019)

2.6 PCA and Kernel-PCA

PCA is a commonly used method in process analytics for dimensionality reduction, feature selection, and unsupervised data exploration. The PCA is limited to investigating the linear relations in the dataset. Schölkopf et al. (1997) introduced KPCA, which provides further utility compared to the conventional, linear PCA. The KPCA aggregates the dataset, transforming it into a high-dimension feature space using a nonlinear mapping. Then, performing dimensionality reduction on the feature space and if a suitable kernel function and parameter is designed makes previously nonlinear data linearly interpretable. There are several kernel functions. The most commonly applied and used in this work are polynomial and radial basis functions (RBF). Both kernel functions have parameters that need to be configured. The KPCA can accommodate underlying nonlinear characteristics and show itself to outperform the PCA when performing feature extraction and classification on datasets with nonlinear behavior. (Lee et al., 2004) Works on fault detection using KPCA can be further viewed in the works by Lee et al. (2004), H. Want and Yao (2015), and He and Zhang (2020). For a fundamental look into Kernel methods, the reader is referred to the work of Schölkopf et al. (1997).

2.7 Analytical Design

Each batch has 15 sensors. FDA is applied 10 of these sensors, which creates 20 new trajectories per batch, 10 for both the 1st and 2nd order derivative. In total, this makes 35 trajectories per batch. Batches are concatenated to relevant campaigns. The chemical composition is measured for every batch before and after the process. 10 and 17 elements are registered before and after, respectively. For every sensor and chemical element, three statistical features are derived. Resulting in 186 features per campaign.

In order to investigate the impact of different methods, the campaign dataset is segmented into several different subsets. Every subset contains 93 campaign samples. The following list details the name, description, and number of features for the eight:

- Full: All data (186 features)
- 0th order: Sensor data without derivatives (45 features)
- 1st & 2nd order: Sensor data of both 1st and 2nd derivative (60 features)
- 1st order: 1st order derivative sensor data (30 features)
- 2nd order: 2nd order derivative sensor data (30 features)
- Chem: Both prior and post elemental composition (81 features)
- Pre chem: Elemental composition before the process (30 features)
- Post chem: Elemental composition after the process (51 features)

Using PCA, the explained variance for each of these dataset will be calculated and compared. The five most significant principal components (PC) will be further investigated, and each PC's five most significant features will also be compared. The fit of the significant PC to the campaign metric will be reviewed using ordinary least squares and the by investigating the coefficient of determination.

The KPCA is modeled for the RBF and polynomial kernel. The parameters for these are dynamic and is presented in results when relevant.

3 Results & Discussions

This section will show how the combined influence of the campaign structure, the FDA smoothing, the 1st and 2nd derivatives, and the SPA, by using PCA and KPCA to identify different phenomenon in the campaign dataset with respect to the campaign features.

The campaign dataset is segmented into eight different datasets, and PCA is performed on all constellations of the Campaign dataset. In Figure 6, the explained variance per principal component (PC) for 15 first components for each dataset is in a scree plot. Beyond 15 components, the explained variance approaches zero and is not included.

In Figure 7, the five samples of the largest explained variance of Figure 6 are extracted, and for each sample, again, the five features with the most significant explained variance are derived. There is overlap between the selected features, e.g., the features for the 1st PC in the Full dataset have similar significant features to the 1st component in the 1st & 2nd order dataset (see the top figure and second figure from the top in Figure 7).

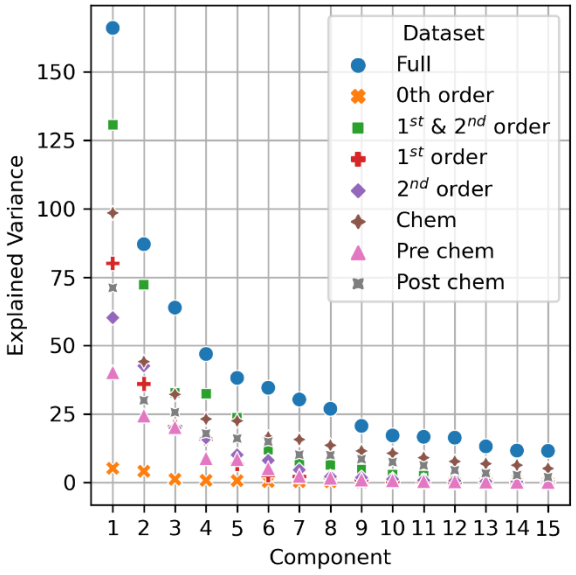

Figure 6. Explained Variance

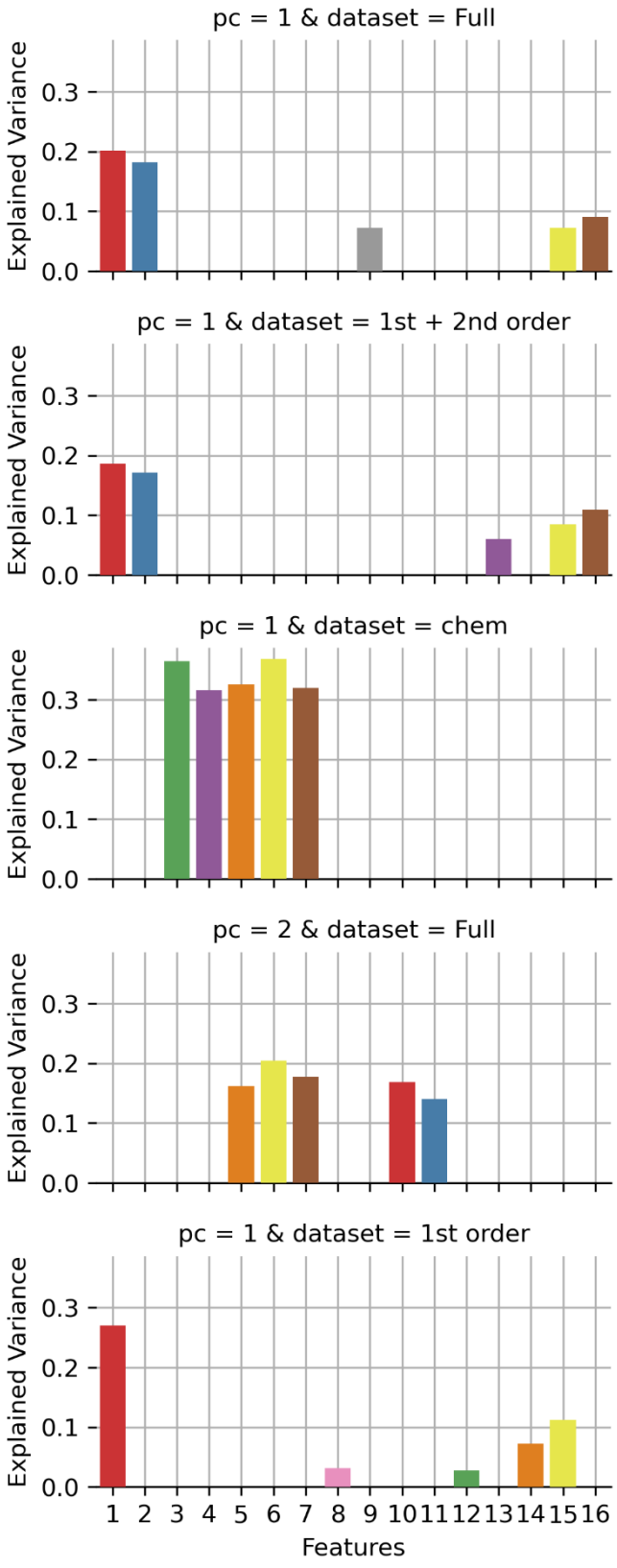

Figure 7. Feature variance of top 5 PCs

Two patterns are noteworthy when observing the data variance in Figure 6 and the variance of the features in Figure 7. First, the 1st PC of the Full dataset coincides with the 1st PC consisting of features from the 1st and 2nd order derivatives and indicates that the sensor derivatives influence the variance of the Full dataset. Further, the 1st PC from the dataset, consisting of only 1st order derivates, also shares features with both aforementioned datasets. The 1st feature seems to be the root of significant variance. Regarding the second discernable pattern, the 2nd PC of the Full dataset and the 1st component of the Chem dataset share three top features. Hence, the Full dataset explains the variation of two datasets with its 1st and 2nd PC.

The five PC is used to model the campaign metric. The coefficient of determination R^2 is calculated for each to determine how well the PCs are able to generalize the campaign metric. None show a significant R^2. Hence, while these PC describes the major variance in the datasets, they cannot be used to generalize the campaign metric.

The KPCA is used on the constellations of datasets. Several different KPCA is constructed using the polynomial and RBF kernels along with their corresponding parameters. Systematically investigating the pcs of the different KPCA constellations shows a weak linear correlation towards the campaign metric. No significant R^2. By observing the relations between the KPCA PC, two interesting patterns are visible.

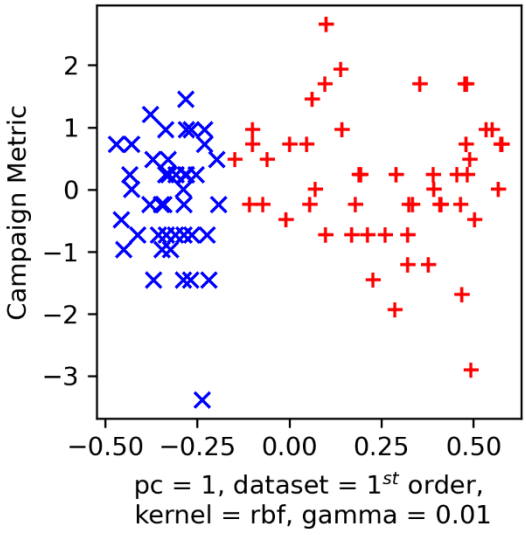

Figure 8. Clustering of campaign metric over PC from KPCA of the 1st order dataset

The first pattern is seen in Figure 8, where the PC is derived from the KPCA with RBF kernel and gamma 0.01 from the 1st order dataset. The 1st PC plotted over the campaign metric shows no significant correlation, but two clusters emerge, as illustrated by the shape and color difference. The features of the 1st order dataset are explored using a kernel density estimation (KDE) plot, and two features are distinct, as seen in Figure 9 and Figure 10, which, respectively, show the skewness and kurtosis of the same sensor. The sensor is the 1st derivative of the temperature sampled for a gas inlet.

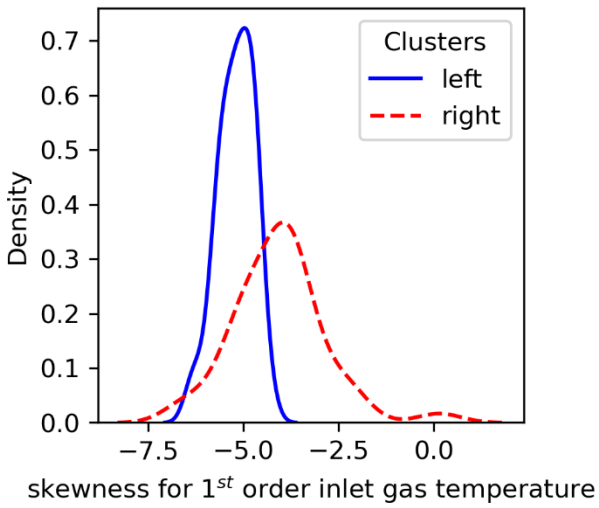

Figure 9. Density plot of skewness for 1st order derivative of inlet gas temp

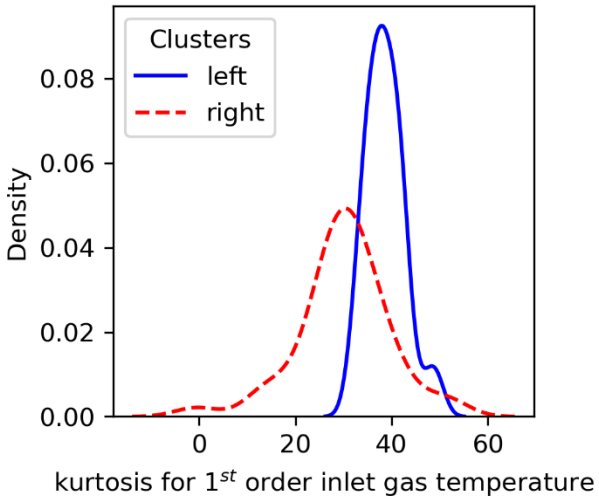

Figure 10. Density plot of kurtosis for 1st order derivative of inlet gas temp

The separation in Figure 9 and Figure 10 shows that the left cluster in Figure 8 has lower skewness and greater kurtosis than the right cluster.

The second pattern, seen in Figure 11, shows a clustering when comparing the campaign metric with the 1st PC derived from a KPCA with the RBF kernel and gamma of 0.001 of the Chem dataset. Figure 12 and Figure 13 further shows how this clustering transfers to the two features of the Chem datasets. Further, both features show the kurtosis for the chemical composition, of the same element, before and after the process. The clustering is overlapping since the distribution in Figure 12 for the right cluster shows two peaks, of which the line up with the other cluster. The right cluster for both figures aligns around where kurtosis is zero, which indicates a tighter spread. Hence, the left cluster is more random regarding the element's content, i.e., it has a more significant deviation.

Considering both the patterns identified via the KPCA (Figure 8 and Figure 11). Isolating the clusters and performing additional analysis could provide further information. Additional campaign samples would be beneficial as they would provide more data for analyzing data subsets. With a total campaign sample size of 93, further, partitioning can prove detrimental.

In general, the approach applied does not explain the campaign metric. Several variables may contribute to expanding the approach, and the rest of this section will reflect on this.

The PCA and KPCA transform the different datasets, and while the PCA is limited to a linear approach, the KPCA is not. However, even with several approaches by KPCA, a relevant interpretation concerning the campaign metric is not discovered. This may be because the analytical approach relies on a parametric framework that assumes the data to conform to underlying statistical distributions. Therefore it would be suitable to include non-parametric methods, such as variation of random forest, to analyze the relationship between the campaign data and metrics. The SPA is not limited to the statistics used in this work, and many other feature-oriented approaches have the potential to derive features that can explain other metrics.

The campaign-based approach unfolds the data batch-wise with respect to a campaign metric. Further, it is common in BDA to divide the batch into phases if the process has different operation modes. Also, it is possible that a campaign can have similar phases, e.g., the first batches are of specific interest and should be separated from the rest. Further, the analysis results of the campaign datasets may be understood if the batch mix is considered, e.g., the clustering is a result of different products or groups of products with similar pro-

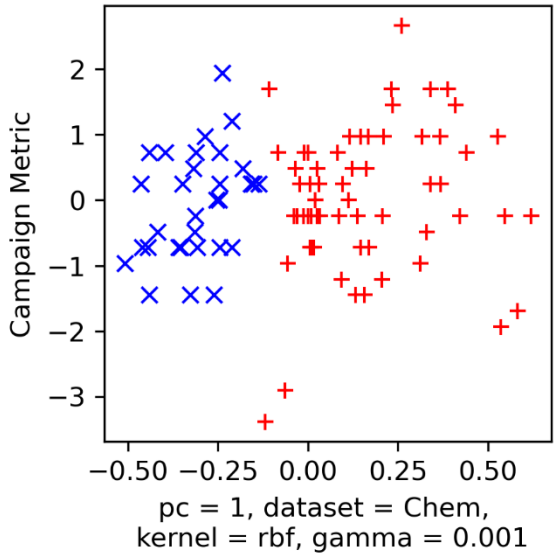

Figure 11. Clustering of Campaign metric over PC from KPCA of the Chem dataset

cess parameters, being overly represented in said campaign. Hence, designing the analysis so that the batch and campaign are divided into relevant phases is suggested. On the other hand, some of the datasets used are already high-dimensional. Considering batch and campaign phases, and adding additional statistical features, would further increase the number of features.

Therefore, an efficient and sustainable feature selection method should be applied so that a more complex and encompassing dataset can be considered.

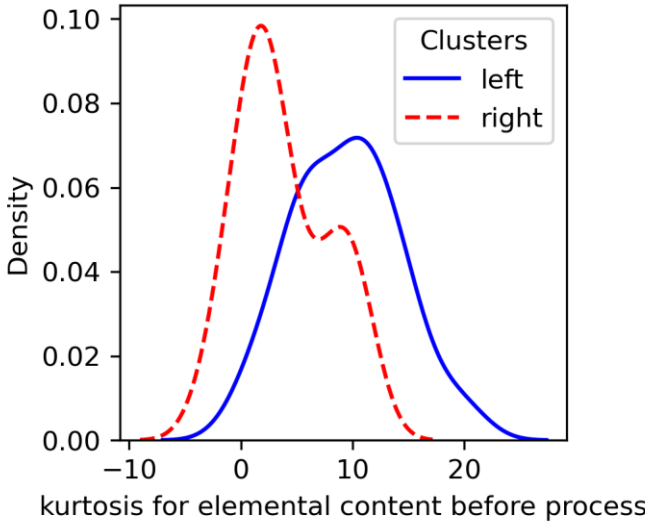

Figure 12. Density plot of kurtosis for elemental content before the process

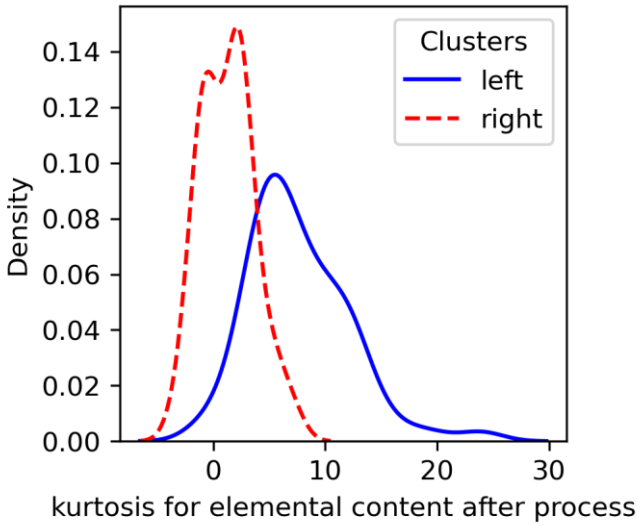

Figure 13. Density plot of kurtosis for elemental content after the process

4 Conclusion

This methodology provides a low complexity and a practical approach to batch process data preprocessing and synthesizes the unaligned three-way array into a two-way array. It is challenging to systematically evaluate the methodology due to a high number of design variables. The approach proves to be poor at generalizing the campaign metric, e.g., unable to explain the degradation mechanics. Several design improvements are discussed to enhance further the potential for the dataset to contain relevant information and increase the number of features, further aggravating the issues that high-dimensional datasets provide. Therefore, it would be valuable to implement a feature selection approach suitable for the campaign structure.

The KPCA approach uncovers interesting patterns in the data. These patterns manage to isolate different modes in the statistical features. The origin of these clusters is not determined, but their existence shows potential for the campaign structure to provide insights. It would be beneficial to increase the number of samples, I.e., increase the number of campaigns, to get a more accurate view of the underlying distributions by investigating data subsets. The challenge to this is that the rate at which data is generated is low. Hence the analytics has to rely on available historical data.

While the feature-oriented approach applied in this work is considered low complexity, the combination of campaign structure and FDA and KPCA makes it an elaborate construct. It shows potential to understand campaign-related phenomena, but further research into proper analysis methods is required.

Acknowledgements

The authors gratefully acknowledge Kanthal AB, Automation Region Research Academy (ARRAY), and the Swedish Knowledge Foundation (KKS) for their support.

References

F. He, and Z. Zhang. Nonlinear Fault Detection of Batch Processes Using Functional Local Kernel Principal Component Analysis. *IEEE Access*, *8*:1–1. 2020. doi:10.1109/access.2020.3004564

Q. P. He, J. Wang, and D. Shah. Feature space monitoring for smart manufacturing via statistics pattern analysis. *Computers and Chemical Engineering*, *126*:321–331. 2019. doi:10.1016/j.compchemeng.2019.04.010

Q. P. He, and J. Wang. Statistics pattern analysis: A new process monitoring framework and its application to semiconductor batch processes. *AIChE Journal*, *57*(1):107–121. 2011. doi:10.1002/aic.12247

J. M. Lee, C. K. Yoo, and I. B. Lee. Fault detection of batch processes using multiway kernel principal component analysis. *Computers and Chemical Engineering*, *28* (9):1837–1847. 2004. doi:10.1016/j.compchemeng.2004.02.036

P. Nomikos, and J. F. MacGregor. Monitoring batch processes using multiway principal component analysis. *AIChE Journal*, *40* (8):1361–1375. 1994. doi:10.1002/aic.690400809

J.O. Ramsay, and B.W. Silvermann. Functional Data Analysis. Springer Series in Statistics. *Biometrical Journal*, *40*

(1):56–56. 1998. doi:10.1002/(sici)1521-4036(199804)40:1<56::aid-bimj56>3.0.co;2-#

R. Rendall, L. H. Chiang, and M. S. Reis. Data-driven methods for batch data analysis – A critical overview and mapping on the complexity scale. *Computers and Chemical Engineering*, *124*:1–13. 2019. doi:10.1016/j.compchemeng.2019.01.014

R. Rendall, B. Lu, I. Castillo, S. T. Chin, L. H. Chiang, and M. S. Reis. A Unifying and Integrated Framework for Feature Oriented Analysis of Batch Processes. *Industrial and Engineering Chemistry Research*, *56* (30):8590–8605. 2017. doi:10.1021/acs.iecr.6b04553

B. Schölkopf, A. Smola, and K. Müller. Kernel principal component analysis. Lecture Notes in Computer Science (Including Subseries Lecture Notes in Artificial Intelligence and Lecture Notes in Bioinformatics), 1327:583–588. 1997. doi:10.1007/bfb0020217

J. Wang, and Q. P. He. Multivariate Statistical Process Monitoring Based on Statistics Pattern Analysis. *Industrial & Engineering Chemistry Research*, *49* (17):7858–7869. 2010. doi:10.1021/ie901911p

H. Wang, and M. Yao. Fault detection of batch processes based on multivariate functional kernel principal component analysis. *Chemometrics and Intelligent Laboratory Systems*, *149*:78–89. 2015. doi:10.1016/j.chemolab.2015.09.018

O. Wu, A. E. F. Bouaswaig, S. M. Schneider, F. M. Leira, L. Imsland, and M. Roth. Data-driven degradation model for batch processes: a case study on heat exchanger fouling. *Computer Aided Chemical Engineering*, *43*:139–144. 2018. doi:10.1016/B978-0-444-64235-6.50026-7

O. Wu, A. E. F. Bouaswaig, L. Imsland, S. M. Schneider, M. Roth, and F. M. Leira. Campaign-based modeling for degradation evolution in batch processes using a multiway partial least squares approach. *Computers and Chemical Engineering*, *128*:117–127. 2019. doi:10.1016/j.compchemeng.2019.05.038

Modelling of snow depth and snow density based on capacitive measurements using machine learning methods.

Nils-Olav Skeie*, Henrik Nikolai Vahl, Håkon Viumdal

Department of Electrical Engineering, Information Technology and Cybernetics (EIK)
University of South-Eastern Norway (USN), N-3918 Porsgrunn, Norway
*(nils-olav.skeie@usn.no)

Abstract

In countries with cold winters, snowpack will affect the hydropower production during the melting periods. To optimize the hydropower production, it is relevant to consider information from the snowpack to estimate the water content when melting. Several techniques and devices can be used to measure the water content of the snowpack. This paper discusses a prototype based on capacitive measurements with a small footprint, and the development of data driven models to estimate the snow density, snow depth and snow water equivalent in a snowpack. The device was deployed in a snowy area throughout the winter with logging while manual reference measurements were made sporadically. Machine learning methods were used for developing the models, and several models were combined to estimate the water content of the snowpack. The developed model estimated the snow density, snow depth and snow water equivalent during the wintertime with good results. However, during the springtime, the capacitive measurements have some limitations.

Keywords: snow density, snow water equivalent, capacitive sensor, model development, machine learning.

1 Introduction

1.1 Background

Measurement of snowpack has been a challenge for a long time, one of the first research papers handling this challenge was published in the early 80s (Denoth et al., 1984). Snowpack is defined as the mass of snow on the ground that is compressed and hardened by its own weight.

Weather forecast is considered the most important input to the models used for predicting hydropower production. However, in areas where snow accumulates during winter and melts in the spring, the inflow and hence the predictions based on these models, will be highly affected.

Today measurements of snow depth and density are often performed manually at the end of the winter season with the aim of estimating the melting inflow. These measurements must often be taken in remote and impassable locations, making it time-consuming and expensive. As an alternative way of measuring the snow depth and density, an autonomous system with a minimal environmental footprint that can be deployed remotely and transmit data is proposed.

In this work a prototype system was developed, based on capacitance measurements, and deployed in a snowy area in autumn 2020. The prototype was used to record measurement values during the winter period 2020/2021 and these measurements were used as input data for the work of a master thesis at University of South-Eastern Norway (USN) spring 2021. The focus of this master thesis is a modelling approach using machine learning methods (Vahl, 2021).

The focus in this work is for hydropower systems. However, the prototype system is a more general system that can also be applied for other purposes based on snowpacks like measuring skiing conditions and evaluating the risk for avalanches.

1.2 Previous work

Since measuring the snowpack has been a challenge for decades, several works and projects have been performed within this area.

An overview of instruments for measurement of the snowpack is described in (Denoth et al, 1984). The focus of these measurements is to estimate the snow water equivalent (SWE) in the snowpack where SWE is defined as

$$SWE = h_s \frac{\rho}{\rho_w}$$

where h_s is the snow depth, ρ is the density of snow and ρ_w is the density of water, measured in g/cm^3. Measurement of dielectric properties of snow is described in (Hallikainen et al. 1982), and an overview

of snow dielectric devices and applications is described in (Denoth and Wilhelmy, 1989).

Newer work about liquid water content in snow is described in (Niang et al., 2006) and (Techel and Pielmeier, 2010).

Some ongoing projects are “Long-term snow water equivalent measurements” at WSL (Wsl, 2021) and “Current snow cover” at CCIN (Ccin, 2021).

The liquid water content in snow is important for hydropower systems as the inflow of water at springtime will be a combination of water from raining and melting of snow. Predicting the amount of inflow is done using models based on among others weather forecasts. However, these models are missing regular inputs from areas where snow accumulates during winter and melts in the springtime.

In Norway, the Norwegian Water Resources and Energy Directorate (NVE) published a report where snow pillows are recommended as automatic snow water equivalent sensors (Stranden et al., 2015). Snow pillows are sensors having a large environmental footprint with a weight and distance sensor to measure the weight and height of the snowpack.

A project was started at USN in 2019, in cooperation with Skagerak Energy AS, to try to develop an autonomous measurement system for snow depth, snow density and snow water equivalent for remote locations, with a small footprint. The first part of the project looked at the system structure of an autonomous measurement system and several possible measurement principles, and a capacitive solution was proposed (Bjerke et al., 2019). A prototype measurement system, based only on capacitance measurements was developed and used for logging (Murillo Abril, 2020), (Murillo Abril et al., 2020). The Covid-19 situation in springtime 2020 with limitation of traveling and the absence of snow at the USN campus limits the number of valid measurements. A new prototype was developed autumn 2020 with five capacitive measurements at different heights in addition to measurement of the atmospheric pressure and temperature. This prototype was deployed in a snowy area, close to Lillehammer (in Norway), throughout the winter season in 2020/2021 with automatic logging of sensor values while manual reference measurements were made sporadically.

1.3 Outline of paper

Section 2 provides a discussion of the system, the prototype developed and deployed, the logging of the sensor values from the prototype, and any manual measurements. Section 3 gives an overview of the machine learning methods. Section 4 gives an overview of the model fitting and validation. The results are discussed in Section 5 and some conclusions are drawn in Section 6.

2 System description

The prototype housing consists of a two-meter heigh grey plastic pipe, with a 90-degree bend on the top. The capacitance sensor devices are located at fixed heights of the plastic pipe, and the temperature and pressure sensor are located at the top of the plastic pipe. The hypothesis for the project was that the snow depth and the snow density could be estimated based on the capacitance measurements at different layers in the snowpack.

A picture of the prototype is shown in Figure 1 covered by about 70 cm of snow, with the two upper capacitance sensors as the black objects pointing to the left from the pipe. The three remaining capacitance sensors are covered by the snow.

Figure 1: The prototype, covered by about 70 cm with snow. The two upper capacitance sensors can be seen as the two black objects pointing to the left of the pipe.

The measurement system of the prototype consists of an Arduino Nano located at the top of the plastic pipe. The Arduino Nano system starts running once a minute, read the sensor values, convert the capacitance sensor outputs to voltage range [0,5] Volt, the temperature to ℃ and the pressure to mBar, and transmit the converted values over the serial line (USB) on a Modbus based

protocol. The capacitive sensor is a “Capacitive Soil Moisture Sensor v1.2” device with a 0-5V interface, the temperature sensor is a TMP36 silicon device with a 0-5V interface, and the pressure sensor is a 4Tech absolute pressure device with a 4-20 mA interface. The 4-20mA interface is converted to a 0-5V interface using a 250 Ohm resistor. However, the pressure sensor must be powered by a separate 12 V DC power supply while the other sensor devices are powered by the 5 V DC output of the Arduino system. The vertical locations of the capacitive sensor devices are 10, 30, 50, 80 and 110 [cm].

A use case diagram, made by Unified Modeling Language (UML), for the Arduino software is shown in Figure 2. As shown in the figure the Arduino software will collect the sensor values and transmit the converted sensor values on the serial line. A remote logging system is needed to record, filter, and store these values.

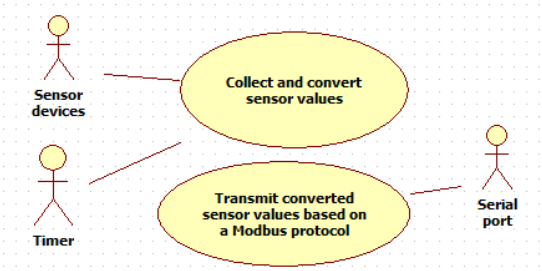

Figure 2: A use case diagram showing the functionality of the Arduino software. Every minute, read the sensor values, convert to the right unit, and transmit on the serial port using a Modbus based protocol.

Machine learning methods were applied, and supervised learning was the selected method as prediction models for the snow depth, snow density and snow water equivalent were needed. Hence corresponding values for snow depth and snow density should be recorded together with the sensor values.

A use case diagram, in UML, for the data storage software (DSS) is shown in Figure 3.

The software has four main functionalities; 1) collect, low pass filter, store and display the values from the measurement system. 2) handle configuration of sensor types, size of low pass filter and how often to store the measurement values on the Comma Separated Values (csv) file. 3) Allow for input of reference values for snow depth and snow density that can be used for the training the models. These values will be stored on the csv file together with the sensor values. 4) Logging of the values on the csv file at specific times independent of receiving data from the measurement system. The default setup was a moving average low pass filter size of 8 and storing the values in csv file every 30 minutes.

The serial port, used for communication between the Arduino system and DSS is an USB port, which also contains the power (5VDC) for the Arduino system.

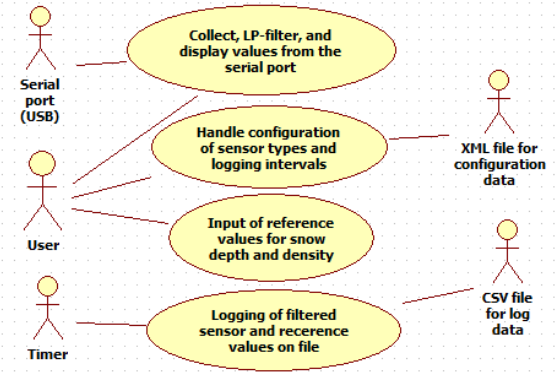

Figure 3: A use case diagram showing the functionality of the logging software, for logging the values from the measurement system.

Figure 4 shows the measuring node to the left, based on a vertical plastic tube with the capacitance sensor devices at fixed height, seen as the white areas in the figure. The lowest capacitance sensor is not visible in this figure. The right side shows the connection between the Arduino system and the DSS, and the protocol used between these systems.

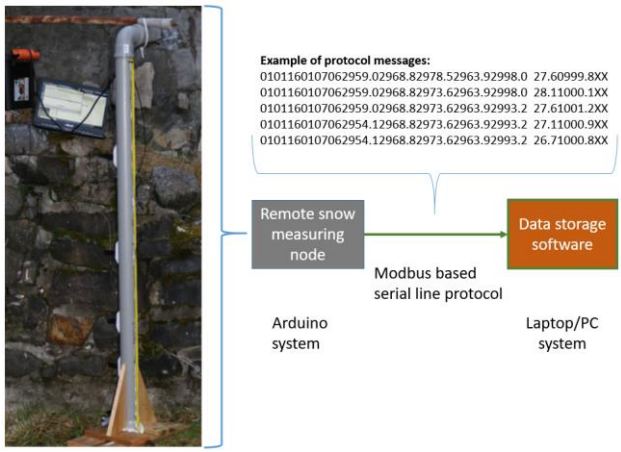

Figure 4: The measurement node to the left with the capacitance sensors at the white areas, and the connection with some examples of the protocol to the right.

The DSS will low pass filter and store the sensor values on a csv file at fixed time intervals, configurable in the DSS. Figure 5 shows a plotting option in DSS when testing manual covering capacitance sensor #2 and #3 with snow. Sensor #2 at 13:40 and sensor #3 at 14:50, with sensor values in mV. Sensor #1 is the lowest sensor device already covered by snow. The change in the voltage is about 100 mV depending on the water content of the snow.

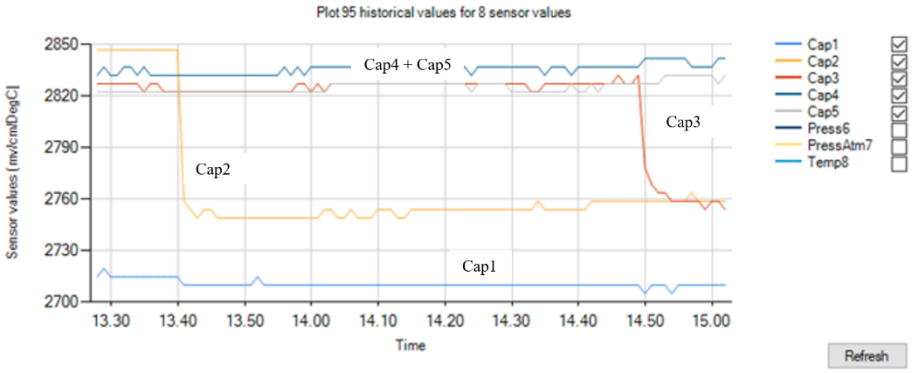

Figure 5: Plotting of the capacitance sensor values when covered by snow. Cap1 is the lowest capacitance sensor, covered by snow. Cap2 is manually covered by snow at 13:40, and Cap3 at 14:50. Cap 4 and Cap 5 is not covered by snow.

The format of the csv file is one line for each measurement containing the time stamp, the values from the capacitance sensors (the lowest one first), temperature sensor, pressure sensors, and any manually measured values for snow depth and snow density. The size of csv file was limited by making a new file for each month.

The manual measurements were made by using a metal pipe with an inner diameter of 6.6 cm inserted into the snowpack, measuring the depth and the weight of the sample. The snow density was calculated based on the pipe diameter and the weight of the snow. All the data needed for the model development are stored in the csv files.

3 Model development

Several tools and frameworks were used for analysis, preprocessing and development of the models. The reason for using several frameworks was to get some experience with the analyzing tools and the process of making models for different frameworks. MATLAB was used for both analyzing, preprocessing and development of the models. ML.NET is a free machine learning framework from Microsoft and was used together with C# for developing models. Keras and TensorFlow was used together with Python to develop models, the tools used in Python was scikit learn. Open Neural Network Exchange (ONNX), an open standard for machine learning models, was evaluated for transferring some of the models between these frameworks but was not used since separate models were developed in each framework.

Supervised learning is used so only the measurement with references can be used for developing the model. The periods for measurements with manual references are 1) 22 to 27-NOV-20, 2) 28 to 31-DEC-20, 3) 12 to 13-FEB-21, and 4) 30-MAR to 2-APR-21. These data were analyzed and some of the data had to be removed because of a power loss error. There is also a challenge

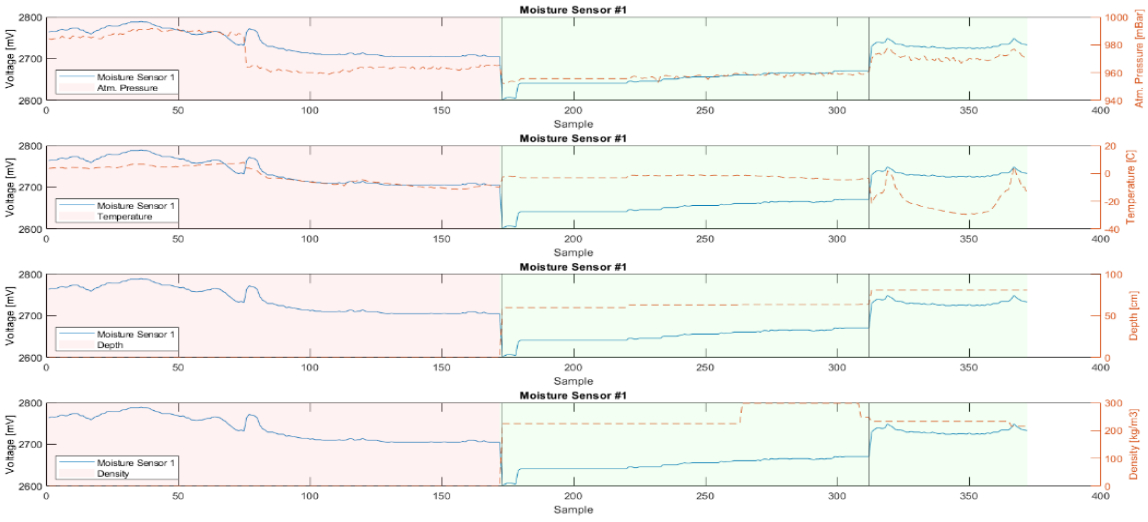

Figure 6: All valid samples for the lowest capacitance sensor with relation to pressure, temperature, depth, and density. Three sections, first section is for November (samples 0 to 172) (without snow), second section for December (samples 172 to 312) and third section for February (samples 313 to 372).

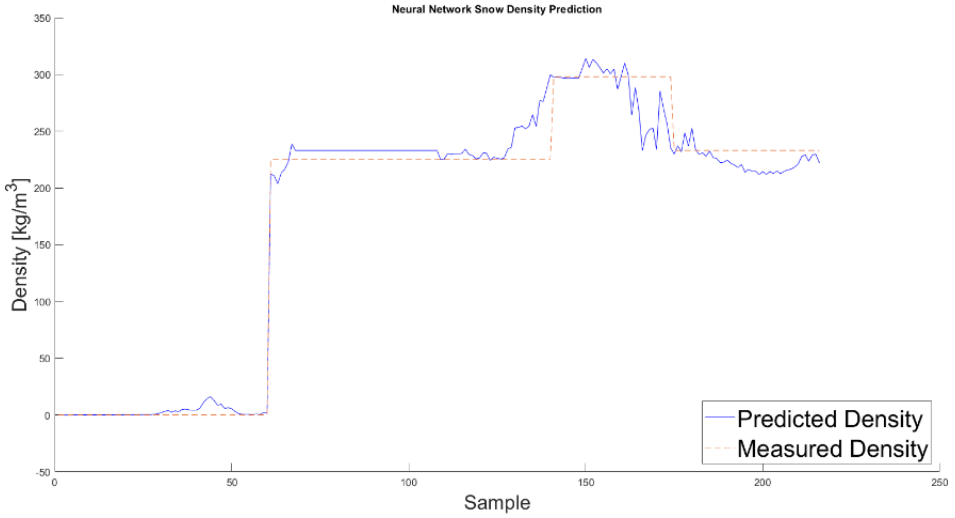

Figure 7: The model for estimating the snow density based on the BR algorithm in MATLAB.

with measurements using a sensor device at fixed location so all the measurements from the last period was removed. This will be discussed as part of the discussion section. The total number of samples that can be used for training of the models are 372.

The valid samples for capacitance sensor #1, the lowest sensor, is shown in Figure 6. The first section, the red section, is the samples for November [1-172], the second section is December [173-312], and the last section is February [313-372]. In each row is the capacitance sensor compared with the pressure, temperature, depth, and density.

A Principal Component Analysis (PCA) was performed indicating that only four principal components are needed to explain 96% of variance in the data. The system has seven variables, 5 capacitance sensor devices, one temperature sensor device and an absolute pressure sensor device. The PCA indicated that all sensor devices were important for the needed information.

The sample set was divided into a training set of 216 samples and a test set of 156 samples.

4 Results

The goal of this project is to develop a model to estimate the Snow Water Equivalent (SWE) parameter for the snowpack, based on the snow depth and snow density. SWE is based on the snow depth and snow density so two separate models must be developed first, one to estimate the snow depth and one model to estimate the snow density.

4.1 Model trained using MATLAB

The Regression Learner app was used in MATLAB to train the models with different algorithms. The best model suggested by the Regression Learner app was

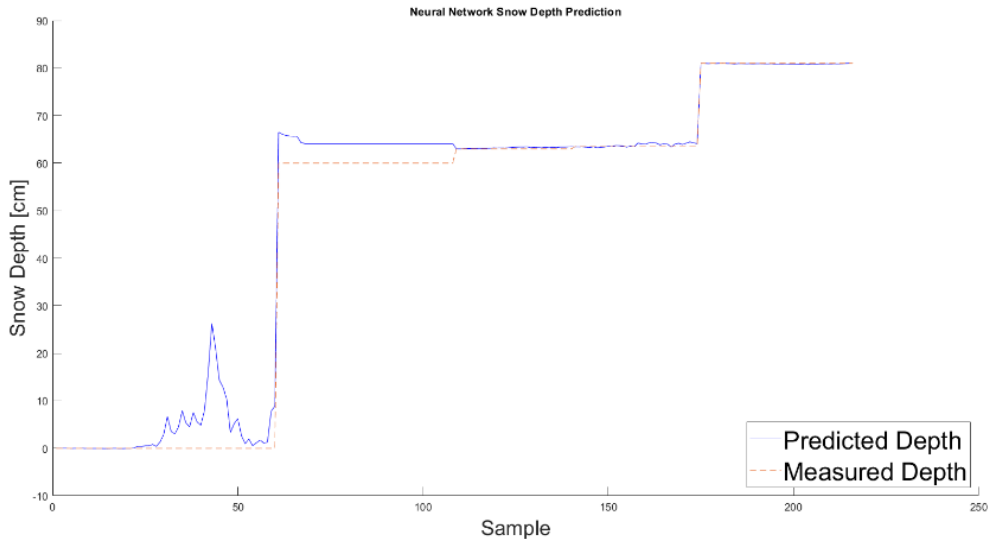

Figure 8: The model for estimating the snow depth based on the BR algorithm in MATLAB.

Gaussian Process Regression (GPP). These models have a challenge in estimating the depth and density in November with no snow. A new model was developed based on neural network with one hidden layer of 50 neurons, using Bayesian Regularization (BR). Figure 8 shows the measured depth and the predicted depth based on the BR model.

The model seems to predict the snow depth ok except for the period in November with no snow, and better than the GPP model. The corresponding model for measured density and predicted density is shown in Figure 7.

4.2 Model trained using ML.NET

ML.NET also contains an automatic trainer but only the algorithm with the best validation results regarding MSE is available at the end of the development process. A test application in C# was developed to plot the measured and predicted values from the models. None of algorithms for the automatic trainer made a model as good as the BR model from MATLAB, and the best results was from the Fast Forrest algorithm. The snow density result is shown in Figure 9 and the snow depth result is shown in Figure 10.

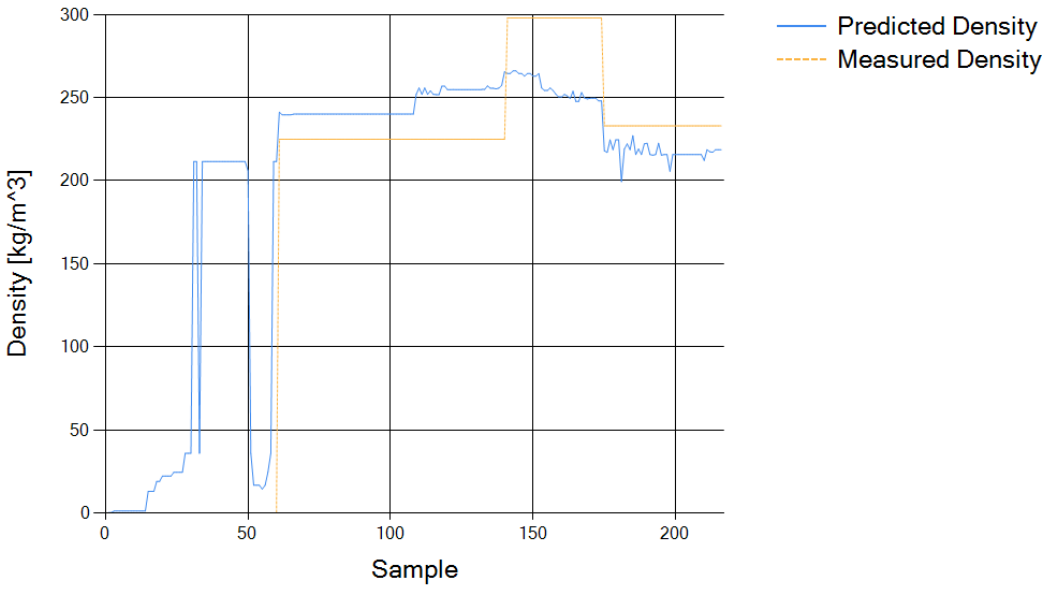

Figure 9: The model for estimation of the snow density based on the ML.NET algorithm.

The model seems to predict the snow density ok, even the November is ok even if there is no snow. There is also a challenge with the density in February, this will be part of the discussion section.

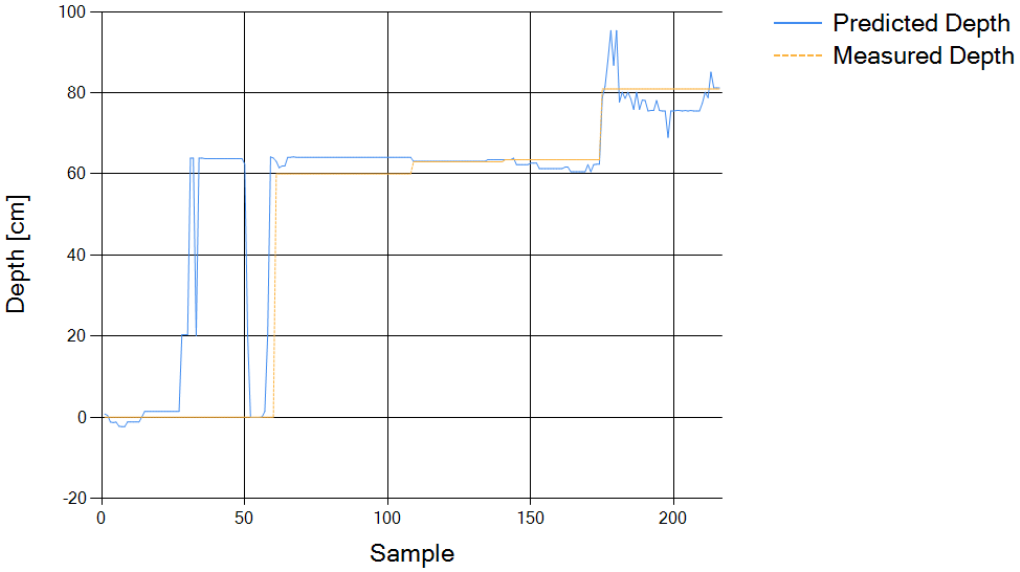

Figure 10: The model for estimation of the snow depth based on the ML.NET algorithm.

Figure 10 shows that the model will not estimate the snow depth very good in November when there is no snow. Most of the models seems to have a challenge with this period. The same challenge with the snow density estimation for the model shown in Figure 9.
The models developed in the MATLAB framework in Figure 7 and Figure 8 seem to estimate the snow depth and snow density better then the models developed in the ML.NET framework.

4.3 Model trained using Keras

Keras is a Python based application programming interface (API) for TensorFlow. Neural network models and the Adam optimizer was used in Keras, with 80% of the samples for training and 20% of the samples used for validation. The selection of samples for these sets were randomized and 1000 epochs was the default for training the models.

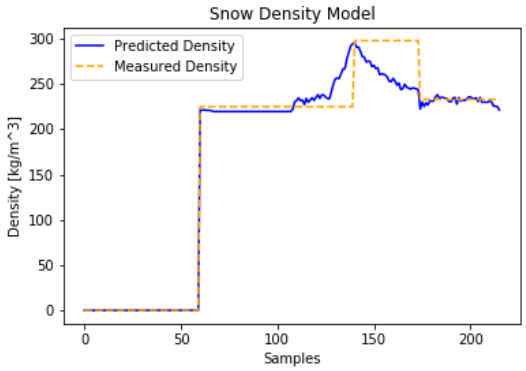

Figure 11: The snow density prediction and measurement based on the Keras framework.

The snow depth model architecture consists of eight hidden layers with between 50 and 200 neurons in each hidden layer. The activation functions used in these layers are Tanh, Relu and Sigmoid types.

The measured and estimated snow depth, based on the Keras model, is shown in Figure 12. The model shows a good prediction also for the November period when there was no snow.

The snow density model architecture consists of six hidden layers with between 25 and 150 neurons in each hidden layer. The activation functions used in these layers are Tanh and Relu types. The architecture for the snow depth model is more complex than the snow density model.

The measured and estimated snow density, based on the Keras model, is shown in Figure 11. The snow density model shows a good prediction of the snow denisty although the density at higher levels is not following the reference optimally.

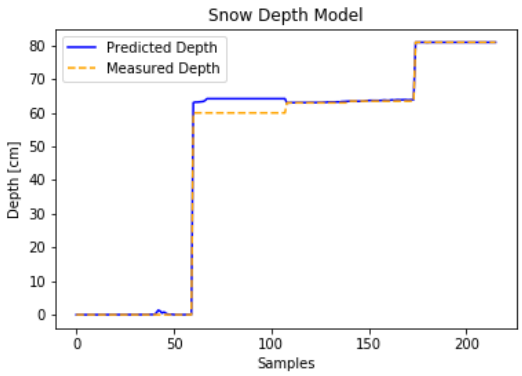

Figure 12: The snow depth prediction and measurement based on the Keras framework.

Since both the snow depth and the snow density models based on the Keras framework seems to perform best on the limited data set, these models were selected as the input for the SWE model.

The SWE model, shown in Figure 13, showing a good prediction of the SWE. Some deviations in the upper regions but still a good fit.

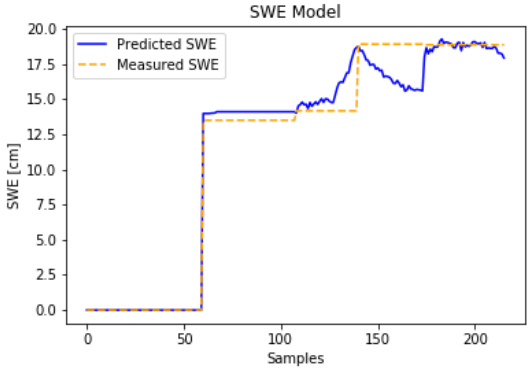

Figure 13: The snow water equivalent (SWE) prediction and measurement based on the Keras framework.

5 Discussion

There are several comments that should be given based on these measurements and results. Many of the models seems to have a challenge predicting the correct snow depth and snow density when no snow, so other weather or environment parameters should be checked and possible added to the system. As always with machine learning methods more data is wanted. In this case there are too few reference measurements with too large jumps in snow depth. This time the reference was based on manual intermittent measurements. The depth measurements were ok, while the density was more of a challenge. First the density was assumed to be almost constant during a day, but in a sunny day the density could vary a lot. The next step will be to have an automatic measurement of the depth and the density as well. Some experiments have been done using an

ultrasonic sensor during the winter and if the calculation is compensated for the temperature and humidity, an ultrasonic sensor will work as depth measurement. A weight cell will also be considered to have a reference measurement for the weight of the snow, estimate the density based on the weight and the depth.

A big challenge with the capacitance sensor devices is that these devices are contact sensors and during the springtime when the snow is melting, the snow crystals will change the shape and size, and will lose contact with fixed objects (Muller, 2020). The capacitance sensor will work in wintertime with temperatures below 0ºC but will lose contact with the snow in springtime and temperatures above 0ºC. This is the reason the last dataset, the dataset from April was not used in the model development process. The current design is not a good solution, another solution should be used to measure the capacitance in the next version of the prototype.

The first versions of the models estimate the parameters as expected. However, the amount of labeled data was too small to get a good and reliable model, and the number of capacitive sensors gave a too rough estimate of the snow depth.

The test and validation set are both collected from the same original dataset, with small variations, especially in the reference. It is therefore likely that the presented Keras model with a huge number of hidden neurons are partly overfitted. Additional new datasets should therefore be tested before the models can be assessed for more conditions in a broader range.

Future work will involve a more robust logging system, a non-contact depth sensor like ultra-sonic or laser sensor and a weight sensor for better calibration data. A new design of the capacitance sensor is needed to better measure the capacitance of the snow during the springtime.

The measurement system is measuring the capacitance at different layers in the snowpack, and estimating the snow depth, the density, and the water content. The focus in this project has been on measurements for hydro power systems. However, properties for other systems like for skiing or avalanches should also be possible with this type of measurements. Skiing properties like snow depth and surface conditions can be estimated based on the measured values from the capacitance sensors. Avalanches are beyond the scope of this study. However, by measuring the capacitance in many layers in the snowpack, with a higher resolution of sensor devices, estimating the condition of each layer can be used for evaluating the risk of avalanches in that area.

6 Conclusion

Three different machine learning framework was used, MATLAB, ML.NET and Keras. The models developed using the Keras framework were the best models, especially in the period with no snow. Two different models were developed for each framework, for prediction of the snow depth and snow density. All models performed ok with a limited set of data samples. The snow density and snow depth models from the Keras framework was used for the SWE model, the goal of this work. The model predicting the SWE was working ok with some limitation. However, the limited set of samples was the largest limitation of making a good model.

References

J. M. Bjerke, M. N. Murillo Abril, A. Jaganjac and N. Pouladi, *Measurement of snow density*, "MSc. Project", University of South-Eastern Norway (USN), Porsgrunn, 2019.

Ccin, Current Snow Cover, Snow Anomaly Tracking, https://ccin.ca/ccw/snow/current/swe, Canadian Cryospheric Information Network, University of Waterloo, 2021.

A. Denoth, A. Foglar, P. Weiland, C. Mätzler, H. Aebischer, M. Tiuri and A. Sihvola, A comparative study of instruments for measuring the liquid water content of snow, *Journal of Applied Physics*, 1984, DOI: 10.1063/1.334215.

A. Denoth and I. Wilhelmy, Snow dielectric devices and field applications, International Snow Science Workshop, 1988.

M. Hallikainen, F. Ulaby and M. Abdel-Razik, Measurements of the dielectric properties of snow in the 4-18 GHz frequency range, *12th European Conference on Microwave*, 1984.

K. Muller, H. Toft Larsen, and G. Sojer, Snøomvandling (in Norwegian), Fact sheet, NVE, 2020

M. N. Murillo Abril, *Development of a remote measurement node for snow density*, "MSc. Thesis", University of South-Eastern Norway (USN), Porsgrunn, 2020.

M. N. Murillo Abril, B. Furenes, N.-O. Skeie, Development of a model to estimate parameters in a snowpack based on capacitive measurements, *SIMS conference*, 2020.

M. Niang, M. Bernier, M. Stacheder, A. Brandelik, and E. van Bochove, Influence of snow temperature interpolation algorithm and dielectric mixing-model coefficient on density and liquid water content determination in a cold seasonal snowpack, *Sensing and Imaging*, 2006, DOI: 10.1007/s11220-006-0020-9.

H. B. Stranden, B. Lirhus Ree and K. M. Møen, Recommendations for automatic measurements of snow water equivalent in NVE, Norwegian Water Resources and Energy Directorate (NVE), 2015.

F. Techel and C. Pielmeier, Point observations of liquid water content in wet snow – investigating methodical, spatial and temporal aspects, *The Cryosphere*, 2011.

H. N. Vahl, *Development of models for estimating snow depth and snow density using machine learning methods*, "MSc. Thesis", University of South-Eastern Norway (USN), Porsgrunn, 2021.

Wsl, Long-term snow water equivalent measurements, https://www.wsl.ch/en/projects/swe-measurements.html, WSL Institute for Snow and Avalanche Research SLF, 2021.

Increasing interpretability and prediction rate by combining self-organizing maps with modeling algorithms

Ivan Ryzhikov[1] Mikko Huovinen[2] Yrjö Hiltunen[1]

[1]Department of environmental and biological sciences, University of Eastern Finland, Finland, {ivan.ryzhikov,yrjo.hiltunen}@uef.fi

[2]Yara, Kuopio, Finland, mikko.huovinen@yara.com

Abstract

We consider supervised learning problems, for which we need not only the accurate model, but also the model, that explains the relation between inputs and a target variable. There are modeling problems, when production experts can measure their confidence in the modeling results by modeling metrics, such as accuracy, but need an explanation for what was the reason of desirable or undesirable situation or system state in the past. In this study we utilize a combination of self-organizing maps and multiple linear modeling to increase the interpretability and accuracy. We assume that the target variable can be explained differently by different patterns that characterizes inputs data. By solving clustering problem for subset of inputs, we have structured data and can relate each cluster to its representative or cluster profile, which explains the cluster. Based on that structure we build linear model for each cluster dataset, and coefficients of this model explain the influence of factors for particular inputs characteristics. To cut the number of inputs we use L1-regularization for linear model. Proposed approach was tested on several industry related problems and implemented in application.

Keywords: explanation, self-organizing map, risk estimation, postprocessing

1 Introduction

Digital transformation makes it possible for industries to find answers on many questions in mathematical models. Machine learning algorithms, statistical analysis and visualization reveal dependencies between production efficiency and processes factors based on observed data. Mathematical models and their applications become a main part of support decision making platforms. Since the models are data-driven, production experts need to measure the adequacy of models, but there is no general way to provide this estimation. Nonlinear models could give a very high prediction rate and good generalization, but due to its complexity it is difficult, if even possible, to interpret the model. On the other hand, simple models can be interpretable, but in some cases give lower prediction rate, so one cannot be confident in modeling results and use the extracted from the model knowledge. In this study we use a combination of clustering approach, such as self-organizing map, and simple modeling approaches proving that these combination makes the final composite model more flexible but still interpretable. Simpler model could be not good at generalizing, because the relation between the inputs and target variables cannot be identified with those simple rules. Another reason of bad generalization is when simple rules meet contradictions in data. But these contradictions could disappear if these are related to patterns in data.

We propose an approach that outperforms simple modeling approaches but keeps its interpretability benefits. This approach increases our confidence in data-driven models and clarifies effects between the target variable and inputs. Applying self-organizing maps helps one to understand the main patterns in the data and helps to see which pattern can be explained with simple models and which cannot and requires nonlinear models. Proposed approach discovers if the main influential factors are different for different patterns in data. This takes place in many cases, for example: seasonal effects or different input materials can lead to situations, where one inputs become more influential on target variable over another. The goal of this approach is to understand what one can do to improve the situation and why. In research we apply linear modeling with and without regularization, and Kohonen's self-organizing maps (SOM) (Kohonen, 1995). Linear models allow us to utilize the well-known statistics, such as p-values and F-score. When we apply l_1 and l_2 regularization (Gareth et al., 2013; Kuhn and Johnson, 2016) and cross-validation, we reduce the number of variables without loss of generalization and prediction rate. Self-organizing maps returns clusters, which can be characterized by their profiles. Profiles can be determined with reference vectors, or average or median values by cluster.

Combination of unsupervised learning and supervised learning can be met in different studies. In some cases, this combination improves the prediction metric. In (Lin et al., 2016) SOM is combined with support vector machine algorithm to improve the forecast of reservoir inflow during typhoon periods.

The proposed approach has been tested on several production data analysis problems and proved its reliability in decision making and understanding the causality between the effects appearing and the system state or input material characteristics.

SOM provides interpretable visualizations. One can see clusters and their properties: number of elements, model prediction rate on train or test data, data pattern that describes the cluster and the most influential variables for that cluster.

An application solving the data analysis and modeling problem with the proposed approach was implemented in R (R Core Team, 2018) and R Shiny (Chang et al., 2021) framework. It allows user to upload the dataset and set the clustering or learning parameters and build clusters and models. As a result, user sees statistics by cluster, modeling results by clusters and cluster profiles in interactive visualization made with "ggiraph" package (Gohel and Skintzos, 2020).

2 Modeling by Clusters

There are many modeling problems, when we are interested not only in the model accuracy, but the in model that explains what factors cause desirable situation. At the same time, model needs to be accurate, otherwise we cannot be confident in explanations that it brings. Linear model, ridge regression and lasso (Gareth et al., 2013; Kuhn and Johnson, 2016) regression give simple explanation on what factors have positive or negative effect on the target variable, but these modeling approaches have low accuracy if the relation between the inputs and outputs is nonlinear (Gareth et al., 2013). Flexible models need specific techniques to reveal the relation between inputs and output, which gives the relative importance of inputs, but leave behind the scenes the detailed explanation. Thus, the production expert cannot decide what condition leads to desirable or undesirable situation.

The main assumption of this study is that there are contradictions in effects of factors on the target variable, which make simple models inaccurate, and these contradictions can be caused by different relation between inputs and outputs for different patterns. The proposed approach is illustrated on Figure 1.

We assume that clusters performed only on a subset of input variable can already give us acceptable result. For example, we can leave out all the process variables and use only the characteristics of inputs materials. The approach consists of three steps, which are given on Figure 1 from the bottom to the top:

1 – We select variables that we will use in clustering analysis.

2 – We provide clustering analysis and reveal patterns in data.

3 – For each dataset related to pattern we solve modeling problem separately.

4 – We analyze the relation between the patterns in data and modeling results.

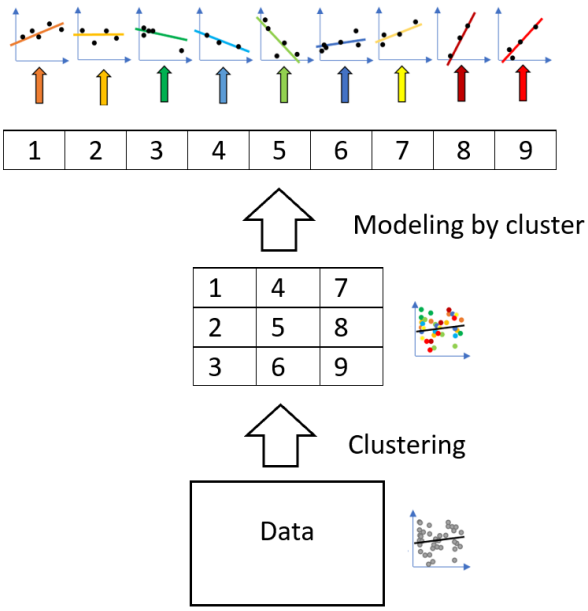

Figure 1. From data to clusters and model for each cluster.

As we mentioned above, linear model does not fit if the relation is nonlinear, but if nonlinearity caused by different patterns in data, we could solve modeling problem for each pattern. That is what one can see in Figure 1. If we use the whole dataset for training, we have a model, which does not give us the satisfactory accuracy level and thus, we cannot trust its coefficients as influence representation. But once we find clusters in the data and solve the modeling problem for each subset that is represented by a cluster, system predictability increases, and we can be more confident in explanations that these models provide. In that case we lessen the contradiction between the influence of different factors, which happens in different system state, according to the patterns found.

Let $X = \{x_1, x_2, \dots, x_s\}$, $x_i \in R^n$, $T = \{t_1, t_2, \dots, t_s\}$, be the observations and times, respectively, s is a dataset size. Let $Y = \{y_1, y_2, \dots, y_s\}$ be the target variable. In this paper we consider regression problem and binary classification problem. When solving binary classification problem, we search for model

$$\begin{gathered} \forall i\ y_i \in \{0,1\}, f_c(\cdot): R \to \{0,1\}, \\ m(\cdot): R^n \to R, \\ \sum_{i=1}^{s} [y_i = f_c(m(x_i))] \to \min, \end{gathered} \tag{1}$$

where f_c is a function that maps the linear model m prediction. Without loss of generality, let classification function f_c map model prediction to the 1st class, if the prediction value is smaller than 0.5.

For regression problem we are interested in model that predicts the output accurately,

$$\forall i\ y_i \in R,\ m(\cdot): R^n \to R,$$
$$\sum_{i=1}^{s} \left(y_i - m(x_i)\right)^2 \to \min. \quad (2)$$

When solving problems (1) and (2) we are interested in model, which can satisfy our expectations in interpretability.

In general, one can solve any other supervised learning problem, but in this study, we focus on (1) and (2). Nevertheless, the developed analytical application allows solving multimodal classification problem.

2.1 Clustering

There are cases when the inputs can reflect different situations: different material types, different content of chemical elements, different shifts, seasons, etc. We expect to see that these factors would affect the relation between the inputs and outputs of the model. But these examples are not the only cases, there could be different patterns in the data that we need to reveal. Because of that we use clustering algorithms to find all the patterns in data.

In this study we utilize self-organizing maps to find the patterns in data. We chose SOM, because it preserves the data structure and makes it possible to visualize the clustering results on two-dimensional plot. Before we train SOM, we center and scale the inputs and keep the scaling parameters to preprocess the new observations. We train SOM on input data only because we need to apply it to new observations and for new observations, we do not know the output value yet.

It is important that clustering problem can be solved for a selection of inputs, which make our clusters more interpretable and allows using of the production experts experience. For example, the input data contain temperatures of machine tools and material analysis. Expert knows that temperatures is something that we cannot control and those change rapidly, but the material analysis changes once in two or three months and there could be some differences in how the process is going. In that part one can test different hypothesis on what variables should we select when do clustering. Let us denote

$$I = \{i_1^c,\ \dots,\ i_q^c\}, \quad (3)$$

as the set of indices of variables, we select for the clustering of the data and q is the number of selected variables.

Once the clustering problem is solved, we have labels or clusters number $C = \{c_1, c_2, \dots, c_s\}$, so each observation has one and only one label $x_i \leftrightarrow c_i$. Now we can split the dataset by clusters:

$$\begin{gathered}\tilde{X}_j = \{x_i \in X,\ i = 1, \dots, s:\ c_i = l_j\},\\ \tilde{T}_j = \{t_i \in T,\ i = 1, \dots, s:\ c_i = l_j\},\\ \tilde{Y}_j = \{y_i \in Y,\ i = 1, \dots, s:\ c_i = l_j\},\\ j = 1, \dots, n_c,\end{gathered} \quad (4)$$

where n_c is number of clusters or patterns and l_j is label of j-th cluster.

SOM requires several parameters. We need to set the grid dimension or the number of neurons and their topology. Let g_v be the number of neurons vertically and g_h be the number of neurons horizontally. The total number of neurons is $g_v \cdot g_h$. Algorithm has the following parameters: number of times the whole dataset will be presented to the network and the radius of neighborhood.

There is "kohonen" package in R (Wehrens and Kruisselbrink, 2018), which we use in this study, when solving the clustering problem. In numerical tests we used the default values for parameters and searched for the grid that is best for the dataset. In application it is possible to set the SOM algorithm parameters.

2.2 Modeling

In this part we do linear model for each of the subset of the dataset (2). First, we consider regression problem and linear models with regularization. To minimize the values of coefficients we use l_2-regularization and to reduce the number of input variables we use l_1-regularization

$$\sum_{i=1}^{s_j} \left(\left(\tilde{Y}_j\right)_i - m_j\left(\left(\tilde{X}_j\right)_i, \theta_j\right)\right)^2 + \alpha P(\theta_j) = \min(\theta_j), \quad (5)$$

$$m_j\left(\left(\tilde{X}_j\right)_i, \theta_j\right) = \sum_{k=1}^{n} \theta_k^j \cdot \left(\left(\tilde{X}_j\right)_i\right)_k + \theta_0^j,$$
$$l_1: P(\theta) = \sum_{i=0}^{n} \left|\theta_i^j\right|,$$
$$l_2: P(\theta) = \sum_{i=0}^{n} {\theta_i^j}^2, \quad (6)$$

where m_j is the j-th linear model for $\tilde{X}_j$ subset that corresponds to cluster l_j, $\left(\tilde{X}_j\right)_i \in R^n$ is the i-th vector of observations in j-th subset, and $\left(a_0^j, a_1^j, \dots, a_n^j\right)$ are the coefficients of j-th linear model and α is parameter.

In this study we also consider binary classification problem, for which both regularizations are applicable:

$$\sum_{i=1}^{s_j} \log\left(\tilde{p}\left(\left(\tilde{Y}_j\right)_i, \left(\tilde{X}_j\right)_i, \theta_j\right)\right) + \alpha P(\theta_j) = \max(\theta_j), \quad (7)$$

$$\tilde{p}\left(\left(\tilde{Y}_j\right)_i, \left(\tilde{X}_j\right)_i, \theta_j\right) = \begin{cases} \sigma\left(m_j\left(\left(\tilde{X}_j\right)_i, \theta_j\right)\right), \left(\tilde{Y}_j\right)_i = 0, \\ \sigma\left(-m_j\left(\left(\tilde{X}_j\right)_i, \theta_j\right)\right), \left(\tilde{Y}_j\right)_i = 1, \end{cases} \quad (8)$$

$$\sigma\left(m_j\left(\left(\tilde{X}_j\right)_i, \theta_j\right)\right) = \frac{1}{1 + e^{-m_j\left(\left(\tilde{X}_j\right)_i, \theta_j\right)}}, \quad (9)$$

When we solve the modeling problem, we split each subset on training, validation, and test sets. Training and validation subsets are used to determined α parameter via the grid search. We pick a trial α value, train the model on the training subset and then calculate the criterion on validation subset and after we check all the trial values, we pick the best α^* value in a sense of validation dataset criterion value. Then we use this α^* to train model on the union of the training and validation dataset and calculate its accuracy on the testing set.

We use "glmnet" R package (Friedman et al., 2016), where lasso, ridge and elastic net regressions are implemented.

2.3 Visualization

Once we have solved the modeling problem for each cluster, it is possible to reveal the statistics of it. First, one can observe the criterion value calculated for the testing set of that cluster and additionally criterion value based on training and validation set. If the model is linear, we can see the p-values and F static. Second, if we are satisfied with the accuracy of the model, we can find the most influential variables by the corresponding coefficients of the linear model and find out which coefficient cause negative or positive effect on the target variable. Third, we can observe the cluster description or cluster profile by its reference vector, vector of medians or mean values of its observations. This profile gives us information about what specifies this cluster. It could be high or low values of the variable.

Visualization of the results includes 3 plots: one with the SOM clusters 2-d plot, another one with selected cluster profile and the last one with coefficients of the linear model built for this cluster.

2.4 Predicting New Observations

When we receive the new observations to make predictions, we need to recognize to which cluster these observations belong to and then use the corresponding model to make a prediction.

Each cluster is represented by its reference vector:

$$V = \{v_1, \ \dots, \ v_{n_c}\}, \tag{10}$$

where $v_k \in R^q$, since we selected q variables for clustering (3).

Let us denote $x_{new} \in R^n$ as new observation and its selected variables (3) for clustering projection is denoted by $x_{new}^c \in R^q$. Now we compare this projection to the cluster reference vectors and determine which cluster is the closest:

$$i_c = \arg\min_i \|x_{new}^c - v_i\| \tag{11}$$

Once we determine the cluster to which projection x_{new}^c belongs, we can make the prediction using the model for specific cluster i_c:

$$y_{new} = m_{i_c}(x_{new}). \tag{12}$$

Criterion (11) is not the only option to determine the cluster, but this question is out of scope in this study. We can also see if there is no cluster close to the new point and realize that this kind of inputs combination is new to us.

3 Experimental Results

We applied approach to find the most influential factors of unwanted effects in a production line. To prevent leakage of commercial information, we rename the variables, and skip the analytical results that relates to the problem domain.

We have a dataset with 61 input variables and solve binary classification problem. Our first class is "good" production state, and our second class is "bad" one. Previously we cleaned the dataset and since observation rate is different for some variables, we modified it to the one we need. We made the standard normalization of the input data because approaches (5)-(6) and (7)-(9) and SOM requires that. When calculating regression or logistic regression with l_1 and l_2 regularization we split the train dataset on train and validation parts and keep 20% of data for validation. Then we use uniform grid on $G = G = [-5, 10]$ with 1000 points and try these values as exponential degrees for α in (5)-(6) and (7)-(9), in other words $\forall p \in G \Rightarrow \alpha = e^p$. Then we look for the best parameter by error on validation dataset and use it to train model on all the train data and after that check it on test dataset.

The next step was to determine the factors we use as the main ones for clustering. Since in the dataset we have sets of variables of different nature, we used one of those. Our choice was discussed with production experts. It is very important to receive a feedback from the production experts or business when selecting the inputs for clustering problem. Variables for clustering will be the first ones the production analyst or decision maker will use, when one needs to make a decision. It does not mean that these variables should be available in advance, but it should be available soon enough, so the decision maker will have explanation in time or not too late.

Once we selected variables (3), we solve the clustering problem and group the data according to the clustering labels (4). In this study we consider different number of clusters. We examined different combinations of clusters on horizontal and vertical axis: $(g_v^i, g_h^i), \forall i: 1 \le g_v^i, g_h^i \le 1, g_v^i \le g_h^i$ and $g_h^i = 1 \Leftrightarrow g_v^i \ne 1$, which means we try the following combinations: $1 \times 2, 1 \times 3, \dots, 1 \times 5, \dots, 2 \times 2, 2 \times 3, \dots, 5 \times 5$. For each of these parameters pair we solve the clustering problem and for each clustering problem solution, we produce the datasets and solve modeling problem.

When we have the combined clustering and models statistics, we can compare the clustering parameters by the total statistics and choose the best settings for considered problem. Let us compare overall train and

test ratings for different combinations of clusters on horizontal and vertical axis. The summary is given in Table 1. In this summary we calculate error rate mean value weighted by number of elements per cluster.

Table 1. Train and Test Error Rate by Number of Clusters

Model	*Train Accuracy*	*Test Accuracy*
No clusters	0.7833	0.7864
1x2	0.8324	0.7517
1x3	0.8371	0.7695
1x4	0.8629	0.7511
1x5	0.8675	0.8041
2x2	0.8582	0.7586
2x3	0.8985	0.8060
2x4	0.9300	0.8387
2x5	0.9599	0.8793
3x3	0.9432	0.8267
3x4	0.9913	**0.9116**
3x5	1.0000	**0.9205**
4x4	1.0000	0.8988
4x5	1.0000	0.9178
5x5	1.0000	0.9030

One can see that there are many combinations that outperforms approach without clustering and modeling by groups of data. One can also see that there are a few combinations which have high prediction rate on test data. Let us consider combination 3×5 as it has the best accuracy rate on test data. It is important to mention that 3×5 combination developed a cluster, which consists only of "good" class cases, so that its actual accuracy rate is higher. This must be considered when one chose the clustering parameters.

In this study we use the "kohonen" R package (Wehrens and Kruisselbrink, 2018) and make visualization with help of "ggplot2" R package (Wickham, 2016).

First, we can visualize clusters and color them according to the number of "bad" observations. In Figure 2 we can see the distribution of "bad" observations and their localization in particular clusters. One can use this information to reveal the relation between the clustering inputs values and pattern these values represent to the target variable. The same is possible for continuous output, for which we can use mean or median value.

Additionally, we can visualize the characteristics of each cluster by its statistics for specific variable or their combinations. For example, we can visualize the average sum of specific components by clusters, or we can see the distribution for a variable among clusters. The general profile or characteristics of the cluster will be described below.

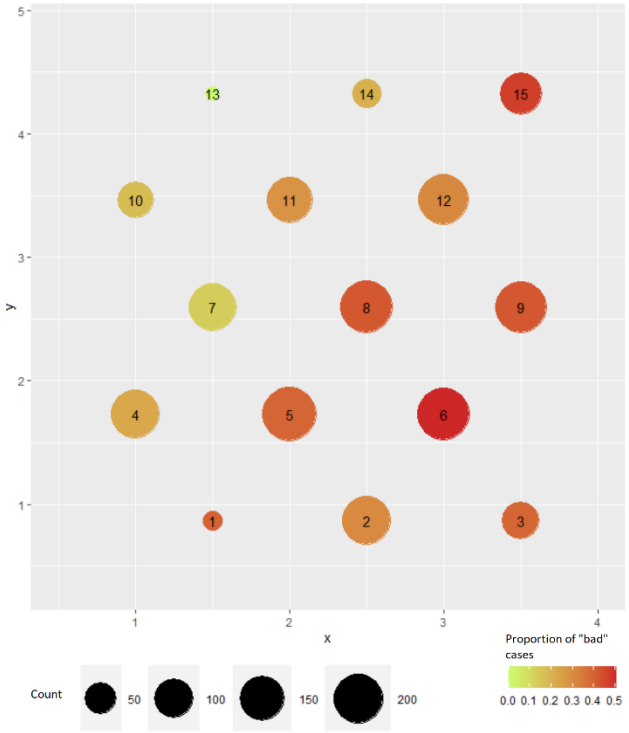

Figure 2. Percent of "bad" cases per cluster.

Second, we can visualize the error on training data for each model. In general, this plot can show us if there are some patterns for which we cannot apply the model we chose, or the data does not allow us to reveal the relation between the inputs and outputs.

Third, we can visualize accuracy on the testing data for each model. This plot is given in Figure 3.

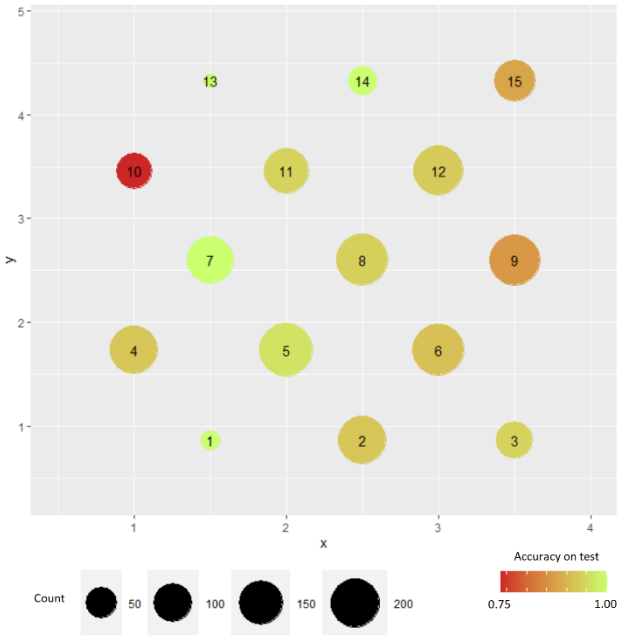

Figure 3. Accuracy on testing data per cluster.

Fourth, we can visualize the precision on the testing data for each model. This plot is given in Figure 4.

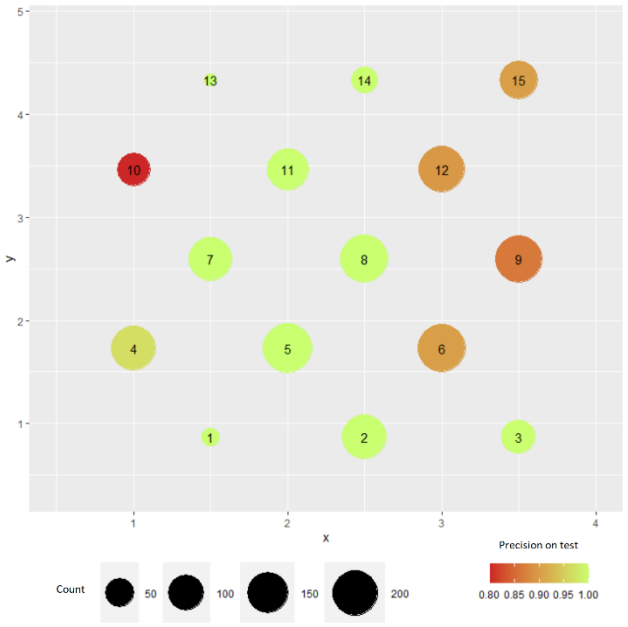

Figure 4. Precision on testing data per cluster.

The final two plots reveal what pattern can we be confident in, when predict the target variable or make any conclusion about relation between inputs and outputs. If the model metric on the test data is low, it means that we cannot be confident in any explanations given by the model that is built on the model of this cluster. For example, one can see that cluster 10 has lower accuracy and precision, comparing to other clusters.

Generally, we can add different statistical characteristics visualizations by clusters.

Now for each cluster one can see its profile and the most influential variables. In application we developed, it is possible to interactively choose the cluster of interest and observe its profile and linear model coefficients with help of R Shiny and "ggiraph" R package. Let us pick cluster "1", which is in left bottom corner in Figures 2-5. An example of cluster profile is given in Figure 5, and model's coefficients for that cluster is given in Figure 6.

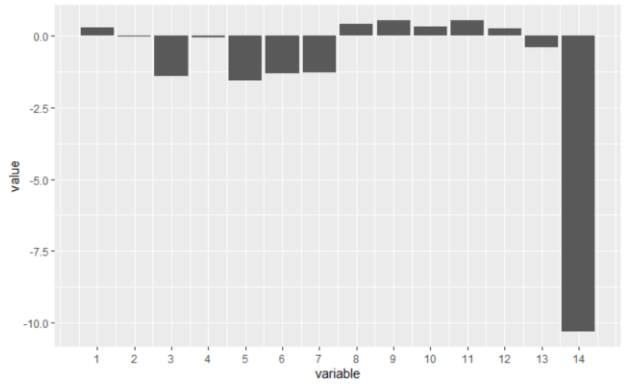

Figure 5. Cluster profile: cluster reference vector.

On profile figure we see the scaled data: 0 means average value for each variable and values above 0 correspond to cases, where these variables were greater than their average. If the value is smaller than 0, we know that this variable usually takes value that is smaller than average. As one can see this cluster can be described by 14th variable, because this variable is sufficiently smaller the mean value. One can also observe that variables 3, 5-7 are also smaller than the mean value. Expert can name this cluster according to its profile and variables nature.

Each cluster can be described by its characteristics. We can use mean, median values or any other metrics that help decision maker understand what each pattern represents. In this study we used reference vectors (10), since we utilize SOM. Reference vectors show values that characterize the cluster in a way, that if there is a new observation, we will compare the reference vector with that observation to make a decision (11) on what cluster does this observation belongs to (12).

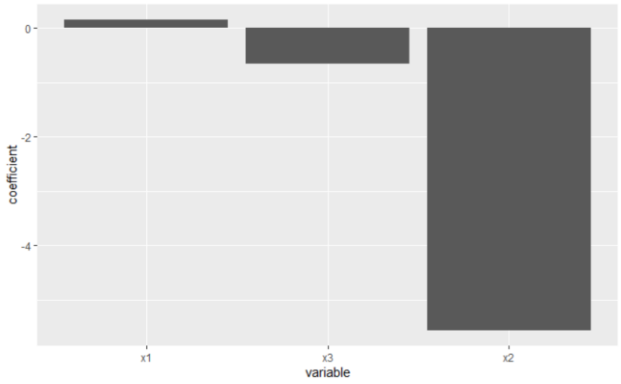

Figure 6. Linear model coefficients for selected cluster.

As one can see, lasso-regression keeps only 3 from 61 variables. Variables selected in model that corresponds to 1st cluster can be interpreted straightforward: increase of **x3** or **x2** lead to negative consequences and increase of **x1** lead to positive ones. Since we applied regularization we cannot calculate the $\boldsymbol{p}$ −value for any of the inputs coefficients the same way as one can do it for linear models without regularization. Nevertheless, one can apply linear modeling without regularization as the step 3, where we solve modeling problems for each data in cluster.

4 Conclusion

When solving modeling problem for business or production we are commonly interested in interpretability of the model. Interpretability lets decision makers and production experts understand the mechanics of the model prediction making. Sometimes this is necessary to validate the model, to be confident in it or to understand the process better. Data-driven modeling provides different view on the interaction between the inputs and outputs, which could reveal the unknown causality. Better understanding of the process is necessary, when one is looking for actions to improve

the process performance, to avoid unwanted states, and lessen production costs.

Proposed approach outperformed modeling without clustering and revealed the patterns that relates to the "bad" cases. We can observe it comparing error rate on train and test in Table 1 for model in the first row, which is built without clustering and any combined model. We can also observe that the model accuracy on train data is increasing with increase of clusters number. At the same time model accuracy on test data increase to some number of clusters. Because of that it is important to investigate what is the best combination of cluster numbers.

Powerful computational and visualization libraries in R along with R Shiny framework allows implementing analytical system, which can solve the combined clustering and modeling problem, reveal the dependencies and pattern and helps looking for actions to improve the process, when new observations appear.

Acknowledgements

This research is a part of the *AI-DA* projects, which is funded by Business Finland, European Regional Development Fund (ERDF), and seven companies.

References

Winston Chang, Joe Cheng, JJ Allaire, Carson Sievert, Barret Schloerke, Yihui Xie, Jeff Allen, Jonathan McPherson, Alan Dipert and Barbara Borges, shiny: Web Application Framework for R. R package version 1.6.0. https://CRAN.R-project.org/package=shiny. 2021

James Gareth, Daniela Witten, Trevor Hastie, Robert Tibshirani, *An Introduction to Statistical Learning*. New York, NY: Springer. 2013

David Gohel, Panagiotis Skintzos, ggiraph: Make 'ggplot2' Graphics Interactive. R package version 0.7.8. https://CRAN.R-project.org/package=ggiraph. 2020

Jerome Friedman, Trevor Hastie, Robert Tibshirani, Regularization Paths for Generalized Linear Models via Coordinate Descent. *Journal of Statistical Software*, 33(1): 1-22. 2016. URL https://www.jstatsoft.org/v33/i01.

Teuvo Kohonen. *Self-Organizing Maps*. Springer, New York. doi:10.1007/ 978-3-642-97610-0. 2001

Max Kuhn, Kjell Johnson, *Applied predictive modeling*. Springer. 2016.

Gwo-Fong Lin, Tsung-Chun Wang, Lu-Hsien Chen, A Forecasting Approach Combining Self-Organizing Map with Support Vector Regression for Reservoir Inflow during Typhoon Periods, *Advances in Meteorology*: 1-12, 2016. https://doi.org/10.1155/2016/7575126

R Core Team. R: A language and environment for statistical computing. R Foundation for Statistical Computing, Vienna, Austria. URL https://www.R-project.org. 2018

Ron Wehrens, Kruisselbrink, Flexible Self-Organizing Maps in kohonen 3.0. *Journal of Statistical Software*, 87(7): 1 - 18. doi : http://dx.doi.org/10.18637/jss.v087.i07. 2018

Hadley Wickham, *ggplot2: Elegant Graphics for Data Analysis*. Springer-Verlag New York, 2016.

Modelling a Cement Precalciner by Machine Learning Methods

Amila C. Kahawalage, M.H. Wathsala N. Jinadasa

Department of Process, Energy and Environmental Technology, Faculty of Technology,
Natural Science and Maritime Sciences, University of South-Eastern Norway, Kjølnes Ring 56, 3918, Porsgrunn, Norway
{amila.c.kahawalage,Wathsala.jinadasa}@usn.no

Abstract

This work is a feasibility study of modelling the calcination process in a cement precalciner by employing machine learning algorithms. Calcination plays a significant role in characterising the clinker quality, energy demand and CO_2 emissions in a cement production facility. Due to the complex nature of the calcination process, it has always been a challenge to reasonably model the precalciner system. This study is an attempt of finding a feasible alternative to answering this challenge. In this study, six machine learning algorithms were tested to analyse three output variables, which are, 1). the apparent degree of calcination, 2). CO_2 molar fraction (dry basis) and 3).water molar fraction in the precalciner outlet stream. Fifteen input variables were used to train the algorithms, of which the values were obtained through a large number of simulated datasets by applying mass and energy balance to the precalciner system. A number of machine learning algorithms showed better predictability and Artificial neural network (ANN) showed the best performance for all three output variables.

Keywords: precalciner, cement manufacturing process, machine learning, degree of calcination

1 Introduction

1.1 Cement manufacturing and calcination

Cement is one of the frequently utilized materials in building infrastructure facilities. Cement manufacturing is a globally crucial industrial sector that is highly energy intensive. It is responsible for a considerable share of global CO_2 emissions. The dominant uses of carbon-intensive fuels, such as coal in clinker making and calcination process, are accountable for a large amount of CO_2 emissions in the cement industry. Calcination in the cement manufacturing process is a complex industrial phenomenon involving mass transfer, heat transfer, and physical and chemical reactions. Materials are subjected to high temperatures so as to cause a chemical and physical change. Process emissions from calcination of limestone are 60%, where 0.5 tonnes of CO_2 is emitted per tonne of clinker production (IEA, 2008). The endotherm reaction at 950 °C in the calciner demands about 1700 MJ/t clinker energy, which is around 50% of total energy (WWFI, 2008).

Figure 1 shows a schematic diagram of a typical dry-based cement manufacturing facility. Most of the modern cement facilities are equipped with a precalciner system located between the preheater and the rotary kiln. In the production process, raw materials, typically 80-90% limestones, are prepared by crushing, grinding and adding chemicals. This preprocessed raw material (which is referred a 'raw meal') is then preheated to 750°C and sent to the precalciner (also called as calciner). Precalciner intiates the chemical decomposition of limestone ($CaCO_3$) into lime (CaO) and carbon dioxide ($CaCO_3 \leftrightarrow CaO + CO_2$). About 90% of raw meal is calcined at this unit (GmbH, 2016). Precalciner system provides direct combustion through solid-gas heat exchange, where it disperses and suspends cement raw meal powder in an airflow. The pre-calcined meal then enters the rotary kiln, where the remaining calcination process is completed. Clinker formation takes place in the kiln and finally the clinker is sent to the clinker cooler.

Stability and the effectiveness of the calcination process directly affects the final clinker quality, smooth operation in the subsequent rotary kiln operation and the energy requirement of the pyroprocessing unit. The exothermic process of fuel combustion and the endothermic process of carbonate decomposition in the raw meal occurs simultaneously in the precalciner. The optimum operation of precalciner conserves energy and reduces emissions associated with both precalciner and rotary kiln. Calcination degree, which is an indicator of the performance of the precalciner, is affected by several parameters such as temperature inside the calciner, residence time of the raw meal in the system, solid gas separation, dust circulation effect and kinetic behavior of raw materials (Mikulčić et al., 2012; Mohammadhadi, 2018).

Calcination degree is expressed in two ways; either *true calcination degree* or *apparent calcination degree* (Tokheim, 1999). The apparent degree of calcination η_{app} is mentioned as ADOC in this paper, which is used as an indicator to monitor the calcination process in the

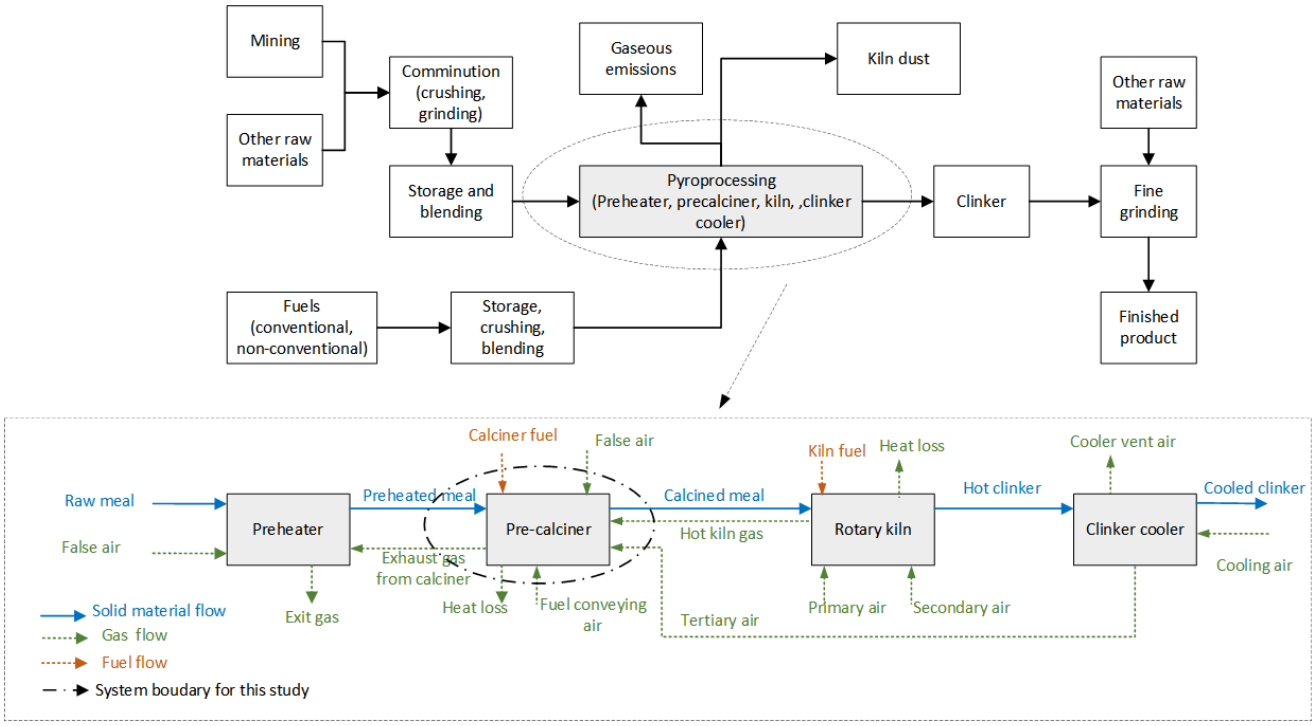

Figure 1. Schematic diagram of a typical cement manufacturing facility with details about input/output flow streams for the pyroprocessing section

cement production line because accurate calcination degree cannot be measured easily. However, it is not easy to measure the apparent degree of calcination online. Instead, samples are extracted from the process line and analyzed offline in the laboratory. The frequency between two subsequent analyses can be one hour or even several hours, depending on the availability of laboratory capacity. The precalciner outlet temperature is therefore used as the primary controlled variable in the precalciner to control the degree of calcination. Oxygen and carbon monoxide levels are also controlled because they are indicators of the fuel combustion and stabilisation of the process, respectively (Osmic et al., 2020)

Figure 2 shows different input and output variables to the cement precalciner system. These variables belong either to basic input streams (i.e. preheated raw meal, fuel and tertiary air) or primary output stream (i.e. calcined meal). Description of symbols can be found in Table 1. Some of these variables can be measured online by appropriate sensors, while others are difficult to measure. In such situations, they are computed using available measurements. The computation can be accomplished on the basis of appropriate assumptions

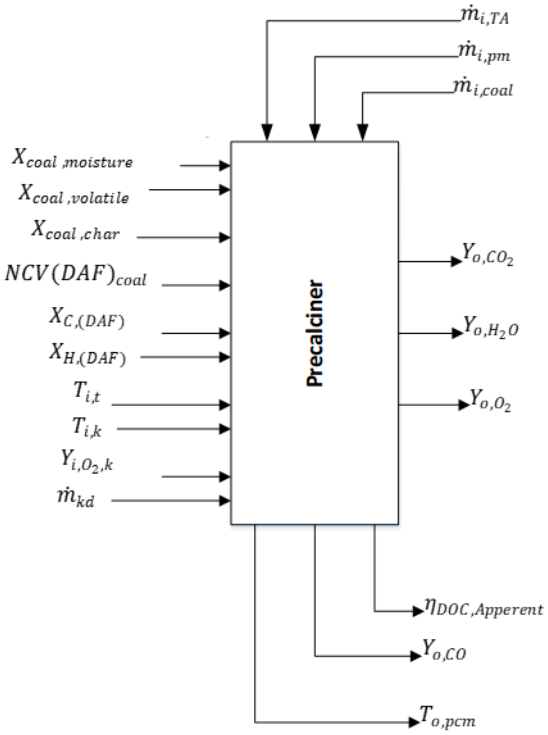

Figure 2. Input, performance and intermediate variables for a precalciner system

.

.

1.2 A modelling approach to assessing the performance of the precalciner

Several researchers have attempted to develop relationships between variables in precalciner process using the soft and hard modelling approach. Coupling, time-varying delay, and nonlinearity of precalciner system make it hard to establish an exact mathematical model to realize performance indicators such as ADOC. Mass and energy balance (MEB) provides a fundamental approach to derive correlation to determine a required process output. Authors in this study have experience in employing MEB to model precalciner. When there are input parameters which are unknown or cannot be measured directly, an iterative procedure is used during the MEB calculation. An example of an alternative approach to MEB is machine learning methods where this iterative process can be skipped.

Machine learning (ML) has shown promising results in modelling complex and nonlinear manufacturing processes that deal with noisy, limited and non-integrated data. Machine learning algorithms such as Support Vector Machine (SVM) and Artificial Neural Network (ANN) have proven their capabilities in this regard. (Gang and Hui, 2010) developed a model by using Least Squares Support Vector Machine (LS-SVM) with radial basis function (RBF) kernel for determining the apparent degree of calcination. The furnace temperature and pressure, the outlet temperature and pressure of the calciner, the temperature of the tertiary air and the lay-off quantity of cement raw were used as inputs to the model. (Griparis et al., 2000) proposed, adaptive, robust and fuzzy control to achieve the desired degree of precalcination of the raw meal, low carbon monoxide, while stabilising the precalcination process considering the multivariable dependencies in the precalciner system. (Yang et al., 2010) developed a back-propagation neural network (BPNN) and Radial basis function neural network (RBFNN) to assess the kiln temperature and oxygen content based on five variables which are coal flow to the kiln, coal flow to the precalciner, raw meal flow, rotary speed of kiln and negative pressure of the preheater exit.

The performance of the machine learning algorithms depends highly on the quality of input data. Therefore, collection and preparation of training dataset is an important step in the modelling process. Training data can be provided in three ways; 1) simulated data 2) actual process data and 3) designed experiment data. Simulated data is generated by theoretical models such as statistical models and computer simulations. Actual process data are randomly selected raw process data and many manufacturing companies have historical data in their database. Designed experimental data can be obtained using a Taguchi or Design of Experiment (DOE) approach. Among these three approaches, training and optimizing a model using a large number of less expensive simulation data and testing the model with a smaller dataset of process data is a cost-effective approach.

This feasibility study aims to provide an alternative approach to conventional mass and energy balance to model precalciner in a cement manufacturing process. Simulated data from MEB calculations were used to train, validate, and test different machine learning models to predict apparent calcination degree, molar fraction of water and CO_2 (dry basis) in precalciner output. They were assessed based on known values of fifteen input variables.

2 Materials and methods

2.1 Input and output data

The first phase of modelling work in this study was selecting input and output variables for models. These variables are listed in Table 2, including their maximum, minimum, mean and standard deviations. The dataset included 20543 samples. The full-factorial design approach, a famous experiment design, was used to generate the synthetic input data matrix. These data were used to obtain the output data matrix by applying mass and energy balance to the precalciner. The system boundary of the model is shown in Figure 1.

2.2 Methodology

Table 1. List of regression algorithms used to train models

Regression Model category	Regression model type
Linear regression model	1). Classical linear 2). Interaction linear 3). Robust linear 4). Stepwise linear
Regression trees	1). Fine Tree 2). Medium tree 3). Coarse Tree
Support vector machines (SVM)	1). Linear SVM 2). Quadratic SVM 3). Cubic SVM 4). Fine Gaussian SVM 5). Medium Gaussian SVM 6). Coarse Gaussian SVM
Gaussian Process Regression	1). Rational quadratic 2). Squared exponential 3). Matern 4). Exponential
Ensemble of Regression Trees	1). Boosted tree 2). Bagged tree
Artificial neural netwrok	1). Levenberg-Marquardt back-propagation

All data were normalized before feeding to the models. Regression Learner App available in Matlab 2019

software was used for model development (Mathworks, 2021).

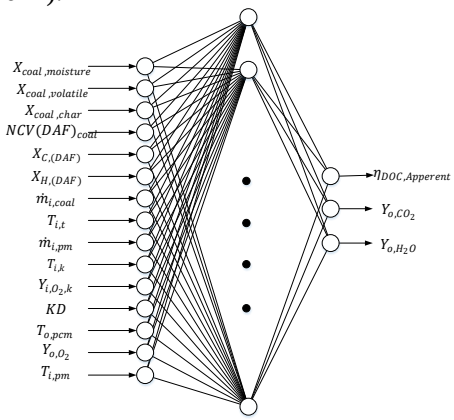

Figure 3. Model network architecture for ANN; The same inputs and outputs were also used for other regression models

Table 1 shows the list of algorithms that were used to train the dataset. These algorithms fall under six regression model categories as linear regression, SVM, regression tree, ensemble gaussian process regression (GPR) and ANN. There are different algorithm types (19 in total) under each of first five categories. The dataset was trained for all these algorithms. For ANN, the data was trained with Levenberg-Marquardt back-propagation algorithm with 20 neurons and one hidden layer. Selection of number of neurons and hidden layers for the ANN model was an arbitrary option. Figure 3 illustrates the ANN network architecture representing inputs and outputs.

Three statistical indicators were used for evaluation of the model performance, which include mean absolute error (MAE), root mean squares error (RMSE) and coefficient of determination (R^2). They were calculated as shown in Equation 1 to 3.

$$MAE = \sum_{i=1}^{m} \frac{(y_i - \hat{y}_i)}{m} \quad (1)$$

$$RMSE = \sqrt{\frac{1}{m}\sum_{i=1}^{m}(y_i - \hat{y}_i)^2} \quad (2)$$

$$R^2 = 1 - \left(\frac{\sum_{i=1}^{m}(y_i - \hat{y}_i)^2}{\sum_{i=1}^{m}(y_i - \bar{y})^2}\right) \quad (3)$$

Here $\hat{y}_i$ is the estimated value by the model, y_i is the actual value of the response process (MEB based simulation data), and m is the number of samples in the dataset.

.

Table 2. Description of input and output variables to the precalciner model

No:	Input/output name	Symbol	Variable type	Unit	Minimum	Maximum	Mean	Standard deviation
1	Moisture content of the fuel	$X_{coal,\ moisture}$	Input	%	0.87	2.27	1.38	0.61
2	Volatile content of the fuel	$X_{coal,\ volatile}$	Input	%	16.17	31.79	24.47	7.15
3	Char content of the fuel	$X_{coal,\ char}$	Input	%	18.84	47.43	34.52	13.40
4	*NCV of coal	$NCV\ (DAF^{\dagger})_{\ coal}$	Input	J/kg	31.47	34.63	33.27	1.34
5	The carbon content of coal (†DAF basis)	$X_{C,\ (DAF)}$	Input	%	86.48	93.47	89.98	3.05
6	Hydorgen content of coal (†DAF basis)	$X_{H,\ (DAF)}$	Input	%	3.93	5.19	4.62	0.59
7	Coal mass flow rate	$\dot{m}_{i,coal}$	Input	kg/s	2.67	3.61	3.07	0.38
8	Tertiary air temperature	$T_{i,t}$	Input	K	742.70	908	821.67	67.32
9	Pre-heated meal mass flow rate	$\dot{m}_{i,pm}$	Input	kg/s	52.37	66	60.14	5.49
10	Pre-heated meal temperature	$T_{i,pm}$	Input	K	950	989	968.92	19.54
11	Kiln gas temperature	$T_{i,k}$	Input	K	1215	1250	1232.10	17.50
12	Kiln gas O_2 molar fraction	$Y_{O2,\ k}$	Input	-	0.04	0.10	0.07	0.03
13	Kiln dust %	$\dot{m}_{kd}$	Input	%	4.00	54.00	28.59	15.95
14	Pre-calcined meal temperature	$T_{o,pcm}$	Input	K	1055	1117	1090.04	30.74
15	O_2 molar fraction of outlet of precalciner	$Y_{o,O2}$	Input	-	0.03	0.05	0.04	0.01
1	Apparent degree of calcination	ADOC= $\eta_{DOC,Apparent}$	Output	%	19.06	100	73.29	17.47
2	CO_2 molar fraction at precalciner outlet	$Y_{o,CO2}$	Output	-	0.19	0.32	0.26	0.02
3	H_2O molar fraction at precalciner outlet	$Y_{o,H2O}$	Output	-	0.05	0.06	0.05	0.003

3 Results and Discussion

As mentioned earlier in Table 1, there were 5 regression model categories which were trained from the dataset. For each category, the model which gave the minimum RMSE was selected to predict the three output variables of apparent calcination degree, CO_2 molar fraction and H_2O molar fraction. The summary of their statistical performance is shown in Table 3. It also shows the ANN model results. In addition, it also shows the *linear regression – classical* model result to give an understanding how the classical linear regression method deviates to other methods.

For predicting the apparent calcination degree, ANN gives the best results while GPR - rational quadratic method also shows successful results. Both Ensemble Bagged Tree and classical linear regression method show poor prediction results. ANN model also showed best performance for building relationship with inputs and CO_2 molar fraction and H_2O molar fraction. Linear regression – stepwise algorithm was also successful for all the three outputs, but it demanded a considerable computational time compared to SVM and regression trees. SVM-medium gaussian and regression tree – fine, gave the third best results for CO_2 molar fraction prediction and H_2O molar fraction prediction respectively. Training by Gaussian process regression algorithms were stopped due to high computational time for the CO_2 and H_2O models.

Figures 4 and 5 illustrate the prediction results for two different models. Figure 4 shows the performance by the ANN model compared to the MEB-based simulated data. ANN model predictions show a fit with R^2=1, and due to the large number of samples tested, data scattering along the 1:1 line is not visible. Therefore, a small section of the x and y-axis was magnified to show the data swarm around the fitting curve. Results show that the ANN model can effectively formulate the relationship between these 15 parameters to the three output properties selected in this study. Figure 5 shows the comparison of *linear regression-classical* model compared to its MEB-simulated data. It shows the least performance compared to other algorithms for this dataset.

Table 3. Statistical details of the model performance

Parameter	Model name	RMSE	R^2	MAE	Training time (sec)
Calcination degree	Linear regression – classical	3.224	0.97	2.5753	6
	Linear regression - stepwise	0.72151	1	0.57324	924
	Tree - Fine	1.9622	0.99	1.6375	8.5
	SVM - quadratic	0.91321	1	0.76053	15
	Ensemble – Bagged tree	2.4634	0.98	1.9776	36
	GPR – rational quadratic	0.03759	1.00	0.02804	1033
	ANN	0.019552493	1	-	-
CO_2 molar fraction (dry basis)	Linear regression - classical	3.3337×10^{-3}	0.98	2.5965×10^{-3}	7
	Linear regression - stepwise	0.4666×10^{-3}	1	0.3633×10^{-3}	1314
	Tree - Fine	1.4738×10^{-3}	1	1.201×10^{-3}	10
	SVM - medium gaussian	1.101×10^{-3}	1	0.898×10^{-3}	16
	Ensemble – Bagged tree	3.12×10^{-3}	0.98	2.471×10^{-3}	24
	GPR	Model training was stopped due to higher computation time			
	ANN	0.04157×10^{-3}	1	-	
H_2O molar fraction	Linear regression - classical	3.476×10^{-4}	0.98	2.085×10^{-4}	3
	Linear regression - stepwise	0.711×10^{-4}	1	0.5873×10^{-4}	1218
	Tree - Fine	1.4129×10^{-4}	1	1.15×10^{-4}	5
	SVM - quadratic	1.6035×10^{-4}	1	1.378×10^{-4}	6
	Ensemble – Boosted tree	3.647×10^{-4}	0.98	2.8007×10^{-4}	12
	GPR	Model training was stopped due to higher computation time			
	ANN	5.97419×10^{-5}	0.99975	-	-

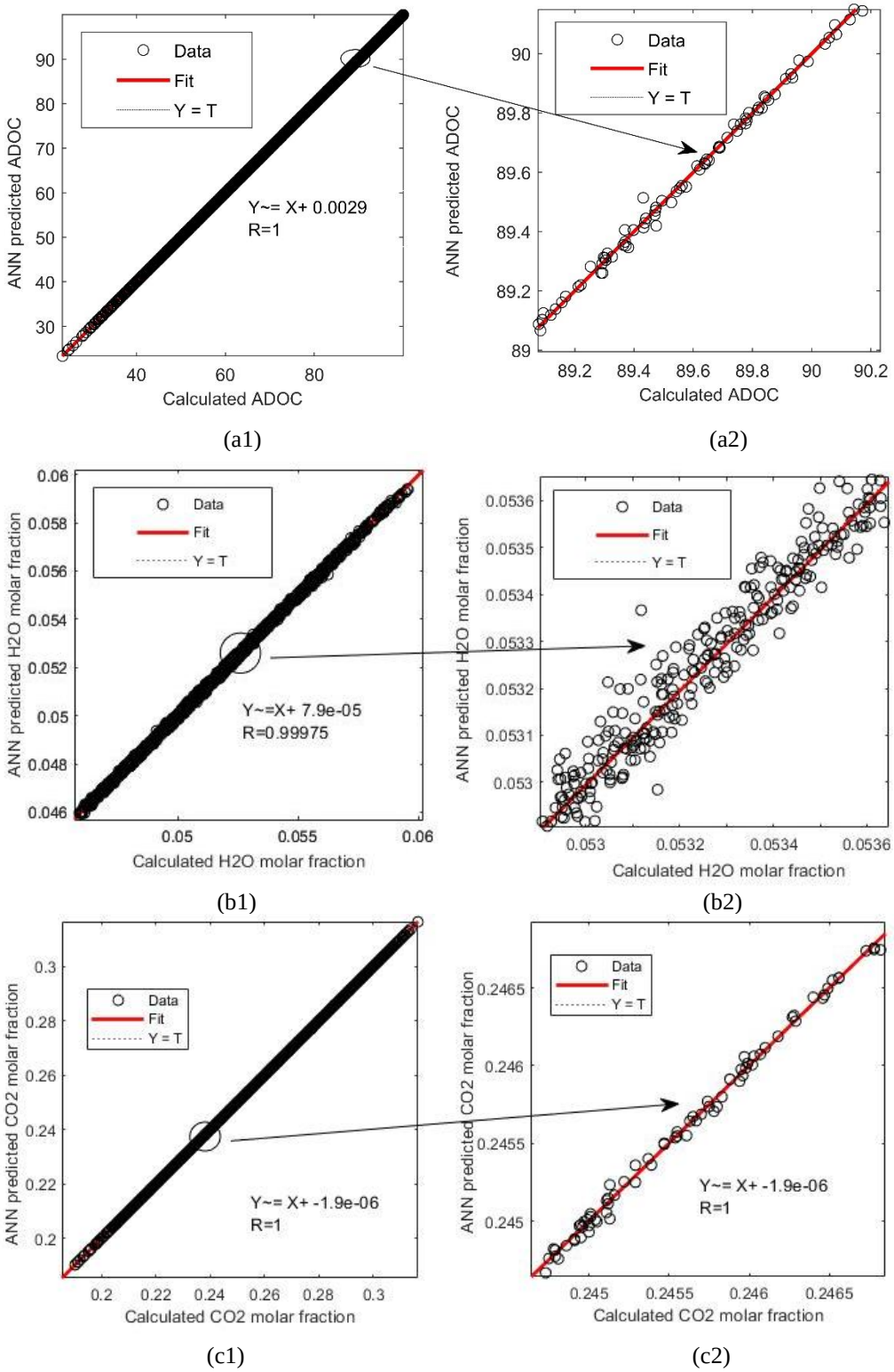

Figure 4. Performance by ANN model. Figure shows the comparison between the calculated data (MEB – based simulataed data) and predicted data (by ANN model); (a1). ADOC; (b1) H_2O molar fraction; (c1). CO_2 molar fraction; a2, b2, and c2 plots are magnified sections from their corresponding left sided plots

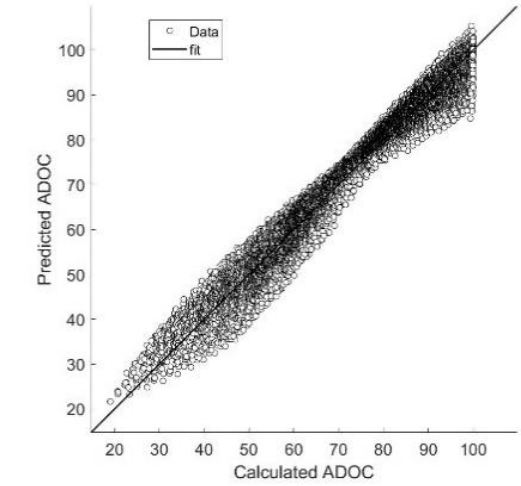

(a)

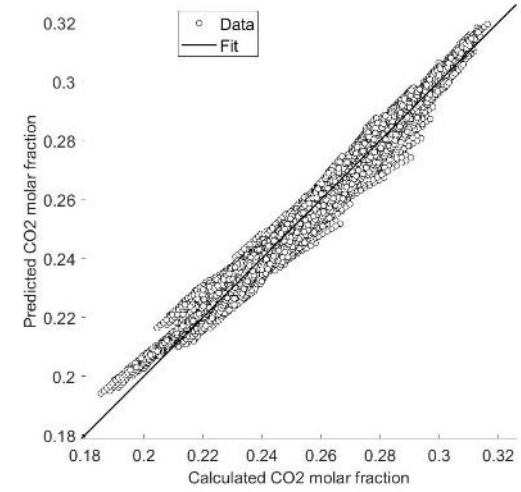

(b)

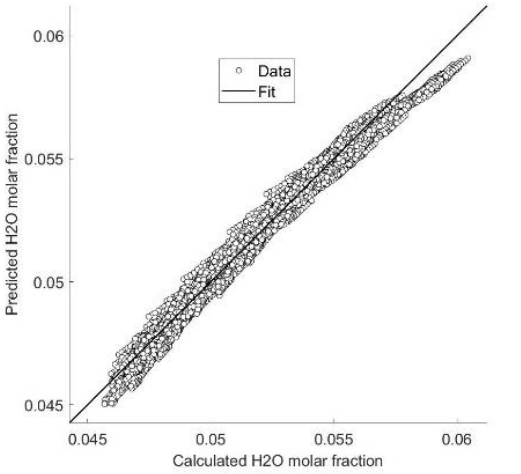

(c)

Figure 5. Performance by classical linear regression model. Figure shows the comparison between the calculated data (MEB – based simulataed data) and predicted data (by classical linear regression model); (a). ADOC; (b) H_2O molar fraction and (c). CO_2 molar fraction

There are both advantages and disadvantages between different machine learning algorithms. Their performance also heavily depends on the type of data. The theory behind these algorithms are not mentioned in this paper and can be found in literature such as in (Shwartz and David, 2014). In general, it is said that SVM and regression trees have fast prediction and training speeds, but they are suitable for handling minor problems and prone to overfitting (Bonaccorso, 2017). Ensemble gives high accuracy and performance for small and medium-size datasets, but tuning is required. Gaussian process is an effective algorithm for both regression and classification. A Gaussian process is a probability distribution over possible functions, and can deal effectively with data uncertainty (Irwin, 1997). The most critical drawback of GP regression is higher computation time. In this study, using GPR algorithm were terminated for H_2O and CO_2 molar fraction prediction. The advantage of modelling by ANN is that the model can be established directly with the input and output data of the application when there is less prior knowledge of the application. It is suitable for the highly nonlinear and uncertain system. ANN model has better online correction capability (Abiodun, Jantan et al., 2018). But it uses a large memory, and training speed can be slow. However, the choices of the quantity and quality of training data, learning algorithm, and topology and type of the network are all critical to the performance of a soft sensor model.

The data used to train the models in this study are simulated data. Some data points used in model development may not be practical in plant operation. The process data generated from real-time plant operation is a mixture of noise from raw materials, energy inputs, equipment, system running state, and time-varying chemical and physical parameters of raw materials and products. Therefore, if the real process data can train the models mentioned in this study, it will be an excellent opportunity to assess the results of this feasibility study. Plant operators can use such models tuned for a prolonged period to reduce downtime and take decisions before the results of offline lab samples arrive. Since plant data always include noise and undefined variations, the way they fit to the models might be different than reported in this study. Therefore it is always recommended to tune the model with a number of plant data before the models are used directly for practical applications.

4 Conclusion and Recommendation

This work describes a regression attempt to determine the apparent degree of calcination, CO_2 molar fraction and H_2O molar fraction in a cement precalciner system by formulating relationships between several input variables. Different types of machine learning algorithms were tested to test their suitability to build relationships with the input data and output data. Since

this is a feasibility study, synthetic data were used to train the models. These data were obtained from applying mass and energy balance. Results show that a number of machine learning algorithms show good performance with respect to the classical linear regression method. Several factors affect the calcination process in the precalciner and adding their contribution as model inputs to tune the developed models are recommended to increase the model robustness. In addition, it will also provide clues whether sampling frequency should be increased or not for experimentally measured parameters used to calculate the precalciner performance.

In particular, training a model using synthetic data can be viewed as a learning process. The advantage of using synthetic data from such theoretical models is that the number of data points can be increased to decrease the error inexpensively. The results can be viewed as a guide for a proposal distribution generator for approximate inference and can be used to draw a formal connection between inputs to optimize network parameters. As the second step of this study, testing the models by selected process data that represent extreme and typical plant operation conditions is recommended. This will lead to develop more realistic models based on the actual plant data. The system boundary used for the model was the precalciner system. However, the model can be more meaningful if the system boundary can be expanded to cover the entire pyroprocessing unit.

Acknowledgements

Financial support from University of South-Eastern Norway, Telemark Fylkeskommune and the Norwegian Research Council is greatly acknowledged.

References

O. I. Abiodun, A. Jantan, A. E. Omolara, K. V. Dada, N. A. Mohamed, and H. Arshad. State-of-the-art in artificial neural network applications: A survey. *Heliyon*, *4*(11), e00938-e00938, 2018. doi:10.1016/j.heliyon.2018.e00938

G. Bonaccorso. *Machine Learning Algorithms*: Packt Publishing Ltd., 2017.

IKN GmbH. CO2 capture from cement production; D 8.1 Status Report on Calciner Technology Revision 2, 2016.

Y. Z. Gang, and L. Hui. *S*oft sensor for apparent degree of calcination in NSP cement production line. Paper presented at the 2nd *International Conference on Computer and Automation Engineering (ICCAE)*, 2010

M. K. Griparis, F. N. Koumboulis, N. S. Machos, and I. Marinos. Precalcination in cement plants (system description and control trends). *IFAC Proceedings* Volumes, *33*(20), 273-278. 2000. doi:10.1016/S1474-6670(17)38062-X

IEA. CO2 capture in the cement industry; Technical Study Report number 2008/3. 2018.

J. D. Irwin *The Industrial Electronics Handbook (The Electrical Engineering Handbook Series)*| CRC Press, 1997.

Mathworks. Regression Learner. Retrieved from https://www.mathworks.com/help/stats/regressionlearner-app.html, 2021.

H. Mikulčić, E. von Berg, M. Vujanović, P. Priesching, L. Perković, R. Tatschl, and N. Duić. Numerical modelling of calcination reaction mechanism for cement production. *Chemical Engineering Science*, 69(1), 607-615. 2012. doi:10.1016/j.ces.2011.11.024

N. Mohammadhadi. *Multi-phase flow and fuel conversion in cement calciner*. PhD thesis. Kgs. Lyngby: Technical University of Denmark (DTU), 2018.

J. Osmic, E. Omerdic, E. Imsirovic, T. Smajlovic, and E. Omerdic. Identification and Control of Precalciner in the Cement Plant. In: J.A.Gonçalves, M.Braz-César, and J.P.Coelho (eds) *CONTROLO 2020*. Lecture Notes in Electrical Engineering, vol 695. 2020. Springer, Cham. doi: 10.1007/978-3-030-58653-9_12

S. S.-Shwartz and S. B.-David. *Understanding Machine Learning: From Theory To Algorithms*: Cambridge University Press. 2014.

L.-A. Tokheim. *The impact of staged combustion on the operation of a precalciner cement kiln*. PhD thesis. NTNU, 1999.

WWFI. A blueprint for a climate friendly cement industry; How to Turn Around the Trend of Cement Related Emissions in the Developing World. 2008.

B. Yang, H. Lu, and L. Chen. BPNN and RBFNN based modeling analysis and comparison for cement calcination process. Paper presented at the *Third International Workshop on Advanced Computational Intelligence*, 2010.

On solving fault detection problem and risk estimation monitoring with deep neural networks and postprocessing

Ivan Ryzhikov[1] Mika Liukkonen[2] Ari Kettunen[2] Yrjö Hiltunen[1]

[1]Department of environmental and biological sciences, University of Eastern Finland, Finland,
{ivan.ryzhikov,yrjo.hiltunen}@uef.fi
[2]Sumitomo SHI FW Energia OY, Relanderinkatu 2, 78200, Varkaus, Finland
{mika.liukkonen, ari.kettunen}@shi-g.com

Abstract

In this study, we consider fault prediction problem and production process risk monitoring based on observational data. We consider case, when there are no variables, by which one could classify the situation preceding to the fault. We propose an approach that is based on a specific auxiliary risk variable and modifications of the modeling accuracy estimation criterion, so the fault detection problem is reduced to supervised learning problem. We use deep learning and examine different model architectures. Trained model produces the risk estimations for new observations, then we use postprocessing to interpret the estimations to decision-maker. This work confirms that data-driven risk estimation can be integrated into digital services to successfully manage plant operational changes and support plant prescriptive maintenance. This was demonstrated with data from a commercial circulating fluidized bed firing various biomass and residues but is generally applicable to other production plants.

Keywords: deep learning, fault detection, risk estimation, postprocessing

1 Introduction

In this paper we consider a real-world problem concentrating on boiler fault prediction in biomass-fired circulating fluidized bed (CFB) power plants. These plants are extremely important and have not only the financial benefits, but also benefits for the environment as they can be used to replace fossil-fuel -based power generation. Plants of this type can utilize challenging fuels such as biomass or waste residues efficiently, but the drawback is that these types of fuel may often cause different problems such as blockages in the material flow. Especially this concerns biomass fractions that include large amounts of alkali metals. Although the consequences of the blockages are serious, we still cannot measure the quality of the fuel accurately and need to control the process using the observational data coming from different other sensors. At the same time rapidly evolving energy market sets challenges to traditional combustion-based power plants as it demands efficiency and flexibility in terms of fuel and load range. For example, the share of biomass as an energy source has increased significantly during recent years and it is expected to keep on increasing. In this study we propose and apply an approach to find patterns in a system state that takes place priorly to the fault.

The fault prediction problem and state monitoring problem appear in many different industries. This problem is serious because faults bring damage to production process and causes loss of profit. Faults can cause production blockage or disfunction and companies require resources to stabilize the process. In (Paltrinieri and Khan, 2016) the importance of risk assessment is considered for chemical industries. In energy sector faults consequences are serious too: any unexpected load limitation or shutdown of a power unit can cause considerable economical losses. Usually, the cost of undoing the damage is much higher than the cost of preventing the fault and that is why it is important to monitor and analyze the system state. The production system state analysis can predict if the process is in risky state and we need to act to lessen the risk.

Production processes are complex so many of those does not have adequate mathematical models based on physics or chemistry. But if even we had a mathematical model, there is still high level of uncertainty: we cannot measure all the inputs and all the system states. Once we met uncertainty, we use data to fight it. This leads us to hypothesis of using the data and data-driven modeling to solve fault prediction problem.

But how do we know that some of the system states causes faults? In general, there are no state variables indicating that situation is getting risky. Even process experts cannot name the conditions by which we could determine the pre-fault state. Anyway, if there are such variables, the approach we consider in this study can be applied too. Commonly, these conditions could be complex, and first we need to recognize those. When we can identify the system state with some value representing how close it is to pre-fault condition, and this is where we use mathematical model. In this case mathematical model is a mapping that reflects the observations to indicative values that shows if the system is risky and earlier it led to one of the fault cases. The next step would be transforming the indicative

value to decision. This next step is based on another mathematical model, which we call a post-processing unit, that helps production expert to categorize the situation.

To sum up, we propose ap approach that is based on recognition of patterns in data that led to failure in the past and help production experts in decision-making by mapping state evaluation to clear and succinct labels. Of course, similar patterns can be met also in common functioning, so it is important part of the approach to deal with interpretation contradictions. But adjustment of proposed decision-making support system needs to involve economical effect calculation. We can make system more sensitive and increase the number of times, when the system indicates, that the current situation is risky, so the production expert needs to act. Or we can make it less sensitive and focus only on patterns that proved their statistical relation to fault. System sensitivity is the question that can be solved with business only and by measuring the economic effect.

Proposed approach helps analyzing the patterns leading to the faults and revealing if similar conditions caused the fault in different cases.

In this study we reduced the fault prediction problem to regression problem, where we use observational data to train the model utilizing machine learning techniques. We adjusted the modeling criterion to fit the problem and applied a specific mapping to the modeling results to interpret the model predictions so the model and its postprocessing unit can work online to solve the risk monitoring problem.

2 Risk Estimation and Fault Prediction

Statistical modeling is applicable to solve various application problems (Kuhn and Johnsson, 2016) and computational resources today allow solving complex modeling problems. We can apply deep neural networks, train them on large datasets and produce a value for the production. Deep learning algorithms proved their efficiency in solving complex modeling problems (Chollet and Allaire, 2018) and (Goodfellow et al., 2016). Digital transformation or Industry 4.0 has high demand in statistical models and modeling methods (Brink et al., 2016) since many of models are data-driven or learning from the data.

In many different studies machine learning algorithms were applied to solve the fault prediction problem, but considered approaches are applicable to specific domain or when there is known variable, by which one can measure how safe is the process. For example, in (Paltrinieri et al., 2019) the machine learning based approach is considered as a promising tool of solving risk estimation problems, but in their study was a variable that represents the risk level. But the process we study does not have such variables. If we could label the system states data, we could apply the approach considered in study (Bondyra et al., 2018). But we have thousands of observations and no information on how we can estimate the degree of risk for each system state.

Approach based on labeled data is also presented in study (Rackshani et al., 2009), where authors consider the fault prediction problem for a power plant boiler and solved it by means of deep neural network. In their study the risk variable was constructed based on the fact of immediate faults and 8-hours operating cycle. This approach is difficult to be applied if there are only a few fault cases in dataset. It also makes it difficult to use this model to make just in time decisions, since the model is trained on aggregated data. It is also hard to detect if the reason for the fault was observed earlier than the working cycle interval. Approach without data aggregation was considered in the study (Hujanen, 2019), where the problem was reduced to the classification problem with 3 classes and deep neural networks were trained.

In this study we propose an approach that is based on recognizing of specific patterns in data, that caused the system fault in the past. We construct the auxiliary risk variable that indicates how dangerous is the current state. We assume that risk starts to grow some time before the fault and all the other time it is low. This risk interpretation is a simplification of the risk definition done by (Kaplan and Garrick, 1981), and we are not estimating the consequences and probabilities.

Having risk variable makes it possible to reduce the fault detection problem to supervised learning problem. But there is uncertainty of the actual risk value for the observations that do not belong to the prior to the fault interval. In following paragraphs, we consider the risk variable construction, the adjustment of criterion and the postprocessing of the modeling results.

2.1 Problem Reduction

The considered process state can be characterized by different inputs that correspond to the sensor data from the different parts of the boiler plant. Each of these inputs can be described as time series with fixed step size: $X = \{x_1, x_2, \dots, x_s\}, T = \{t_1, t_2, \dots, t_s\}$, where s is a sample size. We also know m times at which the fault happened: $t_i^f, i = \overline{1, m}$, so we assume that there had been some time before that, at which the risk began to grow.

2.1.1 Risk Variable Construction

This time before the fault is a parameter Δ of the proposed approach. We put forward a hypothesis, that there is no risk in any other timestamp, than timesteps before the fault limited by the parameter. We also assume that risk increases monotonically starting from zero, and it reaches its maximum value of one by the fault time, so the risk variable can be evaluated by the following function

$$r(t, t^f) = \begin{cases} \frac{t - t^f}{\Delta} + 1, t^f - \Delta \le t \le t^f, \\ 0, otherwise, \end{cases} \quad (1)$$

where t_f is the fault time and Δ is the parameter. Since there could be m different faults, the risk function for whole observation time can be evaluated as a sum of single fault functions (1):

$$r(t) = \sum_{i=1}^{m} r(t, t_i^f). \quad (2)$$

We assume that there is always a normal system state between the different faults, so it is possible to find such Δ that $\nexists i, j,\ t_i^f < t_j^f : t_j^f - t_i^f < \Delta$, so non-zero intervals of the risk functions are not overlapping. According to this approach, we need to find a relation between the system state variables and the risk feature. In this study we assume that the risk is increasing identically before any of the faults.

2.1.2 Criterion Adjustment

We need to split the data on train and test sets to estimate the adequacy of model and its generalization. Since we work with time series, which consists of several intervals corresponding to several faults, we consider two splitting schemes. First option is to leave the data for one of the faults for the test and to keep other faults data for the train. This would help us to understand which faults have similar (or different) patterns corresponding to the risk increase. Second option is to split the data on two subsets, one before some date as train and validation and second after that date as test. In that case we can see, how good is historical data in predicting the future faults. To provide validation we used stratification, so train and validation contain observations from a common process and observations from the interval before the fault.

As a modeling criterion we used the root mean square error

$$I(\tilde{r}) = \sqrt{\sum_{i=1}^{n} \left(r(t_i) - \tilde{r}(x_i)\right)^2}, \quad (3)$$

where n is a test or validation subset size, $r(t_i), i = \overline{1,n}$ are risks (2) at t_i timestamps and $\tilde{r}(x_i), i = \overline{1,n}$ are risk estimations at the same time points by the model. Since we cannot properly estimate the risk for the time, when no fault was detected and we cannot estimate the risk for time intervals right after the fault, we suggested to use specific weights for these errors in the sum (3):

$$I_w(\tilde{r}) = \sqrt{\sum_{i=1}^{n} w(t_i) \cdot \left(r(t_i) - \tilde{r}(x_i)\right)^2}, \quad (4)$$

where $w(t)$ is a weighting function,

$$w(t) = \begin{cases} w_{after}, t \in T_{after}, \\ w_{normal}, t \in T_{normal}, \\ w_{risk}, t \in T_{risk}, \end{cases} \quad (5)$$

and T_{after} are the time intervals corresponding to states after the faults, T_{risk} are the time intervals before the faults and T_{normal} are the other intervals. Here w_{after}, w_{normal} and w_{risk} are weighing coefficients. These coefficients are used for increasing the influence of errors caused at the points, when the risk was growing and decrease the influence of errors of risk estimation for the time intervals for which the risk value is uncertain.

2.1.3 Supervised Learning Problem

The goal of our risk modelling approach is to estimate the risk of the current system state and to observe its dynamics for decision making. It means that we need to have model with optimal parameters α^*, which is adequate in risk estimation and thus minimizing the criterion (4):

$$a^* = \underset{\alpha}{\operatorname{argmin}}\, I_w\left(\tilde{r}(x|\alpha)\right), \quad (6)$$

where $\tilde{r}(x|\alpha)$ is the model prediction in case of its parameters α, and

$$r^*(x) = \tilde{r}(x|a^*), \quad (7)$$

is the best model by criterion (5) for the data we have. The fault prediction problem is reduced to minimization problem (4), where we use specific weight coefficients (5). The solution of reduced problem is optimal model parameters (6), that we use to estimate a risk by system state variables. Now the risk estimation (7) can be used for fault prediction and decision making, but in this study, we consider interpreting risk estimations for decision making in production control.

2.2 Postprocessing

As a result of learning process, we have a model (7), which takes the system state as an input and returns risk prediction as an output. But we cannot use the risk prediction value to make decisions, because the single number cannot be interpreted. To solve the interpretation problem, we need another computational module, which takes the risk predictions and classifies the current situation.

Let $\tilde{r}_t, \tilde{r}_{t-1}, \dots, \tilde{r}_{t-m}$ be the latest m predictions of the model (7) and the postprocessing function is

$$P(\cdot): R^m \to R, \quad P(\tilde{r}_t, \tilde{r}_{t-1}, \dots, \tilde{r}_{t-m}) = l_t, \quad (8)$$

where l_t is the postprocessed value or label that classifies the production process state.

In this study we used three different classes: “good”, “warning” and “dangerous”, so $\forall i, l_i \in \{\text{good}, \text{warning}, \text{dangerous}\}$. First label indicates that process is running regularly, second label requires attention to the production process and the third one indicates that the situation can lead to a fault. In general, one can use any other classes and labels.

We used postprocessing function, which is based on filtering the low values and summation of all the risk values:

$$v_t = \begin{cases} 0 \text{ if } \exists i < m: \tilde{r}_{t-i} > b, \\ \sum_{i=0}^{m} \tilde{r}_{t-i}, \text{otherwise,} \end{cases} \quad (9)$$

where v_t is an intermediate numeric value and b is filter parameter.

Now we use intermediate values (9) to classify the process state:

$$l_t = \begin{cases} \text{"good" if } v_t < q_1, \\ \text{"warning" if } q_1 \le v_t < q_2, \\ \text{"dangerous" if } v_t > q_2, \end{cases} \quad (10)$$

and $q_1 < q_2$ are classification parameters.

2.3 Approach Parameters

Proposed approach has parameters, which need to be tuned. The first group of parameters is related to time intervals: Δ and time after the fault. In general, each interval can be characterized by its own parameters, but it this study we assume that Δ and time after the fault are similar for all fault cases. Production expert opinion is useful in determining time after the fault.

Weights (5) that we use in criterion have strong influence on results. General recommendations are to make $w_{risk} > 10 \cdot w_{normal} > w_{after}$, so recognition of risk increase before the fault is more important than small risk value in case of regular production process. It is also useful to resolve the contradiction if the same pattern led to fault in one case and did not in the other.

Prost-processing parameters are window size m, filter value b, borders q_1 and q_2. These parameters need to be tuned with production and business experts, because of their relation to the decision-making process. Window size depends on dynamical character of the process and rate of observations. Filter value among with the labeling borders can be tuned on the basis of the training data by adjusting the sensitiveness of the postprocessing system.

3 Data-driven Risk Estimation and Monitoring

The production process we want to estimate risk for has many observation variables. Each variable is measured every 15 minutes. We explicitly selected the variables with help of production experts to avoid overfitting and to focus on the factors of the main interest. The dataset contains 50879 observations and has a gap in observations. In given observation time there were 8 faults, each could be caused by own reasons and we do not know that in advance.

In this study we manually tried different time delta parameters and finally used Δ= 2 hours. For that parameter and according to observation step size, we have only 192 observations that can be labelled as leading to the fault. One can see that the dataset is unbalanced: 50687 of "good" observations versus 192 of "leading to the fault" observations. For some production processes, it is typical that the faults occur uniquely, so there is imbalance between classes.

We also consider modeling when we include lags from the previous observations. In this paper we check the last 5 observations, which equals to 1.5-hour lookback. We will label these modes specifically.

The weighs (5) for criterion (4) are set as following: $w_{after} = w_{normal} = 1$, $w_{risk} = 10$. The weights were tuned manually and based on the modeling results feedback from the production experts. Weights (5) are important when adjusting the balance between fault sensitivity and the number of fail detections. In general, these characteristics should be tuned as a part of decision-making support system. It depends on resources company loses with any missed fail and resources company loses when act in case of alarming signal produced by the fault detection system.

We used the Keras framework (Allaire and Chollet, 2018) for modeling, and the application were implemented in R (R Core Team, 2018). We made a web application with R Shiny framework (Chang et al., 2021), that can be deployed to the company server. Since this application has access to the data needed it gives the results in visual form directly to the decision maker.

In this study we tried different deep neural network (DNN) architectures. Previously we tested that the proposed approach works for failure prediction problem solving (Ryzhikov et al., 2020) and now test if the efficiency changes with different DNN models. Each model layer has a dropout with 0.5 probability. When train model we use root mean square back propagation algorithm with a batch size of 5000 and 100 iterations.

For each model given in Table 1, we calculated the root mean square error (RMSE) on train and test data. As one can see, in Table 1 there are models, which include lagged variables. For those models we used lags for the previous 5 observations to check if including the historical data will improve the modeling results.

In this study we use specific learning data splitting: for each fault we produce training dataset, which contains all observations except ones that belong to an interval containing the fault, and test dataset, which is this interval. This splitting helps us to understand if one fault case can be predicted with model, which was trained on another fault cases.

When comparing model, we are interested in how these models predict on train data on intervals before the fault cases and all other intervals, and the same for test dataset. Intervals before fault and all other intervals for train data and for test data are given in Figures 1-4. Since dropout and initial coefficients are random, we provide boxplots of the RMSE and run each problem for 10 times.

Table 1. DNN architectures.

DNN	*Neurons by layer*	*With lag?*
1	64, 64, 64	no
2	64, 64, 64, 64	no
3	128, 64, 64	no
4	256, 64, 64	no
5	128, 64, 8, 64	no
6	64, 64, 64	yes
7	64, 64, 64, 64	yes
8	128, 64, 64	yes
9	256, 64, 64	yes
10	128, 64, 8, 64	yes

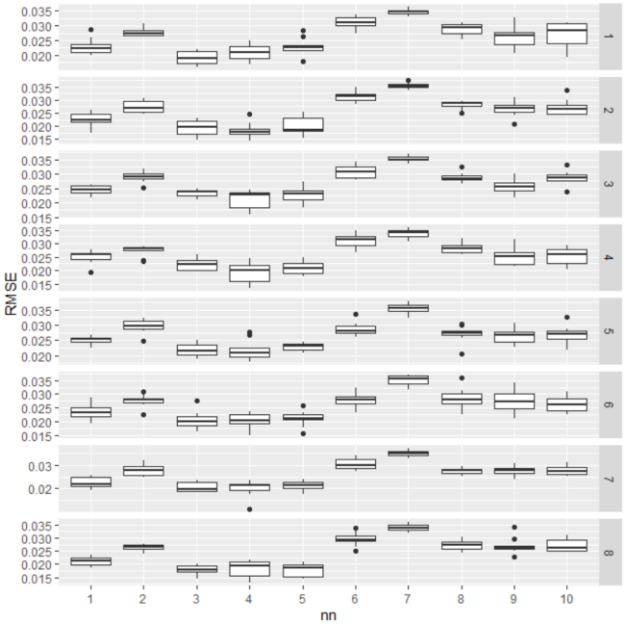

Figure 1. RMSE on train data, fault intervals, by model architecture on x axis and problem on y axis.

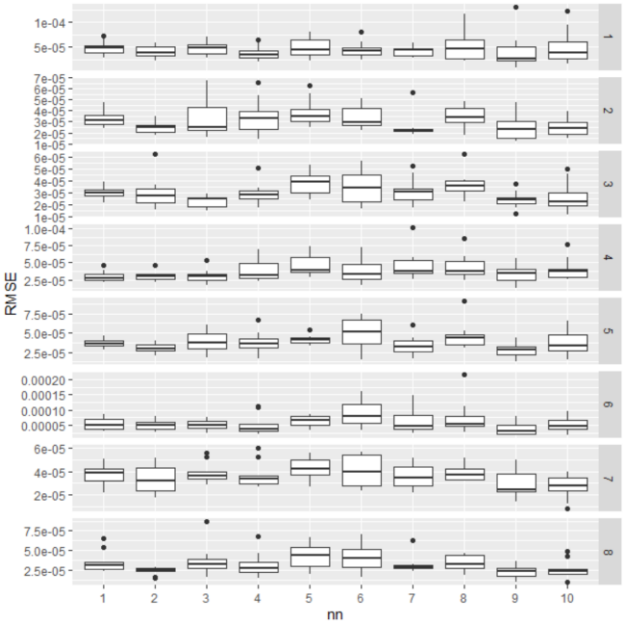

Figure 2. RMSE on train data, regular process intervals, by model architecture on x axis and problem on y axis.

As one can see, some of architectures outperform other architectures on pre-fault intervals risk estimation. Based on pre-fault intervals RMSE statistics we could assume that some of the models are preferable than others. When we look at RMSE statistics on regular process intervals, we can see that the variation of average results is not as big, as it is for fault intervals. Nevertheless, the most important part is prediction for data in test dataset.

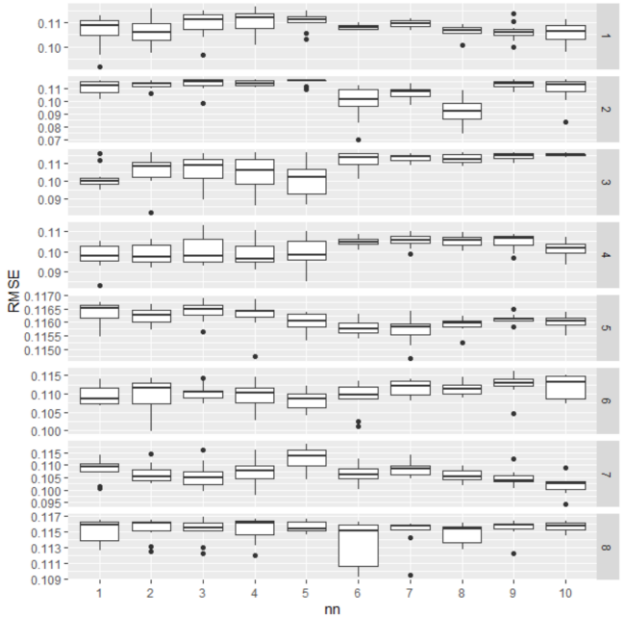

Figure 3. RMSE on test data, fault intervals, by model architecture on x axis and problem on y axis.

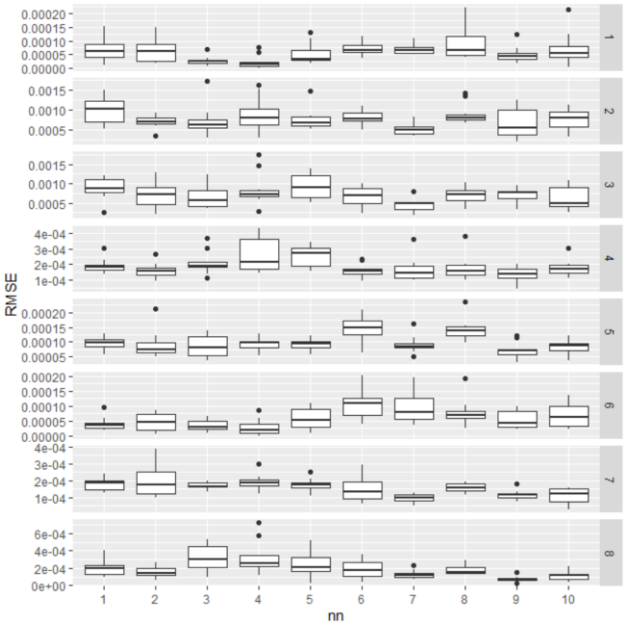

Figure 4. RMSE on test data, regular process intervals, by model architecture on x axis and problem on y axis.

When we compare model performance on test data, we can see some surprising results. For example, architecture 6, which was worse than 1-5 architectures, shows nearly the same or better mean values in 6 problems.

We need to have a closer look at model predictions on train in test data to understand the reason for that effects and why we cannot use RMSE to select the best model. First, our modeling approach assumes (1) and (2), that risk can be explained by the following function. But when we train the model, we are interested in having values greater than 0 in pre-fault intervals and values close to 0 in all other intervals. And models deliver that, but with different magnitude of values. Second, reasons for the faults and selected parameter for pre-fault interval could be different from one fault to another.

We demonstrate this effect in Figures 5-8. Figures 5 and 6 refer to DNN architecture 7, which outperforming statistic we observed above. We randomly selected one of the models from 10 runs for each architecture.

The subject of further research is another metric for comparing modeling results, that is based on ability to predict the fault in advance and

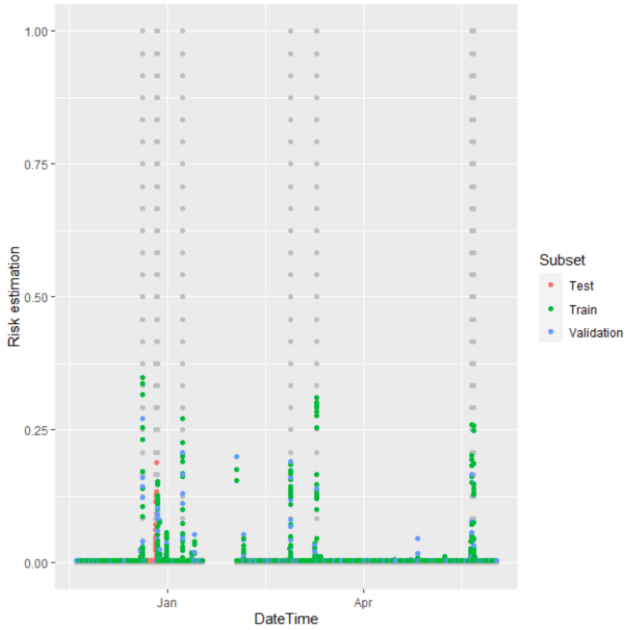

Figure 5. Risk estimation for all dataset, DNN architecture 7.

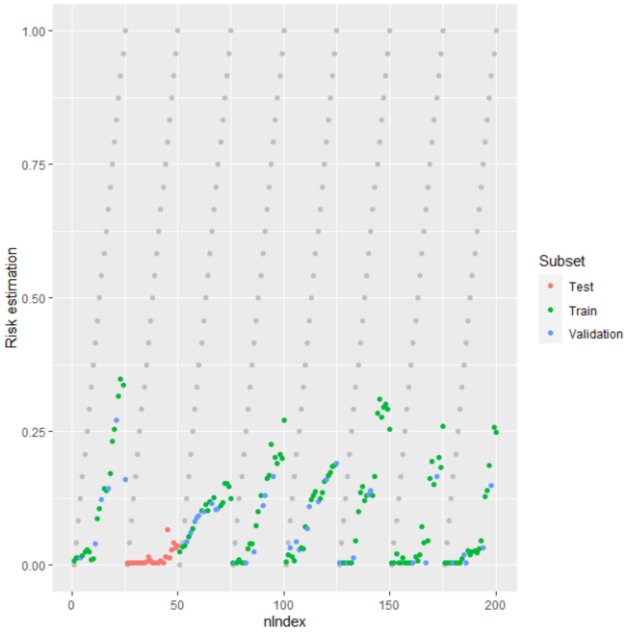

Figure 6. Risk estimation for pre-fault intervals only, DNN architecture 7.

According to plots on Figures 5 and 6, we can assume that model gives a good prediction on a training data, all other observations are near 0 and target interval shows some positive estimations of risk value. The maximum risk value is near 35. Let us compare these two plots with similar ones done for DNN with architecture 2.

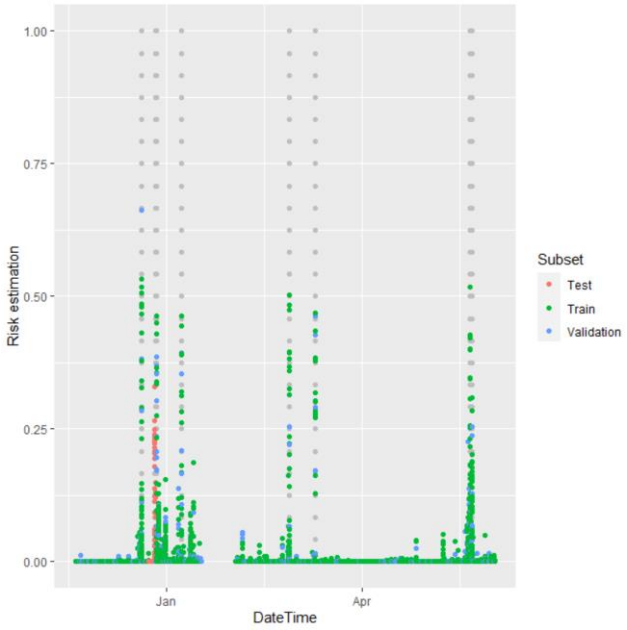

Figure 7. Risk estimation for all dataset, DNN architecture 2.

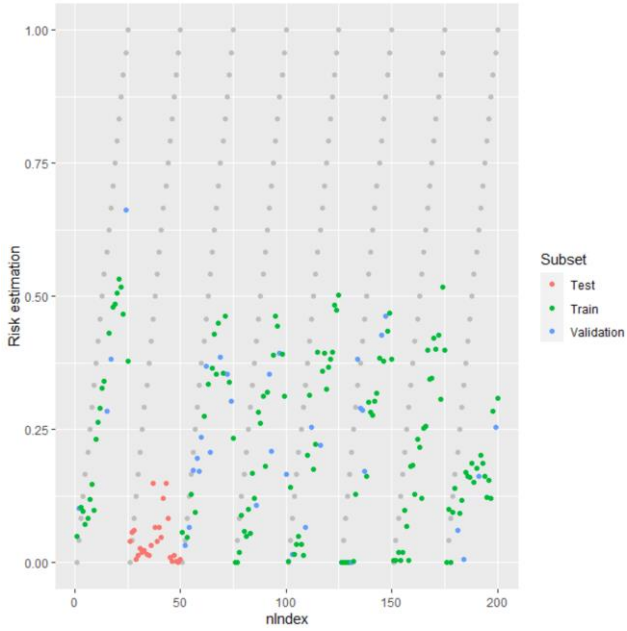

Figure 8. Risk estimation for all dataset, DNN architecture 2.

The prediction on all dataset looks like Figure 5, but fuzzier. The prediction of risk before the target fault is better, according to values, but all the other fault predictions have greater magnitude than ones in Figure 6. This proves our assumption that we need to design and use another criterion co compare different models and architectures, so we could produce them automatically.

In this study and solving real-world fault prediction and risk monitoring problem, we observed all the models manually, running tens and hundreds of model trainings to then choose several. Chosen model was taken as the basis for risk monitoring system. We used model predictions and (8)-(10) postprocessing approach. We adjusted the parameters of postprocessing manually, so these parameters detect the faults in advance.

Data loading, data preprocessing, modeling and postprocessing were implemented in web-application, implemented in R and R Shiny framework. In Figures 9-11 one can see the simulation where model receives new data, estimates risk and then postprocessor signals to application user interface that process is running fine, there is warning, and situation is dangerous. Interface shows also preselected number of previous risk estimations, so the decision-maker can see the situation dynamics.

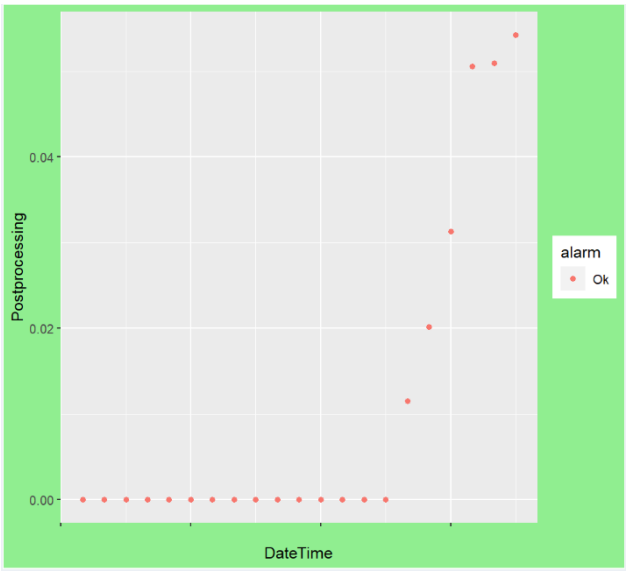

Figure 9. Risk monitoring, postprocessor receiving “Ok” state.

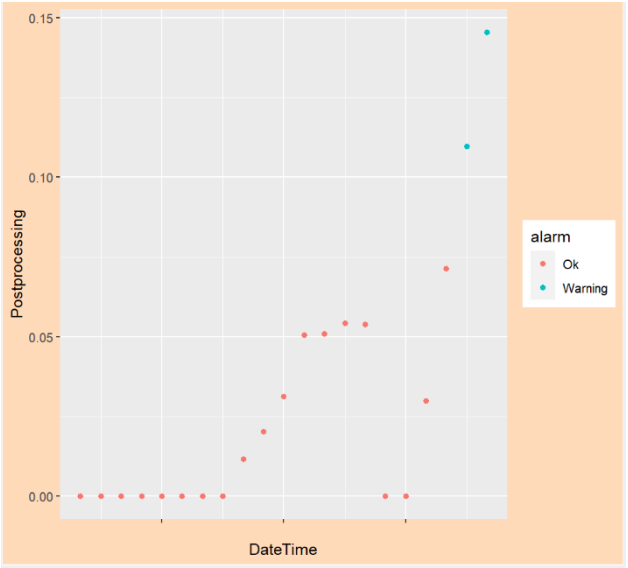

Figure 10. Risk monitoring, postprocessor receiving “Warning” state.

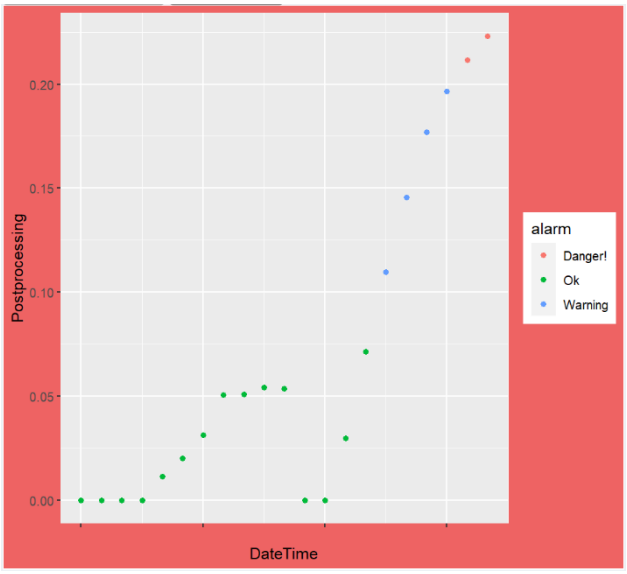

Figure 11. Risk monitoring, postprocessor receiving "Danger!" state.

4 Conclusion

In this study we examined proposed approach of risk estimation and fault detection. We applied postprocessing scheme that is based on filtering and risk summation, which makes possible to interpret the risk estimation model outputs and use this interpretation in decision-making.

Risk is constructed as auxiliary variable that monotonically increases in time interval prior to the fault. This variable makes possible revealing the patterns that possibly caused the faults even if these patterns were observed in different time before the fault and/or during the regular process. Once we apply leave one out testing and validation, we can estimate if the faults caused by similar system states. It is important to mention, that auxiliary risk variable helps us solving the fault detection problem, when there are no variables by which one could detect that there is something wrong with the production process and there is a fault risk.

Postprocessing of the model estimations makes it possible to interpret the results by once adjusting the mapping algorithm. As one can see, different models give risk estimations that differ in magnitude and sensitivity. By adjusting postprocessing we could suggest what is indication fits the production experts most: is one sensitive enough or accurate enough.

Further work is related with automatic model selection. We need to design criterion and searching algorithm that will compare models with different magnitudes of risk estimations and deal with uncertainty of different risk intervals.

We implemented the fault detection and risk estimation as web application with R, keras and R Shiny framework. This application can be deployed to the company network and work online, demonstrating the decision-maker the current estimation of risk.

Acknowledgements

This research is a part of the *AI-DA* projects, which is funded by Business Finland, European Regional Development Fund (ERDF), and seven companies.

References

J.J. Allaire and François Chollet. keras: R Interface to 'Keras'. R package. version 2.4.0., 2021. https://CRAN.R-project.org/package=keras

Henrik Brink, Joseph W. Richards, Mark Fetherolf. *Real-World Machine Learning*, Manning, 2016.

Adam Bondyra, Przemysław Gąsior, Stanislaw Gardecki and Andrej Kasiński. Development of the Sensory Network for the Vibration-based Fault Detection and Isolation in the Multirotor UAV Propulsion System. *In Proceedings of the 15th International Conference on Informatics in Control, Automation and Robotics*, 2: 112-119, 2018. DOI: 10.5220/0006846801120119

Winston Chang, Joe Cheng, JJ Allaire, Carson Sievert, Barret Schloerke, Yihui Xie, Jeff Allen, Jonathan McPherson, Alan Dipert and Barbara Borges, 2021. shiny: Web Application Framework for R. R package version 1.6.0. https://CRAN.R-project.org/package=shiny.

François Chollet, J.J. Allaire. *Deep Learning with R*. Manning. 2018.

Ian Goodfellow, Yoshua Bengio and Aaron Courville. *Deep Learning*. MIT Press. 2016

Jussi Hujanen. Machine Learning Methods for Early Process Deviation Detection in Circulating Fluidized Bed Boilers. *In Proceedings of Nordic Flame Days*, 2019.

Stanley Kaplan, B. John Garrick. On the quantitative definition of risk. Risk Analysis, 1(1): 11-27, 1981.

Max Kuhn, Kjell Johnson. *Applied predictive modeling*. Springer, 2016.

Nicola Paltrinieri, Louise Comfort, Genserik Reniers. Learning about risk: Machine learning for risk assessment. Safety science, *Elseiver*, 118: 475-486, 2019

Nicola Paltrinieri, Faisal I. Khan. *Dynamic Risk Analysis in the Chemical and Petroleum Industry, Dynamic Risk Analysis in the Chemical and Petroleum Industry: Evolution and Interaction with Parallel Disciplines in the Perspective of Industrial Application*. Butterworth-Heinemann. 2016. DOI:10.1016/B978-0-12-803765-2.01001-5.

R Core Team. R: A language and environment for statistical computing. R Foundation for Statistical Computing, Vienna, Austria. 2018. URL https://www.R-project.org

Elyas Rakhshani, Iman Sariri, Kumars Rouzbehi. Application of data mining on fault detection and prediction in Boiler of power plant using artificial neural network. *In proceedings of 2009 International Conference on Power Engineering, Energy and Electrical Drives*, pages 473-478, 2009. DOI: 10.1109/POWERENG.2009.4915186.

Ivan Ryzhikov, Mika Liukkonen, Ari Kettunen, Yrjö Hiltunen. Risk Estimation in Data-driven Fault Prediction

for a Biomass-fired Power Plant. *In Proceedings of the 12th International Joint Conference on Computational Intelligence*, pages 423-429, 2020. DOI: 10.5220/0010113104230429

ANN-Based Correlations for Excess Properties to Represent Density and Viscosity of Aqueous Monoethanol Amine (MEA) Mixtures.

Sumudu S. Karunarathne[1] Khim Chhantyal[2] Lars E. Øi[1]

[1]Department of Process, Energy and Environmental Technology, University of South-Eastern Norway, {sumudu.karunarathne,lars.oi}@usn.no

[2]Sekal, Norway, kc@sekal.com

Abstract

The applicability of Artificial Neural Networks (ANNs) to represent excess properties is discussed. The excess molar volume V^E and excess free energy of activation for viscous flow ΔG^{E*} were calculated from measured density and viscosity at different monoethanol amine (MEA) concentrations and temperatures. Different ANNs with multiple inputs and a single hidden layer were trained, validated and tested to represent V^E and ΔG^{E*}. Developed ANN models show good accuracies in data fitting by giving R^2 as 0.99 and 0.98 for V^E and ΔG^{E*} respectively for the test data. The calculated average absolute relative deviation (AARD) for V^E and ΔG^{E*} are 1.5 % and 1.2 % respectively for the test data that give better predictions for the density and viscosity using a Redlich and Kister polynomial for the regression. The density and viscosity models based on ANN for V^E and ΔG^{E*} give high accuracies, which is an advantage of many aspects in engineering applications.

Keywords: excess properties, ANN, density, viscosity

1 Introduction

Physical properties like density and viscosity of aqueous amine mixtures are useful in the design and simulation of amine-based post-combustion CO_2 capture processes. Density and viscosity appear in most of the correlations proposed to calculate mass transfer coefficients and interfacial area between liquid and gas phases. Various approaches have been proposed to develop correlations to represent measured density and viscosity for solvents such as pure, aqueous, and CO_2 loaded aqueous amine mixtures (Hartono et al. 2014; Weiland et al. 1998).

The applications of ANN (Artificial Neural Network) in post-combustion CO_2 capture radiates into various aspects of the field. Sipöcz et al. (2011) developed an ANN model for a CO_2 capture plant to evaluate the amount of CO_2 captures, specific duty and rich loading in the solvent through the inputs of temperature, flue gas flow rate, CO_2 mass fraction at the inlet flue gas, solvent lean loading, solvent circulation rate and removal efficiency. The ANN is one hidden-layer feed-forward network with a back-propagation learning algorithm. The ANN approach has been used to represent the physicochemical properties of amine solvents for post-combustion CO_2 capture. Hamzehie et al. (2014) discussed the prediction of CO_2 solubility in aqueous amine mixtures using ANN models with two hidden layers. The inputs for the network were established as in theoretical and semi-empirical models as temperature, CO_2 pressure, overall solute's concentration and type of solution (apparent molecular weight). The mass transfer coefficient was predicted through an ANN model by considering various input parameters gas and liquid flow rates, CO_2 partial pressure, liquid concentration, cyclic capacity and physical properties such as density viscosity and diffusion coefficient of CO_2 as illustrated by Fu et al. (2013). Several approaches were reported in literature that describe the implementation of ANN methodology to represent physical properties like density and viscosity of aqueous amine solvents (Pouryousefi et al. 2016; Haratipour et al. 2017; Garg et al. 2015). A previous study of Karunarathne et al. (2020(a)) examined the applicability of ANNs for the predictions of density and viscosity of CO_2 loaded alkanolamine + H_2O mixtures in which mole fractions of amines and CO_2 in the mixture and temperature were inputs for the model while density and viscosity were the outputs.

The excess properties like excess molar volume and excess free energy of activation for viscous flow can be fitted to empirical correlations to represent density and viscosity of liquid mixtures. This work presents ANN-based correlations for excess properties to represent the density and viscosity of aqueous monoethanol amine (MEA) mixtures. The accuracy of the ANN-based correlations was evaluated by comparing the predictions with measured data other empirical correlations.

2 Material and Method

2.1 Excess Properties

The excess properties for molar volume and viscosity can be calculated from measured densities and viscosities of pure and aqueous amine mixtures as shown in (1) and (2). It is possible to fit a Redlich and Kister type polynomial (Redlich and Kister 1948) as

given in (3) to represent excess molar volume and viscosity to develop correlations for the density and viscosity of aqueous amine mixtures (Han et al. 2012; Hartono et al. 2014; Karunarathne et al. 2020(b)).

$$V^E = V - \left(\sum_{i=1}^{i=2} x_i V_i \right) \quad (1)$$

$$\eta^E = \eta - \left(\sum_{i=1}^{i=2} x_i \eta_i \right) \quad (2)$$

$$Y^E = x_1 x_2 \left(\sum_{i=0}^{i=n} A_i (x_1 - x_2)^i \right) \quad (3)$$

where x_i is the mole fraction of the components in the mixture. V, V_i, and V^E are molar volume of the mixture, molar volume of the pure components and excess molar volume of the mixture respectively. η, η_i and η^E are viscosity of the mixture, viscosity of the pure components and excess viscosity of the mixture respectively. Y^E and A are excess property and coefficients respectively in the Redlich and Kister polynomial.

The excess molar volume of different aqueous MEA mixtures was calculated from measured densities as given in (4).

$$V^E = \frac{x_1 M_1 + x_2 M_2}{\rho} - \sum_{i=1}^{i=2} \frac{x_i M_i}{\rho_i} \quad (4)$$

where x_i ρ, ρ_i and M_i are mole fraction of the components in the mixture, density of the mixture, density of the pure components and molecular weights of the pure components. Subscript i = 1 for MEA and i = 2 for H_2O.

The excess molar volume V^E arises due to the intermolecular interactions between the molecules present in the mixture and size and shape of the molecules. Positive V^E reveals the presence of weak interactions or dispersion forces and negative V^E indicates the strong specific interactions between unlike molecules. Further, negative V^E also suggests that molecules are efficiently packed due to the size and shape differences among the constituent molecules (Mahajan and Mirgane 2013; Qi and Wang 2009; Letcher and Baxter 1989).

Eyring's viscosity model (5) provides a theoretical insight into the viscosity of liquid by describing the arise of fluid friction due to the molecular jump over a potential energy barrier (Bird et al. 2002; Eyring 1936). The free energy of activation for viscous flow ΔG^* can be calculated from measured density and viscosity data. Semi-empirical and empirical models can be proposed to fit the calculated ΔG^*. For a binary mixture, the excess free energy of activation for viscous flow ΔG^{E*} is described as given in (6). The sign of ΔG^{E*} reveals the nature of intermolecular interactions among the molecules in the mixture. The positive ΔG^{E*} indicates the presence of strong specific interactions between unlike molecules while negative ΔG^{E*} signifies weak intermolecular interactions like dispersion forces in the mixture (Meyer et al. 1971; Kinart et al. 2002; Ćwiklińska and Kinart 2011; Aminabhavi et al. 1994).

Eyring's viscosity model was adopted to calculate the excess free energy of activation for viscous flow as shown in (6) from measured dynamic viscosities and densities at different MEA mole fractions and temperatures.

$$\eta = \frac{hN_A}{V} exp\left(\frac{\Delta G^*}{RT}\right) \quad (5)$$

$$\frac{\Delta G^{E*}}{RT} = ln(\eta V) - \sum_{i=1}^{i=2} x_i ln(\eta_i V_i) \quad (6)$$

where ΔG^*, ΔG^{E*}, h and N_A are free energy of activation for viscous flow, excess free energy of activation for viscous flow, Planck's constant and Avogadro's number respectively.

2.2 Density and Viscosity Measurements

The density of MEA + H_2O mixtures at different MEA concentrations (30-100 mass% of MEA) and temperatures (293.15 K-363.15 K) was measured using a density meter DMA 4500 from Anton Paar (Graz, Austria). The viscosity of MEA + H_2O mixtures at different MEA concentrations (30-100 mass% of MEA) and temperatures (293.15 K-363.15 K) was measured using a double-gap concentric rheometer Physica MCR 101 from Anton Paar (pressure cell XL DG35.12/PR; measuring cell serial number 8046220) (Graz, Austria). The measured data with associated uncertainties for both density and viscosity measurements are discussed in Karunarathne et al. (2020(b)).

2.3 ANN Network Training and Activation Function

2.3.1 Network Training

For the ANN models, the mole fraction of the components in the mixture and temperature were considered as the inputs to the network. All the networks are comprised of one hidden layer and multiple neurons. A data set with 72 data points were divided into 70%, 15% and 15% randomly for the training, validation and testing. Data sets were then scaled in the range of (-1, 1) as shown in (7). The optimum number of neurons for the

network was decided by examining the cost function of Mean Squared Error (MSE) as given in (8) for the learning algorithm of Bayesian Regularization (BR) for thirty neurons. The BR training algorithm regularizes ANN model parameters to reduce the complexity of the model, which helps to avoid overfitting. Figure 1 illustrates the schematic of the ANN for the excess free energy of activation for viscous flow.

$$Y = (Y_{max} - Y_{min})\left[\frac{X - X_{min}}{X_{max} - X_{min}}\right] + Y_{min} \qquad (7)$$

where Y_{max} and Y_{min} are +1 and -1 respectively. X is the input or output variable. X_{max} and X_{min} are maximum and minimum of variable X.

$$MSE = \frac{1}{2N}\sum_{i=1}^{N}\left\{\left(Y_i^E - Y_i^C\right)^2 + \lambda W^2\right\} \qquad (8)$$

where N, Y_i^E, Y_i^C, λ and W refer to the number of data points, the measured property, calculated property, regularization parameter and weight parameter vector, respectively.

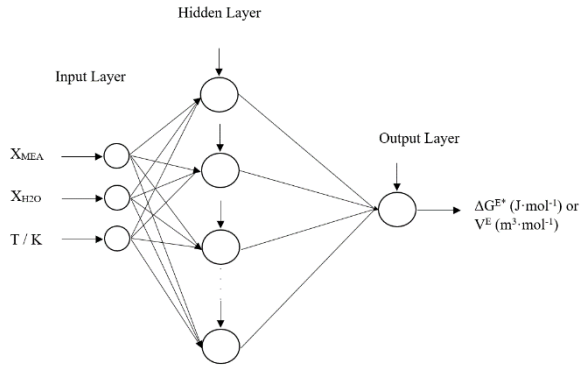

Figure 1: A schematic of feed forward artificial neural network with one hidden layer.

2.3.2 Activation Function

The input for the activation function is the sum of weighted inputs (the input from each independent variable multiplied by an adjustable connection weight) with added hidden layer bias as described in (9) (Rocabruno-Valdés et al. 2015). For the hidden layer, the activation function is a hyperbolic tangent (τ) as given in (10). The output of the ANN is linearly related (ψ) as given in (11) with the weighted output from the hidden layer and output layer bias.

$$\theta_s = IW_{(s,1)}In_1 + IW_{(s,2)}In_2 + \cdots + IW_{(s,k)}In_k + b_s^{(1)} \qquad (9)$$

where In, θ_s, IW, and $b_s^{(1)}$ are the inputs to the network, inputs to the hidden neurons, weight between network input and the hidden neurons and bias term to hidden neurons, respectively. The subscript s and k are for number of hidden neurons and number of inputs, respectively.

$$f = \tau(\theta_s) = \frac{2}{1 + exp(-2\theta_s)} - 1 \qquad (10)$$

$$g = \psi\left(LW \cdot f + b^{(2)}\right) \qquad (11)$$

where LW and $b^{(2)}$ are the input weights and bias in the output layer, respectively.

The ANN-based models were evaluated using average absolute relative deviation (AARD) as given in (12).

$$AARD\ (\%) = \frac{100\%}{N}\sum_{i=1}^{N}\left|\frac{Y_i^E - Y_i^C}{Y_i^E}\right| \qquad (12)$$

where N, Y_i^E and Y_i^C refer to the number of data points, the measured property and calculated property, respectively.

3 Results and Discussion

This section discusses the performance of ANN in excess molar volume V^E and excess free energy of activation for viscous flow ΔG^{E*} predictions for the considered MEA + H_2O mixtures.

3.1 Excess Molar Volume (V^E) From ANN Based Models

The calculated V^E from (4) was used for the train, validate and test a feed forward back propagation ANN. For the MEA + H_2O mixtures, $V^E < 0$ for the considered MEA concentrations and temperatures (Karunarathne et al. 2020(b)). The accuracy of model prediction was analyzed through calculated AARD between calculated V^E and ANN is given in Table 1 for the training, validation and test data sets. Simulation provided a minimum MSE at 25 neurons. The optimum number of neurons of the network was chosen as 7 since it gives a reasonable low value for the MSE of calculated over 30 neurons in the hidden layer. Figures 2 and 3 illustrate the accuracy of the fit between ANN predictions and the calculated V^E. According to Figure 2, V^E calculated from measured properties are fitted with good accuracy into the ANN. Most of the deviation of the ANN predictions for V^E is within 2% and only one data point reported a deviation close to 6% as

illustrated in Figure 3. The developed Redlich and Kister type polynomial was able to fit data with an accuracy of 2.47% AARD and it is higher than 1.5%, which is from the ANN model for the test data set as given in Table 1. A comparison of AARD from ANN models and Redlich and Kister type polynomials for excess properties are given in Table 2. This indicates that the ANN model has a better fit for V^E .

3.2 Excess Free Energy of Activation for Viscous Flow ΔG^{E*} From ANN Based Models

For the ΔG^{E*}, calculated property from (6) was used for the train, validate and test a feed forward back propagation ANN. The ΔG^{E*}> 0 for the MEA + H_2O mixtures at considered MEA concentrations and temperatures. The minimum MSE was found with 26 neurons in the hidden layer and the optimum number of neurons was considered as 7 that gives a reasonable R^2 and AARD in the data fit. Equation (12) was adopted to calculate AARD to analyze accuracy between calculated ΔG^{E*} from (6) and ANN. Table 1 summarized the R^2 and AARD for different data sets reported in Table 1. Figures 4 and 5 show how good the fitting for ΔG^{E*} between predictions from the ANN model and calculation from measured properties. Figure 5 shows that the majority of the data are within a deviation of 3% and only three data points are beyond this limit. The Redlich and Kister type polynomial for ΔG^{E*} was able to fit data with 1.9% AARD, which indicates that the developed ANN model gives a better fit for the data.

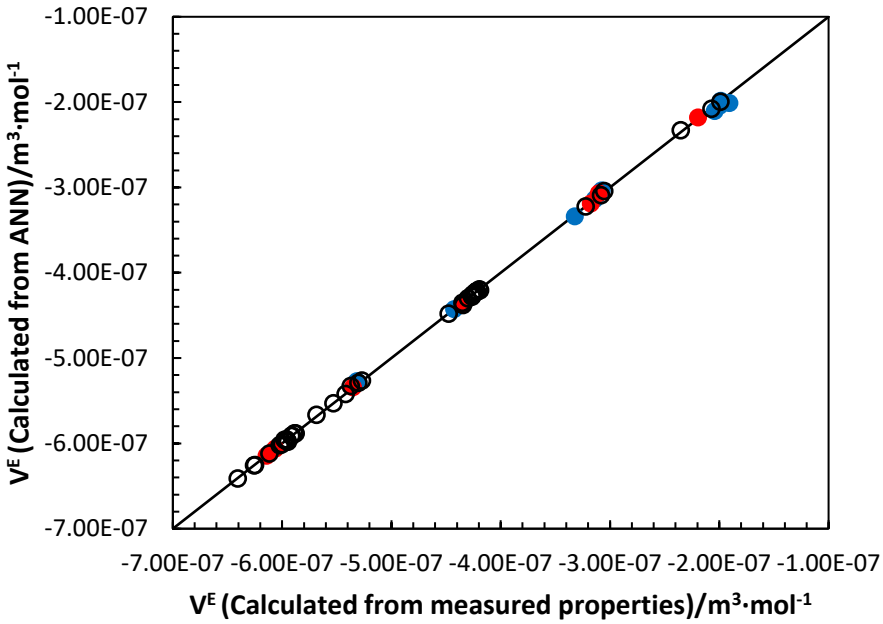

Figure 2. Comparison of correlated V^E with calculated V^E for MEA + H_2O mixtures. ANN: Training data, '○'; Validation data, '●'; Test data, '●'.

Table 1. Performance of trained ANNs for V^E and ΔG^{E*}.

Excess Property	*No. of Neurons in the Hidden Layer*	*Training Data*		*Validation Data*		*Test Data*	
		AARD%	R^2	*AARD%*	R^2	*AARD%*	R^2
V^E ($m^3 \cdot mol^{-1}$)	7	0.2	0.999	0.4	0.999	1.5	0.999
ΔG^{E*}($J \cdot mol^{-1}$)	7	0.5	0.999	0.8	0.999	1.2	0.988

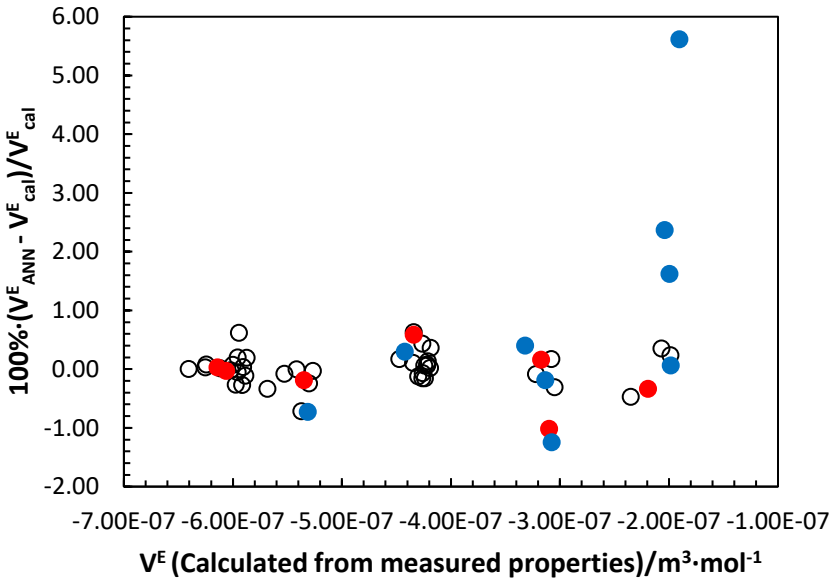

Figure 3. Percentage deviation of correlated V^E from calculated V^E for MEA + H_2O mixtures. ANN: Training data, '○'; Validation data, '●'; Test data, '●'.

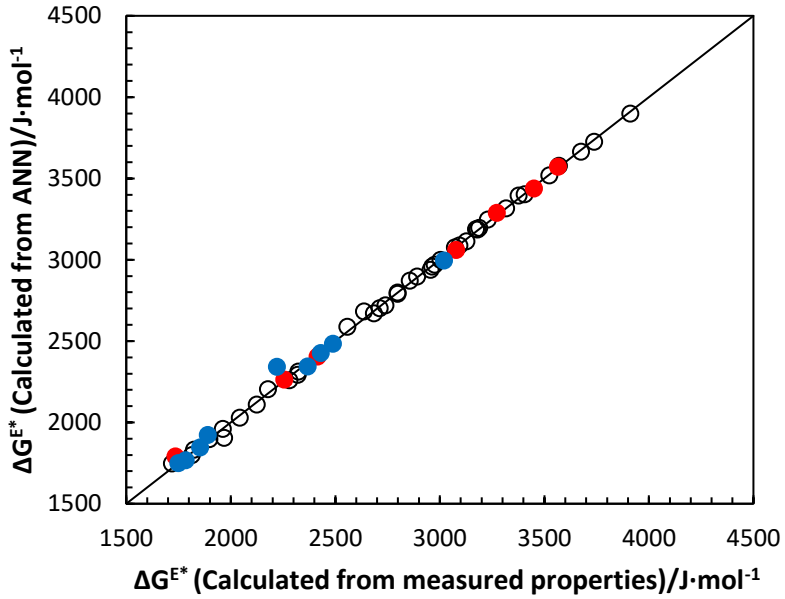

Figure 4. Comparison of correlated ΔG^{E*} with calculated ΔG^{E*} for MEA + H_2O mixtures. ANN: Training data, '○'; Validation data, '●'; Test data, '●'.

Table 2. Accuracies of the data fitting for V^E and ΔG^{E*} from ANN models and Redlich and Kister type polynomials.

Excess Property	*AARD%*	
	ANN	Redlich and Kister
V^E ($m^3 \cdot mol^{-1}$)	1.5	2.47
ΔG^{E*}($J \cdot mol^{-1}$)	1.2	1.9

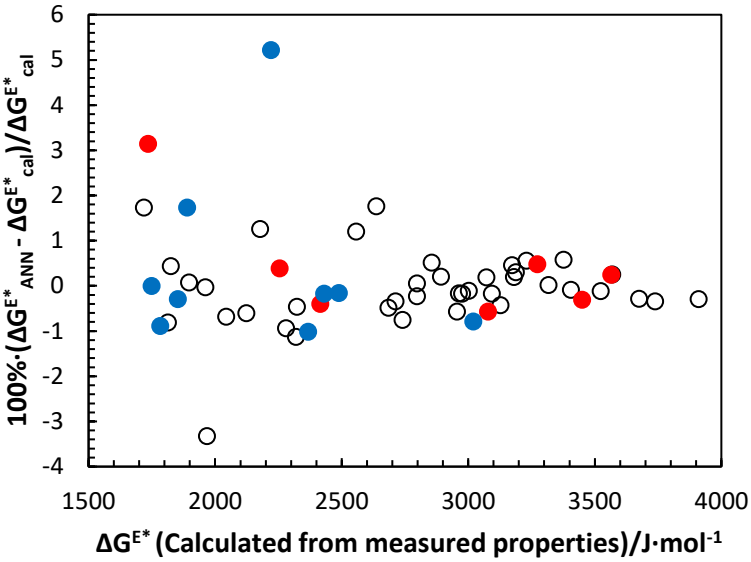

Figure 5. Percentage deviation of correlated ΔG^{E*} from calculated ΔG^{E*} for MEA + H_2O mixtures. ANN: Training data, '○'; Validation data, '●'; Test data, '●'.

Literature provides accuracies for the density and viscosity correlations based on Redlich and Kister polynomial. Han et al. (2012) discussed a density correlation based on Redlich and Kister type polynomial for MEA + H_2O mixtures at different MEA concentrations and temperatures. The correlation was able to represent measured density with an accuracy of AARD 0.042 %. Hartono et al. (2014) used a simplified Redlich and Kister type polynomial for both density and viscosity of MEA + H_2O mixtures at different MEA concentrations and temperatures. Hartono's correlations were able to fit measured data with an accuracy of AARD 0.036 % and 3.5 % for density and viscosity respectively. The developed ANN models in this study for V^E and ΔG^{E*}were used to calculate density and viscosity from (4) and (6). The calculated physical properties show a good accuracy compared to the measured data with AARD 0.018 % and 0.6 % for density and viscosity that is better than the correlations reported based on Redlich and Kister type polynomials in literature.

4 Conclusion

The excess properties of excess molar property and excess free energy of activation for viscous flows were determined from measured densities and viscosities for MEA + H_2O mixtures at different MEA concentrations and temperatures. ANN models were trained to fit calculated excess properties and used to predict density and viscosity of the mixtures.

The proposed ANN model for the excess molar volume V^E was able to fit the data with acceptable accuracy. The calculated AARDs for different data sets of training, validation and test are 0.2, 0.4 and 1.5 % respectively. The ANN model proposed for the excess free energy of activation for viscous flow ΔG^{E*}showed AARDs for different data sets of training, validation and test are 0.5, 0.8 and 1.2 % respectively.

The models were used to predict density and viscosity at different MEA concentrations and temperatures. Results showed a good agreement with measured densities and viscosities. The accuracy for density prediction was 0.018 % AARD and for prediction of viscosity 0.06 % AARD that is higher than the accuracies based on Redlich and Kister polynomials. Accordingly, ANN approach to predict excess properties and physical properties could be used to enhance the accuracy of data fitting. The developed models are useful in the design of process equipment and process modelling for the CO_2 capture processes. Further, this approach can be extended to the mixtures with more than two components.

References

T. M. Aminabhavi, M. I. Aralaguppi, G. Bindu, and R. S. Khinnavar. Densities, shear viscosities, refractive indices, and speeds of sound of Bis(2-methoxyethyl) Ether with Hexane, Heptane, Octane, and 2,2,4-Trimethylpentane in the temperature interval 298.15-318.15 K, *J. Chem. Eng. Data*, 39: 522-528, 1994.

R. B. Bird, W. E. Stewart, and E. N. Lightfoot. 2002. *Transport Phenomena* (John Wiley & Sons, Inc.: USA).

A. Ćwiklińska, and C. M. Kinart. Thermodynamic and physicochemical properties of binary mixtures of nitromethane with {2-methoxyethanol+2-butoxyethanol} systems at T=(293.15, 298.15, 303.15, 308.15, and 313.15)K, *J. Chem. Thermodyn.*, 43: 420-429, 2011.

H. Eyring. Viscosity, Plasticity, and Diffusion as example of absolute reaction rates, *J. Chem. Phys.*, 4: 283-291, 1936.

K. Fu, G. Chen, T. Sema, X. Zhang, Z. Liang, R. Idem, and P. Tontiwachwuthikul. Experimental study on mass transfer and prediction using artificial neural network for CO2 absorption into aqueous DETA, *Chem. Eng. Sci.*, 100: 195-202, 2013.

S. Garg, A. M. Shariff, M. S. Shaikh, B. Lal, A. Aftab, and N. Faiqa. A neural network approach to predict the density of aqueous MEA solution, *Australian Journal of Basic and Applied Sciences*, 9: 415-422, 2015.

M. E. Hamzehie, S. Mazinani, F. Davardoost, A. Mokhtare, H. Najibi, B. Van der Bruggen, and S. Darvishmanesh. Developing a feed forward multilayer neural network model for prediction of CO2 solubility in blended aqueous amine solutions, *Journal of Natural Gas Science and Engineering*, 21: 19-25, 2014.

J. Han, J. Jin, D. A. Eimer, and M. C. Melaaen. Density of water (1) + Monoethanolamine (2) + CO_2 (3) from (298.15 to 413.15) K and surface tension of water (1) + Monoethanolamine (2) from (303.15 to 333.15) K, *J. Chem. Eng. Data*, 57: 1095-1103, 2012.

P. Haratipour, A. Baghban, A. H. Mohammadi, S. H. H. Nazhad, and A. Bahadori. On the estimation of viscosities and densities of CO2-loaded MDEA, MDEA+AMP, MDEA+DIPA, MDEA+MEA, and MDEA+DEA aqueous solutions, *J. Mol. Liq.*, 242: 146-159, 2017.

A. Hartono, E. O. Mba, and H. F. Svendsen. Physical properties of partially CO_2 loaded aqueous monoethanolamine (MEA), *J. Chem. Eng. Data* 59: 1808-1816, 2014.

S. S. Karunarathne, K. Chhantyal, D. A. Eimer, and L. E. Øi. Artificial neural networks (ANNs) for density and viscosity predictions of CO_2 loaded alkanolamine + H_2O mixtures, *ChemEngineering*, 2020.

S. S. Karunarathne, D. A. Eimer, and L. E. Øi. Density, viscosity and free energy of activation for viscous flow of monoethanol amine (1) + H_2O (2) + CO_2 (3) mixtures, *Fluids*, 5,13, 2020.

C. M. Kinart, W. J. Kinart, and A. Ćwiklińska. 2-Methoxyethanol–Tetrahydrofuran–binary liquid system. Viscosities, densities, excess molar volumes and excess Gibbs activation energies of viscous flow at various temperatures, *J. Therm. Anal. Calorim.*, 68: 307-317, 2002.

T. M. Letcher, and R. C. Baxter. Application of the Prigogine-Flory-Patterson theory part I. Mixtures ofn-alkanes with bicyclic compounds, benzene, cyclohexane andn-hexane, *J. Solution Chem.*, 18: 65-80, 1989.

A. R. Mahajan, and S. R. Mirgane. Excess molar volumes and viscosities for the binary mixtures of n-Octane, n-Decane, n-Dodecane, and n-Tetradecane with Octan-2-ol at 298.15 K, *Journal of Thermodynamics*, 2013: 1-11, 2013.

R. Meyer, M. Meyer, J. Metzger, and A. Peneloux. Thermodynamic and physicochemical properties of binary solvent *Journal de Chimie Physique et de Physico-Chimie Biologique*, 68: 406-412, 1971.

F. Pouryousefi, R. Idem, T. Supap, and P. Tontiwachwuthikul. Artificial Neural Networks for Accurate Prediction of Physical Properties of Aqueous Quaternary Systems of Carbon Dioxide (CO2)-Loaded 4-(Diethylamino)-2-butanol and Methyldiethanolamine Blended with Monoethanolamine, *Ind. Eng. Chem. Res.*, 55: 11614-11621, 2016.

F. Qi, and H. Wang. Application of Prigogine–Flory–Patterson theory to excess molar volume of mixtures of 1-butyl-3-methylimidazolium ionic liquids with N-methyl-2-pyrrolidinone, *J. Chem. Thermodyn.*, 41: 265-272, 2009.

O. Redlich, and A. T. Kister. Algebraic representation of thermodynamic properties and the classification of solutions, *Ind. Eng. Chem.*, 40: 345-348, 1948.

C. I. Rocabruno-Valdés, L. F. Ramírez-Verduzco, and J. A. Hernández. Artificial neural network models to predict density, dynamic viscosity, and cetane number of biodiesel, *Fuel*, 147: 9-17, 2015.

N. Sipöcz, F. A. Tobiesen, and M. Assadi. The use of Artificial Neural Network models for CO_2 capture plants, *Appl. Energy*, 88: 2368-2376, 2011.

R. H. Weiland, J. C. Dingman, D. B. Cronin, and G. J. Browning. Density and viscosity of some partially carbonated aqueous alkanolamine solutions and their blends, *J. Chem. Eng. Data*, 43: 378-382, 1998.

Developing a Dynamic Diesel Engine Model for Energy Optimal Control

Viktor Leek, Lars Eriksson

Division of Vehicular Systems, Linköping University, Sweden
viktor.leek@liu.se, lars.eriksson@liu.se

Abstract

A dynamic heavy-duty Euro 6 diesel engine model for energy optimal control is developed. The modeling focus is on accuracy in the entire engine operating range, with attention to the region of highest efficiency and physically plausible extrapolation. The effect of the air-to-fuel ratio on combustion efficiency is studied, and it is demonstrated how this influences the energy optimal transient control. A convenient, physics-based, method for pressure sensor bias estimation is also presented.
Keywords: Diesel engine modeling, Optimal control

1 Introduction

Economy, climate, and diesel engines. Ever since the breakthrough of Rudolph Diesel's engine it has been impossible to consider the first two without the third, and the machine is now one of the two prime movers of globalization (Smil, 2017). As its position in the global economy has risen to the predominant one, so has its impact on the climate. And while it might be possible to imagine a future transportation system without diesel engines, it is impossible to imagine a transition to that system without large investments, so the continued development of the diesel engine is perhaps more important than ever. By reducing fuel consumption, improving emissions, enabling renewable fuels, and increasing reliability, it is possible to improve, individually and in combination, the economy, and the climate. This work aims to help in that effort by developing a diesel engine model for energy optimal control.

The model's intended use is to study the effect of the turbocharger selection on the energy optimal control of the air- and fuel-path of a heavy-duty Euro 6 diesel engine. While being the reason *why* this work is conducted, it is *not* the only area of use. Models are only approximations of reality, and for them to be useful to others it is necessary to show what aspects of reality they reflect, and how accurately they do it. Here, this is done in two parts. This first part describes the development of the model, which include determining the needed properties and settling on the equations. The second part consists of parametrization and validation and is found in (Ekberg et al., 2018).

The contributions include the development of a diesel engine model for studying the turbocharger effect on the energy optimal control, with a novel inclusion of the air-to-fuel ratio effect on the engine efficiency, and is available as open-source (Leek et al.). Another important contribution is a physics-based method for estimating pressure sensor bias in experimental data.

The paper is outlined as follows. Section 2 introduces the subject of modeling for energy optimal control, Section 3 presents the data used for modeling and the method for estimating pressure sensor bias, Section 4 describes the model development, Section 5 demonstrates the energy optimal control of the model, and Section 6 presents the conclusions.

2 Modeling for Energy Optimal Control

With the intention of using the model for energy optimal control, it is necessary to investigate the implications of this on the modeling work. To do that, a basic discussion on optimal control problems, and their numerical solution, is needed.

2.1 Optimal control

An optimal control problem (OCP) can be formulated as:

$$\begin{aligned} \min_{u} \quad & E(t_f, x(t_f)) + \int_0^{t_f} L(t,x,u)\, dt \\ \text{s.t.} \quad & \dot{x} = f(t,x,u),\ t \in [0,t_f], \\ & x(0) \in \mathscr{X}_0, \\ & x(t) \in \mathscr{X},\ t \in [0,t_f], \\ & u(t) \in \mathscr{U},\ t \in [0,t_f], \\ & x(t_f) \in \mathscr{X}_f \end{aligned} \tag{1}$$

The problem consists of finding the optimal control, u^*, and the state trajectory, x^*, that minimize the cost function and does not violate the constraints. The problem's defining characteristic is the differential constraint $\dot{x} = f(t,x,u)$. The objective function consists of two parts. An integral cost $\int L(t,x,u)\,dt$, and a terminal cost $E(t_f, x(t_f))$. There are constraints on the initial value, $x(0) \in \mathscr{X}_0$, path constraints $x(t) \in \mathscr{X}$ and $u(t) \in \mathscr{U}$, and constraints on the final state $x(t_f) \in \mathscr{X}_f$.

2.2 Numerical solution to optimal control problems

There exist several approaches for solving optimal control problems numerically, and an overview can be found in (Rao, 2009). This work focuses on direct methods. They are the most popular methods in general (Diehl et al., 2006), and have proved successful in the optimal control of diesel engines (Asprion et al., 2014; Sivertsson and Eriksson, 2014; Mancini, 2014).

Direct methods are characterized by first discretizing the OCP and turning it into a nonlinear program (NLP), solving that numerically, and then reconstructing the OCP solution from the NLP one. The process of casting the OCP as a NLP is known as transcription. Transcription methods consider some form of grid on which the solution is parameterized. A common, and the most basic of which, is a fixed, equidistant, grid

$$0 = t_0 < t_1 < \cdots < t_{N-1} < t_N = t_f \tag{2a}$$

$$h = t_{n+1} - t_n,\ n = 0, 1, \ldots, N-1 \tag{2b}$$

where h is the fixed step length, and N the number of intervals. The control signal is typically constant over each segment (Diehl, 2011), and consistent with a zero-order hold control system implementation. The state trajectory differs between the individual direct methods, but the two most popular, direct multiple shooting and direct collocation (Diehl et al., 2006), integrate the dynamics separately on each segment, forming a discontinuous trajectory, which is made continuous by introducing defect constraints (Betts, 2010). Based on this, the number of NLP variables resulting from using the direct multiple shooting method is calculated as $Nn_u + (N+1)n_x$, where n_x is the number of states, and n_u the number of control inputs (Andersson, 2013). The corresponding metric for the direct collocation method is $Nn_u + (N(n_{cp}+1)+1)n_x$ where n_{cp} is the number of collocation points. Considering how the NLP variables scale with the number of states and controls, it is preferable that the number of states and controls is kept low, otherwise the NLP risks being too difficult or too expensive to solve, which defeats the purpose.

Literature on optimal control of diesel engines (Asprion et al., 2014) suggests a large NLP, with potentially tens of thousands of variables. To solve that efficiently it is desirable to use a gradient based solver of Newton-type which uses first and second derivatives. As nothing is known of the objective or constraints at the time of modeling, constraints must be passed on to the model. The state trajectory is therefore made, at least, two times differentiable. This has the positive side-effect to aid simulations, as initial value problem solvers assume a sufficiently smooth solution (Ascher and Petzold, 1998).

Based on the characteristics of an optimal solution (Nocedal and Wright, 2006; Asprion et al., 2014), the solution lies at the border of the allowable set and/or in the unconstrained optimum. This has two implications on the modeling work. The first, that the model needs physically plausible extrapolation properties to capture the full set of operating conditions. The second, that the model fit needs to be good in the region of best efficiency, where optimum is expected to be found.

2.3 Modeling implications

Optimization-oriented models need to be *accurate* in order to capture a large set of operating conditions, *small*, for efficient evaluation, provide *plausible extrapolation*, to capture solutions at the border of the feasible set, and be implementable using only *standard mathematical operations*, for algorithmic differentiation applicability. Models for energy optimal control also need *high accuracy in the region of best efficiency*. To successfully meet these demands, it is necessary to combine an approach based on first principles and phenomenology. By formulating the dominating equations from first principles the model is restricted in size, and extrapolation is physically plausible. The phenomenological part consists of, based on available data, determining how the equation parameters change with the operating conditions, and is fundamental to good accuracy over a large operating range.

With the intended use of studying the turbocharger impact on the energy optimal control, it is important with a good model of the turbocharger as it gives rise to the dominating dynamics on the air and fuel path, but also with a good model of its implicit effects on the said path. Larger turbines produce a lower backpressure, which decreases pumping work and thereby increases efficiency (Eriksson et al., 2002). Its larger size also means an increased inertia. This hampers the engine's transient response, and therefore the air-to-fuel ratio is lower during transients. Low air-to-fuel ratio lowers combustion efficiency (Heywood, 1988; Eriksson and Nielsen, 2014), so in order to study the turbocharger impact on the energy optimal control it is necessary to include this effect in the model.

3 Data

Five datasets are used to guide the modeling, and a listing is found in Table 1. Dataset A consists of engine dynamometer experimental data collected in an engine test cell. Dataset B is high-fidelity simulation data from a GT-Power (Gamma Technologies, 2004) model of the engine. Dataset C is a compressor map formed by running measurements in a turbocharger gas stand. Dataset D is a turbine map, also collected from gas stand measurements. Dataset E is data on the throttle area as a function in throttle angle.

The datasets fulfill different aspects of the modeling work. In particular, the high-fidelity simulation data, B, is used instead of cylinder pressure data, which is not available. The simulation data contains information on the torque components, which makes it possible to model the cylinder in better detail than what is possible if only dataset A is used. How the different datasets are fused is found in the validation and parametrization part of this

Table 1. Datasets used to find model parameters.

Dataset	Signals	Samples
A. Engine dynamometer experimental data.	24	235
B. GT Power high-fidelity simulation data.	22	160
C. Compressor map - Gas stand measurements.	4	73
D. Turbine map - Gas stand measurements.	4	73
E. Throttle area - Measurements of angle versus area.	1	11

work (Ekberg et al., 2018).

3.1 Pressure offset estimation

An important part in modeling is having access to reliable data. Unfortunately, measurements contain errors to some degree. Here, dataset A contains bias in the pressure sensors on the intake side. This is compensated for by estimating it. The estimation is based on the observation that flow squared is proportional to the pressure drop over a restriction. By denoting the upstream pressure and temperature by p_{us} and T_{us} respectively, the downstream pressure by p_{ds}, the bias in that sensor by p_{bias}, and the flow by W, the relation is formulated as

$$(p_{\text{us}} - (p_{\text{ds}} + p_{\text{bias}}))\frac{p_{\text{us}}}{\sqrt{T_{\text{us}}}} \propto W^2$$

Rearranging the equation, and introducing the proportionality constant c, the following least squares problem is solved to estimate the bias:

$$\left[p_{\text{us}}/\sqrt{T_{\text{us}}},\ W^2\right]\begin{bmatrix} p_{\text{bias}} \\ c \end{bmatrix} = (p_{\text{us}} - p_{\text{ds}})\frac{p_{\text{us}}}{\sqrt{T_{\text{us}}}} \qquad (3)$$

4 Model

With the model's intended use in mind, a mean value modeling approach is taken. This considerably reduces the model size, when compared to a 1D model, while still being able to capture the relevant quantitative properties of the air and fuel path.

In this work, a model of the throttle is included. The purpose of this is to extend the model's area of use by making it possible to connect it to an aftertreatment system model. As aftertreatment systems are sensitive to temperature, there is a need to control airflow through the system to avoid unnecessary cooling. This means that the model has an extra control volume before the throttle, which means one extra pressure state (boost pressure). Users that do not need this feature can remove it.

4.1 Dynamics

The model is governed by four scalar ODEs: boost pressure dynamics, intake manifold pressure dynamics, exhaust manifold pressure dynamics, and the dominating one, turbocharger rotational dynamics.

The modeling of the control volumes is based on differentiation of the ideal gas law, an isothermal assumption, which means no temperature change in the system, and assumption of mass conservation. The modeling follows (Eriksson and Nielsen, 2014).

Denote the volumes by V, pressures by p, temperatures by T, and let dot notation be used to denote differentiation with respect to time. Introduce the subscript b (boost) for the volume before the throttle, im for the intake manifold, and em for the exhaust manifold. Let R_{a} be the gas constant of air, and R_{e} the gas constant of exhaust gas. Introduce the compressor flow as W_{c}, the throttle flow as W_{thr}, the flow into the cylinders as W_{cyl}, the fuel flow as W_{f}, the turbine flow as W_{t}, and the wastegate flow as W_{wg} (see Figure 2 for an overview). The flows are defined later. The filling and emptying dynamics of the control volumes is then expressed as

$$V_{\text{b}}\,\dot{p}_{\text{b}} = R_{\text{a}}\,T_{\text{b}}(W_{\text{c}} - W_{\text{thr}}) \qquad (4a)$$

$$V_{\text{im}}\,\dot{p}_{\text{im}} = R_{\text{a}}\,T_{\text{im}}(W_{\text{thr}} - W_{\text{cyl}}) \qquad (4b)$$

$$V_{\text{em}}\dot{p}_{\text{em}} = R_{\text{e}}\,T_{\text{em}}(W_{\text{cyl}} + W_{\text{f}} - W_{\text{t}} - W_{\text{wg}}) \qquad (4c)$$

The model builds on the isothermal assumption and should be tested. Figure 1 shows the intake manifold temperature and ambient temperature of dataset A. The data shows a consistent 2 % temperature increase, relative to ambient, which is considered small. This motivates two modeling simplifications, isothermal control volumes, and ideal charge air cooler. Should it be desirable, the intake manifold temperature can be set to 2% above ambient. Furthermore, literature (Wahlström and Eriksson, 2011) suggest only minor differences in observed behavior when using an adiabatic model of the control volumes with temperature state, which further motivates the decision to not include temperature dynamics.

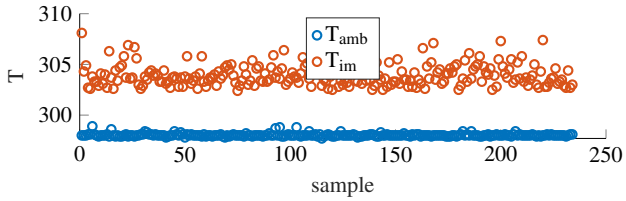

Figure 1. Ambient and intake manifold temperature from dataset A.

Modeling of the turbocharger dynamics follows from Newton's second law of motion. To formulate the equation ω is used to denote angular velocity, J to denote moment of inertia, and subscript tc is used for the turbocharger. The effects of the turbine and compressor on the dynamics is expressed in terms of their power. $P_{\text{t}}\,\eta_{\text{m}}$ is used to denote the turbine power and includes mechanical efficiency, and P_{c} is the compressor power. To obtain torque, power is divided by angular velocity, which means that the model is only valid for positive velocities. The

turbocharger dynamics is formulated as:

$$J_{\mathrm{tc}}\dot{\omega}_{\mathrm{tc}} = \frac{P_{\mathrm{t}}\,\eta_{\mathrm{m}} - P_{\mathrm{c}}}{\omega_{\mathrm{tc}}} \tag{5}$$

With the dynamics presented, it can be concluded that the model has four states x:

$$x = [p_{\mathrm{b}}, p_{\mathrm{im}}, p_{\mathrm{em}}, \omega_{\mathrm{tc}}]^{\mathrm{T}} \tag{6}$$

and to control these, there are three control inputs u. The fuel injection per cycle and cylinder u_{f}, the throttle effective area u_{thr}, and the wastegate effective area u_{wg}:

$$u = [u_{\mathrm{f}}, u_{\mathrm{thr}}, u_{\mathrm{wg}}]^{\mathrm{T}} \tag{7}$$

The engine speed, N_{ice}, is an external input in the model and a model overview is found in Figure 2.

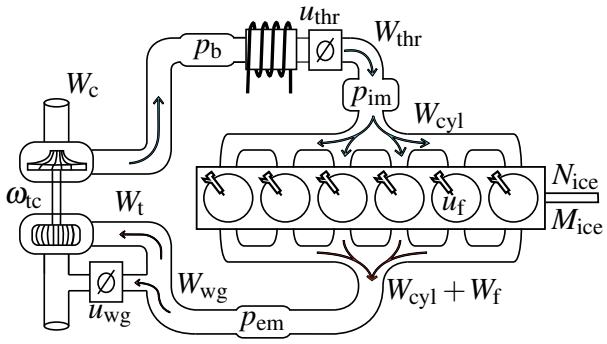

Figure 2. Model overview. Shown are the four states: boost pressure p_{b}, intake manifold pressure p_{im}, exhaust manifold pressure p_{em}, and turbocharger angular velocity ω_{tc}, and the three control inputs: Fuel injection per cycle and cylinder u_{f}, throttle effective area u_{thr}, and wastegate effective area u_{wg}. Also shown are the flows, W, in the model.

4.2 Throttle

Modeling of the throttle follows (Eriksson and Nielsen, 2014), where an isentropic compressible restriction is used. To describe the model, further notation is needed. $A_{\mathrm{thr,max}}$ is the throttle maximum area, $C_{\mathrm{D,thr}}$ the flow coefficient, Ψ_{thr} flow parameter, and the flow is calculated as

$$W_{\mathrm{thr}} = \frac{p_{\mathrm{b}}}{\sqrt{R_{\mathrm{a}}\,T_{\mathrm{b}}}} C_{\mathrm{D,thr}} A_{\mathrm{thr,max}}\, u_{\mathrm{thr}}\, \Psi_{\mathrm{thr}} \tag{8}$$

The effective throttle area $A_{\mathrm{thr,max}}\,u_{\mathrm{thr}}$ is linear in the control input. This is not in accordance with dataset E. Data suggest a cubic relation, but since the relation is injective, the actual control input can be reconstructed from the effective area. So, to avoid nonlinearity, effective area is modeled as linear in the artificial control input u_{thr}.

(Holmbom and Eriksson, 2018) compares different compact models for the flow parameter Ψ_{thr}. Good performance is obtained for the model (Shen and Ohata, 2011), which is based on the conservation of mass, energy, and momentum. By denoting the ratio of specific heats by γ_{a}, and the pressure ratio by Π_{thr}, the model can be expressed as:

$$\Psi_{\mathrm{thr}} = \sqrt{\frac{\gamma_{\mathrm{a}}+1}{2\gamma_{\mathrm{a}}}(1-\Pi_{\mathrm{thr}})\left(\Pi_{\mathrm{thr}} + \frac{\gamma_{\mathrm{a}}-1}{\gamma_{\mathrm{a}}+1}\right)} \tag{9a}$$

$$\Pi_{\mathrm{thr}} = \begin{cases} \frac{p_{\mathrm{im}}}{p_{\mathrm{b}}} & \text{if } \frac{p_{\mathrm{im}}}{p_{\mathrm{b}}} \geq \frac{1}{\gamma_{\mathrm{a}}+1} \\ \frac{1}{\gamma_{\mathrm{a}}+1} & \text{otherwise} \end{cases} \tag{9b}$$

The saturation of flow gives rise to the conditional expression. It does not have a continuous derivative. To circumvent that, the logistic function is used to make the derivative continuous, at the cost of nonlinearity and parametrization effort:

$$\Pi_{\mathrm{thr}} = \Pi^{\mathrm{choke}} + c_{\mathrm{switch}}(\Pi - \Pi^{\mathrm{choke}}) \tag{10a}$$

$$c_{\mathrm{switch}} = 1/\left(1 + e^{-c_\Psi(\Pi - \Pi^{\mathrm{choke}})}\right) \tag{10b}$$

$$\Pi^{\mathrm{choke}} = 1/(\gamma_{\mathrm{a}}+1) \tag{10c}$$

$$\Pi = p_{\mathrm{im}}/p_{\mathrm{b}} \tag{10d}$$

The model contains one tuning parameter, c_Ψ, which determines the steepness of the switch.

4.3 Cylinder

The cylinder air mass flow is based on the modeling of the volumetric efficiency and follows the approach in (Heywood, 1988). By denoting the volumetric efficiency by η_{vol}, the engine displacement by V_{D}, and the engine speed by N_{ice}, the air mass flow is calculated as

$$W_{\mathrm{cyl}} = \eta_{\mathrm{vol}} \frac{2V_{\mathrm{D}}\,p_{\mathrm{im}}}{R_{\mathrm{a}}\,T_{\mathrm{im}} N_{\mathrm{ice}}} \tag{11}$$

The question is how to model volumetric efficiency. A common approach is to base the model on intake manifold pressure and engine speed (Heywood, 1988). The primary modeling dataset, A, does not show such a dependence, see Figure 3, nor does it show a clear correlation with any other variable in the dataset, why constant volumetric efficiency is used.

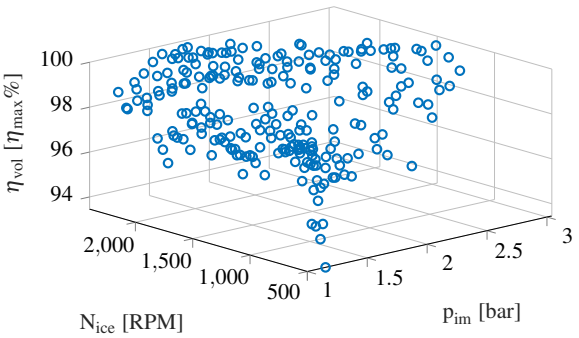

Figure 3. Volumetric efficiency, in circles, relative to the maximum value. Plotted against engine speed and intake manifold pressure.

The fuel mass flow is calculated as $W_{\mathrm{f}} = n_{\mathrm{cyl}} N_{\mathrm{ice}}\, u_{\mathrm{f}}\,/\,2$ and the fuel-to-air equivalence ratio ϕ is calculated as

$\phi = \mathrm{AF_s}\, W_\mathrm{f}/W_\mathrm{cyl}$, where $\mathrm{AF_s}$ is the air-to-fuel stoichiometric ratio. The air-to-fuel equivalence ratio $\lambda = 1/\phi$ is typically used by control engineers instead of ϕ. However, in the model it is preferable to use ϕ as it is not singular for zero fuel flow.

Cylinder out temperature modeling follows (Sivertsson and Eriksson, 2014):

$$T_\mathrm{e} = \eta_\mathrm{sc}\, \Pi_\mathrm{cyl}^{1-1/\gamma_\mathrm{a}}\, r_\mathrm{c}^{1-\gamma_\mathrm{a}} \left(\frac{q_\mathrm{in}}{c_\mathrm{p,a}} + T_\mathrm{im}\, r_\mathrm{c}^{\gamma_\mathrm{a}-1} \right) \tag{12a}$$

$$q_\mathrm{in} = \frac{W_\mathrm{f}}{W_\mathrm{f}+W_\mathrm{cyl}} q_\mathrm{HV}, \;\; \Pi_\mathrm{cyl} = \frac{p_\mathrm{em}}{p_\mathrm{im}} \tag{12b}$$

Here η_sc is a model parameter, γ_a the ratio of specific heats for air, r_c is the compression ratio, and q_HV the fuel lower heating value. The cooling of the gas, before reaching the exhaust manifold, is modeled from (Eriksson, 2002):

$$T_\mathrm{em} = T_\mathrm{amb} + (T_\mathrm{e} - T_\mathrm{amb}) e^{-\frac{c_\mathrm{em,h}}{(W_\mathrm{cyl}+W_\mathrm{f})c_\mathrm{p,e}}} \tag{13}$$

Model parameter is $c_\mathrm{em,h}$, and $c_\mathrm{p,e}$ is the specific heat of the exhaust gas at constant pressure.

4.4 Torque

A large part of the modeling effort is devoted to modeling of the engine work. The engine torque, M_ice, is broken down into the components gross indicated torque M_ig, pumping torque M_pump, and friction torque M_fric:

$$M_\mathrm{ice} = M_\mathrm{ig} - M_\mathrm{pump} - M_\mathrm{fric} \tag{14}$$

As is customary in engine modeling and evaluation, work is normalized with engine displacement, V_D, and expressed in terms of the mean effective pressure (MEP). The relation between torque, M, and mean effective pressure is $4\pi M = V_\mathrm{D}\mathrm{MEP}$. $\mathrm{IMEP_g}$ is the gross indicated mean effective pressure (gross indicate that pumping losses are not included), PMEP is the pump mean effective pressure, and FMEP is the friction mean effective pressure. To be able to separate the different effects, data set B is used.

Indicated work

$\mathrm{IMEP_g}$ is modeled as in (Eriksson and Nielsen, 2014)

$$\mathrm{IMEP_g} = \eta_\mathrm{ig} \frac{q_\mathrm{HV}\, u_\mathrm{f}\, n_\mathrm{cyl}}{V_\mathrm{D}} \tag{15}$$

Achieving a good fit is a matter of modeling η_ig.

A modeling objective is to include the effect of the fuel-to-air ratio on the engine efficiency. The relation between the fuel-to-air ratio, the ratio of specific heats, and engine efficiency is described in (Heywood, 1988; Eriksson and Nielsen, 2014). An important question is how to include it in the model, and how that is done is an important contribution in this work.

The efficiency modeling is started from the efficiency of an ideal otto cycle, $1 - 1/r_\mathrm{c}^{\gamma-1}$, despite being a diesel engine. The reason for using it, is that it is a single parameter model, if the compression ratio r_c is considered given. To find a relation between efficiency and fuel-to-air ratio, the relation $\eta_\mathrm{ig,B} - (1 - 1/r_\mathrm{c}^{\gamma-1}) = 0$, is solved for γ for every datapoint in B, where $\eta_\mathrm{ig,B}$ is the indicated efficiency in the dataset. Figure 4 shows the solution, with γ drawn in circles, and a second order polynomial model of γ in ϕ is drawn in solid. The figure shows that the quadratic model can capture the trend and is like the trends found in literature. This motivates a model of the in-cylinder ratio of specific heats γ_cyl according to

$$\gamma_\mathrm{cyl}(\phi) = c_{\gamma,0} + c_{\gamma,1}\phi + c_{\gamma,2}\phi^2 \tag{16}$$

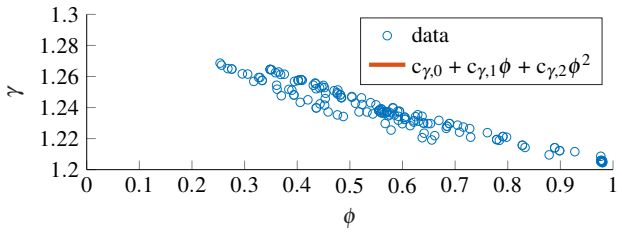

Figure 4. Drawn using circles is the γ that fulfills the relation $\eta_\mathrm{ig,B} - (1 - 1/r_\mathrm{c}^{\gamma-1}) = 0$ for every datapoint in B. Drawn in solid is a quadratic model of γ in ϕ.

The factor $\eta_\mathrm{cal}(N_\mathrm{ice}, u_\mathrm{f})$, is introduced. This gives the following structure for the indicated efficiency:

$$\eta_\mathrm{ig}(\phi, N_\mathrm{ice}, u_\mathrm{f}) = \left(1 - 1/r_\mathrm{c}^{\gamma_\mathrm{cyl}(\phi)-1}\right) \eta_\mathrm{cal}(N_\mathrm{ice}, u_\mathrm{f}) \tag{17}$$

To model η_cal, the same procedure as for γ is used. The equation $\eta_\mathrm{ig} - \eta_\mathrm{ig,B} = 0$ is solved for η_cal for every data point in B, $\eta_\mathrm{ig,B}$. Figure 5 shows the data plotted in circles, with constant coloring for constant engine speed. The data is plotted against fuel injection and engine speed. The figure clearly suggests a dependence on both fuel injection and engine speed. To model that, the model $\eta_\mathrm{cal} = c_\mathrm{cal,2}(u_\mathrm{f} - c_\mathrm{cal,1})^2 + c_\mathrm{cal,0}$ is fitted separately for the different engine speeds in the dataset, see solid lines in Figure 5. Figure 6 shows, drawn in circles, the evolution of the estimated parameters $c_\mathrm{cal,0}$, $c_\mathrm{cal,1}, c_\mathrm{cal,2}$ plotted against engine speed. In the same figure are different polynomial models of the trends plotted, which are estimated from the parameters using a least squares fit, and is used as a basis for modeling how the parameters change with engine speed.

The data and trends suggest the following modeling of the load and speed factor η_cal,

$$\eta_\mathrm{cal}(u_\mathrm{f}, N_\mathrm{ice}) = c_\mathrm{cal,2}(u_\mathrm{f} - c_\mathrm{cal,1})^2 + c_\mathrm{cal,0} \tag{18a}$$

$$c_\mathrm{cal,1} = c_\mathrm{cal,10} + c_\mathrm{cal,11} N_\mathrm{ice} \tag{18b}$$

$$c_\mathrm{cal,2} = c_\mathrm{cal,20} + c_\mathrm{cal,21} N_\mathrm{ice} + c_\mathrm{cal,22} (N_\mathrm{ice})^2 \tag{18c}$$

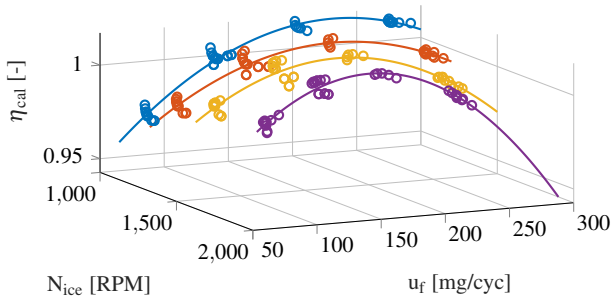

Figure 5. Drawn in circles is the solution to $\eta_{ig} - \eta_{ig,B} = 0$ for η_{ig}, calculated for every data point in B, $\eta_{ig,B}$. Drawn using solid lines is a least squares estimate of the model $\eta_{cal} = c_{cal,2}(u_f - c_{cal,1})^2 + c_{cal,0}$ for each speed-line.

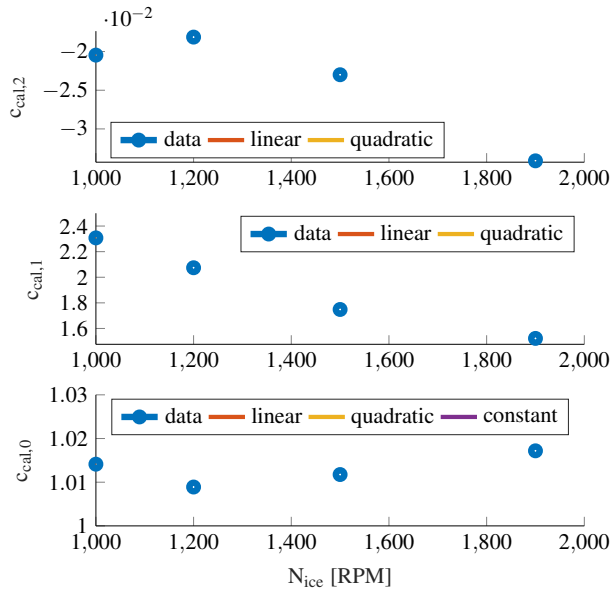

Figure 6. Evolution of $c_{cal,0}$, $c_{cal,1}$, $c_{cal,2}$, plotted against engine speed. Drawn using solid lines is the evolution modeled as polynomials in engine speed for different polynomial degree.

Pump work

The simplest model for the pump mean effective pressure is, PMEP $= p_{em} - p_{im}$. Dataset B gives a bias of 60 kPa for such a model for a least squares absolute error fit, also a linear model gives a bias, why an affine model is selected for the pumping work:

$$\text{PMEP}(p_{im}, p_{em}) = c_{\text{PMEP},0} + c_{\text{PMEP},1}(p_{em} - p_{im}) \quad (19)$$

with model parameters $c_{\text{PMEP},0}$ and $c_{\text{PMEP},1}$.

Friction work

A frequently used model for friction work is a second order polynomial in engine speed (Heywood, 1988). The available data in data set B does not show such a relation. Instead, data suggest the friction mean effective pressure can be modeled as a plane in engine speed, and fuel injection. A plot is available in Figure 7, in which circles

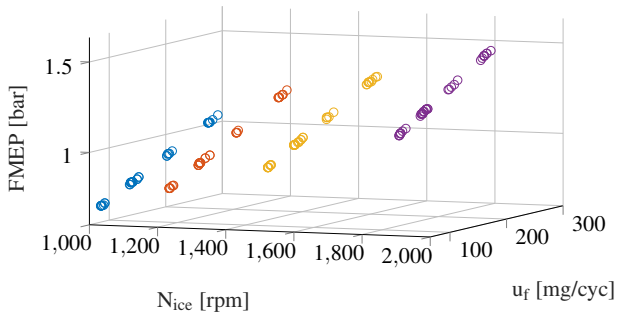

Figure 7. Drawn in circles is FMEP in data set B. Surface plot show the plane, FMEP $= c_{f,0} + c_{f,1}N_{ice} + c_{f,2}u_f + c_{f,3}u_f$, fitted from data.

show the mean effective pressure plotted against fuel injection and engine speed, and a surface plot shows a modeled plane. The model is formulated as follows

$$\text{FMEP}(u_f, N_{ice}) = c_{f,0} + c_{f,1}N_{ice} + c_{f,2}u_f + c_{f,3}u_f N_{ice} \quad (20)$$

in which $c_{f,0}$, $c_{f,1}$, $c_{f,2}$, and $c_{f,3}$ are model parameters.

4.5 Turbine

The turbine power is modeled based on (Eriksson, 2007), which lumps turbine power and the mechanical efficiency of the turbo shaft. By further introducing $c_{p,e}$ as the specific heat of the exhaust gas at constant pressure, and the subscript ats to indicate the aftertreatment system, the power is expressed as

$$P_t \eta_m = W_t c_{p,e} T_{em} \eta_t \left(1 - \Pi_t^{1-1/\gamma_e}\right) \quad (21a)$$

$$\Pi_t = p_{ats}/p_{em} \quad (21b)$$

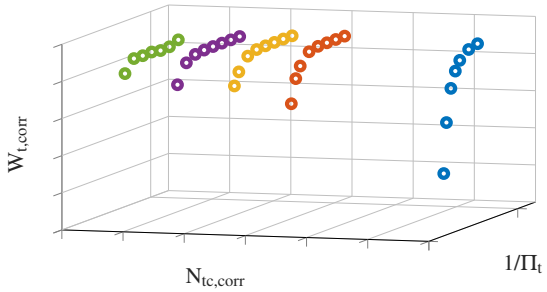

Figure 8. Drawn in circles is the corrected flow in the turbine map, dataset D. The data is plotted against corrected turbo speed $N_{tc,corr}$, and pressure ratio $1/\Pi_t$. Drawn in solid lines is the model $W_{t,corr} = k_0(1 - \Pi_t^{k_1})^{k_2}$ fitted to the different speed lines.

To obtain good accuracy, the square root turbine flow model (Eriksson and Nielsen, 2014) is used and extended with insights from the turbine map, dataset D. Figure 8 shows, drawn in circles, corrected flow $W_{t,corr} = W_t\sqrt{T_{em}}/p_{em}$, plotted against pressure ratio and corrected

turbo speed for dataset D, with constant coloring for constant turbocharger speed. For constant speed, the mass-flow model $W_{\mathrm{t,corr}} = k_0(1-\Pi_{\mathrm{t}}^{k_1})^{k_2}$ is fitted to the data. To settle upon flow equations, it is studied how the parameters k_0, k_1, and k_2 varies with turbocharger speed. A plot is shown in Figure 9, where circles show the value of the parameters for different speeds, and solid lines show different trend models. As is seen in the figure, k_1, and k_2, can be modeled as either linear or quadratic with reasonable results. The flow model is formulated as

$$W_{\mathrm{t,corr}} = k_0\left(1-\Pi_{\mathrm{t}}^{k_1}\right)^{k_2} \tag{22a}$$
$$k_0 = c_{00} + c_{02}N_{\mathrm{tc,corr}}^2 \tag{22b}$$
$$k_1 = c_{10} + c_{11}N_{\mathrm{tc,corr}} \tag{22c}$$
$$k_2 = c_{20} + c_{21}N_{\mathrm{tc,corr}} + c_{22}N_{\mathrm{tc,corr}}^2 \tag{22d}$$
$$N_{\mathrm{tc,corr}} = \frac{\omega_{\mathrm{tc}}}{\sqrt{T_{em}}} \tag{22e}$$

were c_i, $i = \{00, 02, 10, 11, 20, 21, 22\}$ are tuning parameters.

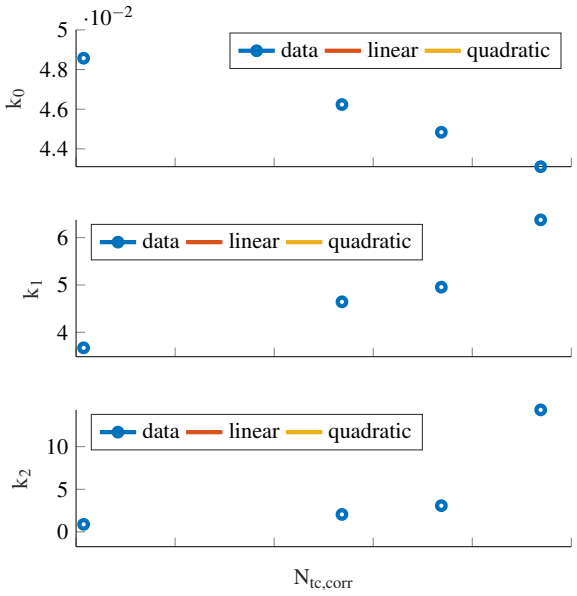

Figure 9. Circles show the evolution of parameters k_0, k_1, and k_2 plotted against turbocharger speed. Solid lines show first and second order polynomial models of the evolution.

The turbine efficiency is modeled based on the blade-speed-ratio (BSR), as defined in (Watson and Janota, 1982)

$$\mathrm{BSR} = \frac{\omega_{\mathrm{tc}} D_{\mathrm{t}}/2}{\sqrt{2c_{\mathrm{p,e}}T_{\mathrm{em}}\left(1-\Pi_{\mathrm{t}}^{1-\frac{1}{\gamma_{\mathrm{e}}}}\right)}} \tag{23}$$

Figure 10 shows the turbine efficiency of data set D plotted against blade-speed-ratio and corrected turbocharger speed. The data suggest the following model structure

$$\eta_t = \eta_{t,\max} - k_\eta(\mathrm{BSR}-\mathrm{BSR_{opt}})^2 \tag{24}$$

with parameters $\eta_{t,\max}$, k_η, and $\mathrm{BSR_{opt}}$ speed dependent, a fit to the different speed lines is shown in the same figure using solid lines.

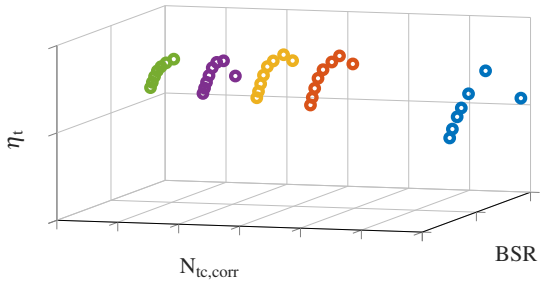

Figure 10. Circles show the turbine efficiency data from dataset D, plotted against corrected turbocharger speed, and blade-speed-ratio. Drawn in solid is a least fit of the model $\eta_t = \eta_{t,\max} - k_\eta(\mathrm{BSR}-\mathrm{BSR_{opt}})^2$ for each speed line.

Figure 11 shows the evolution of $\eta_{t,\max}$, k_η, and $\mathrm{BSR_{opt}}$ with respect to speed. The data suggest that modeling of $\mathrm{BSR_{opt}}$ could be linear or quadratic in speed. The model is formulated as

$$\mathrm{BSR_{opt}} = c_{\mathrm{BSR},0} + c_{\mathrm{BSR},1}N_{\mathrm{tc,corr}} + \tag{25a}$$
$$c_{\mathrm{BSR},2}N_{\mathrm{tc,corr,II}}^2 \tag{25b}$$
$$\eta_{\mathrm{t,max}} = c_{\eta_t,0} + c_{\eta_t,1}N_{\mathrm{tc,corr}} + c_{\eta_t,2}N_{\mathrm{tc,corr}}^2 \tag{25c}$$
$$k_\eta = c_{\mathrm{max},0} + c_{\mathrm{max},1}N_{\mathrm{tc,corr}} \tag{25d}$$

where $c_{\mathrm{BSR},0}$, $c_{\mathrm{BSR},1}$, $c_{\mathrm{BSR},2}$, $c_{\eta_t,0}$, $c_{\eta_t,1}$, $c_{\eta_t,2}$, $c_{\mathrm{max},0}$, and $c_{\mathrm{max},1}$ are model parameters.

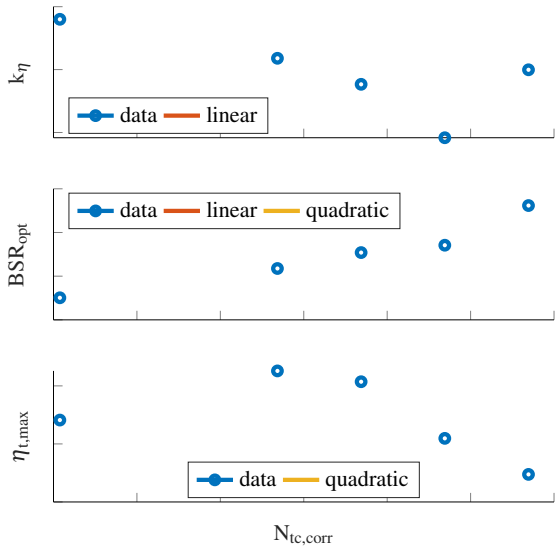

Figure 11. Circles show the evolution of parameters k_η, $\mathrm{BSR_{opt}}$, and $\eta_{t,\max}$ plotted against turbocharger speed. Solid lines show first and second order polynomial models of the evolution.

4.6 Wastegate

Modeling of the wastegate follows that of the throttle, and the mass flow is modeled as

$$W_{\mathrm{wg}} = \frac{p_{\mathrm{em}}}{\sqrt{R_{\mathrm{e}}\, T_{\mathrm{em}}}} C_{\mathrm{D,wg}} A_{\mathrm{wg,max}}\, u_{\mathrm{wg}}\, \Psi_{\mathrm{wg}} \tag{26}$$

The flow head parameter Ψ_{wg} is modeled in the same way as the throttle, with the difference that γ_{a} is replaced by γ_{e}, and pressure ratio Π_{thr} replace by Π_{t}.

4.7 Compressor

The compressor modeling follows that of (Llamas and Eriksson, 2017) and uses the accompanied open-source parametrization tool *LiU CPgui* (Llamas and Eriksson, 2018). The model is a high-fidelity control-oriented compressor model intended to capture a full set of operating conditions. Parameterization data is dataset C. The development of the model component goes beyond the scope of this paper, but the compressor model paper describes the model well, and together with the freely available parameters and parametrization tool, the process is well documented.

5 Energy optimal control

To test the effect of including the air-to-fuel ratio on the energy optimal control, an OCP is presented and solved for the two cases when the effect is included and excluded. The problem is first solved for the presented model, and then using a fixed γ_{cyl} model. γ_{cyl} is then set so that the two solutions have the same average value for $1 - 1/r_{\mathrm{c}}^{\gamma_{\mathrm{cyl}}-1}$. The problem consists of using the least amount of energy to increase engine torque from the initial operating point, $\mathscr{X}_0$, at 200 Nm, to a final operating point $\mathscr{X}_f$, at 2400 Nm, and over the duration of the transient output 1 MJ of work. The engine speed is fixed at 1200 RPM, and the end time t_f is a free parameter. Fuel power is defined as $P_{\mathrm{f}} = q_{\mathrm{HV}} W_{\mathrm{f}}$, and energy consumption is its integral. Engine power is defined as $P_{\mathrm{ice}} = M_{\mathrm{ice}} N_{\mathrm{ice}} \pi/30$ and engine work as $E_{\mathrm{ice}} = \int P_{\mathrm{ice}}$. The engine model is represented by the differential equation $\dot{x} = f(x,u)$, and to avoid soot formation, the air-to-fuel ratio is restricted: $\lambda \geq 1.3$. The problem is formulated as:

$$\begin{aligned}
\min_{t_f,u} \quad & q_{\mathrm{HV}} \int_0^{t_f} W_f \, dt \\
\text{s.t.} \quad & \dot{x} = f(x,u), \\
& x(0) = \mathscr{X}_0,\ x(t_f) \geq \mathscr{X}_f, \\
& [0,0,0]^{\mathrm{T}} \leq u(t) \leq [280,1,1]^{\mathrm{T}}, \\
& \lambda(t) \geq 1.3, \\
& M_{\mathrm{ice}}(t_f) \geq 2400 \text{ Nm}, \\
& E_{\mathrm{ice}}(t_f) \geq 1 \text{ MJ}
\end{aligned} \tag{27}$$

As the end time is a free parameter, the first solution (including the effect of the air-to-fuel ratio) results in the end time 6.5 s, and the second in 4.3 s. Longer lines (blue) thus represent the solution with the original dynamics, and shorter lines (red) the solution with γ_{cyl} fixed. The dashed line shows the smoke limiter value of 1.3. The solutions are presented in Figure 12. For completeness, the figure shows all states and controls except p_{c} and u_{thr} as the throttle remains fully open in both cases. Of particular interest is the engine efficiency, defined as $\eta_{\mathrm{ice}}(t) = P_{\mathrm{ice}}(t)/P_{\mathrm{f}}(t)$, the indicated efficiency η_{ig}, and the air-to-fuel stoichiometric ratio λ. The fixed γ_{cyl} model pushes against the smoke limiter which makes the turbocharger spin up faster, thus reducing transient time and increases work output. Notice that this does not impair efficiency when the effect of the air-to-fuel ratio is excluded from the indicated efficiency model. Because of the higher engine efficiency, the fixed γ_{cyl} model can complete the transient faster, using less fuel. The original model on the other hand is forced to maintain a higher air-to-fuel ratio to maintain good efficiency. The air-to-fuel ratio is lowered at the end, which meets the constraint of engine torque, and at the same time reduces engine efficiency. The results show that the energy optimal control is significantly influenced by the air-to-fuel ratio, both quantitatively and qualitatively, which demonstrate the importance of including this effect in the model.

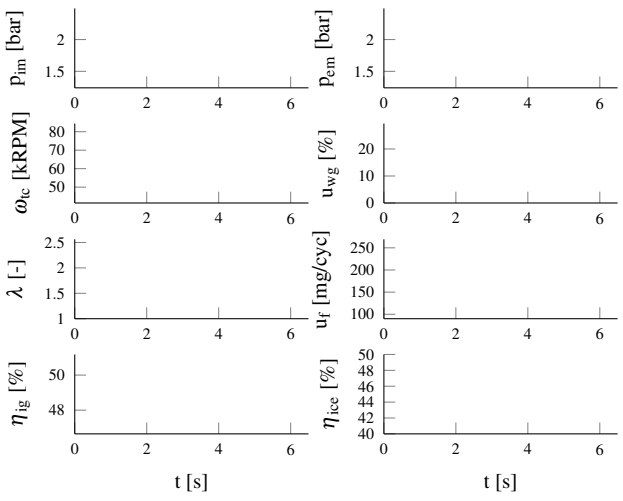

Figure 12. Solution to OCP (27). Longer lines (blue) show the solution to the problem for the presented model. Shorter lines (red) show the solution for a fixed γ_{cyl} model. The dashed line shows the smoke limiter.

6 Conclusions

A diesel engine model for energy optimal control is developed and documented, and available as open-source (Leek et al.). A method for estimating pressure sensor bias in experimental data is also presented. The model's intended use is to investigate the effect of the turbocharger selection on the energy optimal control. The model has a small number of states and controls to reduce the size of optimization problems. The dominating equations are based

on first principles for physically plausible extrapolation. The turbocharger model is detailed in order to accurately capture its effect on the air and fuel path dynamics. The engine efficiency model is dependent on the air-to-fuel ratio in order to include the effect of turbocharger dynamics on the combustion efficiency.

An optimal control problem is formulated and solved for the two scenarios of including the fuel-to-air ratio effect on the engine efficiency, versus excluding it. The results show that the air-to-fuel ratio has a significant quantitative and qualitative effect on the energy optimal transient control, and is an important aspect of turbocharger selection. This indicates that the model is fit for its intended use, but as the paper shows, the model's areas of use goes beyond that and to make it useful to others the development of the model is presented in full.

Acknowledgment

The work was financed by the *Swedish Agency for Innovation Systems* under the program LINK-SIC. The authors would like to thank Scania, especially Erik Höckerdal, Henrik Höglund and Björn Johansson for modeling discussions and data.

References

Joel Andersson. *A general-purpose software framework for dynamic optimization*. PhD thesis, Arenberg Doctoral School, KU Leuven, 2013.

Uri M Ascher and Linda R Petzold. *Computer methods for ordinary differential equations and differential-algebraic equations*, volume 61. Siam, 1998.

Jonas Asprion, Oscar Chinellato, and Lino Guzzella. Optimal control of diesel engines: Numerical methods, applications, and experimental validation. *Mathematical Problems in Engineering*, 2014.

John T Betts. *Practical methods for optimal control and estimation using nonlinear programming*. SIAM, 2010.

M. Diehl, H. G. Bock, H. Diedam, and P. B. Wieber. Fast direct multiple shooting algorithms for optimal robot control. *Lecture Notes in Control and Information Sciences*, 340:65–93, 2006. ISSN 01708643. doi:10.1007/978-3-540-36119-0_4.

Moritz Diehl. Numerical optimal control. Technical report, KU Leuven, 2011.

Kristoffer Ekberg, Viktor Leek, and Lars Eriksson. Modeling and validation of an open-source mean value heavy-duty diesel engine model. *Simul. Notes Eur.*, 28(4):197–204, 2018.

Lars Eriksson. Mean value models for exhaust system temperatures. *SAE Transactions*, pages 753–767, 2002.

Lars Eriksson. Modeling and control of turbocharged SI and DI engines. *Oil & Gas Science and Technology-Revue de l'IFP*, 62(4):523–538, 2007.

Lars Eriksson and Lars Nielsen. *Modeling and control of engines and drivelines*. John Wiley & Sons, 2014.

Lars Eriksson, Simon Frei, Christopher Onder, and Lino Guzzella. Control and optimization of turbocharged spark ignited engines. *IFAC Proceedings Volumes*, 35(1):283–288, 2002.

Gamma Technologies. GT-Power User's Manual. *GT-Suite Version 6.1*, 2004.

John B Heywood. *Internal combustion engine fundamentals*. McGraw-Hill Education, 1988.

Robin Holmbom and Lars Eriksson. Analysis and development of compact models for mass flows through butterfly throttle valves. Technical report, SAE Technical Paper, 2018.

Viktor Leek, Kristoffer Ekberg, and Lars Eriksson. LiU Diesel II - An open-source mean value engine model. Available at. `https://www.vehicular.isy.liu.se/Software/LiUDiesel2/`.

Xavier Llamas and Lars Eriksson. Control-oriented compressor model with adiabatic efficiency extrapolation. *SAE International Journal of Engines*, 10(4), 2017.

Xavier Llamas and Lars Eriksson. LiU CPgui: A toolbox for parameterizing compressor models. Technical report, Linköping University, SE-581 33, Linköping, Sweden, 2018.

Giorgio Mancini. *Automotive diesel engine transient operation: modeling, optimization and control*. PhD thesis, Università di Bologna, 2014.

Jorge Nocedal and Stephen Wright. *Numerical optimization*. Springer Science & Business Media, 2006.

Anil V Rao. A survey of numerical methods for optimal control. *Advances in the Astronautical Sciences*, 135(1):497–528, 2009.

Tielong Shen and Akira Ohata. Modeling and control design for automotive engines-with matlab engine simulator cd-rom. *ISBN 978e-4-339-04610-6*, 2011.

Martin Sivertsson and Lars Eriksson. Modeling for optimal control: A validated diesel-electric powertrain model. In *SIMS 2014-55th Scandinavian Conference on Simulation and Modelling*, pages 49–58. Linköping University Electronic Press, 2014.

Vaclav Smil. Diesel engine at 120 [numbers don't lie]. *IEEE Spectrum*, 54(2):24–24, 2017.

Johan Wahlström and Lars Eriksson. Modelling diesel engines with a variable-geometry turbocharger and exhaust gas recirculation by optimization of model parameters for capturing non-linear system dynamics. *Proceedings of the Institution of Mechanical Engineers, Part D: Journal of Automobile Engineering*, 225(7):960–986, 2011.

Neil Watson and Marian Janota. *Turbocharging the internal combustion engine*. Macmillan International Higher Education, 1982.

Intelligent Micro Grid Controller Development for Hardware-in-the-loop Micro Grid Simulation Subject to Cyber-Attacks

Mike Mekkanen Tero Vartiainen Kimmo Kauhaniemi Duong Dang

School of Technology and Innovation, University of Vaasa, Finland, {mike.mekkanen,tero.vartiainen, kimmo.kauhaniemi,duong.dang}@uwasa.fi

Abstract

This paper develops Hardware-in-the-loop (HIL) simulation against cyber attacks. We design a light-weight intelligent electronic device (IED) that performs Micro Grid Controller (MGC), interfaces are developed based on International Electrotechnical Commission (IEC) 61850 GOOSE protocol from/to the real-time simulation and the MGC. They are executed on two equipment stages, Field Programmable Gate Array (FPGA) and BeagleBoneBlack. CSIL versus CHIL tests are used to evaluate the Micro Grid (MG) behavior against different cyber attacks. We also evaluate the MGC designed control function in accordance with IEC 61850 GOOSE protocol. The results show that the light-weight MGC approach and data modeling of various IEC 61850 predefined data objects, data attributes and logical nodes (LNs) are correct for the design of the power balance control/protection function against cyber attacks in various cyber-attack case studies.

Keywords: Microgrid controller, co-simulation, EC61850, next-generation power system, real time simulator, cyber attack, HIL, IED.

1 Introduction

Renewable energy is considered as one of the solutions to stop global warming, and it has become the fastest-growing energy source in many countries (Dang and Vartiainen 2020; Dang et al., 2021; Eurostats, 2020). Due to the extensive integration interconnected of renewable plants (e.g., wind and solar) and other conventional generators (e.g., coal, oil), intelligent MGCs play very important roles in effectively controlling resources and loads that connect to MGs. For instance, in this study the developed MGC provides the power balance management between generation and consumption within the MG in a dynamic manner. Also, a controller can help to maintain the power balance of a medium voltage network within the limit settled by a distribution system operator.

Therefore, there is increasing interest in MGC's topics (Rajesh et al., 2017). For example, literature has focused on modelling, developing and implementing MG controllers (c.f., Colet-Subirachs et al., 2012; Li et al., 2004; Ruiz-Alvarez et al., 2012; Sen and Kumar, 2018; Ustun et al., 2012; Zia et al., 2018). Also, pilot cases for various types of MG are studied by using early-stage MG controllers with vendor-defined characteristics (Liu et al., 2016). However, although MG standards have been published, the standardization of MG controllers is still under development (Sirviö et al., 2020). Based on the state of the art of standards and up-to-date products, it is argued that there are many issues related to MG controllers' product standards. For example, MG controllers' issues that are related to the interoperability of various systems and functions from different vendors (Baillieul et al., 2016; Reilly and Joos, 2018). Moreover, requirements for the MG controller at the point of interconnection (POI) are established by the standards (Reilly et al., 2017), in which the balance between power generations and loads consumptions (e.g., MG management) is one of the most important requirement for MG controllers that need to be acquired and offered. One possibility can be seen due to the requirements (set by the DSO) of power balance at the connected/Islanded MG situation under different circumstances (e.g., cyber-attack) in (Zhang et al., 2019).When developing and testing the operation of MG and MG controller functions, those issues should be taken into account. The test setup in (Zhang et al. 2019), is based on the software-in-the-loop (SIL) MGC, however, the hardware-in-the-loop (HIL) testing is left for the developer.

Due to these issues, this research aims at developing a controller for MG HIL simulation against cyber-attacks. As a result, we develop MGC from a preliminary computing algorithm that needs to be implemented at a designed light-weight intelligent electronic device (IED). Interfaces are developed based on the IEC 61850 standard GOOSE protocol in the real-time simulation and test platform.

The paper is organized as follows. In Section 2 we illustrate the network development scenarios of the 25-kV medium voltage distribution network MG. Then, Section 3 presents the design light-weight IED with the preliminary power balance control algorithm, as well as IEC 61850 interfaces by libiec61850 library and C

language. Next, Section 4 presents the MGC operation within the CHIL simulations in the real-time simulation platform. The conclusions and discussions are presented in Section 5.

2 Development of MG and Testing Scenarios

A cutting-edge Real-Time Simulator (RTS) is a digital model-based test system that can precisely mimic the reaction of an actual physical system in real time. This digital replica of the actual physical system (digital twin) has been confirmed to be a valuable tool in power system research and studies for several decades. For example, a digital twin helps reduce test stresses on the actual physical system as well as hazardous work. Moreover, it enables the simulation model to interact with external hardware or control algorithms in such a way that external IED does not recognize that the received data is coming from a simulation model rather than actual physical system.

This work studies a MG 120kV grid-connected distribution feeder that can be islanded by opening the point of common coupling (PCC) circuit breaker and operating autonomously as developed in (Zhuang, 2012). The single line diagram of a MG and the cyber-physical structure are depicted in Figure 1. MG assets and their characteristics are depicted in Table 1.

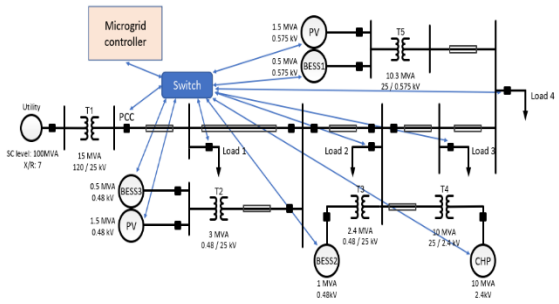

Figure 1: MG single line diagram and the cyber-physical structure, blue lines show the communication links that every MG node entity (DERs, loads, CB, etc.) send measurements, status to the MGC and received controlling signal from the MGC based on GOOSE IEC 61850 standard protocol.

Table 1 MG assets and loads

Asset	Type	Ratings	Operation Modes
Loads			
Load1	Critical	4MW	Always connected
Load2	Critical	4MW	Always connected
Load3	Hybrid	4MW	Can be disconnected on second priority
Load4	Non-Critical	3MW	To be disconnected in Islanded mode
Distributed Energy Resources (DERs)			
Combined Heat and Power (CHP) plant	Gas Turbine	10MW	P/Q (Grid-connected) V/f (Grid forming)
2 x PV Generation System	With Smoothing Battery Energy Storage System	1.5MVA + 0.5MVA (1.2MWh)	MPPT with smoothing battery
3x Battery Energy Storage System (BESS)	Lead Acid	1MW (5MWh)	Power smoothing

The MG is a 25-kV medium voltage distribution network connected to a 120 kV sub-transmission system by means of a 15 MVA delta-wye transformer. The MG consists of 6 DERs, including two 1.5 MVA PV systems, three energy storage systems (ESS) (two of which are 500 kVA ESSs with 1.15 MWh capacity; one is a 1 MVA ESS with 5 MWh capacity), and one 10 MVA CHP unit. The MG also has four aggregated loads: the first two are critical loads rated at 4 MW, the third is a 4 MW priority load, and the fourth is a 5 MW non-critical load. The model does not include relay elements, which are beyond the scope of this study, there is no underlying protection scheme. Each MG asset is linked to a measurement subsystem, which is based on voltage and current measurements; a subsystem measurement component is programmed to produce P, Q, and Vrms measurements. These measurements from the measurement subsystems are sent to the MGC via IEC 61850.

We use the developed computing/controlling algorithm to extract and process those useful measurements from the received GOOSE messages within the MGC. The MGC is designed to provide power balance (calculates the total power generation and the total load consumptions) and manages the dispatch of the assets and load shedding of the non-critical load in the event of islanding. If the difference between the total power generation and the total load consumption exceeds 3MW for any MG actions or attacks, the controlling algorithm output (dispatching signal) will be sent back to the model via additional new GOOSE messages to shed off the non-critical load. In (Zhang et al., 2019) simulates and tests a simple rule-based MGC on the same model using SIL. In contrast, in this paper, we use HIL to test the developed from scratch intelligent external MGC, which is left for the developer. We develop and run two scenarios to

analyze/measure the MG behavior/resiliency of the MG cyber-physical simulation against cyber attacks. In addition, we gain testing results for our developed MGC IED-based design computing algorithm and the MGC interfaces data model's compliance with the IEC 61850 standard.

2.1 Scenario 1: MG Islanding Operation Mode Against a delay attack on Load Shedding Trip

In the first scenario, the MG will be islanded in second 1, in this case the MGC will check the power balance and implement the power balance operation emergency condition (the difference not exceeds 3MW). If the check emergency condition becomes true, the MGC attempts to immediately disconnect the sheddable Load 4 to maintain the MG stability. Be that as a delay attack is introduced to the GOOSE trip command packets sent from the MGC to Load 4, the load shedding function may fail to operate in the required timeframe. In this case this will cause severe unbalance between generation/load relationship and oscillations on MG nominal operation parameters such as e.g., frequency, voltages etc. It may also result in severe consequences like a blackout. Through the C code available delay function within the MGC initial code, a one-second delay attack is applied to the MGC GOOSE message command. Secure Shell (SSH) terminal window is opened to control the MGC and monitor, record the MG physical system's reaction parameters. Wireshark network analyzer/sniffing tool is used for the same purpose, because the interfaces in the HIL test need to be implemented over a physical communication network, such as physical adapters, Ethernet switches, cables, etc.

2.2 Scenario 2: MG Steady State Islanded Operation Mode Against Man-in-the-Middle attack

MGC based on its normal operation will receive measurements that are sent from each MG assists via GOOSE. Be that as a Man-in-the-middle attack is introduced to the load measurements data. Before the load measurements data being received by MGC. The data is manipulated in the middle of its way to the MGC. In this case, the MGC may take incorrect actions based on these received non-critical measurements. According to the test scenario 2, the active power measurement from Load 2 is duplicated by applying a packet manipulation attack to the GOOSE message. In this case, the MGC will take the incorrect action (false tripping) because it perceives the controlling operation emergency condition is true (total load will be more than 3MW greater than the total generation). As a result, a trip command is sent to disconnect Load 3. It also causes oscillations on MG nominal operation parameters such as e.g., frequency, voltages etc.

Comparison between both achieving testing results, SIL and HIL will be made within the rest of this work.

3 Design the light-weight MGC IED

The following describes the development process of the light-weight MGC that will be implemented as CHIL. The development process begins with the creation of an IEC 61850 Substation Configuration Description (SCL) file and its adaptation to two distinct hardware platforms: the BeagleBone Black (BBB) and the Field Programmable Gate Array (FPGA). The concept behind using these boards is based on their low cost, flexibility, support for various interfaces/protocols, I/O pins, and ease of configuration. Within the SCL file, we create the MGC object-oriented data model, which includes selected logical nodes (LN), data objects (DO), and data attributes (DA)s that are appropriate for handling and processing measurements data from the "field," in our case study, data come from the simulation model. In addition, we create and configure the GOOSE control blocks (GCB)s. To build the GCB, GOOSE datasets need to be created. This data set will include all the data attributes that need to be associated with the publishing of the MGC GOOSE messages. We finalize the GCB configuration by configuring the interfaces' GCB parameters such as GOOSE ID, GOOSE configuration revision, GOOSE publishing MAC address, GOOSE subscribing MAC address etc., as illustrated in Figure 2. In particular, the right side of Figure 2 shows the hierarchy structure of the developed MGC IED, including the communication IED section, list of the LNs, list of the GCBs and the list of the data sets. Whereas at the left side of Figure 3, it shows the list of the data attributes that includes the "OV2PTOV" GOOSE data set. These DAs will hold the measurements-status published from the DERs, loads and CBs, within the MG simulation model.

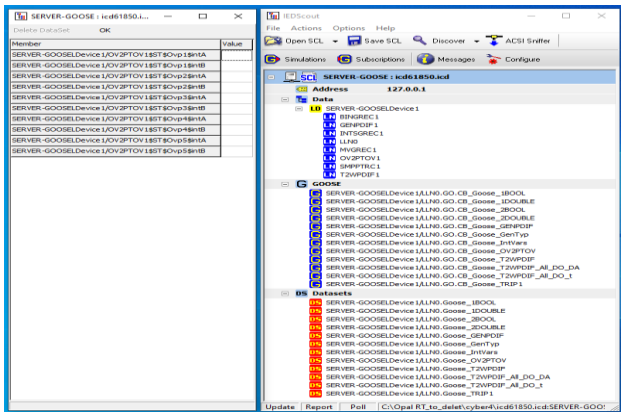

Figure 2. MGC SCL file

At this point the configured SCL file is used to create two files (static_model.c and static_model.h) by

generating source codes (libiec61850 n.d.:61850). The file static_model.c contains the definition of the data structures that build up the IED data model and also contains pre-configured values that are provided by the SCL file. The file static_model.h is intended to be included by the designed project code and defines handles that we can use for efficiently accessing the data model. According to the "model generator" process, each type of IED data model can be mapped directly to a C data structure, resulting in a hierarchy of C data structure. Besides, the generated C files must be accompanied by the platform-specific code to ensure consistency with IEC 61850. Consequently, MGC controlling power balance function in C language was developed in a way that complies with software-in-the-loop (SIL) preliminary algorithms developed by Opal HYPERSIM Power Systems (libiec61850).

The MGC controlling power balance function based on its operation, it needs to subscribe to the GOOSE messages that have been sent from the model with the associated measurements. After a successful subscription by the MGC, it needs to extract these measurements, and run the control function. At this point, the output of the control function based on the assigned emergency conditions that are explained earlier, are True or False. If it is True, the MGC needs to go to step, which is publishing a new GOOSE message that needs to be subscribed by the model. According to this GOOSE message an open CB command is sent. Then, it will return back to the previous step. Whereas, if the output is False, the MGC will send a heartbeat GOOSE messages without any changes. The procedure for designing the "lightweight" MGC HIL controller with all processing steps is presented in Figure 3.

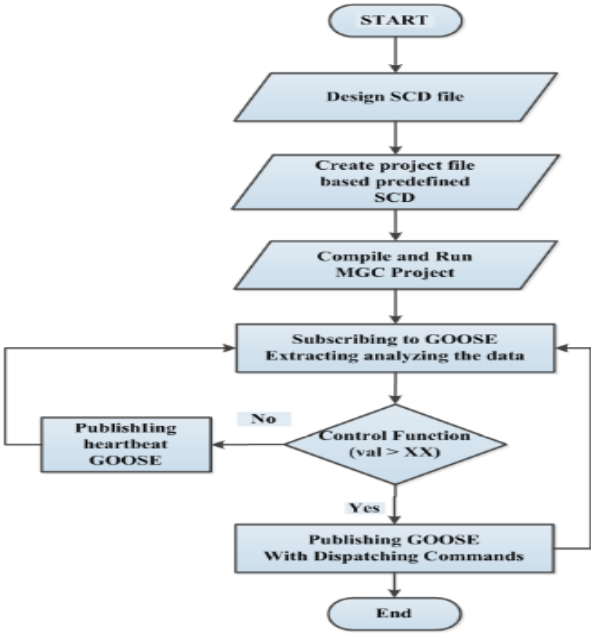

Figure 3: MGC development processing

The testing results will be presented in the next section of this manuscript.

4 CSIL and CHIL Testing Results

4.1 CSIL Testing Results

The workflow of the development of the real-time co-simulation platform consists of use cases development, closed-loop real-time simulations, light-weight MGC IED development, IEC61850 communication implementation, the CSIL, and the CHIL tests. At the beginning and according to the first CSIL scenario test, the MG power system is modeled and MGC is developed and both are implemented via Opal HYPERSIM software as illustrated in Figure 4 and Figure 5. Whereas, the IEC 61850 communication system is emulated in EXata software from Scalable as illustrated in Figure 1. Going into details of the HYPERSIM and EXata simulation/emulation models blocks/elements is out of the scope of this work.

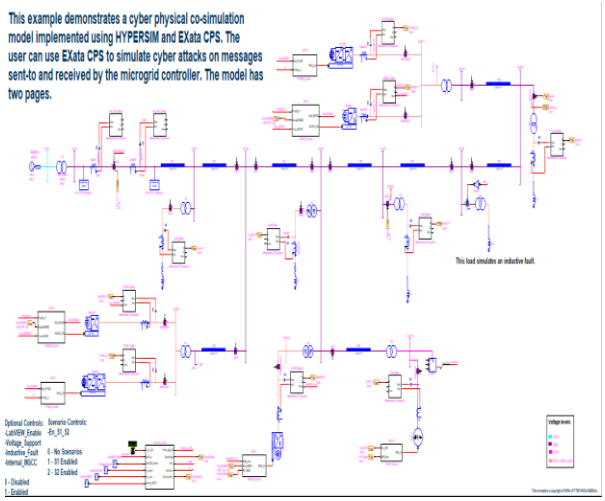

Figure 4. Opal HYPERSIM power system model

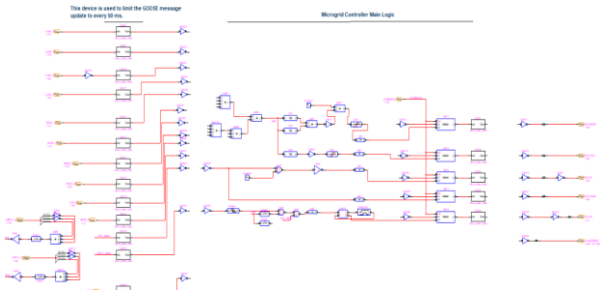

Figure 5. Opal HYPERSIM MGC model as SIL

As the MG goes to islanded mode after one second, the MGC sends a shedding command to load 4 via GOOSE messages in order to fulfill the emergency condition requirements. The results for the first case study are shown in Figure 6, MG returns to power balance after one second that appears in the upper part of Figure 6. Since we did not apply the delay attack yet as shown in the lower part of Figure 6, the sending and

receiving MGC single to shed load 4 is just an overlap which validates the fact that EXata is not adding more delay time within the communication system emulation and implementation.

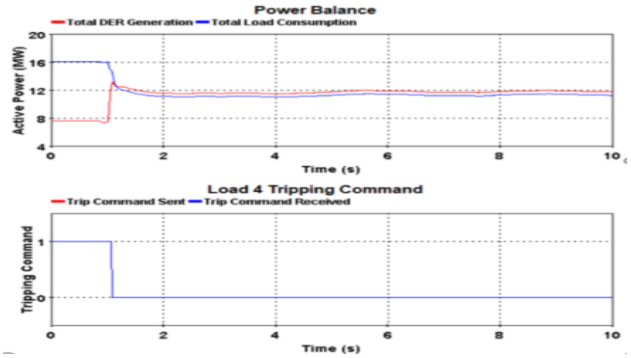

Figure 6. LabVIEW GUI in Opal HYPERSIM scenario 1 normal operation

Whereas, according to the second case study in the first scenario, we implement 1-second delay as a delay attack to MGC signal. Figure 7 illustrates the MG unbalance situation based on this attack, the MG took more time to return back to the balance mode as shown in the upper part of the figure. In the lower part of the figure, the MGC sends the trip command, however based on the attack it will be received by the IED that controls the load 4 CB after 1-second in which it affects the MG operation parameters such as f, V, power Quality, etc.

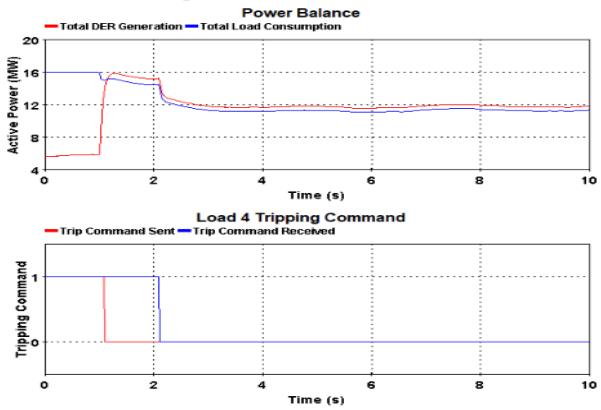

Figure 7. LabVIEW GUI in Opal HYPERSIM scenario 2 delay attack implemented to MG, lower figure shows the (red line) is the original trip signal sent from the MGC to shed off load 4 after the grid is islanded in second one, which it is in time. Whereas the (blue line) is the delayed signal. Trip command sent by the MGC is delayed by one second after we apply the cyber delay attack to the controller signal. Upper picture shows the MG unbalance operation that took a long period (more than 2 seconds).

According to the second scenario, the MG is islanded and in normal operation mode as illustrated in Figure 8. In the first case study, load 2 and load 3 are operated within their nominal operation values that consumes power around 4MW.

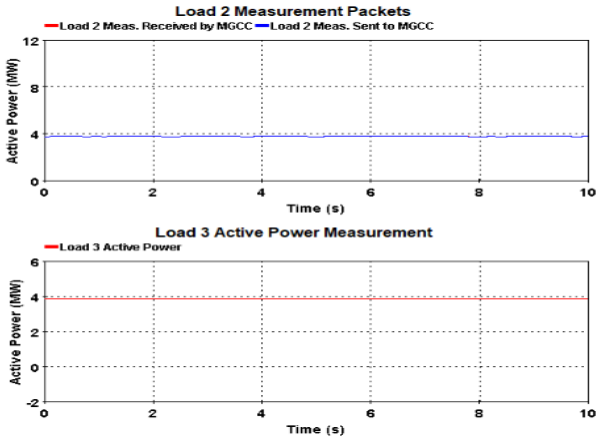

Figure 8. LabVIEW GUI in Opal HYPERSIM scenario 2 normal operation

Whereas, after applying the Man-in-the middle attack to load 2 measurements in its way before it was received by the MGC. Figure 9 illustrates the load 2 measurements manipulation in which it doubled the load 2 power consumption (read curve) as shown in the upper part of the figure 9. In the lower part of the figure 9, it shows load 3 active power consumption that fluctuate between (0 - ≈4MW) based on disconnecting and connecting modes, and the unbalance between the total power generation and total power consumption according to the attack. In addition, this situation also affects other MG operation parameters such as f, V, power quality, etc. that may lead to severe instrument damages or large blackouts.

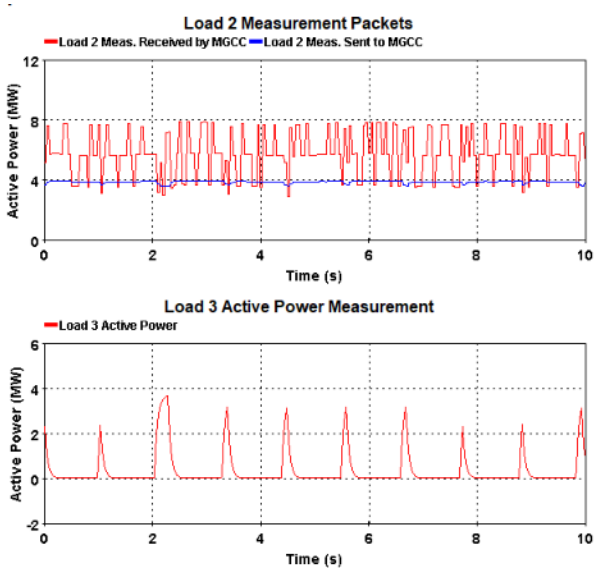

Figure 9. LabVIEW GUI in Opal HYPERSIM scenario 2 man-in-the-middle attack implemented to MG. Upper figure shows load 2 measurements (red curve) are manipulated before they are received by the MGC based on executing the man-in-the-middle attack, (blue curve) is the normal load 2 measurements before executing the attack. Lower figure shows the load 3 active power consumption which fluctuates between (0 and 4MW) since it is connected and disconnected to the grid based on executing the man-in-the-middle attack.

4.2 CHIL Testing Results

For the second part of this work, we show the HIL test and the testbed setup that is illustrated in Figure 10.

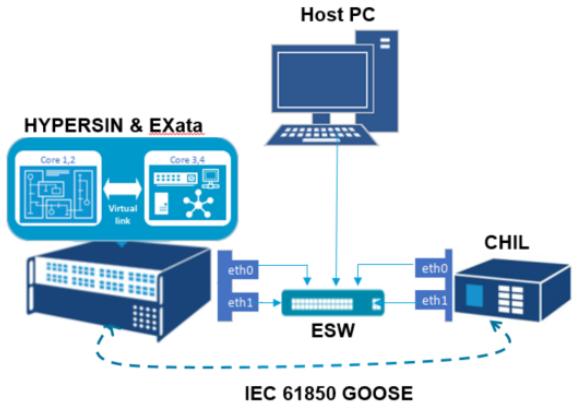

Figure 10. HIL testbed setup

According to the test setup principals, the light-weight MGC is developed that compliance with the IEC 61850 standard, the developed power system model within the HYPERSIM is upgraded and configured, in which the GOOSE publisher will use the physical adapter rather than the virtual adapter to publish the GOOSE messages over the designed communication network as illustrated in Figure 11. RJ45 cables are used to link the test instruments through the Ethernet switch.

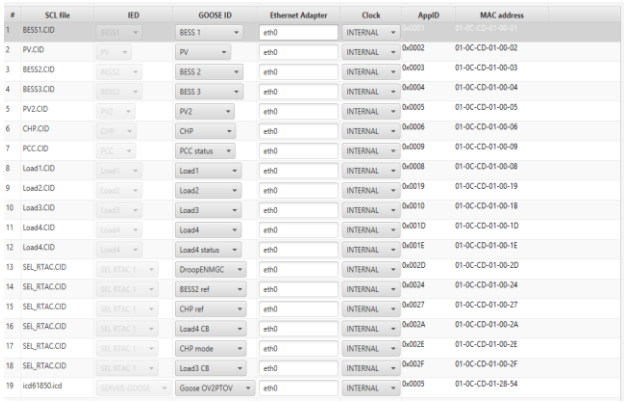

Figure 11. Opal HYPERSIM I/O configuration

The light-weight MGC SSH terminal is used to execute and run the develop MGC project within the microcontroller boards based on Linux environment. Table 1 in Appendix, shows the MGC that has been successfully subscribed to the GOOSE messages published from the real-time simulator. In addition, it shows the tenth measurements that were extracted from the received GOOSE messages. All these extracted parameters are printed out to be shown on the output of the MGC control terminal. As well as, Wireshark sniffing tool is used to capture the GOOSE traffic and also analyzes the tenth measurements associated within the captured GOOSE messages.

Different cyber attacks are implemented within the CHIL test procedure. The first case study is to measure the 1-second delay attack effects on the MG behavior. This delay attack is implemented within the MGC C code. While the second case study in order to simulate the Man-in-the-middle attack, we duplicate load 2 measurements by multiplying the measurements by two before sending it to the MGC. The MGC will extract the manipulated value from the attacked GOOSE message, and implement the check emergency condition in C code. In this case, MGC will send a dispatching command to disconnect load three to fulfill the emergency condition requirements. More analysis of the MGC GOOSE messages received data and discussion should be performed. Appendix Table 1 presents Scenario 1 CHIL data, which will be published as part of the study's continuation. Furthermore, different types of attacks, defender risk assessments, etc., will be tested in the future.

5 Conclusions

The development and performance of an MGC against cyber attack control schemes have been implemented in this paper. These are done by design and deployed on a light-weighted intelligent IED. The MGC control solution and its relevant communication system have been designed in compliance with the IEC 61850 and executed on two equipment stages, FPGA and BeagleBoneBlack. CSIL versus CHIL tests are used to evaluate/assess the MG behavior against different cyber attack scenarios. Moreover, we also evaluated IEC 61850 GOOSE protocol implementation, processing and finally control action performance. The obtained results demonstrate that the light-weight MGC approach and data modeling of various IEC 61850 predefined data object LNs are correct for the design of the power balance control/protection function against cyber attack. In addition, they demonstrate the successful implementations of the designed control/protection function and the modeled MGC LNs in various cyber-attack case studies on reliable detection of the emergency condition. Further work on the analysis of the data received by MGC, implementation of different cyber attacks and power balance detection algorithms is needed to validate the feasibility of the developed approach.

Acknowledgments

This study was partly funded by the European Regional Development Fund and the Regional Council of Ostrobothnia.

References

John Baillieul, Michael C. Caramanis, and Marija D. Ilik. Control Challenges in Microgrids and the Role of Energy-Efficient Buildings. *Proceedings of the IEEE* 104(4):692–96, 2016. doi: 10.1109/JPROC.2016.2532241.

Colet-Subirachs, Alba, Albert Ruiz-Alvarez, Oriol Gomis-Bellmunt, Felipe Alvarez-Cuevas-Figuerola, and Antoni Sudria-Andreu. Centralized and Distributed Active and Reactive Power Control of a Utility Connected Microgrid Using IEC61850. *IEEE Systems Journal* 6(1):58–67, 2012. doi: 10.1109/JSYST.2011.2162924.

Duong Dang, and Tero Vartiainen. Changing Patterns in the Process of Digital Transformation Initiative in Established Firms: The Case of an Energy Sector Company. *PACIS 2020 Proceedings,* 2020.

Duong Dang, Tero Vartiainen, and Mike Mekkanen. Towards Establishing Principles for Designing Cybersecurity Simulations of Cyber-Physical Artefacts in Real-Time Simulation. *Proceedings of the International Conference on Information Systems Development (ISD),* 2021.

Eurostats. Wind and Water Provide Most Renewable Electricity. Retrieved May 10, 2021 (https://ec.europa.eu/eurostat/web/products-eurostat-news/-/ddn-20210108-1), 2020.

Yunwei Li, D. M. Vilathgamuwa, and Poh Chiang Loh. Design, Analysis, and Real-Time Testing of a Controller for Multibus Microgrid System. *IEEE Transactions on Power Electronics* 19(5):1195–1204, 2004. doi: 10.1109/TPEL.2004.833456.

libiec61850. *Libiec61850*.

Guodong Liu, Michael R. Starke, and Andrew N. Herron. *Microgrid Controller and Advanced Distribution Management System Survey Report*. ORNL/TM-2016/288. Oak Ridge National Lab. (ORNL), Oak Ridge, TN (United States), 2016. doi: 10.2172/1287035.

K. S. Rajesh, S. S. Dash, Ragam Rajagopal, and R. Sridhar. A Review on Control of Ac Microgrid. *Renewable and Sustainable Energy Reviews* 71:814–19, 2017. doi: 10.1016/j.rser.2016.12.106.

Jim Reilly, Allen Hefner, Brian Marchionini, and Geza Joos. *Microgrid Controller Standardization: Approach, Benefits and Implementation*. Cleveland, OH, 2017.

Jim Reilly, and Geza Joos. Microgrid Controller Standards for Integration and Interoperability. AIM, 2018.

Albert Ruiz-Alvarez, Alba Colet-Subirachs, Felipe Alvarez-Cuevas Figuerola, Oriol Gomis-Bellmunt, and Antoni Sudria-Andreu. Operation of a Utility Connected Microgrid Using an IEC 61850-Based Multi-Level Management System. *IEEE Transactions on Smart Grid* 3(2):858–65, 2012. doi: 10.1109/TSG.2012.2187222.

Sachidananda Sen, and Vishal Kumar. Microgrid Control: A Comprehensive Survey. *Annual Reviews in Control* 45:118–51, 2018. doi: 10.1016/j.arcontrol.2018.04.012.

Katja H. Sirviö, Mike Mekkanen, Kimmo Kauhaniemi, Hannu Laaksonen, Ari Salo, Felipe Castro, and Davood Babazadeh. Accelerated Real-Time Simulations for Testing a Reactive Power Flow Controller in Long-Term Case Studies. *Journal of Electrical and Computer Engineering* 2020: e8265373, 2020. doi: 10.1155/2020/8265373.

Taha Selim Ustun, Cagil Ozansoy, and Aladin Zayegh. Modeling of a Centralized Microgrid Protection System and Distributed Energy Resources According to IEC 61850-7-420. *IEEE Transactions on Power Systems* 27(3):1560–67, 2012. doi: 10.1109/TPWRS.2012.2185072.

Lixi Zhang, Shijia Li, Lloyd Wihl, Mehrdad Kazemtabrizi, Syed Qaseem Ali, Jean-Nicolas Paquin, and Simon Labbé. Cybersecurity Study of Power System Utilizing Advanced CPS Simulation Tools. *White Paper, OPAL* 13, 2019.

Davy Zhuang. Real Time Testing of Intelligent Relays for Synchronous Distributed Generation Islanding Detection. McGill University, Montréal, Québec, Canada, 2012.

Muhammad Fahad Zia, Elhoussin Elbouchikhi, and Mohamed Benbouzid. Microgrids Energy Management Systems: A Critical Review on Methods, Solutions, and Prospects. *Applied Energy* 222:1033–55, 2018. doi: 10.1016/j.apenergy.2018.04.103.

Appendix

The following Table 1. shows the part from Scenario 1 CHIL test measurements. In this table, columns 2-5 (e.g., Load1 to Load 4) shows the loads active power consumption, while columns 6-11 (e.g., BESS1, PV2, NESS3, PV1, CHP, BESS2) illustrates the DERs active power generation all in Watts. Moreover, columns 12-13 (e.g., PCC, load4) presents the status of the PCC and load 4 circuit breakers, while column 14 (e.g., Time s) shows the time stamp in second. Here, each data object collects three data attributes for each parameter (Val, q, t) i.e., and they are encapsulated in the GOOSE message data set. Row 6 illustrates the first islanding that is implemented in 0.692 s by disconnecting the MG by changing PCC status to true (islanded), whereas load 4 CB will be shed in 0.742 s since at this point no delay attack is implemented. In a similar vein, row 36 shows the MG that is reconnected to the grid and load 4, it is also reconnected and starts consuming active power and column 4 starts showing measurements.

#	Load1	Load 2	Load 3	Load 4	BESS1	PV2	BESS3	PV1	CHP	BESS2	PCC	load4	Time s
1	3875128	3781908	3848320	4745503	324750	12391	313977	657533	5051008	901410	0	1	0.0
2	3886356	3801598	3867824	4767855	259598	12483	298115	657889	6063510	918955	0	1	0.042
3	3895487	3816629	3883259	4787274	274980	12601	377263	658062	7273871	917240	0	1	0.242
4	3875302	3774808	3840516	4734144	247771	12376	426814	653924	6496688	876106	0	1	0.442
5	3628191	3564326	3625103	4470147	263691	16993	441651	637882	7891500	838352	0	1	0.592
6	3765598	3749752	3827546	1686397	248053	23351	461370	631774	10581547	834129	1	1	0.692
7	3909675	3902159	3986019	620417	245663	12185	469602	632663	10463299	804188	1	0	0.742
8	3974832	3972181	4058661	83989	277405	13576	477779	640318	10418736	701015	1	0	0.842
9	3890752	3891604	3976228	11382	255274	13001	300181	639228	10458335	576783	1	0	0.942
10	3826802	3825120	3908149	1550	251834	12469	322624	638311	10355982	451723	1	0	1.042
11	3732894	3727222	3808487	33	245095	11622	391792	637551	10235066	213576	1	0	1.242
12	3690010	3682557	3763187	4	256227	11291	425556	636786	10221290	50770	1	0	1.392
13	3641555	3632102	3711959	0	246946	11559	459342	636631	10287160	16591354	1	0	1.642
14	3633773	3623783	3703827	0	264419	11588	468186	636659	10321279	16508713	1	0	1.742
15	3590677	3583693	3663737	0	257502	11815	297380	636543	10566320	16331793	1	0	1.992
16	3598518	3590426	3670833	0	269892	11909	320684	637715	10613529	16271080	1	0	2.092
17	3609756	3600123	3681195	0	262805	12193	376833	639748	10676801	16190208	1	0	2.242
18	3619217	3608758	3690369	0	255081	12704	416467	640535	10742324	16121152	1	0	2.392
19	3625488	3614647	3696720	0	262562	12717	435432	640812	10775080	16080759	1	0	2.492
20	3626222	3615002	3696941	0	246758	12848	449834	641852	10813148	16045081	1	0	2.592
21	3632638	3621064	3703834	0	268585	13121	469777	643488	10851610	15984287	1	0	2.792
22	3632638	3621064	3703834	0	268585	13121	469777	643488	10851610	15984287	1	0	2.942
23	3626697	3614814	3697480	0	269335	13077	487092	643417	10894398	15908551	1	0	3.142
24	3620534	3608708	3690556	0	253137	12728	492642	642716	10922676	15872675	1	0	3.392
25	3625170	3613655	3695241	0	262391	12730	495402	642562	10947493	15851677	1	0	3.592
26	3635648	3624687	3705456	0	246261	12075	497503	641979	11015321	15833760	1	0	3.842
27	3652699	3642308	3723380	0	261976	11988	498563	641891	11061342	15826077	1	0	3.992
28	3663804	3653738	3734697	0	262258	12213	499013	643486	11097553	15822607	1	0	4.092
29	3682987	3676505	3757403	0	261760	11780	340178	660614	11322578	15817035	1	0	4.392
30	3730492	3723068	3804667	0	246047	12057	416973	676022	11389880	15816532	1	0	4.642
31	3756276	3748616	3830909	0	247682	12198	450782	678971	11427376	15819407	1	0	4.842
32	3744688	3740558	3822954	0	261123	12726	295332	681969	11538362	15825974	1	0	5.042
33	3767777	3761076	3844537	0	270543	12807	383797	687555	11489827	15832647	1	0	5.292
34	3766261	3758344	3841976	0	247153	13027	430778	691158	11444541	15840773	1	0	5.492
35	3420712	3026410	3097530	0	254640	12482	431382	574554	13162528	15900753	1	0	5.592
36	3481128	3080810	3142453	2461343	261153	55416	446532	558530	14976107	15913154	0	1	5.642
37	3695901	3437038	3499438	4124898	248874	12305	296997	640848	8820065	16028727	0	1	5.742
38	3284208	2808361	2857941	3503537	233906	6080	305507	676664	18641205	16206118	0	1	5.842
39	2185473	951665	971935	1210253	170248	16739997	316376	654396	8566525	16347311	0	1	5.992
40	2524608	1476101	1511032	1878933	194460	37169	287098	656788	9263116	16118254	0	1	6.142
41	3003512	2307134	2348593	2904624	216277	890	383725	678090	16462531	16358187	0	1	6.392
42	2183750	947049	966862	1204584	166107	16739091	373027	654642	7105342	16475085	0	1	6.492
43	3365212	2888729	2940613	3631400	229022	5964	478575	685109	15257266	16526335	0	1	6.842
44	2679160	1799928	1833785	2272158	219546	56372	453296	670359	16689547	16598107	0	1	6.942
45	2033099	674768	691849	867267	153846	16725867	422931	645703	4613850	16511752	0	1	7.142
46	2241362	1029269	1054758	1316209	175922	16732549	446194	651958	4286363726	16350067	0	1	7.442
47	3490675	3052096	3109465	3840381	245479	4538	527203	687073	792295	16504408	0	1	7.642
48	3362295	2907956	2960414	3655672	256122	5806	510359	692531	17456987	27897	0	1	7.842
49	3211773	2675600	2725831	3368524	282416	2211	503972	690994	19365029	16742147	0	1	7.992
50	3583477	3274431	3333838	4113662	244491	7432	517104	699436	15932444	16606684	0	1	8.092
51	3605799	3319334	3377019	4166183	244917	9007	508935	700682	15919332	16479252	0	1	8.242
52	3077862	2492068	2538611	3137973	229706	247	489138	695139	4284319804	16716571	0	1	8.442
53	3599355	3349466	3410801	4208360	249106	9223	512640	705241	12373359	410397	0	1	8.642
54	3930460	3927243	3995515	4924185	248776	13423	304915	711150	13442109	718635	0	1	8.842
55	4636077	4653300	4747321	2098696	268523	23734	275530	717507	15092822	729369	1	0	9.092
56	5005018	5031641	5136746	104749	267168	17947	257677	719715	14089063	576036	1	0	9.242
57	4857688	4882122	4983069	2030	277816	16448	255330	713545	13722050	358826	1	0	9.442
58	4616189	4635409	4730578	83	266288	15154	260752	701329	13175867	157475	1	0	9.642
59	4251829	4262130	4349867	12	253596	13391	280713	695326	12272546	16681857	1	0	9.942
60	4134640	4140856	4226667	7	254309	12547	317121	693895	11928201	16611125	1	0	10.042
61	3930348	3929973	4012176	3	269399	11678	389496	692142	11314555	16488264	1	0	10.242
62	3787650	3782931	3862756	1	250291	10521	431577	690397	10939397	16386566	1	0	10.442
63	3703386	3695994	3774444	0	246741	10379	456955	689842	10732796	16302856	1	0	10.642

Level measurements with computer vision - comparison of traditional and machine learning computer vision methods

Eirik Døble, Sindre Haugseter, Christian Mikkelsen, Jørgen Bang Sneisen, Nils-Olav Skeie, Ole Magnus Brastein*

Department of Electrical Engineering, Information Technology and Cybernetics
University of South-Eastern Norway, N-3918 Porsgrunn,
*(ole.m.brastein@usn.no)

Abstract

In this work, modern machine learning methods are compared against traditional image processing techniques, for the purpose of estimating the level of coffee beans in a transparent tank fitted to a coffee machine. Measurements using both approaches are compared against manual level measurements. The resulting algorithm are analysed for repeatability under scene variations, such as orientation of the tank with respect to the camera and the distribution of coffee beans. *Keywords: Level measurement, computer vision, image segmentation, ResNet34*

1 Introduction

1.1 Background

Level measurements is important for a large number of applications in both industry, science and the commercial sector (Bentley, 2005). Popular measurement technologies include guided radar, ultrasonic, capacitance and flotation based sensors principles (Bentley, 2005). In many cases, it is desirable to apply a non-intrusive sensor principle. One possible solution which has received significant scientific interest in recent years is the use of digital cameras together with advanced, typically machine learning (ML) based, algorithms (Goodfellow et al., 2016). This technology has a large range of possible applications, including the non-intrusive level measurement of substances in a partially transparent tank.

In this work, the system of interest is a coffee machine that has been outfitted with an industrial robotic arm. The goal of the project, originating from Bouvet Consulting in Porsgrunn, is to create an *AI barista*. One aspect of this project is to measure the level of coffee beans remaining in the tank of the coffee-machine. Since the machine is a common-of-the-shelf model, there is no level measurement sensor built in. However, as is typically the case for such devices, there is a transparent inspection window which allows users to visually estimate the level of coffee beans in the tank. The facility for visual inspection, together with the obvious need to ensure safe human consumption of the produced coffee, makes the use of vision based sensor technology particularly interesting.

1.2 Previous work

There have been several published works on using computer vision for level estimation for liquids, which is arguably easaier then the granular coffee beans studied in this work. Zepel et.al. used open-source libraries (Numpy, OpenCV, and PySerial) for liquid level monitoring and control in common continuously stirred tank reactor processes. They used Canny Edge detection in order to locate strong horizontal edges to detect the liquid-air interface, and perform decisions to control the pump(s) for manipulating the liquid level. They found that the method gives acceptable results when using computer-vision as part of an autonomous platform to monitor experimental factors and make control decisions. (Zepel et al., 2020).

In (Eppel and Kachman, 2014) a general computer vision method for the recognition of liquid surfaces and liquid levels in various transparent containers is presented. They concluded that making a general recognition method for liquid systems is possible and that it can be achieved with good accuracy in various cases. The best indication of the liquid surface was found to be the relative intensity change, the edge density change and the gradient direction relative to the curve normal.

2 Methods

2.1 Machine learning vs traditional computer vision algorithms

The field of computer vision has experienced a paradigm shift over the last two decades (Goodfellow et al., 2016). The application of machine learning (ML), and in particular multilayer artificial neural networks (ANN), known as *deep learning*, has revolutionised what is possible to achieve with computer vision (Goodfellow et al., 2016), leading to the use of computer vision in many new application. While machine learning certainly has had a profound effect on the computer vision field, there are still much use for non-learning algorithms as well. In many applications, the traditional image processing methods may indeed be advantageous because they tend to be faster w.r.t. execution time.

Before presenting the methods of interest in this work it is instructive to discuss the fundamental difference

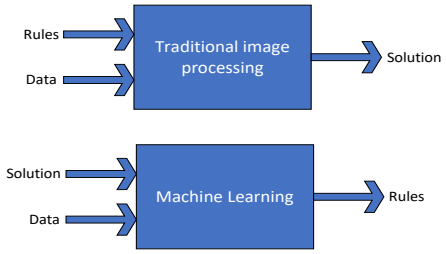

Figure 1. Comparing traditional image processing with machine learning

between the two approaches to image analysis. Before the advent of ML, image analysis was conducted by constructing algorithms using various developed standard techniques, such as filtering and gradient computations (Bradski and Kaehler, 2008). Most analysis tools uses a series of such steps to compute a result. The common denominator for these techniques is that the algorithms consist of a set of rules that describe how an image should be processed to produce an analysis results or solution (Bradski and Kaehler, 2008). In some applications, engineering these rules turns out to be very difficult. Consider the textbook case of distinguishing images of cats and dogs, it is difficult to imagine manually constructing a set of rules that can compute the probability of an image containing a particular animal based solely on the pixel values.

As shown in Fig. 1, machine learning turns the approach to image analysis, and indeed data analysis in general, around. Rather then *engineering* the rules needed to produce a solution, relevant *input data* is coupled by a *desired solution* (Goodfellow et al., 2016; Kuhn and Johnson, 2013). Subsequently, algorithms are used to identify *patterns* between input data and the desired solution. The identified patterns can be considered as *machine generated rules* which in turn is applied to new images in order to compute the desired result (Goodfellow et al., 2016; Kuhn and Johnson, 2013). Naturally, rules generated by a computer by pattern recognition is not necessarily similar in formulation to the rules or instruction steps used in traditional computer vision algorithms, but their use is the same; computing a solution or analysis result for new images of the underlying system of interest.

2.2 Machine learning using fastai

The ML framework of choice in this project is *Fastai* which was created by the Fast.ai organization (Howard and Gugger, 2020). The motivation for developing the framework is to provide a practical approach to machine learning, where the idea is to start learning by doing practical work instead of first requiring a deeper theoretical knowledge of the intricacies of ML. The fastai framework is based on PyTorch (Paszke et al., 2019) and gives the PyTorch library an extra layer of functionality using the API's by offering high-level API's which makes it easier to get started with machine learning.

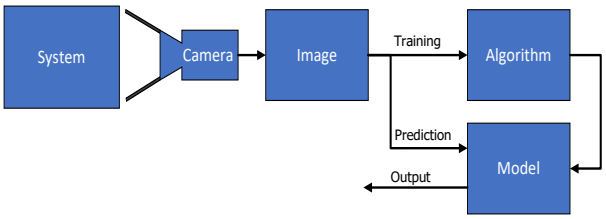

Figure 2. Machine learning and prediction with images

2.2.1 Image classification and segmentation

A fundamental goal of many computer vision analysis algorithms is to *label* the content of an image (Goodfellow et al., 2016). Two distinctly different approaches towards applying labels to various parts of an image are known as *classification* and *segmentation* (Bradski and Kaehler, 2008). Both methods use an algorithm to train a *model* from the images. After a model has been trained, new images is sent to the model and an output is given, as shown in Fig. 2.

In *classification* objects in the image are analysed and labelled as belonging to one of many pre-determined classes, often together with an estimated probability accuracy of the class label being correct (Bradski and Kaehler, 2008; Goodfellow et al., 2016). A class can be, for example, a car, a cat, a house, etc. When training a classification model, a large number of images are pre-labelled and sorted according to the class of object they contain, typically arranged in different folder in the filesystem. The output of an image classifier is a region, typically rectangular, in the input image together with a label that classifies the content of that region.

In contrast, image *segmentation* does not detect discrete objects, but rather seeks to determine non-uniform regions in the image which belong to a particular pretrained class (Bradski and Kaehler, 2008). As such, segmentation can arguably be considered a type of classification, but instead of classifying the object in the image, *each single pixe*l is labelled depending on what class it most likely belongs to. When training a segmentation model, each pixel in the training image is labelled by a class id, typically using different shade of grey in an overlaying image known as a *mask* (He et al., 2016; Deng et al., 2009). By coupling a mask with a training image, the machine learning algorithm learns the pattern that connects image content with segment class. When the trained segmentation model is applied to a new image it will assign a class label to every pixel, such that neighbouring pixels of the same class form an image segment. The segmented image can then be further analysed to locate objects and boundaries like lines and curves in an image.

2.2.2 Estimating tank level from an image

In this work, image segmentation is used to estimate the level of coffee beans in a transparent tank. After applying the segmentation model on a new image, the method outputs a tensor of same dimensions as the input image,

where each tensor element constitutes a class label for the pixel in the corresponding image.

All the training images used in this project are tagged by manually creating masks with three classes: COFFEE, EMPTY_TANK and BACKGROUND. When a new image is segmented using the resulting trained model, the output is a tensor array of the same dimensions as the input image, containing the identified classification of each pixel.This tensor is used to calculate the level in the coffee bean container using:

$$Level\,[\%] = \frac{N_{\text{coffee}}}{N_{\text{coffee}} + N_{\text{tank}}} \tag{1}$$

where N_{coffee} and N_{tank} is the number of pixels after image segmentation classified as belonging to the segments COFFEE and EMPTY_TANK, respectively. The underlying assumption of this approach is that the camera is positioned such that the 2D projection of the coffee tank onto the image sensor produces an image, where the region consisting of coffee beans relative to that of the complete tank, e.g., the empty tank plus the coffee beans, is proportional to the coffee volume of interest. While this assumption is true for the approximate rectangular tank used for this work, a more complex geometry may require a second regression model to be trained in order to estimate the actual volume from the projected 2D regions in an image (Goodfellow et al., 2016; Kuhn and Johnson, 2013).

2.2.3 Transfer learning

Transfer learning (TL) was first introduced in (Bozinovski and Fulgosi, 1976) where they describe a mathematical and geometrical model of TL (Bozinovski, 2020). TL is a method in machine learning where knowledge gained in one task is exploited to improve generalization in different but related task (Goodfellow et al., 2016). For example, knowledge gained from recognizing a car could be used when learning to recognize a truck. TL is a popular approach in computer vision and natural language processing tasks because it can train neural networks with comparatively little data with shorter training time than when training from scratch. In most real-world problems it is difficult to obtain a large number of labelled data points for training of complex models. Hence, a pre-trained model is beneficial. In Computer vision, it is common for the neural network to first find edges in the first layers, general shapes in the middle layers, and finally task-specific characteristics for the last layers. In TL, the first and middle layers are transferred to the new model, while only the last layers must be re-trained. The main advantages of TL is shorter training time, less training data, and in most cases better performance (Bozinovski, 2020).

2.2.4 ResNet

The ML model of choice in this work is a Residual Neural Network (ResNet), which is a continuation of a convolutional neural network (CNN) that has become a popular model for computer vision in the recent years (He et al., 2016). To further improve on the CNN method, the ResNet adds skip connection or shortcuts to jump over some layers. ResNet models typically implements double- or triple- layer skip connections. A weight matrix can be used to find the skip weights in models known as HighwayNets. The skip connections help to avoids the troublesome vanishing gradient problem, which occurs in CNN which preventing further training.

The ResNet model used for this project is ResNet-34 which consist of a network with 34 layers (He et al., 2016). The ResNet-34 model was pre-trained using the ImageNet dataset which consists of millions of pre-labeled images (Deng et al., 2009). Larger networks are better at complex problems but are easy to overfit, takes longer to train and use more memory than smaller networks. Hance, ResNet-34 was chosen because its performance to accuracy trade-off was satisfactory for the problem. Other neural networks like AlexNet, GoogLeNet, DenseNet and SqueezeNet was tested but based on initial experimentation the ResNet-34 model appears to perform adequately for the task.

2.2.5 Model training

The ResNet-34 model was repeatedly re-trained with an increasing number of training images, until a satisfactory result was reached at only 93 images. The relatively low number of training images needed to achieve satisfactory performance shows the strength of using transfer learning on a pre-trained model.

A common method for increasing the variation in the training set artificially is to apply randomised transformations to training set. Examples of transformations are: changing the image size, flipping, rotating, or adding Gaussian blur. By increasing the variation of images in the training set the resulting model will be able to handle a greater variance in images used as inputs when predicting results.

2.3 Traditional approach using OpenCV

The traditional approach to computer vision, i.e., prior to the advent of ML methods, is to construct the algorithms using a sequence of processing steps, typically using a selection of standard computations such as computing gradients, filtering, global or local thresholding, and morphological transformations (Bradski and Kaehler, 2008). These operators are applied to produce new images, typically of the same dimensions in height and width but not necessary the same bit-depth. Input images are typically RGB encoded bitmaps of bit-depth 8, but many other formats exist. Often, building the software for image capture and conversion into the required format requires considerable work (Bradski and Kaehler, 2008). A sequence of capturing and processing steps is often denominated as a *pipeline* in the computer vision field.

One of the main advantages of traditional computer vision algorithms is that the *image operators* , i.e., mathematical processing steps, that is used to build up higher

level algorithms are well known and understood (Bradski and Kaehler, 2008). Hence, there exist highly optimised implementations of these steps. Arguably, the most popular library of such optimised computation methods is the *Open-Source Computer Vision Library (OpenCV)* (Bradski and Kaehler, 2008). As an open-source library, the framework consist of contributions from many of the worlds leading experts in computer vision. Since OpenCV is widely used, its methods and syntax is commonly understood and recognised by software engineers in the field, which helps to speed up the development of new applications (Bradski and Kaehler, 2008). OpenCV supports the programming languages C ++, Python, Java and Matlab, and all major operating systems, e.g., Windows, Linux, Mac OS, and Android.

In this work, OpenCV is used to analyse the images of the coffee bean tank and subsequently provide an estimate of the level of coffee beans. Two promising methods of interest towards this goal is the use of segmentation by *binary thresholding* or edge detection using the *Canny Edge Detection* algorithm. Note that OpenCV also contains several ML based approaches, but in this work it is the non-learning methods in OpenCV that are of primary interest.

2.3.1 Binary threshold

OpenCV supports numerous thresholding functions (Bradski and Kaehler, 2008), including a simple *binary threshold* with or without inversion, i.e., pixels above threshold can be defined as either high (white) or low (black) in the output image.

The simplest thresholding method compares every pixel in the frame against the pre-determined threshold l_{coffee}. In the output image, each pixel value is set depending on being above or below the threshold. If the intensity of the pixel $f_{x,y}$ is greater than that given threshold value l_{coffee}, the output image pixel $\tilde{f}_{x,y}$ will be set to black, e.g., a greyscale value 0 and white or greyscale 255 otherwise, according to:

$$\tilde{f}_{x,y} = \begin{cases} 0, & f_{x,y} > l_{\text{coffee}} \\ 255, & otherwise \end{cases} \quad (2)$$

The application of a threshold assumes that the region of interest can be distinguished from the background by the intensity of the pixel alone. One difficulty with applying this method is choosing an appropriate threshold value, since this value is highly dependant on the scene and lighting conditions.

While the application of the threshold computation is straight forward, building an algorithm around thresholding requires the application of several additional image operators to pre-process the image. In this work, the image is first converted to greyscale by averaging the RGB values of each pixel. Next, a Gaussian blur step is used to smooth the image and reduce the influence of noise on the thresholded image, before finally applying the threshold step. Further, as illustrated in Fig. 3, the

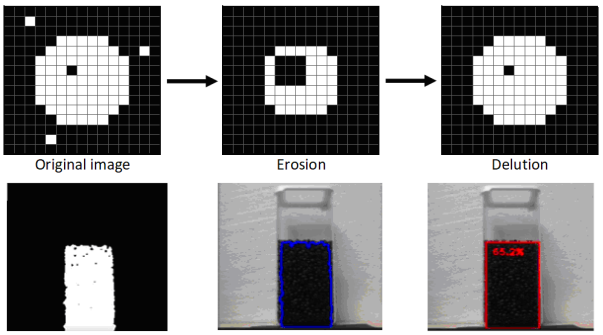

Figure 3. Binary threshold post processing steps.

output of the threshold step is post-processed by the morphological transformations *erosion* and *dilation*, which together forms the operation known as *opening*, to further reduce image noise. The output of the morphological transformation is a binary image where, assuming appropriate threshold value, the coffee bean area is marked as white. The last two steps of the algorithm is to find the contour of the thresholded region and finally fit a rectangle around it. Since the width of the tank is known apriori, the coffee bean level can be estimated from the height vs width ratio of this identified rectangle. A weakens of this approach is that it neglects the possibility of uneven distribution of coffee beans. However, this shortcoming could easily be remedied in future work by either fitting a polygon or multiple rectangle slices across the width direction.

2.3.2 Canny edge detection

Canny Edge Detection (CED) is an algorithm that can be used to detect edges in an image (Bradski and Kaehler, 2008). CED is a multi-step algorithm which consist of the following steps:

1. Noise reduction with a Gaussian filter
2. Finding the intensity gradient compares a pixel's value against its neighbouring pixels and outputs a new image where the larger difference in intensity equates to a higher pixel value
3. Non-maximum Suppression is used to thin the edges
4. Hysteresis thresholding is used to connect neighbouring pixels into a consistent edge

The CED algorithm was tested for the purpose of identifying the edges of the tank and the edge between the two mediums: coffee beans and air. However, the binary threshold algorithm was found to provide more consistent results, hence in the sequel only the binary threshold method is discussed further .

3 Experimental setup

An experimental rig, consist of a wooden plate where a Logitech C922 camera and the coffee tank are mounted, was constructed in order to get repeatability in the pictures w.r.t. camera angle. The camera angle was chosen such that the flat top of the coffee container would not disturb

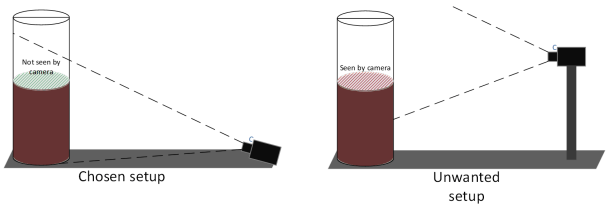

Figure 4. Experimental setup

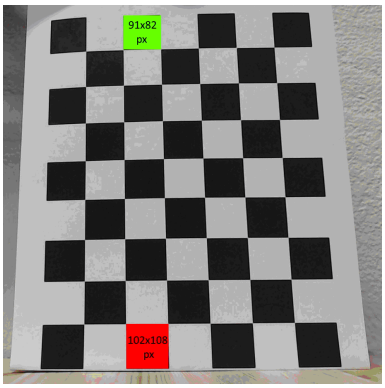

Figure 5. Image shows a A4 25x25mm calibration chessrboard.

the measurement, as shown in Fig. 4. This is because of the method used for measuring level is effectively measuring the area that is in the cameras field of view (FOV).

To get enough variety in the background of the pictures the rig was positioned with different walls in the background, and some black paper was used to show that black does not automatically mean 'coffee' for the ML model. The ideal scenarios are a plain light-coloured background with little disturbances, even lighting, and little to no reflection.

3.1 Perspective distortion

Due to the position of the optical sensor in relation to the tank, as shown in Fig. 4, the captured images are somewhat affected by perspective distortion, which will influence the measured area. As shown in Fig. 5 a rectangle of a given size will occupy a bigger pixel area the further down in the image that it is projected. Observe also that, due to a slight lens distortion effect, the rectangles are not completely square. Compensating for these factors would be recommended for future work and is achievable by standard OpenCV methods.

4 Results and discussion

4.1 Model training

Once the fasai framework is configured and the training images loaded, the model training process consist of repeatedly calling the *fit_one_cycle* method, which advances the model training one iteration, or epoch as is the denomination used in the ML literature. The method returns the loss and accuracy metric in the form of a table for the current training stage. Since segmentation is used to estimate the coffee level, the loss function compares pixel gradients in the training pictures and masks, as discussed in Sec. 2.2.2. To determine the ML model's performance loss, the predicted output is compared with the target value, and the deviation between these determines the loss values, where a large deviation gives a high loss value.

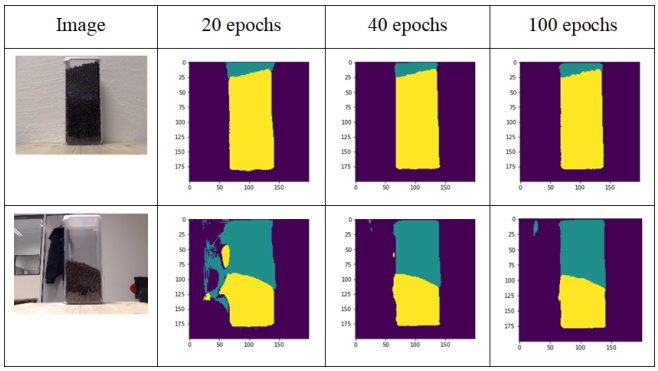

Figure 6. Training with increasing number of epochs. Segments are labeled as coffee (yellow), empty tank (cyan), and background (purple).

The amount of training needed varies from the complexity of the task. Some examples of different situations are shown in Fig. 6. In the first row, an ideal scene configuration with even lighting, little reflection and no noise in the background is shown. Here the machine learning model finds satisfactory results already after just 20 epochs. A more challenging scene is shown on the second row, where a dark jacket is introduced in the background. With only 20 epochs of training, the ML model struggles to differentiate the dark jacket from the container with coffee. At 40 epochs the prediction is much better, and at 100 epochs of training the prediction is close to perfect. This result shows that more complex scene configurations are more challenging to segment and therefore require a more intensively trained ML model. Further, this results shows that it is important to have a variety of scene configurations in the training data since the ML model can only be expected to accurately estimate the image segmentation of images that are similar to the training set used to build the model.

4.2 Optimal scene conditions

The ideal scene configuration is a plain light-colored background with little disturbances providing good contrast with the coffee beans, even lighting, and little or now reflection from the transparent tank. In this situation both OpenCV and fastai detects the area with coffee beans with acceptable accuracy. The mean error from ten different predictions gives fastai an error at 0,7% and OpenCV 3,0% as the results in Fig. 7 and Table 1show. The estimated level accuracy for both methods is considered well within acceptable range for the purpose of a coffee robot.

Note that both methods failed to estimate the level to 0% if the tank is empty, due to how the level is computed

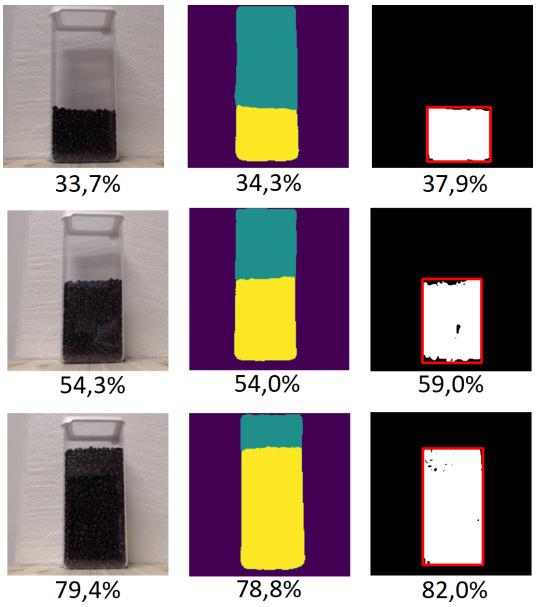

Figure 7. Results of applying both methods under optimal conditions (left: raw image, middle: ML result, right: threshold result).

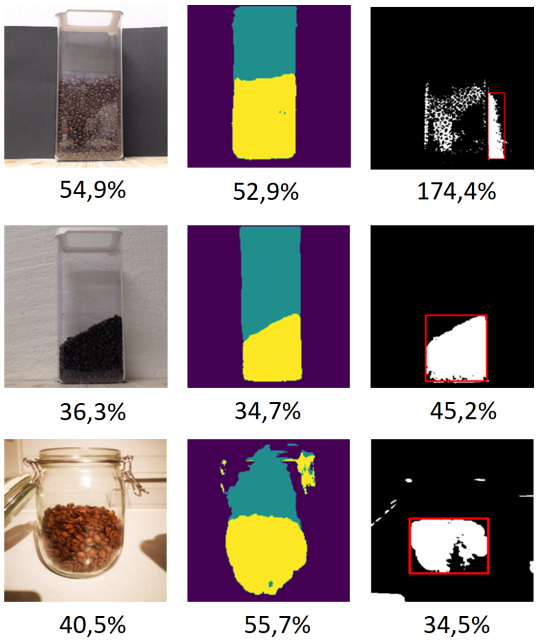

Figure 8. Results of both methods under challenging conditions (left: raw image, middle: ML result, right: threshold result).

from the image analysis results.

4.3 Challenging scene conditions

Figure 8 shows some examples of more challenging scenarios. In the first row a black sheet of paper was added to the background to test if the models could differentiate dark background from the coffee beans. The results show that fastai still segments the coffee accurately, except for a small strip with a lot of reflection on top of the coffee beans. In contrast, the binary threshold method failed completely due to the pre-determined threshold value no longer being suitable for the captured image. The dark background caused the camera to automatically turn up the light sensitivity, which made the coffee too light to be within the threshold. For future work all automatic functions on the camera, like light sensitivity, should be turned off to secure better control over the images.

The second row shows a near ideal scenario, but with the coffee slanted. Here, Fastai also obtains an accurate level estimate while the threshold based method significantly overestimate the level. Since the ML method post processing counts all the marked pixels, while the threshold based method draws a rectangle around the extreme points in the largest contour and find the height from a width to height ratio, the latter is unable to account for an uneven coffee distribution and will therefore always overestimate the level in such conditions. A solution for future work would be to draw a polygon around the coffee instead of a rectangle.

Table 1. Comparing analysis results under ideal conditions.

Ref [%]	ML [%]	Err [%]	OCV [%]	Err [%]
15.2	14.7	0.5	14.6	0.6
25.2	26.4	1.2	26.7	1.5
33.7	34.3	0.6	37.9	4.2
44.3	44.3	0.0	45.8	1.5
54.3	54.0	0.3	59.0	4.7
62.1	62.1	0.0	65.1	3.0
72.0	71.0	1.0	74.3	2.3
79.4	78.8	0.6	82.0	2.6
97.2	96.3	0.9	102.3	5.1
Mean error		0.7		3.0

The images in the third row of Fig. 8 contains a completely different container than used in in the training data. One of the problems with this scene is that the top surface of the coffee is visible, which violates the assumption discussed in Sec. 4. The coffee beans in the picture are also a much lighter colour which further complicates the choice of threshold value. The fastai model, despite the rather large deviation of this particular scene configuration compared with the training images, successfully segmented out the coffee beans. Only some areas around the lid were misclassified. The estimation error of 15% is largely caused by the image violating the assumption of camera angle w.r.t. the coffee surface in the jar being visible. While the threshold method apparently produced a prediction error of only 5%, this result is simply random and must be rejected as false. Since the ratio between the height and the width of the container is different from the assumed tank geometry, the post processing of threshold based method cannot produce reliable results without adapting the assumptions to the new container.

A common challenge encountered in many of the experiments performed in this work is the sensitivity to reflection on the container. The reflections affect the results

on both fastai and the threshold method, resulting in inaccurate level calculations. In fastai the reflections will in some cases be interpreted as the container instead of the coffee beans behind the reflection. In the threshold method the reflection brightness makes the algorithm neglect part of the coffee area as it is brighter than the coffee beans not covered by a reflection.

4.3.1 Adapting to changes in the image scene

As discussed in Sec. 4.3, performing level estimation on an image which deviates from the reference images can cause the level prediction to fail or miscalculate the level. These disturbances and deviations are typically changes in the container geometry, challenging light conditions, colour schemes, reflections, shadows, or new structures in the background.

The fastai model is only capable of accurate segmentation on images that are similar to the training images. However, it can be retrained for new deviations or disturbances, which is done by adding images containing the new conditions to the training set. Next the model is trained through several epochs to prodiuce a new model. The existing training data should be preserved and is used as a starting point when a model is trained with new conditions. This process of adding new data to the training set and subsequently re-training the model is arguably similar to process of creating a new model using transfer learning on the general ResNet-34 model.

In the threshold based method, the expected scene is more closely tied to the chosen method parameters, i.e., the tank geometry and threshold values, which must be set for each specific scenario. Since the threshold value is more highly dependant on light conditions and colour, it is necessary to manually set new threshold values by trial and error. An alternative for future work could be to detect the threshold automaticity by further utilising apriori knowledge of the scene, such as the expected approximately rectangular shape of the coffee area, or indeed the expected location of the coffee beans in the projected image.

The difference in manual labour needed when updating the methods for new conditions or deviations, shows the versatility and adaptability of the fastai training methods compared to the more traditional threshold based method. When compensating for disturbances fastai will retain all previous scenarios, while the threshold method is configured for using specific settings for each scenario.

4.4 Repeatability under experimental variation

To test the *repeatability* of the computer vision based level estimation methods, two experiments were preformed. First, the tank is rotated such that the images are captured from 10 different angles in the range 0 to 90 deg. Next, the beans were repeatedly removed and replaced in the tank to test different distributions of coffee beans. Both experiments used the exact same amount of coffee beans, and consist of 10 repeated images captured with no more than one changing experimental variable for each experiment.

Table 2. Repeatability under altered viewing angle.

	OpenCV [%]	Fastai [%]
Average	59.6	56.4
Std.dev.	4.59	2.04
Max.dev	12.1	3.01

Table 3. Repeatability under altered coffee distribution.

	OpenCV [%]	Fastai [%]
Average	59.6	58.03
Std.dev.	3.39	2.39
Max.dev	8.44	5.67

4.4.1 Rotating tank - altered viewing angle

The results of the first experiment, shown in Table 2, shows that the standard deviation of the thresholding based method is more than twice that of the ML based method. This can be explained by how the threshold method post process the binary output image under the assumption of a known tank geometry height/width ratio. When viewing the tank at an angle, the assumed tank geometry differs significantly from the observed image projections, hence the estimated level is incorrect. In contrast, the ML method segments the tank directly, thus capturing the effective projected width of the tank from any angle, thereby producing accurate estimates level estimates also under varying viewing angles.

4.4.2 Refilling tank - altering distribution of coffee beans in tank

The results of the second repeatability experiment, shown in Table 3, shows that both methods are somewhat robust against the distribution of coffee in the tank. As in the previous experiment, the ML method shows lower estimation errors, but only marginally so for the second experiment. The error in the threshold method is mostly driven by the assumption of a rectangular coffee region, i.e., the use of a fitted rectangle around the detected thresholded region. If an alternative geometry is fitted, e.g., a polygon, the threshold method would likely have similar robustness to coffee distribution as is found for the ML method. Again, the ML method, by use of image segmentation to obtain a detailed shape of the coffee in the tank, produces accurate estimates also under varying distributions of coffee within the tank.

4.5 Timing

An important consideration in any method that utilities ML is the computation time needed to obtain a results. The largest allowable computation time is often denominated as a *hard real-time requirement*. In this work, the real-time requirement is the minimum amount of time it

Table 4. Comparing computation time of both methods.

	OpenCV [s]	Fastai [s]	Relative [x]
Average	0.019	6.35	337
Fastest	0.013	2.75	208
Slowest	0.030	11.7	388

would take to brew a cup of coffee, since the coffee level only needs to be calculated when the level changes.

To verify that the proposed solution meets this requirement, an experiment was done where 40 level predictions was executed with both binary threshold in OpenCV and the re-trained ResNet model in fastai to compare the time usage for each prediction. The experiment used a collection of randomly selected images and gave the results shown in in Table 4. As expected, the threshold method including pre- and post-processing steps vastly outperforms the ML method in terms of computation time, being on average 337 times faster. This can be explained by the relative simplicity of the computations needed in the binary threshold method, compared with the mathematical complexity of evaluating a 34-layer neural net.

However, from manual observation of the AI barista robot, just the task of moving the coffee cup from the machine to the customer is found to take around 12 seconds, hence a maximum computation time of 11.7 seconds for the ML method is more then sufficient w.r.t. the real-.time requirement.

5 Conclusions

The goal of this work was to test the feasibility of using computer vision, both machine learning and more traditional rule-based computations, for non-intrusive coffee bean level estimation in a transparent tank. Further, both approaches was compared on merits of accuracy and computational speed. Both methods are found to be suitable for the specific application in the AI barista project.

Based on the results and analysis presented in this work, it can be concluded that computer vision with machine learning is superior to traditional image processing in terms of accuracy, robustness against scene configuration, and user-friendliness. The traditional methods still produce good level estimation accuracy, but requires significantly more assumption w.r.t. the scene configuration. However, the traditional approach is computationally much faster and therefore less resource demanding. If assuming an ideal scene configuration, e.g., good lighting and without disturbances, the traditional method may be preferable in applications where the real-time requirements are more challenging than for a coffee machine. Over all, the level estimation accuracy and repeatability of both methods are found to be acceptable, with some suggested improvements to improve robustness of the threshold based approach, for the implementation in a coffee machine, but in another application, there may be a higher demand for correcting distortion and the robustness against stacking errors.

In future work, lens and perspective distortion due to camera physics and position should be compensated for. To increase the threshold methods robustness against slanted coffee distributions, the post processing step of fitting a rectangle to the obtained threshold region should be modified to instead fit a more flexible geometric shape, e.g., a polygon or a set of thinner rectangle slices that together make up the full tank width.

References

John P Bentley. *Principles of measurement systems*. Pearson education, 2005.

Stevo Bozinovski. Reminder of the first paper on transfer learning in neural networks, 1976. *Informatica*, 44(3), 2020.

Stevoand Bozinovski and Ante Fulgosi. The influence of pattern similarity and transfer learning upon the training of a base perceptron b2. *Proceedings of Symposium Informatica*, (3-121-5), 1976.

Gary Bradski and Adrian Kaehler. *Learning OpenCV: Computer vision with the OpenCV library*. " O'Reilly Media, Inc.", 2008.

J. Deng, W. Dong, R. Socher, L. Li, Kai Li, and Li Fei-Fei. Imagenet: A large-scale hierarchical image database. In *2009 IEEE Conference on Computer Vision and Pattern Recognition*, pages 248–255, 2009. doi:10.1109/CVPR.2009.5206848.

Sagi Eppel and Tal Kachman. Computer vision-based recognition of liquid surfaces and phase boundaries in transparent vessels, with emphasis on chemistry applications. *arXiv preprint arXiv:1404.7174*, 2014.

Ian Goodfellow, Yoshua Bengio, and Aaron Courville. *Deep learning*, volume 1. MIT press Cambridge, 2016.

Kaiming He, Xiangyu Zhang, Shaoqing Ren, and Jian Sun. Deep residual learning for image recognition. In *Proceedings of the IEEE conference on computer vision and pattern recognition*, pages 770–778, 2016.

Jeremy Howard and Sylvain Gugger. Fastai: A layered api for deep learning. *Information*, 11(2):108, Feb 2020. ISSN 2078-2489. doi:10.3390/info11020108.

Max Kuhn and Kjell Johnson. *Applied predictive modeling*, volume 26. Springer, 2013.

Adam Paszke, Sam Gross, Francisco Massa, Adam Lerer, James Bradbury, Gregory Chanan, Trevor Killeen, Zeming Lin, Natalia Gimelshein, Luca Antiga, et al. Pytorch: An imperative style, high-performance deep learning library. *arXiv preprint arXiv:1912.01703*, 2019.

Tara Zepel, Veronica Lai, Lars PE Yunker, and Jason E Hein. Automated liquid-level monitoring and control using computer vision. *ChemRxiv Preprint*, 10, 2020.

Accurate Simulation for Numerical Optimal Control

Viktor Leek, Lars Eriksson

Division of Vehicular Systems, Linköping University, Sweden
viktor.leek@liu.se, lars.eriksson@liu.se

Abstract

Accurate simulation of the numerical optimal control in software environments where call to simulation routines is explicit, for instance Matlab and SciPy. A discussion on the simulation aspects of numerical optimal control, how it may fail, and how such erroneous results can be detected using accurate simulation. The key contribution is how to accurately include a piecewise constant control input in the simulations, which is discussed in detail, including code examples. The technique is demonstrated on an example problem which show how simulation can be used to analyze optimal control problems with uncertainty, but also demonstrates how erroneous simulation may lead to erroneous conclusions.

Keywords: Simulation, Optimal control, direct multiple shooting, direct collocation

1 Introduction

Numerical optimal control (NOC) is the field devoted to solving optimal control problems (OCPs) numerically. There exist several approaches that can be divided into three main categories: State-space methods, indirect methods, and direct methods. An overview is found in (Rao, 2009). Here, the focus is on *direct methods*, which are characterized by first discretizing the OCP, in a process known as *transcription*, into a parameter optimization problem, and then solved numerically. Often the parameter optimization problem is a nonlinear program (NLP), but may very well be a quadratic program, or some other suitable problem class.

Numerical solution to differential equations, the field underpinning simulation, has been actively researched for well over a century (Butcher, 1996). Too vast to enumerate all relevant publications, a good introduction to the subject can be found in the textbook (Ascher and Petzold, 1998).

Simulation enters NOC is many different ways. It is the key component in the transcription process but can also be used for other purposes. For instance, as a mean of providing an initial guess, as a mean to post-analyze the results, or the results are already from the beginning intended to be used in a simulation, for instance as input to a more complex representation of the system, or as a feedforward/reference signal. It also plays an important role in fine-tuning the transcription process, as it aids the user in selecting a suitable integration method that balance accuracy and execution time.

Perhaps the most important enabler of modern NOC was the release of software package Casadi (Andersson, 2013; Andersson et al., 2019). It provides the building blocks necessary for the user to implement a custom transcription method. The benefit is that the user can formulate and solve a large class of relevant OCPs. The drawback is that the user needs to implement the method themselves from essential building blocks, which is not trivial and therefore opens up for potential pitfalls.

The most vulnerable part of simulating the numerical optimal control is inclusion of a piecewise constant control input. It is well established that discontinuities make simulation more difficult (Shampine et al., 1976), and various solutions can be found (Gear and Osterby, 1984; Majer et al., 1995; Mao and Petzold, 2002). In the field of NOC, much attention is given to how simulation and numerical integration enters NOC (von Stryk and Bulirsch, 1992; Diehl et al., 2006; Betts, 2010; Biegler, 2010; Rawlings et al., 2017), but little attention is given to how NOC enters simulation. An important enabler of NOC in simulation is therefore an explicit investigation of how to handle the incurred difficulties, in particular, an explicit description of handling piecewise constant control inputs, which is the subject here.

The main contribution is how to structure simulations that involve NOC results based on a piecewise constant control input model, and why they should be structured in that way. Secondary contributions include demonstrating how integration in NOC can produce erroneous results and how accurate simulation can help detect that.

The outline is as follows. Section 2 introduces the subject by an example, Section 3 develops a user's model of the transcription process, Section 4 shows how to accurately simulate the optimal control, Section 5 gives an advanced use case in which Monte-Carlo simulation and optimal control is used to test a method for finding robust optimal trajectories, and the conclusions are presented in Section 6.

2 An introductory example

To introduce the subject of simulation in NOC, a simple example has been devised. The purpose is to show the importance of adequately selecting the integration method in the OCP transcription, but also the importance of an accurate simulation of the results.

Begin by denoting the state variable by x, the control

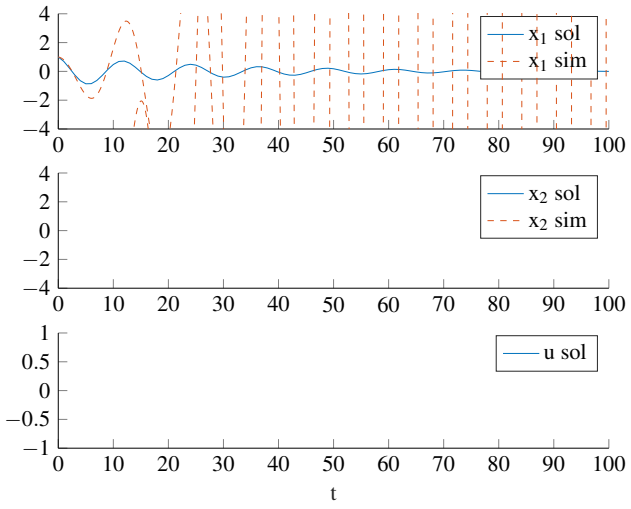

Figure 1. Numerical solution to (2) using implicit euler to discretize the continuous time dynamics. Solid lines (blue) show the numerical solution as obtained from the optimization problem solver. Dashed lines (red) show a validation of the results when the system is driven with the optimal control as input. Y-axis is limited.

input by u, the output by y, and consider the linear system

$$\dot{x} = \begin{bmatrix} \frac{1}{5} & -\frac{13}{50} \\ 1 & 0 \end{bmatrix} x + \begin{bmatrix} 1 \\ 0 \end{bmatrix} u \tag{1a}$$

$$y = \begin{bmatrix} 0 & 1 \end{bmatrix} x \tag{1b}$$

Omitting the control input ($u = 0$), the system is unstable and has poles $1/10 \pm 1/2i$.

Assume it is desired to solve the following optimal control problem, in which the above system dynamics is denoted $\dot{x} = f(x,u)$:

$$\begin{aligned} \min_{u} \quad & \int_0^{t_f} x^{\mathrm{T}} Q x + u^{\mathrm{T}} R u \, dt \\ \text{s.t.} \quad & \dot{x} = f(x,u), \\ & x(0) = x_0, \\ & x(t_f) = x_f \end{aligned} \tag{2}$$

The aim is to drive the state from the initial value x_0, to the final value x_f, while minimizing the quadratic criterion in the objective function, and doing so within the fixed time horizon $t \in [0, t_f]$. To solve the above problem using numerical optimal control a transcription method is needed. Here, the direct collocation method (Hargraves and Paris, 1987) using *implicit Euler* for numerical integration is used.

For the parametrization

$$Q = \begin{bmatrix} 0.1 & 0 \\ 0 & 0.1 \end{bmatrix}, \; R = 1000, \; t_f = 100,$$
$$x_0 = [1,1]^{\mathrm{T}}, \; x_f = [0,0]^{\mathrm{T}}$$

Figure 1 shows, drawn using solid lines (blue), a numerical solution to the problem.

The results are counter intuitive. The system dynamics are unstable, and yet the control input is close to zero. To confirm the results, the system is simulated using the Matlab routine `ode45` (default settings), which is an implementation of Dorman-Prince method (Dormand and Prince, 1980). The results are drawn using dashed lines (red) in Figure 1. It shows that the system is diverging, and not at all driven to the origin, as indicated by the numerical solution to the optimal control problem.

2.1 Analysis

The problem in the above example is that the stability properties of system (1) is not preserved by the implicit Euler method. To analyze the situation, and better appreciate the importance of simulation in numerical optimal control, it is demonstrated with which ease the problem can be constructed.

Consider the system, $\dot{x} = Ax$, where A is a diagonalizable, constant coefficient, $m \times m$ matrix. Take T as a nonsingular matrix consisting of eigenvectors of A. A is then diagonalizable as $A = TDT^{-1}$, where $D = \mathrm{diag}(\lambda_1, \lambda_2, \ldots, \lambda_m)$, is a diagonal matrix with diagonal entries $\lambda_i, i = 1,2,\ldots,m$, being the eigenvalues of A. By introducing the change of variable $z = T^{-1}x$, the decoupled dynamics is obtained as $\dot{z} = Dz$. Applying implicit Euler over the fixed grid

$$0 = t_0 < t_1 < \cdots < t_{N-1} < t_N = t_f \tag{3a}$$

$$h = t_{n+1} - t_n, \; n = 0,1,\ldots,N-1 \tag{3b}$$

for some number of steps N, the discretized dynamics is obtained as $z_{n+1} = (I - hD)^{-1} z_n$. Every component $z^{(i)}$ is of the form

$$z_{n+1}^{(i)} = \frac{1}{1 - h\lambda_i} z_n^{(i)}, \; i = 1,2,\ldots,m$$

For $|1 - h\lambda_i| > 1, i = 1,2,\ldots,m$, a converging sequence $|z_0^{(i)}| > |z_1^{(i)}| > \cdots > |z_n^{(i)}|$ is obtained, regardless of the stability properties of the underlying ODE. So, by construction the matrix from the desired eigenvalues and step size, an unstable ODE, whose stability property is not preserved by the implicit Euler method, can be constructed.

In the example, the poles are $1/10 \pm 1/2i$ and the step length $h = 1$, which gives $|1 - h\lambda_i| = 1 + 37/1250 > 1$.

These types of traps and pitfalls are to be found in simulation, especially when working with simple integration methods, as is typically done in NOC. It shows the importance of properly understanding the type of problem one is simulating, but perhaps even more, the importance of confirming the results by use of simulation.

2.2 Instability

Unstable systems are difficult to simulate, even when control is applied. To demonstrate that the above problem is

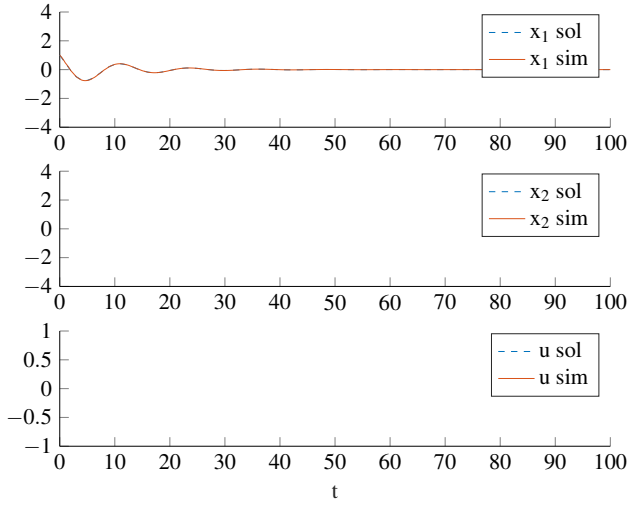

Figure 2. Numerical solution to (2). Drawn using dashed lines (blue) is the results from the OCP solver, using a high order integration method. Drawn in solid lines is the simulation of the results using a different high order integration method.

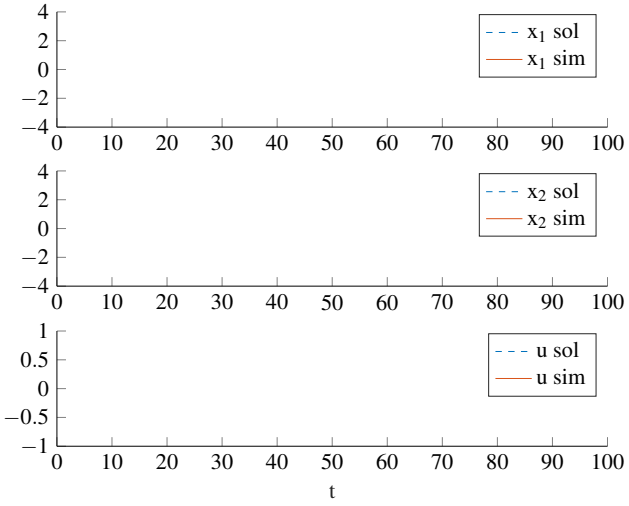

Figure 3. Dashed lines show the actual trajectory, obtained using a correct simulation setup. Solid lines show a faulty confirmation, obtained using the same integration method, with the same default settings as the dashed line, but with a faulty setup. Notice that the control signals are *almost* identical. The perturbation is still large enough to put the system on a completely different trajectory.

simulatable, the OCP (2) is solved using a fifth order Legendre collocation integration method and simulated using `ode45` in Matlab (it can be noted that this is overkill for a linear system). The results are found in Figure 2. Contrary to the first case, the results are consistent with intuition and control is applied forcefully in the beginning to prevent the system from diverging.

2.3 Erroneous simulation

Simulating the numerical results of an optimal control problem is not as trivial as it first appears. Consider Figure 3. Drawn in dashed (blue) is the same solution presented in Figure 2. Drawn in solid (red) is an erroneous simulation of the optimal control. The integration method used to obtain the simulation results presented in Figure 2 and Figure 3 is the same, the Matlab command `ode45`, using default settings in both cases. One trajectory is diverging, the other converging. The difference is in how the simulation is structured, and how to do that accurately is shown in Section 4.

3 Numerical optimal control

In order to structure the simulations correctly, it is necessary to develop a user's model of the transcription process. This section briefly introduces the subject of optimal control and outlines a sufficiently detailed model of the transcription process to structure the simulations.

3.1 Optimal control

A solution to an optimal control problem is seeking the optimal control, u^*, and the optimal state trajectory, x^*, that minimize the cost function and does not violate the constraints. The problem's characteristic feature is the differential constraint $\dot{x} = f(t,x,u)$. The objective function consists of two parts. An integral cost $\int L(t,x,u)\,dt$, and a terminal cost $E(t_f,x(t_f))$. There is an allowable set for the initial value $x(0) \in \mathscr{X}_0$, path constraints $x(t) \in \mathscr{X}$ and $u(t) \in \mathscr{U}$, and an allowable set for the terminal state $x(t_f) \in \mathscr{X}_f$. The problem is formulated as

$$\begin{aligned} \min_{u} \quad & E(t_f,x(t_f)) + \int_0^{t_f} L(t,x,u)\,dt \\ \text{s.t.} \quad & \dot{x} = f(t,x,u),\ t \in [0,t_f], \\ & x(0) \in \mathscr{X}_0, \\ & x(t) \in \mathscr{X},\ t \in [0,t_f], \\ & u(t) \in \mathscr{U},\ t \in [0,t_f], \\ & x(t_f) \in \mathscr{X}_f \end{aligned}$$

3.2 Direct methods for optimal control

Any numerical method for optimal control needs to address the fact that the system of interest is represented by a differential equation. While there are many available methods, the focus here is on *direct methods*, which transcribes the OCP into an NLP, and solves that numerically.

To transcribe the continuous time OCP into an NLP, there are two major considerations to take into account. How to handle the control input, and how to handle the integration of the system dynamics. There is also a third one, the integration of the integral cost $I = \int L(t,x,u)\,dt$. However, by introducing the integration state x_l, $\dot{x}_l = L(t,x,u)$, the integral can be integrated with the system dynamics and rephrased as an terminal cost $I = \int L(t,x,u)\,dt = x_l(t_f)$, and therefore the two main concerns are the state and control trajectory.

Consider again the fixed grid (3). Over it, the control input is parameterized as a piecewise constant signal, with a constant input, u_n, for each step

$$u(t) = u_n,\ t \in [t_n, t_{n+1})$$

While there are several ways of parameterizing the control input (Andersson, 2013), this is the most popular (Diehl, 2011) and corresponds to a zero-order hold control system implementation. It is also more general than it first appears. Consider the following augmentation. Denote the augmented system state by $\tilde{x}$ and augmented control signal by $\tilde{u}$ and let them be defined by

$$\tilde{x} = \begin{bmatrix} x \\ u \end{bmatrix},\ \dot{\tilde{x}} = \begin{bmatrix} f(t,x,u) \\ \tilde{u} \end{bmatrix},\ \tilde{u} = \frac{du}{dt}$$

Given that $\tilde{u}$ is piecewise constant, it then follows that u is piecewise linear. Since this augmentation can be applied arbitrarily many times, it shows that u can be of arbitrarily high order, even if the augmented input is piecewise constant. It should be noted that in a numerical setting, the obtained degree is also influenced by the order of the integration method.

The two most popular direct methods (Diehl et al., 2006), *direct collocation* (Hargraves and Paris, 1987), and *direct multiple shooting* (Bock and Plitt, 1984), integrate the system dynamics over each segment of the grid separately, forming a discontinuous trajectory, consisting of a sequence of initial value problems

$$\dot{x} = f(t,x,u_n),\ t \in [t_n, t_{n+1}),\ n = 0,\cdots,N-1 \quad (4a)$$
$$x(t_n) = x_n \quad (4b)$$

which is parameterized by the initial condition x_n, and state at the terminal boundary by $x(t_N) = x_N$.

To obtain a continuous trajectory, continuity constraints are introduced that bind the trajectory together

$$F(t_n, x_n, u_n) = x_{n+1},\ n = 0,\ldots,N-1 \quad (5)$$

Here, F is the numerical integration of the continuous time dynamics over the segment

$$F(t_n, x_n, u_n) \approx \int_{t_n}^{t_{n+1}} f(t,x,u_n)\,dt$$

A sketch of the process is found in Figure 4.

Omitting the path constraints and only considering box constraints for the initial and terminal constraints, the transcription process results in the NLP

$$\begin{aligned} \min_{\substack{x_0,\ldots,x_N \\ u_0,\ldots,u_{N-1}}} \quad & E(t_f, x_N) + x_{l,N} \\ \text{s.t.} \quad & \begin{bmatrix} x_{0,\min} \\ x_{f,\min} \end{bmatrix} \le \begin{bmatrix} x_0 \\ x_N \end{bmatrix} \le \begin{bmatrix} x_{0,\max} \\ x_{N,\max} \end{bmatrix}, \\ & \begin{bmatrix} F(t_0,x_0,u_0) - x_1 \\ \vdots \\ F(t_{N-1},x_{N-1},u_{N-1}) - x_N \end{bmatrix} = 0 \end{aligned} \quad (6)$$

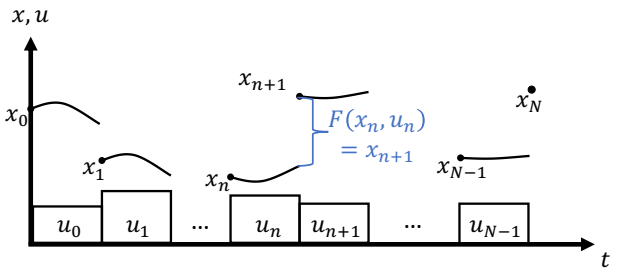

Figure 4. Sketch of a direct method for optimal control. The control input u is piecewise constant, and the state trajectory is discontinuous and parameterized with an initial value for every segment. The state trajectory is made constant by introducing the continuity constraint (5).

As a user's model, the two most important things to note is that the control input can be expected to be piecewise constant, and the state trajectory is integrated separately over the grid segments.

It should also be emphasized that this is an outline of the transcription process, and not a formal description, which can be found in (Biegler, 2010; Betts, 2010).

4 Simulation of the optimal control

The main difficulty in simulating a system with the optimal control as input is handling the piecewise constant control input. Consider the following basic IVP where the intention is to simulate the optimal control. $\dot{x} = h(t,x)$ is used to describe the simulated system, which is a combination of the controlled system and a look-up of the optimal control.

$$\dot{x} = h(t,x),\ t \in [0, t_f] \quad (7a)$$
$$x(0) = x_0 \quad (7b)$$

The controlled system, $\dot{x} = f(t,x,u)$, is contained in $\dot{x} = h(t,x)$. Since the simulated solution is expressed in the two variables t and x, then so is the simulated control, u^s. By introducing the definition $u^s = g(t,x)$, the simulated system can be described by $\dot{x} = h(t,x) = f(t,x,g(t,x))$. The transcription process gives that the optimal control is parameterized in terms of t, so the simulated control is a function in the independent variable only, $u^s = g(t)$. This means that formulation (7) include a look-up of u^* based on the independent variable t. If simulated correctly, $u^s = u^*$, but it is not necessarily so.

The following Matlab code is an example simulation of IVP (7). It uses interpolation based on the current value of the independent variable to look-up the control input. `t` and `x` are the variables the hold the simulation results, `h` is the function that is called by the integration routine `ode45`, `[t0, tf]` is the problem horizon, `x0` is the initial value, `interp1` does piecewise constant interpolation of the optimal control, (`t_sol`, `u_sol`), based on the function parameter `t` which represent the independent

variable, `f` is the function that holds the implementation of the controlled system $f(t,x,u)$, and `der` is the return value that represent $\dot{x}(t)$.

```
[t, x] = ode45(@h, [t0, tf], x0);
function der = h(t, x)
    u = interp1(...
        t_sol, u_sol, t, 'previous');
    der = f(t, x, u);
end
```

This is an example of a naive implementation, and was used to derive the erroneous confirmation in Figure 3 (solid lines). Since the control is interpolated based on the independent variable, the actual control input is dependent on the step length. Unless steps are taken at the exact grid points (3), the simulated control u^s does not equal the optimal control u^*. The problem is remedied by using a variable step-length solver and lowering the tolerance, but it does not solve it. Variable step-length solvers are built on the assumption of a smooth solution, differentiable up to the order conditions, which is why discontinuities are handled poorly (Ascher and Petzold, 1998). Also, the control input is not a dependent variable, so local error control does not have direct mean of estimating the error in that signal. A secondary effect of lowering the tolerance is that the number of function evaluations increases, which increase computational time, so both accuracy and time is lost when structuring the simulation according to (7).

From a user's perspective, an aggravating circumstance of simulating (7) is that it is easy to miss that the optimal control has not been properly reconstructed, since the simulated control, u^s, needs to be reconstructed from the simulation (it is not a state). One might think of using a global variable to store the control, but this approach does not work for variable step-length solvers as not all steps are accepted.

4.1 Event functions

(Ascher and Petzold, 1998; Gustafsson) suggest the use of event functions to tell the integration method that a discontinuous event has occurred. While being a good advice in general, caution needs to be taken. For instance, Matlab (Shampine and Reichelt, 1997) and SciPy (Virtanen et al., 2020) does not use event functions as a mean to direct step length. In other environments such as OpenModelica ans Assimulo (Lundvall et al., 2005; Andersson et al., 2015) events can be used to inform the solver of discontinuities.

4.2 Handling of the control input

To handle the problem of a discontinuous control input in the simulation, the simulation is restarted for every change in the control input, similar to what is done in the transcription process (4)

$$\dot{x} = f(t,x,u_n),\ t \in [t_n, t_{n+1}],\ n = 0,\cdots,N-1 \quad (8a)$$
$$x(t_n) = x_n \quad (8b)$$

This avoids the problem of having to localize the change in control input and ensures $u^s = u^*$, regardless of solver tolerance.

The following is an example Matlab simulation of (8). The code is structured based on the number of segments to simulate, `N`. The first loop iterate is peeled off in order to initialize the variables `t` and `x` which hold the solution. The local solution on each segment (`tt`, `xx`) is appended to the existing solution, without overlap. Notice how the control, `u_sol`, is fixed over each segment `[t_sol(i), t_sol(i+1)]`. The standard Matlab solver `ode45` is used, but it could be any suitable method.

```
f1 = @(t, x) f(t, x, u_sol(1));
[t, x] =  ode45(f1, [t0, tf], x0);
for i=2:N
    fi = @(t, x) f(t, x, u_sol(i));
    [tt, xx] = ode45(fi, [t_sol(i),...
        t_sol(i+1)], x(end,:));
    t = [t; tt(2:end)];
    x = [x; xx(2:end,:)];
end
```

This technique is used in obtaining the results presented in Figure 2 using solid lines (red). The relatively small difference between the code presented at the beginning of this section, and the code presented here, makes all the difference for accurate simulation of optimal control trajectories. The technique is also inline with general methods for handling discontinuities (Ascher and Petzold, 1998; Gustafsson).

5 Example application

In order to demonstrate the close connection between simulation and optimal control, an example application is demonstrated. The example is a variation on the classical OCP, Goddard's Rocket Problem, adapted from (Maurer, 1976; Rutquist and Edvall, 2010). The problem consists of launching a rocket as high up in the air as possible, given a finite amount of fuel.

The aim here is *not* to conduct rocket science so certain aspects are simplified. Instead, the aim is to demonstrate a case where simulation and numerical optimal control interact.

5.1 Rocket Model

The model has three states x: height h, speed v, and fuel mass m_f. The control input, u, is the fuel mass flow rate.

$$x = [h, v, m_f]^{\mathrm{T}},\ u = -\frac{dm_f}{dt}$$

The motion is governed by the ordinary differential equation

$$\dot{x} = f(x,u) = \begin{bmatrix} v \\ \frac{F_p(u) - F_D(v,h) - m(m_f)g(h)}{m(m_f)} \\ -u \end{bmatrix}$$

where F_p is the propulsion force, F_D the drag force, and g the gravitational acceleration. The rocket mass, $m = m_f + m_0$, consist of the fuel mass m_f, and ballast $m_0 = 68$ kg.

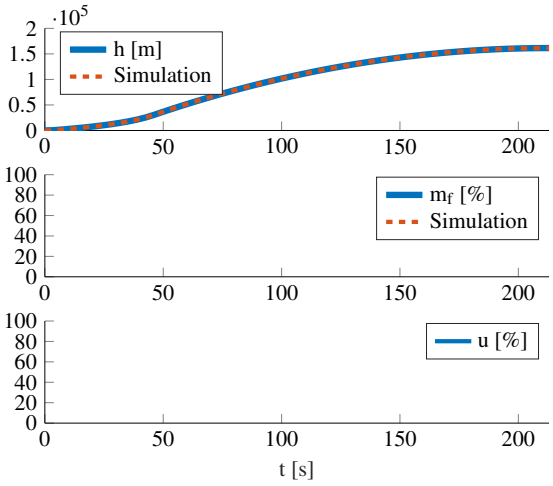

Figure 5. Numerical solution to the nominal formulation of the Goddard Rocket Problem (9), drawn in solid lines (blue). Fuel mass m_f and control (fuel mass flow) u, are presented in percentage of their maximum values. Confirmation by simulation drawn in dashed lines (red).

Propulsive force F_p is proportional to control effort

$$F_p = cu$$

and $c = 2069$ is the proportionality constant. Drag force is nonlinear and dependent on both height and speed

$$F_D = D_0 e^{-\gamma h} v^2$$

where $D_0 = 1.227 \cdot 10^{-2}$ and $\gamma = 1.450 \cdot 10^{-4}$ are model parameters. The gravitational acceleration accounts for how far above the Earth's surface the rocket is

$$g = g_0 \left(\frac{r_0}{r_0 + h} \right)^2$$

and $g_0 = 9.81$ m/s^2, and $r_0 = 6.371 \cdot 10^6$ m is Earth radius.

5.2 Nominal problem formulation

A nominal formulation of the problem is formulated as

$$\begin{aligned} \max_{t_f, u} \quad & h(t_f) \\ \text{s.t.} \quad & \dot{x} = f(x,u),\ t_f \geq 0, \\ & x(0) = [0,0,150]^{\mathrm{T}}, \\ & h \geq 0,\ v \geq 0,\ m_f \geq 0, \\ & 0 \leq u \leq 9.5 \end{aligned} \tag{9}$$

in which the final time, t_f, is a problem parameter. A solution to the formulation is found in Figure 5.

5.3 Problem variation

Assume γ is a parameter that is best described as a random variable on a launch-to-launch basis, but constant over a single launch

$$\gamma = \gamma_{nom} \mathcal{N}(\mu, \sigma^2) \tag{10}$$

with $\gamma_{nom} = 1.450 \cdot 10^{-4}$. Assume that the same reference trajectory is going to be used for every launch and that it therefore is desirable to find a balance between final height, $h(t_f)$, and deviation from the nominal trajectory when γ changes. To measure deviation the root mean square error (RMSE) is used

$$\text{RMSE} = \sqrt{\frac{1}{t_f} \int_0^{t_f} (h^* - h^s)^2 dt} \tag{11}$$

in which the optimal height trajectory is denoted by h^* and the simulated one by h^s for which γ changes.

To balance between height and deviation it is studied how the state trajectory change for a sufficiently small change, ϕ, in a parameter, p and is written as

$$x(t, p + \phi) = x(t,p) + \phi \frac{dx(t,p)}{dp} + \mathcal{O}(\phi^2)$$

Introducing the notation $P = \frac{dx(t;p)}{dp}$, the perturbation matrix function P is governed by the sensitivity equation

$$\dot{P} = \left(\frac{\partial f}{\partial x} \right) P + \frac{\partial f}{\partial p} \tag{12}$$

with the initial condition $P(0) = 0$. See (Ascher and Petzold, 1998) for a derivation. For $p = \gamma$ a cost for the sensitivity $dh/d\gamma$ is included in the objective function as a mean to balance the two objectives:

$$\max_{t_f, x, u} \quad h(t_f) - \beta \int_0^{t_f} \left(W \frac{dh}{d\gamma} \right)^2 dt$$

β is the trade-off parameter, and $W = 10^{-8}$ is a normalization factor that is used to avoid unreasonably small values of β. The formulation penalizes both height and final time t_f. To remedy this, an extra constraint is introduced, $v(t_f) = 0$, which ensures the trajectory reaches the apex.

The full formulation of the problem variation is:

$$\begin{aligned} \max_{t_f, x, u} \quad & h(t_f) - \beta \int_0^{t_f} \left(W \frac{dh}{d\gamma} \right)^2 dt \\ \text{s.t.} \quad & \dot{x} = f(x,u),\ t_f \geq 0, \\ & x(0) = [0,0,150]^{\mathrm{T}}, \\ & h \geq 0,\ v \geq 0,\ m_f \geq 0, \\ & 0 \leq u \leq 9.5, \\ & v(t_f) = 0 \end{aligned} \tag{13}$$

Note that $f(x,u)$ is used ambiguously and in this formulation includes the sensitivity equation (12), with $p = \gamma$.

For $\gamma = \gamma_{nom}$, Figure 6 presents the solution to the problem for a three different values of β, and Figure 7 shows the corresponding sensitivity state trajectory $dh/d\gamma$.

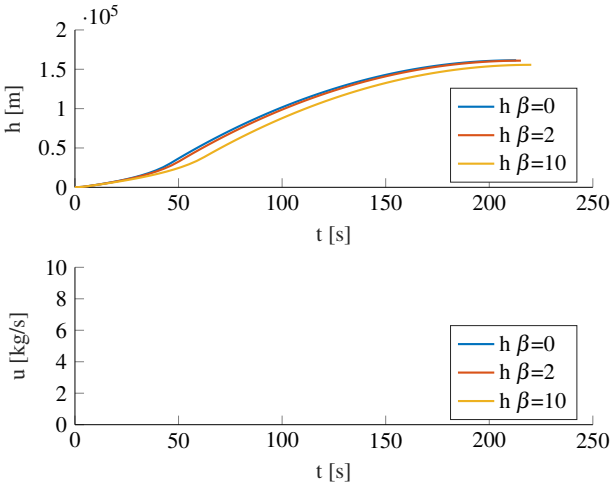

Figure 6. Solution to (13) for three different values of β.

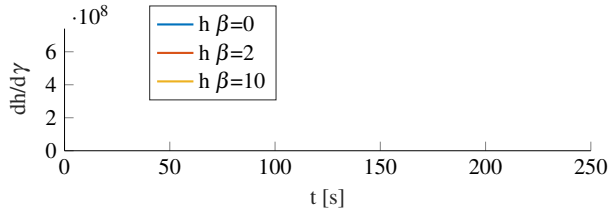

Figure 7. Optimal sensitivity trajectory $\frac{dh}{d\gamma}$ for different values of β.

5.4 Simulation

To quantify the trade-off between the two performance variables, final height $h(t_f)$ and RMSE, the problem (13) is solved for sequence of values of β, for $K = 12$

$$\beta_1 < \beta_2 < \cdots < \beta_K \tag{14}$$

For every solution corresponding to β_k, the optimal control, u_k^*, is simulated, using simulation setup (8), with the parameter γ drawn from the distribution (10). 10'000 simulations are run for every β_k. By completing the procedure for the full sequence of β (14), the results can be plotted, and a Pareto front is formed, see Figure 8. It clearly shows the trade-off between the performance variables.

For $\gamma = \gamma_{nom}\mathcal{N}(1, 0.15)$ Figure 8 shows the trade-off drawn in solid lines (blue), and for $\gamma = \gamma_{nom}\mathcal{N}(0.85, 0.15)$ in dashed lines (red). The height is normalized with maximum height for nominal parameter values, solution to problem (9), and deviation is normalized with the maximum one for the corresponding distribution of β. For the unbiased distribution it can be seen the final height is maximized for the second-most point from the right ($\beta = 1$), although only slightly higher than the nominal trajectory, but deviation is reduced by about 6 %, a free lunch. For the biased estimate, it can be seen that $\beta = 2$ maximizes height, but the most interesting point for both cases is perhaps $\beta = 5$ which gives a significant reduction in deviation while maintaining much of the height. An important aspect of the example is the use of simulation as a mean to gain insights into the optimal control, which shows that simulation too is an integral part of optimal control, not just optimization.

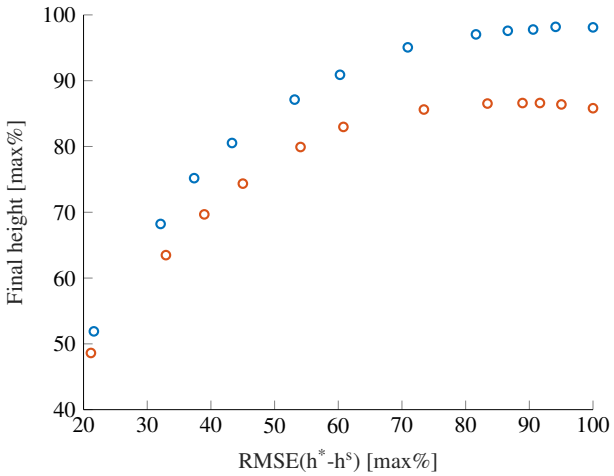

Figure 8. Pareto-optimal solution to (13), for $\beta = \{0, 1, 2, 3, 5, 10, 20, 30, 50, 70, 100, 200\}$. Values to the right correspond to lower values of β. Solid line (blue) correspond to the distribution $\gamma = \gamma_{nom}\mathcal{N}(1, 0.15)$, dashed lines (red), to the distribution $\gamma = \gamma_{nom}\mathcal{N}(0.85, 0.15)$.

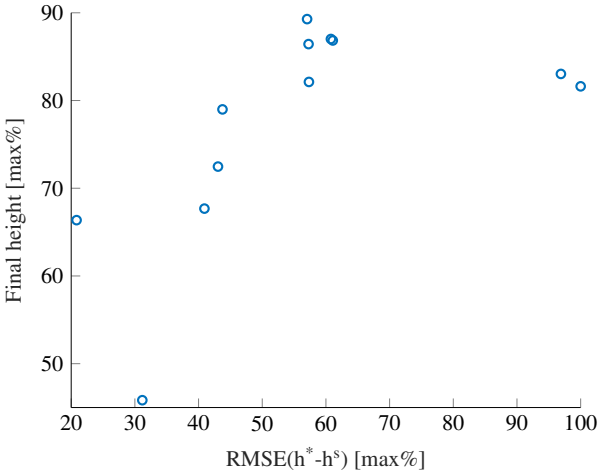

Figure 9. Erroneous Pareto-optimal solution to (13), for $\beta = \{0, 1, 2, 3, 5, 10, 20, 30, 50, 70, 100, 200\}$

As the example is primarily devoted to the simulation aspect, the obtained results are compared to the same analysis but using the look-up based simulation method (7). The simulations are otherwise conducted in the same way, solver and solver settings remains the same. The problem is only solved for the distribution $\gamma = \gamma_{nom}\mathcal{N}(1, 0.15)$ and Figure 9 shows the results. The results are erroneous, and any analysis of the results are therefore useless. In this case, it is obvious that something is wrong, but in a real case it does not have to be as easy to decide, and for those cases it is important to have confidence in the method.

6 Conclusions

It is demonstrated how simulation in NOC can fail and how it can be detected using accurate simulation. A user's model of the transcription process is developed, and based on it, a technique for structuring accurate simulations. The technique is based on the fact that the parameterized control input is discontinuous and to accurately handle that, the simulation is restarted at the discontinuity. MATLAB code, which is simple enough to act as pseudo code for other languages, is provided and is a practical guide for the user on how to apply the technique.The effectiveness and the importance of accurate simulation is demonstrated using an example. It shows how simulation can be used as a tool for getting the most out of optimal control, but also how an inappropriate simulation setup can lead to erroneous results.

References

Christian Andersson, Claus Führer, and Johan Åkesson. Assimulo: A unified framework for ode solvers. *Mathematics and Computers in Simulation*, 116:26–43, 2015.

Joel Andersson. *A general-purpose software framework for dynamic optimization*. PhD thesis, PhD thesis, Arenberg Doctoral School, KU Leuven, Department of Electrical . . . , 2013.

Joel AE Andersson, Joris Gillis, Greg Horn, James B Rawlings, and Moritz Diehl. Casadi: a software framework for nonlinear optimization and optimal control. *Mathematical Programming Computation*, 11(1):1–36, 2019.

Uri M Ascher and Linda R Petzold. *Computer methods for ordinary differential equations and differential-algebraic equations*, volume 61. Siam, 1998.

John T Betts. *Practical methods for optimal control and estimation using nonlinear programming*. SIAM, 2010.

Lorenz T Biegler. *Nonlinear programming: concepts, algorithms, and applications to chemical processes*. SIAM, 2010.

Hans Georg Bock and Karl-Josef Plitt. A multiple shooting algorithm for direct solution of optimal control problems. *IFAC Proceedings Volumes*, 17(2):1603–1608, 1984.

John Charles Butcher. A history of runge-kutta methods. *Applied numerical mathematics*, 20(3):247–260, 1996.

M. Diehl, H. G. Bock, H. Diedam, and P. B. Wieber. Fast direct multiple shooting algorithms for optimal robot control. *Lecture Notes in Control and Information Sciences*, 340:65–93, 2006. ISSN 01708643. doi:10.1007/978-3-540-36119-0_4.

Moritz Diehl. Numerical optimal control. Technical report, KU Leuven, 2011.

John R Dormand and Peter J Prince. A family of embedded runge-kutta formulae. *Journal of computational and applied mathematics*, 6(1):19–26, 1980.

Charles William Gear and O Osterby. Solving ordinary differential equations with discontinuities. *ACM Transactions on Mathematical Software (TOMS)*, 10(1):23–44, 1984.

Kjell Gustafsson. Traps and pitfalls in simulation. Technical report, Ericsson Mobile Communications AB.

Charles R Hargraves and Stephen W Paris. Direct trajectory optimization using nonlinear programming and collocation. *Journal of guidance, control, and dynamics*, 10(4):338–342, 1987.

Håkan Lundvall, Peter Fritzson, and Bernhard Bachmann. *Event handling in the openmodelica compiler and runtime system*. Linköping University Electronic Press, 2005.

C Majer, W Marquardt, and Ernst Dieter Gilles. Reinitialization of dae's after discontinuities. *Computers & chemical engineering*, 19:507–512, 1995.

Guiyou Mao and Linda R Petzold. Efficient integration over discontinuities for differential-algebraic systems. *Computers & Mathematics with Applications*, 43(1-2):65–79, 2002.

H Maurer. Numerical solution of singular control problems using multiple shooting techniques. *Journal of Optimization Theory and Applications*, 18(2):235–257, 1976.

Anil V Rao. A survey of numerical methods for optimal control. *Advances in the Astronautical Sciences*, 135(1):497–528, 2009.

James Blake Rawlings, David Q Mayne, and Moritz Diehl. *Model predictive control: theory, computation, and design*, volume 2. Nob Hill Publishing Madison, WI, 2017.

Per E Rutquist and Marcus M Edvall. Propt-matlab optimal control software. *Tomlab Optimization Inc*, 260(1):12, 2010.

Lawrence F Shampine and Mark W Reichelt. The matlab ode suite. *SIAM journal on scientific computing*, 18(1):1–22, 1997.

LF Shampine, HA Watts, and SM Davenport. Solving nonstiff ordinary differential equations—the state of the art. *Siam Review*, 18(3):376–411, 1976.

Pauli Virtanen, Ralf Gommers, Travis E. Oliphant, Matt Haberland, Tyler Reddy, David Cournapeau, Evgeni Burovski, Pearu Peterson, Warren Weckesser, Jonathan Bright, Stéfan J. van der Walt, Matthew Brett, Joshua Wilson, K. Jarrod Millman, Nikolay Mayorov, Andrew R. J. Nelson, Eric Jones, Robert Kern, Eric Larson, C J Carey, İlhan Polat, Yu Feng, Eric W. Moore, Jake VanderPlas, Denis Laxalde, Josef Perktold, Robert Cimrman, Ian Henriksen, E. A. Quintero, Charles R. Harris, Anne M. Archibald, Antônio H. Ribeiro, Fabian Pedregosa, Paul van Mulbregt, and SciPy 1.0 Contributors. SciPy 1.0: Fundamental Algorithms for Scientific Computing in Python. *Nature Methods*, 17:261–272, 2020. doi:10.1038/s41592-019-0686-2.

O. von Stryk and R. Bulirsch. Direct and indirect methods for trajectory optimization. *Annals of Operations Research*, 37(1):357–373, 1992. ISSN 02545330. doi:10.1007/BF02071065.

Validation of Hygrothermal Numerical Simulation with Experiment for Future Climate Control

Santeri Schroderus[1] Veli-Matti Lähteenmäki[2] Antti Haapala[2] Filip Fedorik[1]

[1]Structures and Construction Technology, University of Oulu, Finland, (santeri.schroderus, filip.fedorik)@oulu.fi

[2]University of Eastern Finland, Joensuu, Finland, (veli-matti.lahteenmaki, antti.haapala)@uef.fi

Abstract

Future climate is expected to be warmer, more humid, and cloudier with more frequent extreme weather conditions. Current building design should consider these changes as they can significantly influence the function of buildings in the future. Here, we study common building envelope assembly subjected to different climatic scenarios. An experiment was set up to validate a numerical model, which is further applied to assess hygrothermal performance (heat and moisture transfer) of the building envelope subjected to different boundary conditions. The assessment is provided via Finnish mould growth model that identifies risk of biological growth through dynamic hygrothermal conditions. Finnish meteorological institute provides data that predicts the climate in 2030, 2050 and 2100. The humidity inside the building envelope is assumed to increase slightly in time, however, increased temperature in the future may cause more favorable conditions for mould growth, especially, if mould sensitive building materials are used. The hygrothermal assessment of building structures with consideration of climate change in structural design is a key factor to provide sustainable building designs. Numerical model was successfully validated with experiments providing data within tolerances of measurement equipment.

Keywords: Numerical simulation, heat and moisture transfer, validation, experiment, climate change

1 Introduction

Building designs are going through a paradigm change in development of new high energy efficient structural systems and materials. High thermal resistance is usually achieved by applying thick layers of insulation, which may cause airtight conditions that slow down moisture diffusion and increase risk for microbial growth (e.g. Fedorik et al., 2015). Hygrothermal performance of building assemblies is currently more important than ever; around 45% of the Finnish national wealth resides in residential or public buildings (ROTI, 2021), which shows the importance of preventing future uncertainties with different methods (Hagentoft et al., 2020) to provide long healthy life cycle and functionality of building elements.

In the future, due to climate change, heating and cooling demand of the buildings will be decreased in Nordic countries by about 20% by 2061 but the moisture problems will be increased by the more humid outdoor climate conditions (Nik, 2012). Humidity has a significant impact on hygrothermal properties of building material, and hence on the hygrothermal performance of entire building envelope. Higher relative humidity increases thermal conductivity, which in turn causes reduction in building energy efficiency. Relative humidity above 80% (≥85% for non-sensitive material) at temperatures between 0 and 50°C may sustain microbial growth (Viitanen & Ojanen, 2007). These hygrothermal conditions may consequentially cause damage and/or deterioration of building material and reduce life span of buildings which in fact increases environmental impact over lifecycle (Marsh, 2017). Therefore, one of the key elements for sustainable building design in long-term is to provide suitable hygrothermal functionality of building assemblies, keeping in mind that today's buildings must also withstand the conditions of tomorrow, and the next 50 to 100 years, thus the ongoing climate change.

The climate is expected to be warmer, wetter, and cloudier with increasing extreme weather conditions (Jylhä *et al.*, 2009). Hence, climate change is transforming the future outdoor circumstances towards more unfavorable for the hygrothermal performance of conventional structures. Prolonged and higher relative humidity and temperature conditions can significantly affect the mould susceptibility of the structures, as these conditions are in a longer period at the favorable range for mould growth (Fedorik *et al.*, 2017; Fedorik *et al.*, 2018). In dry and cold conditions, moulds and other microbes do not usually grow. A previous study has shown that mould growth is mostly affected by the outdoor and

indoor climate conditions than the position of the insulation layers (Kang *et al.*, 2016). This means that hygrothermal performance of structures is important to take into consideration in design of structures to manage future climate.

2 Aims

The aim of the study is to validate a numerical approach with experimental data in a case study of common structural wall-element assemblies. Experimental data is collected with temperature θ and relative humidity φ sensors at two points across element cross-section (Figure 1). The structural assembly is subjected to constant boundary conditions θ=10°C and φ=90% outdoor and θ=21°C and φ=30% of indoor air, respectively.

Validated numerical model is then subjected to future weather conditions following the work by Jokioinen (2004) to assess suitability of a presented structure to the current design approach. Predicted climate change data for 2030, 2050 and 2100 are applied to monitor and study the development of hygrothermal conditions inside the building envelope assembly at these forecasted future conditions (Vinha *et al.* 2013).

3 Methods and Materials

3.1 Structure and Experimental Work

The structure subjected to the study represents a common Finnish timber-frame building envelope consisting of gypsum board, wood fiber insulation board, vapor barrier, wood fiber insulation and windshield board (Figure 1). The experiment was performed for period of 18 days from which the temperature and relative humidity were measured every 10 minutes from within the wall element. Conditions were monitored at 2 points in the direction of heat and mass transfer: at the interface of windshield and thick wool insulation and another at interface of air barrier and inner wool insulation (Figure 1). The experiment setup built inside Memmert climate cabin (CTC256 model) was used to develop the outside conditions that were then used to validate the simulated one-dimensional heat and moisture transfer model.

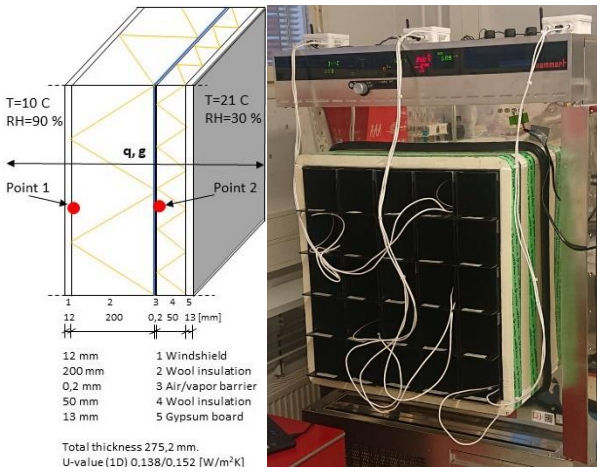

Figure 1. Illustration of building envelope assembly, validation points and laboratory measurement setup.

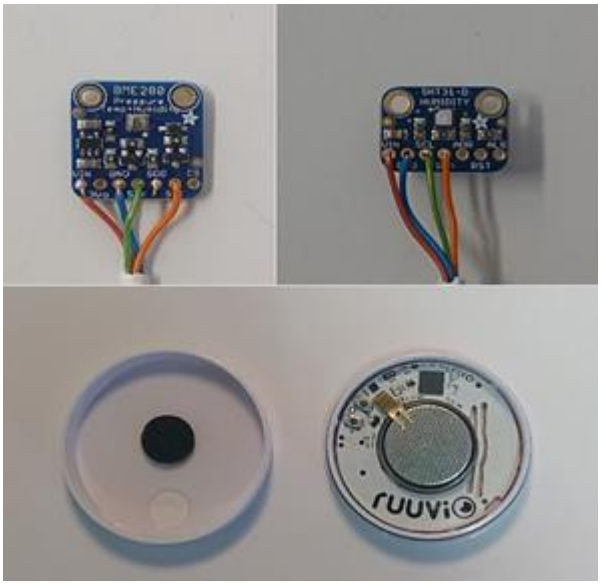

Figure 2. Different types of data collection sensors.

Climate cabin's interior and exterior temperature, relative humidity and barometric pressure were monitored by using Bosch BME280 sensors (top left, Figure 2). This sensor design provides accuracy for temperature ± 1.0°C, relative humidity ± 3% and pressure ± 1hPa. Commercial cased version of the BME280 by Ruuvi Ltd (Figure 2) was used for CTC256 interior measurements because the outside conditions simulated by the cabin were challenging to uncased version. Data collection from the inside of the wall structures was carried out by utilizing the SHT31-D sensors that monitor temperature and relative humidity within tolerances of ± 0.3°C, ± 2%, respectively (top right, Figure 2).

3.2 Future Climate

Finnish Meteorological Institute's building physical test year by Jokioinen (2004) and the future scenarios (for 2030, 2050, 2100) were applied to the structure to investigate its hygrothermal performance and

possible mould growth at the cross-sectional validation points (Figure 1). The future test years are based on a rather pessimistic SRES A2 -climate change scenario for southern Finland. In this scenario, the assumption is that greenhouse gas emissions would continue to rise throughout this century.

3.3 Numerical Approach

Numerical simulations were performed using Comsol Multiphysics simulation software. The model represents dynamic one-dimensional simultaneous heat and mass transfer that is suitable for analysis in hygroscopic range (φ<95%) (Dong *et al.,* 2020). The validation of numerical model was performed for a period of 18 two with a 10-minute time-steps between measurements. Surface convective coefficients were considered the same on both sides of the building assembly, as the outdoor and indoor conditions during the experiment correspond to indoor convective conditions. Hence, surface heat transfer coefficient was h=1/0.13 [W/(m^2·K)] and moisture transfer coefficient is β_p = 2.45·10^{-8} [s/m]. The initial conditions correspond to the initial conditions of the experiment set up.

Simulations applying the current and three future test years were performed for 2-years with 1 hour time step. The initial temperature and relative humidity were considered 21°C and 30%, respectively. The outdoor and indoor surface heat resistances correspond to standard recommendation, where exterior thermal resistance is R_{se}=0.04 [(m^2·K)/W] and indoor R_{si}=0.13 [(m^2·K)/W]. The moisture surface coefficients were set to β_i=2.45·10^{-8} [s/m] and β_e=1.3·10^{-7} [s/m].

Indoor boundary conditions were derived according to Finnish national guideline (RIL 107-2012, 2012) that determines indoor moisture excess more suitable for Finnish weather conditions than ISO 13788:2012 (Vinha *et al.*, 2018). The first-year calculation was performed to eliminate the effect of initial conditions on results. Therefore, the hygrothermal conditions were assessed for the second year of the numerical simulation only.

3.4 Materials Tested

Each layer of a building envelope assembly plays a significant role in the overall hygrothermal performance of a building. The material properties needed for hygrothermal simulation are thermal conductivity λ [W/(m·K)], heat capacity C_p [J/(kg·K)], density ρ [kg/m^3], moisture isotherm w [kg/m^3], liquid transport coefficient D_w [m^2/s] and water vapor resistance factor μ [-]. The individual material properties were obtained from manufacturers, some measured and remaining were taken from literature (Table 1). Density ρ, heat capacity C_p and water vapor resistance factor μ are considered constant for each material. Thermal conductivity, moisture isotherm and liquid transport coefficient vary depending on conditions; where thermal conductivity λ and liquid transport coefficient D_w depend on water content w and moisture isotherm is described by water content w in relation to relative humidity φ.

Table 1. Material properties applied in numerical hygrothermal simulation.

Material	***λ (w)***	***ρ***	***C_p***	***w (φ)***	***D_w (w)***	***μ***
Gypsum board	0.19-0.6	820	1100	0-23.8	0-4.85·10^{-7}	10
Wood fiber insulation board	0.0485-0.6	37	2100	0-15.2	0- 4.85·10^{-9}	1.6
Vapor barrier	0.33	980	1500	0	0	3500
Wood fiber insulation	0.04	60	2100	0-15.2	0-1.07·10^{-7}	1.5
Wind-shield	0.049	235	1500	0-71.3	0-4.85·10^{-9}	13

3.5 Finnish Mould Growth Model

Finnish Mould Growth Model was applied to assess the suitability of building design against biological growth (Viitanen & Ojanen, 2007). It represents a suitable tool for the assessment of different design strategies whether mould growth appears on or inside building components based on dynamic hygrothermal conditions (Lie *et al.*, 2019; Fedorik *et al.*, 2015). The Finnish mould growth model achieves good agreement between the predicted and observed mould growth (Jensen, 2019) and represents the basis for international building standard ASHRAE 160 p (ASHRAE, 2016).

With the Finnish mould growth model, mould growth can be predicted on different building materials in changing hygrothermal conditions. The mould growth risk in the model is presented with a mould index M, which varies between 0-6 and describes amount of the mould appearance on a material surface. Temperature and relative humidity both affect the mould growth rate, and value of mould index M. The model also considers mould decline when hygrothermal conditions are not in favorable area for mould growth. Favorable area for mould growth is defined at a temperature range between 0-50 °C and relative humidity over 80% for sensitive and very sensitive materials and 85% for medium resistant and resistant materials (Ojanen *et al.*, 2010). Hence, the Finnish mould growth model classifies materials for four sensitivity and four decline groups according to their associated factors (surface type,

coating and contact with other materials) (Viitanen & Ojanen, 2007; Vinha *et al.*, 2013).

4 Results

4.1 Validation of Numerical Simulation

The experiment provides hygrothermal data to validate the numerical model (Figures 3 and 4), which can be further applied for future prediction and risk management tools. The numerical results agreed well with the measurement and the calculated hygrothermal conditions are within accuracy (±0.3°C for temperature and ±2.0% for relative humidity) of the measurement system (Figure 3 and 4). The small-scale variation occurring in the experimental setup is not present in the calculated moisture content or temperature.

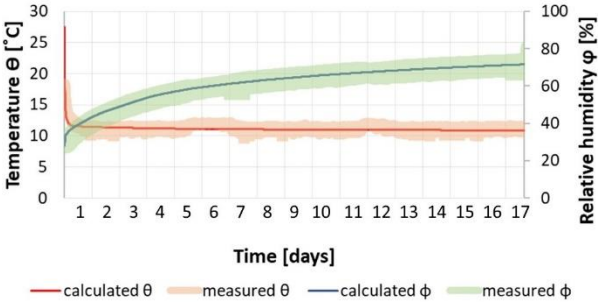

Figure 3. Experimental (expressed with accuracy limits) and simulated temperature and relative humidity at structural analysis point 1.

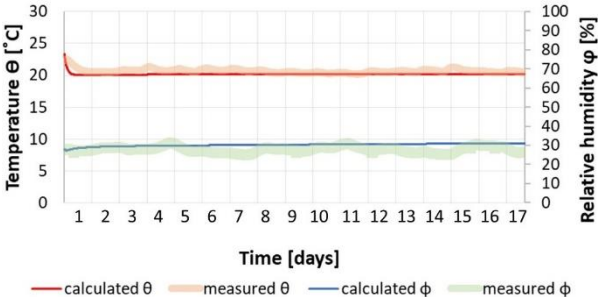

Figure 4. Experimental (expressed with accuracy limits) and simulated temperature and relative humidity at structural analysis point 2.

4.2 Hygrothermal Performance Under Current Building Design Approach

In the simulated climate the temperature is the highest and relative humidity is the lowest in summer. Vice versa in the wintertime temperature has the lowest values and relative humidity has the highest values. However, despite high relative humidity values in wintertime, there was no risk for mould growth because temperature was not continuously in favorable area (0-50°C) for mould growth (Viitanen & Ojanen, 2007). The fluctuation of the temperature and relative humidity at point 1 is greater than at point 2 due to its location closer to the outdoor conditions that change in time. The relative humidity in the wintertime varies from 80% to 90% (Figure 5) at point 1, and is fairly constant at around 40% at the point 2 (Figure 6). The temperature and relative humidity at the point 2 in summertime vary between 15°C and 22°C and 30% and 45%, respectively, and these hygrothermal conditions can be considered unsuitable for biological growth (Figure 6).

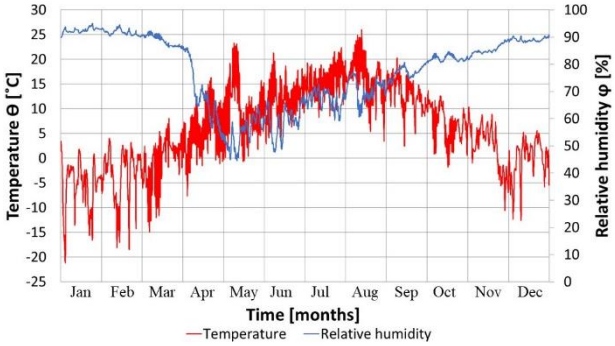

Figure 5. Temperature θ and relative humidity φ at point 1 applying test year data Jokioinen 2004.

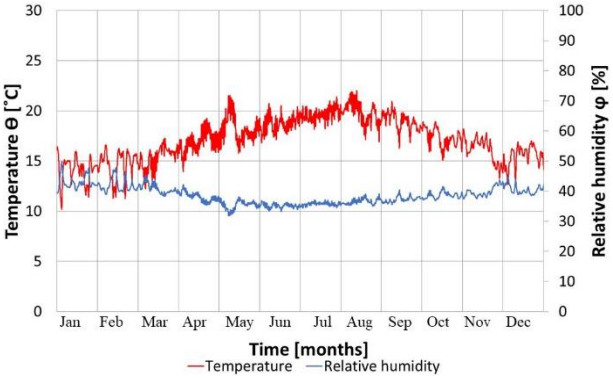

Figure 6. Temperature θ and relative humidity φ at point 2 applying test year data Jokioinen 2004.

Only 2004 results are shown because graphs of temperature and relative humidity were similar in all climate scenarios without any significant differences.

4.3 Hygrothermal Performance Under Different Future Climatic Scenarios

The progress of temperature and relative humidity during one year inside the building envelope (points 1 and 2) subjected to the future scenarios (Jokioinen 2030, 2050 and 2100) are very similar to Jokioinen 2004 test year. The mean annual temperature increases by 1.14°C in 2030, 2.02°C in 2050 and 4.85°C in 2100 in comparison to test year Jokioinen 2004. The relative humidity assumes slight decrease in 2030 by 0.04% but increase in 2050 and in 2100 by 0.25% and 1.12% respectively (Figure 7). Consequently, the annual temperature increases between windshield and wool insulation (point 1) by 1.05°C in 2030, 1.88°C in 2050 and 4.54°C in 2100 scenarios. However, the impact of increasing temperature outdoors in the future is smaller on the

interior surface of the water vapour barrier (point 2) where the thermal conditions are estimated to be increased by 0.27°C in 2030, 0.49°C in 2050 and 1.19°C in 2100 (Figure 7).

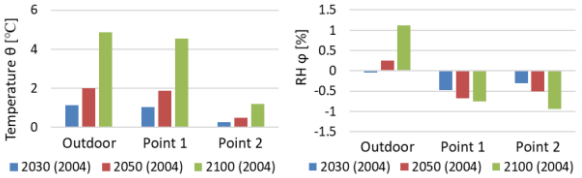

Figure 7. Annual temperature and relative humidity increment for future climate in relation to test year Jokioinen 2004.

The temperature at point 1 with Jokioinen 2100 test year is slightly higher than 2004 test year in the simulated year. The temperature difference between 2004 and 2100 year is almost 3.4°C in mid-April and 4.5°C in mid-October (Figure 8). Between the years in mid-April the temperature increases from 21.9°C to 25.2°C and relative humidity decreases from 46.4% to 46.3% (Figure 8) which means that absolute humidity increases by 1.86 [g/m^3]. Then, dew point increases from 9.7°C to 12.8°C. This reflects the assumption that the outdoor climate will be warmer and more humid in the future.

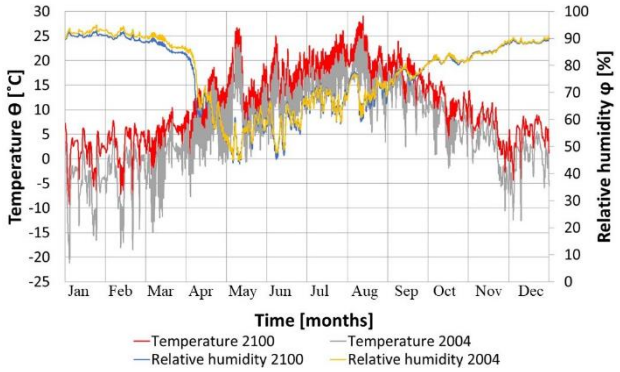

Figure 8. Temperature and relative humidity at structural analysis point 1 for test year Jokioinen 2004 and Jokioinen 2100.

To visually compare all studied (Jokioinen 2004, 2030, 2050 and 2100) scenarios, moving averages of two hundred hours were applied (Figures 9 and 10). Progressive increment in temperature is apparent, especially at structural analysis point 1 (Figure 9), from which the effect of climate change decreases in the wall element from outer wall towards indoors (Figure 10). Therefore, the impact of different climatic scenarios on hygrothermal conditions inside building envelope decreases with the depth of the structure.

The differences in humidity at structural analysis point 1 and 2 referenced to Jokioinen 2004 test year vary between -11% and 2%, with average -0.8% at point 1 and -5% and 1% with average -0.9% at point 2 in 2100, -7% and 1% with average -0.7% at point 1 and -3% and 1% with average -0.5% at point 2 in 2050 and -4% and 1% with average -0.5% at point 1 and -2% and 1% with average -0.3% at point 2 in 2030 (Figure 9 and 10). However, there were no significant differences between relative humidity in longer term cycles.

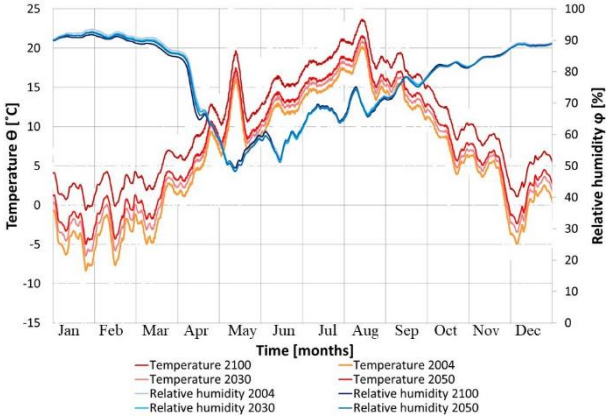

Figure 9. Temperature and relative humidity presented as moving average of two hundred hours at the structural analysis point 1.

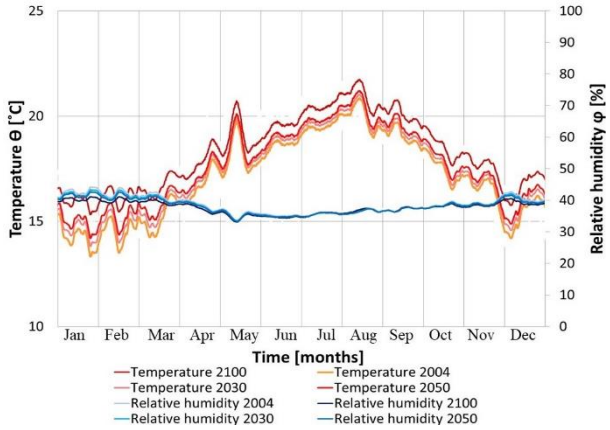

Figure 10. Temperature and relative humidity presented as moving average of two hundred hours at the structural analysis point 2.

4.4 Mould Growth Risk

The temperature and relative humidity data obtained on indoor surfaces of windshield (point 1) and water vapour barrier (point 2) do not show risk for mould growth. At structural analysis point 2, the hygrothermal conditions were unfavorable for mould growth during the entire analyzed period in all climatic scenarios. The reason is relative humidity that varies between 30% and 45%, hence does not exceed critical value of 80%. Hence, the mold index for this area would be 0.

Favorable hygrothermal conditions were obtained only at structural analysis point 1 located between windshield and wood fiber insulation. The wood fiber is mould sensitive material classified in the Finnish mould growth model by class 2. The mould index illustrates the highest risk of mould growth initiation in the case of Jokioinen 2100 test year where the

relative humidity was over 80% for 26.5 weeks during a year. The relative humidity exceeding 80% was achieved especially in wintertime, in which the temperature drops under 0°C, representing unfavorable conditions for biological growth.

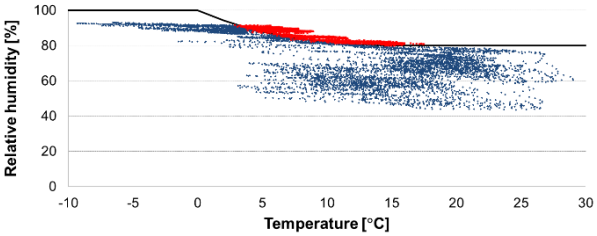

Figure 11. Temperature and relative humidity calculated at each time-step during year using Jokioinen 2100 outdoor conditions (red dots indicate favorable and blue dots unfavorable conditions for mould growth).

However, in all analyzed cases the maximum mould index achieved is below 1 (Table 2) leading to an assumption that the studied assembly following current manufacturer specified wall structure could be considered suitable also for future climate.

Table 2. Maximum mould index achieved at point 1 in different climatic scenarios: Jokioinen 2004, 2030, 2050 and 2100.

Simulated year	***Point 1***
Jokioinen 2004	0.002
Jokioinen 2030	0.009
Jokioinen 2050	0.022
Jokioinen 2100	0.117

5 Conclusions and Future Development

Numerical hygrothermal simulation agrees with measured data in the case of wood fibred insulated wall assembly. Calculated temperature and relative humidity data at analyzed points were within tolerances of measurement equipment.

There is a significant difference between temperatures in 2004 and 2100. Relative humidity is at similar level, which means that the absolute humidity levels and dew points inside the wall structures increase significantly. However, according to the Finnish mould growth model, risk for mould growth remains very low at analyzed points. Validation and future test years models converged with good accuracy and without numerical errors which supports the accuracy of the results.

Study shows that the impact of different climatic scenarios on hygrothermal conditions inside building envelope decrease with depth of the insulated structure. Validated numerical model can be applied for future performance assessment and risk management for healthy long life cycle buildings.

The future work consists of improving dynamic experimental validation and building elements exposed to real conditions.

Acknowledgement

We are grateful for the support of this work through project from the Academy of Finland (Climate Change and Health (CLIHE) project 329885).

References

ASHRAE Standard 160-2016. Criteria for Moisture-Control Design Analysis in Buildings; ASHRAE: Atlanta, GA, USA, 2016.

Wenqiang Dong, Youming Chen, Yang Bao, and Aimin Fang. A validation of dynamic hygrothermal model with coupled heat and moisture transfer in porous building materials and envelopes, *Journal of Building Engineering*, 32, 2020. https://doi.org/10.1016/j.jobe.2020.101484.

Filip Fedorik, Mikko Malaska, Raimo Hannila, Antti Haapala. Improving the thermal performance of concrete–sandwich envelopes in relation to the moisture behaviour of building structures in boreal conditions. *Energy and Buildings*, 107, 226–233, 2015, https://doi.org/10.1016/j.enbuild.2015.08.020.

Filip Fedorik and Antti Haapala. Hygro–thermal and Mould Growth Risk Analysis of Common Foundation Structures. *Energy Procedia 132C*, 111–116, 2017, https://doi.org/10.1016/j.egypro.2017.09.655.

Filip Fedorik and Antti Haapala. Numerical estimation of mould growth on common single-family house building envelopes in boreal conditions. *European Journal of Environmental and Civil Engineering*, 22(10), 1196–1211, 2018. doi: 10.1080/19648189.2016.1245632.

Carl-Eric Hagentoft and Pär Johansson. The Future Climate Moisture Susceptibility of Wall Assemblies: Analysis Based on Monte Carlo Simulation Using a Simplified Deterministic Hygrothermal Simulation Model, *Current Topics and Trends on Durability of Building Materials and Components, Serrat, C., Casas, J.R. and Gibert, V. (Eds)*. 2020. doi: 10.23967/dbmc.2020.197.

Nickolaj F. Jensen, Søren P. Bjarløv, Christopher J. Johnston, Casper F. H. Pold, Morten H. Hansen, and Ruut H. Peuhkuri. Hygrothermal Assessment of North-Facing, Cold Attic Spaces under the Eaves with Varying Structural Roof Scenarios. *Journal of Building Physics*, 44, No 1, pp. 3–36, 2020. https://doi.org/10.1177/1744259119891753.

Kirsti Jylhä, Kimmo Rusoteenoja, Jouni Räisänen, Ari Venäläinen, Heikki Tuomenvirta, Leena Ruokolainen, Seppo Saku, and Teija Seitola. Arvioita Suomen muuttuvasta ilmastosta sopeutumistutkimuksia varten. *ACCLIM-hankkeen raportti 2009*. Ilmatieteen laitos. Raportteja 2009:4. 102 s

Yujin Kang, Seong J. Chang, and Sumin Kim. Analysis of hygrothermal performance of wood frame walls according to position of insulation and climate conditions. *Journal of the Korean Wood Science and*

Technology, 44(2), 264-273, 2016. doi:10.5658/WOOD.2016.44.2.264.

Solrun K. Lie, Thomas K. Thiis, Geir I. Vestøl, Olav Høibø, and Lone R. Gobakken. Can existing mould growth models be used to predict mould growth on wooden claddings exposed to transient wetting?, *Building and Environment*, 152, 192-203, 2019. https://doi.org/10.1016/j.buildenv.2019.01.056.

Rob Marsh. Building lifespan: effect on the environmental impact of building components in a Danish perspective, *Architectural Engineering and Design Management*, 13:2, 80-100, 2017. doi: 10.1080/17452007.2016.1205471, 2017.

Vahid M. Nik. Hygrothermal Simulations of Buildings Concerning Uncertainties of the Future Climate. PhD thesis. Chalmers University of Technology, 2012.

Tuomo Ojanen, Hannu A. Viitanen, Ruut H. Peuhkuri, Kimmo Lähdesmäki, Juha L. Vinha, and Kati Salminen. Mold growth modeling of building structures using sensitivity classes of materials. *ASHRAE Buildings XI Conference*, 2010 Cleawater Beach, Florida, United States, pp. 1-10, Dec. 5-9, 2010.

ROTI 2021 Rakennetun omaisuuden tila -raportti 2021, https://www.ril.fi/media/2021/vaikuttaminen/roti2021_low.pdf.

Hannu Viitanen and Tuomo Ojanen, Improved model to predict mold growth in building materials, *10th Thermal Performance of the Exterior Envelopes of Whole Buildings Conference*. Clearwater Beach, United States, Dec. 2-7, 2007.

Juha Vinha, Anssi Laukkarinen, Mikael Mäkitalo, et al. Ilmastonmuutoksen ja lämmöneristyksen lisäyksen vaikutukset vaipparakenteiden kosteusteknisessä toiminnassa ja rakennusten energiankulutuksessa. Tampere University of Technology. Department of Civil Engineering. Structural Engineering. Research Report 159. 2013. http://urn.fi/URN:ISBN:978-952-15-2949-8.

Juha Vinha, Mikko Salminen, Kati Salminen, Targo Kalamees, Jarek Kurnitski, and Mihkel Kiviste. Internal moisture excess of residential buildings in Finland. *Journal of Building Physics*, 42(3): 239-258, 2018. https://doi.org/10.1177/1744259117750369.

Advanced model-based control of B36:45 LNG engines

Svein Roar Kvåle[1] Roshan Sharma[2]

[1]Bergen Engines AS, Norway,
[2]University of South-Eastern Norway, Porsgrunn, Norway, roshan.sharma@usn.no

Abstract

The framework of model predictive control is used in this paper to optimally control the operation of an B36:45 LNG engine. The model of the engine is based on real life data from an installed B36:45 gas engine in a power plant. Stored data from the plant was used to develop a state space model of the process consisting of 2 manipulatable variables, 3 measured disturbances and 6 measured outputs. The goal is to use global ignition timing and the charge air pressure as control variables to minimize the heat rate while considering constraints on the measured outputs. Heat rate of the engine is directly related to engine performance efficiency. Results show that a model based controller has the potential to be used as an advanced controller for optimal operation of this engine.
Keywords: B36:45 LNG engine, MPC, optimal operation

1 Introduction

Bergen Engines AS is a developer and producer of gas and diesel engines for the marine and land-based power marked. The factory is located just north of Bergen on the west coast of Norway and have been since it moved from the city centre of Bergen in 1965. Bergen Engines was part to the Ulstein group from mid-eighties until 1999 from which it has been a part of Rolls-Royce.The latest LNG (Liquefied Natural Gas) fuel engine type developed is the B36:45 engine family, and a graphical representation of the engine is shown in Figure 1.

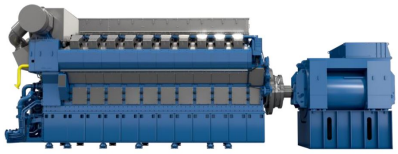

Figure 1. 20 cylinder B36:45 LNG gas engine with generator. (Courtesy: Bergen Engine AS)

For an LNG gas engine, the engine efficiency is in general as shown in Figure 2 for a given power output. It should be noted that the efficiency is not very good below 20% power output and rises slowly from approx. 30% power output to 100% at which the efficiency is close to 50%. The distribution of the efficiency losses can be seen in Figure 2 where most of the losses are to the exhaust gas.

In the search for increasing the engine efficiency, more

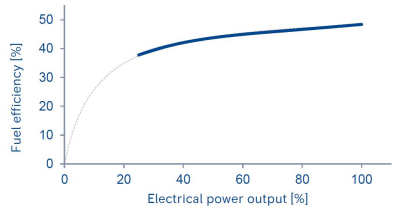

Figure 2. Fuel efficiency for and LNG engine. (Courtesy: Bergen Engine AS)

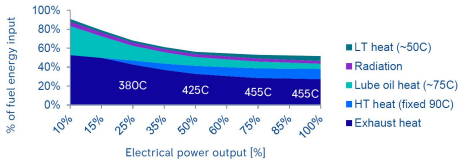

Figure 3. Distribution of losses for an LNG gas engine. (Courtesy: Bergen Engine AS)

complex logic, which takes into account more of the information available, is constantly developed. This has resulted in a large increase in parameters and static maps that interact with each other, which makes the engine tuning phase a complex and time-consuming job.

It is of great interest to Bergen Engines AS to use advanced model based controller such as a model predictive controller (MPC) for generating optimal set points based on measured states of the engine and known disturbances. This is set to be the first step towards a more data driven, self-optimizing algorithms that can use the large amount of data produced. The ultimate goal here is to use a reduced set of parameters which can be used to prioritize different possibilities such that various requirements are reached. For instance one of the requirements for a project can be to reach a given NO_x set point and secondary fuel efficiency, while for another case, it can be the fuel economy as the most important requirement while keeping the NO_x within given constraints.

The main engine controller currently used is an embedded controller from Woodward Inc. The LECM (Large Engine Control Module) is a purpose-built controller with suitable hardware for interfacing large industrial engines. The software for the controller is developed and built in-house at Bergen Engines and hence gives a large flexibility in custom made control algorithms. The control software used in the LECM is developed in MATLAB Simulink with a proprietary library for hardware access to the ac-

tual controller from MotoHawk. The MotoHawk library is a rapid programming development tool which allows engineers to quickly develop control software in Simulink to run on a MotoHawk enabled control module; like the LECM. Even though MotoHawk as many pre-made algorithms available, it does not have any available MPC control structures and hence this must be developed using standard MATLAB and Simulink functions. Thus the main goal of this project work is to add MPC control structure to this existing controller for engine fuel optimization.

MPC has been proven in use for instance in steam generators and servos as illustrated in Richalet (1993). In Koli (1981) an MPC for a turbocharged gasoline engine with EGR (Exhaust Gas Recirculation) has been developed where the dynamics of the model is defined by simple feedforward neural network. It showed that the simple black-box model is sufficient for using with MPC. A paper by Luther (2002) compares neural-net-based modelling to Adiabatic Mean Value Engine Modelling. Some system parts were modeled with good accuracy, but others with large deviations. A neural net based MPC has been used for the non-linear MIMO system with great performance. In Lu et al. (2015) support vector machine for non-linear system identification has been used. The engine model shows the rotation speed of the engine as a function of fuel flow, and an MPC is designed in Simulink.

2 Operational Philosophy

The B36:45 engine family is a medium speed lean-burn single fuel spark ignited internal combustion engine. It mainly uses LNG as fuel source and a run at 720/750 rpm for 60- and 50 Hz applications respectively. It is turbocharged and has a 2-stage water cooled charge air cooler. In most land-based power plants it connected to a generator which is often connected to either a small local grid or a large national grid. The engines nominal power output is 600 kW pr cylinder mechanically and comes in both in inline and Vee configurations. The smallest is an inline 6-cylinder engine and the largest is a Vee 20-cylinder engine.

2.1 Lean burn gas engine - Otto Cycle

A lean-burn gas engine runs with a high air to fuel ratio compared to the required air for a stochiometric combustion. This lowers the combustion temperature and hence reduces NO_x emissions. The B36:45 engine is a lambda 2 engine, indicating that it runs with twice the required amount of air for a stochiometric combustion. This lean mixture is difficult to ignite and hence a pre-combustion chamber is mounted in the cylinder head. A rich mixture is here ignited by a spark plug and the resulting flames will propagate out and into the main chamber where it will ignite the lean mixture. Figure 4 shows an illustration of the engine process and some control loops. The engine is a 4-stroke (also known as the Otto cycle) which means that there are 4 distinct phases for the combustion process.

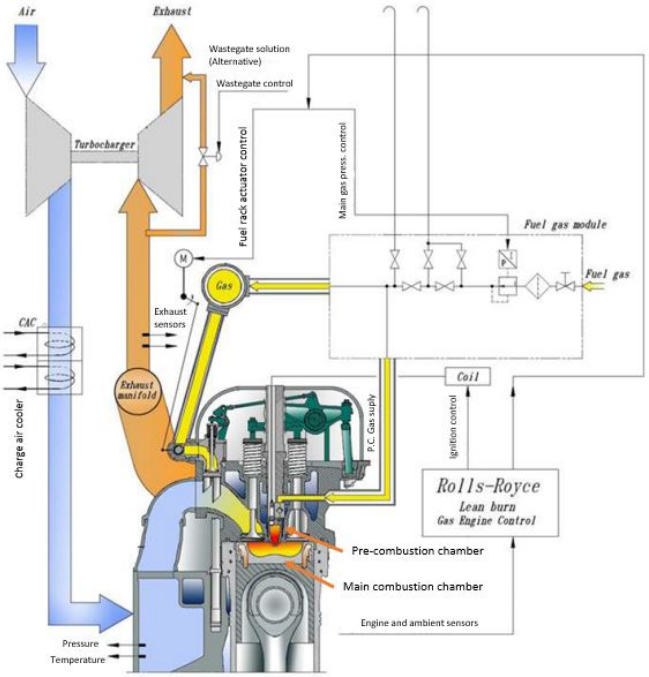

Figure 4. Illustration of the process with some control loops. (Courtesy: Bergen Engine AS)

2.2 Main control loops

This section shortly describes the most common control loops for the combustion process which are controlled by the engine control system today. There some other control loops as well, but the major once are described here.

2.2.1 Speed Control

It is a PID controller which controls the flow of fuel admission in order to keep the engine speed at a desired set point. When connected to a large electricity grid with fixed frequency, speed control loop is used to control the engine power output to a given set point. Increasing the set point for speed will make the speed controller to increase the fuel admission by increasing the fuel flow which will result in an increase of engine power output as the grid frequency cannot change.

2.2.2 Air pressure/AFR control

The AFR, or air pressure control, is a control loop whose main purpose is to control the charge air pressure in the air receiver to a given set point. The set point is based on a map with engine power output and engine speed as inputs. The set point map is derived based on numerous of test runs at the test bed by skilled engineers. Since this is a static map the set point must be biased to a certain degree based on operational conditions. The air pressure control is the most active and influents of all control loops. It dictates most of the engine behaviour as it directly controls the air/fuel ratio under all operational conditions.The output from the air pressure control is a position control signal to a waste gate actuator. The waste gate actuator will control the amount of exhaust by-passing the turbine

part of the turbocharger(s) and hence the energy used to increase the air pressure.The feedback to the air pressure control is the measured air pressure in the air receiver which then forms a closed loop control system. One of the goals of this project is to find the optimum charge air pressure to maximize engine efficiency.

‘

2.2.3 Air temperature control

In order to further control the air/fuel ratio the temperature of the combustion air should be kept at given values. The air temperature is often controlled by a low level PID controller to a given set point based on operational ambient conditions.The control signal from the PID controller is used to control a 3-way valve which will direct, or bypass, water to a 2-stage charge air cooler. By increasing the amount of water going through cooler the temperature can be reduced, and vice-versa. An increase in temperature will lead to an increase in NO_x due to lower air mass added to the combustion process and due to increase in temperature. This will also result in the engine operating closed to the ignition knocking limit.

2.2.4 NO_x control

There are dual NO_x sensors at the exhaust outlets to measure NO_x [ppm] and Oxygen [%]. A PID controller control the NO_x level to a given setpoint. However, the NO_x controller will bias the air pressure controller’s base set point between +10% and -5%, so there is direct interaction between these controllers.

‘

2.2.5 Global ignition timing control

The ignition timing is the time in crank angle (CA) degrees at which the cylinder individual spark plug is ignited in the pre-combustion chamber. The base timing setpoints is created as a map based on various testing on the testbed by engineers. This base timing is adjusted such that a good margin to ignition knocking while maintaining high level of efficiency is achieved. The global timing is adjusted so that the maximum pressure in the cylinder is occurring around 13-15 [degCA] after TDC (Top Dead Center). This will give rise to best performance. The control of the timing location is complex and difficult to maintain.

In this project, this complexity is reduced by allowing an advanced model based controller to find the optimum timing set points given a set of constraints to protect the engine from running into dangerous operational points.

2.3 Global ignition timing and efficiency

In Figure 5, an indication of the relationship between global ignition timing and peak pressure and engine efficiency is shown. These curves are based on data from tests performed on the previous version of the Bergen LNG gas engine, the B35:40. This engine operates at lower brake mean effective pressure (BMEP) than the B36:45 engine and with lower peak pressures. The indicated relationship

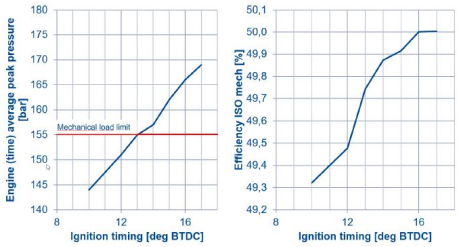

Figure 5. Global timing influence on efficiency and cylinder pressure.

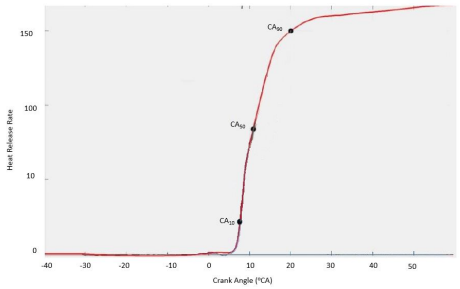

Figure 6. Heat release curve.

however shows similar behaviour also for the B36:45 engine. Earlier ignition timing, i.e. ignition before top dead centre (BTDC) will increase the peak pressure in the cylinder, but it will also increase the efficiency of the engine. There are however, as indicated, a mechanical limit in the construction of the engine on how high the peak pressure can become before there is a risk of mechanical breakdown. The engine control system therefore monitors the peak pressure for all cylinders and in case of too high pressure the engine will shut down. For the MPC, this pressure will be used as a constraint to avoid too high pressure.

2.4 Global ignition timing and heat rate

The accumulated heat release average over a number of combustion cycles are used together with the measured engine load to calculate the heat rate of the engine. The smaller the heat rate of the engine, the less is the amount of fuel used per unit power output. In other words, minimized heat rate will maximize engine efficiency. A typical heat release curve for different ignition timing (crank angle) is shown in Figure 6. The heat release curve is shown with the locations for CA10, CA50 and CA90. These are the locations at which 10%, 50% and 90% of the fuel have been burned in the combustion chamber.

3 Process modelling and description

Operational data collected from a commercial B36:45 engine operating in a power plant in the city of Tabor in Czech Republic was used to develop a data-driven model. The process data is captured at 10 Hz sampling rate by a local data logger. This logger then pushes the data to the cloud every 30 minutes. This data is used both for modelling, fault detection, machine learning and support

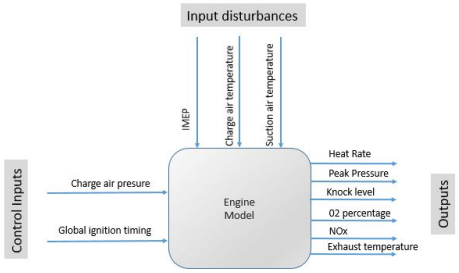

Figure 7. Process functional diagram.

at Bergen Engine AS. A functional diagram of the process showing the control input signals, output signals and the input disturbances is shown in Figure 7.

The two control inputs are the *charge air pressure* and *Global ignition timing*. There are six measured outputs from the system namely *heat rate, peak pressure, knock level, oxygen (O_2) percentage, NO_x* and *Exhaust temperature*. In addition there are three measured input disturbances namely *IMEP (Indicated Mean Efficiency Pressure), charge air temperature* and *suction air temperature*.

3.1 Charge air pressure

The charge air pressure is the pressure of the combustion air entering the combustion chamber from the air receiver. This pressure is controlled by adjusting the waste gate bypass valve such that the pressure is according to set point. Traditionally these set points are found based on testing on a real engine where the emissions are measured and the distance to the knocking limit is observed. In addition, the pressure is mapped towards the turbocharger to prevent any stalling or crossing the surge limit. The charge air pressure set point is usually a map where the set point is based on the engine speed and the power output but biased from several sources to make it adaptable to ambient conditions and ageing. This charge air pressure set point is traditionally highly driven by the engine power output in an almost linear relation. Nominal charge air pressure at 100% power output is approximately 4.2 barg.

3.2 Global Ignition timing

The global ignition timing command is used to set the base ignition timing for the engine. Each individual cylinder will adjust this base timing withing a window of $\pm$-3 [degCA] to balance the peak pressure off the cylinders. The ignition base timing is traditionally found during testing and running the engine close to the knocking limit during controlled environments. It is however not given that the same conditions will be applicable on every project and hence margin must be added on the set point to take into account different fuel compositions and ambient conditions. Ageing is also a factor here. To counter act these changing conditions several set point modifiers are in place which will bias the set point if a change in ignition knocking is detected or if exhaust temperature is increased. In addition, the location of the centre of combustion is measured based on the heat release curve from the combustion process. This location is used as a set point on a second level PID controller which biases the base set point so that this location is kept on set point as well. But none of these measures are there to optimize the fuel consumption over time and to take into account all these constraints as an MPC controller can do.

3.3 Suction air temperature

This is slow varying input disturbance to the system which has the least impact. The suction air temperature is the air temperature measured at the inlet of the compressor part of the turbocharger. This disturbance will inform the system about the ambient conditions under which the engine is currently operating. The ambient temperature, and hence the suction air temperature will wary over a year for a given installation location. This variation might be small or large depending on the location. It might therefor have an impact in some cases and hence it is included here.

3.4 Charge air temperature

The charge air temperature is measured in the air receiver and is the temperature of the combustion air fed into the combustion chamber during the opening time of the inlet valve. This temperature is in some cases actively regulated by a PID controller, while it in some installations are mechanically adjusted at max power output to give a certain temperature. Normal operational temperature here is around 50-55 °C. This might however change if the humid conditions are present such that condensation might occur at this temperature. The temperature of the charge air influences the air mass which is available to the combustion process and hence any change here will impact both NO_x emissions and the resilience towards knocking.

3.5 IMEP

IMEP (Indicated Mean Effective Pressure) is a measure of produced work of the engine including the friction work, i.e. the actual work done by the engine independent of the engine displacement. It is a measure of the average pressure in the combustion chamber of the engine cycle. IMEP is measured directly by the cylinder pressure sensors. The highest and lowest values are removed and the average over the number of cylinders is taken and fed into a moving average filter over 100 cycles. This final value indicates the current loading (power output) of the engine.

3.6 Heat rate

This is the variable that is to be minimized. It is indicative of the relation between the power output and the fuel consumption estimation. The heat rate is given as the relation between the IMEP and the total heat release. The IMEP is measured by the cylinder pressure sensors as well as the total cumulative heat release. The heat release is given as [kJ/cycle] and is estimated based on the pressure rise curve measured by the cylinder pressure sensors.

3.7 Knock level

Knock level is also known as engine detonation and is when the combustion takes place prematurely in part of the compressed air fuel mixture in the cylinder. This knocking can cause severe damage to the engine if not responded to early because of high frequency pressure waves causing very high cylinder pressures potentially above the design limit of the engine. The engines are constantly pushed towards the knocking limit as this area produces better fuel efficiency at higher power outputs. Knocking might occur if the air fuel mixture is not correct or substances such as oil leaks into the combustion chamber causing changes to the burn rate of the air/fuel mixture. Each cylinder is monitored for knock level and any increase in knocking results in that cylinder ignition timing being retarded for some time. If several cylinders experience knocking the global timing point is usually retarded to avoid any further increase into non-operational areas. The knock value is measured by looking at the ripples on the cylinder pressure curve after the ignition location. This value indicates the level of knocking for each cylinder but is averaged for all cylinders here. This will in general only pickup up globally severe knocking. Knocking can also be reduced by lowering engine power output or increasing the amount of air in the air/fuel mixture resulting in a leaner mixture. That will however impact efficiency.

3.8 Peak pressure

The peak pressures are measured from cycle to cycle and is the highest measured pressure in the combustion chamber of the combustion cycle. The peak pressure is a value which must be limited as there are design limitations on the engine for how high pressures the internal components can withstand without damage.

3.9 NO_x

The NO_x emissions are measured in the exhaust outlet after the turbocharger. The emissions are measured with sensor from Continental most commonly used on trucks and cars. This sensor gives the wet NO_x values in ppm directly and is used in a closed loop regulation for controlling the level of NO_x to a given set point. The NO_x values are good indications of how rich or lean the fuel mixture in the combustion is. A high NO_x value indicates a rich mixture and vice versa. The NO_x value is very sensitive to these variations and will rapidly increase in case of the charge air pressure is reduced. It should however be noted that the NO_x values should rarely be seen drifting high during steady operation. During transients a change in NO_x value is expected as the engine increases the air pressure during the transient to get better margins to the knock limit.

3.10 O_2

The same sensors that measures the NO_x level in exhaust will also measure the O_2 level. In the traditional engine controller, the O_2 percentage is used actively for engine limitation. That is if the O_2 level becomes too low, which indicates a too rich mixture, the engine will limit the fuel admittance and hence reduce power output.

3.11 Exhaust temperature

Traditionally the exhaust temperature outlet from each cylinder has been used to balance the engine power output from each cylinder. Before the cylinder pressure sensor era the only possibility to check how much each cylinder contributed to the power output was by looking at the deviation in exhaust temperature between the cylinders. The exhaust temperature used here is the temperature measured in the collecting pipe just prior to the turbine part of the turbocharger. This exhaust will therefore be an indicative of the all cylinders on that pipe collectively. The temperature will increase in case the power output increases and mixture becomes too rich. It is therefore very dependent on the charge air pressure, but also the ignition timing. In case the ignition timing is retarded the temperature will increase and hence this needs to be handled.

3.12 State space model of engine

In order to find the relationship between the control inputs, the measured outputs and the measured input disturbances, system identification toolbox in MATLAB was utilized to obtain a discrete state space model of the form,

$$\begin{aligned} x_{k+1} &= Ax_k + Bu_k + B_d u_{d,k} \\ y_k &= Cx_k \end{aligned} \tag{1}$$

Here, x is the state vector, u is the vector of control inputs, u_d is the vector of measured disturbances and y is the vector of the measured outputs. The state matrix, input matrix, disturbance matrix and the output matrix are $A \in \mathbb{R}^{25\times25}$, $B \in \mathbb{R}^{25\times2}$, $B_d \in \mathbb{R}^{25\times3}$ and $C \in \mathbb{R}^{6\times25}$ respectively. The subscript k denotes the discrete time steps.

4 Optimal control problem formulation

The goal of utilizing an advanced optimal controller is to maximize the engine efficiency. This is achieved by minimizing the heat rate of the engine. To do so, the controller will generate optimal values for the *charge air pressure* and *global ignition timing*. From an optimization point of view, these two are the decision variables. These signals will not directly control the process values but will act as optimal set points for the lower level PID controllers which in turn will adjust accordingly to achieve optimal operation.

The physical constraints for the charge air pressure will be imposed as bounds to the optimizer. By a defined upper limit for what is physical possible and at the same time set a lower bound close to 0 barg. Since the process will not be working on 0 barg air pressure, the lower bound will be set to 0.3 barg and the upper bound to 4.5 barg to give some regulation margin. The charge air pressure

cannot instantly change from one pressure to the next and hence the optimizer is limited based on rate of change of the control value such that it cannot change instantly. Nor can the waste gate valve change instantly and hence such limitations makes sense.

The global base timing will influence the efficiency of the engine but also has an impact on the peak pressures, NO_x generation, knocking and exhaust temperature. By advancing the global timing, the peak pressure increases and this needs to be within the design limit of the engine to prevent mechanical damage to the it. If the ignition is retarded the exhaust temperature increases and the NO_x emissions decreases as the combustion air temperature increases due to longer burn duration. By retarding the ignition timing, the heat rate increases to indicate less efficiency. There are some physical known limitations of the ignition timing that should be obeyed. The global ignition timing is seldom, if at all, below -8.5 [degCA] for a running power plant connected to the grid and producing power at nominal speed. It will also not be possible to advance the timing more than to -20 [degCA]. Nominal global ignition timing is usually in range of -12 [degCA] to -16 [degCA].

The knock level here is included as constraint at it is a limiting factor for advancing the global ignition timing too much or reducing the charge air pressure too much. Typically, the engine is shutdown with a value over 30%.

The nominal peak pressures during 100% power output at nominal speed is usually around 175 [bar]. The control system has alarms and shutdown conditions if sustained operation around 200 bar is experienced and hence the optimizer should avoid operation above 200 bar, and preferably limit operation to 180 bar but with some slack.

The NO_x value would be used as a constraint during the optimization phase such that it can stabilize below at least 150 ppm.

The O_2 is rather critical and hence strict constraints on the low level is to be used. During normal operational conditions the O_2 percentage is somewhere between 8.5% and 12.5%, with nominal condition a approx. 9.5%. The optimization should be rather strict on the lower limit while the upper limit can be broken during given condition. The aim should however be to stay within the limits of 8.5% and 12.5%.

There are limitations from the turbocharger supplier on the max inlet/suction temperature of turbine and hence these needs to be obeyed. The constraints can here be set based on normal operational conditions where the exhaust temperature before the turbocharger turbine should not exceed 600 °C.

Table 1 shows the constraints on the output signals and Table 2 lists the constraints on the control inputs and input disturbances.

In order to minimize the heat rate of the engine while still satisfying the constraints on both the inputs and the output signals, a constrained optimal control problem is

Table 1. Constraints on the outputs.

Signal (symbol)	lower limit	Upper Limit
Peak Pressure (P_p)	0 bar	180 bar
Knock level (K_l)	0%	30%
Heat rate (h_r)		
Exhaust temperature (T_e)	0 °C	600 °C
NO_x (N_{ox})	0 ppm	150 ppm
O_2 (O_2)	8.5%	12.5%

Table 2. Constraints on the control inputs and disturbances.

Signal (symbol)	lower limit	Upper Limit
Charge air Pressure (P_{ca})	0.3 barg	4.5 barg
Global timing (G_t)	-20 degCA	-8.5 degCA
Charge air pressure rate ($\triangle P_{ca}$)	-0.2 barg/s	0.2 barg/s
Global timing rate ($\triangle G_t$)	-0.3 degCA/s	0.5 degCA/s

formulated as,

$$
\begin{aligned}
\min_{P_{ca},G_t,s_1,s_2} \frac{1}{2}\sum_{k=1}^{N} & h_{r,k}^T P h_{r,k} + P_{ca,k-1}^T Q_1 P_{ca,k-1} + G_{t,k-1}^T R_1 G_{t,k-1} \\
& + \triangle P_{ca,k-1}^T Q_2 \triangle P_{ca,k-1} + \triangle G_{t,k-1}^T R_2 \triangle G_{t,k-1} \\
& + s_{1,k}^T M_1 s_{1,k} + s_{2,k}^T M_2 s_{2,k} \\
\text{s.t.} \quad & x_{k+1} = Ax_k + Bu_k + B_d u_{d,k} \\
& y_k = Cx_k \\
& 0 \le T_{e,k} \le 600 \\
& 0 \le N_{ox,k} \le 150 \\
& 8.5 \le O_{2,k} \le 12.5 + s_{1,k} \\
& 0 \le K_{l,k} \le 30 \\
& 0 \le P_{p,k} \le 180 + s_{2,k} \\
& 0.3 \le P_{ca,k} \le 4.5 \\
& -20 \le G_{t,k} \le -8.5 \\
& -0.2 \le \triangle P_{ca,k} \le 0.5 \\
& -0.3 \le \triangle G_{t,k} \le 0.5
\end{aligned}
\tag{2}
$$

For the relaxation of the upper bounds on the output constraints O_2 and P_p, two slack variables s_1 and s_2 are used. The slack variables are then added to the list of decision variables so that the relaxation of the output constraints is a gentle as possible. When the output constraints are within their limits, the variables s_1 and s_2 take values as zeros. In equation 2, $P, Q_1, R_1, Q_2, R_2, M_1$ and M_2 are the weighting matrices of appropriate sizes. The prediction horizon for the MPC is denoted by N. The terms $\triangle P_{ca,k} = P_{ca,k} - P_{ca,k-1}$ and $\triangle G_{t,k} = G_{t,k} - G_{t,k-1}$ denote the rate of change of the control inputs.

To solve this constrained optimization problem, *fmincon* solver in MATLAB has been used. For the receeding horizon strategy of MPC, only the first control move is applied and the optimal control problem given by equation 2 is re-solved at every sampling time.

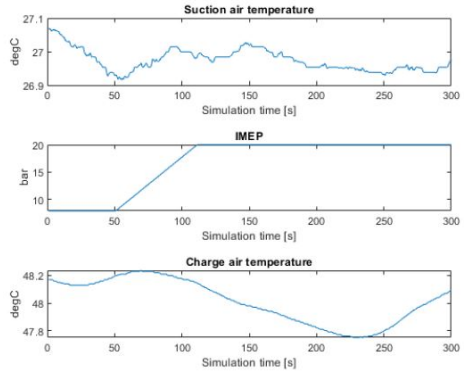

Figure 8. Input disturbances.

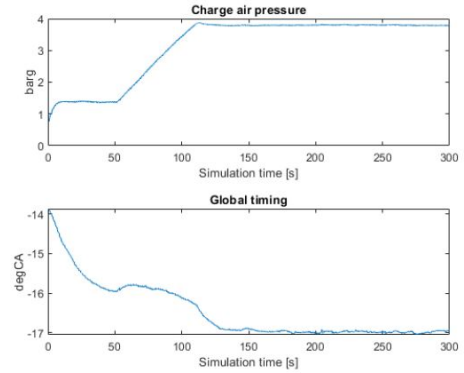

Figure 9. Optimal set points for charge air pressure and global ignition timing under real life disturbances.

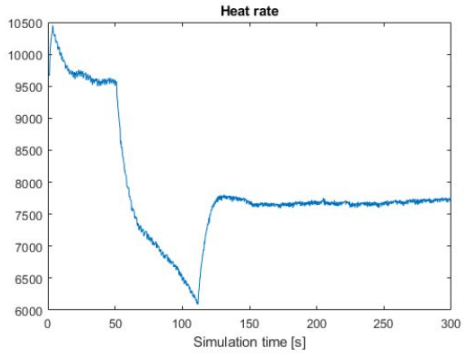

Figure 10. Minimization of the heat rate under real life disturbances.

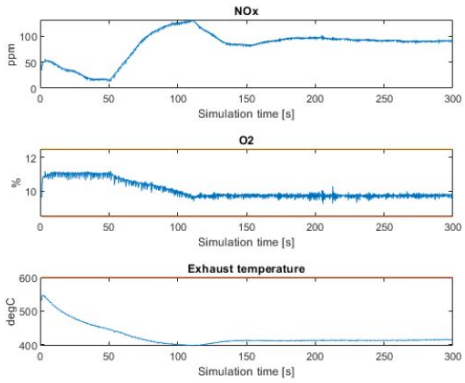

Figure 11. Output variables within their limits under real life disturbances.

5 Results and Discussion

Data from a real power plant operating the B36:45 LNG engine are used for two input disturbances namely for *charge air temperature* and *suction air temperature*. These two input disturbances together with the third disturbance (IMEP) is shown in Figure 8. These input disturbances vary over time and whey they act on the system, they can cause the operation of the plant to be far from optimal. In order to compensate for these disturbances, the optimal controller continuously generates new optimal values of the control inputs which are then fed as variable setpoints to the local PID controllers. Figure 9 shows the optimal values of the control inputs (charge air pressure and Global ignition timing) as calculated by the advanced controller.

When these optimal values of the charge air pressure and global ignition timing is applied to the system, the efficiency of the engine is maximized. As already stated above, this can be shown by the minimization of the heat rate as shown in Figure 10.

During the process of minimizing the heat rate, the optimal controller was also able to satisfy the output constraints. The output variables N_{ox}, O_2 and T_e are well within their limits as shown in Figure 11. In order to further test the advanced optimal controller, data from the real power plant containing large variation in the input disturbances was applied. The real life disturbances are given in Figure 12 for all three input disturbances. In particular, the IMEP covers a range of operational windows from lower values to a peak at full nominal power at 1200-1500 seconds before reducing back down to low level again.

Figure 13 shows the simulated optimal values of the charge air pressure and global ignition timing as calculated by the optimal controller (blue line). In addition it also shows the real values of these two variables from the current engine controller operating in the field (red line). Some differences between these two coloured lines,

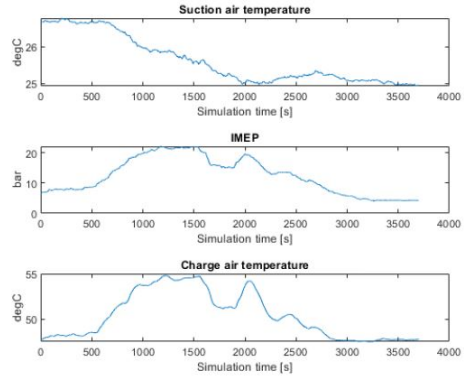

Figure 12. Input disturbances with real life field data.

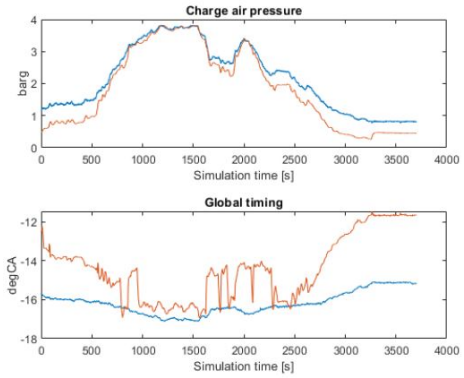

Figure 13. Optimal set points for charge air pressure and global ignition timing for real life field data containing large input disturbance variation. Red line: Measured real values, Blue line: Simulated values.

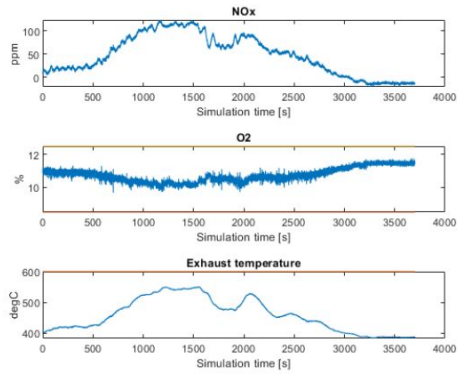

Figure 14. Output variables within their limits for real life field data containing large input disturbance variation.

in particular related to the engine global timing can be observed. The optimal controller utilizes the global ignition timing more than the current controller used in the power plant. This should in principle increase the fuel efficiency. The charge air pressure is also slightly increased to compensate for the increase in burn rate due to the advanced timing generated by the optimal controller. It should be noted that an unlimited possibility of increasing the charge air pressure might not be feasible due to capacity of the turbocharger and a variable upper bound in this value should be established to avoid unrealistic optimal behavior of the optimizer.

At the same time, the output variables N_{ox}, O_2 and T_e are kept within their upper and lower limits in Figure 14 which implies safe operation of the engine. The heat rate output is minimized by the optimizer and the simulated result is shown by blue line in Figure 15. In addition, the measure heat rate from the real field is shown by red line for the same real life input disturbances. It can be noted that values are closely related and share the same form. For the major part of the simulation, the optimized heat rate is also lower than the measured value from the installed engine running traditional control. There is a period around 2250 second mark where the estimated optimize is slightly

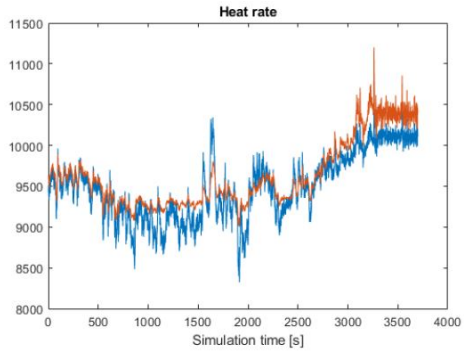

Figure 15. Heat rate minimization for real life field data containing large input disturbance variation. Red line: Measured real values, Blue line: Simulated values.

higher than the measured, but for the majority of the time, the value of the heat rate from the optimal controller is lower. This indicates that the advanced model based controller performs relatively better.

6 Conclusions

The potential of using a model based advanced controller for a B36:45 LNG engine is investigated in this paper. The optimal controller shows promising results in simulations. Compared to the current traditional controller used in the field, the advanced optimal controller could improve the efficiency of the engine. However, the advanced controller requires a dynamic model of the engine, and development of such a model using operational data can be difficult and time consuming. The quality of the results from the optimal controller relies on the quality of the dynamic model. The model used in this paper can be improved in the future and the optimal controller should be tested on a real engine.

References

Rohit V. Koli. Model predictive control of modern high-degree-of-freedom turbocharged spark ignited engines with external cooled egr. *PhD Dissertation, Clemson University*, 1981.

Jun Lu, Weifeng Ma, Yongjun Han, Yuke Gao, Zhaoyuan Guo, Xin Li, and Honglei Niu. Model predictive engine control using support vector machine. In *2015 IEEE International Conference on Cyber Technology in Automation, Control, and Intelligent Systems (CYBER)*, pages 1569–1573, 2015. doi:10.1109/CYBER.2015.7288179.

Jim B. Luther. Advanced neural network engine control. *PhD Dissertation, Technical University of Denmark*, 2002.

J. Richalet. Industrial applications of model based predictive control. *Automatica*, 29(5):1251–1274, 1993.

Bearing Defect and Misalignment Diagnostics Using Local Regularity and Sparse Frequency Analysis

Juhani Nissilä[1] Jouni Laurila[1] Keijo Ruotsalainen[2] Toni Liedes[1]

[1]Intelligent Machines and Systems, University of Oulu, PO Box 4200, 90014 Oulu, Finland,
{juhani.nissila,jouni.laurila,toni.liedes}@oulu.fi
[2]Applied and Computational Mathematics, University of Oulu, PO Box 4500, 90014 Oulu, Finland,
keijo.ruotsalainen@oulu.fi

Abstract

A local regularity signal can be estimated from a vibration measurement with the help of the continuous wavelet transform (CWT). The resulting local regularity signal contains a lot of diagnostic information about different faults states of a machine. It is also typically a sparse signal and thus not well suited for frequency analysis using the discrete Fourier transform (DFT). In this paper, the frequency analysis of the local regularity signal is performed using the Lomb-Scargle periodogram. Another possibility is to use the methods of compressed sensing. Vibration measurements from different fault states from test rigs are utilized in validating the proposed method and comparing it with other methods. The induced fault conditions include a bearing inner ring defect and misalignment of a claw clutch. The results are compared to more traditional spectra calculated directly from the vibration measurement, such as the spectrum of the squared envelope.

Keywords: Hölder regularity, continuous wavelet transform, sparse signals, Lomb-Scargle periodogram, compressed sensing, envelope analysis

1 Introduction

When the CWT of a signal is calculated using a real-valued wavelet, its absolute values form continuous ridges which converge towards the smaller scales. These modulus maxima ridges of the estimated CWT reveal the locations of irregularities in the signal and from their rate of decay, pointwise Hölder exponents of the irregularities can also be read (Mallat and Hwang, 1992). If we don't consider fractal signals, then there are typically only a finite amount of irregularities in a signal and thus only a finite amount of modulus maxima ridges in the CWT. The resulting local regularity signal, i.e. a signal which shows the estimated Hölder regularities or constants related to the sizes of the ridges and their locations, is thus a sparse signal. When these local regularity signals are calculated from vibration measurements of machines, they may contain useful diagnostic information. They have been shown to be useful for diagnosing for example gear tooth cracks and completely lost gear teeth (Loutridis and Trochidis, 2004), local bearing defects (Kotila et al., 2010) and misalignment of a claw clutch and bearing lubrication problems (Nissilä and Laurila, 2019). In (Miao and Makis, 2007) a feature vector calculated from the wavelet modulus maxima ridges is fed to a hidden Markov model for fault classification. Multifractal features extracted from vibration signals are used in bearing diagnostics in (Du et al., 2014).

Wavelet-based methods for extracting weak transients from vibration signals have been successfully applied with bearing faults (Wang et al., 2015) and gear faults (Fan et al., 2015). Wavelet transform was also used for detecting angular misalignment in (Saari et al., 2015). There are also several studies where some kind of sparse representations in some basis are sought and these sparse decompositions also turn out to be useful for gear fault (Zhang et al., 2021; Li et al., 2018) and bearing fault diagnostics (Li et al., 2019; Chen et al., 2017; He et al., 2016).

In machine diagnostics of rotating or reciprocating machines, frequency analysis of measured vibration signals is typically utilized. Methods based on the DFT are easily available, since the measurements are typically equispaced in time. When equispaced measurements are not available, different methods for frequency analysis are needed. This is often the case in astronomical time series and for that reason Lomb and Scargle developed a method that is now called the Lomb-Scargle periodogram (Lomb, 1976; Scargle, 1982). In this study, we calculate these spectra from signals generated using local regularity analysis and they are compared to the spectra of the squared envelope calculated directly from the acceleration measurements. Envelope analysis is a benchmark method in machine diagnostics for diagnosing bearing faults and other faults which cause cyclostationary vibration signatures (Randall et al., 2001).

2 Materials and methods

2.1 Measurements

In this paper, two fault states with six different levels of severity are used for comparing the proposed signal processing methods. The first fault state is a local inner ring fault in a roller bearing. The test rig manufactured by SPM Instrument is shown in Figure 1. The three bearings at the

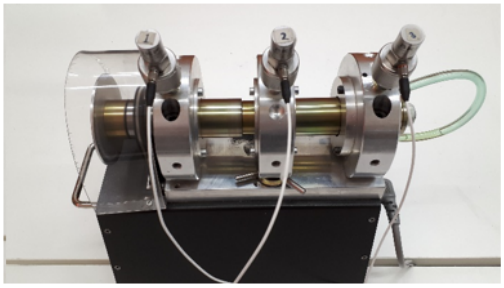

Figure 1. The bearing test rig.

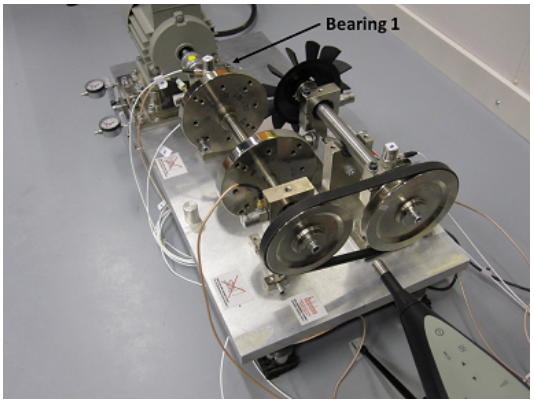

Figure 2. The misalignment test rig.

top support the axle that is driven by a chain drive. The inner ring fault is located in the middle bearing and it is a simple groove that is cut into the inner race. The middle bearing housing can be tightened using a screw and this method gives the six different levels of load. The measurements that we use are recorded using the accelerometer 2 seen in Figure 1 and it is mounted to the bearing housing using a magnet. Sampling frequency is 25.6 kHz and 10 s long measurements from each load level are used.

The test rig used for misalignment measurements is shown in Figure 2. Coupling misalignment in the horizontal direction was induced by moving the motor while keeping the vertical and angular alignment constant. Horizontal measurements from bearing 1 are utilized in this study and the accelerometer was screwed directly into the bearing housing. Sampling frequency is 50 kHz and signal length is 15 s for each misalignment state. The test rig is presented in more detail in (Lahdelma and Laurila, 2012; Lahdelma et al., 2011).

In both measurements, the accelerometer type was Wilcoxon Research 726 with a linear (±5 %) frequency range from 2 Hz to 10 kHz.

2.2 Signal processing

The spectrum of the discrete signal $\boldsymbol{x} = (x_0, \ldots, x_{N-1})^{\mathsf{T}}$ of length $T = \Delta t \cdot N$ is defined using the *discrete Fourier transform* (DFT)

$$\mathscr{F}\{\boldsymbol{x}\}_k = X_k = \frac{1}{N}\sum_{n=0}^{N-1} x_n e^{-i2\pi kn/N}, \tag{1}$$

and the *inverse transform* (IDFT) returns the signal at the sample points (Briggs and Henson, 1995)

$$\mathscr{F}^{-1}\{\boldsymbol{X}\}_n = x_n = \sum_{k=0}^{N-1} X_k e^{i2\pi kn/N}. \tag{2}$$

The *cyclic convolution* of two sampled signals is

$$(\boldsymbol{x} * \boldsymbol{y})_n = \sum_{l=0}^{N-1} x_l\, y_{n-l}, \tag{3}$$

and its DFT is (Briggs and Henson, 1995)

$$\mathscr{F}\{(\boldsymbol{x} * \boldsymbol{y})\}_k = N X_k Y_k. \tag{4}$$

For a discrete time random signal $\mathbf{X}_n$, we define the *squared envelope* (SE) with the expected values $\mathrm{E}\left[|\mathbf{X}_n|^2\right]$ and the *squared envelope spectrum* (SES) by

$$\mathrm{SES}\{\mathbf{X}_n\}(f_c) = \lim_{M\to\infty} \frac{1}{2M+1} \sum_{n=-M}^{M} \mathrm{E}\left[|\mathbf{X}_n|^2\right] e^{-i2\pi f_c n}. \tag{5}$$

In (Dandawate and Giannakis, 1995) it has been proved that under some assumptions, a simple DFT of the squared samples

$$\mathrm{SES}\{\mathbf{X}_n\}\left(\frac{k}{N}\right) \approx \frac{1}{N}\sum_{n=0}^{N-1} \left|x_n\right|^2 e^{-i2\pi kn/N} \tag{6}$$

converges in the mean-square sense to the SES at the cyclic frequency $f_c = k/N$ as $N \to \infty$.

Let us define informally, that a *wavelet* is a brief oscillation. We denote the wavelet by ψ and we want to dilate it by $s > 0$ but retain its L^1 norm

$$\psi_s(t) = \frac{1}{s}\psi\left(\frac{t}{s}\right). \tag{7}$$

The *continuous wavelet transform* (CWT) of a continuous time signal x is

$$\begin{aligned} Wx(s,t) &= (x * \psi_s)(t) \\ &= \frac{1}{s}\int_{-\infty}^{\infty} x(\tau)\psi\left(\frac{t-\tau}{s}\right) \mathrm{d}\tau. \end{aligned} \tag{8}$$

Here t is the point of interest in the signal and s is the positive *scale* that tells how much the wavelet is dilated.

The wavelet that we have chosen for this study is the second derivative of a *central B-spline* (Unser and Blu, 2000) and its DFT is

$$\begin{aligned} B_k &= \frac{1.83}{N}\left(\frac{i2\pi k}{N}\right)^2 \left|\frac{\sin(2\pi k/N)}{2\pi k/N}\right|^5, \\ B_{N/2} &= \frac{1.83}{N}\pi^2\cos(\pi)\left|\frac{\sin(\pi)}{\pi}\right|^5 = 0, \end{aligned} \tag{9}$$

where $-N/2 < k < N/2$. The negative frequencies correspond to $N/2 < k < N$ in our definition of the DFT.

The constant is chosen so that the wavelet's l^1 norm $\|\mathscr{F}^{-1}\{\boldsymbol{B}\}\|_1$ is roughly equal to 1.

The discrete estimate of the CWT at scale s is denoted by $W\boldsymbol{x}_{s,n}$. To calculate its DFT, we first window the measured signal $\boldsymbol{x}$ with a smooth window function called the *Planck-taper window* $\boldsymbol{w}$ (McKechan et al., 2010), i.e. compute $x_n w_n$, calculate its DFT $\mathscr{F}\{x_n w_n\}_k$ and then estimate the DFT of the wavelet transform using (4)

$$\mathscr{F}\{W\boldsymbol{x}_{s,n}\}_k = N\mathscr{F}\{x_n w_n\}_k B_{sk}. \tag{10}$$

Finally, we obtain $W\boldsymbol{x}_{s,n}$ at the desired scales using the IDFT.

Let $\mu \geq 0$. A function x is *pointwise μ-Hölder continuous* at t_0 if

$$|x(t_0+h) - P_m(h)| \leq C|h|^{\mu}, \tag{11}$$

for small values of $|h|$ and P_m is a polynomial of degree $m \leq \mu$.

When traversing a CWT through the scales, a series of connected local maxima or minima are often observed (Mallat, 2009). These are *wavelet transform modulus maxima ridges* (WTMM ridges). In (Mallat and Hwang, 1992), it has been proved that if there are no such ridges at the fine scales on some interval, then x is uniformly Hölder continuous on that interval. Conversely, they proved under some assumptions that if there exists a constant C and a scale s_0 such that all the modulus maxima of $Wx(s,t)$ belong to the cone

$$|t - t_0| < Cs, \tag{12}$$

then x is μ-Hölder at t_0 if and only if

$$|Wx(s,t)| \leq As^{\mu}, \tag{13}$$

at each modulus maxima inside the cone (12). This result means, that if one can recognize the WTMM ridges of isolated irregularities, then their Hölder exponents can be estimated using logarithms and a least squares line fit to

$$\log(|Wx(s,t)|) \leq \log(A) + \mu\log(s). \tag{14}$$

The constant A is related to the height of the ridge, and will also be useful.

The *Lomb-Scargle periodogram* estimates the *power spectral density* (PSD) at the frequencies f of the signal $\boldsymbol{x}$ which has been nonuniformly sampled at the points t_n

$$\begin{aligned} \mathrm{P_{LS}}\{\boldsymbol{x}\}(f) = &\frac{\left(\sum_n x_n \cos\left(2\pi f(t_n-\tau)\right)\right)^2}{2\sum_n \cos^2\left(2\pi f(t_n-\tau)\right)} \\ &+ \frac{\left(\sum_n x_n \sin\left(2\pi f(t_n-\tau)\right)\right)^2}{2\sum_n \sin^2\left(2\pi f(t_n-\tau)\right)}, \end{aligned} \tag{15}$$

where the delay τ is chosen for each frequency f by

$$\tau = \frac{1}{4\pi f}\tan^{-1}\left(\frac{\sum_n \sin(4\pi f t_n)}{\sum_n \cos(4\pi f t_n)}\right). \tag{16}$$

The *discrete cosine transform* (DCT) according to (Ahmed et al., 1974) is defined by

$$\begin{aligned} \mathrm{DCT}\{\boldsymbol{x}\}_0 &= \frac{\sqrt{2}}{N}\sum_{n=0}^{N-1} x_n, \\ \mathrm{DCT}\{\boldsymbol{x}\}_k &= \frac{2}{N}\sum_{n=0}^{N-1} x_n \cos\frac{(2n+1)k\pi}{2N}, \quad k = 1,...,N-1. \end{aligned} \tag{17}$$

When searching for a sparse representation of a discrete signal $\boldsymbol{x} = (x_0,\ldots,x_{N-1})^{\mathsf{T}}$ in some basis, the following minimization problem is addressed

$$\min \|\boldsymbol{v}\|_0, \qquad \text{such that} \qquad \|\boldsymbol{x} - \Theta\boldsymbol{v}\|_2 < \varepsilon. \tag{18}$$

The l^0 pseudo-norm is simply the number of nonzero components of the vector. Many solution algorithms replace it with the l^1 norm. In this paper, the vector $\boldsymbol{v}$ is the sparse DCT of $\boldsymbol{x}$ and the matrix Θ represents the inverse transform and the restriction to using only the sparse signal measurement points. Only those rows which correspond to the sparse local regularity signal are nonzero. To make the problem more tractable, we also limit our attention to only a small portion of the DCT spectrum, and thus only columns of Θ up to some desired maximum frequency are included. The sparse solution in the DCT spectrum is searched using the *orthogonal matching pursuit* (OMP) algorithm (Pati et al., 1993; Mallat, 2009). The DCT is favored in this sparse approximation problem instead of the DFT because it only has one coefficient for each frequency, i.e. no negative frequencies.

3 Results and discussion

3.1 Acceleration measurements and their squared envelope spectra, bearing fault

Calculations were performed with MATLAB R2020b. Samples from the acceleration measurements of the six different load levels in the bearing test are shown in Figure 3. Case 0 is the smallest load level and Case 5 is the largest. It is important to notice, that the shocks caused by the fault are lowest in Case 1 and then start to increase again when the load level is further increased. The rotational frequency of the shaft is roughly 18.6 - 18.2 Hz depending on the load level. As this is also the rotational frequency of the faulty bearing inner race, the shocks caused by the fault are amplified once per revolution of the axle, i.e. whenever the fault passes the loading region. When the fault is passing the loading region, several shocks between the fault and rollers occur and these become more visible when the load level increases. The frequency of these shocks (*ballpass frequency, inner ring*, or BPFI) is roughly 140 - 147 Hz depending on the rotational frequency of the shaft.

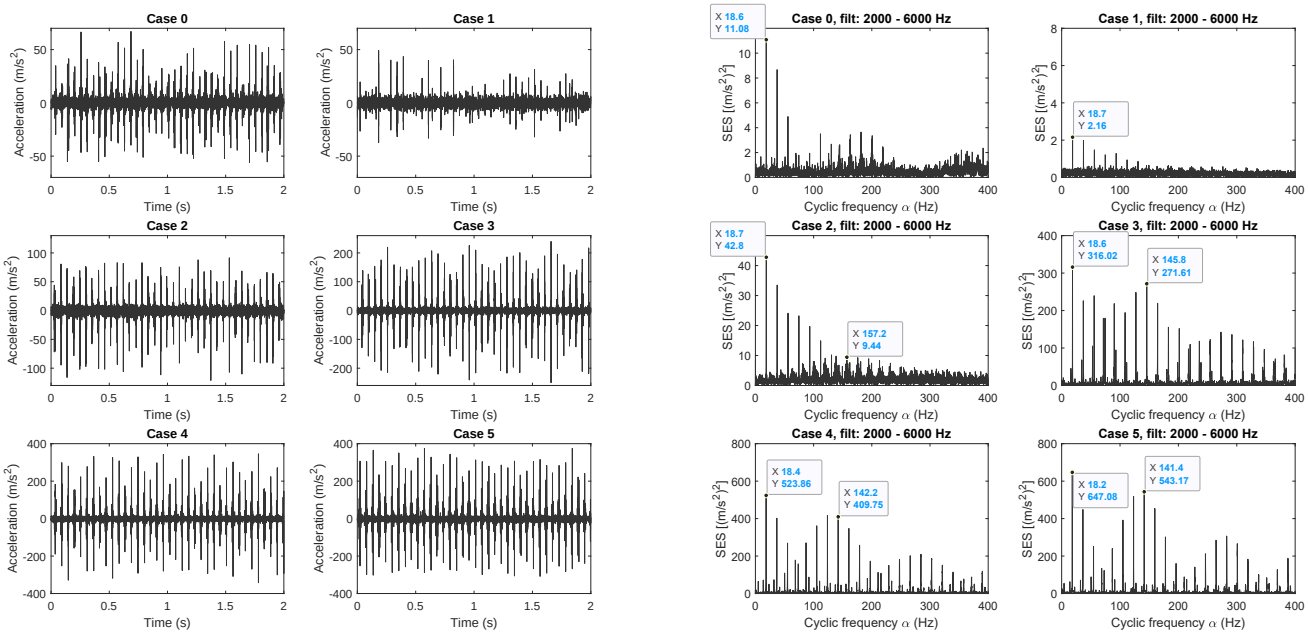

Figure 3. Acceleration measurements from the bearing test rig and their squared envelope spectra.

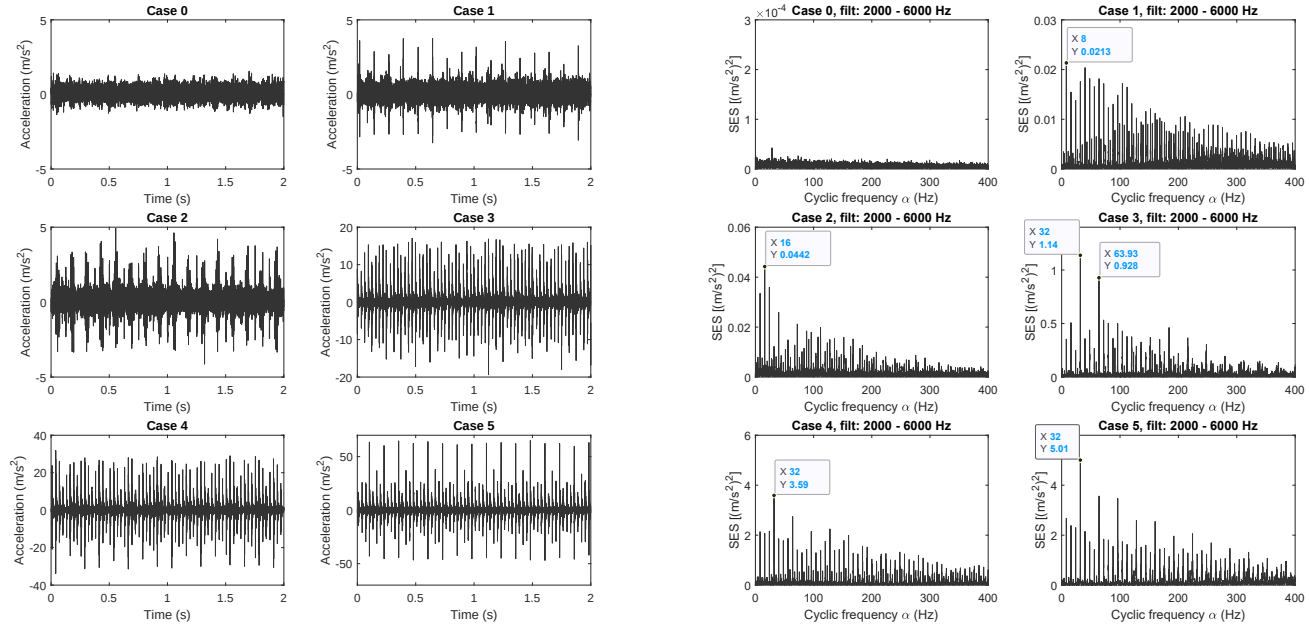

Figure 4. Acceleration measurements from the misalignment test rig and their squared envelope spectra.

The SES of these load cases in Figure 3 are calculated from 10 s long signals and they show us that the strong amplitude modulation is visible as peaks at the shaft speed and its multiples in all load cases. From Case 3 onwards, the BPFI and its sidebands spaced shaft speed apart become clearly visible as a distinct pattern, although faint signs of this pattern already exist in Cases 0 and 2.

3.2 Acceleration measurements and their squared envelope spectra, misalignment

Samples from the acceleration measurements of the six different misalignment states are shown in Figure 4. Case 0 is the no misalignment state and in the following cases the misalignment increases in 0.1 mm increments. Shaft speed is roughly 8 Hz and it is clear, that in Case 1 and 2 there are shocks which repeat mainly at this frequency. From Case 3 onwards, the shocks become more pronounced and they repeat 4 times in every revolution of the shaft, i.e. at the frequency 32 Hz. In Case 5 it is also noticeable that the 4 impacts per revolution are unique and they repeat in a similar fashion. Especially one of them is much bigger in amplitude than the others. The claw clutch located between the motor and bearing 1 has a 4-tooth flexible element which explains these phenomena.

The SES of the different misalignment cases calculated from 15 s long signals are also shown in Figure 4. Shaft speed (8 Hz) and its multiples dominate the spectra from Case 1 onwards. From Case 3 onwards, 32 Hz and its multiples have the largest amplitudes. In these cases, it is also possible to interpret the other multiples of 8 Hz as sidebands of 32 Hz and its multiples. This matches our observations from the time domain signals, mainly that the shocks which occur at 1/32 s intervals are also amplitude modulated by the shaft speed especially in Case 5.

3.3 Local regularity signals and their L-S periodograms and DCT spectra, bearing fault

The CWT of the bearing measurements are estimated at the scales $s = 1.5, 1.6, \ldots, 5.9, 6$, their WTMM ridges are detected and irregularities whose constants A are above 1 are saved. The Hölder exponents and constants A from the bearing measurements are shown in Figure 5. Also here we can see that the vibration is smoothest in Case 1. The Hölder exponents reach quite large negative values. Even in Cases 0 and 1 there are a couple of irregularities with exponents that are less than -3. Such large negative values were also observed in (Nissilä and Laurila, 2019; Kotila et al., 2010) in cases of dry bearing and local bearing faults. We also observe that the amount of irregularities increases with the load level and their constants A get bigger.

For frequency analysis, it was observed that the constants A are more suitable than the Hölder exponents. Figure 6 shows the L-S periodograms of the constants A from all of the load cases. In Case 1 the only recognizable frequency is the axle speed. In Case 0 its multiples are visible and also BPFI with a couple of sidebands spaced axle speed apart. This structure is more emphasized in Case 2 and from Case 3 onwards the axle speed has the biggest amplitude followed with the BPFI. There are also numerous sidebands spaced axle speed apart around BPFI and its multiple. The load level is quite easy to read of from the increasing amplitudes and when compared to the SE spectra in Figure 3, the BPFI is more easily recognized in Cases 0 and 2.

The DCT spectra of constants A in Figure 6 are searched using sparse solutions with 60, 30, 100, 100, 100 and 100 components for the Cases 0 to 5 and for the frequencies shown. In these spectra, we can also observe the BPFI in Cases 0 and 2 and it becomes more distinctive in Cases 3, 4, and 5. The increase in the amplitude of the BPFI with fault severity is not as big as in the L-S spectra.

3.4 Local regularity signals and their L-S periodograms and DCT spectra, misalignment

The CWT of the misalignment measurements are estimated at the scales $s = 1.5, 1.6, \ldots, 5.9, 6$, their WTMM ridges are detected and irregularities whose constants A are above 0.05 are saved. The Hölder exponents and constants A from the misalignment measurements are shown in Figure 7. The Hölder exponents are mainly positive and we see that the number of irregularities and also their constants A increase with the severity of the fault. The amplitudes of the constants A also seem to reflect the periodicity of the shocks caused by the fault.

Also for this fault state, the constants A were better suited for sparse frequency analysis than the Hölder exponents. Figure 8 shows the L-S periodograms of the constants A from all of the fault cases. The amount of irregularities was so small in Case 0, that the estimated spectrum is almost white noise. In Case 1 there are many multiples of the shaft speed (8 Hz) and 8 times the shaft speed has the biggest amplitude. In Case 2 we see that 2 and 11 times the shaft speed are the largest. From Case 3 onwards, four times the shaft speed (32 Hz) is the dominant frequency and it has significant multiples. They also have small sidebands mainly 8 Hz apart. The frequency contents of these spectra are very similar to the SE spectra in Figure 4. The main difference is that the frequency 32 Hz and its multiples are much more prevalent from Case 3 onwards. We can thus confirm, that the diagnostic capability is roughly the same compared to the SES, but possibly the specific nature of the 4-tooth elastic spider element becomes more pronounced when using the L-S spectra of constants A.

The DCT spectra of constants A in Figure 8 are searched using 10, 30, 200, 200, 200 and 200-sparse solutions for the Cases 0 to 5 and for the frequencies shown. It was necessary to decrease the sparsity to obtain spectra where the fault frequency 32 Hz and its multiples become most dominant. When compared to the L-S spectra, it is again observed that the increase in the amplitude of the fault frequency between the cases is not as big. Fault frequency multiples also tend to increase with the severity of the fault, but there is some variation. In Case 1, the frequency 64 Hz has the biggest amplitude.

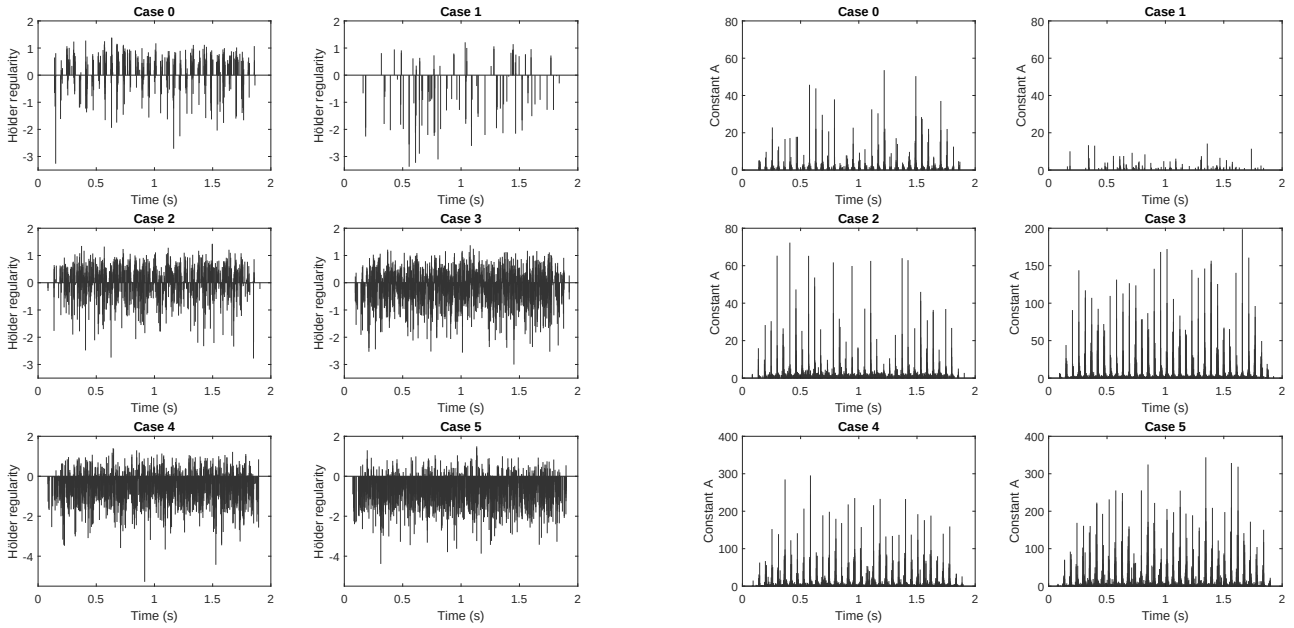

Figure 5. Hölder exponents and constants *A* of the local irregularities from the bearing test rig acceleration measurements.

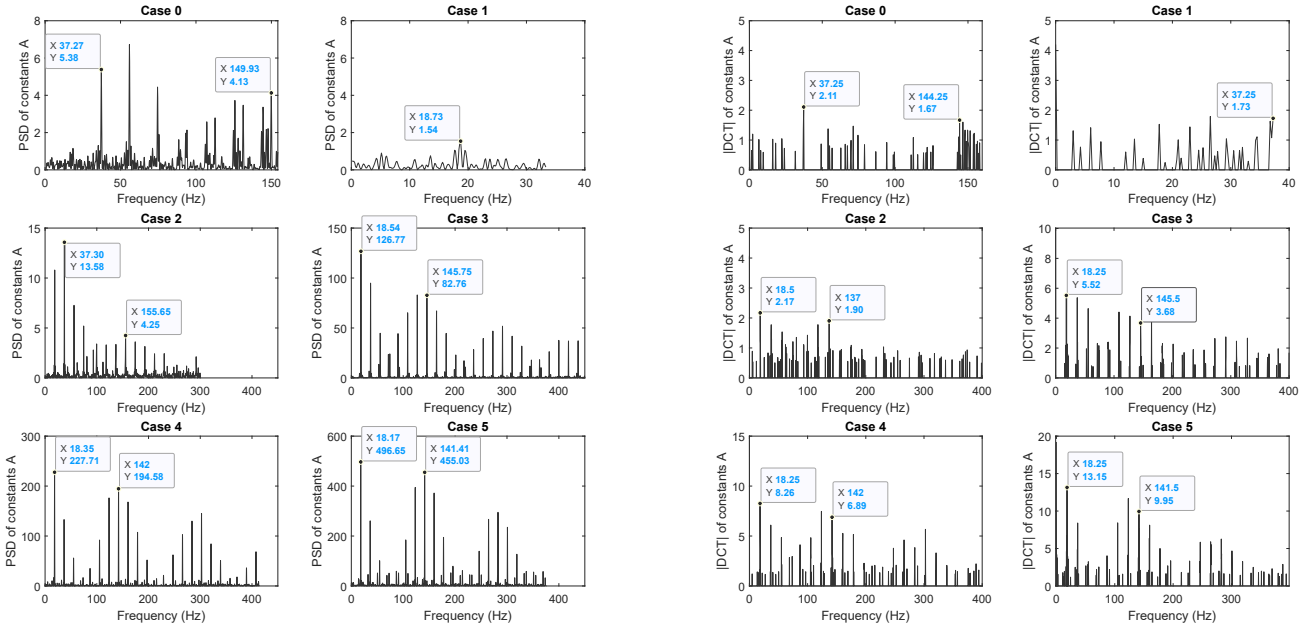

Figure 6. Lomb-Scargle periodograms and absolute values of discrete cosine transforms of the constants *A* from the bearing test rig acceleration measurements.

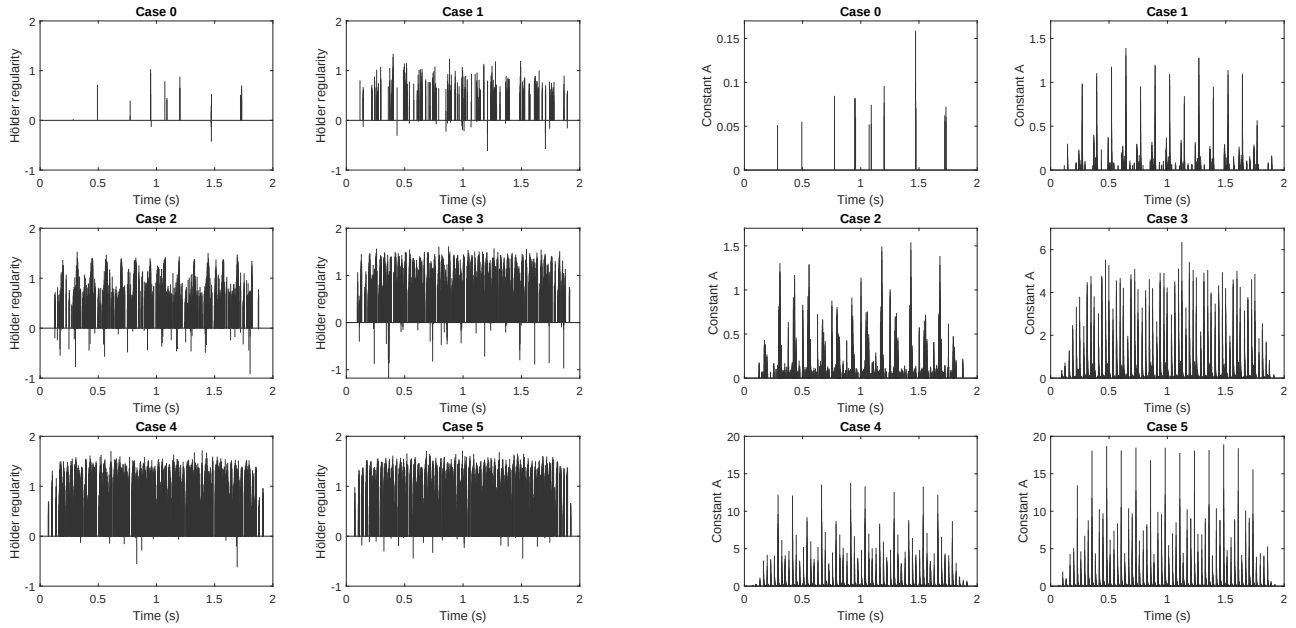

Figure 7. Hölder exponents and constants A of the local irregularities from the misalignment test rig acceleration measurements.

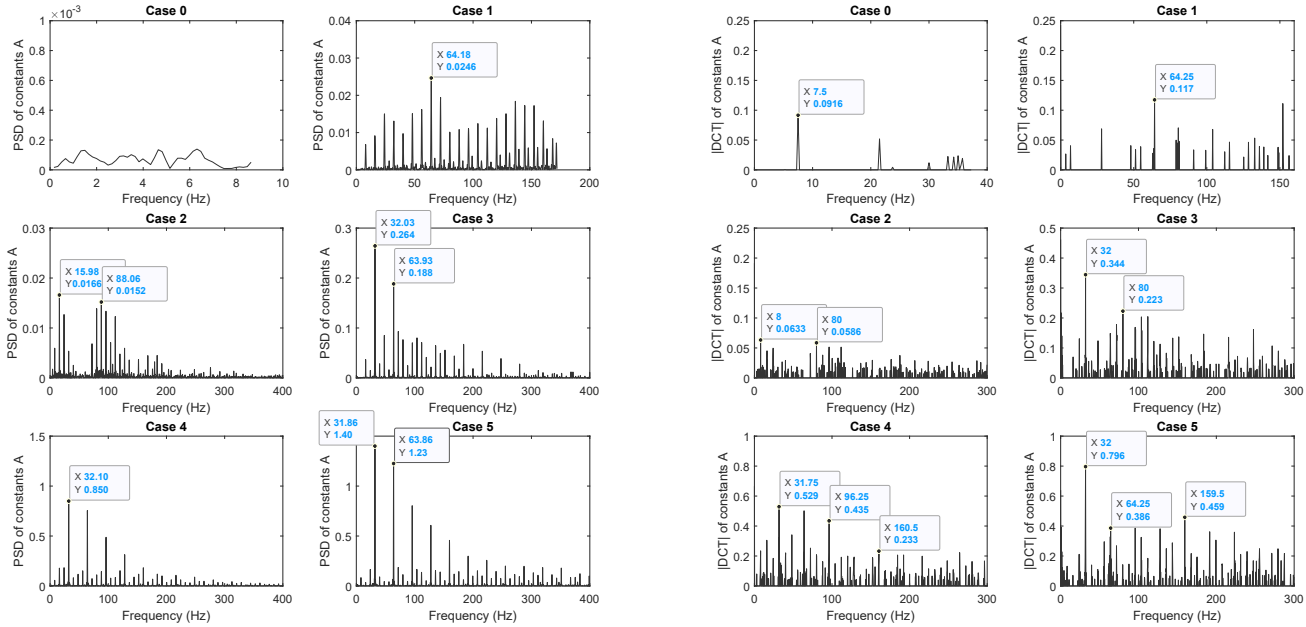

Figure 8. Lomb-Scargle periodograms and absolute values of discrete cosine transforms of the constants *A* from the misalignment test rig acceleration measurements

4 Conclusions

Local regularity analysis in the context of vibration monitoring has been studied for a couple of decades, but mainly as a tool in time domain analysis. The spectral analysis of local irregularities is not a simple task because of their sparse nature. However, the spectra of the constants A of the local irregularities carries at least as much diagnostic information as the squared envelope spectra calculated directly from acceleration signals. All of the tested methods contain different tunable parameters. For SES, these are mainly the bandpass filter's lower and upper limits. For the local regularity analysis, they are the choice of wavelet, the computed scales and the lower limit on how small constants A are taken into the analysis. The computation of the L-S spectrum of constants A is quite straightforward, but when its sparse DCT spectrum is estimated instead, the optimization algorithm and its parameters become tunable parameters as well. Because these parameters are so different for these methods, it is not easy to compare them fairly

For the examples in this paper, 10 and 15 s long signals were used for the estimation of the SES and only 2 s long signals were used for the local regularity analysis. Because of the result (6), it is advantageous to use long signals to estimate the SES. The calculation of the SES is also so simple, that the computational cost is still quite low. In contrast, it is computationally more costly to calculate the local regularity estimation and its sparse spectral analysis for long signals. But we have also demonstrated, that even only 2 s long signals are long enough for good frequency analysis results for both of the examples in this paper.

It is easy to set the lower limit on the constants A to such a level, that in the healthy condition the amount of irregularities is negligible and the spectrum is mostly white noise. This means that changes in the load or health of the machine become easily distinguishable. Especially the Lomb-Scargle periodograms of constants A were found to be very good at detecting and highlighting the fault frequencies.

References

N. Ahmed, T. Natarajan, and K. R. Rao. Discrete Cosine Transform. *IEEE Transactions on Computers*, C-23(1): 90–93, 1974. doi:10.1109/T-C.1974.223784.

W. Briggs and V. E. Henson. *The DFT: An Owner's Manual for the Discrete Fourier Transform*. Society for Industrial and Applied Mathematics, Philadelphia, PA, USA, 1995. ISBN 978-0-898713-42-8.

G. Chen, F. Liu, and W. Huang. Sparse discriminant manifold projections for bearing fault diagnosis. *Journal of Sound and Vibration*, 399: 330–344, 2017. doi:10.1016/j.jsv.2017.03.029.

A. V. Dandawate and G. B. Giannakis. Asymptotic theory of mixed time averages and kth-order cyclic-moment and cumulant statistics. *IEEE Transactions on Information Theory*, 41(1): 216–232, 1995. doi:10.1109/18.370106.

W. Du, J. Tao, Y. Li, and C. Liu. Wavelet leaders multifractal features based fault diagnosis of rotating mechanism. *Mechanical Systems and Signal Processing*, 43(1–2): 57–75, 2014. doi:10.1016/j.ymssp.2013.09.003.

W. Fan, G. Cai, Z. K. Zhu, C. Shen, W. Huang, and L. Shang. Sparse representation of transients in wavelet basis and its application in gearbox fault feature extraction. *Mechanical Systems and Signal Processing*, 56–57: 230–245, 2015. doi:10.1016/j.ymssp.2014.10.016.

W. He, Y. Ding, Y. Zi, and I. W. Selesnick. Sparsity-based algorithm for detecting faults in rotating machines. *Mechanical Systems and Signal Processing*, 72–73: 46–64, 2016. doi:10.1016/j.ymssp.2015.11.027.

V. Kotila, S. Lahdelma, and K. Ruotsalainen. Wavelet-Based Hölder Regularity Analysis in Condition Monitoring. In C. Constanda and M.E. Pérez, editors, *Integral Methods in Science and Engineering, Volume 2: Computational methods*, pages 233–242, Birkhauser, 2010. ISBN 978-0-8176-4896-1. doi:10.1007/978-0-8176-4897-8_22.

S. Lahdelma and J. Laurila. Detecting misalignment of a claw clutch using vibration measurements. In *Proceedings - 9th International Conference on Condition Monitoring and Machinery Failure Prevention Technologies, CM 2012 /MFPT 2012, June 2012, London, UK*, 2012. https://www.researchgate.net/publication/270048637_Detecting_Misalignment_of_a_Claw_Clutch_Using_Vibration_Measurements.

S. Lahdelma, J. Laurila, J. Strackeljan, and R. Hein. Separating Different Vibration Sources in Complex Fault Detection. In *Proceedings - 8th International Conference on Condition Monitoring and Machinery Failure Prevention Technologies, CM 2011 / MFPT 2011, June 2011, Cardiff, UK*, 2011. https://www.researchgate.net/publication/270048457_Separating_Different_Vibration_Sources_in_Complex_Fault_Detection.

G. Li, G. Tang, H. Wang, and Y. Wang. Blind source separation of composite bearing vibration signals with low-rank and sparse decomposition. *Measurement*, 145: 323–334, 2019. doi:10.1016/j.measurement.2019.05.099.

Y. Li, K. Ding, G. He, and X. Jiao. Non-stationary vibration feature extraction method based on sparse decomposition and order tracking for gearbox fault diagnosis. *Measurement*, 124: 453–469, 2018. doi:10.1016/j.measurement.2018.04.063.

N. R. Lomb. Least-squares frequency analysis of unequally spaced data. *Astrophysics and Space Science*, 39: 447–462, 1976. doi:10.1007/BF00648343.

S. Loutridis and A. Trochidis. Classification of gear faults using Hoelder exponents. *Mechanical Systems and Signal Processing*, 18(5): 1009–1030, 2004. doi:10.1016/j.ymssp.2004.01.007.

S. Mallat. *A Wavelet Tour of Signal Processing: The Sparse Way, Third Edition*. Academic Press, Burlington, MA, USA, 2009. ISBN 978-0-12-374370-1.

S. Mallat and W. L. Hwang. Singularity detection and processing with wavelets. *IEEE Transactions on Information Theory*, 38(2): 617–643, 1992. doi:10.1109/18.119727.

D. J. A. McKechan, C. Robinson, and B. S. Sathyaprakash. A tapering window for time-domain templates and simulated signals in the detection of gravitational waves from coalescing compact binaries. *Classical and Quantum Gravity*, 27: 084020. doi:10.1088/0264-9381/27/8/084020.

Q. Miao and V. Makis. Condition monitoring and classification of rotating machinery using wavelets and hidden Markov models. *Mechanical Systems and Signal Processing*, 21(2): 840–855, 2007. doi:10.1016/j.ymssp.2006.01.009.

J. Nissilä and J. Laurila. Diagnosing simultaneous faults using the local regularity of vibration signals. *Measurement Science and Technology*, 30: 045102, 2019. doi:10.1088/1361-6501/aaf8fa.

Y. C. Pati, R. Rezaiifar, and P.S. Krishnaprasad. Orthogonal matching pursuit: recursive function approximation with applications to wavelet decomposition. In *Proceedings - 27th Asilomar Conference on Signals, Systems and Computers, 1-3 November, 1993, Pacific Grove, CA, USA*, pages 40–44, 1993. doi:10.1109/ACSSC.1993.342465.

R. B. Randall, J. Antoni, and S. Chobsaard. The relationship between spectral correlation and envelope analysis in the diagnostics of bearing faults and other cyclostationary machine signals. *Mechanical Systems and Signal Processing*, 15(5): 945–962, 2001. doi:10.1006/mssp.2001.1415.

J. Saari, J. Odelius, J. Lundberg, and M. Rantatalo. Using wavelet transform analysis and the support vector machine to detect angular misalignment of a rubber coupling. In *Proceedings - Maintenance, Condition Monitoring and Diagnostics, Maintenance Performance Measurement and Management, MCMD 2015 / MPMM 2015, 30 September - 1 October, 2015 Oulu, Finland*, 2015. http://urn.kb.se/resolve?urn=urn:nbn:se:ltu:diva-66432.

J. D. Scargle. Studies in astronomical time series analysis. II. Statistical aspects of spectral analysis of unevenly spaced data. *Astrophysical Journal*, 263: 835–853, 1982. doi:10.1086/160554.

M. Unser and T. Blu. Fractional Splines and Wavelets. *SIAM Review*, 42(1): 43–67, 2000. doi:10.1137/S0036144598349435.

Y. Wang, G. Xu, L. Liang, and K. Jiang. Detection of weak transient signals based on wavelet packet transform and manifold learning for rolling element bearing fault diagnosis. *Mechanical Systems and Signal Processing*, 54–55: 259–276, 2015. doi:10.1016/j.ymssp.2014.09.002.

L. Zhang, Y. Li, L. Dong, X. Yang, X. Ding, Q. Zeng, L. Wang, and Y. Shao. Gearbox Fault Diagnosis Using Multiscale Sparse Frequency-Frequency Distributions. *IEEE Access*, 9: 113089–113099, 2021. doi:10.1109/ACCESS.2021.3104281.

Modeling and Simulation for Decision Making in Sustainable and Resilient Assembly System Selection

Juhani Heilala

VTT Technical Research Centre of Finland Ltd, Juhani.heilala@vtt.fi
https://orcid.org/0000-0002-9420-9061

Abstract

Resiliency requires manufacturing system adaptability to internal and external changes, such as quick responses to customer needs, supply chain disruptions, and markets changes, while still controlling costs and quality. Sustainability requires simultaneous consideration of the economic, environmental, and social implications associated with the production and delivery of goods. Due to increasing complexity, the engineering of a production system is a knowledge-intensive process. In this paper, a summary of system adaptation methods are shown, and a holistic methodology for the assembly equipment and system modeling and evaluation is explained. The aim here is to bring resiliency and sustainability considerations into the early decision-making process. The methodology is based on estimations on system performance, using discrete event simulation run results, or other process modeling methods, and the use of Key Performance Indicators (KPI), such as Overall Equipment Efficiency (OEE), connected to cost parameters and environmental aspects analysis. Overall, it is a tool developed through multiple projects for design specification reviews and improvements, trade-off analysis, and investments justification.

Keywords: resilient assembly systems, sustainability, modeling and simulation, decision support

1 Introduction

Manufacturing has to cope with a continuously increasing variety of products, change of volumes, shortening product life cycles, and various disturbances. There has been a shift to the product personalization, customer and market responsive resilient manufacturing. Advanced manufacturing faces challenges: digitization, the shift towards more environmentally sustainable production and transition from Industry 4.0 towards Industry 5.0, and a sustainable, human-centric and resilient European industry (De Nul *et al.,* 2021).

Sustainability is an increasingly important driver. Sustainable Manufacturing has commonly used the following definition (US Department of Commerce, 2007): "*The creation of manufactured products that use processes that minimize negative environmental impacts, conserve energy and natural resources, are safe for employees, communities, and consumers and are economically sound*".

Resiliency is usually defined as the ability of a system to recover from an undesired state and to a desired state. A list of resiliency attributes and their impacts on manufacturing is provided in (Kusiak, 2019; 2020). They include *energy, materials, components, physical assets and processes, transport, supply chain, communications, logistics, efficiency, productivity, capacity, dependability, quality, compatibility, sustainability, workforce, and societal values.* These attributes can be expressed in different forms, metrics, and variables, some of which are measurable. Identification and definition of these variables is important for understanding the nature of manufacturing resiliency and sustainability.

Assembly is one of the last processes within a product realization, a manufacturing operation in which the components and subassemblies are integrated and joined together to get the final product. Resiliency requires system adaptability to internal and external disruptions and changes, e.g., machine setups and job rescheduling for quick responses to customer needs or missing material due to supply chain disturbances. There is a need for the holistic evaluation and decision support methodology in the engineering phase of production and assembly systems.

1.1 Aims

This paper briefly shows how to increase an assembly system resiliency, adaptability to changes in products, and production volumes. Solution is an agile, interoperable, reconfigurable modular system and processes with smart tools, technologies, digitalization, and empowered human operators.

This paper describes holistic methodology for assembly equipment and system evaluation, for design specification reviews and improvements, trade-off analysis, and investments justification. The aim is to bring resiliency and sustainability aspects to the early decision-making process: identify attributes, parameters, visualize, model, simulate, and calculate, in other words use advanced analytics techniques and use

the created information to improve and make better decisions - "*resilience and sustainability-by-design*".

1.2 Sustainable manufacturing

The World Commission on Environment and Development (1987) defined "*Sustainable development is development that meets the needs of the present without compromising the ability of future generations to meet their own needs.*" This elaborated the meaning of sustainability and presented it in three dimensions, i.e., Environmental, Social, and Economic responsibilities, commonly known as the triple bottom line concept (Figure 1).

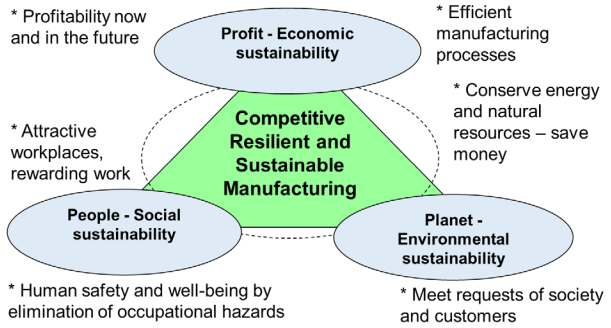

Figure 1. Triple bottom Line (TBL) and Competitive Resilient Sustainable Manufacturing.

The general principle of sustainable manufacturing is to reduce the intensity of materials use, energy consumption, emissions, and the creation of unwanted by-products while maintaining, or improving, the value of products to society and to organizations. Enhancing sustainability performance of the production process is an important contribution to developing a stronger and cleaner economy.

1.3 Resilient and Agile Manufacturing

Resilient Manufacturing is defined as *the ability of a manufacturing system to efficiently mitigate any external disruptions, either derived from the supply chain of the company or resulted from the volatility of the market demand*. Further, the response of the system to these volatile changes must be as rapid as possible in order for the company to maintain their competitive advantage in the market landscape (Mourtzis *et al.,* 2021; Kusiak, 2019).

Resilient manufacturing has similarities to agile and reconfigurable manufacturing. The goal of agile manufacturing is to combine the organizations, people and, technology into an integrated and coordinated whole (Dove 1992; Kidd 1994; Heilala and Voho, 2001). Agility is defined as "*the capability of surviving and prospering in a competitive environment of continuous and unpredictable change by reacting quickly and effectively to changing markets, driven by customer-designed products and services*". Agile manufacturing utilizes effective interoperable systems, process tools, modular reconfigurable systems, human resources, and training to enable manufacturing systems and networks to respond quickly to customer needs and markets changes while still controlling costs and quality (Dove, 1992).

1.4 Requirements and solutions

Flexibility requirements can be classified to static flexibility, where reaction time is typically connected to the planned product life-cycle phases, e.g., production volume changes, new variants, or products in the same system. In dynamic flexibility, reaction time is very short due to customization, lot size one, assembly-to-order, disturbances, machine breaks, repair work, rush orders, and demand fluctuations. Solutions can be physical adaptation on hardware, equipment level or logical, adaptation with software, change of programs, re-planning, re-routing etc. as shown in Table 1.

Table 1. Flexibility solutions adapted from (Heilala and Voho, 2001)

Static flexibility, physical "hardware"	*Dynamic flexibility, logical "programs"*
▪ Layout physical modifications ▪ Level of automation ▪ Re-configurability, re-utilization ▪ Modularity, expandability ▪ Scalable ▪ Exchange of system modules or submodules	▪ Control of tasks and resource settings ▪ Use of information technology ▪ Change of control programs, routines ▪ Robotics, flexible automation, ▪ Human intelligence and skills ▪ Sorting and routing of material and order flow

Technical solutions concepts, e.g., re-configurability at hardware and software defines the capability window of the system (Table 1). System capacity, production volume, can be adapted by increasing work time, e.g., more shifts, increased level of automation, or by adding more resources. Flexibility also depends on logistics and material flow. In a modern supply chain, production network and adaptation can also be done at different organizational levels, e.g., re-routing and re-scheduling can include external suppliers of the network. Requirements for the factory automation are shown by Dotoli *et al.* (2019) and requirements for the smart factory system by Ambkhot *et al.* (2018) and Kusiak (2019). Challenges for the Cyber Physical Production Systems (CPPS), requirements for manufacturing and key success factors for next generation manufacturing are shown by Panetto *et al.* (2019). Findings are similar to (Heilala and Voho, 2001) earlier, with a note that technology has evolved due to the introduction of Industry 4.0, Industrial Internet of Things (IIoT).

Drivers for resilient sustainable manufacturing can be listed as follows:

- Increase operational efficiency by reducing costs and waste;
- Respond to or reach new customers and increase competitive advantage;
- Build long-term business viability and success;
- Protect and strengthen brand and reputation and build public trust;
- Respond to regulatory constraints and opportunities;
- Provide a healthy workplace and empower the workforce; and
- Minimal use of natural resources while reducing environmental impact.

2 Design, modeling and evaluation

Resiliency and agility are about the system and process adaptation to the planned changes and unplanned disturbances. The design of an adaptable manufacturing system involves a number of interrelated subjects, such as tooling strategy, material-handling methods, system size, process and material flow configuration, flexibility needed for future engineering changes, production methods, capacity adjustment, and production floor layout strategy. Sustainable manufacturing system design takes into account the social, economic, and ecological constraints as well.

For analyzing environmental sustainability earlier in the product lifecycle, Brundage *et al.* (2016) suggest use of the SIMA reference model. SIMA, Systems Integration of Manufacturing Applications, reference architecture, developed at NIST (Barkmeyer *et al.*, 1996), addresses product design engineering, manufacturing engineering, production systems engineering, and production activities corresponding to the four top-level activities: (A1) Design Product, (A2) Engineer Manufacture of Product, (A3) Engineer Production System, and (A4) Develop Products (Figure 2).

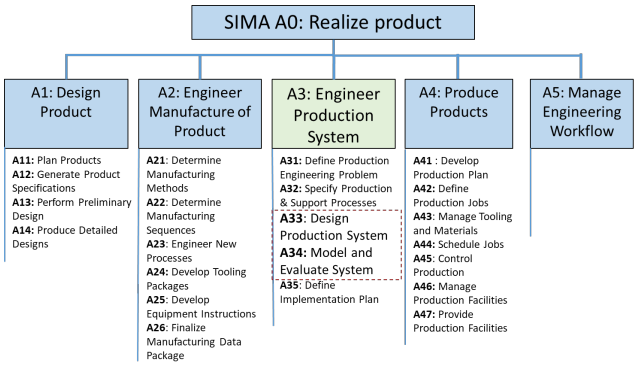

Figure 2. SIMA activities reference model adapted from (Barkmeyer *et al.*, 1996).

SIMA provides the structure of the product realization process. This paper is focused on the A3 Engineering of Production System, specifically to sub phases *(A33) Design Production System and (A34) Model and Evaluate System.* Production systems encompass processes, activities, and includes the resources and controls for carrying out the processes. Process design defines what is being performed in the system. The system design phase emphasis is on details of how, where, and when the process is performed (Phase A33 in Figure 2). In this phase, requirements, needs, strategies, market forecast and product structure, bill of material, production, and auxiliary process are known.

Based on requirements and potential solution designs, life-cycle scenarios are modeled and evaluated (Phase A34 in Figure 2). This can be an iterative process, as shown in Figure 3. The aim is justification of investment into potentially more expensive flexible equipment having a higher re-use value and longer life-time, better adaptation to changes, and/or brings other value, e.g., higher quality rate, and human and environmental aspects.

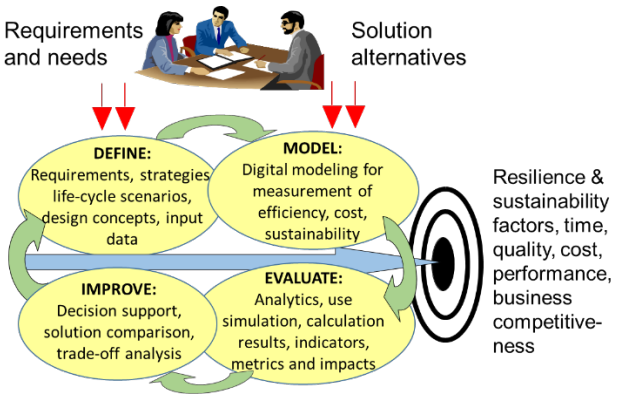

Figure 3. Methodology overview.

2.1 Define requirements and needs

The starting point is strategies, requirements, and needs, e.g., system lifetime scenarios, current and future product mix, and volume estimations. Modular structure of the production system enables use of the unit manufacturing process (UMP) model, as shown in Figure 4.

Product and process information, product structure, bill of material (BOM), production, and auxiliary processes are parameters to the system design. Each of the manufacturing process unit has planned input and output, resources, product and process information, see Figure 4.

In the definition phase, the cost parameters related to inputs are as follows: energy, materials and consumables, and resources: equipment, tools, fixtures, and human operators are identified. The amount of inputs, resource usage, and outputs can be calculated using static process modeling data or using dynamic simulation run results, as shown in the following chapters in this paper.

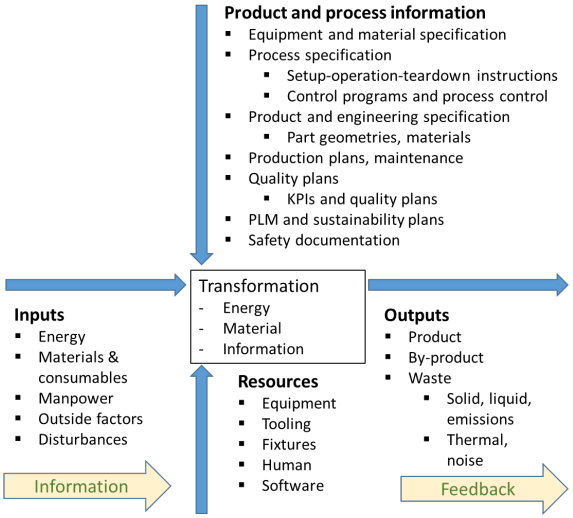

Figure 4. At system- and each module-level information (adapted from ASTM E3012 standard; Mani *et al.* 2016).

2.2 Solution modeling

There are several methods for manufacturing system modeling: analytic, symbolic, and models capturing the dynamics of the systems.

Analytic models, such as mathematical formulas, queue formulas, and linear programming, can give a quick answer. Some are able to give an optimum solution without going through trial and error. Their disadvantages include simplified assumptions that are often unable to account for random behaviors and, thus, a simplified solution to complicated problems.

Symbolic models, such as process flow diagrams, flowcharting, and Integrated DEFinition (IDEF), are suitable for communication, easy to understand, and quick to develop. The focus on the processes in the system are not aimed to resolve resource issues and operational problems too early. The disadvantages include lack of details, little or no quantitative measure of system elements or description of elements, activities, and relationships, and failure to capture the system dynamics. Symbolic models are static models.

Factory simulation measures the effects of process variability and interdependencies on overall system performance. A simulation creates an artificial history of the system. The disadvantages are that models can be difficult to construct – model building can be time-consuming and challenging.

In principle, a combination of the above-mentioned methods should aid engineers in speeding up the design process and improve decision making (Paju *et al.,* 2010). Analytic models in spreadsheets are commonly used by engineers and can be connected to symbolic, static and factory simulation models. Simulation models can read and write to external software, e.g., spreadsheets.

2.2.1 Manufacturing system modeling

Value Stream Mapping (VSM) is a simple-to-use symbolic process-modeling tool (see Figure 5**).** It specifies the activities, cycle times, down-times, and delays, and identifies bottlenecks and non-value-added activities in the production or in the logistics. A snapshot of the process activities in production may be created based on average data. Conventional VSM can be created for one product or product family with a pen and paper, although there are numerous VSM software tools. Combining VSM or similar process modeling to spreadsheets, an engineer can make an estimation of production mix and volumes.

VSM and environmental analysis have merged together in some applications. The US Environmental Protection Agency (EPA) has introduced the Lean and Environment toolkit, which offers practical techniques and strategies for environmentally protective lean decision making (EPA 2007).

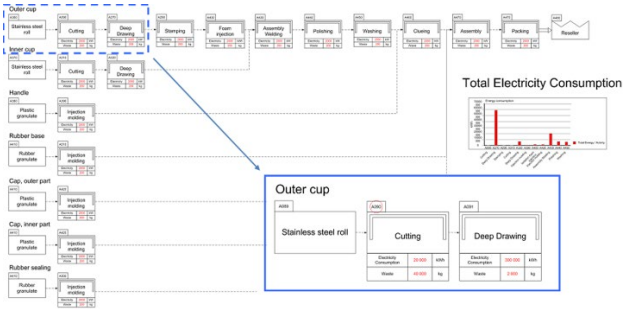

Figure 5. Example of VSM model adapted from (Paju *et al.,* 2010)**.**

Discrete Event Simulation (DES), a factory simulation, allows the experimentation and validation of different products, processes, and manufacturing system configurations (Mourtzis *et al.,* 2018). The simulation model is the virtual image of the planned real system. Discrete event/material flow/factory simulation is used in the design phase to evaluate concepts and optimize system solutions before investments and strategic decisions are made.

The common aim in simulation studies is to identify problem areas, and to quantify or optimize production system performance, such as throughput under average and peak loads, the utilization of resources, labor and machinery, staffing requirements, work shifts, bottlenecks, choke points, queuing at work locations, queuing caused by material handling devices and systems, the effectiveness of the scheduling system, the routing of material, the work in process, and storage needs.

The modular system structure can be implemented to layout planning and modeling systems. For example, in the assembly system layout configuration, model building, using 3D pre-defined and parametric sub-module merging, enables fast scenario creation (Heilala *et al.,* 1998; 2007; 2008a). In some cases, a standardized, parametric simulation submodule, catalogue equipment item can be shared on the internet, e.g., Visual Components public web eCatalog (Visual Components

2021). There are many other factory simulation tools in the market, supporting submodule merging.

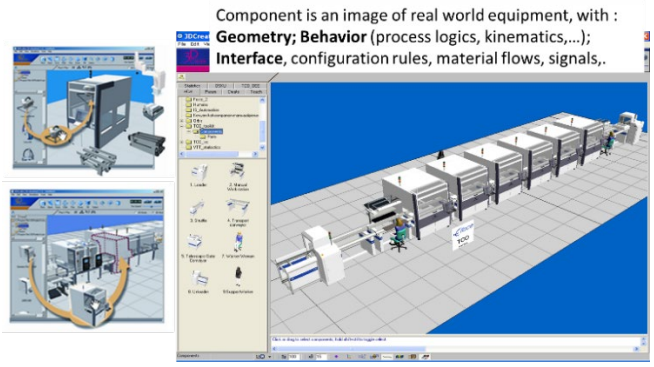

Figure 6. Component-based simulation adapted from (Heilala *et al.*, 2008a).

Modeling modularity is feasible on workstation and at sub-module, e.g. material feeding, jigs, fixtures and tool level as shown in Figure 6. Parametric modeling enables fast model changes. Environmental aspects can also be included in the production simulation analysis, as shown in later in Figure 9 . The environmental aspect analysis with DES or VSM adds the complexity in the input data collection since more data is needed. VSM model parameters and DES simulation run results can be further analyzed in spreadsheet tools, e.g., excel.

2.3 Evaluation and analytics

Modeling for analytics needs a resource, bill of material and product route data, process, order, production schedule, volume, mix, and data for system availability, set-ups, planned maintenance, reliability, machine breaks, and estimated production quality rate data, e.g., yield, rejects, scrap and rework. Use of the UMP model (see Figure 4) enables structure for data collection for each manufacturing unit, and these units can be modeled with VSM or DES, including connection between those units.

The output of analytics is equipment operation data and the percentages of machine statuses (on, off, stand by, under repair), thus allowing the amount of energy needed to be calculated. Using capacity data, we are able to calculate factors such as the piece count and material used during operations. DES shows the dynamics of the system. In Value Stream Mapping (VSM) and combined spreadsheet calculation, production volume data is deterministic, based on static, average data.

2.3.1 Cost and efficiency aspects analytics

Looking at system, equipment, or service purchase price is not enough. Life Cycle Cost (LCC) or Total Cost of Ownership (TCO) is the purchase price of a product or service plus the costs of operation throughout its life cycle. Cost of ownership (COO), as defined by SEMI standards, goes deeper (SEMI E35, SEMI E10, SEMI E79), looking also on profitability, COO of good units. COO depends on the production throughput rate, equipment acquisition cost, equipment reliability, throughput, yield, and equipment utilization, see Figures 7 and 8.

The basic COO is given by the following equation. COO per good unit equals all costs divided by total number of good products during the lifetime of the equipment

$$COO_{\text{per good unit}} = \frac{\text{Total costs}}{\text{Good units}} = \frac{FC + VC + YC}{L \times THP \times U \times Y} \quad (1)$$

where

FC = Fixed costs (amortized for the period under consideration), Acquisition, installation, training, etc.

VC = Operating costs (variable or recurring costs), factory interface, management, maintenance, control, materials, energy, labor costs, etc.

YC = Yield loss costs, scrap, rework,

L = Life time of equipment

THP = Throughput rate (nominal)

U = Utilization

Y = Yield

	Year 0	Year 1/ Period 1	Year 2 Period 2	...	Year n	Σ
FC Fixed costs: - Acquisition, - Facilities, - Decommission + Residual value	Investments, other costs before production	Upgrades, re-configuration, refurbishing or decommissioning				
VC Variable Cost, (recurring cost): - Factory interface, Equipment Management, - Maintenance - Inputs: materials, energy - Personnel: Operation **labor** **YC Yield Cost** Quality/Performance losses - defects, scrap, rework		Capacity/volume, utilization, worktime, quality, ...				
Number of good units, OEE analysis, **simulation**		Volume, loss identification				
COO, NPV, IRR,						

Figure 7. Life cycle cost (LCC), time-based matrix.

Yield loss cost is a measure of the value of units lost through bad quality (e.g., misprocessing, defects) and is broken out separately to demonstrate the importance of yield to both the numerator and denominator. The cost of lost yield increases, if the component travels forward in the processes before detecting the error. Some cost factors are more difficult than others to accurately determine in the concept phase.

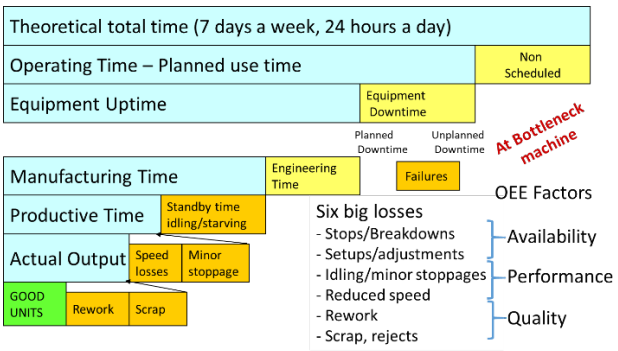

Figure 8. OEE time classification and six big losses.

The number of good products depends on reliability, availability, and maintainability (RAM) and utilization of equipment in a manufacturing environment. OEE (Overall Equipment Efficiency/Effectiveness) is an all-inclusive metric of equipment productivity, i.e., it is based on reliability, (Mean Time Between Failures-MTBF), maintainability (Mean Time To Repair-MTTR), utilization (availability), throughput, and yield.

All of the above factors are grouped into the following three sub-metrics of equipment efficiency.

1. Availability
2. Performance efficiency
3. Rate of quality

The three sub-metrics and OEE are mathematically related as follows: OEE % = Availability x Performance Efficiency x Rate of Quality x 100

OEE is a systematic way to evaluate production losses, normally used as an equipment key performance indicator (KPI). It helps to identify the actual time the system is producing good units, and at the same time it identifies and evaluates the OEE losses, like setups/adjustments, breakdowns, idling/minor stoppages, reduced speed, defects/rework (see Figure 8). In production systems, typically the focus is on the bottleneck machine. In the case of high mix, low volume production, the bottleneck location varies depending on customer orders and workload.

In the case of the DES model, with detailed input data, including data on MTBF, MTTR, cycle time variations, and material flow disturbances, it is possible to define the OEE based on simulation run results. In the case of using the VSM model and spreadsheet analytics, engineers can define the estimated OEE values themselves, by identifying six big losses shown in Figure 8.

In the design review or system sales negotiation phases, it is an advantage to identify potential OEE losses together with the customer, equipment or system user. Thus, there will be fewer surprises during the system utilization phase.

2.3.2 Environmental aspects analytics

VSM and DES are commonly used for manufacturing system analysis and development as shown earlier. Normally, these methods show selected production efficiency key performance indicators. At the same time, both methods create information about the production parameters needed for the calculation and analysis of environmental aspects (see Figure 9.).

Both VSM and DES can provide bookkeeping of production volume, number of products manufactured, cycle time, utilization, and equipment running time (Paju *et al.,* 2010).

Adding environmental data to process and equipment descriptions and planned production rate creates understanding of energy usage, greenhouse gas (GHG) emissions, usage of hazardous materials, waste, emissions, and so on. Usage can be shown per product, resource or process based on piece count or time period. This enables engineers to focus on the most harmful processes and optimize them.

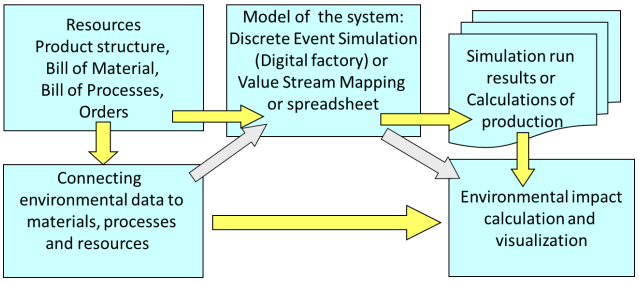

Figure 9. Environmental data connection to production resources, process, and product data.

An example of the categorization of sustainability performance indicators in manufacturing are shown in Figure 10. For air emission, e.g., carbon footprint analysis, the type and amount of material in kg, or energy usage in kWh, is just the starting point. There is a need to know the source of the raw material. Regarding energy, the CO2 emission using fossil fuels is much higher compared to renewal energy sources, e.g., water, wind, or solar energy.

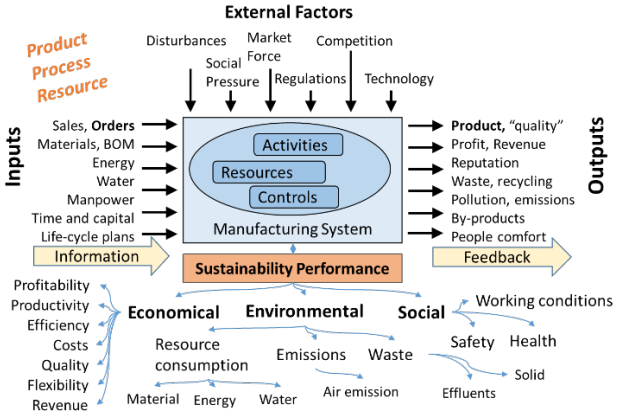

Figure 10. Typical manufacturing sustainability performance indicator adapted from (Beltrami *et al.,* 2021).

With the BOM, environmental data from cradle to the factory gate can be taken from the public LCI data sets, e.g., European Reference Life Cycle Database (ELCD3) (European Commission LCI 2018), or by using commercial data bases.

2.4 Improve decision making

Simulation studies, modeling parameters, input data, and run results, or other modeling methods combined with other relevant information, do provide data for analytics. Decision makers, managers, and development engineers are interested in planned system cost efficiency, investment and operating costs, productivity, throughput, utilization, availability, quality rate, flexibility, and all sustainability performance aspects.

Social sustainability is measuring working conditions, occupational health, and safety. Environmental sustainability is measuring resource consumption, emissions, and waste. Beltrami et al. (2021) show the linkage of industry 4.0 technology and sustainability performance indicators, see Figure 10. The global standards for sustainability reporting (GRI 2020) are one source for defining sustainability indicators.

Environmental aspects are getting more important due to increasing regulation, and they are useful in marketing, in creation of brand, and reputation of the company. Evaluation can be an iterative process, managers and engineers can edit models, and model parameters for optimization, as well as for risk management (Figure 3).

3 Discussion

The presented methodology has evolved during a series of research projects starting in the mid-1990s. The human-friendly agile assembly system concept and modeling methods for modular assembly equipment started in the late 1990s (Heilala and Montonen, 1998; Heilala and Voho, 2001). The cost aspect with performance analytics were introduced in the early 2000s, starting with spreadsheet analytics, later some integration to commercial simulation software (Heilala *et al.,* 2007; 2008a). The development initiated from systems end-user flexibility needs as well as on assembly system vendor ongoing development efforts. Later, the environmental aspects were added, starting with energy consumption and the eco-engineering process during the 2010s (Heilala *et al.,* 2008b; Lind *et al.,* 2009; Paju *et al.,* 2010). This also shows how industrial needs have change, from cost-efficiency-dominant decision making to all sustainability aspects.

The presented methodology usage is not limited to assembly system evaluation, as shown in (Heilala *et al.,* 2007; 2008a; 2008b); in general, the presented principle can be adapted to advanced manufacturing systems development and investment evaluation. Managers and engineers can justify investments to adaptive, human- and environmentally friendly technologies, equipment, and processes. For example, COO analyzes the cost of ergonomics solutions, the physical and cognitive level of automation, and with the OEE evaluation of impact to productivity, benefits of investments can be estimated. It should be noted that in both COO and OEE analyses in spreadsheet tools, it could be for relative comparison, i.e., before versus after change or between competitive solutions. Using these metrics as relative measures, the modeler is not required to build the perfect model or obtain all possible data. In one case, analysis and modeling with normal office tools and advanced spreadsheet calculation were sufficient, e.g., the study on Augmented Reality usage in assembly, shown in (Sääski *et al.,* 2008). In that particular case, laboratory test set-up provided input data for analysis.

This presented methodology is not yet an integrated tool package. It is merely a conceptual methodology. Parts of methodology have been tested in the past in industrial-driven projects, and the results are published. The presented COO and OEE are based on SEMI standards SEMI E35-0305, SEMI E10-0304, and SEMI E79-0304, and these standards have been updated. The next steps would be to adapt to evolving standardization: e.g., ISO - International Organization for Standardization (https://www.iso.org/home.html), SEMI - the global trade association of electronics manufacturing supply chain (https://www.semi.org/en), VDMA - Association of mechanical and plan engineers (https://www.vdma.org/), VDI – The Association of German Engineers (https://www.vdi.de/en/home), ASTM International (https://www.astm.org/), see also (Mani *et al.,* 2016) - just to mention some standardization bodies working on relevant standardization.

4 Conclusions

A resilient system needs agility, re-configurability at various levels, resource and process modularity, re-usability, digitalization, and human and environmental friendliness. One challenge for the manufacturing industry is justification for such equipment, system, or service. The presented methodology is an attempt to improve the decision-making process with modeling and simulation. Currently, the presented methodology is a combination of dynamic analytics, e.g., the use of Discrete Event Simulation (DES) if feasible, combined with selected static modeling and calculation methods in a spreadsheet. Decomposition of aspects under study is the key in analytics.

All sustainability aspects are covered. Social sustainability, human safety, well-being, ergonomics solutions, and related investments, e.g., adjustable worktables, collaborative automation, both physical and cognitive technologies for enhancement, and augmenting human worker performance can be estimated. Economic sustainability, profitability, and efficiency connect the cost parameters of technology, process, or services and evaluate the impact on productivity. Environmental sustainability is looking at environmental impacts as well resource efficiency.

From a cost point of view, the purchase cost of equipment is not enough: evaluate all cost items, fixed and recurring costs, cost of poor quality, cost related to potential upgrades during life-cycle scenarios of the system. The presented cost calculation, Cost of Ownership (COO), also provides data for commonly used investment evaluation methods, and discounted cash flow techniques: Net Present Value (NPV) and Internal Rate of Return (IRR), see Figure 7.

From the production performance point of view, nominal system capacity and throughput are not enough: evaluate disruptive events, such as machine testing, set-ups, planned and unplanned maintenance, quality failures, missing parts, operators, or orders. These events, six big losses (see Figure 8), could lead to full or partial loss of production in the system. Therefore, gaining a fundamental understanding and evaluation of these events and associated impacts on system performance in the design phase will have a significant impact on the economic sustainability.

Environmental aspects can be estimated based on simulation run results or by using (VSM) methodology and spreadsheet calculations for equipment operation hours and the number of products (see Figure 9). Adding environmental data to process and equipment descriptions creates understanding of the energy usage pattern and related CO2 emissions, usage of hazardous materials, chemicals, estimates of the amounts of waste, bi-products, etc. The methodology is not a full Life Cycle Assessment (LCA) but provides data for doing the LCA.

Manufacturing is moving away from the dominating economic paradigm of "maximum gain with minimum capital investment" towards a more sustainable paradigm of "maximum added value using minimal resources and carbon neutrality".

The presented methodology is versatile, a solution-relative comparison without a perfect model, even with normal office tools. Symbolic models, even just with pen and paper, improve communications between stakeholders. Use of dynamic simulation models increases the accuracy of analytics as well complexity in model building.

The presented methodology measures selected resilience and sustainability aspects, to the organization over the planned life cycle of a piece of production equipment - not absolute accurate values in the concept creation phase - but data for comparison. The analytics is as good as input data is; input of false information does not produce the right results. The user should make a risk assessment of results, e.g., use of min, max, and optimal data values in calculation and simulations. The challenges are on getting reliable data in the conceptual phase.

Acknowledgements

The author wishes to acknowledge the financial support received in the past from the national and European funding organizations, VTT, and the Finnish industry, as well as the project's industrial and research partner's fruitful feedback.

References

ASTM E3012-20, Standard Guide for Characterizing Environmental Aspects of Manufacturing Processes, *ASTM International*, West Conshohocken, PA, USA. 2020. doi:10.1520/E3012-20

E. Barkmeyer, N. Christopher, S. Feng, J. Fowler, S. Frechette, A. Jones, K. Jurrens, C. McLean, M. Pratt, H. Scott, M. Senehi, R. Sriram and E. Wallace. SIMA Reference Architecture Part I: Activity Models, NIST Interagency/Internal Report (NISTIR), *National Institute of Standards and Technology,* Gaithersburg, MD, USA, 1996. doi:10.6028/NIST.IR.5939

M. Beltrami, G. Orzes, J. Sarkis, and M. Sartor. Industry 4.0 and sustainability: Towards conceptualization and theory. *Journal of Cleaner Production*, Volume 312, 2021, 127733, ISSN 0959-6526, 2021. doi:10.1016/j.jclepro.2021.127733.

M. Brundage, W. Bernstein, T. Kliks, H. Nishi, S. Hoffenson, Q. Chang and K. Morris. Analyzing environmental sustainability methods for use earlier in the product lifecycle. *Journal of Cleaner Production*, 187: 877-892, 2018. doi:10.1016/j.jclepro.2018.03.187

L. De Nul, M. Breque and A. Petridis. Industry 5.0. Towards a sustainable, human-centric and resilient European industry. *European Commission,* 2021. doi:10.2777/308407

M. Dotoli, A. Fay, M. Miśkowicz, and C. Seatzu. An overview of current technologies and emerging trends in factory automation. *International Journal of Production Research,* 57(15-16): 5047-5067, 2019. doi:10.1080/00207543.2018.1510558

R. Dove. What Is All This Talk About Agility - The 21st Century Manufacturing Enterprise Strategy, *Japan Management Association Research,* Prevision, 1992.

EPA (2007). The Lean and Environment Toolkit. *U.S. Environmental Protection Agency.* https://www.epa.gov/sustainability/lean-environment-toolkit [Accessed July 1 2021].

European Commission LCI. (2018). ELCD 3. Life Cycle Inventory (LCI) data sets. Available via https://eplca.jrc.ec.europa.eu/ELCD3/ [Accessed June 17, 2021].

GRI. *Global Reporting Initiative standards*, 2020. https://www.globalreporting.org/standards. [Accessed 1 July 2021].

J. Heilala and J. Montonen. Simulation-based design of modular assembly system - use of simulation module library. In *Proceedings of 3rd EUROSIM Congress on Modelling and Simulation,* April 14-15, 1998. Helsinki, Finland, pages 493-498. ARGESIM Report 9, 1998. ISBN 978-3-901608-03-2.

J. Heilala and P. Voho. Modular reconfigurable flexible final assembly systems. *Assembly Automation*, 21(1): 20-30, 2001. doi:10.1108/01445150110381646

J. Heilala, O. Väätäinen, J. Montonen, T. Laaksonen and H. Kulmala. Decision Support and Simulation Methods for Assembly System Sales Engineers. In *Proceedings of the 6th EUROSIM Congress*, Ljubljana, Slovenia. 9-13 Sept. 2007. ARGESIM, 2007. ISBN 978-3-901608-32-2.

J. Heilala, J. Montonen and O. Väätäinen. Life cycle and unit-cost analysis for modular reconfigurable flexible light assembly systems. In *Proceedings of the Institution of Mechanical Engineers, Part B: Journal of Engineering Manufacture. Professional Engineering Publishing Ltd.,*

Vol. 222, pages 1289 – 1299. 2008a doi:10.1243/09544054JEM1034

J. Heilala, S. Vatanen, J. Montonen, H. Tonteri, B. Johansson, J. Stahre, and S. Lind. Simulation-Based Sustainable Manufacturing System Design. In *Proceedings of the 2008 Winter Simulation Conference.* pages 1922-1930. 2008b doi:10.1109/WSC.2008.4736284

P.T. Kidd. Agile Manufacturing. Forming New Frontiers, *Addison-Wesley Publishing Company Inc*., 1994. ISBN 0-201-63163-6.

A. Kusiak. Fundamentals of smart manufacturing: A multithread perspective. *IFAC Annual Reviews in Control,* 47: 214–220. 2019. doi:10.1016/j.arcontrol.2019.02.001

A. Kusiak. Resilient manufacturing. *Journal of Intelligent Manufacturing,* 31: 269, 2020. doi:10.1007/s10845-019-01523-7

S. Lind, B. Johansson, J. Stahre, C. Berlin, Å. Fasth, J. Heilala, K. Helin, S. Kiviranta, B. Krassi, J. Montonen, H. Tonteri, S. Vatanen, and J. Viitaniemi. SIMTER - A Joint Simulation Tool for Production Development. Espoo, VTT. 49 p. *VTT Working Papers*; 125. 2009. ISBN 978-951-38-7185-7

M.M. Mabkhot, A.M. Al-Ahmari, B. Salah, and H. Alkhalefah. Requirements of the Smart Factory System: A Survey and Perspective. *Machines* 2018, 6, 23, 2018. doi:10.3390/machines6020023

M. Mani, J. Larborn, B. Johansson, K.W. Lyons, and K.C. Morris. Standard Representations for Sustainability Characterization of Industrial Processes. *ASME. Journal of Manufacturing Science and Engineering.* October 2016; 138(10): 101008. 2016. doi:10.1115/1.4033922

D. Mourtzis, N. Papakostas, D. Mavrikios, S. Makris, and K. Alexopoulos. The role of simulation in digital manufacturing: Applications and outlook. *International Journal of Computer Integrated Manufacturing* 28: 3–24, 2018. doi:10.1080/0951192X.2013.800234

D. Mourtzis, J. Angelopoulos, and N. Panopoulos. Robust Engineering for the Design of Resilient Manufacturing Systems. *Applied Sciences.* 2021, 11, 3067. doi:10.3390/app11073067

M. Paju, J. Heilala, M. Hentula, A. Heikkilä, B. Johansson, S. Leong, and K. Lyons. Framework and indicators for a sustainable manufacturing mapping methodology. In *Proceedings of the 2010 Winter Simulation Conference*, pages 3411–3422, 2010. doi:10.1109/WSC.2010.5679031

H. Panetto, B. Iung, D. Ivanov, G. Weichhart and X. Wang. Challenges for the cyber-physical manufacturing enterprises of the future. *Annual Reviews in Control*, 47: 200-213, 2019. ISSN 1367-5788, doi:10.1016/j.arcontrol.2019.02.002.

SEMI Standard E35 - Guide to Calculate Cost of Ownership (COO) Metrics for Semiconductor Manufacturing Equipment. [available online at www.semi.org].

SEMI Standard E10 - Specification for Definition and Measurement of Equipment Reliability, Availability, and Maintainability (RAM) and Utilization [available online at www.semi.org].

SEMI Standard E79 - Specification for Definition and Measurement of Equipment Productivity [available online at www.semi.org].

J. Sääski, T. Salonen, J. Heilala and J. Mela, J. Economic evaluation of the use of augmented reality in assembly processes. In *Proceedings of Swedish Production Symposium, Stockholm 18-20 November 2008*. Lindberg B., and Stahre J. (eds.). The Swedish Production Academy, pages 409-416. 2008.

Visual Components https://www.visualcomponents.com/ [Accessed August 1 2021].

World Commission on Environment and Development (1987). Our Common Future. Oxford, Great Britain: *Oxford University Press*. 1987.

Extended ATM for Seamless Travel (X-TEAM D2D)

Margarita Bagamanova[1] Abdel el Makhloufi[2] Miguel Mujica Mota[3] Vittorio Di Vito[4] Roberto Valentino Montaquila[4] Giovanni Cerasuolo[4] Bartosz Dziugieł[5] Maciej Maczka[5] Peter A. Meincke[6] Gabriella Duca[7] Raffaella Russo[7] Vittorio Sangermano[7] Mario Ciaburri[7] Stefano Giovannini[8] Luigi Brucculeri[8] Riccardo Enei[9]

[1]AMSIB, Amsterdam University of Applied Sciences, the Netherlands, mm.bagamanova@hva.nl
[2]Faculty of Technology, Amsterdam University of Applied Sciences, the Netherlands
[3]Aviation Academy, Amsterdam University of Applied Sciences, the Netherlands
[4]Italian Aerospace Research Center (CIRA), Italy
[5]Łukasiewicz Research Network – Institute of Aviation (ILOT), Poland
[6]German Aerospace Center (DLR), Germany
[7]Italian Institute for Sustainable Society and Innovation (ISSNOVA),
[8]D-FLIGHT S.p.A, Italy
[9]Institute of Studies for the Integration of Systems (ISINNOVA), Italy

Abstract

X-TEAM D2D project is focused on integrating Air Traffic Management and Urban Air Mobility into an overall multimodal transport network to address the potential increase in efficiency of the overall transportation system in the future, considering the operational domain of the urban and extended urban environment up to a regional extent and passenger-centric perspective. This paper presents the analysis of the Door to Airport trajectory of business passengers until 2035. The results indicate the system's expected performance in 2035 under normal and disrupted scenarios providing insight on the expected impact of future technologies.

Keywords: airport, multimodal transport, passenger service, door-to-door

1 Introduction

The world population will increase to approximately 10 billion people in 2050 and approximately 11 billion around 2100. By 2050, about 68% of the worldwide population will live in urban areas (United Nations, 2019). This growth will dramatically increase mobility and demand for transport, especially air travel demand.

In future (up to 2050), physical infrastructure, transport systems, traffic management, operational processes and information systems will be seamlessly integrated. Combining emerging information technologies and transport modes with a passenger-centric view will revolutionise future mobility (Organisation for Economic Co-operation and Development and International Transport Forum, 2020). From the aviation perspective, a key enabler for this is integrating Air Traffic Management (ATM) and Urban Air Mobility (UAM) and related U-Space services into overall multimodal transport systems that will provide its stakeholders with standard and comprehensive information of the door-to-door (D2D) travel flows and improve accessibility and passenger service level (Bao et al., 2016). To achieve such integration and facilitate reaching the goals of Flightpath 2050 (European Commission, 2011), it is necessary to explore how different existing, emerging, and new transport technologies can be integrated and define the related integrated service concept as well as the policies that could help such systems function most efficiently. These tasks comprise the scope of the X-TEAM D2D project.

This paper presents preliminary results of simulation experiments for the business traveller's use case considering technological changes in the passenger journey in 2025 and 2035 and is organised as follows. Section 2 introduces project goals. The project methodology and the relevant elements are described in Section 3. Modelling and simulation approach for validation of Concept of Operations (ConOps) is presented in Section 4. First simulation experiments with the ConOps validation tool are described in Section 5, and their preliminary results are discussed in Section 6. Section 7 concludes the paper and discusses future work direction.

2 Project Goals

The X-TEAM D2D project aims to explore and analyse the integration of ATM (and UAM with related U-Space services into the overall multimodal transport system, considering currently available transportation modalities and the emerging mobility forms envisaged for the next decades. Moreover, the X-TEAM D2D focuses on developing the ConOps for seamless D2D mobility in urban and extended urban areas (up to

regional). The developed ConOps will be validated and evaluated against relevant key performance areas and performance indicators, using a simulation-based platform that considers the most relevant future transport elements. Furthermore, specific use cases of the D2D journey under different scenarios will be analysed to validate the ConOps and enable decision support tools.

The X-TEAM D2D will bring the following improvements in the state-of-the-art research:

- Enhancing understanding of seamless D2D travel in integrated ATM and multimodal transport modes.
- Integrating modelling D2D travel into ATM and multimodal transport.

3 Methodology

The X-TEAM D2D research methodology comprises the definition and validation of the ConOps, based on reference scenarios and application in use cases. The ConOps for ATM integration into multimodal transport will describe the characteristics of the proposed system from the perspective of passengers and transport modes through several use cases in 2025, 2035, and 2050. Figure 1 shows the project methodology, which includes extensive literature research as well as use of public transport data from different existing mobility service providers. In cases, where are no data available, e.g., for future mobility technologies, the project members agree on assumption regarding the required operational parameters.

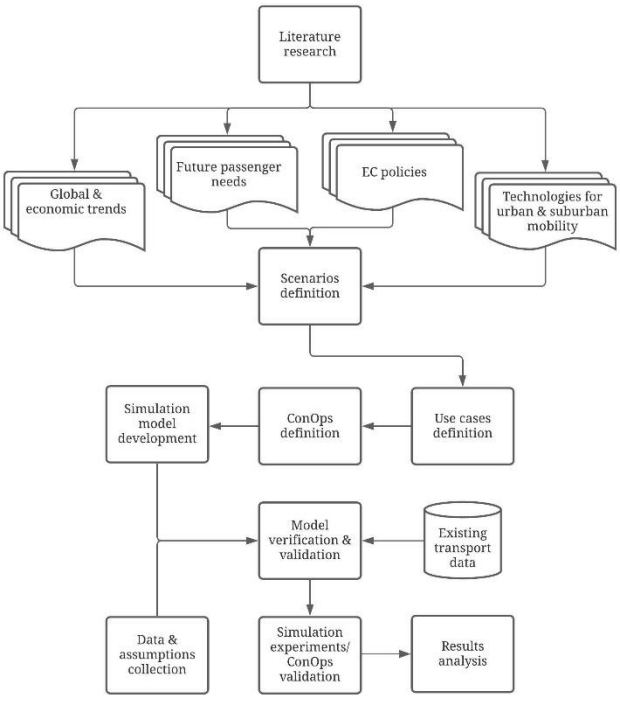

Figure 1. X-TEAM D2D methodology flowchart.

3.1 Reference Scenarios Definition

To formulate ConOps applicable to three considered time horizons, three reference scenarios describing the state of the transportation system in these years were defined. They assume that energy transition, green mobility and transport, and circular economy will occur in 2025 and 2035, supported by a significant increase in digitalisation and automation in 2050 (Eurocities, 2021). The defined scenarios are not alternatives but subsequent possible future states. The analysis of the potential integration of ATM and other modes shows that most technologies will be partly achieved by 2035 (electric vehicles, autonomous/electric bus in connection with the airport, transit elevated bus, autonomous cars, shared electric micro-mobility) and fully deployed by 2050. The defined reference scenarios characteristics are as follows:

In 2025:

- Intensifying use of New Mobility Services (NMS) (Kamargianni et al., 2016), emerging of connected, cooperative, automated mobility (CCAM) (European Comission, 2018).
- Further development of Trans-European Transport Network (TEN-T) (mainly rail and maritime) (European Comission, 2021), shift to rail and maritime logistics.
- Million public recharging stations and 500 hydrogen refuelling stations (European Commission, 2020).
- Eurovignette (AGES, 2021).

In 2035:

- Emerging of UAM, intensifying use of CCAM.
- The Core TEN-T Network completed, smart pricing, shift to lower emission modes.
- Three million public recharging stations and 1000 hydrogen refuelling stations.
- Intensifying multimodality among the soft modes of travel, mass transit, NMS, CCAM.

In 2050:

- Net-zero emissions in transport.
- The Comprehensive TEN-T Network completed.
- Walkable cities, domination of soft modes, mass transit, NMS, CCAM, UAM.

The scenario development adopted and implemented a passenger-centred approach, which incorporates concepts of inclusive design, transgenerational design, and context of use. Inclusive design aims to optimise the use of a system or a service for a specific user with specific needs. Eventually, inclusive design results in a system and/or service accessible to and usable by as many people as reasonably possible without the need for adaptation or specialised design for specific user categories. The inclusive design embeds the concept of transgenerational design, aiming to make systems and

services compatible with physical and sensory impairments associated with human ageing (Pirkl, 1994). Thus, the inclusive design considers the full range of human diversity to cover individual passengers' permanent or temporary needs (Inclusive Design Research Centre, 2021). The concept of context of use represents the combination of goals, characteristics, tasks, objects and environment describing the situation in which the users operate a system or service. The context of use considers the variety of real-world contexts under different time horizons, concerning which transport mode is more efficient and responds better to the needs of travellers.

The passenger-centred approach allows the identification of the main actions of passengers and their characteristics during the multimodal D2D journey. Based on the three scenarios mentioned in Section 3.1, a set of most representative use cases was defined. These use cases are "ATM-centred", meaning that they include the central role of ATM in multimodal transport.

3.2 Definition of Use Cases

Definition of the use cases for a given time scenario consists of the identification of the most representative passenger profiles, the expected mobility patterns, the identification of new modes of transport, and the integration of ATM with multimodal transport modes through data exchange, with special focus on tools and solutions that enable efficient travel planning, management and resilience to various disruptions.

To determine the relevant passengers' needs, the following key aspects were considered:

- Services and facilities should have affordable prices, considering the demand market segmentation.
- The options and solutions provided should be easy to use and easy to understand.
- Frequent railroad connections to the city centre should be an asset if an attractive alternative to road-based transport to/from airports exists.
- Information provided should be exhaustive and of high quality, particularly in case of disruptions.
- Reliability of services should be guaranteed by providing alternative solutions, e.g., in case of unexpected disruptions.

The specifications of the use cases include type, characteristics, profile and expected behaviour of different passengers, new modes of transport, the transport integration and data exchange that cover planning, management, and resilience to disruptions during multimodal D2D journey. In total, 18 use cases were identified. Figure 2 gives an overview of the defined use cases and the corresponding scenarios.

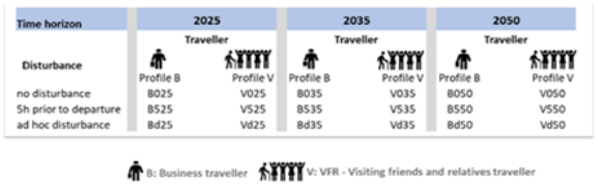

Figure 2. Overview of use cases within the time horizons.

The key characteristics of passengers' profiles and their expected behaviour are based on the distinction between two types: the business traveller (BT) and visiting friends and relatives (VFT). These characteristics and corresponding expected behaviour are then projected in the future according to three time horizons: 2025, 2035 and 2050. Table 1 gives an example of the BT key characteristics and corresponding behaviour in 2035.

Table 1. Business traveller profile key points for 2035.

Characteristics	*Expected behaviour*
• Travels alone (mainly). • Very high comfort standard. • Expect a very short travel time. • Few budget limits. • Travels for a short stay, small luggage. • Frequent traveller. • Adult (18-70 years), generally in normal health condition (minor physical or sensorial impairments). • Relies on dedicated business services for travel arrangements (no reservation or payment methods constraints). • Complete flexibility for a travel plan change.	• Spends little time in planning the trip; the trip is not arranged a long time in advance. • Personalised/on-demand travel services, even at higher costs. • Chooses the fastest multimodal journey combination. • Chooses the most comfortable, effortless travel means. • Might choose travel means to show status, according to the position in the organisation. • Might choose travel means to reinforce sustainability policies of his/her company.

Various assumptions have been made for specifying current and future transport modes in determining the use cases according to the defined scenarios. For example, in scenario 2025, it is assumed that data sharing will impact the efficiency of the transport system, especially short-range airlines connections. There is a good connection between the hub and regional airports, and there is a good connection between the hub airport and the city by numerous transport modes (trains, bus connections, taxis).

4 Modelling and Validating ConOps

An essential part of the X-TEAM D2D project is developing a simulation framework for evaluating and validating the created ConOps. This framework represents high-level door-to-door travel where target passenger groups use different transport means to reach their destination. As X-TEAM D2D is focused on the role of ATM and airports in future multimodality, the simulation framework is built around two types of airports: regional airport and hub airport.

The framework consists of two parts which represent door-to-airport and airport-to-door phases of the passenger journey. The schematic representation of typical passenger journeys simulated in the framework is shown in Figure 3. This paper presents only the first half of the door-to-door trip of the simulation framework, reflecting the business traveller's door-to-airport journey in 2025 and 2035. The characteristics of the model and simulation experiments set up are described in the following sections.

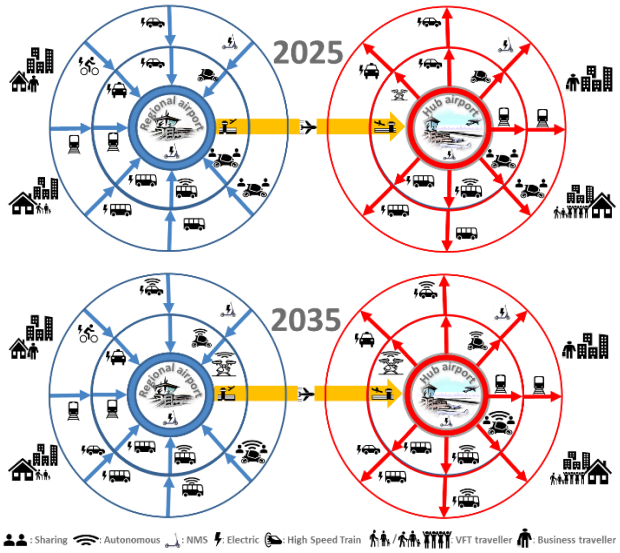

Figure 3. Multimodal passenger trips in 2025 and 2035.

4.1 Simulation Model Architecture

The developed simulation framework aims at evaluating the impact of future concepts of operations on the passenger journey. The simulation framework is based on a multiple-layer approach, where first, the existing transportation network is created. Then, future transport technologies are added on top of that as an additional layer considering relevant time horizon assumptions and ConOps. Such an approach allows simulating different time horizons using the same simulation model, which reduces required model building time and allows flexible integration of different transport means into an overall multimodal network.

There are three groups of elements implemented in the model. The first group, dynamic entities, represents passengers and vehicles transporting passengers from their origin to the airport. The second group, static elements, represent transport stations that the passengers can use to embark/disembark on and off transport vehicles. These stations serve as the entry, transfer, and exit points with a fixed position for the interconnected multimodal transport networks and are modelled as capacitated servers. The third group is the set of nodes and edges connected into a network that vehicles and passengers use to move through the space between transport stations. Figure 4 shows a part of the simulation model representing door-to-airport journey.

Figure 4. X-TEAM D2D simulation model view.

In the model, the arrival of passengers and most transportation means is generated stochastically based on the initial assumptions. Some transport means (such as buses and trains) are generated on a schedule, as observed in real-life operations. An overview of modelling assumptions is given in Section 4.2.

The model is implemented in a general-purpose discrete event simulation software, using the concepts described above.

4.2 Modelling Assumptions

In the simulation model, the following transport technologies have been considered:

- Public buses
- Railroad transport (trains)
- Taxi vehicles, running on fossil-based fuel
- Electric scooter or similar form of individual transport (eScooter)
- Electric taxi vehicles (eTaxi)
- Electric vertical take-off and landing aircraft (eVTOL)

The following assumptions have been considered in the model:

- The road infrastructure and its operational conditions remain unchanged through all time horizons and correspond to the existing infrastructure state in 2020.
- Only individual business passengers travelling to the airport are simulated.

- Passenger arrival remains stochastic across scenarios and follows the same distribution as shown in Figure 5. The arrival rate pattern was adapted from NV Nederlandse Spoorwegen (2020).
- All passengers have pre-purchased travel tickets; therefore, no purchasing time is considered during the journey.
- Travelling time in the first transport modality also includes walking time to the first transport station from the passenger's origin location.
- All transport modes in 2035 are carbon-neutral (electric transport).
- eVTOL operation does not consider possible airspace limitations and regulations.

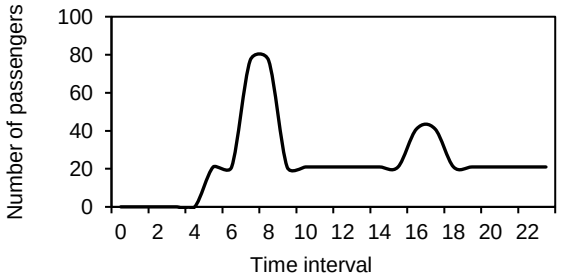

Figure 5. Passengers' arrival rate per hour.

The rest of the assumptions is scenario-specific and described in Section 5.

5 Simulation Experiments

In the scope of this paper, a journey of BT passengers in two time horizons, 2025 and 2035, was simulated in normal and ad-hoc disturbance conditions according to four scenarios defined in the first phase of the X-TEAM D2D project. The characteristics of these scenarios can be found in Table 2 and Table 3. Where it was possible, the operational characteristics of mobility services were adapted from the corresponding service operators (Connexxion, 2021; Electric Scooter Guide, 2021; EV Database, 2021; NV Nederlandse Spoorwegen, 2021). It is important to notice that only trains and buses operated on an on-schedule basis in these scenarios—the rest of the transport modes operated based on demand.

The simulated scenarios represent the following situations:

- In 2025, BT passengers use public buses to get to the city train station, from which they take a train to the airport. The next scenario, 2025d, implies that a disruption occurs when a passenger arrives at a train station and the trains no longer operate. To catch the flight on time, BT passenger has to get a taxi to reach the airport.
- In 2035, BT passengers use a form of pooled individual electric transport, such as an electric scooter (eScooter), to get to the landing site of eVTOL, from which they can take a direct flight to the airport. When a disruption occurs with eVTOLs in scenario 2035d, BT passenger has to take an electric taxi from the landing site to the airport.

Table 2. Overview of simulation scenarios for 2025.

Parameter	*2025*	*2025d*
Use case	B025	Bd25
Operation	Normal	Ad-hoc disturbance
Transport used	Bus, train	Bus, taxi
Travel distance 1st mode, km	Uniform(0,3)	Uniform(0,3)
Average travel speed 1st mode, km/h	18	18
Transfer time to 2nd mode, min	Uniform(1,15)	Uniform(1,15)
Travel distance 2nd mode, km	26	22
Average travel speed 2nd mode, km/h	65	60
Disruption location	-	Train station
Reaction to disruption time, min	-	Uniform(1,5)

Table 3. Overview of simulation scenarios for 2035.

Parameter	*2035*	*2035d*
Use case	B035	Bd35
Operation	Normal	Ad-hoc disturbance
Transport used	eScooter, eVTOL	eScooter, eTaxi
Travel distance 1st mode, km	Uniform(0,14)	Uniform(0,14)
Average travel speed 1st mode, km/h	27.5	27.5
Capacity 1st mode, passengers	1	1
Transfer time to 2nd mode, min	Uniform(1,15)	Uniform(1,15)
Travel distance 2nd mode, km	13	22
Average travel speed 2nd mode, km/h	200	60
Capacity 2nd mode, passengers	4	1

Disruption location	-	eVTOL landing site
Reaction to disruption time, min	-	Uniform(1,5)

The total travelled distance and total travel time were tracked across the simulation experiments to compare multimodal system performance in the presented scenarios. Each experiment simulated 25 hours of passengers travelling from a small European town to an international airport. The results of these experiments are discussed in Section 6.

6 Results

Experiments in scenarios 2025 and 2025d reflect the transportation network performance closest to the current state of multimodal connectivity. Scenarios 2035 and 2035d reveal some effects of emerging transport technologies integrated into existing transportation networks and replacing existing modes of transport. The results of simulation experiments are shown in Figure 6 and Figure 7.

Scenario 2025d resulted in a 14% shorter travel distance than in scenario 2025, as passengers could take the taxi directly to the airport. This difference, however, can be strongly dependent on the particular infrastructure layout. In this study, there is no fast train connection from the passengers' origin town, which results in longer travel. In 2035, such layout inefficiency is considered to be solved by establishing a direct air connection to the airport. Consequently, as can be seen in Figure 6, the travel distance was reduced by 26%.

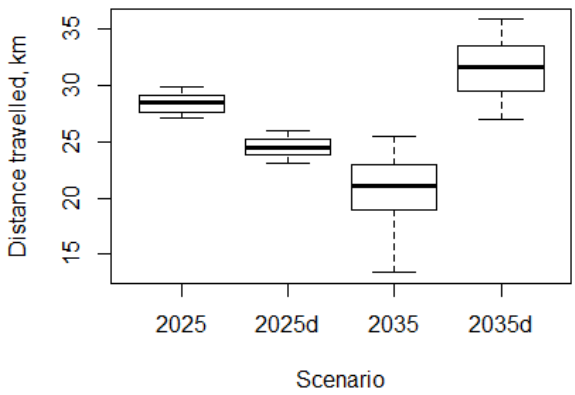

Figure 6. Travel distance statistics.

When comparing the distance travelled by business passengers in all four scenarios, it can be noticed from Figure 6 that the shortest distance corresponds to 2035. This result matches a scenario where eVTOL technology replaces road and railroad transport and provides the most direct connection to the airport. However, if eVTOL operations are disrupted and business passengers only learn about such disruption when they arrive at the landing site (scenario 2035d), relying on road transport for a quick solution to reach the airport creates a significant increase in travel distance – by 50% on average.

A similar effect can be observed in travel times. As shown in Figure 7, using a taxi in scenario 2025d allows reducing travel times by 5% on average. However, in 2035d, using an electric taxi in case of disruptions increases travel time by 40%, which means 8% longer travel than in scenario 2025d.

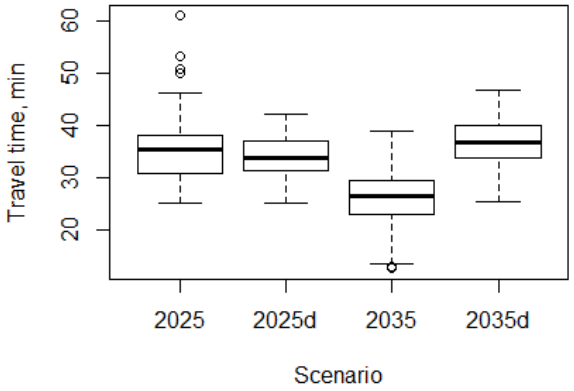

Figure 7. Travel time statistics.

To summarise, business travellers are expected to win significantly in travel time and distance if new technologies like electric scooters and eVTOL are introduced into transportation networks. Nevertheless, if the existing road infrastructure and its speed limitations remain unchanged up to 2035, the improvement of travel times will be lost for business passengers who encounter disruptions on their way to the airport. The latter means that not only technological and IT advancements are required for the improvement of passenger travel, but a system-wide redesign of the transportation network and consideration of potential inefficiencies in the concepts of future transport operations are needed.

7 Conclusions and Further Work

For seamless integration of existing and future transport technologies into an overall multimodal network with a high level of passenger service, the Concept of Operations (ConOps) have to be developed and validated. These concepts will ensure the inclusiveness and resilience of the future transportation network for all types of passengers. To define and validate such operational concepts, project X-TEAM D2D performed an extensive technological review for 2025, 2035, and 2050 and developed a simulation platform to assess the system performance.

In this paper, the authors used the framework to obtain preliminary results of the door-to-airport trip of business passengers. According to these initial results, emerging technologies such as individual electric transport and electric vertical take-off and landing aircraft can improve business passengers travel times in

2035 by 26%. However, considering the assumptions taken, if these passengers rely on on-demand road transport in case of disruptions, the resulting journey duration will be almost as long as in 2025.

In the simulated scenarios, it was assumed that the passengers noticed the disruption only when they arrived at the eVTOL port, which might not be the case if relevant journey planning systems are integrated sufficiently in 2035. As future work, the simulation framework will be expanded to reflect the state of the transportation networks in 2050. The developed ConOps will be integrated into the framework to perform their validation and evaluation. Furthermore, more performance indicators, visiting friends and families and other passenger profiles will be added to the framework to reflect better passenger-specific needs and goals of the multimodal systems in 2025, 2035 and 2050.

Acknowledgements

Project X-TEAM D2D has received funding from the SESAR Joint Undertaking with GA No 891061 under European Union's Horizon 2020 research and innovation program. The authors would like to express their gratitude to the Dutch Benelux Simulation Society (www.dutchBSS.org) and EUROSIM for disseminating the results of this work.

References

AGES. Eurovignette. The easy way to pay, 2021. URL https://www.ages.de/en/eurovignette.html.

Connexxion. Up-to-date travel information, 2021. URL https://www.connexxion.nl/en/travel-information/up-to-date-travel-information.

Electric Scooter Guide. Best electric scooters of 2021: according to science and exclusive data, 2021. URL https://electric-scooter.guide/best-rated/best-electric-scooters/.

Eurocities. Stories, 2021. URL https://eurocities.eu/stories/.

European Commission. Trans-European Transport Network (TEN-T), 2021. URL https://ec.europa.eu/transport/themes/infrastructure/ten-t_en.

European Commission. Cooperative, connected and automated mobility (CCAM), 2018. URL https://ec.europa.eu/info/law/better-regulation/have-your-say/initiatives/1957-Cooperative-connected-and-automated-mobility-CCAM-_en.

European Commission. A European green deal, 2020. URL https://ec.europa.eu/info/strategy/priorities-2019-2024/european-green-deal_en.

European Commission. Flightpath 2050. Europe's vision for aviation, 2011. doi: 10.2777/50266

EV Database. Top speed of full electric vehicles cheatsheet, 2021. URL https://ev-database.org/cheatsheet/top-speed-electric-car.

Inclusive Design Research Centre. What is Inclusive Design, 2021. URL https://legacy.idrc.ocadu.ca/about-the-idrc/49-resources/online-resources/articles-and-papers/443-whatisinclusivedesign.

Maria Kamargianni, Weibo Li, Melinda Matyas, and Andreas Schäfer. A Critical review of New Mobility Services for urban Transport. In *Transportation Research Procedia*, pages 3294–3303, 2016. doi: 10.1016/j.trpro.2016.05.277.

NV Nederlandse Spoorwegen. Travel information, 2021. URL https://www.ns.nl/en/travel-information.

NV Nederlandse Spoorwegen. Traveller behaviour, 2020. URL https://dashboards.nsjaarverslag.nl/reizigersgedrag/schiphol-airport.

Organisation for Economic Co-operation and Development, International Transport Forum. Leveraging digital technology and data for human-centric Smart Cities. The case of Smart Mobility, 2020.

James J. Pirkl. *Transgenerational design: products for an aging population*. Van Nostrand Reinhold. 1994.

United Nations, Department of Economic and Social Affairs, Population Division. World Population Prospects 2019: Highlights, 2019.

Formulation of Stochastic MPC to Balance Intermittent Solar Power with Hydro Power in Microgrid

Madhusudhan Pandey, Dietmar Winkler, Roshan Sharma, Bernt Lie*

TMCC, University of South-Eastern Norway, Bernt.Lie@usn.no

Abstract

In a microgrid with both intermittent and dispatchable generation, the intermittency caused by sources such as solar power and wind power can be balanced using dispatchable sources like hydro power. Both generation and consumption are stochastic in nature and require future prediction. The stochasticity of both generation and consumption will drift the grid frequency. Improved performance of the grid can be achieved if the operation of the microgrid is optimized over some horizon, for instance formulating Model Predictive Control (MPC), with the added problem that intermittent sources vary randomly into the future. In this paper, first, we have formulated a deterministic MPC and compared it with a PI controller. Second, a stochastic MPC (SMPC) based on a multi-objective optimization (MOO) scheme is presented. Results from deterministic MPC show that the overall performance of MPC is better than the PI controller for dispatching the required amount of hydro power into the grid and simultaneously constraining the grid frequency. Results from SMPC indicate that there exists a trade-off between the amount of water flow through the turbine and the rate of change of the turbine's valve while constraining the grid frequency.

Keywords: microgrid, load and generation balance, intermittent injection, dispatchable hydro power, frequency stability, stochastic MPC

1 Introduction

1.1 Background

The demand for electricity generation from renewable energy is increasing because of oil insecurity, climatic concern, and the nuclear power debate. Renewable energy consists of intermittent and dispatchable energy sources. Intermittent generation from sources such as solar power, wind power, and tidal power exhibit fluctuating power production and creates an imbalance between generation and load. However, renewable dispatchable sources such as hydro power plants play a significant role in balancing out the variability caused by intermittent sources.

For instance, in a microgrid supplying electrical power to a common consumer load with generation from intermittent solar power and a dispatchable hydro power plant, injection of intermittent solar power into the grid creates a fluctuation in grid frequency. Assuming that he grid frequency must be maintained at the range of $(50 \pm 5\%)$ Hz, it is of interest to dispatch the required amount of hydro power into the grid for balancing out the load and the generation while maintaining the grid frequency in that range.

However, the required amount of hydro power production can not be dispatched instantaneously. In reality, changes in hydro power production are constrained by inertia in water and rotating mass, and the need to avoid wear and tear in actuators and other equipment. Furthermore, both solar power and consumer load are not known perfectly. The solar power and consumer load intermittency cause power imbalance into the grid and drifting in grid frequency. Improved performance can be achieved if the operation of the microgrid is optimized over some horizon with the added problem that intermittent power varies randomly into the future. Optimal management of dynamic systems over a future horizon with disturbances is often posed as an MPC problem.

1.2 Previous Work

An MPC approach had been applied for controlling water flow into the turbine in (Zhou, 2017). The use of MPC with consideration of dynamical model of hydro power systems is presented in (Munoz-Hernandez et al., 2012). Simulation results with different operating conditions and disturbances from previous work emphasize the use of an MPC-based approach over the optimal PI controllers (Avramiotis-Falireas et al., 2013; Bhagdev et al., 2019; Reigstad and Uhlen, 2020). In a recent study of (Pandey et al., 2021) stochastic analysis of deterministic MPC for a dynamical model of microgrid was performed. It is of interest to further extend the work of (Pandey et al., 2021) with SMPC with the addition of comparison between a PI controller and deterministic MPC.

1.3 Outline of the Paper

Section 2 provides a system description. The mathematical model of the microgrid is detailed in Section 3. The implementation of a deterministic MPC and a stochastic MPC is given in Section 4 and Section 5, respectively. Section 6 provides results and discussions. Conclusions and future work are outlined in Section 7.

2 System Description

Consider a microgrid as in Figure 1 a) operated at consumer load P_ℓ and supplied with intermittent solar power

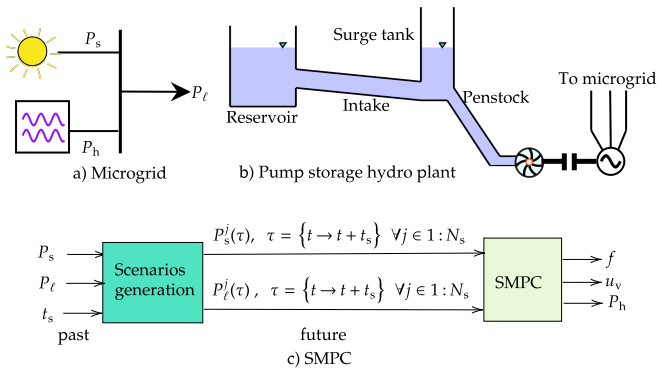

Figure 1. System description.

P_s. The difference between the intermittent generation and load is balanced with dispatchable hydro power P_h. Figure 1 b) shows the hydro power plant with reservoir, intake, surge tank, penstock, and turbine connected to the microgrid with an electrical generator. Figure 1 c) shows the N_s future scenarios generated in SMPC from the past data of P_s and P_ℓ. SMPC, as shown in the figure, keeps track of the constraint violation in grid frequency f for $50 \pm 5\%$ Hz and generates the turbine valve signal u_v and hydro power P_h dispatched into the grid based on the stochastic input from solar and consumer load.

3 Mathematical Model

3.1 Hydro Power Plant

The mathematical model for a hydro power plant shown in Figure 1 b) is taken from (Pandey et al., 2021) and given as

$$\frac{dh}{dt} = \frac{\dot{V}_s}{A_s} \tag{1}$$

$$\frac{d\dot{V}_s}{dt} = \frac{A_s}{\rho h}(p_n - p_a) - \frac{\pi D_s \dot{V}_s \mid \dot{V}_s \mid}{8A_s^2} f_{D,s} - gA_s \tag{2}$$

$$\frac{d\dot{V}_p}{dt} = \frac{A_p}{\rho L_p}(p_n - p_t) - \frac{\pi D_p \dot{V}_p \mid \dot{V}_p \mid}{8A_p^2} f_{D,p} + gA_p \frac{H_p}{L_p}, \tag{3}$$

with algebriac equations given by

$$p_t = p_a \left(1 + \left(\frac{\dot{V}_p}{C_v u_v}\right)^2\right) \tag{4}$$

$$\frac{d\dot{V}_i}{dt} = \frac{A_i}{\rho L_i}(p_a + \rho g H_r - p_n) - \frac{\pi D_i \dot{V}_i \mid \dot{V}_i \mid}{8A_i^2} f_{D,i} + gA_i \frac{H_i}{L_i} \tag{5}$$

$$\dot{V}_i = \dot{V}_s + \dot{V}_p \tag{6}$$

$$P_h = \eta_h (p_t - p_a) \dot{V}_p, \tag{7}$$

where the intake, the surge tank, and the penstock are subscripted with i, s and p, respectively. h is is the water level and $\dot{V}$ is the volumetric flow rate. Readers are requested to follow (Pandey et al., 2021) for notation.

3.2 Solar Power and Consumer Load

Solar power is calculated based on the solar irradiance k_I and given by

$$P_s = \eta_s A k_I \tag{8}$$

where η_s is the efficiency of a solar panel and A is the effective area of panels in the solar farm.

In contrast, the consumer load P_ℓ is modeled with the measurement data.

3.3 Grid

The grid is modeled with the *swing* equation given as

$$\frac{df}{dt} = \frac{P_m - P_e}{4\pi^2 f J} \tag{9}$$

where P_m is the mechanical power input into the microgrid with

$$P_m = P_h + P_s \tag{10}$$

and P_e is the electrical power load from the grid. The total inertia of the grid is represented by J.

3.4 Canonical Representation of the Model

The differential algebraic equations (DAEs) can be written in a canonical form of

$$\begin{aligned} \frac{dx}{dt} &= f(x,z,u,w;\theta) \\ 0 &= h(x,z,u,w;\theta) \\ y &= g(x,z,u,w,v;\theta), \end{aligned}$$

where x, z, u, and θ represents system states, algebraic variables, inputs, and parameters respectively. w is the process disturbances and v is the measurement noise. For the microgrid shown in Figure 1 a) represented by mathematical equations from Eqs. (1) to (10), we have

$$\begin{aligned} x &= \left(h, \dot{V}_s, \dot{V}_p, f\right) \\ z &= \left(p_t, p_n, \dot{V}_i, P_h, P_m\right) \\ u &= u_v \\ w &= P_s \\ \theta &= \left(H_j, L_j, D_j, A_j, H_r, \eta_h, C_v\right), \forall j = \{i,s,p\} \\ y &= P_e, \end{aligned} \tag{11}$$

where the intermittent solar power P_s is considered as process disturbance and all states are assumed to be measured.

3.5 Case Study

It is of interest to see how a 5 MW hydro power plant can be used for balancing a 4 MW rated consumer load supplied with solar power. Table 1 lists specifications for power plants containing rated information, geometrical dimensions and efficiencies.

Table 1. Specifications of the power plants.

Parameters	Symbols	Values
Hydro power plant:		
Rated power	$P_{\mathrm{h}}^{\mathrm{r}}$	5 MW
Nominal head, discharge, valve signal	$H^{\mathrm{n}}, \dot{V}^{\mathrm{n}}, u_{\mathrm{v}}^{\mathrm{n}}$	$120\,\mathrm{m}, 4\,\mathrm{m}^3/\mathrm{s}, 0.95$120 m, 44 m^3/s,0.95
Height difference of reservoir, intake, surge tank and penstock	$H_{\mathrm{r}}, H_{\mathrm{i}}, H_{\mathrm{s}}, H_{\mathrm{p}}$	$20\,\mathrm{m}, 20\,\mathrm{m}, 50\,\mathrm{m}, 70\,\mathrm{m}$
Length of intake, surge tank and penstock	$L_{\mathrm{i}}, L_{\mathrm{s}}, L_{\mathrm{p}}$	$1000\,\mathrm{m}, 50\,\mathrm{m}, 80\,\mathrm{m}$
Diameter of intake, surge tank and penstock	$D_{\mathrm{i}}, D_{\mathrm{s}}, D_{\mathrm{p}}$	$3\,\mathrm{m}, 2\,\mathrm{m}, 2\,\mathrm{m}$
Hydraulic efficiency of hydro turbine	η_{h}	0.96
Inertia of turbine-rotor	J_{h}	$1 \cdot 10^3\,\mathrm{kgm}^2$
Solar power plant:		
Rated power and irradiance	$P_{\mathrm{s}}^{\mathrm{r}}, k_{\mathrm{I}}^{\mathrm{r}}$	$2.5\,\mathrm{MW}, 600\,\mathrm{W}/\mathrm{m}^2$
Effective area of total panels	A	$25000\,\mathrm{m}^2$
Solar panel efficiency	η_{s}	0.14

4 Deterministic MPC

A deterministic MPC can be formulated assuming known inputs from solar power P_{s} and consumer load P_ℓ. We want to formulate a setpoint tracking problem for P_ℓ.

4.1 Cost Function

The chosen cost function for formulating optimal control problem (OCP) for the deterministic MPC is taken from (Pandey et al., 2021) given as

$$\min_{u_k} \; J_{\mathrm{d}} = \sum_{k=1}^{N_{\mathrm{p}}} (y_k - r_k)^2 + p \cdot \Delta u_{k-1}^2 \tag{12}$$

s.t.

$$\begin{aligned} x_{k+1} &= f(x_k, z_k, u_k, w_k; \theta) \\ 0 &= h(x_k, z_k, u_k, w_k; \theta) \\ y_k &= g(x_k, z_k, u_k, w_k, v_k; \theta) \\ x_\ell &\le x_k \le x_{\mathrm{h}} \\ u_\ell &\le u_k \le u_{\mathrm{h}} \\ \Delta u_\ell &\le \Delta u_k \le \Delta u_{\mathrm{h}}, \end{aligned}$$

where ℓ and h represents low and high bounds for states, inputs, and rate of change of inputs. N_{p} is the number of future samples in the prediction horizon where OCP is formulated. p is scalar weight for tuning the controller. r is the reference taken for consumer load power P_ℓ.

4.2 OCP Formulated in JuMP.jl

The internal structure of OCP is formulated in the Julia language[1] using JuMP.jl (Dunning et al., 2017), a Julia package for modeling mathematical optimization problems. JuMP provides an easy way of describing optimization problems containing linear and nonlinear constraints. JuMP also supports automatic differentiation (AD) using the package ForwardDiff.jl (Revels et al., 2016) which is a most useful property rarely supported by other modeling languages. Several open-source solvers are available for solving models described in JuMP. Our choice of JuMP solver is Ipopt[2]. We have represented the plant by a Modelica model, and the controller model is implemented in Julia. These interact via OMJulia[3]. OMJulia is an OpenModelica-Julia interface providing application programming interfaces (APIs) for advanced model analysis in Julia.

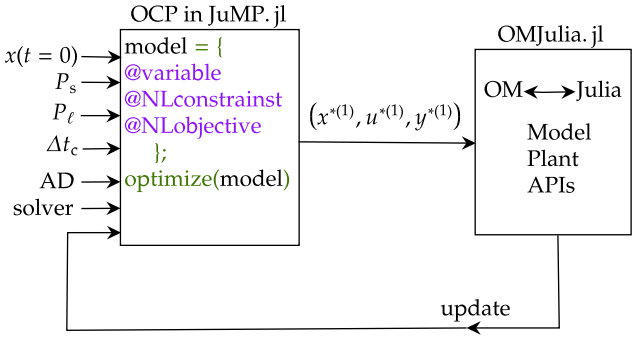

Figure 2. OCP formulated for deterministic MPC in JuMP.jl.

Figure 2 shows the internal structure of OCP formulated in JuMP.jl for deterministic MPC. In the figure, $\left(x^{*(1)}, u^{*(1)}, y^{*(1)}\right)$ represents first optimal values of states, control inputs and control outputs from OCP. We have assumed that all the states are known. These optimal control inputs are then applied to the emulated real plant developed in OpenModelica[4]. Similarly, both the optimal states and the control inputs are applied to the mathematical model. The states, inputs, and outputs are accessed through OMJulia APIs for further iteration.

[1] https://julialang.org/

[2] https://github.com/jump-dev/Ipopt.jl

[3] https://github.com/OpenModelica/OMJulia.jl

[4] https://www.openmodelica.org/

5 Stochastic MPC

Several stochastic MPC algorithms can be used for handling uncertainty in the system (Camacho and Bordons, 2016). A comparative study on stochastic MPC is given in (González et al., 2020). Comparison of the different stochastic MPC algorithms are out of the scope of this paper. In this paper, more focus is on the implementation of the dynamic formulation of the microgrid with stochastic solar power and load power. We have chosen multi-objective optimization (MOO) based stochastic MPC with similar formulation from the previous work our institution (Menchacatorre et al., 2020) as it is easier to formulate and have a quick analysis. In MOO-based stochastic MPC, we create scenarios of random disturbances; and in our case the random disturbances are P_s and P_ℓ. Each scenario is then assigned with an objective function or a constraint. When each of the objective functions is summed together by assigning weights to each of the objectives, a single objective function is created which is called a weighted-sum MOO.

5.1 Cost Function

The MOO based cost function for N_s number of stochastic scenarios for P_s and P_ℓ is given as

$$\min_{u_k} \; J_\mathrm{s} = \sum_{s=1}^{N_\mathrm{s}} \left(\sum_{k=1}^{N_\mathrm{p}} (y_k^s - r_k^s)^2 + p \cdot \Delta u_{k-1}^2 \right) \tag{13}$$

s.t.

$$\begin{aligned} x_{k+1}^s &= f(x_k^s, z_k^s, u_k, w_k^s; \theta) \\ 0 &= h(x_k^s, z_k^s, u_k, w_k^s; \theta) \\ y_k &= g(x_k^s, z_k^s, u_k, w_k^s, v_k^s; \theta) \\ x_\ell &\le x_k^s \le x_\mathrm{h} \\ u_\ell &\le u_k \le u_\mathrm{h} \\ \Delta u_\ell &\le \Delta u_k \le \Delta u_\mathrm{h}, \end{aligned}$$

where we have considered each of the scenarios to be equally important; thus the total objective is formulated summing objective function of each of the scenarios. This cost function is used for formulating OCP for stochastic MPC. A stochastic MPC is formulated by solving OCP for each iteration considering N_p number of future samples in the prediction horizon.

5.2 Stochastic Scenarios for P_s and P_ℓ

Real measurement for solar irradiance is taken for Kjølnes Ring 56, Campus Porsgrunn, University of South-Eastern Norway, 9.6714 longitudes and 59.13814 latitudes from www.solcast.com. The measurement data is updated at every 5 min throughout the day. The real measurement for consumer load is taken for monthly hourly averaged load for Norway from ENTOS-E[5]. The magnitude of measurement data for electrical demand is modified as per our case study with a microgrid with a power capacity of 5 MW keeping the load dynamics preserved in hourly data. Furthermore, the hourly sampled data is interpolated for creating consumer load with a sampling of 5 min.

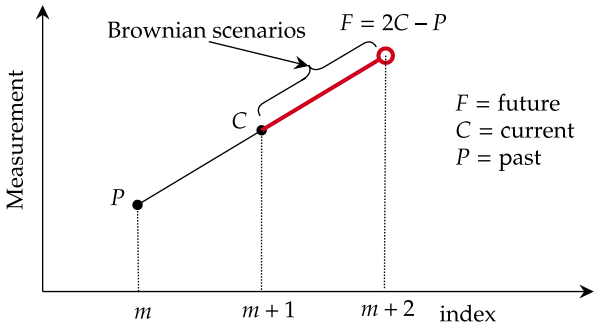

Figure 3. Scenarios generation based on the past measurement.

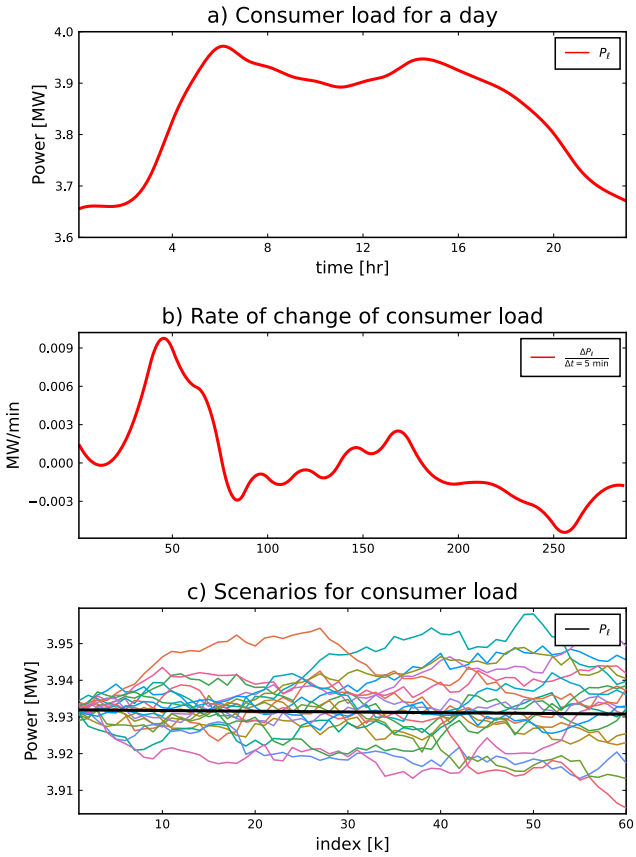

Figure 4. Scenarios generation for P_ℓ.

Between each of the measurements, scenarios are generated using a stochastic evolution equation considering a *Brownian* motion[6]. The stochastic evolution equation based on the Brownian motion is used as a *generatrix* and a straight line between the two measurements is used as a *directrix*.

Figure 3 shows the method for generating future scenarios based on the past and current measurements sampled

[5] https://www.entsoe.eu/data/power-stats/

[6] https://en.wikipedia.org/wiki/Brownian_motion

at 5 min. In the figure, the future measurement F is predicted from past measurement P and current measurement C. Assuming measurement P, C and F are co-linear we have

$$\frac{F-C}{(m+2)-(m+1)} = \frac{C-P}{(m+1)-m},$$

which gives

$$F = 2C - P.$$

The stochastic scenarios are then creating using Brownian motion between current measurement C and future prediction F.

Figure 4 a) shows consumer load on a typical day with measurement data taken at 5 min. Figure 4 b) shows rate of change of consumer load for $\Delta t \to 5$ min where the data points within a day consist of 288 data points and represented as $P_\ell = \{P_\ell[m] \ \forall m \in 1:288\}$. The figure shows that the bound for $\frac{\Delta P_\ell}{\Delta t = 5\,\text{min}}$ lies in $[-0.002, 0.009]$. The standard deviation for Brownian motion for creating scenarios is then set to > 0.011. Figure 4 c) shows the future predicted P_ℓ from the past measurement P and current measurement C considering co-linear existence between P, C and F as shown in Figure 3. For P_ℓ in Figure 4 b) we have assumed that $P = P_\ell[99]$, $C = P_\ell[100]$ and $F = P_\ell[101]$. Figure 4 c) shows 20 scenarios generated using Brownian motion. The same procedure is applied for predicting P_s as shown in Figure 5 where the standard deviation for Brownian motion is set to > 0.3 which is comparatively larger than in case of consumer load scenarios generation. The standard deviation in scenarios is much higher in case of prediction of P_s because of the clouds. A more rigorous algorithm for predicting scenarios of P_s depends on the information of clouds injected into the prediction algorithms. Since we have only focused on formulation of stochastic MPC, we neglected the part of considering cloud information while generating scenarios for P_s.

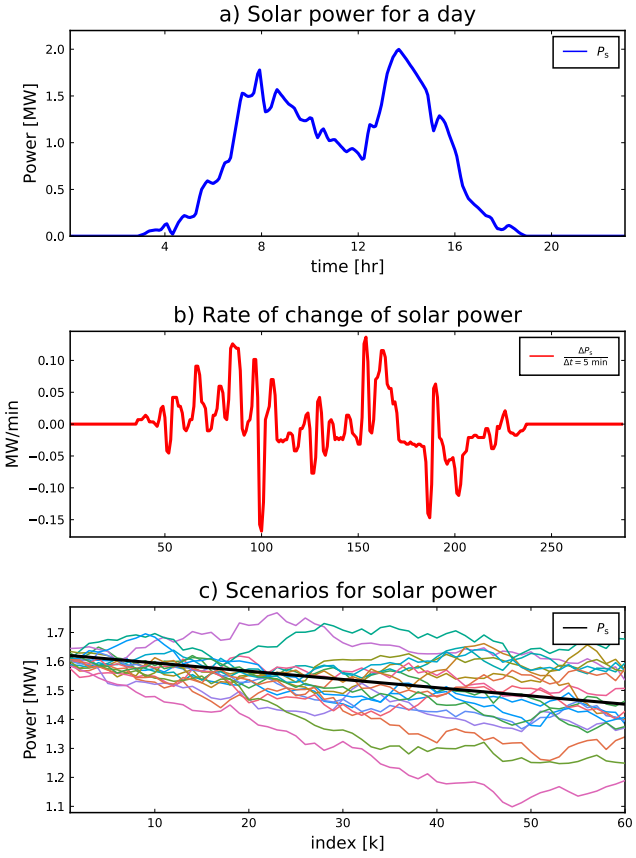

Figure 5. Scenarios generation for P_s.

5.3 Stochastic OCP

We have considered the prediction horizon of $N_p = 10$. The discretization time of the controller for SMPC is chosen to be $\Delta t = 5$ s based on our previous work for a microgrid with around 5 MW (Pandey et al., 2021). For moving along the stochastic prediction horizon of P_s and P_ℓ, the states and the outputs are updated taking the mean of the first value of each of the scenarios of states and outputs from the stochastic OCP.

6 Results and Discussions

6.1 Deterministic MPC

Figure 6 shows setpoint tracking formulation of consumer load P_ℓ using both deterministic MPC and a PI controller. The MPC is characterized by tuning parameter $p = 0.1$, $N_p = 5$ and $\Delta t = 1$ s. Similarly, the PI controller is characterized with $K_p = 0.05$ and $T_i = 3$ s. The initial tuning of the PI controller is based on the SIMC method (Skogestad, 2001) and the final tuning was performed manually. The setpoint tracking of P_ℓ using the PI controller is performed using OpenHPL in OpenModelica while the MPC is formulated as in Figure 2 in conjunction with real plant considering from OpenHPL and the control model is formulated in Julia. The control model is discretized using Euler discretization.

Figure 6 a) shows the setpoint tracking using both MPC and PI controller. A step change in P_ℓ is performed at time =25 s while a step change in P_s is performed at time =50 s. Figure 6 b) shows the hydro power dispatched into the grid from both the MPC and the PI controller. The control input, turbine valve signal u_v, for controlling the flow rate through the penstock for balancing the load and the generation is shown in Figure 6 c). Similarly, Figure 6 d) shows the grid frequency f of the microgrid. In Figure 6 c) we see that u_v in case of the MPC is smoother and less fluctuating than u_v in case of the PI controller. Furthermore, since an MPC works based on the future horizon, in Figure 6 c) the turbine valve signal u_v in case of the MPC is increased from 0.4 to 0.6 at time ≈23 s keeping the constraint in grid frequency for $f \approx 50$ Hz (small deviation not shown in the figure). Contrary to the performance of the MPC, from the figure the turbine valve signal is increased exactly at time =25 s while the grid frequency f fluctuates from 50 Hz to 47.5 Hz. The PI controller is able to regain

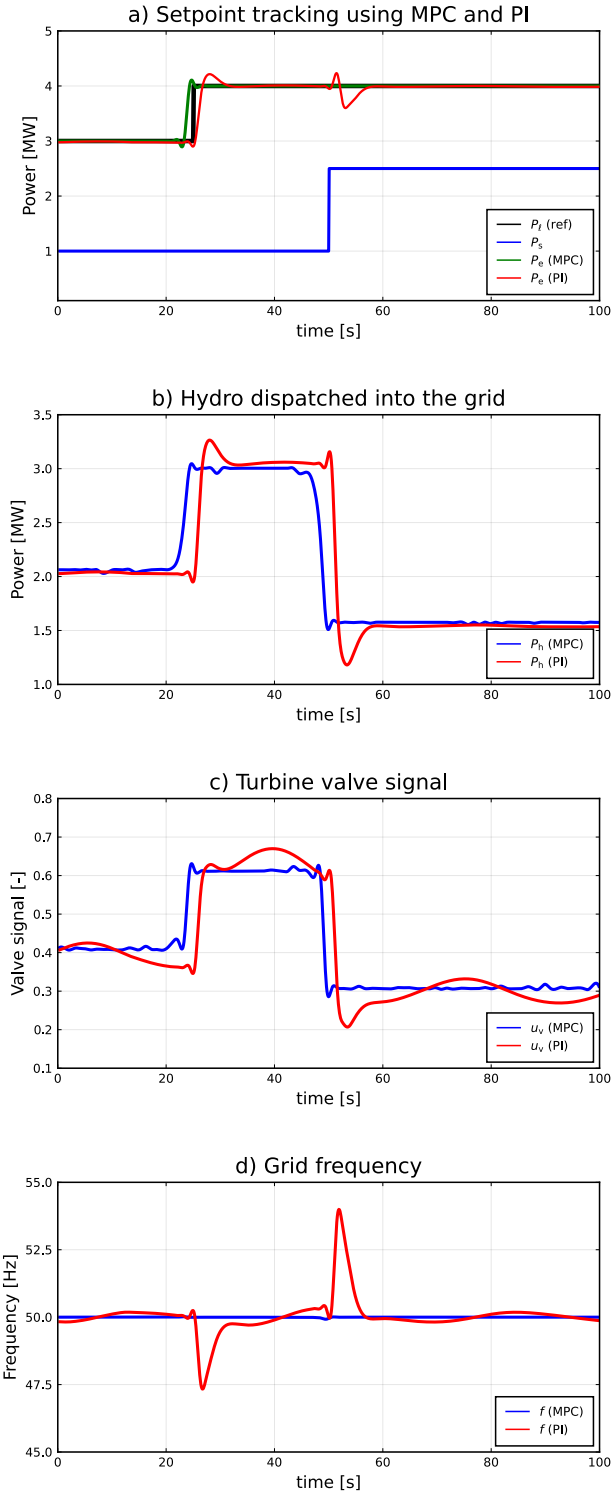

Figure 6. Setpoint tracking using deterministic MPC and PI controller.

the grid frequency around 50 Hz after ≈ 5 s. Similar, results can be seen in the case of hydro power P_h dispatched into the grid and the electrical power P_e. The similar dynamics of P_ℓ and P_e with u_v in case of both the MPC and the PI controller can be related from Equations (4), (7), and (9). Overall, the performance of the MPC is better than that of the PI controller.

6.2 Stochastic MPC

Figure 7 shows the tracking of the future predicted consumer load P_ℓ based on the future prediction of solar power P_s into the grid where both future predicted P_ℓ and P_s are taken from Section 5.2. The MOO based stochastic MPC is characterized by $N_p = 10$, $N_s = 20$, $p = 0.1$ and $\Delta t = 5$ s. The next scenarios for P_ℓ and P_s are updated every 5 min $= 300$ s using the current measurement C and the past measurement P as shown in Figure 3.

Figure 7 a) shows the turbine valve signal u_v generated for each of the scenarios considering a deterministic MPC. The results for u_v from the deterministic MPC for each of the scenarios are considered as an ensemble of trajectories for u_v. In the figure, $u_v\,(\mathrm{MOO})$ is the results from the stochastic MPC based on MOO in tandem with the ensemble of results from deterministic MPC for each of the scenarios. The fluctuation in the grid frequency is negligible as in the range of $1 \cdot 10^{-4}$ rad/s for both the deterministic and stochastic case as shown in Figure 7 f). Figure 7 b), c), d) and e) show the results from both the deterministic and stochastic case for hydro dispatched P_h, electrical power into the grid P_e, flowrate into the penstock $\dot{V}_p$, and the water mass oscillation inside the surge tank h, respectively.

7 Conclusions and Future Work

In this paper formulation of a deterministic and a stochastic MPC is performed for a microgrid supplied with intermittent solar power and dispatchable hydro power for constraining the grid frequency at $f = 50$ Hz. A deterministic MPC is compared with a PI controller. Furthermore, for the stochastic MPC, the scenarios for solar power and the consumer load are predicted using Brownian motion using past and current measurement data. A MOO-based stochastic MPC is implemented.

Results indicate that the deterministic MPC performs better for constraining the grid frequency of the microgrid at $f = 50$ Hz than to the PI controller. The stochastic MPC based on MOO shows better result than deterministic MPC while constraining the grid frequency.

Future work includes the implementation of stochastic MPC with scenario generation for solar power with the inclusion of cloud factors.

References

Iason Avramiotis-Falireas, Athanasios Troupakis, Farzaneh Abbaspourtorbati, and Marek Zima. An MPC strategy for automatic generation control with consideration of deterministic power imbalances. In *2013 IREP Symposium Bulk Power System Dynamics and Control-IX Optimization, Security and Control of the Emerging Power Grid*, pages 1–8. IEEE, 2013. doi:10.1109/IREP.2013.6629359.

Dishant Bhagdev, Rajasi Mandal, and Kalyan Chatterjee. Study and application of mpc for agc of two area interconnected thermal-hydro-wind system. In *2019 Innova-*

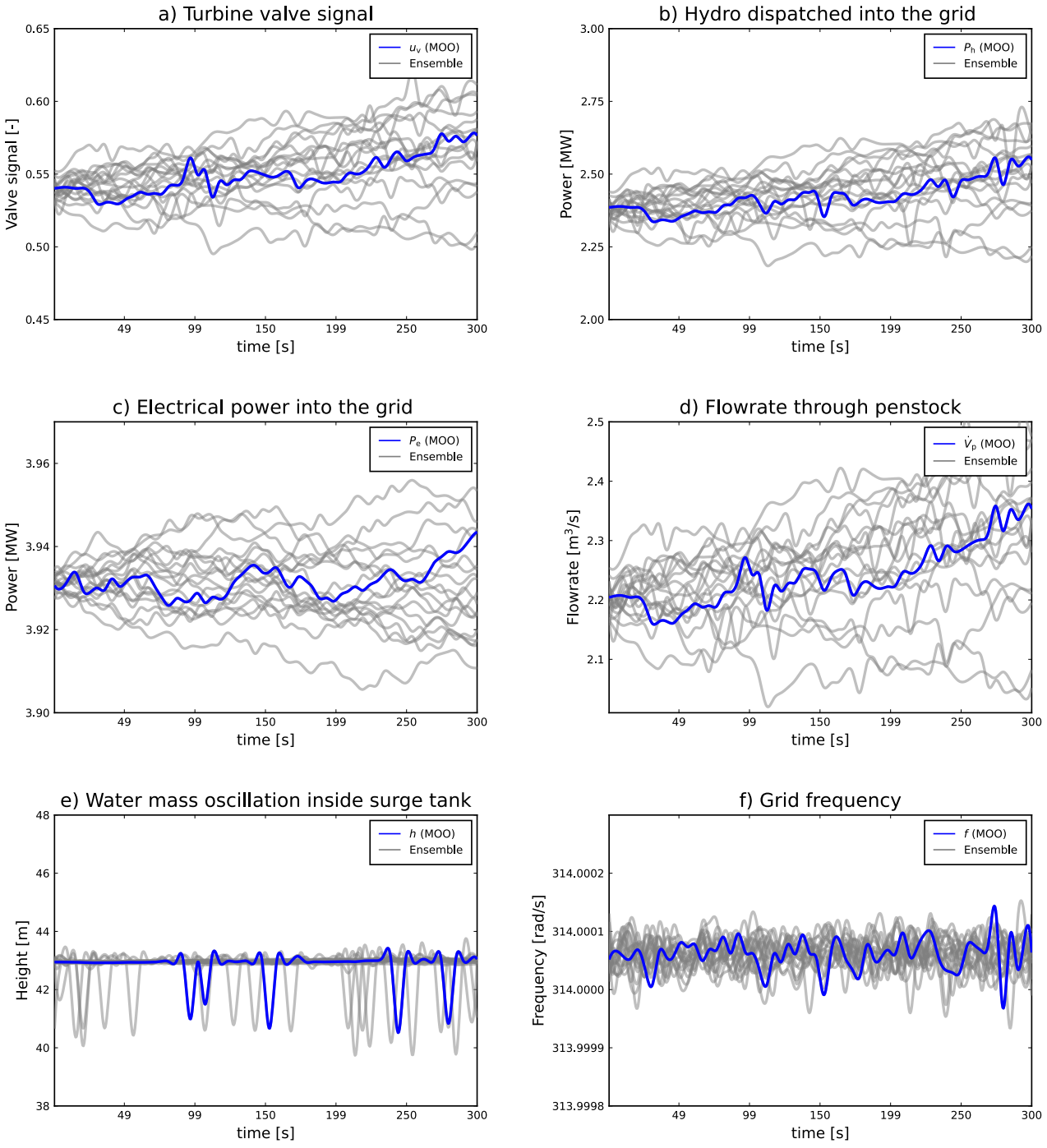

Figure 7. Deterministic and stochastic comparison for scenarios generated for P_s and P_ℓ in Section 5.2.

tions in Power and Advanced Computing Technologies (i-PACT), volume 1, pages 1–6. IEEE, 2019. doi:10.1109/i-PACT44901.2019.8960124.

Eduardo F Camacho and Carlos Bordons. *Model predictive control: Classical, robust and stochastic*. Springer International Publishing, 2016.

Iain Dunning, Joey Huchette, and Miles Lubin. Jump: A modeling language for mathematical optimization. *SIAM Review*, 59(2):295–320, 2017. doi:10.1137/15M1020575.

Edwin González, Javier Sanchis, Sergio García-Nieto, and José Salcedo. A comparative study of stochastic model predictive controllers. *Electronics*, 9(12):2078, 2020. doi:10.3390/electronics9122078.

Itsaso Menchacatorre, Roshan Sharma, Beathe Furenes, and Bernt Lie. Flood Management of Lake Toke: MPC Operation under Uncertainty. In *Proceedings of The 60th SIMS Conference on Simulation and Modelling SIMS 2019, August 12-16, Västerås, Sweden*, number 170, pages 9–16. Linköping University Electronic Press, 2020. doi:10.3384/ecp201709.

German Ardul Munoz-Hernandez, Dewi Ieuan Jones, et al. *Modelling and controlling hydropower plants*. Springer Science & Business Media, 2012. doi:10.1007/978-1-4471-2291-3.

Madhusudhan Pandey, Dietmar Winkler, Roshan Sharma, and Bernt Lie. Using MPC to Balance Intermittent Wind and Solar Power with Hydro Power in Microgrids. *Energies*, 14(4): 874, 2021. doi:10.3390/en14040874.

Tor Inge Reigstad and Kjetil Uhlen. Optimized control of variable speed hydropower for provision of fast frequency reserves. *Electric Power Systems Research*, 189:106668, 2020. doi:10.1016/j.epsr.2020.106668.

J. Revels, M. Lubin, and T. Papamarkou. Forward-mode automatic differentiation in Julia. *arXiv:1607.07892 [cs.MS]*, 2016. URL `https://arxiv.org/abs/1607.07892`.

Sigurd Skogestad. Probably the best simple pid tuning rules in the world. In *AIChE Annual Meeting, Reno, Nevada*, volume 77, 2001. URL `https://folk.ntnu.no/skoge/publications/2003/tuningPID/more/old-original_rejected_version_from_July01/tuningpaper.pdf`.

Wenjing Zhou. Modeling, Control and Optimization of a Hydropower Plant. 2017. Doctoral dissertations at the University College of Southeast Norway;33.

Droop Control of Hydro Power System in OpenHPL

Madhusudhan Pandey, Roshan Sharma, Bernt Lie*

TMCC, University of South-Eastern Norway, Bernt.Lie@usn.no

Abstract

OpenHPL is an open-source hydro power library for modeling, design, and analysis. Currently, OpenHPL consists of mechanistic models for waterways from a reservoir to tailrace, Francis and Pelton turbine models, a simple generator model, hydro power speed governor model, etc. However, the library lacks a *controller* for the parallel operation of hydro powers. This paper mainly focuses on extending OpenHPL with power-frequency droop control for a multi-generator system. Two simulation case studies are carried out for the parallel operation of hydro power units.

Keywords: Parallel operation of hydro powers, multi-generator system, Droop control, OpenHPL

1 Introduction

1.1 Background

Electricity generation from renewable sources is increasing because of oil insecurity, climatic concern, and the nuclear power debate. Renewable energy is a combination of intermittent and dispatchable energy sources. Intermittent sources like solar, wind, and tidal power plants exhibit fluctuating power production that creates an imbalance between generation and load. In this regard, renewable dispatchable sources like hydro power plants play a significant role in balancing out the variability caused by intermittent sources. Current hydro power modeling, design, and analysis tools are free or available commercially. Freely available tools include CASiMiR-Hydropower[1], LVTrans[2], and OpenHPL[3], while commercial tools include Alab[4] and Modelon Hydro Power Library (HPL)[5]. This drives a motivation for an open-source hydro power library development for modeling, design, and analysis.

A mechanistic model of hydropower systems had been developed in (Splavska et al., 2017) using mass and momentum balances which leads to a Modelica[6] based open-source hydropower library OpenHPL, and was initiated in a PhD study (Vytvytskyi, 2019). OpenHPL is under development at the University of South-Eastern Norway. Currently, OpenHPL has units for the flow of water in filled pipes (inelastic and elastic walls, incompressible and compressible water) (Vytvytsky and Lie, 2017), a mechanistic model of a Francis turbine (including design of turbine parameters) (Vytvytskyi and Lie, 2018), etc. The library is further extended with mechanistic models of different kinds of surge tanks and draft tubes (Pandey and Lie, 2020, Submitted). In addition, some accompanying work on analysis tools has been developed in scripting languages (Python, Julia) related to state estimation, structural analysis, etc (Vytvytskyi and Lie, 2019). The library has been tested on real power plant data (Pandey and Lie, 2020). The library can be interfaced with other Modelica libraries, for example, OpenIPSL[7] for generator and grid, PhotoVoltaics[8] for solar power plants, and WindPowerPlants[9] for wind power plants as in (Pandey et al., 2021; Pandey and Lie, 2020). However, the library lacks hydro power controllers for parallel operation of hydro power and load frequency control in an interconnected power system network.

In this regard, it is of interest to extend OpenHPL with hydro power controller models. This paper mainly focuses on developing a droop control mechanism applied for the parallel operation of hydro turbine generating units in OpenHPL.

1.2 Outline of the Paper

Section 2 presents a speed governing mechanism in a hydro power plant. Section 3 provides the concept of droop control in the parallel operation of hydro power plants. The implementation of droop control is tested via case-studies in Section 4. Finally, conclusions and future work are presented in Section 5.

2 Speed Governor for Single Hydro Power Plant

2.1 Governing mechanism

Figure 1 a) shows the speed governing mechanism in a hydro power plant. In the figure, T is the turbine, G is the generator and P_g is the generated power from the T-G aggregate which is supplied to cover the consumer load P_ℓ. When there is a difference in power generation and consumer load, the volumetric discharge $\dot{V}$ through the turbine is controlled which in turn controls the generation

[1] http://www.casimir-software.de/save_download.php?language=2

[2] http://svingentech.no/about%20lvtrans.html

[3] https://github.com/simulatino/OpenHPL

[4] http://www.alab.no/Alab-Hydropower-Software/Functionality-Alab-Hydropower-Software/Operation-simulation-with-waterway

[5] https://www.modelon.com/library/hydro-power-library/

[6] https://www.modelica.org/

[7] https://github.com/OpenIPSL/OpenIPSL

[8] https://github.com/christiankral/PhotoVoltaics

[9] https://github.com/christiankral/WindPowerPlants

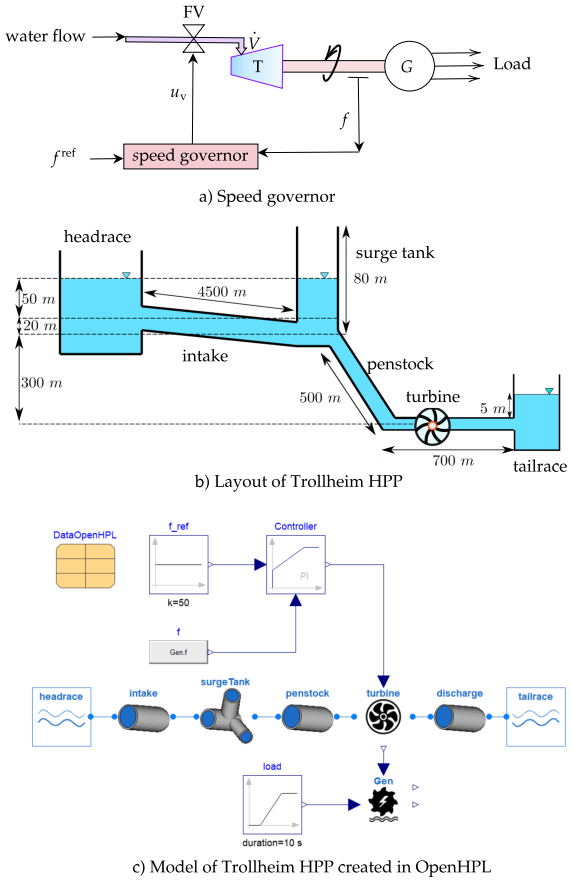

Figure 1. Speed governing in a hydro power system.

from the generator. To achieve this generation control, the shaft speed $\omega = 2\pi f$ of the T-G aggregate system is compared with the reference speed $\omega^{\text{ref}} = 2\pi f^{\text{ref}}$ by the speed governing system to generate a valve signal u_{v} for controlling the flow valve FV. It is of interest to design a speed governing system using a PI-controller in OpenHPL using a case study of a real hydro power plant.

2.2 Trollheim Hydro Power Plant

Figure 1 b) shows the layout of Trollheim hydro power plant (HPP) in Norway, with nominal power output 130 MW, nominal discharge rate 40 m/s^2, and nominal rated speed 380 rpm. The diameter of the intake tunnel is 7 m, and the diameter of both the surge tank and the penstock is 4 m. Figure 1 c) shows the model of Trollheim HPP created in OpenHPL. Models in OpenHPL are created simply by "dragging and dropping" hydro power units, and then connecting them together from the outlet of one unit to the inlet of another unit as in the case of the surge tank and the penstock shown in the figure. In Figure 1 c) a controller is used to maintain the frequency of T-G aggregate to $f^{\text{ref}} = 50$ Hz while controlling the flow through the turbine to balance the generation and the load. The controller is a PI controller taken from the built-in Modelica Standard Libraryand is characterized by a proportionality gain K_{p} and an integral time constant T_{i}.

2.3 Tuning of PI Controller

The PI controller is tuned based on the SMIC-PI tuning rule (Skogestad, 2001). In the SMIC-PI tuning method, a process is considered as a first-order system plus delay with a generalized transfer function as

$$G(s) = \frac{k}{\tau s + 1} e^{-\theta s}. \tag{1}$$

Controller parameters K_{p} and T_{i} are selected as

$$K_{\text{p}} = \frac{1}{k}\left(\frac{\tau}{\tau_{\text{c}} + \theta}\right) \tag{2}$$

$$T_{\text{i}} = \min\left(\tau, 4\left(\tau_{\text{c}} + \theta\right)\right) \tag{3}$$

where τ_{c} is considered as the tuning parameter and acts as a trade-off between (i) a fast controller response, and (ii) stability, robustness, and small input usage. For a reasonable response with good robustness we set $\tau_{\text{c}} = \theta$. In addition, the controller response becomes faster as the value of τ_{c} is decreased, and slower/smoother as the value of τ_{c} is increased.

2.4 Step Change in Load Power P_ℓ

Figure 2 shows the step responses from the PI controller for Trollheim HPP. The PI controller is specified by $K_{\text{p}} = 0.2$ and $T_{\text{i}} = 5$. Figure 2 shows the respective generated power P_{g} from the hydro power plant to balance the consumer load P_ℓ. Figure 2 also shows the turbine valve signal for controlling the water flow through the turbine to balance the load and the generation while maintaining the system frequency at 50 Hz.

3 Control of Multiple Hydro Power Plants

3.1 Problem Description

Next, consider operation of multiple hydro power plants connected to the same grid as shown in Figure 3 a), with generator i supplying power $P_{\text{g},i}$ to a common consumer load P_ℓ. For each of the T-G aggregates, what happens if we use the same speed governing mechanism as in Figure 1 a)? The grid frequency is determined by the "swing equation", essentially

$$J_{\text{eq}} \frac{d\omega}{dt} = \frac{1}{\omega}\left(\sum_i P_{\text{g},i} - P_\ell\right) \tag{4}$$

where ω is the common electric grid angular velocity related to frequency f by $\omega = 2\pi f$, and J_{eq} is the equivalent moment of inertia of all generators, referred to the electric grid frequency. If we use PI controllers as in Section 2, we essentially try to specify a single variable (f or ω) by changing many guide vane openings, one for each generator. This implies that we have many more unknowns (guide vane openings) than equations (specifying f or ω),and there is no unique solution. In practice, using

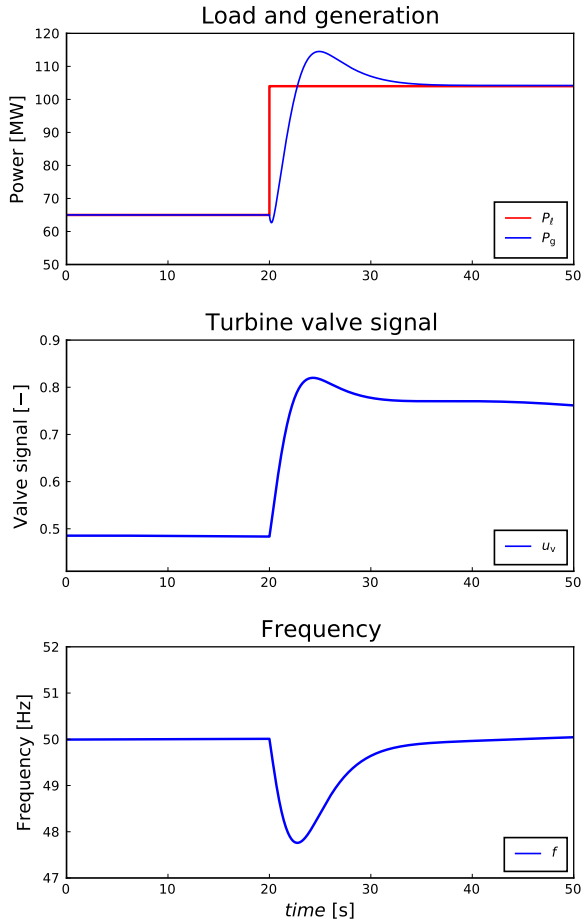

Figure 2. Step response from the PI controller for Trollheim HPP. a) Step change in load power P_ℓ from 50% loading to 80% loading and the corresponding generation P_g from the hydro turbine, b) turbine valve signal u_v, and c) frequency f of the plant.

one PI controller per generator will lead to wildly oscillating control outputs, and the system will break down

(Schavemaker and Van der Sluis, 2017). In summary, we can only use one PI controller when controlling a single variable (the grid frequency). Thus a different strategy is needed for multiple generators.

In practice, the Transmission System Operator (TSO) makes a prediction of the next-day power consumption, P_ℓ^{ref}. In a competitive power market, power producers make a bidding on amount of power produced at a suggested price, and the TSO allots a share $P_{\ell,i}^{\text{ref}}$ of the predicted power load to generator i (alternatively: to a power area i) such that $P_\ell^{\text{ref}} = \sum_i P_{\ell,i}^{\text{ref}}$.

The *real* next-day power load P_ℓ will differ from the predicted/reference power load P_ℓ^{ref} leading to a frequency f which differs from the reference frequency f^{ref} (typically 50 Hz or 60 Hz), and a mechanism is needed to distribute the difference $P_\ell - P_\ell^{\text{ref}}$ among all the generators in a way which takes into account their capacity and drives f towards f^{ref}. This distribution of the difference is commonly done using a *droop control mechanism* as illustrated in Figure 3 a). The droop control mechanism can be

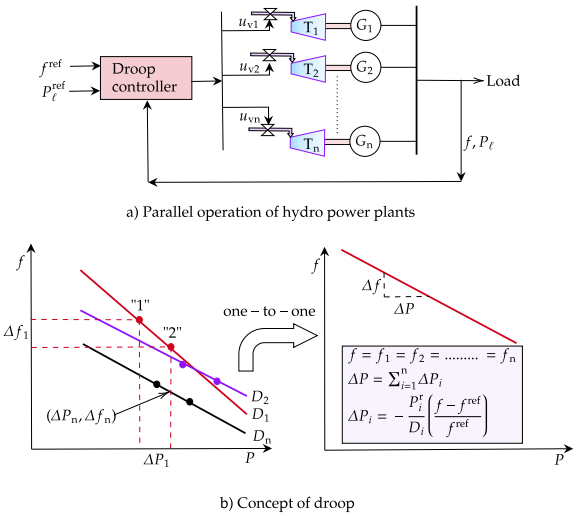

Figure 3. Concept of droop control for parallel operation of hydro power plants.

applied in diverse filed of engineering. Typical examples include the use of droop control in microgrid (Pota, 2013), inverters (Zhong and Zeng, 2016), oil and gas (Sharma et al., 2011), etc. The load power P_ℓ and the grid frequency f are compared with the reference load power P_ℓ^{ref} and the reference frequency f^{ref} . The droop controller makes a *one-to-one* power-frequency relation as in Figure 3 b) and distributes the proportioned signal to each of the generators' controller to restore the grid frequency. The droop controller operates based on the droop characteristics of each of the generators.

3.2 Concept of Droop Control

Figure 3b) shows the concept of the droop power-frequency control in a hydro power system. A droop is a slope of two independent variables in a dynamical system. For instance, the slope between the consumer P_ℓ and the frequency of the system f in a hydro turbine-generator power system can be represented by a power-frequency droop. When there is a sudden change of a consumer load there is a change in the system frequency. When the consumer load is greater than the generation, the system frequency decreases, and vice-versa. The droop D in case of power-frequency relation is expressed, thus, with the negative slope and defined as,

$$D = -\frac{\Delta f / f^{\text{ref}}}{\Delta P / P^{\text{r}}} \tag{5}$$

where f^{ref} and P^{r} are the reference frequency (normally taken as 50 Hz or 60 Hz depending on the power system network) and the rated power for the hydro power system, respectively. Δf is the change in frequency for the change in generation and load represented by ΔP. The values of the droop for a typical hydro power system are set in the range of $(2\% - 6\%)$.

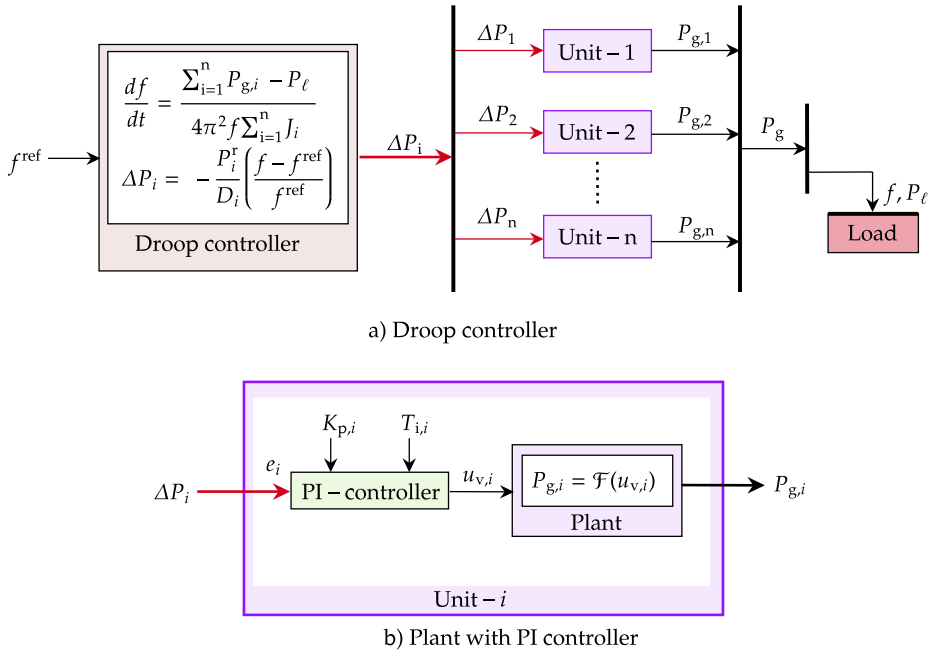

Figure 4. a) Internal structure of a droop controller b) Error from droop controller for the plant with PI-controller.

Figure 3b) shows the power-frequency characteristics or the droop characteristics for the operation of a multi-generator systems. The operation of the plant with droop characteristics D_1 at position "1" is shifted to position "2" when the consumer load changes suddenly by ΔP_1 with a drop in frequency Δf_1; and so on for the other systems with droop characteristics $D_2, D_3, ...D_n$. The relationship between droop characteristics of each of the parallelly ran multi-generator systems is transferred into one-to-one $P-f$ relation. In the figure, ΔP is the overall difference in the generation and the load which is distributed to each of the generators for restoring f from the droop controller. The generation to be increased by the i^{th} generator to cope with the total variation ΔP in the multi-generator system, is given as,

$$\Delta P_i = -\frac{P_i^r}{D_i}\left(\frac{f - f^{ref}}{f^{ref}}\right). \tag{6}$$

3.3 Internal Structure of Droop Controller

Figure 4 a) shows the internal structure of a droop controller. The grid frequency f is calculated based on the measurement available for the generation $P_{g,i}$ and the load P_ℓ using the swing equation. For each of the generators, based on the droop D_i, power rating P_i^r and the grid frequency f, an error signal ΔP_i is generated for the PI controller of the generator which is used to change the guide vane opening of the hydro turbine as shown in Figure 4 b) which drives the grid frequency f towards f^{ref}.

Table 1. Parallel operation of two turbines for Trollheim HPP.

Units	P^r	D	K_p	T_i
Unit-1	65 MW	4%	0.03	3
Unit-2	65 MW	5%	0.03	3

4 Case Studies

4.1 Case Study-1

We now consider Trollheim HPP with two hydro turbine units operating in parallel for supplying to a common consumer load P_ℓ. The droop, rated power, and values of K_p and T_i are given in Table 1.

Figure 5 a) shows the total load and the generation from the hydro power units. In the figure, at time $= 30$ s load is increased from 65 MW to 90 MW. To compensate the increase in 25 MW load, according to Eq. (6), Unit-1 should produce $\frac{D_2}{D_1+D_2}\Delta P = \frac{5}{4+5} \cdot 25 \approx 14$ MW and Unit-2 should then produce ≈ 11 MW as shown in the figure. As the generating Unit-1 has a lower droop than Unit-2, Unit-1 will add more power into the grid according to Eq. (6). Figure 5 b) shows the turbine valve signal for both the hydro power units. Figure 5c) shows the grid frequency and frequencies of both synchronous generating units. As the consumer load increases, the grid frequency of the system decreases and to compensate for the increased power both flow in the turbine units should be increased which will accelerate the generators of Unit-1 and Unit-2. The frequency of generators and the grid will be the same after the steady-state condition is reached.

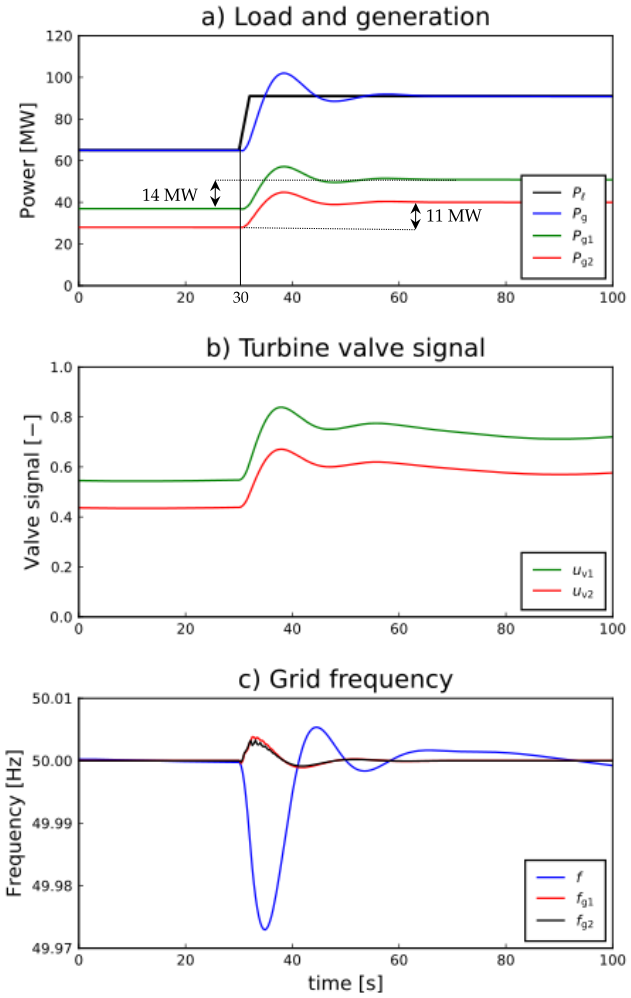

Figure 5. Droop control for parallel operation of two hydro units for Trollheim HPP.

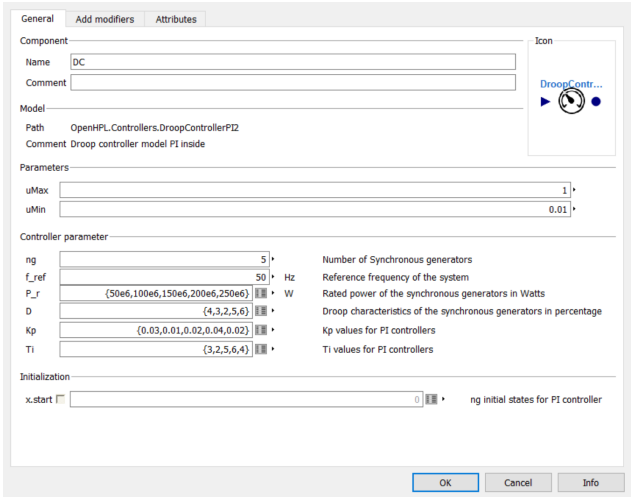

a) Parameters for droop control in OpenHPL

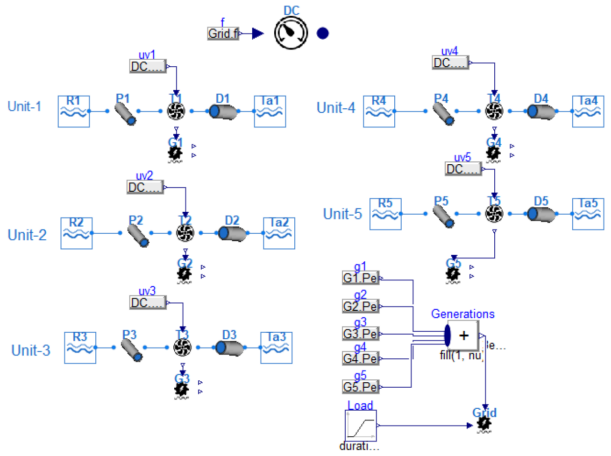

b) Models of parallel operation of five hydro power plants in OpenHPL with droop control

Figure 6. Droop control in OpenHPL.

4.2 Case Study-2

We now consider models of five hydro power plants operating in parallel to supply a common consumer load as shown in Figure 6 b). Figure 6 a) shows the initialization and droop controller parameter GUI in OpenHPL. For the icon shown in the top-right of the figure, the input to the controller is the grid frequency f and output from the controller is the turbine valve signal u_{v}. To initialize the droop control for n number of synchronous generators, rated power P^{r}, droop D, K_{p} and T_{i} values for PI-controller for each of the turbine-generator plant should be given as in Figure 6 a). For the purpose of the case study, P^{r}, D, and K_{p} and T_{i} values for the PI-controller for five hydro power plants are given in Table 2.

Figure 7 a) shows the generation and load in the case of five hydro power plants operating in parallel. Figure 7 b) shows the respective generation from each of the hydro power units supplying to balance the difference in the load and the generation. The generation from each of the hydro power units are distributed based on their power rating and droop characteristics. In the figure, Unit-1 has the least contribution and Unit-4 has the highest contribution to balance the generation and the load. Figure 7 c) shows the turbine valve signals for controlling flow through each of the turbine units. From the figure we can see that to cope with the load and the generation variation flow through Unit-3 is the highest and flow through Unit-1 is the least. The flow $u_{\mathrm{v},i}$ depends on D_i, $K_{\mathrm{p},i}$ and $T_{\mathrm{i},i}$. Similarly, 7 d) shows the grid frequency and frequencies of each of the generator units supplying to a common consumer load.

From Figure 4 b) we see that if $T = \sum_{i=1}^{5} T_{\mathrm{i},i}$ is the equivalent integral time constant at which the grid frequency of the system is restored then the valve signal for the units are given as

$$u_{\mathrm{v},i} = K_{\mathrm{p},i}\Delta P_i + \frac{K_{\mathrm{p},i}}{T_{\mathrm{i},i}} \int_0^T \Delta P_i dt \tag{7}$$

where

$$\Delta P_i = -\frac{P_i^{\mathrm{r}}}{D_i}\left(\frac{\Delta f}{f^{\mathrm{ref}}}\right). \tag{8}$$

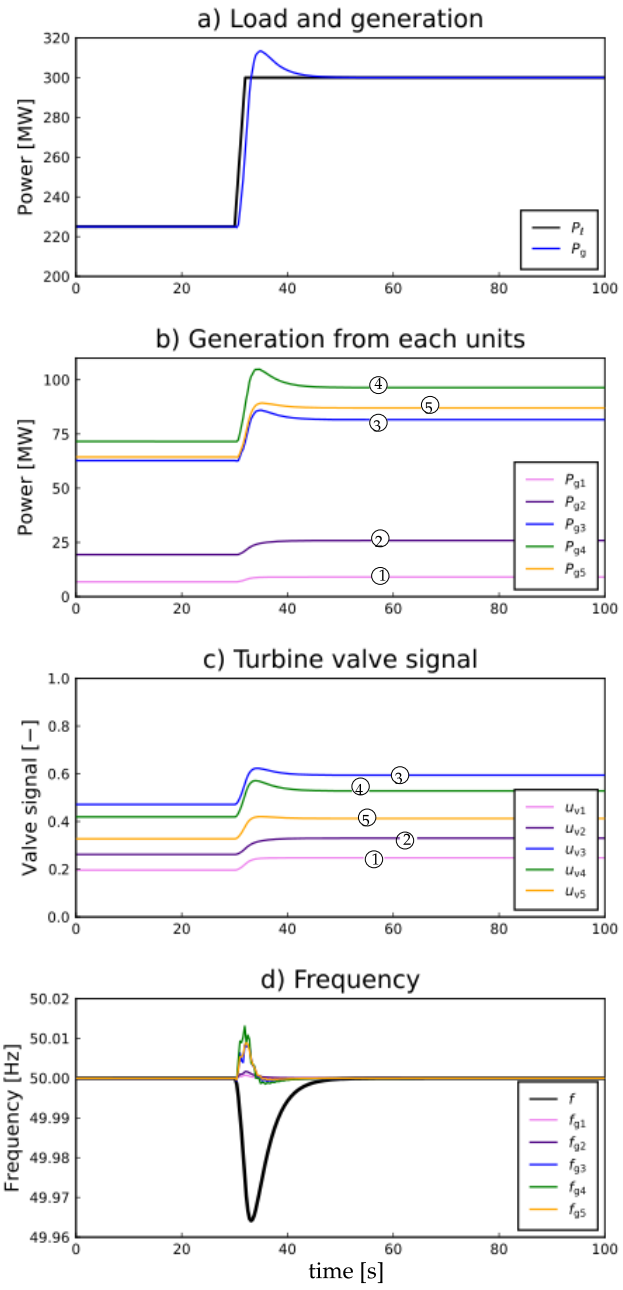

Figure 7. Droop control for five generators operating in parallel index by numbers from 1 to 5.

Table 2. Specifications of power plants.

P^{r}	D	K_{p}	T_{i}
50 MW	4%	0.03	3
100 MW	3%	0.01	2
150 MW	2%	0.02	5
200 MW	5%	0.04	6
250 MW	6%	0.02	4

Table 3. Valve signal and power shared after the steady state is reached at sudden increment in the load power.

$u_{\mathrm{v},i}$	$\Delta u_{\mathrm{v},i}$	ΔP_i
0.23	0.03	2 MW
0.3	0.04	5 MW
0.6	0.13	16 MW
0.55	0.12	27 MW
0.4	0.03	25 MW
		$\sum \Delta P_i = 75$ MW

Putting Equation (8) into (9) we get

$$u_{\mathrm{v},i} = K_{\mathrm{p},i}\left(1 + \frac{1}{\frac{T_{\mathrm{i},i}}{T}}\right)\Delta P_i$$

which can be further expressed as

$$u_{\mathrm{v},i} = -K_{\mathrm{p},i}\left(1 + \frac{1}{\frac{T_{\mathrm{i},i}}{T}}\right)\left(\frac{P_i^{\mathrm{r}}}{D_i}\frac{\Delta f}{f^{\mathrm{ref}}}\right) \tag{9}$$

where $\frac{T_{\mathrm{i},i}}{T}$ is the integral time constant for the valve signal $u_{\mathrm{v},i}$ and depends on total integral time constant given by $T = \sum_{i=1}^{5} T_{\mathrm{i},i}$. This adheres that as the number of hydro turbine increases the plant with a lower value of T_{i} will have a smooth control over u_{v} as shown in Figure 7 c).

From Figure 7 d) f is the grid frequency. Figure 7 a) shows that at $t = 30$ s the load power P_ℓ increases from 225 MW to 300 MW with an increment of 75 MW. This addition of the load will be sensed by the decrement in the grid frequency as shown in Figure 7 d) where f is the grid frequency. From Figure 7 d) we see that in response to the addition of the load into the grid there is a change in the grid frequency given as $\Delta f \approx 0.037$ Hz. With $T = \sum_{i=1}^{5} T_{\mathrm{i},i} = 20$ s and the values taken from Table 2 for all the generators, the required valve signal for each of the hydro turbines can be calculated from Equation (9). The steady state values of the valve signal $u_{\mathrm{v},i}$ after the grid frequency is restored is given in Table 3. Similarly, the power shared among the generators shown in Figure 7 b) is also given in Table 3.

5 Conclusions and Future Work

This paper presents the droop control mechanism applied for the parallel operation of hydro power plants for an open-source hydro power library OpenHPL. The droop controller is a feature extension for OpenHPL. The difference in total generation and load is shared among all the generators operated in parallel to cope with the difference. This is achieved by controlling the flow through the turbines. For an i^{th} generator operating in parallel in a multi-generator system, the turbine valve control signal depends particularly on K_{p} and T_{i} of the PI-controller for that unit, power rating P^{r}, the droop D and the total integral time constant $T = \sum_i T_{\mathrm{i},i}$.

Future work includes an extension of OpenHPL with automatic generation control (AGC) or load frequency control (LFC) in the case of the interconnected power system network.

References

Madhusudhan Pandey and Bernt Lie. The role of hydropower simulation in smart energy systems. In *2020 IEEE 7th International Conference on Energy Smart Systems (ESS)*, pages 392–397, 2020. doi:10.1109/ESS50319.2020.9160193.

Madhusudhan Pandey and Bernt Lie. Mechanistic modeling of different types of surge tanks and draft tubes for hydropower plants. In *Proceedings of The 61th SIMS Conference on Simulation and Modelling SIMS 2020, September 22-24, Oulu, Finland*. Linköping University Electronic Press, 2020, Submitted.

Madhusudhan Pandey, Dietmar Winkler, Roshan Sharma, and Bernt Lie. Using MPC to Balance Intermittent Wind and Solar Power with Hydro Power in Microgrids. *Energies*, 14(4): 874, 2021.

Hemanshu R Pota. Droop control for islanded microgrids. In *2013 IEEE Power & Energy Society General Meeting*, pages 1–4. IEEE, 2013.

Pieter Schavemaker and Lou Van der Sluis. *Electrical power system essentials*. John Wiley & Sons, 2017.

R Sharma, K Fjalestad, and B Glemmestad. Modeling and control of gas lifted oil field with five oil wells. In *52nd International Conference of Scandinavian Simulation Society, SIMS*, pages 29–30, 2011.

Sigurd Skogestad. Probably the best simple pid tuning rules in the world. In *AIChE Annual Meeting, Reno, Nevada*, volume 77, 2001.

Valentyna Splavska, Liubomyr Vytvytskyi, and Bernt Lie. Hydropower systems: comparison of mechanistic and table look-up turbine models. In *Proceedings of the 58th Conference on Simulation and Modelling (SIMS 58) Reykjavik, Iceland, September 25th–27th, 2017*, number 138, pages 368–373. Linköping University Electronic Press, 2017.

Liubomyr Vytvytsky and Bernt Lie. Comparison of elastic vs. inelastic penstock model using OpenModelica. In *Proceedings of the 58th Conference on Simulation and Modelling (SIMS 58) Reykjavik, Iceland, September 25th–27th, 2017*, number 138, pages 20–28. Linköping University Electronic Press, 2017. doi:http://dx.doi.org/10.3384/ecp1713820.

Liubomyr Vytvytskyi. *Dynamics and model analysis of hydropower systems*. PhD thesis, University of South-Eastern Norway, 2019. URL `http://hdl.handle.net/11250/2608105`.

Liubomyr Vytvytskyi and Bernt Lie. Mechanistic model for Francis turbines in OpenModelica. *IFAC-PapersOnLine*, 51(2):103–108, 2018. doi:https://doi.org/10.1016/j.ifacol.2018.03.018.

Liubomyr Vytvytskyi and Bernt Lie. Combining measurements with models for superior information in hydropower plants. *Flow Measurement and Instrumentation*, 69:101582, 2019.

Qing-Chang Zhong and Yu Zeng. Universal droop control of inverters with different types of output impedance. *IEEE access*, 4:702–712, 2016.

Energy Reduction in Lithium-ion Battery Manufacturing using Heat Pumps and Heat Exchanger Networks

Håkon Guddingsmo* Petter Martinussen* Daniel Stjernen* Asanthi Jinasena Anders Hammer Strømman Odne Stokke Burheim

Department of Energy and Process Engineering, Norwegian University of Science and Technology, Norway,
{haakogud,pettma,daniestj}@stud.ntnu.no,
{asanthi.jinasena,anders.hammer.stromman,odne.s.burheim}@ntnu.no
* Equally contributed

Abstract

Global electric mobility is rapidly expanding. Hence, the demand for lithium-ion batteries is also increasing fast. Therefore, understanding energy minimization options in this rapidly growing industry is crucial for reducing the environmental impact as well as developing low-cost and sustainable batteries. The biggest contribution to greenhouse gas emissions is the cell manufacturing process. The most energy-intensive steps of cell manufacturing are electrode drying and dry room conditioning. Therefore, we developed process models for these two systems that can be used for evaluating various energy optimization techniques, such as heat pumps and heat exchanger networks. Further, various process options can be tested and benchmarked in terms of their overall energy consumption using these models. The results show that the power requirement may be reduced through all the options assessed, and available energy efficiency measures may substantially lower the energy footprint of cell production with strong relevance for subsequent greenhouse gas footprints.

Keywords: lithium-ion battery, energy optimization, electric vehicle, electrode drying, dry room, sustainable energy, pinch analysis, heat pump

1 Introduction

Today's transport sector is shifting from fossil-fueled vehicles to electric vehicles. Although this is currently a slow transition, the global market for electric vehicles is expected to grow rapidly in the future. The demand for lithium-ion batteries (LIB) for these vehicles is also expected to increase simultaneously. Having a low carbon footprint is a requirement for ensuring climate change mitigation with this growth. Life cycle assessment studies on battery electric vehicles have shown that the carbon footprint of LIB production may contribute to significant greenhouse gas emissions (Kurland, 2020; Ellingsen et al., 2016). One of the main drivers for these emissions is identified as the energy usage of the cell manufacturing process (Kurland, 2020). Although emissions vary over different regions, energy saving is always important.

Therefore, today's LIB research is advancing towards energy-efficient, low-cost, and sustainable cell manufacturing techniques. Adaption of less energy-intensive technologies such as advanced drying technologies (Bryntesen et al., 2021) or semisolid-state and solid-state battery manufacturing technologies is becoming popular in this regard. Identifying various energy minimization options for the conventional cell manufacturing process is equally crucial for today's battery industry.

The most energy-intensive steps of conventional cell manufacturing are electrode drying and dry room conditioning (Dai et al., 2019; Yuan et al., 2017; Jinasena et al., 2021). Energy for a convective cathode drying and a solvent recovery system is modeled by Ahmed et al. (2016b), while different dry room air conditioning systems using solid desiccant wheels are modeled by Vogt et al. (2021) and Ahmed et al. (2016a). Although these processes have been studied individually, and their energy impacts were analyzed in detail, there are no studies that explore the energy minimization options of the combined process. There are possibilities of applying a heat pump to facilitate exchanges between the electrode drying process and the dry room air conditioning system. In addition, the general use of heat exchanger networks to exchange various heating and cooling loads is also of interest.

Therefore, this study's main objective is to explore these two possibilities to minimize the total energy requirement of the energy-intensive process steps of LIB cell manufacturing. For this, we have developed process models for electrode drying and dry room air conditioning such that various process options can be tested and benchmarked in terms of their overall energy consumption.

2 System Description

A $LiNi_{1/3}Mn_{1/3}Co_{1/3}O_2$ (NMC111) cell production factory of 530 MWh annual capacity is selected for the study. Out of the cell production process, only the electrode drying process, solvent recovery system and the dry room air dehumidification system were considered for the study due to their high energy intensity. Different options of energy recovery is explored between these systems. The modeling approaches for each system is described in this section.

2.1 Electrode Drying

Conventionally, the drying is performed using convective heat transfer and high temperature air circulating over the electrode films. Alternatively, this can also be performed using radiation drying. Drying rate and drying time differ depending on solvent used and the temperature inside the chamber. To reduce the amount of energy consumed during drying, a multistage drying process can potentially be utilized. This alternative drying process can consist of splitting the drying chamber into multiple sections with different temperatures, ranging from low to high temperature drying. Alternatively, the temperature can be controlled in intervals when utilizing a batch dryer. This will reduce the overall heating load in comparison to a single-stage heating process, as it will reduce the amount of air that needs to be heated.

The electrode drying process is modeled using a reduced-order model for two different technologies, convection drying (CD) using hot air and infra-red radiation drying (RD) using radiation heaters (Oppegård et al., 2020). For more details on the model see Oppegård et al. (2020).

2.2 Solvent Recovery System

Water soluble N-Methyl-2-pyrrolidone (NMP) can be used as a solvent for the mixing of cathode material powders during LIB manufacturing. The need for recovering and recycling this solvent is prominent due to its polluting and hazardous nature. For this, an intricate filtration process is applied. A typical NMP recovery system is shown in Figure 1. Condensation is used in order to extract the NMP from the air exiting the drying stage. However, the complete solvent recovery system is not modeled in the study, where the solvent removal columns are omitted. The heat and mass transfer of the thermal units are modeled using Aspen Plus. Based on Ahmed et al. (2016b), the air needs to be cooled to approximately 6°C. The required cooling energy is assumed to be equal to that of the heating when considering conservation of energy.

Furthermore, this is mainly applicable to the cathode, as most of the anode material mixing are usually water-based. Due to the use of water as solvent, the anode is assumed to not require a solvent recovery process.

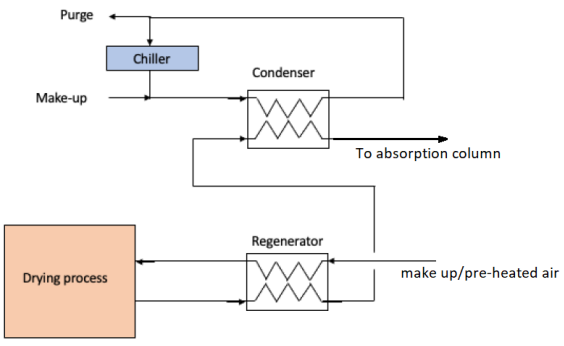

Figure 1. The NMP recovery system.

2.3 Dry Room Air Dehumidification System

A dry room is an enclosure with low humidity and a certain level of cleanness. It is an essential part for processes that require a dry and clean environment, such as the cell assembly stages in a battery manufacturing process. Liquid electrolyte filling is highly sensitive to water vapor. The dry air supply for the dry room can be obtained by an air dehumidification system. Common air dehumidifiers are mostly operated by either a solid desiccant wheel or a liquid desiccant system.

The liquid desiccant system is a mechanism that removes humidity and sensible heat from the air through the use of a liquid desiccant material and thermal energy. Calcium chloride ($CaCl_2$) is a commonly used desiccant for this purpose. Figure 2 depicts a basic configuration.

Here, the absorber and regenerator columns are connected through a piping system. The water in the humid air entering the absorber column is bound to the liquid desiccant, and the dried air then exit at the top of the same column. A heater increases the temperature of the water-filled desiccant to 100°C upon entry of the regenerative column. The water is then evaporated, while the residual desiccant is pumped into the absorber column while subsequently being cooled to 25°C, closing the loop. The heat and mass transfer of the complete system with an additional heater for dry air heating is modeled in Aspen Plus.

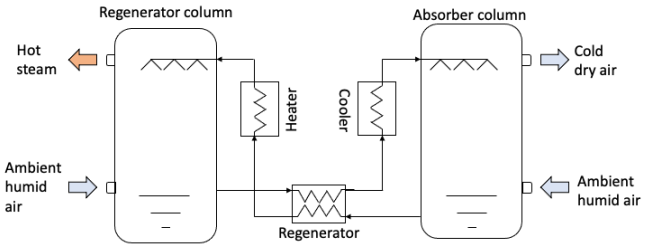

Figure 2. The liquid desiccant system.

2.4 Heat Pump

A heat pump is a system that transfers energy between two thermal reservoirs of different temperatures. The system is based on the vapor compression refrigeration cycle. A common configuration of a heat pump is shown in Figure 3 which consists of an evaporator, compressor, condenser and expansion valve. At the inlet of the evaporator (low temperature), the circulating fluid of the cycle is a vapor-liquid mixture. When passing through the evaporator, the liquid evaporates using the energy transferred from the cold reservoir. The fluid then enters the compressor, which increases the pressure of the fluid to become saturated vapor. The high temperature vapor then enters the condenser which absorbs energy by converting the fluid from vapor to saturated liquid. In this process, the energy is released in the form of heat, which is then transported into the hot reservoir. The fluid is then expanded adiabatically through an expansion valve which returns it to the

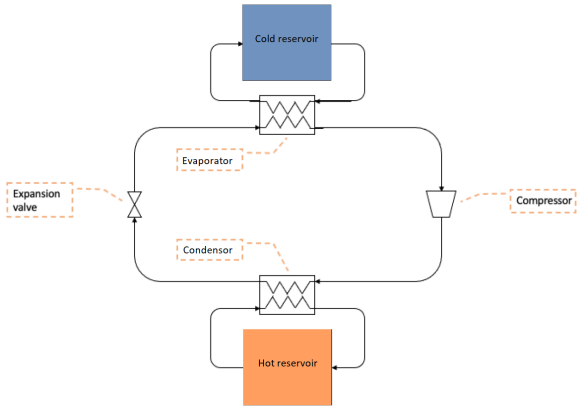

Figure 3. A typical heat pump configuration.

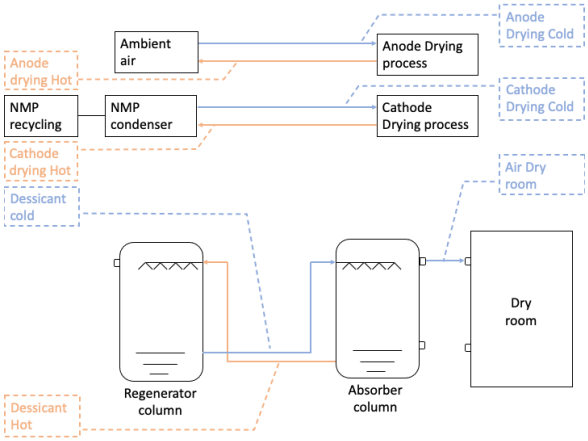

Figure 4. Streams evaluated using pinch approach.

same state as the evaporator inlet, closing the loop (Moran et al., 2018).

The heat pump is modeled in Aspen and various refrigerants were used as the working fluid of the heat pump based on the availability and thermodynamic characteristics. The refrigerants are R-22 (chlorodifluoromethane), R-134a (tetrafluoroethane) and R-600a (isobutane). Different condensation and evaporation temperature and pressure characteristics were also tested to find out the optimum operational conditions.

2.5 Heat Exchanger Networks

A Maximum Energy Recovery (MER) network is a system that is based on pinch analysis and consists of a network of heat exchangers optimally placed for maximum energy recovery within the system. A further option investigated utilizing different MER-network designs within the entire systems heat exchangers. These networks are designed using the heat exchanger details resulted from the models and the corresponding pinch analyses were performed. How the streams of the network are connected in the network configurations is depicted in Figure 4. This was the basis for simulation. The streams shown in the figure are categorized as hot and cold. The cold streams are in need of heating, while hot streams are in need of cooling. The figure also shows all the material streams involved in the production process. These streams consisted of three groups. The first of these being the anode streams, with both inlet and outlet from the drying process. Secondly, the cathode streams were connected between the drying process and the NMP recycling unit. Finally, the dry room streams consisted of the two streams within the desiccant system, between the absorber and regenerator column, as well as the airflow into the dry room. The streams presented here essentially represent the total system before any connections were made.

The minimum temperature difference was set to 10°C. Aspen Energy Analyser was used to design the MER-network, based on the input streams listed in Table 1. The number of stream splits allowed was set to zero, in order to simplify the design. The design yielded the energy requirements and heat exchanger sizes required for the design. A series of designs were produced connecting different heat exchangers based on the pinch approach. The simplicity of the connections and the total costs were considered during the design.

Table 1. The input values for the pinch analysis in Aspen Energy Analyser.

Stream	*Temperature range [°C]*	*Mass flow rate [kg/h]*	*Heat cap. [kJ/kgK]*
Desiccant hot	78–25	2 000	3.71
Desiccant cold	6–100	2 000	3.71
Air dry room	5–23	32 000	1.00
Cathode hot	140–6	34 200	1.00
Cathode cold	6–140	34 200	1.00
Anode hot	140–8	34 200	1.00
Anode cold	8–140	34 200	1.00

3 Results and Discussion

3.1 Effect of Parameters on the Evaporation Energy of Drying

For the drying process, the evaporation energy and drying time are heavily impacted by the parameters of the air entering the convective dryer, with temperature, velocity and humidity being the prominent factors.

Figure 5 shows the effect of these parameters on the power requirement for the evaporation of solvent and Figure 6 shows the effect on the evaporation energy for one batch of NMC111 cathode production. Parameters were changed one at a time and all the parameters were normalized for illustration. The process parameters have a significant effect on the evaporation energy in both CD and RD. However, in comparison to the other energy values in the cell production process, the evaporation energy is insignificant (less than 0.2 Wh/Wh) which makes the variations of process parameters less significant for evaporation energy consumption. It is important to note that although

faster drying rates can be achieved with high temperatures, drying rate is controlled to prevent binder migration and cracking of electrodes (Jaiser et al., 2016; Rollag et al., 2019; Westphal et al., 2015). Therefore, multi-stage drying is preferred (Oppegård et al., 2020).

The initial conditions are selected according to the battery chemistry specifics and the heat source temperature is taken as 140°C. For an NMC111 cathode, the CD time and evaporation power is 19.2 minutes and 28.7 kW, respectively. For a graphite anode, the CD time is 13.7 minutes and the power needed for evaporation becomes 41.9 kW. Thus, the load needed for evaporation using CD is collectively 70.6 kW for a NMC111-based cell.

Similarly, the power and energy requirements are calculated for RD, resulting in 40.9 kW (0.089 Wh/Wh) for cathode and 58.2 kW (0.086 Wh/Wh) for anode, respectively (see Figure 7). For both anode and cathode drying, RD is faster than CD due to faster drying rates towards the end of the drying process. The drying time has a significant effect on the power requirement as the power is higher for RD than CD. However, the total energy requirement can be considered similar between CD and RD as the change in values is comparatively low (0.003 Wh/Wh).

3.2 Effect of Drying Temperature and Regenerator Size on the Energy of Solvent Recovery System

The solvent recovery system was tested for different drying temperatures of 80°C and 140°C (for CD), as well as for various heat exchanger sizes. Table 2 shows the heating and cooling loads for the cathode drying system when operating at these temperatures. The total load is for the heating of the anode, and the heating and cooling of the cathode. The regenerator is an additional heat exchanger to the system shown in Figure 1 to be used in the heat pump and for further energy recovery. Regenerator load zero represents the original solvent recovery system without additional energy recovery.

Through the implementation of a regenerative unit, the decrease in required power is shown to be linear for the heating and cooling loads. When the regenerator size is bigger with higher load, the total heat exchanger load is lower than the original system, which shows that more energy can be recovered by the regenerator. Lowering the dryer air temperature also show a significant impact on the power requirement. However, as discussed in Section 3.1, the decrease in temperature results in a increase in drying time, which would affect the production capacity and the energy consumption per cell.

For anode drying, it is assumed that the anode utilizes water as solvent instead of NMP, and does not require a solvent recovery process. This removes the need for cooling. However, a regenerative unit can still be implemented for the anode air stream. The anode heating load would be equal to the cathode heating load of 1208 kW and 707

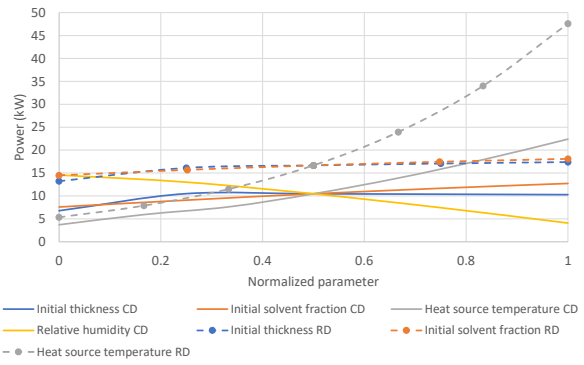

Figure 5. Effect of initial and operating conditions on the power requirement for evaporation by convection and radiation.

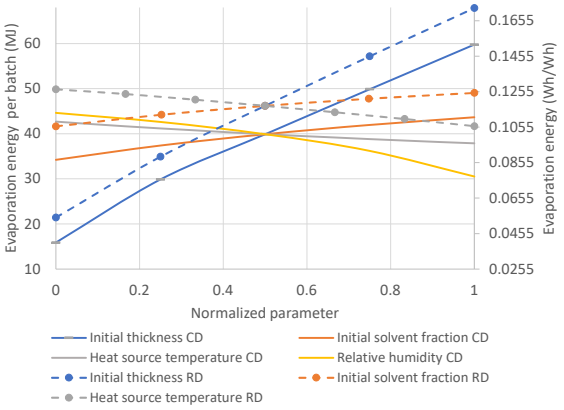

Figure 6. Effect of initial and operating conditions on the evaporation energy by convection and radiation.

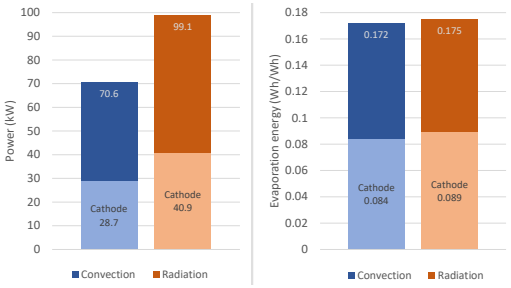

Figure 7. Power and energy requirements for evaporation of anode and cathode solvents by convection and radiation.

Table 2. The heat exchanger loads with various regenerator sizes for a 80°C and 140°C CD process.

Temperature (°C)	*Regenerator [kW]*	*Heating [kW]*	*Cooling [kW]*	*Total [kW]*
80	0	663	663	1989
	100	563	563	1689
	250	412	412	1236
	500	163	163	489
140	0	1208	1208	3624
	100	1108	1108	3324
	250	958	958	2874
	500	707	707	2121

kW for 140°C, without and with a 500 kW regenerator, respectively.

For both cathode and anode drying the total load amounts to 3624 kW for the original system at 140°C and 2121 kW with two 500 kW regenerators (one for each drying process). Similarly, for RD, the heating load for cathode drying is taken as 742 kW, where the required heating and cooling loads without regeneration amounts to a total of 2226 kW.

3.3 Energy Consumption with Heat Pump

The heat pump that is applied between the drying system and the dehumidification system is shown in Figure 8. The different regenerator sizes tested in Section 3.2 are used here. The selected refrigerants were also tested, which yielded different pressure ranges for the condenser and evaporator of the heat pump. Further, the required compressor energy was found for the desired operating conditions of the heat pump. It is observed that the lower pressure ranges have a higher required compressor power for the heat pump to be able to operate under ideal conditions.

The heat pump design is highly based on the characteristics of the attached systems. For example, for a dry room heater load of 132.1 kW, the heat pump requires a regenerator duty of 1090 kW or alternatively an additional heat exchanger connected to the desiccant system to assist in cooling the stream.

Therefore, using a heat pump requires a large sized regenerator, since the heating load for the desiccant system is selected as 150 kW. This would require a regenerator duty of 940 kW. The resulting temperature ranges of the streams connected to the heat pump would be 20–6°C for the electrode drying stream and 8–23°C for the dry room air flow. The temperature difference is too small to use a regular heat exchanger and using a heat pump is therefore viable.

Table 3 displays the compressor power, pressure ranges and coefficient of performance of the compressor based on tested refrigerants. R–600a is selected as the refrigerant for the study due to the lower pressure range. The heat pump in this proposed design covers the entire heating load for air entering the dry room as well as contributing to cooling the air stream for NMP extraction. The potential power savings are considered as 247.9 kW, although, this is highly dependent on the refrigerant used.

Table 3. The pressure ranges and compressor power requirement for different refrigerants in the heat pump. COP: coefficient of performance

Refrigerant	*Pressure (bar)*	*Compressor power (kW)*	*COP factor*
R–22	4.37–12.67	9.3	14.10
R–134a	2.53–8.25	16.2	8.17
R–600a	1.37–4.33	20.1	6.58

3.4 Energy Consumption with MER-Network

The composite curve and the grand composite curve for the system is shown in Figure 9. The composite curve is parallel showing a high possibility of energy recovery. A clear pinch point is also seen at 10°C. According to the grand composite curve there is an energy pocket up to 150 kW, which indicates excess energy that cannot be used for a heat exchanger due to the available low temperature range. However, theoretically, this allows a heat pump to be operated based on the temperature ranges that were analyzed for the operation of heat pump in section 3.3. Therefore, implementing a heat pump in combination with a MER-network has the potential to theoretically save around 300 kW, including both heating and cooling.

Three MER networks (named MER-1, MER-2 and MER-3) were designed and one of the designed MER-networks (MER-1) are shown in Figure 10. The blue horizontal lines of the network represent the cold streams and the orange horizontal lines represent the hot streams in the total system. The heat exchanger connections are indicated by the vertical connection lines between the streams, where blue dots indicate the coolers connected to the cold utility stream (refrigerant/cooling water), orange dots indicate the heaters connected to the hot utility stream (steam/hot water), while the gray dots indicate the regenerators interconnected to process streams. The minimum temperature difference for the pinch analysis is taken as 10°C for all the designs.

For MER-1 and 2, the utility streams were chosen arbi-

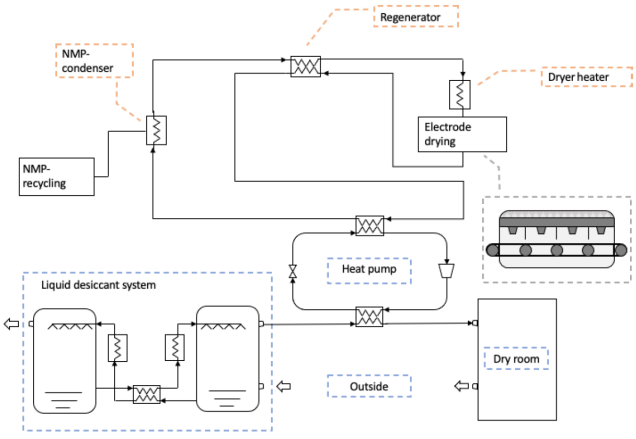

Figure 8. Applied heat pump configuration.

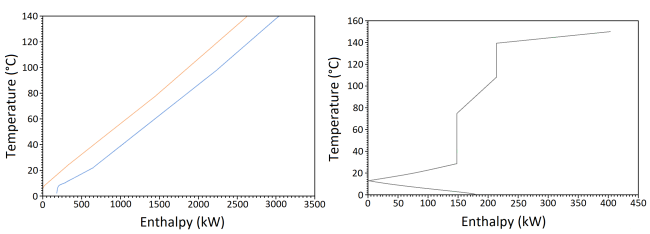

Figure 9. The composite and grand composite curves.

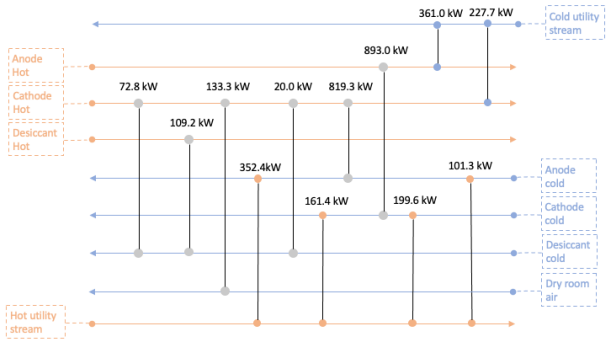

Figure 10. MER-network design one (MER-1).

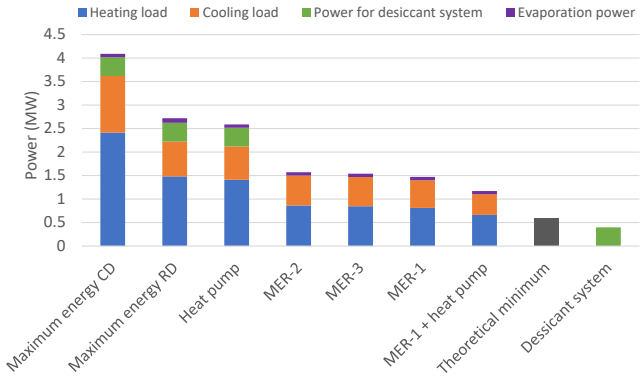

Figure 11. A comparison of power requirements with different energy reduction methods including a heat pump and MER heat exchanger network designs.

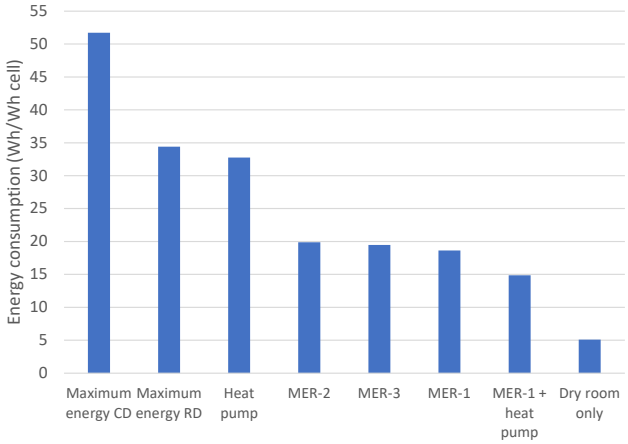

Figure 12. The energy consumption for different energy optimization methods.

trarily since it does not impact the energy demand. However, this impacts the required area of the heat exchangers representing cooling and heating units, which directly affects the capital cost which is not considered in the study. MER-1 network consists of twelve heat exchangers, where four of them are heaters and two are coolers. The total heating and cooling requirements for this design are 814.7 kW and 588.7 kW, respectively, and 1403.4 kW in total. The largest regenerator in this design needs a heat exchanger area of 775 m^2 and the total area for heat exchangers is 2058 m^2.

Similarly, for MER-2, thirteen heat exchangers are used including four heaters and two coolers. The power requirement for this design is 864.7 kW for heating and 638.6 kW for cooling which gives a total power of 1503.3 kW. This is a slightly higher power requirement than the first design. The largest heat exchanger in this design is of an area of 900 m^2 and the total area for heat exchangers is 1825 m^2.

The third design, MER-3 was done using four heaters, three coolers and five regenerators. The power requirement for this design is similar to MER-1 with a total of 1471.2 kW, where 848.7 kW for heating and 622.5 kW for cooling, respectively. In MER-3, the largest heat exchanger is 697 m^2 with a total heat exchanger area of 1928 m^2.

All the network designs have two remaining low temperature coolers at the top right and a low temperature heating load to the bottom left in the respective designs. There is a potential for connecting a heat exchanger between these two heating and cooling loads which can further reduce the total power requirement of all three designs.

3.5 Comparison of the Used Energy Optimization Methods

Total power requirement from all the assessed methods are compared together as shown in Figure 11. The total system without any energy recovery is used as the maximum power requirement for the system either with a convective (4090 kW or 51.7 Wh/Wh) or radiation (2720 kW or 34.3 Wh/Wh) drying process. The system with RD is lower in energy, about 17.3 Wh/Wh (1370 kW) compared to the CD system. The energy recovery methods are applied only to the system with CD.

The addition of a regenerator in the solvent recovery system, and the heat pump between the regenerator and desiccant system heater, has decreased the power requirements by 1503 kW (19 Wh/Wh). The MER-network designs have reduced the power requirements further down by 2620 kW (33.1 Wh/Wh), 2520 kW (31.8 Wh/Wh) and 2552 kW (32.2 Wh/Wh) for MER-1, MER-2 and MER-3, respectively. The difference of each network is by approximately 100 kW between each other. By implementing a heat pump together with the MER-1 design, the total power is further decreased by 300 kW (3.8 Wh/Wh). A theoretical minimum power requirement (581 kW) for the MER-networks is also included as a comparison followed by the power requirement for the dry room dehumidification system which can be compared with production processes without drying, such as semi-solid-state batteries.

The energy requirements for the same optimization methods are calculated with respect to the produced cell capacity for NMC111 cell production. The total energy consumption values are shown in Figure 12 for the se-

lected energy saving options. A similar reduction of energy trend can be seen from the figure.

The results suggest that the energy requirement can be reduced through all the options assessed. In total, the results indicate a potential for substantial improvements in overall energy intensity for the production of different battery chemistries (energy usage in Wh per Wh of produced battery) when heat exchanger networks are used for heat recovery. This can be further enhanced by combining the heat exchanger networks with the heat pumps. In summary, this work suggests that available energy efficiency measures may substantially lower the energy footprint of LIB production with strong relevance for subsequent greenhouse gas footprints.

3.6 Comparison with Literature Values

The energy values for the range of various energy optimization methods are compared together with the energy values reported in literature. The MWh to GWh scale plant data reported by Yuan et al. (2017), Pettinger and Dong (2017), Schünemann (2015), Dai et al. (2019), and Sun et al. (2020) are considered here. Further, the models developed by Ahmed et al. (2016a,b) and Jinasena et al. (2021) are also included in the comparison. The compared values for dry room and drying energy consumption are shown in Figure 13.

The values are not comparable with their variation due to the different plant capacities. However, the values for dry room and drying with MER-networks are well comparable with similar capacity values of a 0.7 GWh plant data by Schünemann (2015, cited in Thomitzek et al., 2019). The values of this study are slightly higher than the values from Schünemann (2015, cited in Thomitzek et al., 2019), which could be due to the slightly lower plant capacity of this study.

Ahmed et al. (2016b) investigated the energy for cathode drying and solvent recovery process for an annual plant capacity of 1 GWh. For their base case of a CD process of 37 m^3/s air flow, the power for the electrode dryer is 130 kW, where in our study the maximum power (out of various initial drying conditions) is 26 kW for a flow of 7.5 m^3/s cathode dryer air flow. The total power for their process is given as 5851 kW (42.1 Wh/Wh pack) where 1470 kW of electrical power and 4381 kW of thermal power. This amount (42.1 Wh/Wh) is the second highest energy requirement out of the reported values, where the highest is 51.2 Wh/Wh for a 18.2 MWh plant reported by (Yuan et al., 2017). Further, this value is only for the cathode drying which suggest the energy values will be higher for both cathode and anode drying. The plant consists of a fuel fired air heater of 3752 kW, a chiller of 1169 kW (electricity), and a condenser of 3508 kW which is connected to an air-to-air heat exchanger for energy recovery (2700 kW). The total electric power for air blowers is 301 kW. Additionally, there is a 236 kW re-heater for the regeneration air of the desiccant wheel, and a 394 kW heater for the distillation column where the recovered NMP is further purified for reuse. The total power requirement in their study for various process parameters is in the range of 3346–7304 kW (24.1–52.6 Wh/Wh). In our study we haven't included the blowers or the NMP purification column which gives a slightly underestimated value for the energy requirement.

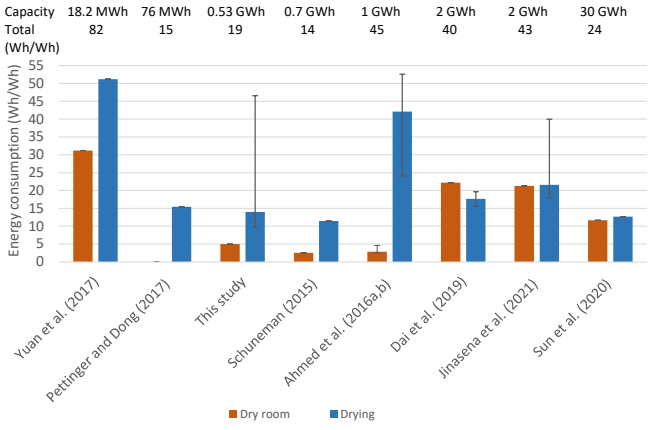

Figure 13. The comparison of energy consumption values for drying and dry room with reported literature values. The average total energy and the annual capacity of each production facility are also stated.

Similarly, Ahmed et al. (2016a) modeled a 16 000 m^3 dry room for a dry air flow of 20 m^3/s. The system uses a zeolite wheel for moisture removal, and consists of a cooler (426 kW), pre-cooler (57 kW), heater (63 kW), regenerator (30 kW) and blowers (167 kW). For a base case of operating conditions the total power was determined as 398 kW. Assuming that they produced 10 kWh battery packs (similar to Ahmed et al. (2016b)) this value is around 2.9 Wh/Wh which is comparatively low.

Further, Thomitzek et al. (2019) reported a 133.6 Wh/Wh for drying and 448.7 Wh/Wh for dry room for a 48 kWh annual capacity pilot plant. For this plant, Vogt et al. (2021) report a total power of 271.8 kW for a dry room which supplies 2.74 m^3/s dry air flow. This includes two pre-coolers of 54.8 kW and 43.8 kW, a process fan of 15 kW, a re-heater of 33.2 kW, and a regeneration heater of 125 kW with a 15 kW heat recovery.

These results show that comparing the values of different scales is difficult because of the high variance of the reported values. Therefore, the models need to be scaled up or redesigned for giga factory scale for a proper comparison. Vogt et al. (2021) have reported scaling-up of their pilot scale energy data. They report a reduction of energy consumption of the dry room from 20.98 kWh per cell (Wessel et al., 2021) to 1.45 kWh per cell. However, this is equivalent to approximately 47 Wh/Wh and is still higher than the other reported values. Therefore, scaling-up of smaller scale plant data and models, and development of giga scale plant models need to be further explored for accurate energy consumption estimations for battery industry.

4 Conclusions

Process models were developed for a dry room air conditioning system and electrode drying processes of a lithium-ion battery production process, for analyzing different energy optimization options. For the drying process, different drying techniques were explored, namely convection air drying and infra-red radiation drying. The energy consumption for radiation drying is lower than for convection drying without any energy recovery in the convection process. Application of a heat pump and use of maximum energy recovery heat exchanger network design based on pinch analysis are explored as energy optimization techniques. For the system with convection drying, a heat pump reduced the energy usage considerably. Application of heat exchanger networks reduced the energy usage more than the heat pump. The combination of both these techniques resulted in the most energy reduction for the total process system from 51.7 Wh/Wh to 14.9 Wh/Wh.

Acknowledgement

We acknowledge Freyr Battery AS (grant 02-2019-IP172-FREYR) for the funding of the study.

References

Shabbir Ahmed, Paul A. Nelson, and Dennis W. Dees. Study of a dry room in a battery manufacturing plant using a process model. *Journal of Power Sources*, 326:490–497, 2016a. doi:10.1016/j.jpowsour.2016.06.107.

Shabbir Ahmed, Paul A. Nelson, Kevin G. Gallagher, and Dennis W. Dees. Energy impact of cathode drying and solvent recovery during lithium-ion battery manufacturing. *Journal of Power Sources*, 322:169–178, 2016b. doi:10.1016/j.jpowsour.2016.04.102.

Silje Bryntesen, Anders Strømman, Ignat Tolstorebrov, Paul Shearing, Jacob Lamb, and Odne Burheim. Opportunities for the State-of-the-Art Production of LIB Electrodes—A Review. *Energies*, 14:1406, 2021. doi:10.3390/en14051406.

Qiang Dai, Jarod C. Kelly, Linda Gaines, and Michael Wang. Life cycle analysis of lithium-ion batteries for automotive applications. *Batteries*, 5(48), 2019. doi:10.3390/batteries5020048.

Linda Ellingsen, Bhawna Singh, and Anders H. Strømman. The size and range effect:Life-cycle greenhouse gas emissions of electric vehicles. *Environmental Research Letters*, 11:1–9, 2016.

Stefan Jaiser, Marcus Müller, Michael Baunach, Werner Bauer, Philip Scharfer, and Wilhelm Schabel. Investigation of film solidification and binder migration during drying of li-ion battery anodes. *Journal of Power Sources*, 318:210–219, 2016. doi:https://doi.org/10.1016/j.jpowsour.2016.04.018.

Asanthi Jinasena, Odne S. Burheim, and Anders H. Strømman. A Flexible Model for Benchmarking the Energy Usage of Automotive Lithium-Ion Battery Cell Manufacturing. *Batteries*, 7(1):14, 2021. doi:10.3390/batteries7010014.

Simon Davidsson Kurland. Energy use for GWh-scale lithium-ion battery production. *Environmental Research Communications*, 2(1):012001, 2020. doi:10.1088/2515-7620/ab5e1e.

Michael J. Moran, Howard N. Shapiro, Daisie D. Boettner, and Margaret B. Bailey. *Fundamentals of Engineering Thermodynamics*. Wiley, 9th edition, 2018. ISBN 978-1-119-39138-8.

Emil Oppegård, Asanthi Jinasena, Anders H. Strømman, Jon A. Suul, and Odne S. Burheim. Study of an Industrial Electrode Dryer of a Lithium-Ion Battery Manufacturing Plant: Dynamic Modelling. In *61st Conference on Simulation and Modelling*, pages 77–84, Virtual, 2020. doi:10.3384/ecp2017677.

Karl Heinz Pettinger and Winny Dong. When does the operation of a battery become environmentally positive? *Journal of the Electrochemical Society*, 164(1):A6274–A6277, 2017. ISSN 19457111. doi:10.1149/2.0401701jes.

Kelsey Rollag, Daniel Juarez-Robles, Zhijia Du, David L. Wood, and Partha P. Mukherjee. Drying Temperature and Capillarity-Driven Crack Formation in Aqueous Processing of Li-Ion Battery Electrodes. *ACS Applied Energy Materials*, 2(6):4464–4476, 2019. doi:10.1021/acsaem.9b00704.

Jan-Hinnerk Schünemann. *Modell zur Bewertung der Herstellkosten von Lithiumionenbatteriezellen*. Sierke, 1st edition, 2015. ISBN 978-3-86844-704-0.

Xin Sun, Xiaoli Luo, Zhan Zhang, Fanran Meng, and Jianxin Yang. Life cycle assessment of lithium nickel cobalt manganese oxide (NCM) batteries for electric passenger vehicles. *Journal of Cleaner Production*, 273:123006, 2020. ISSN 09596526. doi:10.1016/j.jclepro.2020.123006.

Matthias Thomitzek, Nicolas Von Drachenfels, Felipe Cerdas, Christoph Herrmann, and Sebastian Thiede. Simulation-based assessment of the energy demand in battery cell manufacturing. *Procedia CIRP*, 80:126–131, 2019. ISSN 22128271. doi:10.1016/j.procir.2019.01.097.

Marcus Vogt, Klemens Koch, Artem Turetskyy, Felipe Cerdas, Sebastian Thiede, and Christoph Herrmann. Model-based energy analysis of a dry room HVAC system in battery cell production. *Procedia CIRP*, 98:157–162, 2021. doi:10.1016/j.procir.2021.01.023.

Jacob Wessel, Artem Turetskyy, Felipe Cerdas, and Christoph Herrmann. Integrated Material-Energy-Quality Assessment for Lithium-ion Battery Cell Manufacturing. *Procedia CIRP*, 98:388–393, 2021. ISSN 22128271. doi:10.1016/j.procir.2021.01.122.

Bastian Westphal, Henrike Bockholt, T. Gunther, W. Haselrieder, and Arno Kwade. Influence of convective drying parameters on electrode performance and physical electrode properties. *ECS Transactions*, 64(22):57–68, 2015. doi:10.1149/06422.0057ecst.

Chris Yuan, Yelin Deng, Tonghui Li, and Fan Yang. Manufacturing energy analysis of lithium ion battery pack for electric vehicles. *CIRP Annals - Manufacturing Technology*, 66(1): 53–56, 2017. doi:10.1016/j.cirp.2017.04.109.

Develop a Cyber Physical Security Platform for Supporting Security Countermeasure for Digital Energy System

Mike Mekkanen Tero Vartiainen Duong Dang

School of Technology and Innovation, University of Vaasa, Finland,
{mike.mekkanen,tero.vartiainen,duong.dang}@uwasa.fi

Abstract

The paper develops a cyber physical system (CPS) security platform for supporting security countermeasures for digital energy systems based on real-time simulators. The CPS platform provides functions that trainers or trainees can be able to operate and test their scenarios with a state-of-the-art integrated solution running at a real-time simulator. Those integrated solutions include energy systems simulation software and communication systems simulation/emulation software. The platform provides practical "hand-on-experiences" for participants and they are able to test, monitor and predict behaviors of both systems at the same time. The platform also helps achieve training's objectives that meet skilled requirements for the future generation in both smart energy systems evaluation and cyber physical security fields. In particular, we present the CPS platform's architecture and its functionalities. The developed CPS platform has also been validated and tested within different simulated threat cases and systems.

Keywords: cyber physical system laboratory, critical infrastructures, attack vectors, real time simulator, operational technology, information technology

1 Introduction

Numerous energy firms are undergoing digital transformations (Dang and Vartiainen 2019; Dang et al., 2021; Mekkanen et al., 2021; Mekkanen and Kauhaniemi 2018) and digital transformation has significant impact to the energy sector (Dang and Vartiainen, 2020; Mekkanen, 2021). It also brings threats to the sector as the information and communications technology (ICT) is embedded in energy systems. For example, cyber-attacks are one of the most common threats in the energy sector that causes severe consequences to organizations and even national security. To prevent cyber-attacks, several solutions are proposed, such as legislations, standards (Pearson, 2011), or testbeds (Sun et al., 2018). In particular, testbeds often use a Real-Time Simulator as a tool to test different scenarios that cannot test in a real physical system or it is very challenging if we put the real physical system in hazard mode as it may cause damage to the real-world systems. As a result, Real-Time Simulators thus have been widely used in the energy sector (Vellaithurai et al., 2017). In addition, one of the conventional solutions to prevent cyber attack is training persons-in-charges to acquire practical skills through a real time simulator.

However, engineering training faces several difficulties. First, the difficulties of setting up and executing scenarios in a diverse environment that allow learners to conduct and evaluate cases that align between labs' environments (e.g., equipment, software, threads, and technologies) and real-world environments (e.g., digital twins). Second, the difficulties in the multidisciplinary nature of energy systems that also integrate ICT and its threat to the systems. For example, smart grid systems increase cybersecurity threats. In that sense, if an attack happens in the energy systems, the damage is likely costly and it could potentially impact national security as in the case of cyber-attacks physically destroying Iran's nuclear centrifuges (Pearson, 2011).

This paper aims to tackle this issue by developing a cyber physical system (CPS) for an education environment. We use a state-of-the-art integrated solution running at real-time simulator. Those integrated solutions are the energy systems simulation software and the communication systems simulation/emulation software. We propose a CPS platform that provides abilities for trainers to train or coach trainees (e.g., students/security experts) for conducting tasks with a real simulator via online power system modeling, communication system emulation and cyber-attack emulation integrating and running in real-time in one target. Here a CPS is understood as a co-simulation platform, which links software that simulates the modern digital energy system (energy system unites, ICT and threats) aspects, and captures the complex interactions between them which meet the requirements of physical processes (Ison et al., 2020; de Reuver et al., 2018). The co-simulation allows more adaptable setup, scalable, simpler cyber-attacks testing/mitigation,

and comprehensive instrumentation via software probes to discover exactly what happened at every component of the CPS.

Our proposed platform has an ability to mimic the operation of the real instruments subject to cyber-attack at the lab's environment. Through the platform, trainees can perform their tasks in a state-of-the-art integrated solution real-time simulator via online physical/virtual devices, such as personal computers (PCs), servers, routers, firewalls, intrusion detection system (IDS), protocols, defender, intelligent agent, simulate attack and other information technology/operational technology (IT/OT) CPS system management solutions/tools that connected via different existing/designed communication protocols/medium to the real-time simulator, such as hardware-in-the-loop (HIL), software-in-the-loop (SIL), and processor-in-the-Loop (PIL). By doing so, it is expected that learners can learn practical "hand-on-experiences" and they become physical security experts in the future.

The remainder of this study is structured as follows. First, the background section is presented. Second, we describe the development of the CPS platform. Third, the CPS platform scenarios are presented. Finally, we present the conclusions.

2 Background

2.1 A brief history of simulation development

A simulation has been widely employed in electrical *system planning and design for decades. There are a* wide range of energy sector applications that have successfully developed simulation for their experiments. The rapid evolution of computing technologies has helped the improvements of simulation tools during the past decades. Figure 1 shows the timeline of the evolution of real-time simulators from physical/analog to fully digitalization.

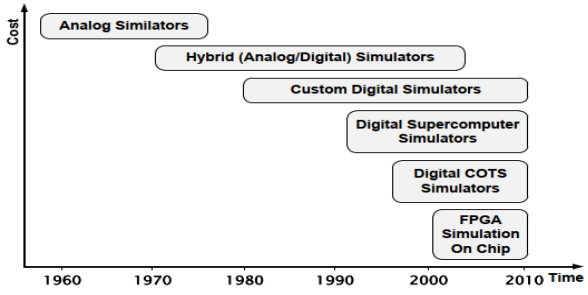

Figure 1. Real-time simulator evolution

Moreover, the emergence of low-cost multi-core processors has also paved the way for the development of simulators as it considerably helps more affordable and scalable real-time simulators. The ability of a real-time simulator to distribute work across different dedicated cores within a multi-core processor dramatically reduces processing time and allows the integration of different tools, as well as the capacity to interact with other software, applications, and devices, resulting in a co-simulation-approach. Co-simulations are a complex combination of different sorts of simulations that are run or solved in separate runtime environments. Real time co-simulations merge multiple types of simulations to create a hybrid simulation model (power system, ICT, cyber-security etc.), where various representations must be synchronized in order to run in universal time.

2.2 Real-time simulation

A simulation is "a representation of the operation or features of a system through the use or operation of another" (Sun et al., 2018). In this paper, we use a discrete-time simulation or fixed time-step simulation for the platform development as it is suitable for the real-time simulation. Each system state or variable will be solved mathematically based on a selected solver at a given time-step. We obtain the results via off-line and in real-time simulations, however offline is faster than online. A given discrete time-step simulation might be differ (e.g., shorter or longer) in comparison to the actual required time to compute equations and functions that represent a system model. Figure 2. represents these two possibilities: (a) computing time is shorter than a fixed time-step, (b) computing time is longer than a fixed time-step. Whereas in (c) both times are synchronized. It also shows all operations including driving inputs and outputs (I/O) to and from externally connected devices. In addition, it is noted that the solving system speed relies upon the accessible calculation power and the system numerical model complexity.

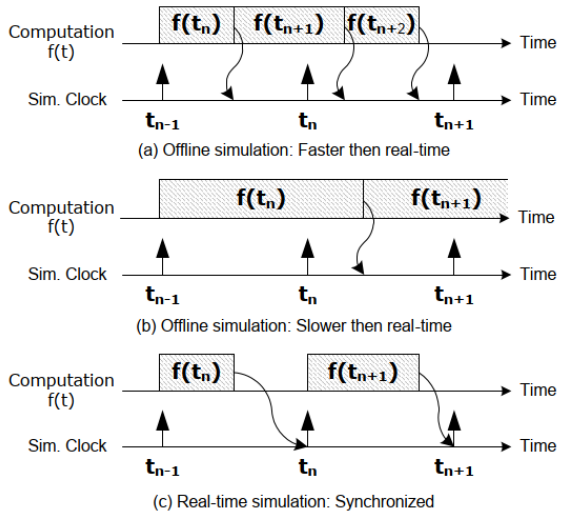

Figure 2. Real-time simulator computation

Computation accuracy is determined by two factors: the precise dynamic representation of the system and the time required for producing results. The accuracy and

validity of a real-time simulation is determined by performing all internal computations and performing results outputs that are compared to actual devices.

2.3 Model for designing and testing a real-time simulation

We apply the Mode-based Design (MBD) method. MBD is a mathematical and graphical methodology for expressing the system under test, and it adheres to the "V" diagram workflow as shown in Figure 3.

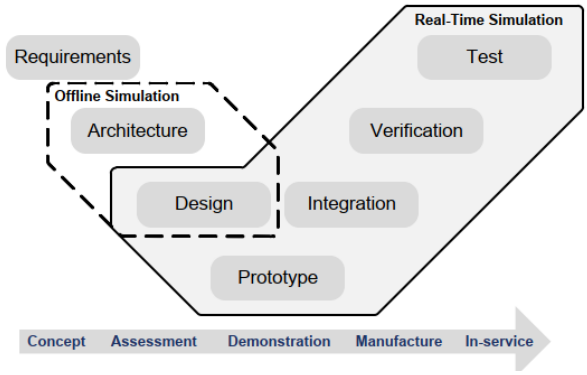

Figure 3. Model-based Design Workflow

This model provides a comprehensive view of the system under development with diverse domain knowledge. It also provides abilities for engineers who are involved in designing, modeling, testing, and utilizing models in an efficient and organized manner. For example, it allows automated testing with different parameters under different circumstances. It is reusable and the designed environment can remain homogeneous through different design tools via import/export model tool's features. The majority of those tools provide an automatic code generator for the designed models. As a result, the import/export features in those tools are easy to use. Even if they are developed using different design tools, the predesigned/old model will be imported and included as a block in the new design model. Thus, the use of an automatic code generator adds value to real-time simulation in MBD.

Combining an automatic code generator and a real-time simulator make a rapid control prototyping (RCP) implementation from the testing model point view with minimal effort. The prototype can then be used to speed up integration and verification testing, something that offline simulation cannot do. The same concept is valid also for the HIL testing. By using an HIL test, hardware testing can be performed earlier in the process, sometimes before an actual plant is available. For example, electrical system automotive controller testing functionality can be performed early even before a physical plant is completed. As a result, designed issues can be identified earlier in the process, allowing required tradeoffs to be determined and applied, lowering development cycle/costs.

2.4 Cyber physical security platform

As discussed in the aforementioned section, the energy system is a multidisciplinary study due to the involvement of various fields, ranging from electric power, ICT systems, cyber security to computing science. As a result, universities have recently updated their engineering programs curriculum, such as adding new courses or updating materials for existing courses (Langner, 2011; de Reuver et al., 2018). Those courses are often designed with lab practices, this leads to a high demand for labs that allow learners to be able to practice and learn hands-on-skills. The dilemma is that an energy system contains several devices (e.g., generators, transmission line transformer) while establishing a lab and managing those devices are challenging in terms of technical difficulties, costs, and human resources.

A real-time CPS platform includes a simulator that combines energy system simulation software and emulation (e.g., communication system and cyber physical security), software/tools (e.g., co-simulation). The platform provides a holistic experience to both trainers and trainees. Also, it enables the trainer to visualize their specific energy system and/or communication network environments in a manageable laboratory setting (digital twins; replica of real physical system). Moreover, CPS platform provides functions to analyze a variety of "what if" scenarios in order to assess impacts of different circumstances.

CPS platform supports researchers who are working to find solutions beyond the state-of-the-art. This is because of its designed and development capabilities, such as energy system components, communication system interfaces/protocols and cyber security entities.

3 Development of CPS Platform

A digital energy system has a cross-disciplinary nature that has different domain competencies. This cross-disciplinary is amplified by combining required CPS competence with others (e.g., power system simulation model, communication simulation/emulation model) competencies. To this end, educators are subject to a variety of tools and concepts that are associated with various domains. Subsequently, new instructive teaching/training methods/techniques should be developed along with tools. This enables relevant parties in dealing with various domains and combining their knowledge into a single solution. This solution enables educators to comprehend coupling and interaction among entities that comprise the integrated developed solution. As a result, it is natural that the CPS platform be developed in such a way that educators can learn by bridging the gap between theory and real-world application.

To achieve this goal, we design a CPS platform with a real-time simulator as the mean core of the lab, along

with other different development boards and Field-programmable gate arrays (FPGAs). The simulator is from Opal RT (e.g., OP5700 Real-Time Simulator) with HYPERSIM modeling software which simulates the power system. Our platform's emulator is Scalable EXata communication simulation/emulation software, which simulates/emulates the communication network with cyber-attack modules. This HYPERSIM-software's simulator has the capability to accurately mimic the response of an actual physical system in real-time. Also, it has multiple interface modules, including analog and digital channels, as well as, a variety of communication protocols including IEC 61850 Generic Object-Oriented Substation Event (GOOSE) and SV, IEEE C37.118, DNP3, Modbus.

In the context of CPS, using an RTS allows a simulation to interface with a cyber system in real-time and achieve a more complete and realistic testing environment. Here, SCALABLE has developed a highly-specialized kernel to exploit contemporary multi-core architectures for real-time execution of large-scale, high-fidelity network and cyber models. It uses a network digital twin to represent entire CPS communication networks, various protocol layers, application layers, physical layers, and devices. It includes a low-skew synchronization kernel to connect with live applications and equipment, which communicates throughout the digital twin just as it would run on physical networks. A suite of simulated cyberspace attacks and defenses interact with every layer of the emulated network. These include network security protocols, firewall models, port and network scanning, DoS, stimulation of intrusion detection systems, vulnerability exploitation, packet modification, virus and worm propagation and defense, backdoors, rootkits, botnets, and others. The system can also integrate real exploitation tools into a safe lab environment. Running real data feeds e.g., GOOSE, though the system can subject these feeds to delay, degradation or even substitution. The system enables actual cyber defense technologies to be deployed and integrated with the emulated network, the cyberspace attacks, and the virtual representations of systems to assess the effectiveness of tools, techniques and architectures to ensure system-of-systems availability. These two software are tightly linked together via a developed functionality to automate virtual link creation. Using the virtual links ensures mapping between HYPERSIM and EXata dedicated sender and receiver, that a packet being sent at one interface of the link will be only received at the other interface as illustrated in Figure 4.

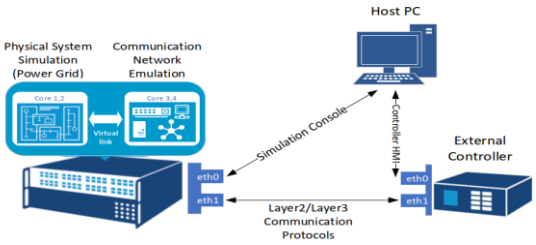

Figure 4. CPS platform setup

The closed-loop testing environment offered by CPS platform will allow the unit under test to interact with the CPS platform in a real-time manner. Using this closed-loop testing specifically for cyber security research is more beneficial, because in this situation, based on cyber incidents cascaded events in the energy system that will generate large-scale disruption. Studying such events by performing after-fault analysis, developing prediction strategies, and testing mitigation solutions can be easily implemented by using the automatic statistical reports generation for each entity with the test.

In addition, the CPS platform has great benefits that has a graphical user interface on the Host PC to facilitate scenario creation and real-time visualization of the power system and the communication system parameters. In addition, it can be used at runtime to launch cyber-attacks, or alternatively, the attacks can be predefined in the scenario while it's running which accelerates the workflow and eliminates human errors in configuration. Given the benefits of using a real-time simulator, particularly with this new integrated solution, there's several challenges to consider.

4 CR-DES CPS Platform scenarios

The provided SIL "Cyber-Physical Simulation of a Microgrid Subject to Cyber-Attacks" example developed by Opal RT and Scalable EXata forms the basis for the development of HIL use-cases. These examples are used to validate and test the CPS platform's operation and results validation. The first SIL is an example of a cyber-physical simulation involving a cyber-attacked microgrid. An OPAL-RT Real-Time Simulator co-simulates a microgrid system, including its distributed energy resources (DERs), power converters, and loads modeled in HYPERSIM, as well as the underlying communication network in EXata CPS as illustrated in Figure 5. Technical descriptions of microgrid units and testing results discussions are beyond the scope of this paper and will be published in other works as part of the CR-DES project dissemination plan.

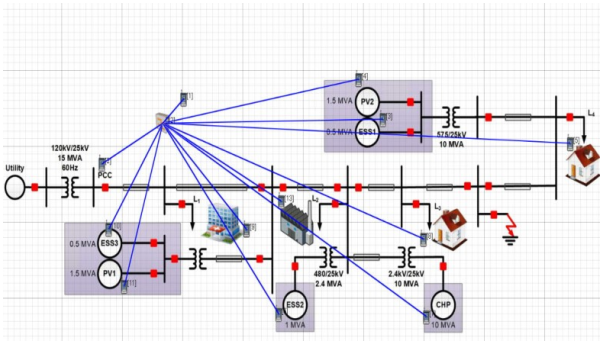

Figure 5. SIL microgrid subject to cyber attack, blue lines show the communication links that every MG node entity (DERs, loads, CB, etc.) send measurements, status to the MGC and received controlling signal from the MGC based on GOOSE IEC 61850 standard protocol

Each microgrid asset has a subsystem measurement that generates P, Q, and Vrms measurements based on voltage and current measurements. Internal microgrid controller MGC (Node 1) is a simulated MGC that has been implemented on the same model (SIL). The primary role of the MGC is to receive measurements from measurement subsystems and use these measurements to send reference set points to some of the DERs. As well as to keep the balance between the generated and consumed power by the DERs and loads respectively. Two scenarios had been designed and tested as follows.

1.1 Scenario 1

The first scenario the grid will be islanded in second 1, and in this islanded mode in order to insure the power balance between DERs power generation and load power consumption. The MGC is designed in a way that needs to send a dispatching signal to shed loads 4 (noun critical load), if there is a difference between DERs power generation and load power consumption as fast as possible. This power difference should be more than 3MW. The MGC is using the IEC 61850 GOOSE protocol for sending and receiving via EXata communication emulation features. In addition, MGC attempts to enable voltage support and keep the microgrid physical parameters measurement values such as (frequency, grid RMS voltages etc.,) close to the nominal operation values.

Next step within scenario one, a delay cyber-attack module will be introduced (1 second delay) via EXat emulation software. According to this delay attack the trip command within the GOOSE messages that send from MGC to open CB Load4 (disconnect Load 4) will be delayed by 1 second. This delay attack will initiate large disturbance that might lead to blackout e.g., Large frequency deviation, before being regulated back to its nominal value, hard and longer voltage dip down under its nominal value, with increased voltage oscillations as illustrated in Figure 6.

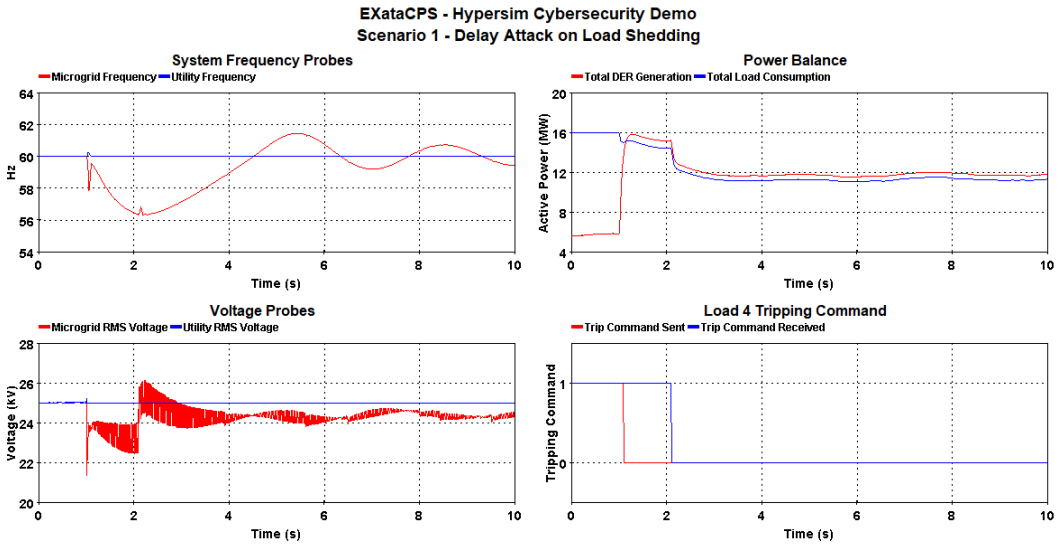

Figure 6. Microgrid subject to delay attack scenario 1. In the bottom right of the figure, the red line is the original trip signal sent from the controller to shed load 4 after the grid is islanded in the second one, which it is in time. Whereas the blue line is the delayed signal. Trip command sent by the MGC is delayed by one second after we apply the cyber delay attack to the controller signal. The bottom left figure shows a hard and longer voltage dip down to 23 kV, with increased voltage oscillations happening along with execution of the delay attack. Also, on the up left figure shows large frequency deviation, before being regulated back to its nominal value after second two. In the right up of the figure it shows the power unbalance and the mismatching between power supply (red curve) and demand (blue curve) before second two (based on the delay attack). However, the grid attempts to tackle the problem and return back to normal operation after the second and keep the balance between the generated and consumed powers.

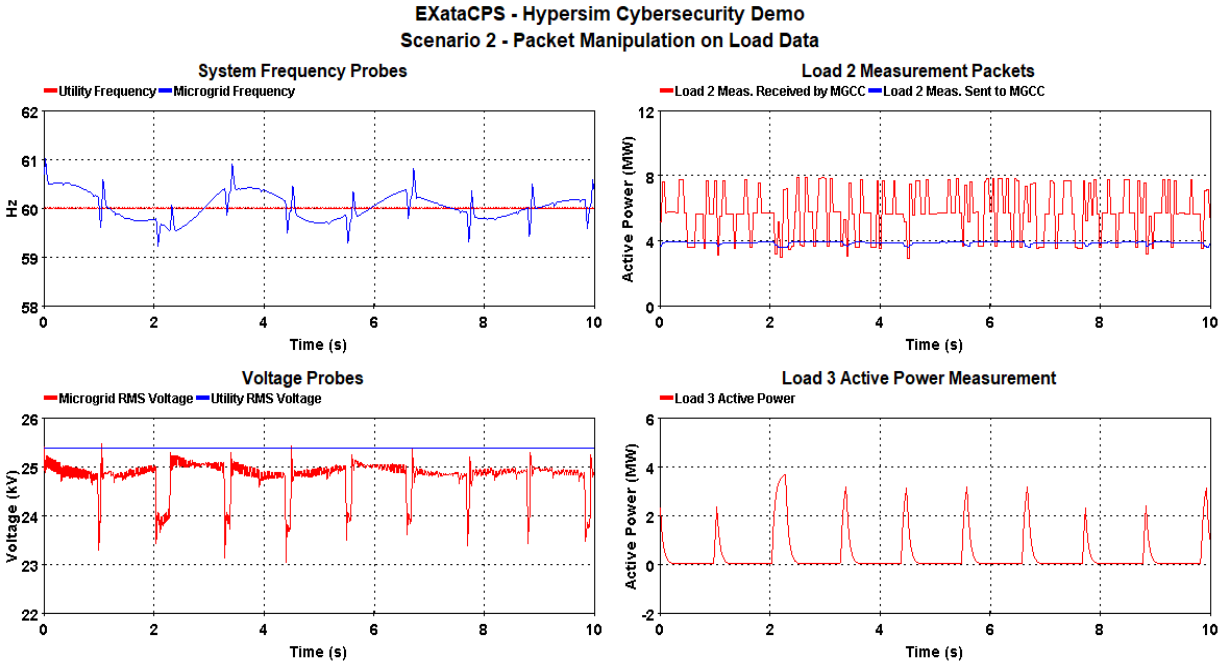

Figure 7. Microgrid subject to man-in-the-middle attack scenario 2. In the top right picture load 2 measurements, red curve is manipulated before they are received by the MGC based on executing the man-in-the-middle attack, blue curve is the normal load 2 measurements before executing the attack. The bottom right shows the load 3 active power consumption which is fluctuated between (0 and 4MW) since it is connected and disconnected to the grid based on the executing the man-in-the-middle attack that duplicate load 2 consuming power and the MGCC is programmed to shed the priority load 3 if the mismatch between generation and load exceeds 3 MW. Smart grid also suffers from declining power quality voltage oscillations as shown in the bottom left of the figure and also high frequency oscillations as shown in the up left of the figure.

1.2 Scenario 2

Microgrid is landed in steady state operation mode subject to man-in-the-middle cyber-attack. According to this scenario manipulation to Load 2 power consumption metermen's is duplicated within the EXata software (cyber-attack modules) on its way before it is received by the MGC. In this case MGCC will periodically trips and reconnects load 3 since MGCC is programmed to shed the priority load 3 if the mismatch between generation and load exceeds 3 MW. In addition, the microgrid under test also suffers from declining power quality, including high frequency and voltage oscillations as illustrated in Figure 7.

Consequently, various types of cyber-attacks, such as denial of service (DoS), buffer issues, virus sniffing, etc., can be carried out. Different monitoring and defensive network techniques, such as firewalls, intrusion detection ID, intelligent agents, defenders, etc., can also be designed and implemented for effective operational testing and assessing the resilience of energy system communication networks to cyber threats.

5 Conclusions

The CPS security platform is proposed in this paper and we show the requirements for testing of complex design systems in a variety of situations (e.g., steady state, transition, and attack) during both the development phase and prior to final system commissioning. As well as we present the feasibility of the developed CPS security platform to accomplish these tasks. Furthermore, we demonstrate one case study (SIL) in which real-time traffic based on the IEC 61850 GOOSE protocol has been exchanged between the smart grid nodes and controller. This real-time traffic is subject to cyber attack. We also present the architecture of cybersecurity and resilience of digital energy systems as well as its basic functionalities.

Acknowledgments

This study was partly funded by the European Regional Development Fund and the Regional Council of Ostrobothnia.

References

Duong Dang and Tero Vartiainen. Digital Strategy Patterns in Information Systems Research. *Pacific Asia Conference on Information Systems (PACIS) 2019 Proceedings,* 2019.

Duong Dang and Tero Vartiainen. Changing Patterns in the Process of Digital Transformation Initiative in Established Firms: The Case of an Energy Sector Company. *Pacific Asia Conference on Information Systems (PACIS) 2020 Proceedings,* 2020.

Duong Dang, Tero Vartiainen, and Mike Mekkanen. Towards Establishing Principles for Designing Cybersecurity Simulations of Cyber-Physical Artefacts in Real-Time Simulation. *Proceedings of International Conference on Information Systems Development (ISD),* 2021.

Stephen Ison, Lucy Budd, Magdi S. Mahmoud, and Yuanqing Xia, eds. Chapter 13 - Secure Estimation Subject to Cyber Stochastic Attacks. Pp. 373–404 in *Cloud Control Systems*, *Emerging Methodologies and Applications in Modelling*. Academic Press, 2020.

R. Langner, Stuxnet: Dissecting a Cyberwarfare Weapon. *IEEE Security Privacy* 9(3):49–51, 2011. doi: 10.1109/MSP.2011.67.

Mike Mekkanen, and Kimmo Kauhaniemi. Wireless Light-Weight IEC 61850 Based Loss of Mains Protection for Smart Grid. *Open Engineering* 8(1):182–92, 2018. doi: 10.1515/eng-2018-0022.

Mike Mekkanen, Tero Vartiainen, Kimmo Kauhaniemi, and Duong Dang. Intelligent Micro Grid Controller Development for Hardware-in-the-Loop Micro Grid Simulation Subject to Cyber-Attacks. Oulu, Finland, 2021.

Mike Mekkanen. Cybersecurity and Resilience of Digital Energy Systems. Opal-RT 21, Conference, 2021.

Ivan L. G. Pearson. Smart Grid Cyber Security for Europe. *Energy Policy* 39(9):5211–18, 2011. doi: 10.1016/j.enpol.2011.05.043.

Mark de Reuver, Carsten Sørensen, and Rahul C. Basole. The Digital Platform: A Research Agenda. *Journal of Information Technology* 33(2):124–35, 2018. doi: 10.1057/s41265-016-0033-3.

Chih-Che Sun, Adam Hahn, and Chen-Ching Liu. Cyber Security of a Power Grid: State-of-the-Art. *International Journal of Electrical Power & Energy Systems* 99:45–56, 2018. doi: 10.1016/j.ijepes.2017.12.020.

C. B. Vellaithurai, S. S. Biswas, and A. K. Srivastava. Development and Application of a Real-Time Test Bed for Cyber–Physical System. *IEEE Systems Journal* 11(4):2192–2203, 2017. doi: 10.1109/JSYST.2015.2476367.

MPC Operation with Improved Optimal Control Problem at Dalsfoss Power Plant

Changhun Jeong[1] Beathe Furenes[2] Roshan Sharma[1]

[1]Natural Sciences and Maritime Sciences Department of Electrical engineering, Information Technology and Cybernetics, University of South-Eastern Norway, Porsgrunn, Norway
{Changhun.Jeong,Roshan.Sharma}@usn.no
[2]Skagerak Kraft AS, Norway

Abstract

The operational conditions at the Dalsfoss power station are complicated due to many requirements such as environmental regulations and safety constraints. Model predictive control (MPC) has been in use at this power station to control the floodgates at the Dalsfoss dam. However, the current formulation of MPC at the power plant does not have routines to explicitly handle output constraints. In this paper, a new improved optimal control problem (OCP) is formulated for the operation of the flood gates at the Dalsfoss power station. This new OCP formulation is thought to be relatively easier for the operators to understand and it is more flexible to the violation of constraints. The aim of this paper is to extend the current MPC used at the power plant so that the output constraints are systematically included in the new improved MPC formulation. Two alternatives are presented and their robustness to an uncertain disturbance is analyzed through robustness analysis.

Keywords: Model predictive control, optimal control problem, flood management, uncertainty, robustness analysis

1 Introduction

Kragerø watercourse is one of many watercourse systems that Skagerak Kraft operates. The watercourse contains one dam and five hydropower stations which are located between lake Toke and the sea sequentially along the watercourse as shown in Figure 1. Its catchment area is over 1200 square kilometres and lies mainly in Telemark, Norway. The uppermost power plant is the Dalsfoss power plant which is located next to the dam (SkagerakKraft, 2021b). The system has intakes to three turbines and two flood gates (SkagerakKraft, 2021a).

Skagerak Kraft is fully responsible for the safety of the operations at the Dalsfoss power station. Therefore, requirements by the Norwegian Water Resource and Energy Administration (NVE) must be complied with to ensure safe and environmental-friendly operation. Some of these requirements are environmental-related and are imposed to prevent damages to the inhabitants and the ecosystem

Figure 1. Overview of the Kragerø watercourse (SkagerakKraft, 2021b).

around the water system. One of the most important constraints is to maintain the level of water at Merkebekk within a specific range. The range is not constant and changes over the months within a year (NVE, 2021). It is not easy to satisfy the requirement all the time during the operation due to two uncertainties in the system. One is the power production plan to meet the energy demand. The other is the water inflow to the lake/dam. Skagerak Kraft creates the power production plan and uses it to operate the plant. Water inflow to the lake is predicted by using a complex hydrological model and weather forecast information. As the result, the predicted water inflow is given as 50 possible future scenarios for the next 13 days.

MPC is known as an attractive multivariable constrained control approach with its ability to effectively deal with the complex dynamics of systems with multiple inputs and outputs and constraints. (Morari and H. Lee, 1999; Mayne, 2014). Therefore, a reference region tracking MPC based on a mathematical model of the system was suggested for the operation of the Dalsfoss power station (Lie, 2014). More research has been conducted since the first MPC was suggested in 2014. A better parameter fitting on the model was suggested due to a poor description of the model during a severe flood in September 2015

(Kvam et al., 2017). To obtain optimal operation under the uncertainty of water inflow, the use of multi-objective optimization (MOO) MPC was investigated with the OCP used in the reference region tracking MPC (Menchacatorre et al., 2019).

However, in the works of Lie (2014) and Menchacatorre et al. (2019) the water level at the dam (which is an output of the system under consideration) has not been explicitly handled as an output constraint, but is rather dealt indirectly using a complex cost/objective function during the formulation of the control problem. In this paper, two alternatives have been proposed to handle the concession requirements of the level at the dam by explicitly considering them as output constraint. Pros and cons of these two alternatives are discussed thoroughly in Section 3.

2 System Description

2.1 System model

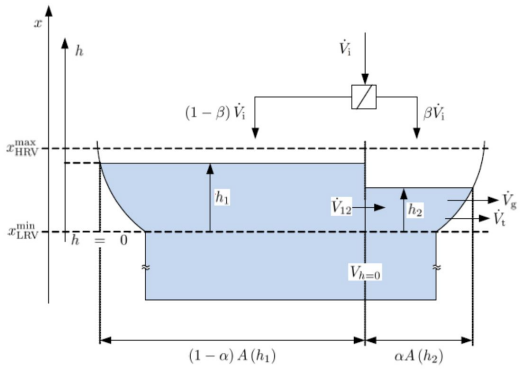

Figure 2. Schematic of lake Toke (Lie, 2014)

Figure 2 depicts a simplified layout of the lake Toke. The layout is divided into two parts. The left side of the layout represents the upper stream of lake Toke, Merkebekk. The right side describes the lower stream of lake Toke, near the Dalsfoss dam.

h_1 and h_2 are the height of water level above the minimal low regulated level value, $x^{\min}_{\mathrm{LRV}}$, at Merkebekk and Dalsfoss respectively. The water levels are states of the system. $\dot{V}_\mathrm{i}$ is the time-varying volumetric flow into Lake Toke from its catchment. $\dot{V}_\mathrm{i}$ is split to both Merkebekk and Dalsfoss as shown in Figure 2. Skagerak Kraft has a hydrological model to calculate $\dot{V}_\mathrm{i}$ with the weather forecast information they subscribe to. It is an input disturbance to the system. The other disturbance is the power demand denoted as W_e. It is scheduled by specialists in Skagerak Kraft. W_e is used to calculate the turbine flow, $\dot{V}_\mathrm{t}$, which means the required water flow rate to generate electrical power. $\dot{V}_\mathrm{t}$ is limited as operational condition by $36\mathrm{m}^3/\mathrm{s}$. $\dot{V}_\mathrm{g}$ is the flow rate through floodgates. Water that flows through flood gates does not produce any electrical power since they are not sent through turbines but simply discarded from the dam. Ideally, the flood gates should be kept closed as much as possible to conserve water in the dam for energy production and they should be activated only in a flood situation to satisfy concession requirements. Figure 3 shows the simplified schematic of the floodgate at the Dalsfoss dam. The gate opening height denoted h_g is the control input for the system.

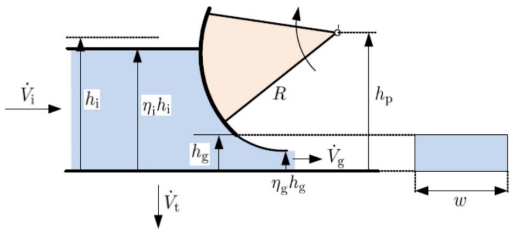

Figure 3. Structure of floodgate (Lie, 2014)

The model of lake Toke was developed and its update has been suggested (Lie, 2014; Kvam et al., 2017). A summary of the model follows:

The heights of water level relative to sea level at Merkebekk and Dalsfoss, denoted x_M and x_D, are given by:

$$x_\mathrm{M} = h_1 + x^{\min}_{\mathrm{LRV}} \tag{1}$$

$$x_\mathrm{D} = h_2 + x^{\min}_{\mathrm{LRV}} \tag{2}$$

The area of the surface curve at lake Toke is calculated as:

$$A(h) = \max(28\times10^6\cdot1.1\cdot h^{\frac{1}{10}}, 10^3) \tag{3}$$

Inter compartment flow $\dot{V}_{12}$ is expressed as:

$$\dot{V}_{12} = K_{12}\cdot(h_1-h_2)\sqrt{|h_1-h_2|} \tag{4}$$

where K_{12} is Inter compartment flow coefficient.
The equation to calculate $\dot{V}_\mathrm{t}$ from the electrical power demand W_e is:

$$\dot{V}_\mathrm{t} = a\frac{\dot{W}_\mathrm{e}}{x_\mathrm{D}-x_\mathrm{q}} + b \tag{5}$$

where a and b are coefficients from data fitting. x_q means downstream level after the turbine which can be obtained by solving the following cubic equation:

$$\begin{aligned} 0 = {} & c_1x_\mathrm{q}^3 + (c_2 - c_1x_\mathrm{D})x_\mathrm{q}^2 \\ & + (c_3 - c_2x_\mathrm{D} + c_4\dot{V}_\mathrm{g})x_\mathrm{q} \\ & + \dot{W}_\mathrm{e} - c_3x_\mathrm{D} - c_4\dot{V}_\mathrm{g}x_\mathrm{D} - c_5 \end{aligned} \tag{6}$$

where c_1, c_2, c_3, c_4, and c_5 are coefficient obtained from polynomial model fitting.
At Dalsfoss power plant there are two flood gates. The model for flow rate through floodgate j, $\dot{V}_{\mathrm{g},j}$, is:

$$\dot{V}_{\mathrm{g},j} = C_\mathrm{d}w_j\cdot\min(h_\mathrm{g},h_2)\sqrt{2g\cdot\max(h_2,0)} \tag{7}$$

where C_d is discharge coefficient and g is acceleration of gravity.
The total water outflow from the Dalsfoss power station, $\dot{V}_o$, is calculated as:

$$\dot{V}_o = \dot{V}_t + \sum^{j} \dot{V}_{g,j} \tag{8}$$

The dynamic model of states, h_1 and h_2, are expressed as:

$$\frac{dh_1}{dt} = \frac{1}{(1-\alpha)A(h_1)}((1-\beta)\dot{V}_i - \dot{V}_{12}) \tag{9}$$

$$\frac{dh_2}{dt} = \frac{1}{\alpha A(h_1)}(\beta\dot{V}_i + \dot{V}_{12} - \dot{V}_t - \dot{V}_g) \tag{10}$$

Parameters for the model are given in Table 1.

2.2 Operational constraints

Operational constraints on lake Toke are specified by NVE. They are designed to achieve (i) operational safety, (ii) securing ecological diversity, and (iii) avoiding property damage, e.g., by maintaining certain minimum and maximum levels at Merkebekk. The key constraints for a flood situation are:

1. The total water outflow from the Dalsfoss power station, V_o, should remain as steady as possible. This requirement is to keep people and animals safe from the sudden change of the water outflow and level at the downstream.

2. The minimum flow rate of the total water outflow should be bigger than $4\mathrm{m}^3/\mathrm{s}$. This restriction is not to disturb the ecosystem in the downstream, e.g to allow fishes to move freely, etc.

3. The water level at Merkebekk, x_M, must stay within a range:

$$x_M \in [x_{LRV}, x_{HRV}]$$

   where x_{LRV} and x_{HRV} denote the low regulated value and the high regulated value for the water level respectively. The seasonal change on level constraints throughout a year is briefly shown in Figure 4. This level constraint exists for not disturbing fauna along the shoreline, but also to prevent damages or inconvenience such as flooding properties or putting boats on dry land, etc. This constraint can be violated to satisfy the second constraint by going lower than x_{LRV} . However, the level of water at Merkebekk should never exceed the maximal high regulated value denoted as x_{HRV}^{max}.

4. When severe flooding occurs x_M can exceed x_{HRV}. However, after the culmination of flooding ends, x_M must reach x_{HRV} as soon as possible.

5. When the winter operation is terminated, the water level in the reservoir must reach x_{LRV}^{summer} quickly. However, the flow rate at the downstream, V_o, is limited to $20\mathrm{m}^3/\mathrm{s}$ until the water level is at the target level.

6. Although there is the minimum required flow rate at the downstream, $V_o \geq 4\mathrm{m}^3/\mathrm{s}$, it is more beneficial economically to have the flow rate larger than $10\mathrm{m}^3/\mathrm{s}$, which enables the operation of the four sequentially located power plants along the watercourse.

The fourth and fifth constraints mentioned above requires the judgement of the professional on sites such as when flooding begins and when the winter operation is completed. Therefore, in this paper, the two constraints are not considered.

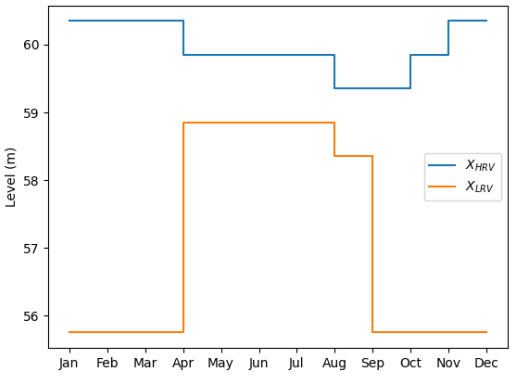

Figure 4. Water level constraint changes throughout year

3 Optimal Control Formulation

In this section, two alternative OCP formulations to improve the the current MPC used at Dalsfoss hydropower plant are presented. These two alternative MPC formulations can be regarded as extensions of the current MPC.

3.1 Reference region tracking OCP with output constraints

In the reference region tracking MPC currently being used at Dalsfoss, the water level at the dam is controlled to lie between the upper and the lower limits (see Figure 4) by formulating a complex objective function containing a reference region as,

$$\min \sum_{i=1}^{N} \omega_R R^2(x_{t+i}) + \omega_{\Delta u} \Delta u_{c,t+i-1}^2 + \omega_u u_{c,t+i-1}^2 \tag{11}$$

Here ω is a weight matrix and N is length of the prediction horizon. u is control input and it has operational constraint such as $u_{c,i} \in [0, h_{g,max}]$. $h_{g,max}$ means the maximal

Table 1. Parameters for Lake Toke model

Parameter	Value	Unit	Comment
α	0.05	-	Fraction of surface area in compartment 2
β	0.02	-	Fraction of inflow to compartment 2
K_{12}	800	$\mathrm{m}^{\frac{3}{2}}/\mathrm{s}$	Inter compartment flow coefficient
C_d	0.7	-	Discharge coefficient, Dalsfoss gate
w_1	11.6	m	Width of Dalsfoss gate 1
w_2	11.0	m	Width of Dalsfoss gate 2
$x_{\mathrm{LRV}}^{\min}$	55.75	m	Minimal low regulated level value
$x_{\mathrm{HRV}}^{\max}$	60.35	m	Maximal high regulated level value
g	9.81	$\mathrm{m/s}^2$	Acceleration of gravity

allowed opening height of the floodgate. Δu denotes the gate opening changes which is:

$$\Delta u_{\mathrm{c},t} = u_{\mathrm{c},t} - u_{\mathrm{c},t-1} \tag{12}$$

The level reference term in Equation 11, $R^2(x_{t+i})$, is expressed as:

$$R(x_{t+1}) = \min(x_{\mathrm{M},t+1} - \gamma_{t+i}^{\mathrm{l}}, 0) + \max(x_{\mathrm{M},t+1} - \gamma_{t+i}^{\mathrm{u}}, 0) \tag{13}$$

where $\gamma_{t+i}^{\mathrm{l}}$ and $\gamma_{t+i}^{\mathrm{u}}$ work as lower and upper boundaries of the reference region. They are calculated by:

$$\gamma_i^{\mathrm{l}} = (1 - X_\mathrm{R}) x_{\mathrm{LRV},i} + X_\mathrm{R} x_{\mathrm{HRV},i} \tag{14}$$

$$\gamma_i^{\mathrm{u}} = f(x_{\mathrm{HRV}}) - \delta_{\mathrm{HRV}} \tag{15}$$

where X_R and δ_{HRV} are the variable inputs that engineers can put their insight into. A typical value for X_R is 0.75. The purpose of δ_{HRV} is to have a slight margin wrt. the maximal allowed level for x_M. $f(x_{\mathrm{HRV}})$ is decided based on whether excessive flooding occurs or not as follow:

$$f(x_{\mathrm{HRV}}) = \begin{cases} x_{\mathrm{HRV}}^{\max}, & \text{for excessive flooding} \\ x_{\mathrm{HRV}} & \text{otherwise} \end{cases}$$

The reference level term in Equation 11 becomes zero when the water level at Merkebekk stays in the reference range defined by Equations 14 and 15. The reference term is only activated when the water level is outside of the reference range. Therefore, the weight on the use of floodgates (i.e. control inputs) and the rate of change of control inputs are more emphasized when the water level remains in the specified reference range. In this formulation, the only constraints are the input constraints, and the constraints on the water level are really only handled as a complex cost function. It is a well-known fact that only using a cost function does not guarantee constraint satisfaction. In this paper, the addition of output constraints on the water level at Merkebekk is suggested as,

$$x_{\mathrm{LRV}} \leq x_\mathrm{M} \leq f(x_{\mathrm{HRV}})$$

3.2 New OCP with constraint relaxation

When handling the flood gates, care should be taken that the water from the dam is not let out through flood gates unnecessarily. This would result in loss of water which otherwise could be used to produce electricity. In this sense, saving as much water as possible (i.e. having as high water level as possible) in the dam while still satisfying the concession requirements also becomes necessary. In this newly formulated OCP, the objective function is designed to maximize the water level at Merkebekk and is simpler compared to the objective function in the reference region tracking OCP, Equation 11 as:

$$\min \sum_{i=1}^{N} \omega_\mathrm{R} R_{\mathrm{new}}^2(x_{t+i}) + \omega_{\Delta\mathrm{u}} \Delta u_{\mathrm{c},t+i-1}^2 + \omega_\mathrm{u} u_{\mathrm{c},t+i-1}^2 + p^2 \omega_\mathrm{p} \tag{16}$$

The new reference term in Equation 16 is expressed as:

$$R_{\mathrm{new}}(x_{t+1}) = x_{\mathrm{M},t+1} - f(x_{\mathrm{HRV}}) v \tag{17}$$

Equation 17 is simpler than Equation 13. It is not only more effective to preserve the water as much as possible in the reservoir, but also easier for operators and engineers to understand.

The last term, $p^2\omega_p$ which is the penalty for violation of level constraints, is newly added. The variable p is the slack variable which is used to modify the level constraints as:

$$x_{\mathrm{LRV}} + p \leq x_\mathrm{M} \leq f(x_{\mathrm{HRV}})$$

The value of the slack variable is automatically decided by the optimizer since it is added to the list of the decision variable (Sharma, 2020). This term can offer more flexibility on optimization when the constraints are violated, for example when x_M goes lower than x_{LRV} to satisfy the minimum flow rate requirement on the total outflow, $V_\mathrm{o} = 4\mathrm{m}^3/\mathrm{s}$, the optimization would not fail (due to infeasibility) and cause the malfunction of the controllers in the system.

4 Simulation of Nominal MPC

This section presents the simulation results of nominal MPC using the two alternative OCP formulations as described in Section 3. For the simulation, the two disturbances, the power production plan and the water inflow to the lake Toke must be described.

For the simplicity of the simulation, the power production plan is assumed to generate maximum power. This can be achieved by setting a fixed value on V_t as $36\text{m}^3/\text{s}$. This is the maximum flow rate that can pass through the turbine at Dalsfoss hydropower station.

The actual data of water inflow prediction stored by Skagerak Kraft is applied for the simulation. The water inflow prediction is given each day as 50 possible future scenarios for the next 13 days. An example of the water inflow prediction is shown in Figure 5. It is the historical inflow prediction data recorded on 15th April 2020. The deviation of the inflow prediction tends to be bigger as time marches further into the future. The prediction data can be expressed in matrix form as Equation 18.

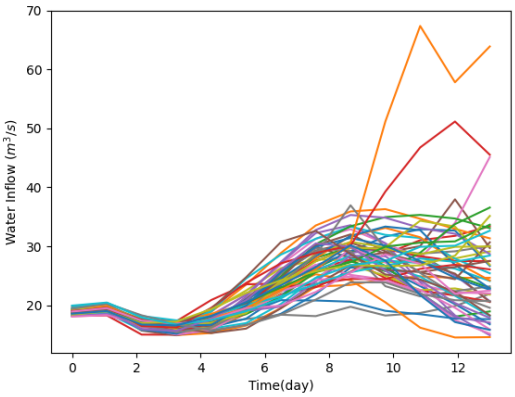

Figure 5. 50 ensembles of the water inflow prediction to lake Toke on April 15 2020

$$\dot{V}_{\text{i},t} = \begin{pmatrix} \dot{V}_{\text{i},t}^{(1)} & \dot{V}_{\text{i},t}^{(2)} & \cdots & \dot{V}_{\text{i},t}^{(50)} \\ \dot{V}_{\text{i},t+1}^{(1)} & \dot{V}_{\text{i},t+1}^{(2)} & \cdots & \dot{V}_{\text{i},t+1}^{(50)} \\ \vdots & \vdots & \ddots & \vdots \\ \dot{V}_{\text{i},t+12}^{(1)} & \dot{V}_{\text{i},t+12}^{(2)} & \cdots & \dot{V}_{\text{i},t+12}^{(50)} \end{pmatrix} \tag{18}$$

The rows in Equation 18 shows the time evolution of the water inflow prediction and the column represents the different 50 possible scenarios of water inflows. The prediction of the inflow to the lake is updated every 24 hours. For simulation of nominal MPC, the average value of the water inflow prediction is used. It is calculated as:

Table 2. Parameters for the simulations

Parameter	Value	Unit
X_{R}	0.75	-
δ_{HRV}	0.05	m
ω_{R}	10	-
$\omega_{\Delta\text{u}}$	1	-
ω_{u}	1	-
ω_{p}	100	-
$h_{\text{g,max}}$	5.6	m

$$\dot{V}_{\text{avg},t} = \begin{pmatrix} \text{Mean}(\dot{V}_{\text{i},t}^{(1)} & \dot{V}_{\text{i},t}^{(2)} & \cdots & \dot{V}_{\text{i},t}^{(50)}) \\ \text{Mean}(\dot{V}_{\text{i},t+1}^{(1)} & \dot{V}_{\text{i},t+1}^{(2)} & \cdots & \dot{V}_{\text{i},t+1}^{(50)}) \\ \vdots & \vdots & \ddots & \vdots \\ \text{Mean}(\dot{V}_{\text{i},t+12}^{(1)} & \dot{V}_{\text{i},t+12}^{(2)} & \cdots & \dot{V}_{\text{i},t+12}^{(50)}) \end{pmatrix} \tag{19}$$

The average is calculated on each time step with a new set of the water inflow prediction. The water inflow prediction based on the historical data is multiplied by a flood coefficient to simulate the flooding situations. The flood coefficient is set as 3 for the nominal MPC.

The period of simulation is set from April 15 to May 15 and includes a drastic change of the level constraints at Merkebekk. The simulation is performed with two different initial points for the water level to demonstrate two different situations. One initial point for the water level is located lower than the reference region and the other initial point is located in the reference region. Parameters for the OCPs are presented in Table 2. For the optimization, IPOPT in CasADi is used in Python (Andersson et al., 2019).

4.1 Simulation result: Initial water level below the reference region

Figure 6 shows the result of the simulation of nominal MPC at Dalsfoss power station using the reference region tracking MPC with output constraints when the initial water level at Merkebekk is below the reference region. The upper figure shows the level control and the lower figure shows the control actions during the simulation. The floodgate is supposed to remain closed to make the water level reach the reference region. However, floodgates are drastically opened several times and remain opened. It causes the water level to drop since the water is being thrown out from the reservoir. This abnormal action is due to the optimization problem becoming infeasible and the time-varying level constraints not being satisfied at such low water level. The optimizer then fails to find an optimal solution and produces incorrect and abnormal results.

Figure 7 shows the result of the simulation of nominal MPC using the newly formulated OCP with constraint relaxation as described in Section 3.2. The upper plot in Figure 7 represents the level changes and the lower plot shows the floodgate openings during the simulation. Thanks to

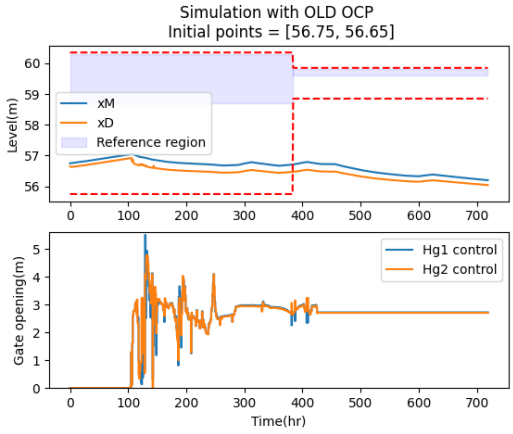

Figure 6. Simulation result of MPC at Dalsfoss station using the reference region tracking OCP with output constraints for initial water level lower than reference region. (upper plot - level control, lower plot - floodgate opening)

the penalty term, $p^2\omega_p$, in Equation 16, in the newly formulated OCP, output constraint (water level) relaxation is possible due to the use of slack variables. This does not cause any failures of optimization problem during the simulation. Therefore, as it is supposed to be, the floodgate stays closed. Despite the violation of the level constraint at around 380 hours, the water level is maximized and the level constraints are satisfied later at around 400 hours. The reason that the level constraint (lower constraint) is not fulfilled at ca. 380 hours is due to the control signals being saturated. The flood gates are completely closed and the inflow to the lake is not sufficiently large. Under this circumstance, this is the best the new OCP can perform without failing due to constraint relaxation.

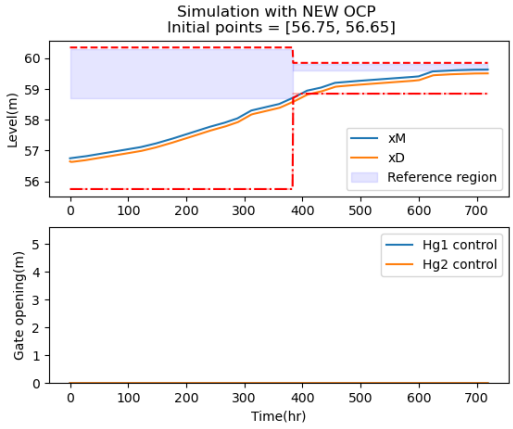

Figure 7. Simulation result of MPC at Dalsfoss station using the new OCP with constraint relaxation for initial water level lower than reference region. (upper plot - level control, lower plot - floodgate opening)

4.2 Simulation result: Initial water level in the reference region

Figure 8 shows the simulation result of nominal MPC using the reference region tracking MPC with output constraints. The initial point for the water level at Merkebekk is located inside of the reference region. The upper plot in Figure 8 shows the level change and the lower plot shows the gate openings during the simulation. The water level remains nearly constant but the water level is not maximized. The gate stays constantly opened and thus results in unnecessary loss of water through the flood gates.

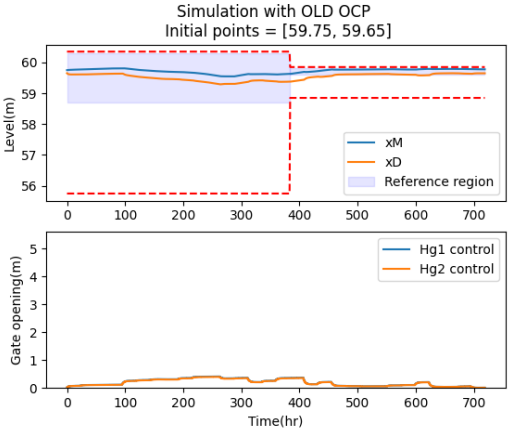

Figure 8. Simulation result of MPC at Dalsfoss station using the reference region tracking MPC with output constraints for initial water level in reference region. (upper plot - level control, lower plot - floodgate opening)

The simulation result of nominal MPC using the new OCP with constraint relaxation with an initial water level lying inside of the reference region is displayed in Figure 9. The upper plot shows the level change and the lower plot shows the gate openings during the simulation. The water level is maximized as intended to save as much useful water as possible in the dam. Achieving a higher level at the dam while still satisfying the concession requirement means more water is preserved in the reservoir, and this extra water can then be sent through the turbine later on to produce useful electric power (increased profit). This shows that the new OCP with constraint relaxation results in an improved operation of the hydropower plant.

5 Robustness Analysis

The realization of all possible water inflow, which means the first data of water inflow prediction on every update of the prediction every day, is presented in Figure 10.

With robustness analysis, the goal is to use the nominal MPC to all the individual 50 ensembles of the water inflow predictions. In order words, robustness analysis enables us to study the effect of applying a nominal/deterministic MPC to an uncertain system. Here uncertainty lies in the fact that any one of the 50 possible inflow forecasts can occur in the future in the real plant. The robustness analy-

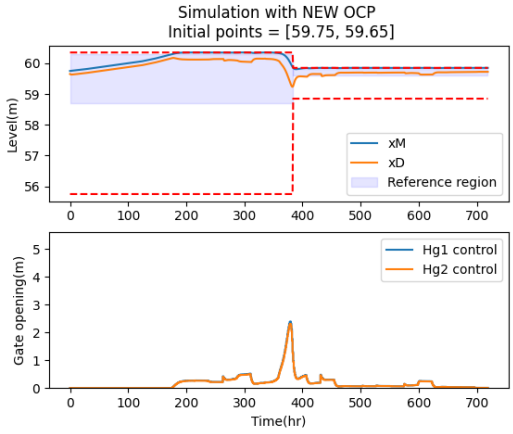

Figure 9. Simulation result of MPC at Dalsfoss station using the new OCP with constraint relaxation for initial water level in reference region. (upper plot - level control, lower plot - floodgate opening)

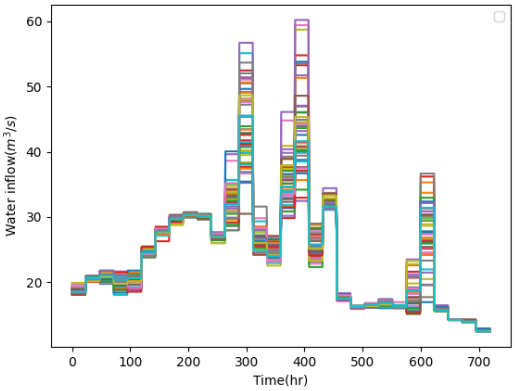

Figure 10. Plot of water inflow prediction

sis shows the possibility of constraint violation due to the influence of uncertainty. Since there are significant deviations in the realization of water inflow in each scenario, this section presents the result of the robustness analysis of nominal MPC using both OCPs as described in Section 3 at the Dalsfoss power station.

For robustness analysis, the nominal scenario must be chosen to get a sequence of the applied control input throughout the simulation time. Then, the sequence of the applied control input is used to evolve the states with different inflow forecast scenarios of the uncertainty by the system model as shown in Figure 11. The first scenario of water inflow prediction, $(\dot{V}^{(1)}_{\mathrm{i},t}, \cdots, \dot{V}^{(1)}_{\mathrm{i},t+12})$ in Equation 18, is chosen as the nominal prediction set and the other scenarios are considered as the possible future occurrences.

The flooding coefficient is set as 3 for the analysis. The initial water levels are located inside of the reference region so that the OCP for the reference region tracking MPC with output constraints does not fail to converge due to the violation of the time-varying level constraints (i.e., due to infeasibility).

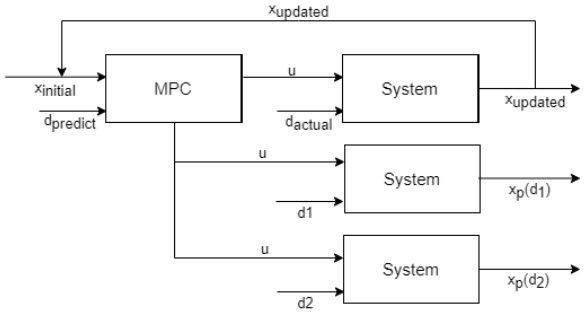

Figure 11. Scheme of robustness analysis

Figure 12 displays the result of the robustness analysis of nominal MPC with the reference region tracking OCP with output constraints. The violation of the level constraint does not occur. However, the water level is remained in the reference region instead of achieving the optimal states, i.e., maximizing the water level.

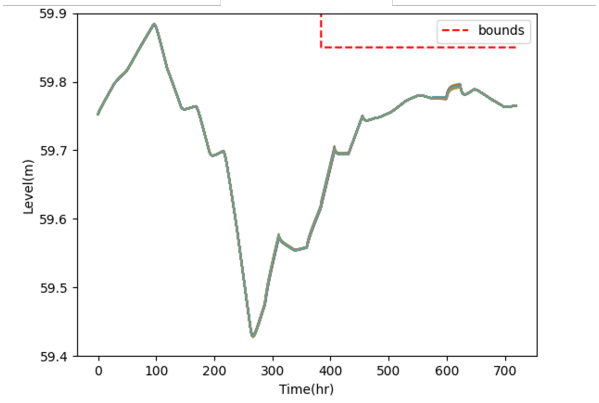

Figure 12. Robustness analysis on level control at Dalsfoss power station using the reference region tracking MPC with output constraints

The robustness analysis result with the new OCP with constraint relaxation is shown in Figure 13. The areas marked by blue and green colours in Figure 13 are displayed in Figure 14 and Figure 15 respectively. The potential violation of the level constraint is detected by 1384 times throughout the simulation period. when the nominal MPC with new OCP is applied to the uncertain system, the level constraints are not always satisfied for all the possible water inflows to the lake that can happen in the future. Some realizations can result in the violation of constraints. This reflects reality since in the real plant, water inflow to the lake can be dictated by one (or some other) of the possible forecast realizations.

6 Conclusion

The new OCP with constraint relaxation shows some improvements over the OCP for the reference region tracking MPC with output constraints. As presented in Section 4, it not only saves more water in the reservoir compared to the reference region tracking with output constraints but

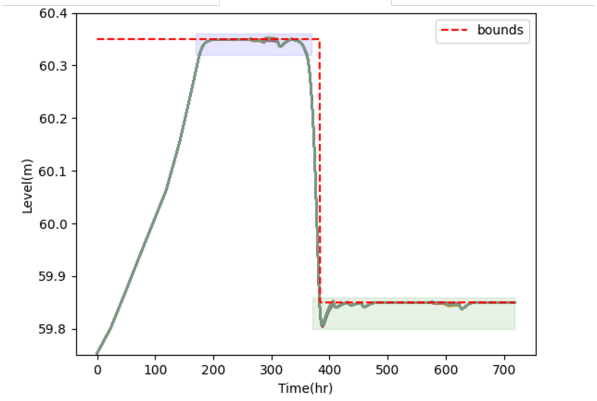

Figure 13. Robustness analysis on level control at Dalsfoss power station using the new OCP with constraint relaxation

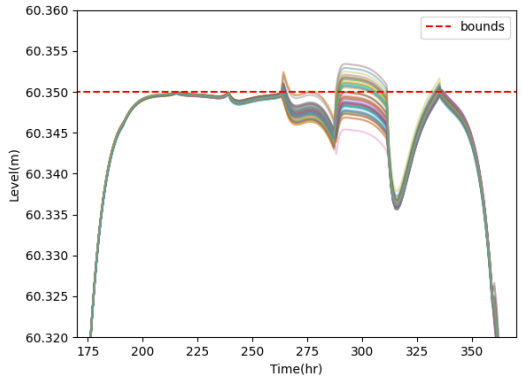

Figure 14. Enlarged robustness analysis on level control at Dalsfoss power station using the new OCP with constraint relaxation : time = [170,370]

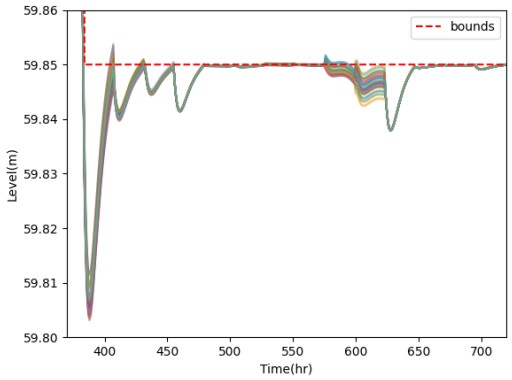

Figure 15. Enlarged robustness analysis on level control at Dalsfoss power station using the new OCP with constraint relaxation : time = [370,720]

also, did not cause any failure on optimization due to infeasibilities. Also, since the new OCP with constraint relaxation is simpler, it should be easier for the operators and engineers on the site to understand. More study should be performed with the new OCP with constraint relaxation by using more realistic operational scenarios including the use of power production plan in the future.

In robustness analysis, a flood situation is assumed by setting the flood coefficient as 3. The new OCP with constraint relaxation shows the vulnerability compared to the reference region tracking MPC in terms of the robustness of MPC. While the reference region tracking MPC has no potential violations on the level constraint, the MPC with new OCP displays 1384 times of the potential violation. However, this kind of possible constraint violation can be mitigated by employing a stochastic MPC or putting the safety margin. For the use of the stochastic MPC, the new OCP with constraint relaxation in this paper may be more beneficial to use due to its flexibility on output constrained optimization and its behaviour to save more water at the dam.

References

Joel A E Andersson, Joris Gillis, Greg Horn, James B Rawlings, and Moritz Diehl. CasADi – A software framework for nonlinear optimization and optimal control. *Mathematical Programming Computation*, 11(1):1–36, 2019. doi:10.1007/s12532-018-0139-4.

Kristian D. Kvam, Beathe Furenes, Åsmund Hasaa, Alexander Zhang Gjerseth, Nils-Olav Skeie, and Bernt Lie. Flood control of lake toke: Model development and model fitting. 2017. ISSN 1650-3686. URL `http://hdl.handle.net/11250/2466966`.

Bernt Lie. Final report: Kontrakt nr inan-140122 optimal control of dalsfos flood gates- control algorithm. 2014.

David Q Mayne. Model predictive control: Recent developments and future promise. *Automatica (Oxford)*, 50(12): 2967–2986, 2014. ISSN 0005-1098.

Itsaso Menchacatorre, Roshan Sharma, Beathe Furenes, and Bernt Lie. Flood management of lake toke: Mpc operation under uncertainty. 2019. ISSN 1650-3686.

Manfred Morari and Jay H. Lee. Model predictive control: past, present and future. *Computers chemical engineering*, 23(4): 667–682, 1999. ISSN 0098-1354.

NVE. Supervision of dams, (accessed: 24.05.2021). `https://www.nve.no/supervision-of-dams/?ref=mainmenu`, 2021.

Roshan Sharma. Lectures note for course iia 4117 : Model predictive control in university of south-eastern norway. 2020.

SkagerakKraft. Dalsfos, (accessed: 24.05.2021). `https://www.skagerakkraft.no/dalsfos/category1277.html`, 2021a.

SkagerakKraft. Kragerø watercourse system, (accessed: 24.05.2021). `https://www.skagerakkraft.no/kragero-watercourse/category2391.html`, 2021b.

Feasibility study on the use of electrolyzers for short term energy storage

Esin Iplik[1] Johannes Warsinski[2] Ioanna Aslanidou[3] Konstantinos Kyprianidis[1]

[1]Future Energy Center, Mälardalen University, Sweden , esin.iplik@mdh.se
[2]Enercon - WRD GmbH, Germany
[3]Innovation and Product Realisation, Mälardalen University, Sweden

Abstract

Electricity grid flexibility is vital for renewable energy to be used effectively. Power-to-gas technologies are investigated to connect electricity grid to gas grid and to tackle capacity challenges. Grid management expenses consist of redispatch and feed-in management. These management procedures, next to being costly, cause a significant energy loss. Proton-exchange membrane electrolyzer installations were studied to reduce these expenses and recover energy. The change in the levelized cost of hydrogen production with varying electrolyzer capacities was presented. The sensitivity of the levelized cost and net present value with respect to installation costs, maintenance costs, and electricity prices were investigated. While the electricity prices have the most significant effect on the levelized cost of hydrogen production, the net present value was affected considerably by the hydrogen selling price. Possible energy savings were calculated between 2 – 23 GWh for 2, 5, 10, 20 MW installations. The annual grid management expense savings were in the range of 0.2 – 2.3 million Euros, increasing with the increasing electrolyzer capacity.

Keywords: electrolysis, power-to-gas, renewable energy

1 Introduction

The share of intermittent renewable sources (wind and solar) reached a significant level that causes various issues in the grid. One of these challenges is the uncontrollable amount and geographical distribution of power generation. As the storage capacity of the grid is limited, the electricity prices can be negative, or generators have to shut down to ensure grid stability. When the transmission operator changes the active generators holding the same energy production to avoid congestion, it is called redispatch. It might cause shutting off renewable power plants due to their location and maybe use fossil alternatives instead. It is called feed-in management when certain generators are shut down because the production exceeds the grid transmission capacity. In 2015, it was reported that the transmission system operators in Germany paid 412 million Euros for redispatch and 478 million Euros for feed-in management (Bundesnetzagentur, 2016). According to this report, Schleswig - Holstein is the most affected state from these measures. As a matter of fact, 65.5% of the feed-in management expenses are affiliated with this state. Its low population density (Hinz et al., 2018), high wind power (Maruf and Islam, 2021) and weakly connected grid to the demand owner states (Bencs et al., 2020) contribute significantly to the situation. Water electrolysis can utilize the redundant energy and produce hydrogen that can be sold to process industries or stored to be converted back to electricity when needed. Expenses of grid management are not the only point to consider; Schleswig - Holstein has lost over 1000 GWh of energy due to an inflexible grid in 2014 (Schermeyer et al., 2017).

Hydrogen is widely used in process industries, especially for ammonia and methanol production (Nicita et al., 2020). When it is produced from renewable resources, it has a lower carbon footprint than its fossil production route. A gray hydrogen production route, steam-methane reforming, has a global warming potential of approximately 12000 g CO_{2eq}/kg H_2, and this value is 970 g CO_{2eq}/kg H_2 for electrolysis by wind energy and 2412 g CO_{2eq}/kg H_2 for electrolysis by solar energy (Cetinkaya et al., 2012). Currently, most of the industrial hydrogen is produced via steam-methane reforming (Carapellucci and Giordano, 2020). In the last decades, hydrogen gains importance as an environmentally friendly energy carrier and as a product of power-to-gas research. It is a good candidate for decarbonizing the systems where high energy density is required. Hydrogen use in aviation (Bauen et al., 2020) and steel industry (Gielen et al., 2020) can undoubtedly contribute to achieve the lower greenhouse gas emission aims.

A variety of electrolysis methods are available for different scales with different current densities and operating conditions. Alkaline electrolysis is a mature technology. Norsk Hydro operated this type of electrolyzers for over 50 years in Norway (Posdziech et al., 2019). Although they are mature, they have low current densities and lower efficiency than the other options (Grigoriev et al., 2020). Solid-oxide electrolysis operates at a high temperature (Lei et al., 2019), and it is a very efficient system. However, the high temperature condition makes it harder to integrate into intermittent systems. The start-up time is longer to reach the 800 – 1300 K temperatures. Proton-exchange membrane (PEM) electrolysis operates

at a lower temperature (350 K), and has a higher current density and efficiency than the alkaline method (Lümmen et al., 2019).

There are studies in the literature, discussing electrolysis installations for Italy (Minutillo et al., 2021), Norway (Ulleberg and Hancke, 2020) and Korea (Lee et al., 2020). These studies show the location dependency of the costs, prices, and energy availability. In this work, the German state of Schleswig - Holstein is selected as the location of a PEM type electrolyzer to reduce the penalty costs and lost energy. The levelized cost of hydrogen production and the net present value of electrolyzer installation are calculated for different capacities. The sensitivities of the levelized cost and the net present value are estimated based on the expenses. The savings are calculated in terms of energy and grid management cost reduction. Finally, the internal rate of return is presented with a discussion on the feasibility of this application. New stations are planned to increase the state's existing hydrogen filling capacity; therefore, the produced hydrogen can be sold locally (Posdziech, 2019).

The next section presents the equations and parameters used to evaluate electrolyzers from an economic perspective. Additionally, case scenarios are created with varying costs and product prices, operating hours, and electricity prices to analyze the commercial possibilities. The results are presented based on these scenarios and discussed in the section that follows. Finally, in the last section, the outcomes of this work are summarized next to possible points for future investigations.

2 Methods

To assess the economic conditions of hydrogen production via electrolysis, the levelized cost of hydrogen production (LCOH) is used. LCOH is calculated by Equation 1. As can be seen in the equation, this value shows the cost per kg of hydrogen production.

$$LCOH = \frac{\sum_{y=1}^{N} \frac{CapEx_y + E_y}{(1+d)^y}}{\sum_{y=1}^{N} \frac{m_{h,y}}{(1+d)^y}} \tag{1}$$

The net present value of the installations are calculated by Equation 2.

$$NPV = \sum_{y=0}^{N} \frac{Cash_{in} - Cash_{out}}{(1+d)^y} \tag{2}$$

The internal rate of return (IRR) is also calculated to show the expected return generated by the investment. IRR is the discount rate that results in a zero NPV, which is given in Equation 3.

$$\sum_{y=0}^{N} \frac{Cash_{in} - Cash_{out}}{(1+IRR)^y} = 0 \tag{3}$$

The variables used for these equations are given in Table 1. The value of time is taken into consideration by the discount factor in all the economic assessment methods used.

Table 1. Variables used for levelized cost, net present value, and internal rate of return calculations.

Variable	*Description (Unit)*
LCOH	Levelized Cost (EUR/kg Hydrogen)
y	Year index
N	Electrolyzer lifetime (year)
$CapEx_y$	Capital expenses in year y (EUR)
$OpEx_y$	Operational expenses in year y (EUR)
E_y	Electricity cost in year y (EUR/kWh)
$m_{h,y}$	Produced hydrogen in year y (kg/year)
d	Discount factor (%)
NPV	Net present value (EUR)
$Cash_{in}$	Cash inflow (EUR)
$Cash_{out}$	Cash outflow (EUR)
IRR	Internal rate of return (%)

Capital expenses (CapEx) and maintenance expenses are calculated by using factors changing according to the capacity of the electrolyzer. These factors are given in Table 2 for PEM electrolysis.

Table 2. Variables used for levelized cost and net present value calculations.

Capacity (MW)	*CapEx*[1] (EUR/kW)	*Maintenance*[2] (EUR/kW)
2	1400	500
5	1300	455
10	1250	445
20	1200	420

The electrodes have a shorter lifetime than the system. Therefore, maintenance is considered for electrode change every five years. The electricity cost is the only operational expense that is included in this study. Instead of using a factor, this expense is calculated by using 6 ¢EUR/kWh electricity price, the capacity of the electrolyzer, and the running hours of the system. This value is the lower limit of industrial electricity price in Germany (Schmitz et al., 2020). For the base scenario, 6 EUR/kg hydrogen selling price is used. A 6000-hour operation per year is assumed for the electrolyzers considering that the high electricity prices would cause infeasible operation.

Scenarios

- *Base Scenario:* LCOH, NPV and IRR are calculated for capacities of 2, 5, 10, and 20 MW, and electrolyzer lifetime of 10, 15, and 20 years.
- *Dependency on costs and product price variation:*

[1](Saba et al., 2018)
[2](Lee et al., 2020)

Each expense parameter (CapEx, OpEx, and maintenance) is reduced by 10%, and the change in LCOH is presented. In addition to the expense reduction scenarios, the change in NPV with respect to a 10% hydrogen selling price increase is calculated.

- *Runtime:* Operating hours per year is varied between 3000 – 8000 with 1000 h/y increments, and the LCOH changing trend is studied.
- *Electricity price:* A high electricity price is considered to observe the change in LCOH. Negative prices are discussed and an electricity price limit is suggested to run the systems.
- *Savings:* The annual energy savings of each electrolyzer is calculated based on the curtailment hours of the state. The payback period, when NPV reaches zero, is calculated.

The next section follows the order of these scenarios, reporting the values and discussing them against each other.

3 Results and Discussions

Base scenarios

Levelized cost, net present value and internal rate of return calculations are performed for 2, 5, 10, and 20 MW capacity, and the results are given in Figure 1, 2 and 3 for 10, 15 and 20 years lifetime. LCOH decreases with a longer lifetime of the installation, but this decrease is not linear. The installation of 2 MW has an LCOH of below 5.5 EUR/kg, which is below the selling price of hydrogen even with the shortest lifetime.

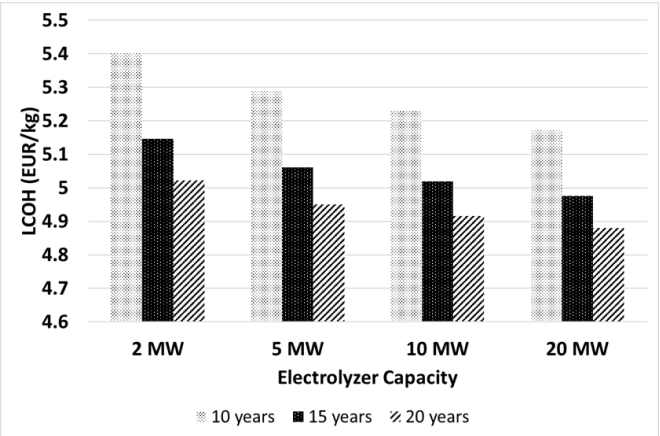

Figure 1. Levelized cost of the electrolyzers with respect to capacity and lifetime.

NPV increases with the electrolyzer lifetime, and similar to the LCOH decrease, this increasing trend is not linear.

IRR and NPV show the same trend as expected. The increasing capacity lowers the effect of a longer lifetime on the generated value. These values of LCOH, NPV, and IRR, calculated for 6000 h/y operating period and 6 ¢EUR/kWh electricity price, are taken as the base cases, and all the percentage calculations use these values.

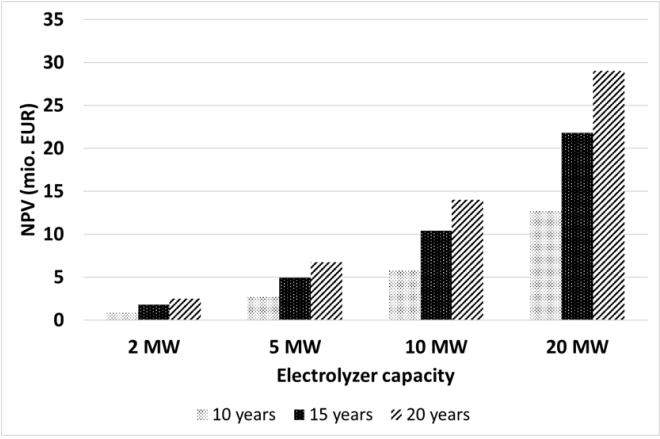

Figure 2. Net present value of the electrolyzers with respect to capacity and lifetime.

Additionally, these results show the low effect of the capacity on LCOH and IRR. The electrolyzer stacks can be installed as needed, as a bigger capacity brings only a slight LCOH improvement.

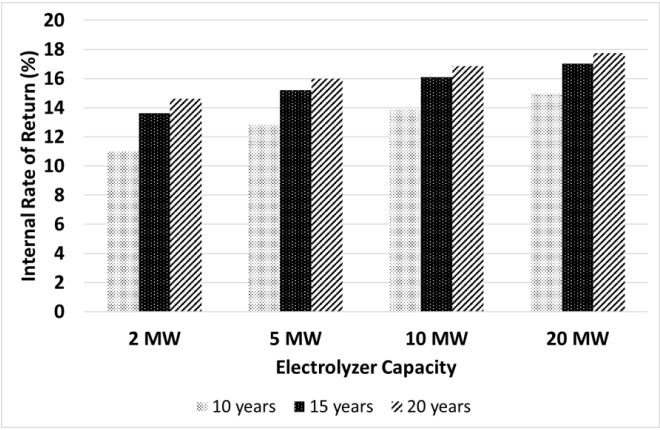

Figure 3. Internal rate of return of the electrolyzers with respect to capacity and lifetime.

The effect of expenses and product price on LCOH and NPV

PEM electrolysis is a hot research topic, and the ongoing scientific work increases the expectations of cost reduction. The sensitivity of LCOH is investigated based on expected technological improvements to decrease the CapEx, OpEx, maintenance cost, and electricity price. The decrease in the LCOH with a 10% decrease in each of these expenses is given in Figure 4 for all evaluated electrolyzer capacities. Electricity price change has the most significant effect on LCOH, followed by CapEx and maintenance, respectively. Therefore, it can be said that it is more critical to reach cheaper electricity compared to

technological advances. The sensitivity of LCOH with respect to CapEx and maintenance slightly decreases with the increasing capacity. However, since the electricity consumption increases with the increased capacity, the higher capacity electrolyzer has a more sensitive LCOH to the electricity price.

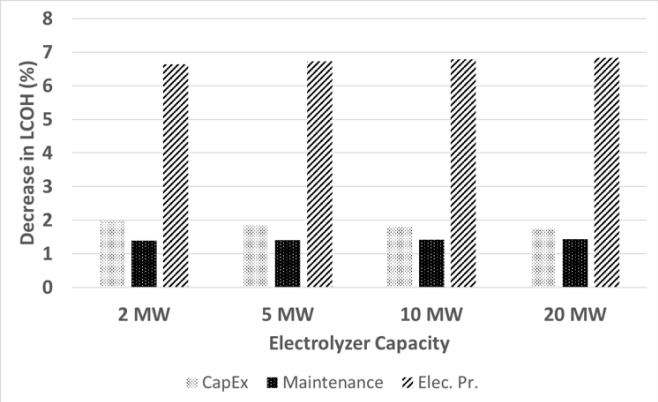

Figure 4. Decrease in LCOH with respect to 10% decrease in each expense type.

The sensitivity of NPV is also investigated concerning the same expenses. Additionally, NPV depends on the hydrogen selling price. Therefore, the effect of a 10% increase in the hydrogen selling price is also investigated. The results are given in Figure 5. For the 2 MW capacity, almost 65% increase is observed with a 10% increase in the hydrogen selling price. As all the expenses are lower for the small scale, the product creates more value. NPV becomes less sensitive to the product price with the increasing capacity, although this value is still the most important parameter. The expenses affect the NPV in the same order as they affect LCOH. However, the sensitivity decreases with the increasing capacity. Both LCOH and NPV used for the sensitivity analysis are for 20 years electrolyzer lifetime. Of course, a 10-year lifetime causes a higher dependency on the expenses.

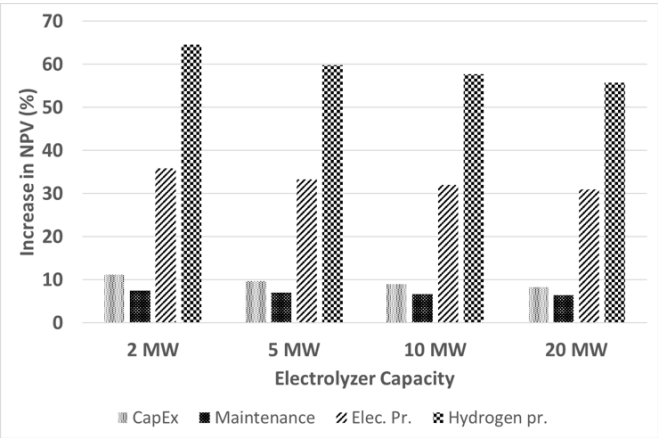

Figure 5. Increase in NPV with respect to 10% increase in hydrogen selling price and 10% decrease in each expense type.

The effect of runtime on LCOH

If the 2 MW electrolyzer runs less than 5000 hours a year, the production costs exceed the selling price of 6 EUR/kg, and the net present value after 20 years becomes negative. Of course, a higher-capacity electrolyzer can tolerate more extended downtime due to higher production. The change in the LCOH with respect to the runtime of the electrolyzer is given in Figure 6 for different capacities for 10, 15, and 20 years lifetime. The LCOH values are quite high for the low operating hours. However, in an average node in Schleswig - Holstein, 1443 hours of curtailment occurred in 2015 (Schermeyer et al., 2017). Considering that the electricity price will be zero (or lower) for these hours, LCOH will be affected by the annual curtailment events significantly.

Electricity price

The electricity price and lifetime – runtime analyses show the importance of when to run the electrolyzer decision. The electricity price has the highest effect on LCOH. Germany has relatively higher prices for small-scale industrial electricity; the highest value for the large-scale industry is around 14 ¢EUR/kWh (Schmitz et al., 2020). If the highest electricity price is considered, LCOH increases significantly. The LCOH values for the expensive electricity scenario are given next to the percent increase compared to the base case scenario in Table 3.

Table 3. LCOH for the high electricity price and percent increase from the base scenario.

10 years	*LCOH (EUR/kg)*	*% increase*
2 MW	9.8	82.28
5 MW	9.7	84.05
10 MW	9.6	84.97
20 MW	9.6	85.91
15 years	*LCOH (EUR/kg)*	*% increase*
2 MW	9.5	86.37
5 MW	9.5	87.82
10 MW	9.4	88.56
20 MW	9.4	89.32
20 years	*LCOH (EUR/kg)*	*% increase*
2 MW	9.4	88.5
5 MW	9.3	89.77
10 MW	9.3	90.41
20 MW	9.3	91.07

On the other hand, average electricity prices can be misleading. In 2020, electricity price was below zero for 298 hours, and from February to May, the price range was generally 0 – 3 ¢EUR/kWh (Kern, 2021). If the selling price is kept constant, up to 8 ¢EUR/kWh, a feasible operation is possible. As the selected PEM electrolyzer has a fast start-up, 15-minute prices of the power market can be used for

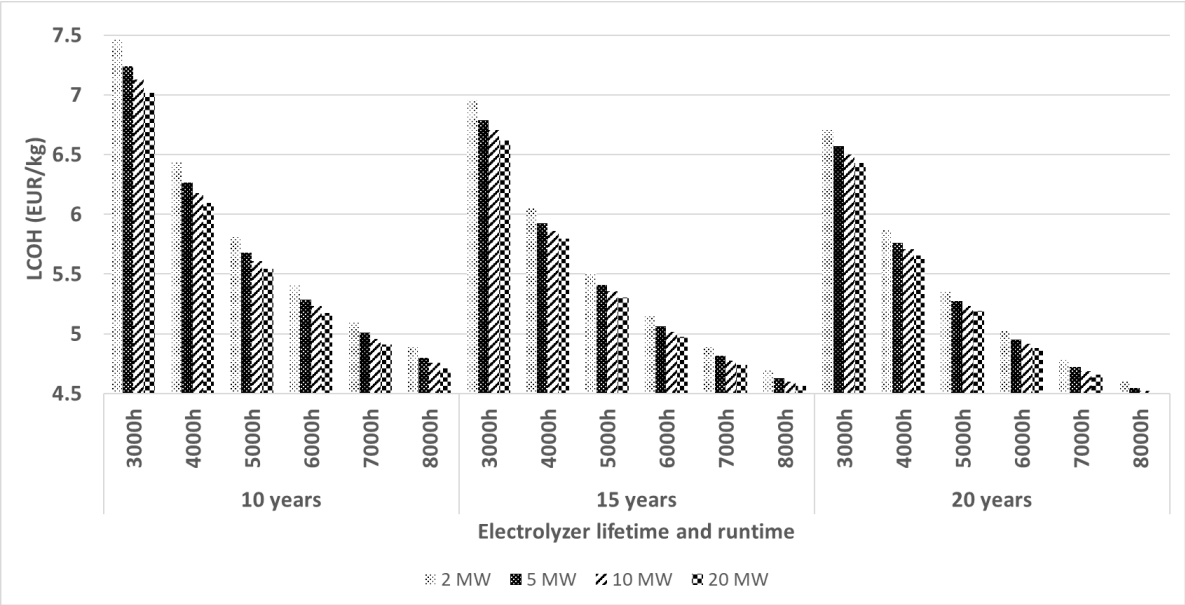

Figure 6. Change of LCOH for changing running hours of electrolyzers.

this decision, rather than a fixed average price.

Savings

If the electrolyzer of 2 MW capacity ran on the curtailment hours (1443 h/y), 2.31 GWh energy would have been saved if the conversion efficiency is 80 %. For the 5, 10, and 20 MW electrolyzers, energy savings would be 5.77, 11.5, and 23.1 GWh, respectively. Additionally, the transmission system operators could reduce the feed-in management costs by a rate of 101 EUR/MWh (Bundesnetzagentur, 2016). The cost reduction for each electrolyzer capacity is given in Table 4.

Table 4. Feed-in management cost reduction by the electrolyzer capacity.

Capacity (MW)	2	5	10	20
Cost reduction (Mio. EUR)	0.23	0.58	1.16	2.34
% of CapEx	8.21	8.92	9.28	9.75

Thanks to the German Renewable Energy Sources Act (EEG), many renewable energy producers have a guaranteed selling price (BGBI. I S. 1066, 2014). It should be noted that part of the grid management savings might be shifted to the EEG surcharge (EEG-Umlage) due to the difference between the guaranteed price and the market price. This difference might be high, considered that the curtailment events mainly occur when there is a high renewable share in the grid.

For this study, an average value of 6 EUR/kg is taken as the selling price of hydrogen. There are studies taking higher and lower values (Song and Ozkan, 2010; Dufo-López et al., 2009). The price range of gray hydrogen is much lower, around 1.8 EUR/kg (Salkuyeh et al., 2018). An effort from governments to use a mixed hydrogen stream can make the high price range justifiable. Thanks to a similar effort, market diesel is a mix of petrodiesel and bio-diesel in Germany as in many other countries (BGBI. I S. 590, 1318, 2016). The investment might be feasible when the savings' rate to CapEx and feed-in management costs, given in Table 4, are also considered. These values show the economic potential of the electrolyzer from different perspectives. If the transmission system operators can cut grid management costs, the business case will be less dependent on the hydrogen selling price.

Water electrolysis produces high purity oxygen gas next to hydrogen. As it is not relevant to the energy calculations, the monetary value of this side product is not considered for this work. However, selling high purity oxygen can bring additional value.

4 Conclusions

The state of Schleswig – Holstein has high grid management expenses due to the high share of wind power generation. Four different capacities for PEM electrolysis are investigated for this state to save energy and cut expenses. LCOH and NPV are calculated for economic assessment, and how these values change according to CapEx, maintenance, and electricity expenses are shown. Their trend shows the importance of cheap electricity. CapEx and maintenance costs affect the LCOH much less than the electricity price. The feasibility is found highly dependent also on the hydrogen selling price. However, the possible grid management cost reduction of up to 9% of the CapEx can lower its effect. Internal rate of return values are found satisfactory, ranging between 14 - 17 % for the 20-year lifetime electrolyzers. With its possible product utilization alternatives of electricity generation, heat generation, and chemical feedstock, electrolysis is a substan-

tial investment candidate to gain grid flexibility. Future work can focus on the comparison of different alternatives to cut grid management costs of this state. Additionally, instead of selling the produced hydrogen to process industries, different scenarios for converting it back to electricity can be considered.

References

Ausilio Bauen, Niccolò Bitossi, Lizzie German, Anisha Harris, and Khangzhen Leow. Sustainable aviation fuels: Status, challenges and prospects of drop-in liquid fuels, hydrogen and electrification in aviation. *Johnson Matthey Technology Review*, 64(3):263–278, 2020.

Peter Bencs, Mohammed Al-Ktranee, and Károly Marcell Mészáros. Effects of solar panels on electrical networks. *Analecta Technica Szegedinensia*, 14(1):50–60, 2020.

BGBI. I S. 1066. Gesetz für den ausbau erneuerbarer energien, 2014. http://www.gesetze-im-internet.de/eeg_2014/EEG_2021.pdf Accessed on 15.06.2021.

BGBI. I S. 590, 1318. Verordnung zur durchführung der regelungen der biokraftstoffquote, 2016. http://www.gesetze-im-internet.de/bimschv_36/36._BImSchV.pdf Accessed on 15.06.2021.

Bundesnetzagentur. Quartalsbericht zu Netz- und Systemsicherheitsmassnahmen. Technical report, Arbeitsgruppe Energie-Monitoring, 2016.

Roberto Carapellucci and Lorena Giordano. Steam, dry and autothermal methane reforming for hydrogen production: A thermodynamic equilibrium analysis. *Journal of Power Sources*, 469:228391, 2020.

E Cetinkaya, I Dincer, and GF Naterer. Life cycle assessment of various hydrogen production methods. *International journal of hydrogen energy*, 37(3):2071–2080, 2012.

Rodolfo Dufo-López, José L Bernal-Agustín, and Franklin Mendoza. Design and economical analysis of hybrid pv–wind systems connected to the grid for the intermittent production of hydrogen. *Energy Policy*, 37(8):3082–3095, 2009.

Dolf Gielen, Deger Saygin, Emanuele Taibi, and Jean-Pierre Birat. Renewables-based decarbonization and relocation of iron and steel making: A case study. *Journal of Industrial Ecology*, 24(5):1113–1125, 2020.

SA Grigoriev, VN Fateev, DG Bessarabov, and P Millet. Current status, research trends, and challenges in water electrolysis science and technology. *International Journal of Hydrogen Energy*, 45(49):26036–26058, 2020.

Fabian Hinz, Matthew Schmidt, and Dominik Möst. Regional distribution effects of different electricity network tariff designs with a distributed generation structure: The case of germany. *Energy Policy*, 113:97–111, 2018.

Timo Kern. Deutsche strompreise an der börse epex spot in 2020. Technical report, Forschungsgesellschaft fuer Energiewirtschaft mBH, 2021.

Hyunjun Lee, Boreum Lee, Manhee Byun, and Hankwon Lim. Economic and environmental analysis for pem water electrolysis based on replacement moment and renewable electricity resources. *Energy Conversion and Management*, 224: 113477, 2020.

Libin Lei, Jihao Zhang, Zhihao Yuan, Jianping Liu, Meng Ni, and Fanglin Chen. Progress report on proton conducting solid oxide electrolysis cells. *Advanced Functional Materials*, 29 (37):1903805, 2019.

Norbert Lümmen, Assma Karouach, and Stine Tveitan. Thermo-economic study of waste heat recovery from condensing steam for hydrogen production by pem electrolysis. *Energy Conversion and Management*, 185:21–34, 2019.

Md Maruf and Nasimul Islam. A novel method for analyzing highly renewable and sector-coupled subnational energy systems—case study of schleswig-holstein. *Sustainability*, 13 (7):3852, 2021.

M Minutillo, A Perna, A Forcina, S Di Micco, and E Jannelli. Analyzing the levelized cost of hydrogen in refueling stations with on-site hydrogen production via water electrolysis in the italian scenario. *International Journal of Hydrogen Energy*, 46(26):13667–13677, 2021.

A Nicita, G Maggio, APF Andaloro, and G Squadrito. Green hydrogen as feedstock: Financial analysis of a photovoltaic-powered electrolysis plant. *International Journal of Hydrogen Energy*, 45(20):11395–11408, 2020.

Nina Posdziech. Schleswig-holstein's first hydrogen filling station opens in handewitt, 2019. Retrieved 09.09.2021 from https://www.now-gmbh.de/en/news/pressreleases/schleswig-holsteins-first-hydrogen-filling-station-opens-in-handewitt/.

Oliver Posdziech, Konstantin Schwarze, and Jörg Brabandt. Efficient hydrogen production for industry and electricity storage via high-temperature electrolysis. *International Journal of Hydrogen Energy*, 44(35):19089–19101, 2019.

Sayed M Saba, Martin Müller, Martin Robinius, and Detlef Stolten. The investment costs of electrolysis–a comparison of cost studies from the past 30 years. *International journal of hydrogen energy*, 43(3):1209–1223, 2018.

Yaser Khojasteh Salkuyeh, Bradley A Saville, and Heather L MacLean. Techno-economic analysis and life cycle assessment of hydrogen production from different biomass gasification processes. *International Journal of Hydrogen Energy*, 43(20):9514–9528, 2018.

Hans Schermeyer, Michael Studer, Manuel Ruppert, and Wolf Fichtner. Understanding distribution grid congestion caused by electricity generation from renewables. In *Smart Energy Research. At the Crossroads of Engineering, Economics, and Computer Science*, pages 78–89. Springer, 2017.

Joachim Schmitz, Sonja Rinne, and Sebastian Pieper. Strompreise: Neue wege bei der finanzierung. Technical report, Bundesministerium fur Wirtschaft un Energie, 2020.

Hua Song and Umit S Ozkan. Economic analysis of hydrogen production through a bio-ethanol steam reforming process: Sensitivity analyses and cost estimations. *International journal of hydrogen energy*, 35(1):127–134, 2010.

Øystein Ulleberg and Ragnhild Hancke. Techno-economic calculations of small-scale hydrogen supply systems for zero emission transport in norway. *international journal of hydrogen energy*, 45(2):1201–1211, 2020.

Model Based Control and Analysis of Gas Lifted Oil Field for Optimal Operation

Nima Janatian Kushila Jayamanne Roshan Sharma

Department of Electrical Engineering, IT and Cybernetics, University of South-Eastern Norway, Norway,
{Nima.Janatianghadikolaei,Kushila.R.Jayamanne,Roshan.Sharma}@usn.no

Abstract

This paper describes mathematical modeling, optimization, and analysis of a gas lift oil field with five wells. A global sensitivity analysis using the variance-based method is performed to classify the parameters, which are highly sensitive and uncertain simultaneously. An improved model is further used to design a model-based predictive controller to optimally distribute a limited supply of lift gas among the oil wells. Several simulation cases showed an increase in the total oil production, and all the constraints were fully satisfied when the deterministic NMPC was applied to the nominal model. The effect of parametric uncertainty is studied by applying the deterministic NMPC to the plant model containing the uncertain parameters. It has been shown that under the presence of uncertainty, robust constraint satisfaction is not guaranteed with some constraints not being satisfied, leading to unachievable and unrealistic lift gas distribution.

Keywords: Gas Lifted Oil Wells, Model Predictive Control, Global Sensitivity Analysis, Dynamic Modeling and Simulation, Parametric Uncertainty

1 Introduction

It is always of interest to manage and plan resources efficiently to obtain profit as much as possible from a given resource. In this sense, the oil and gas industry is not an exception. Hence, the optimal distribution of available gas is crucial to maximizing total oil production in a gas-lifted oil field where the multiple oil wells share the lift gas supplied by a common source.

In a gas lifted oil field, an artificial external mechanism is exploited to bring the dead wells back to life or increase the production rates from the naturally flowing wells. A continuous flow gas lifted oil field normally consists of multiple gas lift oil wells sharing lift gas from a common supply pipeline. A single gas lifted oil well is shown in Figure 1.In this system which is mostly used to extract the lighter crude oils, the high-pressurized natural gas is continuously injected into the annulus of the well through the gas lift choke valve. The injected gas finds its way into tubing at some points located at proper depths and mixes with the multiphase fluid from the reservoir. As a result of this mixing, the density of the fluid in the tubing will be reduced, which means that the flowing pressure losses in the tubing reduce. Consequently, the reservoir pressure will be able to overcome the flowing resistance in the well and push the reservoir fluid to the surface.

Each well has its own inflow characteristics. For example, two oil wells in the same field may produce different amount of oil even when the same amount of lift gas is injected into them. In other words, there is no rule of thumb on how to distribute the available lift gas among the oil wells to obtain the maximum possible oil production from the field. For optimal distribution of lift gas among the wells, model based real-time optimizer (RTO) can be used. For this an accurate mechanistic model of the process, which should be simultaneously simple enough to be used for real-time optimization and control purposes should be used.

Modeling and control of gas lifted oil field has been studied before in (Sharma et al., 2011), where some simplifying assumptions were made that may not reflect reality. For example, the fluid that comes out of the reservoir was assumed to be pure oil (without gas coming from the reservoir) and all the well parameters were assumed to be deterministic. This model had been used further in optimization of lift gas allocation as nonlinear optimization in (Sharma et al., 2012). This model has been improved in (Krishnamoorthy et al., 2016) by considering the gas to oil ratio. The long term production optimization under uncertainty has been studied in (Capolei et al., 2015; Hanssen et al., 2017) using economic MPC. But when it comes to the short-term optimization, most of the works either consider a deterministic model, which means they simply disregard uncertainty, or they limit the research scope to steady-state optimization using a very simplified linear model (Hanssen and Foss, 2015). Recently, a few papers have been published on real-time process optimization under the presence of uncertainty (Krishnamoorthy et al., 2019) to address the challenges in this area.

The first purpose of this paper is to improve the existing mathematical model of gas lifted oil fields with more realistic assumptions. To achieve this goal, the fluid that comes out of the reservoir is considered to be a mixture of oil, water, and gas. Furthermore, parametric uncertainties are considered for some parameters such as gas to oil ratio and productivity index. The second aim of the paper is to classify parameters that are both highly sensitive and uncertain simultaneously. Therefore, a global sensi-

tivity analysis is performed to study how the uncertainty in output (total oil production from the field) can be apportioned to different sources of uncertainty in the model parameters. The first order and total-effect sensitivity indices are calculated using the variance-based method due to its valuable features, such as the inclusion of interaction effects among input factors (Saltelli et al., 2008). The third goal is to study the effect of parametric uncertainty on lift gas distribution optimization problem. Considering the operational constraints of the process and the inherent robustness (to a certain extent) of the receding horizon strategy, a deterministic nonlinear model based predictive controller is designed based on the nominal plant model to optimally distribute a limited supply of lift gas being shared to several oil wells in the field. Several simulation cases are performed to study the performance of the optimal controller under varying operational scenarios. Simulation results show that the total oil production will be increased and all the constraints will be satisfied when the deterministic NMPC is applied to the nominal model. The effect of parametric uncertainty is shown by applying the deterministic NMPC to the plant model containing uncertain parameters and it has been shown that some constraints will be violated which suggests that the uncertainties should be considered explicitly in the optimal control problem.

The rest of the paper is organized as follows. Section 2 describes mathematical modeling of the gas lifted oil field system, openloop simulation results and the sensitivity analysis. Standard nonlinear model predictive control design, simulation results and stochastic analysis are presented in Section 3 before concluding in Section 4.

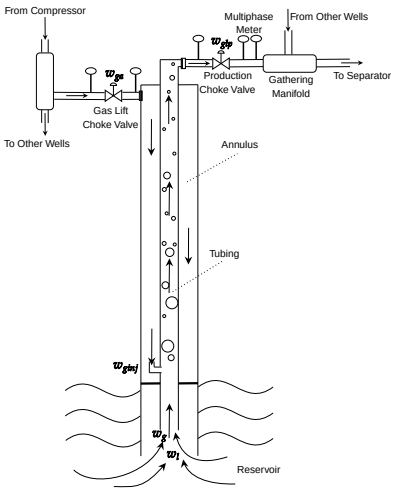

Figure 1. Schematic diagram of a single gas lift oil well

2 Modeling and Sensitivity Analysis

The considered gas lifted oil field of this paper consists of five oil wells that share a common gas distribution pipeline and common gathering manifold. A compressor discharges highly pressurized lift gas into the common gas distribution pipeline where it should be distributed among the oil wells. Considering a single oil well, the lift gas mass flow rate from the common distribution manifold into the well's annulus is denoted by w^i_{ga} where the superscript i refers to the i^{th} oil well. Then, the high pressure lift gas is injected from annulus into tubing (w^i_{ginj}) at a proper depth through the gas injection valve which is always open and only passes the flow in one direction. The injected gas mixes with the multiphase fluid (mixture of oil, water, and the gas from the reservoir) and reduces its density. This causes the hydrostatic pressure of the fluid column in tubing above the injection point and consequently the bottom hole pressure to drop. As a result, the differential pressure between the reservoir and the bottom hole pressure will increase and pushes the liquid column to flows upward to the surface. The produced mixture flows out through all the production choke valves (w^i_{glp}) is collected in the common gathering manifold and finally transported to the separator where they are separated into their corresponding compartments. The gas is then sent back to the compressor system and recycled to be used for lifting purposes.

Friction losses in the pipelines have not been taken into account since it might not be important for the sole purpose of control. All phases of the multiphase fluid are assumed to be evenly distributed with no slugging. The temperature of lift gas and the multiphase fluid is assumed to be constant at 280 K at all sections of the pipelines and the reservoir pressure is assumed to be constant at 150 bar. All the assumption are based on expert knowledge from Equinor ASA.

2.1 Model Description

The model is developed considering all the components of a typical gas lifted oil well as shown in Figure 1. The differential equations in model are obtained from the mass balances of each compartment. The algebraic equations are mostly density models, pressure models, flow models, and so on, which are obtained from equations of states, valve equations, and first principal modeling techniques.

Considering the mass of lift gas in annulus m^i_{ga}, mass of the gas in the tubing above the injection point m^i_{gt}, and mass of the liquid (mixture of oil and water) in the tubing above the injection point m^i_{lt} as three states and applying the mass balance, three corresponding differential equations are given by:

$$\dot{m}^i_{\text{ga}} = w^i_{\text{ga}} - w^i_{\text{ginj}} \tag{1}$$

$$\dot{m}^i_{\text{gt}} = w^i_{\text{ginj}} + w^i_{\text{g}} - w^i_{\text{gp}} \tag{2}$$

$$\dot{m}^i_{\text{lt}} = w^i_{\text{l}} - w^i_{\text{lp}} \tag{3}$$

w^i_{ga} is the mass flow rate of the injected lift gas into each well from the gas lift choke valve (system input), w^i_{ginj} is the mass flow rate of the gas injection from the annulus into the tubing, w^i_{gp} and w^i_{lp} are the produced gas and

liquid phase mass flow rates from the production choke valve, respectively, and w^i_{g} and w^i_{l} are the gas and liquid mass flow rates from the reservoir into the well. w^i_{glp} is the total mass flow rate of all phases from the production choke valve and w^i_{op} is the oil compartment of the w^i_{lp}. All the flow equations are given by:

$$w^i_{\text{ginj}} = K^i Y^i_2 \sqrt{\rho^i_{\text{ga}} \max(P^i_{\text{ainj}} - P^i_{\text{tinj}}, 0)} \tag{4}$$

$$w^i_{\text{gp}} = \frac{m^i_{\text{gt}}}{m^i_{\text{gt}} + m^i_{\text{lt}}} w^i_{\text{glp}} \tag{5}$$

$$w^i_{\text{lp}} = \frac{m^i_{\text{lt}}}{m^i_{\text{gt}} + m^i_{\text{lt}}} w^i_{\text{glp}} \tag{6}$$

$$w^i_{\text{l}} = PI^i \max(P_r - P^i_{\text{wf}}) \tag{7}$$

$$w^i_{\text{g}} = GOR^i w^i_{\text{l}} \tag{8}$$

$$w^i_{\text{glp}} = C_v(u^i_2) Y^i_3 \sqrt{\rho^i_{\text{m}} \max(P^i_{\text{wh}} - P_s, 0)} \tag{9}$$

$$w^i_{\text{op}} = \frac{\rho_o}{\rho_w}(1 - WC^i) w^i_{\text{lp}} \tag{10}$$

P^i_{a} is the pressure of lift gas in annulus downstream the gas lift choke valve, P^i_{ainj} is the pressure upstream the gas injection valve in the annulus and P^i_{tinj} is the pressure downstream the gas injection valve in the tubing, and P^i_{wh} and P^i_{wf} are the well head and bottom hole pressure respectively. All the pressures are given by:

$$P^i_{\text{a}} = \frac{z m^i_{\text{ga}} R T^i_{\text{a}}}{M A^i_{\text{a}} L^i_{\text{a\_tl}}} \tag{11}$$

$$P^i_{\text{ainj}} = P^i_{\text{a}} + \frac{m^i_{\text{ga}}}{A^i_{\text{a}} L^i_{\text{a\_tl}}} g L^i_{\text{a\_vl}} \tag{12}$$

$$P^i_{\text{tinj}} = \frac{z m^i_{\text{gt}} R T^i_{\text{t}}}{M V^i_G} + \frac{\rho^i_{\text{m}} g L^i_{\text{t\_vl}}}{2} \tag{13}$$

$$P^i_{\text{wh}} = \frac{z m^i_{\text{gt}} R T^i_{\text{t}}}{M V^i_G} - \frac{\rho^i_{\text{m}} g L^i_{\text{t\_vl}}}{2} \tag{14}$$

$$P^i_{\text{wf}} = P^i_{\text{tinj}} + \rho^i_{\text{l}} g L^i_{\text{r\_vl}} \tag{15}$$

ρ^i_{ga} is the average density of gas in the annulus. ρ^i_{gl} is the density of liquid phase (oil and water mixture), ρ^i_{m} is the average density of multiphase mixture in tubing above the injection point. Y^i_2 and Y^i_3 are the gas expandability factor for the gas that passes through gas injection valve and production choke valve, respectively. V^i_G is the volume of gas present in the tubing above the gas injection point, and $C_v(u^i_2)$ is the production choke valve characteristics as its opening. All the densities and other variables are given by:

$$\rho^i_{\text{ga}} = \frac{M(P^i_{\text{a}} + P^i_{\text{ainj}})}{2 z R T^i_{\text{a}}} \tag{16}$$

$$\rho^i_{\text{l}} = \rho_w WC^i + \rho_o(1 - WC^i) \tag{17}$$

$$\rho^i_{\text{m}} = \frac{m^i_{\text{gt}} + m^i_{\text{lt}}}{A^i_{\text{t}} L^i_{\text{t\_tl}}} \tag{18}$$

$$Y^i_2 = 1 - \alpha_{\text{Y}} \frac{P^i_{\text{ainj}} - P^i_{\text{tinj}}}{\max(P^i_{\text{ainj}}, P^{\min}_{\text{ainj}})} \tag{19}$$

$$Y^i_3 = 1 - \alpha_{\text{Y}} \frac{P^i_{\text{wh}} - P_s}{\max(P^i_{\text{wh}}, P^{\min}_{\text{wh}})} \tag{20}$$

$$V^i_G = A^i_{\text{t}} L^i_{\text{t\_tl}} - \frac{m^i_{\text{lt}}}{\rho^i_{\text{l}}} \tag{21}$$

$$C_v(u^i_2) = \begin{cases} 0 & \text{if } u^i_2 < 5 \\ 30.303 u^i_2 - 151.788 & \text{if } 5 < u^i_2 < 50 \\ 136.5 u^i_2 - 5460 & \text{if } 50 < u^i_2 \end{cases} \tag{22}$$

Note that the dynamic model 1 to 22 could be written as an explicit ODE (ordinary differential equations) by simply eliminating the algebraic variables. So the model in compact form is given by:

$$\dot{x} = f(x, u) \tag{23}$$

$$y_1 = h_1(x, u) \tag{24}$$

$$y_2 = h_2(x, u) \tag{25}$$

where x and u are the states and system inputs, and y_1 and y_2 are two desired outputs

$$x = \begin{bmatrix} m^1_{\text{ga}} & \dots & m^5_{\text{ga}} & m^1_{\text{gt}} & \dots & m^5_{\text{gt}} & m^1_{\text{lt}} & \dots & m^5_{\text{lt}} \end{bmatrix}^T \tag{26}$$

$$u = \begin{bmatrix} w^1_{\text{ga}} & w^2_{\text{ga}} & w^3_{\text{ga}} & w^4_{\text{ga}} & w^5_{\text{ga}} \end{bmatrix}^T \tag{27}$$

$$y_1 = \sum_{i=1}^{5} w^i_{\text{op}} \tag{28}$$

$$y_2 = \sum_{i=1}^{5} w^i_{\text{glp}} \tag{29}$$

2.2 Uncertainties

In this work, the productivity index PI which is a mathematical means of expressing the reservoir's ability to deliver fluids to the wellbore, gas to oil ratio GOR which is defined as the mass ratio of produced gas to produced liquid (oil and water), and water cut WC which is defined as the volumetric flow rate of water to the total produced liquid, are considered to be constant but unknown parameters. Considering the five oil wells, there exist fifteen uncertain parameters in the system that makes it visually impossible to show the uncertainty region. Nevertheless, the uncertainty region of one well is shown in Figure 2 as

an example. All the uncertain parameters of all the five wells in this paper are assumed to have the same ±20% deviation from their nominal values and uniform distribution. The reason of choosing uniform distribution is to challenge the controller.

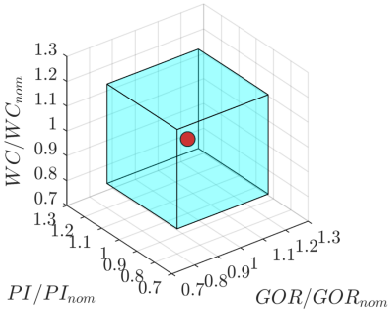

Figure 2. Unceratainty region with ±20% deviation.

2.3 Open Loop Simulation

The system is simulated in open loop using the nominal values of parameters provided in Table 1 and P_r and P_s are assumed to be 150 and 30 bar, respectively. The presented results in Figure 3 show that a decrease in the injected lift gas flow rates causes an increase in bottom hole pressures, and consequently, the oil production flows decrease. This means that the model is capable of showing all the necessary dynamics of gas lifted oil field and will be used further to perform sensitivity analysis and to design nonlinear model predictive control.

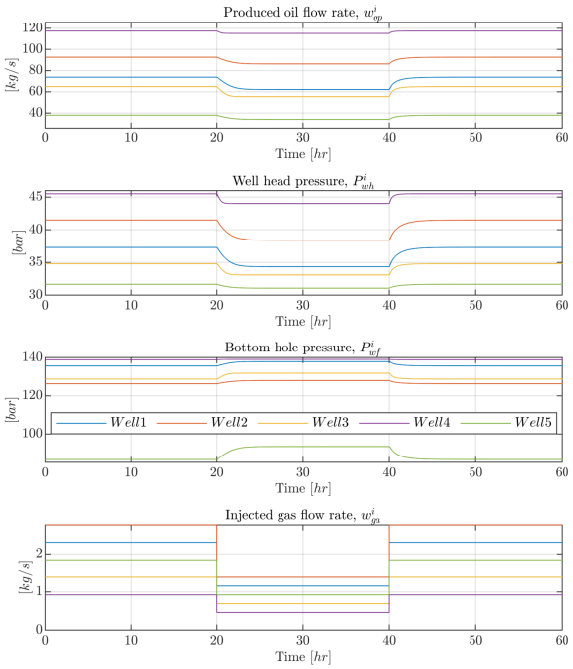

Figure 3. Open loop simulations of the nominal model

2.4 Global Sensitivity Analysis

It is useful to figure out which parameters have a strong/weak influence on the model output, especially under the presence of uncertainties, because the model based control design will be more problematic and needs more care if the uncertain parameters are sensitive as well. Variance based global sensitivity analysis method is selected due to its valuable features such as model independence, capacity to capture the influence of the full range of variation of each input factor, and appreciation of interaction effects among input factors.

The first order and total sensitivity indices are calculated using the variance based method introduced in (Saltelli et al., 2008) which is an improved extension of the original approach provided by (Sobol, 1993) and (Homma and Saltelli, 1996). Here only the results are presented and the readers are referred to the main reference for more information about the method due to the word limitation.

A number of 136000 Monte Carlo simulations have been done to calculate the sensitivity indices. Both sensitivity indices presented in Figure 4 show that for the considered uncertainty region introduced in Figure 2, gas to oil ratio is the most sensitive/influential parameter and productivity index and water cut are at the second and third place, respectively. In other words, the standard controller based on the nominal model will be more robust to deviation in water cut. On the other hand, a slight deviation in the gas to oil ratio leads to a severe mismatch between the nominal and uncertain model, therefore, poor performance is expected. These interpretations will be verified by stochastic analysis results in the following section.

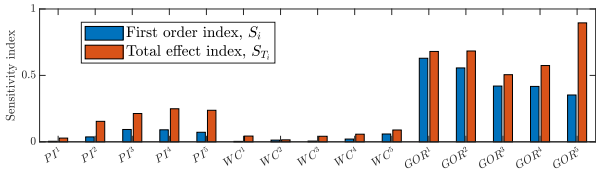

Figure 4. Sensitivity indices

3 Standard NMPC and Stochastic Analysis

3.1 Design of deterministic standard NMPC

The primary control objective is to maximize the total oil production of the field (output y_1) by manipulating the injected lift gas (u). Additionally, u and Δu are introduced to penalize excessive lift-gas utilization and large fluctuations in the control signals. Apart from the model equations, which obviously should be satisfied, the process is subjected to operational constraints. For example, the total injected lift gas should be equal to or less than the total available lift gas ($W_{\text{gc}}^{\max}$) and the total produced fluid should not exceed the maximum capacity of the separator ($W_{\text{s}}^{\max}$). There are also upper and lower bounds on control

Table 1. Nominal values of well parameters used for simulation.

Parameter	*Well1*	*Well2*	*Well3*	*Well4*	*Well5*	*Unit*
K	68.43	67.82	67.82	69.26	66.22	$[\frac{\sqrt{\frac{\text{kgm}^3}{\text{bar}}}}{\text{hr}}]$
PI(1.0e+4)	2.51	1.63	1.62	4.75	0.232	$\frac{\text{kg/hr}}{\text{bar}}$
GOR	0.05	0.07	0.03	0.04	0.06	$[\text{kg/kg}]$
WC	0.20	0.10	0.25	0.15	0.05	$[\text{m}^3/\text{m}^3]$
$L_{\text{a\_tl}}/L_{\text{t\_tl}}$	2758	2559	2677	2382	2454	$[\text{m}]$
$L_{\text{a\_vl}}/L_{\text{t\_vl}}$	2271	2344	1863	1793	1789	$[\text{m}]$
A_{a}	0.0174	0.0174	0.0174	0.0174	0.0174	$[\text{m}^2]$
A_{t}	0.0194	0.0194	0.0194	0.0194	0.0194	$[\text{m}^2]$
$L_{\text{r\_vl}}$	114	67	61	97	146	$[\text{m}]$

inputs and change of control due to the physical limitation of the actuators (valves). Therefore, the optimal control problem formulation is given by:

$$\min_{x,u} \quad \sum_{k=0}^{N-1}\left(-Q(y_{1,k})^2 + R\sum_{i=1}^{5} u_k^{i^2} + S\sum_{i=1}^{5}\Delta u_k^{i^2}\right) \tag{30}$$

$$\text{s.t.} \quad x_{k+1} = f\left(x_k, u_k, \theta_k\right) \tag{31}$$

$$\sum_{i=1}^{5} u_k^i \leq W_{\text{gc,k}}^{\max} \tag{32}$$

$$y_{2,k} \leq W_s^{\max} \tag{33}$$

$$u_{\text{LB}} \leq u_k^i \leq u_{\text{UB}} \tag{34}$$

$$\Delta u_{\text{LB}} \leq \Delta u_k^i \leq \Delta u_{\text{UB}} \tag{35}$$

where Q, R, and S are tuning weights and are chosen to be 1, 0.5, and 50, respectively. The total available lift gas $W_{\text{gc}}^{\max} = 9.22$[kg/s] and the maximum capacity of the separator $W_{\text{s}}^{\max} = 520$[kg/s]. The lower and upper bounds on the control signal are 0.323 and 11.66[kg/s]. Change of control also is limited between ± 0.15[kg/s]. A sampling time of 10 seconds and a prediction horizon of 25 timesteps (4.1 min) is used. These values are maintained constant throughout this paper.

3.2 Stochastic analysis of parametric uncertainty

In the first scenario, the deterministic NMPC was applied to the nominal model. As shown in Figure 5, open loop simulation started within the feasible region and the controller activated after 1 hour. The simulation results show a 12% increased in the total oil production from the field while all the constraints on the total available lift gas, capacity of separator and actuator limitations are fully satisfied.

In the other scenarios, the same controller is applied to the models containing uncertainties to see whether the controller can cope with the uncertainties in the model. For the extreme cases where the uncertain parameters take their maximums and minimums in the uncertainty region, severe oscillations were observed that led to instability.

Figure 6 shows the result of applying the nominal controller to the plant that only has -10% deviations in water cut, while the gas to oil ratio and productivity index are equal to their nominal values. It can be seen that the total oil production has been increased while the constraint on the maximum capacity of separator is violated. Although this case is not practically implementable, it worth to be noted that the same, or even smaller deviation (about 4%) in gas to oil ratio and productivity index leads to instability. This observation is consistent with the outcome from the sensitivity analysis that says the model is less sensitive to water cut rather than either gas to oil ratio or productivity index.

Figure 7 is the last scenario with -5, 8, and -2 percent deviations in productivity index, water cut, and gas to oil ratio, respectively, from their nominal values. The mismatch between the nominal and uncertain models can be observed from the total fluid production graph. In essence, it can be concluded that the deterministic NMPC is not sufficient for the gas lifted oil field model with uncertain parameters.

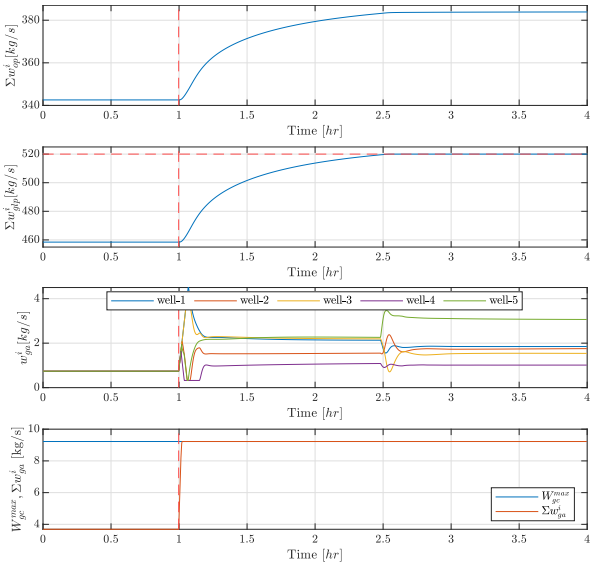

Figure 5. Performance of standard NMPC when it is applied to the nominal model.

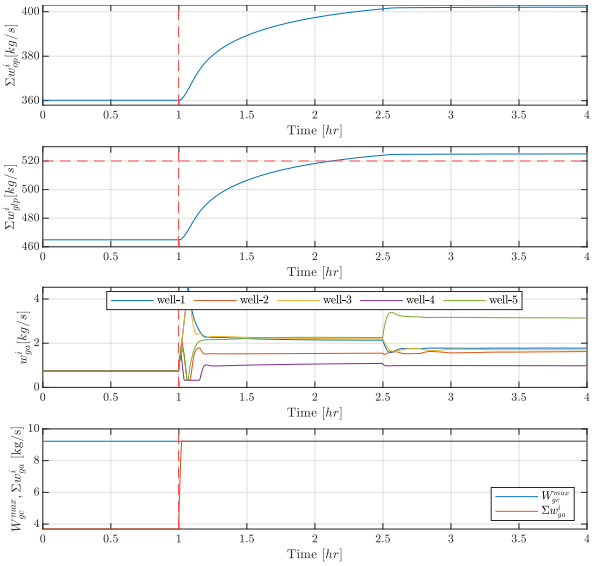

Figure 6. Performance of standard NMPC when it is applied to the uncertain model.

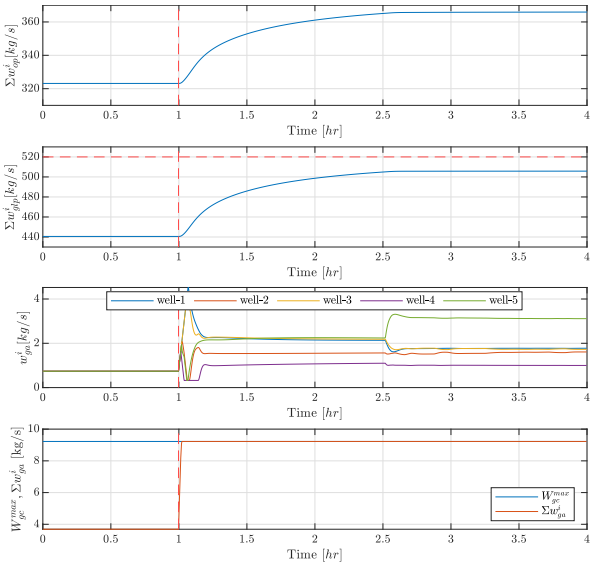

Figure 7. Performance of standard NMPC when it is applied to the uncertain model.

4 Conclusion

This paper presented a modeling framework for the gas lifted well system and total oil production maximization as a dynamic optimization control problem. The simulation results showed that the deterministic NMPC based on nominal model is capable of maximizing the total oil production of the nominal model while fulfills all the operational constraints subjected to the process; however, when the deterministic NMPC is applied to the model contains uncertainties, simulation results showed some constraints violations. This means that a deterministic NMPC is not sufficient to handle parametric uncertainties for this problem. Feasibility issues showed that the uncertainties need to be considered explicitly inside the optimization problem using robust or stochastic model predictive control. The future work includes using such advanced control methods to maximize total oil production while ensuring robust constraint satisfaction for all possible values of the uncertainties.

Acknowledgments

We gratefully acknowledge the economic support from The Research Council of Norway and Equinor ASA through Research Council project “308817 - Digital wells for optimal production and drainage” (DigiWell).

References

Andrea Capolei, Bjarne Foss, and John B. Jørgensen. Profit and risk measures in oil production optimization. *IFAC-PapersOnLine*, 48(6):214–220, 2015. doi:10.1016/j.ifacol.2015.08.034.

Kristian G. Hanssen and Bjarne Foss. Production optimization under uncertainty - applied to petroleum production. *IFAC-PapersOnLine*, 48(8):217–222, 2015. doi:10.1016/j.ifacol.2015.08.184.

Kristian G. Hanssen, Andrés Codas, and Bjarne Foss. Closed-loop predictions in reservoir management under uncertainty. *SPE Journal*, 22(5):1585–1595, 2017. doi:10.2118/185956-PA.

Toshimitsu Homma and Andrea Saltelli. Importance measures in global sensitivity analysis of nonlinear models. *Reliability Engineering & System Safety*, 52(1):1–17, 1996. doi:10.1016/0951-8320(96)00002-6.

Dinesh Krishnamoorthy, Bjarne Foss, and Sigurd Skogestad. Real-time optimization under uncertainty applied to a gas lifted well network. *Processes*, 52(4), 2016. doi:10.3390/pr4040052.

Dinesh Krishnamoorthy, Sigurd Skogestad, and Johannes Jäschke. Multistage model predictive control with online scenario tree update using recursive bayesian weighting. *18th European Control Conference (ECC)*, pages 1443–1448, 2019. doi:10.23919/ECC.2019.8795839.

Andrea Saltelli, Marco Ratto, Terry Andres, Francesca Campolongo, Jessica Cariboni, Debora Gatelli, Michaela Saisana, and Stefano Tarantola. *Global Sensitivity Analysis: The Primer*. John Wiley & Sons, 2008. ISBN 978-0-470-72517-7.

Roshan Sharma, Kjetil Fjalestad, and Bjørn Glemmestad. Modeling and control of gas lifted oil field with five oil wells. *the 52nd International Conference of Scandinavian Simulation Society*, pages 47–59, 2011.

Roshan Sharma, Kjetil Fjalestad, and Bjørn Glemmestad. Optimization of lift gas allocation in a gas lifted oil field as nonlinear optimization problem. *Modeling, Identification and Control*, 33(1):13–25, 2012.

Ilya M. Sobol. Sensitivity analysis for non-linear mathematical models. *Mathematical modelling and computational experiment*, 1:407–414, 1993.

Sensitivity Analysis of Oil Production Models to Reservoir Rock and Fluid Properties

Bikash Sharma, Ali Moradi, Britt Margrethe Emilie Moldestad
[1] Department of Process, Energy and Environmental Technology, University of South-Eastern Norway, Norway.
{sharmabikash59@yahoo.com, ali.moradi@usn.no, britt.moldestad@usn.no}

Abstract

Improving the efficiency and optimization of oil recovery with a special focus on digitalization is on the spotlight. Achieving an optimized and successful automatic production highly depends on the ability to monitor and control the well performances. This requires a suitable dynamic model of the oil field and production equipment over the production lifetime. One of the main barriers to developing such dynamic models is that generally, it is very difficult to observe and understand the dynamic of fluid in a porous medium, describe the physical processes, and measure all the parameters that influence the multiphase flow behavior inside a reservoir. Consequently, predicting the reservoir production over time and respond to different drive and displacement mechanisms has a large degree of uncertainty attached. To develop long-term oil production models under uncertainty, it is crucial to have a clear understanding of the sensitivity of such models to the input parameters. This helps to identify the most impactful parameters on the accuracy of the models and allows to limit the time of focusing on less important data. The main goal of this paper is to do sensitivity analysis for investigation of the effect of uncertainty in each reservoir parameter on the outputs of oil production models. Two simulation models for oil production have been developed by using the OLGA-ROCX simulator. By perturbation of reservoir parameters, the sensitivity of these model outputs has been measured and analyzed. According to the simulation results after 200 days, it can be argued that the most affecting parameter for accumulated oil production was the oil density with sensitivity coefficients of -1.667 and 1.610 and relative permeability (-0.844 and 0.969). Therefore, decreasing the degree of uncertainty in those input parameters can highly increase the accuracy of the outputs of oil production models.

Keywords: sensitivity analysis, OLGA, ROCX, Norne field, oil production

1 Introduction

Oil is a crucial element of our modern society and plays an important role in improving the welfare of human beings. There is no immediate alternative for oil and as a result, oil production cannot be stopped over a night. In order to achieve maximized oil recovery with minimized carbon footprint, accurate and efficient modelling and simulation of oil production are of key importance. The performance of oil simulation models for the evaluation and prediction of oil production highly depends on the reservoir parameters. Uncertainty in any of these parameters can considerably impact the accuracy of such models. Therefore, it is very important to identify which reservoir parameters are the most impactful parameters on the accuracy of the models. The sensitivity analysis assesses the contribution of the uncertainty of each model input to the uncertainty of the model outcomes and identifies the most important parameters of the system. This allows to limit the time for focusing on less important data and improve the accuracy and efficiency of the models.

Oil reservoirs have different properties, and each reservoir performs differently during various methods of oil recovery. This paper provides insight into the most important reservoir rock and fluid properties needed for accurate modeling of horizontal wells with Inflow Control Device (ICD) completion during primary oil recovery. This is achieved by doing sensitivity analysis for two near-well simulation models for two reservoirs with different properties. One of these models is based on the realistic characteristics of the Norne field located in the Norwegian Sea and the other one is developed for a synthetic reservoir. Moreover, the OLGA simulator which is a dynamic multiphase-flow simulator in combination with the ROCX module which is a near-wellbore reservoir simulator is used in this study.

2 Sensitivity Analysis

It has been in the trend since old days that before putting some engineering equipment to work, it must be designed and tested first. Several methods and approaches can be used to achieve that. One of the methods is to develop a model using several logical steps to determine the parameters which influence the results the most. This method is known as ‘Sensitivity Analysis’ and it is not only important for validation of a model but also guides to future research (Hamby, 1994).

Depending upon the complexity of the model and the type of parameters being used there are many sensitivity analysis methods. The different methods are differential analysis, one-at-a-time sensitivity measures, factorial design, sensitivity index, importance factors, subjective

sensitive analysis. All the methods are unique and can be used for the models that are suitable according to the type of results needed. In this paper, differential analysis method is applied which is the simplest and the generalized method of the analysis. Because of its simplicity and generalization, this method is also considered as the backbone of all other analysis techniques (Hamby, 1994).

Differential analysis also known as the direct method, is a technique structured based on the model with a set of specific input parameter values. Assuming this case as a base case scenario, where all other input parameters are held constant, they are set to their mean value. A sensitivity coefficient (ϕ_i) is termed to the value that describes the change of the output parameter. Basically, sensitivity coefficient is the ratio of change in output to change in input by keeping all other parameters constant(Hamby, 1994).

$$\phi_i = \frac{\%\Delta Y}{\%\Delta X_i} \quad (1)$$

where $\frac{\%\Delta Y}{\%\Delta X_i}$ is the partial derivative of Y with respect to X_i and ϕ_i is a dimensionless quantity.

3 Characteristics of the Reservoir for the Simulation Models

The simulations that increase the knowledge about sensitivity analysis of various reservoir parameters requires a model. This model could be either realistic or synthetic. Evaluating the sensitivity analysis in only one model could be specific to that case only which may or may not be the generalized case for all the models. Therefore, two models, one from the Norne field and one synthetic case are simulated and evaluated. Hence, the characteristics of each of these models need to be studied.

3.1 The Norne Model

Since Norne had potential for yielding high amount of oil and gas, there were several wells developed for maximum and optimized extraction of oil. Well 6608/10-D-2H is one of the wells, and the data needed as input for OLGA/ROCX were taken and calculation of the well was performed.

The well test data gave the temperature values for the reservoir near Well 6608/10-D-2H which is 115℃ (388 K). Based on pressure formation data, the pressure was approximated to be 277 bar.

The OLGA/ROCX requires the value of viscosity in the form of dynamic viscosity but the values from Equinor's crude summary report provided the values in the form of kinematic viscosity at different temperatures (Equinor, 2021). MATLAB was used to extrapolate the value of the viscosity from the available data. Equation 2 is the empirical equation and by using the linear regression technique the value of viscosity was extrapolated for the given temperature and pressure value.

$$\mu = Ae^{B/T} \quad (2)$$

where μ is viscosity [cP], T is temperature[K] and A and B are unknown constant parameters which should be defined empirically. To calculate the value of viscosity at reservoir condition (388K) curve fitting is used. The values obtained from linear regression and the MATLAB code is then used to extrapolate the value as shown in Figure 1. At temperature 388K the oil viscosity was found to be 0.471cP.

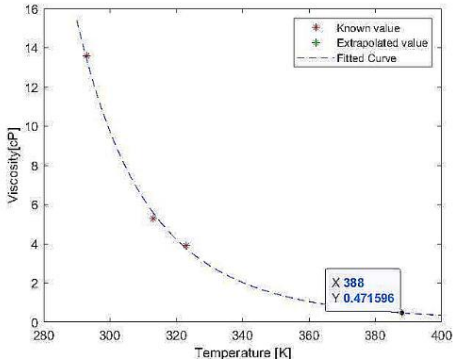

Figure 1. Extrapolated value of viscosity at reservoir conditions by curve-fitting

Permeability anisotropy (a) is the ratio of vertical permeability (k_v) to horizontal permeability (k_H). Well 6608/10-D-2H of the Norne field is divided into several layers and each layer or formations have different values for net pay thicknesses , effective porosity (ϕ_e) and shale volume (V_{sh}). These layers are called zones and the values for each zone are shown in Table 1.

Table 1. Zone thickness and the values of the rock parameters

Zones	Net Pay Thickness	Effective porosity (ϕ_e)	Shale volume (V_{sh})
Zone 1	35 m	0.2	0.31
Zone 2	46 m	0.24	0.15
Zone 3	55 m	0.27	0.14

Based on the analysis of well logs from NPD factpage, the value of average effective porosity (ϕ_e) for well 6608/10-D-2H is 0.23 and the median permeability (k) near this well is 0.3D.

By using the given data in Table 1, and Equations 3, 4 and 5 which are empirical correlations for the sandstone reservoir, the anisotropy permeability, $a = k_v / k_H$, near Well 6608/10-D-2H can be calculated (Igbokoyi et al., 2012).

$$k_H = \sqrt{k_x k_y} \quad (3)$$

$$k = \sqrt[3]{k_x k_y k_z} \quad (4)$$

$$k_v = k_z = 0.0718 \times \sqrt{\left[\frac{k_H(1-V_{sh})}{\phi_e}\right]^{2.0901}} \quad (5)$$

The results obtained from Table 1 and Equations 3, 4 and 5 for permeability anisotropy is shown in Table 2.

Table 2. Permeability anisotropy near Well 6608/10-D-2H

Parameters	k_x	k_y	k_z	a
Values	0.469D	0.469D	0.121D	0.257

The value of rock compressibility usually ranges from 1.5×10^{-6} to 20×10^{-6} 1/psi and the value used in OLGA/ROCX was 0.0001 1/bar that is approximately 1.4×10^{-5} 1/psi (Satter et al., 2016).

The data for relative permeability and capillary pressure for different saturations is not available in the NPD fact page so, the relative permeability and capillary pressure data are obtained from the OPM database (Open datasets, OPM, 2021). The calculated relative permeability curves for water and oil shown in Figure 2 can be used for the Norne field.

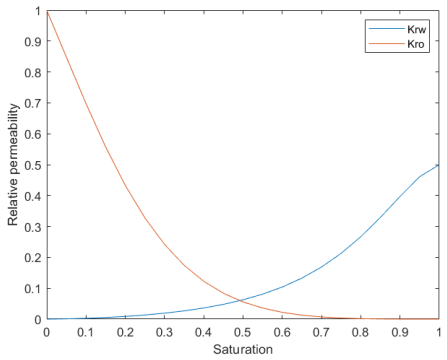

Figure 2. Relative permeability curve for Norne field

The values for oil density and Gas Oil Ratio (GOR) were 860 kg/m^3 and 82 Sm^3/ Sm^3, respectively (Norwegian Petroleum Dirctorate, 2021).

3.2 Synthetic Model

In the synthetic model, reasonable values for all the parameters required in OLGA/ROCX were concidered based experience and the ranges of values used in literature. Table 3 shows the values chosen for the synthetic model.

Table 3. Reservoir fluid and rock properties of synthetic model

Parameters	**Values**
Oil density	880 kg/m^3
Porosity	0.27
Viscosity	5 cP
Gas Oil Ratio (GOR)	40 Sm^3/ Sm^3
Rock Compressibility	0.0001 1/bar
Permeability anisotropy	0.3
Reservoir temperature	80 ℃
Reservoir pressure	200 bar

4 Development of the OLGA/ROCX Model

In this section, a simulation model was developed using OLGA/ROCX. The methodology adopted to build the dynamic reservoir wellbore model is described along with the selection of different input parameters for the model.

4.1 Development of the Reservoir Model for the Norne Model in ROCX

Based on data from various sources for Well 6608/10-D-2H at the Norne field, a model was developed in ROCX. Developing the model includes many step-by-step processes which is explained in detail.

4.1.1 Determining the Dimensions of the Reservoir Drainage Area and the Grid Setting

To prepare a reservoir model, drainage area of the near-well reservoir must be made. In actual practice the area of the drainage is ellipsoidal. However, when modelling in ROCX, it is not possible to feed the data for an ellipsoidal area, and therefore a rectangular reservoir is used.

The dimensions of the rectangular well need to be defined for the Well 6608/10-D-2H. For the calculation of the horizontal length of well, Total Vertical Depth (TVD) and Measured Depth (MD) of the well is needed which are 2647m and 4174m respectively (Norwegian Petroleum Directorate, 2021). Kickoff point is the point from which the deviation starts for drilling the hole in horizontal direction, and the length ($L_{kick\text{-}off}$) is also needed to determine the measured depth:

$$L_{MD} = L_{TVD} + L_{horizontal} + L_{kickoff} \quad (6)$$

Based on the types of horizontal well, it is assumed that Well 6608/10-D-2H is a long horizontal well so the value for $R_{kickoff}$ is 457.2 m and from all these values the length of the horizontal section of the well is calculated to be 945m. When dividing the wellbore in zones, approximating the length of the well as 992 m was easier for modelling and did not affect the output of the well.
The thickness of net pay reservoir near Well 6608/10-D-2H can be calculated from Table 1 which is 136m (35+46+55=136m). The width, however, was determined by simulation of test model for oil production of five test cases done in OLGA. This is done by keeping the height and length of the drainage area constant and varying the width between 230m and 310m. The result is shown in Figure 3 where it is clearly seen that changing the width of the drainage area seems to have very less effect on the output of oil production. The drainage width was assumed to be approximately 270m (twice the thickness) but the results from the five simulations indicates that considering the width to be 230m seems to have almost same results as with width 270m.

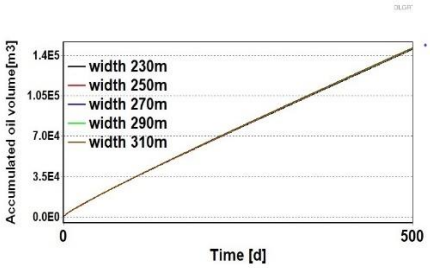

Figure 3. Different widths simulation for 500 days

Now based on the dimensions approximated for Well 6608/10-2H, the geometry of the drainage area and the position of the well are schematically shown in Figure 4. In the figure, the position of well is kept near the surface away from the aquifer to prevent early water breakthrough.

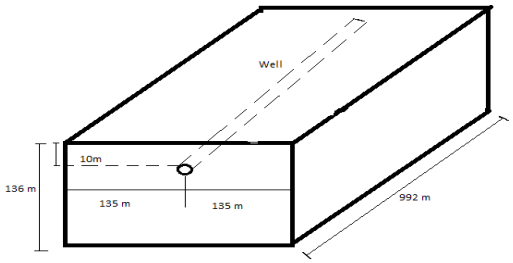

Figure 4. Geometry of the drainage area and position of well

The computational simulation should be accurate and time efficient. Finer grids and small-time steps give more accurate results but require a significant amount of time as well as computational resources. Finer mesh towards the well in y-direction was chosen with 19 cells in the Y direction and 24 cells in the Z-direction. The simulation was done using 8 equivalent ICDs, hence the length of the well was divided into 8 zones of equal size. The developed grid dimensions are shown in Figure 5. Finer mesh size in the places with high variation of fluid properties and coarser mesh size in the other places were adopted for the reservoir. This is done in order to maintain the accuracy of the results.

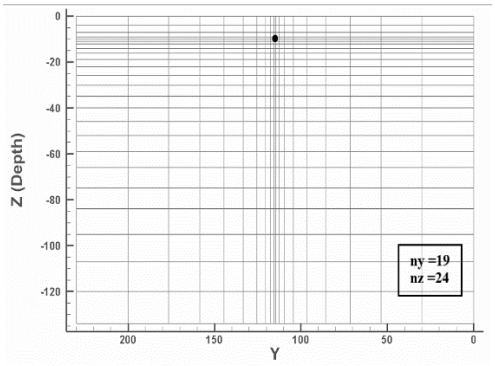

Figure 5. Grid setting for model base case of Norne well

4.1.2 Fluid Properties

It is essential to know the Pressure Volume Temperature (PVT) relation of the fluids that is used in simulations. The crude oils have a wide range of physical and chemical properties. One of the models used to estimate the PVT relations is the black oil fluid model. The black oil fluid model is a model that assumes that the oil components will always be in the liquid phase and does not evaporate at any conditions. So, the black oil model was selected over the PVT table model in ROCX. The basic properties of light oil used in the simulations are presented in Table 4.

Table 4. Oil properties used for ROCX

Parameters	Values
Oil Viscosity(cP)	0.471
Oil specific gravity	0.86
Gas specific gravity	0.64
GOR (Sm^3/ Sm^3)	82

The values of these parameters were considered at measured reservoir temperature of 115℃ and pressure of 277 bar.

4.1.3 Reservoir Properties

In the reservoir properties, the rock properties of the Norne oil field are specified. There are some assumptions made while feeding the inputs to the parameters where porosity of the Norne oil field is constant everywhere and the rock thermal properties has no effect on the production. The permeabilities in x, y and z directions are included for a rectangular drainage area. Table 5 represents the values that are used in ROCX for reservoir properties of Well 6608/10-D-2H.

Table 5. Reservoir properties for the Norne field

Parameters	Values
Porosity	0.23
Rock compressibility	0.0001 1/bar
Permeability(x-direction)	469 mD
Permeability(y-direction)	469 mD
Permeability(z-direction)	121 mD

4.1.4 Initial Condition

The initial values of temperature and pressure (115℃ and 277 bar) are the same as provided in the fluid property setting. The values of saturations of water (s_w), oil (s_o) and gas (s_g), are 0.3, 0.7 and 0 respectively.

4.2 Development of the Reservoir Model for the Synthetic Model in ROCX

The ROCX model for the synthetic case are based on the same procedures as for Well 6608/10-D-2H, with some changes in the drainage area of the reservoir. The values of the rock and fluid parameters of the well were also changed.

4.2.1 Dimensions of the Reservoir Drainage Area and the Grid Setting

The dimensions of drainage area for the synthetic model are shown in Table 6. The length of the reservoir is divided in 8 zones of equal length with one ICD in each zone. Just as for the Norne well, ICDs were installed along the length of the well.

Table 6. Dimension of reservoir of synthetic model

Parameters	Span (m)
Length	2000
Width	70
Thickness	30

The location of the horizontal well is in X-direction and the well location in the drainage area is show in Figure 6.

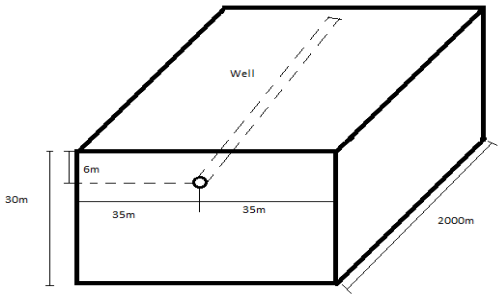

Figure 6. Location of well in drainage area of reservoir

After the location was defined for the synthetic case, the drainage area was needed to be discretized. Figure 7 shows the discretization of grid in *Y-Z* plane where the value of number of grids in Y and Z directions are 13 and 8 respectively. The length of the well along x axis is divided into 8 zones of 250 m each.

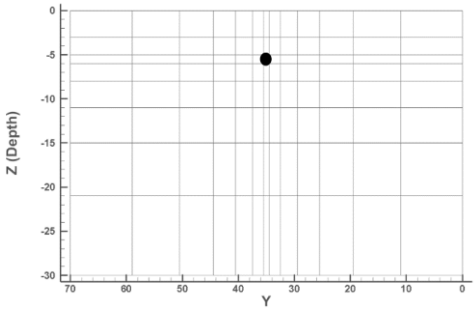

Figure 7. Grid setting for base case of synthetic well

The fluid properties for the synthetic model is presented in Table 7. The PVT selection is the same as for the Norne field. The reservoir properties needed for ROCX are shown in Table 8. The assumptions made for the Norne field for porosity and the rock thermal properties are also used in the synthetic model. The initial conditions for reservoir temperature and pressure were 80℃ and 200 bar respectively. The saturation values of fluids of water, oil and gas are s_w = 0.15, s_o = 0.85 and s_g = 0 respectively.

Table 7. Fluid property setting for synthetic model

Parameters	Values
Oil Viscosity(cP)	5
Oil specific gravity	0.88
Gas specific gravity	0.65
GOR (Sm^3/ Sm^3)	40

Table 8. Reservoir properties of synthetic model

Parameters	Values
Porosity	0.27
Rock compressibility	0.0001 1/bar
Permeability(x-direction)	2000 mD
Permeability(y-direction)	2000 mD
Permeability(z-direction)	600 mD

4.3 Development of the Well Model for the Norne Model in OLGA

There are two pipes, one for wellbore (annulus) where various flow components are installed, and the other is the production tubing. The information about each of these pipelines is required in OLGA model. The diameter of production tubing is 0.1397 m (5.5 inches), and the length is 992 m long. The diameter of the wellbore is 0.2286 m (9 inches) and has same length as the production pipe. The value of surface roughness (ε) is 0.00015 m. Each zone is further divided in two hypothetical sections and the details of these zones are presented in Figure 8.

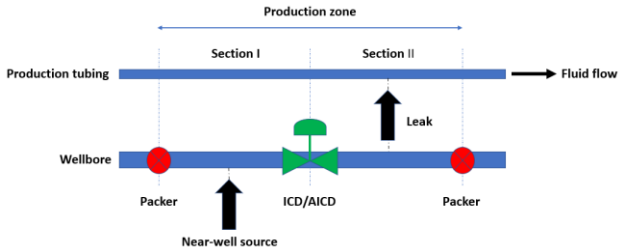

Figure 8. Simplified representation of a single production zone (Moradi et al, 2020).

Each of the zones contains two sections in the wellbore and has four components. The first component is a packer, which is used to separate zones by preventing the fluid to flow from one zone to another. The near-well source in first section of each zone is connected with ROCX and presents the fluid flow from the reservoir to the annulus. The ICD valves are installed on the wall of the pipeline, and the flow through the ICD, enters the pipeline from the annulus. The leak gives the connection from the ICD to the production pipeline. The coefficient of discharge (CD) for each valve is different as required in the wellbore. Production occures from all zones in the well, and the fluid moves towards the heel.

Considering the frictional pressure drop in the well and pressure difference across the ICDs, the pressure drawdown for this well is assumed to be 12 bar. Moreover, the hole diameter of the equivalent valve is

calculated as d = 0.09m. The simulation of this model is run for 200 days and the cumulative oil production and volumetric flow rate of oil and water are recorded.

4.4 Development of the Well Model for the Synthetic Model in OLGA

Similarly for the model development of the synthetic case in OLGA, few changes were made in the value of some parameters and apart from that, the flow component setup was exactly same as shown in Figure 8.

The length of the wellbore and production tubing were 2000m and were divided into 8 equal zones (250m each). The diameter of production tubing is 0.2159m and that of wellbore is 0.1397m. The material of pipe used is same in both cases so, the surface roughness is 0.000015m for both pipes. The pressure drawdown in the synthetic case is 10 bar and the orifice diameter is 0.015m. The simulations were run for 200 days.

4.5 Simulated Cases

Once all the parameters were set and the model was completed in OLGA/ROCX, a base case model was developed and a sensitivity analysis was performed for different rock and fluid properties of Well 6608/10-D-2H and for the synthetic model.

For the Norne oil field, the sensitivity analysis was done by increasing and decreasing the value of parameters by 20% from their mean value given in Table 10.

Table 10. Simulated cases of Norne field

Parameters	Base case	Case 1 (20% increase)	Case 2 (20% decrease)
Viscosity	0.471cP	0.565	0.376
Porosity	0.23	0.276	0.184
GOR	82 Sm^3/Sm^3	98.4	65.6
Initial water saturation	0.3	0.36	0.24
Oil density[1]	860 kg/m^3	951.5	778.5
Absolute Permeability	0.3 D	0.36	0.24
Permeability anisotropy	0.257	0.309	0.206
Rock compressibility	0.0001 1/bar	0.00012	0.00009

The relative permeability curves and capillary pressure table in ROCX were also changed from their mean values and simulated in OLGA.

[1] Oil density was changed by ± 10% only because increasing by 20% gave a value greater than 1000 which is practically not possible.

The simulated cases for the synthetic model are presented in Table 11. In these cases, the values of the parameters were increased and decreased by 10% from their mean values.

Table 11. Simulated cases of synthetic case

Parameters	Base Value	Case 1 (10% increase)	Case 2 (10% decrease)
Viscosity	5 cP	5.5	4.5
Porosity	0.27	0.297	0.243
GOR	40 Sm^3/Sm^3	44	36
Initial water saturation	0.15	0.165	0.135
Oil density	880 kg/m^3	968	792
Absolute Permeability	1.3 D	1.43	1.17
Permeability anisotropy	0.3	0.33	0.27
Rock compressibility	0.0001 1/bar	0.00012	0.00009

5 Results and Discussion

In this section, the base case model of Well 6608/10-D-2H of Norne field and of synthetic well are graphically explained. The method used for the simulations is described. A sensitivity analysis for oil and water production is carried out for Norne and the synthetic well.

5.1 Cumulative Oil and Water Production

For the sensitivity analysis of the two reservoirs, a model for a base case is developed. The graphs obtained from these cases are for accumulated volume of oil and water for the Norne well and for the synthetic case. These graphs give the idea of the quantity of oil and water in the reservoir after a certain period. The water breakthrough time can be determined based on these graphs. From Figure 9, the oil production at the end of 200 days for Norne is approximately 140000 m^3 and that for synthetic case is around 220000 m^3. Similarly, the water production for the Norne case and the synthetic case are somewhere near 11000 m^3 and 35000 m^3.

5.2 Oil and Water Flow Rate

The volumetric flow rate is another important factor which must be taken into consideration for the sensitivity analysis. The peak value of flow rate of oil for Norne in Figure 10 is around 1100 m^3/d. This value is very close to the original value which is 1250 m^3/d which indicates that the model is accurate. Also, the

ratio of the peak values of water flow rate to oil flow rate from Figure 10 is around 0.2 (200/1100). Comparing this value with the relative permeability curve for Norne in Figure 2 by dividing the rises of water and oil saturations of relative permeability, the values are approximately the same(0.2/0.68 ≈ 0.3). This is another verification of accuracy of the model.

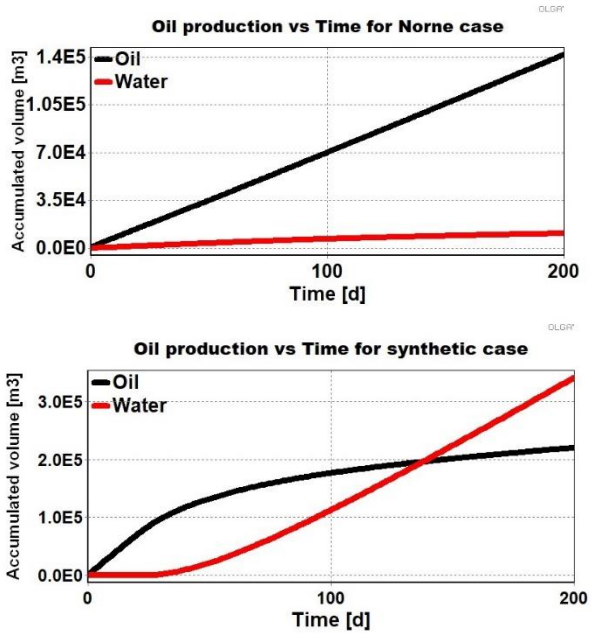

Figure 9. Accumulated oil and water production from Norne well and synthetic well

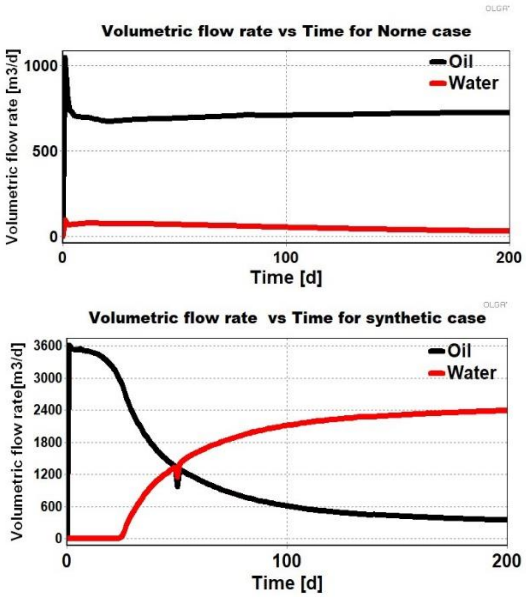

Figure 10. Volumetric flow rates of oil and water for Norne well and synthetic well

5.3 Sensitivity Coefficient for Oil Production

The parameters in the base case that are analyzed are changed in OLGA/ROCX by keeping all other parameters constant. In case of the Norne oil field, the parameter values have been changed by ± 20% and for the synthetic case, the parameter values were changed by ± 10%.

The model with the new parameter values was simulated for 200 days and the accumulated oil and water volume flows were registered. Based on the production data from the new case and the base case, the sensitivity coefficients for the different parameters were calculated. Figure 11 shows the comparison of the most affecting and the least affecting parameters for Norne and for the synthetic reservoir.

For the Norne oil field, the most affecting parameter is oil density with sensitivity coefficients -1.667 and 1.610. Oil density is then followed by initial water saturation, relative permeability, oil viscosity, and absolute permeability. The least affecting parameter is the porosity.

For the synthetic case, the most affecting parameter is the relative permeability with sensitivity coefficients of -0.844 and 0.969 for increase and decrease of the parameter values, respectively. Relative permeability is followed by porosity, oil density, initial water saturation down to capillary pressure which is the least affected parameter.

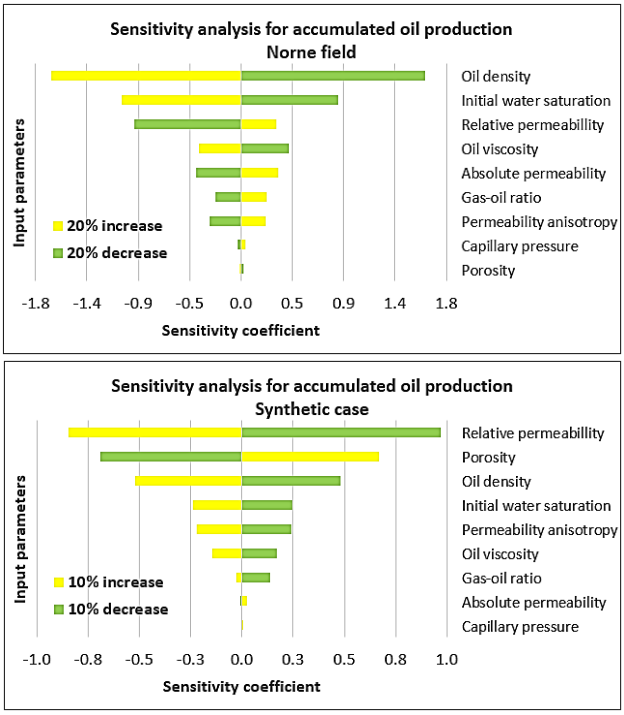

Figure 11. Sensitivity analysis of oil production of rock and fluid parameters of two cases

5.4 Sensitivity Coefficient for Water Production

The results presented in Figure 12 are obtained from the sensitivity analysis in OLGA/ROCX regarding water production.

The most affecting parameter in case of sensitivity analysis of water production for the Norne field is the initial water saturation with sensitivity coefficients of 4.516 and -3.592 for increase and decrease in the

parameter values, respectively. The initial water saturation is followed by relative permeability, oil viscosity, oil density and absolute permeability. For the synthetic case, the most affecting parameter is relative permeability with sensitivity coefficients of -0.467 and 0.323 for increase and decrease of the parameter values, respectively.

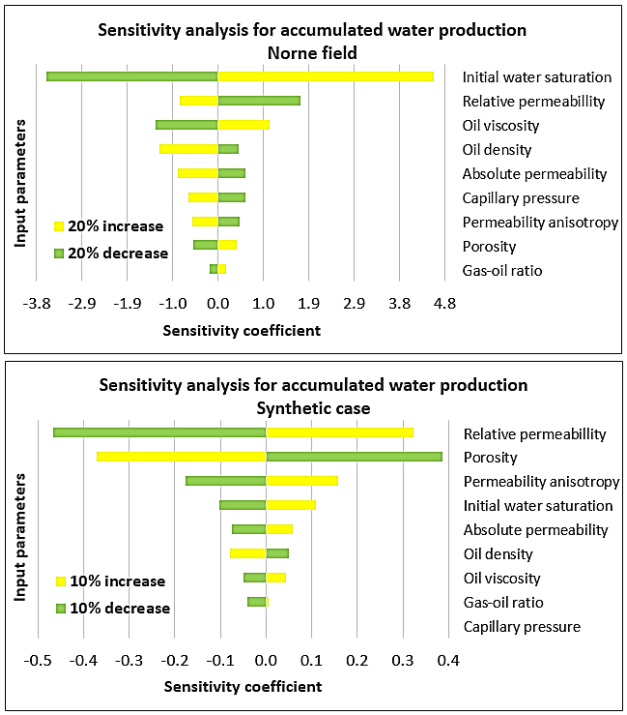

Figure 12. Sensitivity analysis of water production of rock and fluid parameters of two cases

6 Conclusion

The results obtained from the sensitivity analysis of rock and fluid parameters based on 200 days of production simulated in OLGA/ROCX shows the following key points. In the case of the Norne oil field, the most affecting parameter for accumulated oil volume was oil density with sensitivity coefficients -1.667 and 1.610 for increase and decrease of values respectively, followed by initial water saturation, relative permeability, oil viscosity, and absolute permeability. The least affecting parameter was porosity. The change in rock compressibility seemed to have no effect on the production output.

For the water production at Norne, the most affecting parameter was the initial water saturation with sensitivity coefficients of 4.516 and -3.592 for increase and decrease in the parameter values. The initial water saturation is followed by relative permeability, oil viscosity, oil density and absolute permeability.

In the synthetic case, the most impactful parameter for accumulated oil production was found to be the relative permeability (-0.844 and 0.969) followed by porosity, oil density, and initial water saturation.

For the accumulated water production, the most impactful parameter was relative permeability (-0.467 and 0.323) followed by porosity, permeability anisotropy and initial water saturation. In the synthetic case, the rock compressibility and capillary pressure seemed to have no effect on the production output.

Therefore, it can be concluded that the most affecting parameters in oil field varies based on the type of oil fields. Two different reservoirs have different parameters for the most and least affecting properties.

Acknowledgments

We gratefully acknowledge the economic support from the Research Council of Norway and Equinor through Research Council Project No. 308817, “Digital Wells for Optimal Production and Drainage” (DigiWell).

References

Equinor. Crude oil assays.2021
https://www.equinor.com/en/what-we-do/crude-oil-and condensate-assays.html

David M. Hamby. A review of techniques for parameter sensitivity analysis of environmental models. *Environmental Monitoring and Assessment*, 32(2): 135-154,1994. doi: 10.1007/BF00547132.

Philip C. Iheanacho, Djebbar Tiab and Alpheus O. Igbokoyi. Vertical-Horizontal Permeability Relationships for Sandstone Reservoirs. In Proceedings - *SPE Nigeria Annual International Conference and Exhibition*, 2012. doi:10.2118/163011-MS.

Ali Moradi and Britt M.E. Moldestad. Near-well simulation of oil production from a horizontal well with ICD and AICD completions in the Johan Sverdrup field using OLGA/ROCX. *In Proceedings - The 61st SIMS Conference on Simulation and Modelling SIMS 2020, September 22-24, Virtual Conference, Finland*, 2020.

Norwegian Pertoleum Directorate. Fact Pages. 2021 https://factpages.npd.no/en/field/pageview/all/43778

Open Porous Media. Open datasets, OPM. 2021.
https://opm-project.org/?page_id=559

Abdus Satter and Ghulam M. Iqbal. *Reservoir Engineering. The Fundamentals, Simulation, and Management of Convential and Unconvential Recoveries*. Gulf Professional Publishing, 2016.

Uncertainty Analysis of a Simplified 2D Control-relevant Oil Reservoir Model

Ashish Bhattarai, Bernt Lie

University of South-Eastern Norway, Porsgrunn, Norway, Bernt.Lie@usn.no

Abstract

In this paper, a simplified 2D control relevant model for a slightly slanting wedge-shaped black oil reservoir is made more realistic by incorporating model uncertainty. The uncertainty in the model is computed via Monte Carlo simulation. Furthermore, based on this model with uncertainty, a Proportional + Integral (PI) controller is implemented to increase oil production while minimizing water production. A PI controller is used to control the valve opening of the Inlet Control Valves (ICVs) in the production well. Implementation of a PI controller enhanced the oil recovery in 1000 days by 1.79%, while the total water production is reduced by 2.59%.

Keywords: uncertainty analysis, Monte Carlo simulation, oil reservoir model, production control

1 Introduction

1.1 Background

Norway is one of the leading suppliers of oil and gas to the global market. Revenues from sales of oil and gas have played a vital role in creating modern Norwegian society. Oil and gas are trapped in the subsurface formation of relatively thin slabs of porous rock. Oil wells are drilled into the subsurface with an oil rig to extract the oil and gas from the reservoir. The production of oil can be increased by predicting and managing the future performance of the oil reservoir. However, because of the subsurface complexity and limited data, numerous uncertainties are present in oil reservoir characterization. These uncertainties should be considered for better future prediction of oil reservoir performance. In project no. 308817, "DigiWell", of the Research Council of Norway, it is of interest to combine reservoir models and well transport models under uncertainty; these models operate under very different time scales, which poses a numeric problem. It is of interest to formulate simplified models for conceptual studies. A potential reservoir model in such a conceptual study could be a 2D, wedge-shaped black-oil model.

1.2 Previous Work

A number of simulation tools exist for prediction of oil reservoir performance, e.g., ECLIPSE, MRST, INTERSECT, MEERA, OLGA ROCKX[1]. Most of these tools are commercial; a few of them support simulation under model uncertainty. In project "DigiWell", tool MRST will be a working tool.

Zolotukhin and Ursin (2000) give an introduction to petroleum production, how to find experimental data/-model parameters from laboratory analysis, and indicate basic model formulation. Chen et al. (2006a) focus more on general model formulation. Lie (2019) presents the modeling framework used in simulation tool MRST.

Zhang (2013) developed a simplified 2D, control relevant model of a slightly slanting, 2D wedge-shaped black oil reservoir. The model was implemented in MATLAB, using fixed step-length Explicit Euler discretization. A PI controller was used to control the valve opening of the inflow control valves (ICVs) in the production well. Minimum water saturation S_w over the reservoir was taken as a set-point for the PI controller. Because this minimum saturation is not available from measurements, a different approach is needed for a realistic solution.

1.3 Structure of Paper

Bhattarai (2021) re-formulated the model from (Zhang, 2013) and implemented the model in computer language Julia, using the DifferentialEquations.jl package with variable step-length solver Tsit5(). Different saturation vs. relative permeability correlations were used, and simple parameter uncertainty was introduced, allowing for Monte Carlos simulations posed as EnsembleProblem in Julia. A more realistic PI controller that reduces the water cut (WC) was implemented. This work is presented here. In Section 2, the simulation model is developed. Section 3 presents model uncertainty and the PI controller. Section 4 provides simulation results. Finally, some conclusions are drawn in Section 5.

2 Model Overview

2.1 Two-phase Flow in a Porous Media

A black oil reservoir model has a water component, as well as hydrocarbon components divided into a gas component and an oil component with no mass transfer between the water phase and the other two phases (oil and gas) (Chen et al., 2006a,b). We further simplify the black

[1] https://en.wikipedia.org/wiki/Reservoir_simulation

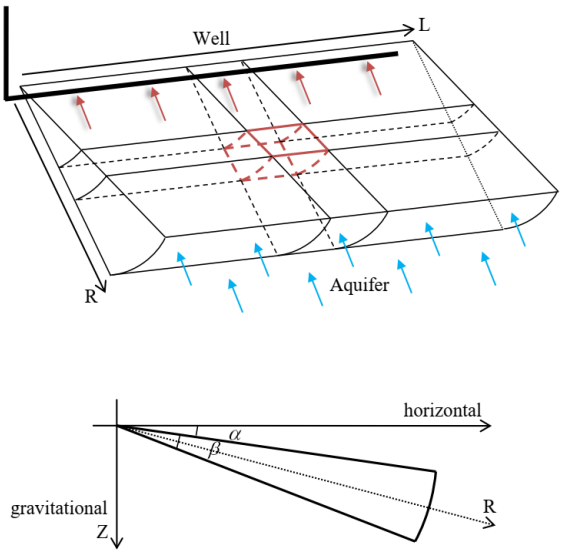

Figure 1. (a) Schematic view of the reservoir and (b) geometrical characteristics of the reservoir (Zhang, 2013).

oil model by considering a relatively new heavy oil reservoir without gas.

2.2 Reservoir Overview

The model in this work is developed for a slightly slanting wedge-shaped horizontal black oil reservoir with homogeneous dispersion of water and homogeneous in its geological features permeabilities, porosities, etc., Figure 1.

A natural aquifer with constant pressure P_a and constant relative permeability k_{wa} is located at the bottom of the reservoir, while a horizontal well is located at the top of the wedge-shaped reservoir. We use coordinates length $\ell \in [0, L]$ along the well, and radius $r \in [0, R]$ from the well towards the aquifer. The boundary conditions are zero flux at $(\ell = 0, r)$, $(\ell = L, r)$, and at (ℓ, r) for the slanting angles $\theta = \alpha \pm \frac{\beta}{2}$. A water flux exists at $(\ell, r = R)$ and a flux of oil and water mixture at $(\ell, r = 0)$ into the well. The total production rate of the mixture of oil and water from the reservoir $q_{\text{mix,tot}}$ is specified to be constant. The spatial-temporal variables are represented by (r, ℓ), and t, respectively.

The wedge-shaped reservoir model is combined with the well model. From the combined reservoir and well model, we are interested in finding how the water saturation S_w, reservoir pressure P, water and oil volumetric production rates ($q_{w,s}$, and $q_{o,s}$, respectively), well pressure P_{rw}, well bottom hole pressure P_{bh}, etc., vary with time.

2.3 Reservoir Model

With bulk volume V_b and pore volume V_p of the reservoir, porosity is given as $\phi \triangleq \partial V_p / \partial V_b$. Fluid saturation S_η for fluid $\eta \in \{o, w\}$ (oil, water) is defined as $S_\eta \triangleq \partial V_\eta / \partial V_p$ where V_η is the volume taken up by fluid η. It follows that $\sum_\eta S_\eta = 1$. For two-phase flow (Zhang, 2013)

$$\frac{\partial (\rho_\eta \cdot \phi \cdot S_\eta)}{\partial t} = \frac{1}{r} \cdot \frac{\partial (\rho_\eta \cdot u_{\eta,r} r)}{\partial r} + \frac{\partial (\rho_\eta \cdot u_{\eta,\ell})}{\partial \ell} - q_{\eta,s}. \tag{1}$$

The velocity terms in Equation 1 are given by Darcy's law:

$$u_\eta = -\lambda_\eta (\nabla P_\eta - \rho_\eta \cdot g \cdot \nabla z), \tag{2}$$

where, $\lambda_\eta = \frac{k_{\text{rel},\eta}}{\mu_\eta} K$, K is the absolute permeability, $k_{\text{rel},\eta}$ is a relative permeability for phase η, μ_η is the viscosity of phase η, P_η is the fluid pressure, and g is the acceleration of gravity.

The z-term has to be projected to the r-coordinate according to Figure 1 (b).

$$z = r \sin\left(\alpha + \frac{\beta}{2}\right). \tag{3}$$

Here, angle α is the slope of the wedge, while angle β is the angular width of the wedge, Figure 1.

2.4 Well Model

According to Chen and Zhang, the pressure close to the well declines much faster than near the aquifer. Therefore, a small step size Δr near the well is required for accurate pressure calculation in the reservoir cell at the neighborhood of the well. This can be handled by using local grids refinement in the neighborhood of the well. However, this can lead to restrictions on time steps in the numerical simulation (Chen et al., 2006a). The alternative solution is to derive an analytical solution for the steady-state flow model that yields the Peaceman equation (Peaceman, 1993). As-suming only radial flow in grids near the well,

$$q_{\eta,s,r,\ell} = -\left(\frac{2\pi\Delta\ell}{\ln\left(\frac{r_{\text{well}}}{r_e}\right)} \cdot \lambda_{\eta,r} \left(P_{rw,\eta} - P_{re,\eta} - h_\eta \left(r_{\text{well}} - r_e\right)\right) \right)_{r,\ell}. \tag{4}$$

Total *specified* flow rate $q_{\eta,s,\text{tot}}$ is the sum of the flow rates from all perforated zones

$$q_{\eta,s,\text{tot}} = -\sum_{n=1}^{N_v} \frac{2\pi\Delta\ell}{\ln\left(\frac{r_{\text{well}}}{r_e}\right)} \cdot \lambda_{\eta,r} \left(P_{rw,\eta} - P_{re,\eta} - h_\eta \left(r_{\text{well}} - r_e\right)\right), \tag{5}$$

where, N_v is the total number of perforated zones of the well, and $(r, \ell) \in [0, \Delta r] \times [0, L_{\text{well}}]$.

Specified total oil and water mixture production rate $q_{\text{mix,tot}}$ can be written as

$$q_{\text{mix,tot}} = q_{w,s,\text{tot}} + q_{o,s,\text{tot}}, \tag{6}$$

where, $q_{w,s,\text{tot}}$ and $q_{o,s,\text{tot}}$ are the total production rate of water, and oil, respectively.

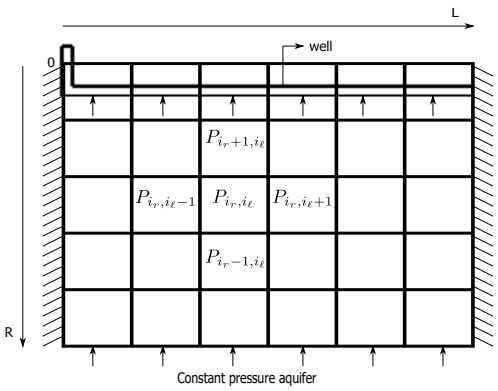

Figure 2. The block-centered grid system and a five-point stencil scheme (Zhang, 2013).

Total oil, and water mixture production rate for each cell near the well $q_{\text{mix},r,\ell}$ can be written as

$$q_{\text{mix},r,\ell} = q_{\text{w,s},r,\ell} + q_{\text{o,s},r,\ell}. \tag{7}$$

2.5 Simplifying Assumptions

To simplify the implementation of the model, it is convenient to number the grids by i_r and i_ℓ, where we number the grid for $(i_r, i_\ell) \in \{1,\ldots,n_r\} \times \{1,\ldots,n_\ell\}$ as shown in Figure 2.

The following simplifying assumptions are made:

1. Both rock and fluid are incompressible, leading to constant density and formation volume factor.
2. Immiscible two-phase flow.
3. Capillary pressure is assumed to be equal to zero, i.e., $P_{\text{cow}} = P_{\text{o}} - P_{\text{w}} = 0$. Here, P_{o} and P_{w} are pressure exerted by oil and water, respectively.
4. Effect of temperature is neglected.
5. Uniform rock porosity, i.e., $\phi_{i_r,i_\ell} = \phi$.
6. Isotropic medium $K_r = K_\ell$

With these assumptions, and introducing the definition

$$\begin{aligned} \Delta z_{\Delta i_r,i_\ell} &\triangleq z_{i_r+\frac{1}{2},i_\ell} - z_{i_r-\frac{1}{2},i_\ell} \\ \Delta z_{i_r,\Delta i_\ell} &\triangleq z_{i_r,i_\ell+\frac{1}{2}} - z_{i_r,i_\ell-\frac{1}{2}}, \end{aligned} \tag{8}$$

Equation 1 can be simplified to

$$\begin{aligned} \phi\left(\frac{dS_\eta}{dt}\right)_{i_r,i_\ell} = &\frac{\Delta\left(\lambda_\eta\left(\frac{\partial P}{\partial r} - h_\eta\right)r\right)_{\Delta i_r,i_\ell}}{r_{i_r,i_\ell}\cdot\Delta r} \\ &+ \frac{\Delta\left(\lambda_\eta\left(\frac{\partial P}{\partial \ell}\right)\right)_{i_r,\Delta i_\ell}}{\Delta\ell} \\ &- \frac{q_{\eta,\text{s}_{i_r,i_\ell}}}{\beta r_{r,\ell}\Delta r\Delta\ell}. \end{aligned} \tag{9}$$

The well model is,

$$q_{\eta,\text{s}_{i_r,i_\ell}} = -\left(\frac{2\pi\Delta\ell}{\ln\left(\frac{r_{\text{well}}}{r_{\text{e}}}\right)}\cdot\lambda_\eta\left(P_{\text{rw}} - P_{\text{re}} - h_\eta\left(r_{\text{well}} - r_{\text{e}}\right)\right)\right)_{i_r,i_\ell}. \tag{10}$$

2.6 Valve and Pipe

The valves are represented by a homogeneous flow model of sub-critical flow through a pipe containing restriction as

$$\Delta P_{\text{valve}} = 2C_{\text{u}}\frac{\rho_{\text{mix}}}{2C_{\text{v}}^2 A_{\text{valve}}^2} q_{\text{mix}}^2, \tag{11}$$

where

$$\rho_{\text{mix}} \triangleq \frac{q_{\text{w,s}}\rho_{\text{w}} + q_{\text{s,o}}\rho_{\text{o}}}{q_{\text{mix}}}, \tag{12}$$

and

$$\Delta P_{\text{valve}} = P_{\text{rw}} - P_{\text{bh}}, \tag{13}$$

here, C_{u} is a unit conversion constant, C_{v} is a dimensionless flow coefficient of the valve, A_{valve} is the constriction effective area, ρ_{mix} is the density of the fluid mixture, q_{mix} is the volumetric flow rate of the mixture, P_{rw} is the well pressure, and P_{bh} is the bottom hole pressure.

The pipes are modeled as a hydraulic network using the following equation:

$$\Delta P_{\text{pipe}} = f\rho_{\text{mix}}\frac{8\Delta L_{\text{pipe}}}{\pi^2\left(2r_{\text{p}}\right)^5} q_{\text{mix}}, \tag{14}$$

with

$$\left(\Delta P_{\text{pipe}}\right)_{i_r,i_\ell} = P_{\text{bh},i_r,i_\ell} - P_{\text{bh},i_r,i_\ell-1}, \tag{15}$$

where $(i_r, i_\ell) \in n_r \times \{1,\ldots,n_{\text{well}}\}$, f is the fanning friction factor, ΔL_{pipe} is the pipe step length which assumed to be equal to well step length $\Delta\ell_{\text{well}}$ and reservoir step length $\Delta\ell$, r_{p} is the radius of a production pipe.

2.7 Water Saturation Versus Relative Permeability

The data for water saturation S_{w} and corresponding relative permeabilities are typical values provided by the industry. This is achieved through least-square fit using a standard package in Julia called *LsqFit*[2]. Comparison of water saturation and permeability relation for actual data and least-square function is shown in Figure 3

2.8 Mobility Determination

Most of the works in the literature use an upstream scheme to evaluate the mobilities (Cordazzo et al.).The mobility λ at the integration point is evaluated upstream of the flow.

[2]https://julianlsolvers.github.io/LsqFit.jl/latest/tutorial/

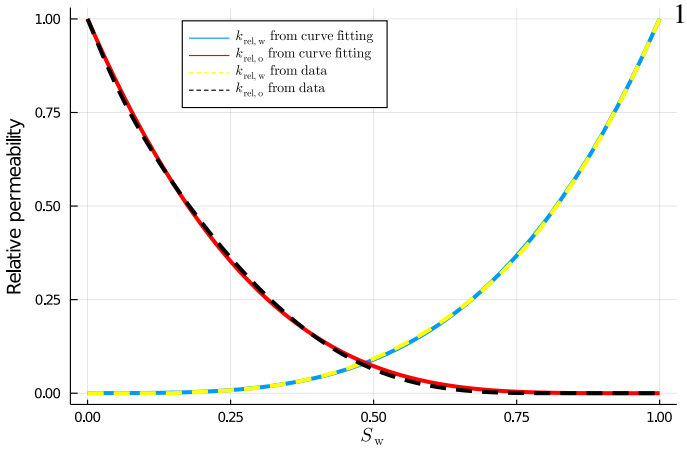

Figure 3. Relation between water saturation S_{w} and relative permeabilities.

2.9 Numerical Solution

In the numerical simulation, the finite difference method uses finite differences to approximate derivatives of ordinary differential equations. The forward difference method is used in this work.

$$\begin{aligned}\phi\left(\frac{dS_\eta}{dt}\right)_{i_r,i_\ell} &= a_{\eta,1,i_r,i_\ell}P_{i_r+1,i_\ell} + a_{\eta,2,i_r,i_\ell}P_{i_r,i_\ell-1}\\ &+ a_{\eta,3,i_r,i_\ell}P_{i_r,i_\ell} + a_{\eta,4,i_r,i_\ell}P_{i_r,i_\ell+1}\\ &+ a_{\eta,5,i_r,i_\ell}P_{i_r-1,i_\ell} - a_{\eta,6,i_r,i_\ell},\end{aligned} \tag{16}$$

where,

$$\begin{aligned}a_{\eta,1,i_r,i_\ell} &= \frac{(\lambda_\eta r)_{i_r+\frac{1}{2},i_\ell}}{r_{i_r,i_\ell}\cdot\Delta r^2}\\ a_{\eta,2,i_r,i_\ell} &= \frac{\lambda_{\eta,i_r,i_\ell-\frac{1}{2}}}{\Delta\ell^2}\\ a_{\eta,3,i_r,i_\ell} &= -\frac{(\lambda_\eta r)_{i_r-\frac{1}{2},i_\ell}}{r_{i_r,i_\ell}\cdot\Delta r^2} - \frac{(\lambda_\eta r)_{i_r+\frac{1}{2},i_\ell}}{r_{i_r,i_\ell}\cdot\Delta r^2} - \frac{\lambda_{\eta,i_r,i_\ell-\frac{1}{2}}}{\Delta\ell^2}\\ &- \frac{\lambda_{\eta,i_r,i_\ell+\frac{1}{2}}}{\Delta\ell^2}\\ a_{\eta,4,i_r,i_\ell} &= \frac{\lambda_{\eta,i_r,i_\ell+\frac{1}{2}}}{\Delta\ell^2}\\ a_{\eta,5,i_r,i_\ell} &= \frac{(\lambda_\eta r)_{i_r-\frac{1}{2},i_\ell}}{r_{i_r,i_\ell}\cdot\Delta r^2}\\ a_{\eta,6,i_r,i_\ell} &= \left(\frac{(\lambda_\eta r)_{i_r-\frac{1}{2},i_\ell}}{r_{i_r,i_\ell}\cdot\Delta r} - \frac{(\lambda_\eta r)_{i_r+\frac{1}{2},i_\ell}}{r_{i_r,i_\ell}\cdot\Delta r}\right)h_\eta\\ &+ \frac{q_{\eta,\mathrm{s},i_r,i_\ell}}{\beta r_{r,\ell}\Delta r\Delta\ell}\end{aligned} \tag{17}$$

2.10 Pressure Equation

To derive the pressure equation, we sum Equation 16 for the oil and water phases, and using the fact that $S_{\mathrm{w}}+S_{\mathrm{o}}=1$, we deduce

$$\begin{aligned}\phi\left(\underbrace{\frac{dS_{\mathrm{w}}}{dt}+\frac{dS_{\mathrm{o}}}{dt}}_{=\frac{d}{dt}(S_{\mathrm{w}}+S_{\mathrm{o}})=0}\right)_{i_r,i_\ell} &= (a_{\mathrm{w},1}+a_{\mathrm{o},1})_{i_r,i_\ell}P_{i_r+1,i_\ell}\\ &+ (a_{\mathrm{w},2}+a_{\mathrm{o},2})_{i_r,i_\ell}P_{i_r,i_\ell-1}\\ &+ (a_{\mathrm{w},3}+a_{\mathrm{o},3})_{i_r,i_\ell}P_{i_r,i_\ell}\\ &+ (a_{\mathrm{w},4}+a_{\mathrm{o},4})_{i_r,i_\ell}P_{i_r,i_\ell+1}\\ &+ (a_{\mathrm{w},5}+a_{\mathrm{o},5})_{i_r,i_\ell}P_{i_r-1,i_\ell}\\ &- (a_{\mathrm{w},6}+a_{\mathrm{o},6})_{i_r,i_\ell}\end{aligned} \tag{18}$$

where we set

$$\begin{aligned}a_{\mathrm{w},1}+a_{\mathrm{o},1} &= a_1\\ a_{\mathrm{w},2}+a_{\mathrm{o},2} &= a_2\\ a_{\mathrm{w},3}+a_{\mathrm{o},3} &= a_3\\ a_{\mathrm{w},4}+a_{\mathrm{o},4} &= a_4\\ a_{\mathrm{w},5}+a_{\mathrm{o},5} &= a_5\\ a_{\mathrm{w},6}+a_{\mathrm{o},6} &= a_6.\end{aligned} \tag{19}$$

This leads to

$$\begin{aligned}a_{6,i_r,i_\ell} &= a_{1,i_r,i_\ell}P_{i_r+1,i_\ell} + a_{2,i_r,i_\ell}P_{i_r,i_\ell-1} + a_{3,i_r,i_\ell}P_{i_r,i_\ell}\\ &+ a_{4,i_r,i_\ell}P_{i_r,i_\ell+1} + a_{5,i_r,i_\ell}P_{i_r-1,i_\ell}\end{aligned} \tag{20}$$

The pressure Equation 20 can be written in matrix form

$$AP = B, \tag{21}$$

where A is a five-diagonal sparse matrix, and P is a vector of unknown pressures,

$$A = \begin{bmatrix} \times & \times & & & \times & & & & \\ \times & \times & \times & & & \times & & & \\ & \times & \times & \times & & & \times & & \\ & & & \cdot & & & & \times & \\ \times & & & & \cdot & & & & \times \\ & \times & & & & \cdot & & & \\ & & \times & & & \times & \times & \times & \\ & & & \times & & & \times & \times & \times \\ & & & & \times & & & \times & \times \end{bmatrix}$$

$$P = \begin{bmatrix} P_{1,1}\\ P_{1,2}\\ \vdots\\ P_{1,n_\ell}\\ P_{2,1}\\ \vdots\\ P_{i_r,i_\ell}\\ \vdots\\ P_{n_r,n_\ell}\end{bmatrix}, \qquad B = \begin{bmatrix} B_{1,1}\\ B_{1,2}\\ \vdots\\ B_{1,n_\ell}\\ B_{2,1}\\ \vdots\\ B_{i_r,i_\ell}\\ \vdots\\ B_{n_r,n_\ell}\end{bmatrix}$$

The pressure is solved from this implicit, linear equation.

Table 1. Monte Carlo simulation setup.

Symbol	Range	Value	Unit
ϕ	Lower limit	$0.27 \times 80\%$	-
	Upper limit	$0.27 \times 120\%$	
S_{w_0}	Lower limit	$0.15 \times 80\%$	-
	Upper limit	$0.15 \times 120\%$	
K	Lower limit	$1500 \times 80\%$	mD
	Upper limit	$1500 \times 120\%$	
n_{sim}	-	100	-

3 Model Uncertainty and PI Controller

3.1 Uncertainty Analysis

Some of the methods developed for uncertainty in the field of the petroleum industry are experimental design, response surface, multiple realization tree, and Monte Carlo simulations. In this work, we use the Monte Carlo method, which implies simulating an ensemble of cases where uncertain parameters are drawn from some statistical distribution (Zhang, 2003). Uncertain reservoir parameters include porosity, saturation, and permeability.

We assume uniform distributions for porosity, permeability, and initial water saturation where these parameters are varied by $\pm 20\%$, Table 1.

Monte Carlo simulation is performed using *EnsembleProblem* in Julia which interfaces well with the standard differential equation solving package *DifferentialEquations.jl*.

3.2 PI Controller

There are a number of inflow control devices (ICD; passive) with the flow that is contained in an *inner pocket* in the production pipe. Inflow control valves (ICV; active) give a controlled flow out of this *inner pocket* and into the production pipe. It is assumed that the ICVs are installed at every 60 m length along the oil production pipe, i.e., at each segment of the pipe length. The group of ICVs receives the same control signals. In other words, there are 20 ICVs installed at the production pipe in which the group of valves at $n_{\text{well}} = \{1,\ldots,5\}$, $n_{\text{well}} = \{6,\ldots,10\}$, $n_{\text{well}} = \{11,\ldots,15\}$, and $n_{\text{well}} = \{16,\ldots,20\}$ receive the same control signals, respectively.

The standard methods for SISO PID controller tuning are Skogestad's method, Ziegler-Nichols method, the Good Gain method, etc. Because the reservoir system is a MIMO system with strong interactions, these standard methods fail, and we instead tune the PI controller manually through trial and error. The values of K_{p} and T_{i} are taken as $7.506 \cdot 10^{-6}$, and $2.9376 \cdot 10^{9}$, respectively, for all loops.

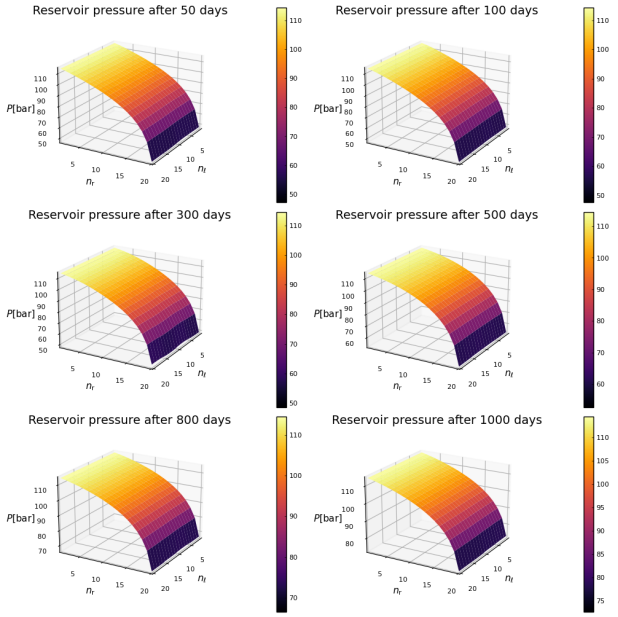

Figure 4. Pressure profile for model with PI controller.

4 Simulation Results

The value of parameters used in the simulation of the model is shown in Table 2.

Figure 4 shows 3D water saturation profiles after 50, 100, 300, 500, 800, and 1000 days of production, respectively. Water from the aquifer slowly advances towards the production well. When the water flooding front reaches the wellbore at $r = 0$, water breakthrough occurs. In Figure 5, it can be observed that the water saturation slowly starts to increase along the reservoir radius with increase in production time. In these water saturation profiles, the water coning effect is not visible because the volumetric flow rate of fluids in the well is assumed to be evenly distributed.

In the water saturation profile after 300 days of production, the water saturation at grids $n_r = 10$ to $n_r = 20$ are the same as the initial water saturation of the reservoir i.e., 0.15. However, after 500 days of production, we can observe that the water saturation at grids $n_r = 20$ is higher than 0.15. This is because the water breakthrough already occurred after 390 days of production. After 1000 days of water production, the average water saturation at $n_r = 20$ is observed to be 0.249.

Figures 6 and 7 demonstrate the effect of PI controller in total production of oil and water in 1000 days, respectively. In these figures, we can see that the total oil production, after implementing the PI controller, is increased by 1.79% while the total water production is decreased by 2.59%.

Figure 8 demonstrates the total volumetric flow rate of oil and water after implementing the PI controller. The average oil volumetric flow rate per day is increased by

Table 2. Description of parameters used in oil reservoir model.

Symbol	Description	Value	Unit
ϕ	Porosity	0.27	-
R	Reservoir radius	200	m
L	Reservoir length	1200	m
K	Absolute permeability of a reservoir	1500	mD
k_{wa}	Relative permeability of an aquifer	1	-
λ_{wa}	Mobility of aquifer water	$\frac{k_{\text{wa}}}{\mu_{\text{w}}}K$	$\text{m}^3\text{s}/\text{kg}$
ρ_{w}	Water density	1050	kg/m^3
ρ_{o}	Oil density	950	kg/m^3
μ_{o}	Oil viscosity	$100 \cdot 10^{-3}$	Pa.s
μ_{w}	Water viscosity	10^{-3}	Pa.s
α	Inclination angle of a reservoir	20	degree
β	Arch angle of a wedge shaped reservoir	25	degree
r_{well}	Well radius	0.124	m
h_{o}	Oil pressure head	$\rho_{\text{o}} \cdot g \cdot \sin\left(\alpha + \frac{\beta}{2}\right)$	$\text{kg}/\text{m}^2/\text{s}^2$
h_{w}	Water pressure head	$\rho_{\text{w}} \cdot g \cdot \sin\left(\alpha + \frac{\beta}{2}\right)$	$\text{kg}/\text{m}^2/\text{s}^2$
r_{e}	Equivalent radius	$0.5 \cdot \Delta r$	m
d_{valve}	Maximum orifice diameter of a valve	$3.217 \cdot 10^{-3}$	m
L_{well}	Horizontal well length	1200	m
n_r	Number of grids along reservoir radius	20	-
n_ℓ	Number of grids along reservoir length	20	-
n_{well}	Number of grids along well length	20	-
Δr	Step length along reservoir radius	$\frac{L}{n_r}$	m
$\Delta \ell$	Step length along reservoir length	$\frac{L}{n_\ell}$	m
$\Delta \ell_{\text{well}}$	Step length along well length	$\frac{L_{\text{well}}}{n_{\text{well}}}$	m

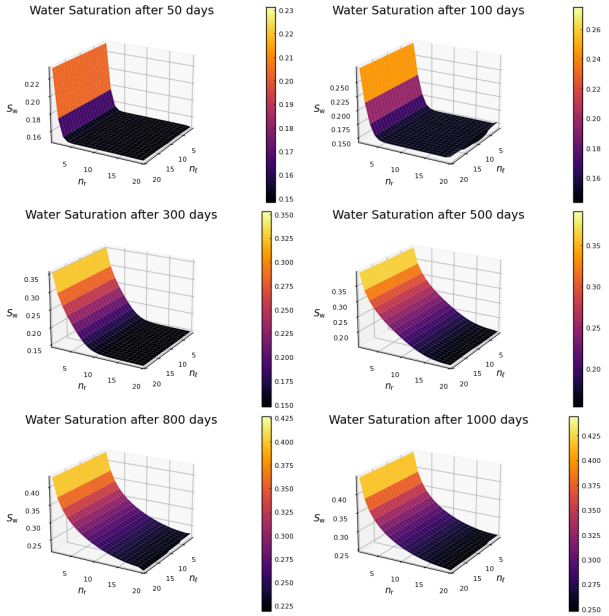

Figure 5. Saturation profile for model with PI controller.

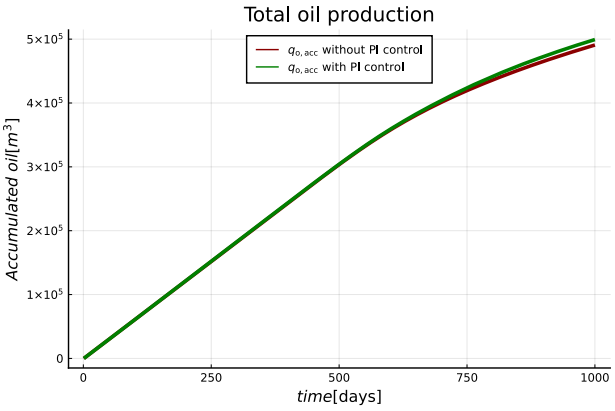

Figure 6. Comparison of total production of oil in 1000 days with and without PI controller.

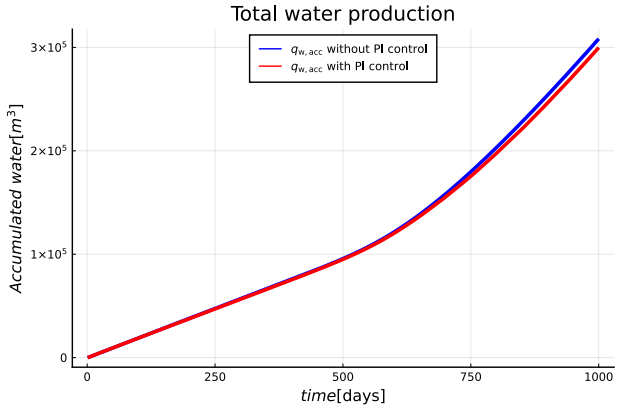

Figure 7. Comparison of total production of water in 1000 days with and without PI controller.

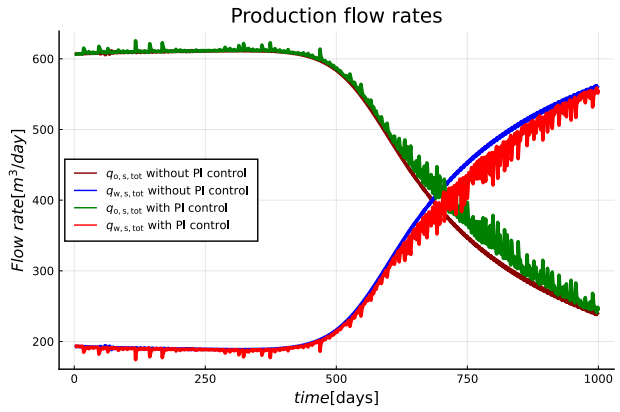

Figure 8. Comparison of total volumetric flow rates of oil and water with and without PI controller.

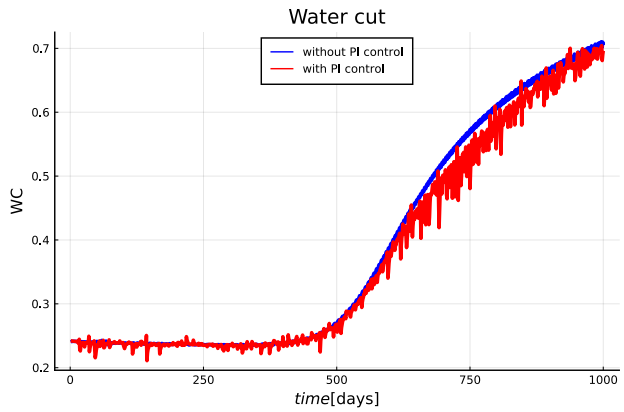

Figure 9. Comparison of water cut at the well at $\ell = 0.5L$ with and without PI controller.

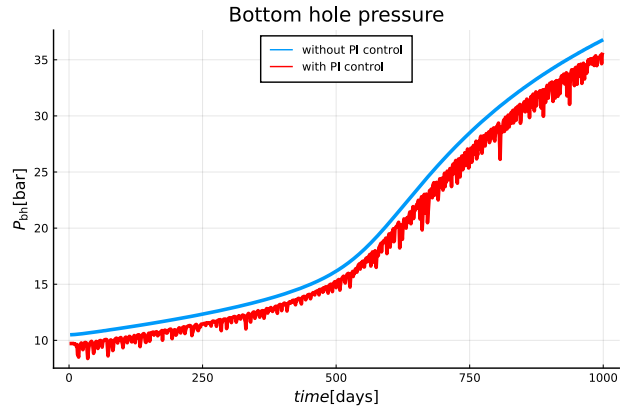

Figure 10. Comparison of bottom hole pressure at the well heel with and without PI controller.

1.738%, while the average water volumetric flow rate per day is decreased by 2.7715%. Similarly, Figure 9 shows the effect of PI controller on water cut at $\ell = 0.5L$ or $n_\ell = 10$. The average water cut is decreased by 2.755% after implementing the PI controller. Finally, in Figure 10, we can observe that the bottom hole pressure tends to decrease after the use of the PI controller.

The PI controller is implemented in a model with uncertainties. The comparison for the total oil and water production volume after implementing PI controller is shown in Figures 11 and 12, respectively. In Figure 11, the solid lines with maroon color represent uncertainties in total oil production volume without PI controller, while the green dot lines represent uncertainties in total oil production with PI controller. In this figure, we can observe that the minimum total oil production volume in 1000 days after implementing the PI controller is $359.0391 \cdot 10^3$ m^{3}which is higher than that of the model without PI controller i.e., $326.4863 \cdot 10^3$ m^3. However, the maximum total oil production volume in 1000 days after implementing the PI controller is $614.6868 \cdot 10^3$ m^3 which is lower than that of the model with PI controller i.e., $657.2351 \cdot 10^3$ m^3.

Similarly, In Figure 12, blue solid lines represent uncertainties in total water production volume without PI con-

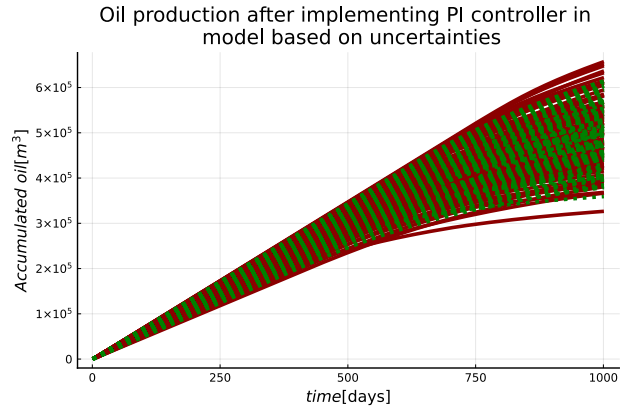

Figure 11. Comparison of Monte Carlo simulation for production of oil in 1000 days with PI controller (green dot lines) and without PI controller (maroon solid lines).

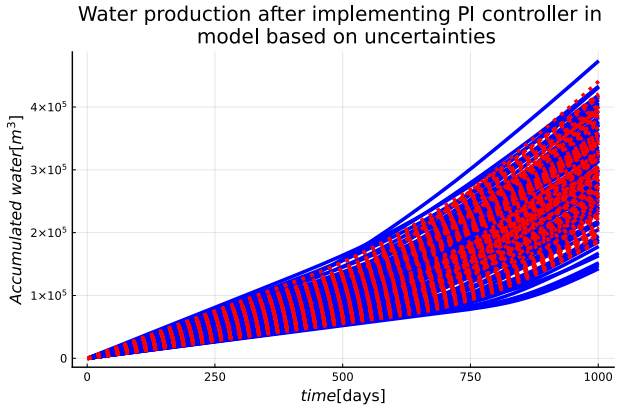

Figure 12. Comparison of Monte Carlo simulation for production of water in 1000 dayswith PI controller (red dot lines) and without PI controller (blue solid lines).

troller, while the red dot lines represent uncertainties in total water production with PI controller. In this figure, the maximum total water production volume in 1000 days after implementing the PI controller is $440.9470 \cdot 10^3\,\mathrm{m}^3$ which is lower than that of the model without PI controller i.e., $473.5101 \cdot 10^3\,\mathrm{m}^3$. However, the minimum total water production volume in 1000 days after implementing the PI controller is $185.3096 \cdot 10^3\,\mathrm{m}^3$which is higher than that of the model without PI controller i.e., $142.7613 \cdot 10^3\,\mathrm{m}^3$.

5 Conclusions

An overview of an oil well holding black oil, with a reservoir, and pipes is given. A simplified 2D control-relevant model is developed and implemented in Julia programming language, and solved using an efficient, variable time step method.

Results such as total production volume of oil and water, water cut, volumetric flow rates of oil and water, bottom hole pressure etc., are compared to those in Zhang (2013). Even when the :parameter values used in this work differ from those in (Zhang, 2013), the results are qualitatively similar to those of (Zhang, 2013). Further-more, uncertainties in the model are discussed and studied by Monte Carlo simulation. Finally, a PI controller is im-plemented in the model based on uncertainties to enhance the oil production, while minimizing the water production. The PI controller helps to increase the oil production by manipulating the ICVs at the production well. Implemen-tation of PI controller improved the total oil production in 1000 days by 1.79%. However, the effect is not very sig-nificant due to the limited capability of a PI controller. In this case, a more effective controller is required, such as MPC.

References

Ashish Bhattarai. *Improved Oil Recovery through Advanced Control*. Master's thesis, University of South-Eastern Norway, Kjølnes ring 56, N-3918 Porsgrunn, Norway, 2021.

Zhangxin Chen and Youqian Zhang. Well flow models for various numerical methods. *International Journal of Numerical Analysis and Modeling*, 9(6):375–388, 2009.

Zhangxin Chen, Guanren Huan, and Yuanle Ma. *In Computational Methods for Multiphase Flows in Porous Media*. SIAM, Philadelphia, PA, USA, 2006a. ISBN 0-89871-606-3.

Zhangxin Chen, Guanren Huan, and Yuanle Ma. *In Computational methods for multiphase flows in porous media*. Society for Industrial and Applied Mathematics, 2006b. ISBN 978-0-89871-894-2. doi:https://doi.org/10.1137/1.9780898718942. URL `https://epubs.siam.org/doi/abs/10.1137/1.9780898718942`.

Jonas Cordazzo, Clovis Raimundo Maliska, and Silva. Interblock transmissibility calculation analysis for petroleum reservoir simulation. In *In* Proceedings from the 2nd Meeting on Reservoir Simulation, November, 2002, Buenos Aires. pages 6–6.

Knut-Andreas Lie. *In* An Introduction to Reservoir Simulation Using MATLAB/GNU Octave: User Guide for the MATLAB Reservoir Simulation Toolbox (MRST). Cambridge University Press, Cambridge,UK, 2019. ISBN 978-1108492430.

DW Peaceman. Representation of a horizontal well in numerical reservoir simulation. *SPE Advanced Technology Series*. 1(1):7–16, 1993.

Guohong Zhang. Estimating uncertainties in integrated reservoir studies. PhD thesis, Texas AM University, December 2003.

Jianghui Zhang. *Improved oil recovery through advanced control*. Master's thesis, University of South-Eastern Norway, Porsgrunn, Norway, 2013.

Anatoly B. Zolotukhin and Jann-Rune Ursin. *In Introduction to Petroleum Reservoir Engineering*. HøyskoleForlaget, Kristiansand, Norway, 2000. ISBN 82-7634-065-2.

Simulation of heavy oil production using smart wells

Ali Moradi, Britt Margrethe Emilie Moldestad
Department of Process, Energy and Environmental Technology, University of South-Eastern Norway, Norway.
{ali.moradi@usn.no, britt.moldestad@usn.no}

Abstract

The application of long horizontal wells, especially in heavy oil reservoirs with a water drive, is associated with some challenges including the early breakthrough of water into the well. To solve this challenge, smart horizontal wells completed with downhole flow control devices (FCDs) and zonal isolation are widely used today. Therefore, evaluating the functionality of different types of FCDs in reducing water cut is necessary to achieve a successful design of smart wells for heavy oil production. In this paper, heavy oil production from smart wells completed with the main types of FCDs is modeled and simulated through a case study. According to the obtained results, compared to conventional wells, by using smart wells more oil and at the same time, less water can be produced from heavy oil reservoirs. Besides, in comparison with ICDs, AICDs and AICVs have better functionality in improving oil recovery and reducing water cut. It can also be concluded that among the main types of FCDs, AICVs have the best performance in achieving cost-effective heavy oil production.

Keywords: smart wells, ICD, AICD, AICV, heavy oil

1 Introduction

Despite the rapid growth of renewable energies, the world is still dependent on oil in years to come. Therefore, the focus must be on improving oil recovery with less carbon footprint to meet future energy demands. One of the main principles to achieve this purpose is maximizing the well-reservoir contact by using long horizontal wells. One of the main challenges of using such wells, especially in heavy oil reservoirs, is early water breakthrough. This problem happens due to the heel-toe effect and heterogeneity along the horizontal wells. To tackle this problem, smart wells are widely applied today. Smart (advanced or intelligent) wells are horizontal wells equipped with downhole Flow Control Devices (DFCs), zonal isolation as well as monitoring and control systems, etc. DFCs are the key elements of smart wells. The main types of such devices are passive Inflow Control Devices (ICDs), Autonomous Inflow Control Devices (AICDs), and Autonomous Inflow Control Valves (AICVs). In order to achieve a successful design of smart wells, a suitable type of these devices must be chosen for completion of the well based on the characteristics of the reservoir. So far, few studies have been performed for investigating the performance of FCDs in reducing water cut in heavy oil reservoirs with a large water aquifer. This paper aims to provide more insight into the functionality of the main types of FCDs in heavy oil reservoirs needed for the suitable design of smart wells. The study is performed through near-well simulation of heavy oil production from a smart horizontal well with zonal isolation and FCD completion in a synthetic heavy oil reservoir with a strong water drive. The OLGA® simulator coupled with the ROCX® simulator is used for developing the simulation models.

2 Inflow control technologies

2.1 Passive inflow control devices

ICDs have been developed since the 1990s for mitigating the risk of early water and/or gas breakthrough in horizontal wells. ICDs are mounted on the production tubing as a passive flow restrictor device with no moving part. ICDs are used for counteracting the non-uniform inflow throughout the length of the horizontal by adding extra pressure drop. Figure 1 shows the functionality of such devices to delay the early water breakthrough by balancing the inflow along the well (Aakre, 2017).

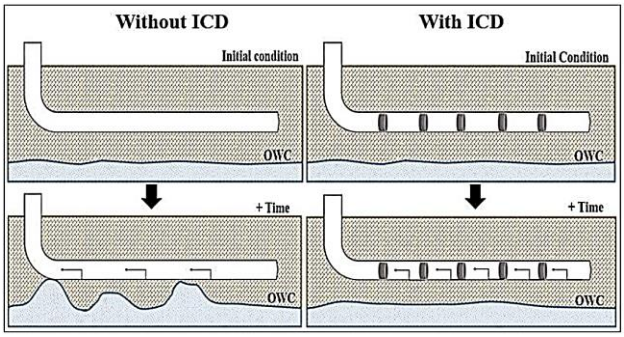

Figure 1. Application of ICDs in mitigation of the early water breakthrough (Chammout et al., 2017).

One of the main disadvantages of ICDs is not having the capability for choking unwanted fluids (water or gas) back after the breakthrough. As a result, the well must be shut in to avoid producing unwanted fluids more than the capacity of the separation facilities (Aakre, 2017).

One of the common types of ICDs is the orifice ICD and the mathematical equation governing the behavior of this type of ICDs is:

$$\dot{Q} = C_D A \sqrt{\frac{1}{1-\beta^4}} \cdot \sqrt{\frac{2\Delta P}{\rho}} \qquad (1)$$

where $\dot{Q}$ is the volume flow rate of the fluid passing through the ICD, ΔP is the pressure drop over the ICD and ρ is the fluid density. In this equation, C_D is called *discharge coefficient* and it can be calculated as $C_D = A / A_{vc}$ in which A is the cross-sectional area of the orifice hole and A_{vc} is the minimum jet area just downstream of the orifice. Moreover, $\beta = d / D$ in which *d* and *D* are the diameters of the orifice and production tubing respectively (The Engineering ToolBox, 2004).

2.2 Autonomous inflow control devices

Since passive ICDs can not choke the unwanted fluids back after breakthrough, AICDs have been developed as a robust alternative in recent years. Owing to the special design of AICDs, they can be partially closed for low-viscosity fluids compared to oil like water and gas. Consequently, in addition to delaying the water or gas breakthrough, AICDs are able to reduce the production of unwanted fluids after breakthrough autonomously and thereby increase oil production (Aakre, 2017).

Rate-Controlled Production valves (RCPs) that are also known as the Equinor AICD is one of the most widely used types of AICDs today. Figure 2 shows the schematic of an RCP valve that is consists of a body, nozzle, and a moving plate. These types of valves are designed based on the fluid properties in such a way that the moving plate rests at the sit and consequently the valve is fully open when oil passes through the valve. However, when low-viscosity fluids compared to oil enter the valve, according to Bernoulli's equation, the pressure at the inlet becomes lower. Therefore, the total force acting on the moving plate pulls it towards the inlet and the valve gets partially closed. Owing to this mechanism, these types of valves can reduce the flow rate of unwanted fluids like water or gas autonomously (Mathiesen et al., 2011; Askvik and Sørheim, 2017).

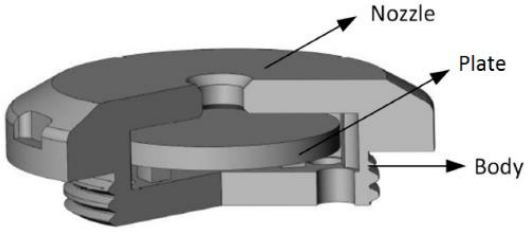

Figure 2. Schematic sketch of RCP-type AICDs (Mathiesen et al., 2011).

The empirical function describing the behavior of the RCP valves developed and validated by Equinor is represented by Equations 2 and 3 as:

$$\Delta P = f(\rho, \mu) \cdot a_{AICD} \cdot \dot{Q}^x \tag{2}$$

$$f(\rho, \mu) = \left(\frac{\rho_{mix}^2}{\rho_{cal}} \right) \cdot \left(\frac{\mu_{cal}}{\mu_{mix}} \right)^y \tag{3}$$

where $\dot{Q}$ is the volumetric flow rate of fluid passing through the RCP, and ΔP is the pressure drop over the RCP. In this equation a_{AICD}, *x* and *y* are user-input parameters that depend upon the RCP design and fluid properties. $f(\rho,\mu)$ is an analytical function of fluid density and viscosity in which ρ_{cal} and μ_{cal} are specified as calibration density and viscosity respectively. Moreover, ρ_{mix} and μ_{mix} are the density and viscosity of the mixture of fluids passing through the RCP valve and are calculated by Equation 4 as:

$$\begin{aligned} \rho_{mix} &= \alpha_{oil}\rho_{oil} + \alpha_{water}\rho_{water} + \alpha_{gas}\rho_{gas} \\ \mu_{mix} &= \alpha_{oil}\mu_{oil} + \alpha_{water}\mu_{water} + \alpha_{gas}\mu_{gas} \end{aligned} \tag{4}$$

where α_{oil}, α_{water} and α_{gas} are the volume fraction of oil, water, and gas in the mixture respectively (Halvorsen et al., 2016).

2.3 Autonomous inflow control valves

AICVs are the newest generation of inflow control devices developed by InflowControl AS. Unlike the AICDs that are capable to be partially closed against unwanted fluids, AICVs can be almost completely closed when low viscous fluids like water or gas pass through them. AICVs are self-regulating and reversible and are able to reopen when oil is the surrounding fluid. AICVs act rests on the difference in pressure drop in laminar and turbulent flow restrictors. The pressure drop across a laminar and turbulent flow restrictor is expressed by Equation 5 and 6 respectively as:

$$\Delta P = \frac{32\mu\rho v L}{D^2} \tag{5}$$

$$\Delta P = k\frac{1}{2}\rho v^2 \tag{6}$$

Figure 3 shows the principle of AICV technology which is based on a combination of laminar and turbulent flow restrictors in series. According to Equations 5, the pressure drop across a laminar flow restrictor depends on density and viscosity. Therefore, when a viscose fluid like oil passes through a laminar flow restrictor, it experiences a higher pressure drop compared to low-viscosity fluids like water and gas. Because of less pressure drop after the laminar flow restrictor, low-viscosity fluids have higher pressure in the chamber between the laminar and turbulent flow restrictors. Therefore, low-viscosity fluids move with higher velocity before passing through the turbulent flow restrictor. Based on Equation 6, the pressure drop across a turbulent flow restrictor is proportional to density and velocity squared. As a result, low-viscosity fluids experience higher pressure drop across the turbulent flow restrictor compared to oil. Based on these principles AICVs are designed to remain open for oil and get almost completely closed for unwanted fluids (Mathiesen et al., 2014).

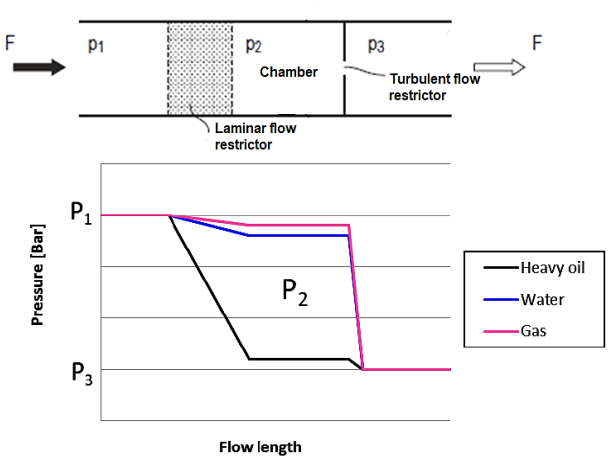

Figure 3. Combination of laminar and turbulent flow restrictor in series (Mathiesen et al., 2014).

2.4 Characteristics of the synthetic reservoir

For simulation of heavy oil production from smart wells, a synthetic (with hypothetical properties) reservoir is considered for developing the simulation models. However, to achieve realistic results, the rock and fluid properties of the synthetic reservoir are specified to be similar to those of a real reservoir. The characteristics of the synthetic reservoir are given in Table 1.

Table 1. Characteristics of the reservoir used for developing the simulation models.

Parameter	Value
Oil Density	950 kg/m^3
Oil Viscosity	10 cP
Water Density	1050 kg/m^3
Water Viscosity	0.45 cP
Gas-Oil Ratio (GOR)	50 Sm^3/Sm^3
Absolute Permeability	*Kx*=*Ky*=2000, *Kz*=600 mD
Porocity	0.25
Capilary Pressure	3 bar @ Sw=0.12, 0 bar @ Sw=1
Initial Water saturation	0.12
Reservoir Temperature	80 ˚C
Reservoir Pressure	200 bar

It is assumed that the reservoir has a mixed-wet wettability state. The Corey model is used for determining the oil and water relative permeability curves. Figure 4 shows the relative permeability curves for oil and water obtained based on the recommended Corey model parameters for a mixed-wet reservoir.

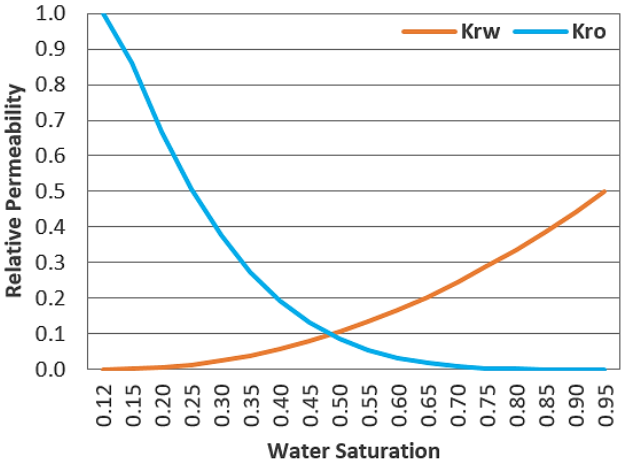

Figure 4. Relative permeability curves used for developing the simulation models.

3 Development of the OLGA/ROCX model

OLGA is a dynamic multiphase flow simulator and ROCX is a near-wellbore reservoir simulator that can be coupled to the OLGA simulator. The OLGA-ROCX coupling is commonly used for dynamic modeling and simulation of multiphase flow behavior from the reservoir pore to the production pipe and process facilities. When the OLGA simulator is combined with the ROCX simulator, an implicit scheme couples the OLGA and ROCX simulators based on the same PVT file. The OLGA simulator calculates the wellbore pressure and sends the information to the ROCX simulator. Then the ROCX simulator calculates the flow rate for each phase of the reservoir fluids and sends the information back to the OLGA simulator for calculating the new wellbore pressure. Likewise, the simulation is moved forward and completed (Schlumberger, 2020).

3.1 Development of the near-well reservoir model in the ROCX module

One of the main steps in developing a near-wellbore reservoir model in the ROCX simulator is determining the geometry and dimensions of the drainage area near the well. In reality, the drainage area of a horizontal well has an ellipsoidal shape. However, due to the ROCX limitations, a rectangular drainage area as it is illustrated in Figure 5 is considered for developing the near-wellbore reservoir model. In this study, the length of the reservoir is assumed to be the same as that of the horizontal well and equal to 992 m. The thickness and width of the reservoir are considered to be 30 m and 70 m respectively. It is also assumed that the well is located 5.5 m below the top of the drainage area.

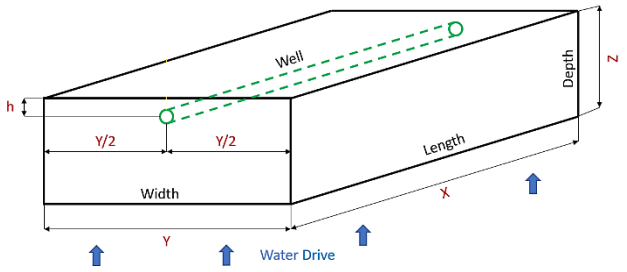

Figure 5. Schematic geometry of the reservoir near the well (Moradi and Moldestad, 2020).

The cross-section of the reservoir is located in the *Y*-*Z* plane and the well is in the *X*-direction. Therefore, the fluid pressure experiences higher variations in the *Y* and *Z* directions compared to the *X* direction. To achieve a suitable grid setup, in the *Y* and *Z* directions finer meshes have been used near the wellbore and uniform meshes are considered in the *X*-direction (Moradi, 2020). In order to develop the near-well reservoir model, for simplifying the model it is assumed that the horizontal well has 8 equivalent joints, each 124 m long. As a result, 8 uniform cells are considered for the reservoir in the *X* direction. The grid resolution in *Y* and Z directions is illustrated in Figure 6.

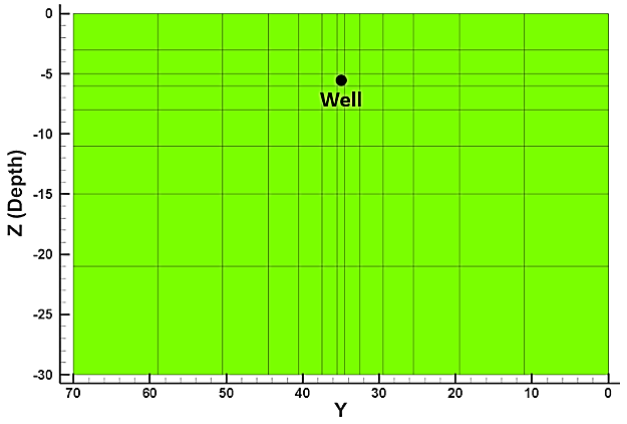

Figure 6. Grid resolution in the *Y*-*Z* plane.

3.2 Development of the well model in the OLGA simulator

For developing the well model in the OLGA simulator, one pipe with a length of 992 m, a diameter of 5.5 inch, and roughness of 15 µm is considered for representing the production tubing. Another pipe with the same length but a diameter of 8.5 inch is considered for representing the wellbore. It is assumed that the well consists of 8 equivalent joints with only one equivalent inflow control device for each joint. Besides, for each joint, the wellbore is isolated by two packers to stop flowing the reservoir fluids between different zones in the annulus. As a result, oil is produced from 8 separated zones. The simplified model for oil production from each zone in the OLGA simulator is illustrated in Figure 7. As can be seen in the figure, each production zone is divided into two sections. The wellbore in section one is connected to the ROCX simulator via the near-well source. The reservoir fluids enter the second section of the wellbore after passing FCDs. Then the reservoir fluids enter the production tubing through a leak connected to the second section of the production tubing and in this way oil is produced from each zone. This setup has been proposed and used in (Aakre, 2017).

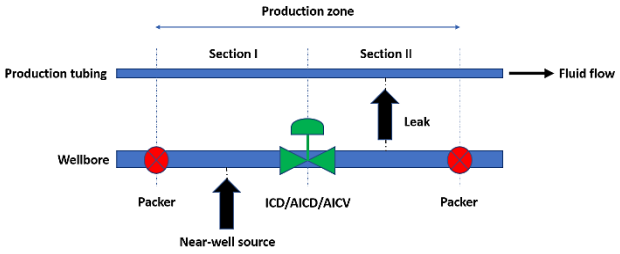

Figure 7. Simplified model of a single production zone in the OLGA simulator (Moradi and Moldestad, 2021).

The pressure drawdown used for developing the simulation models is considered to be 10 bar. For modeling ICDs in the OLGA simulator, a simple orifice valve with a diameter of 0.01 m is used. In order to model AICDs and AICVs, a controller is added to the ICD model for choking the orifice valve based on the characteristics of AICDs and AICVs. Moreover, to add a regulating flow valve to the model for keeping the total liquid production rate under a specific value, a valve with a PID controller is used.

4 Results and discussion

In this chapter, the obtained simulation results from the OLGA-ROCX model are presented and discussed. The functionality of ICDs, AICDs and AICVs in reducing water cut and improving heavy oil recovery is evaluated and compared with an open-hole well. The simulations have been conducted under two production strategies. In Case a, it is assumed that oil is produced from the smart wells by a constant pressure drawdown of 10 bar without any limitations for total liquid production. In Case b, the production strategy is the same as Case a, but it is assumed that oil production is constrained by the maximum liquid production of 800 m^3/day. Case a is a hypothetical case assuming no limit for the transportation and separation of the total liquid produced from the well. Case a has been chosen to investigate the unrestricted functionality of different FCDs where there are no limitations for fluid production from the well. However, since in reality there is a limitation in the transportation system and the separation unit, Case b has been chosen to evaluate the performance of different FCDs in a realistic case.

4.1 Cumulative oil and water production

To investigate the functionality of the different types of inflow valves, accumulated oil and water are the two most important parameters that must be taken into account. Figure 8 illustrates the accumulated oil and

water produced by the smart well compared to the open-hole well in Case a. In Case a, there is no restriction for the total liquid production rate. So, as can be seen in the figure, both the total oil production and the total water production from an open-hole well in Case a is more than those of smart wells. However, the increase in water production from the open-hole well is significantly higher than the increase in oil production from the open-hole well compared to smart wells. Therefore, although in this case more oil can be produced, much more water is also produced. Besides, in Case a, the smart well with AICDs and AICVs has produced relatively less oil but considerably less water compared to the smart well with ICDs.

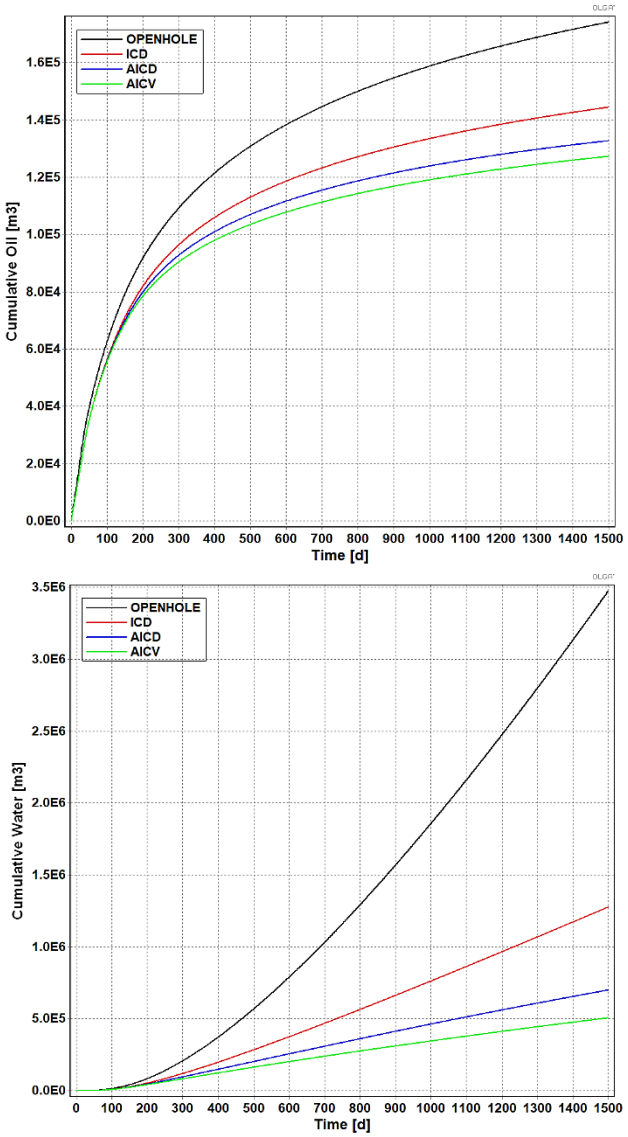

Figure 8. Cumulative oil and water production in Case a.

The cumulative oil and water production from the smart well compared to the open-hole well in Case b are shown in Figure 9. In Case b, there is a flow regulating valve for limiting the total liquid produced from the well. Therefore, in Case b, the smart well can produce more oil with less water compared to the open-hole well. Moreover, according to the figure, a relatively higher amount of oil with considerably less amount of water can be produced by using AICDs and AICVs compared to ICDs. The smart well completed with AICVs produces the lowest amount of water and has the best performance in reducing water cut compared to ICDs and AICDs.

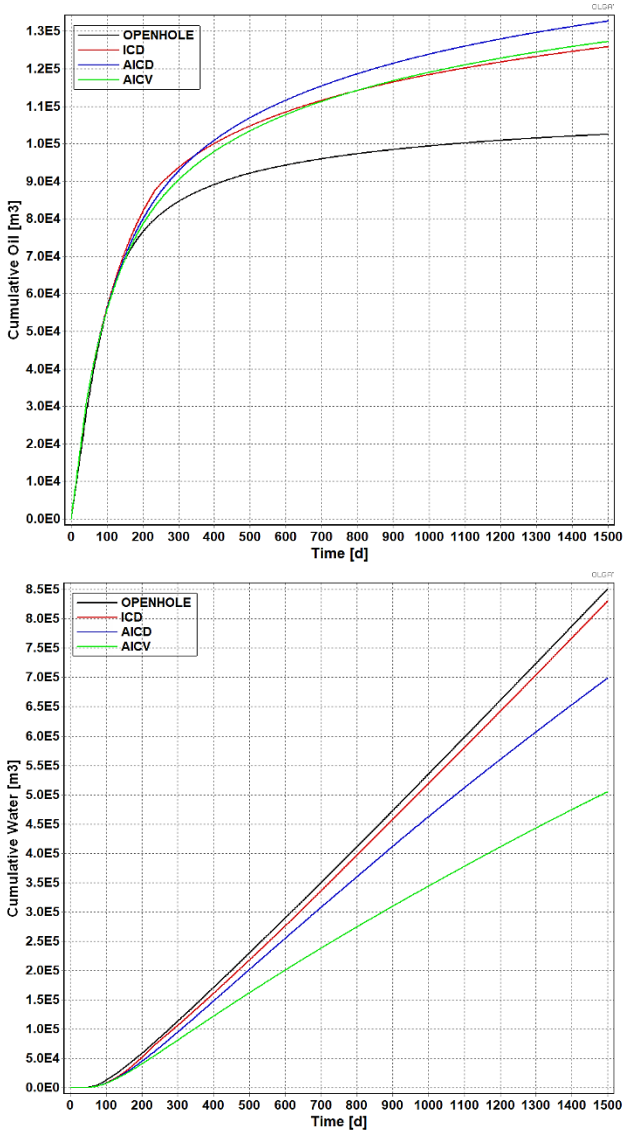

Figure 9. Cumulative oil and water production in Case b.

The values of cumulative oil and water production for the smart well with ICD, AICD, and AICV completions compared to the open-hole well after 1500 days of production are presented in Table 2. According to the obtained results, in Case a, the total oil production from the smart well completed with ICDs, AICDs, and AICVs compared to the open-hole well is decreased by 17.1%, 23.8%, 26.9% respectively. In the same way, the total water production is reduced by 63.3%, 79.9%, 85.5%.

According to Table 2, unlike Case a, the total oil produced from the smart well with ICD, AICD and AICV completions in Case b is increased by 22.7%,

29.4%, 24.1% respectively compared to the open-hole well. At the same time, the total water production is decreased respectively by 2.4%, 17.9%, 40.7%. for ICD, AICD and AICV completions in Case b.

Table 2. The values of cumulative oil and water production in Case a and b after 1500 days.

Parameter [m^3]	Open-Hole	ICD	AICD	AICV
Cum. Oil (Case a)	174143	144423	132706	127262
Cum. Water (Case b)	3475290	1277150	699178	505078
Cum. Oil (Case a)	102530	125841	132695	127251
Cum. Water (Case b)	851399	830752	699178	505078

4.2 Oil and water flow rate

Figure 10 illustrates the volumetric flow rate of oil and water in Case a during 1500 days.

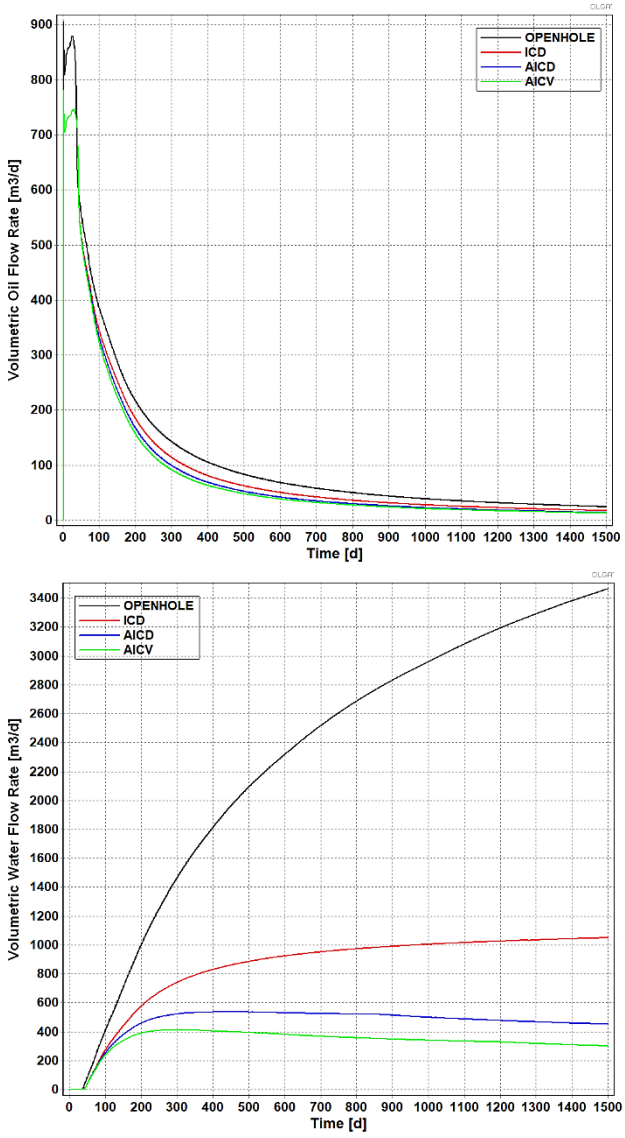

Figure 10. Volumetric oil and water flow rate in Case a.

As can be seen in Figure 10, in Case a, the rate of oil production for the open-hole well and the smart well with ICD completion is slightly higher than the smart well with AICD and AICV completions. This is due to the fact that for the open hole-well and the ICD completion (after the water breakthrough), the cross-sectional area for entering reservoir fluid to the well is bigger compared to AICD and AICV completions. However, unlike the open hole well and the smart well with ICD completion, after a while, the rate of water production from the smart wells completed with AICDs and AICVs experience a decreasing trend. This is based on the autonomous behavior of AICDs and AICVs for choking the unwanted fluids after the breakthrough.

The volumetric flow rate of oil and water in Case b are shown in Figure 11. In Case b, there is a regulating flow valve to limit the rate of total fluid production by using a valve with a PID controller. As a result, the diagrams of oil and water flow rate for the open-hole well and the smart well with ICD are noisy.

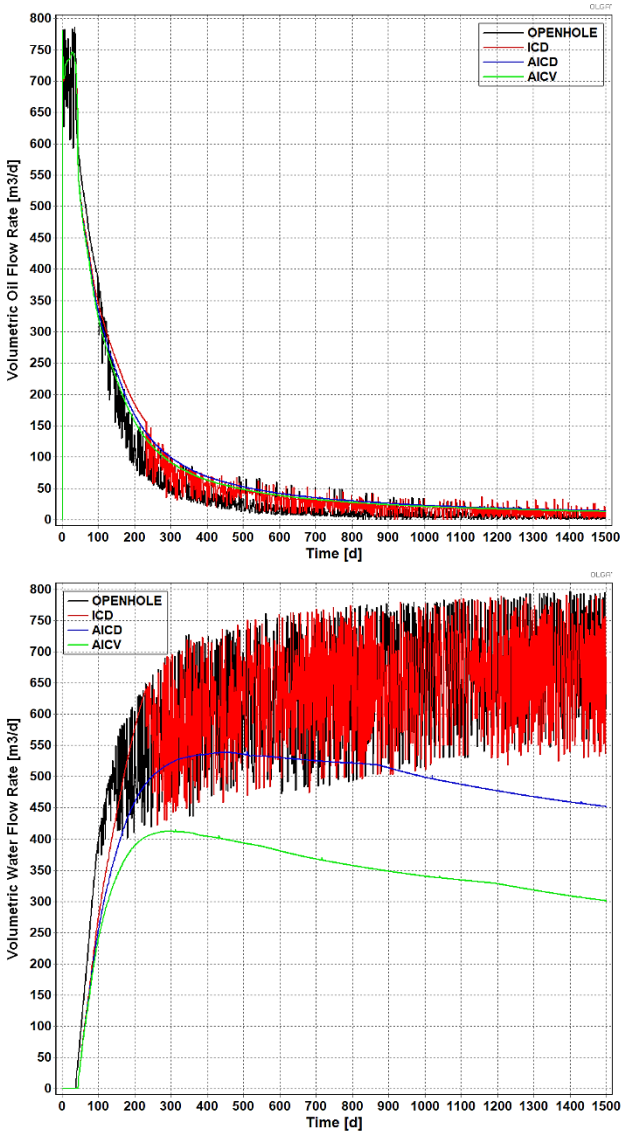

Figure 11. Volumetric oil and water flow rate in Case b.

As can be seen in Figure 11, due to the existence of a regulating flow valve, the flow rate of water for the open-hole well and the well with ICD completion remains below 800 m^3/day during the whole period of production. However, owing to the capability of AICDs for getting partially closed against water, the flow rate of produced water is autonomously decreased after almost 500 days for the smart well with AICD completion. AICVs are able to be close almost completely when water passing through them. Consequently, as can be seen in the figure, after almost 300 days the rate of water production is reduced for the smart well with AICV completion.

The values of volumetric oil and water flow rate in Case a and b after 1500 days have been given in Table 3. According to the given data in this table, the flow rate of oil after 1500 days in Case a is respectively decreased by 28.6%, 43.3%, 46.9% for ICD, AICD and AICV completions compared to the open-hole well. In the same way, comparing the open-hole well, the flow rate of water is reduced by 69.7%, 87.0%, 91.3% with ICD, AICD, and AICV completions sequentially.

In Case b, the flow rate of oil after 1500 days is increased by 77.7%, 165.7%, 150.3%, and the flow rate of water is decreased by 5.0%, 37.7%, 58.5% for the smart well with ICD, AICD and AICV completions compared to the open-hole well respectively.

Table 3. The values of oil and water production rate for Case a and b after 1500 days.

Parameter [m^3/day]	Open-Hole	ICD	AICD	AICV
Oil Rate (Case a)	24.5	17.5	13.9	13
Water Rate (Case b)	3464.3	1049.9	451.8	300.9
Oil Rate (Case a)	5.2	9.2	13.8	13.0
Water Rate (Case b)	725.6	689.3	451.8	300.9

4.3 Water cut

Since extracting, transporting, and then separating the produced water from an oil well is costly, reducing water cut is of key importance to achieve cost-effective oil production. Figure 12 shows the diagram of outlet water cut for the smart well completed with ICD, AICD, and AICV compared to the open-hole well in Case a (up), and Case b (down). As can be seen in the figure for both cases, oil is produced with considerably lower water cut buy using AICDs and AICVs compared to the open-hole well and the smart well with ICD completion. Besides, according to the obtained results, AICVs have better functionality in reducing the water cut compared to AICDs. This is due to the fact that AICVs have more capability for choking water back after breakthrough compared to AICDs.

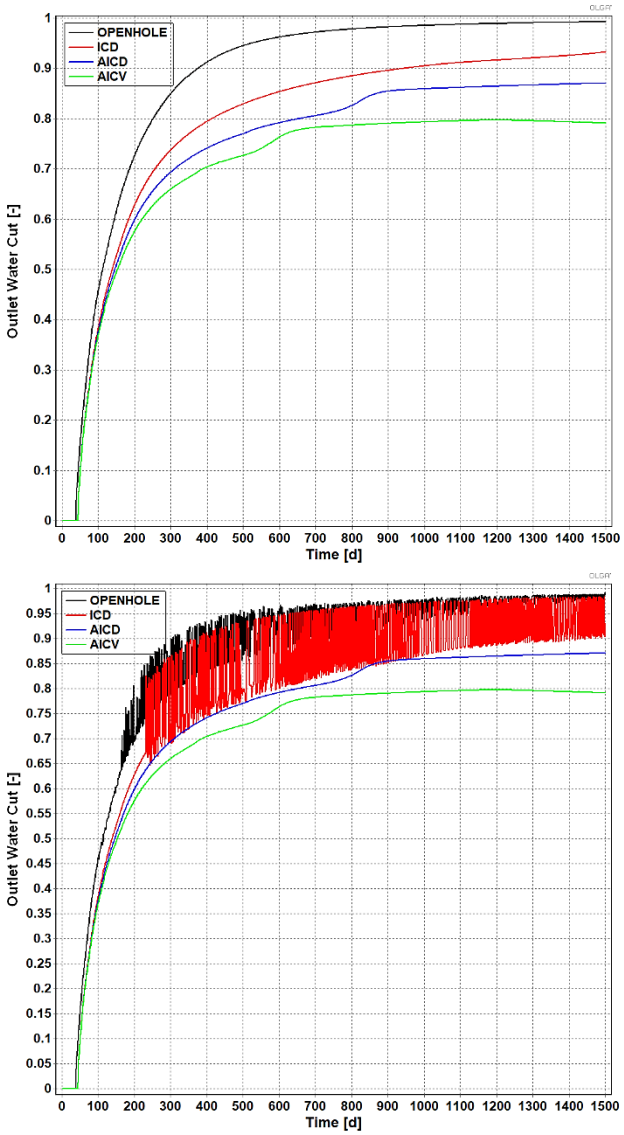

Figure 12. Outlet water cut in Case a (up), and Case b (down).

The values of outlet water cut in Case a and b after 1500 days of production are presented in Table 4. According to the given values, comparing the open-hole well, the water cut is decreased by 6.0%, 12.3%, 20.3% by completing the smart well with ICDs, AICDs, and AICVs sequentially compared to the open-hole well. Also, with a negligible difference with Case a, in Case b the water cut can be decreased by 6.5%, 11.4%, 19.5% when ICDs, AICDs, and AICVs are used for completing the smart well respectively.

Table 4. The values of outlet water cut for Case a and b after 1500 days.

Parameter [%]	Open-Hole	ICD	AICD	AICV
Water cut (Case a)	99.3	93.3	87.1	79.1
Water cut (Case b)	98.2	91.8	87.1	79.1

5 Conclusion

According to the presented simulation results, the breakthrough of water from the aquifer into the horizontal wells leads to a significant drop in oil production from heavy oil reservoirs. Considering the realistic case (Case b) it can be concluded that by using smart wells more oil and at the same time, less water can be produced from heavy oil reservoirs compared to using open-hole horizontal wells. The obtained results show that compared to the open-hole well, smart wells with ICD, AICD, and AICV, are able to increase heavy oil production by 22.7%, 29.4%, 24.1% respectively. At the same time, the amount of water produced from the smart wells using ICD, AICD, and AICV completions is reduced by 2.4%, 17.9%, 40.7% sequentially, compared to the open-hole well. Also, the outlet water cut after 1500 days of production is decreased by 6.5%, 11.4%, 19.5% when ICDs, AICDs, and AICVs are used for completing the smart well respectively, compared to using the open-hole well. Therefore, applying smart wells can noticeably improve the heavy oil recovery by reducing the water cut. Moreover, based on the simulation results, it can be said that autonomous inflow control devices (AICDs and AICVs) have better functionality for increasing oil production and reducing water production in comparison with passive inflow control devices (ICDs). Besides, it can be argued that among the main types of inflow control devices, AICVs have the best performance in reducing water cut during heavy oil production. As a result, more cost-effective oil production can be achieved from heavy oil reservoirs by using AICV completion for smart wells compared to AICD and ICD completions.

Acknowledgments

We gratefully acknowledge the economic support from the Research Council of Norway and Equinor through Research Council Project No. 308817, “Digital Wells for Optimal Production and Drainage” (DigiWell).

References

Haavard Aakre. *The impact of autonomous inflow control valve on increased oil production and recovery*. PhD thesis, University College of Southeast Norway, 2017.

Stian M. Askvik and Ivar L. J. Sørheim. *Dynamic Autonomous Inflow Control Device-Performance prediction and experimental investigation of a specific rate controlled production valve design*. Master's thesis, NTNU, 2017.

Omar J. Chammout, Bisweswar Ghosh, and Mohamad Y. Alklih. Downhole flow controllers in mitigating challenges of long reach horizontal wells: A practical outlook with case studies. *Journal of Petroleum and Gas Engineering*, 8 (10): 97-110, 2017.

Martin Halvorsen, Martin Madsen, Mathias V. Mo, Ismail I. Mohd, and Annabel Green. Enhanced oil recovery on troll field by implementing autonomous inflow control device. In Proceedings - *SPE Bergen One Day Seminar, Norwey*, 2016.

Vidar Mathiesen, Bjernar Werswick, Haavard Aakre, and Geir Elseth. Autonomous Valve, A Game Changer Of Inflow Control In Horizontal Wells. In Proceedings - *Offshore Europe Oil and Gas Conference and Exhibition, UK*, 2011.

Vidar Mathiesen, Bjørnar Werswick, and Haavard Aakre. The next generation inflow control, the next step to increase oil recovery on the Norwegian continental shelf. In Proceedings - *SPE Bergen One Day Seminar, Norway*, 2014.

Ali Moradi. *Cost-effective and safe oil production from existing and near-future oil fields.* Master's thesis, University of South-Eastern Norway, 2020.

Ali Moradi and Britt M. E. Moldestad. A Proposed Method for Simulation of Rate-Controlled Production Valves for Reduced Water Cut. *SPE Production & Operations*, 36 (03): 669–684, 2021.

Ali Moradi and Britt Margrethe Emilie Moldestad. Near-well simulation of oil production from a horizontal well with ICD and AICD completions in the Johan Sverdrup field using OLGA/ROCX. In Proceedings - *The 61st SIMS Conference on Simulation and Modelling SIMS 2020, September 22-24, Virtual Conference, Finland*, 2020.

Schlumberger. OLGA ROCX. 2020. https://www.software.slb.com/products/olga/olga-wells-management/rocx.

The Engineering ToolBox. Orifice, Nozzle and Venturi Flow Rate Meters. 2004. file:///C:/Users/alimo/OneDrive/Skrivebord/Orifice/Orifice,%20Nozzle%20and%20Venturi%20Flow%20Rate%20Meters.html.

On Uncertainty Analysis of the Rate Controlled Production (RCP) Model

Soheila Taghavi[1,2] Ali Ghaderi[3]

[1]Process, Energy and Environmental Technology, University of South-Eastern Norway, Norway, Soheila.t.hosnaroudi@usn.no

[2]InflowControl AS, Norway, Soheila.taghavi@inflowcontrol.no

[3]Mathematics and Science Education, University of South-Eastern Norway, Norway, Ali.Ghaderi@usn.no

Abstract

Rate controlled production (RCP) model is used to simulate and investigate the performance of the oil wells which are completed by autonomous inflow control devices. In order to quantify the performance of the RCP model, a dimensionless version of the model is considered, and its parameters are estimated. We demonstrate how the model and the measurement uncertainties can be quantified within the Bayesian statistical inference framework. In this relation, Hamilton Monte Carlo (HMC) is used to draw samples from the joint posterior probability distribution. We demonstrate that at the calibration step the modified model is able to capture the variations in the measurements. However, the cross- validation with the new data has revealed that the modified model tends to overpredict the pressure drop. This inadequacy cannot be explained by the measurement noise or the uncertainty in the estimated parameters. These results also imply that the original RCP model needs revision.

Keywords: AICV performance, RCP model, Bayesian inference, parameter estimation, MCMC, Stan

1 Introduction

Increase in oil production and recovery have been always the main objective of the oil industry. Hence, different methods and technologies have been developed to achieve this goal. One of the proven methods is to drill long horizontal wells, which increases the reservoir contact and consequently makes the oil production feasible and more economical.

However, long horizontal wells are likely to experience more pressure differences between the heel and toe section. This leads to non-uniform flow and consequently breakthrough of unwanted fluids in the heel section of the well, as shown in Figure 1.This phenomenon is known as heel to toe effect (Mathiesen, et al., 2014).

Autonomous Inflow Control Valve (AICV) together with Autonomous Inflow Control Devices (AICD's) like RCP valves are among the newest technologies that have been developed for Increased Oil Recovery (IOR). By balancing reservoir drawdown, these valves delay the onset of water and/or gas breakthrough and in case of breakthrough, it will restrict the production of these unwanted fluids significantly.

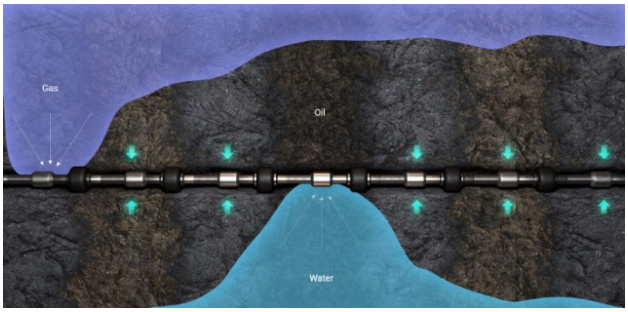

Figure 1.Uneven flow along the wellbore resulting in water and gas breakthrough.

A mathematical model describing the performance of the RCP valve was originally developed by Mathiesen et. al. in 2011 (Mathiesen, et al., 2011).This model is later being used to describe the AICV performance too. In recent years, both lab and production data from various oil wells have been used to check the validity of the model (Mohd Ismail, et al., 2018; Langaas, et al., 2020). This model has been implemented in reservoir simulators such as NETool and Eclipse in order to simulate the performance of the valve under static and dynamic conditions.

In order to be able to employ the model, one needs to estimate the model parameters prior to its deployment. It appears that one of the methods used by many practitioners for parameter estimation prior to utilization of the model in NETool is the trial-and-error method (Aakre, et al., 2018; Halvorsen, et al., 2016). Nevertheless, if one assumes that the model is correct, in most practical cases, the classical least square or similar methods are sufficient to produce good estimates for the model parameters (Moradi, et al., 2021). However, there are some evidences that the model does not explain all the variations in the data (Langaas, et al., 2020). There has also been attempts to modify the model (Voll, et al., 2014).

In order to be able to verify model inadequacy, two pre-conditions are needed to be satisfied. The first one

is accurate and precis measurements of the valve behaviour and the second one is the quantification of the different sources of the uncertainty. In this short paper, we will demonstrate how results from accurate measurements can be used within the Bayesian statistical inference framework to quantify and model the sources of the uncertainty and check how good the model explains the variations in the measurements.

2 AICV Principle

AICV utilizes viscosity and density differences between the reservoir fluids in such a way that it will keep the valve open for oil and closed for unwanted fluids like gas and water. Figure 2 illustrates AICV in open and closed position, respectively.

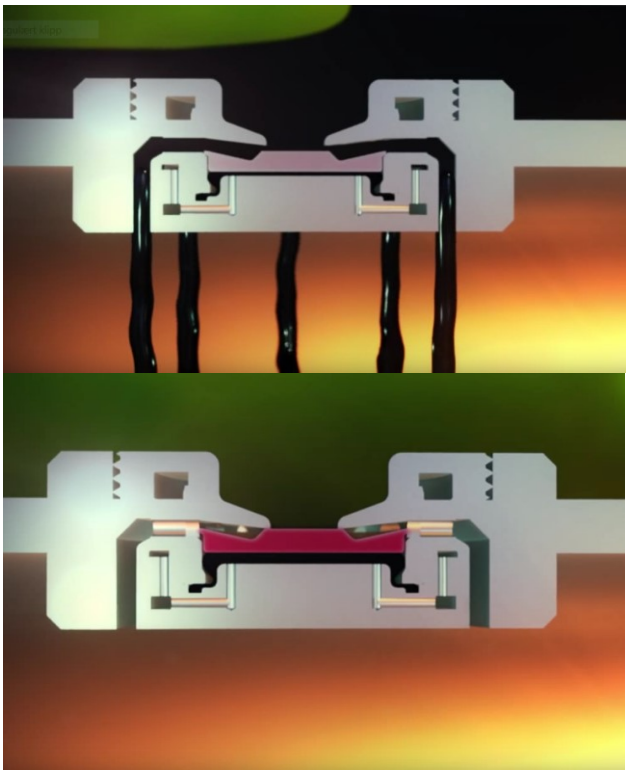

Figure 2. AICV is open for oil, illustrated by the black region (top) and closed for gas, illustrated by the green region (bottom).

This is achieved by taking advantage of the pressure differences in the Laminar Flow Element (LFE) and Turbulent Flow Element (TFE). These two flow restrictors are connected in series, which is illustrated in Figure 3 . AICV consists of two flow paths: the main flow path and the pilot flow path. Pilot flow path consists of two flow restrictors of LFE and TFE. When reservoir fluid enters the main path, a small portion of the flow is guided through the pilot flow, which is located near the main path. If a fluid with high viscosity enters the AICV, its flow through LFE will lead to a higher pressure drop over LFE. This phenomenon can be explained by Darcy-Weisbachs equation:

$$\Delta P = f \times \frac{L\rho v^2}{2D} = \frac{64}{Re} \times \frac{L\rho v^2}{2D} = \frac{32\mu v L}{D^2} \qquad (1)$$

where

ΔP is the pressure drop.

f is the friction factor (64/Re)

Re is Reynolds number.

ρ is the fluid density.

μ is the fluid viscosity.

v is the fluid velocity.

L and D are the length and diameter of the LFE respectively.

After passing through the LFE, which is a pipe segment, fluid enters a chamber. The second flow restrictor TFE, which is a nozzle, is placed in this chamber. The pressure drop across the TFE as described by Bernoulli, is calculated using the equation:

$$\Delta P = \frac{C}{2}\rho v^2, \qquad (2)$$

in which, C is a geometrical constant. Combination of these two flow restrictors results in a pressure drop, which determines how the AICV functions. As it is shown in Figure 3, high P2 will move the piston upwards closing the AICV for unwanted fluids while low P2 will keep the piston at its neutral position that maintains the oil production.

The concept and principle of AICV is described in detail in earlier SPE papers (Taghavi, et al., 2019; Aakre, et al., 2014).

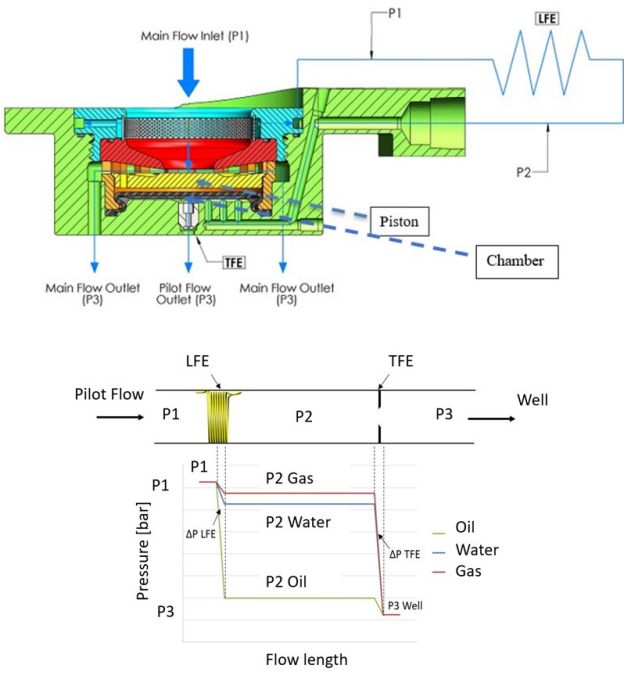

Figure 3. Combination of the laminar and turbulent flow restrictors in series in the AICV pilot flow.

3 RCP Model

The RCP model for the valve can be described as:

$$\Delta P_{Tot} = \left(\frac{\rho_{mix}^2}{\rho_{cal}}\right) \cdot \left(\frac{\mu_{cal}}{\mu_{mix}}\right)^y \cdot a_{AICD} \cdot Q^x \qquad (3)$$

where ΔP_{Tot} is the differential pressure across the AICV ρ_{cal} and μ_{cal} are the calibration fluid density and viscosity, and ρ_{mix} and μ_{mix} are the mixture fluid density and viscosity. The parameter a_{AICD} is a valve characteristic given by the ICD strength, Q is the volumetric mixture flow rate, and x and y are constants (Mathiesen, et al., 2011).

In order to reduce the complexity in this short article, we will concentrate our efforts on a single-phase oil flow. In addition, the model will be evaluated for three types of oil with different densities and viscosities.

The model described by Eq. (3), is dimensionally inconsistent. In order to avoid handling this inconsistency and its consequences, we study the flow rate vs. pressure drop with respect to a reference fluid at the same temperature. Therefore, we have chosen water at 20 degrees and a flow rate around 120 l/h. The measured pressure drop for water under these conditions is around 10 bar. Consequently, since a_{AICD} is a geometric parameter and hence independent of the fluid type, it will not play a role in the analysis. Then from Eq. (3) follows that the relative pressure drop with respect to water is

$$\frac{\Delta P_{oil}}{\Delta p_{water}} = \left(\frac{\rho_{oil}}{\rho_{water}}\right)^2 \left(\frac{\mu_{water}}{\mu_{oil}}\right)^y \left(\frac{Q_{oil}}{Q_{water}}\right)^x \qquad (4)$$

As it was mentioned earlier, there are some indications that the RCP model does not explain all the variations in the data. For this reason, we propose to use a multiplicative noise term in order to quantify possible model discrepancies. The *modified dimensionless RCP model* is

$$\frac{\Delta P_{oil}}{\Delta p_{water}} = \alpha \left(\frac{\rho_{oil}}{\rho_{water}}\right)^2 \left(\frac{\mu_{water}}{\mu_{oil}}\right)^y \left(\frac{Q_{oil}}{Q_{water}}\right)^x \qquad (5)$$

where α denotes the multiplicative noise term. Since the relative pressure drop is positive, we assume that a priori α is distributed according to Gamma distribution, with its mode at one. An α-value very close to one is an indication that the model can adequately describe the variations in the data. The statistical inference will reveal the probable values of α. In the following, Eq. (5) along with the experimental data are used to estimate the parameters α, x and y. These estimates are used to evaluate the performance of the modified RCP model.

4 Experimental Setup

The experiments were performed on the AICV prototype test rig at InflowControl's multiphase test facility located in Porsgrunn, Norway. A simplified schematic of the test rig showing the key elements of equipment and key measurement locations is shown in Figure 4. The tests can be carried out with water, pressurized air, and silicone oil as test fluid. The test facility is designed for single- and multiphase oil, water, and gas. A multistage centrifugal pump increases the water/oil pressure from the water/oil supply. Compressed air at room temperature can be regulated to the desired pressure for each case, up to maximum 200 bar. Flow rates, density and temperature are measured close to the inlet of the test vessel by a Coriolis flowmeter. A pressure transmitter measures the inlet pressure, whereas a differential pressure transmitter measures the differential pressure over the test vessel. Multiphase flow tests can be performed by injecting the desired oil flow rate to the test vessel, which is already filled with gas. The desired oil flow rate is injected from a separate test rig, which is connected to the single-phase test rig. The green dashed line in Figure 4 show the multiphase test flow path.

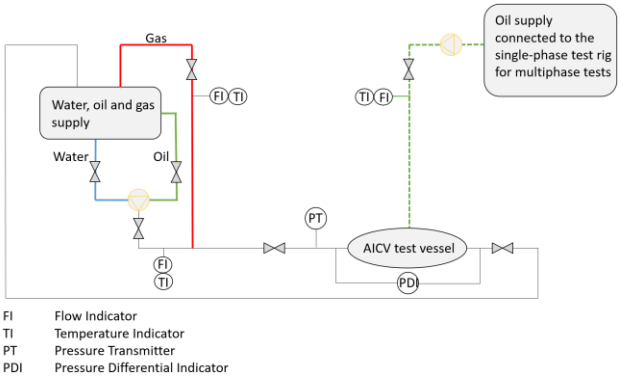

Figure 4. AICV prototype test rig setup.

4.1 Test Conditions and Data

Single-phase flow tests were performed with silicone oil as test fluid. The system conditions such as temperature and pressure, flow rates, pressure drops over the AICV and fluid properties, such as viscosity and density are controlled and measured in each test. The data obtained during the tests are listed in Table 1 in the Appendix. Temperature, density, and mass flow rate were measured using a Coriolis flow meter and the differential pressure across the AICV were measured by using a high precision pressure transmitter. Viscosity was measured and calculated manually using an Ubbelohde type viscometer. Viscosity measurements were performed several times under stable conditions in order to minimize the uncertainties. The accuracy of the different measuring tools employed in the tests are listed in Table 2 in the Appendix.

5 Bayesian Inference

The calculus of Bayesian inference is based on the application of two rules, the product, and the sum rules of the probability theory. One of the useful forms of the

product rule is the Bayes theorem. In the present context, we have noisy measurements, D and a model, M with unknown parameters represented by θ. We are seeking to estimate θ. Then by the Bayes theorem we have

$$P(\theta|D,M,I) = P(D|\theta,M,I) \times \frac{P(\theta|M,I)}{P(D|I)} \qquad (6)$$

$P(\theta|D,M,I)$ is the posterior distribution over the possible values of θ consistent with the measurements, the model and any other available and relevant background information denoted by I; like any information about the valve construction. On the right-hand side of the above equation, $P(D|\theta,M,I)$ is the likelihood, which is a statement about how likely it is to measure D given the model and specific values for θ. The term $P(\theta|M,I)$ is known as the prior distribution. In the present context, it models the expert opinion about the possible values of the θ. The last term $P(D|I)$ functions as the normalization constant and is independent of θ and hence not relevant in the present context. We remind the reader that the letters in the parentheses stand for logical propositions and "," denotes the logical "AND" operation. However, in calculations we work with algebraic expressions. The context will determine the use.

Often, as in the present case, the inference on θ also depends on some other parameters, for which neither their true values are known nor are they of primary interests. Nevertheless, due to dependency of inference on them, they must be part of the estimation process. These parameters are known as the *nuisance parameters*. Here the sum rule of the probability theory can be useful. Let ω denote the vector of the nuisance parameters, then by the sum rule we have

$$P(\theta|D,M,I) = \int_{\Omega} P(\theta,\omega|D,M,I)d\omega \qquad (7)$$

The above operation is called marginalization. Basically, calculating the above integral is the same as averaging the integrant over all possible values of ω. Marginalization is a very powerful concept and will be used in the next section. The reader is referred to (Kruschke, 2015) for further reading on Bayesian inference.

6 Statement of the Inference

In the following, let the model parameters, the nuisance parameters, data, and the model be denoted by θ, ω, D and M, respectively. That is,

$\theta = (\alpha, x, y)$
$\omega = (\Delta p_w, Q_w, \sigma_\mu, Q_o, \mu_o)$
$D = (\Delta p_{od}, Q_{od}, \mu_{od}, \rho_o, \rho_w, \mu_w, \sigma_p, \sigma_q)$
$M = M(\theta,\omega) = \Delta p_o(\theta,\omega)$

The description of each symbol is listed in Table 3 in the Appendix. The main reason for the choice of the nuisance parameter vector ω, is that we are uncertain about the true values of these parameters. For example, even though we have taken great care in measuring the viscosity, there is no guaranty that the conditions under which the oil flows through the valve are exactly the same as the viscometer. Therefore, we have chosen to include σ_μ as one of the nuisance parameters. Similar reasons are behind the choice of other components of ω. We emphasise that this is an important component in quantification of the sources of the uncertainty. The lack of knowledge about the true values of the parameters under different test conditions, which are not possible to be controlled during the experiments, constitute an important source of the uncertainty.

By the Bayes theorem, the joint posterior distribution is

$$p(\theta,\omega|D,M,I) \propto p(D|\theta,\omega,M,I) \times p(\theta,\omega|M,I). \quad (8)$$

The choice of the likelihood is determined by the measurements noise, while the choice of the prior distribution is based on the uncertainty in the expert knowledge about the true values of the parameters, before considering the measurements. For example, as was mentioned previously, α represents the multiplicative noise. It is positive and we expect its value to be one. However, there are reasons to believe that the model tends to overestimate the pressure drop over the valve. Therefore, we suspect that there is a good chance that α can attain values below one. For these reasons, we choose $\gamma(2,2)$, the gamma distribution with the parameters $(2,2)$, to represent our prior knowledge about α. The expected value of this distribution is one and its mode is at one-half. However, after seeing the data, the posterior distribution of α might be different, which as we shall see, is indeed the case. Note that $\gamma(2,2)$ has non-zero mass for all $\alpha > 0$. That is, the prior distribution does not exclude any positive values of α. It only makes some values less probable. The marginal posterior distribution of α will allow the data to modify the belief represented by the prior. In a similar manner, the expert knowledge on the other parameters can be incorporated in the inference process through appropriate choice of the prior distributions for each parameter. We have summarized the choices of the priors and the likelihoods for each parameter in Figure 5.

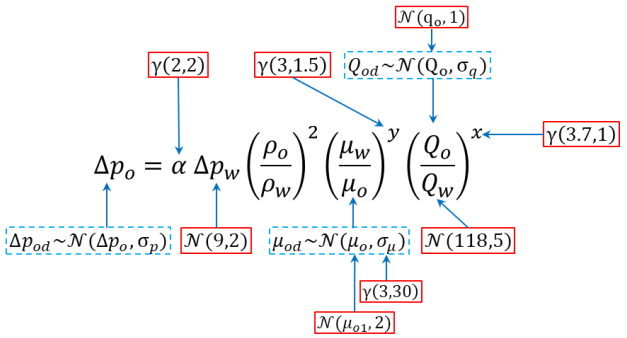

Figure 5. The choice of prior distribution (in red/whole) and the likelihood (in blue/dashed).

Due to *logical* independence between the parameters, the joint posterior distribution in Eq. (8) is the product of all the distributions listed in Figure 5. All the parameters are positive and in case of x, it is larger than 2. This means that all the normal distributions are truncated at zero. In the case of x, we have a truncated gamma distribution with lower limit being 2. The marginal posterior distribution is found by integrating over the domain of ω.

7 Markov Chain Monte Carlo Simulation

It is difficult to find an analytical expression for the joint- and the marginal posterior distributions of the parameters. This is generally a challenging task in Bayesian statistics. A common approach is to approximate the joint posterior distribution by large number of samples. The generation of samples are often conducted by a class of dependent sampling methods known as Markov Chain Monte Carlo (MCMC). Roughly explained, the method works by sampling the distribution relative to the height of the distribution function on its domain. The frequency distribution of these samples will on the long run converge to the true distribution. Computationally, one starts with a random sample and generates a chain of samples following certain sets of rules, which will guaranty that the chain will eventually visit all the regions relative to their probability mass. Since in practice one can only generate finite number of samples, it is important to check if the chain has found the regions of highest probability mass. There is a so-called *burn-in* period, below which all the samples are discarded. The reason for this is to make sure that in a set containing a finite number of samples, the samples from regions with low probability mass are not over-represented.

For the purpose of this study, we run a MCMC method known as *Hamiltonian Monte Carlo* (HMC), using the statistical software known as *Stan*, which comes also as a R package known as *RStan* (Stan development team, 2019). We have run four chains, each with different starting points. Figure 6 shows the output of the chains for each of the model parameters.

As it can be seen, regardless of the initial starting point of the chain, after a burn-in period of roughly 10K, all the chains are stabilized and converged. For more details, we refer the reader to (Kruschke, 2015).

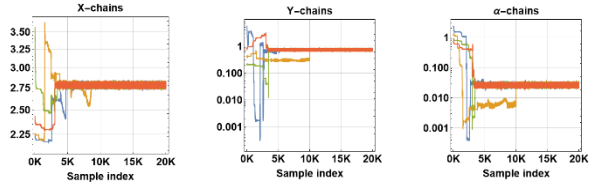

Figure 6. The trace plot of the MCMC chains for model parameters.

After ignoring the burn-in samples, the pairs plot can be used to represent the marginal posterior distributions of the model parameters. The plot consists of both single and pairwise marginal posterior distributions of the model parameters. It is basically 1D and 2D histogram of the samples of the model parameters (see Figure 7).

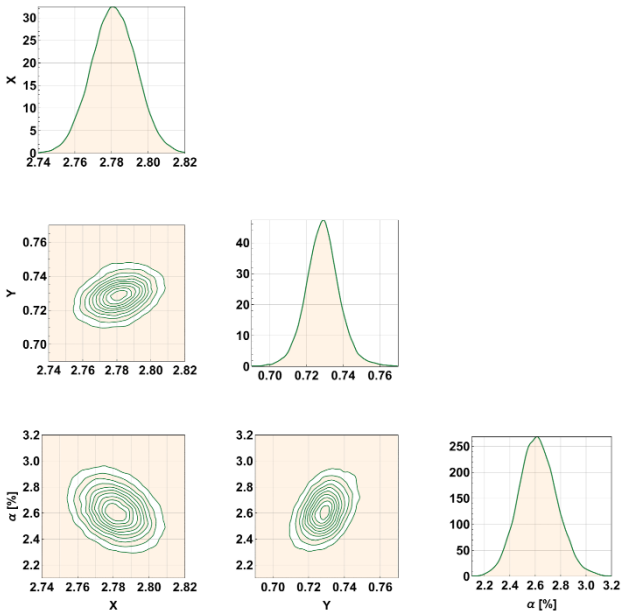

Figure 7. Pairs plot of the model parameters.

The histogram density of the parameter α reveals that the model is hugely over predicting the relative pressure drop over the valve. More specifically, the pressure drops over the valve have to be scaled down to 2.2%-3.2% of their predicted values by the model in order to be consistent with the measurements.

7.1 Calibration and Validation

The dataset D used in the MCMC simulation is generated by running experiments on two different oil types with viscosities 6.6 cP and 36.4 cP (see Table 4 in the Appendix). The measurements and the posterior samples from the MCMC with 99% credible intervals are plotted in Figure 8. Except for two points, for the case of 36.4 cP oil, all the pressure drops predicted by the model are within the 99% credible interval. That is,

at the calibration step, the model can describe most of the variations in the measurements. At this stage, without further measurements, it is difficult to explain the reason(s) for the two borderline outliers observed in the dataset for 36.4 cP oil.

The validation is conducted on a new dataset, which was not used in the estimation of the model parameters. This second dataset is generated by running the experiment on an oil with viscosity 12.6 cP. For this, we need to find the posterior predictive distribution.

Indeed, let $D_N = (\Delta p_{oN}, Q_{oN})$ denote the unobserved new data. Then the posterior predictive distribution is defined as $p(D_N \,|D, M, I)$. In order to be able to use the model M, one needs to know the model parameters.

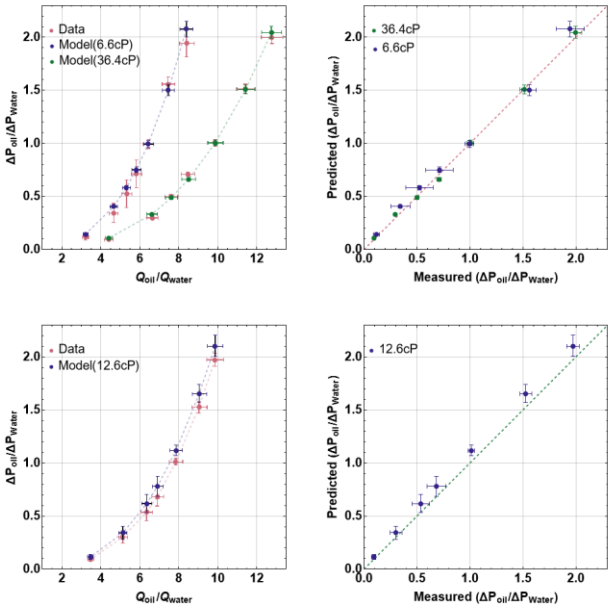

Figure 8. Calibration (top row) and validation (bottom row). The dashed lines are drawn for visualization purpose.

By application of the marginalization, we get

$$p(D_N \,|D, M, I) = \int_\Lambda p(D_N\,, \theta, \omega|D, M, I) d\theta d\omega \quad (9)$$

Note that by the product rule, the integrant can be expressed as

$$p(D_N\,, \theta, \omega|D, M, I) = p(D_N \,|\theta, \omega, D, M, I) \times p(\theta, \omega|D, M, I) \quad (10)$$

The observant reader recognizes that the second term on the right-hand side is the joint posterior distribution defined by Eq. (8). The first term on the right-hand side is called the *sampling distribution* and its functional form is same as the likelihood. The difference is that unlike likelihood, which is a function of the model parameters, the sampling distribution is a function of D_N and is normalized to unity over the domain of D_N. By applying the following algorithm, one can generate samples from the posterior predictive distribution,

1. Generate (θ_i, ω_i) from $p(\theta, \omega|D, M, I)$
2. Generate D_{Ni} from $p(D_N \,|\theta_i, \omega_i, D, M, I)$
3. $i = i + 1$, go to step 1.

The above algorithm is iterated a given number of times. The histogram of the generated samples D_{Ni} can then be considered as an estimate for the posterior predictive distribution defined by Eq. (9). Note that we are already in disposition of the samples (θ_i, ω_i). They are the samples generated from the joint posterior distribution during the calibration step. Thus, we only need to conduct the step 2 in the above algorithm. From the product rule, and the nature of measurements noise, follows that the sampling distribution can be expressed as product of two normal distributions

$$p(D_N \,|\theta, \omega, D, M, I) = p(\Delta p_{oN} \,|\mathrm{M}(\theta, \omega), Q_{oN}, D, I) \times p\left(Q_{oN} \,|q_{oN}, \sigma_q, I\right) \quad (11)$$

in which

$$p(\Delta p_{oN} \,|\mathrm{M}(\theta, \omega), Q_{oN}, D, I) = \mathcal{N}(\Delta p_{oN}|\mathrm{M}(\theta, \omega), Q_{oN}, D) \quad (12)$$

and

$$p\left(Q_{oN} \,|q_{oN}, \sigma_q, I\right) = \mathcal{N}\left(Q_{oN}|q_{oN}, \sigma_q\right). \quad (13)$$

In the above expressions q_{oN} is the given flow rate for which one seeks to calculate the corresponding pressure drop. The algorithm for generating samples from the sampling distribution can be formulated as follows

2.1. Generate Q_{oNi} from $\mathcal{N}\left(q_{oN}, \sigma_q\right)$
2.2. Generate Δp_{oNi} from $\mathcal{N}(\Delta p_{oN}|\mathrm{M}(\theta, \omega), Q_{oNi}, D)$

The result of the cross-validation with 99% credible error-bars is given in Figure 8. For low flow rates or equivalently low-pressure drops, the model prediction is within the 99% credible interval of the measurements. However, it appears that for high flow rates, the model has some tendency to over-predict the differential pressure over the valve.

8 Conclusions

In this paper, we demonstrated how the model and the measurement uncertainties can be quantified within the framework of the Bayesian statistics. In order to avoid complications due to dimensional inconsistency of the original model, we proposed a dimensionless version of the model. The result of our analysis revealed discrepancies, which could not be explained by the measurement noise or the uncertainty in the estimated parameters. The model inadequacy can be divided into global and local categories. The most serious problem observed was at the global level. Indeed, the predictions of the dimensionless model given by Eq. (5) had to be scaled down to 2.2%-3.2% of their values in order to be at the same level as the measurements. This has not been observed before or reported in literature. We believe that

the main reason for this is that this type of scaling would in general be absorbed into the a_{AICD} factor and hence would slip away unnoticed. Further studies are needed to determine the source(s) of this inconsistency. If one accepts the correction factor α and hence the modified dimensionless model given by Eq. (5), the deviation at the local level is less significant. The model validation has revealed that there is a tendency for the modified model to over-predict the pressure drop. A closer study of the results has revealed that a slight increase in oil viscosity during its passage through the valve can explain most of the overestimated pressure drop tendencies by the model. Further studies under more stringent conditions will be conducted in order to uncover the causes of these observations.

References

H. Aakre, B. Moldestad, B. Werswick, and V. Mathiesen. Autonomous Inflow Control Valve for Heavy and Extra-Heavy Oil. *In Proceedings- SPE Heavy and Extra Heavy Oil Conference. - Latin America, Medellín, Colombia*, 2014. doi: 10.2118/169233-MS.

H. Aakre, V. Mathiesen, and B. Moldestad. Performance of CO2 flooding in a heterogeneous oil reservoir using autonomous inflow control. *Journal of petroleum science & engineering,*167:654-663, 2018.

M. Halvorsen, M. Madsen, Mo. M. Vikøren, I. Mohd Ismail, and A. Green. Enhanced Oil Recovery on Troll Field by implementing Autonomous Inflow Control Device. *In Proceedings- SPE Bergen One Day Seminar. Bergen, Norway, 2016*. doi: 10.2118/169233-MS

J. Kruschke. *Doing Bayesian Data Analysis, A Tutorial with R,JAGS and Stan.* Elsevier Inc, Bloomington, USA, 2011.

K. Langaas,O. Urazovskaya, N. Gueze, E. Jeurissen. Attic Oil Recovery in the Alvheim Field. *In Proceedings-SPE Norway Subsurface Conference,Virtual. -Bergen, Norway,2020*. doi: 10.2118/169233-MS

V. Mathiesen, B. Werswick, H. Aakre, and G. Elseth. The Autonomous RCP Valve – New Technology for Inflow Control in Horizontal wells. *In Proceedings-SPE Offshore Europe Oil and Gas Conference and Exhibition, Aberdeen, 2011.* doi: 10.2118/169233-MS

V. Mathiesen , B. Werswick, and H. Aakre. The Next Generation Inflow Control the Next Step to Increase Oil Recovery on the Norwegian Continental Shelf. *In Proceedings - SPE Bergen one day seminar,2 April. - Bergen, Norway, 2014*. doi: 10.2118/169233-MS

I. Mohd Ismail, N.A .Che Sidik, F. Syarani wahi, G. Lin Tan, T. Focht, and F. Hillis. Increased Oil Production in Super Thin Oil Rim Using the Application of Autonomous Inflow Control Devices. *In Proceedings - SPE Annual Technical Conference and Exhibition, Dallas, Texas,2018*. doi: 10.2118/191590-MS

A. Moradi and B. Moldestad. A Proposed Method for Simulation of Rate-Controlled Production Valves for Reduced Water Cut. *SPE Prod & Oper*. 36(03): 669–684, 2021. doi: 10.2118/205377-PA

Stan development team Stan Reference Manual [Online]. -. - 2.27.2019. URL: https://mc-stan.org/docs/2_27/reference-manual/index.html

S. Taghavi, H. Aakre, S. Swaffield, and B.R. Brough. Verification of Autonomous Inflow Control Valve Flow Performance Within Heavy Oil-SAGD Thermal Flow Loop. *In Proceedings - SPE Annual Technical Conference and Exhibition. - Calgary, Alberta, Canada, 2019*. doi: 10.2118/196216-MS

B.A. Voll, I. Mohd Ismail, and I. Oguche. Sustaining Production by Limiting Water Cut And Gas Break Through With Autonomous Inflow Control Technology. *In Proceedings - SPE Russian Oil and Gas Exploration and Production Technical Conference and Exhibition. - Moscow,Russia,2014*. doi: 10.2118/171149-MS

Appendix

Table 1. Experimental results with model oil of different viscosities.

Differential Pressure [bar]	*Mass Flow [kg/h]*	*Density [kg/m3]*	*Temperature [°C]*	*Volume Flow [m3/h]*
Test#1; Oil 6.6 cP				
19.44	929.65	922.53	19.59	1.01
15.58	824.79	921.59	19.50	0.89
9.93	710.16	920.60	19.18	0.77
7.12	642.89	920.01	18.94	0.70
5.23	587.78	919.54	18.85	0.64
3.42	514.06	919.13	19.62	0.56
1.17	353.74	918.34	18.06	0.39
Test#2; Oil 12.6 cP				
19.73	1109.32	937.98	20.02	1.18
15.49	1021.85	937.51	19.34	1.09
10.12	882.52	936.54	19.25	0.94
6.82	774.99	935.77	18.93	0.83
5.36	712.71	935.48	19.11	0.76
3.02	575.30	934.97	18.61	0.62
0.92	388.95	934.03	19.57	0.42
Test#3; Oil 36.4 cP				
19.97	1460.89	953.18	21.95	1.53
15.13	1305.44	952.57	20.46	1.37
10.05	1126.45	951.34	20.31	1.18
7.08	966.33	951.62	20.28	1.02
4.99	868.67	952.29	20.54	0.91
2.96	760.25	953.07	20.88	0.80
0.93	503.04	950.56	20.05	0.53

Table 2. Accuracy of the test devices

Device	*Measured Property (ies)*	*Accuracy*
Coriolis	Mass flow, Temperature, Density	0.1 %
Pressure transmitter	Differential pressure	0.04 %
Viscometer	Viscosity	0.2 %

Table 3. Data and parameters description**.**

Name	*Description*
x, y, α	Model parameters
Δp_w	True differential pressure of water
Q_w	True volume flow rate of water
σ_μ	Standard deviation of oil viscosity
Q_o	True oil flow rate
μ_o	True oil viscosity
Δp_{od}	Measured differential pressure of oil
Q_{od}	Measured volume flow rate of oil
μ_{od}	Measured oil viscosity
ρ_o, ρ_w	Oil and water density
μ_w	Water viscosity $= 1$
σ_p	Standard deviations of the Δp measurements
σ_q	Standard deviations of the flow measurements
$\boldsymbol{\Delta p_o}$	True differential pressure of oil

Table 4. Calibration data set.

ρ_o *[kg/m3]*	Δp_{od} *[bar]*	σ_p *[bar]*	Q_{od} *[L/h]*	q_o *[L/h]*	σ_q *[L/h]*	μ_{od} *[cP]*	μ_{o1} *[cP]*
920	19.44	0.47	1007.72	1006.41	4.69	6.6	6.4
920	15.58	0.21	894.97	894.73	4.07	6.6	6.4
920	9.93	0.13	771.40	771.83	1.53	6.6	6.4
920	7.12	0.50	698.79	697.72	2.32	6.6	6.4
920	5.23	0.50	639.21	636.61	5.09	6.6	6.4
920	3.42	0.35	559.29	558.47	5.46	6.6	6.4
920	1.17	0.11	385.19	385.44	2.78	6.6	6.4
950	19.97	0.10	1532.66	1530.58	2.81	36.4	36.2
950	15.13	0.08	1370.44	1370.49	1.28	36.4	36.2
950	10.05	0.08	1184.07	1183.58	0.93	36.4	36.2
950	7.08	0.04	1015.46	1015.78	1.09	36.4	36.2
950	4.99	0.05	912.19	912.41	1.38	36.4	36.2
950	2.96	0.03	797.69	799.07	2.22	36.4	36.2
950	0.93	0.05	529.20	529.44	6.00	36.4	36.2

Modeling and Simulation of an Electrified Drop-Tube Calciner

Martin H. Usterud Ron M. Jacob Lars-André Tokheim

Department of Process, Energy and Environmental Technology, University of South-Eastern Norway
{137010, Ron.Jacob, Lars.A.Tokheim}@usn.no

Abstract

About 65 % of the carbon dioxide emissions from a modern cement kiln system are generated through calcination (decarbonation). The calcium carbonate in the limestone is the primary source of CO_2, and the rest comes from fuel combustion. This gives a calciner exit gas consisting of N_2, O_2, CO_2, and H_2O, the CO_2 constituting up to 30 % of the mixture. In the future, electric power will have to come from renewable energy. Electrification of the calciner, i.e., replacing fuel combustion with electrically generated heat, will eliminate the fuel combustion exhaust gases. The calciner exit gas will then be pure CO_2 and removes the need for a separate CO_2 capture plant. Such a process may require a new type of calcination reactor, different from the currently used reactors in most cement kiln systems. In the current work, an electrically heated drop-tube reactor (DTR) is used to calcine the meal. The DTR may replace the traditional entrainment calciner. Essential characteristics in developing a DTR include the particle size distribution (PSD), particle settling velocity, operational temperature of the tube wall, and velocity of the product gas. A PSD ranging from 0.2 to 180 µm, where most particles have a diameter < 30 µm, was investigated. Also, to assess the effect of clustering, an effective particle diameter of 500 µm was evaluated. Two different DTR designs were compared, 1) co-current flow of gas and particles, 2) counter-current flow of gas and particles. The dimensions of a calcination reactor were calculated using simulations in Python 3.8. The tube diameter was selected as the key parameter to see how the overall design of the reactor was influenced.

Keywords: Drop tube reactor, electrification, CO_2 capture, calcination, Python 3.8

1 Introduction

Concrete is one of the most used construction materials in the world. The key additive in concrete is cement, and about 4.1 billion tonnes of cement are produced globally every year, resulting in a global anthropogenic CO_2 emission of up to 8 % (Andrew, 2018). Hence, strategies such as improving the energy efficiency of existing cement plants and using lower carbon fuels and green electricity to decarbonize the raw meal should be implemented (Norcem, 2021).

Producing cement clinkers has two significant sources of CO_2 emission: calcination of the raw materials and fuel combustion. Calcination is a thermally driven chemical reaction where the calcium carbonate ($CaCO_3$) in the limestone will decompose and form lime (CaO) and CO_2: $CaCO_3 + heat \rightarrow CaO + CO_2$. The decarbonation of raw meal accounts for about 65 % of the CO_2 emissions in a modern cement kiln system, while fuel combustion accounts for about 35 % (Tokheim et al., 2019).

Modern calciners are based on raw meal particles being entrained by hot combustion gases, which at the same time provide the required heat transfer to the particles. However, expecting a greener future, the cement clinker production process will have to be powered by electricity generated by renewable energy sources. Implementing green electricity to power the calciner instead of fossil fuels can prove to be an efficient way to reduce CO_2 emissions: The CO_2 produced from the standard fuel combustion is eliminated, and the CO_2 produced from the calcination process is pure, which removes the need for a separate CO_2 capture facility.

Different reactors may be applied in a process where the heat is transferred indirectly to the meal, for example rotary calciners (Tokheim et al., 2019), fluidized bed calciners (Samani et al., 2020), or drop tube calciners.

Calcination by indirect heat transfer in drop tube calciners has been tested in the Leilac project (Leilac, 2021), but in that project, fuel combustion is the source of energy used for calcination (Hills et al., 2017; Hodgson et al., 2018).

In this work, we study indirect heat transfer in an electrified drop tube reactor and address the following key questions:

- What is the settling velocity of the particles?
- How will the CO_2 from the calcination reaction impact the particle flow in the reactor?
- What factors are decisive for the tube diameter and length?

The purpose of this study is to investigate, through modeling and simulation, how variable design parameters and operational settings will impact the industrial calcination in an electrified DTR. Two different designs are considered; co-flow and counter-flow of meal and gas.

2 Method

To design an electrically heated DTR in order to calcine the raw meal, the particle settling process and the heat transfer from the heated tube wall to the particles in the reactor are modelled. A modified shrinking core model (SCM) is used to study the kinetics of the calcination reaction. The reaction rate coefficient of the reaction, which is dependent on the equilibrium pressure and the partial pressure of CO_2, is modelled. The models are implemented in Python 3.8 for simulation purposes to investigate how different particle sizes, wall temperatures, and fluid velocities will impact the system design.

3 Process description

The upper part of Figure 1 shows a typical modern cement kiln system. The raw meal is preheated in two preheaters before being calcined in the calciner. The precalcined meal is then sent to a rotary kiln, where the meal is fully calcined and cement clinker is produced. Finally, the clinker is cooled in a clinker cooler.

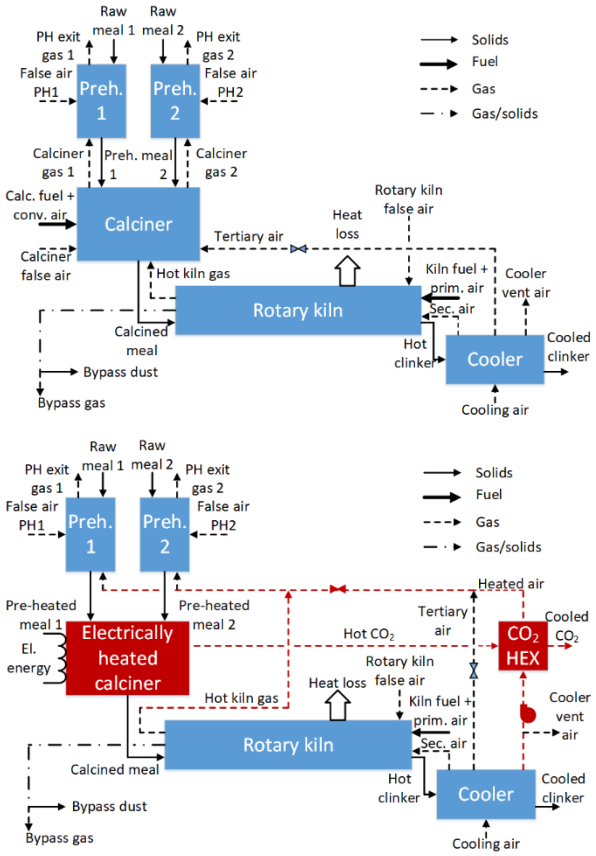

Figure 1. A regular cement kiln system with two preheater strings (top) and a system equipped with an electrified calciner (bottom) (Tokheim et al., 2019).

The lower part of Figure 1 shows a system where the fuel-fired calciner has been replaced by an electrified calciner. The fuel in the calciner fuel has now been replaced by heat provided from electrical energy. The combustion air is no longer required, so this air stream and the hot rotary kiln exit gas are both routed to the preheater, where the sensible heat can be utilized. Hence, the only gas component in the exit gas stream from the calciner is CO_2 coming from the decarbonation. The red-colored process units in Figure 1 are considered in the present study.

Figure 2 shows a process flow diagram of a DTR (i.e., the electrically heated calciner) and adjacent units such as a de-dusting cyclone, a heat exchanger, and a fan.

The preheated raw meal enters the top of the reactor at a temperature of about 650 °C. As the particles continuously fall through the reactor, the heat generated from electricity will heat the particles to a calcination temperature of about 900 °C. During the calcination of the particles, CO_2 is produced. A fan is implemented to force the normally buoyant gas down through the bottom of the DTR, as shown in Figure 2. A de-dusting cyclone is implemented to separate the particles and exit gas. Heat exchangers cool down the pure CO_2 gas before it is sent to storage or further processing. The calcined meal is sent to the rotary kiln. In this study, two different DTR designs are compared; co-current flow of gas and particles (shown in Figure 2), and counter-current flow of gas and particles. In the latter concept, the CO_2 will exit at the top of the DTR instead of at the bottom, but otherwise the flow diagram will be the same.

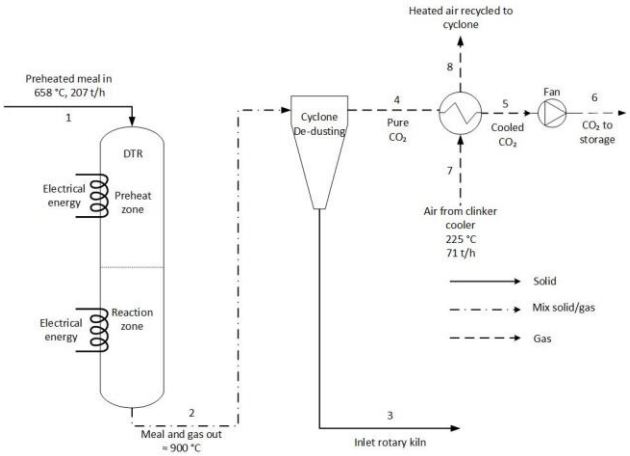

Figure 2. Process flow diagram of DTR and adjacent units.

Implementing the DTR in an existing cement kiln system is expected to have a relatively small constructional impact: 1) Replacement of the existing entrainment calciner with the DTR, 2) Installation of de-dusting cyclone(s), 3) installation of heat exchanger(s) for utilization of sensible heat in the hot CO_2 and 4) installation of a fan to pull the CO_2 out of the calciner and send it to a CO_2 processing unit (required for storage and transport).

The DTR itself will have to be implemented in the form of a number of parallel tubes, each processing a fraction of the preheated meal.

Figure 3 shows the cumulative particle size distribution of a typical raw meal, collected from

Norcem AS Brevik. The diameter ranges from 0.2 to 180 µm.

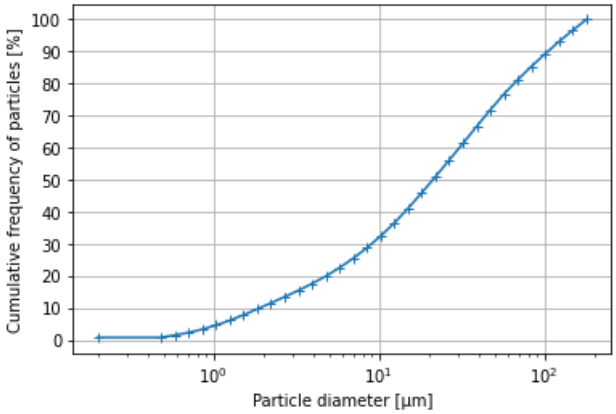

Figure 3. Cumulative frequency of particles with a size range of 0.2-180µm in diameter.

Table 1. Design basis values.

Parameter	Unit	Value
Feed rate of raw meal	t/h	207
Fraction of calcium carbonate in raw meal	kg/kg	0.776
Calcination degree	%	94
Reference temperature	K	298
The temperature of the preheated meal	K	931
Calcination temperature	K	1173
Wall temperature	K	1323
Overall heat transfer coefficient	W/(m²K)	250
Enthalpy of calcination	MJ/kgCO_2	-3.6
Enthalpy of other meal-related reactions	MJ/kgCO_2	0.3
Electricity-to-heat efficiency	%	98
Emissivity	-	0.9
Gravitational acceleration	m/s²	9.807
Particle diameter	µm	0.2-180, 500
Dynamic viscosity CO_2	Pa s	$4.65 \cdot 10^{-5}$
Density $CaCO_3$	kg/m³	2711
Density CaO	kg/m³	1520
Gas velocity	m/s	0.1-2.0, 0.5
Partial pressure of CO_2	atm	1
Specific heat capacity $CaCO_3$ at 931 K, constant pressure	J/mol K	134
Specific heat capacity $CaCO_3$ at 1173 K, constant pressure	J/mol K	140

Table 1 is a list of design basis values used in the simulations. The input values are the same as used in a previous study, in which a rotary calciner was used in an electrified calcination process (Tokheim et al., 2019).

4 Modelling

The DTR must be dimensioned in such a way that efficient calcination of the raw meal occurs. Thus, the settling velocity of particles, reaction kinetics, mass and energy balances, heat transfer, and design dimensions have been modelled.

4.1 Particle settling velocity

The settling velocity of the particles inside the DTR is modelled as a function of particle diameter. The following simplifications have been made:

- Initial particle acceleration period neglected
- No impact from particle-wall interactions
- Direct transition from laminar to turbulent flow regime (neglecting the transition region)
- No interaction between particles

For small particles, the settling is laminar, and the settling velocity can then be calculated using Equation 1, where g [m/s²] is the gravitational constant, D_p [m] is the particle diameter, μ [Pa·s] is the dynamic viscosity and ρ_p and ρ_{gas} are the densities [kg/m³] of the particle and the gas, respectively (Zevenhoven and Kilpinen, 2001):

$$v_t = \frac{g \cdot D_p^2 \cdot (\rho_p - \rho_{gas})}{18 \cdot \mu} \quad (1)$$

Equation 2 is used to confirm that the Reynolds number, Re_D, indicates laminar settling. If $Re_D < \sim 1$, the flow is in the Stokes regime and regarded as laminar.

$$Re_D = \frac{\rho_{gas} \cdot v_t \cdot D_p}{\mu} \quad (2)$$

However, if the Reynolds number from Equation 2 is found to be larger than ~1, this indicates that the settling is turbulent. Then the Archimedes number is calculated according to Equation 3, whereas an empirical Reynolds number is calculated from Equation 4, and, finally, Equation 5 is utilized to determine the settling velocity in the turbulent flow regime:

$$Ar = \frac{\rho_{gas} \cdot (\rho_p - \rho_{gas}) \cdot g \cdot D_p^3}{\mu^2} \quad (3)$$

$$Re = 0.1334 \cdot Ar^{0.7016} \quad (4)$$

$$v_{t,turb} = \frac{Re \cdot \mu}{\rho_{gas} \cdot D_p} \quad (5)$$

As the calcination reaction occurs within the DTR, the particles are gradually decarbonated, a process that changes the density of the particles. Thus, to compensate for the velocity of the calcined ($v_{94\%,calcined}$) and uncalcined ($v_{uncalcined}$) particles, Equation 6 is used as a representative average value.

$$v_{mid} = \frac{v_{uncalcined} + v_{94\%,calcined}}{2} \quad (6)$$

The effective settling velocity for both designs is calculated by Equation 7 (co-current) and Equation 8 (counter-current).

$$v_{eff,t,co} = v_{mid} + u_m \quad (7)$$

$$v_{eff,t,counter} = v_{mid} - u_m \quad (8)$$

Figure 4 shows the calculated effective settling velocity of the particles. The green and the yellow curves represent the counter-current design, whereas the blue and red lines give the effective settling velocity for the co-current design. These calculations are done with a constant gas velocity of 0.5 m/s (cf. Table 1), and for the counter-current case, the effective velocity is negative for particles smaller than 226 µm.

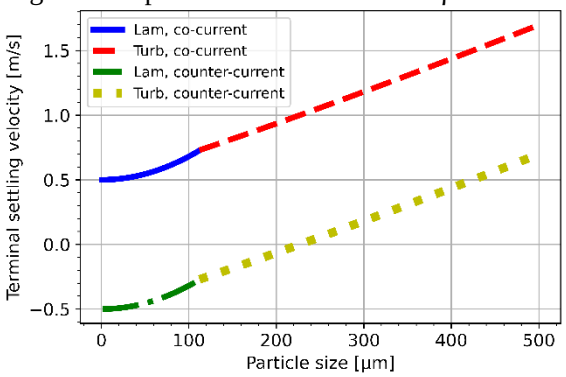

Figure 4. Settling velocity for the counter-current and co-current flow designs as a function of particle diameter. Including laminar and turbulent flow regimes.

In the calculations shown above, it was assumed that the particles do not interact with each other. However, due to the high solids loading in the system, it is likely that the particles will interact with each other and form clusters that effectively behave as bigger particles. This means that the actual settling velocity may be significantly higher than the values calculated above. Hence, in the simulations in Section 5, a larger effective particle diameter was used.

4.2 Reaction kinetics

The shrinking core model (SCM) describes the changes in a particle when a chemical reaction occurs, assuming that the particle size remains unchanged whereas the reaction front will gradually move towards the center of the particle, so that the unreacted core gradually shrinks, from a diameter equal to the particle diameter, to zero.

To calculate the conversion factor of the particles, the correlations and results from (Milne et al., 1990) have been used. The calcination conversion factor is calculated by Equation 9, where k_r [$m^{0.6}$/s] is the reaction rate coefficient, d_0 [$m^{0.6}$] is the initial diameter of the particle and t_{cal} [s] is the calcination time.

$$X = 1 - \left(1 - \frac{k_r}{d_0^{0.6}} \cdot t_{cal}\right)^3 \quad (9)$$

The reaction rate coefficient is determined by implementing the equilibrium pressure, P^* [atm], and partial pressure of CO_2 inside the reactor, P_{CO2} [atm]. These are given by Equations 10 and Equation 11, respectively (Stanmore and Gilot, 2005).

$$k_r = A \cdot \exp\left(\frac{-E}{R \cdot T}\right) \cdot (P^* - P_{CO2}) \quad (10)$$

$$P^* = 4.192 \cdot 10^9 \cdot \exp\left(\frac{-20474}{T}\right) \quad (11)$$

In this study, where CO_2 is the only gas in contact with the meal, and the system is operating at ambient pressure, the partial pressure of CO_2 is assumed to be equal to 1 atm. T [K] is the calcination temperature, which is set to 1173 K in this study. In Equation 10, the pre-exponential factor A is 0.012 mol/(m²·s·kPa), and the activation energy E is 33.47 kJ/mol.

4.3 Mass and energy balance

A mass and energy balance for the DTR at steady-state conditions was conducted, assuming no heat loss to the surroundings.

The mass balance was used to determine the mass flow rate of produced CO_2 from calcination, given by Equation 12, where $\dot{m}_{phm,in}$ [t/h] is the inlet feed rate of preheated meal (cf. Table 1), $\dot{m}_{CO2,prod}$ [t/h] is the mass flow rate of produced CO_2, and $\dot{m}_{meal,cal}$ [t/h] is the mass flow rate of calcined meal.

$$\dot{m}_{phm,in} = \dot{m}_{CO2,prod} + \dot{m}_{meal,cal} \quad (12)$$

Equation 13 is used to calculate the amount of produced CO_2 assuming 100 % conversion from $CaCO_3$ to CaO and CO_2, where $w_{CO2,phm}$ is the weight fraction of CO_2 in the $CaCO_3$. To find the mass flow rate of produced CO_2 at 94 % calcination degree (X), Equation 14 is used (cf. Table 1).

$$\dot{m}_{CO2,phm,100\%} = w_{CO2,phm}\dot{m}_{phm,in} \quad (13)$$

$$\dot{m}_{CO2,prod} = \dot{m}_{CO2,phm,100\%}\, X \quad (14)$$

By dividing the DTR into two section – one preheating and one calcination section – the amount of heat required to process the meal was determined.

Equation 15 is the energy balance for the preheating section, where $E_{el,ph}$ [MW] is the energy supplied into the system to preheat the raw meal to calcination temperature. $C_{p,phm}$ [J/mol K] is the specific heat capacity of the preheated meal (cf. Table 1).

$$E_{el,ph} = \dot{m}_{phm} \cdot C_{p,phm} \cdot (T_{cal} - T_{phm}) \quad (15)$$

Equation 16 is the energy balance for the calcination section based on how much energy must be supplied to the reactor for the reactions to occur. The mass flow rate of CO_2 is calculated based on the mass balance (cf. Equation 13 and 14), and H_{cal} and H_{other} are the enthalpies of reaction for calcination and other meal related reactions, respectively (cf. Table 1).

$$E_{el,cal} = \dot{m}_{CO2,prod} \cdot (H_{cal} + H_{other}) \quad (16)$$

4.4 Radiation heat transfer

The particles are heated by conduction, convection, and radiation heat transfer. However, at the high temperature prevailing in the calciner, radiation heat transfer is much more significant than the two other mechanisms. Thus,

radiation is here assumed to be the only acting heat transfer mechanism.

CO_2 is a polyatomic gas and will absorb some of the radiation, contributing to a reduced effect of the radiation heat flux. The effect of the absorption was investigated and found not to significantly affect the radiation heat flux. Hence, the main effect is the direct radiation from the hot wall to the particles, and this is the mechanism used in the model.

For radiation heat transfer from the hot wall at temperature T_{wall} [K] to the particles at temperature T [K], Equation 17 can be applied to estimate the radiation heat flux, where ε is the wall emissivity and σ is the Stefan-Boltzmann constant ($5.67 \cdot 10^{-8}$ $\frac{W}{m^2 K^4}$) (Incropera et al., 2017).

$$q''_{rad} = \varepsilon \cdot \sigma \cdot (T^4_{wall} - T^4) \quad (17)$$

4.5 DTR design

To effectively process the raw meal to the desired calcination degree, the diameter and heat of the reactor tube have been determined. The diameter of a cylindrical tube is found by Equation 18.

$$D = \sqrt{\frac{4 \cdot A_{cross}}{\pi}} \quad (18)$$

Here, the cross-sectional area, A_{cross} [m²], is given by Equation 19, where $\dot{V}$ [m³/s] is the volumetric flow rate of fluid, and u_m [m/s] is the fluid velocity chosen based on the settling velocity of the particles.

$$A_{cross} = \frac{\dot{V}}{u_m} \quad (19)$$

The necessary heat transfer area of the reactor tube can be determined based on the energy balance and the radiation heat flux calculations, given by Equation 20.

$$A_{heat,preheat} = \frac{Q_{preheat}}{q''_{preheat}} \qquad A_{heat,calcination} = \frac{Q_{calcination}}{q''_{calcination}} \quad (20)$$

Based on the energy required for heating the raw meal to the calcination temperature, the height of the section can be determined with Equation 21.

$$h_{t,preheating} = \frac{A_{heat,preheating}}{\pi \cdot D} \quad (21)$$

The necessary height of the calcination section is found by Equation 22, based on the required residence time of the particles (cf. Figure 5), and the effective particle settling velocity (cf. Figure 4).

$$h_{t,calcination} = t_{res} \cdot v_{eff.t} \quad (22)$$

Further, the total height can be found by Equation 23 by adding the preheating section height ($h_{t,preheating}$) and the calcination section height ($h_{t,calcination}$).

$$h_t = h_{t,preheating} + h_{t,calcination} \quad (23)$$

4.6 Simulations

The models described above were implemented in Python 3.8. Both system designs – co-current and counter-current – are highly dependent on the tube diameter. Thus, the diameter was selected as a key parameter to vary in the determination of the DTR design.

By having a counter-current flow of gas and particles, the buoyant CO_2 gas may be problematic regarding smaller particles. The particles processed in the co-current flow of gas and particles will have an increased effective settling velocity. Thus, the height of the DTR is expected to increase accordingly. However, this design is not impaired by the CO_2 gas, which is forced to flow downwards with the particles.

5 Results and discussion

Figure 5 shows the calcination degree as a function of time and effective particle size. The smaller particles in the PSD have a short calcination time, meaning that complete conversion from $CaCO_3$ to CaO will happen rapidly. Given a calcination time, some of the larger particles may, however, not achieve the desired calcination degree.

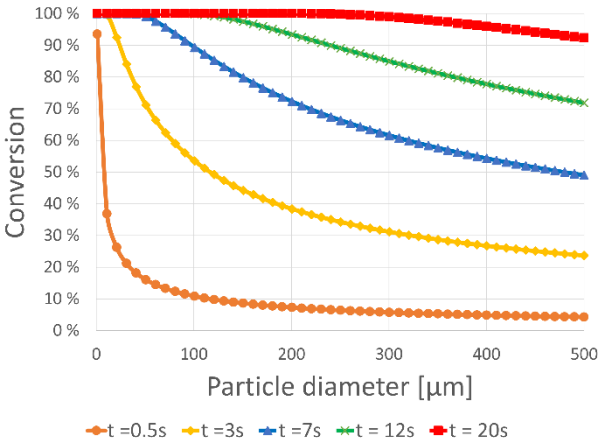

Figure 5. Calcination degree (conversion) as a function of time particle size. The calcination temperature is 1173 K. Each curve represents a given calcination time.

Figure 6 shows the gas velocity and the required number of tubes as a function of the tube diameter. The gas velocity should be low in order to reduce the number of particles being forced out of the reactor by friction (relevant for the counter-current concept).

For the co-current flow of gas and particles, the effective settling velocity increases with increased fluid velocity. Thus, to reduce the height of the tube, the gas velocity should be minimized.

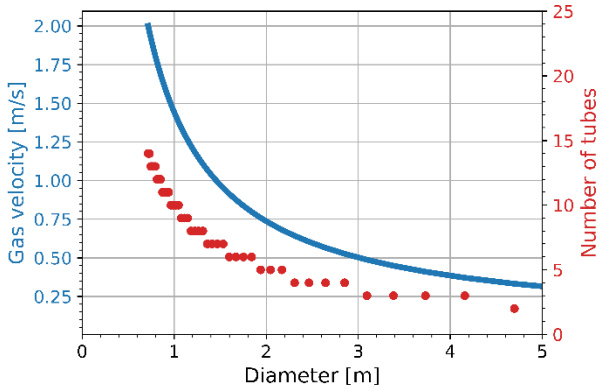

Figure 6. Gas velocity and number of tubes as a function of tube diameter (counter-current flow).

Figure 7 illustrates the reaction process and shows the heat necessary to preheat the raw meal to the calcination temperature, and the calcination reaction assuming 94 % conversion to CaO from $CaCO_3$ in the DTR. A feed rate of 207 t/h generates about 66 t/h CO_2 from the reaction, and about 141 t/h of calcined meal is produced.

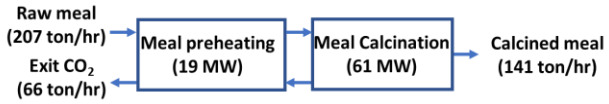

Figure 7. Shows the results from the mass and energy balances listed in Section 4.3.

Figure 8 shows the heat flux with varying temperature. The temperature is varied in the range 1200 – 1500 K, and the green cross marks the flux when operating at 1323 K, which results in a flux of 60 kW/m^2. Increasing the temperature will decrease the required height as then the heat flux increases. However, it may be difficult to find materials that can operate at very high temperatures for a long period of time. A wall temperature of 1323 K (1050 °C) may be a suitable trade-off between heat transfer efficiency and material availability.

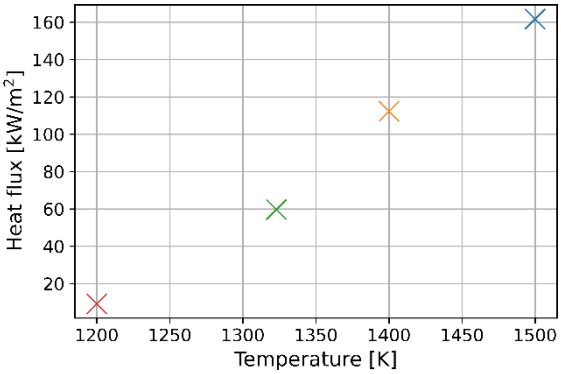

Figure 8. Radiation heat flux as a function of wall temperature.

The upper part of Figure 9 shows the required number of tubes as a function of the diameter. The calculations are based on a constant feed rate of 207 t/h, a residence time of 20 s, a constant gas velocity of 0.5 m/s, effective particle diameter of 500 µm, and wall temperature of 1323 K (cf. Table 1.).

The lower part of the figure shows the tube height (cf. Equation 23), where the slight increase in height comes from the preheating part of the tube, which increases because of fewer processing tubes.

Based on Figure 9, several combinations of diameter, height and number of tubes can be used, depending on the requirements and specifications on the system where it should be installed. However, a relatively small diameter is necessary to ensure efficient heat transfer.

A viable option may be to use 15 processing tubes with a diameter of 2.6 m and a height of 37.6 m, each processing a feed of 13.8 t/h. However, it could be that the heat transfer will be impaired with such a big diameter, and another option could be 40 tubes with a diameter of 1.6 m and a height of 37.5 m, each tube processing 5.3 t/h. If fewer operating DTRs were to be used, the diameter would greatly increase. The efficiency of heat transfer would decrease since the heat may not reach the particles furthest away from the tube wall (the heat source).

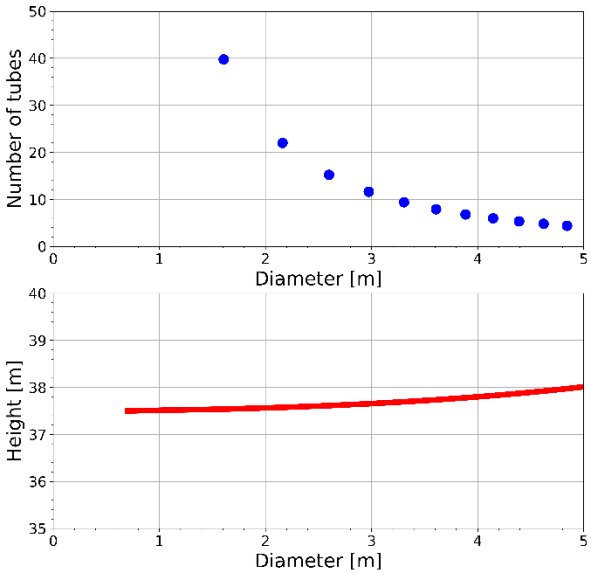

Figure 9. Number of tubes and height necessary to process the raw meal (co-current) as a function of the tube diameter.

Figure 10 shows the number of tubes and the tube height as a function of the tube diameter (counter-current design) for the same conditions as in Figure 9. The most significant difference between Figure 9 and Figure 10 is the tube height due to the effective particle settling velocity (cf. Equations 7 and 8).

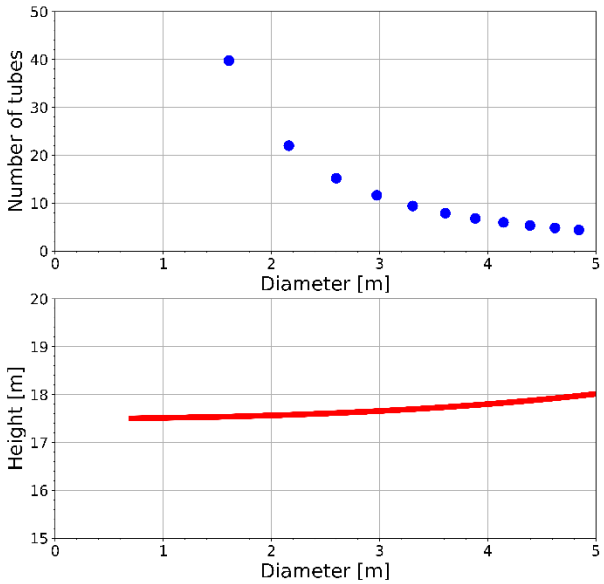

Figure 10. Number of tubes and height necessary to process the raw meal (counter-current) as a function of the tube diameter.

As mentioned before, the difference between the co-current and counter-current design is the impact of the gas velocity on the particles settling velocity. One major consideration when choosing the preferred design is the available area for the installation of the system. If height is a limiting factor at the site where the DTR is to be installed, the counter-current design should be considered.

6 Conclusion

Two concepts were investigated for calcination of raw meal in a drop tube reactor, 1) co-current flow of particles and gas, 2) counter-current flow of particles and gas.

The settling velocity is dependent on the particle size. Small raw meal particles with a low settling velocity will be affected by the buoyant CO_2 gas for the counter-current design if the fluid velocity is 0.5 m/s. This is not the case for the co-current design. However, the required height of the tube increases as a result of the increased settling velocity of the particles.

Due to the high loading of solids in the system, it is likely that the particles will interact with each other and form clusters that effectively behave as bigger particles. The settling velocity is a function of the particle size, and about 1.2 m/s is achieved for particles with an effective size of 500 µm. Using a gas velocity of 0.5 m/s, the effective settling velocity of the particles was accordingly found to be 1.7 m/s and 0.7 m/s for the co-current and counter-current designs, respectively.

Simulations show that operating with a high fluid velocity decreases the diameter of the reactor tube. Larger tube diameters will likely impair the heat transfer.

Both designs are influenced by decreasing the tube diameter. The particles in the co-current design will achieve a higher effective settling velocity, increasing the height of each reactor tube. The particles in the counter-current design will achieve a reduced effective settling velocity, increasing the residence time of the particles and reducing the necessary tube height. However, small particles (with a settling velocity less than the fluid velocity) may be entrained by the buoyant CO_2 gas and exit at the top of the reactor.

Mass and energy balances were used to determine how much heat is required to preheat and calcine the meal, and how much CO_2 is produced during calcination of $CaCO_3$. About 80 MW in total is required for both processes when calcining a feed rate of 207 t/h. The process results in about 66 t/h produced CO_2 and 141 t/h calcined meal.

Increasing the number of processing tubes and dividing the total feed rate of raw meal between the tubes decreases the diameter while ensuring the correct fluid velocity of the gas.

The decisive factor for the tube diameter is the fluid velocity. To achieve an acceptable gas velocity and maintain a high heat transfer coefficient, a relatively high number of processing tubes is required.

Which design (co- or counter-current) and what configuration of the system with regards to diameter, height and number of operating tubes are heavily dependent on the system where the DTR is to be installed. However, if the PSD consist of small particles and the buoyant CO_2 is a problem, then the co-current design should be used. The proposed dimensions by calculations and simulations to ensure efficient heat transfer can be 40 DTRs, each with a diameter of 1.6 m and a height of 37.5 m.

The counter-current flow of gas and particles is impaired if clustering of particles does not occur. For a case with no interaction between the particles, a minimum effective diameter of 226 µm is required to avoid particles rising with the buoyant CO_2 gas when operating with a gas velocity of 0.5 m/s in a counter-current design. If the installation of the DTR system is heavily dependent on minimizing the height of tubes because of height limitations, the counter-current design should be used. Considering the same number of operating DTRs and the same diameter as for the co-current design, the height may then be reduced to 17.5 meters.

In order to numerically verify the results, future work could include CFD simulations of the flow process.

Acknowledgements

This study was carried out as part of the research project "Combined calcination and CO_2 capture in cement clinker production by use of CO_2-neutral electrical energy – Phase 2". Gassnova and Norcem are greatly acknowledged for funding this project.

References

Robbie M. Andrew. Global CO2 emissions from cement production, 1928–2017, Earth Syst. Sci. Data, 10, 2213–2239, https://doi.org/10.5194/essd-11-1675-2019, 2018

Thomas P. Hills, Mark Sceats, Daniel Rennie, and Paul Fennella. LEILAC: Low cost CO_2 capture for the cement and lime industries. Energy Procedia 114, pp. 6166–6170, 2017, doi: 10.1016/j.egypro.2017.03.1753

Phil Hodgson, Mark Sceats, Adam Vincent, Daniel Rennie, Paul Fennell, Thomas Hills. Direct Separation Calcination Technology for Carbon Capture: Demonstrating a Low Cost Solution for the Lime and Cement Industries in the LEILAC Project. 14th International Conference on Greenhouse Gas Control Technologies (GHGT-14), 21st–25th October, Melbourne, Australia, 2018

Frank P. Incropera, David P. Dewitt, Theodore L. Bergman, Adrienne S. Lavine. Principles of heat and mass transfer. John Wiley & Sons, Global edition, 2017.

Leilac, Low Emissions Intensity Lime & Cement, project web site, https://www.project-leilac.eu/, 2021

C. R. Milne, G. D. Silcox, D.W. Pershing, D.A. Kirchgessner. Calcination and sintering models for application to high-temperature, short-time sulfation of calcium-based sorbents. *American Chemical Society*, 29, 139-149, 1990. doi: https://doi.org/10.1021/ie00098a001

Norcem Heidelbergcement Group. *Cement production and emissions*. Retrieved (08.01.2021). Available online: https://www.norcem.no/en/Cement_and_CCS

Nastaran A. Samani, Chameera K. Jayarathna and Lars-André Tokheim. Fluidized bed calcination of cement raw meal: Laboratory experiments and CPFD simulations, Linköping Electronic Conference Proceedings (Proceedings of the 61st SIMS, September 22nd - 24th, virtual conference), pp. 399–406, 2020, https://doi.org/10.3384/ecp20176407

B. Stanmore, P. Gilot. Review – Calcination and carbonation of limestone during thermal cycling for CO_2 sequestration, *Fuel processing technology*, 86: 1707 – 1743, 2005

Lars-André Tokheim, Anette Mathisen, A., Lars E. Øi, Chameera Jayarathna, Nils H. Eldrup and Tor Gautestad. Combined calcination and CO_2 capture in cement clinker production by use of electrical energy, SINTEF proceedings, 4, pp 101-109, 2019

Ron Zevenhoven, Pia Kilpinen. Control of pollutants in flue gases and fuel gases, Helsinki University of Technology, 2001

Comparison of absorption and adsorption processes for CO_2 dehydration

Lars Erik Øi[*], Philip Nitsche, Solomon Aromada
[1]Department of Process, Energy and Environmental Technology, University of South-Eastern Norway
Corresponding author's email address: lars.oi@usn.no

Abstract

Captured carbon dioxide (CO_2) must be dehydrated prior to transport or storage because of possibilities for corrosion and hydrate formation. CO_2 dehydration can be performed by absorption, typically into triethylene glycol (TEG) followed by desorption or by adsorption on a solid (typically a molecular sieve) followed by desorption. In this work, the process simulation program Aspen HYSYS is used to calculate material and heat balances for a TEG based absorption process and a molecular sieve adsorption process to achieve less than 30 ppm water in the dehydrated gas. The absorption and stripping columns were modelled using a specified Murphree stage efficiency on each absorption and stripping stage. In the base case, the absorption and adsorption pressure was 40 bar and the inlet temperature was 30 °C. An additional stripping column was added below the desorption column to obtain a low water content. In the molecular sieve based process, all the process units except the adsorption/stripping units were simulated in Aspen HYSYS. It is simulated reasonable process alternatives for CO_2 dehydration down to water levels of 30 and 5 ppm. The simulations combined with cost estimation indicate that a TEG based process is the most economic process both for dehydration down to 30 ppm and to 5 ppm water in dehydrated gas.

Keywords: Dehydration, Carbon capture, Adsorption, Absorption, Aspen HYSYS

1 Introduction

CO_2 dehydration is the process of reducing the water content of captured CO_2 down to an acceptable value prior to transport or storage. The reasons are to avoid problems like corrosion and hydrate formation. Possible specifications are discussed in the references (Cole et al., 2011; Uilhorn, 2013; Buit, 2011). Water specifications are normally in the range between 5 and 500 ppm (parts per million by volume).

The most mentioned processes for dehydration are based on absorption and adsorption. The most traditional method for large scale dehydration is by absorption into triethylene glycol (TEG). For very low water levels, adsorption processes (typically using molecular sieves) are claimed to be necessary (Kohl and Nielsen, 1997; Kemper et al., 2014). Processes for glycol dehydration of CO_2 down to water levels below 5 ppm (Øi and Fazlagic, 2014) using stripping gas and an extra stripping column have been simulated. Øi and Rai (2018) simulated the alternative including an extra stripping column and a Drizo process achieving a water level down to 1 ppm. Glycol based processes are evaluated and compared by Kinigoma and Ani (2016), Kong et al. (2019) and Affandy et al. (2020).

Most commercially planned processes for CO_2 dehydration are based on molecular sieve technologies, eg. the operating facility at Melkøya (Equinor, 2016), in Brevik (Norcem, 2019) and Fortum Oslo Varme (2020). However, CO_2 dehydration has also been performed large scale using glycol processes, eg. at the Quest project in Canada (Dharwadkar, 2011).

The main purpose of this paper is to perform simulation, dimension and cost estimation of a glycol based and molecular sieve dehydration process for a traditional specification of 30 ppm to compare the two alternatives. To our knowledge, such comparisons have not been documented in open literature before.

2 Process description

2.1 Process description of traditional process

A traditional process for CO_2 dehydration using TEG is shown in Figure 1. The inlet gas flows upwards in the contactor/absorber while lean glycol (glycol with little water) flows downwards. The rich glycol (with water) flows to a heat exchanger and a regenerator where the water is evaporated. The regenerated glycol is cooled in the heat exchanger and flows back to the contactor.

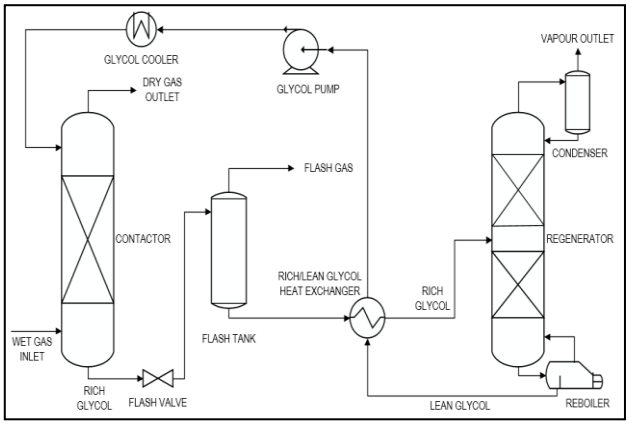

Figure 1. Process flow diagram of a standard TEG dehydration process (Øi and Rai, 2018)

A traditional adsorption based dehydration process has at least two columns filled with an adsorbent like molecular sieves. While one of the columns is in adsorption mode, the other is in desorption mode. After a scheduled time, the operation mode is switched between the columns by opening and closing control valves.

2.2 Process description of simulated processes

Figures 2 and 3 were used as a basis for process simulation. Figure 2 is based on information from Øi and Fazlagic (2014) and Øi and Rai (2018). Compared to Figure 1, the process in Figure 2 takes stripping gas from the flash gas which is contacted countercurrently with regenerated glycol in an extra stripping column. The advantage with using stripping gas and an extra stripping column is that the water content in regenerated glycol can be reduced considerably. This makes it possible to obtain considerably less water in dehydrated gas out from the absorber.

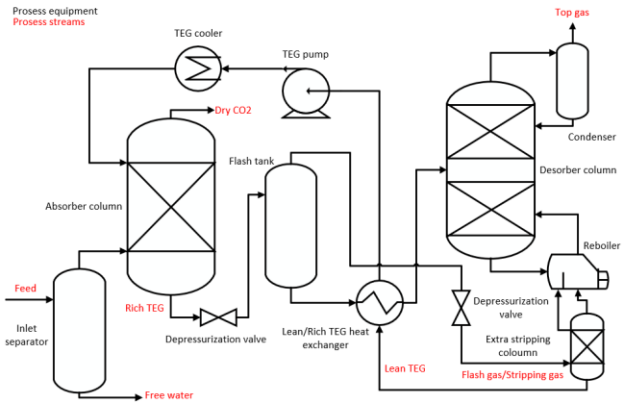

Figure 2 Flowsheet of TEG dehydration unit with extra stripping column and flash gas as stripping gas (Nitsche, 2020).

Figure 3 is a simplified version of the process information from Fortum (2020). The feed (wet CO_2) is first brought to an inlet separator to remove any free water. The CO_2 then flows into the column in adsorption mode where the water is adsorbed on molecular sieves. The dry CO_2 exits at the bottom. A portion of the dry CO_2 is heated and goes through the column operating in regenerating mode. The water is released from the molecular sieves and exits with the regeneration gas. This gas is now cooled, and the water is separated out. A compressor is used to recycle the gas back to mix it with the inlet gas.

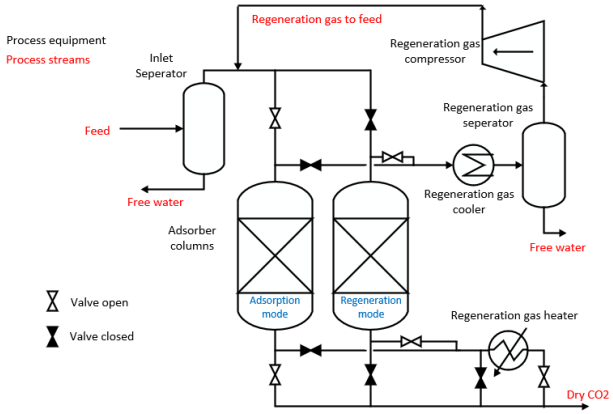

Figure 3. Process flow diagram of the molecular sieve based process (Nitsche, 2020).

3 Simulations

3.1 Specifications and simulation of TEG process and molecular sieve process

The simulation is performed using the glycol package in Aspen HYSYS based on the vapour/liquid equilibrium model Twu et al. (2005). The simulation is similar to the simulations in Øi and Fazlagic (2014) and in Øi and Rai (2018). In these simulations, the Peng-Robinson (PR) model and the Twu-Sim-Tassone (TST) model have been used. The specifications are given in Table 1. An Aspen HYSYS flow diagram is shown in Figure 4. The desorption column and the extra stripping column were simulated as one column in Aspen HYSYS with heating at an intermediate stage.

Table 1. Aspen model parameters and specifications for the TEG simulation

Parameter	Value
Feed flowrate [kg/h]	55000
CO_2 content in Feed [mol%]	0.9960
Water content in Feed [mol%]	0.40
Absorber column temperature [°C]	30
Absorber column pressure [kPa]	4000
Lean TEG temperature [°C]	35
Lean TEG pressure [kPa]	4000
Lean TEG circulation rate [kg/h]	1337
Number of stages in absorber column	8
Murphree efficiency in absorber column	0.5
Flash drum pressure [kPa]	110
Lean-Rich TEG heat exchanger ΔT_{min} [°C]	10
Number of stages in desorber column	7
Murphree efficiency in desorber column	1.0
Reboiler temperature [°C]	200
Desorber column pressure [kPa]	101.3
Reflux ratio in desorber column	0.5

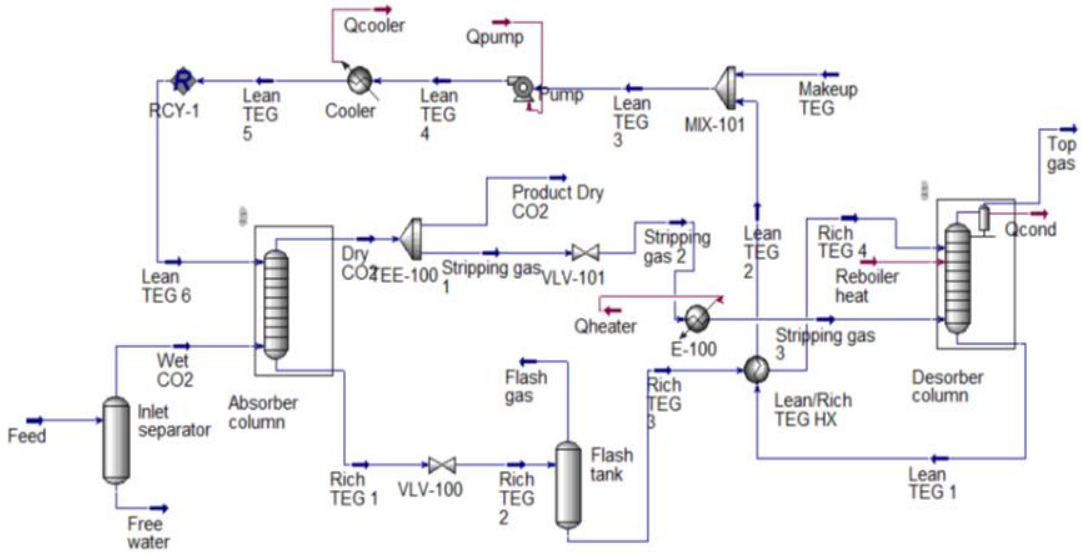

Figure 4. Aspen HYSYS flow diagram of the TEG dehydration process (Nitsche, 2020)

Table 2. Aspen model parameters and specifications for the mol sieve simulation

Parameter	Value
Feed flowrate [kg/h]	55000
CO_2 content in Feed [mol%]	99.6
Water content in Feed [mol%]	0.4
Regeneration gas flow rate [kmole/h]	125.3
CO_2 content in Regeneration gas (same as in Wet CO_2) [mol%]	99.79
Water content in Regeneration gas (same as Wet CO_2) [mol%]	0.21
Adsorber inlet and outlet temperature [°C]	30
Adsorber / regeneration inlet pressure [kPa]	4000
Pressure drop in regenerator [kPa]	5
Adsorber column outlet and inlet [kmole/h]	1373
Regeneration column inlet temperature [°C]	278

A simulation of the molecular sieve based process was performed based on the specifications in Table 2. The two adsorption/regeneration columns were not simulated in Aspen HYSYS, so the calculation was divided in three. An Aspen HYSYS flow diagram is shown in Figure 5. The first part starts with the feed and the regeneration gas and ends before the column in adsorption mode. The second and middle part starts after the column in adsorption mode and ends before the column in regeneration mode. The third starts after the column in regeneration mode and ends with the regeneration gas. The resulting flow in the regeneration gas in the third part equals the flow to the first part. The Aspen HYSYS flow diagram is shown in Figure 5.

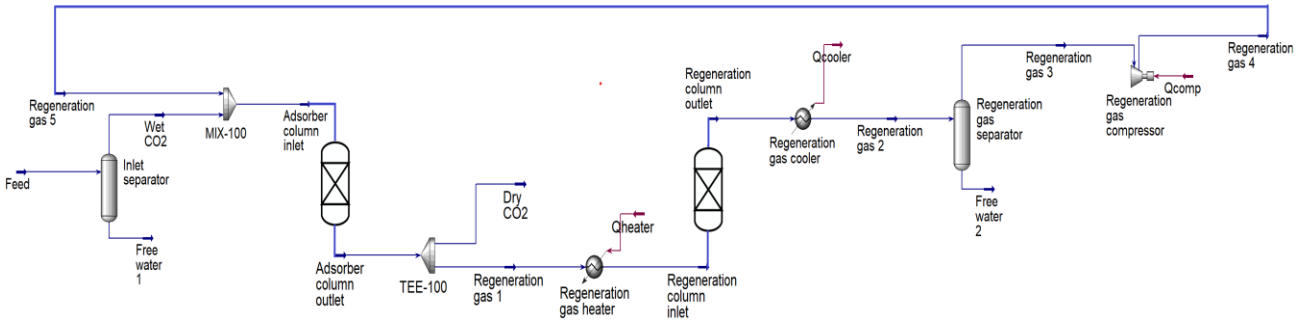

Figure 5. Aspen HYSYS flow diagram of the molecular sieve based process (Nitsche, 2020)

4 Dimensioning and cost estimation

4.1 Dimensioning specifications

The basis for the dimensioning is the material and heat balance from the Aspen HYSYS simulations.

For the TEG dehydration process, gas velocity was specified to 0.32 m/s to calculate the cross section and diameter. The estimated gas velocity through the structured packing is calculated from a traditional value of 2 m/s at atmospheric conditions divided by the square root of the pressure ratio (40). The packing height of the absorption and desorption column is 1 meter per stage with a specified stage efficiency. The total height of the absorption column, desorption column and extra stripping column were specified to be 17 m, 8 m and 7 m, respectively. The extra height is due to distributors, demister, gas inlet, outlet and sump. The heat transfer numbers (U-values in $W/(m^2K)$) were estimated to 300 for the lean rich heat exchanger, 900 for the reboiler, 500 for the condenser and 300 for the cooler.

The adsorption and stripping columns were dimensioned by assuming gas velocities (0.12 m/s) based on an Ergun equation from GPSA, relative water capacity (0.13 kg water/kg for 1/8") of the molecular sieves, retention time and operation time between switching between adsorption and stripping modes (12 hours). The adsorber height was calculated by finding the height of the saturation zone and the mass transfer zone. The total height and diameter for the two adsorbers were then specified to 6.1 m and 1.4 m, respectively.

The separator tanks were dimensioned by a traditional Souders Brown factor of 0.07 using data for physical properties from the Aspen HYSYS simulation. For the tanks, traditional design pressure based on operating pressure was assumed. Standard corrosion allowance was also assumed. The adiabatic efficiency for the compressor was specified to 0.75.

4.2 Cost estimation specifications

The Enhanced Detailed Factor (EDF) method from Ali et al. (2019) was used in the cost estimation. For each equipment unit, the Aspen In-plant version 10.0 was used to estimate the procured cost. Stainless steel was specified for all process units. Then an installation cost was calculated based on a detailed factor table (Ali et al., 2019). Then the unit cost was corrected for currency and year index.

Table 3. Assumptions made for CAPEX calculation

Parameter	Value
Currency exchange rate (20.11.18)	9.7135 NOK/EU
Currency exchange rate (20.11.20)	10.6613 NOK/EU
Cost index (Nov.2018)	109.8
Cost index (Nov.2020)	112.4

Table 4. Assumptions for OPEX calculations

Maintenance cost	4 % of CAPEX
Electricity price	0.50 NOK/kWh
Steam price	0.13 NOK/kWh
Operational time	8000 hours/yr

4.3 Scope of dimensioning and cost estimation

The cost analysis is limited to the equipment listed in the flowsheets in Figure 4 and 5. No pre-treatment like inlet gas purification is considered, and no treatment after processing like purification, compression, transport or storage is considered. The cost estimate is limited to installed cost of listed equipment. It does not include eg. land procurement, preparation, service buildings or owners cost.

5 Results and Discussion

5.1 CAPEX results

Based on the cost estimation described in section 4, the capital cost was calculated for the process based on glycol dehydration (the TEG unit) and the process based on molecular sieve adsorption. The results are presented in Figure 6.

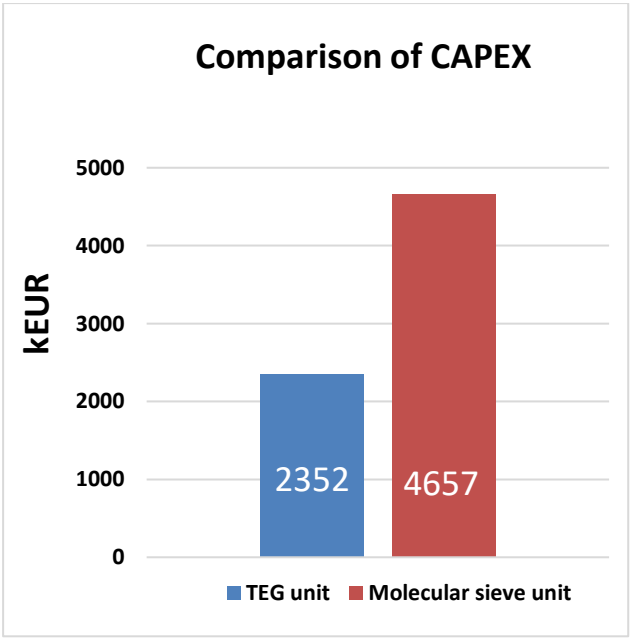

Figure 6. Comparison of CAPEX between the TEG and molecular sieve unit [kEUR] (Nitsche, 2020)

The comparison of the CAPEX shows that the capital cost is considerably higher for the molecular sieve based unit. There are two main reasons. The recirculation compressor unit is expensive, and the molecular sieve columns are large due to a lower gas velocity through the molecular sieve compared to the gas velocity in the absorption column.

The processes are compared for the base case conditions and selected specifications. The inlet and operating pressure of 30 bar is based on optimum absorption conditions between 30 and 50 bar from literature (Øi and Fazlagic, 2014). Other specifications as pressure drop and regeneration flow rate for the mol-sieve process are also recommended values from industry (GPSA, 1987). Other choices of the specifications are not expected to change much on the differences between the compared processes.

5.2 Opex results

The yearly operating cost was calculated for both dehydration processes. The dominant operation cost is energy which is due to heating, compression and pumping. Maintenance cost estimated as 4 % of CAPEX is also included. The results are presented in Figure 7.

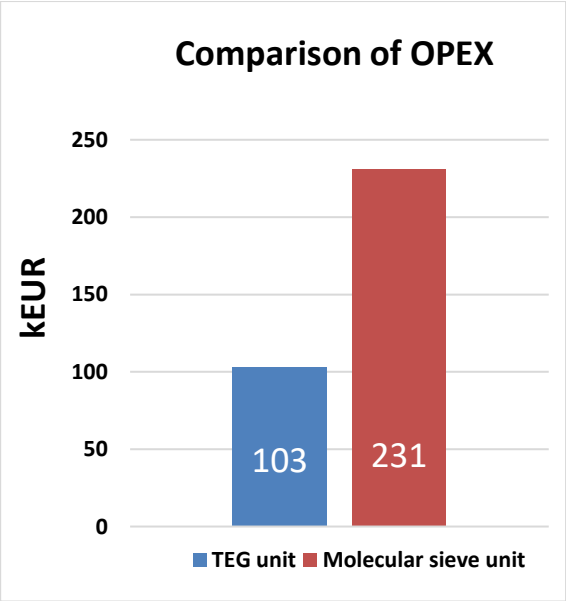

Figure 7. Comparison of yearly OPEX between the TEG and molecular sieve unit [kEUR] (Nitsche, 2020)

The comparison of OPEX also shows considerably higher operating cost for the molecular sieve based process. The two main reasons are that the heat demand is higher for the adsorption case because of more indirect heating, and that the compressor has a high energy demand. It is assumed that electricity is necessary to heat the regeneration gas. For the glycol unit, it is possible to use cheaper heat as steam.

If the same heat source (like steam or electricity) was used for both processes, the operating cost difference would be less. But because the heat demand is higher for the molecular sieve based process, the operating cost for the molecular sieve alternative would still be higher.

5.3 Results for 5 ppm water specification

Some references (Kohl and Nielsen1997; Kemper et al., 2014) claim that a molecular sieve based process is necessary to obtain low water levels. A glycol based process which achieved less than 5 ppm was simulated with a higher absorption column than in the standard case. This is compared with the molecular sieve process in Figure 8. The capital cost for the molecular sieve unit is assumed to be only slightly increased to obtain 5 ppm water in dehydrated gas.

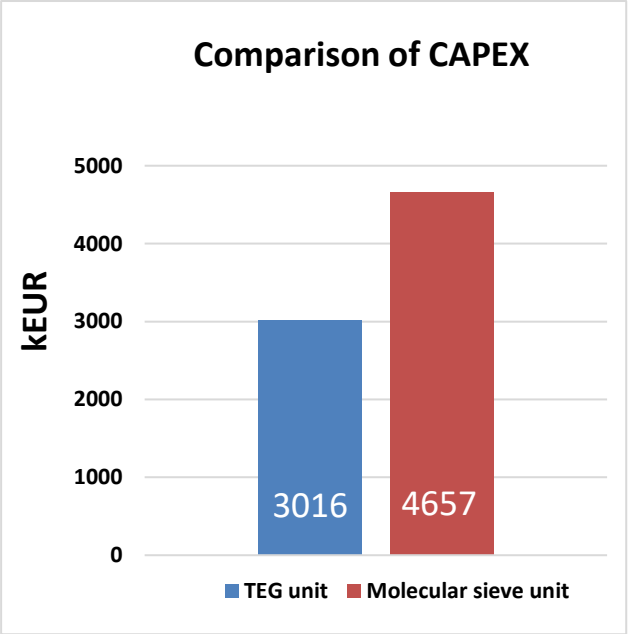

Figure 8. Comparison of CAPEX between the TEG and molecular sieve unit [kEUR] for dehydration down to 5 ppm (Nitsche, 2020)

The results show that the CAPEX is still considerably higher for the molecular sieve based process for obtaining less than 5 ppm in dehydrated gas.

There might be other criterias than cost when comparing a glycol based and molecular sieve based dehydration process like stability, robustness and risk. These factors are however assumed to be comparable for the two dehydration processes. There is no reason to claim that it is not possible to achieve 5 ppm water with both a glycol based and a molecular sieve based process.

6 Conclusion

In this work, the process simulation program Aspen HYSYS is used to calculate material and heat balances for a TEG based absorption process and a molecular sieve adsorption process to achieve less than 30 ppm water in the dehydrated gas. The absorption and stripping columns were modelled using a specified Murphree stage efficiency on each absorption and stripping stage. In the base case, the absorption and adsorption pressure were 40 bar, the inlet temperature was 30 °C, and the processes achieved less than 30 ppm water in the dehydrated gas. An additional stripping column was added below the desorption column. Both processes were cost estimated using the Aspen In-Plant cost estimation tool for the equipment cost, using a detailed factor method to estimate the capital cost and typical utility cost data for heat and electricity.

For the base case (with less than 30 ppm water in the dehydrated gas), the capital cost was calculated to 2.4 mill. EURO for the TEG unit and 4.7 mill. EURO for the molecular sieve process. The yearly operating cost was calculated to 0.1 mill. EURO for the TEG process and 0.23 mill. EURO for the molecular sieve process. The process was also calculated for dehydration down to 5 ppm. To achieve that in the TEG process, a higher absorption column is necessary. The cost of the TEG based process did not increase considerably, so the TEG absorption process was also most economical for those conditions.

It is simulated reasonable process alternatives for CO_2 dehydration down to water levels of 30 and 5 ppm. The simulations combined with cost estimation indicate that a TEG based process is the most economic process both for dehydration down to 30 ppm and to 5 ppm water in dehydrated gas.

References

S. A. Affandy, A. Kurniawan, R. Handogo, J. P Sutikno and I-L. Chien. Technical and economic evaluation of triethylene glycol regeneration process using flash gas as stripping gas in a domestic natural gas dehydration unit. *Engineering Reports*, 2020;2:e12153, 2020. https://doi.org/10.1002/eng2.12153. [Accessed: Nov. 29, 2020].

H. Ali. *Techno-economic analysis of CO_2 capture concepts*. PhD Thesis, University of South-Eastern Norway, 2019.

L. Buit, M. Ahmad, W. Mallon and F. Hage. CO_2 EuroPipe study of the occurrence of free water in dense phase CO_2 transport. *Energy Procedia*, 4:3056-3062, 2011.

I.S. Cole, P. Corrigan, S. Sim and N. Birbilis. Corrosion of pipelines used for CO_2 transport in CCS: Is it a real problem? *International Journal of Greenhouse Gas Control*, 5(7):749-756, 2011.

M. Dharwadkar, *TECHNOLOGY SELECTION REPORT-CAPTURE*. Shell Canada Energy, 2011. Available: https://open.alberta.ca/dataset/46ddba1a-7b86-4d7c-b8b6-8fe33a60fada/resource/b3b052a0-b2ef-4cfc-95b1-b363b9272546/download/technology_selection_report.pdf. [Accessed: Nov 29, 2020].

H. Secker and E. Bergene. *Drying of CO_2 in Process Applications using Molecular Sieves*. Gas Processors Association, Tulsa, Oklahoma, 2016.
file:///C:/Users/cacca/Downloads/GPApaperCO2Drying290316%20(1).pdf

Fortum Oslo Varme. *FEED Study Report DG3 (redacted version)*. Fortum Oslo Varme AS, Oslo, Norway, no. NC03-KEA-A-RA-0025, 2020.

G. P. S. A. (GPSA), *Engineering Data Book, 10. ed.*, Tulsa, Oklahoma, Gas Processing Suppliers Association, 1987.

J. Kemper, L. Sutherland, J. Watt and S. Santos. Evaluation and analysis of the performance of dehydration units for CO_2 capture. *Energy Procedia*, 63:7568-7584, 2014.

B. S. Kinigoma and G. O. Ani, Comparison of Gas Dehydration Methods based on Energy Consumption. *J. of Appl. Sci. and Environmental Management*, 20(2):253-258, 2016.

A.L. Kohl and R. Nielsen. *Gas purification, 5th ed.*, Gulf Publication, Houston. 1997.

Z. Y. Kong, A. Mahmoud, S. Liu and J. Sunarso. Development of a techno-economic framework for natural gas dehydration via absorption using Tri-Ethylene Glycol: a comparative study on conventional and stripping gas dehydration processes. *J Chem Technol Biotechnol*, 94:955-963, 2019.

P. Nitsche. *Comparison of absorption and adsorption processes for CO_2 dehydration*. Master thesis, University of South-Eastern Norway, Porsgrunn, Norway, 2020.

Norcem. *Redacted version of FEED Study (DG3) Report*. Norcem HeidelbergCement Group, Brevik, Norway, no. NC03-NOCE-A-RA-0009, 2019.

K. I. Okoli. *Comparison of CO_2 dehydration processes after CO_2 capture*. Master thesis, University College of South-Eastern Norway, 2017.

Prosernat. *Glycol dehydration best process*. http://www.prosernat.com/en/solutions/upstream/gas-dehydration/drizo.html. [Accessed: April 11, 2016].

Shell Canada Energy. *Quest Carbon Capture and Storage Project - ANNUAL SUMMARY REPORT* 2018, Shell Canada Energy, 2019. [Online]. Available: https://open.alberta.ca/dataset/c7969bcb-d510-48b4-aef5-7cc6d92d183a/resource/b1480661-2efa-4b9d-a6e6-5ca47021c399/download/quest-annual-summary-alberta-department-of-energy-2018.pdf. [Accessed Nov. 29, 2020].

C.H. Twu, V. Tassone, W.D. Sim and S. Watanasiri. Advanced equation of state method for modeling TEG–water for glycol gas dehydration. *Fluid Phase Equilibria*, 228-229: 213-221, 2005.

F.E. Uilhorn. Evaluating the risk of hydrate formation in CO_2 pipelines under transient operation. *International Journal of Greenhouse Gas Control*. 14(5):177-182, 2013.

L.E. Øi and M. Fazlagic. *Glycol dehydration of captured carbon dioxide using Aspen Hysys simulation*. Sims 55 Conference, Aalborg, Denmark. In Linköping Electronic Conference Proceedings SIMS 55, pp. 167-174, 2014.

L.E. Øi and B. Rai. *Simulation of Glycol Processes for CO_2 Dehydration*. 9th EUROSIM Congress on Modelling and Simulation, Oulu, Finland 12-16 September 2016. In Linköping Electronic Conference Proceedings, pp. 168-173. DOI: 10.3384/ecp17142168.

Automated Cost Optimization of CO_2 Capture Using Aspen HYSYS

Lars Erik Øi*, Andrea Haukås, Solomon Aforkoghene Aromada, Nils Eldrup
[1]Department of Process, Energy and Environmental Technology, University of South-Eastern Norway
Corresponding author's email address: lars.oi@usn.no

Abstract

CO_2 can be captured by absorption into monoethanol amine (MEA) followed by desorption. In this work, three configurations; standard, vapour recompression and a simple split-stream (rich split) have been simulated with an equilibrium-based model in Aspen HYSYS™ V10.0 using flue gas data from a natural gas based power plant. Adjust and recycle blocks available in Aspen HYSYS are used to automate the energy and material balance for a specified configuration. Optimization can be performed by minimizing the total cost calculated in an Aspen HYSYS spreadsheet. The equipment cost was obtained from Aspen In-plant Cost Estimator™ V10.0, and an enhanced detailed factor (EDF) method was used to estimate the total investment cost. Parametric studies of absorber packing height, minimum approach temperature in the main heat exchanger, flash pressure and split ratio were performed at 85 % capture efficiency for the three configurations. The calculated cost optimum process parameters for the standard process were 15 m packing height and 13 °C minimum approach temperature. For the vapor recompression case, a flash pressure of 150 kPa provided the lowest total cost. The calculated optimum rich split ratio was 12 %. Automated calculations are dependent on stable convergence of the simulations. A specific challenge is the adjustment of the amine recirculation to obtain a specified total capture rate.

Keywords: Carbon capture, Aspen HYSYS, simulation, cost estimation, optimization

1 Introduction

1.1 Aim

The aim of this work has been to calculate cost optimum process parameters for a standard CO_2 capture process based on amines, with emphasis on the possibility to automate the calculations. Optimization of different configurations, especially vapour recompression and a split stream (rich split) are also evaluated. Such optimizations have been only scarcely documented in literature, and especially a cost optimization of the split-stream ratio has not been found in earlier work.

1.2 Literature

This work is a continuation of previous work at the Telemark University College and the University of South-Eastern Norway (USN). Some references are (Kallevik, 2010; Øi, 2012; Park and Øi, 2017; Aromada and Øi, 2017; Øi et al., 2020). This work is based on the Master thesis work of Haukås (2020).

Several of these projects have involved process simulation, dimensioning and cost estimation of CO_2 capture using the process simulation tool Aspen HYSYS. Capture rate, energy demand and capture cost per ton CO_2 have been calculated.

By changing process parameters, such as the minimum temperature difference in the main heat exchanger, an optimum solution can be found. To keep the specified conditions stable under optimization, different strategies to adjust the process have been used. A traditional challenge is to make sure that the recirculation stream to the amine absorber is the same as in previous iterations. A recycle block available in the simulation program is traditionally used to obtain this. The next challenge is to keep the capture rate constant during iterations. This can be done by adjusting the amine circulation flow to achieve the desired capture rate, either manually or with an adjust block.

1.3 Simulation of process configurations

There have been suggested a number of process improvements of the standard CO_2 capture process (Cousins, 2011a; Moullec et al., 2011; Dubois and Thomas, 2017). Vapour recompression is an alternative where the regenerated amine is pressure reduced, and then the flashed gas is recompressed in a compressor and used as stripping steam in the reboiler. Cost optimization of vapour recompression has been performed by Fernandez et al (2012), Øi et al. (2014), Aromada and Øi (2017) and Øi et al. (2017).

Optimum conditions for a rich split have been evaluated earlier by Cousins et al. (2011b) and Karimi et al. (2011). These publications have emphasis on comparison of energy consumption between different configurations, and on energy optimization by adjusting different parameters for a given configuration.

1.4 Process description

Figure 1 shows a standard process for CO_2 absorption followed by desorption. The equipment units in the flowsheet are an absorption column, a stripping column including a reboiler and condenser, circulating pumps and heat exchangers. The process is described in more detail in Øi (2012), and in Haukås (2020).

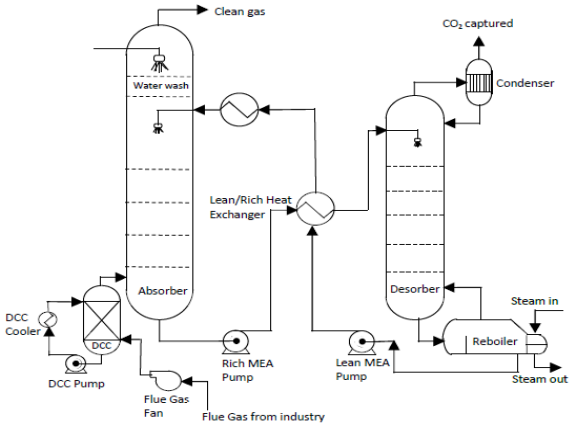

Figure 1. Process flow diagram of a standard amine-based CO_2 capture process (Aromada et al., 2020)

2 Specifications and simulations

2.1 Specifications and simulation of standard CO_2 capture process

The specifications for the base case in Table 1 correspond to 85 % CO_2 removal efficiency and a minimum approach temperature of 10 °C in the lean/rich heat exchanger. The process simulation tool Aspen HYSYS version 10 was used with the amine package (which has now been replaced as the recommended equilibrium model by Aspen HYSYS).

The calculation sequence is similar to earlier works (Aromada and Øi, 2015; Øi et al., 2020). The calculation strategy is based on a sequential modular approach (Kisala et al., 1987; Ishii and Otto, 2008).

Prior to the CO_2 capture process, the flue gas is cooled in a direct contact cooler (DCC) with circulating water. Then the absorption column is calculated from the inlet gas and the lean amine (which is specified in the first iteration). The amine with absorbed CO_2 from the bottom of the absorption column is pumped through the rich/lean heat exchanger with the temperature after the heat exchanger specified. The hot amine solution is entering the desorption column which separates the feed into the CO_2 product at the top and hot regenerated amine at the bottom. The regenerated amine is pumped to a higher pressure in a pump, then passes through the lean/rich heat exchanger and is further cooled in the lean cooler. After the lean amine cooler, the amine solution is checked in a recycle block whether the flow and composition is sufficiently close to the amine stream from the last iteration.

There are two adjust operations in the flowsheet to get an automated simulation model. One is adjusting the minimum approach temperature in the lean/rich heat exchanger by varying the temperature on the hot side after the exchanger. The other is adjusting the removal efficiency by varying the lean amine mass flow. The Aspen HYSYS process flowsheet is shown in Figure 2.

The traditional process converged after some trial and error. Due to a small water loss (and in some case water build-up) in the process, water must be added to the process. The make-up water was in some simulations adjusted manually and in some calculations the make-up water was calculated by a material balance.

Table 1. Aspen HYSYS model parameters and specifications for the base case alternative

Parameter	
Inlet flue gas temperature [°C]	40.0
Inlet flue gas pressure [kPa]	101/121
Inlet flue gas flow rate [kmol/h]	85540
CO_2 content in inlet gas [mole %]	3.73
Water content in inlet gas [mole %]	6.71
Lean amine temperature [°C]	40.0
Lean amine pressure [kPa]	101.0
Lean amine rate [kg/h]	$1.103 \cdot 10^6$
MEA content in lean amine [mass %]	29.0
CO_2 content in lean amine [mass %]	5.4
Number of stages in absorber [-]	15
Murphree efficiency in absorber [m^{-1}]	0.15
Rich amine pump pressure [kPa]	500.0
Rich amine temp. out of HEX [°C]	103.6
Number of stages in desorber [-]	12
Murphree efficiency in desorber [m^{-1}]	0.5
Reflux ratio in stripper [-]	0.4
Reboiler temperature [°C]	120.0
Lean amine pump pressure [kPa]	500.0

2.2 Specification of vapour recompression and split stream processes

The Aspen HYSYS flowsheet for the vapour recompression process is presented in Figure 3. After the desorber, the bottom stream is depressurized through a valve to a flash tank. The gas after the flash tank with a specified flash pressure is compressed and sent back to the desorber. The advantage with the vapour recompression configuration is that the CO_2 content in regenerated amine can be reduced. The drawback is capital and operating cost due to the compressor. Extra specifications are given in Table 2.

Table 2. Aspen HYSYS model parameters and specifications for the vapour recompression case

Parameter	
Flash pressure [bar]	1.0
Compressor outlet pressure[bar]	2.0
Lean pump, delta P [bar]	6.0
Lean MEA flow rate [kmol/h]	92885
CO_2 content in lean amine [mass %]	5.04
Water content in lean amine [mass %]	68.85
MEA content in lean amine [mass %]	29.11

The Aspen HYSYS flowsheet for the split-stream (rich split) alternative is shown in Figure 4. After the absorption column and the rich MEA pump, the rich amine is split into two streams. One is sent to the top of the desorber while the other stream goes through the main heat exchanger before entering the desorber at a lower feed point. The advantage is that the energy consumption is reduced (Cousins, 2011b). The disadvantage is increased complexity.

2.3 Parameter variations

10 stages, 85 % removal efficiency and 10 °C as minimum approach temperature were specified in the base case simulation. For all the configurations, the packing height and minimum approach temperature were varied. For the vapour recompression case, the flash pressure was varied. For the split-stream case, the split ratio was varied. In the parameter variation simulations, all other specified parameters were kept constant.

When a parameter is varied, the traditional way in a process simulation program like Aspen HYSYS, is to change the parameter to a new value and perform the simulation once more. In many cases it is necessary to perform some adjustments in the flow-sheet to obtain a converged solution. Another possibility is to make use of the Case study function in Aspen HYSYS. In that case a series of calculations can be performed automatically. When using the Case study function, it is not possible to perform other adjustments for each new parameter value.

2.4 Process convergence

The calculation strategy in this work is sequential, even though the Aspen HYSYS simulation tool is in principle equation based. Recycle blocks are used to solve the flowsheet in Aspen HYSYS. Recycle blocks compare the in-stream to the block with the stream from the previous iteration. Adjust functions are used to vary a parameter to obtain a specified result elsewhere in the simulated process. Different tolerances were used in the recycle blocks and adjust functions to obtain stable and fast convergence. In the columns, the Modified Hysim Inside-Out algorithm with adaptive damping was used according to a recommendation by Øi (2012).

Flow-sheet convergence was discussed by Kisala et al. (1987), Ishii and Otto (2008), Holoboff (2019) and Øi et al. (2020).

As indicated in the subsection about parameter variation, the need for stable convergence is especially important when running a Case study in Aspen HYSYS.

2.5 Simulation and cost estimation procedure

The following procedure was implemented for the cost estimation, similar to the procedure in Øi et al. (2020):

1. Simulation of the CO_2 capture process in Aspen HYSYS with specifications in Table 1 and 2
2. Dimensioning of the equipment
3. Calculation of equipment cost for each unit using Aspen In-Plant cost estimator
4. Calculation of installation cost based on a detailed factor table (Ali, 2019)
5. Correction for currency and index
6. Estimation of annual operational costs based on energy requirement from simulations
7. Calculation of net present value based on a given discount rate and project lifetime

2.6 Dimensioning and cost estimation

To determine the packing height, a constant stage (Murphree) efficiency corresponding to 1 meter of packing was assumed. Murphree efficiencies of 0.15 and 0.5 were specified for the absorber and the desorber (in Table 1). For the absorber and desorber internals, a structured packing was selected.

The absorption column diameter was calculated based on a gas velocity of 2.5 m/s and the desorption column is based on a gas velocity of 1 m/s as in Park and Øi (2017) and Øi et al. (2020). The total height of the absorption column and desorption column is specified to be 40 m and 16 m respectively. The extra height is due to distributors, water wash packing, demister, gas inlet, outlet and sump.

Centrifugal pumps with 75 % adiabatic efficiency were used in the process simulations.

The direct contact cooler and the flash tank were dimensioned using a Souders Brown equation with k-parameter 0.15 and 0.075 respectively (Souders and Brown, 1934; GPSA, 1987). Overall heat transfer coefficient values have been specified for the lean/rich heat exchanger 550 W/(m^{2}K), lean amine cooler 800 W/(m^{2}K), reboiler 1200 W/(m^{2}K) and condenser 1000 W/(m^{2}K). These values are the same as in Øi (2012) and Park and Øi (2017) and less than the numbers in Øi et al. (2020) which are regarded as optimistic.

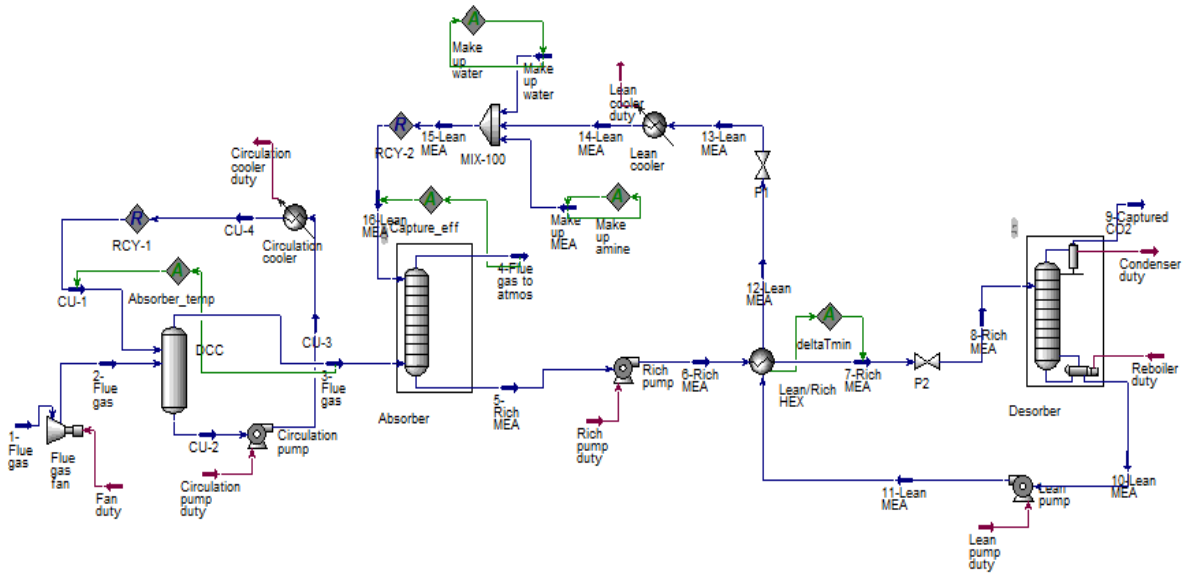

Figure 2. Aspen HYSYS flow-sheet of the base case simulation

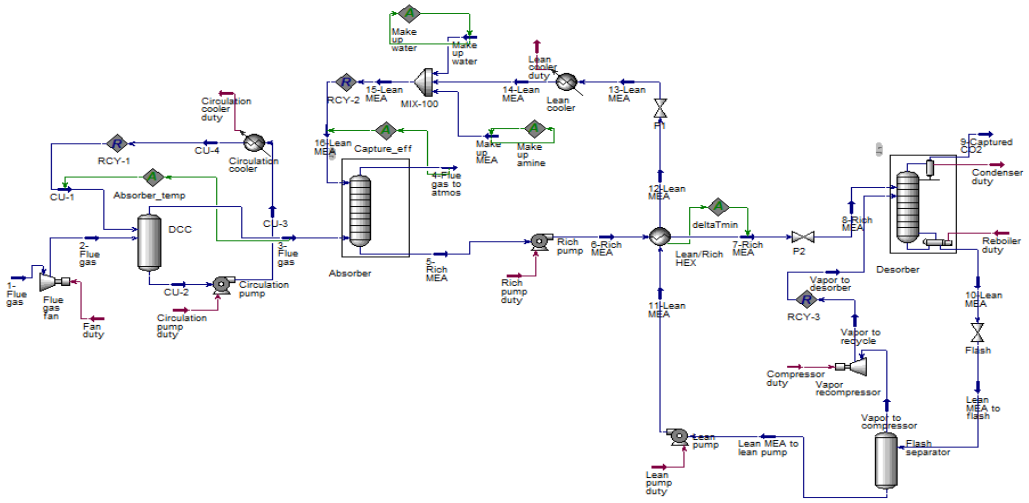

Figure 3. Aspen HYSYS flow-sheet of the vapour recompression case simulation

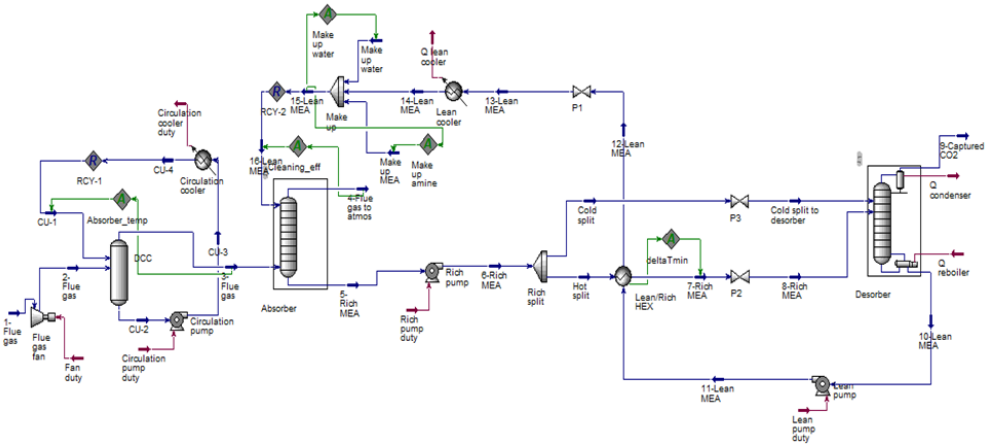

Figure 4. Aspen HYSYS flow-sheet of the split stream simulation

2.7 Capital cost estimation methods

The equipment costs were calculated in Aspen In-plant Cost Estimator (v.10), which gives the cost in Euro (€) for Year 2016 (1st Quarter). A generic location (e.g. Rotterdam) was assumed. Stainless steel (SS316) with a material factor of 1.75 was assumed for all equipment units. For pumps, fan and compressor, a material factor of 1.3 was used as in Øi et al. (2020).

In the detailed factor method, each equipment cost (in carbon steel) was multiplied with its individual installation factor to get equipment installed cost, as in Øi et al. (2020). The detailed installation factor is a function of the site, equipment type, materials, size of equipment and includes direct costs for erection, instruments, civil, piping, electrical, insulation, steel and concrete, engineering cost, administration cost, commissioning and contingency. The updated installation factors for 2016 (Eldrup, 2016) were used. More details can be found in Haukås (2020) and Øi et al. (2020).

Table 3. Cost calculation specifications

Parameter	Value
Plant lifetime	20 years
Discount rate	7.5 %
Maintenance cost	4 % of installed cost
Electricity price	0.5 NOK/kWh
Steam price	0.13 NOK/kWh
Annual operational time	8000 hours
Location	Rotterdam
Currency exchange rate 2016	9.21
Cost index 2016	103.6
Cost index September 2020	111.3

2.8 Operating cost calculation

This project includes OPEX estimations for the use of electricity and steam. Electricity cost was specified to be 0.5 NOK/kWh (approximately 0.05 Euro/kWh). The steam cost was specified to be 25 % of the electricity cost, 0.13 NOK/kWh.

2.9 Aspen HYSYS optimization

The spreadsheet unit in Aspen HYSYS was used to calculate the detailed cost estimation of CAPEX, OPEX and NPV (net present value).

For the case of optimizing the temperature difference in the main heat exchanger, the calculation could be performed effectively by using the Case Study option in Aspen HYSYS.

For the case of optimizing the number of absorber stages, each calculation was performed independently by specifying the number of stages in each calculation. The flash pressure was optimized by running a series of calculations with different pressures. This was performed both as an Aspen HYSYS Case study and by independent calculations. The split-stream process was also optimized both by a Case study in Aspen HYSYS and with a series of individual calculations.

3 Results and Discussion

3.1 Base case cost results

In Table 4, the results for the capital cost estimation of the base case is given for all the equipment units. The cost is given partly in Euro and partly in NOK, because the Aspen In-plant gives the results in Euro, while the detailed factor method is based on NOK. In the figures 5 to 12 a conversion rate of 10.0 was used to obtain approximate numbers in Euro. At the end of 2020, the conversion rate was exceeding 10.0 (10.2). For the base case, the CAPEX was estimated to 1.3 billion NOK or 130 million Euro.

Table 4. Base case cost results.

Equipment	Eq. cost CS [kEUR2016]	Eq. cost CS [kNOK2016]	Total cost factor CS	Piping factor	Total cost factor SS	Inst. cost [kNOK2020/pcs]	Number of units	Installed cost [kNOK2020]
Flue gas fan	5951	55291	3.59	0.29	3.98	236234	-	236234
DCC tower	1985	18443	3.59	0.29	4.56	90299	-	90299
DCC packing*	867	8058	-	-	2.00	17314	-	17314
DCC circ. pump	475	4417	4.93	0.48	5.37	25497	-	25497
DCC circ. cooler	125	1158	6.10	0.65	7.34	9126	6	54754
Absorber shell	2432	22596	3.59	0.29	4.56	110633	-	110633
Absorber packing*	9980	92724	-	-	2.00	199232	-	199232
Water wash*	3327	30911	-	-	2.00	66417	-	66417
Rich pump	174	1612	6.10	0.65	6.60	11417	-	11417
Lean/rich HEX	133	1233	6.10	0.65	7.34	9732	28	272499
Desorber, shell	508	4716	4.44	0.41	5.50	27855	-	27855
Desorber, packing*	1318	12243	-	-	2.00	26307	-	26307
Condenser	56	520	7.20	0.83	8.57	4778	1	4778
Reboiler	128	1188	6.10	0.65	7.34	9416	17	160073
Lean pump	181	1679	6.10	0.65	6.60	11890	-	11890
Lean cooler	100	929	7.20	0.83	8.57	8539	2	17077
Total installed cost								1332277

*Cost estimated in SS 316 in Aspen In-Plant Cost Estimator

3.2 Optimization of column height

The result from the base case is given in Figure 5. It shows an optimum (lowest NPV) for 15 stages equivalent to 15 meter packing height. This is similar to results in earlier work (Kallevik, 2010; Øi et al., 2014; Aromada and Øi, 2017).

Optimum height is also shown for the vapour recompression configuration and the split-stream configuration. Because the change in number of stages has to be performed manually, all the points on the curves in Figures 5, 6 and 7 are performed individually.

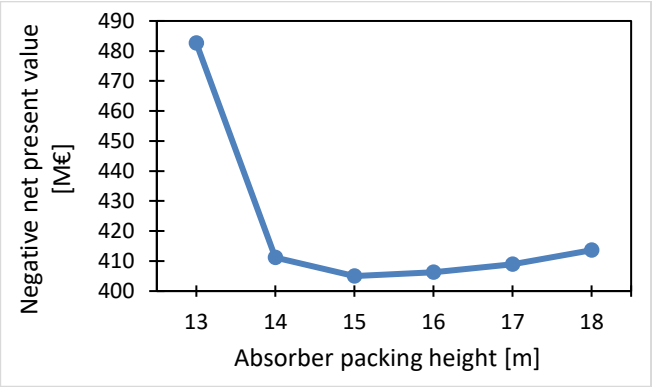

Figure 5. Optimization of number of stages for the standard case.

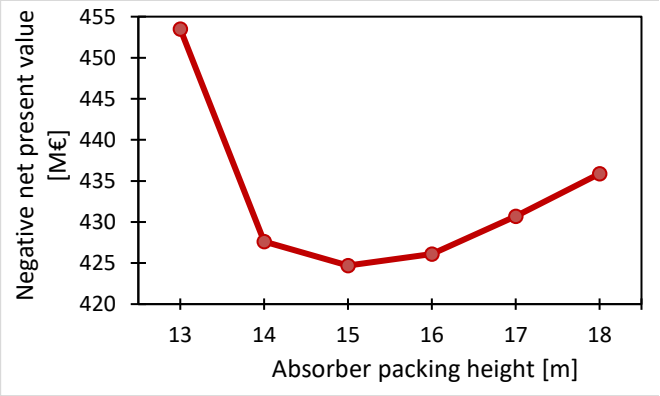

Figure 6. Optimization of number of stages for the Vapour Recompression case

An optimum column height for the vapour recompression case close to the standard process was also found in Øi et al. (2014) and in Aromada and Øi (2017).

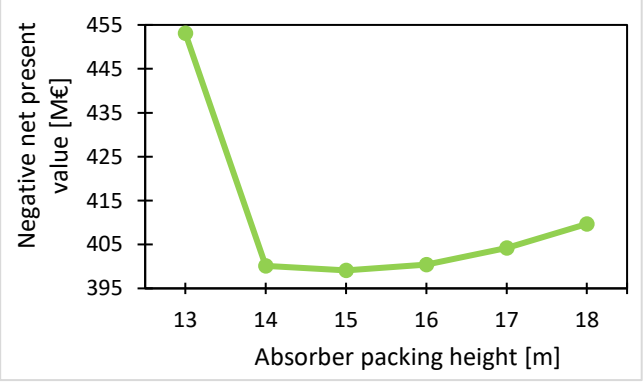

Figure 7. Optimization of number of stages for the Split-Stream configuration

3.3 Optimization of flash pressure

The flash pressure is optimized by a series of calculations. The lowest NPV is at 150 kPa in Figure 8. In this optimization, the column height was 15 meter, and the minimum temperature approach was 10 K. A possible optimum might be found between 150 and 200 kPa, but in that case the extra compressor is not reasonable. The standard process will then be regarded as optimum.

The optimum is sensitive to the cost of the compressor. An optimization was performed with a lower-cost compressor. Then, the cost optimum flash pressure was calculated to 120 kPa. This is closer to other optimization calculations (Øi et al., 2014).

The energy optimum has been calculated to a lower value than the cost optimum by Karimi et al. (2011), Fernandez et al. (2012) and Øi et al. (2014).

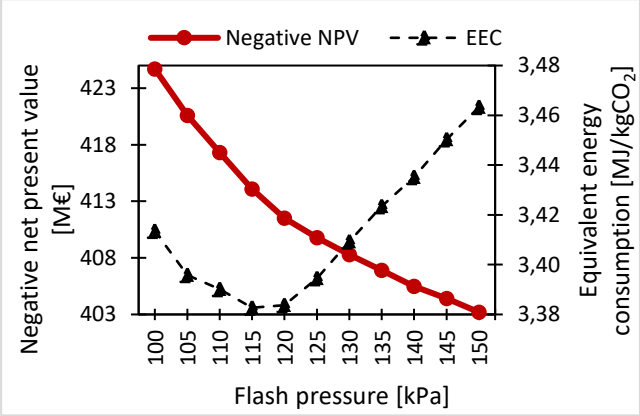

Figure 8. Optimization of flash pressure

3.4 Optimization of split ratio

The optimization in Figure 9 was performed by a Case study in Aspen HYSYS. It shows that the curve is very smooth, and this makes the optimization efficient. The calculated optimum is shown to be 12 %.

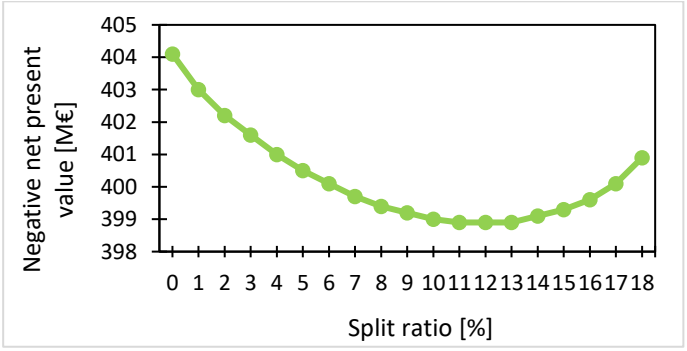

Figure 9. Optimization of the split ratio in a split-stream configuration based on a Case study.

The curve in Figure 9 is very smooth. When the same optimization was performed by manual variation and adjustment of the simulations, the curve was less smooth.

The optimum split ratio was calculated for different specifications. In the optimization in Figure 9, the column height was 15 meter, and the minimum temperature approach was 10 K and optimum lean amine pressure was 500 kPa. The optimum split ratio was calculated to values between 10 and 16 % when these parameters were varied. The optimum capture cost was approximately 40 Euro per ton CO_2 captured in these optimizations. The lowest calculated cost of 39 Euro per ton CO_2 captured was obtained when the pressure increase in the rich amine pump was reduced to 79 kPa.

3.5 Optimum minimum T approach

Minimum temperature approach optimization for the standard, vapour recompression and split-stream configurations are shown in Figure 10, 11 and 12, respectively. The absorber packing height was 15 m in these optimizations. The optimum value can be found as the one with minimum (negative) NPV. The resulting optimums are 13, 12 and 9 K for three cases. Also, Øi et al. (2014) and Aromada and Øi (2017) get about the same optimum for the different configurations. The optimum minimum temperature approach differs in literature between 10 and 15 K. This is due to different ratios between cost of heat exchangers and cost of heat. All the curves in these three figures are performed by Case studies in Aspen HYSYS. This means that the convergence is rather stable.

Another possibility to optimize is to add a minimization procedure in a spreadsheet connected to the process simulation program. The Aspen HYSYS spreadsheet do not have this as a function. But one possibility is to link the Aspen HYSYS simulation to another tool like an Excel spreadsheet. This is discussed by Sharma and Rangaiah (2016).

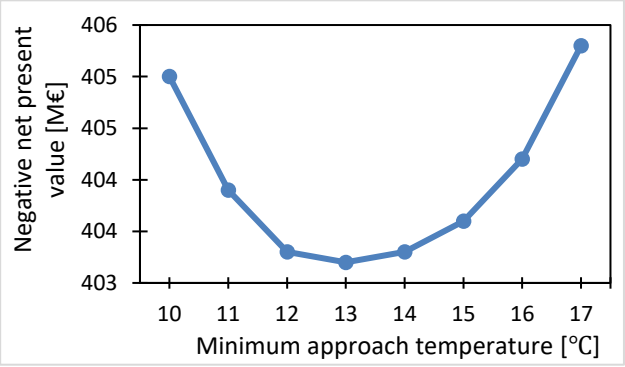

Figure 10. Optimization of minimum approach temperature for the base case

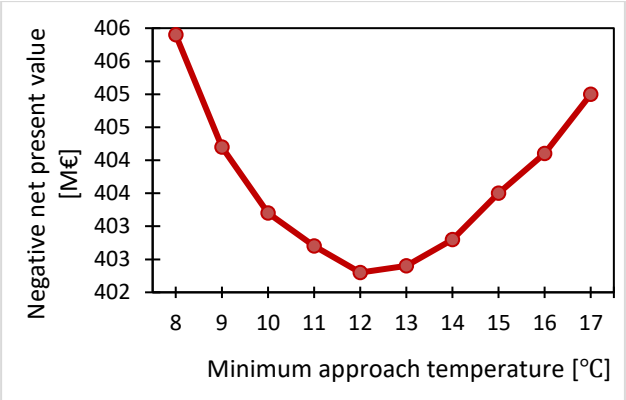

Figure 11. Optimization of minimum approach temperature for the vapour recompression case.

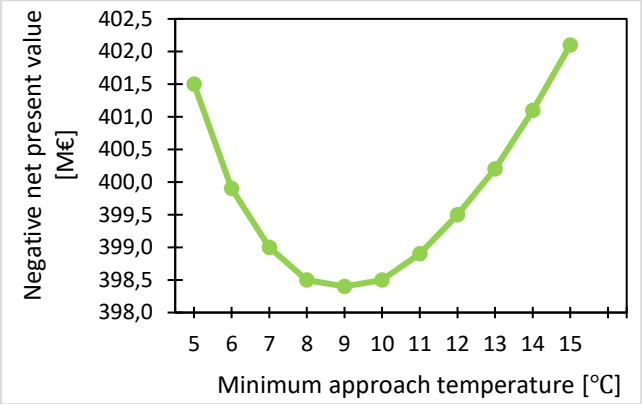

Figure 12. Optimization of minimum approach temperature for the split-stream case.

The optimum capture cost was calculated to approximately 40 Euro per ton CO_2 captured in these optimizations. This is in order of magnitude the last year's quota price for CO_2. When cost of transport and storage is added, the cost of capture, transport and storage is still higher than the quota price.

4 Conclusion

In this work, three configurations; standard, vapour recompression and a simple split-stream (rich split) have been simulated with an equilibrium-based model in Aspen HYSYS™ using flue gas data from a natural gas based power plant. Adjust and recycle blocks available in Aspen HYSYS are used to automate the energy and material balance for a specified configuration. Optimization can be performed by minimizing the total cost calculated in an Aspen HYSYS spreadsheet. The equipment cost was obtained from Aspen In-plant Cost Estimator™ V10.0, and an enhanced detailed factor (EDF) method was used to estimate the total investment cost. Parametric studies of varying absorber packing height, minimum approach temperature, flash pressure and split ratio were performed at 85 % capture efficiency for the three configurations. The calculated

cost optimum process parameters for the standard process were 15 m packing height and 13 °C minimum approach temperature. For the vapour recompression case, a flash pressure of 150 kPa provided the lowest total cost. The calculated optimum for the rich split configuration was 10-16 % split ratio. The minimum capture cost was calculated to 39-40 Euro per ton CO_2 in these optimizations. Automated calculations are dependent on stable convergence of the simulations. A specific challenge is the adjustment of the amine recirculation to obtain a specified total capture rate.

References

H. Ali. *Techno-economic analysis of CO_2 capture concepts*. PhD Thesis, University of South-Eastern Norway, 2019.

S. A. Aromada and L. E. Øi. *Simulation of Improved Absorption Configurations for CO_2 Capture*. In Linköping Electronic Conference Proceedings, SIMS 56, pp. 21-29, 2015. doi:http://dx.doi.org/10.3384/ecp1511921

S. A. Aromoda and L. E. Øi. Energy and Economic Analysis of Improved Absorption Configurations for CO_2 Capture. *Energy Procedia*, 114:1342-1351, 2017.

S. A. Aromada, N. H. Eldrup, F. Normann and L. E. Øi. *Simulation and Cost Optimization of different Heat Exchangers for CO_2 Capture*. In Linköping Electronic Conference Proceedings, SIMS 61, pp. 22-24, 2020. doi:10.3384/ecp20176318

A. Cousins, L. T. Wardhaugh, and P. H. M. Feron, Preliminary analysis of process flow sheet modifications for energy efficient CO_2 capture from flue gases using chemical absorption, *Chemical Engineering Research and Design*, 89(8):1237-1251, 2011.

A. Cousins, L. T. Wardhaugh, and P. H. M. Feron. A survey of process flow sheet modifications for energy efficient CO_2 capture from flue gases using chemical absorption. *International Journal of Greenhouse Gas Control*, 5(4):605-619, 2011.

L. Dubois and D. Thomas. Comparison of various configurations of the absorption-regeneration process using different solvents for the post-combustion CO_2 capture applied to cement plant flue gases. *International Journal of Greenhouse Gas Control*, 69:20-35, 2017.

N. H. Eldrup. *Installation factor sheet - Project Management and Cost Engineering*. Master's Course. University College of South-Eastern Norway, Porsgrunn, 2016.

E. S. Fernandez, E. J. Bergsma, F. M. Mercader, and E. L. V. Goetheer. Optimisation of lean vapour compression (LVC) as an option for post-combustion CO_2 capture: Net present value maximisation, *International Journal of Greenhouse Gas Control*, 11:114-121, 2012.

G. P. S. A. (GPSA), Engineering Data Book, 10. ed., Tulsa, Oklahoma: Gas Processing Suppliers Association, 1987.

A. L. Haukås, J. Helvig, I. Hæstad and A. M. Lande. *Automatization of Process Simulation and Cost Estimation of CO_2 capture in Aspen HYSYS*. Master's Project, University of South-Eastern Norway, 2019.

A. L. Haukås. *Process simulation and cost optimization of CO_2 capture Using Aspen HYSYS*. Master's Thesis, University of South-Eastern Norway, Porsgrunn, 2020.

J. Holoboff. *Improving flowsheet convergence in HYSYS*. Available online (30.11.2019): http://processecology.com/articles/improving-flowsheet-convergence-in-hysys

Y. Ishii and F. D. Otto. Novel and fundamental strategies for equation-oriented process plowsheeting Part I: A basic algorithm for inter-linked, multicolumn separation processes. *Computers and Chemical Engineering*, 32:1842-1860, 2008.

O. B. Kallevik. *Cost estimation of CO_2 removal in HYSYS*. Master's Thesis, Telemark University College, Porsgrunn, 2010.

M. Karimi, M. Hillestad, and H. F. Svendsen. Capital costs and energy considerations of different alternative stripper configurations for post combustion CO_2 capture. *Chemical Engineering Research and Design*, 89(8):1229-1236, 2011.

T. P. Kisala, R. A. Trevino-Lozano, J.F. Boston and H. I. Britt. Sequential modular and simultaneous modular strategies for process flowsheet optimization. *Computers and Chemical Engineering*, 11(6):567-579, 1987.

Y. Le Moullec, T. Neverux, A. Chikukwva and A. Hoff. Process modifications for solvent-based post-combustion CO_2 capture. *International Journal of Greenhouse Gas Control*, 31:96-112, 2011.

K. Park and L. E. Øi. *Optimization of gas velocity and pressure drop in CO_2 absorption column.* In Linköping Electronic Conference Proceedings SIMS 58, pp. 292-297, 2017. doi: 10.3384/ecp17138292

S. Sharma and G.P. Rangaiah. *Mathematical Modeling, Simulation and Optimization for Process Design. Chemical Process Retrofitting and Revamping, Techniques for Retrofitting and Revamping*, G. P. Rangaiah, Ed., 1. ed. ProQuest Ebook Central: John Wiley & Sons, Incorporated, 2016, pp. 97-127, 2016.

M. Souders and G. G. Brown. Design of Fractionating Columns I. Entrainment and Capacity. *Industrial & Engineering Chemistry*, 26:98-103, 1934.

L. E. Øi. *Removal of CO_2 from exhaust gas*. PhD Thesis, Telemark University College, Porsgrunn, 2012.

L. E. Øi, T. Bråthen, C. Berg, S. K. Brekne, M. Flatin, R. Johnsen, I. G. Moen and E. Thomassen. Optimization of Configurations for Amine based CO_2 Absorption Using Aspen HYSYS. *Energy Procedia*, 51: 224-233, 2014.

L. E. Øi, E. Sundbø, and H. Ali. *Simulation and Economic Optimization of Vapor Recompression Configuration for Partial CO_2 capture*. In the 58th Conference on Simulation and Modelling, SIMS 58, Reykjavik, Iceland, September 25th – 27th, 2017.

L. E. Øi, N. Eldrup, S. Aromada, A. Haukås, J. Helvig, I. Hæstad and A.M. Lande. *Process Simulation and Cost Estimation of CO_2 Capture using Aspen HYSYS*. In Linköping Electronic Conference Proceedings, SIMS 61, pp. 326-331, 2020. doi:10.3384/ecp20176326

Simulation Based Cost Optimization Tool for CO_2 Absorption Processes: Iterative Detailed Factor (IDF) Scheme

Solomon Aforkoghene Aromada[1], Nils Henrik Eldrup[1,2], Lars Erik Øi[1]
[1]Department of Process, Energy and Environmental Technology, University of South-Eastern Norway
[2]SINTEF Tel-Tek, SINTEF Industri, Forskningsparken, Hydrovegen 67, 3936 Porsgrunn, Norway

Corresponding author's email address: solomon.a.aromada@usn.no; saromada@gmail.com

Abstract

A simple, fast, and accurate process simulation based cost estimation and optimization scheme was developed in Aspen HYSYS based on a detailed factorial methodology for solvent-based CO_2 absorption and desorption processes. This was implemented with the aid of the spreadsheet function in the software. The aim is to drastically reduce the time to obtain cost estimates in subsequent iterations of simulation due to parametric changes, studying new solvents/blends and process modifications. All equipment costs in a reference case are obtained from Aspen In-Plant Cost Estimator V12. The equipment cost for subsequent iterations are evaluated based on cost exponents. Equipment that are not affected by any change in the process are assigned a cost exponent of 1.0 and the others 0.65, except the absorber packing height which is 1.1. The capital cost obtained for new calculations with the Iterative Detailed Factor (IDF) model are in good agreement with all the reference cases. The IDF tool was able to accurately estimate the cost optimum minimum approach temperature based on CO_2 capture cost, with an error of less than 0.2%.

Keywords: Carbon capture, Aspen HYSYS, simulation, cost estimation, techno-economic analysis

1 Introduction

Amine based post-combustion carbon capture technology is generally recognized as the most mature and promising technology that can be deployed industrially to reduce CO_2 emissions, which has become necessary for climate change mitigation (Karimi et al., 2011). The current challenge remains the economic implications of the huge energy consumption and the large capital investment requirements (Aromada and Øi, 2017).

This has led to several techno-economic studies. The focus of some of the research is on evaluating the representative costs for carbon capture and storage (CCS) (Stone et al., 2009). The objective of some other studies is on cost reduction and optimization (Fernandez et al., 2012).

Costs are projected to be reduced as research continues and as the first set of industrial CO_2 capture plants start operations (Sprenger, 2019; Aromada et al., 2021). The resulting new concepts and innovations will always be subjected to techno-economic evaluation and optimization or sensitivity analysis.

The common procedure for conducting carbon capture cost estimation and cost optimization studies is to import mass and energy balance data from a simulation software to Microsoft Excel or other applications for analysis each time a simulation is performed (Schach et al., 2010; Lassagne et al., 2013; Aromada and Øi, 2017).

Parametric variation or sensitivity analyses of costs that involve running the entire process simulation several times, and performing new equipment dimensioning, obtaining new costs for all the equipment, and recalculating the capital and operating costs can be very time consuming.

Applying a detailed factorial scheme for chemical plant's initial cost estimation has great advantages of accuracy and capabilities for different types of projects: new plant construction, retrofit or modification projects, small and large plant construction cost estimation (Gerrard, 2020; Ali et al., 2019; Aromada et al., 2021). However, it comes with much more work, and thus much more time to implement compared to methodologies that are founded on a uniform or single overall plant installation factor on all equipment irrespective of cost.

Therefore, there is a need to develop a cost estimation and optimization tool that will drastically reduce the overall economic analysis and optimization calculation time yet giving accurate cost estimates.

2 Model description

The iterative detailed factor (IDF) model is developed based on the Enhanced Detailed Factorial (EDF) method (Ali et al., 2019; Aromada et al., 2021). At Telemark University College and University of South-Eastern Norway (USN) there has been much focus on

calculation of cost optimum parameters in CO_2 absorption-desorption processes. This involves varying different process parameters and different configurations (flowsheet modifications). The procedure commences from process development and simulation of the system's process flow diagram (PFD) to equipment dimensioning and cost estimation.

Each time any parameter is varied, this process is repeated. Consequently, in previous works (Kallevik, 2010; Aromada and Øi, 2017), there is a change in the cost of the equipment, when one of its parameters is being varied, but the costs of all other equipment are kept constant. Similarly, energy consumption by other equipment is also kept constant, while that of the equipment with parameters being optimized can vary. This procedure does not capture the effect of every change in the process caused by varying a specific parameter in the evaluation for optimum cost.

In addition, it is an aim to enable subsequent calculations of all the processes from simulations to cost estimation and optimization in not more than a minute.

The Enhanced Detailed Factorial (EDF) method used at USN has several advantages such as capability for new and modification projects (Aromada et al., 2021). Each equipment unit's installation factor is a function of its cost. This ensures that a very expensive equipment is not over-estimated, and a relatively cheaper equipment are not underestimated. This also comes with a challenge of relatively more work due to the details. Thus, it takes much more time to implement.

Therefore, the Iterative Detailed Factor (IDF) scheme was developed to consider all the effects caused by any parametric variation on the entire process, and to drastically reduce the time to implement cost estimation and other economic analyses of subsequent simulation iterations. The flowchart in Figure 1 explains how the scheme is developed and works. The arrows show how the process flows as well as where inputs come from and where they are used. The steps (and the directions of the arrows) are explained below:

1. Start: The PFD is developed and simulated in Aspen HYSYS.
2. Equipment dimensioning calculations based on mass and energy balances from the simulation are done in a separate Aspen HYSYS Spreadsheet as shown in Figure 2.
3. In the first simulation/cost estimation (base case), all equipment costs are obtained directly from a reliable (reference) source based on the calculated dimensions. In this work, equipment cost data were obtained from Aspen In-Plant Cost Estimator Version 12.
4. In subsequent iterations, when parameters are varied, a change to another solvent/blend is implemented, change in technical and/or economic underlying assumptions are made, or when the process configuration is modified, equipment cost is obtained by cost adjustment, utilizing cost exponents, capturing all the changes caused by the change of a process parameter or system as shown in equation (1):

$$EC_{new} = EC_{Base\ case}\left(\frac{Size_{new}}{Size_{Base\ case}}\right)^{n} \quad (1)$$

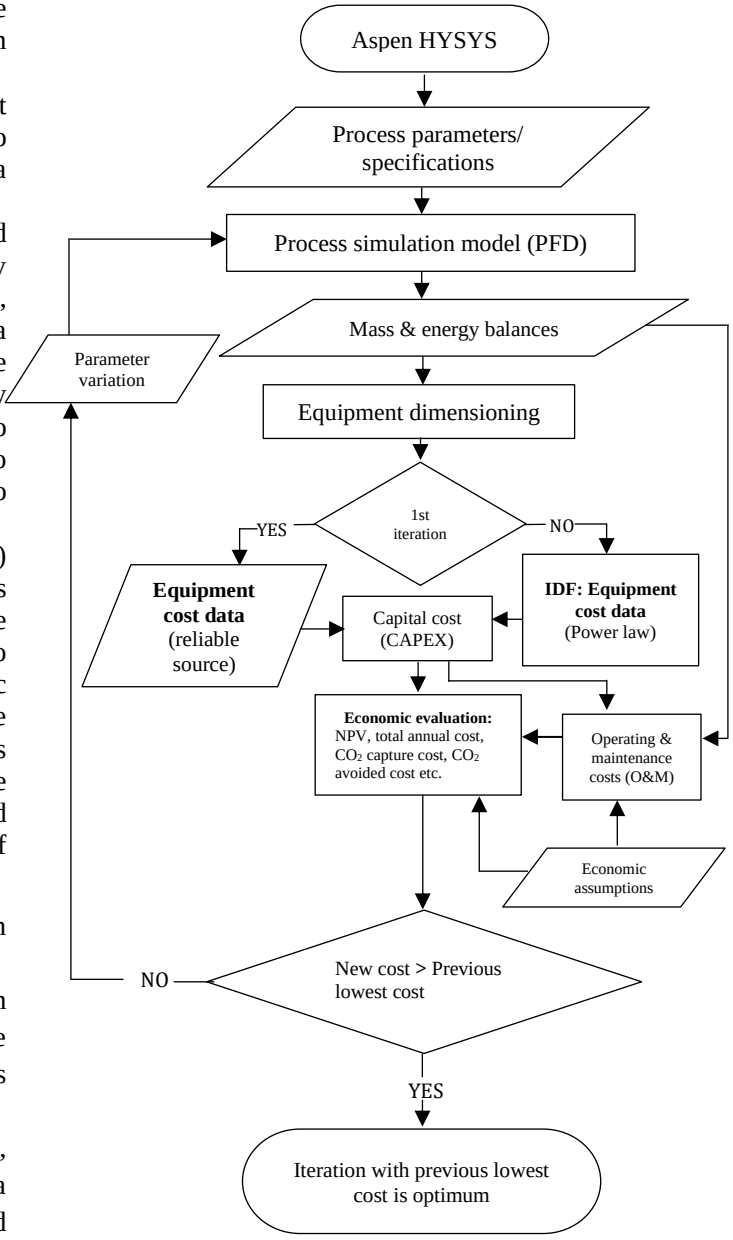

Figure 1. Flow chart describing the iterative detailed factor carbon capture cost optimization model

where $EC_{Base\ case}$ and $Size_{Base\ case}$ are equipment cost and size in the Base case obtained directly from the Aspen In-Plant Cost Estimator. EC_{new} and $Size_{new}$ are the new equipment cost and size for the new simulation evaluated using equation (1). And n is the cost exponent. All equipment costs in a reference case are obtained from a reliable source. The equipment cost for subsequent iterations are evaluated based on cost exponents (Power Law). Equipment that are not affected by any change in the process are assigned a cost exponent of 1 and the others 0.65, except for the absorber packing height (see Section 3.3).

5. All other costs and cost indices already programmed during the first iteration are automatically available after a minor check of the detailed installation factors. Further improvements can be achieved by avoiding manual adjustments of the installation factors between each iteration.
6. The cost optimum parameter is identified when the new cost estimated is less than the costs obtained in previous iterations, and in some cases, also less than cost obtained from subsequent simulations.
7. The capital cost, operating costs and other economic analysis are all done in separate Aspen HYSYS Spreadsheets as can be seen at the bottom of Figure 2.

2.1 Process simulation

The simulation sequence is the same as in (Aromada and Øi, 2015; Aromada et al., 2020a). The base case simulation was performed using the process specifications in Table 1. They are from a 400 MW natural gas combined cycle (NGCC) power plant. It is a 90% amine based CO_2 absorption and desorption in Aspen HYSYS Version 12.

Table 1. Specifications for simulation

Specifications	
Flue gas	
Temperature [°C]	80
Pressure [kPa]	121
CO_2 mole-fraction	0.0375
H_2O mole-fraction	0.0671
N_2 mole-fraction	0.8954
O_2 mole-fraction	0
Molar flow rate [kmol/h]	85000
Flue gas from from DCC to absorber	
Temperature [°C]	40
Pressure [kPa]	121
Lean MEA	
Temperature	40
Pressure [kPa]	121
Molar flow rate [kmol/h]	101595
Mass fraction of MEA [%]	29
Mass fraction of CO_2 [%]	5.30
Absorber	
No. of absorber stages	15
Absorber Murphree efficiency [%]	11- 21
ΔT_{min}, lean/rich heat exchanger [°C]	10
Desorber	
Number of stages	10
Desorber Murphree efficiency [%]	50
Pressure [kPa]	200
Reboiler temperature [°C]	120
Reflux ratio in the desorber	0.3
Temperature into desorber [°C]	104.6

The Aspen HYSYS process flow diagram (PFD) is shown in Figure 2. The absorption and desorption columns were simulated as equilibrium stages with 11 – 21% Murphree efficiencies (changing linearly from bottom to top) and 50% constant Murphree efficiency respectively.

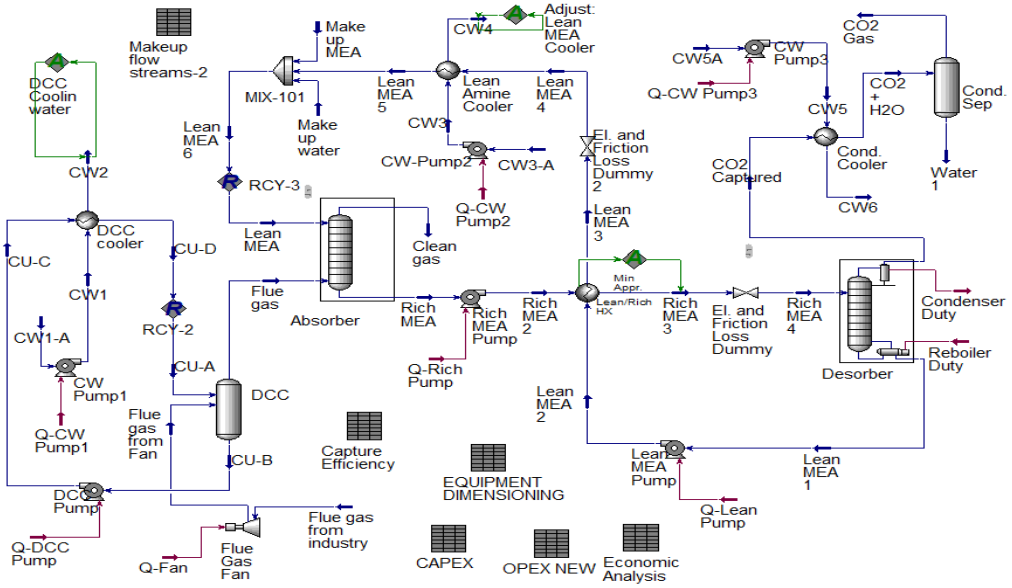

Figure 2. Aspen HYSYS process flow diagram (PFD) of the standard CO_2 capture process

2.2 Equipment dimensioning

Mass and energy balances from the simulations were used to size the equipment in Figure 2.

Table 2. Equipment dimensioning factors and assumptions

Equipment	Sizing factors	Basis/Assumptions
DCC Unit	Tangent-to-tangent height (TT), iterations: mass (*kg*); Packing height, internal and external diameters (all in [*m*]), iterations: volume (m^3);	Velocity using Souders-Brown equation with a k-factor of 0.15 m/s. TT =15 *m*, 1 *m* (structured) packing height/stage (4 stages)
Absorber		Superficial velocity of 2.5 m/s, TT=40 *m*, 1 *m* packing (structured) height/stage (15 stages)
Desorber		Superficial velocity of 1 *m/s*, TT=22 *m*, 1 *m* packing (structured) height/stage (10 stages)
Separator		Vertical vessel, Velocity using Souders-Brown
Lean/rich heat exchanger	Heat transfer area, A [m^2]	Duty, Q [*kW*], U = 0.73 $kW/m^2.K$ (Nwaoha et al., 2019). FTS-STHX
Reboiler		Duty, Q [*kW*], U = 0.8 $kW/m^2.K$, U-tube Kettle type
Condenser		Duty, Q [*kW*], U = 1.0 $kW/m^2.K$, UT-STHX
Coolers		Duty, Q [*kW*], U = 0.8 $kW/m^2.K$, UT-STHX
Pumps	Flow rate [*l/s*] and duty [*kW*], iterations: duty [*kW*]	Centrifugal. Efficiency = 0.75
Fans	Flow rate [m^3/h] and duty [*kW*], iterations: duty [*kW*].	Centrifugal. Efficiency = 0.75

The sizing factors, basis and assumptions for equipment dimensioning are summarized in Table 2. They are the same as in previous works (Aromada et al., 2020a) but on a different system. FTS-STHX refers to fixed tube-sheets Shell and tube heat exchanger, and the U-tube type is UT-STHX. More details on the equipment dimensioning can also be found in (Aromada et al., 2020; Aromada et al., 2021).

2.3 Capital Cost Assumptions

The capital cost in this work is the sum of each equipment installed cost. The IDF scheme is based on the EDF method (Ali et al., 2019; Aromada et al., 2021). All equipment is assumed to be manufactured from stainless steel (SS) with exception of the fan which is constructed from carbon steel (CS). Equipment costs in SS are converted to their corresponding costs in CS. Each equipment installed cost is obtained as a product of the equipment cost in CS and its individual detailed installation factor.

The cost year is 2020 and the cost currency is Euro (€). Therefore, the 2020 updated detailed installation list was used (Eldrup, 2020). The factors are derived based on the site, equipment type, materials, size of equipment and includes direct costs for erection, instruments, civil, piping, electrical, insulation, steel and concrete, engineering cost, administration cost, commissioning and contingency.

2.4 Operating costs scope and assumptions

Operating costs in this work include cost for electricity, steam, cooling water, solvent, maintenance and salaries. The economic assumptions are tabulated in Table 3.

Table 3. Economic assumption for operating cost

	Unit	Value/unit
Operational hours	Hours/year	8 000
Steam	€/kWh	0.026
Electricity	€/kWh	0.059
Cooling water	€/m^3	0.075
Process water	€/m^3	6.77
MEA	€/m^3	1514
Maintenance	€	4% of TPC
Supervisor (1)	€	156 650
Operators (6)	€	80 000

3 Results and Discussion

3.1 Process Simulation Results

The specific reboiler heat obtained in the base case is 4.10 GJ/t CO_2, and the rich loading is 0.46. The rich loading is the mole ratio of CO_2 to the MEA in the rich stream exiting the absorber. The results have good agreement with literature. Sipöcz and Tobiesen (2012) calculated a reboiler heat of 3.97 GJ/t CO_2 and 0.47 rich-loading. In addition, Sipöcz et al. (2011) for an NGCC's exhaust gas also obtained 3.93 GJ/t CO_2 and 0.47 rich loading.

For a case with a minimum approach temperature of 5°C in the main heat exchanger, a reboiler heat of 3.78 GJ/t CO_2 and 0.47 rich loading were calculated. This is also close to the results obtained by Dutta et al. (2017), which are 3.70 GJ/t CO_2 reboiler heat and 0.47 rich loading.

3.2 Base Case Capital and Operating Costs

The capital cost estimated in the base case is €135 million. The capital cost in this work is limited to the total plant cost (TPC). It also does not include CO_2 compression or other flue gas pre-treatment sections other than the direct contact cooling loop. This is sufficient as all the sensitivity analysis conducted in this work are merely within the main CO_2 capture process between the absorber and the desorber. Nth-of-a-kind (NOAK) was also assumed. It is important to state that a first-of-a-kind (FOAK) plant would cost 115 – 155% of a NOAK plant (Boldon and Sabharwall, 2014; Aromada et al., 2020b). In a similar work (NOAK) that included the compression section, the TPC was estimated to €189 million (Aromada et al., 2021).

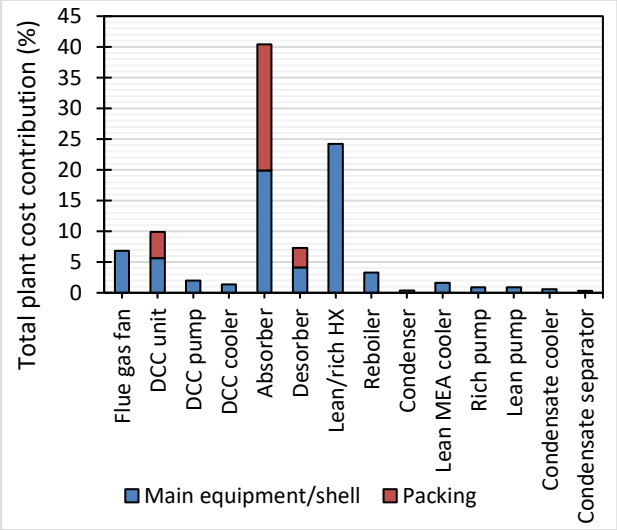

Figure 3. Capital cost distribution

The capital cost distribution is shown in Figure 3. It can be observed that the absorber and the lean/rich heat exchanger are the main cost contributors to the capital costs. Their contributions are 40% and 24% respectively. Therefore, the absorber and the main heat exchanger are the most important equipment for cost optimization in this capture process. Consequently, the IDF tool for process cost optimization based on process parameter variation was tested on the two equipment units for validation.

The cost of the lean/rich heat exchanger in initial cost estimation is a function of the required heat transfer area (m^2). The area varies much with the temperature difference (ΔT_{min}). The required area is doubled if the ΔT_{min} is 5°C instead of 10°C (Karimi et al., 2011). Therefore, ΔT_{min} has often been a very important process parameter to optimize in different solvent-based carbon capture processes (Aromada et al., 2020b; Aromada and Øi; 2017; Øi, 2012; Karimi et al., 2011).

In previous works, the absorption column, especially the packing height has been given attention for optimization, to reduce the entire cost of the process (Øi et al., 2020; Aromada and Øi, 2017; Kallevik, 2010).

3.3 Validation of the IDF Scheme: Capital Cost

To validate the accuracy of the scheme, it is important to perform cost estimation of the same process, with equipment cost data obtained from a reliable or reference source, and equipment costs estimated using the IDF scheme on the same process.

To evaluate the performance of the IDF scheme, equipment costs were first obtained from Aspen In-Plant Cost Estimator for each simulation iteration. These costs were used to estimate capital cost for each iteration, capturing the effect of the variation of a specific process parameter on all equipment in the process. These reference costs are referred to as the "original cost" since the equipment costs are directly obtained from a reliable cost database. This process is time consuming.

The IDF scheme is then applied for estimating the capital cost, operating cost, and CO_2 capture cost in each parameter variation simulation iteration. The IDF tool equipment costs were estimated from the base case equipment purchase cost based the Power law as described in Section 2.

The equipment costs in the IDF Scheme were calculated with a cost exponent of 0.65 for all the equipment that changes in size when a specific process parameter is varied, except for the absorber packing height. The larger the packing volume, the more the column and packing supports and auxiliaries are needed. Thus, costing the entire column may not necessarily follow economy of scale principle by using a cost exponent of 0.65. A range of cost exponents where then tested: 0.65, 0.85, 0.9, 1.0 and 1.1. To differentiate the results of each cost exponent, each cost exponent was designated PH-cost exponent. PH signifies packing height, which is being varied, while the number refers to the cost exponent used for estimating the new costs of the new packing size (volume). For example, in the case of PH-0.65 results, it means that as the packing height (PH) of the absorption column was varied between 12 *m* and 25 *m*, the costs of the new packing heights (12 *m*, 18 *m*, 20 *m*, 22 *m*, and 25 *m*) were estimated using a cost exponent of 0.65. New packing costs were also similarly estimated using cost exponents of 0.85 (PH-0.85), 0.90 (PH-0.90), 1.0 (PH-1.00), and 1.10 (PH-1.10). The results are plotted together and are compared with the original cost, that is the cost obtained directly from Aspen In-Plant Cost Estimator version 12.

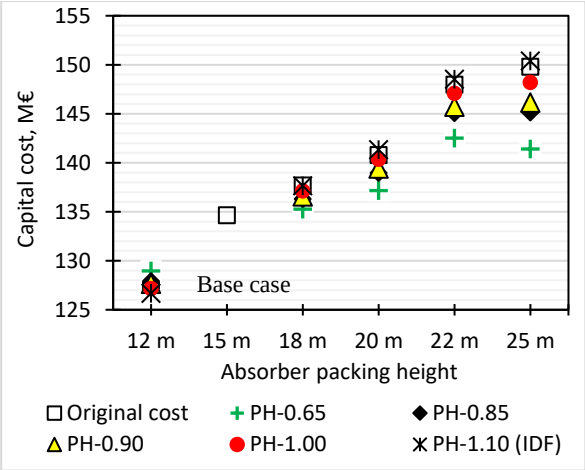

Figure 4. Impact of varying absorber packing height on the plant's capital cost with different cost exponents

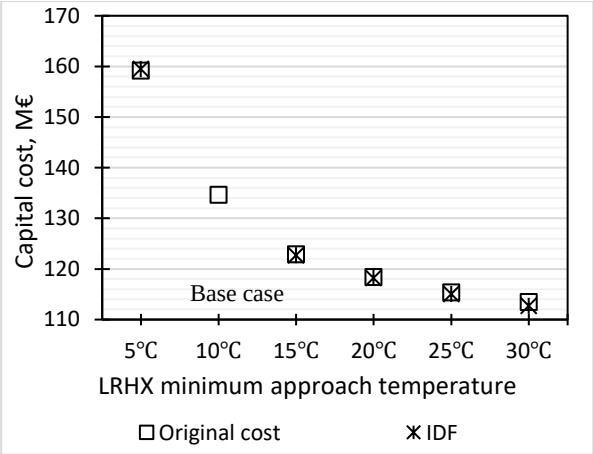

Figure 5. Comparison of IDF Scheme capital costs with reference capital cost when the temperature difference in the lean/rich exchanger is varied

Figure 4 shows that the cost exponent of 1.1 has the best agreement with the original cost for new sizes higher than the base case, and 0.85 for the size (12 *m* packing height) less than the base case (15 *m* packing height). However, cost exponent 1.00 also has a good agreement. Therefore, a cost exponent of 1.10 was used in the IDF scheme to estimate the cost of the absorber packing volume from the Base case (original cost) for higher volumes and 0.85 for volume less than in the base case where the absorber packing height is 12. The results suggest that due to the peculiarity of the cost of the packings/auxiliaries/supports/installations, not necessarily following economy of scale when the size of the column increases, new cost due to size adjustment using Power Law would require a cost exponent of 1.1 to minimize the estimation error or deviation from the original (reference) cost.

The ΔT_{min} of the main heat exchanger was varied from 5°C to 30°C in steps of 5°C. The IDF Scheme capital costs in each iteration were similarly estimated but with a cost exponent of 0.65 for all equipment apart from the columns and their packings, which were estimated with a cost exponent of 1 as they were kept constant. Varying ΔT_{min} will not have any effect on the absorber. Figure 5 presents the comparison of capital cost estimates from the IDF tool with the original capital costs. Original or reference costs are the cost obtained directly from Aspen In-Plant Cost Estimator. The agreement is quite good. The trend of the estimates is also similar to results in (Aromada et al., 2020b).

3.4 CO_2 Capture Cost

Trade-off analyses of the resulting capital and operating costs due to varying of the two process parameters were conducted, using the economic cost metric of CO_2 capture cost. This was estimated as follows:

$$CO_2\ capture\ cost\left(\frac{€}{tCO_2}\right) = \frac{Total\ annual\ cost(€)}{Mass\ of\ CO_2\ captured\ (tCO_2)} \quad (2)$$

where, the total annual cost is the sum of the annual capital cost and yearly operating expenses as done in (Aromada et al., 2020a). The results are presented in Figure 6 and Figure 7. The agreement with the original cost is very good. In Figure 6, IDF estimates used 0.85 as cost exponent for absorber packing height of 12 *m* and 1.1 for packing heights above that of the Base case (15 *m*) as explained in the previous section. However, capture cost was also estimated using 1.1 for 12 *m*, which is represented by a "red circle". The agreement is also good but using 0.85 is more accurate. This implies that the IDF scheme will still give good estimates if 1.1 is used as the cost exponent for all packing height iterations.

Figure 7 is specifically a cost optimization result. The cost optimum ΔT_{min} is 15°C which is the same cost optimum temperature difference calculated in (Aromada et al., 2020b) even though both process specifications, CO_2 concentrations and capture rates are different. Aromada et al. (2021) also calculated the cost optimum ΔT_{min} to be 15°C for a similar process but including CO_2 compression process. Kallevik (2010) estimated the minimum cost at 90 % CO_2 capture as in this study to be 15°C. The results obtained show that apart from drastically reducing the work and time required for cost estimation and cost optimization calculations in subsequent process simulation iterations, the IDF tool can give accurate or acceptable capital cost and operating cost.

The specific reboiler heat plot in Figure 7 indicates that the capital cost dominates at 5°C. The capital cost influence declines till the cost optimum, after which the energy cost (operating cost) begins to dominate.

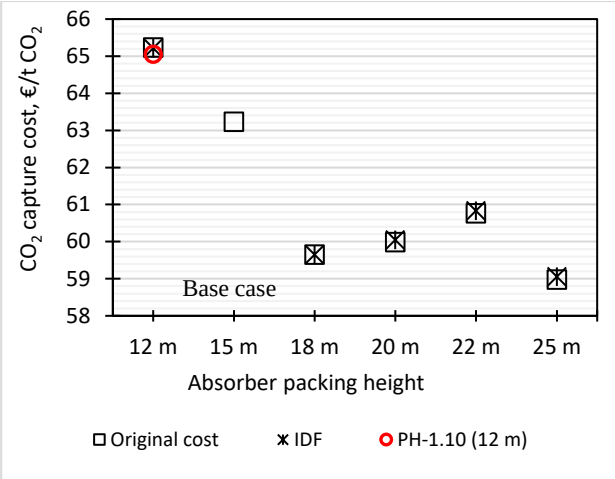

Figure 6. Impact of varying absorber packing height on CO_2 capture cost

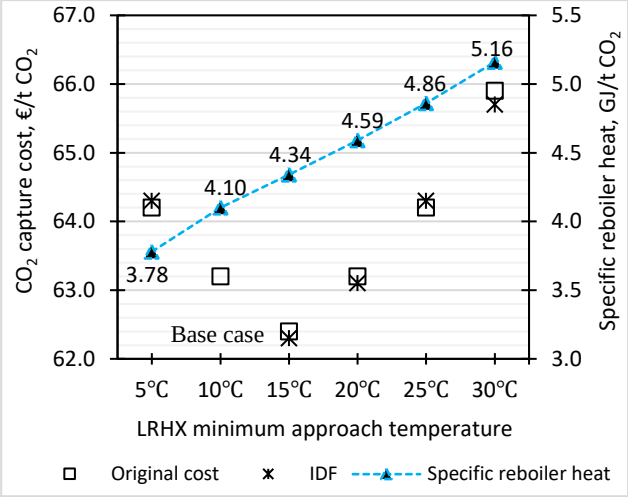

Figure 7. Impact of varying the minimum approach temperature in the lean/rich exchanger on CO_2 capture cost

3.5 Accuracy

We conducted an error analysis of the IDF tool using a simple percentage of differences between the IDF Scheme results and the original costs. This was performed as follows:

$$Error\ (\%) = \frac{(IDF\ result - Original\ cost)}{Original\ cost} \times 100 \qquad (3)$$

A negative value indicates that the IDF Scheme estimate is less than the original or reference cost and vice versa. The IDF Scheme's errors in both the capital cost and CO_2 capture cost estimates for absorber packing height and lean/rich heat exchanger's temperature difference iterations are presented in Figures 8 and 9, respectively.

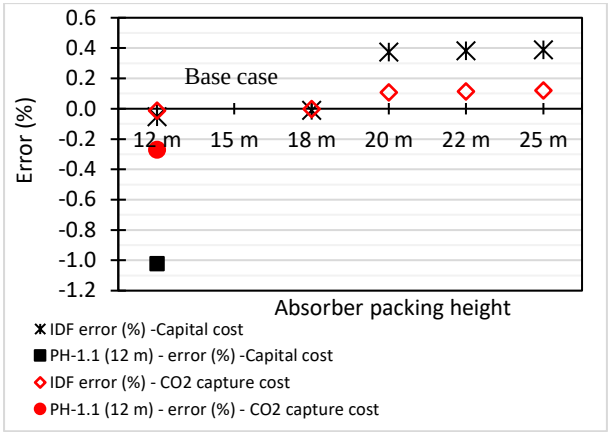

Figure 8. Error analysis of resulting capital costs by varying the absorber packing height

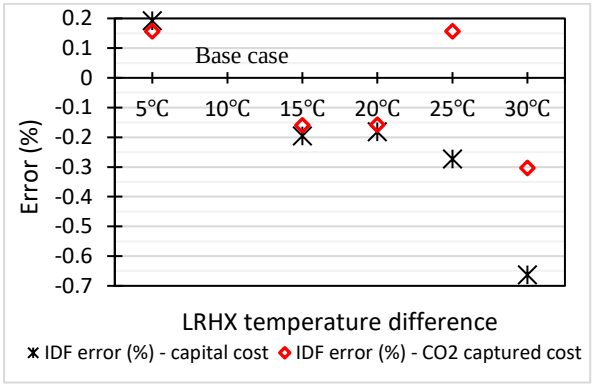

Figure 9. Error analysis of resulting capital costs by varying the minimum approach temperature in the lean/rich exchanger

In the case of varying the absorber packing height, the error in the capital cost estimates of the scheme is between 0.01 to 0.39%, while it is 0 to 0.12% for CO_2 capture cost (Figure 8). If 1.1 is used as cost exponent for 12 *m* which is less than the Base case size (15 *m*), the errors at that point increase to approximately 1% and 0.3% for the capital cost and CO_2 capture cost respectively, as can be observed in Figure 8. That is why 0.85 cost exponent is adopted for packing height less than the Base case in the IDF Scheme. This is because of the peculiarity of the absorption column and packings in respect of economy scale principle as explained earlier.

In the case of the lean/rich heat exchanger temperature difference iterations, the IDF tool errors for the capital cost and CO_2 capture cost estimates are between -0.66 to 0.18% and -0.30 to 0.16%.

These are very small errors and are acceptable. They do not have any effect on cost optimization calculations or sensitivity analysis results when process parameters are varied several times. Therefore, the IDF tool is suitable for quick and accurate cost estimation and other economic analysis of solvent-based CO_2 capture processes involving several iterations of the entire process from simulation to cost estimation.

DOI: 10.3384/ecp21185301

4 Conclusion

A simple scheme was developed in Aspen HYSYS for quick and accurate iterative process simulations, equipment dimensioning and cost estimation of a CO_2 capture process. We refer to it as the Iterative Detailed Factor (IDF) Scheme. It is implemented by the aid of the Aspen HYSYS spreadsheet's function. It was validated in this work. The average error in all the iterations is 0.2% of the reference cases. The cost optimum temperature difference in the lean/rich heat exchanger estimated using the IDF tool with fixed tubesheets shell and tube heat exchangers (FTS-STHX) is 15°C. This agrees with recent literature.

Application of detailed factorial methodology in cost estimation is time-consuming. However, the IDF tool reduces the time required for economic analysis of CO_2 capture processes for subsequent iterations to less than a minute after simulation.

Therefore, with the IDF Scheme, accurate cost optimization of CO_2 capture processes, sensitivity analysis of process parameters and economic assumptions as well as market conditions, solvent and blends cost analysis and other iterative cost studies of CO_2 capture processes can be conducted using detailed factorial method in relatively short time (minutes instead of hours or days).

References

H. Ali, N. H. Eldrup, F. Normann, R. Skagestad, and L. E. Øi. Cost Estimation of CO_2 Absorption Plants for CO_2 Mitigation–Method and Assumptions. *International Journal of Greenhouse Gas Control*, 88, 10-23, 2019.

S. A. Aromada and L. E. Øi. Simulation of Improved Absorption Configurations for CO_2 Capture. In Proceedings of the 56th Conference on Simulation and Modelling (SIMS 56), October, 7-9, 2015, Linköping University, Sweden. *Linköping Electronic Conference Proceedings*, 21-29, 2015. doi:http://dx.doi.org/10.3384/ecp1511921

S. A. Aromoda and L. E. Øi. Energy and Economic Analysis of Improved Absorption Configurations for CO_2 Capture. *Energy Procedia*, 114, 1342-1351, 2017.

S. A. Aromada, N. H. Eldrup, F. Normann, and L. E. Øi. Techno-Economic Assessment of Different Heat Exchangers for CO_2 Capture. *Energies*, 13(23), 6315, 2020a.

S. A. Aromada, N. H. Eldrup, F. Normann and L. E. Øi. Simulation and Cost Optimization of different Heat Exchangers for CO_2 Capture. In Proceedings of the 61st International Conference of Scandinavian Simulation, SIMS 2020, September 22-24, Virtual Conference, Oulu, Finland. *Linköping Electronic Conference Proceedings*, 22-24, 2020b.

S. A. Aromada, N. H. Eldrup, and L. E. Øi. Capital cost estimation of CO_2 capture plant using Enhanced Detailed Factor (EDF) method: Installation factors and plant construction characteristic factors. *International Journal of Greenhouse Gas Control*, 110, 103394, 2021.

L. M. Boldon and P. Sabharwall. *Small modular reactor: First-of-a-Kind (FOAK) and Nth-of-a-Kind (NOAK) Economic Analysis* (No. INL/EXT-14-32616). Idaho National Lab. (INL), Idaho Falls, ID (United States), 2014. doi: 10.2172/1167545

R. Dutta, L.O. Nord and O. Bolland. Selection and design of post-combustion CO_2 capture process for 600 MW natural gas fueled thermal power plant based on operability. Energy, 121, 643-656, 2017.

N. H. Eldrup. *Installation factor sheet - Project Management and Cost Engineering*. Master's Course. University College of Southeast Norway, Porsgrunn, 2020.

E. S. Fernandez, E. J. Bergsma, F. de Miguel Mercader, E. L. Goetheer, T. J. Vlugt. Optimisation of lean vapour compression (LVC) as an option for post-combustion CO_2 capture: Net present value maximisation. *International Journal of Greenhouse Gas Control*, 11, 114–121, 2012.

O. B. Kallevik. *Cost estimation of CO_2 removal in HYSYS*. Master's Thesis, Telemark University College, Porsgrunn, 2010.

N. Sipöcz, A. Tobiesen, and M. Assadi. Integrated modelling and simulation of a 400 MW NGCC power plant with CO_2 capture. *Energy Procedia*, 4, 1941-1948, 2011.

N. Sipöcz and F.A. Tobiesen. Natural gas combined cycle power plants with CO_2 capture–Opportunities to reduce cost. *International Journal of Greenhouse Gas Control*, 7, 98-106, 2012.

M. Sprenger. Carbon capture is cheaper than ever. Norwegian SciTech News, Research News from NTNU and SINTEF, Norway. April 10, 2019. Accessed on 10.01.2021. Available: https://norwegianscitechnews.com/2019/04/carbon-capture-is-cheaper-than-ever

E. J.Stone, J. A. Lowe, and K. P. Shine. The impact of carbon capture and storage on climate. *Energy & Environmental Science*, 2(1), 81-91, 2009.

L. E. Øi. Aspen HYSYS simulation of CO_2 removal by amine absorption in a gas based power plant. In Proceedings *The 48th Scandinavian Conference on Simulation and Modelling (SIMS 2007)*, Göteborg, Sweden. Linköping *Electronic Conference Proceedings* 27(8), 73-81, 2007.

L. E. Øi. *Removal of CO_2 from exhaust gas*. PhD Thesis, Telemark University College, Porsgrunn. TUC 3: 2012.

Simulation and Impact of different Optimization Parameters on CO_2 Capture Cost

Solomon Aforkoghene Aromada[1], Sumudu Karunarathne[1], Nils Eldrup[1,2], Sina Orangi[1], Farzan Farsi Madan[1], Katarzyna Grazyna Fajferek[1], Njål Torgeir Sæter[1], Syaiful Bahri[1], Lars Erik Øi[1]

[1]Department of Process, Energy and Environmental Technology, University of South-Eastern Norway
[2]SINTEF Tel-Tek, SINTEF Industri, Forskningsparken, Hydrovegen 67, 3936 Porsgrunn
solomon.a.aromada@usn.no, saromada@gmail.com

Abstract

The influence of different process parameters/factors on CO_2 capture cost, in a standard amine based CO_2 capture process was studied through process simulation and cost estimation. The most influential factor was found to be the CO_2 capture efficiency. This led to investigation of routes for capturing more than 85 % of CO_2. The routes are by merely increasing the solvent flow or by increasing the absorber packing height. The cost-efficient route was found to be by increasing the packing height of the absorber. This resulted in 20 % less cost compared to capturing 90 % CO_2 by increasing only the solvent flow. The cost optimum absorber packing height was 12 *m* (12 stages). The cost optimum temperature difference in the lean/rich heat exchanger was 5°C. A case with a combination of the two cost optimum parameters achieved a 4 % decrease in capture cost compared to the base case. The results highlight the significance of performing cost optimization of CO_2 capture processes.

Key words: simulation, CO2, optimization, techno-economic analysis, Aspen HYSYS.

1 Introduction

An economic optimization of a standard CO_2 absorption and desorption process can be conducted by the aid of process simulation and parametric variation (sensitivity analysis). There are different studies on different process parameters optimization (Schach et al., 2010; Øi, 2012; Li et al., 2016). In this work, we emphasise how the influence of different parameters on the capture cost compare. Such comparison is important to understand the most influential parameter or factors on the cost of the capture process. Then, the process engineer can pay more attention to it.

Important parameters frequently cost optimized in a standard solvent based CO_2 absorption and desorption are the absorber packing height (Øi et al., 2020; Aromada & Øi, 2017; Kallevik, 2010), and the minimum temperature difference in the main heat exchanger (ΔT_{min}) (Schach, 2010; Karimi et al., 2011; Øi et al., 2014; Li et al., 2016; Aromada et al., 2020a). The CO_2 capture efficiency in literature is typically within 85 – 90 % (IEAGHG, 2008; IEAGHG, 2013). Several of such studies have been conducted (Aromada & Øi, 2017; Øi et al., 2020), but none of those studies has shown or compared the effect of these parameters on the capture cost, to understand which parameter has the greatest influence on the capture cost.

The first CO_2 capture plant to capture CO_2 from a cement plant's flue gas is being constructed at Brevik in Norway (Thorsen, 2020). The plant is designed to capture only 50 % of the CO_2 from the cement plant. Soon, it might be necessary to increase this capture rate due to climate change mitigation demands. There are generally two ways to achieve higher CO_2 capture: (1) to retain the current packing height and increase the solvent circulation rate, or (2) to increase the packing height.

The question is, what is the most cost efficient route between (1) and (2) above, to capture additional CO_2, more than 85%? To increase the absorption column packing height will lead to increase in capital cost. The operating cost will increase when the solvent circulation rate increases. It is important to perform a trade-off analysis to show the most cost efficient route to increase the CO_2 removal rate.

This work presents extended results from a group project at the University of South-Eastern Norway (Orangi et al., 2020). The aim is to investigate for the most influential process parameter or factor on CO_2 capture cost, and to show the most economic way to increase CO_2 capture efficiency.

2. Methods

2.1 Scope of Analysis

The focus of this work is on investigating the influence of certain process parameters or factors on carbon capture cost. It is sufficient to limit the analysis to only the main CO_2 capture process described in Figure 1. The scope does not cover CO_2

compression, transport and storage, costs, insurance, taxes, first fill cost, and administrative costs are not included in the operating cost. Therefore, the compression section is not necessary. The important equipment in the main capture process includes the absorber, desorber, lean/rich heat exchanger, lean amine cooler, reboiler, condenser, and the rich and lean pumps. The flue gas cooling process before the CO_2 absorption is also included in this study. The flue gas is from a 400 MWe natural gas combined cycle (NGCC) power plant.

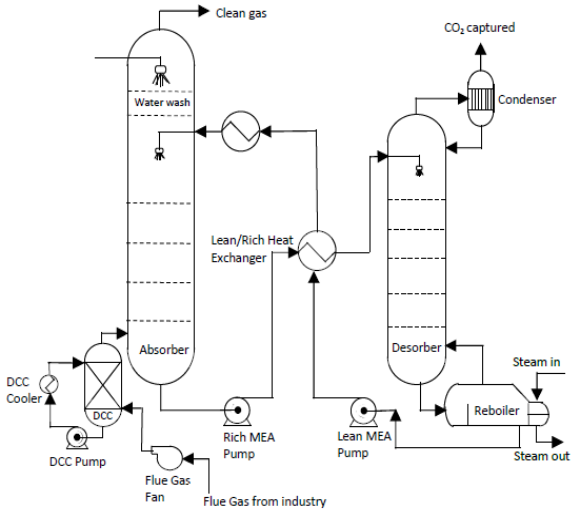

Figure 1. Flowsheet of the standard process (Aromada et al., 2020a)

2.2 Process Specifications and Simulation

The process specifications used for the base case simulation are presented in Table 1. The process simulation in this work applies the same strategy used in (Øi, 2007; Aromada et al., 2015). The simulations were conducted using the equilibrium based Aspen HYSYS Version 10.

Table 1. Specifications for process simulation

Parameter	Value	Unit
Inlet flue gas temperature	40	℃
Inlet flue gas pressure	101.0	kPa
Inlet flue gas flow rate	1.091×10^5	$kgmol/h$
CO_2 content in inlet gas	3.30	$mol\ \%$
Water content in inlet gas	6.90	$mol\ \%$
Lean amine temperature before and after pump	120	℃
Lean amine pressure before pump	200	kPa
Lean amine pressure after pump	300	kPa
Lean amine pressure to absorber	110	kPa
Lean amine rate to absorber	1.175×10^5	$kgmol/h$
CO_2 content in lean amine	2.98	$mole\ \%$
Number of stages in absorber	10	-
Rich amine pressure before pump	110	kPa
Rich amine pressure after pump	200	kPa
Number of stages of stripper	6 + Reboiler + Condenser	-
Reboiler temperature	120	℃

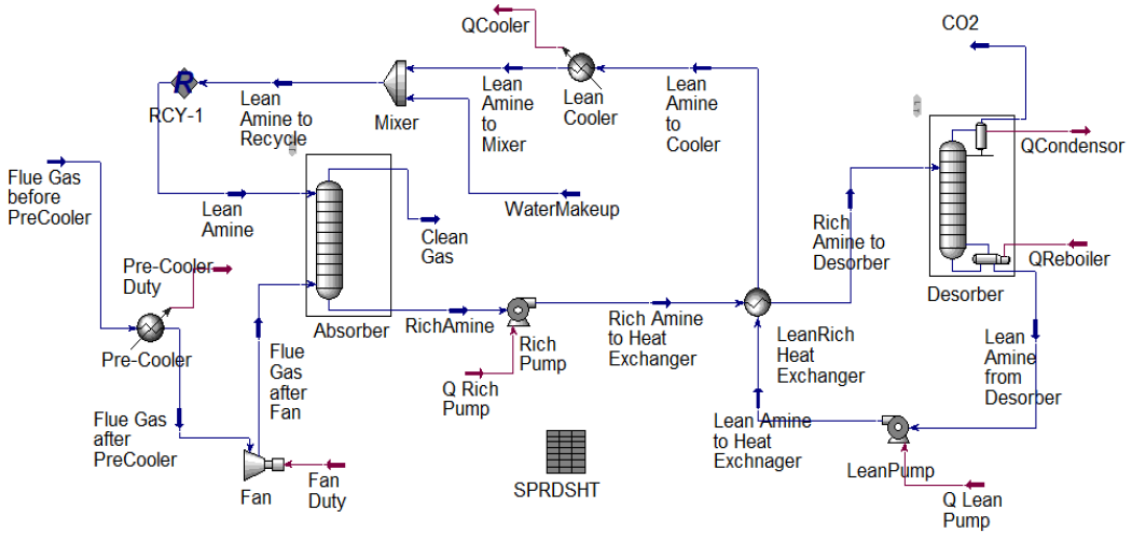

Figure 2. Simulation PFD in Aspen HYSYS

The base case was simulated to capture 85 % CO_2 from exhaust gas from a natural gas combined cycle (NGCC) power plant (Øi, 2007). The process consists of an absorber with 10 packing stages (10 *m*), a desorber with 6 packing stages (6 *m*), and 10 ℃ temperature difference in the main heat exchanger.

The parametric optimization were performed by varying the absorber packing height between 8 and 14 stages in step of 2 stages. The temperature difference in the main heat exchanger was varied between 5 ℃ and 15 ℃ in step of 2.5 ℃. Simulations were also performed for 87.5 % and 90 % CO_2 capture efficiencies with constant (10 *m*) and changing absorber packing heights. The flue gas fan and the pumps were simulated with specified adiabatic efficiency of 75 %.

The Aspen HYSYS simulation process flow diagram showing all the equipment included in the scope of the study is shown in Figure 2.

2.3 Equipment Sizing

The absorber and desorber were dimensioned based on a superficial gas velocity of 2.5 *m*/s and 1.0 *m*/s respectively. Their packing heights in the base case are 10 *m* and 6 *m* respectively where each stage was assumed to be 1 *m*. Murphree efficiencies of 0.25 and 1.0 were also specified for the absorber and stripper respectively. Structured packing with a normal area of 250 m^2/m^3 was also assumed for both columns' packing. This is because of low pressure drop, high efficiency and high capacity (Øi, 2012; Brickett, 2015). It is most likely close to the economical optimum (Øi, 2012).

All the heat exchange equipment were sized based on the effective heat transfer area calculated from their respective heat duties. These are directly obtained from Aspen HYSYS. Overall heat transfer coefficients of 500 W/m^2K, 800 W/m^2K, 1000 W/m^2K and 800 W/m^2K were specified for the lean/rich heat exchanger, reboiler, condenser and the coolers respectively (Aromada et al., 2020b; Ali et al., 2019).

The fan and pumps were dimensioned based on volumetric flows and duties.

All equipment unit except the flue gas fan is assumed to be constructed from stainless steel (SS) for corrosion resistance purpose. The flue gas fan is manufactured from carbon steel (CS). The details of material conversion from other materials to CS have been provided for different capital cost estimation methods in (Aromada et al., 2021).

2.4 Capital Cost Estimation

All the cost estimation was performed using the Enhanced Detailed Factor (EDF) method (Ali et al., 2019; Aromada et al., 2021). The capital cost is the sum of the installed costs of all the equipment within the scope of analysis.

The costs of equipment were obtained from Aspen In-plant Cost Estimator Version 10. The cost year is 2016. The costs were then escalated to 2019 using the chemical engineering plant cost index (CEPCI). The assumed default location is Rotterdam in Netherlands. It has a location factor of 1.

Some equipment not included in the simulation which may affect the overall cost are accounted for in the capital cost. These are all the equipment units in the water-wash section of the absorption column, tanks, and mixers. They are categorized as "unlisted equipment" in this project and are assumed to be 20% of the total plant cost.

The EDF method is prepared for equipment cost in CS. Thus, material factors of 1.75 and 1.30 were used to convert equipment cost in SS to their corresponding costs in CS for welded and machined equipment respectively.

This is an Nth-of-a-kind project (Aromada et al., 2020b). A project life of 20 years with two years of plant construction and discount rate of 7.5 % were assumed.

2.5 Operating Cost Estimation

The scope of the operating cost in this study is limited to maintenance cost which is 4 % of the capital cost, steam cost (€0.03/kWh), electricity cost (€0.13/kWh), solvent cost (€2035.90/m^3), and cooling water cost (€0.22/m^3). These are seen to be the most important and they vary when a process parameter is changed. Other operating costs such as wages and salaries are usually fixed, so, parametric change which is the objective of this work does not affect them.

2.6 Annual Cost and Capture Cost

Different cost metrics are used in carbon capture studies. While the most important metric in climate change perspective may be CO_2 avoidance cost, for mere economic consideration, CO_2 capture cost is sufficient. So, in this project, which is focused on economic optimization, CO_2 capture cost is used:

$$\text{CO}_2 \text{ capture cost} = \frac{\text{Total annual cost}}{\text{Mass of CO}_2 \text{ Captured}} \qquad (1)$$

The annual capital cost is obtained as follows:

$$\text{Annual capital cost} = \frac{\text{capital cost}}{\text{Annualized factor}} \quad (2)$$

The annualised factor is calculated as follows:

$$\text{Annualised factor} = \sum_{i=1}^{n}\left[\frac{1}{(1+r)^n}\right] \quad (3)$$

where n is the years of operation and r is the interest rate.

3 Results and Discussion

3.1 Simulation Results

Table 2 presents the process simulation results for the base case and parametric optimization. The reboiler specific heat consumption in this work is 3.77 GJ/tCO_2. This is close to the 3.65 GJ/tCO_2 and 3.71 GJ/tCO_2 calculated by (Øi, 2007) and (Aromada et al., 2021) respectively for a similar process with 85 % CO_2 capture.

Table 2. Main simulation results

	Reboiler heat [GJ/tCO_2]	Optimum parameter
Base case	3.77	-
Energy optimum packing height	3.50	14 stages
Energy optimum temperature difference	3.41	5°C
90% capture, N=10m	5.24	-
92% capture, N=15m	3.55	-

The absorber packing height (N) was reduced to 8 m and also increased to 12 *m* and 14 *m*. The energy optimum was 14 *m*, which shows that the desorption heat requirement decreases with increase in the absorption column packing height.

The lowest specific heat consumption was achieved by the case with a temperature difference of 5°C in the lean/rich heat exchanger.

Another important observation is that there is a drastic increase of 39 % in the heat requirement for desorption when the base case capture rate was increased from 85% to 90%. However, when the packing height was increased by 50%, that is to 15 *m*, the steam demand by the stripper was reduced by 6% to 3.55 GJ/tCO_2 for 92% CO_2 capture rate.

3.2 Sensitivity Analysis of different Process Parameters/Factors on Energy Consumption

The complete results of the influence of the different process parameters/factors on specific reboiler heat consumption are presented in Figure 3. When the absorber packing height (1 *m*/packing height) was increased from 8 *m* to 10 *m*, the specific reboiler heat consumption decreased from 4.20 GJ/tCO_2 to 3.77 GJ/tCO_2. That is 10 % reduction in steam consumption. Increasing the absorption column packing height further to 12 *m* yielded a 6 % reduction of steam consumption (3.53 GJ/tCO_2) compared to 10 *m* packing height. However, a further increase from 12 *m* to 14 *m* resulted in less than 1 % reduction in reboiler energy demand (3.50 GJ/tCO_2).

While increase in the absorption packing height caused decrease in the reboiler steam demand, increasing the minimum approach temperature (ΔT_{min}) in the lean/rich heat exchanger result in increase in the decrease in the steam consumption in the reboiler. This is because as the ΔT_{min} increases, the amount of heat recovered in the lean/rich heat exchanger by the rich amine stream reduces. The specific reboiler heat consumption with 5 °C, 5 °C, 5 °C and 5 °C are 3.41 GJ/tCO_2, 3.58 GJ/tCO_2, 3.77 GJ/tCO_2, 3.82 GJ/tCO_2 and 3.92 GJ/tCO_2 respectively. The specific reboiler heat consumption for the standard amine based CO_2 capture process reported in literature with different parameters and capture rate are in the range of 3.5 – 5.2 GJ/tCO_2 (Nwaoha et al., 2018; Hu et al., 2018). The values obtained in this work are within this range.

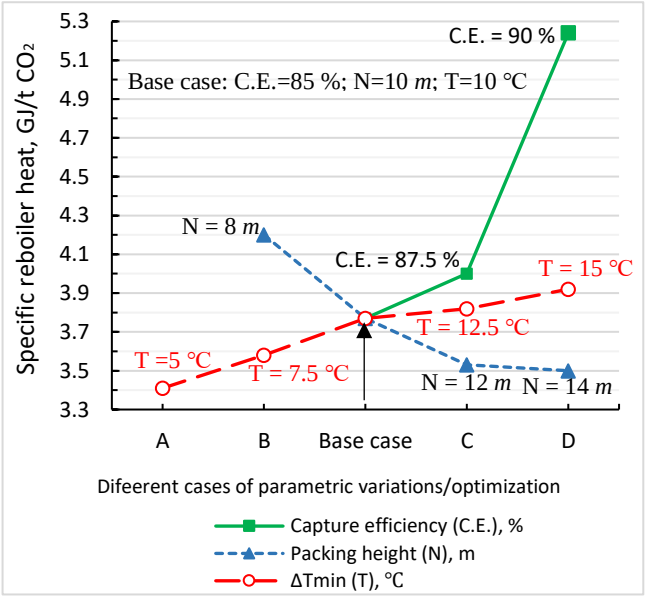

Figure 3. Impacts of different process parameters or factors on specific reboiler heat consumption

Sensitivity of the CO_2 capture rate was also conducted by increasing it to 87.5 % and 90 %. The steam requirement increased by 6 % when the capture efficiency was increased from 85 % to 87.5 %. Increasing the CO_2 capture rate from 87.5 % to 90 % caused a very high increase (31 %) in the reboiler heat consumption. It is important to state that the capture efficiency increase was only achieved by mere increase in the solvent circulation rate of the base case.

3.3 Sensitivity Analysis of different Process Parameters/Factors on CO_2 capture Cost

The results of economic optimization of different process parameters are summarized in Figure 4. The cost optimum absorber packing height is 12 *m*, even though the energy optimum is 14 *m*. The CO_2 capture cost is €63.9/tCO_2. This indicates that the capital cost dominates at 14 *m*. Therefore, the trade-off favours 12 *m* absorber packing height. This implies that it is important to conduct capital and operating costs trade-off analysis before making an economic conclusion on any energy optimum process, which could have been achieved due to higher process complexity. For example, by adding other equipment or increasing the size of one or more equipment units as done in this study.

Varying the temperature difference in the main heat exchanger shows the cost optimum to be 5 °C with a capture cost of €63.8/tCO_2. This agrees with the work of Li et al. (2016) which suggested that the optimum is within the 5 – 10 °C. Schach et al. (2010) calculated the cost optimum to be a logarithmic mean temperature difference of 7.5 °C which is close to this work. However, it is different from what is obtained in the work of Karimi et al. (2011) which calculated the cost at 10 °C to be less than the capture cost at 5 °C. The reason is because the equipment purchase cost for the heat exchanger employed as lean/rich heat exchanger in this work is lower than some other studies (Karimi et al., 2011; Kallevik, 2010; Aromada & Øi, 2017; Aromada et al. 2020a; Aromada et al., 2021). This indicates that the energy (steam) cost dominated in this work. Aromada et al. (2020a) and Aromada et al. (2021) estimated the cost optimum ΔT_{min} with shell and tube heat exchangers to be 15°C. However, in Aromada et al. (2020a), a cost optimum ΔT_{min} of 5°C was estimated when the type of heat exchanger was changed to plate heat exchanger. This revealed that the cost optimum ΔT_{min} depends on the process and the economic assumptions, especially the cost of the heat exchanger and the cost of steam.

Changing the capture rate to 87.5 % and 90 % increased the CO_2 capture cost from €65/tCO_2 to €70/tCO_2 and €85/tCO_2 respectively. And by this, increasing the capture rate by increasing solvent circulation rate has the highest impact on the CO_2 capture (Figure 3). Therefore, it is worth to look at finding a more economical way to capture more CO_2, that is more than 85 % at a lower cost. This is done in the subsequent section.

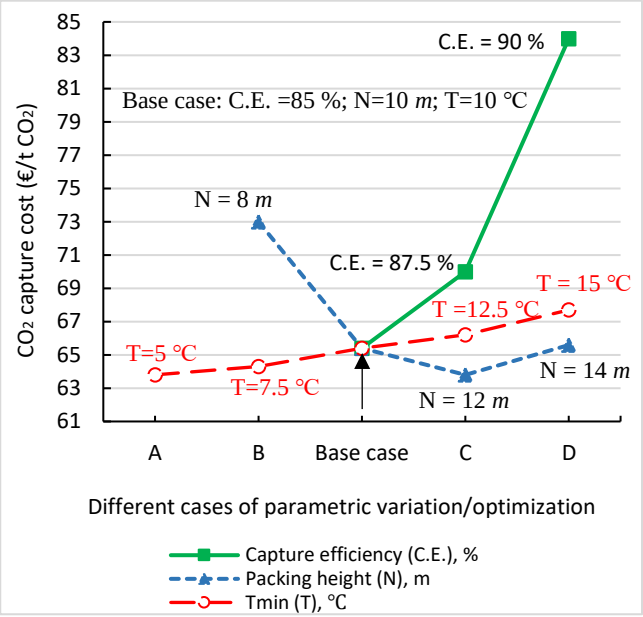

Figure 4. Impacts of different process parameters or factors on CO_2 capture cost

3.4 Different Routes of Capturing More CO_2

The results of the second objective of this work are presented in Figure 5. That is to find out a more economical way to capture more than 85 % of CO_2 from industry's flue gas. The two routes for increasing the capture efficiency from 85 % to 90 % and above are by increasing the solvent flow rate and by increasing the absorber packing height.

When the CO_2 capture rate was increase to 87.5 % and 90 %, the new route (route 2) compared to Figure 3, resulted in reduction of €5/tCO_2 and €17/tCO_2 respectively in CO_2 capture cost. These are 7 % and 20 % reduction respectively. They are significant numbers. According to this work, the cost efficient route to capture more CO_2 is not by merely increasing the solvent flow, but by increasing the absorber packing height. When solvent flow is increased, more CO_2 is captured but at a high steam cost. High steam need requires larger effective heat exchange area in the reboiler (more units). The capital cost of the heat exchanger network to meet the heat exchange area requirement also increases when the solvent flow increases.

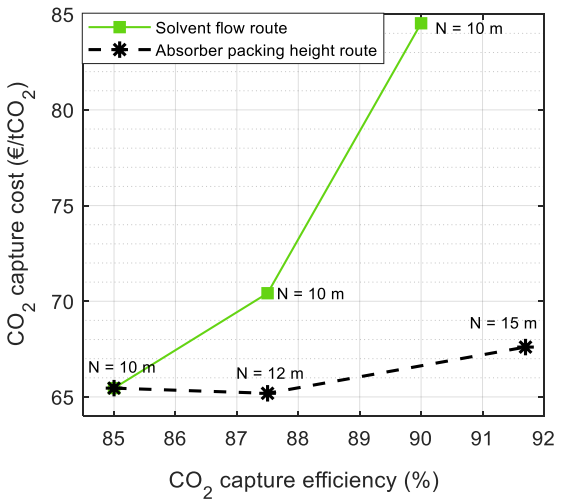

Figure 5. Economic implications of two different routes to increase the CO_2 capture rate above 85%

For route (2), increasing the absorber packing height effectively led to both less solvent flow due to increase in retention (CO_2 and solvent contact) time, relatively smaller heat exchange area, and significantly less desorption steam requirement. In route (2), the minimum CO_2 capture cost (in €/tCO_2) is not 85% as in route (1) but 87.5%.

There is no literature to compare the results with, however, further studies will find the results very useful, especially in reducing the cost of capturing when 90 % and more CO_2 capture is needed.

3.5 Estimated Capital and Operating Costs

The capital and operating costs that are used for all the trade-off analyses to obtain the cost optimum parameters as well as for capturing 90 % of CO_2 and above are shown in Figure 6 and Figure 7 respectively. The treated exhaust gas is from 400 MWe NGCC power plant, and the compression section was not included. The capital cost here is only the total plant cost (TPC).

A look at Figures 6 and Figure 7 shows that the case of 90 % route (1), which is through increase of solvent flow has the highest capital cost and the highest operating cost. The high capital cost is mainly due to the increase in the reboiler heat transfer area to meet the substantial (39 %) increase in the steam needed for desorption.

The cost implication of increasing the heat transfer area of the lean/rich exchanger using shell and tube heat exchangers is also usually relatively large (Karimi et al., 2011; Aromada et al., 2020a). The lowest capital cost was obtained by the case of the cost optimum packing height and the minimum annual operating cost was obtained by the case of the cost optimum temperature difference. The 92 % route (2) has a reduced operating cost compared to 90 % route (1) due to the decrease in the steam requirement. The high capital cost in the 92 % route (2) case is a result of increase in the absorber packing height from 10 *m* to 15 *m*.

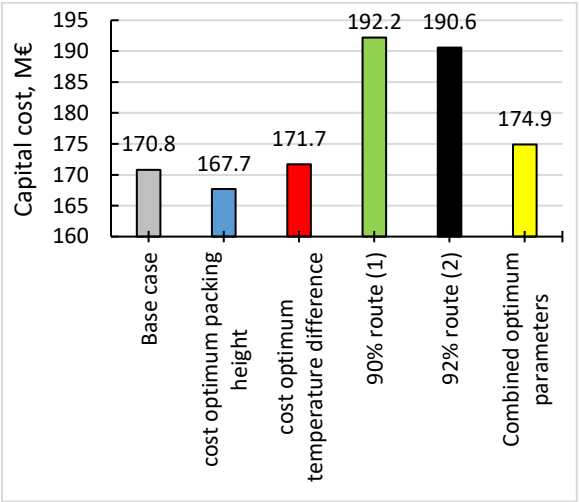

Figure 6. Capital cost estimates of the different cases

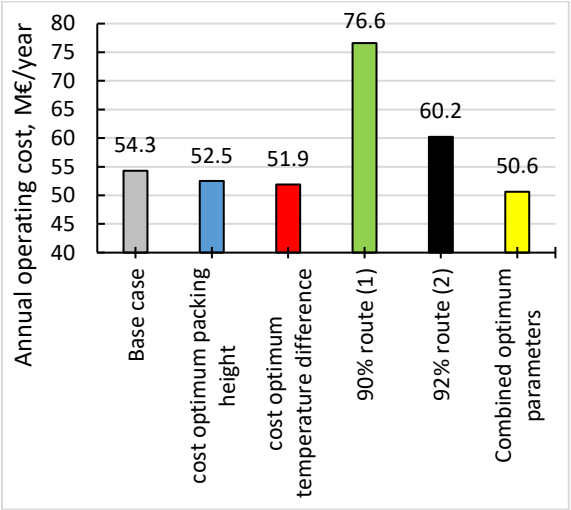

Figure 7. Capital cost estimates of the different cases

The combined effects of the two cost optimum parameters for the 85 % CO_2 capture process on the capital and operating cost were also evaluated and are shown in Figure 6 and Figure 7. The capital cost of the combined optimum parameters' case is higher than that of the base case and the two individual cost optimum parameters cases. However, it achieved the lowest annual operating cost.

Table 3. Summary of results

	Base case	cost optimum packing height	cost optimum temperature difference	90% route (1)	92% route (2)	Combined optimum parameters
Capital cost (TPC) (million €)	170.8	167.7	171.7	192.2	190.6	174.9
Annualized capital cost (million €)	16.8	16.5	16.8	18.9	18.7	17.2
Annual operating cost (million €)	54.3	52.5	51.9	76.6	60.2	50.8
Total annual cost (million €)	71.1	69.0	68.7	95.5	78.9	67.9
CO_2 capture cost (€/tCO_2)	65.4	63.9	63.8	84.5	67.3	62.9
Specific reboiler heat (GJ/tCO_2)	3.77	3.50	3.41	5.24	3.55	3.33
Annual cost savings (%)	-	-2	-2	29	3	-4
Energy savings (%)	-	-7	-10	39	-6	-12

3.6 Summary of Analyses

The results of the simulations and economic analyses of all the important cases are summarized in Table 3. The percentage of annual cost savings and the savings in desorption steam requirements are also shown. Negative percentage values indicate savings compared to the base case, while positive percentage values signify more expensive cases.

4 Conclusion

A study of the impact of different process optimization parameters or factors in a standard amine based CO_2 Capture process on the capture cost was conducted through process simulation and cost estimation. The study was carried out to reveal the most important influential factor on CO_2 capture cost, which led to investigating two routes of capturing more than 85% of CO_2 from an industry flue gas.

The most influential factor was found to be the CO_2 capture efficiency. To increase CO_2 removal rate above 85% without increasing the absorber packing height will result in drastic increase in the amount of steam needed for desorption, and a significant increase in the cost of the main heat exchanger if the shell and tube heat exchangers are used. These will in turn result in a drastic increase in capture cost. The cost efficient route to capture more than 85% of CO_2 is by increasing the packing height of the absorber to increase the contact time between CO_2 and the solvent.

The cost optimum number of stages of absorber packing height when the CO_2 removal efficiency and temperature difference in the main heat exchanger were kept constant at 85% and 10°C respectively is 12 *m* (12 stages). The cost optimum temperature in the lean/rich heat exchanger when other base case's parameters were kept constant is 5°C.

An 85% CO_2 capture case with combination of the cost optimum parameters achieved a 12% reduction in the amount of steam needed for desorption. That resulted in a 4% decrease in the base case CO_2 capture cost. These emphasizes the importance of performing cost optimization of CO_2 capture process.

References

H. Ali, N.H. Eldrup, F. Normann, R. Skagestad, and L. E. Øi. Cost Estimation of CO_2 Absorption Plants for CO_2 Mitigation–Method and Assumptions. *International Journal of Greenhouse Gas Control*, 88, 10-23, 2019. doi: 10.1016/j.ijggc.2019.05.028.

S. A. Aromada, N. H. Eldrup and L. E. Øi. Capital Cost Estimation of CO_2 Capture Plant using Enhanced Detailed Factor (EDF) Method: Installation Factors and Plant Construction Characteristic Factors. *International Journal of Greenhouse Gas Control*, 1 10, 103394, 2021.

S. A. Aromada, N. H. Eldrup, F. Normann and L. E. Øi. Techno-Economic Assessment of Different Heat Exchangers for CO_2 Capture. *Energies*, 13(23), 6315, 2020b. https://doi.org/10.3390/en13236315

S. A. Aromada and L. E. Øi. Simulation of Improved Absorption Configurations for CO_2 Capture. In Proceedings of the 56th Conference on Simulation and Modelling (SIMS 56), October, 7-9, 2015, Linköping University, Sweden. Linköping Electronic Conference Proceedings, 119(2), 21-29, 2015. http://dx.doi.org/10.3384/ecp1511921

S. A. Aromada and L. E. Øi. Energy and Economic Analysis of Improved Absorption Configurations for CO_2 Capture. *Energy Procedia*, 114: 1342-1351, 2017. doi: 10.1016/j.egypro.2017.03.1900

S. A. Aromada, N. H. Eldrup, F. Normann and L. E. Øi. Simulation and Cost Optimization of different Heat Exchangers for CO_2 Capture. Proceedings of The 61st SIMS Conference on Simulation and Modelling SIMS 2020, September 22-24, Virtual Conference, Finland. Linköping Electronic Conference Proceedings, 176(45), 318-325, 2020a. https://doi.org/10.3384/ecp20176318

L. Brickett. Carbon Dioxide Capture Handbook. National Energy Technology Laboratory. 2015. Available on: www.netl.doe.gov (Accessed on 10.11.2020)

Y. Hu, Y. Gao, Y., H. Lv, G. Xu, S. Dong. A new integration system for natural gas combined cycle power plants with CO_2 capture and heat supply. *Energies*, 11(11), 3055, 2018.

IEAGHG. Deployment of CCS in the cement industry. Cheltenham, UK. 2013.

IEAGHG R&D Programme, 2008. CO_2 capture in the cement industry. Cheltenham, UK. 2008/3.

O. B. Kallevik. Cost estimation of CO_2 removal in HYSYS. Master's thesis. Høgskolen i Telemark, 2010.

M. Karimi, M. Hillestad, and H. F. Svendsen. Capital costs and energy considerations of different alternative stripper configurations for post combustion CO_2 capture. *Chemical Engineering Research and Design*, 89(8), 1229–1236, 2011.

K. Li, W. Leigh, P. Feron, H. Yu and M. Tade. Systematic study of aqueous monoethanolamine (MEA)-based CO_2 capture process: Techno-economic assessment of the MEA process and its improvements. *Applied Energy*, 165, 648-659, 2016.

C. Nwaoha, M. Beaulieu, P. Tontiwachwuthikul, M. D. Gibson, M. D. Techno-economic analysis of CO2 capture from a 1.2 million MTPA cement plant using AMP-PZ-MEA blend. *International Journal of Greenhouse Gas Control*, 78, 400-412, 2018.

S. Orangi, F. F. Madan, K. G. Fajferek, N. T. Sæter, S. Bahri. Process simulation and cost estimation of CO_2 capture in Aspen HYSYS using different estimation methods. Master's Group Project Report, University of South-Eastern Norway, Porsgrunn. 2020.

M. O. Schach, R. Schneider, H. Schramm and J. U. Repke, J. U. Techno-economic analysis of postcombustion processes for the capture of carbon dioxide from power plant flue gas. *Industrial & Engineering Chemistry Research*, 49(5), 2363-2370, 2010.

T. E. Thorsen. Therefore, this is a big day for Grenland-LEADER: The government's "yes" to the capture and storage of CO_2 in Brevik is big. Varden. 2020, September 21. Available online: https://www.varden.no/meninger/derfor-erdette-en-stor-dag-for-grenland/ (Accessed: 03.04.2021).

L.E. Øi, N. Eldrup, S. Aromada, A. Haukås, J. HelvigIda Hæstad, & A. M. Lande. Process Simulation, Cost Estimation and Optimization of CO_2 Capture using Aspen HYSYS. In Proceedings of The 61st SIMS Conference on Simulation and Modelling SIMS 2020, September 22-24, Virtual Conference, Finland. Linköping Electronic Conference Proceedings 176:46, 326-331, 2020. https://doi.org/10.3384/ecp20176326

L. E. Øi, T. Bråthen, C. Berg, S. K. Brekne, M. Flatin, R., Johnsen, I. G. Moen, & E. Thomassen. Optimization of configurations for amine based CO_2 absorption using Aspen HYSYS. *Energy Procedia*, 51:224-233, 2014. doi:10.1016/j.egypro.2014.07.026.

L. E. Øi. Removal of CO_2 from Exhaust Gas. Ph.D. Thesis, Department of Process, Energy and Environmental Technology, Telemark University College, Porsgrunn, Norway, 2012.

L. E. Øi. Aspen HYSYS simulation of CO_2 removal by amine absorption from a gas based power plant. In The 48th Scandinavian Conference on Simulation and Modeling (SIMS 2007); 30-31 October; 2007; Göteborg. Linköping Electronic Conference Proceedings 27 (8), 73-81, 2007. http://www.ep.liu.se/ecp_article/index.en.aspx?issue=027;article=008

Simulation and economic analysis of MEA+PZ and MDEA+MEA blends in post-combustion CO_2 capture plant

Sina Orangi [1*], Solomon Aforkoghene Aromada [1], Neda Razi [2], Lars Erik Øi [1]

[1] Department of Process, Energy and Environmental Technology, University of South-Eastern, Norway,
[2]Safezak AS, Asker, Norway,
*sina.orangi@gmail.com
Solomon.A.Aromada@usn.no, Lars.Oi@usn.no, neda11365@yahoo.com

Abstract

The energy requirement of the amine based CO_2 capture process is the main drawback of the technology. Studies on energy demand reduction are therefore important. This work presents energy optimization and economic analysis of an 85% CO_2 capture process using pure monoethanolamine (MEA), and processes with blends of methyl diethanolamine (MDEA) and piperazine (PZ). The process with 30 wt% MEA was the base (reference) case in this study. The regeneration energy requirement for the base case was 3.77 / . The blends of (30 wt% MEA+5 wt% PZ) and (30 wt% MEA+15 wt% MDEA) were calculated to achieve 4.9% and 7.5% reduction in regeneration energy respectively. The economic analysis also indicated that 4.1% and 4.3% total annual cost savings can be achieved by the MEA+PZ and MEA+MDEA blends processes respectively. The work further shows that the cyclic capacity is enhanced by using these blends instead of pure MEA.

Keywords: CO_2 capture, simulation, energy-optimal, cost estimation, solvent, blend, regeneration energy, economy.

1 Introduction

Our planet has been faced with rising atmospheric concentration of greenhouse gases like carbon dioxide, methane, nitrous oxide and chlorofluorocarbons especially in recent decades. According to the Intergovernmental Panel on Climate Changes (IPCC), more than 50% of this increase results from CO_2 emissions (Abu-Zahra et al., 2007). Although the post combustion amine-based process requires huge amount of energy especially for regenerating amine, the mentioned process is the most mature method to highly cut down CO_2 emissions from flue gas exiting from plants or industries (Zang et al., 2017), mainly from combustion of fossil fuels such as coal, oil and gas in power plants.

Applying 30 wt% monoethanolamine (MEA) is regarded as the reference solvent for CO_2 capture at atmospheric pressure (Øi, 2010; Rochelle et al., 2011). A sketch of this process is presented in Figure 1. The whole or a part of the flue gas is conveyed to the bottom of an absorption column where amine solvent comes into the absorber from the top. The two inlet streams flow counter-currently in the absorption column. As they come in contact, a chemical reaction is initiated where the CO_2 in the flue gas is absorbed by the amine solvent. This solution leaves the absorber, and it is pumped to the stripper where the CO_2-rich amine solution is regenerated by heat supply from steam (endothermic reaction). The regenerated amine is pumped back into the absorption column for subsequent cycle of CO_2 absorption-desorption. Other main plant items such as heat exchangers, pumps in different parts of process are used to form the whole cycle.

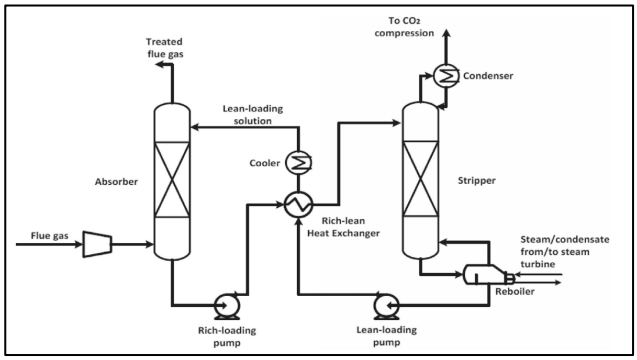

Figure 1. Standard or conventional CO_2 capture process (Hosseini-Ardali et al., 2020)

MEA is classified among the primary solvent group which has high reactivity with CO_2, but this amine requires a high heat of regeneration. This problem is the most outstanding one for MEA solvent. (Lee et al., 2013) claimed that using MEA as solvent could lead to up to a 30% reduction in the overall efficiency of the power plant and a corresponding 80% increase to the cost of electricity. Various experiments and simulations have been conducted to reduce the energy requirement (Abu-Zahra et al., 2007; Hosseini-Ardali et al., 2020; Le et al., 2013; Nwaoha et al., 2017). Such reduction in the needed regeneration heat could be achieved through three general approaches, which include (Dubois & Thomas, 2018):

- Improved absorption configurations, that is flowsheet modifications, for example, lean vapour recompression configuration (Aromada & Øi, 2015; Cousins et al., 2011),
- Optimization of operational conditions e.g., pressure and temperature of absorber and stripper columns (Abu-Zahra et al., 2007),
- Switching from the reference monoethanolamine (MEA) to other solvents e.g., methyl diethanolamine (MDEA), piperazine (PZ) or their blends.

This work focuses on the third strategy. MDEA, a tertiary solvent, was favored in recent years due to advantages like low corrosion, high loading capacity, resistance to thermal and oxidative degradation and lower heat of regeneration than MEA and some other solvents (Mudhasakul et al., 2013). Nevertheless, there a major disadvantage of low reaction rate with CO_2. Piperazine (PZ) is known as a cyclic secondary amine, having a rapid reaction rate with CO_2. PZ is highly resistant to oxidative and thermal degradation (up to 150). This amine is used as additive to other amines (Borhani & Wang, 2019). A complete study of advantages and disadvantages of the different amines is found in (Borhani & Wang, 2019). The main concept of blending different amines is to combine the favorable characteristics of different solvents to overcome their various shortcomings. A careful selection of amine concentrations in a blend requires considering various parameters because each solvent has a distinctive chemical structure with different properties from other ones. This is why finding an optimal concentration of blends to bring more benefits to the removal process is important but demanding. This matter is an interest of various studies.

In this work, firstly, a standard base case where 30 wt% MEA is selected as solvent will be introduced. This case is specified as the reference case for comparison with other simulated cases where other solvents or blends are used. Those ranges of MDEA and PZ which can be added to the base case (30% MEA) to present MEA+PZ and MEA+MDEA blends with lower regeneration energy have been assessed. Moreover, an optimization in suggested ranges which results in lowest regeneration energy compared to base case is presented. The work proceeded with a cost estimation of the CO_2 capture plant for simulated cases in order to investigate the cost savings' potential due to switching from MEA to the mentioned solvents or blends.

Since implementing other solvents/blends directly affects the lean, rich and cyclic loading parameters in the process, they will be investigated in this work.

Various studies have been performed to study various concentrations of solvents and/or their blends in CO_2 capture processes. Some other works have attempted to study the economic implication of selecting different solvent blends. Finding a work where energy-optimal concentrations of solvents/blends with the economic analysis of the total plant is a rarity. In this work, besides finding energy-optimal concentrations of amine-blends, the cost estimation for each solvent or blend is performed to investigate the economy of plant. This is because an energy-optimal amine solvent or blend may not necessarily give economically optimal process. The economic analysis of this work covers the whole lifetime of the plant.

2 Process simulation program and specifications

2.1 Process simulation program

All simulations in this work have been conducted with Aspen HYSYS version 10, which is a commercial process simulation program from AspenTech. The program has several property packages so that each one implies a specific equilibrium model. Acid gas chemical solvents is used in this work because this package supports a wide range of solvents and their blends.

Absorption and desorption columns in the standard process are the key items. These columns can be simulated with equilibrium stages including a stage efficiency (Øi et al., 2017). In this work, the efficiency of stages for CO_2 is assumed to be 0.25 in the absorption column. This parameter in the desorption column is presumed to be 1.0.

2.2 Specifications to conventional CO_2 capture process

The depicted process in Figure 1 is known as standard or conventional CO_2 absorption and desorption process. The process specifications in this work are given in Table 1, which are similar to ones in (Øi et al., 2017).

Table 1. Specifications for the conventional CO_2 capture process for 85% removal efficiency using 30 wt% MEA

Parameter	Value (Unit)
Inlet flue gas temperature to process	40 (℃)
Inlet flue gas pressure to process	101 (kPa)
Inlet flue gas flow rate	1.091e5 ($kgmol/h$)
CO_2 content in inlet gas	3.30 ($mol\%$)
Water content in inlet gas	6.90 ($mol\%$)
Nitrogen in inlet gas	89.8 ($mol\%$)
Lean amine temperature before and after pump	120 (℃)
Amine pressure before rich pump	200 (kPa)
Amine pressure after rich pump	300 (kPa)
Lean amine pressure to absorber	101 (kPa)
Lean amine rate to absorber	1.175e5 ($kgmol/h$)

CO_2 content in lean amine	2.98 $(mole\%)$
Number of stages in absorber	10 (-)
Rich amine pressure before pump	110 (kPa)
Rich amine pressure after pump	200 (kPa)
Number of stages of stripper	6 (-)
Reboiler temperature	120 (°C)
Efficiency of stages in absorber	0.25 (-)
Efficiency of stages in stripper	1.0 (-)

Minimum approach temperature in the lean rich heat exchanger is kept 10°C. Figure 2 represents a simulated standard process in Aspen HYSYS.

material to satisfy the requirements of each item. In addition, dimensioning shapes initial data for cost estimation.

Equipment cost could be obtained by different methods. The most reliable source is to obtain them from manufacturers. Though, in many cases, it is difficult to have access to such data (Ali et al., 2019). The use of commercial databases like Aspen In-Plant Cost Estimator is practical. The equipment cost data in this work were obtained from Aspen In-Plant Cost Estimator version 10, where the cost year is 2016. Other costs including direct costs, engineering costs and administration costs are added to form total installed costs for equipment (Aromada et al., 2021).

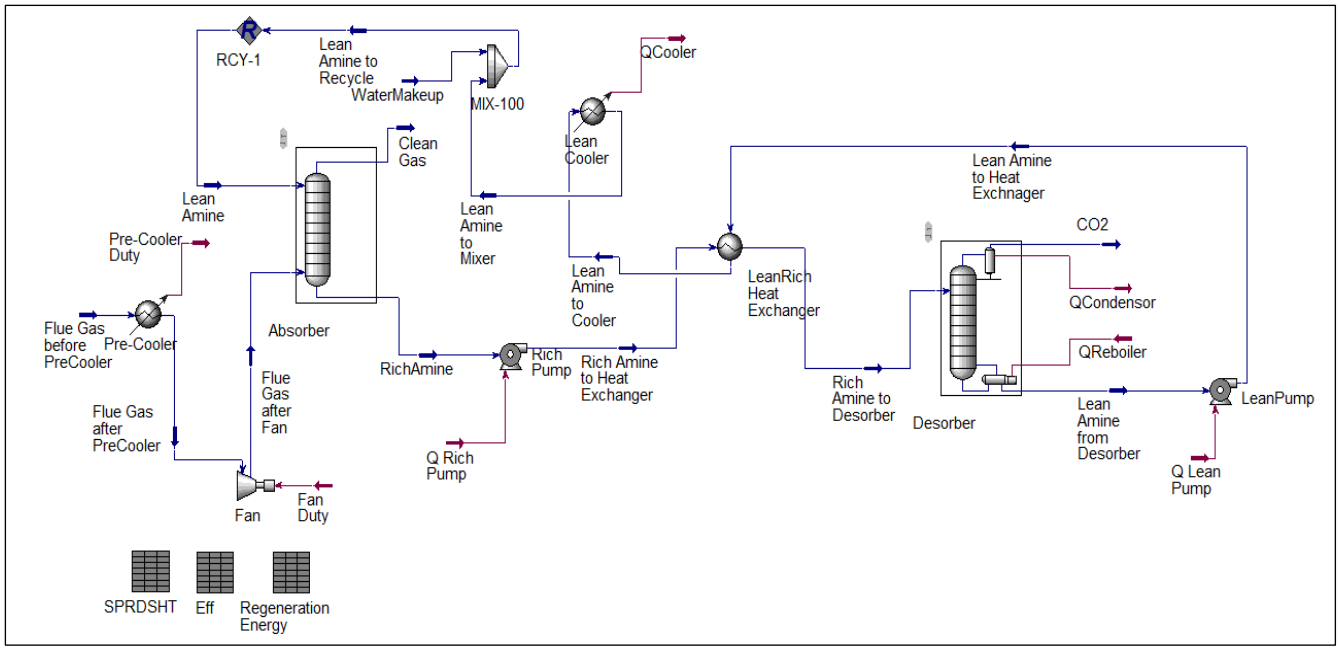

Figure 2. Aspen HYSYS flow-sheet of conventional process

2.3 Simulations with blends

As mentioned earlier, other solvents or their blends can be used in CO_2 capture process instead of MEA. In this work, both blends of MEA+MDEA and MEA+PZ are used as solvent. Various simulations with different concentrations of mentioned blends have been tested to investigate their effects on the process. Simulations with the blends have the same specifications of the standard base case listed in Table 1. Thus, there is no difference in the configuration of process with the standard base case in Figure 2. The results from simulations will be presented in the following sections.

3 Dimensioning and cost estimation

The main objective of dimensioning is to specify proper equipment to the capture plant. These items should be proper in different parameters especially size and

The total capital expenditure (CAPEX) for the CO_2 capture plant is the sum of all the equipment installed cost. In addition to CAPEX, operating expenditures (OPEX) were also estimated. In this work, OPEX comprises only the cost of electricity, cooling water, steam, solvents and maintenance. Other items for OPEX calculation like labour and supervision costs, insurance and direct overheads are not included in this work. Because the main objective of current work is to study possible cost saving of other solvents or their mixtures relative to pure MEA process.

3.1 Assumptions for dimensioning

Dimensioning was implemented for each piece of equipment used in the carbon dioxide removal plant. Calculation of the diameter for the absorption column is done by assumption of gas velocity to be 2.5 m/s. Gas velocity for the desorption column is assumed to be 1.0

m/s (Øi et al., 2017). The tangent-to-tangent height of the columns are calculated based on the required space for the structured packings and washing sections. Flooding phenomenon must be included in dimensioning for both columns. In this work, 22 meters and 10 meters are assumed as the tangent-to-tangent heights of the absorber and the stripper respectively.

Heat exchangers are sized based on the required heat transfer area. The Logarithmic Mean Temperature Difference (LMTD) and duties for each heat exchanger are extracted from the simulation results. In this work, the overall heat transfer coefficients are assumed to be 500 $W/(m^2K)$ for the lean rich heat exchanger, 800 $W/(m^2K)$ for the reboiler and the lean amine cooler, and 1000 $W/(m^2K)$ for the condenser (Ali et al., 2019; Aromada et al., 2020). All the heat exchangers in this work are assumed to be shell and tube type. More possibilities for other types of heat exchangers can be found in (Aromada et al., 2020).

In the plant, pumps are responsible for conveying the rich and lean amine flows. Volumetric flow rates of the lean and rich streams determine the required power for pumps. In this work, centrifugal pumps with adiabatic efficiency of 75% are assumed (Øi et al., 2017; Aromada et al., 2020). The fan is assumed to be a sort of centrifugal one with adiabatic efficiency of 75% (Aromada et al., 2020).

Stainless steel (SS316) is selected for almost all items except for the fan, which is assumed to be carbon steel (CS). The main reason for selecting SS316 material is resistance to corrosion (Ali et al., 2019).

Using other solvents, especially piperazine might bring some benefits to the capturing process in terms of material selection instead of pure MEA. For instance, (Rochelle et al., 2019) indicated that if PZ solvent selected for a CO_2 absorption plant, there is a possibility for specifying cheaper carbon steel for the stripper. Moreover, (Rochelle et al., 2011) evaluated positive effects of piperazine solvent like more resistant to degradation and volatility compared to pure MEA.

3.2 Assumptions for cost estimation

Although there are various works in which cost estimations for carbon dioxide removal plants have been estimated, considerable differences can be found in literature which results from applying different methods, assumptions and scope of study.

In this work, adjusting equipment costs in CAPEX calculation to total installed costs was conducted with the Enhanced Detailed Factor (EDF) method (Ali et al., 2019; Aromada et al., 2020; Aromada et al., 2021). This method is briefly explained in the following section.

Equipment cost data were obtained directly from Aspen In-Plant Cost Estimator version 10 with cost year of 2016, while current work is in 2021. This adjustment was implemented using the Chemical Engineering Plant Cost Index (CEPCI) where:

$$Cost_{\,2021} = Cost_{2016} \times \frac{CEPCI_{2021}}{CEPCI_{2016}} \quad (1)$$

The cost indices for 2016 and 2021 are 542 and 655 respectively (Chemical Engineering Essentials for the CPi Professional. 2021).

The total lifetime for the plant is assumed to be 20 years. Since the value of money during this time is not constant, interest rate is implemented into the CAPEX calculation to update the value of money for each time slot. Time slot in this work is assumed to be one year with the interest rate of 7.5% (Aromada et al., 2020). Total annual hours of operation for the plant in this work is presumed to be 8000 $hours/year$ (Øi et al., 2017; Ali et al., 2019; Aromada et al., 2020). Maintenance costs of this work is 4% of total CAPEX.

Other important item in the plant is the cost of solvents. Table 2 below provides the prices for the selected solvents in current study. While the unit prices of the utilities in the plant are provided in Table 3.

Table 2. Prices for applied amines in this work (Gomes et al., 2015)

Amine	Value (€/$litre$)
MEA	30.50
PZ	68.70
MDEA	51.60

Table 3. Prices for applied utilities in the plant (Aromada et al., 2020)

Utility	Value ($unit$)
Electricity	0.132 [€/kWh]
Steam	0.032 [€/kWh]
Cooling water	0.022 [€/m^3]

3.3 Cost estimation method

In the EDF method, each piece of equipment has its distinct installation factor based on its costs. These installation factors are prepared in for equipment in carbon steel. Therefore, since almost all the equipment in the plant is constructed from SS316. To use the EDF installation factor list (Aromada et al, 2021), the cost of equipment in SS has to be converted to their corresponding cost in CS using the EDF material factors provided in Table 4 as follows:

$$F_{total,SS} = F_{total,CS} + ([f_{mat} - 1].[f_{equipment} + f_{piping}]) \quad (2)$$

where, $F_{total,SS}$ is the total cost factor of stainless steel. $F_{total,CS}$ is the total installation factor of the equipment in carbon steel, f_{mat} is the material factor, $f_{equipment}$ and f_{piping} refer to the equipment and piping installation factors respectively.

Table 4. EDF method material factors

Sort of material	Material factor
Stainless steel (SS316) welded	1.75
Stainless steel (SS316) machined	1.30
Glass-reinforced plastic	1.00
Exotic materials	

The CAPEX is the sum of total installed cost for each piece of equipment in the plant. To estimate the total annual cost, the CAPEX was annualized and the first year OPEX was estimated. The annualized factor and annualized CAPEX are estimated using equation (3) and (4) respectively.

$$Annualized\ factor = \sum_{1}^{n} \frac{1}{(1+i)^n} \qquad (3)$$

where, i is the interest rate and n is plant lifetime.

$$Annualized\ CAPEX = \frac{CAPEX}{Annualized\ factor} \qquad (4)$$

4 Results and discussion

4.1 Results for energy consumptions

According to analysis of the simulated standard base case, this process requires 3.77 / . (Nwaoha et al., 2017) investigated various literature where they applied 30 wt% MEA solvent. The required regeneration energy is 3.3 to 4.4 / which validates the result of this work. Regeneration energy has been assessed for other simulations with 30 wt% MEA and blending with different amounts of piperazine, ranging from 5 wt% to 15 wt% as presented in Figure 3. From the results obtained in this work, 5 – 10 wt% PZ as additive to 30 wt% MEA reduces required regeneration energy in the CO_2 capture process. The solvent blend of 30 wt% MEA+5 wt% PZ gave the energy optimum specific reboiler heat consumption of 3.59 / . This is a 4.9% reduction compared to the standard base case. Different concentrations of PZ in MEA are presented in Figure 3.

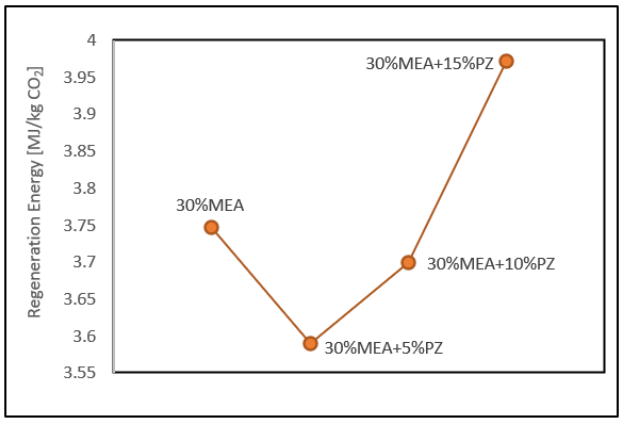

Figure 3. Assessment of adding different concentrations of piperazine to MEA in term of regeneration energy

Similar work has been performed for blends of MEA+MDEA. Among the results of the simulations performed with the blends of 30 wt% MEA and different concentrations of MDEA as additive, a range of 5 to 25 wt% MDEA presents lower regeneration energy than the reference pure MEA process as can be seen in Figure 4. The energy optimum blend of MEA+MDEA was found to be a blend of 30 wt% MEA+15 wt% MDEA. This optimum value is 3.49 / , which is 7.5% saving in regeneration energy compared to the standard base case.

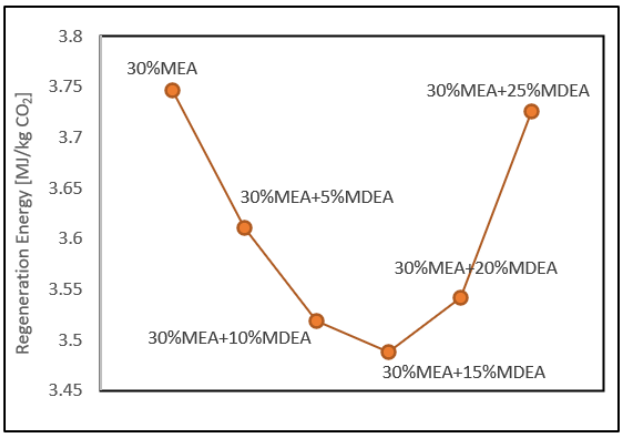

Figure 4. Assessment of adding different concentrations of MDEA to MEA in term of regeneration energy

Thus, both blends of (30 wt% MEA+5 wt% PZ) and (30 wt% MEA+15 wt% MDEA) have potential for lower regeneration energy based on the simulations results.

(Mudhasakul et al., 2013) simulated the effect of adding different concentrations of piperazine through a physical property package of acid gas removal unit into Aspen Plus. Their work clearly shows that 4 wt% to 5 wt% piperazine as additive has the best trade-off between CO_2 recovery and energy consumption. In addition, (Abd & Naji,, 2020) with a steady state simulation in the Aspen HYSYS program has

determined that the effects of adding various concentrations of piperazine up to 10 wt% with maintaining the constancy of the entire amine strength of 45 wt%. Their results indicate that 5 wt% piperazine provides the best consequence in terms of energy.

(Idem et al., 2006) experimented 4:1 molar ratio of MEA+MDEA blend in a pilot plant and their results emphasized a huge heat-duty reduction relative to the pure MEA process. (Li & Wang., 2013) also experimented different concentrations of MEA+MDEA blend in an amine scrubber. Their work showed a 2:1 weight portion of MEA+MDEA can reduce the regeneration energy by 22%.

4.2 Results for cost estimations

Cost estimation of the standard base case has been performed based on the EDF method. Cost estimation for suggested blends has also been performed to investigate whether they can bring cost saving to the plant.

The CAPEX for the standard base case process is 122.3 million euros for a lifetime based on calculations for the year 2016. Adjusting this value to year 2021 results in 147.9 million euros. The annualized CAPEX for this case is calculated to 14.5 million euros per year. The distribution of CAPEX for the standard base case is presented in Figure 5. The annual OPEX distribution is given in Figure 6.

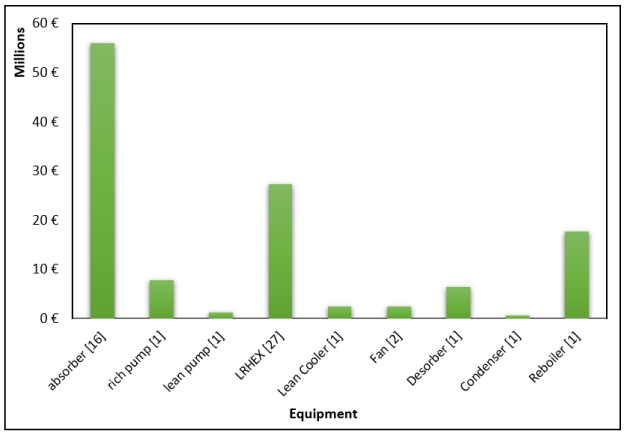

Figure 5. Distribution of the CAPEX for the standard base case plant. (Value in [] indicates the number of that particular item applied in the process)

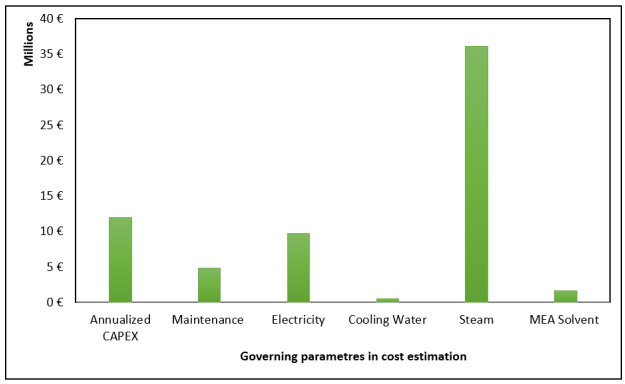

Figure 6. Distribution of governing parameters in total economy of plant for the standard base case

Total annual cost for the standard base case is calculated to be 78.6 million euros. From Figure 6, it is obvious that steam has the highest share of the annual costs of the capture process. This is more than 55% of the total cost per year. Amine-based solvent capture processes are regarded as energy-intensive and any reduction in regeneration energy might bring cost savings.

Although MEA is the least expensive solvent compared to MDEA and piperazine, the economic analysis of the capture processes with the two suggested blends in Section 4.1 resulted in saving in annual costs. The blend of (30 wt% MEA+5 wt% PZ) yields a 4.1% cost saving per year. A 4.3 % cost savings per year for the blend of (30 wt% MEA+15 wt% MDEA) was estimated. The economic analysis of the carbon capture process for the two blends is presented in Figure 7 as well as for the standard base case.

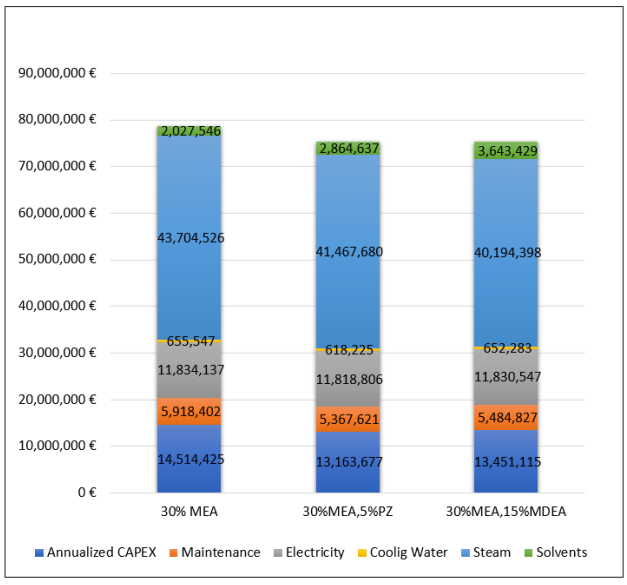

Figure 7. Economy analysis of CO_2 removal process for three different solvents/blends

4.3 Results for lean, rich and cyclic loadings

The lean and rich loading are defined as,

$$\alpha = \frac{n_{CO_2}}{n_{amine}} \quad (5)$$

where, lean and rich amines have been shown in Figure 2. The difference between the lean and rich loadings is referred to as the cyclic loading,

$$\alpha_{cyclic} = \alpha_{rich} - \alpha_{lean} \quad (6)$$

Achieving higher amount of cyclic capacity is highly desirable thanks to its improvements in the regeneration energy. (Nwaoha et al., 2017) asserts that an ideal solvent or blend requires to have a higher cyclic loading. The cyclic capacities of the different concentrations of MEA+MDEA and MEA+PZ blends have been evaluated and compared with the same concentration if only pure MEA solvent is used. The results are shown in Figure 8 and Figure 9 respectively.

Figure 8 indicates that adding MDEA to MEA enhances cyclic loading compared to the pure MEA process. It is obvious that the blend of 30 wt% MEA+ 15 wt% MDEA achieved the highest cyclic loading compared to other concentrations.

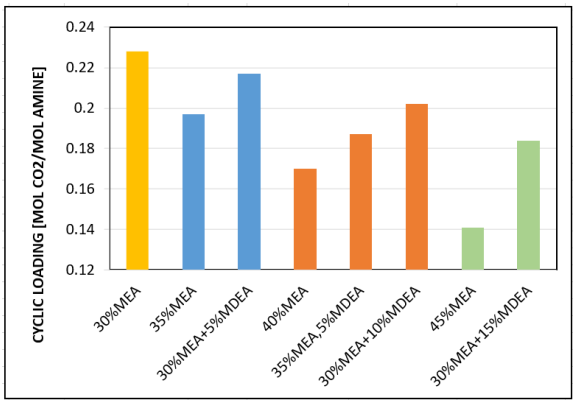

Figure 8. Assessment of cyclic loading for different concentrations of the blend of MEA+MDEA compared to the identical weight fraction of pure MEA

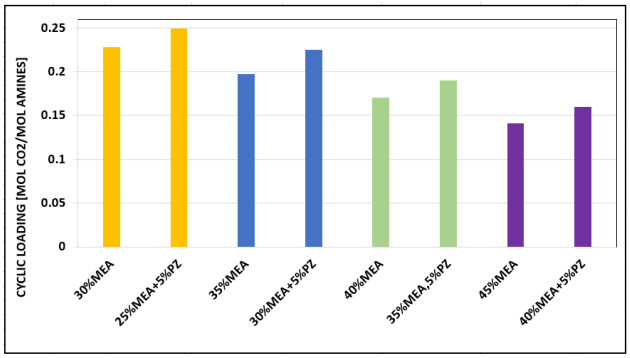

Figure 9. Assessment of cyclic loading for different concentrations of the blend of MEA+PZ compared to the identical weight fraction of pure MEA

Similar analysis was performed for the blend of MEA+PZ, resulting in Figure 9. According to the Figure 9, all concentrations of MEA+PZ blend present a larger cyclic loading than the same concentration of pure MEA, which means PZ can enhance cyclic loading in this blend.

Benefits for switching from individual MEA to other solvents or blends are not only limited to regeneration energy, but also economy of the plant and cyclic loading. Other important factors like degradation, foaming and precipitation have potential for future study. In addition, it will be reasonable to proceed the work in the future with experimental data in order to validate the results.

4.4 Uncertainties

Regarding the uncertainties in this work, Murphree efficiency could be mentioned. This factor in all simulated processes has been assumed to be equal, while each blend requires to have a specific one. This work is an option for future work. Secondly, this work has been based on vapor-liquid equilibrium model. Other models could be investigated and compared with current results.

5 Conclusion

In this work performed in Aspen HYSYS version 10, a standard CO_2 removal process has been simulated with various concentrations of individual and mixtures of MEA, MDEA and PZ solvents. It was concluded that the blend of MEA+PZ and MEA+MDEA have potential to improve the process especially in term of regeneration energy. Based on the performed simulations, two blends of (30 wt% MEA+5 wt% PZ) and (30 wt% MEA+15 wt% MDEA) present energy-optimal processes compared with other concentrations.

In addition, the cost analysis based on the EDF method for the simulated plants has been performed to investigate the effect of implementing other solvents than MEA on the economy of plant. The results indicated that both suggested blends have potential to bring considerable cost savings to the CO_2 removal process.

Acknowledgements

This work is part of a continuous development at the University of South-Eastern Norway to assess CO_2 capture processes from different views. Thank you for contributions from staff and students to this project.

References

A. A. Abd, S. Z. Naji. Comparison study of activators performance for MDEA solution of acid gases capturing from natural gas: Simulation-based on a real plant. *Environmental Technology & Innovation*, 17, 100562, 2020.

M. R. Abu-Zahra, L. H. Schneiders, LJ. P. Niederer, P. H. Feron, G. F. Versteeg. CO_2 capture from power plants: Part I. A parametric study of the technical performance

based on monoethanolamine. *International Journal of Greenhouse gas control,* 1(1), 37-46, 2007.

H. Ali, N. H. Eldrup, F. Normann, R. Skagestad, R., L. E. Øi. Cost Estimation of CO_2 Absorption Plants for CO_2 Mitigation–Method and Assumptions. *International Journal of Greenhouse Gas Control*, 88, 10-23, 2019.

S. A. Aromada, N. H. Eldrup, F. Normann, L. E. Øi. Techno-Economic Assessment of Different Heat Exchangers for CO_2 Capture. *Energies*, 13(23), 6315, 2020.

S. A. Aromada, N. H. Eldrup, L. E. Øi. Capital cost estimation of CO_2 capture plant using Enhanced Detailed Factor (EDF) method: Installation factors and plant construction characteristic factors. *International Journal of Greenhouse Gas Control*, 110, 103394, 2021.

S. A. Aromada, L. E. Øi. Simulation of improved absorption configurations for CO_2 capture. In Proceedings of the 56th Conference on Simulation and Modelling (SIMS 56), October, 7-9, 2015, Linköping University, Sweden. Linköping University Electronic Press, 119, 21-29, 2015, November. Doi: 10.3384/ecp1511921.

T. N. Borhani, M. Wang. Role of solvents in CO_2 capture processes: The review of selection and design methods. *Renewable and Sustainable Energy Reviews*, 114, 109299, 2019.

Chemical Enginnering Essentials for the CPi Professional . 2021. Available online: https://www.chemengonline.com/pci-home. Accessed: 08.02.2021.

A. Cousins, L. T. Wardhaugh, P. H. M. Feron. A survey of process flow sheet modifications for energy efficient CO_2 capture from flue gases using chemical absorption. International Journal of Greenhouse Gas Control, 5(4), 605-619, 2011. doi: **http://dx.doi.org/10.1016/j.ijggc.2011.01.002**

L. Dubois, D. Thomas. Comparison of various configurations of the absorption-regeneration process using different solvents for the post-combustion CO2 capture applied to cement plant flue gases. International Journal of Greenhouse Gas Control, 69, 20-35, 2018.

J. Gomes, S. Santos, J. Bordado. Choosing amine-based absorbents for CO_2 capture. *Environmental technology*, 36(1), 19-25, 2015.

S. M. Hosseini-Ardali, M. Hazrati-Kalbibaki, M. Fattahi, F. Lezsovits. Multi-objective optimization of post combustion CO_2 capture using methyldiethanolamine (MDEA) and piperazine (PZ) bi-solvent. *Energy*, 211, 119035, 2020.

R. M. Idem, M. Wilson, P. Tontiwachwuthikul, A. Chakma, A Veawab, A. Aroonwilas, D. Gelowitz, D. Pilot plant studies of the CO_2 capture performance of aqueous MEA and mixed MEA/MDEA solvents at the University of Regina CO_2 capture technology development plant and the boundary dam CO_2 capture demonstration plant. *Industrial & engineering chemistry research*, 45(8), 2414-2420, 2006.

B. A. Khan, A. Ullah, M. W. Saleem, A. N. Khan, M. Faiq, M. Haris. Energy Minimization in Piperazine Promoted MDEA-Based CO_2 Capture Process. *Sustainability*, 12(20), 8524, 2020.

A. S. Lee, J. C. Eslick, D. C. Miller, J. R. Kitchin. Comparisons of amine solvents for post-combustion CO_2 capture: A multi-objective analysis approach. *International Journal of Greenhouse Gas Control*, 18, 68-74, 2013.

X. Li, S. Wang, C. Chen. Experimental study of energy requirement of CO_2 desorption from rich solvent. *Energy Procedia*, 37, 1836-1843, 2013.

S. Mudhasakul, H. M. Ku, P. L. Douglas. A simulation model of a CO_2 absorption process with methyldiethanolamine solvent and piperazine as an activator. *International Journal of Greenhouse Gas Control,* 15, 134-141, 2013.

C. Nwaoha, T. Supap, R. Idem, C. Saiwan, P. Tontiwachwuthikul, M. J. AL-Marri, A. Benamor. Advancement and new perspectives of using formulated reactive amine blends for post-combustion carbon dioxide (CO_2) capture technologies. *Petroleum*, 3(1), 10-36, 2017.

G. T. Rochelle, Y. Wu, E Chen, K. Akinpelumi, K. B. Fischer, T. Gao, T, C. T. Liu, J. L. Selinger, J. L. Pilot plant demonstration of piperazine with the advanced flash stripper. *International Journal of Greenhouse Gas Control*, 84, 72-81, 2019.

G. Rochelle, E. Chen, S. Freeman, D. Van Wagener, Q Xu, A. Voice. Aqueous piperazine as the new standard for CO_2 capture technology. *Chemical engineering journal*, 171(3), 725-733, 2011.

R. Zhang, X. Zhang, Q. Yang, H. Yu, Z. Liang, X. Luo. Analysis of the reduction of energy cost by using MEA-MDEA-PZ solvent for post-combustion carbon dioxide capture (PCC). Applied Energy, 205, 1002-1011, 2017.

L. E. Øi. CO_2 removal by absorption: challenges in modelling. *Mathematical and Computer Modelling of Dynamical Systems*, 16(6), 511-533, 2010.

L. E. Øi, E. Sundbø, H. Ali. Simulation and economic optimization of vapour recompression configuration for partial CO_2 capture. *Linköping Electronic Conference Proceedings*, 298-303, 2017. Doi:10.3384/ecp171382982017.

Studying the effect of pyrolysis gas composition on the gasification syngas composition using CPFD simulation

Ahmad T. Dawod Britt M. E Moldestad Hildegunn H. Haugen Janitha C. Bandara

Department of Process, Energy and Environmental Technology, University of South-Eastern Norway, Norway,
ahmad.dawod93@hotmail.com {britt.moldestad, hildegunn.h.haugen, janitha.bandara}@usn.no

Abstract

A CPFD model for biomass gasification in a bubbling fluidized bed was developed using the Barracuda Virtual Reactor 17.4.1 commercial CFD code. Three simulation cases were performed at varying the reactor temperature and pyrolysis gas compositions. The effect of the pyrolysis step was found to be significant, especially on the production of CO, H_2, and CH_4. This is mainly because that the pyrolysis step converts 85% of the biomass weight into volatiles.

Comparing the simulation results with the experimental data showed a good agreement on predicting CH_4 and H_2, whereas CO_2 was overestimated, and CO was underestimated. This might be due to inaccuracies in the pyrolysis gas composition or high rates in the water-gas-shift reaction used in the simulation.

The effects of temperature on the synthesis gas composition were further investigated. Increasing the temperature from 800°C to 900°C, increased the concentration of CO and H_2 by 2.4% and 1.6% respectively, while decreased the concentration of CO_2 and CH_4 by 1.3% and 0.5%, respectively. The trends of gas compositions showed a good agreement with other literature data, except the trend of CH_4. This might be due to the neglect of tar composition in the volatiles.

Keywords: Pyrolysis, Biomass gasification, CPFD.

1 Introduction

Waste generation has increased greatly in the ongoing many years, and there are no signs of decline. 2.01 billion tons of municipal solid waste (MSW) is generated globally every year (Kaza *et al*., 2018). According to the World Bank estimation, the overall waste generation will increase by around 70% to 3.4 billion tons by 2050. This is due to various components, such as population growth, urbanization, economic development, and customer shopping habits (Ellis, 2018). At least 33% of the generated waste worldwide is not managed in an environmentally safe way and instead dumped or openly burned (Kaza *et al*., 2018).

Biomass resources, also known as bio-renewable resources, refer to all types of organic non-fossil materials, such as plant, animal, and waste materials (Luo & Zhou, 2012) (Alternativ Energy Tutorials, 2015). Biomass fuels are classified as environmentally friendly, and the use of biomass for energy production is on the rise. As a result, all available biomass resources are becoming increasingly important (Rosendahl, 2013).

1.1 Pyrolysis and gasification of biomass

Pyrolysis of biomass is one of the thermal treatment technologies that breaks biomass into bio-oil, solid biochar, and gases. Pyrolysis is defined as the breaking down of any solid (or liquid) hydrocarbon by heating to high temperatures in the absence of oxygen (Basu, 2013). Bio-oil from the pyrolysis is an increasing interest due to its economical storage and transportation compared to solid biomass, which can be alternative combustion fuel for power generation and transportation (Luo *et al*., 2012). Biochar has different industrial applications such as solid fuel in boilers and the production of activated carbon. Finally, the gas fraction can be used as a fuel for industrial combustion or in supplying the energy required for the pyrolysis process itself (Goyal *et al*., 2008).

Biomass gasification process, in contrast to pyrolysis, tends to maximize the gas fraction by rearranging the biomass molecular structure in the presence of a gasifying agent such as air, oxygen or steam (Rosendahl, 2013) (Basu, 2013). Biomass particles undergo a chain of conversion processes, which include drying, pyrolysis, combustion, and char gasification (Sun, 2014; Basu, 2013). The product gas mixture is called synthesis gas or syngas, which consists of CO_2, CO, CH_4, H_2, H_2O, and small amounts of heavier hydrocarbons (Monilo *et al*., 2016).

There are three types of reactors (gasifiers) used for biomass gasification: fixed or moving bed, fluidized bed, and entrained flow gasifiers. They differ mainly in their flow conditions, gas-solid contact mode, and residence time of biomass inside the reactors (Monilo *et al*., 2016; Badeau *et al*., 2009). Fluidized bed gasification reactors are characterized by effective temperature distribution and high mass and heat transfer rates compared to other reactor types (Rosendahl, 2013). The bed material (e.g., sand) inside the reactor act as a heat carrier and a mixing enhancer (Basu, 2013). The fluidized bed gasification reactors are classified into two types: bubbling fluidized beds and circulating fluidized

beds. They differ mainly in fluidized gas velocity and gas path (Gomez-Barea & Leckner, 2010).

1.2 CPFD simulations

The multiphase particle in cell (MP PIC) method is used in the Barracuda VR, which has found to be an efficient tool for the simulation of fluidized bed reactors and other gas particle processes. Barracuda VR is specialized CFD software that is commonly used for simulation and analysis of fluidized bed reactors and other gas-solid processes (CPFD, 2019). The software is competent in optimizing operational conditions, geometry, inlets and outlets, flow rates, and particle properties, where some of them is difficult to achieve with experiments (CPFD Software, 2021). This numerical approach solves the fluid phase with the Eulerian computational grid and models the solid phase with Lagrangian computational particles (Perera, 2013). A given number of particles having the same properties are expressed by parcels to minimize the computational costs (CPFD Software, 2021). The present work uses the Barracuda VR software for the simulation of the biomass gasification process.

1.3 Objectives

The overall aim was to simulate a fluidized bed gasification reactor using a computational particle fluid dynamic (CPFD) and using actual experimental data from pyrolysis as an input.

Another aim is to study the composition of the synthesis gas obtained from gasification of wood pellets and compare them with the experimental results performed at USN and conducted by Bandara (Bandara, 2021). Further, the aim is to study the effect of pyrolysis gas composition and reactor temperature on the synthesis gas composition.

2 Material and methods

The experimental works of a previous study was used for the comparison with the simulation results. The experimental method is discussed briefly, and further details were presented in previous publications (Bandara, 2021).

2.1 Experimental methods

The gasification experimental rig is a bubbling fluidized bed reactor with a fuel capacity of 20kW and is installed at the University of South-Eastern Norway. Figure 1 show a schematic diagram of the biomass gasification rig. The reactor has a diameter of 100mm and a height of 1000mm. Three electrical heaters are installed on the reactor wall which heats up the reactor during operation. The gasifying air is heated by an air heater before it flows into the reactor.

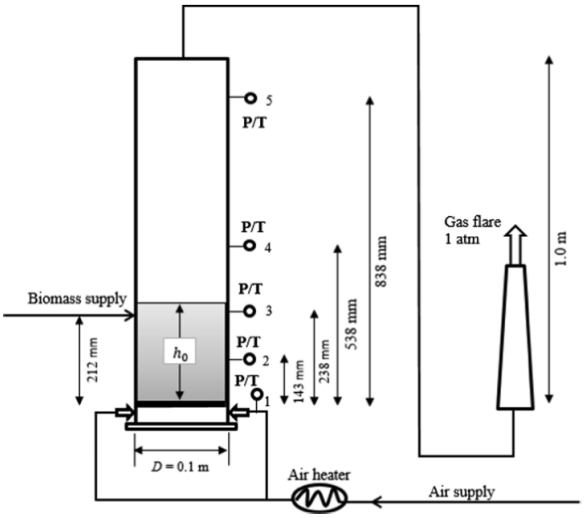

Figure 1. Schematic diagram of the biomass gasifier.

Temperature and pressure sensors are placed in different locations along the reactor height to measure the variation in pressure and temperature during the operation. The fuel is stored in a silo and supplied to the reactor using two screw conveyers. The bed material (sand) is supplied to the reactor from the funnel type opening placed at the reactor wall. A constant nitrogen flow of 0.5 L/min is maintained across the silo to avoid any gas leakages from the reactor to the silo. A sampling line is attached at the reactor outlet. A gas chromatograph (GC) SRI 8610C using helium as a carrier gas, is used to determine the gas composition fraction (O_2, N_2, CH_4, CO_2, and CO).

The experiments were carried out using wood pellets of 6 mm in diameter and 5-30 mm in length. The experiments were performed at USN and conducted by Bandara (Bandara, 2021).

2.2 CPFD methods

Computational particle fluid dynamic (CPFD) software was used to simulate the biomass gasification reactor. The Barracuda Virtual reactor (VR) version 17.4.1 software simulates multiphase hydrodynamics, heat balance, and chemical reactions of fluid-particle systems in three dimensions. The Lagrange approach is used for the particle phase, and the Eulerian approach is used for the gas phase. Pyrolysis data obtained from different studies were used as an input for the simulation.

It should be noted that the simulation was done using a square-sectioned geometry to avoid small and missing grid sections that can arise in a cylindrical-shaped geometry. According to the study done by (Bandara, 2021), at least one biomass particle should be able to fit within the cell to avoid computational errors. However, the geometry has the same cross-section area as the cylindrical geometry used in experiments.

This section discusses the simulation setup and procedure used in Barracuda software to establish the simulation model.

2.2.1 Mesh and geometry

For the simulation of biomass gasification in bubbling fluidized bed, a geometry with 8.83 cm square cross-section and 100 cm height was created using the SolidWorks software. Figure 2 shows the meshed geometry (Grid), initial bed material, dimension of the geometry, and the locations of transient data points.

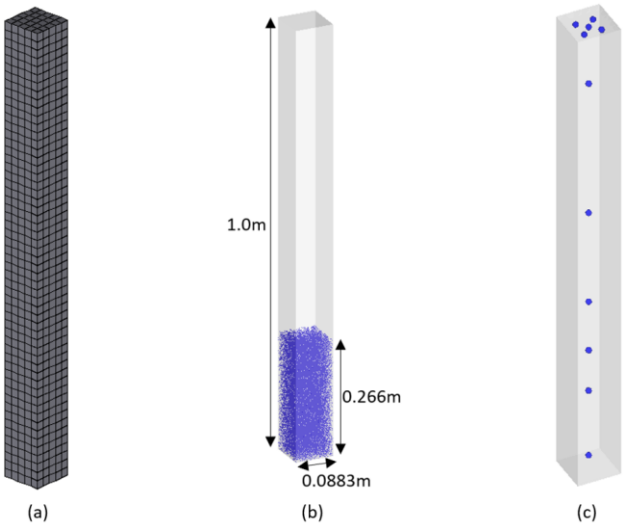

Figure 2. Simulation set-up: (a) Meshed geometry (b) Initial bed material and geometry dimensions (c) Transient data points.

As illustrated in Figure 2a, the simulated grid was generated with 6000 cells in total. Sand (SiO_2) particles with a mean diameter of 300µm and density of 2650 kg/m^3 were used as the bed material. The transient data points (sensors), as depicted in Figure 2c located along the center line of the reactor are used to measure the temperature and the pressure at different locations of the reactor, whereas datapoint located at the top surface measures the gas composition.

2.2.2 Initial and boundary conditions

The boundary conditions used in the geometry were specified as shown in Figure 3. Air was used as the gasification agent, which was implemented as a flow boundary. The syngas exit at the reactor top was a pressure boundary. The biomass inlet flow boundary was at 0.254m above the reactor bottom. Figure 3b shows the thermal boundary condition used to specify the constant temperature reactor wall, which was maintained by electrical heating elements during the experiments.

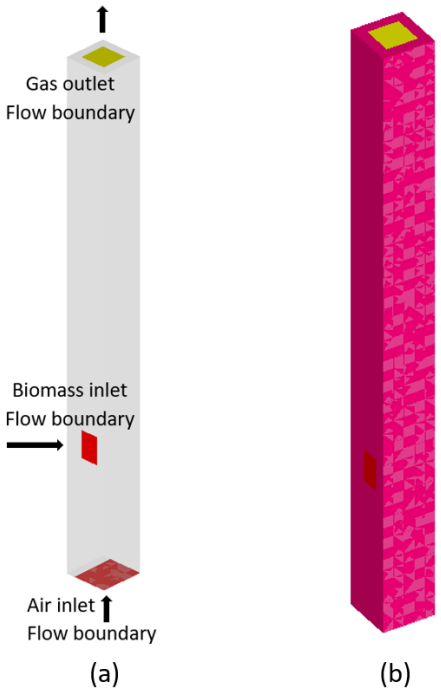

Figure 3. Boundary conditions: (a) Flow boundaries (b) Thermal boundary.

The reactor was initially filled with pure nitrogen at 1 atm and the temperature was varied according to the simulated case. The bed material is initially 100% sand (SiO_2) with a particle volume fraction of 0.6. The bed material was initially at 0.266 m height as illustrated in Figure 2b. depicted with blue color. The starting temperature was specified to be similar to the target operational temperature for all simulated cases.

2.2.3 Input data

Wen-Yu/Ergun drag model was adopted for the simulation as it was proven to give better predictions (Jaiswal, 2018). Table 1 shows the specified biomass properties, inlet flows, and simulation parameters used in the simulation.

Table 1. Biomass particle properties, inlet flows, and simulation parameters used in the simulation.

Biomass properties	
Type	Wood pellets (spherical shaped)
Size	2 mm
Inlet temperature	27°C (300K)
Density	1000 kg/m^3
Char density (after pyrolysis)	300 kg/m^3
Inlet flows	
Air	3 kg/h
Biomass	2.4 kg/h
Biomass carrier gas (N_2)	0.5 L/min
Air-Fuel ratio	1.25
Simulation parameters	
Close-pack volume fraction	0.6
Maximum momentum redirection from collision	40%
Normal-to-wall momentum retention coefficient	0.85
Tangent-to-wall momentum retention coefficient	0.85
Diffuse bounce	3
Drag model	Wen-Yu/Ergun

To define the wood pellets in the simulation software, the fraction of the volatiles and solid must be clarified. From the proximate analysis, wood pellets are broken into 83.9 wt.% volatiles, 15.55 wt.% fixed carbon, 0.55 wt.% ash, and 7.9 wt.% moisture in the pyrolysis stage. The amount of ash is very small; thus, the ash content was neglected. The moisture content was included in the volatile phase. Biomass char is considered to consist of pure carbon.

Hundreds of chemical reactions might occur in a gasification reactor. However, only the major reactions were considered, and the chemical kinetics are presented in Table 2.

Table 2. Chemical reactions and Kinetics for air gasification

Chemical reactions	Kinetics
Water gas shift reaction (Ismail *et al.*, 2019) R1: $CO + H_2O \leftrightarrow CO_2 + H_2$	$r = 6.4 \times 10^9 T \exp\left(\frac{-39{,}260}{T}\right)$
CO combustion (Gomez *et al.*, 2010) R2: $CO + 1/2O_2 \rightarrow CO_2$	$r = 4.78 \times 10^8 \exp\left(\frac{-6.69 \times 10^4}{RT}\right) [CO][O_2]^{0.3}[H_2O]^{0.5}$
H_2 combusion (Desroches *et al.*, 1998) R3: $H_2 + 1/2O_2 \leftrightarrow H_2O$	$r = 2.2 \times 10^9 \exp\left(\frac{-1.09 \times 10^5}{RT}\right) [H_2][0_2]$
Methane reforming (Kumar *et al.*, 2019) R4: $CH_4 + H_2O \leftrightarrow CO + 3H_2$	$r = 3.015 \times 10^8 \exp\left(\frac{-1.2552 \times 10^5}{RT}\right) [CH_4][H_20]$
Char oxidation (Kumar *et al.*, 2019) R5: $2C + O_2 \leftrightarrow 2CO$	$r = 1.47 \times 10^5 \exp\left(\frac{-1.13 \times 10^8}{RT}\right) [0_2]$
Steam gasification (Kumar *et al.*, 2019) R6: $C + H_2O \leftrightarrow CO + H_2$	$r = 8.28 \exp\left(\frac{-1.882 \times 10^8}{RT}\right) [H_2O]$
Boudouard reaction (Radmanesh *et al.*, 2006) R7: $CO_2 + C \leftrightarrow 2CO$	$r = 3.42\,T \exp\left(\frac{-15600}{T}\right) [C0_2]$

2.2.4 Simulation procedure

Three simulation cases were established by changing the reactor and pyrolysis temperatures. and fitting the pyrolysis gas compositions according to data from the literature. The specific data of pyrolysis gas composition for each case are tabulated in Table 3.

Table 3. Input data for the simulation cases (Santamaria, et al., 2021).

Case number	**Gas composition (wt.%)**					
	H_2O	H_2	CH_4	CO_2	CO	Tar (benzene)
Case-A	9	2	12	36	41	
Case-B	9	1	11	24	37	18
Case-C	9	2	12	36	41	

For Case-A, the reactor temperature was set to 800°C and the pyrolysis gas composition for 800°C was fitted. Case-B was modified by setting the reactor temperature to 800°C and fitting the pyrolysis gas composition for 700°C. It was assumed that if the mixing is not efficient

at the feeding point, the temperature can drop down to 700°C. In this case, the composition of tar (benzene) was included because pyrolysis yields more liquid at lower temperatures. Case-C is modified by increasing the reactor temperature up to 900°C and use the pyrolysis gas compositions for 800°C. The special aim of these cases was to study the effect of temperature and pyrolysis gas composition on biomass gasification. And thereby, compare the results with the experimental results from other studies performed at the USN gasification rig.

The total simulation time for each case was set to 200 seconds with a time step of 0.001 seconds. The gas compositions measured by the transient data points were averaged for the last simulated 100 seconds.

3 Results and discussion

This section discusses the simulation data for each case. The data were further compared against experiments.

3.1 Case-A

Case-A was modified by setting the reactor temperature to 800°C using the pyrolysis gas composition for 800°C. Figure 4 shows the mass fraction of product species at the reactor outlet plotted after 100s of simulated time. The average mass fraction of CO was 10.4%, CO_2 was 39.4%, CH_4 was 4.2% and H_2 was 1.1%.

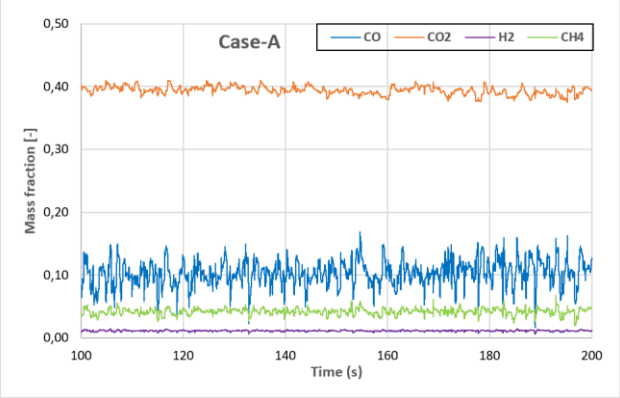

Figure 4. Case-A: Outlet mass fraction variation with time.

Figure 5 shows an outline of the (a) fluid temperature (b) particle temperature and (c) particle volume fraction across the bed at 200s. The fluid and particle temperatures are above 800°C (1073K), which is the desired temperature. This indicates that the gasification reactions are continuously maintained. From Figure 5c, the particles seem to be well mixed, which is good in terms of temperature distribution. The air flow might be a little bit high, but as long the particles remain within the bed it is accepted. However, limited air flows can reduce the generation of combustible gases such as CO, H_2, and CH_4.

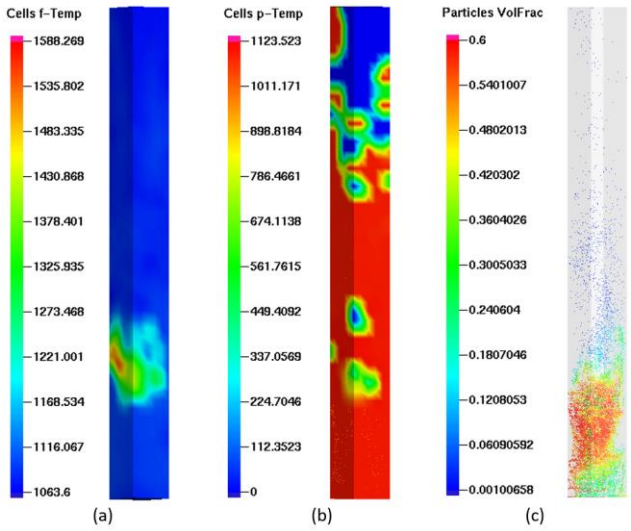

Figure 5. Reactor conditions (a) Fluid temperature [K] (b) Particle temperature (c) Particle's volume fraction.

3.2 Case-B

In Case-B, the reactor temperature was kept at 800°C and the pyrolysis gas composition for 700°C was fitted. Figure 6 shows the mass fraction of product species at the reactor outlet plotted after 100s of simulated time. The average mass fraction of CO was 13.2%, CO_2 was 32.4%, CH_4 was 4.1% and H_2 was 0.9%. As the pyrolysis gas composition for 700°C was fitted in this case, the tar content is significant. Thereby, the tar composition was modified within the volatiles and the tar reactions were included in the simulation. The tar was assumed by a single component, that is benzene C_6H_6.

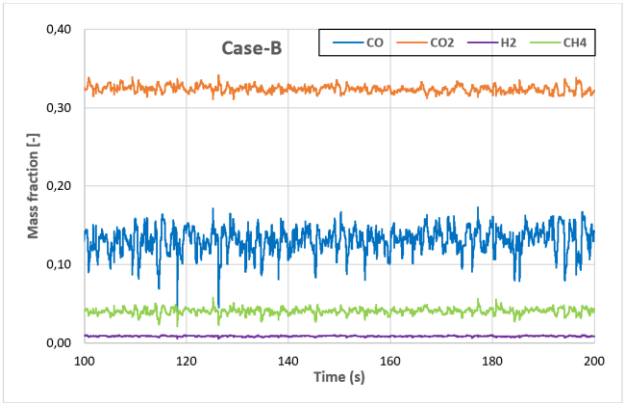

Figure 6. Case-B: Outlet mass fraction variation with time.

3.3 Case-C

Finally, Case-C was modified by setting the reactor temperature to 900°C and fitting the pyrolysis gas composition for 800°C. Figure 7 shows the mass fraction of product species at the reactor outlet plotted after 100s of simulated time. The average mass fraction of CO was 13.1%, CO_2 was 37.9%, CH_4 was 3.9% and H_2 was 1.2%.

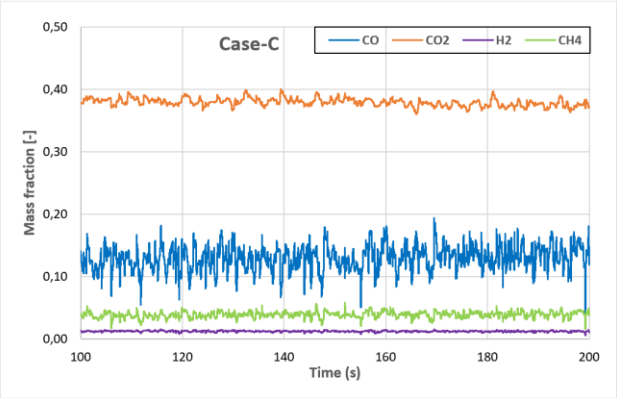

Figure 7. Case-C: Outlet mass fraction variation with time.

From Figure 4, Figure 6, and Figure 7, the calculated product mass fractions are showing a noisy and unsteady behavior where, the steady-state is never reached. This is due to the unsteady characteristics of the fluidized bed, where different chemical and physical transformations are taking place. However, it was noticed from the plots that the average mass fractions were stable over time.

3.4 Comparison of the cases

The molar compositions of the syngas from simulations and experiments at 800°C is given in Figure 8 and Table 4. In all cases, N_2 contributed to the highest molar concentration and ranged between 41.5% and 43.5% of the total. This is reasonable, as nitrogen is an inert gas and does not involve in the reactions. The molar concentrations of O_2 were monitored to be very close to zero. This is mainly due to the occurrence of oxidation reactions. The H_2O molar concentrations were measured to be 2.5%, 1.6%, and 1.2% for Case-A, B, and C, respectively. The lower percentage of H_2O produced in Case-C is mainly due to the increase of temperature to 900°C. Higher temperatures enhance the steam gasification reaction (R6) to proceed forward, which in turn produces more H_2. In all cases, the molar concentration of CO_2 was highest followed by H_2 and CO, respectively. The lowest produced gas component was CH_4.

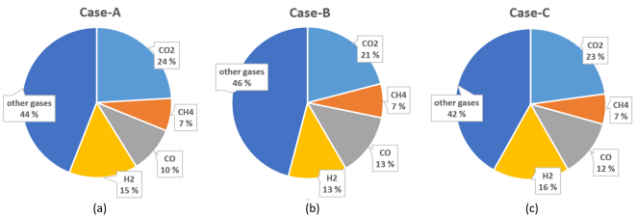

Figure 8. Molar compositions of the gas species monitored at the reactor outlet for (a) Case-A (b) Case-B (c) Case-C.

Case-A and Case-B were simulated using the same reactor temperature but different pyrolysis gas compositions. Therefore, the results from the two cases are compared to study the effect of the pyrolysis step. Figure 9 and Figure 10 show the input pyrolysis gas compositions for Case-A and B respectively, compared to the synthesis gas compositions.

The molar concentration of CO_2 increased slightly by 3% and 2.6% in the synthesis gas for Case-A and B, respectively. In the contrast, the CO concentration decreased significantly by 27% and 29.9% in the synthesis gas for Case-A and B, respectively. The concentration of CH_4 decreased by 6.9% and 7.1% in the synthesis gas for Case-A and B, respectively. The concentration of H_2 decreased by 8.2% and 4.7% in the synthesis gas for Case-A and B, respectively.

The increase of CO_2 is mainly due to the oxidation of char and CO in the gasifier. Oxidation and water gas shift reaction (R1) are the main drives for the reduction of CO. Consumption of methane is mainly due to steam methane reforming reaction (R4), which is in turn produces more CO.

It was observed that higher concentrations of the combustible gases including CH_4, CO, and H_2 released in the pyrolysis stage contributed to higher concentrations of these gases in the synthesis gas. Therefore, pyrolysis stage is critical in deciding how much CH_4, CO, and H_2 will be in the synthesis gas. This is mainly because that the pyrolysis step converts 85% of the biomass weight into volatiles.

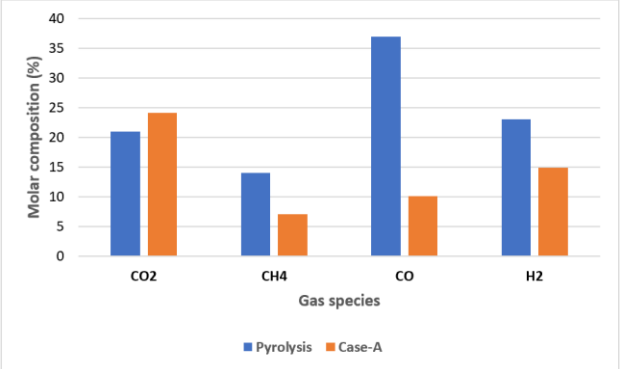

Figure 9. Case-A: Input pyrolysis gas composition compared to synthesis gas composition.

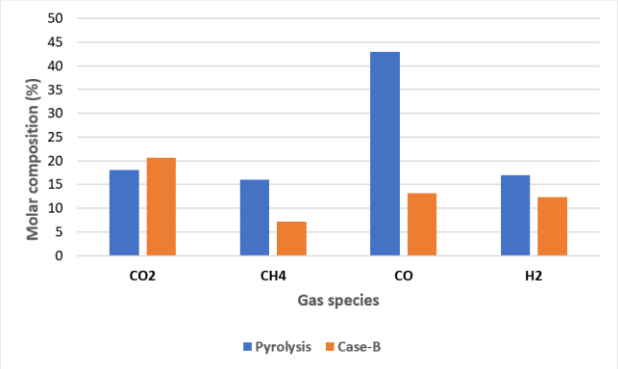

Figure 10. Case-B: Input pyrolysis gas composition compared to synthesis gas composition.

Figure 11 shows the average gas compositions from the simulation of Case-A and B compared with the

experimental results. It should be noted that only Case-A and B are comparable with the experimental results, as they have the same reactor temperature. Both cases show a good agreement with the experimental results for CH_4 and H_2. Case-B gave a closer prediction on CO_2 and CO, which is not as expected because Case-B uses the pyrolysis gas composition for 700°C. This might be due to the tar that was defined in Case-B. However, in both cases, the concentration of CO_2 was overestimated, CO was underestimated while CH_4 was slightly overestimated.

The overestimation of CO_2 and underestimation of CO might be due to some inaccuracies in the pyrolysis gas composition or high rates in the water-gas-shift reaction (R1) where CO is consumed, and more CO_2 is produced. Moreover, there can also be some experimental uncertainties in measuring the gas composition, especially related to the GC measurements and the gas sampling. During the experiment, biomass feeding was not continuous in contrast to the simulation. As the pyrolysis gas composition highly affects the final syngas composition, discontinuous feeding might cause deviations in the actual measured value. In the simulation, it is possible to take a wide range of measurements, which is difficult during the experiments.

However, the deviation between experiment and simulation cannot be avoided. This is mainly because the reaction network is decreased, devolatilization is simplified and the tar generation is minimized or ignored.

Table 4. Average gas composition (mole basis) from the simulated cases and experiment.

	Case-A	Case-B	Case-C	Experiment
CO_2	24.1	20.6	22.82	14
CH_4	7	7.1	6.5	4
CO	10	13.1	12.4	19
H_2	14.8	12.3	16.4	17

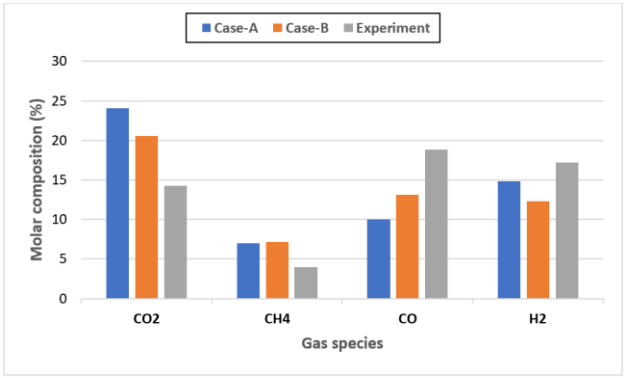

Figure 11. Average product gas composition from the three cases compared to the experimental results.

Case-A and C are compared with each other to study the effect of temperature on the synthesis gas composition. Two cases are defined with the same pyrolysis gas composition but with different temperatures. Figure 12 shows the product gas composition from Case-A and Case-B with varying reactor temperature. Increasing the temperature from 800°C to 900°C, the CO molar concentration increased from 10% to 12.4%, CO_2 decreased from 24.1% to 22.8%, CH_4 decreased slightly from 7% to 6.5% and H_2 increased from 14.8% to 16.4%. This is mainly due to the reactions that are enhanced with increasing temperature including, char partial oxidation reaction (R5), water gas shift reaction (R1), and the Boudouard reaction (R7). Further, the reactor temperature has a significant effect on the syngas product yields. Therefore, increasing the reactor temperature contributes to higher gas composition and lower tar yields. However, the trends show a good agreement with literature and other experiments except for the trend of CH_4. This might be due to the neglect of the tar composition in the volatiles.

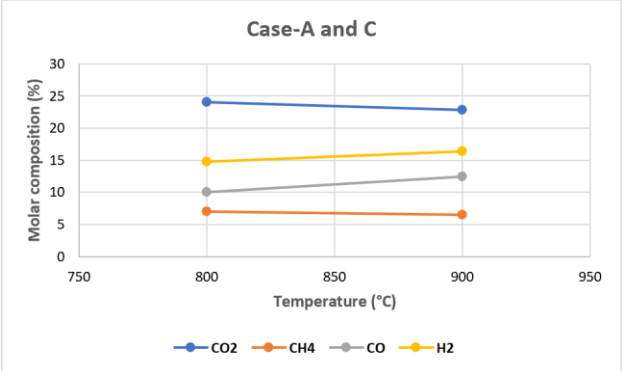

Figure 12. Product gas molar fraction for Case-A and Case-C at different temperatures.

4 Conclusion

Computational particle fluid dynamic (CPFD) simulations were carried out to study the composition of the synthesis gas obtained from the air gasification of wood pellets. Three simulation cases were created by varying the temperature and the pyrolysis gas compositions.

In all the cases, production of CO_2 was highest, and then come H_2, CO, and CH_4, respectively. The effect of the pyrolysis step on synthesis gas composition was found to be significant, especially on the production of CO, H_2, and CH_4. This is mainly due to the 85% by weight of the synthesis gas was produced during the pyrolysis of biomass.

Comparing Case-A and B with experimental data showed a good agreement on predicting CH_4 and H_2 while overestimation of CO_2 and underestimation of CO. The deviation of CO_2 and CO might be due to uncertainty in the pyrolysis gas composition or high kinetic rates of water-gas shift reaction used in the simulation. Including the decomposition of tar in the simulation seems to give better prediction performance, especially for CO_2 and CO.

The effect of temperature was established by comparing Case-A and C, where the temperature was varied from 800°C up to 900°C. Increasing the temperature increased the concentration of CO and H_2 by 2.4% and 1.6% respectively and decreased the concentration of CO_2 and CH_4 by 1.3% and 0.5%. The trends showed a good agreement with other experiments from the literature, except the trend of CH_4. This might be due to the neglect of the tar compositions in the volatiles.

References

Alternativ Energy Tutorials. *Biomass Resources*. Retrieved 03 2021, from https://www.alternative-energy-tutorials.com/biomass/biomass-resources.html

J.P. Badeau, A. Levi. *Biomass Gasification: Chemistry, Processes and Applications.* New York: Nova Science Publishers. 2009.

J. Bandara. *Simulation and parameter optimization of fluidized-bed and biomass gasification.* University of South-Eastern Norway, 2021.

P. Basu. *Biomass Gasification, Pyrolysis and Torrefaction* (2nd ed.). Elsevier, 2013.

CPFD Software. *Complements Other Tools*, 2021. Retrieved from https://cpfd-software.com/technology/complements-other-tools/

CPFD Software LLC. *CPFD Software Realeases Barracuda Virtual Reactor 17.4*. Retrieved 05.03.2021: https://cpfd-software.com/news/cpfd-software-releases-barracuda-virtual-reactor-17.4

E. Desroches-Ducarne, J. C.Dolignier, E. Marty, G. Martin, L. Delfosse. Modeling of gaseous pollutants emissions in circulating fluidized bed combustion of municipal refuse. *Fuel*, 77(13): 1399-1410, 1998.

C. Ellis. *World Bank: Global waste generation could increase by 70% by 2050.* World Bank: Global waste generation could increase 70% by 2050 | Waste Dive, Industry Dive 2018.

L. Fagbemi, L. Khezami, R. Capart. Pyrolysis products from different biomasses: application to the thermal cracking of tar. *Applied Energy*, 69(4), 293-306, 2001.

A. Gomez-Barea, B. Leckner. Modeling of biomass gasification in fluidized bed. *Progress in Energy and Combustion Science*, 36(4): 444-509, 2010.

H. B. Goyal, D. Seal, R. C. Saxena. Bio-fuel from thermochemical conversion of renewable resources: A review. *Elsevier*, 12(2): 504-517, 2008.

M. T. Ismail, A. Ramos, M. A. El-Salam, E. Monteiro, A. Rouboa. Plasma fixed bed gasification using a Eulerian model. *International Journal of Hydrogen Energy*, 44(54): 28668-28684, 2019.

R. Jaiswal, R. *Computational modeling and experimental studies on fluidized bed regimes.* University of South-Eastern Norway, 2018.

S. Kaza, L. Yaw, P. Bhada-Tata, F. V. Woerden. *What a Waste.* Washington: International Bank for Reconstruction and development. 2018.

U. Kumar, M. C. Paul. CFD modeling of biomass gasification with a volatile break-up approach. *Chemical Engineering Science, 195*: 413-422, 2019, doi: https://doi.org/10.1016/j.ces.2018.09.038

Z. Luo, J. Zhou. Thermal Conversion of Biomass. *Handbook of Climate Change Mitigation*: pp. 1001-1042. New York: Springer, 2012.

A. Monilo, S. Chianese, D. Musmarra. Biomass gasification technology: The state of the art overview. *Journal of Energy Chemistry*, 25(1): 10-25, 2016.

C. K. Perera, *Optimization of biomass gasification reactor.* Telemark University College, 2013.

R. Radmanesh, J. Chaouki, C. Guy. Biomass gasification in a bubbling fluidized bed reactor: Experiments and modeling. *AIChE Journal*, 52(12): 4258-4272, 2006. doi: https://doi.org/10.1002/aic.11020

L. Rosendahl. *Biomass Combustion Science, Technology and Engineering.* Sawston: Woodhead Publishing Limited, 2013.

L. Santamaria, M. Beirow, F. Mangold, G. Lopez, M. Olazar, M. Schmid, G. Scheffknecht. Influence of temperature on products from fluidized bed pyrolysis of wood and solid recovered fuel. *Fuel*, 283, 2021.

K. Sun. *Optimization of biomass gasification reactor using Aspen Plus.* Telemark University College. 2014.

Fluidization of fine calciner raw meal particles by mixing with coarser inert particles – Experiments and CPFD simulations

Ron M Jacob Britt M.E. Moldestad Lars-Andre Tokheim

Department of Process, Energy and Environmental Technology, University of South-Eastern Norway
{ron.jacob, britt.moldestad, Lars.A.Tokheim}@usn.no

Abstract

The calciner has a significant role in the production of cement. It is the most energy-intensive process unit in the production process. Most modern calciners are entrainment-based, i.e., a hot gas pneumatically conveys the particles through the calciner. A fluidized bed is an alternative to the entrainment calciner, which may be of special interest if the calcination process is to be electrified, so that the raw meal is mainly calcined by heat transfer from a hot surface and not by direct contact with hot combustion gases. The fine particle size of the raw meal, however, makes it a challenge to fluidize. This study looks into an alternative solution in which the cement raw meal is mixed with coarse sand particles to enhance the fluidization behavior.

Experiments are first conducted to fluidize pure cement raw meal (fine particles) and sand (coarse particles) separately. Then they are mixed at fine/coarse mass ratios of 25%/75% and 50%/50%.

Simulations are then performed, using a commercial CPFD software (Barracuda ®, version 20.0.0), to replicate the results from the experiments.

The experimental results indicate that it is technically feasible to fluidize cement raw meal by mixing it with coarse inert particles at the mentioned fine/coarse mass ratios. Stable fluidization was observed at a superficial gas velocity of 0.3 m/s. The pressure drop results from simulations and experiments matched quite well at both mixing ratios. Hence, the CPFD simulations may be used as an aid in the design of a potential full-scale calciner applying this concept.

Keywords: Fluidization, Cement, Binary particles, Calcination, Electrification

1 Introduction

Around 7% of the global CO_2 emissions are from the cement industry (IEA, 2020). In modern cement plants, the CO_2 comes from the decarbonation of the calcium carbonate in the raw meal (about 70 %) and from the fuel combustion (about 30 %). Reducing the CO_2 emissions from such plants can be done by post-combustion capture of the CO_2 in the exhaust gas from the plant. However, calcination by electrification of the calciner will generate a pure gas CO_2, which makes it possible to significantly reduce the CO_2 emissions without building a separate capture plant, provided the electricity is produced from a renewable energy source. This method can reduce around 70 % of the CO_2 emissions from a modern cement plant (Tokheim *et al.*, 2019).

Most modern calciners operate in the entrainment mode where the raw meal is entrained by the combustion flue gases while providing heat for calcination reaction (Becker *et al.*, 2016). It may be possible to electrify the entrainment calciner by inserting heating rods. However, the main challenge with this concept is the potential heat loss from a large amount of recycling gas required for raw meal entrainment (Jacob and Tokheim, 2021).

An alternative solution to this concept is a fluidized bed calciner, which will operate at a lower velocity and will require much less recycle gas. Moreover, a high heat transfer coefficient and a uniform temperature distribution due to good mixing in the system are additional advantages (Kunii and Levenspiel, 1991). However, due to the small particle size in a traditional cement raw meal, it may not be feasible to fluidize the particles properly (Samani, 2020).

A raw meal typically has a particle size distribution in the range 0.5 – 250 µm, where 70-80% of the particles fall in the range of the Geldart C particle size class. Geldart C particles are difficult to fluidize due to their cohesive nature (Geldart, 1973). A previous investigation demonstrated this challenge as rat hole formation in the bed was observed (Samani *et al.*, 2020).

Mixing the cement raw meal with coarse particles could be an alternative way of fluidizing these particles (Samani *et al.*, 2020). This concept of mixing cement raw meal with coarse inert particles is called "Powder-Particle Fluidized Bed (PPFB)" (Kato *et al.*, 1991). The PPFB concept was demonstrated experimentally at a limestone feeding rate of 15 g/hr and a superficial gas velocity of 0.45 m/s. The static bed height of coarse particles was varied in the range 0.1 – 0.2 m. The experiment was done in a column with a diameter of 0.03 m and a height of 0.65 m (Tashimo *et al.*, 1999).

This study aims to investigate the feasibility of fluidizing a binary mixture by mixing fine cement raw meal and coarse sand particles at a mass ratio that may be appropriate for a full-scale process. The feasibility is tested experimentally with a cold-flow lab-scale fluidized bed at different mass ratios. Computational particle and fluid dynamics (CPFD) simulations are

further performed with the commercial software Barracuda ®, version 20.0.0, to check if the results from the experiments can be replicated through computer simulations. The intention is to use the results from this study to design a full-scale calciner.

2 Experimental Method

The experimental setup, the particle characteristics, and the experimental procedure are described below.

2.1 Experimental setup

The experiments were conducted in a lab-scale fluidized bed. The lab-scale fluidized bed is a cylindrical tube made of Lexan plastic. The internal diameter and the height of the tube are 0.085 and 1.4 m, respectively. The tube has nine pressure transmitters placed along its axial direction, and a LabVIEW® programme records the pressure readings. The experimental setup is shown in Figure 1.

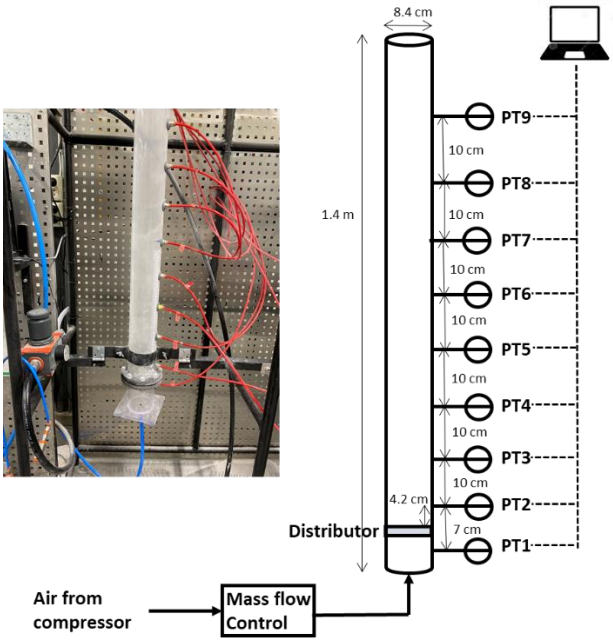

Figure 1: Experimental setup

The distance between PT1 and PT2 is 7 cm, and the other transmitters have an equal spacing of 10 cm, as shown in Figure 1. The particles are fluidized with air at ambient conditions. The mass flow rate of the air is controlled with a flowmeter.

The air distributor, made of a highly porous sintered stainless steel (Siperm R20®, Tridelta Siperm GmbH), is placed between the fluidizing air and particles. The porosity of the distributor is 37-42 %.

The pressure drop from the air distributor (ΔP_d) was measured at different gas velocities by passing air through the distributor without any presence of particles. The pressure drop versus air velocity was then fitted to a non-linear equation. The experimental result of pressure drop and the prediction from the non-linear equation are shown in Figure 2.

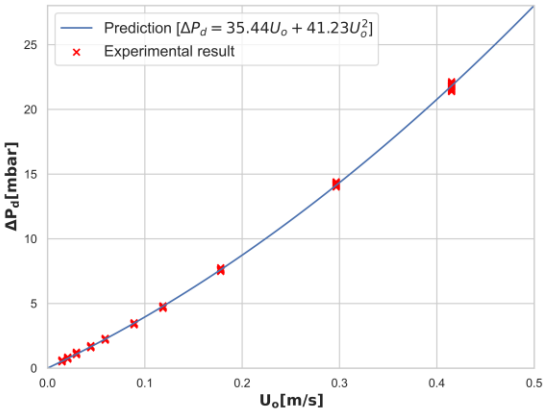

Figure 2: Fitting pressure drop across the distributor to second order velocity function.

2.2 Particle characteristics

A regular cement raw meal from a local Norwegian cement plant was used as fines in the experiment. The fine particles had a size distribution between 0.5 and 250 µm, and almost 80 % of the particles were below 30 µm. Sand with a particle size between 100 and 600 µm was used as the coarse particles in the experiment.

Four different mass fractions of fines were used in the experiments; 0, 25, 50 and 100 %. The total mass of fine and coarse particles was 900 g in all experimental cases. An overview of the experimental cases and the particle properties is shown in Table 1.

Table 1: Experimental cases and particle properties

Parameters	100% fines	50% fines	25% fines	0% fines
Mass of raw meal [kg]	0.9	0.45	0.225	0
Mass of sand [kg]	0	0.45	0.675	0.9
Average particle density [kg/m³]	2897	2774	2712	2650
Bed Height [cm]	15.2	11.7	10.4	10.2
Bulk density [kg/m³]	1053	1368	1540	1570
Void fraction [-]	0.64	0.51	0.43	0.41

Laser diffraction with a HELOS (RODOS dry dispersion) particle size analyzer was used to measure the particle size distribution (PSD) for each case. The resulting distribution is shown in Figure 3.

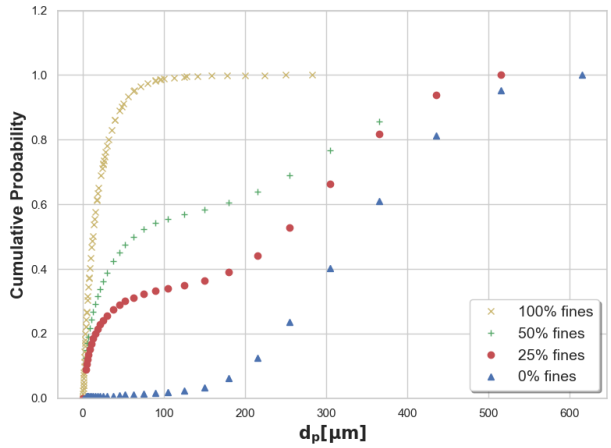

Figure 3: Cumulative particle size distribution (PSD) plot for the experimental cases

2.3 Experimental procedure

The particles were carefully weighed and poured into the column. The bed height in each case was noted down (cf. Table 1).

The air velocity was then increased in steps to different levels. By experience it was found that the system reached a pseudo-steady state within 160 seconds at a certain level. Hence, for each step, the velocity was held constant for 200 seconds. The pressure measurements between 160 and 200 s were used to determine the mean pressure and pressure fluctuations at the pseudo-steady state conditions. A high standard deviation in these fluctuations may indicate a bubbling behavior in the bed (Jaiswal *et al.*, 2018).

3 Modelling methods

Monte-Carlo simulations were used to numerically determine the PSD of the mixtures. Computational particle and fluid dynamics (CPFD) modelling was used to simulate the particle behaviour in the bed, applying a suitable drag model. These models, as well as the simulation setup, are described below.

3.1 Monte-Carlo simulations to analyze PSD

A Monte-Carlo simulation may be used to analyze the particle size distribution (PSD). According to the law of large numbers, as the sample size increases, the distribution of the sampled particles tends to have its original distribution. Samples may be generated from the distribution using various algorithms. In this study, a modified version of the inverse sampling algorithm is used:

1. Generate a random number between 0 and 1 from a uniform distribution. This number represents the cumulative probability (y-axis) in Figure 3.
2. At the randomly generated cumulative probability, read the value of diameter (d_p) by linear interpolation. This value of d_p is the generated sample.
3. Repeat step 1 and step 2 to get the required number of samples (10,000 in our case).

The histogram of the generated sample may, however, not be smooth enough to make inferences. Kernel density estimation (KDE) is a non-parametric method to estimate the probability density from random variates. It is used for data smoothening where inferences about the data must be made. The KDE algorithm implemented in the Seaborn package of Python 3.8 was used to smoothen the distribution. This method is useful for predicting the probability density of the mixture if the probability density of pure components is known. The prediction test is also simulated in this study.

3.2 CPFD method

Computational particle and fluid dynamics (CPFD) is a method to simulate gas-solids multiphase flow. This method is based on Eulerian-Lagrangian coupling, and it uses a unique concept called the multiphase-particle-in-cell (MP-PIC) method (Andrews and O'Rourke, 1996). The MP-PIC method solves the gas phase equation by the Eulerian approach and the solid phase equations by the Lagrangian approach. This approach makes it quite similar to the traditional discrete element method (DEM). However, some differences, such as the particle-to-particle force calculations and the assumption of numerical particles, make the CPFD method much more computationally efficient than the traditional DEM method for an industrial system (Snider, 2007).

The simulations were performed at the experimental conditions to study the physics of particles in each case.

The volume-averaged continuity and momentum equation for a two-phase incompressible flow is (Snider 2007),

$$\frac{\delta \theta_f}{\delta t} + \nabla \cdot \left(\theta_f u_f\right) = 0 \tag{1}$$

$$\frac{\delta \left(\theta_f u_f\right)}{\delta t} + \nabla \cdot \left(\theta_f u_f u_f\right) = \frac{-1}{\rho_f}\nabla p - \frac{1}{\rho_f} F + \theta_f g + \frac{1}{\rho_f}\nabla \cdot \tau \tag{2}$$

Here, θ_f is the fluid volume fraction, u_f is the fluid velocity, ρ_f is the fluid density, p is the fluid pressure, τ is the fluid stress tensor, g is the gravitational constant, and F is the momentum exchange rate per volume between fluid and the particles.

The acceleration in the particles can be further modelled by (Snider, 2007),

$$\frac{\delta u_p}{\delta t} = D(u_f - u_p) - \frac{1}{\rho_p}\nabla p + g - \frac{1}{\theta_p \rho_p}\nabla \tau_p + F_S \quad (3)$$

Here, u_p is the particle velocity, ρ_p is particle density, D is the interphase drag function, θ_p is the particle void fraction, τ_p is the particle normal stress and F_S is the particle friction.

The particle-to-particle forces are modelled with the normal stress of particle (τ_p), and this is given by (Snider 2001),

$$\tau_p = \frac{P_s {\theta_p}^{\beta}}{max[\theta_{cp} - \theta_p, \varepsilon(1 - \theta_p)]} \quad (4)$$

Here the constant P_s has a unit of pressure, θ_{cp} is particle void fraction at close packing, β is a constant with a recommended value between 2 and 5, ε is a very small number activated when particle void fraction comes very close to its close pack limit.

The blended acceleration model (BAM) is an extra option implemented in Barracuda to account for the fluidization behavior of particles of different size. The particles with different size have a lower relative motion due to sustained particle contacts. BAM is used to simulate this phenomenon, and without BAM, the segregation of particles in simulations may be higher than in reality.

Particle to wall interaction modelling in Barracuda is controlled mainly by three variables; normal-to-wall momentum retention (r_N), tangent-to-wall momentum retention (r_T) and diffuse bounce index (d_{bi}).

A schematic of a particle colliding with a wall with initial velocity (u^n) and attaining a final velocity (u^{n+1}) is shown in Figure 4.

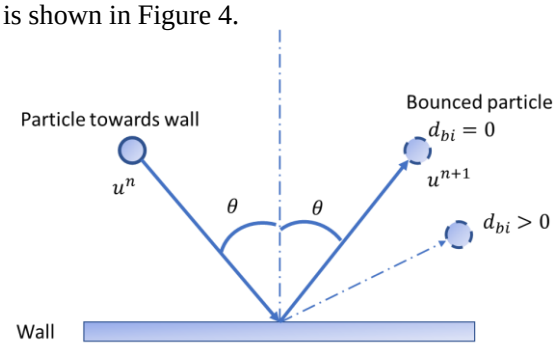

Figure 4: Schematic of particle collision with the wall

The diffuse bounce index (d_{bi}) defines the degree of scattering of particles after the collision (cf. Figure 4). This parameter applies to a rough wall, which is usually present in an industrial system. The normal-to-wall momentum retention (r_N) is the fraction of the normal component of particle momentum retained after a collision with wall. The tangent-to-wall momentum retention (r_T) is the fraction of tangential component of particle momentum retained after a collision with wall.

The choice of values for the parameters discussed in this section varies in the literature. The values used in this study are shown in Table 2.

Table 2: Particle interaction parameters used in this study

Particle-to-particle interaction		Particle-to-wall interaction	
Parameter	**Value**	**Parameter**	**Value**
$\boldsymbol{P_s}$	1	r_N	0.4
$\boldsymbol{\beta}$	3	r_T	0.95
$\boldsymbol{\varepsilon}$	10^{-8}	d_{bi}	2

3.3 Drag modelling

The interphase drag function (D) is used to model particle acceleration. There are many models available for drag modelling.

The Ergun drag model defines this function as (Beetstra *et al.*, 2007),

$$D = 0.5\left(\frac{c_1 \theta_p}{\theta_f Re} + c_o\right)\frac{\rho_f(u_f - u_p)}{r_p \rho_p} \quad (5)$$

Here, c_o and c_1 are model coefficients and recommended value for c_o is 2 and for c_1 is 180 (Beetstra *et al.*, 2007). This model was developed using data for a dense bed.

The Wen-Yu drag model was developed based on fluid void fraction and single-particle drag (Wen and Yu, 1966). The drag coefficient is defined as,

$$C_d = \begin{cases} \frac{24}{Re}{\theta_f}^{n_o} & Re < 0.5 \\ \frac{24}{Re}{\theta_f}^{n_o}(c_o + c_1 Re^{n_1}) & 0.5 \le Re \le 1000 \\ c_2 {\theta_f}^{n_o} & Re > 1000 \end{cases} \quad (6)$$

Here, the drag coefficient (C_d) is related to the interphase drag function by,

$$D = \frac{3}{8} C_d \frac{\rho_f(u_f - u_p)}{r_p \rho_p} \quad (7)$$

The Wen-Yu drag model is more appropriate for dilute flows, while the Ergun drag model is more appropriate for dense flows. Using a blend may capture the best of both drag models. The blended model is given by,

$$D = \begin{cases} D_1 & \theta_p < 0.75\theta_{CP} \\ \frac{(D_2 - D_1)(\theta_p - 0.75\,\theta_{cp})}{0.85\theta_{cp} - 0.75\theta_{cp}} + D_1 & 0.75\theta_{cp} \le \theta_p \le 0.85\theta_{cp} \\ D_2 & \theta_p > 0.85\theta_{CP} \end{cases} \quad (8)$$

Here, D_1 is the drag function from the Wen-Yu equation and D_2 is the drag function from the Ergun equation.

In this study, the blended model was used for the coarse particles and the mixture cases, whereas the Wen-Yu model was used for the fine cement raw meal.

3.4 Simulation setup

The simulations were set up to match the experimental conditions. A three-dimensional geometry of the tube

was developed with an internal diameter of 0.085 and a height of 1.4 m. A uniform grid with a total of 17600 (10×10×176) cells in the tube was created. The pressure sensors were placed at the height of 4.2 cm and 14.2 from the bottom to replicate the PT2 and PT3 sensors. The resulting mesh and the pressure monitoring points are shown in Figure 5.

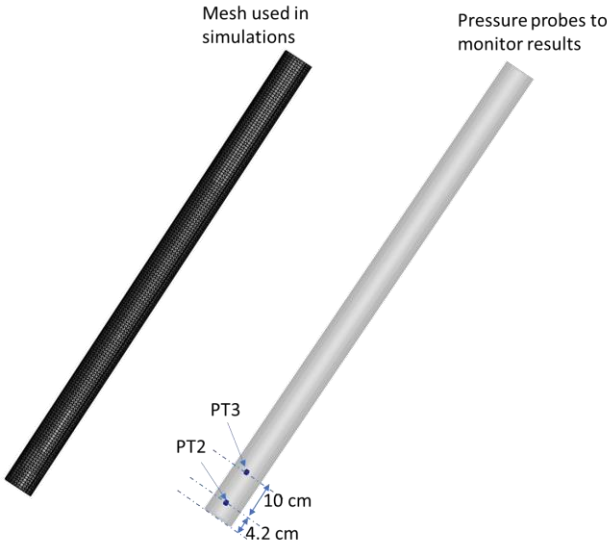

Figure 5: Mesh used in the simulations and pressure probe to monitor results

The simulation results are presented after simulating for 30 seconds in each case as it was found that a pseudo-steady state was reached after 30 seconds of simulations.

4 Results and Discussions

4.1 Monte-Carlo simulation results

The PSDs from the Monte-Carlo simulations are given in Figure 6. Results from mixing pure particles are given in Figure 7. The results indicate that Monte-Carlo sampling is an efficient algorithm to estimate the particle size distribution of mixed powders.

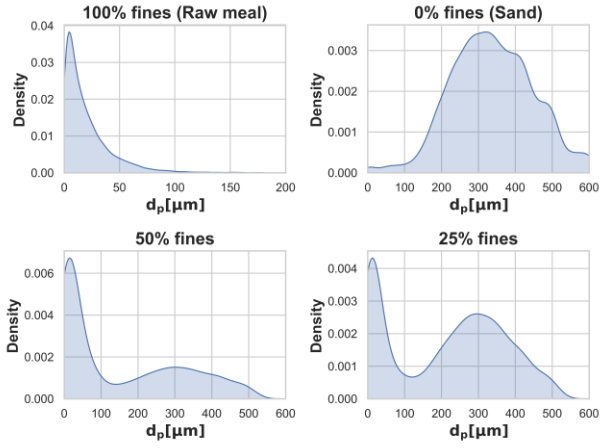

Figure 6: Probability distribution of the particles

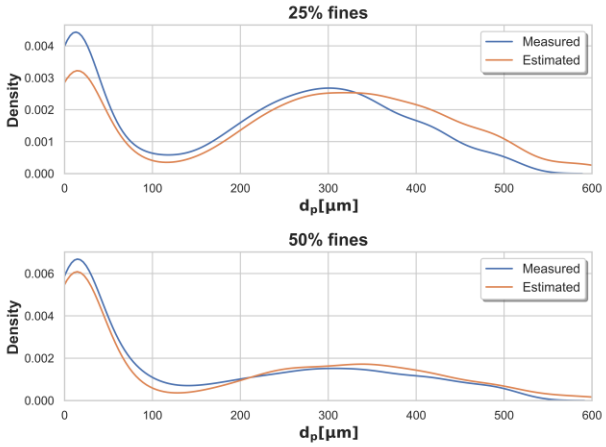

Figure 7: Sampling from measured PSD vs estimated PSD by sampling from pure powders

4.2 Pure particle results

A corrected pressure drop between PT1 and PT2 (cf. Figure 1) was calculated by subtracting the pressure drop over the distributor from the measured pressure drop between point 1 and 2 (cf. Figure 2). The corrected bed pressure drop between PT1 and PT2 (excluding distributor pressure drop), ΔP_{12}, is shown in Figure 8. The standard deviation of the pressure drop (σ_P) is plotted as a band and also as a separate dotted line.

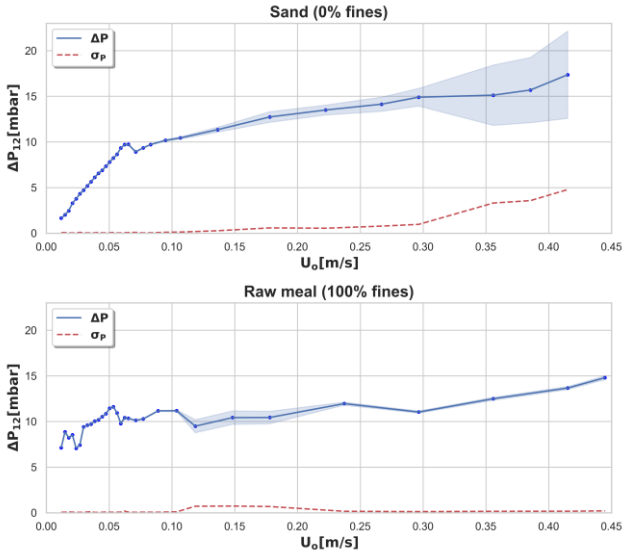

Figure 8: Pressure drop profile for pure particle fluidization

The minimum fluidization velocity (U_{mf}) for the pure coarse particles is at a superficial gas velocity of 0.06 m/s. The minimum fluidizing velocity (U_{mf}) of the fine particles could not be measured accurately as the disturbances in the bed started at the lowest superficial gas velocity of 0.01 m/s. Both coarse and fine particles had similar pressure drop readings at the fluidizing conditions because the weight of both particles is the same. The pressure drop fluctuations for coarse particles are high when the velocity is high. In contrast, for the

fine cement raw meal, the fluctuations were low. These results indicate an excellent fluidization behavior of the sand particles and poor fluidization behavior of the fine cement raw meal. This inference is also consistent with visual observation of the bed.

The corrected bed pressure drop between PT1 and PT2 (excluding distributor pressure drop), ΔP_{12}, is not directly comparable to the simulation results as pressure point 1 in the experiment is not present in the simulation model. So, the experimental pressure drop between sensor PT2 and PT3 (ΔP_{23}) is compared against the simulation results for pure particles in Figure 9.

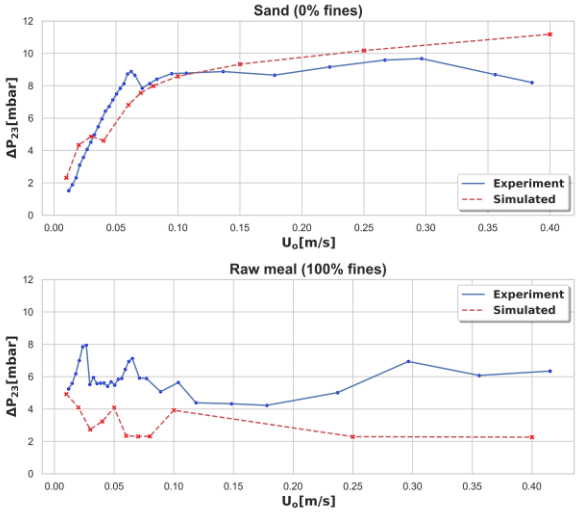

Figure 9: Pressure drop profile comparison of experiments and simulations for pure particles

The results for the coarse particles show that the measured and simulated pressure drop match quite well. In the experiments, a pressure drop peak corresponding to the minimum fluidization velocity is observed. In the simulation, however, the peak is predicted at a lower velocity. This peak may not be the minimum fluidization velocity as the pressure drop keeps increasing almost at the same gradient after the peak. The simulated pressure drop curve starts to flatten out at a velocity higher than the minimum fluidization velocity predicted from experiment. Thus, the minimum fluidization velocity value predicted from the simulation is higher than the experimental value. The coarse particles have a wide size distribution (cf. Figure 3), which means an interaction between particles of different sizes is expected. Some of the interaction effects are neglected in the CPFD model and could be a reason for the deviation. This effect may be modelled with the BAM feature (cf. Section 3.2). However, for this work, the current results are considered good enough for further analysis.

The results for the fine particles show that the pressure drop is under-predicted in all the cases. In a real system, the particles tend to agglomerate, and this increases the pressure drop in the system. This agglomeration effect may be the reason for the deviation as it is not modelled in this study. Still, the results are considered good enough for further study.

4.3 Experimental results of binary particle

The pressure drop (ΔP_{12}) results from fluidizing binary particles were estimated in the same way as in Section 4.2. The results are shown in Figure 10.

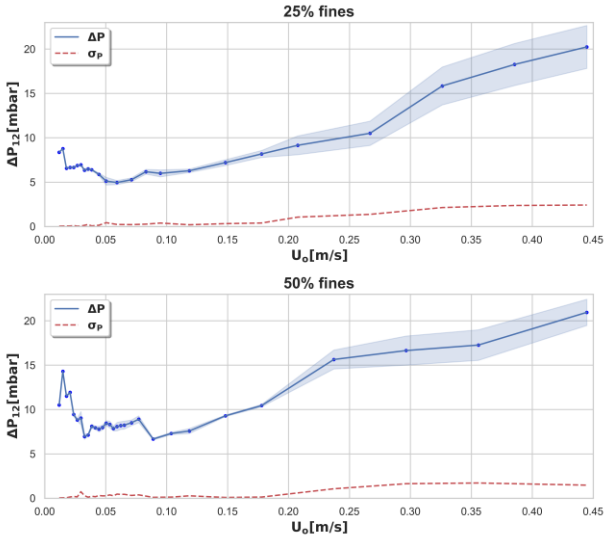

Figure 10: Pressure drop profile for mixed particles

The minimum fluidizing velocity (U_{mf}) could not be accurately determined as the disturbances started at the lowest velocity (0.01 m/s) in both cases of binary particle fluidization. A low minimum fluidizing velocity for a binary mixture may be expected for a large particle size ratio (Rao and Curtis, 2011). A large particle size ratio is present in this study, as the Sauter mean diameter of the fine cement raw meal is 5µm and that for the coarse sand is 226 µm. Sharp peaks in the pressure drop are observed when the binary particles are fluidized. One explanation for the sharp peaks is the phenomenon of entrapment. According to this phenomenon, if some of the fine particles in the top layer are entrapped by the coarse particles, at a sufficiently high gas velocity, the fines may gain enough momentum to break through the bed, causing pressure drop peaks (Rao and Curtis, 2011).

The primary outcome of this study is the fluidization conditions of the binary particles. The pressure drop fluctuations had a relatively high standard deviation in both cases of binary mixing. This observation may indicate good bubbling behavior. However, the visual observation showed a better bubbling behavior for the case with a 25%/75% fine/coarse mass ratio. This mixing ratio may be good for operating the fluidized bed calciner. However, additional studies on the segregation pattern should be done to determine if the fine cement raw meal particles may be removed easily from the binary mixture.

4.4 Simulation of binary particles

A comparison of pressure drop readings in experiments and simulations is shown in Figure 11.

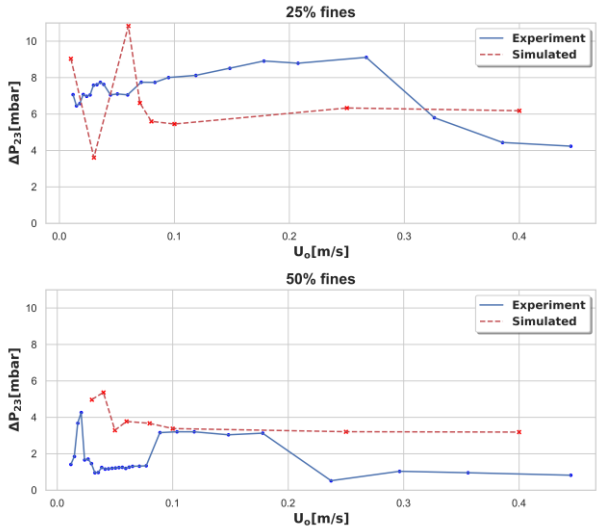

Figure 11: Pressure drop profile comparison of experiment and simulations for mixed particles

The deviations in the pressure drop profile may be due to the deviations in the pure component (discussed in Section 4.2). Additional deviations may be due to segregation effects in the mixed state. However, the pressure drop results are in the same range. Thus, the results may be useful for additional simulations of a full-scale calciner.

Simulation results are shown in Figure 12 and Figure 13. The results are displayed at different superficial gas velocities (U_o) after 30 seconds of simulation (system reached a pseudo-steady state). The fine particles are displayed in green color and coarse particles are displayed in red color.

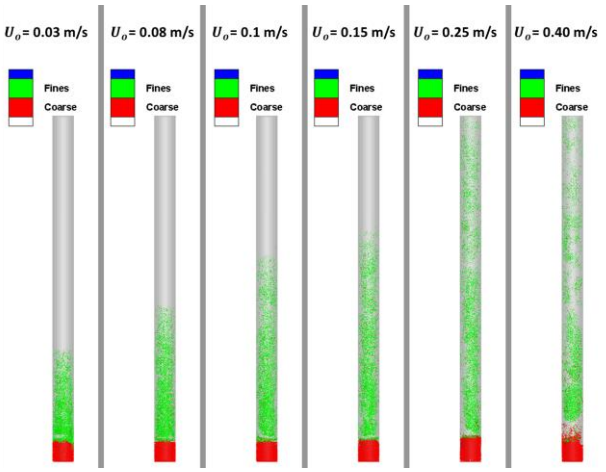

Figure 12: Simulation results from 25% fines at different superficial gas velocities (U_o) (Green = Fines, Red = Coarse)

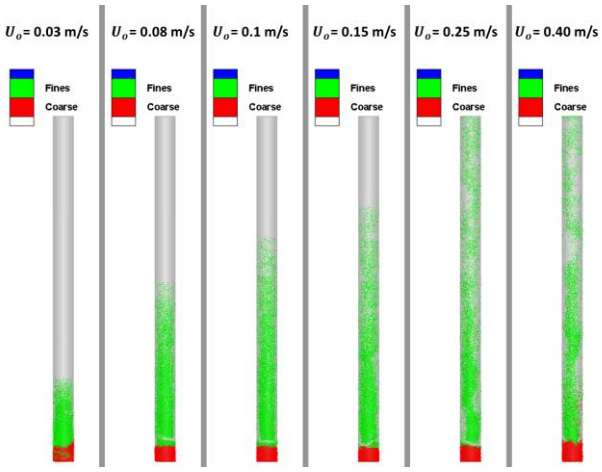

Figure 13: Simulation results from 50% fines at different superficial gas velocities (U_o) (Green = Fines, Red = Coarse)

The snapshots of simulation results shows that the fine particle rises in the column as the superficial gas velocity is increased. At superficial gas velocity of around 0.25 m/s, the fine particles are entrained up to the total column length. The fine particles are further entrained outside the column at this gas velocity. These results may be useful while designing a full-scale calciner.

5 Conclusion

Fluidizing fine cement raw meal (fines) by mixing with sand (coarse) particles appears to be technically feasible. The standard deviation of the pressure fluctuation is a good measure to determine the fluidization conditions. The pure coarse particles had the best fluidizing quality, as expected, while the pure fine particles did not fluidize. For the binary mixtures, stable fluidization was observed with a superficial gas velocity higher than 0.25 m/s at fine/coarse mass ratios of 25%/75% and 50%/50%.

Visually, the fluidization quality was better with a fine/coarse mass ratio of 25%/75%. This condition may be used to operate a fluidized bed calciner by mixing cement raw meal and inert coarse particles.

Simulations were performed to replicate the results from the experiments. The results showed some deviations in pressure drop predictions. However, results were not too far off, so simulations may be applied to a scaled-up version of the calciner.

In practice, some other factors such as segregation, separation efficiency, effect on capacity and energy with 25 % fines, should be addressed in further studies. Considering these effects, an appropriate height should be selected to remove the fines from the top of the bed. Alternatively, a classifier (Jayarathna et. al., 2019) may be placed downstream to separate the fines and the coarse particles. These factors may be included in later studies of a scaled-up version of the calciner.

Acknowledgements

This study was carried out as part of the research project "Combined calcination and CO_2 capture in cement clinker production by use of CO_2-neutral electrical energy – Phase 2". Gassnova and Norcem are greatly acknowledged for funding this project.

References

M. J. Andrews, P. J. O'Rourke. The multiphase particle-in-cell (MP-PIC) method for dense particulate flows. *Int. J. Multiphase Flow*, Vol. 22, No. 2, pp. 379-402, 1996

Simon Becker, Robert Mathai, Kristina Fleiger, Giovanni Cinti. Status report on calciner technology. *CEMCAP*, Rev. 2, 2016.

R. Beetstra, M. A. van der Hoef, J. A. M. Kuipers. Drag force of intermediate Reynolds number flow pas mono- and bidisperse arrays of spheres. *AIChE Journal*, Vol. 53, 2007.

D. Geldart. Types of gas fluidization. *Powder Technology*, Vol 7, pp. 285-292, 1973.

IEA, Technology Roadmap - Low-Carbon Transition in the Cement Industry. 2018.

Ron M. Jacob, Lars-André Tokheim. Electrification of an entrainment calciner in a cement kiln system – heat transfer modelling and simulations. Submitted to the *SIMS conference*, 2021.

Rajan Jaiswal, Cornelius E. Agu, Rajan K. Thapa, Britt M. E. Moldestad. Study of fluidized bed regimes using computational particle fluid dynamics. *SIMS*, 59, 2018.

Chameera K. Jayarathna, Michael Balfe, Britt M.E. Moldestad, Lars-Andre Tokheim. Improved multi-stage cross-flow fluidized bed classifier. *Powder Technology*, Vol 342, pp. 621-629, 2019.

K. Kato, T. Takarada, N. Matsuo, T. Suto, N. Nakagawa. Residence time distribution of fine particles in a powder-particle fluidized bed. Kagaku Kogaku Ronbunshu, Vol. 17, pp. 970-975, 1991.

Daizo Kunii, Octave Levenspiel. Fluidization Engineering, *Butterworth-Heinemann series in chemical engineering*, Edition 2, 1991.

Akhil Rao, Jennifer S. Curtis. Classifying the fluidization and segregation behavior of binary mixtures using particle size and density ratios. *AIChE Journal*, Vol. 57, No. 6, 2011.

Nastaran Ahmadpour Samani. Calcination in an electrically heated bubbling fluidized bed applied in calcium looping, *Master's thesis*, USN, 2020.

Dale M. Snider. An incompressible three-dimensional multiphase particle-in-cell model for dense particle flows. *Journal of Computational Physics*. 170, pp. 523-549, 2001

Dale M. Snider. Three fundamental granular flow experiments and CPFD predictions, *Powder Technology*, Vol. 176, pp. 36-46, 2007.

Tsutomu Tashimo, Tomohiko Suto, Jun Murota, Kunio Kato. Calcination of fine limestone particles by a powder particle fluidized bed. *Journal of chemical engineering of Japan*, Vol. 32, pp. 374-378, 1999.

Lars-André Tokheim, Anette Mathisen, A., Lars E. Øi, Chameera Jayarathna, Nils H. Eldrup and Tor Gautestad. Combined calcination and CO_2 capture in cement clinker production by use of electrical energy, SINTEF proceedings, 4, pp 101-109, 2019

C. Y. Wen, Y. H. Yu. Mechanics of fluidization. Chemical Engineering Process Symposium, pp. 100-111, 1966.

CPFD Simulations on a Chlorination Fluidized Bed Reactor for Aluminum Production: An Optimization Study

Zahir Barahmand[1] Chameera Jayarathna[2] Chandana Ratnayake[1,2]

[1] Department of Process, Energy and Environmental Technology, University of South-Eastern Norway
zbarahmand@gmail.com
[2] SINTEF Tel-Tek, SINTEF Industry, Porsgrunn, Norway

Abstract

Early CPFD simulation studies on designing a fluidized bed reactor for alumina chlorination showed that the model suffers from high particle outflow and dense phase bed channeling. The present study is aimed to optimize the previous alumina chlorination fluidized bed reactor model through modified geometry, parameter modifications, and improved meshing. To optimize the performance of the reactor, complex geometry with an extended top section was combined with a regular cylindrical reactor. Besides, the gas inlet pattern was changed from an ideal uniform distribution to a non-uniform one. Besides, the reactor's inlet diameter is reduced, and the value for the particle sphericity and voidage has been updated based on experimental observations. The results show that the new reactor with an extended cross-sectional area on top has a significantly lower particle outflow even with the higher inlet superficial gas velocity. The paper discusses the optimization steps and relevant changes in reactor performances in detail.

Keywords: Optimization, fluidized bed reactor (FBR), alumina chlorination, Barracuda, CPFD simulation

1 Introduction

Aluminum is now the world's second most used metal (Donaldson & Raahauge, 2013). Since aluminum has a unique combination of appealing properties and functionalities, it allows significant energy savings in many applications, such as vehicles and buildings. Although this energy-saving leads to lower CO_2 emissions, the production process of aluminum still dramatically impacts the environment.

In 1889, the melted cryolite-alumina electrolysis process known as Hall-Héroult (H-H) was started, and the commercial production of metallic aluminum started, and this process has been used almost exclusively in the aluminum production industry (Prasad, 2000). This process has been independently developed and patented, after two young men, oceans apart, around 140 years ago in the United States and France. This discovery in 1886 by C. Hall and P. Héroult has provided the world with the gleaming light metal at reasonable prices. In this method, solid alumina (Al_2O_3) is dissolved in an electrolyte predominantly composed of liquid cryolite (Na_3AlFe_6). The electrolyte is altered with calcium fluoride, aluminum fluoride, and other additives (Peterson & Miller, 2007).

In a typical alumina reduction cell, multiple prebaked carbon anodes are immersed in the electrolyte, and as an intermediate product, oxide ions from alumina dissolution are discharged electrolytically onto the anodes. On the other hand, the oxide intermediate reacts further with the carbon anodes, eventually consuming them by producing gaseous carbon dioxide (CO_2). Inside the electrolyte is a molten aluminum reservoir enclosed in a preformed composite lining and thermally sealed by refractory and insulation components inside a steel shield (Thonstad, 2001). Hence, aluminum is molded by reducing aluminum-containing anions at the electrolyte-metal interface. Although the term cathode is often used to refer to the whole tank of liquid metal and electrolyte, the actual acting cathode is the metal pad or aluminum pool's top surface. The following reaction is the overall reaction of dissolved alumina with carbon to form the products (Barahmand, Jayarathna, et al., 2021d).

$$½\, Al_2O_3\,(dissolved) + ¾\, C\,(s) \rightarrow Al\,(l) + ¾\, CO_2\,(g) \quad (1)$$

This process's total energy conversion is approximately 0.16–0.2 MJ/ton (Barahmand, 2021a). Using titanium diboride cathodes will also substantially reduce energy consumption (up to 20%). The manufacturing of a permanent anode is a more challenging task, and while large-scale experiments are in progress in Japan, Europe, and the United States, no success has been reported. More immediately, sophisticated controls can increase H-H cell efficiency by up to 5%. To anticipate anode effects and optimize its positioning, the pattern of individual cell voltage variations can be monitored and analyzed. Higher energy costs also induce cells to run at lower current densities, resulting in higher efficiency (*Survey of Potential Processes for the Manufacture of Aluminum*, 1979).

The search for feasible alternative processes for aluminum production has been accelerated by rising prices and a lack of large blocks of electrical energy. For instance, the electrolysis of aluminum chloride, sulfide,

nitride; carbothermic reduction of ore or alumina; and the disproportioning reactions of aluminum sulfide or the mono-chloride route can be considered possible alternatives (Barahmand, 2021a). The aluminum industry is undergoing significant changes. It can no longer be selective when it comes to developing sites based on the cost of electricity. Due to the limited electricity available for expansion, the next generation of aluminum smelters must optimize their energy efficiency. This shift has also impacted the importance given to alternative process technology (Grjotheim & Welch, 2016). All of the non-electrolysis processes necessitate extremely high temperatures that can only be reached in an electric furnace. In each case, electrical energy consumption (17.6-22 kWh/kg) is estimated to be higher than that of a Hall-Héroult cell (13.2-17.6 kWh/kg) (*Survey of Potential Processes for the Manufacture of Aluminium*, 1979).

Except for the Alcoa chlorination process, there is no technology for producing aluminum metal that can compete with the Hall-Héroult process in electrical energy consumption. There are some other significant advantages, although, that make the chlorination process attractive. This process does not necessitate the use of pure aluminum oxide as a raw material exclusively. Consequently, the Bayer process could be skipped, eliminating the issue of disposing of vast amounts of red sludge (Barahmand, Jayarathna, et al., 2021a). Carbochlorination can result in relatively high CO_2 concentrations in the process gas, making CO_2 capture and storage easier to implement (Barahmand, 2021a). Carbon's mechanical properties, which are merely a chemical reactant in the chlorination of aluminum chloride, are not required. Consequently, biocarbon may be used instead of coke from petroleum refineries, which the Hall-Héroult process requires, necessitating high mechanical strength and density anodes (Øye, 2019).

The industry has turned its attention to the two-step process of converting alumina to aluminum chloride and then further reducing the aluminum chloride to aluminum metal after failing to find a cost-effective procedure for direct carbothermic reduction of alumina. In the patent literature (Rao & Soleiman, 1986), two chlorination processes are mentioned. The first is a fluidized bed that converts aluminum to aluminum chloride ($AlCl_3$) at a temperature of 590°C. Hydrogen chloride, aluminum hydroxy chloride, aluminum oxychloride, and sodium chloride are also delivered significantly. The sodium comes from the alumina, which contains sodium as an impurity from the Bayer process (Barahmand, 2021a). The stoichiometry of chlorination of gaseous reactants is as follows,

$$Al_2O_3\,(s) + 3Cl_2 + 3CO \rightarrow 2AlCl_3 + 3CO_2 \quad (2)$$

In continuation of the studies on a New Sustainable Aluminum Production (NSAP) process (Barahmand, Aghaabbasi, et al., 2021; Barahmand, Jayarathna, et al., 2021d, 2021a, 2021c, 2021b), this optimization study aims to design an industrial alumina chlorination fluidized bed reactor (isothermally) to achieve the minimum particle outflow and to improve the hydrodynamics inside the reactor by minimizing the channeling effect in the dense phase bed.

2 Overall Design Criteria

The present study aims to design an industrial fluidized bed reactor for pure γ-alumina chlorination in the presence of equimolar carbon monoxide and chlorine gas mixture under the isothermal condition at 700°C. The reactor should be designed for handling 0.6 kg/s of alumina feed. There are no specified limitations for the reactor dimensions or the geometry. However, it is recommended to minimize internals (specifically for cooling and solid circulation). Moreover, because of some technical considerations, such as the possibility of having a considerable percentage of α-alumina in the feed, at the first step, the rector has been designed with no circulation. In the following sections, the main design factors and considerations are discussed.

Circulation System: An early study (Barahmand, Aghaabbasi, et al., 2021) ended up having a turbulent regime using an internal circulation system, but the reactor will be designed for a bubbling regime with better hydrodynamics. On the other hand, considering the highly corrosive environment inside the reactor and the existence of α-alumina impurity in the system, which is not favorable, it avoids circulation internally or externally.

Gas-Solid Separator: The project's primary goal is to minimize the solid escape from the system. Therefore, an external high-efficiency cyclone with an efficiency of 99% will be designed to handle maximum solid carryover. The cyclone is designed for half of the inlet solid flow rate to the reactor (0.01-0.3 kg/s). The other design parameters, such as pressure, fluid properties, and average particle size, will be calculated from simulations.

Regime and Bed Type: As mentioned earlier, the reactor should be designed for the bubbling regime. A free bubbling bed with no internal baffles is recommended to use. To have a smaller bubble size and lower rise velocity, the superficial velocity is chosen in a range close to the minimum bubbling velocity.

Bed Aspect Ratio (H/D): The bed height (H) to the bed diameter (D) ratio is known as the bed aspect ratio (H/D), which is one of the most crucial factors for reactor design calculations (Shaul et al., 2012). The superficial gas velocity by matching the required fluidization regime is used to determine the bed diameter. The bed is generally called tall or deep if the aspect ratio is more significant than unity. On the other side, a shallow bed has an aspect ratio of one or less than one. The precise aspect ratio that marks the transition

between a deep and shallow fluidized bed has yet to be determined (Sathiyamoorthy & Horio, 2003). To have better hydrodynamics in the bed, it has been avoided using a shallow bed. The minimum aspect ratio has been about unity as a safe value (Kunii & Levenspiel, 1991). The given bed aspect ratio selected by the authors in an early study (Barahmand, Jayarathna, et al., 2021a) has been used in the current study.

Reactor Diameter: Based on the carbon monoxide and chlorine mixture's stoichiometry and physical properties, the needed volumetric flow rate of the fluid at the inlet to handle 0.6 kg/s of solid can be calculated easily. On the other hand, the fluid's superficial velocity range is chosen before being very close to minimum bubbling velocity (Regime and Bed Type), which can be calculated too (Barahmand, Aghaabbasi, et al., 2021).

Reactor height: The height of a fluidized bed reactor can be divided into dense and lean phases. Solids lose density as they rise in height. The lean process's height (or freeboard) can be separated into two zones, with the lower section known as the Transport Disengaging Height (TDH). If there is no secondary reaction in the freeboard region, the reactor outlet can be located on top of TDH or above. Otherwise, it can reduce the freeboard and add a more efficient cyclone to the system. Both dense-phase and TDH can be calculated for a bubbling regime (Kunii & Levenspiel, 1991).

Operating Pressure: These parameters highly affect hydrodynamics by influencing fluid's physical properties (Barahmand, Aghaabbasi, et al., 2021). There is no specific pressure in the system because the pressure at the bottom and top of the reactor is not identical, and there is a pressure drop to overcome the bed height of the reactor. The upstream pressure is the bottleneck to define a pressure for the system. It is enough to calculate the needed pressure at the reactor's bottom by choosing a pressure for the fluidized bed outlet. Depending on how the flow boundary at the inlet is defined, this pressure can be calculated automatically by the simulation software (Barracuda®) or defined manually.

Gas Distributor: The distribution mechanism in the gas inlet of the fluidized bed reactor significantly affects hydrodynamics. For example, it can contribute to channeling in the bed or change the bubble size or regime in the bed (Kunii & Levenspiel, 1991). At the first step, a uniform and flat distribution throughout the whole inlet area will be used. In the next step, a grid plate or sparger should be considered a uniform distributing system to be more realistic. Figure 1 shows different types of sparger arrangements in a fluidized bed.

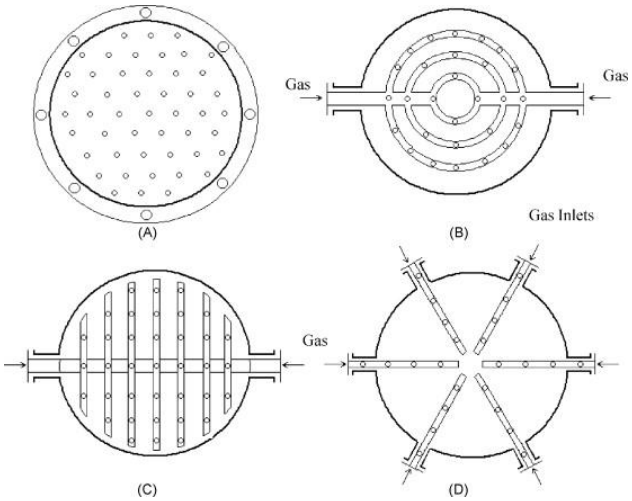

Figure 1. (a) Sieve plate sparger, (b) multiple ring sparger, (c) spider, and (d) pipe sparger (Kulkarni et al., 2009).

Alumina: Many types of alumina have different properties (Barahmand, Jayarathna, et al., 2021d). In the present study, pure γ-alumina has been taken into account, and the effect of impurities is neglected. Each solid particle has many characteristic properties which affect the fluidized bed system. Parameters properties such as particle size distribution, sphericity, voidage, and density should be defined as accurately as possible (Barahmand, Jayarathna, et al., 2021b).

Reactor Geometry: A simple cylindrical reactor with a uniform circular cross-section has been used in early studies (Barahmand, Aghaabbasi, et al., 2021; Barahmand, Jayarathna, et al., 2021a). The reactor's optimum dimensions should be chosen by changing the bed aspect ratio, superficial velocity, and reactor height. An exit geometry should be selected between smooth and abrupt (Harris et al., 2003; Mabrouk et al., 2008). Any change in the reactor geometry can be applied to achieve lower particle escape and desirable hydrodynamics. For example, cylindrical FB reactors inherited several weak points. Yang et al. have investigated the effect of the expanded cross-section at the top of the reactor and related hydrodynamics.

Reaction kinetics: The present study simulates the single overall reaction (2) in Barracuda®. The reaction kinetics are based on (Barahmand, Jayarathna, et al., 2021d). Although the alumina chlorination at 700℃ is very fast and the reactor height can be reduced, the hydrodynamics inside the reactor plays a crucial role. The H/D highly affects the overall reactor height, and the reported value is minimum equal to unity (Kunii & Levenspiel, 1991) for Geldart A particles. On the other hand, reaction kinetics is highly correlated with temperature, particle size distribution, and porosity (Barahmand et al., 2021d).

Heat Transfer: Although the primary goal of the present study is to touch the project objectives under isothermal conditions at 700℃, the thermal study of the chlorination process is one of the most critical design considerations (Barahmand et al., 2021c). The literature confirms that the best and optimum temperature for the alumina chlorination process is 700℃, but taking the industrial design limitations into account, 600℃ will be the optimum temperature (Gokcen, 1983).

Solid Feeder: The current fluidized bed is a continuous reactor that alumina is fed to the reactor with a feeding rate of 0.6 kg/s. In general, the powder can be transported mechanically or pneumatically (or air-assisted). The screw feeder, as an example of a mechanical conveyor or pneumatic conveying system, can be used in the design. In this project, it is considered that the powder is injected pneumatically using CO_2. Another critical point is the location and direction of the injection. In some cases, particles' downward movement positively affects the reaction (For example, alumina chlorination in fluidized bed (Gokcen, 1983)). However, taking the other considerations, such as possible particle outflow, into account, placing the particle injection at the reactor's bottom side-wall is beneficial.

Construction Material: Although the current study does not directly deal with the materials, reactor design is affected by general considerations. The typical fluidized bed uses a carbon steel shell lined with a particular alumina refractory (Barahmand, Aghaabbasi, et al., 2021).

Erosion: There are three primary sources for erosion in a fluidized bed, temperature, chemicals, and solid particles (Barahmand, 2021b). All the internal surfaces that contact a corrosive or very high-temperature fluid are in danger of erosion. On the other hand, in higher velocities, solid particles can cause erosion, and usually, it is associated with transitional and directional changes in the system. For example, most erosive wear may occur in the internal cyclone wall or near the elbow of bent pipes. In the present study, a particular alumina refractory is considered a reactor lining to protect against very high temperatures and chemical corrosion. Although alumina particles are highly abrasive (Haugland et al., 2019), this effect may be minimal because of the low superficial velocity in the system. The erosion has not been considered in this study.

Drag Model: The force acting on a particle by the fluid flow around it is determined by the particle's drag model. The Barracuda® provides a range of predefined drag models that the WenYu-Ergun blended drag model could be more suitable for the current study. Since the Wen and Yu correlation is appropriate for more dilute systems and the Ergun relationship is appropriate at higher packing fractions, proposed a drag function blending both the Wen-Yu and Ergun functions as the following (Gidaspow, 2012).

For $\theta_p < 0.75\theta_{cp}$, the drag model can be calculated by the Wen-Yu model (D_1).

$$D_1 = \begin{cases} \frac{24}{Re}\theta_f{}^{-2.65} & Re < 0.5 \\ \frac{24}{Re}\theta_f{}^{-2.65}(1 + 0.15Re^{0.687}) & 0.5 \le Re \le 1000 \\ 0.44\theta_f{}^{-2.65} & Re > 1000 \end{cases} \quad (3)$$

For $\theta_p > 0.85\theta_{cp}$, the drag model can be calculated by the Ergun drag function (D_2) as below.

$$D_2 = 0.5\left(\frac{180\theta_p}{\theta_f Re} + 2\right)\frac{\rho_f|u_f - u_p|}{r_p\rho_p} \quad (4)$$

For $0.75\theta_{cp} \le \theta_p \le 0.85\theta_c$, the following equation can derive the drag model:

$$D = (D_2 - D_1)\left(\frac{\theta_p - 0.75\theta_{cp}}{0.85\theta_{cp} - 0.75\theta_{cp}}\right) \quad (5)$$

Where θ_p and θ_f are the particle and fluid volume fraction respectively, θ_{cp} is the particle volume fraction at the close pack[1], Re is the Reynolds number, u_f and u_p are fluid and particle velocity, ρ_p is particle density and r_p is the average particle radius.

3 3D Multiphase Particle-in-Cell Approach

Barracuda®'s technology is based on 3D Multiphase Particle-in-Cell (3D-MP-PIC), a patented computational technique for CFD simulation of gas-particle flows that includes close fluid-particle coupling as well as careful consideration of thermal physics and reaction chemistry (Ahmadpour Samani et al., 2020). For dense particle flows, a three-dimensional, multiphase particle-in-cell approach is presented. The computational technique uses a continuum model to solve the governing equations of the fluid phase and a Lagrangian model to solve the governing equations of the particle phase (Snider, 2001). Through mapping particle properties to an Eulerian grid and then mapping back-calculated stress tensors to particle positions, the difficulties associated with estimating inter-particle interactions with dense particle flows with volume fractions above 5% have been removed. A robust sub-grid particle normal stress model for isolated particles that eliminates the need for an implicit measurement of normal particle stress on the grid has been presented. The properties of interpolation operators that provide compact support, conservatism, and a quick solution for

[1] The close pack volume fraction specifies the maximum volume fraction of particles when they are packed randomly.

a broad particle population are defined. The solution scheme allows for particle forms, sizes, and mass distributions with no numerical diffusion from the Lagrangian particle equations. The fluid momentum and pressure equations are indirectly solved, resulting in a stable solution.

There are two approaches to this, the Continuum and the Particulate Phase. The continuity equation for a fluid with no interphase mass transfer is (Verma & Padding, 2020).

$$\frac{\partial \theta_f}{\partial t} + \nabla.\left(\theta_f u_f\right) = 0 \tag{6}$$

The momentum equation for the fluid will be as (7).

$$\frac{\partial\left(\theta_f u_f\right)}{\partial t} + \nabla.\left(\theta_f u_f u_f\right) = -\frac{1}{\rho_f}\nabla P - \frac{1}{\rho_f}\mathrm{F} + \mathrm{g}\theta_f \tag{7}$$

where, g is the acceleration gravity, F is "the rate of momentum exchange per volume between the fluid and particle phases," P is fluid pressure, and ρ_f is the fluid density. In the Particulate Phase, the particle probability distribution function $\emptyset\,(X, u_p, \rho_p, \Omega_p, t)$ is used to define the dynamics of the particle process, where X is the particle position, u_p is the particle velocity, ρ_p is the particle density, and Ω_p is the particle volume (Snider, 2001). For the time being, it is thought that each particle's mass remains stable over time (i.e., no mass transfer between particles or to the fluid), although particles may vary in size and density. The time evolution is obtained by solving a Liouville equation (Williams, 1985) for the particle distribution function.

$$\frac{\partial \emptyset}{\partial t} + \nabla.\left(\emptyset\, u_p\right) + \nabla_{u_p}.(\emptyset A) = 0 \tag{8}$$

where ∇_u is the divergence operator concerning velocity. Using the definition from (Andrews & O'Rourke, 1996), the discrete particle acceleration, A, can be defined as,

$$A = D_p\left(u_f - u_p\right) - \left(\frac{1}{\rho_p}\nabla P + \frac{1}{\theta_p \rho_p}\tau\right) + \mathrm{g} \tag{9}$$

where, the terms describe acceleration due to aerodynamic drag, pressure gradient, interparticle stress gradient, and gravity, respectively, the Gidaspow drag model (Gidaspow, 2012), which is a combination of the Wen and Yu (Wen & Yu, 1966) and the Ergun (Ergun, 1952) drag models (3-5), can be used in (9). The present study optimizes the alumina chlorination in a fluidized bed reaction having a bubbling regime. The superficial velocity of the fluid is close to the minimum bubbling velocity.

4 CPFD Simulations

The standard range for the bed aspect ratio (H/D) is not thoroughly investigated and discussed in the literature. The best aspect ratio used in the present study is based on the authors' previous work (Barahmand et al., 2021a), equal to 2. The reaction kinetics and alumina properties are explained elsewhere (Barahmand et al., 2021d). The base model was developed with simple cylindrical geometry and a smooth exit in the first step. The smooth exit does not affect the hydrodynamics of the reactor top (Mabrouk et al., 2008).

4.1 Base Model

The chlorine concentration (as a factor of conversion rate) and particle distribution (as a factor of reactor hydrodynamics) have been studied in the model. In the first step, the gas reactants are distributed homogeneously from the bottom of the reactor (ideal distribution). Figure 3 illustrates the particle mass flux in different heights in the reactor. As seen in the figure, the red ring emphasizes particle escape through the reactor wall.

Studying the particle outflow shows that for uniform inflow, the average particle outflow at the pseudo-steady-state is about 0.38 kg/s, almost 63% of the particle inflow (Figure 2). On the other hand, the particle escape through the wall harms reaction conversion. 'Due to high resistance within the particle bed, the fluid temps to escape close to the reactor wall, increasing fluid velocity in the near-wall region. As a result, the reactants have less time to react.

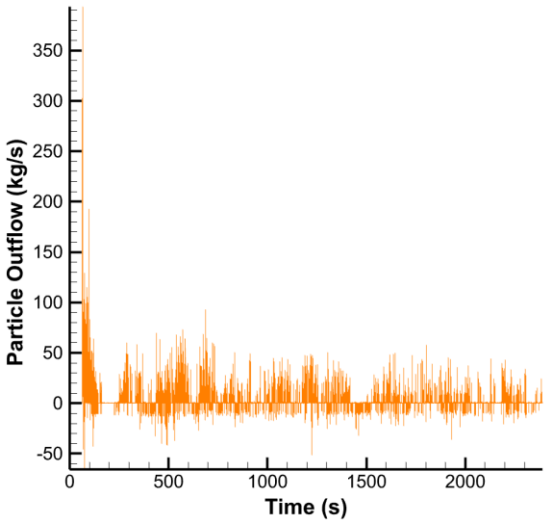

Figure 2. Particle outflow (kg/s) with uniform distribution

A non-uniform distribution pattern (Figure 4) with higher velocity in the middle and gradually decreasing toward the inner walls (Figure 5) has been applied to the system to solve this problem. The results have shown a significant change in the reactor hydrodynamics and particle escape.

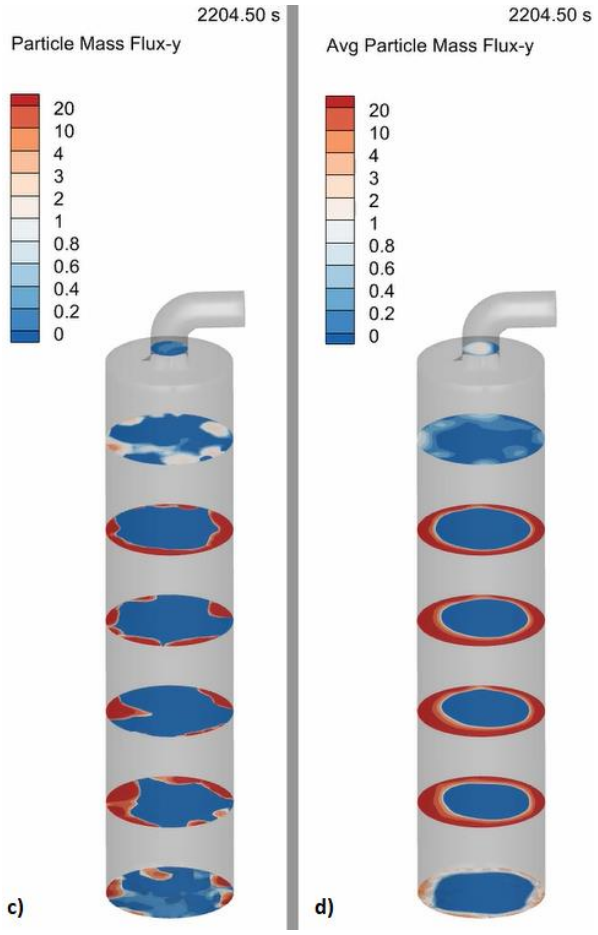

Figure 3. The particle mass flux (kg/sm^2) in different heights with a uniform distribution. c) Particle mass flux at the specific time, and d) Average particle mass flux in the last 300 seconds.

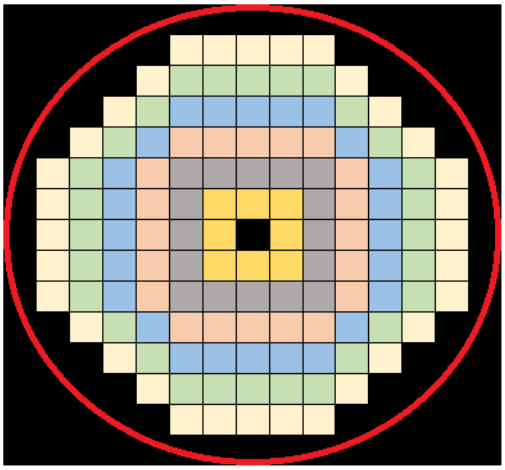

Figure 4. Defined non-uniform ring distribution in Barracuda®

Changing the fluid distribution pattern shows a considerable change in the bed's hydrodynamics. As seen in Figure 6, the ring area is turned to a crescent shape. Compared with uniform distribution, the particle outflow is 0.59 kg/s which is two times more and almost identical to the particle feed rate.

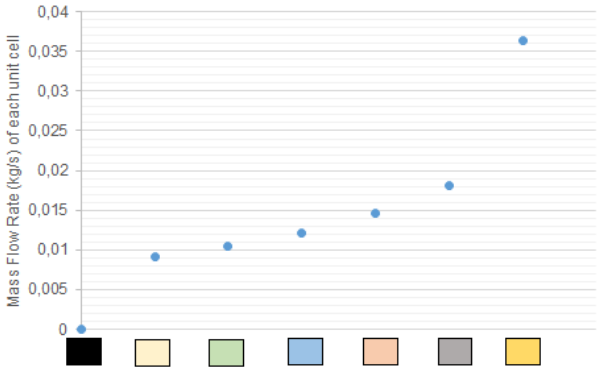

Figure 5. Inlet gas ($CO+Cl_2$) mass flow rate of each cell-color scale refers to Figure 4.

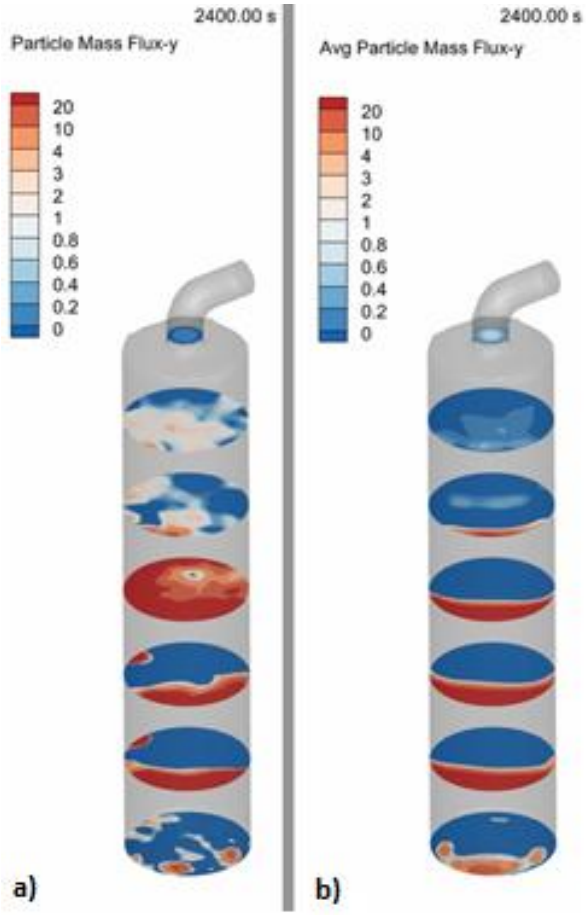

Figure 6. The particle mass flux (kg/s.m^2) in different heights with the non-uniform distribution. a) Particle mass flux at the specific time, and b) Average particle mass flux in the last 300 seconds.

Although the hydrodynamics has experienced a considerable change, the chlorine concentration through the reactor is almost constant due to the very high reaction rate. Table 1 gives the chlorine concentration through the reactor from bottom to top in the specified heights in Figure 3 and Figure 6. Although the results confirm that the conversion rate becomes complete at the bottom of the reactor, reducing the reactor height is

not suggested to keep the best hydrodynamics (Barahmand, 2021a).

Table 1. Average Cl_2 concentration (mg/l) in different heights of the reactor.

Level	**Uniform**	**Non-Uniform**
0	289.27	65.23
1	0.35	0.59
2	0.05	0.04
3	0.03	0.02
4	0.02	0.02
5	0.02	0.04
6	0.03	0.03
7	0.02	0.03

In these simulations, the particle escape from the top of the reactor is the biggest challenge.

4.2 Optimized model

As discussed in Section 2, Yang et al. have used an expanded section to reduce the slugging and to solve this problem effectively. Therefore, it may positively affect reducing particle outflow (Yang & Keairns, 1980). Figure 7 illustrates a schematic view of the new geometry with the expanded cross-sectional at the top. In the current simulation, a total number of 65000 cells have been used.

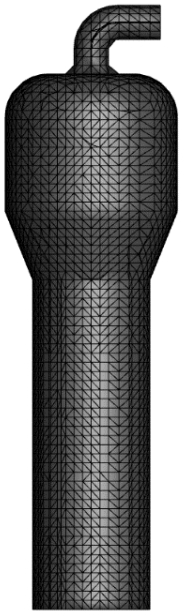

Figure 7. The meshed geometry with the expanded cross-sectional area on top

Similarly, for uniform and non-uniform distributions, the bed hydrodynamics, particle outflow, and Cl_2 concentration have been studied. As expected, the geometry shows no effect on the reaction and chlorine consumption.

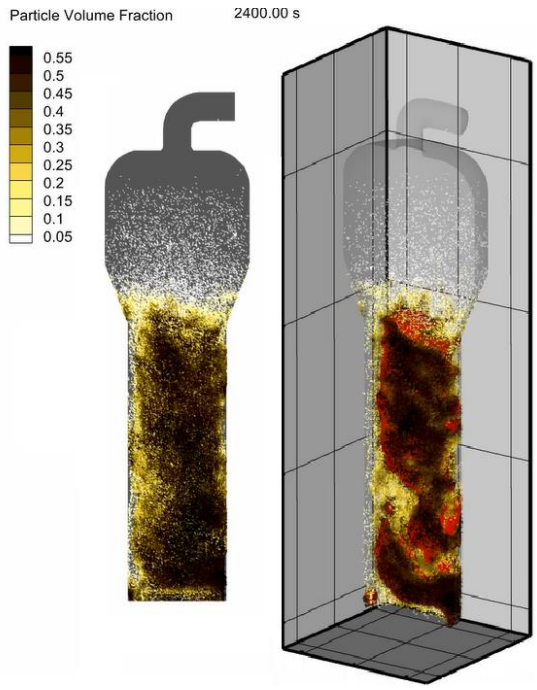

Figure 8. Particle distribution through the reactor with the non-uniform flow.

As seen in Figure 8, the expanded bed is located in the bottom cylindrical section of the reactor. As a result, a negligible effect on particle escape through the reactor wall has been expected. In comparison with cylindrical models, Figure 9 and Figure 10 confirm this phenomenon.

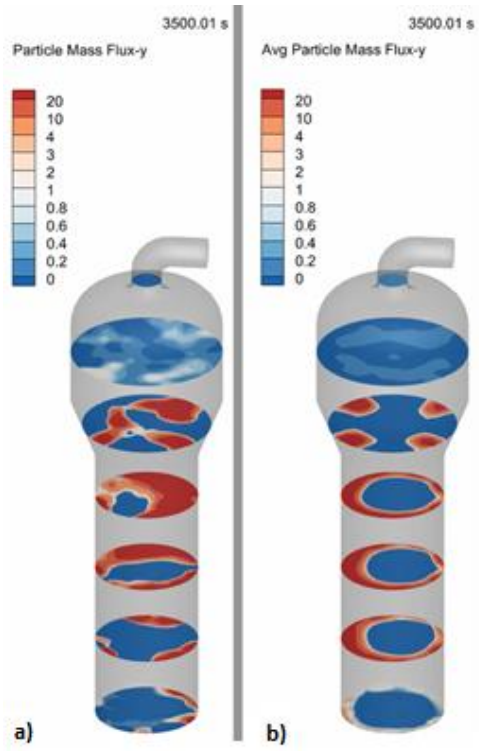

Figure 9. The particle mass flux (kg/s.m^2) in different heights with a uniform distribution. a) Particle mass flux at

the specific time, and b) Average particle mass flux in the last 300 seconds.

Nevertheless, in both cases, particle outflow has been dropped significantly. Table 2 gives comparative data for all cases.

Table 2. Particle outflow (kg/s) in different cases

	Uniform gas Distribution	Non-Uniform gas Distribution
Cylindrical	0.38	0.59
New Design	0.15	0.0004

Although the optimized geometry has shown a remarkable performance in reducing the particle escape from the top of the reactor, this design may suffer from the possibility of particle deposition and caking phenomenon in the conical top sections. Applying a non-uniform inlet flow pattern has reduced the channeling effect, and has resulted less scape through the sidewall has been observed. Figure 11 shows a channel created inside the bed.

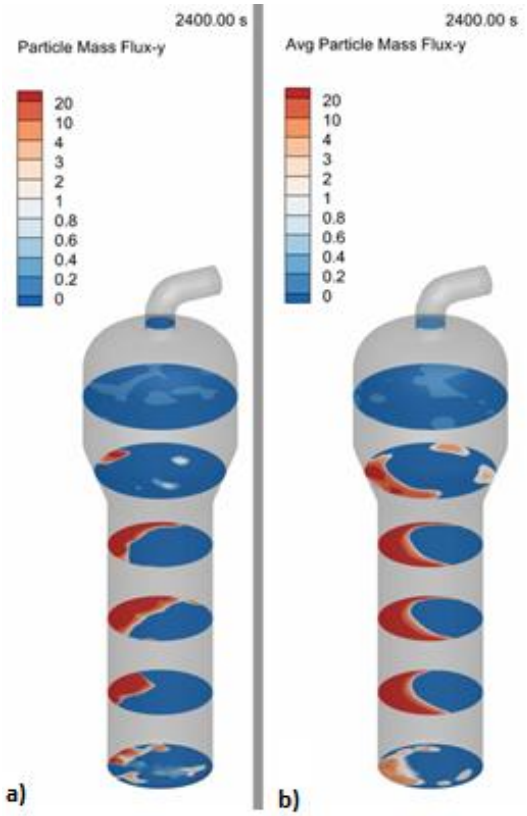

Figure 10. The particle mass flux (kg/s.m^2) in different heights with the non-uniform distribution. a) Particle mass flux at the specific time, and b) Average particle mass flux in the last 300 seconds.

5 Conclusion

The modified geometry leads to minimizing the particle outflow significantly and helps the reactor's hydrodynamics. On the other hand, in contrast with simple cylindrical geometry, non-uniform gas distribution contributes to reducing high gas escape close to the wall, enhancing the reaction. Combining geometrical modification and change in gas injection, the reactor has now shown quite promising performances. It is crucial to validate the CFD simulation data with a lab-scale experimental unit as future work. Moreover, even though current simulations are done based on mess specifications from CPFD software (Barracuda®), the mesh convergence can be helpful to find the right mesh size and further improvement of the model.

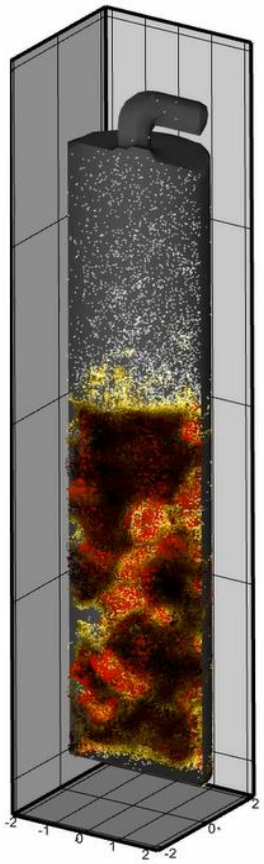

Figure 11. Channeling effect in a cylindrical reactor with uniform distribution.

References

N. Ahmadpour Samani, C. Jayarathna, and L. A. Tokheim. CPFD simulation of enhanced cement raw meal fluidization through mixing with coarse, inert particles. *In proceedings - 61st SIMS Conference on Simulation and Modelling SIMS 2020*, Finland, 2020. doi:10.3384/ecp20176399

M. J. Andrews and P. J. O'Rourke. The multiphase particle-in-cell (MP-PIC) method for dense particulate flows. *International Journal of Multiphase Flow*, *22*(2), 379–402. 1996. doi:10.1016/0301-9322(95)00072-0

Z. Barahmand. *Design of an Industrial Chlorination Reactor using CPFD Simulations*, Master's Thesis. University of South-Eastern Norway, 2021a.

Z. Barahmand, O. Aghaabbasi, E. K. L. Rustad, J. L. Salcido, C. Jayarathna, and C. Ratnayake. Designing of a medium-scale circulating fluidized bed reactor for chlorination of processed aluminum oxide. *In proceedings - 1st SIMS EUROSIM Conference on Modelling and Simulation*, Finland, 2021.

Z. Barahmand, C. Jayarathna, and C. Ratnayake. CPFD modeling of the hydrodynamics and reaction kinetics of alumina chlorination in an industrial fluidized bed reactor. *In proceedings - 1st SIMS EUROSIM Conference on Modelling and Simulation*, Finland, 2021a.

Z. Barahmand, C. Jayarathna, and C. Ratnayake. Sensitivity and uncertainty analysis in a fluidized bed reactor modeling. *In proceedings - 1st SIMS EUROSIM Conference on Modelling and Simulation*, Finland, 2021b.

Z. Barahmand, C. Jayarathna, and C. Ratnayake. Study of the thermal performance of an industrial alumina chlorination reactor using CPFD simulation. *In proceedings - 1st SIMS EUROSIM Conference on Modelling and Simulation*, Finland, 2021c.

Z. Barahmand, C. Jayarathna, and C. Ratnayake. The effect of alumina impurities on chlorination in a fluidized bed reactor: A CPFD study. *In proceedings - 1st SIMS EUROSIM Conference on Modelling and Simulation*, Finland, 2021d.

D. Donaldson and B. Raahauge. *Essential Readings in Light Metals, Alumina and Bauxite*. John Wiley & Sons, 2013.

S. Ergun. Fluid flow through packed columns. *Fluid Flow Through Packed Columns*, *48*, 89–94. Scopus, 1952.

D. Gidaspow. *Multiphase Flow and Fluidization: Continuum and Kinetic Theory Descriptions, 2012*.

N. A. Gokcen. *Rates of chlorination of aluminous resource*, pages 28, U.S. Department of the Interior, Bureau of Mines, 1983.

K. Grjotheim and B. Welch. Impact of Alternative Processes for Aluminium Production on Energy Requirements. In G. Bearne, M. Dupuis, & G. Tarcy (Eds.), *Essential Readings in Light Metals: Volume 2 Aluminum Reduction Technology*, pages 1049–1055. Springer International Publishing, 2016. doi:10.1007/978-3-319-48156-2_154

A. T. Harris, J. F. Davidson, and R. B. Thorpe. Influence of exit geometry in circulating fluidized-bed risers. *AIChE Journal*, *49*(1), 52–64, 2003. doi:10.1002/aic.690490107

I. B. Haugland, O. Kjos, A. Røyset, P. E. Vullum, T. A. Aarhaug, and M. Halstensen. Alumina Scale Composition and Growth Rate in Distribution Pipes. In C. Chesonis (Ed.), *Light Metals 2019* (pp. 697–706). Springer International Publishing, 2019. doi:10.1007/978-3-030-05864-7_86

A. V. Kulkarni, S. V. Badgandi, and J. B. Joshi. Design of ring and spider type spargers for bubble column reactor: Experimental measurements and CFD simulation of flow and weeping. *Chemical Engineering Research and Design*, *87*(12), 1612–1630, 2009. doi:10.1016/j.cherd.2009.06.003

D. Kunii and O. Levenspiel. *Fluidization Engineering*. Butterworth-Heinemann, 1991.

R. Mabrouk, J. Chaouki, and C. Guy. Exit effect on the hydrodynamics of the internal circulating fluidized bed riser. *Powder Technology - POWDER TECHNOL*, *182*, 406–414, 2008. doi:10.1016/j.powtec.2007.07.008

B. Øye. Could the chloride process replace the Hall-Héroult process in aluminum production?. 2019, March 28.

W. S. Peterson and R. E. Miller. *Hall-Héroult Centennial: First Century of Aluminum Process Technology*, 2007.

S. Prasad. Studies on the Hall-Héroult aluminum electro winning process. *Journal of the Brazilian Chemical Society*, *11*, 245–251, 2000. doi:10.1590/S0103-50532000000300008

Y. K. Rao and M. K. Soleiman. *Alumina chlorination*. United States Patent No. US4565674A, 1986. https://patents.google.com/patent/US4565674A/en

D. Sathiyamoorthy and M. Horio. On the influence of aspect ratio and distributor in gas fluidized beds. *Chemical Engineering Journal*, *93*(2), 151–161, 2003. doi:10.1016/S1385-8947(02)00257-7

S. Shaul, E. Rabinovich, and H. Kalman. Generalized flow regime diagram of fluidized beds based on the height to bed diameter ratio. *Powder Technology*, *228*, 264–271, 2012. doi:10.1016/j.powtec.2012.05.029

D. M. Snider. An Incompressible Three-Dimensional Multiphase Particle-in-Cell Model for Dense Particle Flows. *Journal of Computational Physics*, *170*(2), 523–549, 2001. doi:10.1006/jcph.2001.6747

Survey of potential processes for the manufacture of aluminium (ANL/OEPM-79-4). Little (Arthur D.), Inc., Cambridge, MA (USA), 1979. doi:10.2172/5669730

J. Thonstad, J. Aluminium electrolysis: Fundamentals of the Hall-Héroult process, 2001.

V. Verma and J. T. Padding. A novel approach to MP-PIC: Continuum particle model for dense particle flows in fluidized beds. *Chemical Engineering Science: X*, *6*, 100053, 2020. doi:10.1016/j.cesx.2019.100053

C. Wen and Y. Yu. Mechanics of fluidization. *The Chemical Engineering Progress Symposium Series*, *62*, 100–111, 1966.

F. A. William. *Combustion Theory*. The Benjamin/Cummings Publishing Company, Inc, 1985.

W. Yang and D. Keairns. *The effect of an expanded section on slugging*, 1980. doi:10.1002/AIC.690260124

Sensitivity and Uncertainty Analysis in a Circulating Fluidized Bed Reactor Modeling

Zahir Barahmand[1] Chameera Jayarathna[2] Chandana Ratnayake[1,2]

[1] Department of Process, Energy and Environmental Technology, University of South-Eastern Norway
zbarahmand@gmail.com
[2] SINTEF Tel-Tek, SINTEF Industry, Porsgrunn, Norway

Abstract

As in many real applications, in the world of fine powders and small particles, depending on the accuracy of the relevant method, there are uncertainties and vagueness in the parameters such as particle size, sphericity, initial solid void fraction, envelope density, etc. In some cases, there are different methods to measure a parameter, such as a particle size that depends on the method (based on length, weight, and volume); the measured values may be significantly different from each other. Therefore, there is no crisp or exactly known parameter in many cases because of the fine powders' inherent uncertain nature. On the other hand, being characteristic of the dynamic systems, physical parameters such as temperature and pressure fluctuate but can be kept in an acceptable range, affecting the main design parameters such as fluid density and dynamic viscosity.

The most traditional tools and methods for simulating, modeling, and reasoning are crisp, deterministic, and precise, but these values are estimated or changing (randomly or stochastically). Several approaches can describe this phenomenon. Moreover, when it comes to uncertainties, mathematical tools are probably the best solutions. With the fuzzy set theory method, linguistic variables or ranges can be converted to mathematical expressions, and consequently, instead of crisp values, these can be applied to the equations. The uncertainty analysis can be more important when the model is susceptible to one parameter. A preliminary sensitivity analysis on a fluidized bed application has shown that the solid void fraction has the highest, and the fluid density has the lowest sensitivity to its operation. The performed uncertain theoretical approach has been validated by CPFD simulation using Barracuda v20.1.0.

Keywords: Fuzzy set theory, Sensitivity analysis, uncertainty analysis, circulating fluidized bed reactor, CPFD simulation

1 Introduction

In general, a solid particle in a fluid behaves in a state of uncertainty. This fact motivates to study the behavior of uncertain phenomena. Most traditional formal modeling, reasoning, and computing tools are crisp, deterministic, and precise. In order to model uncertainty, it is essential to know the uncertainty causes in nature and how it is possible to deal with it. In real-life applications, the system complexity inevitably results in weak models with a high degree of parametric or functional uncertainty. If the controlled system has a multi-valued function or exhibits several modes of behavior during the operation, the problem gets much more complex (Herzallah, 2005).

Generally, gas-solid systems perform pretty in different ways under minor changes of process conditions. For example, changing the velocity from below the minimum fluidization velocity up to a very high velocity, the system experiences many regimes such as the fixed bed, minimum fluidization, smooth, bubbling, slugging, turbulent fluidization, and finally lean phase fluidization with pneumatic transport (Kunii & Levenspiel, 1991). For instance, the hydrodynamics in the fluidized bed is heavily influenced by solid particle properties such as size distribution, sphericity, and voidage. The measurement error, for instance, maybe the most crucial factor for the uncertainty of the particle size distribution (Tinke, 2020).

There are different approaches to categorizing uncertainties in a system. These can be classified into two categories. The first is the uncertainty in a mathematical sense due to the difference between measured, estimated, and actual values, including errors in observations or calculations (Zhu, 2015). The second is the sources of uncertainty, including uncertainty in the particle and fluid physical properties, reaction kinetics (Valkó & Turányi, 2020), reactor temperature, etc.

Traditional and deterministic approaches to a complex system study (such as powder and particulate systems) would not deal with the above uncertainties. Therefore, as seen in Figure 1, the most used uncertainty modeling techniques include probabilistic, possibilistic, and hybrid possibilistic–probabilistic methods, information Gap decision theory (IGDT), and robust optimization (Aien et al., 2016).

These approaches are primarily used to assess the effect of uncertain input parameters on system output parameters. The critical distinction between these

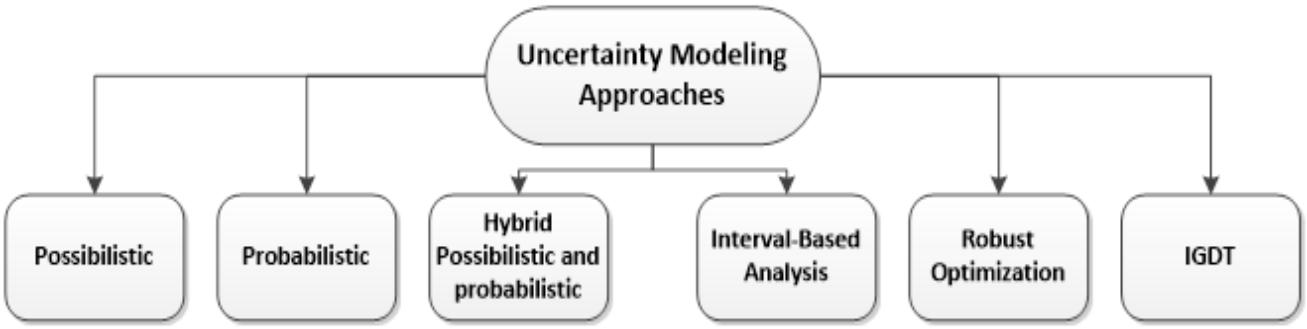

Figure 1. The uncertainty modeling approaches

methods is that they use different ways to describe the ambiguity of input parameters. The following is a short overview of how the above approaches can be used to model uncertainty:

• *Probabilistic approach:* it is assumed that the probability distribution functions of input variables are known. One of the earliest works in stochastic programming was done by (Dantzig, 1955).

• *Possibilistic approach:* a membership function is assigned to model input parameters in this approach (Zadeh, 1999).

• *Hybrid possibilistic–probabilistic approaches:* in this approach, both random and possibilistic parameters are used to handle the uncertain input parameters (Aien et al., 2014; Soroudi & Ehsan, 2011).

• *Information Gap Decision Theory (IGDT):* contrary to probabilistic and possibilistic decision theory, this does not use probability distribution or membership function. Instead, it measures the deviation of differences between parameters and their estimates, but not the probability of outcomes (Ben-Haim, 2001).

• *Robust optimization:* For describing the uncertainty of input parameters, uncertainty sets are used. Obtained decisions are optimal for the worst-case realization of the uncertain parameter within a given set by using this technique (Soyster, 1973).

• *Interval analysis:* The unknown parameters are assumed to take their values from a known interval. It resembles probabilistic simulation with a uniform probability distribution function in several ways (Moore et al., 2009).

Between these causes, the lack of information and measurement errors found in the system can be modeled with the fuzzy set theory, which was first introduced in 1965 (Zadeh, 1965). Reducing the weaknesses of the probability theory, Zadeh introduced the possibility theory (Zadeh, 1999), which naturally complements the fuzzy set theory for handling uncertainty induced by fuzzy and incomplete pieces of information. Possibility theory turns out to be a non-probabilistic view of uncertainty that aims to model states of partial or complete ignorance rather than capture randomness. Using this theory, Dubois and parade (Dubois & Prade, 1983) have studied the ranking of fuzzy numbers considering the possibility and necessity of events. (Goetschel & Voxman, 1986) have introduced a model for ranking fuzzy numbers, which become the primary notion for introducing possibilistic moments by Carlson and Fuller (Carlsson & Fullér, 2001).

On the other hand, the term "sensitivity" describes how our outcomes vary when assumptions in our model are changed. When sensitivity is high, the results fluctuate dramatically when specific assumptions are changed; these assumptions must be extremely well established (Fragoulakis et al., 2015). The Sensitivity Analysis (SA) method is a numerical model that examines how uncertainties in one or more input variables might lead to uncertainties in the output variables (Pichery, 2014). In general, there are two approaches to sensitivity analysis, global and local. The behavior of input parameters on the change of the model output is the focus of global SA, while a local SA looks at sensitivity concerning a single parameter value change. In contrast, a global analysis looks at sensitivity throughout the parameter field (Abedi et al., 2016).

The present study aims to find the parameters that a circulating fluidized bed is sensitive to (using the local SA method) and apply the fuzzy set theory to the mathematical calculations. As numerical examples, the calculated minimum fluidization velocity and cyclone efficiency for the alumina chlorination FBR (Barahmand et al., 2021a) will be compared with the CPFD results. The mathematical approach focuses on Generalized Trapezoidal Fuzzy Numbers (GTrFN) algebraic operations through α-cuts (Zhang et al., 2014) and its application in the CFB.

The present paper describes the fuzzy sets' basic definitions and algebraic operations, properties, and sensitivity analysis. Finally, some numerical examples have adopted the fuzzy model to calculate the minimum fluidization velocity and cyclone efficiency under uncertainty.

2 Fuzzy Set Basics

This section introduces the basic concepts and definitions used in fuzzy sets theory to facilitate future discussions. The notation and concepts introduced by (Carlsson & Fullér, 2001), (Fullér & Majlender, 2003), and (Zimmermann, 1985) are used in this section.

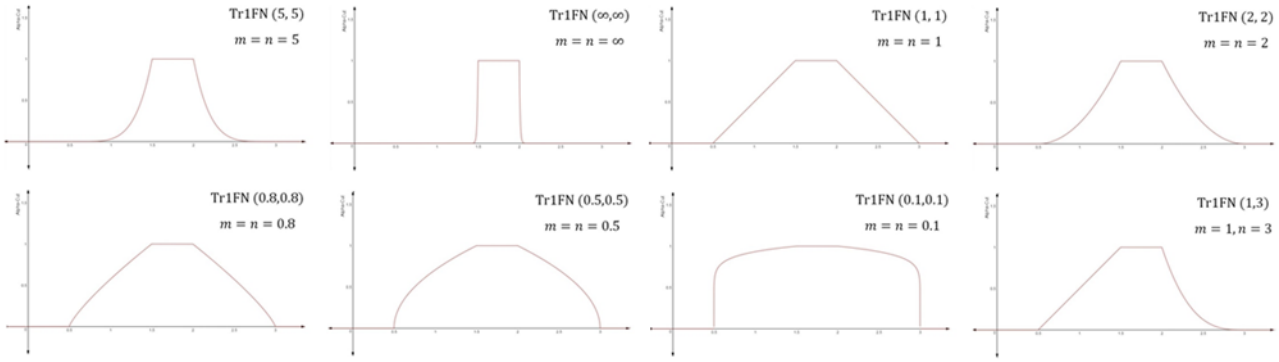

Figure 2 The generalized trapezoidal fuzzy number applying for different orders

2.1 Definitions

Definition 1 fuzzy set A, denoted $\tilde{A}$, is characterized by a Membership Function (MF) $\mu_{\tilde{A}}(x)$, where $x \in X$ (Thavaneswaran et al., 2009).

$$\tilde{A} = \{(x, \mu_A(X)) | x \in A\} \quad , \quad \mu_A(X): X \to \{0,1\} \qquad (1)$$

$\mu_{\tilde{A}}(x)$ is the degree of membership of X in $\tilde{A}$. The closer the value of $\mu_{\tilde{A}}(x)$ is to 1, the more x belongs to $\tilde{A}$.

Definition 2 Let $\tilde{A}$ be a fuzzy set in X. Then the support of $\tilde{A}$, denoted by $Supp(A)$, is the crisp set given by,

$$Supp(A) = \{x \in X: \mu_{\tilde{A}}(x) > 0\}, \qquad (2)$$

Definition 3 Let $\tilde{A}$ be a fuzzy set in X. The height $h(A)$ of $\tilde{A}$ is defined as,

$$Sh(A) = \sup_{x \in X} \mu_{\tilde{A}}(x) \qquad (3)$$

Definition 4 If $h(A) = 1$, then the fuzzy set $\tilde{A}$ is called a normal fuzzy set.

Definition 5 A Fuzzy Number $\tilde{A}$ is a fuzzy set on the real-line $\mathcal{R}$, which possesses the following properties (Carlsson & Fullér, 2001).

(1) A is a normal, convex fuzzy set on R,
(2) The $A(\alpha)$ is a closed interval for every $\alpha \in (0,1]$,
(3)The membership function is an upper semi-continuous, and
(4) The support of $\tilde{A}$, $S(A) = \{x \in A : \mu_A(X) > 0\}$, is bounded.

Definition 6 As shown in Figure 2, a trapezoidal fuzzy number $\tilde{A} = [a_1, a_2, a_3, a_4]_{(m,n)}$ is defined to be Generalized Trapezoidal Fuzzy Number having orders of m and n (GTrFN or TrFN(m, n)) if the MF is given by,

$$\mu_A(x) = \begin{cases} 0 & x \le a_1 \\ h(A)\left(\frac{x - a_1}{a_2 - a_1}\right)^m & a_1 \le x \le a_2 \\ h(A) & a_2 \le x \le a_3 \\ h(A)\left(\frac{x - a_4}{a_3 - a_4}\right)^n & a_3 \le x \le a_4 \\ 0 & x \ge a_4 \end{cases} \qquad (4)$$

Definition 7 An $\alpha - cut$ (interval of confidence) denoted by $A(\alpha)$ is the crisp set of elements x$\in\mathcal{R}$ whose degree of belonging to the fuzzy set $\tilde{A}$ is at least α (Thavaneswaran et al., 2013).

$$A(\alpha) = \{x \in A | \mu_A(X) \ge \alpha \in (0,1]\} = A(\alpha) = \left[a_1^{(\alpha)}, a_2^{(\alpha)}\right] \qquad (5)$$

Putting membership functions in definition 6 equal to α, and by finding x, the equation (5) will be reached.

$$A(\alpha) = \left[a_1^{(\alpha)}, a_2^{(\alpha)}\right] = \left[a_1 + (a_2 - a_1)\left(\frac{\alpha}{h(A)}\right)^{\frac{1}{m}}, a_4 + (a_3 - a_4)\left(\frac{\alpha}{h(A)}\right)^{\frac{1}{n}}\right. \qquad (6)$$

Definition 8 Defuzzification (Karnik & Mendel, 2001) of a fuzzy set $\tilde{A}$ with Center of Gravity (CoG) method can be defined as whose domain, $x \in X$, is discretized into N sub-areas, $A_1, A_2, A_3, \dots, A_N$, is given as,

$$c_{\tilde{A}} = \frac{\sum_{i=1}^{N} x_i A_i}{\sum_{i=1}^{N} A_i} \qquad (7)$$

where, x_i is the CoG in sub-areas.

Definition 9 The f-weighted possibilistic mean value of a fuzzy number $(\tilde{A} = [a_1, a_2, a_3, a_4]_{(m,n)})$ is defined as (Carlsson & Fullér, 2001; Fullér & Majlender, 2003),

$$\bar{M}(A) = \frac{a_1 + a_4}{2} + \frac{(a_2 - a_1)m}{(2m + 1)} + \frac{(a_3 - a_4)n}{(2n + 1)} \qquad (8)$$

3 Sensitivity Analysis

The local sensitivity analysis (Zhou & Lin, 2008) technique defines how an independent variable will impact a specific dependent variable under a given set of assumptions. In this model, the sensitivity of the minimum fluidization velocity to five different parameters (which have uncertainty in nature) has been studied. These parameters are the voidage at the minimum fluidization condition, fluid and solid

particles density, average particle diameter, particle sphericity, and gas viscosity.

In the simplified case, with microscopic particles ($Re_{mf} < 20$), the minimum fluidization velocity can be calculated by,

$$u_{mf} = \frac{d_p^2 \left(\rho_s - \rho_g\right) g}{150\,\mu} \cdot \frac{\varepsilon_{mf}^3\, \emptyset_s^2}{1 - \varepsilon_{mf}} \tag{9}$$

where, Re_{mf} is Reynolds number at the minimum fluidization condition, g is the acceleration gravity, ε_{mf} is the voidage at the minimum fluidization condition, ρ_g and ρ_s are the fluid and solid particles density, respectively, d_P is the average particle diameter, μ is the fluid dynamic viscosity and $\emptyset_s$ is the particle sphericity.

Table 1. Sensitivity Analysis of minimum fluidization velocity in a fluidized bed

	Output	**Input**
	u_{mf}	ε_{mf}
Initial	0.00452	0.4
Secondary	0.01059	0.5
% changed	134%	25%
Sensitivity	134/25 = 5.36	
	u_{mf}	ρ_g
Initial	0.01059	0.93
Secondary	0.01059	2
% changed	0%	115%
Sensitivity	0/115 = 0	
	u_{mf}	d_P
Initial	0.01059	0.000098
Secondary	0.01588	0.000120
% changed	49.9%	22.5%
Sensitivity	49.9/22.5 = 2.22	
	u_{mf}	$\emptyset_s$
Initial	0.00939	0.8
Secondary	0.01188	0.9
% changed	26.5%	12.5
Sensitivity	26.5/12.5 = 2.12	
	u_{mf}	μ
Initial	0.01059	0.000042
Secondary	0.00747	0.000060
% changed	-29.5%	42.8%
Sensitivity	29.5/42.8 = 0.68	

The results in Table 1 show that the highest sensitivity belongs to the ε_{mf}. On the contrary, the model is not sensitive to the ρ_g. The fluid's dynamic viscosity has the second-lowest sensitivity. When it comes to defining a value for each, the value for the voidage must be chosen as accurately as possible because it has the highest sensitivity in the model.

4 Fuzzy Models

4.1 Minimum Fluidization Velocity

Using definition (6), except for solid particle density and acceleration of gravity can be assumed as deterministic parameters, other parameters are considered as a GTrFN. Therefore,

$\tilde{d}_p = (\tilde{d}_{p1}, \tilde{d}_{p2}, \tilde{d}_{p3}, \tilde{d}_{p4}, h(\tilde{d}_p))_{m,n}$

$\tilde{\rho}_g = (\tilde{\rho}_{g1}, \tilde{\rho}_{g2}, \tilde{\rho}_{g3}, \tilde{\rho}_{g4}, h(\tilde{\rho}_g))_{m,n}$

$\tilde{\varepsilon}_{mf} = (\tilde{\varepsilon}_{mf1}, \tilde{\varepsilon}_{mf2}, \tilde{\varepsilon}_{mf3}, \tilde{\varepsilon}_{mf4}, h(\tilde{\varepsilon}_{mf}))_{m,n}$

$\tilde{\mu} = (\tilde{\mu}_1, \tilde{\mu}_2, \tilde{\mu}_3, \tilde{\mu}_4, h(\tilde{\mu}))_{m,n}$

$\widetilde{\emptyset}_s = (\widetilde{\emptyset}_{s1}, \widetilde{\emptyset}_{s2}, \widetilde{\emptyset}_{s3}, \widetilde{\emptyset}_{s4}, h(\widetilde{\emptyset}_s))_{m,n}$

The fuzzy form of the equation (7) is,

$$\tilde{u}_{mf} = \frac{\tilde{d}_p^2 \left(\rho_s - \tilde{\rho}_g\right) g}{150\,\tilde{\mu}} \cdot \frac{\tilde{\varepsilon}_{mf}^3\, \widetilde{\emptyset}_s^2}{1 - \tilde{\varepsilon}_{mf}} \tag{10}$$

Based on the introduced procedure in (Appadoo, 2006) and definition (7), the upper and lower α–cuts of the $\tilde{u}_{mf}$ ($\tilde{u}_{mf} = \left[\tilde{u}_{mf}^1(\alpha)\,, \tilde{u}_{mf}^2(\alpha)\,\right]$), can be written as below:

$$\begin{aligned} &\tilde{u}_{mf}^1(\alpha) \\ &= \frac{\tilde{d}_{p1}^2 \left(\rho_s - \tilde{\rho}_{g1}\right) g \tilde{\varepsilon}_{mf1}^3\, \widetilde{\emptyset}_{s1}^2}{150\,\tilde{\mu}_1 (1 - \tilde{\varepsilon}_{mf1})} \\ &+ \left(\frac{\tilde{d}_{p2}^2 \left(\rho_s - \tilde{\rho}_{g2}\right) g \tilde{\varepsilon}_{mf2}^3\, \widetilde{\emptyset}_{s2}^2}{150\,\tilde{\mu}_2 (1 - \tilde{\varepsilon}_{mf2})}\right. \\ &\left. - \frac{\tilde{d}_{p1}^2 \left(\rho_s - \tilde{\rho}_{g1}\right) g \tilde{\varepsilon}_{mf1}^3\, \widetilde{\emptyset}_{s1}^2}{150\,\tilde{\mu}_1 (1 - \tilde{\varepsilon}_{mf1})}\right) \left(\frac{\alpha}{h(\tilde{u}_{mf})}\right)^{\frac{1}{m}} \end{aligned} \tag{11}$$

$$\begin{aligned} &\tilde{u}_{mf}^2(\alpha) \\ &= \frac{\tilde{d}_{p4}^2 \left(\rho_s - \tilde{\rho}_{g4}\right) g \tilde{\varepsilon}_{mf4}^3\, \widetilde{\emptyset}_{s4}^2}{150\,\tilde{\mu}_4 (1 - \tilde{\varepsilon}_{mf4})} \\ &+ \left(\frac{\tilde{d}_{p3}^2 \left(\rho_s - \tilde{\rho}_{g3}\right) g \tilde{\varepsilon}_{mf3}^3\, \widetilde{\emptyset}_{s3}^2}{150\,\tilde{\mu}_3 (1 - \tilde{\varepsilon}_{mf3})}\right. \\ &\left. - \frac{\tilde{d}_{p4}^2 \left(\rho_s - \tilde{\rho}_{g4}\right) g \tilde{\varepsilon}_{mf4}^3\, \widetilde{\emptyset}_{s4}^2}{150\,\tilde{\mu}_4 (1 - \tilde{\varepsilon}_{mf4})}\right) \left(\frac{\alpha}{h(\tilde{u}_{mf})}\right)^{\frac{1}{n}} \end{aligned} \tag{12}$$

As a result, the standard form of the fuzzy minimum fluidization velocity will be:

$$\tilde{u}_{mf} = (\tilde{u}_{mf1}, \tilde{u}_{mf2}, \tilde{u}_{mf3}, \tilde{u}_{mf4}, h(\tilde{u}_{mf}))_{m,n} \tag{13}$$

where, $h(\tilde{u}_{mf})$ can be calculated as the following,

$$h(\tilde{u}_{mf}) = Min\{h(\tilde{d}_p), h(\tilde{\rho}_g), h(\tilde{\varepsilon}_{mf}), h(\tilde{\mu}), h(\widetilde{\emptyset}_s)\} \tag{14}$$

$$\mu_{\tilde{u}_{mf}}(x)=\begin{cases}0 & x\le \tilde{u}_{mf1}\\ h(\tilde{u}_{mf})\left(\dfrac{x-\dfrac{\tilde{d}_{p1}^2\,(\rho_s-\tilde{\rho}_{g1})g\tilde{\varepsilon}_{mf1}^3\,\tilde{\emptyset}_{s1}^2}{150\,\tilde{\mu}_1(1-\tilde{\varepsilon}_{mf1})}}{\dfrac{\tilde{d}_{p2}^2\,(\rho_s-\tilde{\rho}_{g2})g\tilde{\varepsilon}_{mf2}^3\,\tilde{\emptyset}_{s2}^2}{150\,\tilde{\mu}_2(1-\tilde{\varepsilon}_{mf2})}-\dfrac{\tilde{d}_{p1}^2\,(\rho_s-\tilde{\rho}_{g1})g\tilde{\varepsilon}_{mf1}^3\,\tilde{\emptyset}_{s1}^2}{150\,\tilde{\mu}_1(1-\tilde{\varepsilon}_{mf1})}}\right)^m & \tilde{u}_{mf1}\le x\le \tilde{u}_{mf2}\\ h(\tilde{u}_{mf}) & \tilde{u}_{mf2}\le x\le \tilde{u}_{mf3}\\ h(\tilde{u}_{mf})\left(\dfrac{x-\dfrac{\tilde{d}_{p4}^2\,(\rho_s-\tilde{\rho}_{g4})g\tilde{\varepsilon}_{mf4}^3\,\tilde{\emptyset}_{s4}^2}{150\,\tilde{\mu}_4(1-\tilde{\varepsilon}_{mf4})}}{\dfrac{\tilde{d}_{p3}^2\,(\rho_s-\tilde{\rho}_{g3})g\tilde{\varepsilon}_{mf3}^3\,\tilde{\emptyset}_{s3}^2}{150\,\tilde{\mu}_3(1-\tilde{\varepsilon}_{mf3})}-\dfrac{\tilde{d}_{p4}^2\,(\rho_s-\tilde{\rho}_{g4})g\tilde{\varepsilon}_{mf4}^3\,\tilde{\emptyset}_{s4}^2}{150\,\tilde{\mu}_4(1-\tilde{\varepsilon}_{mf4})}}\right)^n & \tilde{u}_{mf3}\le x\le \tilde{u}_{mf4}\\ 0 & x\ge \tilde{u}_{mf4}\end{cases} \quad (15)$$

The membership function of the $\tilde{u}_{mf}$ can be calculated from equation (15).

4.2 Cyclone Efficiency

In general, cyclones are the most common kind of mechanical separator. This basic system has very high efficiency with a low-pressure drop without any moving mechanical components, which are the most favorable advantages. A cyclone is a device that separates solid particles from a fluid by centrifugal force and works simply by the kinetic energy of the incoming mixture (flow stream) and the geometry of the cyclone. Particle (in fluid) velocity and residence time are two main factors in cyclone design (Cooper & Alley, 2010). A typical cyclone scheme is shown in Figure 3.

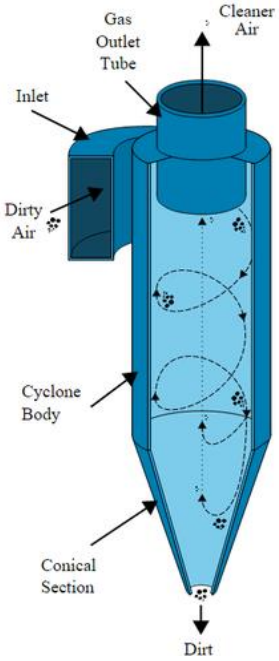

Figure 3. Components of a vertical axis tangential entry cyclone (Afework et al., 2018)

Because of the cyclone's cylindrical form and the tangential entrance of the gas, the gas-solid suspension flows in two concentric vortices around the cyclone. The outer vortex is heading downward, while the central vortex is moving upward. Solids with a higher density than flue gas exit the outer vortex and pass against the wall due to centrifugal force. The comparatively clean gas rises through the inner vortex and leaves through a vertical exit on the cyclone's top (Basu, 2015).

Many parameters affect cyclone efficiency. Table 2 shows the effect of design and process parameters on cyclones' efficiency (Cooper & Alley, 2010). If the parameter increases, the cyclone's efficiency will:

Table 2. Effect of parameters on the cyclone efficiency

Parameter	
Particle size	Increase
Particle density	Increase
Dust loading	Increase*
Inlet gas velocity	Increase*
Cyclone body diameter	Decrease
The ratio of body length to diameter	Increase
The smoothness of cyclone's inner wall	Increase
Gas viscosity	Decrease
Gas density	Decrease
Gas inlet duct area	Decrease
Gas exit pipe diameter	Decrease

*With these parameters, cyclone efficiency can only increase to a certain point and then decrease.

Similarly, as explained in Section 4.1, the uncertainty has been applied to the cyclone calculations based on the

Table 3. Model's deterministic and fuzzy parameters

		Crisp	Normal Linear Trapezoidal Fuzzy	Weighted	Defuzzified
	Value	Value	Number	P-Mean	(CoG method)
d_p	μm	98	$(20, 75, 115, 190, 1)_{1,1}$	103	102
ρ_s	kg/m^3	3958	-	-	-
ρ_g	kg/m^3	9.29e-01	$(1.04, 9.38e\text{-}01, 9.19e\text{-}01, 8.24e\text{-}01, 1)_{1,1}$	9.32e-01	9.31e-01
ε_{mf}	-	0.4	$(0.35, 0.39, 0.41, 0.42, 1)_{1,1}$	0.39	0.4
g	m/s^2	9.8	-	-	-
μ	kg/ms	4.2e-05	$(3.68e\text{-}05, 4.23e\text{-}05, 4.39e\text{-}05, 5.04e\text{-}05, 1)_{1,1}$	4.3e-05	4.3e-05
$\emptyset_s$	-	0.85	$(0.5, 0.65, 0.75, 0.90, 1)_{1,1}$	0.7	0.7

Lapple method (Cooper & Alley, 2010). As a result, the cyclone efficiency can be calculated by equation 16.

$$\eta = \frac{1}{1+\left(\frac{d_{50}}{d_p}\right)^2} \tag{16}$$

where, η is the cyclone efficiency, d_p is the average particle diameter and d_{50} can be calculated by the equation below.

$$d_{50} = \sqrt{\frac{9\mu W}{2\pi\vartheta_{in}(\rho_p - \rho_g)N_A}} \tag{17}$$

where, ϑ_{in} in the fluid's superficial velocity inlet to the cyclone, W is the cyclone's inlet width and N_A is:

$$N_A = \frac{L_b + 0.5L_c}{H} \tag{18}$$

where, L_b is the cyclone main body height, L_c is the height of the conical part of the cyclone, and H is the height of the inlet of the cyclone. All the parameters in this equation are deterministic. In equations 16 and 17, except N_A, ρ_p and W other parameters can be assumed as the fuzzy number as below,

$\tilde{d}_p = (\tilde{d}_{p1}, \tilde{d}_{p2}, \tilde{d}_{p3}, \tilde{d}_{p4}, h(\tilde{d}_p))_{m,n}$

$\tilde{\rho}_g = (\tilde{\rho}_{g1}, \tilde{\rho}_{g2}, \tilde{\rho}_{g3}, \tilde{\rho}_{g4}, h(\tilde{\rho}_g))_{m,n}$

$\tilde{\vartheta}_{in} = (\tilde{\vartheta}_1, \tilde{\vartheta}_2, \tilde{\vartheta}_3, \tilde{\vartheta}_4, h(\tilde{\vartheta}_{in}))_{m,n}$

$\tilde{\mu} = (\tilde{\mu}_1, \tilde{\mu}_2, \tilde{\mu}_3, \tilde{\mu}_4, h(\tilde{\mu}))_{m,n}$

In equation 15, defining the fuzzy d_p is sufficient because the value for d_{50} (which all the uncertainties have been considered) will be calculated accordingly.

Equation 16 is an intermediate equation that can be used in the central equation. Therefore, the *possibilistic mean value* of the uncertain parameters can be used to calculate d_{50}. Based on definition 9, equation (17) can be written in the following form:

$$\bar{d}_{50} = \sqrt{\frac{9\bar{\mu}W}{2\pi\bar{\vartheta}_{in}(\rho_p - \bar{\rho}_g)N_A}} \tag{19}$$

where, $\bar{\mu}$, $\bar{\vartheta}_{in}$, and $\bar{\rho}_g$ are the possibilistic mean value for the corresponding parameters.

Now, the fuzzy form of the cyclone's efficiency can be written as,

$$\tilde{\eta} = \frac{1}{1+\left(\frac{\bar{d}_{50}}{\tilde{d}_p}\right)^2} \tag{20}$$

Based on definition 7, the upper and lower α–cuts of the $\tilde{\eta}$ can be written as below:

$$\tilde{\eta} = \frac{1}{1+\left(\frac{\bar{d}_{50}}{\tilde{d}_{p1}}\right)^2} + \left(\frac{1}{1+\left(\frac{\bar{d}_{50}}{\tilde{d}_{p2}}\right)^2} - \frac{1}{1+\left(\frac{\bar{d}_{50}}{\tilde{d}_{p1}}\right)^2}\right)\left(\frac{\alpha}{h(\tilde{\eta})}\right)^{\frac{1}{m}} \tag{21}$$

$$\tilde{\eta} = \frac{1}{1+\left(\frac{\bar{d}_{50}}{\tilde{d}_{p4}}\right)^2} + \left(\frac{1}{1+\left(\frac{\bar{d}_{50}}{\tilde{d}_{p3}}\right)^2} - \frac{1}{1+\left(\frac{\bar{d}_{50}}{\tilde{d}_{p4}}\right)^2}\right)\left(\frac{\alpha}{h(\tilde{\eta})}\right)^{\frac{1}{n}} \tag{22}$$

where, $h(\tilde{\eta})$ can be calculated as the following,

$$h(\tilde{\eta}) = Min\{h(\tilde{d}_p), h(\tilde{\rho}_g), h(\tilde{\vartheta}_{in}), h(\tilde{\mu})\} \tag{23}$$

5 Numerical Examples

5.1 Minimum fluidization Velocity

The following trapezoidal fuzzy parameters are defined for the alumina chlorination in a fluidized bed reactor (Barahmand et al., 2021b). There are different methods to define a fuzzy number. For fuzzy particle diameter,

as an example, this can be achieved by fitting a trapezoidal to the size distribution diagram (Figure 4). In this case, the fuzzy particle diameter can be defined as,

$\tilde{d}_p = (20, 75, 115, 190, 1)_{1,1}$

This fuzzy number shows that the particles with a diameter less and more than 25 and 190 microns do not belong to this fuzzy set (the range is between extreme values). The other helpful information given by this fuzzy number is that the particles with a diameter of 85-125 microns 100% belong to this set. To make it more straightforward, as an example, assume a set defined as the black balls. The white, light grey, dark grey, and black balls belong to this set with different belonging degrees. In this case, the belonging degree in the range [0, 1] for these balls is 0, 0.2, 0.8, and 1, respectively.

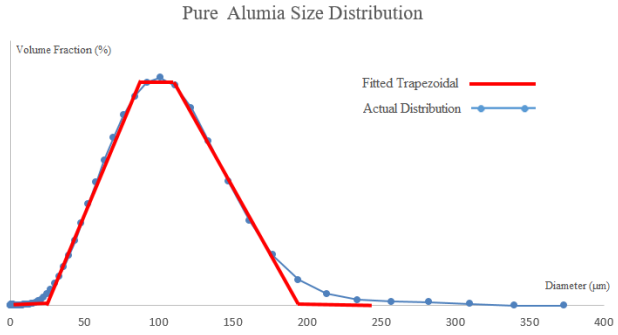

Figure 4. Fitted trapezoidal to the alumina size distribution

Similarly, the other parameters can be defined by operating conditions, results from the dynamic system (fluctuations), experiments, etc.

Table **3** gives the deterministic and fuzzy values used in the numerical example. As an example, for the fluid's density and dynamic viscosity, the interval of the midpoints and endpoints are calculated based on ± 10℃ and ± 40℃, respectively.

By applying the data into equations 11 and 12, the minimum fluidization velocity α–cuts can be derived as,

$$\tilde{u}_{mf} = \left[\tilde{u}^1_{mf}(\alpha), \tilde{u}^2_{mf}(\alpha)\right] = [0.00012 + 0.00256\alpha, 0.02133 - 0.014\alpha]$$

To find the interior and endpoints, let $\alpha = 1$ and $\alpha = 0$ in equation (13). As a result, the fuzzy minimum fluidization velocity can be defined as below,

$\tilde{u}_{mf} = (0.00012, 0.00268, 0.00733, 0.02136)$, where the membership function is,

$$\mu_{\tilde{u}_{mf}}(x) = \begin{cases} 0 & x \le 0.00012 \\ \dfrac{x - 0.00012}{0.00256} & 0.00012 \le x \le 0.00268 \\ 1 & 0.00268 \le x \le 0.00733 \\ \dfrac{x - 0.02136}{-0.014} & 0.00733 \le x \le 0.02136 \\ 0 & x \ge 0.02136 \end{cases}$$

Now, based on the above membership and calculated α-cuts (Table 4) and the graphical fuzzy minimum fluidization velocity is presented in Figure 5.

Table 4. $\tilde{u}_{mf}$ α-cuts with linear membership functions

α	0.00	0.20	0.40	0.60	0.80	1.00
$\tilde{u}^1_{mf}$	**0.012**	0.063	0.114	0.166	0.20	**0.27**
α	0.00	0.20	0.40	0.60	0.80	1.00
$\tilde{u}^2_{mf}$	**2.14**	1.72	1.43	1.29	1.01	**0.73**

Considering all uncertain and certain parameters, the calculated fuzzy minimum fluidization velocity is given in Figure 4.

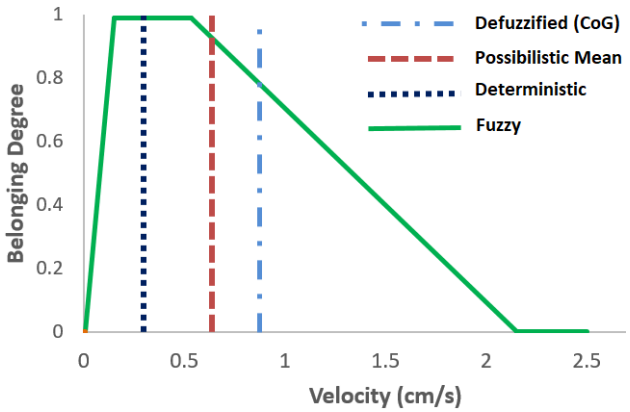

Figure 5. Calculated fuzzy minimum fluidization velocity with linear membership functions.

The results show that the minimum fluidization velocity without considering uncertainty has been calculated as 0.32 cm/s, ideally in the range with the highest belonging degree in the fuzzy number. The fuzzy minimum fluidization velocity gives more information. This analysis illustrates that considering all the defined uncertainties, the minimum fluidization velocity will not be more than 2.14 cm/s and not drop below 0.012 cm/s, but the velocities in the range [0.27, 0.73] cm/s have the highest belonging degree to this set. As seen in Figure 5, the average deterministic value of this fuzzy number (defuzzified based on the center of gravity method and possibilistic mean). Instead of the deterministic calculated value, these values can be used in further reactor design calculations, representing the model's uncertainty.

5.2 Cyclone Efficiency

5.2.1 Base model

To study the performance of the cyclone in a specific operating condition, a CPFD simulation has been done to study the performance of the cyclone in a specific operating condition. The cyclone diameter has been

chosen 0.5 m, and all other dimensions can be calculated accordingly. The model has been simulated under the following operating condition, as shown in Table 5.

Figure 6 shows a snapshot of the cyclone simulation in an isothermal condition. As it is clear, most of the particles leave the system from the bottom. Therefore, the average cyclone efficiency can be calculated by dividing the average particle mass flow rates between the bottom and the inlet.

Table 5. Cyclone's operating conditions used for the simulations

Number of cells in setup grid:	500000
Fluid superficial velocity (inlet)	36.5 m/s
Particle duty in:	0.3 kg/s
Temperature:	973.15 K
Outlet pressure:	1.5 bars
Average particle diameter:	20 microns
Fluid density:	1.3318 kg/m^3
Fluid dynamic viscosity:	0.0000287893 pa.s
Cyclone type:	High-Efficiency
Nominal efficiency:	99%
Particle density:	2100 kg/m^3

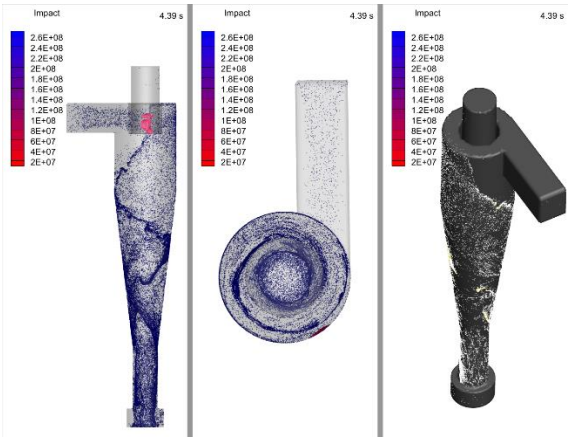

Figure 6. Particle distribution inside the cyclone

5.2.2 Uncertainty in Theoretical Approach

As discussed in Section 4.2, for the first step, the fuzzy parameters should be defined. The particle diameter and superficial velocity inlet to the cyclone are assumed as fuzzy numbers with linear membership functions (m and n equal to 1). Other parameters are kept the same as Table 5.

$\tilde{d}_p = (10, 18, 20, 22, 1)$

$\tilde{\vartheta}_{in} = (35.64, 36.42, 36.92, 37.34, 1)$

Following the procedure in Section 4.2, in the second step, using definition 9, $\bar{d}_{50}$ can be calculated by using possibilistic mean values in equation 19. From equations 21 and 22, the fuzzy efficiency of the cyclone can be calculated as Figure 7.

5.2.3 Uncertainty in CPFD Model

In the base model, the particle duty entered into the system has been set to 0.3 kg/s. To study the uncertainty using Barracuda® as the best alternative, the particle duty inlet to the cyclone has been chosen because all other uncertain parameters directly or indirectly affect the particle mass concentration.

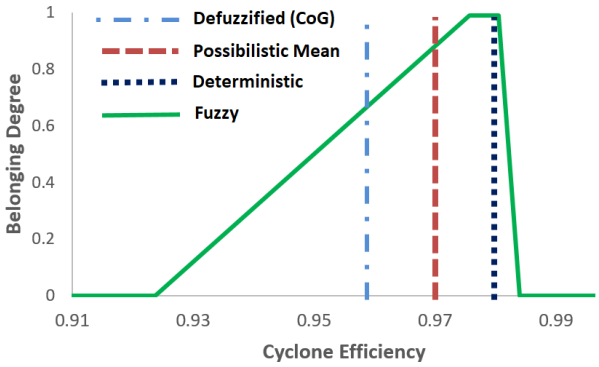

Figure 7. Fuzzy cyclone efficiency

According to Table 6, by increasing the particle duty, the cyclone's efficiency will increase, and after a certain point, it will start to drop. By investigating this with the CPFD simulation, the following results have been observed (Table 6).

Table 6. Sensitivity of Cyclone efficiency to particle concentrations inlet to the cyclone

Particle duty (kg/s)	Particle Escape (kg/s)	Efficiency (%)
0.05	0.002676	94.6
0.1	0.005447	94.6
0.2	0.007239	96.4
0.3	0.008284	97.2
0.4	0.011694	97.1

The calculated fuzzy efficiency is in the overall range of 92.3-98.3%. On the other hand, the CPFD simulation shows the efficiency in the range 94.6-97.1%. Using the parameters in Table 5 and applying equation 16, the theoretical efficiency can be calculated at 98%. Figure 7 clearly shows these calculated efficiency ranges with the highest belonging degree (97.5-98%). On the other hand, there is more information about the efficiency of the system. Considering all the defined uncertainties, the possibility of having efficiency lower than 92.3% and higher than 98.3% is very low, and the efficiency will be in the range of 92.3-98.3%. This range covers the range resulted from CPFD simulation.

6 Conclusion

Solid particles and fine powders in many industrial systems behave in a state of uncertainty. In a circulating fluidized bed, specifically, both sources of uncertainty are available. These sources are the uncertainty in a mathematical sense due to the difference between measured, estimated, and actual values, including errors in observations or calculations, and the uncertainty in particle and fluid physical properties, reaction kinetics, reactor temperature, etc.

The fuzzy set theory is one of the robust tools which can model these uncertainties mathematically. Moreover, applying generalized trapezoidal fuzzy sets to fluidized bed calculation gives designers and analysts a more dependable tool to analyze the uncertainty. As can be seen in the result, the fuzzy model is efficient and valuable, and without introducing this method, it would not be possible to consider this genuine uncertainty.

Overall, it is pretty clear that except for engineering, this fuzzy modeling method has applications in most branches of science and life, such as biomedical sciences, finance, social sciences, etc. Furthermore, future research could extend our model by type-2 incorporating different heights for fuzzy inputs.

References

V. Abedi, R. Hontecillas, A. Carbo, C. Philipson, S. Hoops, and J. Bassaganya-Riera. Chapter 8 - Multiscale Modeling: Concepts, Technologies, and Use Cases in Immunology. In J. Bassaganya-Riera (Ed.), *Computational Immunology* pages 145–173. Academic Press, 2016. doi:10.1016/B978-0-12-803697-6.00008-4

B. Afework, J. Hanania, K. Stenhouse, and J. Donev. *Cyclone separator—Energy Education, 2018*.

M. Aien, A. Hajebrahimi, and M. Fotuhi-Firuzabad. A comprehensive review on uncertainty modeling techniques in power system studies. *Renewable and Sustainable Energy Reviews*, *57*, 1077–1089, 2016. doi:10.1016/j.rser.2015.12.070

M. Aien, M. Rashidinejad, and M. Fotuhi-Firuzabad. On possibilistic and probabilistic uncertainty assessment of power flow problem: A review and a new approach. *Renewable and Sustainable Energy Reviews*, *37*, 883–895, 2014. doi:10.1016/j.rser.2014.05.063

S. S. Appadoo. *Pricing financial derivatives with fuzzy algebraic models: A theoretical and computational approach*, Ph.D. thesis, University of Manitoba, 2006.

Z. Barahmand, C. Jayarathna, and C. Ratnayake. CPFD simulations on a chlorination fluidized bed reactor for aluminum production: An optimization study. *In Proceedings - 1st SIMS EUROSIM Conference on Modelling and Simulation*, Finland, 2021a.

Z. Barahmand, C. Jayarathna, and C. Ratnayake. The effect of alumina impurities on chlorination in a fluidized bed reactor: A CPFD study. *In Proceedings - 1st SIMS EUROSIM Conference on Modelling and Simulation*, Finland, 2021b.

P. Basu. *Circulating Fluidized Bed Boilers: Design, Operation and Maintenance*. Springer International Publishing, 2015. doi:10.1007/978-3-319-06173-3

Y. Ben-Haim. *Information Gap Decision Theory: Decisions under Severe Uncertainty* (1st edition). Academic Press, 2001.

C. Carlsson and R. Fullér. On possibilistic mean value and variance of fuzzy numbers. *Fuzzy Sets and Systems*, *122*(2), 315–326, 2001. doi:10.1016/S0165-0114(00)00043-9

C. D. Cooper and F. C. Alley. *Air Pollution Control: A Design Approach, Fourth Edition*. Waveland Press, 2010.

G. B. Dantzig. Linear Programming under Uncertainty. *Management Science*, *1*(3–4), 197–206, 1955. doi: 10.1287/mnsc.1.3-4.197

D. Dubois and H. Prade. Ranking fuzzy numbers in the setting of possibility theory. *Information Sciences*, *30*(3), 183–224, 1983. doi:10.1016/0020-0255(83)90025-7

V. Fragoulakis, C. Mitropoulou, M. S. Williams, & G. P. Patrinos. Chapter 5—Advanced Methodological Aspects in the Economic Evaluation. In V. Fragoulakis, C. Mitropoulou, M. S. Williams, & G. P. Patrinos (Eds.), *Economic Evaluation in Genomic Medicine* (pp. 65–96). Academic Press, 2015. doi:10.1016/B978-0-12-801497-4.00005-9

R. Fullér and P. Majlender. On weighted possibilistic mean and variance of fuzzy numbers. *Fuzzy Sets and Systems*, 136, 363–374, 2003. doi:10.1016/S0165-0114(02)00216-6

R. Goetschel and W. Voxman. Elementary fuzzy calculus. *Fuzzy Sets and Systems*, *18*(1), 31–43, 1986. doi:10.1016/0165-0114(86)90026-6

R. Herzallah. Incertainty in control problems: A survey. *IFAC Proceedings Volumes*, *38*(1), 82–90, 2005. https://doi.org/10.3182/20050703-6-CZ-1902.01092

N. N. Karnikand J. M. Mendel. Centroid of a type-2 fuzzy set. *Information Sciences*, *132*(1), 195–220, 2001. doi:10.1016/S0020-0255(01)00069-X

D. Kunii and O. Levenspiel. *Fluidization Engineering*. Butterworth-Heinemann, 1991.

R. E. Moore, R.B. Kearfott, and M. J. Cloud. *Introduction to Interval Analysis* (1st edition). Society for Industrial and Applied Mathematics, 2009.

C. Pichery. Sensitivity Analysis. In P. Wexler (Ed.), *Encyclopedia of Toxicology (third edition)*, pages 236–237. Academic Press, 2014. doi:10.1016/B978-0-12-386454-3.00431-0

A. Soroudi and M. Ehsan. A possibilistic-probabilistic tool for evaluating the impact of stochastic renewable and controllable power generation on energy losses in distribution networks: A case study. *Renewable and Sustainable Energy Reviews*, *15*(1), 794–800, 2011.

A. L. Soyster. Convex Programming with Set-Inclusive Constraints and Applications to Inexact Linear

Programming. *Operations Research*, *21*(5), pages 1154–1157, 1973.

A. Thavaneswaran, S. S. Appadoo, and J. Frank, J. Binary option pricing using fuzzy numbers. *Applied Mathematics Letters*, *26*(1), 65–72, 2013. doi: 10.1016/j.aml.2012.03.034

A. Thavaneswaran, S. S. Appadoo, and A. Paseka. Weighted possibilistic moments of fuzzy numbers with applications to GARCH modeling and option pricing. *Mathematical and Computer Modelling*, *49*(1), 352–368, 2009. doi: 10.1016/j.mcm.2008.07.035

A. Tinke. *Minimum Sample Size and Measurement Uncertainty in the Particle Size Distribution Analysis of Powders, 2020*. doi: 10.13140/RG.2.2.12086.45127

É. Valkó and T. Turányi. *Uncertainty Quantification of Chemical Kinetic Reaction Rate Coefficients*, pages 35–44, 2020. doi:10.1007/978-3-030-50388-8_3

L. A. Zadeh. Fuzzy sets. *Information and Control*, *8*(3), 338–353, 1965. doi: 10.1016/S0019-9958(65)90241-X

L. A. Zadeh. Fuzzy sets as a basis for a theory of possibility. *Fuzzy Sets and Systems*, *100*, 9–34, 1999. doi: 10.1016/S0165-0114(99)80004-9

H. Zhang, L. Shu, and S. Liao. Generalized Trapezoidal Fuzzy Soft Set and Its Application in Medical Diagnosis. *Journal of Applied Mathematics*, 2014. doi: 10.1155/2014/312069

X. Zhou, and H. Lin. Local Sensitivity Analysis. In S. Shekhar & H. Xiong (Eds.), *Encyclopedia of GIS* (pp. 616–616). Springer US, 2008. doi: 10.1007/978-0-387-35973-1_703

J. Zhu. *Optimization of Power System Operation*. Wiley-IEEE Press, 2015.

H. J. Zimmermann. Fuzzy Sets—Basic Definitions. In H.-J. Zimmermann (Ed.), *Fuzzy Set Theory—And Its Applications*, pages 11–23. Springer Netherlands, 1985. doi: 10.1007/978-94-015-7153-1_2

Design of a Medium-Scale Circulating Fluidized Bed Reactor for Chlorination of Processed Aluminum Oxide

Zahir Barahmand[1] Omid Aghaabbasi[1] Jose Luis Salcido[1] Emmy Kristine L. Rustad[1]
Chameera Jayarathna[2] Chandana Ratnayake[1,2]

[1] Department of Process, Energy and Environmental Technology, University of South-Eastern Norway
zbarahmand@gmail.com
[2] SINTEF Tel-Tek, SINTEF Industry, Porsgrunn, Norway

Abstract

Fluidization is a well-established and widely used technology in the process industry. The production stability and the large effective contact area between the active substances, resulting in high mass and heat transfer between the phases, are some of the main advantages of fluidization. However, this technology has not yet been adequately developed for alumina chlorination as a standard solution on an industrial scale. Although a circulating fluidized bed reactor design is complex by its nature, it is advantageous to simulate the process compared to running experiments on a lab scale. The Computational Particle-Fluid Dynamic (CPFD) simulation lays a foundation for studying the given reaction process.

The reaction between the solid alumina particles and the gaseous chlorine and carbon monoxide results in the products (aluminum chloride and carbon dioxide). The present study aims to design a circulating fluidized bed reactor by simulating the process in Barracuda®. Simulations with a simple geometry contributed to a better understanding of the reaction process. Then the simulation results are compared with values from both a theoretical approach and parallel simulations in Aspen Plus®. The comparison revealed that the results from Barracuda® Virtual Reactor (VR), such as product flow rate, are within a reasonable range of what could be expected in a full-scale plant. The promising preliminary results imply that CPFD could be a promising approach for future research on the design, optimization, and implementation of the industrial alumina chlorination process. The final design includes a fluidized bed reactor with a 2.4 m internal diameter and 8 m height and four parallel internal cyclones on top.

Keywords: CPFD Simulation, Alumina Chlorination, Circulating Fluidized Bed Reactor (CFBR), Reactor Design, Barracuda, Fluidization, Multiphase flow

1 Introduction

The earth's crust is rich in aluminum. It can only be found in mineral compositions, for example, alumina-silicates, clays, and hydrated oxides like bauxite. Producing aluminum from bauxite is mainly done by extraction in a Bayer process (Survey of Potential Processes for the Manufacture of Aluminium, 1979). This is done by dissolving alumina with soda ash and lime in steel digesters and converting it to pure aluminum by an electrochemical process, namely Hall-Héroult (Thonstad, 2001). This process has a considerable power requirement and greenhouse gas (GHG) emissions. Because of that, it is important to evaluate an alternative process. The challenge lies in finding a proper and economical solution, considering the complexity of alumina's carbothermic reduction (Rao & Soleiman, 1986). Even if alumina is pure, the result is aluminum metal and aluminum carbide. This again needs to decompose carbide to metal at 2100°C.

The solution could be a two-step process that converts alumina to aluminum chloride ($AlCl_3$) and then reduces it to metal aluminum. At first, it was suggested to reduce $AlCl_3$ with manganese, but it was not an excellent economical choice (*Survey of Potential Processes for the Manufacture of Aluminum*, 1979). Alcoa® proposed a solution for this second step as the electrolysis of $AlCl_3$ with alkali and alkaline earth chlorides (Rhamdhani et al., 2013). This solution appears to be a more economical and energy-saving method. Current research and development study has been focusing on producing aluminum chloride from alumina.

One proposed technology for the chlorination of alumina is a fluidized bed reactor (National Fuels and Energy Conservation Act, 1973). This technology has a wide range of possible applications. The upward flow of a fluid through a bed of solid particles is a technique that results in an efficient heat and mass transfer and generally offers a stable and efficient production. The challenge of using a Circulating Fluidized Bed (CFB) reactor lies in the design of the reactors due to the complexity of the flow patterns and the flow dynamics with multiphase situations within the reactors. This makes it hard to ensure that optimal conditions and dimensions are obtained (Cocco et al., 2014).

Traditionally the preliminary design of processes has been done by the experiments on a lab scale. The execution of experiments of CFB reactors can be both

expensive and not necessarily applicable since the scale-up processes of a fluidized bed reactor are difficult and complex. The extrapolation from lab-scale to industrial size is unreliable, especially when the Fluidized Bed Reactor (FBR) involves a reaction (Kunii & Levenspiel, 1991). Over the last decades, the possibility of simulating processes has been under constant development, compared to the traditional approach with experiments. Moreover, as computational power and knowledge increase, making accurate designs through simulations increases.

The fluidized bed technology has a wide range of applications in the process industry. The upward flow of a fluid through a bed of solid particles is a technique that results in an efficient heat and mass transfer and generally offers the process a stable production. However, due to the complexity of the flow pattern and the flow hydrodynamics within the gas-solid multiphase, the challenge of using a fluidized bed reactor rests in the design.

The current work aims to design a medium-scale chlorination reactor for producing a stream of AlCl3 that may later be converted into pure aluminum. First, the basic geometry and the size of the reactor specifications are figured out for suitable hydrodynamics based on the available gas-solid fluidization theories. Then, the design and operation of the reactor are evaluated and analyzed by the CFD simulations for actual operating and process conditions.

As the first step of the study, a circulating fluidized bed reactor (CFBR) preliminary mechanical design is completed using SOLIDWORKS®. The reactor model is then simulated/optimized with the use of CFD software called Barracuda VR® version 17.4.

Alumina chlorination is an aggressive exothermic reaction that occurs at higher temperatures (~700°C) (Bjarte, 2018), and the Cl_2 and $AlCl_3$ as a reactant and product are highly corrosive. Therefore the specification of material and the cooling system are essential parts of the design process. However, these are not considered within the scope of the current study.

2 Fluidization Process

Several variables affect the regimes in a fluidized bed; among them are the fluid properties of particles and fluid included in the process. Different regimes can categorize the behavior of the system. Generally, at the low velocity of the fluid, the bed of particles is stagnant, and flowing fluid passes through the void spaces of the particles. By rising velocity above minimum fluidization condition, the system's behavior depends on which kind of interface we have. In liquid-solid systems, a velocity above minimum fluidization gives a smooth expansion of the bed. However, in gas-solid systems, having a velocity above minimum fluidization velocity causes the expansion of the bed.

Further increase of the superficial gas velocity causes bubbles and movement of particles to go stronger. As a result, the bed height remains the same as it was at minimum fluidization condition. This regime is known as a bubbling fluidized bed (Kunii & Levenspiel, 1991).

2.1 Industrial application

The fluidized bed process has a long history in the industry. The first commercial process was introduced in the 1920s with the advent of the Winkler coal gasifier in Germany. Further, that produced high-octane gasoline by fluidized catalytic cracking units (FCCUs) in the 1940s (Cocco et al., 2014). After that, in the United States, it was suggested to use natural gas instead of petroleum fractions to produce gasoline with the fluidized bed. From the first attempts to use the fluidized bed in industry and until now, many processes have been changed and improved; thus, the range of applications has been raised. This is because of the usefulness of fluidized beds in process operation, especially for uniform temperature requirements for sensitive reactions (Kunii & Levenspiel, 1991).

Heat exchangers are an example of an application of fluidized beds due to their high rate of heat transport and uniform temperature. An example of a process that needs a high heat transfer rate is producing alloy with specific properties, a quench, and a tempering process (Liu et al., 2020). For this purpose, the utilization of a fluidized bed is often seen as a solution. Solidification of melt to produce granules is another application of fluidized bed in industry and is based on spraying molten urea by falling through a tower and passing cold air upward to solidify droplets and form granules. Another practical application is coating solids with plastic by suspending plastic particles through the air to collide a hot metal with a higher temperature than the melting point of plastic and perform coating it with plastic. Drying solids as a dryer for wet particles through hot gas is widely used to apply fluidized beds since it has a large capacity with low construction cost, high thermal efficiency, and easy operability (Chandran et al., 1990). In addition to the applications above, fluidized beds have many useful and extensive commercial applications based on physical operations. Among them are adsorption, transportation, mixing of fine powders, and chemical operations like carbonization, solid catalyzed reaction, and combustion (Kunii & Levenspiel, 1991).

2.2 Fluidized Bed Pros and Cons

Fluidized beds have three main advantages (Ahmadpour Samani et al., 2020). The first is the excellent heat and mass transfer between solids and fluids, leading to the low surface area needed for heat exchangers within the fluidized bed. The second one is the easy movement of solids, like fluid causes continuous operation and rapid mixing to the isothermal condition that avoids abrupt

temperature changes, making it a safe and stable method. The third one is the ability to process solids with a wide range of size distributions. As a result, they are suitable for all scale operations and have high gas and solid throughput.

There are some challenges in designing and building fluidized beds as they have inherent difficulties scaling up from lab-scale experiments. They also tend to have erosion because of the collision of particles into surfaces of vessels and pipes. The substantial losses can raise operating costs, especially if they are expensive catalysts. In addition, the rapid mixing and attrition of solids make non-uniform residence time for solids. Managing the giant bubbles in mass transfer cases are another challenge for fluidized bed (Cocco et al., 2014).

Despite these mentioned challenges, the benefits of the fluidizing bed raise interest in the widespread industrial application making it a proper method in many industrial processing operations.

3 Reactor Design

Based on the given chlorination reaction (Figure 1), the following steps have been taken to design an industrial CFBR for alumina chlorination, classifying them into six different categories as 1) theoretical calculations, 2) fluidization regime selection, 3) CPFD simulations, 4) design optimization, 5) corrosion analysis and material selection, and 6) mechanical design.

The fluid's superficial velocity directly affects the fluidization regime and thus the reactor performances. As discussed in Section 3.1.2, the favorable regime can be achieved by choosing the fluid's velocity inside the reactor based on the calculated velocities.

3.1 Theoretical Calculations

In this section, the main calculations will be discussed step by step.

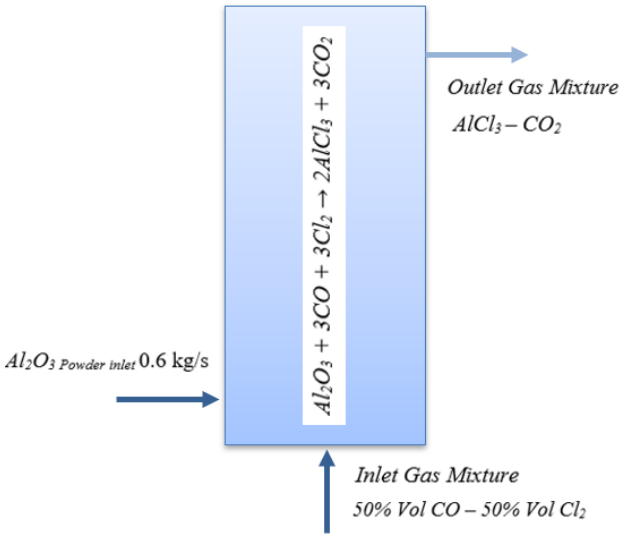

Figure 1. Illustration of the FBR

3.1.1 Mass Balance

As seen in Figure 1, the reactor should be designed for the given reaction (0.6 kg/s solid alumina with an equimolar mixture of Cl_2 and CO) at 700 ℃.

The overall reaction and mass balance are given in equations (1) and (2).

$$Al_2O_3 + 3Cl_2 + 3CO \rightarrow 2AlCl_3 + 3CO_2 \quad (1)$$

$$\dot{n}_{Al_2O_3} M_{Al_2O_3} + \dot{n}_{Cl_2} M_{Cl_2} + \dot{n}_{CO} M_{CO} = \dot{n}_{AlCl_3} M_{AlCl_3} + \dot{n}_{CO_2} M_{CO_2} \quad (2)$$

where, M is molecular weight and $\dot{n}$ is molar flow rate. Table 1 shows the calculated mass and molar flow rate for the reactants and products.

Table 1. Summarized results of the mass balance

Component	M ($\frac{g}{mole}$)	$\dot{m}$ ($\frac{kg}{s}$)	$\dot{n}$ ($\frac{mole}{s}$)
Al_2O_3	101.9	0.6	5.88
Cl_2	70.9	1.252	17.65
CO	28.01	0.494	17.65
$AlCl_3$	133.34	1.569	11.77
CO_2	44.01	0.777	17.65

3.1.2 Effect of superficial gas velocity on fluidization

There are several important velocities in a fluidized bed reactor hydrodynamics, such as minimum fluidization (u_{mf}), minimum bubbling (u_{mb}) and terminal (u_t) velocity. Although many factors affect the fluidization regime, such as solid particle Geldart classification (Kunii & Levenspiel, 1991), the fluid's superficial velocity significantly affects the bed regime. As discussed earlier, choosing the velocities below minimum fluidization velocity leads to having a fixed bed. By rising velocity above that velocity, a smooth expansion of the bed will happen accordingly. In a multiphase (gas-solid) system, bubbles are generated for velocities above minimum bubbling velocity, particles' movement is stronger, and bed height increases relatively. In the velocities above terminal velocity, fluidization will be transferred to a pneumatic transport scenario.

The given alumina sample can be categorized as Geldart A, as per its characteristic properties. Therefore, the minimum fluidization velocity can be calculated by solving the following quadratic equation:

$$\frac{1.75}{\varepsilon_{mf}^3 \, \emptyset_s}(Re)^2 + \frac{150 - (1 - \varepsilon_{mf})}{\varepsilon_{mf}^3 \, \emptyset_s^2}(Re) = \frac{d_p^3 \, \rho_g \, (\rho_s - \rho_g) g}{\mu^2} \quad (3)$$

$$Re = \frac{d_p \, u_{mf} \, \rho_g}{\mu} \quad (4)$$

where, Re is the Reynolds number, ε_{mf} is the voidage at minimum fluidization condition, $\emptyset_s$ is the solid sphericity, d_p is the average particle diameter, μ is the

fluid's dynamic viscosity, g is the acceleration gravity and ρ_g and ρ_s are fluid and solid density.

It is investigated that u_{mb}/u_{mf} is highly dependent on the weight fraction of particles smaller than 45μm (Abrahamsen & Geldart, 1980). Based on experiment on 23 different particle types and 5 different types of fluidized gases, they found the following equation to calculate the minimum bubbling velocity for fine particles as below (Kunii & Levenspiel, 1991):

$$u_{mb} = u_{mf} \frac{2300 \rho_g^{0.13} \mu^{0.52} \ e^{0.72 P_{45\mu m}}}{d_p^{0.8} \left(\rho_s - \rho_g\right)^{0.93}} \quad (5)$$

where, $P_{45\mu m}$ is the weight fraction of particles smaller than 45μm.

One way to calculate the terminal velocity is using Stokes law as below (Barahmand, 2021):

$$u_t = \frac{d_p^2 ((\rho_s - \rho_g) g}{18 \mu} \quad (6)$$

Based on the parameters in Table 2, the velocities have been calculated as $u_{mf} = 0.0106\, m/s$, $u_{mb} = 0.1\, m/s$, $u_t = 0.489\, m/s$.

Table 2. Input parameters for velocity calculations

Parameter	Value	Unit
$\emptyset_s$	0.85	-
d_p	0.000098	*m*
g	9.81	*m/s²*
ρ_s	3958	*Kg/m³*
ρ_g	0.906	*Kg/m³*
μ_g	4.45*10^{-5}	*Pa.s*
$P_{45\mu m}$	0.0897	-

3.1.3 Reactor Diameter Calculation

The required superficial velocity (u_{req}) is equal to the inlet fluid volumetric flow rate ($\dot{V}_{in}$) divided by the cross-sectional area (which is a circle in this case). Hence, the reactor diameter (d_t) can be calculated by:

$$d_t = \left(\frac{4 \dot{V}_{in}}{u_{req} \pi}\right)^{\frac{1}{2}} \quad (7)$$

In a fluidized bed reactor, the required superficial velocity can vary between the minimum bubbling velocity of 0.1 m/s and the terminal velocity of 0.489 m/s, as per the values presented in Table 2, which give values from 5.94 m to 2.47 m for reactor diameter, respectively based on the demand of the inlet gas volumetric flow rate. The flow rate of gas is calculated from the flow rate of particles set by the industrial requirements. The current study is decided based on the stoichiometry of the chlorination reaction. This means that the flow rate of gas, 2.35 m^3/s, can only be adjusted by changing the mass flow rate of particles or the number of reactors. The starting point was a somewhat arbitrary diameter, then the volumetric flow rates and the velocity were calculated stepwise. Then the three parameters were varied until an acceptable result was obtained, meaning that the velocity should be inside an acceptable range, the number of reactors was reasonable, and the diameter seemed appropriate. It ended with an internal diameter of 2.4 m, which resulted in the need for five reactors to handle 0.12 kg/s of solid particle feed in each reactor.

3.1.4 Reactor Height Calculation

An FBR has several heights with different definitions, and it is essential to differentiate between them. The fixed bed height (L_m), the height of the bubbling bed (L_f) and the height of the reactor itself (H_R) are the main ones (Kunii & Levenspiel, 1991). Determining the height depends on several factors, but an important one is the fluid's superficial velocity inside the reactor.

As discussed in Section 3.1.3, the desired superficial velocity passing through the reactor can be achieved by adjusting the reactor diameter. Nevertheless, calculating the reactor height is relatively challenging. This is because many parameters, such as superficial velocity, terminal velocity, and fluidization regime, affect the reactor height simultaneously.

As shown in Figure 2, the height of a fluidized bed reactor can be divided into two main sections: the dense and lean phases. The density of solids decreases with height (Kunii & Levenspiel, 1991). The lean phase (also known as freeboard) height can be divided into two zones, where the lower part of this makes up the Transport Disengaging Height (TDH). Above the TDH is where the reactor outlet or inlet to the cyclone should be placed (Cocco et al., 2014).

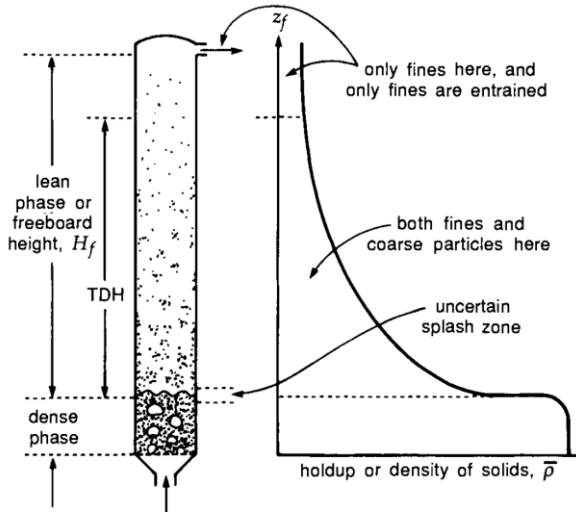

Figure 2. Different heights in a fluidized bed reactor (Kunii & Levenspiel, 1991)

The reactor height can be chosen above TDH. As a result, the minimum reactor height can be calculated by calculating the dense phase height and the TDH. The dense phase or bubbling bed height (L_f) can be calculated by series of equations ab below:

$$L_f = \frac{L_m\,(1 - \varepsilon_m)}{1 - \varepsilon_f} \quad (8)$$

where, L_m is the fixed bed height, ε_m is the voidage in a fixed bed condition and ε_f is the void fraction in a fluidized bed as a whole.

$$\varepsilon_f = \delta + (1 - \delta)\varepsilon_{mb} \quad (9)$$

where, δ is the height of bed at minimum fluidization, and ε_{mb} is the voidage at minimum fluidization condition.

$$\delta = \frac{u_o - u_{mf}}{u_b - u_{mf}} \quad (10)$$

where, u_o is the superficial gas velocity through a bed (empty vessel) and u_b is the velocity of a bubble rising through a bed.

$$u_b = u_0 - u_{mf} + u_{br} \quad (11)$$

where, u_{br} is the velocity of a bubble rising through the bed (Kunii & Levenspiel, 1991).

$$u_{br} = 0.711(g d_b)^{1/2} \quad (12)$$

$$d_b = 0.853[1 + 0.272(u_0 - u_{mf})]^{1/3}(1 + 0.0684z)^{1.21} \quad (13)$$

where, z is any height in the reactor.

Considering $u_0 = 0.175\ m/s$, $L_m = 1.6\ m$, and $\varepsilon_{mb} = 0.6$, the dense phase height will be 4.2 m. By adding 2.5 m as TDH according to Figure 3, the acceptable height for the reactor will be almost 7 meters. In the case of using an internal cyclone or other consideration, higher values can be chosen.

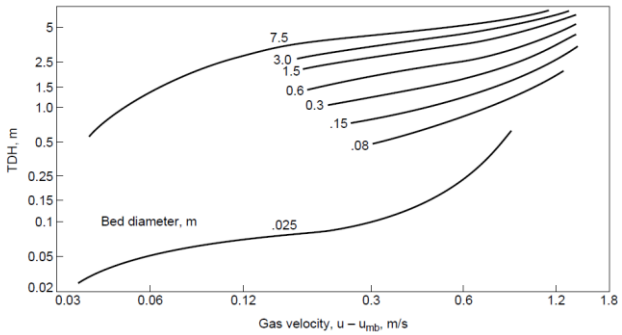

Figure 3. Estimating TDH (Perry, 1950)

4 CPFD Simulation and the Results

The CPFD simulations are based on the particle size distribution. Although in the theoretical calculation in Section 3, the average particle size has been used to calculate u_{mf} and u_{mb}. Based on these theoretical values, the required superficial gas velocity inside the fluidized bed reactor is estimated. This value is then fed into the CFD simulations as one of the inputs, and more sophisticated calculations are done with CFD to study the hydrodynamics of the bed with the entire distribution of particles. The reaction kinetics are based on an isothermal condition at 700℃ (Barahmand et al., 2021b). The activation temperature and pre-exponential factor in the Arrhenius equation are 4000 K and 4583 L.mol−1s−1 for a second-order reaction. As the first step, a preliminary reactor height of 15 meters was selected as an initial estimate to prevent particle escape through the exit through the top of the reactor. As shown in Figure 4, by visual observation and studying the particle mass flow rate through the reactor, CPFD simulation shows that the maximum height particles can achieve at steady-state is around 10 meters, which are slightly higher than the calculated value of 7 m Section 3.1.4. This may happen because of the model uncertainties (Barahmand et al., 2021a). However, the cylindrical reactor height selected is sufficient to contain the particles once it reaches a steady state.

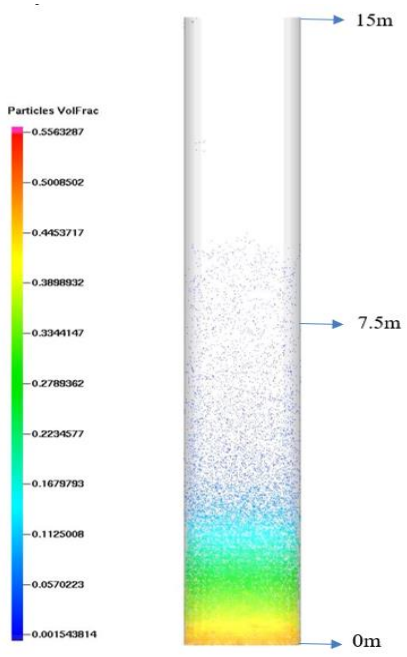

Figure 4. Bed height at the steady-state

The alumina chlorination is an exothermic and fast reaction. Due to the low reaction time, the residence time for particles could be lower as well. Based on the transient barracuda simulations, the reactor is predicted to be stabilized in around two minutes of operational time. Figure 5 shows the variation of the $AlCl_3$ and CO_2 produced at the reactor based on the reaction (1).

Based on the reaction stoichiometry, the mole fraction of produced aluminum chloride and carbon dioxide at steady-state should be 2:3, equivalent to 2:1 mass fraction. Therefore, at the steady state, the average mass flow rate of $AlCl_3$ and CO_2 have been calculated as 0.381 kg/s and 0.188 kg/s, respectively.

The chlorination product composition in the outlet has been calculated and compared with the results based on theoretical manual calculation, process simulations (Aspen Plus®), and CFD simulations (see Table 3).

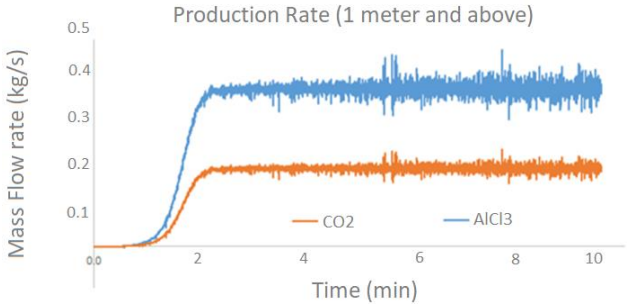

Figure 5. Product's mass flow rate at the outlet

Table 3. Component mass flow rates (kg/s) at the outlet

	Mass Flow Rates (kg/s)		
	CPFD Simulation (Barracuda®)	Theoretical	Process simulations (Aspen Plus®)
$AlCl_3$	0.381	0.314	0.313
CO_2	0.188	0.155	0.155
CO	0.00145	0	0.00021
Cl_2	5×10^{-7}	0	0.00055

By changing the fluid's superficial velocity from minimum bubbling to higher velocities, the reactor experiences different regimes. As the second step, the effect of the superficial velocity inside the reactor on the reaction and hydrodynamics has been studied. Table 4 shows the aluminum chloride ($AlCl_3$) production rate is low (minimum bubbling), medium, and high (terminal) velocities.

Table 4. Effect of the fluid velocity on $AlCl_3$ production

Velocity *m/s*	Particles Inflow Rate (kg/s)	Number of Reactors[1]	Total Production Rate (kg/s)
0.1	0.12	5	1.9040
0.3	0.35	1.7	1.9409
0.52	0.6	1	1.9862

As shown in Table 4, a higher production (around 1%) can be achieved by increasing the velocity, but the number of reactors is reduced from 5 to 1. Therefore, in the next step, the design will be optimized based on the turbulent regime.

5 Design Optimization

The reactor has been optimized based on the turbulent regime (fast fluidization), with four internal cyclones designed based on the Lapple cyclone design (Barahmand et al., 2021a). The reactor diameter has been kept the same as before (2.4 m).

The inlet of the cyclones has a height of 7 meters which gives the reactor height 9.7 m. The cyclones have been designed for 99% efficiency, and the cyclones' arrangement has been chosen based on a Gasifier design reported in the Barracuda® training material (*Barracuda User Manual*, 2021). Figure 6 shows the particle distribution in the reactor.

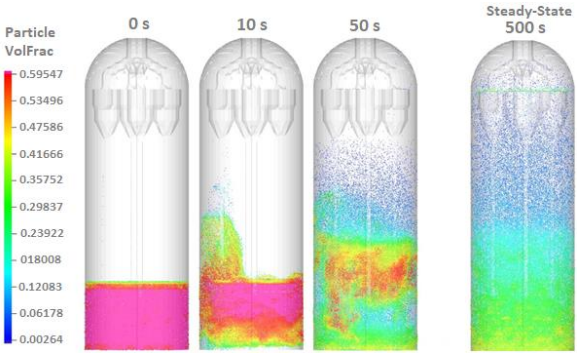

Figure 6. Simulated alumina chlorination reactor (fast fluidized bed with four internal cyclones)

6 Mechanical Design and the Material Selection

Operating conditions in this application (700°C and 50% dry-chlorine) are challenging to handle. A very high temperature decreases the resistance of the metals, and a high concentration of chlorine at the given temperature is insanely corrosive (Chang & Wei, 1991). Most of the strong alloys can tolerate just 2% of chlorine in long-term operations. Figure 7 provides a simple guide to select the different alloys for dry chlorine conditions and indicates design parameters for internals such as tubes in heat exchangers and vessel components or pipes (Davies, 2018). The corrosion rates are based on short-term tests and should not be considered a solution in long-term operations or higher concentrations.

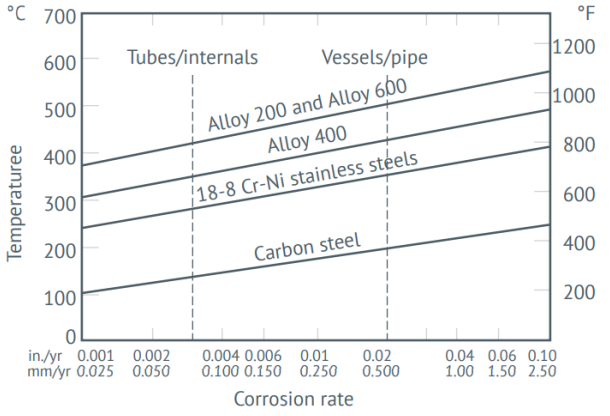

Figure 7. Upper design limits for various alloys in dry chlorine (Davies, 2018)

[1] To reach 0.6 kg/s.

Some of the alloys, specifically nickel-base ones, are more resistant in these kinds of conditions. However, it should not be forgotten that all these experiments and results have been tested in dilute chlorine, which is not the case in a real-life application.

As seen in Figure 8, HAYNES® 214 alloy shows remarkable resistance to corrosion in high-temperature chlorine. Test results are shown for less than 500 hours of contact in a flowing gas mixture of Ar + 20% O_2 + 0.25% Cl_2. Note that the metal loss showed by HAYNES® 214 alloys is very low compared to other alloys tested. Another alternative to this is INCONEL® alloy 600 (*HAYNES® 214® ALLOY*, 2008).

In many cases, constructing a massive reactor with these materials is not economical for design and cost. A carbon steel reactor with special refractory linings, as an example, should be replaced in industrial-scale design.

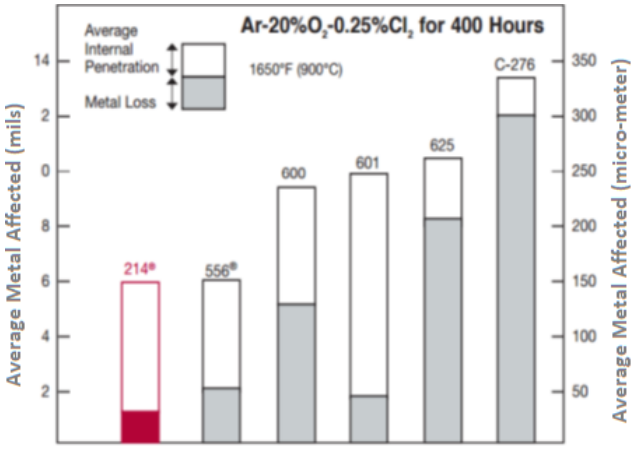

Figure 8. Resistance to chlorine corrosion (*HAYNES® 214® ALLOY*, 2008)

Using the process data, the overall mechanical design for the reactor (Figure 9) has been used to draw the 3D model of the reactor (Figure 10). As discussed earlier, the preferred material for the reactor itself is a combination of carbon steel and refractory lining. Despite being cost-beneficial, this method has more operational safety because of the high temperature. Therefore, two layers of semi-silica brick and high-alumina refractory (150 mm each) have been chosen for the lining. The lining's thickness and materials can be modified during detail engineering.

Figure 11 shows the four internal parallel cyclone's arrangement in the fast fluidized bed reactor. Figure 12 illustrates the top and bottom views of the reactor both internally and externally. For the gas distribution system, a perforated (Kunii & Levenspiel, 1991) pipe sparger mechanism (Kulkarni et al., 2009) has been designed and located at the bottom of the reactor.

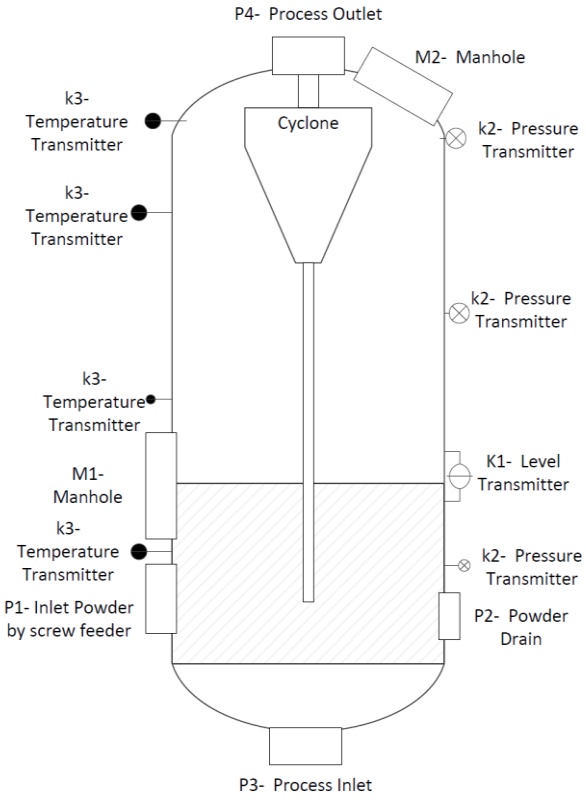

Figure 9. Overall assembly design of the reactor

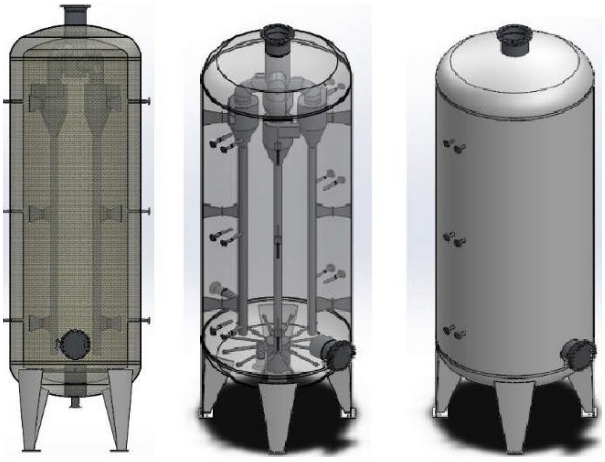

Figure 10. Reactor general assembly

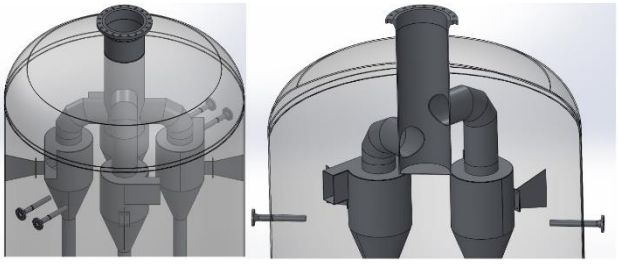

Figure 11. The cyclones arrangement

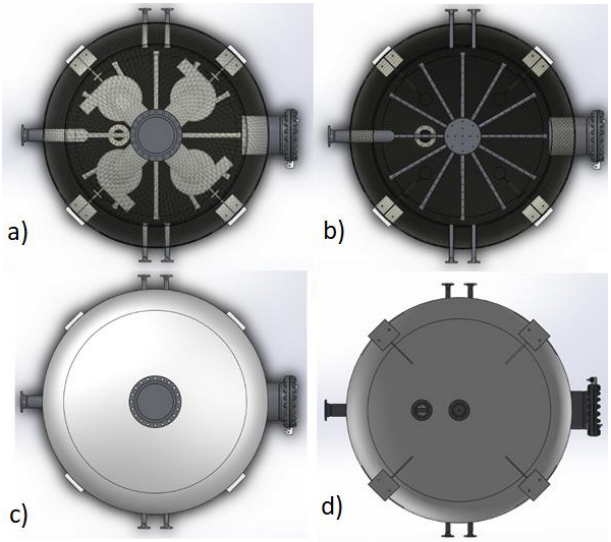

Figure 12. a) Internal top view, b) internal bottom view, c) external top view, and d) external bottom view

7 Conclusion and future development

The present study results have been evaluated and implied that the present approach can be a practical solution for industrial aluminum production with lower environmental effects as CO_2 produced from the process can be separated directly after the crystallization of $AlCl_3$. It can be concluded that the promising results suggest continuing the work and research towards implementing a real-life industrial-scale reactor. It is crucial to validate the CFD simulation data with a lab-scale experimental unit as future work. However, the results have been verified within the considered design parameters with theoretical methods and Aspen Plus® simulations. The overall internal diameter and height of the reactor are 2.4 m and 8 m, respectively. The circulation unit includes four parallel cyclones with a 0.45 m diameter.

References

A. Abrahamsen and D Geldart. Behavior of gas-fluidized beds of fine powders part I. Homogeneous expansion. *Powder Technology*, *26*(1), 35–46, 1980. doi:10.1016/0032-5910(80)85005-4

N. Ahmadpour Samani, C, Jayarathna, and L.A.Tokheim. Fluidized bed calcination of cement raw meal: Laboratory experiments and CPFD simulations. *In Proceedings - 61st SIMS Conference on Simulation and Modelling SIMS 2020*, 2020. doi:10.3384/ecp20176407

Z. Barahmand. *Design of an Industrial Chlorination Reactor Using CPFD Simulations*, Master Thesis, University of South-Eastern Norway, 2021.

Z. Barahmand, C. Jayarathna, and C. Ratnayake. Sensitivity and uncertainty analysis in a fluidized bed reactor modeling. *In Proceedings - 1st SIMS EUROSIM Conference on Modelling and Simulation*, Finland, 2021a.

Z. Barahmand, C. Jayarathna, and C. Ratnayake. The effect of alumina impurities on chlorination in a fluidized bed reactor: A CPFD study. *In Proceedings - 1st SIMS EUROSIM Conference on Modelling and Simulation*, Finland, 2021b.

Barracuda User Manual. CPFD Software, 2021. https://cpfd-software.com/

Ø. Bjarte. *Carbochlorination routes in production of Al*, pages 57, SINTEF Industry, 2018.

A. N. Chandran, S. S. Rao, and Y. B. G. Varma. Fluidized bed drying of solids. *AIChE Journal*, *36*(1), 29–38, 1990. doi:10.1002/aic.690360106

Y. N. Chang and F. I. Wei. High-temperature chlorine corrosion of metals and alloys. *Journal of Materials Science*, *26*(14), 3693–3698, 1991. doi: 10.1007/BF01184958

R. Cocco, S. Karri, and T. Knowlton. Introduction to Fluidization. *Chemical Engineering Progress*, *110*, 21–29, 2014.

M. Davies. *Alloy selection for service in chlorine, hydrogen chloride and hydrochloric acid*. Nickel Institute, 2018.

HAYNES® 214® ALLOY. Haynes International, Inc. 2008. haynes.ch/doc/haynes/214_h3008.pdf

A. V. Kulkarni, S. V. Badgandi, and J. B. Joshi. Design of ring and spider-type spargers for bubble column reactor: Experimental measurements and CFD simulation of flow and weeping. *Chemical Engineering Research and Design*, *87*(12), 1612–1630, 2009. doi:10.1016/j.cherd.2009.06.003

D. Kunii and O. Levenspiel. *Fluidization Engineering*. Butterworth-Heinemann, 1991.

Z. Liu, G. Wang, and J. Yi. Study on heat transfer behaviors between Al-Mg-Si alloy and die material at different contact conditions based on inverse heat conduction algorithm. *Journal of Materials Research and Technology*, *9*(2), 1918–1928, 2020. doi:10.1016/j.jmrt.2019.12.024

National Fuels and Energy Conservation Act. S. 2176, U.S. Government Printing Office, 1973.

J. H. Perry. *Chemical Engineers' Handbook* (Third Edition). McGraw-Hill, New York, 1950.

Y. K. Rao and M. K. Soleiman. *Alumina chlorination*. United States Patent No. US4565674A, 1986.

M. A. Rhamdhani, M. Dewan, G. Brooks, B. Monaghan, and L. Prentice. Alternative Al Production Methods: Part 1. A Review. *Mineral Processing and Extractive Metallurgy IMM Transactions Section C*, *122*, 87–104, 2013.

Survey of potential processes for the manufacture of aluminium, ANL/OEPM-79-4. Little , D. Arthur, Inc., Cambridge, MA, USA, 1979. doi:10.2172/5669730

J. Thonstad. *Aluminium Electrolysis: Fundamentals of the Hall-Héroult Process*. Aluminium-Verlag, 2001.

CPFD modeling to study the hydrodynamics of an industrial fluidized bed reactor for alumina chlorination

Zahir Barahmand[1] Chameera Jayarathna[2] Chandana Ratnayake[1,2]

[1] Department of Process, Energy and Environmental Technology, University of South-Eastern Norway
zbarahmand@gmail.com
[2] SINTEF Tel-Tek, SINTEF Industry, Porsgrunn, Norway

Abstract

Aluminum is one of the most used metals. Since aluminum has a unique combination of appealing properties and effects, it allows significant energy savings in many applications, such as vehicles and buildings. Although this energy-saving leads to lower CO_2 emissions, the production process of aluminum still dramatically impacts the environment.

The process used exclusively in the aluminum industry is the Hall-Héroult process with a considerable carbon footprint and high energy consumption. As the best alternative, Alcoa's approach (which is not industrialized yet) is based on the chlorination of processed aluminum oxide, reducing the traditional method's negative impacts.

Further to Alcoa's effort, this study aims to investigate the possibility of a new low-carbon aluminum production process. This aim can be achieved by designing an industrial fluidized bed reactor with an external (due to high corrosion inside the reactor) gas-solid separation unit. The aim is to handle 0.6 kg/s of solid reactants and produce aluminum chloride as the main product. The research focuses on determining the best bed height based on the available reaction rates, choosing the best reactor dimension to reduce particle outflow under isothermal conditions (700°C). Autodesk Inventor® and Barracuda® are used for 3D modeling of the reactor and CFD simulation for multiphase (solid-gas) reactions, respectively. Although results have shown that the bed aspect ratio (H/D; H- bed Height and D- bed Diameter) does not affect the reaction, it highly affects the reactor's hydrodynamics and particle outflow. The final design shows the best hydrodynamics belongs to bed aspect ratio equal to 2.

Keywords: CPFD simulation, Bubbling regime, Fluidized bed reactor, Reactor design, Alumina Chlorination

1 Introduction

Aluminum is now the second most used metal globally (Bray, 2021). This is because aluminum has a unique combination of appealing properties and functionalities allowance for significant energy savings in many applications, such as vehicles and buildings. Besides, recycled aluminum is highly energy-efficient, using only 5% of primary production energy (Mapping Resource Prices: The Past and the Future, 2012). Although this energy-saving leads to lower CO_2 emissions, the production process of aluminum still has a massive impact on the environment (The Aluminium Effect, 2021). One of the aluminum industry's key targets (such as many other sectors) has remained aluminum manufacturing with the lowest carbon footprint possible, thanks to growing concern about global climate change (Adoption of the Paris Agreement, 2015). The industrial sector contributes approximately 21% of global greenhouse gas (GHG) emissions, with aluminum industries accounting for 1.0 percent (11.5 tons of CO_2 per ton of aluminum) (Clemence, 2019), and many key players in the global aluminum sector have taken the lead and made progress in reducing CO_2 emissions in their smelting operations. This becomes more important when the significant increase in the global aluminum market size from around 150 billion dollars in 2019 to 250 billion by 2027 with a compound annual growth rate of 5.7% during the period is reported (Aluminium Market Size, Trends | Global Industry Forecast [2027], 2021).

The process which is used almost exclusively in the aluminum industry is the Hall-Héroult process. This process has turned aluminum metal into a commodity product since its invention in 1886 (Kovács et al., 2020). Alumina is dissolved in a cryolite bath in this continuous process, and aluminum is produced by electrolysis. In this cryolite-alumina melt electrolysis, aluminum oxide is dissolved in molten cryolite (Na_3AlF_6) and afterward electrolytically reduced to aluminum at almost 960°C. Carbon anodes are used in the process, consumed during electrolysis, resulting in the formation of CO_2. This process suffers from relatively high heat loss from the electrolytic cells and increased CO_2 emissions from the anodes, even though manufacturers have gradually improved their production processes. Besides, the Hall-Héroult process moves down to its potentially lowest energy consumption and CO_2 emissions during decades (Prasad, 2000).

Alternative aluminum processing strategies have been under intense investigation due to the comparatively high energy usage and carbon footprint

associated with anode consumption (Thonstad, 2001). In continuation of this, in 1973, an innovative process was introduced by Alcoa Corporation, and it had several advantages compared to the commonly used method (Hall-Héroult) at that time (*National Fuels and Energy Conservation Act, S. 2176*, 1973). Alcoa's process is based on the chlorination of processed aluminum oxide. The chlorination process has the advantages of being more compact and operating at a lower temperature than the Hall-Héroult process, normally 700°C. The chemical carbon footprint of the two processes, however, is similar since aluminum chloride is created by carbochlorination of aluminum oxide, which includes aluminum oxide reacting with carbon (C) and chlorine gas (Cl_2) to form aluminum chloride ($AlCl_3$) and CO_2. As a result, the same amount of CO_2 is extracted per kilogram of aluminum in classical electrolysis. However, there are some significant differences although that make this process fascinating. First, this process does not necessitate the use of pure aluminum oxide as a raw material exclusively.

Consequently, the Bayer process could be skipped, eliminating the issue of disposing of vast amounts of red sludge (*Survey of Potential Processes for the Manufacture of Aluminium*, 1979). Second, carbochlorination can result in relatively high CO_2 concentrations in the process gas, making CO_2 capture and storage easier to implement (Øye, 2019). The third, the mechanical properties of carbon, which is merely a chemical reactant in aluminum chloride production by chlorination, are unnecessary. As a result, biocarbon can be used instead of coke from petroleum refineries, required by the Hall-Héroult process requires anodes with high mechanical strength and density (Øye, 2019).

Around the time of the Alcoa process's implementation, a great deal of work was conducted on both the process and the chlorination of raw materials. Later, interest somewhat waned, but it has recently reappeared. Theoretically, many minerals containing sufficient amounts of aluminum can be directly chlorinated. So naturally, minerals with such a weak thermodynamic bond to aluminum, such as clay minerals bauxite and kaolinite, as well as hydrated aluminum sulfates, are preferred (Peterson & Miller, 2007).

Until now, fluidized bed technology has been studied in a wide range of applications. Even though it is a well-known technology, designing such a reactor with ideal and realistic operating conditions continues to be a challenge without advanced numerical calculations. The complexity of hydrodynamics and the uncertain nature of the particles' behavior with their enormous influential characteristics in the fluidized bed reactor make this engineering process complex (Barahmand, Aghaabbasi, et al., 2021). A highly corrosive environment inside the reactor adds the design further challenges.

2 Hydrodynamics

The hydrodynamic models depict solid motion and distribution, gas-solid mixtures, bubble size, velocity, growth, the relationship between the bubble and emulsion phases, and mass and heat transfer processes (Yang, 2003). The balance of forces between particles and gas velocity defines the hydrodynamics of a fluidized bed. It is possible to set the required fluidization regime by adjusting the gas velocity (Philippsen et al., 2015). The fixed bed has a low gas velocity, which keeps the bed static. The minimal fluidization regime is the fluidization regime's beginning point. When the gas velocity exceeds the minimum fluidization velocity, the bubbles form, causing flow instability. When the gas velocity exceeds the terminal velocity, the pneumatic transfer of particulates occurs, and it is employed in circulating fluidized beds (Kunii & Levenspiel, 1991).

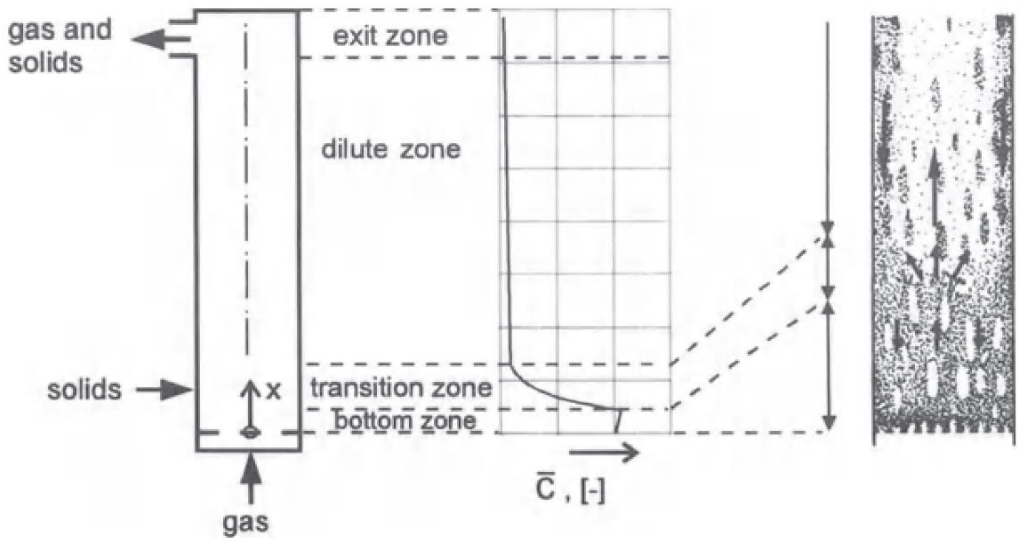

Figure 1. Solids motion and of different solids volume fractions zones (Horio, 1997)

Because of interactions between the gas and solid phases, fluidized beds have highly complex hydrodynamics. The movements of gases and solids are tough to define and explain. Hydrodynamics in a fluidized bed reactor deals with the mechanics of gas-solid suspensions and the hydrodynamic properties of gas-solid contacts. The dilute suspension's clustering nature, first observed from the relatively high gas-solid slip velocity, has been the most significant point of concern from a theoretical perspective. On the other hand, the impact of structural factors such as column diameter, wall shape, gas distributor design, exit configuration, solid separation and recycling equipment, as well as operating conditions, on the performance of circulation systems are the main hydrodynamic concerns from an engineering standpoint which is relatively interrelated with scientific aspects (Horio, 1997).

Any mechanical interactions in the model must be considered in a mathematical model to correctly simulate all of the flow processes associated with gas-solid flows. These interactions, which are dependent on the mean and fluctuating components of the gas and solid velocity fields, are described by (Sinclair & Jackson, 1989) as 1) the interaction between average gas and solid velocity results in the drag force between the two phases, 2) the gas-phase Reynolds stresses are created by the interaction of average and fluctuating gas velocities, 3) the interaction between average and fluctuating solid velocities in the solid assembly that causes stresses., and 4) the interaction of particles with a fluctuating gas velocity, resulting in an interfacial flux of kinetic energy correlated with arbitrary motion.

The properties of the particles have a significant effect on fluidization. Geldart (Geldart, 1973) divided particle behavior in fluidization into four categories, which are now generally recognized and applied in fluidized bed modeling.

- Group A: The particles are small (30–150 μm) and have a low density (1.4 g/cm^3). The fluidization is simple, smooth, and consistent. It allows operating with modest gas flows while still controlling the size and speed of the bubbles.
- Group B: Medium-diameter particles (40–500 μm) having a density of 1.4 – 4 g/cm^3. For high gas flow rates, fluidization is appropriate. Bubbles emerge at the onset of fluidization and expand rapidly.
- Group C: Particles with a diameter of less than 30 μm. Fluidization is a complex process.
- Group D: Particles that are dense and big (d > 500 μm). Fluidization is complex and uneven, making spouted beds suitable.

2.1 Particle motion and solids mixing mechanisms

Studying fluidized bed hydrodynamics (Hartge et al., 1988; Zhang et al., 1991) has indicated that the solids volume concentrations in the fluidized bed reactor can be classified into mainly four regions (Figure 1). First, cross-sectional average solids volume concentrations of usually 0.1 to 0.2 characterize the bottom region, where solid particle acceleration occurs. Next, a dilute region follows the transition zone, occupying most of the riser height and marked by low solids volume concentrations (> 1%). Finally, the exit geometry governs the fluid dynamics throughout the exit zone at the reactor's top (smooth or abrupt exit) (Horio, 1997).

2.1.1 Particle motion in the dense bed

In a previous work (Svensson et al., 1993), it is reported that the dense bottom zone of a fluidized bed experiences hydrodynamic activity similar to bubbling or turbulent fluidized beds, with fluidization gas flowing through the reactor's bottom typically in the form of voids, based on pressure variations at the bottom. These voids break and push solids into the transfer zone as they hit the bottom zone's surface. Since there have not been enough local experiments on solids mixing in the bottom zone of a fluidized bed, it is safe to conclude that the mixing processes are identical to those in bubbling fluidized beds. According to (Kunii & Levenspiel, 1991), "the transport in the wakes of rising voids is the essential mixing mechanism."

2.1.2 Particle motion in the dilute zone

The presence of two phases (lean and dense phase) can describe the dilute region. According to studies in local hydrodynamics (Hartge et al., 1988), the lean phase comprises an upward-moving dilute suspension, while the dense phase comprises downward traveling particle clusters. The dense phase is made near the riser wall for the most part and has solids concentrations at least marginally more significant than the lean phase. For the sake of convenience, the dense phase is often believed to be constrained to a layer near the wall. Figure 2 demonstrates radial profiles of local solids mass fluxes collected by a suction probe as an example of solids motion in the dilute zone (Kruse & Werther, 1995). Reduced solids fluxes[1] are plotted against r/R to demonstrate the results. The upward solids mass fluxes are highest at the reactor's core and decline as they approach the sidewall, while the downward mass fluxes are the opposite. Under these operating conditions, comparatively high downward-moving mass fluxes have been observed at the wall.

The presence of a radial profile of local average solids velocities is another feature of the dilute region. It is

[1] Averaging the local disparity between upward and downward mass fluxes across the cross-sectional area.

reported that the reactor's core has the highest solids velocities (Figure 3), with mean solids velocities of 1.5 to 2 times the superficial gas velocity (Yang et al., 1992). Showing a dominant downward movement of solid particles near the sidewall, negative values are registered. In 1992 (Rhodes et al., 1992), a high-speed video camera to perform a more thorough analysis of the acceleration of downward flowing solids in regions near the wall was used. At velocities ranging from -0.3 to -0.4 m/s, high-density particle swarms were observed descending in contact with the wall. Falling solids were observed to drop with a velocity of -1 m/s as strands a few millimeters from the wall.

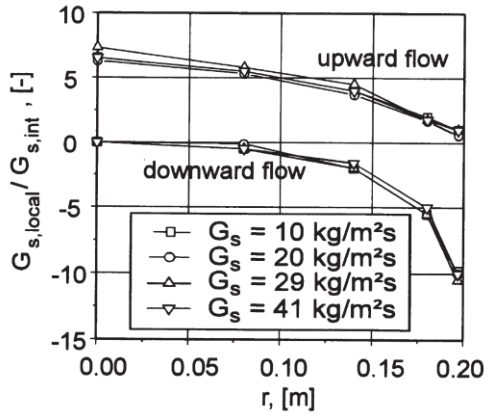

Figure 2. Radial profiles of solids mass fluxes (Horio, 1997)

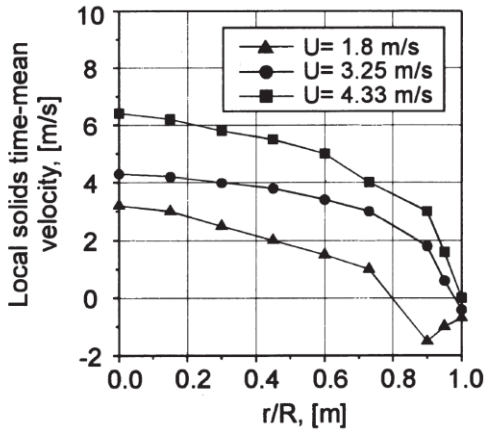

Figure 3. Radial profiles of solids velocities (Horio, 1997)

2.1.3 Particle motion in the transition zone

A transition from the dense bottom zone to the dilute zone happens in this zone, with low solids volume concentrations of solid and the gas phase (Senior & Brereton, 1992). Significant volumes of solids are released from the bottom zone into the transition zone through bursting voids. Solids from the dilute zone are carried back into the zone by dropping clusters. As a consequence, this is a high-intensity mixing region. Solid particles mix in the transfer region; on the other hand, the phenomenon has not yet been studied separately (Horio, 1997).

2.1.4 Particle motion in the exit zone

In the literature, two primary forms of exit geometries have been identified as smooth and abrupt exits. The first is a smooth bent pipe from the top of the fluidized bed reactor to the gas separation unit (cyclone) entry, with no impact on the reactor's flow regime, and the second geometry includes a sharp 90° take-off below the reactor's end cap. Experiments using an abrupt exit (Mabrouk et al., 2008) have revealed increasing solids concentrations at the top of the riser. This effect is caused by solids colliding with the reactor's end cap. Heavier particles, which cannot follow the gas flow through the outlet, are mirrored at the riser's top, allowing solids to accumulate in this region (Horio, 1997).

2.2 Heterogeneous particles fluidization

Solid segregation happens when different solids with varying sizes and densities are fluidized, closely related to solids mixing. Solids segregation in bubbling fluidized beds has gained much interest recently (Nienow, 1985). The consequences of segregation are commonly unfavorable and harm hydrodynamics inside the reactor (Barahmand et al., 2021c).

2.3 Particle's classification

In (Zhang et al., 2014), The fluidization state has been described using a generalized flow regime diagram with the Reynolds number as a function of the Archimedes number. As seen in Figure 4, the Archimedes number (or Geldart classification) and the height to bed diameter ratio may be used to classify diverse materials properly. These experiments have studied the effect of different H/D based on hundreds of powders in different Geldart classifications on the fluidized bed hydrodynamics. In practice, there are, in many cases, there are different alumina types in a process that have different physical properties (Barahmand et al., 2021c). Hence, considering and studying the possibility of segregation is essential for designers.

3 CPFD simulations and discussion

The main goal of the present study is to simulate the alumina chlorination reaction under an isothermal condition at 700℃ in a simple cylindrical fluidized bed reactor and study the effect of different bed aspect ratios (H/D) on the reaction conversion rate and hydrodynamics of the system. The reactor height has been chosen relatively high enough to avoid particle escape in fluidization. The alumina size and reaction

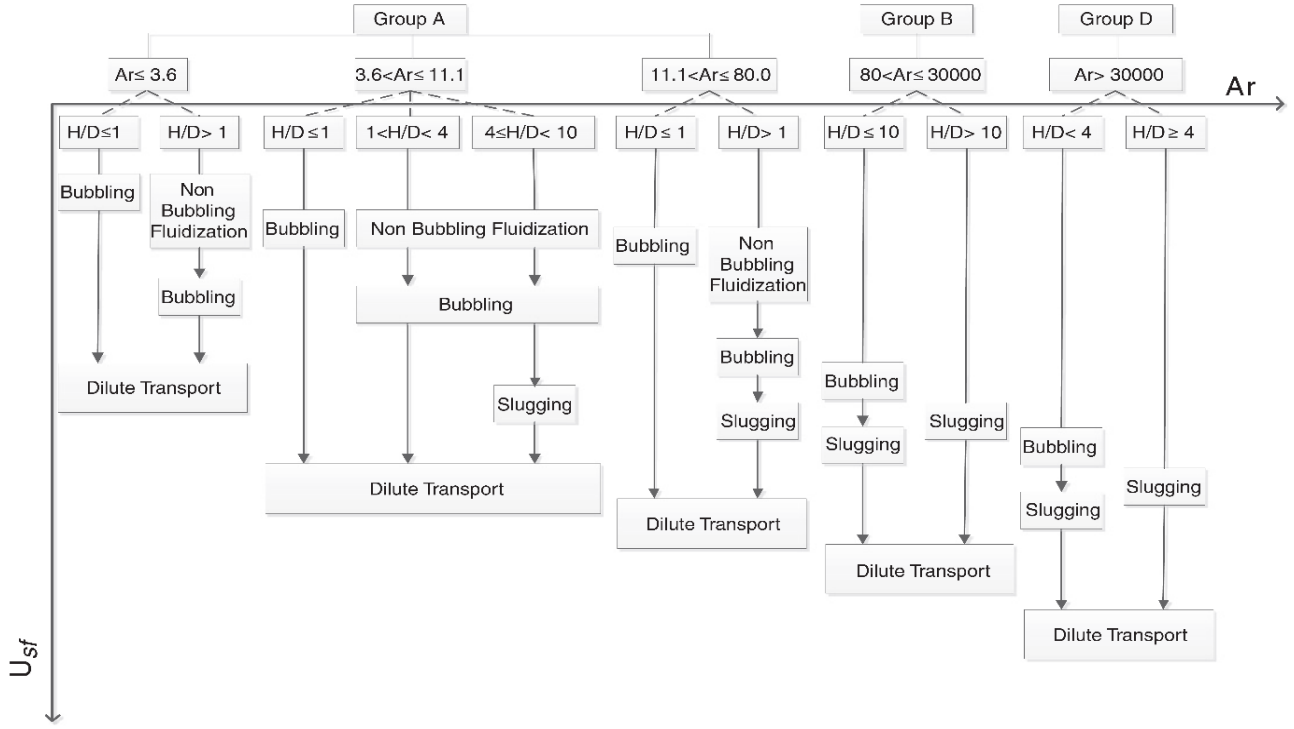

Figure 4. Block flow regime diagram for different particle classification in a fluidized bed (Shaul et al., 2012)

kinetics are based on (Barahmand et al., 2021b). The Archimedes number for the alumina sample can be calculated as 3.59 (Geldart group A). Therefore, H/D below and above unity has been considered into simulations. This study investigates the effect of different bed aspect ratios and operating pressures on the reaction conversion rate. The overall reaction and mass balance are given in equations (1) and (2).

$$Al_2O_3 + 3Cl_2 + 3CO \rightarrow 2AlCl_3 + 3CO_2 \qquad (1)$$

3.1 Bed aspect ratio (H/D)

To study the effect of bed aspect ratio on reactor hydrodynamics and reaction efficiency, different H/Ds have been chosen (0.5, 1, 1.5, 2, 2.5, and 3).

Figure 5 shows the initial bed at the time 0 for 6 different cases. Almost 1500 seconds after fluidization, the system experiences a steady-state. The expanded beds are shown in Figure 6, where the red color represents the solid region in the bed. In all cases, the bed's solid regions cause the fluid to escape through the area between the reactor wall and the bed.

The Cl_2 average mass concentrations and mole fractions at the outlet are given in Table 1. As shown in Figure 7, the highest and lowest Cl_2 concentration belongs to H/D equal to 3 and 1, respectively. Thus, the results show that the bed aspect ratio (above unity) harms the reaction conversion.

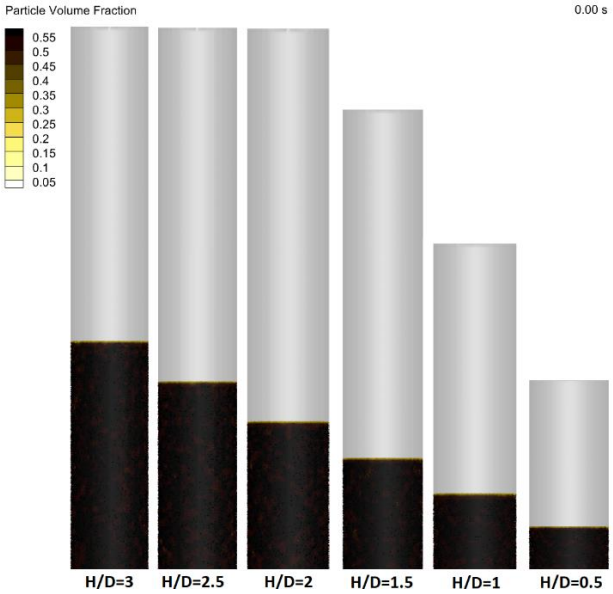

Figure 5. Initial bed for different H/Ds

Table 1. Cl_2 concentration and mole fraction at the outlet

H/D	Mass Concentration (g/m^3)	Mole Fraction
3	38.15	0.0375
2.5	21.2	0.0161
2	19.2	0.0146
1.5	5.6	0.0043
1	0.62	0.0005
0.5	1.96	0.0015

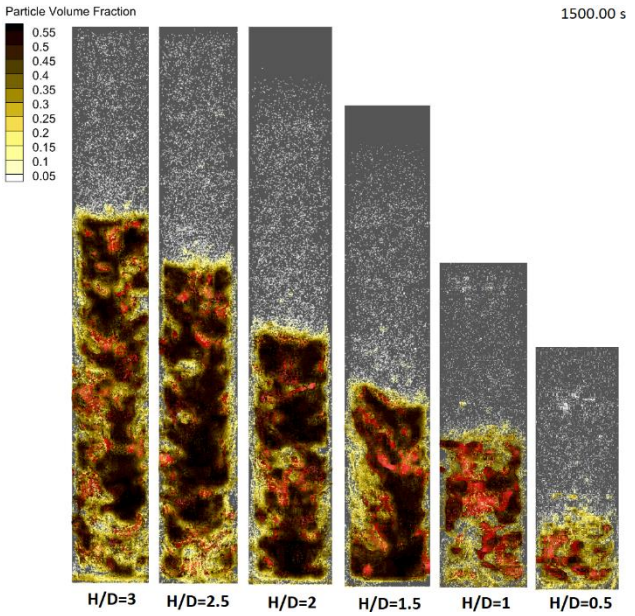

Figure 6. Solid regions in the bed at steady-state

Although the H/D equal to unity shows the best performance in reaction conversion, to choose a proper bed aspect ratio, it is necessary to consider the whole hydrodynamics of the bed (Barahmand et al., 2021a, 2021b). Too low H/D can cause channeling, and it may reduce the reaction efficiency. As a result, Cl_2 concentration at the reactor outlet may increase. Even a tiny amount of Cl_2 at the outlet could cause problems if there is no purification process on Cl_2. Too high H/D may also cause channeling because of creating strong solid regions in the bed. Simultaneously, too high H/D will increase energy consumption significantly due to the increased pressure drop of the reactor.

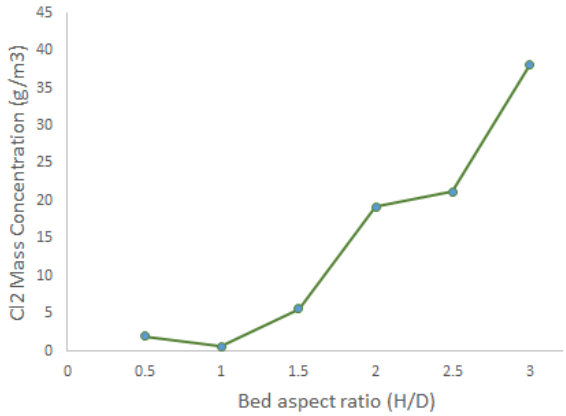

Figure 7. Average Cl_2 concentration in the outlet vs. H/D

3.2 Pressure Effect

In the next step, the present work aims to study the effect of the operating pressure on the reactor's chemical performance. The outlet pressure boundary condition directly affects the fluid's superficial velocity for a certain fluid mass flow rate. Choosing H/D=1, several simulations have been done in different conditions. Each simulation has a duration of at least 1500 seconds to reach the pseudo-steady-state. As seen in Figure 8, the average Cl_2 mass concentration in the outlet increases by increasing the outlet pressure. Therefore, it can be concluded that it is favorable to operate the reactor with the lowest pressure to have better reaction conversion.

There is a negative correlation between the reactor's outlet pressure and the reaction conversion. Studying the effect of outlet pressure on Cl_2 mass concentration illustrates that the minimum concentration belongs to the range when outlet pressure is between 1 and 2 bars.

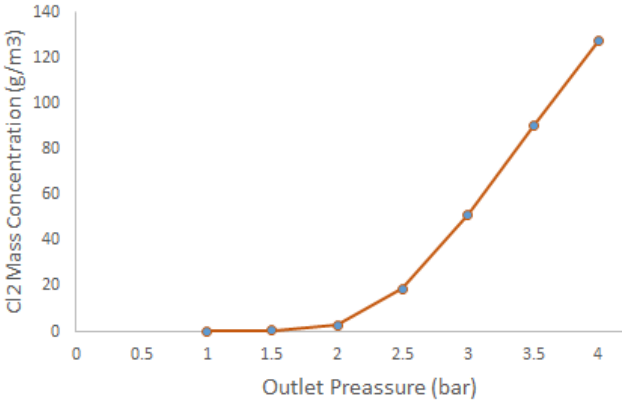

Figure 8. The effect of the pressure on the Cl_2 concentration

4 Conclusions

As simulation results show, almost all the Cl_2 are consumed within the first meter of the reactor, which means the current range of bed and reactor height may not be fully activated in an actual chlorination process. However, the H/D value has a significant role when it comes to suitable hydrodynamics of the reactor. Therefore, selecting the reactor specification for good hydrodynamics of the gas-solid fluidized bed reactor is very important. Too low and high H/D can cause channeling. A low H/D may reduce the reaction efficiency. Too high H/D may also cause channeling because of creating strong solid regions or increasing energy consumption significantly. The results show that the reactor performs best (minimum Cl_2 mass concentration at the outlet) when the outlet pressure ranges between 1 and 2 bars.

Considering all factors to ensure the reliable and effective operation of the fluidized bed reactor (such as hydrodynamics, change in Cl_2 concentration over height, and particle outflow, etc.), the suitable height to diameter ratio (H/D) can be considered as 2. Results of further simulations related to the selected H/D ratio are reported by (Barahmand, 2021).

References

Adoption of the Paris Agreement (FCCC/CP/2015/L.9/Rev.1). United Nations, 2015. https://unfccc.int/resource/docs/2015/cop21/eng/l09r01.pdf

Aluminium Market Size, Trends | Global Industry Forecast [2027], 2021.

Z. Barahmand. *Design of an Industrial Chlorination Reactor Using CPFD Simulations* [Master Thesis]. University of South-Eastern Norway, 2021.

Z. Barahmand, O. Aghaabbasi, E. K. L. Rustad, J. L. Salcido, C. Jayarathna, and C. Ratnayake. Designing of a medium-scale circulating fluidized bed reactor for chlorination of processed aluminum oxide. *In Proceedings - 1st SIMS EUROSIM Conference on Modelling and Simulation*, Finland, 2021.

Z. Barahmand, C. Jayarathna, and C. Ratnayake. CPFD simulations on a chlorination fluidized bed reactor for aluminum production: An optimization study. *In Proceedings - 1st SIMS EUROSIM Conference on Modelling and Simulation*, Finland, 2021a.

Z. Barahmand, C. Jayarathna, and C. Ratnayake. Study of the thermal performance of an industrial alumina chlorination reactor using CPFD simulation. *In Proceedings - 1st SIMS EUROSIM Conference on Modelling and Simulation*, Finland, 2021b.

Z. Barahmand, C. Jayarathna, and C. Ratnayake. The effect of alumina impurities on chlorination in a fluidized bed reactor: A CPFD study. *In Proceedings - 1st SIMS EUROSIM Conference on Modelling and Simulation*, Finland, 2021c.

E. L. Bray. *Aluminum Statistics and Information*. United State National Minerals Information Center, 2021. https://www.usgs.gov/centers/nmic/aluminum-statistics-and-information

C. Clemence. *Leaders Emerge In The Aluminium Industry's Race To Zero Carbon*. Aluminium Insider, 2019. https://aluminiuminsider.com/leaders-emerge-in-the-aluminium-industrys-race-to-zero-carbon/

D. Geldart. Types of gas fluidization. *Powder Technology*, 7(5), 285–292, 1973. doi:10.1016/0032-5910(73)80037-3.

E. Hartge, D. Rensner, and J. Werther. Solid concentration and velocity patterns in circulating fluidized bed. In P. Basu & J. F. Large (Eds.), *Circulating Fluidized Bed Technology*, pages 165–180. Pergamon, 1988. doi:10.1016/B978-0-08-036225-0.50020-4

M. Horio. *Circulating Fluidized Beds* (J. R. Grace, A. A. Avidan, & T. M. Knowlton, Eds.). Springer Netherlands, 1977. doi:10.1007/978-94-009-0095-0_2

A. Kovács, C. Breward, K. Einarsrud, S. Halvorsen, E. Nordgård-Hansen, E. Manger, A Münch, and J. Oliver. A heat and mass transfer problem for the dissolution of an alumina particle in a cryolite bath. *International Journal of Heat and Mass Transfer*, 162, 120232, 2020. doi:10.1016/j.ijheatmasstransfer.2020.120232

M. Kruse and J. Werther. 2D gas and solids flow prediction in circulating fluidized beds based on suction probe and pressure profile measurements. *Chemical Engineering and Processing: Process Intensification*, 34(3), 185–203, 1995. doi:10.1016/0255-2701(94)04004-4

D. Kunii, O. Levenspiel. *Fluidization Engineering*. Butterworth-Heinemann, 1991.

R. Mabrouk, J. Chaouki, and C. Guy. Exit effect on hydrodynamics of the internal circulating fluidized bed riser. *Powder Technology - POWDER TECHNOL*, 182, 406–414, 2008. doi:10.1016/j.powtec.2007.07.008

Mapping resource prices: The past and the future. ENV.G.1/FRA/20410/0044; pages 370. ECORYS, 2012.

National Fuels and Energy Conservation Act, S. 2176. U.S. Government Printing Office, 1973.

A. W. Nienow. Fluidization of dissimilar materials. *Fluidization*, 357–381, 1985.

B. Øye, B. Could the chloride process replace the Hall-Héroult process in aluminium production? *SINTEFblog*, 2019, March 28. https://blog.sintef.com/sintefenergy/energy-efficiency/could-the-chloride-process-replace-the-hall-heroult-process-in-aluminium-production/

W. S. Peterson and R. E. Miller. *Hall-Heroult Centennial: First Century of Aluminum Process Technology*, 2007.

C. Philippsen, A. Vilela, and L. Zen. Fluidized bed modeling applied to the analysis of processes: Review and state of the art. *Journal of Materials Research and Technology*, 4(2), 208–216, 2015. doi:10.1016/j.jmrt.2014.10.018

S. Prasad. Studies on the Hall-Heroult aluminum electrowinning process. *Journal of the Brazilian Chemical Society*, 11, 245–251, 2000. doi:10.1590/S0103-50532000000300008

M. Rhodes, H. Mineo, and T. Hirama. Particle motion at the wall of a circulating fluidized bed. *Powder Technology*, 70(3), 207–214, 1992. doi:10.1016/0032-5910(92)80055-2

R. Senior and C. Brereton. Modelling of circulating fluidised-bed solids flow and distribution. *Chemical Engineering Science*, 47(2), 281–296, 1992. doi:10.1016/0009-2509(92)80020-D

J. Sinclair, and R. Jackson. *Gas-particle flow in a vertical pipe with particle-particle interactions*, 1989. doi:10.1002/AIC.690350908

Survey of potential processes for the manufacture of aluminium (ANL/OEPM-79-4). Little (Arthur D.), Inc., Cambridge, MA (USA), 1979.

A. Svensson, F. Johnsson, and B. Leckner. Fluid-dynamics of the bottom bed of circulating fluidized bed boilers. *In Proceedings - 12th International Conference on Fluidized-*Bed Combustion, 2, 887–897, 1993.

The Aluminium Effect—European Aluminium. 2021. https://european-aluminium.eu/about-aluminium/the-aluminium-effect/

J. Thonstad. *Aluminium Electrolysis: Fundamentals of the Hall-Héroult Process*. Aluminium-Verlag, 2001.

M. Van de Velden, J. Baeyens, J. Degrève, and J. Seville. The residence time distribution of the gas phase in circulating fluidized beds (CFB). *In Proceedings - European Congress of Chemical Engineering*, 16–20, 2007.

W. Yang. *Handbook of Fluidization and Fluid-Particle Systems*. CRC Press, 2003.

Y. Yang, Y. Jin, Z. Yu, and Z. Wang. Investigation on slip velocity distributions in the riser of dilute circulating fluidized bed. *Powder Technology*, 73(1), 67–73, 1992. doi:10.1016/0032-5910(92)87008-X

H. Zhang, L. Shu, and S. Liao. Generalized Trapezoidal Fuzzy Soft Set and Its Application in Medical Diagnosis. *Journal of Applied Mathematics*, e312069, 2014. doi:10.1155/2014/312069

W. Zhang, Y. Tung, F. Johnsson. Radial voidage profiles in fast fluidized beds of different diameters. *Chemical Engineering Science*, 46(12), 3045–3052, 1991.

Study of the Thermal Performance of Industrial Alumina Chlorination Reactor Based on CPFD Simulation

Zahir Barahmand[1] Chameera Jayarathna[2] Chandana Ratnayake[1,2]

[1] Department of Process, Energy and Environmental Technology, University of South-Eastern Norway
zbarahmand@gmail.com
[2] SINTEF Tel-Tek, SINTEF Industry, Porsgrunn, Norway

Abstract

As a part of the new sustainable aluminum production process under study, alumina chlorination plays a crucial role. The relevant process is an exothermic reaction in a fluidized bed reactor. The solid alumina reacts with chlorine and carbon monoxide and produces aluminum chloride and carbon dioxide as the main products. Then carbon dioxide can be separated efficiently. The optimum temperature for the alumina chlorination is 700℃. The reactor's temperature should be kept in the range of 650-850℃ (most preferably 700℃) because below that temperature range, the reaction rate drops, and above that range, the alumina (which usually is γ-alumina) transfers to other alumina types, which is not desirable for the purpose.

Extending other simulation studies by authors on alumina chlorination in an isothermal condition, the CPFD method has been utilized to thermal study and simulate the overall heat transfer of the system, including convective fluid to the wall, fluid to particle, and radiation heat transfer. Radial and axial heat transfer coefficient profiles at different levels show that almost all the heat should be transferred in the lower half of the reactor, making the design more challenging. At the steady-state, the range for the fluid temperature inside the reactor has been recorded 700-780℃.

Keywords: Heat transfer, fluidized bed reactor, alumina chlorination, exothermic reaction, Barracuda, radiation, thermal simulation, CPFD simulation

1 Introduction

The Hall-Héroult process used almost exclusively in the aluminum industry suffers from relatively high heat loss from the electrolytic cells and increased CO_2 emissions from the anodes, even though manufacturers have gradually improved their production processes (Kovács et al., 2020). In 2001, Jomar Thonstad, professor of Electrochemistry at the Norwegian university of science and technology (NTNU), and his colleagues, in their book (Thonstad, 2001), mentioned that "the Hall-Héroult process remains the only modern method of producing aluminum today, having withstood many attempts to replace it. No other mechanism seems to be threatening it for the next twenty years or so," and it has been 20 years now.

Alternative aluminum processing strategies have been under intense investigation due to the comparatively high energy usage and carbon footprint associated with anode consumption (Thonstad, 2001). In continuation of this, in 1973, an innovative process was introduced by Alcoa Corporation, and it had several advantages compared to the commonly used method (Hall-Héroult) at that time (*National Fuels and Energy Conservation Act, S. 2176*, 1973). Alcoa's process is based on the chlorination of processed aluminum oxide in a fluidized bed. The chlorination process has the advantages of being more compact and operating at a lower temperature than the Hall-Héroult process, normally 700℃ as well as less carbon footprint.

During the last decades, fluidized bed reactors (FBR) have been used in a wide range of applications in the industry due to the inherited uniform thermal distribution through the reactor, high heat and mass transfer, and flexibility in operation in large-scale applications (Zhang & Wei, 2017). In a fluidized bed, solid particles are suspended by a stream of fluid that flows upward, causing the solid suspension to move fluidly (Alagha & Szentannai, 2020). Fluidized bed technology has become widely employed in power generation due to its superior mixing and heat transport characteristics (Basu, 2006; Scala, 2013), chemical (Kunii & Levenspiel, 1991; Yang, 2003), pharmaceutical industries (Almendros-Ibáñez et al., 2019; Miller et al., 2018), etc.

Heat transfer occurs either spontaneously or intentionally in many gas fluidized bed applications. Heat transfer may occur between the solid and gas phases, the two-phase mixture, a solid surface, or both (Yang, 2003). The fluidized chlorination of alumina, for example, is a process in which alumina particles are fluidized by an equimolar mixture of carbon monoxide and chlorine at 700 ℃. The exothermic chlorination of alumina at the particle surface raises particle temperature, which leads to natural heat transfer from the heated particles to the fluidizing gas mixture (Barahmand et al., 2021b). To keep the bed's overall energy balance (the reactor temperature should be kept around 700 ℃), heat must be transferred from the particle to the gas medium and then to a cooling surface,

such as heat exchanger tubes, reactor jacket, or any other cooling apparatus.

In the FBR, several heat transfer mechanisms could be identified, such as fluid convection, solid particle conduction or convection, and radiation (Nauman, 2001). Thermal diffusion (heat conduction), convection, and radiation are the three primary modes of heat transfer. These mechanisms may exist simultaneously, or one of them may predominate under particular circumstances (Fan & Zhu, 1998). These conduction and convection modes are similar to their fluid-based counterparts in terms of momentum transfer. Thermal radiation, a type of energy transport via electromagnetic waves, is regulated by a distinct set of principles and can even occur in a perfect vacuum. It should also be noted that due to the similarities of their governing equations, mass transfer and heat transfer (without radiation) may be compared.

Intraparticle heat transport is dominated by conductive heat transfer. Conductive heat transfer is essential for fluid heat transfer at low Reynolds number flow conditions (Tsotsas, 2019). In addition to heat conduction, thermal convection enhances heat transfer from a thermal surface exposed to a flowing fluid (Garcia-Gutierrez et al., 2020). In a bubbling fluidized bed, the convective heat transfer mechanism occupies the total heat transfer flux (Qiu et al., 2016). Natural convection in a gas-solid system is generally negligible, even though thermal convection generally comprises forced and natural convection (Fan & Zhu, 1998). In a thermally radiative condition, absorption, reflection, refraction, and diffraction have happened for an element in the system. Not only can the element transmit incoming radiative heat fluxes but also emits its radiative heat flux (Fan & Zhu, 1998). Gray bodies can represent most solid materials in gas-solid fluxes, including particles and pipe walls. The term *scattering* can describe several modes of radiative energy transmission (Filla et al., 1996).

In thermal studies, solids not only alter the size as a result of pyrolysis, but the rates of reactions and fluid temperatures can also be affected by solid surface areas, solid material types, and discrete solid temperatures (Snider et al., 2011). The particle phase can be modeled in a variety of ways utilizing discrete computational particles or components. Only a small number of particles can be calculated using the direct numerical solution and Lattice Boltzmann computations. The CPFD approach to simulating a reactive thermal fluid-solid flow is reported in the current manuscript. The multi-phase-particle-in-cell (MP-PIC) technique is used in the CPFD numerical methodology to calculate dense particle flows (Snider, 2001). The MP-PIC technique is a hybrid numerical approach that solves the fluid phase with an Eulerian computational grid and models the solids with Lagrangian computational particles (Snider et al., 2011).

The current simulation work aims to study heat transfer between reactive materials in an industrial FBR reactor (dedicated for alumina chlorination) and its wall. To maintain the pseudo-steady-state, the heat produced from exothermic reactions should be transferred outside the reactor (cooling). Further investigations are done on temperature gradient and its variations through the height of the reactor.

2 Energy balance

A flow reactor's thermal energy balance can be written in a reasonably general way as below,

$$\frac{dU}{dt} = \dot{H}_i - \dot{H}_e + \dot{W}_f + \dot{W}_V + \dot{Q}_r + \dot{Q}_T \qquad (1)$$

where, $\frac{dU}{dt}$ is the accumulation of energy, $\dot{H}_i$ and $\dot{H}_e$ are convective enthalpy of input and output streams, respectively, $\dot{Q}_r$ is the heat generated by the reaction, $\dot{Q}_T$ is the heat transferred to the environment[1] (radiation, convection, and conduction), $\dot{W}_V$ is added work associated with the volume change, and $\dot{W}_f \geq 0$ is the friction work.

By neglecting volume and friction work, equation (1) can be simplified as,

$$\frac{dU}{dt} = \dot{H}_i - \dot{H}_e - \dot{Q}_r - \dot{Q}_T \qquad (2)$$

In thermodynamics, one of several energy expressions is *enthalpy H*, which simply is defined as (Lie, 2019),

$$H \triangleq U + PV \qquad (3)$$

Working on the left-hand side of equation (2) results,

$$U = H - PV \Rightarrow \frac{dU}{dt} = \frac{d(H - PV)}{dt} = \frac{dH}{dt} - P\frac{dV}{dt} - V\frac{dP}{dt} = \frac{dH}{dt}$$

$$H = m\widehat{H} \Rightarrow \frac{dH}{dt} = \frac{d\left(m\widehat{H}\right)}{dt} = m\frac{d\widehat{H}}{dt} + \widehat{H}\frac{dm}{dt} = m\frac{d\widehat{H}}{dt}$$

$$\frac{dU}{dt} = \frac{d}{dt}(\hat{\rho}V) \qquad (4)$$

In the same manner, by simplification of the right-hand side, the thermal energy balance is turned to,

$$\frac{d}{dt}\left(\hat{\rho}V\widehat{H}\right) = \dot{V}_{in}\rho_{in}\widehat{H}_{in} - \dot{V}_{out}\rho_{out}\widehat{H}_{out} + \hat{r}_A V\Delta\widehat{H}_r + \dot{Q}_r - \dot{Q}_T \qquad (5)$$

This is an integral balance that can be applied to the whole system. The enthalpies are defined relative to a

[1] This terms is positive when the heat leaves the control volume and includes all heat transport mechanisms

reference temperature (T_{ref}). The temperature would commonly be used to replace the enthalpy expressions.

$$H = \int_{T_{ref}}^{T} C_p \qquad (6)$$

Where, C_p is the average specific heat capacity for the entire reactant mixture. Taking the thermodynamics convenient into account, for exothermic reactions $\Delta H_r < 0$. The heat-generation expression refers to the net effect of all reactions where there are several reactions. As a consequence, the $\Delta H_r r$ expression is an implicit summation of all m potential reactions (Nauman, 2001):

$$\Delta H_r r = \sum_{Reactions} (\Delta H_r)_i (r)_i = \sum_{i=1}^{m} (\Delta H_r)_i (r)_i \qquad (7)$$

3 Heat Transfer Mechanisms

Barracuda® can quantify temperature gradients within the model due to initial particle and fluid temperatures, boundary state temperatures, thermal walls, or chemical reactions. In the computational particle fluid dynamics (CPFD) simulation, the following mechanisms can be studied by Barracuda® (*Barracuda User Manual*, 2021): the convective fluid-to-wall heat transfer, which includes lean-phase and dense-phase heat transfer, fluid-to-particle heat transfer, and radiation, including P-1 model for thermal radiation and Wall to particle radiation.

3.1 Convective fluid-to-wall heat transfer

The sum of the coefficients for a lean and dense phase in the fluidized bed is often used to indicate the effective heat transfer coefficients as below (Yang, 2003),

$$h_{fw} = h_l + f_d h_d \qquad (8)$$

$$f_d = 1 - e^{-10(\theta_p/\theta_{cp})} \qquad (9)$$

where, h_{fw} is the local fluid-wall heat transfer coefficient, h_l is a combination of contributions from a lean gas phase heat transfer coefficient, θ_{cp} is the close pack value fraction, θ_p is the particle volume fraction at the wall, and a dense particle phase's coefficient, h_d. The fluid-to-wall heat transfer coefficient is weighted by the function f_d , which is the fraction of contact time by the dense particle phase. The time fraction of dense phase contact, f_d is a function of the particle volume fraction at the wall.

For the heat transfer in a lean phase, the general form of heat transfer coefficient is,

$$h_l = \left(\left(c_0 Re_L^{n_1} Pr^{n_2} + c_1 \right) \frac{k_f}{L} + c_2 \right) \qquad (10)$$

where, c_0, c_1, c_2, n_1, and n_2 are adjustable model parameters, k_f is the thermal conductivity of the fluid, L is the cell length, and Re_L is the Reynolds number, and Pr is the Prandtl number (Bergman et al., 2011).

In these simulations, the following default lean phase heat transfer coefficient, based on the correlation of Douglas and Churchill (Yang, 2003), has been used.

(c_0 = 0.46, c_1 = 3.66, c_2 = 0.0, n_1 = 0.5, and n_2 = 0.33)

In the dense phase, the general form of the heat transfer coefficient is as below,

$$h_d = \left(c_0 Re_L^{n_1} \right) \frac{k_f}{d_p} \qquad (11)$$

where, d_p is the particle diameter.

Similarly, the following default dense phase heat transfer coefficients (Yang, 2003) have been used in the simulation.

(c_0 = 0.525, n_1 = 0.75)

3.2 Fluid-to-particle heat transfer

The fluid-to-particle heat transfer coefficient is used to describe heat transmission between the fluid and particle phases.

$$h_l = \left(\left(c_0 Re_p^{n_1} Pr^{0.33} + c_1 \right) \frac{k_f}{d_p} + c_2 \right) \qquad (12)$$

where, the Reynolds number and Prandtl number are defined as,

$$Re_L = \frac{\rho_f |U_f - U_p| d_p}{\mu_f} \quad , \quad Pr = \frac{\mu_f c_{p,f}}{k_f} \qquad (13)$$

where, U_f is the fluid velocity, U_p is the particle velocity, ρ_f is the fluid density, μ_f is the fluid's dynamic viscosity, and $c_{p,f}$ is the fluid heat capacity.

In a fluidized bed, when the Reynolds number is less than 20, the Nusselt number for a single sphere is typically higher than the particle Nusselt number. A single sphere in a quiescent fluid has a Nu_p = 2, representing the limit of conductive heat transfer. On the other hand, the bubbling phenomena cause the observed magnitude of Nu_p to be less than 2 in a fluidized bed. Low Reynolds numbers correspond to tiny particle beds (small d_p and U_p) with entrained particles clouding the bubbles. This reduces the efficiency of particle-gas interaction below the assumed plug flow level, resulting in lower Nu_p values. As particle diameter rises (coarse particle beds), the "bubbles" become less cloudy, and gas-particle interaction improves.

Barracuda® uses a correlation for fluid-to-particle heat transfer coefficient dependent on McAdams' correlation to capture fluid-to-particle heat transfer in a fluidized bed (Fan & Zhu, 1998).

(c_0 = 0.37, c_1 = 0.1, c_2 = 0.0, and n_1 = 0.6)

3.3 Radiation model

3.3.1 P-1 radiation model:

This model, which is the simplest case of the more general P-N model (*ANSYS FLUENT User Guide*, 2021), addresses the heat transfer, where thermal radiation between particles, particles and fluid, particles and thermal walls, and fluid and thermal walls are taken into account. In the P-1 radiation model, the incident radiation transfer equation is:

$$\nabla \cdot (\Gamma \nabla G) + 4\left(an^2\sigma T^4 + E_p\right) - \left(a - a_p\right)G = 0 \quad (14)$$

where, Γ is the diffuse radiation coefficient, G is the incident radiation to be solved, a is the absorption coefficient of the fluid mixture, n is the refractive index of the fluid mixture, σ is the Stefan-Boltzmann constant, T is the fluid temperature in units of K, E_p is equivalent emission of the particles, and a_p is the equivalent particle absorption coefficient.

By defining a thermal boundary condition, the Marshak boundary condition (Elshin et al., 2018) is used for the radiative heat flux at the thermal wall (q_w) as the following:

$$-q_w = \Gamma_w\left(\frac{\partial G}{\partial n}\right) = \frac{\varepsilon_w}{2(2-\varepsilon_w)}\left(4\sigma T_w^4 - G_w\right) \quad (15)$$

$$\Gamma = \frac{1}{3\left(a + a_p + \sigma_f + \sigma_p\right)} \quad (16)$$

Where, ε_w is the emissivity of the thermal wall, w is subscript for thermal wall, σ_f is equivalent fluid scattering coefficient, and σ_p is identical particle scattering factor.

3.3.2 Particle to Wall Radiation:

The model is only used under thermal wall boundary conditions and only considers radiation between a thermal wall and the particle phase and ignores radiative heat transfer between particles-walls or wall-fluid. The radiation between a thermal wall cell and nearby particles (q_{wp}) is calculated as (*Barracuda User Manual*, 2021),

$$q_{wp} = A_w F_{wp} \varepsilon_{wp} \sigma \left({T_w}^4 - {\bar{T}_p}^4\right) \quad (17)$$

$$\Gamma\varepsilon_{wp} = \left(\frac{1}{\bar{\varepsilon}_p} + \frac{1}{\varepsilon_w} - 1\right) \quad (18)$$

where, A_w is the area of the thermal wall, F_{wp} is a calculated view factor, ε_{wp} is the effective emissivity between the wall and the particles in a cell, T_w is the temperature of the wall, $\bar{T}_p$ is the mass-weighted average temperature of particles in a cell, and $\bar{\varepsilon}_p$ is the volume-weighted average of particle emissivity.

4 CPFD simulations

The CPFD simulations are based on the particle size distribution and reaction kinetics (pure γ-alumina chlorination) in an isothermal condition at 700℃ (Barahmand et al., 2021b). The geometry (cylindrical reactor with extended section) and other operational conditions (Barahmand et al., 2021a) for the pure γ-alumina chlorination. In Barracuda®, the thermal wall of a model applies a user-defined temperature to the reactor wall. Energy can be transferred via the reactor wall depending on the temperature in between the wall and the fluid near the wall. The model has been simulated under the following operating condition (Table 1):

Table 1. Reactor's Operating Condition

Number of cells in setup grid:	65000
Bed aspect ratio (H/D)	1.8
Wall temperature	973.15 K
Reactor initial temperature:	973.15 K
Outlet pressure:	1.5 bars
Particle diameter:	Distribution[2]
Particle density (envelope):	2100 kg/m^3
Particle sphericity	0.7
Initial bed void fraction	0.44
Fluidization regime	Bubbling

The alumina chlorination reaction is a rapid and exothermic reaction that mainly occurs at the bottom of the reactor (Barahmand et al., 2021b). As a result, the generated heat will not be distributed homogeneously through the entire height of the particle bed. Therefore, the surface area of the reactor has been divided into 7 different sections, as shown in Figure 1

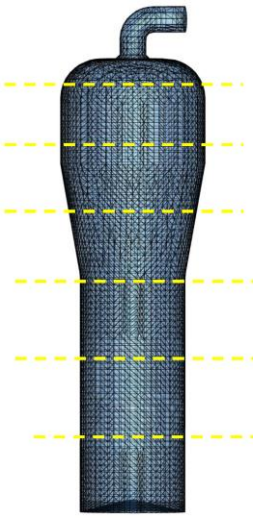

Figure 1. Reactor geometry and thermal-wall sections

[2] Based on (Barahmand et al., 2021b) with the average diameter of 98 microns.

5 Result and discussion

Due to a lack of information about the reactor wall emissivity, the heat transfer has been studied in three different cases. The first case is in the absence of radiation (emissivity = 0). In the second simulation, maximum possible radiation (emissivity = 1) has been set into the calculations, and in the last step, a relatively high emissivity (0.85) has been used.

5.1 Thermal model without radiation

The thermal simulations need much more time to reach pseudo-steady-state. Figure 2 shows the average fluid temperature distribution inside the reactor (middle cross-section). It seems like the local temperature is somewhat evenly distributed at the bottom part of the bed. The temperature at the bottom of the reactor is the highest since the reaction conversion is very high in that area.

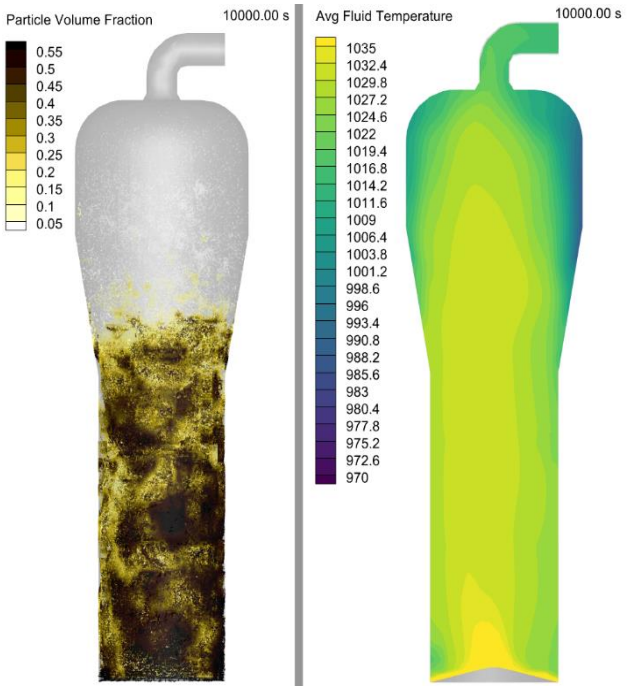

Figure 2 Particle distribution (left), and temperature distribution (right) at steady-state.

Figure 3 shows the heat transfer through the wall of the reactor. It seems it is necessary to transfer 1.56 MW of heat through the reactor wall at pseudo-steady-state to keep the reactor wall at 700℃. Theoretically, the heat duty transferred through the wall is not equally distributed. Table 2 gives the information about the heat transfer rate in different reactor sections in Figure 1. Starting from bottom to top, the sections are named from 1 to 7. Most of the heat leaves the reactor through the bottom half due to high energy generation from the exothermic chlorination reaction in the specific area.

Figure 4 illustrates the average fluid temperature in different sections of the reactor. Comparing figures 2 and 4 confirms that the fluid temperature inside the reactor is almost gradually decreasing from bottom to top. The highest recorded temperature is 792℃, and the average fluid temperature leaving the system is about 744℃.

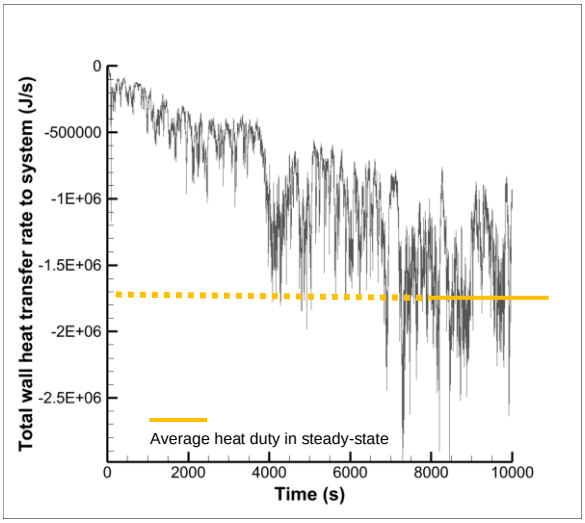

Figure 3. Overall heat transfer through the reactor wall

Table 2 Heat transfer in different sections

Section	Heat Transfer (MW)	(%) of total
1	0.22	14.2
2	0.41	26.2
3	0.61	39
4	0.26	16.6
5	0.31	2
6	0.016	1
7	0.013	< 1

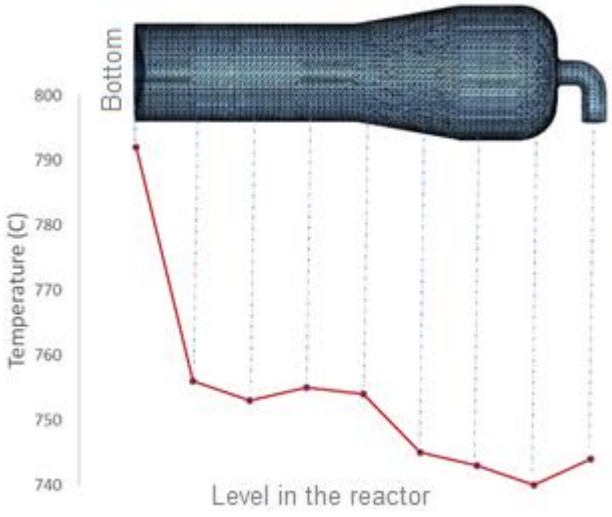

Figure 4. The fluid average temperature profile in different heights

5.2 Thermal model with radiation

5.2.1 Radiation (emissivity = 1)

By activating the P-1 model with maximum possible emissivity, the overall heat transfer through the reactor wall increases significantly. In this case, the overall heat transfer is 2 MW, almost 30 % higher than the heat transfer with no radiation (Figure 5). The portion of the convective mode is 29 % by 0.58 MW, and radiative heat transfer is 71 % by 1.4 MW (see Figure 6). In the current simulation, radiation is the dominant heat transfer mechanism.

Table 3 gives the overall view of heat transfer in the different sections of the reactor. Convective heat transfer has not been observed at the three upper sections of the reactor. The average fluid temperature in the middle vertical cross-section of the reactor is given in Figure 7. The fluid temperature is considerably lower because of the higher heat transfer (compared to the case with no radiation).

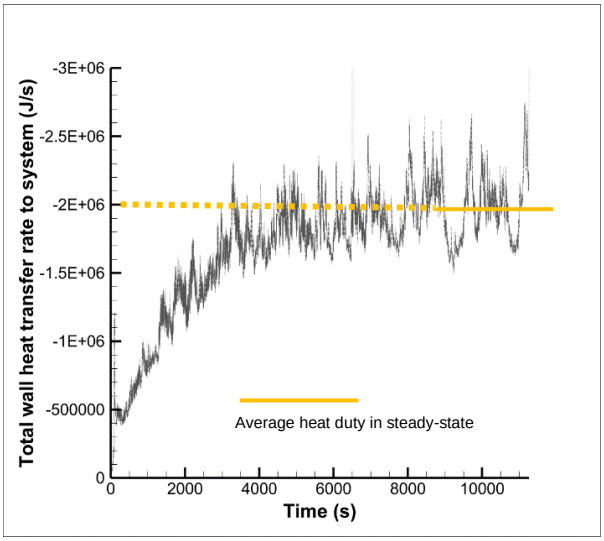

Figure 5 Reactor's overall heat transfer with maximum radiative heat transfer.

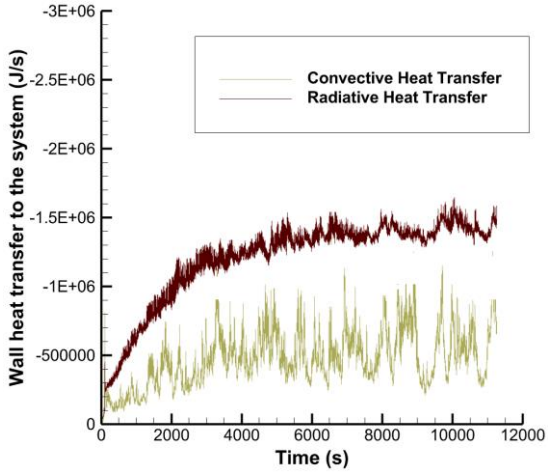

Figure 6. Convective and radiative heat transfer in the reactor (max emissivity)

Table 3. Convective and radiative Heat transfer in different sections of the reactor

Section	Convection		Radiation	
	Heat Transfer (kW)	(%)	Heat Transfer (MW)	(%)
1	92.4	16	264.8	19
2	163	28	240.6	17
3	224.9	39	266	19
4	90.3	16	180.4	13
5	6	1	192.5	14
6	2.9	< 1	224.3	16
7	2.1	~0	46.1	3

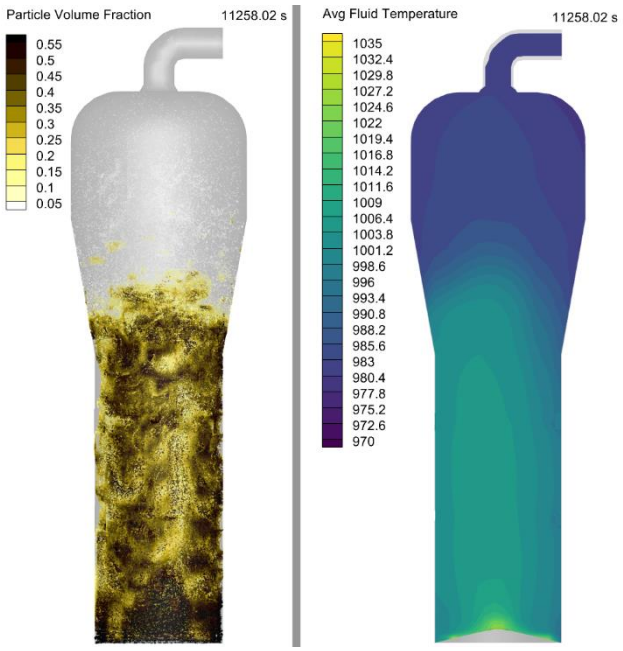

Figure 7. Particle distribution (right), and temperature distribution (left) in steady-state.

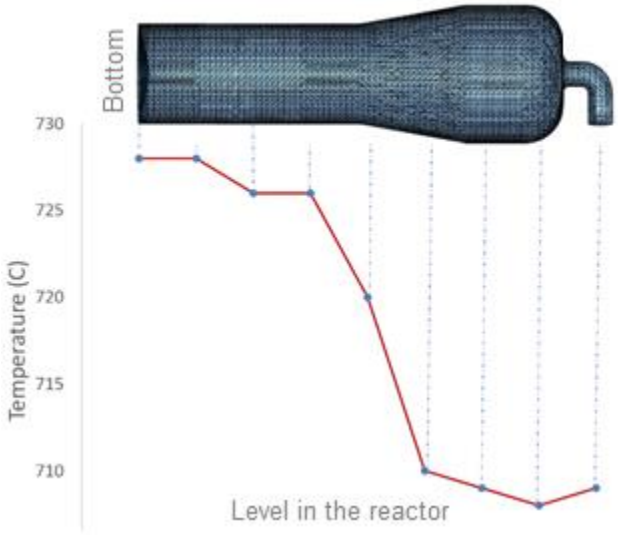

Figure 8. The fluid average temperature profile in different heights

Figure 8 illustrates the average fluid temperature in different sections of the reactor. The reactor temperature distribution can be divided mainly into three areas. The temperature in the first and the last three sections are almost constant. Nevertheless, in the middle section (4th), the reactor experienced a 20 ℃ temperature drop which can easily be observed in Figure 7. The average fluid temperature in the outlet is 709 ℃ which is very close to the desired temperature.

5.2.2 Radiation (emissivity = 0.85)

In Sections 5.1 and 5.2.1, the extreme modes for the radiation (emissivity 0 and 1) have been investigated. In the last step, the emissivity is set to 0.85. The average overall heat transfer is 1.94 MW (Figure 9) which is 2.5 percent lower than the case with the maximum emissivity.

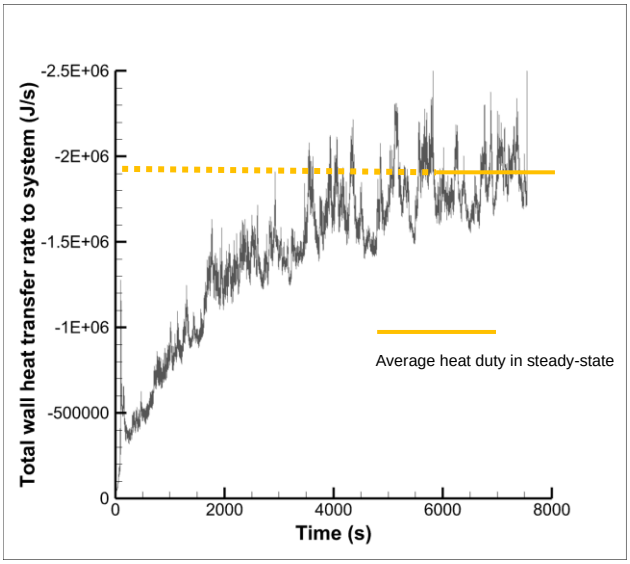

Figure 9. Reactor's overall heat transfer with maximum radiative heat transfer.

Table 4. Convective and radiative Heat transfer in different sections of the reactor

	Convection		Radiation	
Section	Heat Transfer (KW)	(%)	Heat Transfer (MW)	(%)
1	879	15	241.4	18
2	141.2	24	214.5	16
3	229.6	39	242.1	18
4	110.7	19	178.5	13
5	8	1	204.3	15
6	3.9	< 1	226.3	17
7	2.9	< 1	46	3

As expected, change in emissivity shows no effect on the convective heat transfer. The radiative heat transfer has been dropped to 1.35 MW. As seen in Table 4, the portion on each heat transfer mechanism in the different sections is almost the same as before. The average Outlet temperature has been recorded at 711℃ in comparison with 709℃ in the previous case.

To compare the heat duty calculated by the CPFD method, the reaction has been simulated in Aspen Plus® using the Gibbs reactor. A Gibbs reactor is a reactor that uses equilibrium processes to minimize the Gibbs free energy (Haydary, 2018). The Gibbs reactor simulation gave the 1.6 MW, which is slightly higher than the heat transfer in the absence of radiation and much lower than the cases with radiation. Several reasons may cause this variation, such as the difference in enthalpy value or heat formation in the libraries and different conditions in the outlet (because of the system's dynamics in CPFD simulation).

The enthalpy equation is used to explain energy. Energy transport in the fluid phase and energy transfer from the solid phase is described by energy conservation. Using a turbulent Prandtl number approximation, the turbulent thermal diffusion is derived from eddy conductivity. For each gas species, a transport equation is solved. Particle chemistry transfers mass and energy between solid and fluid phases. The enthalpy for each gas species includes the heat of formation from breaking and establishing chemical bonds.

6 Conclusion

Design an exothermic reactor with an efficient heat transfer performance is probably the most critical task from an engineering perspective. The efficiency of the reaction is highly affected by temperature. The CPFD method is applied to an industrial alumina chlorination reactor. The alumina chlorination calculation is three-dimensional, with chemistry in a large industrial hot reactor. The CPFD method provided a chlorination solution to 10000 seconds and took 47 days computation time on a single Intel Xeon E5 computer.

The Gibbs reactor simulation in Aspen Plus® shows lower heat transfer than thermal analysis by CPFD simulation. In CPFD simulation, at the steady-state, the reactor temperature range is 744-792℃ in the case with emissivity equal to 0, 709-728℃ for the case with the maximum emissivity, and 711-730℃ in the case with emissivity equal to 0.85. The possibility of having higher radiation by using the material with high emissivity helps to reach more heat transfer and lower temperature in the reactor. As a result, less cooling duty will be needed. For future studies, it is suggested to validate the model with other computational or experimental studies. Moreover, the mesh convergence test can help future studies find the best mesh size for the model.

References

M. Alagha and P. Szentannai. Analytical review of fluid-dynamic and thermal modeling aspects of fluidized beds for energy conversion devices. *International Journal of Heat*

and Mass Transfer, *147*, 118907, 2020. doi:10.1016/j.ijheatmasstransfer.2019.118907

J. Almendros-Ibáñez, M. Fernández-Torrijos, M. Díaz-Heras, J. Belmonte, and C. Sobrino. A review of solar thermal energy storage in beds of particles: Packed and fluidized beds. *Solar Energy*, *192*, 193–237, 2019. doi:10.1016/j.solener.2018.05.047

ANSYS FLUENT User Guide. 2021. https://www.afs.enea.it/project/neptunius/docs/fluent/html/th/node112.htm

Z. Barahmand, C. Jayarathna, and C. Ratnayake. CPFD simulations on a chlorination fluidized bed reactor for aluminum production: An optimization study. *In proceedings - 1st SIMS EUROSIM Conference on Modelling and Simulation*, Finland, 2021a.

Z. Barahmand, C. Jayarathna, and C. Ratnayake. The effect of alumina impurities on chlorination in a fluidized bed reactor: A CPFD study. *In proceedings - 1st SIMS EUROSIM Conference on Modelling and Simulation*, Finland, 2021b.

Barracuda User Manual. 2021. CPFD Software. https://cpfd-software.com/

P. Basu. *Combustion and Gasification in Fluidized Beds*. CRC Press, 2006.

T. Bergman, F. Incropera, D. DeWitt, and A. Lavine. *Fundamentals of Heat and Mass Transfer*. John Wiley & Sons, 2011.

A. Elshin, K. Muraveva, A. Borisenko, and A. Kalutik. Mark and Marshak boundary conditions in surface harmonics method. *Journal of Physics: Conference Series*, 2018. doi:10.1088/1742-6596/1133/1/012017

L. Fan, and C. Zhu. *Principles of Gas-Solid Flows*. Cambridge University Press, 1998.

M. Filla, A. Scalabrin, and C. Tonfoni. Scattering of thermal radiation in the freeboard of a 1 MWt fluidized bed combustion with coal and limestone feeding. *Symposium (International) on Combustion*, 26(2), 3295–3300, 1996. doi:10.1016/S0082-0784(96)80176-7

L. Garcia-Gutierrez, F. Hernández-Jiménez, E. Cano-Pleite, and A. Soria-Verdugo. Experimental evaluation of the convection heat transfer coefficient of large particles moving freely in a fluidized bed reactor. *International Journal of Heat and Mass Transfer*, *153*, 119612, 2020. doi:10.1016/j.ijheatmasstransfer.2020.119612

Haydary. Reactors. In *Chemical Process Design and Simulation* (pp. 101–124). John Wiley & Sons, 2018. https://doi.org/10.1002/9781119311478.ch5

A. Kovács, C. Breward, K. Einarsrud, S. Halvorsen, E. Nordgård-Hansen, E. Manger, A. Münch, and J. Oliver. A heat and mass transfer problem for the dissolution of an alumina particle in a cryolite bath. *International Journal of Heat and Mass Transfer*, *162*, 120232, 2020. https://doi.org/10.1016/j.ijheatmasstransfer.2020.120232

D. Kunii and Levenspiel. *Fluidization Engineering*. Butterworth-Heinemann, 1991.

B. Lie. *Modeling of Dynamic Systems* [Unpublished book], 2019.

D. Miller, C. Pfutzner, and G. Jackson. Heat transfer in counter-flow fluidized bed of oxide particles for thermal energy storage. *International Journal of Heat and Mass Transfer*, *126*, 730–745, 2018. doi:10.1016/j.ijheatmasstransfer.2018.05.165

National Fuels and Energy Conservation Act, S. 2176. U.S. Government Printing Office, 1973.

B. Nauman, B. *Handbook of Chemical Reactor Design, Optimization, and Scaleup*. McGraw-Hill Professional, 2001. doi:10.1036/9780071395588

K. Qiu, F. Wu, S. Yang, K. Luo, K. Luo, and J. Fan. Heat transfer and erosion mechanisms of an immersed tube in a bubbling fluidized bed: A LES–DEM approach. *International Journal of Thermal Sciences*, 100, 357–371, 2016. https://doi.org/10.1016/j.ijthermalsci.2015.10.001

F. Scala, F. *Fluidized Bed Technologies for Near-Zero Emission Combustion and Gasification* (1st edition). Woodhead Publishing, 2013.

D. Snider. An Incompressible Three-Dimensional Multiphase Particle-in-Cell Model for Dense Particle Flows. *Journal of Computational Physics*, *170*(2), 523–549, 2001. doi:10.1006/jcph.2001.6747

D. Snider, S. Clark, P. & O'Rourke. Eulerian–Lagrangian method for three-dimensional thermal reacting flow with application to coal gasifiers. *Chemical Engineering Science*, 66(6), 1285–1295, 2011. doi:10.1016/j.ces.2010.12.042

J. Thonstad. *Aluminium Electrolysis: Fundamentals of the Hall-Héroult Process*. Aluminium-Verlag, 2001.

E. Tsotsas. Particle-particle heat transfer in thermal DEM: Three competing models and a new equation. *International Journal of Heat and Mass Transfer*, 132, 939–943, 2019. https://doi.org/10.1016/j.ijheatmasstransfer.2018.12.090

W. Yang. *Handbook of Fluidization and Fluid-Particle Systems*. CRC Press, 2003.

Y. Zhang and Q. Wei. CPFD simulation of bed-to-wall heat transfer in a gas-solids bubbling fluidized bed with an immersed vertical tube. *Chemical Engineering and Processing: Process Intensification*, 116, 2017. doi:10.1016/j.cep.2017.03.007

The Effect of Impurities on γ-Alumina Chlorination in a Fluidized Bed Reactor: A CPFD Study

Zahir Barahmand[1] Chameera Jayarathna[2] Chandana Ratnayake[1,2]

[1] Department of Process, Energy and Environmental Technology, University of South-Eastern Norway
zbarahmand@gmail.com
[2] SINTEF Tel-Tek, SINTEF Industry, Porsgrunn, Norway

Abstract

Alumina is one of the most widely used materials today, with a total annual production of millions of tonnes of highly pure alumina. A large portion of this is used to make metal aluminum. Apart from that, a growing amount of alumina is used in ceramics, refractories, catalysts, and various other products. In nature, alumina can be found in different phases. These phases can be transformed into each other in different temperatures. Among these, γ-alumina is used in the chlorination process in the aluminum production industry because of the higher reaction rates. Previously, the chlorination of pure γ-alumina has been considered in the CPFD simulations. Extending previous researches, the present study investigates the effect of seven percent α-alumina impurity on the overall chlorination reaction, bed hydrodynamics, and composition of the outflow of the reactor. Commercial CPFD software Barracuda® v20.1.0 is used for the simulations. The results are compared with the pure γ-alumina simulations, and the results show that the impurity has no considerable effect on the chlorine concentration at the outlet. However, the mass balance of the bed shows an unfavorable accumulation of α-alumina in the fluidized bed reactor.

Keywords: Barracuda, CPFD simulation, α-Alumina chlorination, γ-alumina chlorination, Fluidized bed reactor (FBR),

1 Introduction

The Romans called materials with a styptic or astringent flavor "alumen." Impure forms of aluminum sulfate and alum could have been among them naturally occurring in volcanic areas. Term alumina appears to be derived from the mineral alumen (Beckmann, 1846). Alumina is the raw material used for the production of metal Aluminum.

The process which is used almost exclusively in the aluminum industry is the Hall-Héroult process. This process has turned aluminum metal into a commodity product since its invention in 1886 (Kovács et al., 2020). Alumina is dissolved in a cryolite bath in this continuous process, and aluminum is produced by electrolysis. In this cryolite-alumina melt electrolysis, aluminum oxide is dissolved in molten cryolite (Na_3AlF_6) and afterward electrolytically reduced to aluminum at almost 960 °C. Carbon anodes are used in the process, consumed during electrolysis, are resulting in the formation of CO_2. This process suffers from relatively high heat loss from the electrolytic cells and increased CO_2 emissions from the anodes, even though manufacturers have gradually improved their production processes. Besides, the Hall-Héroult process moves down to its potentially lowest energy consumption and CO_2 emissions during decades (Prasad, 2000). The following reaction (2.1) can be the overall reaction of dissolved alumina with carbon to form the products (Thonstad, 2001).

$$½\ Al_2O_3\ (dissolved)\ +\ ¾\ C\ (s) \rightarrow\ Al\ (l)\ +\ ¾\ CO_2\ (g) \quad (1)$$

Alternative aluminum processing strategies have been under intense investigation due to the comparatively high energy usage and carbon footprint associated with anode consumption (Thonstad, 2001). In continuation of this, in 1973, an innovative process was introduced by Alcoa Corporation, and it had several advantages compared to the commonly used method (Hall-Héroult) at that time (*National Fuels and Energy Conservation Act, S. 2176*, 1973). Alcoa's process is based on the chlorination of processed aluminum oxide. The chlorination process has the advantages of being more compact and operating at a lower temperature than the Hall-Héroult process, normally 700 °C. Unlike the Hall-Héroult process, which needs pure alumina, one of the main advantages of the chlorination process is the possibility of using impure alumina. The following simplified general reaction can be used to reflect carbothermic chlorination of alumina (Rao & Soleiman, 1986):

$$Al_2O_3\ +\ (n)C\ +\ 3Cl_2 \rightarrow\ 2AlCl_3\ +\ (2n-3)CO\ +\ (3-n)CO_2 \quad (2)$$

where, $1.5 \leq n \leq 3$. The following sequential reactions can explain the carbothermic chlorination of alumina as the reaction progresses with the production of carbon dioxide and carbon monoxide:

$$Al_2O_3\ +\ 3CO\ +\ 3Cl_2\ \rightarrow\ 2AlCl_3\ +\ 3CO_2 \quad (3)$$

$$C\ +\ CO_2\ \rightarrow\ 2CO\ ,bounded\ reaction \quad (4)$$

The experimental techniques for obtaining gas-solid contact and extracting gaseous materials containing

$AlCl_3$ and impurity elements are crucial in deciding the chlorination rate.

Experiments of different CO/Cl_2 molar ratios revealed that $CO/Cl_2 = 1$ has the highest chlorination rate, and this is clear from overall reactions (3), which involve equimolar concentrations of CO and Cl_2 (Gokcen, 1983). The optimal temperature for chlorinating aluminous resources with $CO + Cl_2$ is between 600° and 900°C, with 650 to 750°C being the most expected range. According to (Alder et al., 1977), 600°C could be a reasonable operating temperature for an alumina chlorination fluidized bed. In an industrial chlorination reactor, erosion and chlorination of reactor lining are significantly reduced at lower temperatures. Hence, chlorination at low temperatures tends to be desirable for designers.

Commercial chlorination reactor construction materials must be kept cold enough to prevent being chlorinated. As a result, it seems that externally heated chambers are not feasible. An appropriate series of reactions must be chosen to produce enough heat to keep the internal reactor temperature up while retaining a temperature gradient that allows for a relatively cold and nearly non-reacting wall (Gokcen, 1983).

The Alcoa process's overall chlorination reaction has been introduced by equations (2-4), where solid-phase alumina (mainly Al_2O_3) reacts with the gaseous chlorine and carbon monoxide at 700 ℃. It is vital to know that many alumina particles have different purities and size distribution, affecting the reaction rate.

α-Alumina has outstanding mechanical properties and superb thermal properties at high temperatures; polycrystalline α-alumina is used as a structural ceramic. As a result, this type has much lower reaction rates in the chlorination process. The present study aims to investigate the effect of an impurity (α-alumina) in an industrial γ-alumina chlorination fluidized bed reactor under the isothermal condition at 700 ℃. First, some critical information about the stoichiometry of alumina chlorination, reactants, and products is given. Next, the alumina chlorination kinetics for both types have been introduced, which are used from previous studies. In the current study, SOLIDWORKS® has been used for the mechanical design of the fluidized bed reactor, and the reactor model is then simulated/optimized with the use of CFD software called Barracuda VR® version 20.1. At the final step, the results have been compared with the same model reacting pure γ-alumina (Barahmand et al., 2021).

2 Alumina chlorination stoichiometry

The stoichiometry of chlorination of reactants is as reaction (5),

$$Al_2O_3\,(s) + 3Cl_2 + 3CO \rightarrow 2AlCl_3 + 3CO_2 \quad (5)$$

Al_2O_3: In nature and different thermal conditions, alumina is found in different phases. These phases can be transformed into each other. Table 1 (Aswad, 2012) shows some properties of three main types of alumina. The density of the alpha type is more than other types.

Table 1 Properties of different types of alumina

Type	Envelope Density (kg/m^3)	Melting Temp (°C)
α-alumina	2600	2051
γ-alumina	2100	γ →δ:700-800
θ-alumina	2330	θ →α:1050

$AlCl_3$: because of low vapor pressure (1 atm) at 169.7℃, the gas phase is almost all Al_2Cl_6 (g). However, during chlorination at high temperatures, both gaseous $AlCl_3$ and Al_2Cl_6 are present in the process. It has a shallow melting point of about 192℃.

$$2AlCl_3 \rightleftarrows Al_2Cl_3 \quad (6)$$

$AlCl_3$ in the gaseous phase is in equilibrium with Al_2Cl_6. Table 2 shows their volume percentage at different temperatures (Gokcen, 1983).

Table 2 Volume percentage of $AlCl_3$ and Al_2Cl_6 in equilibrium

Temperature (K)	600	800	1000	1200
$AlCl_3$ (%)	2.1	35.5	88.4	98.7
Al_2Cl_6 (%)	97.9	64.5	11.6	1.3

CO and Cl_2: At the 1 atm pressure, CO and Cl_2 are in equilibrium with phosgene ($COCl_2$). The volume percentage of each in a mixture with different temperatures is given in Table 3 (Gokcen, 1983).

Table 3 Volume percentage of $CO + Cl_2$ and $COCl_2$ in equilibrium

Temperature (K)	800	1000
CO (%)	30.8	48.16
$COCl_2$ (%)	30.8	48.16
Cl_2 (%)	38.4	3.68

An equimolar mixture of CO and Cl_2 can contain small amounts of $COCl_2$ in the normal temperature range of chlorination. However, This is not an issue because the reaction of alumina with phosgene is faster than an equimolar mixture of CO and Cl_2 (Bertóti et al., 1981).

$$Cl_2 + CO \rightleftarrows COCl_2 \quad (7)$$

3 Process kinetics

3.1 γ-Alumina chlorination kinetics

In 1981 the temperature and partial pressure dependency and the influence of photo-irradiation of the reactive gases were studied to find reaction rate for γ-alumina chlorination with carbon monoxide and chlorine (Tóth et al., 1982) and phosgene (Bertóti et al., 1981) in different temperatures. To experiment with carbon

monoxide and chlorine, the isothermal TG measurements were taken at temperatures ranging from 327 to 850°C. It has been shown that the reaction conversion and the specific initial reaction rate (R_0) have a significant temperature dependency. The reaction rates for phosgene are higher than the mixture of CO and Cl_2 up to around 920 K, as observed, while the data obtained with both are almost the same as results in (Bertóti et al., 1981). Unlike (Milne, 1976), solid samples have been preheated before chlorination, and as a result, they have been gotten rid of the uncontrolled behavior of the change in the sample's reactivity due to structural changes. The Arrhenius style of specific reaction rate (R_0) is illustrated in Figure 1.

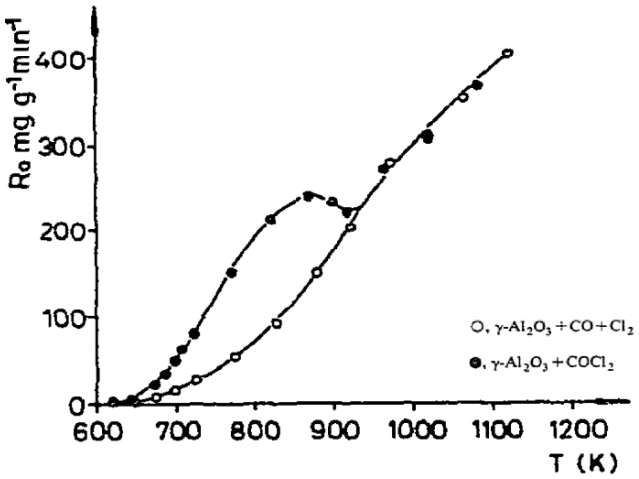

Figure 1. The specific initial reaction rate (R0) vs. temperature (T) in reaction with phosgene (black) and $CO+Cl_2$ mixture (white) (Tóth et al., 1982)

For the reaction with $CO+Cl_2$ mixture, the activation energies (E_1) computed by the rate constant of the first-order kinetic equation and initial reaction rate are 106 and 118 kJ/mole. Between temperatures 775-878 K, E_2 is almost half of the E_1 and equal to 56 kJ/mole, and for the range between 920-1123 K, E_3 is the lowest and equal to 23 kJ/mole, indicating that the process at these temperatures is effectively regulated by external mass transfer.

Figure 2 verifies the above-described phenomenon, as the results of an experimental investigation (Milne, 1976) studied chlorination of two different sizes (7.9 mm and 0.125 mm) of γ-alumina with an equimolar mixture of CO and Cl_2. The particle's surface area directly impacts the reaction (Kunii & Levenspiel, 1991). As per the findings of this experiment, it is expected that the fluidized bed's reaction rate will be much quicker than the experiment when very tiny alumina particles are used in the reactor.

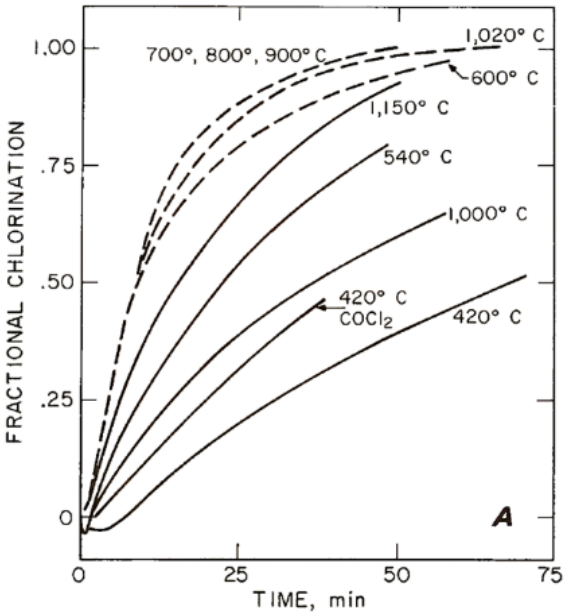

Figure 2. Chlorination of γ-alumina with CO/Cl_2=1. Solid lines are for 9.7 mm particles; broken lines are for 0.125 mm particles (Milne, 1976).

3.2 α-Alumina chlorination kinetics

As (Soleiman & Rao, 1987) reported, the reaction rate and activation energy of the α-alumina in a carbo-chlorination reaction is much lower than that of the γ type. In the range 800-900°C, the activation energy is 32±2.5 kJ/mole. In general,

$$r_{exp} = K\left(P_{cl_2}\right)^m (P_{CO})^n \quad (8)$$

where, P_x is the partial pressure of component x, m and n are reaction orders, K is the reaction constant, and r_{exp} is an experimentally calculated reaction rate. Table 4 gives calculated m and n in different temperatures.

Table 4. Reaction orders in different temperatures

	Reaction Temperatures (°C)				
	800	**835**	**870**	**910**	**950**
m	0.71	0.60	0.59	0.56	0.48
n	0.77	0.72	0.66	0.65	0.65

The rate expression for the particular case considered under the experiment considerations can be written as,

$$r_{exp} = \tilde{k}\left(P_{cl_2}\right)(P_{CO}) \quad (9)$$

where, $\tilde{k}$ is the apparent rate constant in $gg^{-1}min^{-1}atm$. Table 5 shows the different values for the apparent rate constant,

Table 5. Values of $\tilde{k}$ obtained by regression analysis of r_{exp} vs $\left(P_{cl_2}\right)(P_{CO})$ results

T (°C)	800	835	870	910	950
$\tilde{k}$	0.0234	0.0256	0.0281	0.0313	0.0368
$ln\tilde{k}$	-3.755	-3.665	-3.572	-3.464	-3.302
10000/T	9.3197	9.0253	8.8479	8.4531	8.1766

4 CPFD model

The CPFD method is applied to an industrial alumina chlorination reactor with modified geometry (cylindrical reactor with a section with an extended diameter on top) with a smooth exit on top (Figure 5), and the bed aspect ration (H/D) equal to 2 has been used (Barahmand *et al.*, 2021). The alumina chlorination calculation is three-dimensional, with chemistry in a large industrial reactor at isothermal conditions (700℃). The CPFD method provided a chlorination solution for 3600 seconds. The calculation took 5 days to complete the computation on a single Intel Xeon E5 computer using 55000 cells in total.

An equimolar mixture of CO and Cl_2 enters continuously from the bottom of the reactor, and the products leave the reactor from the top. The initial bed contains mainly γ-alumina with only 7% of α-alumina as the impurity. The amount of γ (top) and α-alumina (bottom) types are patched in the particle bed as shown in Figure 5 (right). In terms of the concentration, the same percentage of the impurity (α-alumina) has been applied to injected solid particles through the feeder (total particle feed is 0.6 kg/s). Specifications of the particles have a crucial role in the fluidized bed hydrodynamics, such as size distribution, sphericity, porosity, and the void fraction of the particle bed. The particle size distribution given in Figure 3 is used for both γ and α alumina types.

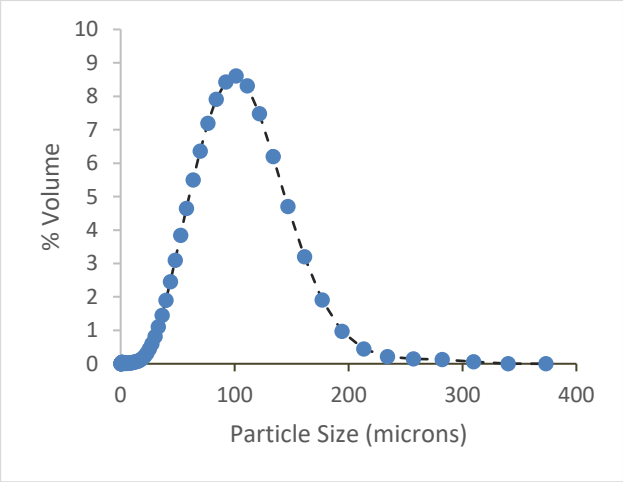

Figure 3. Particle size distribution of the alumina sample

The particle sphericity, envelop density, and bed void fraction cannot be calculated easily and need special measuring apparatus and procedures. However, an extensive range of values has been reported in the literature. To get closer to the acceptable range, an experiment has been done. Finding a reasonable estimation of sphericity, a random sample has been studied under a microscope[1].

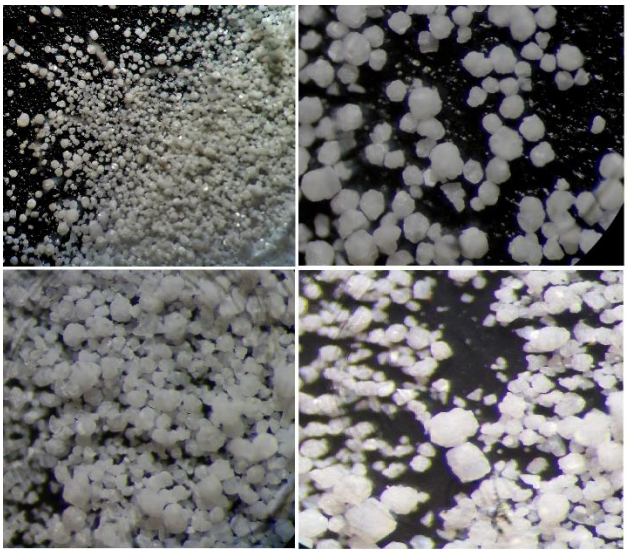

Figure 4. Alumina sample under the microscope

It has been observed that this shows a considerable amount of cracked particles (by attrition), which might be created during the process. Based on the approximation guideline (Liang et al., 2016), the cracked particles mostly have sphericity below 0.5, but the sphericity for the not cracked particles could be estimated close to 0.9 (Figure 4). All in all, 0.9 for the average sphericity of this alumina is somewhat optimistic, and finally, 0.7 has been chosen.

The parameters defined for the γ-alumina particles in the simulation are given in Table 6. Except for the envelope density, other parameters are the same in both alumina types. The envelope density of α-alumina has been set to 2600 kg/m^3.

Table 6. γ-Alumina Properties

Parameter	Effects on	Used-values
Average diameter	H, R	98 microns
Sphericity	H	0.7
Emissivity	R,HT	0.75
Envelope Density	H	2100 kg/m^3
Bulk Density	H	1.19 kg/m^3
Diffusion coefficient	R	2.2E-06 cm^2/s
Void Fraction	H	0.46

(H: Hydrodynamics, R: Reaction, HT: Heat Transfer)

The WenYu-Ergun drag model (Xie et al., 2018) has been used, and the reaction rate has been set using the information in Sections 3.1 and 3.2. The superficial velocity has been set close to the minimum bubbling velocity (0.1 m/s). The pressure boundary in the outlet has been assumed 1 atm.

[1] Nikon smz745T

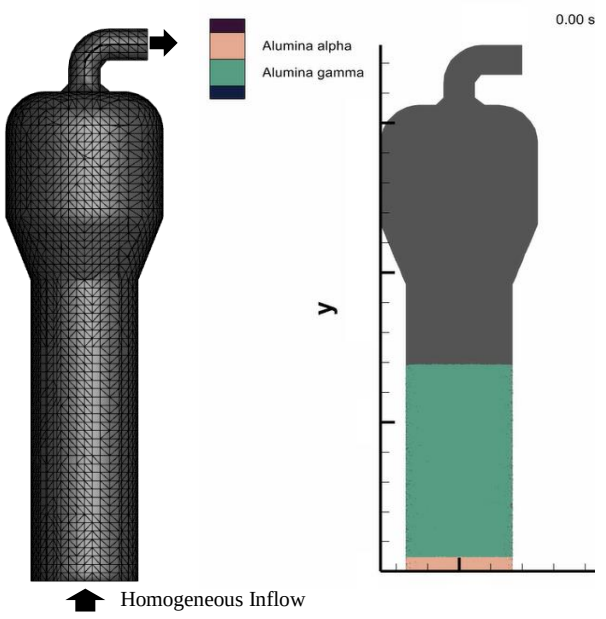

Figure 5. Reactor meshed geometry (left), different types of alumina in the initial bed (right)

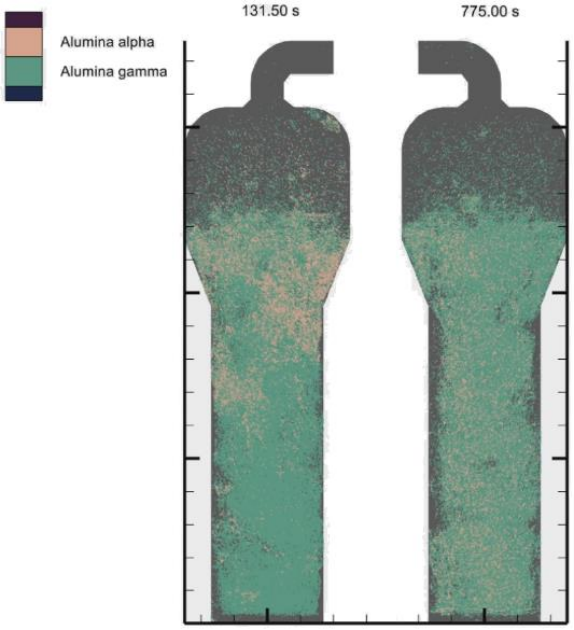

Figure 6. Different types of alumina particle's distribution after fluidization (left) in steady-state (right)

5 Results and discussion

Comparing the chlorine concentration in the outlet with pure γ-alumina (Barahmand et al., 2021) with the present study confirms that 7% impurity in the alumina sample does not affect reaction conversion. The average chlorine concertation in both cases is below 0.0003 mole/m^3 in the outlet. Although the reaction kinetics clearly shows that the reaction rate for α-alumina is much slower than the γ-alumina, the impurity shows no adverse effect on the Cl_2 concentration in the outlet because the chlorination reaction is rapid. On the other hand, there are more solid particles than needed to react with the gaseous reactants.

Figure 6 shows the α and γ-type alumina particle distribution through the reactor. However, because of the densification, α-alumina is relatively heavier than γ-alumina. After only 700 seconds, it has been distributed homogeneously through the bed.

Studying the particle outflow in the pseudo-steady-state shows that the overall particle escape is 156 g/s, almost one-fourth of the feed. The average escaping rate of α-alumina (from 500 seconds in steady-state) particles has been recorded as only 6 g/s, almost 3.8 percent, while this percent is 7 for the feed. As a result, α-alumina may accumulate inside the reactor. One reason can be the higher density (about 25 percent) of α-alumina. Figure 8 shows that the distribution of the particles leaving the reactor. Almost 97 % of these particles have a mean diameter below 20 microns.

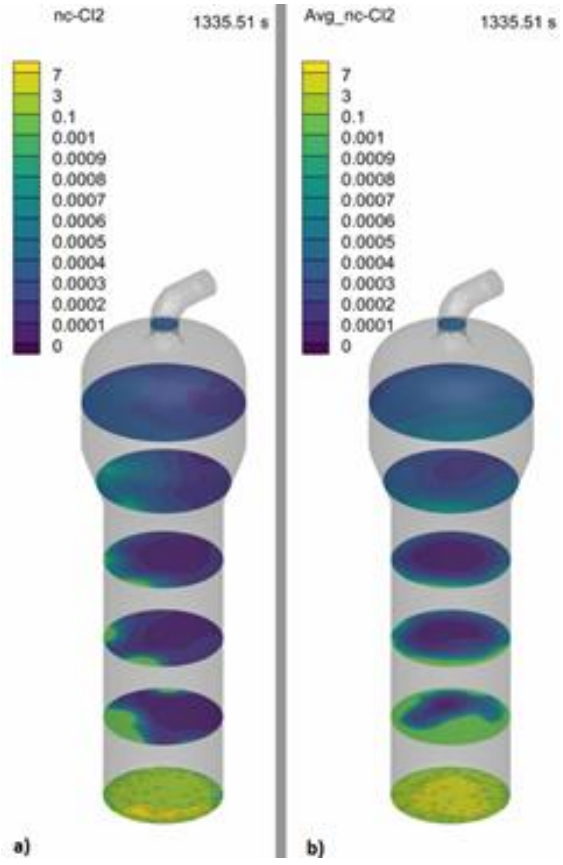

Figure 7. Cl_2 concentration (mole/m^3) in different heights, a) Cl_2 concentration at the specific time, and b) Average Cl_2 concentration in the last 300 seconds.

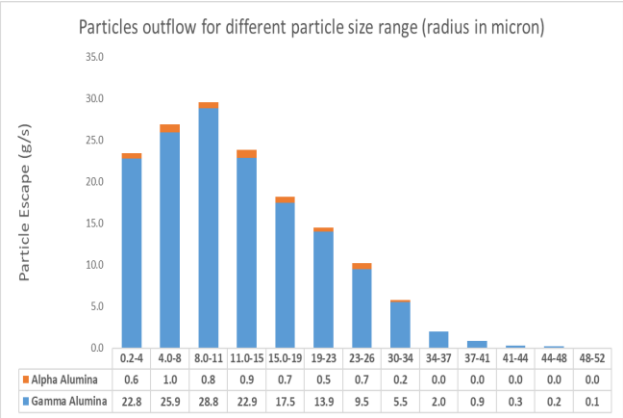

Figure 8. Composition of the particle outflow

Figure 9 and Figure 10 show the size distribution of the different alumina components leaving the reactor. The biggest γ-alumina particle that can leave the system is in the range of 48-52 microns. This value for the α-alumina is in the range of 30-34 microns, emphasizing the higher density of these particles, leading to higher terminal velocity.

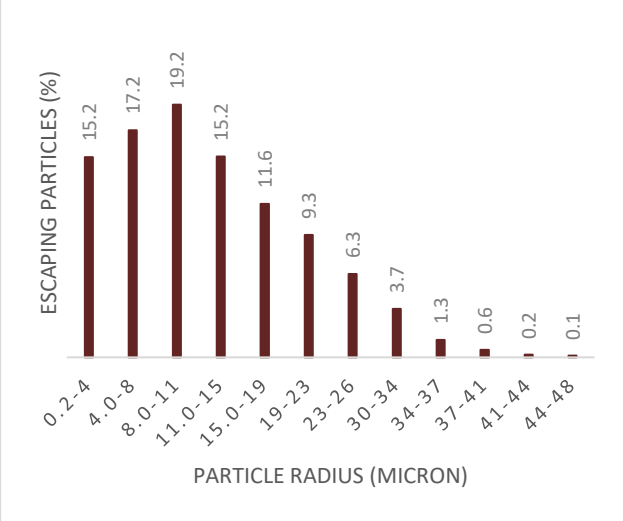

Figure 9. γ-Alumina size distribution in the outlet

The mass balance of the bed shows an unfavorable accumulation of α-alumina in the fluidized bed reactor. During the one-hour simulation period, α-alumina is accumulated at the rate of 5 g/s, and the bed losses γ-alumina at the same rate. Although the alumina inflow rate is constant (0.6 kg/s with a fixed 7 % impurity), α-alumina in the bed is increased, and the overall reaction efficiency of the reactor went down. To minimize the harmful effects of the accumulated α-alumina particles, the particles inside the reactor should be replaced periodically.

An increased amount of non-reactive particles in bed may also increase the particle outflow, but that could be minimized by introducing a proper solid circulation mechanism. However, this may not completely stop the α-alumina accumulation within the system. Nevertheless, the circulation system for particles can increase the particles' residence time, which may help α-alumina particles reach complete chlorination.

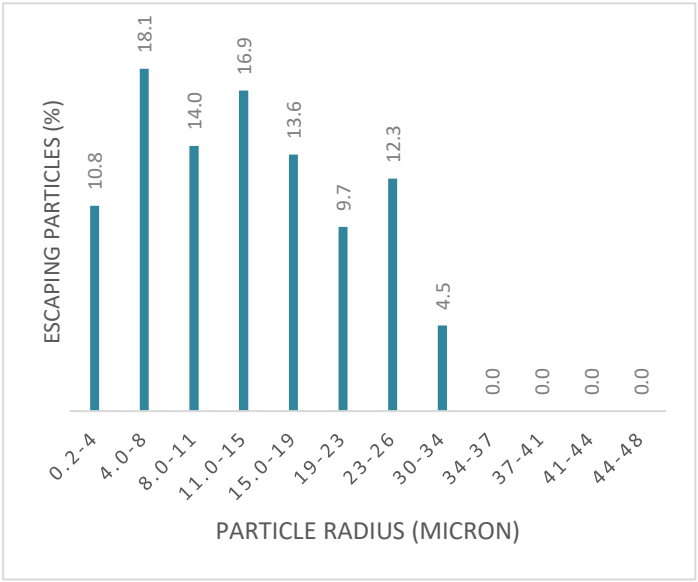

Figure 10. α-Alumina size distribution in the outlet

6 Conclusion

Compared with the model with pure γ-alumina, the results show that, as an impurity, α-alumina does not affect the chlorine concentration at the outlet. The overall particle outflow has become slightly higher in the case of pure γ-alumina. Compared with the α-alumina inflow, which is 7 % of the total inflow, only 3.8 % of the total particle outflow is belongs to α-alumina. In the long run, as a result, α-alumina will be accumulated in the reactor, which is not favorable. In the operating temperature, the reaction rate of α-alumina is much slower, and the accumulation of α-alumina will affect the overall reaction negatively. As remedies, adding a circulation path or speeding up the fluid inside the reactor to a certain point may be helpful, which can be investigated in future works.

References

H. Alder, H. Muller, W. Richarz. Kinetic Study of the Alumina Chlorination with Carbon Monoxide and Chlorine. *Light Metals*, 1977.

Z. Barahmand, C. Jayarathna, and C. Ratnayake. CPFD simulations on a chlorination fluidized bed reactor for aluminum production: An optimization study. *In Proceedings - 1st SIMS EUROSIM Conference on Modelling and Simulation*, Finland, 2021.

J. Beckmann. *History of Inventions, Discoveries, and Origins*. H.G. Bohn, 1846.

I. Bertóti, A. Tóth, T. Székely, and I. Pap. Kinetics of γ-alumina chlorination by phosgene. *Thermochimica Acta*, *44*(3), 325–331, 1981. doi:10.1016/0040-6031(81)85025-3

N. Gokcen. *Rates of chlorination of aluminous resource*, pages 28. U.S. Department of the Interior, Bureau of Mines, 1983.

A. Kovács, C. Breward, K. Einarsrud, S. Halvorsen, E. Nordgård-Hansen, E. Manger, A. Münch, and J. Oliver. A heat and mass transfer problem for the dissolution of an alumina particle in a cryolite bath. *International Journal of Heat and Mass Transfer*, *162*, 120232, 2020. doi:10.1016/j.ijheatmasstransfer.2020.120232

D. Kunii and O. Levenspiel. *Fluidization Engineering*. Butterworth-Heinemann, 1991.

F. Liang, M. Sayed, G. Al-Muntasheri, F. Chang, and L. Li. A comprehensive review on proppant technologies. *Petroleum*, *2*(1), 26–39, 2016. doi:10.1016/j.petlm.2015.11.001

J. Milne. The chlorination of alumina and bauxite with chlorine and carbon monoxide. *Proc Aust Inst Min Metall*, *260*, 23–31, 1976.

National Fuels and Energy Conservation Act, S. 2176, U.S. Government Printing Office, 1973.

S. Prasad. Studies on the Hall-Heroult aluminum electrowinning process. *Journal of the Brazilian Chemical Society*, *11*, 245–251, 2000. doi:10.1590/S0103-50532000000300008

Y. Rao, and M. Soleiman. *Alumina chlorination* (United States Patent No. US4565674A), 1986.

M. Soleiman and Y. Rao. Kinetics and Mechanism of Chlorination of Alumina Grains with He–CO–Cl2 Gas Mixtures—I. Experimental. *Canadian Metallurgical Quarterly*, *26*(3), 207–215, 1987. doi: 10.1179/cmq.1987.26.3.207

J. Thonstad. *Aluminum Electrolysis: Fundamentals of the Hall-Héroult Process*. Aluminium-Verlag, 2001.

A. Tóth, I. Bertóti and T. Székely. Kinetics of γ-alumina chlorination by carbon monoxide and chlorine. *Thermochimica Acta*, *52*(1), 211–215, 1982. doi: 10.1016/0040-6031(82)85198-8

J. Xie, W. Zhong and A. Yu. MP-PIC modeling of CFB risers with homogeneous and heterogeneous drag models. *Advanced Powder Technology*, *29*(11), 2859–2871, 2018. doi: 10.1016/j.apt.2018.08.007

The application of the Lattice Boltzmann Method in the calculation of the virtual mass

Nastaran Ahmadpour Samani Ali Moradi Britt M. E. Moldestad

Department of Process, Energy and Environmental Technology, University of South-Eastern Norway,
nastaran.samani@usn.no
ali.moradi@usn.no
britt.moldestad@usn.no

Abstract

Virtual mass is an important quantity in the analysis of the unsteady motion of objects underwater or other fluids or unsteady flow around bodies, for example, the virtual mass effect is important in the inertia of ships, floaters, swimmers' organs, airplanes, and bubbles. The additional mass resulting from the fluid acting on the structure can be calculated by solving the equation of potential flow around the object. In this paper, a system in which a square object is immersed in a channel of fluid and moves parallel to the wall has been considered. The corresponding virtual mass at a determined distance $\boldsymbol{S}$ from the wall and for the object size $\boldsymbol{D}$ (the side of the square object) is calculated via the Lattice Boltzmann Method. Here, it is tried to change $\boldsymbol{D}$ and $\boldsymbol{S}$ separately and investigate their effects on the virtual mass. According to the simulation results, for the systems in which the distance from the wall is more than four times the object size ($\boldsymbol{S} > 4\boldsymbol{D}$), the distance does not influence the added mass. Furthermore, the virtual mass rises when the object approaches the wall and experiences its maximum value as it reaches the wall ($\boldsymbol{S} \rightarrow \boldsymbol{0}$). As a result, in this case, the virtual mass is about 75% larger than in the case of $\boldsymbol{S}=4\boldsymbol{D}$. In addition, the simulations reveal that by increasing the dimensions of the object $\boldsymbol{D}$ the virtual mass increases and vice versa.

Keywords: Lattice Boltzmann simulation, added/virtual mass, variable size, various distance, bounce-back boundary condition

1 Introduction

The Lattice Boltzmann Method (LBM) which is a mesoscopic method based on simplified kinetic equations, has been significantly taken into consideration in classical statistical physics. LBM can be an appropriate alternative approach to the current finite difference, finite element, and finite volume techniques for solving the Navier Stokes equations. According to this method, it has been concluded that if only collective macroscopic flow behavior is investigated, the macroscopic behavior of a fluid system is generally not very sensitive to the underlying microscopic behavior of the particle. In LBM, the simulation is based on the modeling of fluid flow as a collection of particles colliding over a discrete lattice sphere. In this method, the Boltzmann equation is solved on a discrete lattice and instead of solving Navier Stokes equations, the density of the fluid is simulated during two steps including streaming and collision. Owing to its underlying kinetic property, the ability to combine microscopic interactions, and using bounce back boundary conditions, the LBM has been increasingly applied in the simulation of fluid flow especially interfacial dynamics and complicated boundaries and geometries, such as multiphase/multicomponent flows in porous media (Hinebaugh et al., 2012; Tu et al., 2018; Succi, 2001). The Lattice Boltzmann Method has been used in the simulation of a wide variety of fluid dynamical applications. The method is really practical in the simulation of turbulent single-phase flow, flow in porous media, and multiphase flows in several industrial applications (Chen and Doolen, 1998). LBM has been applied in various simulations such as flow in porous media (Pan et al., 2006; Nabovati et al., 2009), colloidal suspensions (Kutay et al., 2006), multiphase and multicomponent flows (Yang and Boek, 2013; Inamuro et al., 2004), and several other applications.

In this study, the additional mass of a two-dimensional object is simulated using the Lattice Boltzmann Method. Numerous forces are exerted on a body moving in a fluid. Lift and drag forces are exerted on bodies in a fluid due to surface friction and the variation of pressure around the bodies. In order for a moving body to move in a fluid, it must counteract the fluid and move it. Therefore, not only should the body move its weight, but it should also move the surrounding fluid. Hence, to counteract the fluid's inertia, the body faces additional forces, and it senses further weight than that of its weight. If the density of the body is greater than that of the fluid, the additional force can be overlooked. Otherwise, it must be considered. The additional force which is caused by the fluid inertia is called added mass. Other titles such as virtual mass, hydrodynamic mass, effective mass, inertial mass, apparent mass, and induced mass are also applied. The calculation of virtual mass is a challenging procedure in the analysis of bodies moving in the water.

In (Cebeci et al., 2005) the low-speed unsteady airfoils were investigated by researchers, and it was demonstrated that further forces are exerted on airfoils in moving fluids. Additional mass for various geometries was calculated by employing the complex function methods by Korotkin (Korotkin, 2008). The value of the body acceleration did not have any effect on the value of additional mass (Wakaba and Balachandar, 2007). The additional mass for various figures in low-depth water was calculated (Zhou et al., 2005). The additional mass for a cylinder which was placed between two parallel plates was measured by Kharlamov (Kharlamov, 2012). The additional mass for a hydrofoil with cavitation was calculated by Benaouicha (Benaouicha et al., 2012). Investigated vibration characteristic of a thin layer in the air by implementing empirical methods was studied in (Yuanqi et al., 2011). Furthermore, the additional mass for a swimmer, the effects of deformation, and the size of a swimmer, i.e. a man or a woman were studied by Caspersen (Caspersen et al., 2010). The influence of additional mass on the forces exerted on insect wings was studied by Yan (Yan et al., 2011). Guo investigated the added mass effect of seawater on pipeline vibration (Guo et al., 2013).

In this investigation, initially, the additional mass for a body when it is far from a wall is calculated and it is compared with the exact results. Afterward, the effects of the wall near the body on additional mass are investigated. Moreover, the dimensions of the deformed body and its effects on the additional mass are taken into consideration.

2 Fundamental equations

Figure 1 presents the investigated problem of this study, which is a square body with dimensions that moves parallel to the wall. In order to determine the additional mass, potential fluid around the body is considered. Laplacian equation for the potential equation is as follows (Versteeg and Malalasekera, 2007):

$$\frac{\partial^2 \varphi}{\partial x^2}+\frac{\partial^2 \varphi}{\partial y^2}=0 \qquad (1)$$

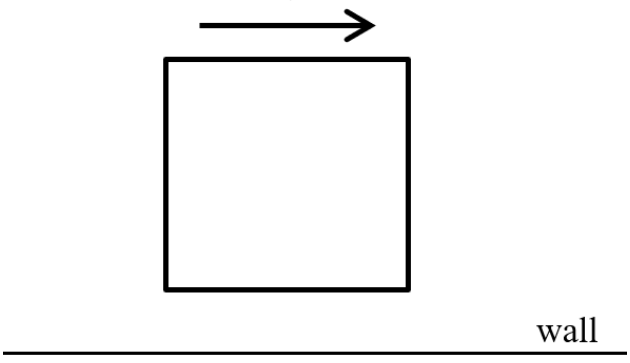

Figure 1. Figure of square moving body

It is feasible to assume that the fluid is moving instead of the body. Boundary conditions are depicted in Figure 2. For a uniform potential fluid flow in the *x*-direction, the potential function changes linearly with *x*. The gradient of the potential function in the direction of perpendicular on the surface for the wall, the body, and the top boundary condition is equal to zero. The value of the potential equation is assumed for the right and left boundaries, which are zero, and φ_0 for the left and right boundaries, respectively. The length of the solution must be considered in a way that satisfies $\partial\varphi/\partial y$ and $\partial\varphi/\partial x$ in the regions which are near the wall boundaries. In fact, the amplitude of the solution should be chosen so that integration on the solution amplitude yields the proper results. The dimensions of solution amplitude are represented in Figure 3. The distance between the body and the wall is specified by *S* and 9*D* is the length of the solution range. The accuracy of the presented dimensions is investigated in the results section. The dimensionless parameters are defined as (Mohamad, 2011):

$$Y\equiv\frac{y}{D} \qquad \phi=\frac{\varphi}{\varphi_0}\frac{L}{D} \qquad U\equiv\frac{uL}{\varphi_0} \qquad \mathrm{X}\equiv\frac{x}{D} \qquad \phi=\frac{T-100}{100} \qquad (2)$$

L is the solution amplitude.

$$\frac{\partial^2 \phi}{\partial X^2}+\frac{\partial^2 \phi}{\partial Y^2}=0 \qquad (3)$$

$$\phi(\frac{+L}{2},X)=\frac{L}{D} \qquad \phi(\frac{-L}{2},Y)=0 \qquad (4)$$

On the top and bottom boundary:

$$\frac{\partial \phi}{\partial Y}=0$$

And on the body:

$$\frac{\partial \phi}{\partial n}=0$$

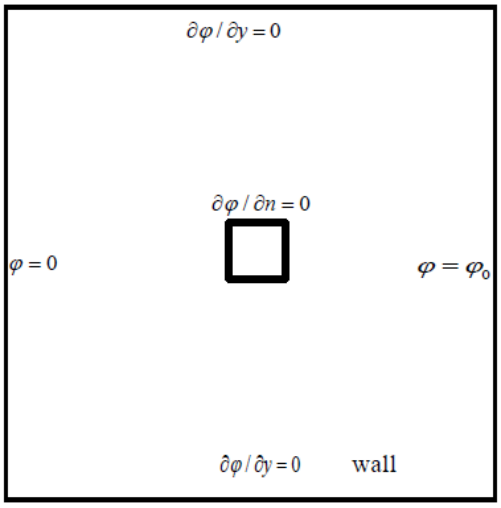

Figure 2. Boundary conditions

Based on the 2D or 3D body dimensions, the additional mass has numerous components. In this study, a two-dimensional body with one-dimensional moving and one component additional mass is taken into account. Additional mass is going to be dimensionless regarding the following equation.

$$M = \frac{m}{\rho D^2} \tag{5}$$

The mass, m [kg/m] is defined as the additional mass of the object at a specified distance from the wall. ρ [kg/m^3] is fluid density and D [m] is the distance from the wall.

After determining the potential equation, the value of additional mass is calculated from (Graebel 2007):

$$M = \iint M_{11}(X,Y)\,dX\,dY \tag{6}$$

$$M_{11}(X,Y) = \left(\frac{\partial \phi}{\partial X} - 1\right)^2 + \left(\frac{\partial \phi}{\partial Y}\right)^2 \tag{7}$$

In contrast to regions near the body, the value of $M_{11}(X, Y)$ is zero in regions far from the body.

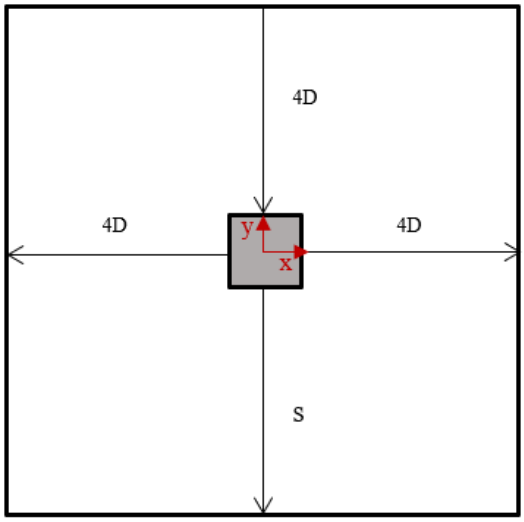

Figure 3. Dimensions of solution amplitude

3 Boltzmann Method

The Boltzmann procedure is explained by Mohamad (Mohamad, 2011). The solution amplitude is divided into nodes of equal size. D_2Q_9 is implemented in this study and the $g(i)$ distribution equation is employed. The following correlation is governed for the $g(i)$ equations (Mohamad, 2011):

$$g_i(\vec{r} + \vec{e}_i \delta t, t + \delta t) = g_i + \frac{g_i^{eq} - g_i}{\tau} \tag{8}$$

$\vec{r}$ is the position vector of a node, τ is the relaxation time, and g_i^{eq} is the vector of the distribution equation. $\vec{e}_i$ vectors are depicted in Figure 4 and its value is as follows. In addition, g_i^{eq} is presented as (Mohamad, 2011):

$$\left\|\vec{e}_0\right\| = 0, \qquad \left\|\vec{e}_{1,2,3,4}\right\| = 1, \qquad \left\|\vec{e}_{5,6,7,8}\right\| = \sqrt{2} \tag{9}$$

$$\left\{ \begin{array}{l} g_0^{eq} = 0 \\ g_1^{eq} = g_2^{eq} = g_3^{eq} = g_4^{eq} = \frac{1}{6}\phi \\ g_5^{eq} = g_6^{eq} = g_7^{eq} = g_8^{eq} = \frac{1}{12}\phi \end{array} \right\} \tag{10}$$

Boltzmann correlation is solved at the two stages of collision and stream (Mohamad, 2011):

$$g_i(\vec{r}, t + \delta t) = g_i + \frac{g_i^{eq} - g_i}{\tau} \tag{11}$$

$$g_\alpha\left(\vec{r} + \vec{e}_i t, t + \delta t\right) = g_\alpha\left(\vec{r}, t + \delta t\right) \tag{12}$$

At the collision stage, Equation 11, the values of distribution equations are calculated from the previous stage. Each node at the stream stage transfers to another node in the opposite direction.

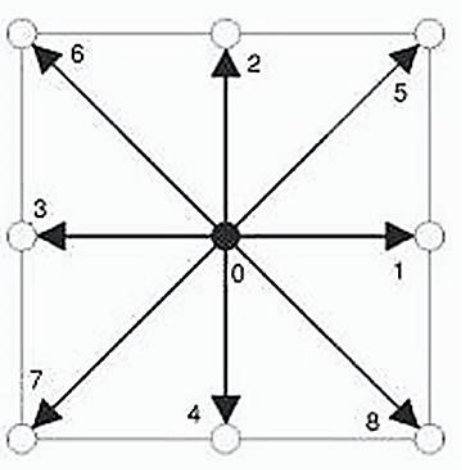

Figure 4. D2Q9 Lattice model

After the determination of the distribution equation in each node, the value of the potential equation and its derivatives are determined as follows (Mohamad, 2011);

$$\phi = \sum_{i=0}^{8} g_i \tag{13}$$

$$\vec{\nabla}\phi = \frac{\tau - 0.5}{\tau} \sum_{i=0}^{8} \vec{e}_i g_i \tag{14}$$

At the stream stage, no value is transferred to the distribution equations, i.e., $g(i)$ on the boundaries. There are three paths on each node, in which no value is transferred to them so that the boundary conditions for these nodes can determine the distribution functions on unknown nodes. For example, the values of g_3, g_6, and g_7 are unknown for the right boundary because there is no node after the right boundary to transfer the values

based on Equation 12 to these functions. The value of the potential equation is known for the right boundary ($\varphi_R \equiv L/D$):

$$\varphi_R = g_0 + g_1 + ... + g_8 \quad (15)$$

The value of the potential equation is constant at the direction of this boundary and hence the potential equation is zero in this direction:

$$\frac{\partial \phi}{\partial Y} = \frac{\tau - 0.5}{\tau}(g_2 + g_6 + g_5 - g_4 - g_7 - g_8) = 0 \quad (16)$$

According to the bounce-back condition, the value of the distribution equation is equal for the directions normal to the boundary, thus for the right boundary:

$$g_3 = g_1 \quad (17)$$

From Equations 15 and 16, it is concluded that:

$$g_6 = \frac{\phi_R}{2} - (\frac{g_0}{2} + g_1 + g_2 + g_5) \quad (18)$$

$$g_7 = \frac{\phi_R}{2} - (\frac{g_0}{2} + g_1 + g_4 + g_8) \quad (19)$$

The procedure for the left boundary is the same as the right boundary.

The values of g_4, g_7, and g_8 are unknown for the top boundary. This is due to the fact that on this boundary $\frac{\partial \varphi}{\partial y} = 0$, and Equation 16 is accurate if:

$$g_4 = g_2, \qquad g_7 = g_6, \qquad g_8 = g_5 \quad (20)$$

Therefore, the value of *g(i)* which is unknown for the nodes is equal to its symmetry concerning the boundary. The current method is used for the bottom boundary and the outer of the body. For the entire calculations in this study $\tau = 1.5$ is assumed. The procedure of solving is started with an initial condition by assuming the value φ is zero for every node. Afterward, this procedure continues until the variations of φ or M become insignificant between two-time steps.

4 Results

In this contribution, the value of additional mass for a square body that is placed far from a wall is initially investigated, and in this case, *M*=1.189 is deduced. The problem is solved for the various node distances in order to determine the best number of nodes. The effect of node number on the value of additional mass is presented in Table 1. Regarding the presented relative error on the table, the distance between the nodes has been chosen to be 1/69. The number of nodes is 630×630.

Table 1. The influence of the number of nodes on added mass

ΔX	M	$E\%$
1/9	2.225	87
1/19	1.448	22
1/29	1.300	9.32
1/39	1.246	4.8
1/49	1.219	2.5
1/59	1.204	1.3
1/69	1.195	0.5

The constant potential lines and M_{11} distribution are presented in Figure 5. The potential equation at the places far from the body is linear, and the velocity reaches its final constant value. According to the horizontal moving of the body, the M_{11} variations are higher at the front and back sides of the body.

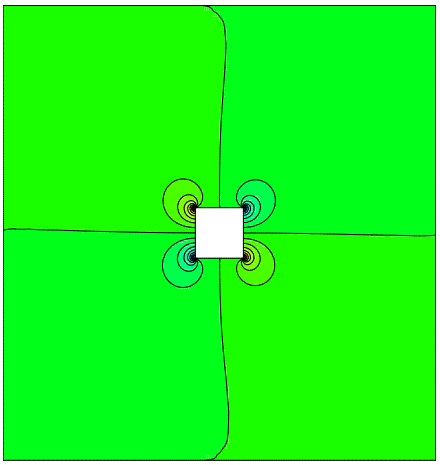

Figure 5. M_{11} distribution, for dimension of D×D and S=4D

Figure 6 represents potential lines and M_{11} distribution for the case in which the body is approaching the wall and *S=D*. By approaching the wall, the displacement of the body is going to be more complicated, and this is due to an additional mass increase in the regions near the wall. The problem is solved for *S/D*= 4, 3, 2, 1, 0.75, 0.5, 0.25, 0. The variation of additional mass versus the distance from the wall is shown in Figure 7. By approaching the wall, the value of additional mass increases, and its value increased by approximately 75% as the body reach the wall. The diagram of Figure 7 can be expanded by applying Equation 21. The equation has been achieved by curve fitting in MATLAB.

$$M = 0.857\, e^{(-3.2(S/D)+1.182)} \quad (17)$$

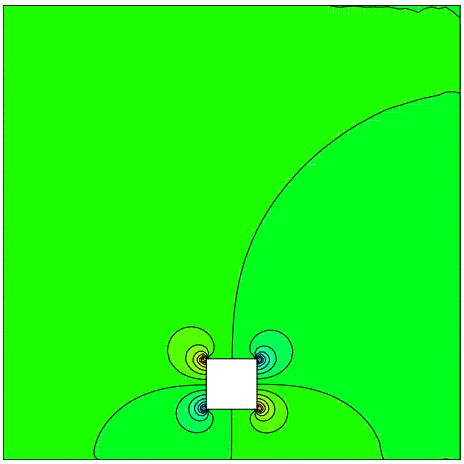

Figure 6. M_{11} distribution, for dimension of D×D and S=D

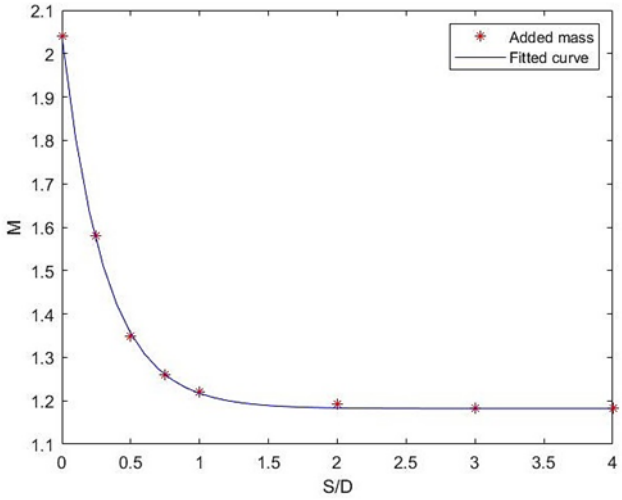

Figure 7. The variation of additional mass versus the distance from the wall

Moreover, the dimensions of the body have been changed and its influences upon additional mass are calculated. Constant potential lines and M_{11} distribution are presented in Figure 8 for a body with $0.8D\times D$ dimensions. Figure 9 demonstrates potential lines and M_{11} distribution for a case in which the body approaches the wall, i.e., $S=D$. By approaching the wall, body displacements become much harder, and this is because of the additional mass increase near the wall. The problem is solved for S/D= 4, 3, 2, 1, 0.75, 0.5, 0.25, 0. It is concluded that additional mass decreases by the decrease in the dimensions of the body.

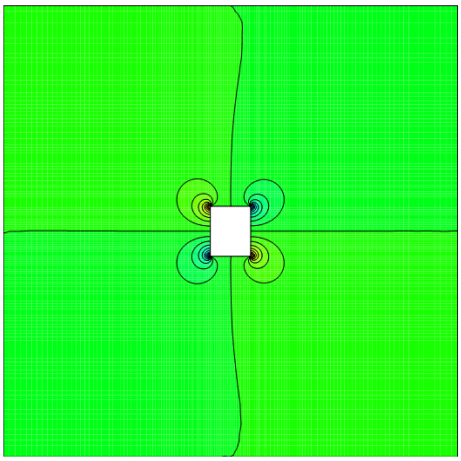

Figure 8. M_{11} distribution for dimension of 0.8D×D and S=4D

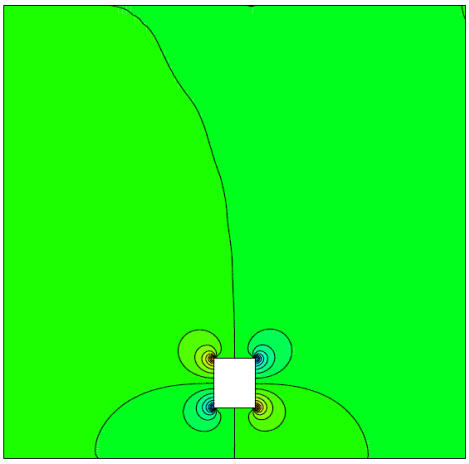

Figure 9. M_{11} distribution, for size of 0.8D×D and S=D

Figure 10 shows constant potential lines and M_{11} distribution for a body with $1.2D\times D$ dimensions. Figure11 shows potential lines and M_{11} distribution for a case in which the body approaches the wall, i.e. $S=D$. The displacement of the body becomes much more complicated as the body approaches the wall, and this is because of the increase in the values of additional mass in the regions near the wall. The problem is considered by determining S/D= 4, 3, 2, 1, 0.75, 0.5, 0.25, 0, and it is concluded that additional mass increases by increasing the dimensions of the body.

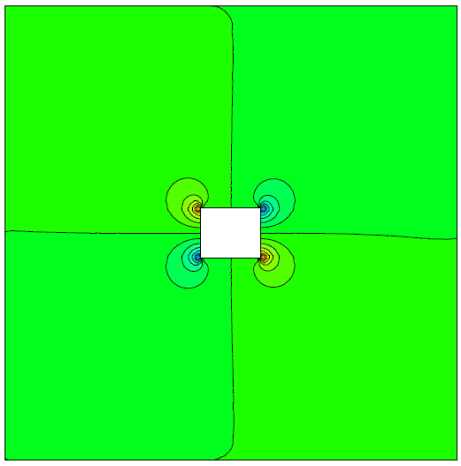

Figure 10. M_{11} distribution, for dimension of 1.2D×D and S=4D

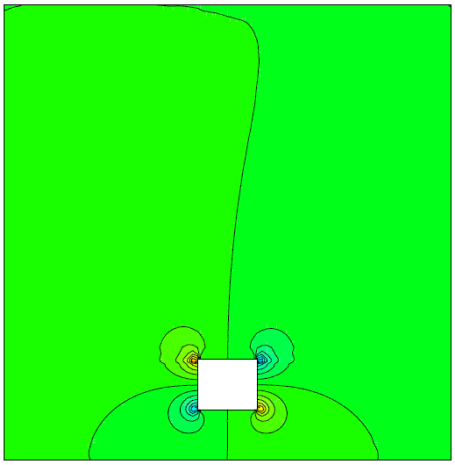

Figure 11. M_{11} distribution, for the dimension of 1.2D×D and S=D

The added masses of the body in the different dimensions in the distance equal to 4*D* from the wall have been validated by the results by Korotkin, in 2008. The results in Table 2 revealed that the added masses calculated by the Lattice Boltzmann Method have a very good constancy with the results in (Korotkin, 2008). The deviation between measured added masses and data in (Korotkin, 2008) varies between 0.9 % and 5 %, and the root mean square error is 2 %.

Table 2. Validation of the calculated added mass from Lattice Boltzmann Method for different dimensions in the distance equal to 4D from the wall with the results in (Korotkin, 2008)

Dimensions	*M_calculated [kg]*	*M (Korotkin 2008) [kg]*
0.4D×D	1.053	1.115
0.8D×D	1.148	1.162
D×D	1.182	1.193
1.2D×D	1.211	1.23
1.4D×D	1.234	1.257
1.6D×D	1.254	1.28
1.8D×D	1.27	1.304
2D×D	1.284	1.327

Furthermore, this procedure is employed for the cases in which the dimensions of the body are 2*D*×*D*, 1.8*D*×*D*, 1.6*D*×*D*, and 1.4*D*×*D*, and the value of additional mass is calculated. Figure 12 represents the variations of the calculated added masses of a body with various dimensions at different distances from the wall. Figure 13 shows the effects of the dimension of the body on the calculated added mass.

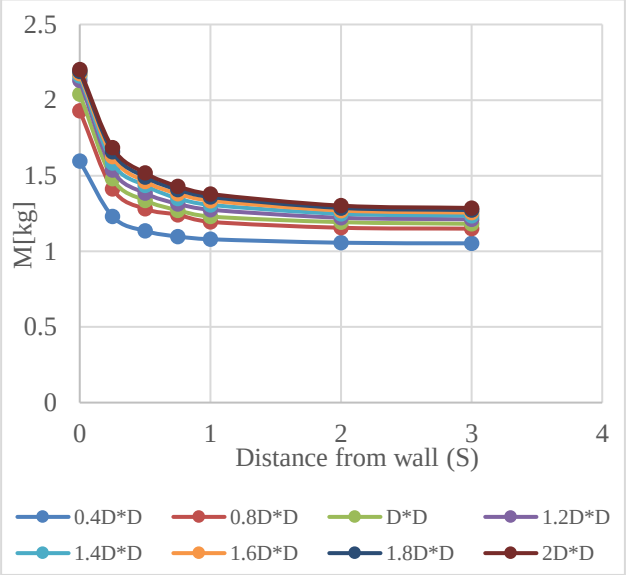

Figure 12. The variation of added masses of different sizes of body versus distance from the wall

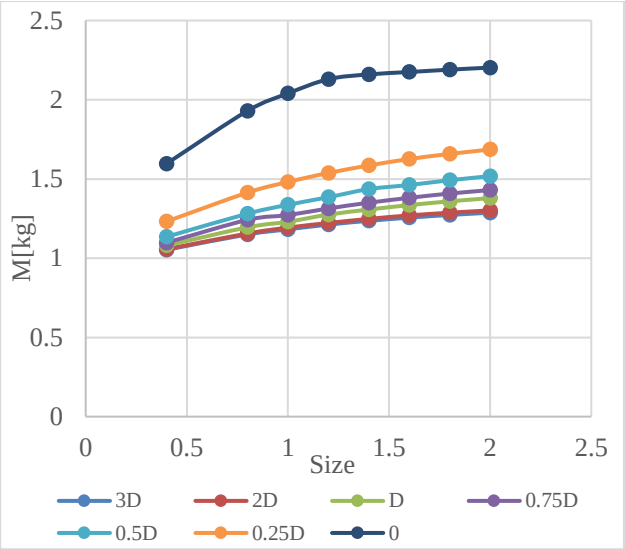

Figure 13. The variation of virtual masses of a body in different distances of the wall versus the dimension of the body

5 Conclusion

Added mass is an important quantity in the analysis of the motion of a submerged object, for example, ships crossing canals. The added mass increases when the object approaches the wall and reaches its maximum value as it moves on the wall ($\boldsymbol{S \rightarrow 0}$). In this case, the added mass is about 75% larger than for the case with $\boldsymbol{S}$=4$\boldsymbol{D}$. In addition, it is observed that the added mass increases by an increase of the object size $\boldsymbol{D}$ and vice versa. By increasing the size of the object to twice, the amount of added mass enhances between 8 to 15% depending on the distance of the object from the wall. The results of the measured added mass using the Lattice Boltzmann Method at the distance of 4D from the wall were validated with the results in the book by Korotkin and the results have a good consistency (RMSE =2%).

References

Mustapha Benaouicha, and Jacques-André Astolfi. Analysis of added mass in cavitating flow. *Journal of fluids and structures.* 31:30-48, 2012.

Cecilie Caspersen, Petter A. Berthelsen, Mari Eik, Csaba Pâkozdi, and Per-Ludvik Kjendlie. Added mass in human swimmers: age and gender differences. *Journal of Biomechanics*. 43, no. 12: 2369-2373, 2010.

Tuncer Cebeci, Max Platzer, Hsun Chen, Kuo-Cheng Chang, and Jian P. Shao. *Analysis of low-speed unsteady airfoil flows*. Springer Berlin Heidelberg, 2005.

Shiyi Chen, and Gary D. Doolen. Lattice Boltzmann method for fluid flows. *Annual review of fluid mechanics*. 30, no. 1: 329-364, 1998.

William Graebel. *Advanced fluid mechanics*. Academic Press, 2007.

Boyun Guo, Shanhong Song, Ali Ghalambor, and Tian Ran Lin. *Offshore pipelines: design, installation, and maintenance*. Gulf Professional Publishing, 2013.

J. Hinebaugh, A. Bazylak, and P. P. Mukherjee. Multi-scale modeling of two-phase transport in polymer electrolyte membrane fuel cells. *Polymer electrolyte membrane and direct methanol fuel cell technology*. pp. 254-292e. Woodhead Publishing, 2012.

Takaji Inamuro. Lattice Boltzmann methods for moving boundary flows. *Fluid Dynamics Research* 44. no. 2: 024001, 2012.

A. A. Kharlamov. The virtual mass coefficients of a circular cylinder moving in an ideal fluid between parallel walls. *Journal of Applied Mathematics and Mechanics*. 76, no. 1: 98-102, 2012.

Alexandr I. Korotkin. *Added masses of ship structures*. Vol. 88. Springer Science & Business Media, 2008.

Muhammed E. Kutay, Ahmet H. Aydilek, and Eyad Masad. Laboratory validation of lattice Boltzmann method for modeling pore-scale flow in granular materials. *Computers and Geotechnics* 33, no. 8 (2006): 381-395.

A. A. Mohamad. *Lattice Boltzmann Method*. Vol. 70. London: Springer, 2011.

Aydin Nabovati, Edward W. Llewellin, and Antonio CM Sousa. A general model for the permeability of fibrous porous media based on fluid flow simulations using the lattice Boltzmann method. *Composites Part A: Applied Science and Manufacturing* 40, no. 6-7: 860-869, 2009.

Chongxun Pan, Li-Shi Luo, and Cass T. Miller. An evaluation of lattice Boltzmann schemes for porous medium flow simulation. *Computers & fluids* 35, no. 8-9: 898-909, 2006.

Sauro Succi. *The lattice Boltzmann equation: for fluid dynamics and beyond*. Oxford university press, 2001.

Jiyuan Tu, Guan Heng Yeoh, and Chaoqun Liu. *Computational fluid dynamics: a practical approach*. Butterworth-Heinemann, 2018.

Henk Kaarle Versteeg, and Weeratunge Malalasekera. *An introduction to computational fluid dynamics: the finite volume method*. Pearson education, 2007.

Y. J. Lee, Kim-Boon Lua, T. T. Lim, and K. S. Yeo. A quasi-steady aerodynamic model for flapping flight with improved adaptability. *Bioinspiration & biomimetics* 11, no. 3: 036005, 2016.

L. Wakaba, and S. Balachandar. On the added mass force at finite Reynolds and acceleration numbers. *Theoretical and Computational fluid dynamics* 21, no. 2: 147-153, 2007.

Xingyao Yan, Shanan Zhu, Zhongdi Su, and Hongjun Zhang. Added mass effect and an extended unsteady blade element model of insect hovering. *Journal of Bionic Engineering* 8, no. 4: 387-394, 2011.

Jianhui Yang, and Edo S. Boek. A comparison study of multi-component Lattice Boltzmann models for flow in porous media applications. *Computers & Mathematics with Applications* 65, no. 6: 882-890, 2013.

Li Yuanqi, Lei Wang, Zuyan Shen, and Yukio Tamura. Added-mass estimation of flat membranes vibrating in still air. *Journal of Wind Engineering and Industrial Aerodynamics* 99, no. 8: 815-824, 2011.

Z. X. Zhou, Edmond YM Lo, and S. K. Tan. Effect of shallow and narrow water on added mass of cylinders with various cross-sectional shapes. *Ocean engineering* 32, no. 10: 1199-1215, 2005.

Possible concepts for digital twin simulator for WWTP

Tiina M. Komulainen[1] Hilde Johansen[2]

[1]Department of Mechanical, Electronics and Chemical Engineering, Oslo Metropolitan University, Norway, tiina.komulainen@oslomet.no

[2]Veas - Vestfjorden Avløpsselskap, Norway, hj@veas.nu

Abstract

Application of advanced modeling and simulation technologies is essential to meet future requirements for higher wastewater treatment capacity and increased discharge water quality without large investments in construction projects.

This article describes an industrial pre-project for digital twin simulator for Veas wastewater treatment plant in Norway. The desired main functionalities of the digital twin simulator were:

- Data- and model-based management as well as decision support for process operators
- Predictive operational support and process optimization for engineers
- Testing of process modifications, control system modifications, new procedures and other changes
- Competency building and knowledge transfer between the operators and engineers

Commercially available technologies were compared according to the functional design specification and four possible digital twin simulator concepts were developed for wastewater treatment facilities.

Keywords: dynamic modeling, simulator, digital twin, water treatment, wastewater treatment plant.

1 Introduction

As growing cities produce more wastewater, climate change increases storm water intensity, and legislative requirements for the discharge water quality tightens, the capacity in the wastewater treatment facilities must be increased. In order to meet these future requirements without large investments in comprehensive construction projects, it is essential to develop innovative technology for process optimization and knowledge building in the organization.

During the past decade, research and development in artificial intelligence (Kapelan et al,, 2020), digital twins (Molin, 2021; Valverde-Pérez et al., 2021) and advanced process control solutions (Zlatkovikj et al., 2020; ABB, 2021a; Dahlquist et al., 2019) in the water sector has increased significantly. Experiences with simulators (Komulainen and Sannerud, 2018) and digital twins (Cameron et al., 2018) in the oil industry have shown good results in terms of knowledge building, process optimization and plant integrity. There is a high potential for use of digital twins at wastewater treatment plants as several commercial simulator tools and AI products are available in the international market.

Currently, the wastewater treatment plants in Viken county, Norway, are dominated by traditional control technology and do not use simulators or digital twins for operator training, process optimization, energy efficiency or other purposes.

This article describes the results of the DTS VANN pre-project, a collaboration between Veas wastewater treatment plant in Asker, Norway and Oslo Metropolitan University during 1.9.2020-31.5.2021, funded by RFF Viken (Johansen, 2021). During the pre-project, a functional design specification for a digital twin simulator for the wastewater treatment plant was developed, and available technologies were compared according to the specification. The comparison was further developed into possible digital twin simulator concepts for water treatment facilities.

The research question was “Which digital twin simulator concepts can provide a platform for 1. Online process optimization 2. Offline process optimization and modification studies 3. Operator training?”

1.1 Nomenclature

AI artificial intelligence
APC advanced process control
BOD, COD biological and chemical oxygen demand
DCS distributed control system
FDS functional design specification
OPC open platform communications (originally object linking and embedding for process control)
OPC UA open platform communications unified architecture
PAX, PIX preconditioning chemicals
P&ID piping and instrumentation diagram
PS process simulator (high fidelity)
RFI request for information
TSS total suspended solids
VEAS Vestfjorden Avløpsselskap
WWTP wastewater treatment plant

1.2 Plant description

The Veas plant is Norway's largest wastewater treatment plant and a crucial contributor to the efforts in keeping the Oslo Fjord clean. The process plant has an annual production of around 100 million m^3 of treated wastewater, about 40 000 tons of Veas-soil and 10 million standard m^3 of biogas (2019). Wastewater from the equivalent of 835 000 inhabitants (2020) in Oslo, Bærum and Asker is transported via the Veas tunnel to the treatment plant at Bjerkås in Asker. The plant is required to remove at least 70% of nitrogen, 90% of phosphorus, and organic material: 70% BOD and 75% COD.

The main processing facilities of the Veas plant include:

1. Pumping of the wastewater from the Veas tunnel to the Veas WWTP facility with centrifugal pumps.
2. Mechanical treatment includes removal of bulky, large solids and garbage with screens, and removal of sand and skimming of fat in grit chambers.
3. In chemical treatment the suspended and colloid fractions are removed from the water: water is preconditioned with iron chlorides (PIX), aluminum chlorides (PAX), and polymers prior to sedimentation.
4. In biological processes Nitrogen and organic materials are removed: these processes include water screening, aerobic process in an aerated basins with nitrification filter (bacteria on granules), flow equalization, methanol addition, and anaerobic process in a basin with denitrification filter. The cleaned water is disposed to Oslo fjord.
5. Reject water from sludge treatment (after chamber filter presses) is treated to remove nitrogen. The process includes a stirred flow equalization tank, screening, air stripping of ammonia in a countercurrent column, absorption of ammonia to nitric acid solution in a counter current column. The resulting ammonium nitrate is sold to industry.
6. Actiflo-facility for excess rainwater includes the following processing units stirred coagulation tank with iron addition, stirred tanks with micro sand and polymer addition, sedimentation basin with bottom scraper, sludge cyclone. The cleaned water is disposed to Oslo fjord.
7. Sludge treatment and soil production includes the following processes fiber removal with rotating screening drums, polymer addition, dewatering with drum screen, sludge buffer tank, sludge heating, sludge buffer tank; 20 day long batch process in mesophilic anaerobic digester stirred with recirculated biogas and recirculated, heated sludge; sludge buffer tank with aeration to stop digestion; sludge buffer tank, sludge screening, lime conditioning in a stirred tank, stirred tank with polymer addition, dewatering with chamber filter press using pressure up to 250 bar, sterilization using hot membrane water (80°C); dried sludge is transported via conveyor belt system to a stirred silo, export.
8. Biogas treatment and liquefaction: gas from digesters through H_2S filter, first stage CO_2 removal in absorber using amine solution, gas pre-cooler, reciprocating compressor, second stage CO_2 removal in absorber using amine solution, gas cooler, gas drier, amine regeneration; gas cooler, gas condenser, export pump (centrifugal), export system; systems for cooling medium. The liquefied biogas is sold to industry.
9. Heat production using a pellet boiler and a biogas/oil boiler, primary and secondary hot water loops, heat pump, plate heat exchangers and centrifugal pumps.
10. Cooling medium systems with glycol, water and sea water.

2 Materials and methods

This qualitative study was conducted using the following materials and methods.

2.1 Materials

The materials for this study included:

- Piping and instrumentation diagrams (P&ID) and the distributed control system screens of the the process systems at Veas wastewater treatment plant Process areas included were water treatment, sludge treatment, biogas production, biogas refining and liquefaction and mechanical treatment of solids.
- Technical documentation and presentations of simulator and digital twin products, provided by selected vendor companies.

2.2 Methods

The methods in this study included:

- Preparation of functional design specification for Veas WWTP analyzing the process documentation (P&ID, DCS screens) and interviews with the Veas process engineers and system engineers.
- Extraction of operational challenges from the interviews with process engineers.
- Selection of possible commercial simulator and digital twin vendors.
- "Request for Information" – a questionnaire with quantitative and qualitative questions on offline/online simulator products (modules and functionalities) and digital twin functionalities based on the functional design specification.
- Comparison of available simulator and digital twin products using the companies answers to the "Request for Information", and technical material and presentations provided by the technology vendors.
- Development of possible concepts fulfilling the goals for digital twin simulator for wastewater treatment plants.

3 Results

First, a short version of the functional design specification is presented and some typical operational challenges are described. Then, the formulation of documents "request for information" and "request for project information" are presented briefly. Finally, possible solutions fulfilling the goals of the digital twin simulator are described.

3.1 Functional Design Specification

A functional design specification (FDS) was prepared for the Veas wastewater treatment processes, in short the contents are as follows:

3.1.1 Overall goals of the digital twin simulator

The overall goal of the digital twin simulator is to

- Minimize the environmental impact
- Optimize the chemical consumption
- Optimize the energy use
- Improve the quality of the products

The digital twin simulator should provide:

Goal1: Online process optimization in order to achieve better products and minimize chemical consumption and energy use. Data- and model-based predictive support for daily process optimization. To start with as a decision support tool (open-loop, operators implement suggestions manually to DCS), and in longer perspective as automatic control (closed-loop, using programmable logic controllers and advanced process control algorithms).

Goal2: Testing of possible modifications to optimize the WWTP process operation (tightening regulations, population growth, climate changes). Tool for offline process optimization, and testing of future modifications for cost-effective operation as well as providing the opportunity to utilize the margins in existing infrastructure before expensive construction projects are necessary.

Goal3: Training system that ensures effective competency building among engineers and operators.

3.1.2 Description of the Veas wastewater treatment processes and instrumentation

The detailed description of the process and instrumentation included the three pretreatment stages, the three chemical and biological treatment stages with equipment, instruments and sensors. The pre-treatment stages include inlet pumps, screening station, and grit chamber. The main treatment stages include sedimentation, nitrification and denitrification states. The water treatment processes include 45 controllers, 123 transmitters, 446 valves, 203 pumps, tanks, mixers and motors, and 16 other equipment, in total 833 objects with a total of 5214 tags in the DCS system.

3.1.3 System integration

The digital twin simulator will be integrated with ABB's 800xA distributed control system and SCADA. version 6.1. The data can be shared via OPC server, preferably with OPC-DA, OPC-HDA, OPC-AE. It is desired that the digital twin simulator can be integrated together or co-simulated with other dynamic models, for example DHI's MIKE model of the urban drainage tunnel leading wastewater to the Veas facility.

3.1.4 Simulator specification

The simulator specification includes typical simulator functionalities for all user groups, like initial conditions, scenarios, basic functions, process equipment details and failure modes. Special functions are required for engineering simulator, operator and instructor interfaces. In addition the simulator should be run online, parallel to the real process with adaptation of the simulator model parameters, possibility for snapshots and predictive what-if-scenarios towards future.

3.1.5 Digital twin specification

The digital twin functionalities were not specified in detail, but the functionalities should fulfill the goals 1-3 listed in the beginning of the FDS.

3.2 Operational challenges – need for digital twin simulator

Based on review work the functional design specification and interviews with the Veas process engineers, the following areas of interest were identified:

3.2.1 Early warning and monitoring with virtual sensors

- General measurement quality using mass, molar or energy balance based approach
- Screens, conveyor belts and transport screws: blocking of these with solids, and faulty level measurement around these equipment due to build-up
- Basins: accumulation of sedimented particles and sludge
- Biological filters: effectivity and activity of bacteria
- Filters: fouling and timing for backwash cycle, as increased pressure difference over filter increases energy use in downstream pumps;
- Pumps: pump effect, energy use, wear-and-tear, challenges with sludge pumps
- Mixers: solids build-up/fouling, wear-and-tear, insufficient mixing of polymer
- Digesters: monitoring of the rotting process, stop in gas-circulating compressor leads to foaming;
- Heat exchangers: efficiency, heat transfer coefficients, stopping, leakage

- Tank after digesters: end the rotting process with aeration.
- Chamber filter press: many components and multi-stage sequences with high pressure and high temperature, degree of sterilization is dependent on hot water temperature in membrane water system
- Water tanks: decreasing level due to small inlet flow or leakage.
- Oil tanks: high pressure/temperature leads to process shutdown
- Gas tanks: possible hazards like leakage, emergency shutdown

3.2.2 Process optimization and/or advanced process control

- Inlet pumps: during varying hydraulic loads optimize the load sharing between eight inlet pumps.
- Chemical addition: optimize dosing of chemicals PIX, PAX, methanol, lime slurry, polymer and micro-sand based on influent quality.
- Sedimentation basins: optimize sludge pumping out of basin to avoid accumulation
- Nitrification basin: optimize aeration rate
- Denitrification basins: balance flow between the eight basins
- Nitrification, denitrification and stripping: optimize degree of purification with process parameters including backwash
- Digesters: optimize biogas production using parameters such as sludge retention time based on total suspended solids (TSS) in, sludge heating and circulation, biogas circulation and mixing; balance organic load between the tanks.
- Digesters: improve temperature setpoint tracking in digester tank with sludge heating and circulation.
- Filters: optimize pressure difference over the rag filters and dewatering of sludge in drum screens.
- Chamber filter presses: improve temperature setpoint tracking in membrane water system.

3.2.3 Operator training

- All scenarios given above, especially process optimization and advanced process control should be included to operator training.
- Emergency scenarios especially with biogas production, refining and liquefaction should be included to operator training.
- Process shutdown scenarios related to the logic in the safety and alarm system should be included to operator training. For example, pump stop in “less critical” parts of the plant can lead to full process shut down.

3.2.4 Simulation studies on possible modifications

- Case studies for increasing water treatment capacity with current equipment
- Case studies for new parallel operations (keeping in mind the limited space available), i.e. replacing existing water treatment equipment with new, more effective alternatives.
- Case studies with control system modifications.

3.3 Selection of companies

The possible vendors were selected from list of technology companies working with water, water networks and wastewater.

The following companies answered positively to the RFI: ABB, Aquasight, Aspentech, Corys, DHI, Hatch/Hydromantis, Kongsberg, KrügerKaldnes/Veolia, and Statsoft.

The following companies did not reply to our request for information or gave a negative answer: Andritz, Createch 360, Cybernetica, Envidan, EnviroSim, H2Ometrics, Perceptive Engineering, Prediktor, Royal Haskoning DHV, Xylem (Emnet).

We also invited presentations from ABB Västerås about MPC solution for a WWTP facility in the FUDIPO EU-project (Dahlquist, 2021), from ABB Italy about advanced process control for WWTP facilities (ABB, 2021a) and collaboration with DHI in the Singapore PUB project (ABB, 2021b) and ri.se about digital twin projects for WWTP facilities (Molin, 2021; Valverde-Pérez et al., 2021).

3.4 Request for information

To get an idea of the dynamic simulation modules and digital twin functionalities the available commercial tools have, a request for information (RFI) was sent to the companies. The request of information included three sections, Veas plant description, a multiple-choice questionnaire on dynamic simulation modules and system integration, and open written questions on system integration and digital twin functionalities. The multiple-choice part was divided to five categories:

Generic dynamic simulation modules including: Pipelines with two phase flow (liquid and solids), Pipelines with two phase flow (gas and liquid), Control valves, on/off valves, manual valves, safety valves, Centrifugal pumps (water), Eccentric U-pump (sludge), Heat exchangers: plate, spiral and tube, Fans, Stirred tanks, Buffer tanks, Cyclones, Pellet boiler, Biogas boiler, ESD/PSD system.

Wastewater treatment-specific dynamic process modules including: Grit chambers, Sedimentation basin, Basin/reactor with nitrification filter and aeration, Basin/reactor with denitrification filter, Continuous stirred tanks with chemical, sand or polymer additions.

Sludge treatment dynamic process modules including: Digester tank (anaerobic sludge rotting), Buffer tank with air inlet from bottom, Chamber filter press

Biogas specific dynamic process modules including: Gas coolers, CO_2-absorbtion and stripping columns, Gas compressor (piston and screw), Gas drying/H2O

removal: absorption in silica gel, H_2S-filter, Flare system, Gas cooler (plate heat exchanger), Gas condenser, Pump (LNG, glycol), Expansion drum, Coalescer (oil droplet removal), Drum for gas/liquid separation

Mechanical processing and transportation of dry solids dynamic process modules including:

Screens, Screws (transport of solids), Conveyor belts, Flip-flops, Containers, Fiber/rag removal with rotating screening drum

System integration including:

Communication via OPC-DA/HDA communication protocol, two-way communication with third party process modeling software, online simulation and requirements for communication outside Veas firewalls.

Open-ended questions

- Supported system integration protocols
- Maximum amount of signals
- References to previous projects with system integration to a control system like ABB's 800xA
- References to previous projects with system integration to third-party simulation software.
- Experience with co-simulation
- Description of digital twin functionalities for WWTP

4 Analysis: Possible solutions with commercial tools for WWTP

The information gathered from FDS, interviews with Veas engineers, presentations and discussions with the companies were merged and compared with the goals Veas has for the digital twin simulator.

4.1 Goal1: online process optimization

The first goal of the digital twin simulator is to provide online process optimization. If the decision support system is to suggest manual control actions to process operators, either an online simulator covering the whole plant or an AI tool for specific operational cases can be implemented.

An online simulator based on high-fidelity process models, gives holistic approach to the whole plant operation and covers more than cases in AI tools, i.e. the process interactions. Available online simulator simulator tools include DHI's TwinPlant (DHI, 2021a), Hatch's Mantis.AI (Hatch Hydromantis, 2021a), and Kongsbergs K-Spice Assure (Kongsberg, 2021a; 2021b). All of the online simulators can be run with ABB's 800xA DCS simulator (ABB, 2021c) for example using OPC-UA protocol.

Data-driven, artificial intelligence or model-based tools use real-time data to monitor selected process units and assist process operators. Products like Aquasight's Apollo (Aquasight, 2021), Veolia's Hubgrade (Krüger Kaldnes Veolia, 2021), or Statsoft's TIBCO (TIBCO, 2021) can be applied case-based for process units with largest potential for cost savings. Examples of research projects on digital twins, virtual/ soft sensors based on artificial intelligence and models can be found from (Molin, 2021; Valverde-Pérez et al., 2021)

If closed-loop control is desired, advanced process control packages like ABB's APC (ABB, 2021d) can be applied case-based to cover the process units with largest potential cost savings in energy and chemicals. In order to minimize the model mismatch between the simplified model in the APC algorithm and the "real process", an online simulator or an extended Kalman filter can be used to update the model parameters. Examples on MPC applications for wastewater treatment plants can be found from research projects (Dahlquist, 2021) and commercial projects (ABB, 2021b).

4.2 Goal 2: offline process optimization and modification studies

Testing of possible modifications to optimize the WWTP process operation for future requirements requires a holistic tool that covers the interconnections of the whole wastewater treatment plant. This can only be done with high/medium fidelity process simulators. The functionalities of six different commercial simulator products were compared according to the functional design specification and the request for project information. The modeling score, presented in Table 1, were calculated based on the vendors answers to the request for information. Only GPS-X modeling tool from Hatch Hydromantis (Hatch Hydromantis, 2021b) covers all the wastewater treatment, sludge treatment, biogas production, biogas refining and liquification. An older version of the Indiss Plus modeling tool from Corys (2015) covers the different process stages excluding some parts of the sludge treatment and mechanical processing, conversion to the new modeling tool will be necessary. The WEST modeling tool from DHI (DHI, 2021b) covers unit operations in general WWTP processing, wastewater treatment, sludge treatment and biogas production, but lack most of biogas liquefaction and mechanical processing. The K-SPICE modeling tool from Kongsberg (2021c) is developed for oil and gas processing and lacks ions, pH and solids. Therefore, it can calculate rough approximations for unit operations in general WWTP process, wastewater treatment, sludge treatment, biogas production and mechanical processing. K-SPICE covers well the biogas refining and liquefaction processes. The Apollo process modeling tool from Aquasight (2021) was not well enough described and demonstrated well enough to compare with the other products. The documentation and presentation from Aspentech also lacked necessary information about the AspenPlus

modeling tool and APM solutions tool for WWTP unit operations (AspenTech, 2021).

4.3 Goal 3: operator training system

Training system that ensures effective competency building among engineers and operators should also rely on a holistic view of all the Veas processes, because fluid/mass flow and heat flow between the different parts of the wastewater treatment plant are heavily interconnected. High/medium-fidelity process model with a virtual replica of the distributed control system will give realistic look-and-feel for the training system. It is possible to build case-based training scenarios with partial models, like data-driven AI models, but these will most likely not be able to replicate the interconnected nature of the WWTP processes.

Table 1. Dynamic simulation modules from process simulator vendors.

Process modeling product	*AspenPlus*	*Apollo*	*GPS-X*	*IndissPlus*	*K-Spice*	*WEST*
Vendor	*Aspentech*	*Aquasight*	*Hatch*	*Corys*	*Kongsberg*	*DHI*
Total modeling score (max 5)	**1,4**	**2,6**	**5**	**4,3**	**2,5**	**3,2**
General process modules	0,4	0,7	1	1	0,8	0,7
Wastewater treatment	0	1	1	1	0,2	1
Sludge treatment and biogas production	0	0,7	1	0,7	0,2	0,9
Biogas refining and liquefaction	0,8	0	1	1	1	0,4
Mechanical processing	0,2	0,2	1	0,6	0,3	0,2

Table 2: Overall assessment of simulator tools, AI tools and APC tools according to project goals. PS=process simulator, CB=case-based

	Process simulator (PS)	DCS simulator	Online simulator	AI tool	APC
Goal1a: Online optimization with manual control	Partly	With PS	YES	CB	CB
Goal1b: Online optimization with closed loop control	No	No	No	No	CB
Goal2: Offline optimization and modification studies	Yes	With PS	No	No	No
Goal 3: Operator training	Yes	With PS	Partly	No	No

5 Conclusions and further work

5.1 Overall assessment of possible digital twin simulator concepts

Possible digital twin simulator concepts fulfilling the goals are:

- offline process simulator with DCS simulator (G2, G3) and online simulator with decision support interface (G1 manual control)
- offline process simulator (G2, G3) and online simulator with decision support interface (G1 manual control)
- offline process simulator (G2, G3) and AI-based decision support system (G1 manual control)
- offline process simulator (G2, G3) and advanced process control (G1 closed-loop control)

In order to fulfill goals 2 and 3, it is recommended to base the digital twin simulator on a high/medium-fidelity process simulator. To add realistic DCS functionalities in the simulator, a DCS simulator should be considered. In order to fulfill goal 1 with manual control, it is recommended to add an online simulator with decision support interface, or an AI tool for the most-profitable cases. In order to fulfill goal1 with closed-loop control, it is recommended to implement advanced process control for most-profitable cases. The overall assessment is further illustrated in Table 2.

5.2 Research and development possibilities

Future work is recommended for development of virtual sensors, process optimization and advanced control for cases given in Section 3.2 using data-driven and model-based algorithms. The algorithms can be effectively tested with a high-fidelity process simulator to quantify the environmental and economical benefits, and to increase the operators trust before implementation in the plant. Possibilities within vocational education research include evaluation of the learning process during the process simulator commissioning and training, and evaluation of the effects to life-long learning, work-place competency development, workplace safety and working environment.

Acknowledgements

The authors would like to thank the RFF Viken for funding the pre-project number 316678. Active participation of Veas system engineers Jonas Pettersen,

Yves Le Naour and Veas process engineers Andrea Hillestad, Anne-Kari Marsteng, Annett Hafslund, Jonas Bråten, Linn Ringdal Steiner, Morten Grøndal and Theresa Liedtke in process review, interviews, vendor presentations and project meetings were essential for successful completion of the project. We greatly acknowledge the inspiring presentations from vendors: ABB Norway, ABB Italy, Aquasight, Aspentech, Corys, DHI, Hatch Hydromantis, Kongsberg, KrügerKaldnes/Veolia, and Statsoft, and hands-on simulator workshops with DHI and Hatch. We would also like to thank ABB Västerås for interesting presentation on the FUDIPO project and ri.se for sharing research insights in digital twin projects.

6 References

ABB. *Process control and automation solutions for water and wastewater industry*, 2021a. https://new.abb.com/control-systems/industry-specific-solutions/water-wastewater-treatment.

ABB. *PUB, Singapore's National Water Agency selects ABB to automate world's largest membrane bioreactor*, 2021b. https://new.abb.com/news/detail/70644/pub-singapores-national-water-agency-selects-abb-to-automate-worlds-largest-membrane-bioreactor.

ABB. *ABB Ability™ System 800xA Simulator - realistic DCS simulation*, 2021c. https://new.abb.com/control-systems/service/customer-support/800xA-services/800xA-training/800xa-simulator.

ABB. *800xA APC - Advanced Process Control*, 2021d. https://new.abb.com/control-systems/system-800xa/800xa-dcs/embedded-systems/advanced-process-control.

Aquasight. *Efficient Wastewater treatment and recovery*, 2021. https://www.aquasight.io/apollo.html.

AspenTech. *Aspen APM - Water & Wastewater*, 2021. https://www.aspentech.com/en/industries/water-and-wastewater.

David B, Cameron, Arild Waaler, and Tiina M Komulainen. Oil and Gas digital twins after twenty years. How can they be made sustainable, maintainable and useful? *The 59th Conference on Simulation and Modelling (SIMS 59)*. Oslo: Linköping University Electronic Press. 9-16, 2018. doi:10.3384/ecp181539.

Corys. *Indiss Plus Dynamic simulation platform*, 2015. https://www.corys.com/en/indiss-plusr.

Erik Dahlquist. *FUDIPO - future directions of production planning and optimized energy and process industries*, 2021. https://fudipo.eu/.

Erik Dahlquist, Eva Nordlander, Eva Thorin, Christian Wallin, and Anders Avelin. Control of waste water treatment combined with irrigation. *11th International Conference on Applied Energy, 2019.* Västerås: Linköping University Electronic Press.

DHI. *TwinPlant - Optimise the performance of your treatment plant on-line*, 2021a. https://www.dhigroup.com/operational-services/twinplant.

DHI. *WEST - WWTP modeling that does it all*, 2021b. https://www.mikepoweredbydhi.com/products/west.

Hatch Hydromantis. *Mantis.AI - A "Digital Twin" for your Treatment Facility*, 2021a. https://www.hydromantis.com/MantisAI.html.

Hatch Hydromantis. *GPS-X - Premium Water & Wastewater Modelling and Simulation Software*, 2021b. https://www.hydromantis.com/GPSX.html.

Hilde Johansen. *DTS VANN Digital tvillingsimulator for vannrenseanlegg.* 04 09, 2021. https://veas.nu/forskning-utvikling/dts-vann.

Zoran Kapelan, Emma Weisbord, and Vladan Babovic. *Artificial Intelligence for the water sector.* London: International Water Association, 16, 2020. https://iwa-network.org/wp-content/uploads/2020/08/IWA_2020_Artificial_Intelligence_SCREEN.pdf.

Tiina M. Komulainen and Ronny Sannerud. Learning transfer through industrial simulator training: Petroleum industry case. *Cogent Education* (Cogent) 5 (1): 1-19, 2018. doi:10.1080/2331186X.2018.1554790.

Kongsberg. *Online operator training simulator - improve operational efficiency*, 2021a. https://www.kongsberg.com/digital/products/process-simulation/online-operator-training-simulator/.

Kongsberg. *Production monitoring system - Full picture production and look-ahead calculations*, 2021b. https://www.kongsberg.com/digital/products/process-simulation/production-monitoring-system/.

Kongsberg. *K-Spice process simulation*, 2021c. https://www.kongsberg.com/digital/products/process-simulation/.

Krüger Kaldnes Veolia. *Hubgrade, Veolia's smart monitoring solution*, 2021. https://www.veolia.com/en/solution/smart-services-smart-monitoring-solutions.

Hanna Molin. *Implementation of digital twins at water resource recovery facilities.* Industrial Electrical Engineering and Automation , Lund University, Lund: Lund University, 21, 2021. Accessed 2021. https://www.iea.lth.se/publications/Reports/LTH-IEA-7276.pdf.

TIBCO. *TIBCO makes it possible to unlock the potential of your real-time data for making faster, smarter decisions*, 2021. https://www.tibco.com/.

Borja Valverde-Pérez, Bruce Johnson, Christoffer Wärff, Douglas Lumley, Elena Torfs, Ingmar Nopens, and Lloyd Townley. *Digital Water - Operational digital twins in the urban water sector: case studies.* London: IWA - international water association, 17, 2021. https://iwa-network.org/wp-content/uploads/2021/03/Digital-Twins.pdf.

Milan Zlatkovikj, Valentina Zaccaria, Ioanna Aslanidou, and Konstantinos G Kyprianidis. Simulation study for comparison of control structures for BFB biomass boiler. *61st SIMS Conference on Simulation and Modelling.* Virtual: Linköping University Electronic Press, pages 107-115, 2020. doi:10.3384/ecp20176107.

Averaging Level Control for Urban Drainage System

Yongjie Wang[1] Finn Aakre Haugen[2]

[1]Faculty of Technology, Natural Sciences and Maritime Sciences. Department of Electrical engineering, Information Technology and Cybernetics. University of South-Eastern Norway (USN), Porsgrunn, Norway.
{Yongjie.Wang, Finn.Haugen}@usn.no

Abstract

In the work, averaging level control using model-based control and estimation algorithm on a buffer tank system is studied. Implementation of Model Predictive Control (MPC) and Proportional-Integral (PI) control together with Kalman filter for state and disturbance estimation show decent benefits and potentials. Results show that acceptable setpoint tracking of water level in the basin under varying inflow can be achieved. MPC precedes PI for smoother pump actions. Python as a popular programming language is adopted and showed potential for real-time control (RTC).

Keywords: Averaging level control, MPC, PI, Extended Kalman filter, Urban Drainage System

1 Introduction

Real-time control (RTC) of Urban Drainage System (UDS) is an important part for different goals in the drainage network.

Literature review (Lund *et al.*, 2018) shows that MPC is an efficient tool for UDS control, and there have been a few projects provided promising results, even though the total number of operational implementations is limited. MPC has been used for controlling different components in UDS, including basin, pipe, junction, reservoir, etc. with linear and/or nonlinear models available internally or externally. More than 60 percent of 113 references addressed using MPC for UDS control from 1983 to 2018 in a few cities globally. Reported applications are mostly found in North America and central European countries. In particular, more active research projects can be found in Span, Canada and Denmark.

Kalman filter is an important data assimilation algorithm in weather forecast to combine numerical methods and observations (Sun *et al.*, 2016).

We present results from a research project, which is about potential use of automatic control on an existing UDS in Norway. Figure 1 illustrates a 42 km long tunnel, which is a main component of the drainage system, transports total volume up to 110 million m^3/year combined sewage overflow (CSO) to one of the largest Water Resource Recovery Facility (WRRF) in Norway named VEAS. An equalization magazine downstream the tunnel works as a buffer tank of the wastewater before it enters the VEAS plant, being processed and discharged into the Oslo Fjord.

Due to the process requirement at VEAS and flow control along the tunnel, the combined drainage must be controlled for different purposes:

- Smoothed inflow to the plant.
- Relatively short retaining time of water inside the tunnel.
- The water flow has certain constraints/ limits, i.e., the tunnel should not be total empty, meanwhile, as less overflows into the Oslo Fjord as possible.
- Dealing with precipitation according to weather data/ forecast.

A laboratory buffer tank in Figure 2 is to be used to emulate the actual basin part in the end of the tunnel. Details of the system is to be presented in Section 2.1.

This work aims at:

1. Mathematical modelling of the buffer tank.
2. Averaging level control using model-based control.
3. Inflow estimation using Extended Kalman filter (EKF).

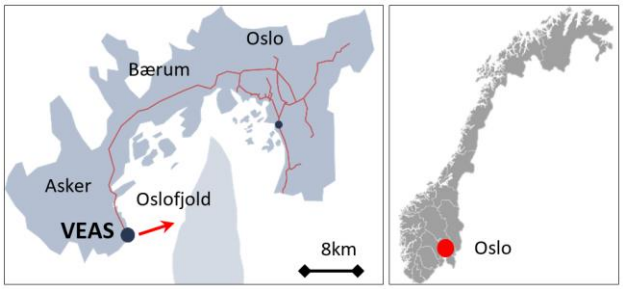

Figure 1. VEAS tunnel for transporting wastewater from urban areas to the treatment plant. (VEAS, 2018)

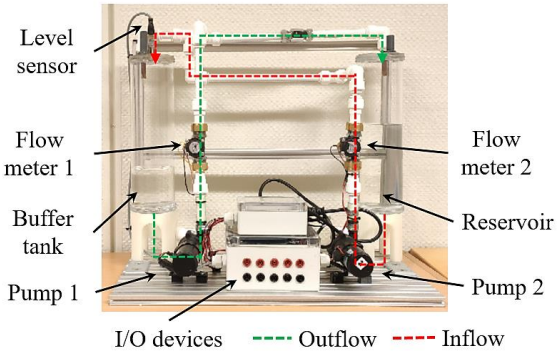

Figure 2. Buffer tank system for averaging level control.

2 Materials and methods

The simulated buffer tank as the testing bench and algorithms for control and estimation are introduced.

2.1 Buffer tank system

Main components of the laboratory buffer tank in Figure 2 consist of:

- Left-hand side: A buffer tank equipped with an ultrasonic level transmitter (Level sensor); a pump (Pump 1) followed by a flowmeter measuring the flowrate of outflow from the buffer tank;
- Right-hand side: A tank as a reservoir of outflow; a pump (Pump 2) to transport simulated varying "precipitation and wastewater" into the buffer tank.
- Bottom center: I/O devices for communication between computer and the buffer tank system. Power supply unit for powering the electronic devices and electrical components. Table 1 lists the main components used in the system.
- Local PI controllers: The flow from each pump is controlled based on readings of inline flow meters.

Table 1. Main components in the buffer tank system for averaging level control.

Component	*Brand/ Model*	*Measurement range*
Pump (x2)	Johnson Pump/ SPXFlow CM30P7-1	<26 L/min
Level sensor	Pepperl Fuchs/ UB300-18GM40-I-V1	35~300 mm
Flow meter (x2)	Sea/ YF-S201	1~30 L/min
I/O device	National Instruments/ USB-6008	AO: 0~5V AI: 0~5V

2.2 Simulation and testing environment

Python (Python.org, 2021) with open libraries for computation and interfaces is used as the simulation and testing environment in this project. The open-access libraries are listed in Table 2.

Table 2. Open-access libraries for averaging level control.

Module	*Function*	*Reference*
Numpy	Matrix and random noise related calculation	(numpy.org, 2021)
Scipy	Optimization	(SciPy.org, 2021b)
nidaqmx	Interface for NI-DAQmx driver	(National Instruments, 2017)
Matplotlib	Data visualization	(Matplotlib.org, 2021)

2.3 Mathematical modelling

The mathematical model of the system can be derived from mass balance of the water tank, given in continuous state-space form by (1):

$$\begin{cases} \dot{h} = \frac{1}{a}(F_{in} - F_{out}) + w \\ y = h + v \end{cases} \quad (1)$$

where,

- h [cm], the process state variable, the water level inside the tank.
- y [cm], the process output, the water level measurement.
- F_{out} [cm^3/s], the control variable of the pump to manipulate the outflow from the buffer tank.
- a [cm^2], the tank cross-sectional area. In this system, a cylindrical tank is installed vertically so $a = \pi D^2/4$ is a constant, with tank inner diameter $D = 8.5$ cm. In reality, the basin cross-sectional area varies with the water level, i.e., $a = H(h)$, where H is a nonlinear function.
- F_{in} [cm^3/s], inflow into the tank, which in the real VEAS case is unknown.
- w and v are process noise and measurement noise with covariances $Q = E[w^2]$ and $R = E[v^2]$, respectively.

2.4 Control and estimation algorithms

MPC and PI as the control algorithms and EKF as the estimation method are introduced in this section.

2.4.1 Averaging level control

The overall purpose of averaging level control is to smooth the inflow in real-time through the buffer tank so that the variation of outflow from the buffer tank is smoothed (Haugen, 2010). Block diagram of such principle is presented in Figure 3.

The level of water inside the buffer tank is to be maintained close to a user-specified value by manipulating Pump 1 based on the level measurement from Level sensor. Situations like full tank and empty tank are restricted.

The pump control signals are limited to be:

$$u \in [u_{min}, u_{max}] \quad (2)$$

where, u_{min} and u_{max} are the allowed minimum and maximum flow, respectively. In addition, to have smooth pump actions as the process required, constraint for Δu is introduced as:

$$\left|\frac{\Delta u_k}{T_s}\right| = \left|\frac{u_k - u_{k-1}}{T_s}\right| \le L \quad (3)$$
$$\Rightarrow u_k \in [u_{k-1} - L \times T_s, u_{k-1} + L \times T_s]$$

where, L=10 cm^3/s^2 is the user-specified limit, T_s=0.2 s is the time step, the pump action u_k is limited to be:

$$u_k \in [u_{k-1} - 2\ \text{cm}^3/\text{s}\ , u_{k-1} + 2\ \text{cm}^3/\text{s}]$$

2.4.2 State and inflow estimation

The water level measurement is the only measurement for feedback control in the buffer tank.

As mentioned, the inflow F_{in} in (1) is a random variable representing the unknown precipitation and wastewater flowing into the buffer tank/ basin. Extended Kalman filter (EKF) is used for the inflow estimation in this work (Simon, 2006). To estimate the inflow, the state vector is augmented with inflow disturbance as is given by (4):

$$\dot{x} = \begin{bmatrix} \dot{h} \\ \dot{F}_{in} \end{bmatrix} = \begin{bmatrix} \frac{1}{a}(F_{in} - F_{out}) \\ 0 \end{bmatrix} + \boldsymbol{w} \qquad (4)$$

where, $\dot{F}_{in}$ [cm^3/(s^2)] is the first order derivative of the inflow, $\dot{F}_{in} = \frac{dF_{in}}{dt}$. The only measurement $y = h$ is used to update the EKF in this work. $\boldsymbol{w} = \begin{bmatrix} w_1 \\ w_2 \end{bmatrix} \sim \mathcal{N}(0, \delta_{\boldsymbol{w}}^2)$ is assumed Gaussian noise vector for the augmented state vector with zero-means and variance matrix $\delta_{\boldsymbol{w}}^2 = \begin{bmatrix} \delta_{w_1}^2 \\ \delta_{w_2}^2 \end{bmatrix}$ to be determined by experiments.

Process distribution covariance:

$$Q = \begin{bmatrix} Q_h & 0 \\ 0 & Q_{F_{in}} \end{bmatrix} = \begin{bmatrix} \delta_{w_1}^2 & 0 \\ 0 & \delta_{w_2}^2 \end{bmatrix}$$

Tuning of the EKF with covariance matrices is done by using:

$$Q_{KF} = Q, R_{KF} = 10 \times R$$

2.4.3 Discretized state-space model

Based on the model (1), discretization of (4) gives the process model in discretized state-space form as in (5):

$$\begin{aligned} x_{k+1} &= Ax_k + Bu_k + w_k \\ y_k &= Cx_k + v_k \end{aligned} \qquad (5)$$

where, the system matrices are

$$A = \begin{bmatrix} 1 & \frac{T_s}{a} \\ 0 & 1 \end{bmatrix}, B = \begin{bmatrix} -\frac{T_s}{a} \\ 0 \end{bmatrix}, C = [1 \quad 0]$$

with state vector $x_k = \begin{bmatrix} h_k \\ F_{in,k} \end{bmatrix}$, control variable $u_k = F_{out,k}$, time step $T_s = 0.2$s, process noise vector $w_k \sim \mathcal{N}(0, Q_k)$, measurement noise $v_k \sim \mathcal{N}(0, R_k)$.

The controllability matrix $\mathcal{C}$ and observability matrix $\mathcal{O}$ can be calculated as:

$$\mathcal{C} = [B \; AB] = \begin{bmatrix} -\frac{T_s}{a} & -\frac{T_s}{a} \\ 0 & 0 \end{bmatrix}$$

$$\mathcal{O} = \begin{bmatrix} C \\ CA \end{bmatrix} = \begin{bmatrix} 1 & 0 \\ 1 & \frac{T_s}{a} \end{bmatrix}$$

Checking the rank of these matrices, giving:
$Rank(\mathcal{C}) = 1$, h is controllable.
$Rank(\mathcal{O}) = 2$, the system is observable.

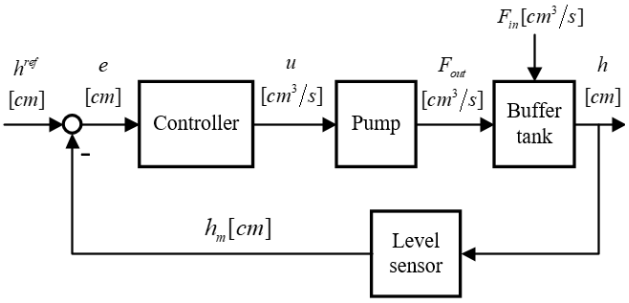

Figure 3. Block diagram of averaging level control.

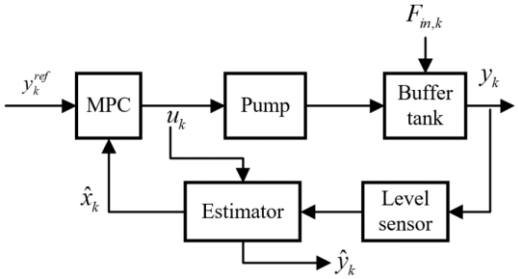

Figure 4. Block diagram of output feedback MPC.

2.4.4 Output feedback MPC

The main idea of implementing MPC is to solve an open-loop optimal control problem over a moving horizon with finite length at each sampling time, starting at the current state. At the next time step, the computation is repeated starting from the new state and over a shifted horizon.

In an output feedback MPC, feedback of states is obtained through an estimator, i.e., EKF, to recursively estimate the states based on the measurement at every time step. The estimated states $\hat{x}_k = \begin{bmatrix} \hat{h}_k \\ \hat{F}_{in,k} \end{bmatrix}$ is sent to MPC, instead of the states measured directly from the process x_k.

Figure 4 shows the block diagram of the principle of output feedback MPC.

For a Single-Input-Single-Output (SISO) MPC, the cost function in this case is defined by (6):

$$\min_{u_k} J = \frac{1}{2}\left\{\sum_{k=1}^{N_p} M \times e_k^2 + \sum_{k=1}^{N_c} N \times \Delta u_k^2\right\} \qquad (6)$$

where,

- u_k is the control signal to be optimized. Control error $\Delta u_k = u_k - u_{k-1}$.
- Constraints on u_k and Δu_k are as in (2) and (3).
- $e_k = y_k^{ref} - y_k$, is the prediction error defined as the difference between the setpoint y_k^{ref} and process output y_k.
- N_p and N_c are the length of prediction horizon ($T_{predict} = N_p \times T_s$) and control horizon ($T_{control} = N_c \times T_s$), respectively.
- $M \in \mathbb{R}^{1\times1}$ and $N \in \mathbb{R}^{1\times1}$ are positive definite weighting matrices for prediction error and control error, respectively.

2.4.5 PI control

PI is a control algorithm widely used in various industries. The PI controller in time domain to be used is of the discretized form (Haugen, 2010) in (7):

$$u_k = u_{k-1} + [u_{0,k} - u_{0,k-1}] + K_p[e_k - e_{k-1}] + \frac{K_p T_s}{T_i} e_k \quad (7)$$

where,

- u_k, controller output at time step t_k with constraints introduced as in (2) and (3).
- u_0, manual control input.
- $e_k = y_k^{ref} - y_k$, where y_k and y_k^{ref} are the measurement and the reference at t_k, respectively.
- K_p, T_i, proportional gain and integral time of the PI controller. Skogestad's method as a model-based tuning method (Haugen, 2010) is used for tuning of these parameters.

3 Results and discussion

In this section, results of averaging level control are presented and discussed.

3.1 Averaging level control using PI

Experiment results are shown in Figure 5 with controller settings: K_p^h= -5.67 (direct actions), T_i^h=20 s.

In general, the water level h showed smooth changes in the meantime of tracking the setpoint h_{sp}, as can be seen from the top plot. The real-time measurement h_m and the estimated signal $\hat{h}$ match each other well, except for slight deviation in the beginning phase (< 10 s) due to a guessed initial value used for the EKF estimator.

PI controller calcucates $F_{out,k}$ based on the estimated inflow $\hat{F}_{in,k}$ for updating the pump actions at each time step. The estimated inflow $\hat{F}_{in,k}$ started to reflect the real data after about 10 s as the middle plot shows. The large deviation of the estimated inflow from the real value in the beginning phase caused delayed controller actions, in addition to the $\Delta u/\Delta t$ constraint for smooth pump actions shown in the bottom plot. Even though the estimation of inflow is noisy, the Pump 1 control actions $u = F_{out}$ slowly resembled the varying inflow, including conditions of two stepwise changes at t=0 s and t=50 s. The Pump 1 control actions fluctuated at low flow rate, i.e., from t=50 s to t=100 s when the inflow is ~20 cm^3/s shown in the middle plot, caused by the nonlinear pump characteristics.

3.2 Averaging level control using MPC

Results of MPC control algorithm are presented in Figure 6, with the following controller settings:

- Optimization method: SLSQP (SciPy.org, 2021a), tolerance = 0.001.
- Constraint/ boundaries: as in (2) and (3).

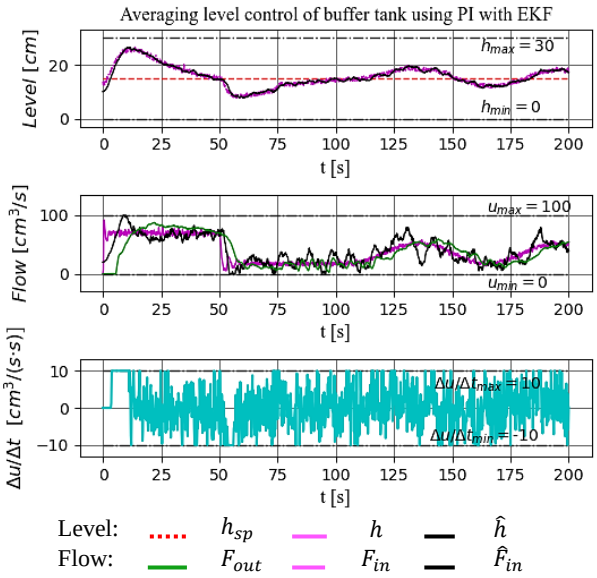

Figure 5. Results of implementing PI for buffer tank averaging level control.

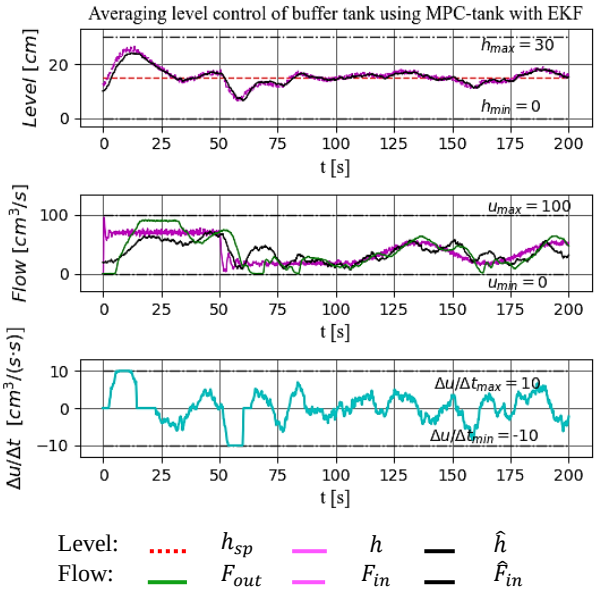

Figure 6. Results of implementing MPC for buffer tank averaging level control.

- $T_{predict} = T_{predict}$ =10 s, and $N_c = N_p$=20.
- Weighting matrices: M = 5, N = 1.
- F_{in}: Estimated inflow at each time step $F_{in,k}$ is used for prediction and cost function calculation, meaning that the inflow is a "fixed" value for the entire prediction horizon N_p.

Comparing the results from MPC to from PI control, one can firstly notice that the MPC outperforms PI with "smoother" F_{out} (middle plot) and much less varied outflow $\Delta u/\Delta t$ (bottom plot). This is because of the moving horizon and optimization algorithm used for optimal control in the prediction horizon, given the same constraints of on F_{out} and $\Delta u/\Delta t$ as for PI controller.

It is worth noting that, with smoother outflow, more overall setpoint deviation of the water level should have

been observed since the volume would have varied more to buffer against inflow. However, from the results, the differences are noticeable but not obvious, comparing the two "level" plots in Figure 5 and Figure 6.

Estimation of both water level $\hat{h}$ and the inflow $\hat{F}_{in}$ are about the same overall performance as in PI controlled case. However, the less noisy control actions led to less noisy $\hat{F}_{in}$.

Both PI controller and MPC can be tuned for less tracking error suffering more abrupt control action changes or more varied water level with less fluctuated pump actions.

3.3 "Time" issue in real-time control

One problem of using Python for real-time control (RTC) is how to ensure the time step T_s during the computation, since Python is not designed for real-time purpose and the computation speed is dependent on many factors.

Figure 7 presents the differences between computational load for the averaging level control using MPC and PI, given computer configurations in Table 3. The two upper plots are the cycle time for each cycle (totally 200 s / 0.2 s = 1000 cycles). The lower histogram plots show the distribution of the cycle time for both control algorithms, in which the 1000 cycles are binned into 40 groups with the largest group marked red.

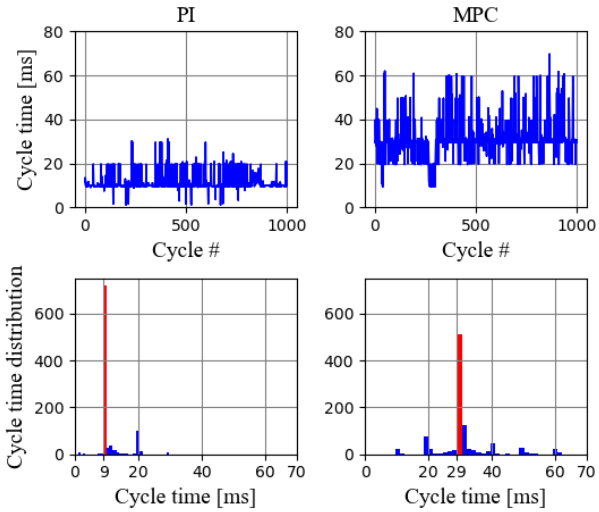

Figure 7. Comparison of computation load of PI and MPC for averaging level control.

Table 3. Computer configurations.

Hardware	Processor: Intel(R) Core(TM) i7-8750H @ 2.20GHz Installed RAM: 32.0 GB
Operating system	Windows 10 Enterprise 64-bit Version 20H2 OS build 19042.985

The computational load is relatively less heavy using PI control than using MPC. In the experiments based on PI control, more than 70% cycles have about 9~10 ms computation time (not the "average" computation time) and maximum cycle time is ~31 ms. For MPC case, more than 50% cycles have 29~31 ms running time and maximum is ~70 ms, both are much higher than using PI control. As can be seen from the histogram, the cycle time distribution for MPC is much "wider", meaning the cycle time varies a lot from loop to loop. This is because MPC is an optimization-based algorithm. The computation depends highly on the problem construction, optimization method, and solver setup, etc. A few other factors can also influence the cycle time including file I/O, hardware communication and setup, computer configurations, etc.

In this work, Python built-in "time" module is used with the following method to handle the issue:

1. Define a time step/ cycle time, i.e., T_s = 0.2 s. The value has to be far greater than the largest actual cycle time, which can be determined from experiments.
2. For each loop:
   a. Count the actual cycle time $T_{cycle,k}$ [s] of each loop k.
   b. "Wait" for $T_{wait,k} = T_s - T_{cycle,k}$ [s] at the end of each loop. In Python, the built-in "time" module can be used as:
      `time.sleep(T_wait_k)`
   c. If for some reason $T_{wait,k} \geq T_s$, let $T_{wait,k} = 0$.
   d. Pump control signal u_k is maintained until next time step.

To speed up the simulation/ shorten the cycle time, some options are recommended: Cython (Cython.org, 2020), multi-threading and multi-processing (Python.org, 2021), use well-accepted open libraries and proper setup of modules, separate file I/O and computational tasks, etc.

4 Conclusions and future development

The work presents a demonstration of using model-based control algorithms for averaging level control of urban drainage system, to be specific, a wastewater equalization magazine using a small-scale buffer tank. The conclusions are:

- Averaging level control using model-based control algorithms is successful, with unknown inflow.
- MPC is based on the system model and optimization solver. PI controller does not require the system model to compute the control action. With proper settings, MPC can achieve smoother control actions than PI control.
- The process can benefit from both PI and MPC algorithms for averaging level control, given constrained control signal with upper/ lower limits

($[u_{max}, u_{min}]$) and allowed maximum change of flow rate ($|\Delta u/\Delta t|$).

- For the buffer tank system, the inflow is observable so that it can be estimated as an augmented state with water level as the only measurement. EKF is easy to implement for the estimation but some effort is required for tuning.
- Python is a promising option for programming for real-time control. As one can see, a number of open libraries are available for the purpose.

To improve the MPC performance in the future, instead of using a "fixed" F_{in} for the entire prediction horizon, a "forecast horizon" N_f can be used to obtain a sequence of "future inflow" for the MPC optimization, i.e., $\left[F_{in,t_k}, F_{in,t_{k+1}}, \dots, F_{in,t_{k+N_f}}\right]$. Choosing of N_f is based on the information available and computation resource. $N_f \geq N_p$ is suggested so that the inflow information is available throughout the prediction horizon N_p for the optimizer. Different algorithms for estimating/ forecasting inflow can be tested, i.e., Particle Filter (PF), Ensemble Kalman filter (EnKF), Moving Horizon Estimation (MHE), neural network, etc. Trade-off between extra computational load and performance should be taken into consideration.

References

Finn A. Haugen. *Basic DYNAMICS and CONTROL*. TechTeach. 2010.

N. S. V. Lund, A. K. V. Falk, M. Borup, H. Madsen, and Peter S. Mikkelsen. Model Predictive Control of Urban Drainage Systems: A Review and Perspective towards Smart Real-Time Water Management. *Critical Reviews in Environmental Science and Technology* 48 (3):279–339. 2018. doi: 10.1080/10643389.2018.1455484.

Dan Simon. *Optimal State Estimation: Kalman, H Infinity, and Nonlinear Approaches*. John Wiley & Sons. 2006.

L. Sun, O. Seidou, I. Nistor, and K. Liu. Review of the Kalman-Type Hydrological Data Assimilation. *Hydrological Sciences Journal* 61 (13):2348–66. 2016. doi: 10.1080/02626667.2015.1127376.

National Instruments. *NI-DAQmx Python API Documentation*. Release 0.5.0. 2017.

VEAS.nu. From Sewage Treatment Plant to Biorefinery - Brochure in English with Key Numbers for 2018. 2018. https://www.veas.nu/global/upload/rBPPQ/files/5155-VEAS-profileringsbrosjyre-A5-ENG-v1-oppslag.pdf.

Cython.org. Cython 3.0a0 Documentation. 2020. https://cython.readthedocs.io/en/latest/. numpy.org. NumPy User Guide. 2021. https://numpy.org/doc/stable/user/index.html.

Matplotlib.org. Matplotlib: Python Plotting - Matplotlib 3.4.2 Documentation. 2021. https://matplotlib.org/.

Python.org. Python 3.9.5 Documentation. 2021. https://docs.python.org/3.9/.

SciPy.org. Minimize(Method='SLSQP') - SciPy v1.7.0 Manual. 2021a. https://docs.scipy.org/doc/scipy/reference/optimize.minimize-slsqp.html#optimize-minimize-slsqp.

SciPy.org. SciPy v1.4.1 Reference Guide. 2021b. https://docs.scipy.org/doc/scipy/reference/generated/scipy.optimize.minimize.html#rdd2e1855725e-12.

Moving Bed Biofilm Process in Activated Sludge Model 1 for Reject Water Treatment

Vasan Sivalingam Gamunu Samarakoon Carlos Dinamarca

Department of Process, Energy and Environmental Technology, University of South-Eastern Norway, Norway.
{vasan.sivalingam, Gamunu.arachchige, carlos.dinamarca}@usn.no

Abstract

A moving bed biofilm (MBB) process was modelled in AQUASIM using the standard activated sludge model 1 (ASM1) as a baseline. The model was controlled against experimental data from a pilot Hybrid Vertical Anaerobic Biofilm (HyVAB) reactor installed at Knarrdalstrand wastewater treatment plant, Porsgrunn, Norway. High ammonium concentration removal from reject water was studied by applying different aeration schemes at the plant and the modelling tool. Results show that the standard ASM1 model was poor to fit experimental data. Simulation results evidenced missing biochemical mechanisms related to anaerobic ammonium oxidation (Anammox) and short cut nitrogen removal processes. However, the essential simulation outputs are biofilm thickness, substrates concentration variation, and biomass distribution, partially validated with experimental results. The model, therefore, helped to realise the nature of the bioprocess observed at the pilot reactor.

Keywords: Moving bed biofilm reactor, Reject water, Activated sludge model, Intermittent aeration, AQUASIM

1 Introduction

Reject water originated from digested sludge dewatering is usually rich in ammonium (Guo et al., 2010). The untreated discharge causes many environmental and health hazards (i.e., eutrophication and blue baby syndrome) that strictly requires proper treatment. Mixing reject water into the mainstream wastewater line is a common practice (Sivalingam et al., 2019). However, the higher nutrient load of reject water causes process instabilities. Reject water requires, therefore, an additional treatment before mixing with the mainstream treatment process.

A pilot Hybrid Vertical Anaerobic Biofilm (HyVAB) reactor was installed in the reject water line (Figure 1). Intermittent aeration was implemented into the aerobic chamber to achieve simultaneous nitrification and denitrification. The intermittent aeration strategy has several advantages compared to the conventional activated sludge process; thus, less aeration energy requirement and a single rector setup are sufficient to achieve aerobic and anoxic treatments (Di Bella and Mannina, 2020).

Authors have earlier investigated different intermittent aeration patterns to remove higher ammonium concentrations from Knarrdalstrand wastewater treatment plant (KWWTP) reject water (Sivalingam et al., 2020). However, experimentally examining various aeration schemes is tedious and resource-intensive. Therefore, a theoretical study was carried out by modelling and simulation.

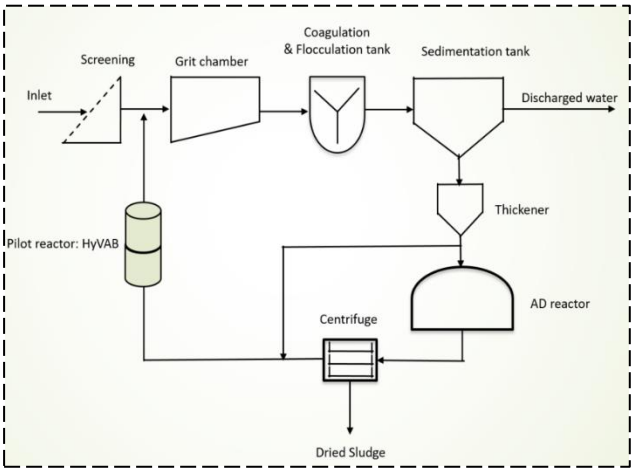

Figure 1. HyVAB pilot reactor integration at KWWTP.

This research develops a moving bed biofilm (MBB) model to study the impact of intermittent aeration on the HyVAB pilot reactor, treating reject water. The standard activated sludge model 1 (ASM1) is applied to the MBB compartment in the HyVAB reactor modelled by AQUASIM software. We present the preliminary simulation results of the 1D multi-substrate and multispecies biofilm model to give an overview of the possible process parameters examination when integrating the MBB process and ASM1 model into AQUASIM.

1.1 Activated Sludge Model 1

The ASM1 was introduced in 1983 and has been extensively studied (Nelson and Sidhu, 2009); it was developed futher to investigate the activated sludge organic and nitrogen removal process (Van Loosdrecht et al., 2015). Only a few key elements are briefly presented here to ensure the proper reading flow of this article.

In ASM1, oxygen and nitrate are the primary electron acceptors. The organic matters are classified into biodegradable chemical oxygen demand (COD), non-biodegradable COD, and active biomass. The active biomass has two subsets pertaining to heterotrophic and autotrophic organisms. The ASM1 model consists of 13 state variables. Some of the essential variables are: Active heterotrophic and autotrophic biomass, alkalinity, ammonium, nitrate, soluble and biodegradable organics, and dissolved oxygen.

The ASM1 consists nitrification and denitrification as conventional single-step reactions, converting ammonia to nitrate (nitrification) and nitrate to nitrogen gas (denitrification) (Henze et al., 2000). However the intermittent aeration facilitates conventional, short cut and anaerobic ammonium oxidative pathways to remove nitrogen from the wastewater (Miao et al., 2018)

1.2 Moving Bed Biofilm Process

Moving bed biofilm process is a Norwegian technology specially designed for nutrient removal from wastewater (Rusten et al., 1997). It is an attractive solution for high strength wastewater treatment (Sivalingam et al., 2020b) due to stable biofilm growth into a protected surface area, which is more tolerant to the process variance.

The biofilm consists of different layers of mixed culture microorganism clusters, referred to as attached growth. The diversity of microorganisms depends on nutrient and oxygen gradients along with the biofilm thickness (Wang et al., 2019). For instance, in an aerated system, the outer layer of the biofilm is rich in aerobic culture. In contrast, the inner layers favour anoxic growth, and the layers near to the substratum contain anaerobic cultures. The different cultures perform specific biochemical reactions, such as nitrification occurs at the outer layer and denitrification happens at the inner layers. This is a key benefit of using moving beds (bio carriers) in this pilot study, facilitating biofilm growth.

2 Material and methods

The HyVAB pilot reactor has two compartments, the anaerobic part is at the bottom, and the aerobic part is at the top. The purpose of the anaerobic part is to recover energy as biogas. The anaerobic effluent enters to the aerobic compartment to undergo a nutrient removal process, especially ammonium removal. The aerobic part contains BWT15® type carriers (Biowater Technology AS, Tønsberg, Norway). The sketch of the reactor is presented in Figure 2, adapted from (Sivalingam et al., 2020a).

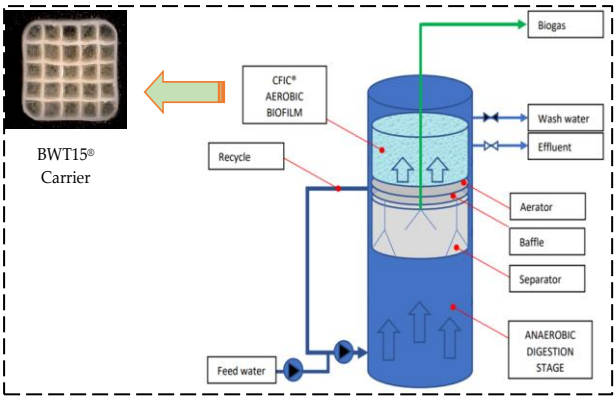

Figure 2. HyVAB reactor and matured moving bed bio carrier.

2.1 Reactor operation and experiments

Centrifuged effluent from the KWWTP anaerobic digestor was used as the reject water feed to the HyVAB reactor. The hydraulic retention time was one day, and the operational temperature was 30±2 °C. Two different intermittent aeration schemes were tested, i.e., (1) 5 min on/ 15 min off (20 min. Aeration cycle); (2) 3 min on/4 min off (7 min aeration cycle). The 2nd aeration pattern achieved 50% ammonium removal. The complete experimental study is presented in (Sivalingam et al., 2020a). The 2nd aeration scheme is used here to compare the simulation results.

2.2 Model Development

Since ammonium removal is our primary concern in reject water treatment, only the aerobic part of the pilot reactor (Biofilm compartment) and the ASM1 are modelled. The activated sludge process was incorporated into the biofilm compartment (attached growth).

The biofilm compartment in AQUASIM has been modified to comply with the biofilm part of the pilot reactor. The following assumptions are adapted from a similar study (Wanner and Morgenroth, 2004): (1) The type of reactor is confined; (2) The pore volume consists only a liquid phase and dissolved solids; (3) The biofilm matrix is in rigid form, and the volume can be changed only due to microbial activities; (4) The surface detachment velocity was assumed as a global value of 0.5*UF, where UF is the velocity by which the biofilm surface displaced due to the production and decay of microbial mass in the biofilm; (5) Biofilm surface area is constant at 10 m^2. The porosity rate was considered zero by assuming that the fraction of pore water volume of the biofilm is constant.

Nitrification, denitrification, aeration, autotrophic inactivation, heterotrophic inactivation, and aerobic heterotrophic growth are the main processes taken into account in the biofilm compartment. The complete process kinetics and stoichiometry coefficients are adapted from (Henze et al., 2000).

2.3 Intermittent Aeration implementation

Two approaches were performed to implement the intermittent aeration into this model. Firstly the aeration process activated in the biofilm compartment when aeration is 'on' and deactivated when aeration is 'off'. After activation and deactivation of the aeration process, the model was simulated with appropriate on/off time via the start/continue option from the simulation tool. It was challenging to simulate the model for a long time, like 250 days for a concise aeration cycle.

Therefore, in approach an aeration switch was introduced. First, a formula variable called 'AerSwitch' was created. The expression was defined as a sinusoidal function 207*(sin(500*t) ^2). This expression was determined by trial and error to match with experimentally calculated gas-liquid mass transfer coefficient (K_La). The desired 3 min on/off cycle was achieved by increasing the omega terms in the sine function (ω of sin ωt). Then 'AerSwitch' was assigned as the expression for K_La.

Approach 2 provides an equal time interval for both the 'on' and 'off' cycle because of the sine function. Therefore, if we indeed need more accurate cycles, the 'AerSwitch' function should be fine-tuned. However, in our experimental case, on/off cycle was 3 min on and 4 min off. Therefore 3 min on/off was considered as a reasonable number for the simulations.

The initial conditions and the input values derived from the experimental study (Sivalingam et al., 2020a) are presented in Tables 1 and 2. Other required parameters are adapted from (Rauch et al., 1999; Mannina et al., 2011; Reichert, 1998), listed in Table 3.

Table 1. Initial conditions for the model.

Variable	*Description*	*Initial values*	*Units*
L_f	Biofilm thickness	1e-005	m
X_{het}	Heterotrophs	0.1*rho	mgL^{-1}
X_{aut}	Autotrophs	0.1*rho	mgL^{-1}
C_{HCO_3}	Alkalinity	1e-005	mgL^{-1}
C_{NH_4}	Ammonium	1e-005	mgL^{-1}
C_{NO_3}	Nitrate	1e-005	mgL^{-1}
$C_{S_{Org}}$	Soluble organics	1e-005	mgL^{-1}
C_{O_2}	Dissolved oxygen	1e-005	mgL^{-1}

Table 2. Model input parameters.

Variable	*Description*	*Inputs*	*Units*
Q_{in}	In flow rate	0.065	m^3d^{-1}
X_{het}	Heterotrophs	0	mgL^{-1}
X_{aut}	Autotrophs	0	mgL^{-1}
C_{HCO_3}	Alkalinity	1952	mgL^{-1}
C_{NH_4}	Ammonium	450	mgL^{-1}
$C_{S_{Org}}$	Soluble organics	100	mgL^{-1}
C_{O_2}	Dissolved oxygen	0.5	mgL^{-1}

3 Results and Discussion

Figure 3 shows the biofilm propagation. On day 75, the biofilm thickness (L_f) reached steady-state at 1.16 mm. The biofilm contains both autotrophic (X_{Aut}) and heterotrophic (X_{het}) biomass. The distribution along the biofilm matrix is presented in Figure 4. Heterotrophic growth dominates the biomass composition. At substratum, heterotrophic biomass concentration decreases with time, the opposite happens for autotrophic biomass concentration. This could be due to the diffusion limitation of substrates.

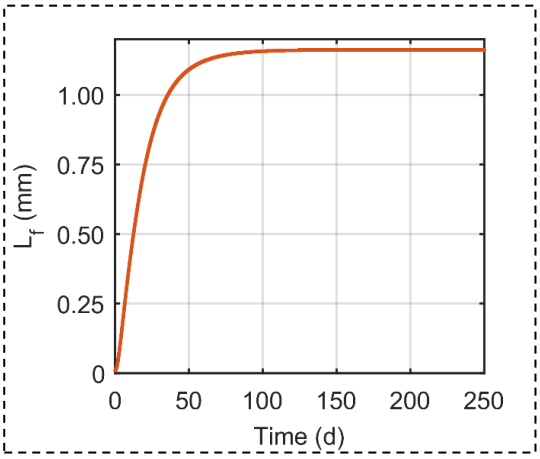

Figure 3. Biofilm thickness progression.

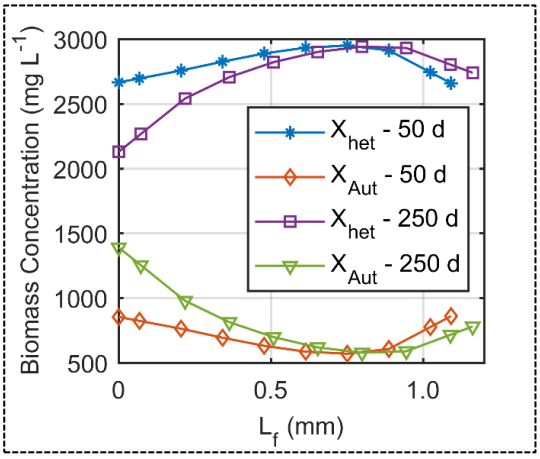

Figure 4. Autotrophic and heterotrophic bacterial distribution in the biofilm matrix on 50th and 250th days.

Table 3. Model parameters.

Symbol	*Parameter description*	*Values*	*Units*	*Reference*
DS_{O2}	Diffusion coefficient of oxygen	2.1	cm^2d^{-1}	(Rauch et al., 1999)
DS_{Org}	Diffusion coefficient of organic matter	0.58	cm^2d^{-1}	(Rauch et al., 1999)
DS_{NO_3}	Diffusion coefficient of nitrate nitrogen	2	cm^2d^{-1}	(Rauch et al., 1999)
DS_{NH_4}	Diffusion coefficient of ammonium nitrogen	1.8	cm^2d^{-1}	(Rauch et al., 1999)
DS_{HCO3}	Diffusion coefficient of alkalinity	2	cm^2d^{-1}	(Reichert, 1998)
DS_{N_2}	Diffusion coefficient of nitrogen gas	1.9	cm^2d^{-1}	(Reichert, 1998)
DX	Diffusion coefficient of biomass	1e-7	cm^2d^{-1}	(Reichert, 1998)
μ_{Het} and μ_{Anox}	Maximum growth rate heterotrophs	2.8	d^{-1}	(Mannina et al., 2011; Rauch et al., 1999)
μ_{Aut}	Maximum growth rate autotrophs	1.0	d^{-1}	(Mannina et al., 2011)
Y_{het}	Heterotrophic yield coefficient	0.65	$\frac{mgCOD}{mgCOD}$	(Rauch et al., 1999)
Y_{Aut}	Autotrophic yield coefficient	0.22	$\frac{mgCOD}{mgNH_4}$	(Mannina et al., 2011)
b_{het}	Heterotrophic decay rate	0.1	d^{-1}	(Mannina et al., 2011)
b_{Aut}	Autotrophic decay rate	0.06	d^{-1}	(Mannina et al., 2011)
η_{het}	Coefficient for anoxic heterotrophic growth	0.80	-	(Mannina et al., 2011)
iXB_{aut}	Ammonia fraction in biomass	0.08	$\frac{mgN}{mgCOD}$	(Mannina et al., 2011)
iXP_{aut}	Ammonia fraction in particulate fraction	0.06	$\frac{mgN}{mgCOD}$	(Mannina et al., 2011)
K_{NH}	Saturation coefficient for ammonia	1	mgL^{-1}	(Mannina et al., 2011)
$K_{S_{Org}}$	Saturation coefficient for organic matter	20	mgL^{-1}	(Mannina et al., 2011)
K_{NO_3}	Saturation coefficient for nitrate	0.5	mgL^{-1}	(Mannina et al., 2011)
K_{O_2}	Saturation coefficient for oxygen	0.2	mgL^{-1}	(Mannina et al., 2011)
$K_{O_{2het}}$	Saturation coefficient for oxygen heterotrophic organism	0.2	mgL^{-1}	(Mannina et al., 2011)
K_La	Oxygen transfer coefficient	207	d^{-1}	Calculated

The X_{Aut} and X_{het} biomass distribution in the biofilm bulk profiles are depicted in Figure 5. In the beginning, the X_{het} reached 30 mg L^{-1}, which is six times higher than $X_{Aut.}$ However, after 50 days of operation, it levelled at 10 mg L^{-1}, while the X_{Aut} remained stable at around 5 mg L^{-1}. The lack of soluble organics is the reason for such a remarkable reduction in X_{het}.

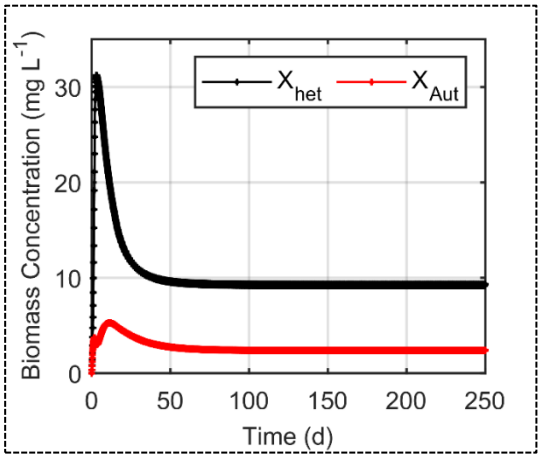

Figure 5. Autotrophic and heterotrophic biomass distribution in the biofilm bulk.

Figure 6 illustrates the dissolved oxygen (DO) concentration during the changes in aeration cycles. The on/off aeration scheme facilitates the nitrification and denitrification process, resulting in 13% ammonium removal. In addition, nitrogen gas evolution was observed. Small amounts of nitrate were also produced. All these nitrogen species concentration profiles are shown in Figure 7.

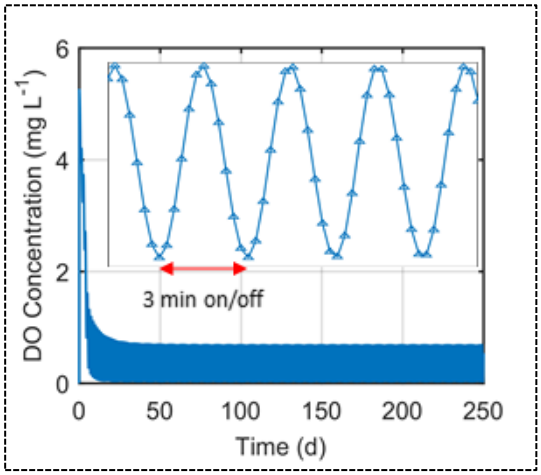

Figure 6. On/off aeration scheme enlarged version.

The DO concentration along the biofilm thickness was investigated when the aeration was switched 'on' (aerobic) and switched 'off' (anoxic). The simulation results are depicted in Figure 8. Oxygen concentration (along with biofilm thickness) is higher when aeration is "on" than where aeration is "off". The significant change in the aeration profile proves that DO concentration is the rate-limiting factor for the nitrogen removal process. However, the DO difference in those two conditions is less significant at the substratum, while a notable difference is in the outermost layer.

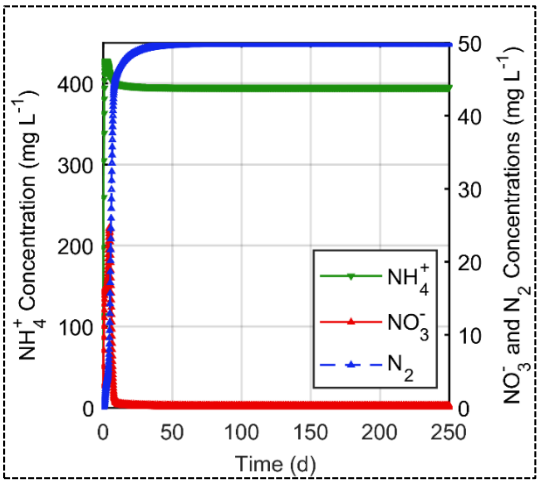

Figure 7. Nitrogen species variation in the bulk liquid.

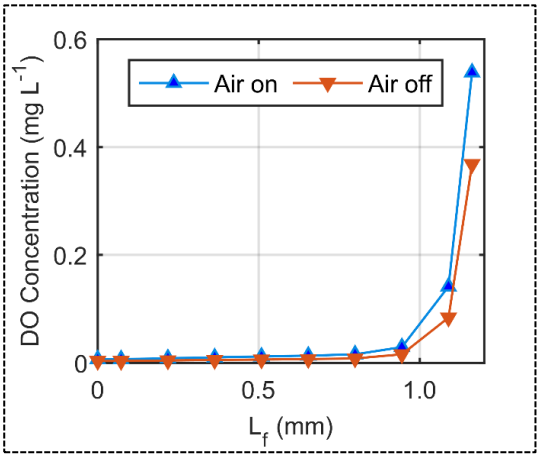

Figure 8. DO concentration profiles along with the biofilm thickness at aerobic and anoxic conditions.

Ammonium, nitrate, soluble organics, and nitrogen gas concentration changes along with the biofilm matrix at 250th day are presented in Figure 9. The ammonium, nitrate and soluble organic concentration trends have corresponded to each other; however, the gradient differs due to the different diffusion coefficients. The nitrogen gas concentration remains stable at 50 mg L^{-1} throughout the entire biofilm matrix. It is reasonable because of very sparingly soluble behaviour.

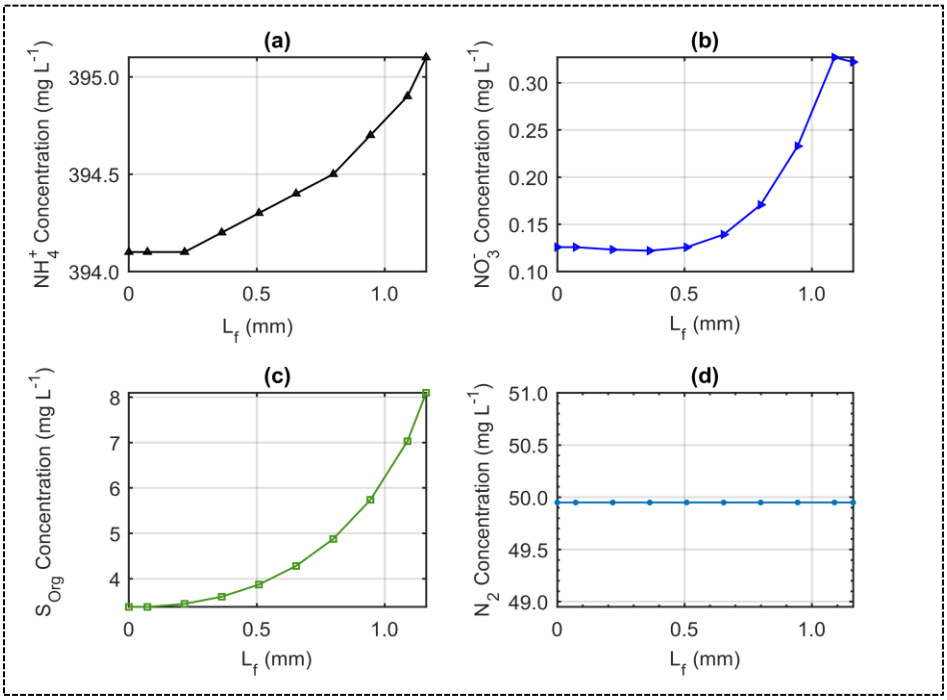

Figure 9. Substrate concentration profiles along the biofilm matrix at 250th day. (a) Ammonium, (b) Nitrate, (c) Soluble organics and (d) Nitrogen gas.

4 Conclusion and Further Development

The MBB model with activated sludge processes was successfully implemented in AQUASIM software. The simulation results illustrate that the model can study the impact of intermittent aeration on biofilm thickness, biomass and substrate distribution within the biofilm, biomass and substrates concentration in the bulk liquid.

The simulation results showed lower ammonium removal efficiency (13%) than the experimentally achieved efficiency (50%) from the pilot reactor. This is because the ASM1 does not include the possible shortcut and anaerobic ammonium oxidative pathways that occur in the experiment. Therefore, the model requires further development by integrating all possible ammonium nitrogen removal pathways to match the experimental results.

Acknowledgements

The authors would like to thank Knarrdalstrand Wastewater Treatment Plant, Porsgrunn, Norway and Biowater Technology AS, Tønsberg, Norway, for their support throughout the experimental study.

References

G. Di Bella and G. Mannina. Intermittent Aeration in a Hybrid Moving Bed Biofilm Reactor for Carbon and Nutrient Biological Removal. *Water*, 12 (2), 2020. doi: 10.3390/w12020492.

C. H. Guo, V. Stabnikov, and V. Ivanov. The removal of nitrogen and phosphorus from reject water of municipal wastewater treatment plant using ferric and nitrate bioreductions. *Bioresour. Technol*, 101(11): 3992–3999, 2010.

M. Henze, W. Gujer, T. Mino, and M. C. M. van Loosdrecht. *Activated sludge models ASM1, ASM2, ASM2d and ASM3*. IWA Publishing, 2000.

G. Mannina, D. D. Trapani, G. Viviani, and H. Ødegaard. Modelling and dynamic simulation of hybrid moving bed biofilm reactors: Model concepts and application to a pilot plant. *Biochem. Eng. J*, 56 (1): 23–36, 2011. doi: 10.1016/j.bej.2011.04.013.

Y. Miao, Y. Ping, L. Zhang, B. Li, X. Li, L.Wu, and S. Wang. Partial nitrification-anammox (PNA) treating sewage with intermittent aeration mode-Effect of influent C/N ratios. *Chem. Eng. J*, 334: 664–672, 2018. doi: 10.1016/j.cej.2017.10.072.

M. I. Nelson and H. S. Sidhu. Analysis of the activated sludge model 1. *Appl. Math. Lett*, 22(5): 629–635, 2009. doi: 10.1016/j.aml.2008.05.003.

W. Rauch, H. Vanhooren, and P. Vanrolleghem. A simplified mixed-culture biofilm model. *Water Res*, 33(9), 1999. doi: 10.1016/S0043-1354(98)00415-1.

P. Reichert. *Aquasim 2.0 User manual*. Swiss Federal Institute for Environmental Science and Technology, Switzerland, 1998.

B. Rusten, O. Kolkinn, and H. Odegaard. Moving bed biofilm reactors and chemical precipitation for high efficiency treatment of wastewater from small communities. *Water Sci. Technol*, 35(6): 71–79, 1997. doi: 10.1016/S0273-1223(97)00097-8.

V. Sivalingam. "*Nitrogen transformation in biofilm*". University of South-Eastern Norway, Porsgrunn, 2019.

V. Sivalingam, C. Dinamarca, E. Janka, S. Kukankov, S. Wang, and R. Bakke. Effect of Intermittent Aeration in a Hybrid Vertical Anaerobic Biofilm Reactor (HyVAB) for Reject Water Treatment. *Water*, 12(4), 2020a. doi: 10.3390/w12041151.

V. Sivalingam, O. Ibrahim, S. Kukankov, B. Omodara, E. Janka, S. Wang, C. Dinamarca, H. Haugen, and R. Bakke. Chemical equilibrium model to investigate scaling in moving bed biofilm reactors (MBBR). In *Proceedings of The 60th SIMS Conference on Simulation and Modelling SIMS 2019, 12-16 August*, 2020, *Västerås, Sweden*, pages 139–144, 2020b. doi:10.3384/ecp20170139.

M. C. M. Van Loosdrecht, C. M. Lopez-Vazquez, S. C. F. Meijer, C. M. Hooijmans, and D. Brdjanovic. Twenty-five years of ASM1: past, present and future of wastewater treatment modelling. *J. Hydroinformatics*, 17(5): 697–718, 2015. doi: 10.2166/hydro.2015.006.

S. Wang, S. Parajuli, V. Sivalingam, and R. Bakke. Biofilm in Moving Bed Biofilm Process for Wastewater Treatment. *Bact. Biofilms*, 2019. doi: 10.5772/intechopen.88520.

O. Wanner and E. Morgenroth. Biofilm modeling with AQUASIM. *Water Sci. Technol*, 49(11–12): 137-144, 2004. doi.org/10.2166/wst.2004.0824.

Detectability of Fault Signatures in a Wastewater Treatment Process

Heidi L. Marais[1] Valentina Zaccaria[1] Jean-Paul A. Ivan[2] Eva Nordlander[1]

[1]Future Energy Center, Mälardalen University, Sweden, {heidi.marais, valentina.zaccaria, eva.nordlander}@mdh.se
[2]Center for Applied Autonomous Sensor Systems, Örebro University, Sweden jean-paul.ivan@oru.se

Abstract

In a wastewater treatment plant reliable fault detection is an integral component of process supervision and ensuring safe operation of the process. Detecting and isolating process faults requires that sensors in the process can be used to uniquely identify such faults. However, sensors in the wastewater treatment process operate in hostile environments and often require expensive equipment and maintenance. This work addresses this problem by identifying a minimal set of sensors which can detect and isolate these faults in the Benchmark Simulation Model No. 1. Residual-based fault signatures are used to determine this sensor set using a graph-based approach; these fault signatures can be used in future work developing fault detection methods. It is recommended that further work investigate what sizes of faults are critical to detect based on their potential effects on the process, as well as ways to select an optimal sensor set from multiple valid configurations.
Keywords: fault detection, wastewater treatment, detectability, isolation

1 Introduction

Fault detection (FD) is an important part of process supervision; monitoring the state of the process, identifying undesirable states, and initiating action to prevent negative consequences (Isermann, 2006, pg. 13). The safe and reliable operation of a process depends on the process supervision, this is no less the case in a wastewater treatment plant (WWTP) where poor performance can result in the release of untreated wastewater subsequently endangering human health and the environment (Ryder, 2017). The successful implementation of automatic control also hinges on the quality of process supervision. Control and automation in WWTPs has historically lagged behind other industrial processes, but is becoming increasingly important as effluent standards have become more strict and processes move from wastewater treatment to recovery (Olsson et al., 2005).

In a WWTP there are numerous types of faults that can occur, such as instrument faults and process faults. Specific process faults that have been the focus of FD research include: a decrease in the growth rate of autotrophic bacteria causing a decrease in nitrification (Choi and Lee, 2004; Lee et al., 2003, 2004b,a; Yoo and Lee, 2006), a decrease in the growth rate of heterotrophic bacteria (toxicity fault) (Aguado and Rosen, 2008; Borowa et al., 2007; Garcia-Alvarez et al., 2009; Yin et al., 2017; Yu, 2012), a combined decrease in growth rate and increase in death rate of heterotrophic bacteria (inhabitation fault) (Aguado and Rosen, 2008; Garcia-Alvarez et al., 2009; Yin et al., 2017), a decrease in ammonification rate (Yu, 2012), and a decrease in the settling velocity to simulate a bulking fault (Aguado and Rosen, 2008; Choi and Lee, 2004; Garcia-Alvarez et al., 2009; Yoo and Lee, 2006).

Each of these faults possess a fault signature based on how they affect the measurable states. These fault signatures are independent of any particular FD strategy (Ding, 2013, pg. 52), and knowledge of their detectability and isolability can be beneficial when quantifying the performance of different FD methods (Basseville, 2001).

Sensors and measurement devices are pivotal to FD as they provide information about the state of the process. However, the hostile environment in a WWTP commonly places sensors at risk of, for example, clogging and biofouling (Li et al., 2017). This can result in high maintenance costs due to required cleaning and calibration. Additionally, the sensors themselves are costly, can disturb the process, and in some cases are unavailable. Due to this, it is important to strategically select and place sensors in order to obtain as much information as possible while minimising the costs associated with monitoring.

There are numerous ways to approach the problem of sensor placement, such as considering observability and redundancy within the process (Villez et al., 2016, 2020), or considering fault detectability and isolability (Krysander and Frisk, 2008; Jung et al., 2020). In this work we consider the latter approach, focusing also on the determination of fault signatures for common process faults within a WWTP.

This type of analysis has been done extensively in other fields. For example, in gas turbines analysing fault signatures based on sensitivity (Chen et al., 2015), correlation (Stenfelt et al., 2019), and measurement uncertainty (Chen et al., 2015; Zaccaria et al., 2020) are all common procedures to determine a sensor set. However, a correlation based method is not easily applicable to a WWTP. WWTPs consist of process units in series, with

similar biochemical mechanisms occurring in each unit. This structure inherently leads to high correlation between measurements in successive units and renders futile the use of correlation analysis for sensor selection.

An alternative approach is to utilise the structural information of the process model. In this method variables and equations are represented as separate node sets in a bipartite graph and a graph theoretic approach is used to select a minimal sensor set (Krysander and Frisk, 2008). This approach yields 'best case' results for an ideal system. Using a distinguishability criterion that facilitates the specification of thresholds on the probability of false alarms and missed detections the method can be extended to a more realistic case, and when combined with model analysis a greedy stochastic search method can be used to determine an optimal sensor set to satisfy the requirements (Jung et al., 2020)

In this work a combined approach is used. Simulations are performed to observe the effects of faults on the various measurements, and responses that are below noise thresholds are discarded. The remaining fault-measurement combinations are represented as a bipartite graph, with non-zero residuals specifying the edges. Detectability and isolability conditions are defined in terms of neighbourhoods on the graph, and both a greedy approach and a Monte Carlo approach are implemented to obtain a minimal sensor set to satisfy the requirements.

2 Method

2.1 Simulation

The Benchmark Simulation Model No. 1 (BSM1) was used for simulating the WWTP. The benchmark plant consists of five biological reactors in series, where two are anoxic (total volume 2000 m^3) and three are aerated (total volume 3999 m^3), the reactors are modelled with the Activated Sludge Model No. 1 (ASM1). The reactors are followed by a secondary settler with a volume of 6000 m^3 which is modelled as a nonreactive ten layer settler with the Takács model (Gernaey et al., 2014, pg. 9–10). The model assumes a constant temperature of 15 °C. The BSM1 is used with the two standard control loops for NO_3-N and dissolved oxygen control, with set-points of 1 $g\,N\,m^{-3}$ and 2 $g\,O_2\,m^{-3}$ respectively (Gernaey et al., 2014, pg. 55–56). The layout of the process is shown in Figure 1 with the control loops, and the locations where for this study it was considered feasible to place sensors.

The MATLAB Simulink implementation of the steady-state form of the BSM1 was run with constant influent. The steady-state model utilises ideal sensors in the control loop but is otherwise similar to the normal BSM1. This simulation set-up was used to be able to easily detect the new steady-state that is reached after a fault has occurred.

The simulation model was modified to allow for the introduction of process faults. These faults were added as bias faults, where the size of the step was a percentage of the normal value of the parameter. Table 1 shows the list of faults, along with the normal values for the single parameters. The fault sizes used for simulation were 1 %, 5 %, 10 %, 20 %, 30 %, 40 %, 50 %, and 75 %. Considering each fault fault-size combination as a unique fault, a total of $n_f = 96$ faults were tested.

Table 1. Summary of faults that were introduced to the system. The fault symbol shows whether there was an increase or a decrease in the parameter. All growth rates are maximum specific growth rates as used in the ASM1.

Faulty Parameter(s)	*Normal Value*	*Symbol*	*Fault No.*
Ammonification rate	0.05[a]	$+k_a$	1
		$-k_a$	2
Heterotrophic growth rate	4 d^{-1}	$+\mu_H$	3
		$-\mu_H$	4
Heterotrophic death rate	0.3 d^{-1}	$+b_H$	5
		$-b_H$	6
Heterotrophic growth rate Heterotrophic death rate	4 d^{-1} 0.3 d^{-1}	I[b]	7
Autotrophic growth rate	0.5 d^{-1}	$+\mu_A$	8
		$-\mu_A$	9
Autotrophic death rate	0.05 d^{-1}	$+b_A$	10
		$-b_A$	11
Settling velocity	NA[c]	$-v_s$	12

[a] The ammonification rate constant has units of $m^3\,gCOD^{-1}\,d^{-1}$.
[b] The inhabitation fault is a combination of $-\mu_H$ and $+b_H$.
[c] The settling velocity is calculated from the double-exponential settling velocity function and therefore has no single normal value.

The simulation was loaded from a predetermined steady-state and run for 50 days before introduction of a fault. After the fault was introduced the simulation continued until the system reached a new steady-state. The post-fault steady-state values were used for the residual analysis.

2.2 Sensors and Measurement Noise

The starting set of sensors was taken as those variables that are commonly measured and have available commercial sensors. These included flow rates (Q), dissolved oxygen (S_O), alkalinity (S_{ALK}), total suspended solids (TSS), as well as nitrate/nitrite nitrogen (S_{NO}), and ammonium/ammonia nitrogen (S_{NH}) (Olsson et al., 2005; Rieger et al., 2003). All six variables were considered to be measurable at the eight locations indicated in Figure 1. These locations are used as subscripts to describe a specific sensor, e.g. $S_{O,5}$ indicates the dissolved oxygen measurement in the fifth reactor. Additional flow rates were measured in the wastage (Q_w) and internal recycle (Q_a). It was also assumed that the oxygen mass transfer coefficient (K_La), which represents the airflow into the final reactor, is known or measured. This resulted in a starting set of 51 measurements; 40 concentration sensors, 10 flow rate

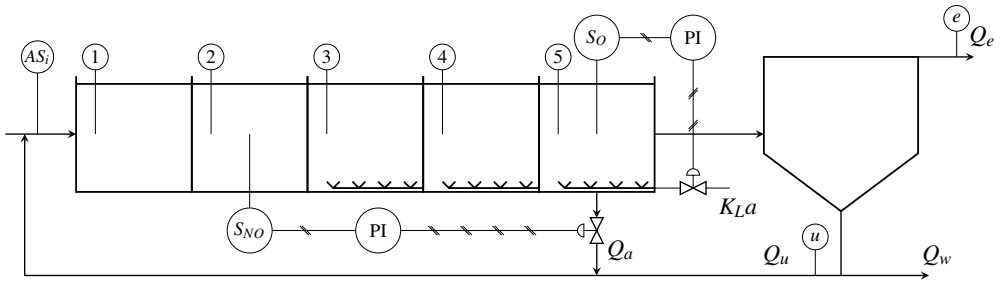

Figure 1. The plant layout for the BSM1 WWTP, the two standard control loops are shown on the diagram with the measurements involved, as well as all locations where it is assumed possible to install sensors and take measurements marked by 1-5 (inside biological reactors), e and u (in settler effluent and underflow respectively), and AS_i (in the inflow to biological reactors).

sensors, and the K_La value in the fifth tank. We represent the total number of sensors with n_s.

As stated previously, ideal sensors were used in the simulation of the process. However, sensor ranges and measurement uncertainty were considered when analysing the residuals. In the non-ideal BSM1 measurement noise is specified as 2.5 % of the maximum measurement range boundary for the sensor of interest, and measurement ranges for variable-specific sensors are provided (Gernaey et al., 2014; Rieger et al., 2003). We denote the measurement noise for sensor j as σ_j^2.

A sensitivity analysis was performed by changing the noise to 1 % (Rosen et al., 2008) and 4 % and comparing the main results.

2.3 Analysis of Residuals

Residuals were calculated for each fault, fault size, and sensor based on the normal operating conditions and the post-fault steady states obtained from simulations performed using the modified BSM1. These residuals form an $n_f \times n_s$ influence matrix M', where $M'_{i,j}$ represents the size of the residual detected by sensor j caused by fault i. We then construct an $n_f \times 2n_s$ binary influence matrix M as follows:

$$M_{i,j} = \begin{cases} 1, & M'_{ij} > \sigma_j^2 \\ 0, & \text{otherwise} \end{cases} \quad M_{i,j+n_s} = \begin{cases} 1, & M'_{ij} < -\sigma_j^2 \\ 0, & \text{otherwise} \end{cases} \tag{1}$$

If we represent this matrix blockwise $M = [M_+ M_-]$ then the block M_+ shows that fault i caused a positive residual above the noise threshold of sensor j; block M_- shows the same thing for negative residuals.

This can be interpreted as the biadjacency matrix of a bipartite graph $G = (F, S, E)$, where $F = \{f_i\}_{i=1}^{n_f}$ is a set of vertices representing faults, $S = \{s_j^+, s_j^-\}_{j=1}^{n_s}$ is a set of vertices representing positive or negative residuals on sensors, and E is the set of edges. A fault, f_i, is detectable only if it is connected to at least one sensor s_j^+ or s_j^-. Formally, we can say that the neighbourhood of a detectable fault in G is non-empty, i.e. $N(f_i) \neq \emptyset$. A fault can be isolated if it is detectable and the residual set it creates is distinct from all others, i.e. $N(f_i) = N(f_j)$ if and only if $i = j$.

Call a subgraph $H = (F, S', E')$ of G a minimal sensor graph if: 1) all faults which are detectable in G are detectable in H, 2) all faults which are isolable in G are isolable in H, 3) removing any vertex pair (s_j^+, s_j^-) from S' would violate 1) or 2). To find a minimal sensor graph in G we used both a greedy method for removing vertices from G, as well as a Monte Carlo approach.

For the greedy method residual pairs (s_j^+, s_j^-) are iterated through, if a pair is found which can be removed without affecting the overall isolability and detectability, it is removed. This continues until no more residual pairs can be removed. The Monte Carlo approach samples from the existing residual pairs randomly and removes pairs while preserving isolability and detectability. When the subgraph stagnates the search terminates.

3 Results and Discussion

Following the procedure detailed above, both the greedy method and the Monte Carlo approach identified a minimum of eleven sensors as necessary to detect and isolate the maximum number of fault cases. Ten thousand iterations of the Monte Carlo approach resulted in no changes to the minimum number of sensors, but different combinations of sensors were identified. Future work will investigate additional criteria which may be used to determine an optimal sensor set from the results of the Monte Carlo approach, however, this work considers the set obtained with the greedy method. These sensors are: $S_{NH,1}$, $S_{NH,3}$, $S_{NO,3}$, $S_{O,3}$, $S_{O,4}$, $S_{NO,e}$, $S_{ALK,e}$, TSS_e, TSS_u, $TSS_{AS_{in}}$, K_La_5.

3.1 Fault Detectability and Isolability

Considering the faults described in Table 1, faults $+k_a$ and $+\mu_H$ were found to be undetectable by any of the possible sensors, given the sensor noise thresholds. This is not unexpected as they were unconventional faults; increasing either of these parameters may in some circumstances be beneficial, however, any deviation from the desired operating point satisfies the definition of a fault.

Additionally, small deviations, the 1 % and 5 % fault sizes, were found to be undetectable. Considering that the smallest deviation in these parameters that was found in the literature was 6 % (Lee et al., 2003), with 40 % to 60 %

being more common sizes for changes in the parameters, this is an expected result. Future work should consider the effect that different fault sizes have on the performance of the WWTP in order to understand which sizes are critical to detect. These aforementioned non-detectable faults account for 36 of the original 96 tested faults.

Figure 2 shows for the detectable faults and fault sizes, at what size each fault became detectable, and where the signatures were unique. From this Figure we can see that 31 of the original 96 faults were detectable *and* isolable, while 43 were detectable.

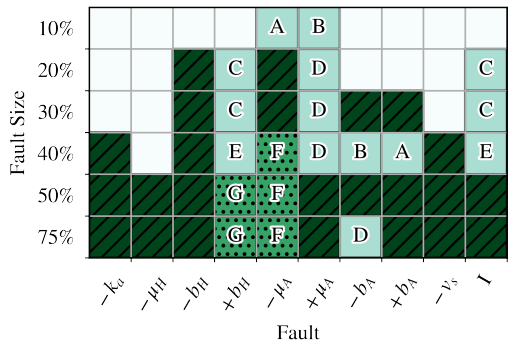

Figure 2. The detectability and isolability of faults is shown for different sizes of faults. White indicates an undetectable fault while colored indicates a detectable fault. The dark green with hatching shows completely unique fault signatures, green with a dotted pattern indicates that within a particular fault different sizes have the same signature, and the unpatterned light green shows identical signatures in different fault types. The letters show which fault signatures are the same.

There are several interesting observations to be made from this Figure. Firstly, we see that certain faults at particular sizes can resemble different faults at either the same, or different fault sizes. Consider the faults marked 'A' as an example of the latter case; this occurs at a 10 % deviation for fault $-\mu_A$, and at 40 % for $+b_A$ and shows that these two faults share the same signature. This makes sense as a decrease in growth rate and an increase in death rate of the autotrophic bacteria can be expected to have a similar effect on the process. However, the faults are distinguishable if their evolution is monitored as they only share a signature at one size. The faults marked 'B' and 'D' show a similar relationship between $+\mu_A$ and $-b_A$, but identical signatures also exist *within* the $+\mu_A$ fault across several sizes as shown by the 'D' faults.

Faults $+b_H$ and I are interesting due to the appearance of 'C' and 'E', marking two unique signatures shared by these two faults at the same sizes. This is likely due to the fact that I, as mentioned previously, is a combination of $+b_H$ and $-\mu_H$. In Figure 2, fault $-\mu_H$ is seen to be undetectable until a size of 50 %, this is the size at which the signatures of $+b_H$ and I become distinct from each other, indicating that at smaller sizes the dominant effect was $+b_H$ and we could expect the two signatures to be equal. From this observation we can state that it is likely that if an additional fault was tested that was the combination of $+b_A$ and $-\mu_A$, this fault would share signatures with $-\mu_A$ until fault size 30 %.

The uniqueness of signatures across fault sizes, within a fault, can be a useful property as fault sizes can be identified purely from the *signs* of the residuals, without analysis of the *size* of the residuals. In the case where certain fault sizes require immediate action this property can provide an early warning if the evolution of fault signatures are monitored.

3.2 Fault Signatures

Discussing now the fault signatures, in Figure 3 all fault signatures are shown. Each subplot is for a single fault, the columns represent the different sizes of the fault, and the rows show which sensor is used in detecting that occurrence of the fault. The sign of the residual is shown by the fill on the Figure.

The first observation to make from Figure 3 is that, when considering fault pairs of "+" and "−" of the same parameter, we observe similar residual patterns yet opposite signs. This is an expected response, and if the process were perfectly linear we would expect identical but oppositely signed residual patterns. There are three pairs to observe this behavior in: μ_A, b_A, and b_H.

Secondly, pairs of parameters that have a similar effect on the process have similar residual patterns. These pairs are the oppositely signed changes of growth and death rates of either the autotrophic or heterotrophic bacteria. This was mentioned in the discussion of Figure 2 in relation to the labelled pairs of identical signatures ('A', 'B', 'C', etc.). Considering 'C' and 'E' which were seen between faults $+b_H$ and I, these are easily identified in Figure 3. We see $S_{O,4}$, TSS_{AS_i}, TSS_u, and K_La_5 responding to both of these faults identically up until fault size 50 % where the effect of $-\mu_H$ becomes significant.

Considering some specifics, the sensor TSS_e is only used to detect a decrease in the settling velocity ($-v_s$). This suggests that despite this fault having a more complex signature based on the sensor set, it could be identified and isolated with that single sensor if the size of the fault was not of interest. Similarly, $S_{ALK,e}$ is only used in fault $-\mu_A$ and causes size 20 % and 30 % to be distinguishable. If we were uninterested in isolating the sizes of this fault based on the binary residual approach followed, this sensor could be excluded from the sensor set.

Finally, if we consider K_La_5 in the fault $-\mu_A$, the residual can be observed to change sign as the fault size increases which is a clear indicator of nonlinearities in the process.

3.3 Sensitivity to Measurement Noise

Sensitivity of the selected sensor set and detectable faults to measurement noise can be evaluated by repeating the analysis for different sensor noise levels. Table 2 shows the maximum possible number of isolable faults, the number of sensors required for fault isolation, and the changes

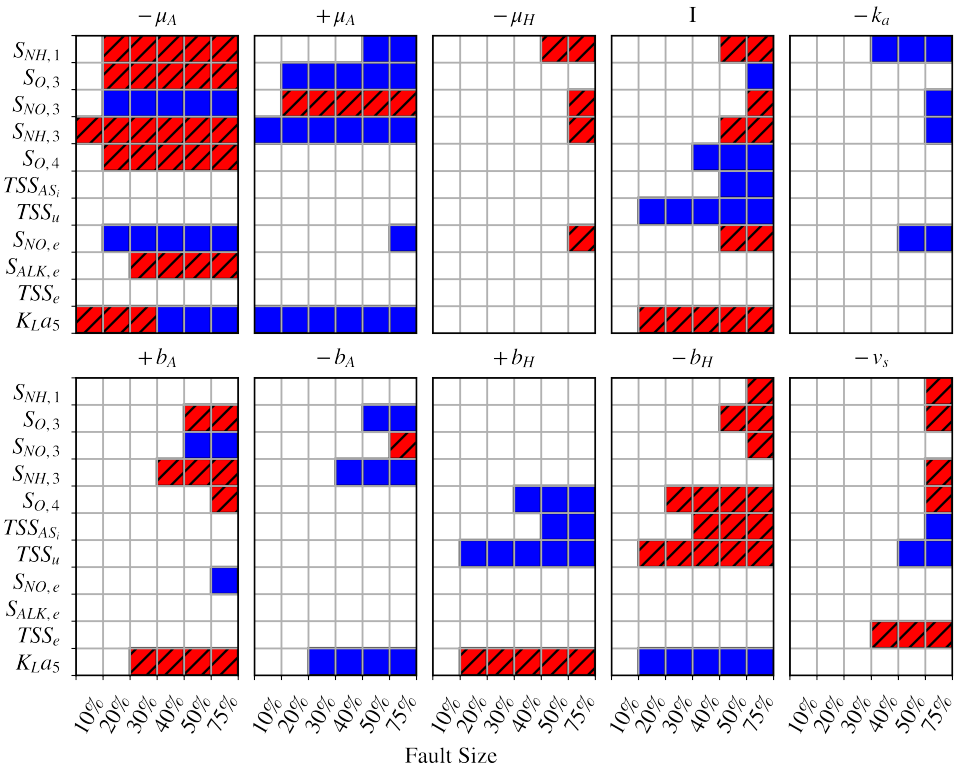

Figure 3. Fault signatures for the tested, detectable, faults. The hatched red squares indicate a positive residual observed in a specific sensor while unpatterned blue indicates a negative residual.

to the sensor configuration specified previously.

Table 2. Sensitivity of analysis to measurement noise.

	1 %	2.5 %	4 %
Isolable faults	34	31	31
Number of sensors	13	11	10
Sensors to remove	-	-	$S_{ALK,e}$, $S_{O,4}$
Sensors to add	$S_{NH,4}$, Q_a	-	$S_{NH,4}$

An interesting observation is the addition of sensor $S_{NH,4}$ in both cases, this suggests that including this sensor in the recommended sensor set may make the FD and isolation more robust to variations in noise and uncertainty. The additional number of sensors required to detect the faults with less noise is due to more sensors producing residuals above the threshold and subsequent isolation of the faults requiring more information. We can similarly discuss the fewer number of sensors required to isolate the same number of faults with the 4 % noise when compared to 2.5 %. As the noise increases the number of residuals above the threshold decreases, which means fewer sensors may be required to isolate the same number of faults. This suggests that clearly defining a threshold for each sensor is a vital step in the FD procedure.

4 Conclusions and Recommendations

Using a combined simulation based-graph theoretic approach a minimal sensor set was suggested in order to allow for the detection and isolation of the maximum number of fault fault-size combinations. The required sensors were $S_{NH,1}$, $S_{NH,3}$, $S_{NO,3}$, $S_{O,3}$, $S_{O,4}$, $S_{NO,e}$, $S_{ALK,e}$, TSS_e, TSS_u, $TSS_{AS_{in}}$, K_La_5; a total of eleven. However, other combinations of eleven sensors were capable of detecting the same faults and future work should consider how to select the optimal combination of sensors. It was found that replacing $S_{ALK,e}$ with $S_{NH,4}$ may increase the robustness to variations in measurement noise, and the importance of defining a noise threshold was highlighted.

Fault signatures were identified for faults relating to changes in the growth and death rates of the autotrophic and heterotrophic bacteria, as well as changes to the ammonification rate, and settling velocity. It was observed that small changes to these parameters do not produce residuals that are distinguishable from measurement noise, and it is recommended that future work investigate the effect that different fault sizes have on the performance of the WWTP in order to highlight which fault sizes are critical to detect.

The results were based on a binary approach, considering only the sign of the residual and not its magnitude. It may be possible to reduce the sensor set and increase isolability by considering residual magnitude, and this can be investigated further in future work. Following the binary approach simplifies the residual analysis and is easier to visualise; which is an important consideration in terms of potential implementation in industry.

5 Acknowledgements

This study has been done within the international project Control4Reuse with partners from Sweden, France and Brazil. The project is part of the IC4WATER programme, in the frame of the collaborative international consortium of the 2017 call of the Water Challenges for a Changing World Joint Programme Initiative (Water JPI). The authors would like to thank Formas (Project No 2018-02213) for funding the Swedish part of this project, within the above mentioned initiative.

References

D. Aguado and C. Rosen. Multivariate statistical monitoring of continuous wastewater treatment plants. *Engineering Applications of Artificial Intelligence*, 21(7):1080–1091, Oct. 2008. doi:10.1016/j.engappai.2007.08.004.

M. Basseville. On Fault Detectability and Isolability. *European Journal of Control*, 7(6):625–637, Jan. 2001. doi:10.3166/ejc.7.625-637.

A. Borowa, M. A. Brdyś, and K. Mazur. Detection of Unmeasured Process Abnormalities in Wastewater Treatment Process using MS-PCA. *IFAC Proceedings Volumes*, 40(9):262–267, Jan. 2007. doi:10.3182/20070723-3-PL-2917.00042.

M. Chen, L. Quan Hu, and H. Tang. An Approach for Optimal Measurements Selection on Gas Turbine Engine Fault Diagnosis. *Journal of Engineering for Gas Turbines and Power*, 137(7), July 2015. doi:10.1115/1.4029171.

S. W. Choi and I.-B. Lee. Nonlinear dynamic process monitoring based on dynamic kernel PCA. *Chemical Engineering Science*, 59(24):5897–5908, Dec. 2004. doi:10.1016/j.ces.2004.07.019.

S. X. Ding. *Model-Based Fault Diagnosis Techniques Design Schemes, Algorithms and Tools*. Advances in industrial control. Springer London, London, 2nd ed. edition, 2013. ISBN 978-1-4471-4799-2.

D. Garcia-Alvarez, M. J. Fuente, P. Vega, and G. Sainz. Fault Detection and Diagnosis using Multivariate Statistical Techniques in a Wastewater Treatment Plant. *IFAC Proceedings Volumes*, 42(11):952–957, Jan. 2009. doi:10.3182/20090712-4-TR-2008.00156.

K. V. Gernaey, U. Jeppsson, P. A. Vanrolleghem, and J. B. Copp. *Benchmarking of Control Strategies for Wastewater Treatment Plants*. IWA Publishing, Sept. 2014. ISBN 978-1-84339-146-3.

R. Isermann. *Fault-Diagnosis Systems: An Introduction from Fault Detection to Fault Tolerance*. Springer-Verlag, Berlin Heidelberg, 2006. ISBN 978-3-540-24112-6. doi:10.1007/3-540-30368-5.

D. Jung, Y. Dong, E. Frisk, M. Krysander, and G. Biswas. Sensor selection for fault diagnosis in uncertain systems. *International Journal of Control*, 93(3):629–639, Mar. 2020. doi:10.1080/00207179.2018.1484171.

M. Krysander and E. Frisk. Sensor Placement for Fault Diagnosis. *IEEE Transactions on Systems, Man, and Cybernetics - Part A: Systems and Humans*, 38(6):1398–1410, Nov. 2008. doi:10.1109/TSMCA.2008.2003968.

J.-M. Lee, C.-K. Yoo, and I.-B. Lee. Statistical Process Monitoring with Multivariate Exponentially Weighted Moving Average and Independent Component Analysis. *Journal of Chemical Engineering of Japan*, 36(5):563–577, 2003. doi:10.1252/jcej.36.563.

J.-M. Lee, C.-K. Yoo, S. W. Choi, P. A. Vanrolleghem, and I. Lee. Nonlinear process monitoring using kernel principal component analysis. *Chemical Engineering Science*, 59(1): 223–234, Jan. 2004a. doi:10.1016/j.ces.2003.09.012.

J.-M. Lee, C.-K. Yoo, and I.-B. Lee. Statistical process monitoring with independent component analysis. *Journal of Process Control*, 14(5):467–485, Aug. 2004b. doi:10.1016/j.jprocont.2003.09.004.

T. Li, M. Winnel, H. Lin, J. Panther, C. Liu, R. O'Halloran, K. Wang, T. An, P. K. Wong, S. Zhang, and H. Zhao. A reliable sewage quality abnormal event monitoring system. *Water Research*, 121:248–257, Sept. 2017. doi:10.1016/j.watres.2017.05.040.

G. Olsson, M. Nielsen, Z. Yuan, A. Lynggaard-Jensen, and J.-P. Steyer. *Instrumentation, Control and Automation in Wastewater Systems*. IWA Publishing, Apr. 2005. ISBN 978-1-900222-83-9.

L. Rieger, J. Alex, S. Winkler, M. Boehler, M. Thomann, and H. Siegrist. Progress in sensor technology - progress in process control? Part I: Sensor property investigation and classification. *Water Science and Technology*, 47(2):103–112, Jan. 2003. doi:10.2166/wst.2003.0096.

C. Rosen, L. Rieger, U. Jeppsson, and P. A. Vanrolleghem. Adding realism to simulated sensors and actuators. *Water Science and Technology*, 57(3):337–344, Feb. 2008. doi:10.2166/wst.2008.130.

G. Ryder. The United Nations world water development report, 2017: Wastewater: the untapped resource. Technical report, UNESCO World Water Assessment Programme, Paris, 2017.

M. Stenfelt, V. Zaccaria, and K. Kyprianidis. Automatic Gas Turbine Matching Scheme Adaptation for Robust GPA Diagnostics. In *Proceedings of the ASME Turbo Expo*, volume 6, Phoenix, United States, June 2019.

K. Villez, P. A. Vanrolleghem, and L. Corominas. Optimal flow sensor placement on wastewater treatment plants. *Water Research*, 101:75–83, Sept. 2016. doi:10.1016/j.watres.2016.05.068.

K. Villez, P. A. Vanrolleghem, and L. Corominas. A general-purpose method for Pareto optimal placement of flow rate and concentration sensors in networked systems – With application to wastewater treatment plants. *Computers & Chemical Engineering*, 139:106880, Aug. 2020. doi:10.1016/j.compchemeng.2020.106880.

S. Yin, X. Xie, and W. Sun. A Nonlinear Process Monitoring Approach With Locally Weighted Learning of Available Data. *IEEE Transactions on Industrial Electronics*, 64 (2):1507–1516, Feb. 2017. doi:10.1109/TIE.2016.2612161. Conference Name: IEEE Transactions on Industrial Electronics.

C. K. Yoo and I. Lee. Nonlinear multivariate filtering and bioprocess monitoring for supervising nonlinear biological processes. *Process Biochemistry*, 41(8):1854–1863, Aug. 2006. doi:10.1016/j.procbio.2006.03.038.

J. Yu. A nonlinear kernel Gaussian mixture model based inferential monitoring approach for fault detection and diagnosis of chemical processes. *Chemical Engineering Science*, 68(1): 506–519, Jan. 2012. doi:10.1016/j.ces.2011.10.011.

V. Zaccaria, A. D. Fentaye, M. Stenfelt, and K. G. Kyprianidis. Probabilistic Model for Aero-Engines Fleet Condition Monitoring. *Aerospace*, 7(6):66, June 2020. doi:10.3390/aerospace7060066.

Challenges in connecting a wastewater treatment plant to a machine learning platform

Christian Wallin[1,2] Eva Nordlander[1]

[1]Future Energy Center, Mälardalen University, Sweden, {eva.nordlander}@mdh.se
[2]ABB AB, Sweden, christian.wallin@se.abb.com

Abstract

Treatment of wastewater is fundamental to protect the environment and to ensure a healthy water supply. Higher demands are put on the treatment of the effluent from wastewater treatment plants (WWTP) to reduce more pollutants as well as remove pharmaceutical residues. To be able to deliver better water quality monitoring and control is of importance but wastewater treatment is far behind many industrial processes when it comes to automation. Digital twins and machine learning could offer many benefits but not much work has been done in this field concerning wastewater treatment. How do you move from an existing traditional process automation system to an integrated machine learning platform?

This paper investigates the challenges of implementing an integrated machine learning platform for a wastewater treatment plant. The paper is based on experience from a project where a number of different processes, including a WWTP where integrated into a machine learning platform in an online cloud environment. In this paper we focus on the integration of the WWTP. On the platform a model is run in real-time using process data. Machine learning algorithms are used to treat the process data and for sensor fault detection. The challenges and considerations are many, such as cyber-security when it comes to data access and data transfer and how to convert the process data to a format that can be used by the model.

Multiple defining choices must be made along the way that can have a major impact on the final platform functionality. It is important not only to evaluate these choices but also to have enough knowledge and jurisdiction to make both the right decisions and to also make them in time. Many projects run out of time and/or money for different reasons and strategies will be discussed for how to mitigate risk factors.

Keywords: Wastewater Treatment, Machine Learning, Cloud Environment

1 Introduction

Many wastewater treatment plants today have sensors to measure water quality and also to control parts of the plants. A common control is the aeration of the biological treatment to send enough air in to the water to fulfill a set-point of the level of oxygen in the water. Other common measurements is the level of ammonia and nitrate in the water and some plants also use these measurements as control parameters. The wastewater treatment plant of Västerås, that was used as reference plant in this project, have all of the above mentioned measurements as well as water temperature, water flow-rate and phosphor concentration sensors. Data from these sensors have been stored in a historical database since at least 5 years back to produce graphs for operators of the plant and to create reports to authorities. The goal was to do more with all this data and use modern machine learning technologies to achieve better control and monitoring of the water and the treatment plant.

2 Method

Historical data at the WWTP were stored in a process database. A model had also been developed of the WWTP based on the BSM2G Matlab Simulink simulation model (Vrecko et al., 2006) but for other purposes than was intended within this project. The model was used for online simulations of the plant and needed to be adapted to connect to the data from sensors and analysis. It also needed to be stable and have a reasonable simulation time. In the end a BSM2 model (Jeppsson et al., 2007) adapted for the plant was used, but the ASM1 (Henze et al., 1987) and BSM2G models were also tested. Since sensor data would be used for the models, sensor fault detection was also of importance and multiple strategies were evaluated. In addition we wanted to add Model Predictive Control (MPC) as extra functionality to optimize the process.

2.1 Using a Cloud Platform

To ensure the existing data was not altered by mistake and to avoid unauthorized access the data needed for new models and analysis was cloned from the existing database. The cloned data and models could either be hosted on-site or using an online cloud platform. There are benefits with self-hosting since data never leaves the site but there are also drawbacks in terms of accessibly and scaling as well as needing new hardware to be purchased and maintained. For this project a cloud-based solution was selected. With a cloud-based solution initial costs for investing in infrastructure could be avoided and it made it possible to get started before the full benefit and return value of an investment could determined.

2.2 Models

Throughout the project numerous different models and model interfaces have been used and evaluated. To build a scale-able platform that is able to support effortless integration of as many different models as possible it is important to choose a platform that is not built only to support a specific model vendor. As the project was founded by the EU Research and Innovation program ”Horizon 2020” all models were required to be open source models. This does not limit the use of commercial software such as MATLAB but requires the final models created to be exported to an open-source format. One of the benefits with open-source models is that they allow for better sharing of experiences between organisations. Another benefit is that the open-source models are often less platform-dependent which also gives more options to the final user.

The models used in this project was built using MATLAB Simulink. MATLAB models can be run outside of MATLAB using runtime dll-file but it still requires a MATLAB runtime license. This could be a working solution for many but with our requirement to be fully open-source it was not possible to use this in our project. Another possibility is to convert an existing model to an open-source model, but the resulting model would essentially be a new model which would require time to build and test it. In this project it was solved by using the Simulink model but compile it is an open-source model using the Modelon "FMI TOOLBOX FOR MATLAB/SIMULINK" (Modelon AB, 2021). This toolbox makes it possible to compile a Simulink model as a Functional Mock-up Unit (FMU) which creates a file with the simulation model based on the Functional Mock-up Interface (FMI) which is an open standard for simulation models.

2.3 Data

Data was extracted in two ways: Initially historical data of interest was extracted and then followed by a continuous extraction of new data. The data was extracted using Excel-scripts and the two different types of extractions had to be treated separately. As Excel has limitations in how much data that can be stored in one file and the amount of data from certain sensors that had been storing data for several years where extensive. The historical data had to be extracted for one sensor at a time and in some cases also in batches of as little as a few months while the continuous extraction of new for all sensors could fit in a single file. Even though the time-resolution varied among the different sensors, the extracted files was created using batches of data based on one-minute averages for each sensor. Intervals of 15-minutes were used between extractions, meaning each extracted file contained 15 lines, one for each minute, of the data for each sensor for the last 15-minute period.

The chosen time resolution of 1 minute and 15 minutes between extractions impacted the amount of storage space required to store the extracted data as well as what models can be run using the data. The time resolution was chosen to work well with all models used and could be increased if too much storage would be consumed. 15 minutes between each batch of new data was also considered enough since the models would not be used for direct control. A delay of up to 15 minutes would be sufficient to decide the set-points of faster controllers or to detect sensor failing over time. If the models should instead be used for direct control of for example valves or pumps the time resolution and time between extractions would need to be reconsidered.

2.4 Integration

The models need to be connected to the data storage. Between the storage of data and the model the data needs to be checked as well as translated into a form that can be used as input by the model. The model results also need to be stored as well as the model state in case of state-based models. An alternative to storing the model state is to have a default state and an initialization period before each batch of new data feed into the model.

The data and model integration framework used to handle management of data between the data-store and the models used in this project was Node-RED (JS Foundation, 2021). In addition to data management the framework also contains the functionality to create websites to visualize data and model output as well as providing the possibility to get user input to models. Having such a framework is essential to prepare raw data from the database storage in a suitable input format for each of the models and to sort through the model output to format and store essential model output. We decided to have a full separation of stored raw data from the treatment plant and the data stored from model output to never risk losing track of the origin of the stored data.

Some of the models that were used required data from chemical analysis as well as sensor data for model input. The chemical analyses are made at the plant manually about once every week. The data from the analysis were stored separately from the sensor data. Each of the analysed values was assumed to remain the same until a new analysis was made. The load on the plant varies over the day but since the analysis are made as collected samples each week the values does not reflect daily variations. Instead to simulate daily variations, a normal daily variation curve was used. The resolution was 15 minutes and the average for each day was the chemical analysis value for the week the day belonged to.

2.5 Output and presentation

One of the most important parts for a project like this to be considered successful is to make good use of the produced outputs. The performance of the models does not matter much if the outputs cannot be visualized to an end user to make better or more informed decisions or to optimize actions as plant control or maintenance planning. Writing information back to the control system can be a real chal-

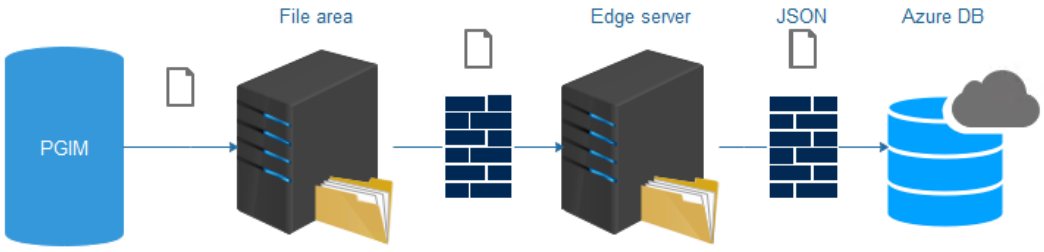

Figure 1. File transfer from historian database to cloud storage

lenge from a security perspective and it should be handled with care. Even if the write-back of data to the system is secured, the models also need to be thoroughly tested before actual control actions can be taken based on the model results. It would also be advisable to have model input and output validation to make sure that all variables are within reasonable levels. If any of the variables would deviate a default fallback option ignoring the models could be used as a fail-safe.

In this project nothing was written back to the system, results were instead presented on a webpage for operators to read to take actions, with a security air-gap between the new cloud models and the control system.

3 Results

3.1 Implemented models

Several physical simulation models both of generic and plant specific tuned models have been integrated in the platform. All physical plant simulation models used originates form MATLAB Simulink models that was wrapped as Function Mockup Units (FMU:s) so they could be run in any environment without the requirement of a Simulink runtime. First the generic benchmark model BSM1 (Alex et al., 2008) got implemented as a proof of concept to validate that the FMU models would produce the same results as when they were run inside Simulink which was successful. Following that the more complex models BSM2 (Jeppsson et al., 2007) and BSM2G (Vrecko et al., 2006) modified and tuned as digital twins of the Västerås wastewater treatment plant named Kungsängsverket were also integrated and tested in the platform.

Some live sensors have been connected to these models and the current ongoing task is to create the required influent datapoints from live sensors together with information gather from recent lab measurements. This is needed as the models requires a large set of input parameters which is not directly measured with live sensors as the contamination in the incoming water make continuous measurements very challenging.

Models for Model Predictive Control (MPC) was also developed in Matlab Simulink using the MPC Toolbox and like the full plant model they were exported to FMU. Several different FMU:s have been tested to run the BSM1 and the BSM2 models. For security reasons no write-back to plant is currently allowed and would have to be solved in future project which make closed-loop MPC impossible but the possibility to manually read MPC output and use this as manual input to the control system is still useful whilst not as manageable as a closed-loop solution. The output from the MPC in all cases have been supervisory control as in set-points for existing PI controllers. The main improvement observed is in the possibility to lower the amount of aeration during lower plant load to save energy but a small improvement to water quality has also been seen in some scenarios.

To compare and analyze the correlation between multiple oxygen and air-flow sensors a Bayesian Network model was developed using the Hugin tool (HUGIN EXPERT A/S, 2021). However, this model required a lot of training data to provide accurate results which was not available in the quantities needed. Instead the fault detection was moved to Python models. A model to classify normal data from disturbance data from event of sensor cleaning was developed and tested with good result using historical data. This was not suitable to classify new datapoints from continuous sensor measurements and instead focus was moved an Auto-regressive Integrated Moving Average Model (ARIMA) model to look at multiple airflow sensors together with oxygen sensor readings to determine normal conditions and detect deviations from this.

3.2 Data Extraction

A file is cyclically exported from PGIM database and put in an internal file area and a scheduled job is moving this to an area where an edge server can consume this file. This flow is illustrated in Figure 1.

The edge server is a virtual machine placed inside Mälarenergi network which runs on Ubuntu operating system. Edge server ingest data from a share drive located in Mälarenergi network and then performing data processing, anonymization and transfer to JavaScript Object Notation (JSON) format, and sending to cloud will be managed by scheduled data collecting modules. JSON files are processed directly to database by scripts that runs in Azure functions. Functions are triggered on incoming files at Azure BLOB Storage. Data is continuously transferred from history database to Azure Cloud MS SQL Server and

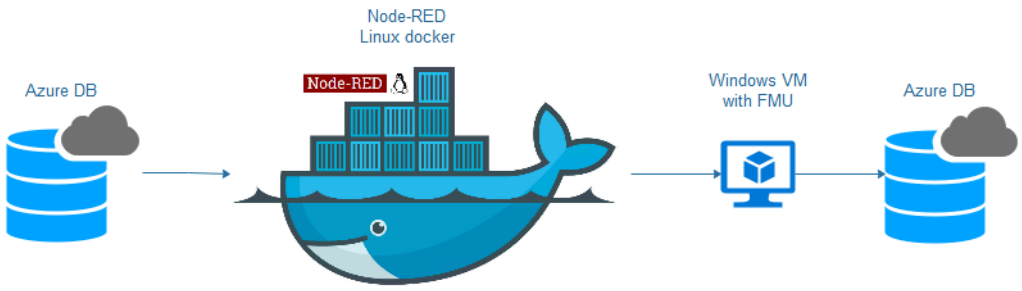

Figure 2. Data flow in cloud environment

the data is available in the cloud storage less than 5 minutes after the data has been written from the control system to the history database.

3.3 Data and Model Integration

Using a variety of Microsoft Azure resources; virtual machines, storage, databases and application-services, it is possible to use the data originating from the customer site database to call i.e. a FMU-model and store back the model results. The results could later be used to control the plant or give suggestions to plant staff of how to optimize the process of running the plant or optimize maintenance. Data flow from database through data preparation stages to model execution, retrieving model results and finally writing results back to a database is illustrated in Figure 2.

The process of running the models inside the cloud platform was built in the flow-based programming tool named Node-RED which is running inside a Linux Docker container in the MS Azure cloud. Inside Node-RED a flow is created which retrieves the necessary data from the MS Azure Database pre-process the data to a format suitable for the intended model to be run and send a http request to a Windows virtual machine also running in the MS Azure environment. This virtual machine, which has the necessary run-times required to run the models, run a web-service that listens for request on different ports for different models to know what model should run with what data. Once data is sent to a web-socket a program execute the corresponding model based and feed it the input data sent to the virtual machine. Once the model has finished running the results are sent back the Node-RED flow which then take care of the model output and make it possible to store it back in the cloud database. An example of how such a Node-RED data-flow is created within the Node-RED user interface has been illustrated in Figure 3. Here each node i.e. SQL code to retrieve or store data to a database or JavaScript code to prepare data for model execution.

4 Discussions

Making sensor data available to be processed and accessed by modern machine learning algorithms and simulation models is the start of a new era of process control. There are numerous studies simulating the WWTP and different possible advanced control strategies. This implementation and evaluation framework is a step to bring advanced control closer toward full-scale testing and final implementation. Having a framework in place where data can very easy be made accessible to new model developers also reduce both the complexity and the effort required in any future project looking to further improve the process. Adding feed-forward and feedback MPC to the existing aeration control strategy give both the possibility to reduce effluent violations and to reduce the energy used during periods when the aeration demand is lower.

When adding more algorithms and models to a system the quality of input data become increasingly important. Sensor maintenance already requires a lot of work for plant owners and maintenance personnel. When this maintenance can be planned in according to where and when a sensor is in most need of maintenance such as cleaning with addition of added sensor diagnosis tools both the cost of maintenance and the accuracy of sensor data could be improved. Today every sensor is cleaned in intervals based on experience but with the possibility of analyzing actual sensor performance it could be both better and without requiring experienced staff to plan the work.

Digital Twin(s) give endless comparison opportunities both for process control and sensor maintenance. Future control strategies should be evaluated by numerous clones with different settings and models can also be made accessible for experienced operators to try new strategies without the risk of affecting the process. The platform can also be a valuable tool for new personnel to train, learn and experiment with the process in a safe environment. It would also be possible to record special scenarios to be replayed either to try strategies or to teach already know strategies.

The biggest achievement is the implementation of the platform itself and the endless possibilities for further development of new models and possible plant control. It has been shown that it is possible to achieve better water quality and reduce energy consumption by applying MPC to the aeration process of a WWTP. Having a full plant model implemented in a cloud environment connected to live data, makes it possible to evaluate strategies in a close to live environment which further increase the possibility to develop and test new strategies.

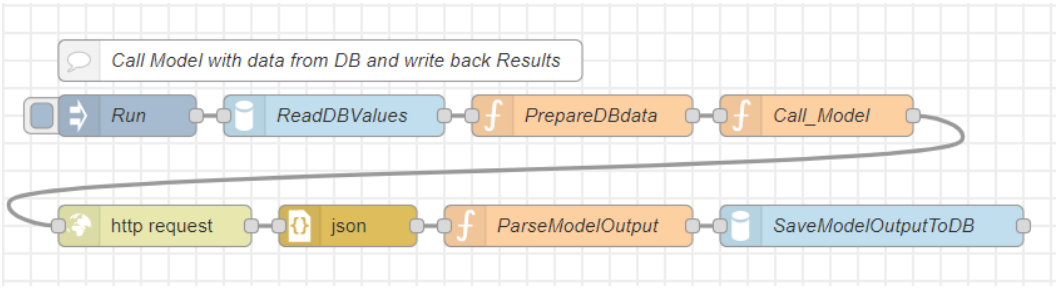

Figure 3. Example of Node-RED data flow editor

Numerous papers and research project already exit outside of this project at a theoretical level and having this implementation and evaluation framework is a step to take the theories toward further testing and finally implementing actual control of treatment plants using new technologies.

With many models to integrate, strategies to evaluate and a complex platform it is important to start with getting the simplest model (or simply just present data) to fully work as a proof of concept before moving to more complex tasks. Hopefully the information within this paper can serve as a guide for others to more easily accomplish this.

5 Conclusions

In this study an integrated machine learning platform was implemented for a WWTP. Data was extracted every 15 minutes from the plant's historical database to a cloud storage. In the cloud storage data cleaning and fault detection was performed. The data was used to run models of the WWTP and create suggestions of control actions for the operators. It shows an important step towards implementation of advanced control in wastewater treatment. Further work is needed but it is possible in the future that advanced models could be run in the cloud to directly control wastewater treatment plants and optimize their performance.

6 Acknowledgment

The authors gratefully acknowledge the financial support from European Union's Horizon 2020 research and innovation program under grant agreement No 723523 through FUDIPO project (http://fudipo.eu/).

References

Jens Alex, Lorenzo Benedetti, Jb Copp, Krist Gernaey, Ulf Jeppsson, Ingmar Nopens, MN Pons, Leiv Rieger, Christian Rosen, and J-P Steyer. Benchmark simulation model no. 1 (bsm1). *Report by the IWA Taskgroup on Benchmarking of Control Strategies for WWTPs*, 01 2008.

Mogens Henze, Leslie Grady Jr, W Gujer, G. Marais, and T Matsuo. Activated sludge model no 1. *Wat Sci Technol*, 29, 01 1987.

HUGIN EXPERT A/S. Hugin. `https://www.hugin.com/`, 2021. Accessed: 2021-07-12.

Ulf Jeppsson, Marie-Noëlle Pons, Ingmar Nopens, Jens Alex, Jb Copp, Krist Gernaey, Christian Rosen, J-P Steyer, and Peter Vanrolleghem. Benchmark simulation model no 2—general protocol and exploratory case studies. *Water science and technology : a journal of the International Association on Water Pollution Research*, 56:67–78, 02 2007. doi:10.2166/wst.2007.604.

JS Foundation. Node-red. `https://nodered.org/`, 2021. Accessed: 2021-07-12.

Modelon AB. Modelon functional mock-up interface. `https://www.modelon.com/functional-mock-up-interface-fmi/`, 2021. Accessed: 2021-07-12.

Darko Vrecko, Krist Gernaey, Christian Rosen, and Ulf Jeppsson. Benchmark simulation model no 2 in matlab-simulink: Towards plant-wide wwtp control strategy evaluation. *Water science and technology : a journal of the International Association on Water Pollution Research*, 54:65–72, 02 2006. doi:10.2166/wst.2006.773.

A screening method for urban drainage zones

Tiina M. Komulainen[1] Tolli Lavrans Mørk[1] Ali Riyad Al-Shiblawi[1] Jakub Roemer[1,2]

[1]Department of Mechanical, Electronics and Chemical Engineering, Oslo Metropolitan University, Norway,
{tiina.komulainen, jakub.roemer}@oslomet.no

[2]AGH University of Science and Technology, Poland

Abstract

Due to climate change, the storms have intensified leaving the urban drainage system and wastewater treatment plants hard to tackle with the large water quantities. In this study we develop a data-based screening method to identify which drainage zones would benefit most of blue-green infrastructure to avoid spilling of uncleaned water. First the precipitation and drainage zone flow rate data are pre-processed and de-seasonalized to remove the flow rate due to consumer wastewater. Then, system identification is applied for the rain periods and transfer function parameters for first order plus time delay model are collected. The screening index is calculated from the transfer function model parameters. The results show that the system is very nonlinear, but the mean values for the screening index is statistically significantly different for the drainage zones included to this study. The screening index clearly separates the different types of drainage zones and gives a reasonable suggestion for which drainage zones should be considered further for implementation of blue-green infrastructure like nature-based solutions.

Keywords: dynamic modeling, system identification, urban drainage system, nature-based solutions, blue-green infrastructure, flood risk mitigation.

1 Introduction

It is expected that the climate change is going to have increasing impact on urban water resources. Currently, for the most European regions the rainfall patterns and temperature regimes are changing (Field, 2014). Precipitation frequency and temporal distribution leads to shorter but more intense rainfall events.

In rapidly expanding urbanization the urban drainage system and wastewater treatment plants are unprepared for treatment of large water quantities. This causes flooding in cities and disposal of uncleaned water to nearby sea/rivers/lakes. Flood damages the city buildings and polluted urban water systems have high economical and ecological consequences for the citizens and marine life (Leal Filho, 2019).

In recent years the idea of nature-based solutions (NBS) has gained significant attention for storm water mitigation (Dolman, 2020, Kalsnes, 2019). Nature-based solutions are blue-green infrastructures implemented at the human habitats (Somarakis, 2019). The main goal of NBS is to support sustainable and resilient city growth, mitigate climate change and restore the local ecosystem. Nature-based solutions can potentially be used for flood risk mitigation and water quantity and quality improvement. The principal of NBS lies in natural process of water evapotranspiration, phytoremediation and infiltration (Haase, 2015, Beloqui, 2020). Rainwater, instead of being transported directly into the storm channels grid, can be accumulated in NBS and slowly disposed hours or even days after the precipitation event. Thanks to this ability, the water runoff peak can be flattened and prolonged. Lowered runoff amplitude is easier to handle by wastewater treatment facilities, which makes the city more flooding resilient (Eisenberg 2018).

There are many types of NBS dedicated to support surface water regulation function in the city areas. The most effective are arboretums, residential parks, green roofs (intensive/smart), detention ponds (dry), retention ponds (wet), biofilters and mounds (Somarakis, 2019, Eisenberg, 2018). Recently, green roofs have been implemented at Fossum Terrasse in Bærum. At the moment the constructed wetlands are built at Hovseterdalen in Oslo.

1.1 Drainage zones and storm water problem

A drainage zone is an area of land, forest, buildings, infrastructure and a subterranean urban drainage pipeline network that leads the rainwater and wastewater from households towards a joint urban water tunnel. The joint urban water tunnel collects water from the drainage zones in Oslo, Bærum and Asker municipalities and leads the water to the Veas wastewater treatment plant. In Asker municipality the rainwater is flowing in its own pipelines whereas in many parts of Oslo and Bærum the rainwater and household water are flowing in the same subterranean pipelines. During heavy rain the joint urban water tunnel

can get filled up with water, and the excess uncleaned water will be spilled to the Oslo fjord. This is a major threat to the marine life the Oslo fjord and closes of beaches along the fjord.

1.2 Problem statement and research questions

More targeted efforts are needed to reduce disposal of uncleaned water to the Oslo Fjord during heavy storms. The Veas wastewater treatment plant and municipalities at Oslo, Bærum and Asker have challenged researchers at OsloMet to develop a screening method that can pinpoint drainage zones which have the greatest influence to the excess water into the Veas tunnel during rainy periods.

We aim to develop a screening method based on dynamic characterization of the drainage zones using collected time series. The screening method should illustrate which drainage zones could benefit most of blue-green infrastructures by slowing down the water flow through the drainage zone, and thereby flattening the flow profile into the tunnel.

Our research questions are: RQ1: Is it possible to approximate the dynamic behavior of water flow through a drainage zone with a simple time-series model? RQ2: Can the drainage zones be classified using an index based on the dynamic model parameters?

Table 1. Bærum drainage zones with precipitation stations, number of inhabitants and maximum values for precipitation and flow sensors.

Drainage zone	Precipitation station	Persons	Max precipitation [mm]	Max flow [L/s]
Bjørne-gård	Gjettum_II	914	15.4	92.2
Sør-aasen	Aurevann	2882	8.9	208.7
Evjebakken	Gjettum_II	2072	15.4	250.8
Jar	Øvrevoll	8497	6.0	341.8
Sand-vika	Bærum_kommunegården	9264	12.3	435.9
Ha-mang	Økeriveien, Bærums_verk,Øvre_Toppenhaug,Gjettum_II	34582	17.0	915.1
Sta-bekk	Storøya	9358	6.1	966.5

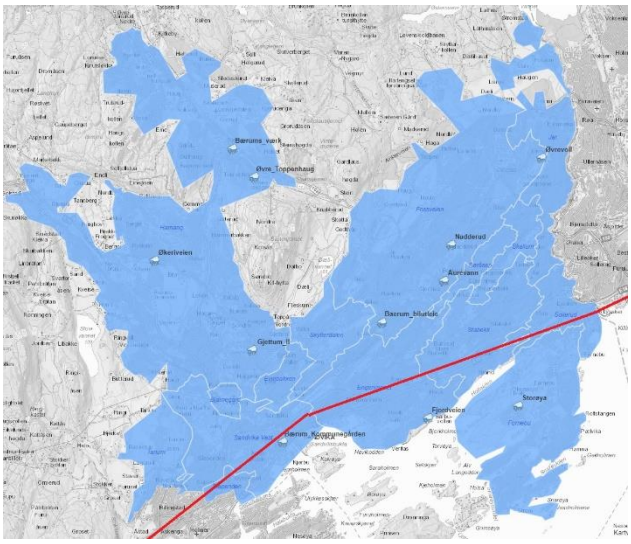

Figure 1. Drainage zones (blue text) and precipitation stations (black text) in Bærum municipality. The joint urban water tunnel (red line) is built along the coast.

1.3 Scope of the study, Bærum municipality

The scope of this case study is the urban drainage system in Bærum, because the data set for this area is more complete than data sets collected for Oslo and Asker municipalities. The drainage zones, the precipitation stations, the number of inhabitants and the maximum values for the precipitation and flow measurements are given in Table 1 and Figure 1. The drainage zones omitted from this study due to missing data are Engervann, Fossveien, Fornebu, Skallum Skytterdalen, Slependen, and Tanum.

Rainwater is measured at precipitation stations, located in different drainage zones. Some drainage zones do not have its own precipitation station, and therefore, the closest precipitation measurement is used to estimate the rain fall in this zone. The rainwater and wastewater from one drainage zone are led into an inlet point to the joint urban drainage tunnel. The flow measurement device is installed at this inlet point.

2 Modeling of urban drainage systems

Hydrology refers to water, its occurrence, distribution, circulation as well as its physical and chemical properties (Marshal, 2013). Hydrological phenomena like rainfall, interception, infiltration, transportation, evaporation or storage are components of water cycle. There are many hydrologic models trying to represent water behavior. These models can be divided into three categories, depending on used parameters and physical principles applied (Devia, 2015).

First group consists of empirical models representing a data-driven approach. Water behavior modeling is based on finding relations between input (usually rainfall) and output (water runoff) without taking into

account actual the complex physics. The second group covers parametric-based models. These models try to represent the water runoff behavior with a multi-parameter equations. The parameters are usually obtained empirically and calibrated for each specific case. The physically based models are the third group. Their principle of operation is based on modeling physics behind hydrological processes. The water dynamics is usually represented with differential equations.

2.1 Physically based approach

MIKE SHE is one of the most widely used physically based hydrological models (Ma, 2016). The principle of operation lies in dividing the watershed into a unit grid horizontally for discrete calculations of complex terrain. The relationship between the ecohydrological processes (precipitation, evaporation etc.) and water runoff is calculated through continuity and motion equations (Zhou, 2013). The MIKE SHE contains three modules: water body motion module, water quality module and water balance tool, as well as several submodules, including snow melting module, overland flow module, rivers and lakes module, evapotranspiration module, unsaturated flow module and saturated flow module. The accurate calculations require selection of proper set of modules. It is a complex and challenging task depending on multidisciplinary skills.

2.2 Parameter based approach

SWIMM model is one of well-recognized parameter-based models used for dynamic rainfall-runoff simulation (Rossman, 2015). It can be used for single event as well as for long-term simulations. The modeled land area is divided into subcatchment areas, which are characterized by different the soil types and ground covers. The SWIMM model collects the subcatchment areas that generate rainwater runoffs as a result of precipitation. The SWIMM model then simulates the water transportation through pipes and channels. Water storage and treatment devices (pumps and regulators) can be also implemented. The SWIMM can model both runoff quantity and quality, separately for each subcatchment area, pipe or channel.

2.3 Data-driven approach with system identification

System identification is a data-driven method to create models from time-series data (Ljung, 1999). The system identification toolbox in Matlab uses subspace algorithm to identify parameters for models with pre-defined structures such as transfer functions, state-space models and many more.

2.4 The idea for simplified modeling for urban drainage zone

In order to develop a simple screening method, we need to characterize the dynamic behavior between precipitation and flow. We assume that the hydrological system, i.e. the soil and built infrastructure, in a drainage zone can be approximated as a first order transfer function system. Further we assume that the hydraulic system, i.e. the water flow through the subterranean pipelines in a drainage zone, can be approximated as plug-flow. This gives us a first order plus time delay (FOPTD) transfer function model structure between precipitation P(s) and flow F(s) to the joint urban drainage tunnel:

$$F(s) = \frac{K_p}{T_p s+1} \cdot e^{-T_d s} \cdot P(s) \qquad (1)$$

Where K_p is the process gain, T_p is the time constant and T_d is the time delay.

2.5 The idea for screening method for urban drainage zones

Assume that the drainage zones can be modeled with FOPTD system and the dynamic characteristics of the precipitation are similar to a pulse signal. Then, the rainwater flow from each drainage zone will be a pulse response. Further, assume that these pulse responses from each the drainage zone can be summed up using the principle of superposition. The total flow profile into the joint urban water tunnel is then the sum of the flow profiles from each drainage zone.

Now, the drainage zone with the largest process gain and the shortest time delay and shortest time constant, will have the sharpest flow profile that contributes most to the problem of overflow in the joint urban water tunnel.

We suggest to construct the screening index for drainage zone i, S_i, as follows:

$$S_i = \frac{K_{pi}}{T_{pi}+T_{di}} \qquad (2)$$

Drainage zones with high Si have most aggressive flow profile whereas drainage zones with low Si index have smoother flow profile.

Constructing blue-green infrastructure to drainage zones with high Si would flatten the total flow curve into the joint urban water tunnel. Thus, inhibiting the sharp flow peaks into the tunnel that forces the excess water to the Oslo fjord.

3 Materials and methods

3.1 Data collection

The data was collected from Bærum municipality during January 2018 – December 2019 using resolution of 10 minutes. The data consists of precipitation measurements in [mm] at the 11 precipitation stations and flow rate measurements in [L/s] at the Veas tunnel inlet points from the drainage zones.

3.2 Software tools

Matlab R2021a with system identification toolbox was used for data pre-processing and modeling.

3.3 Data pre-treatment

The dataset contains flow rate and precipitation measurements collected by several stations in Bearum municipality. Some of the drainage zones do not have a measuring station. Thus, the first data pre-treatment step was to assign the closest precipitation measurement to those areas which do not have their own station. In the next step, all winter months (November-April) were excluded from further processing. Snow melting impact is hard to evaluate and including winter months could affect further modelling. In the next step, data were synchronized in the manner that flow rate measurement sampling was changed from 1/minute to 1/10minutes.

3.4 Removal of seasonal trends

The joint urban drainage tunnel collects stormwater, but also municipal wastewater. The municipal wastewater flow with daily and weekly variation had to be removed to improve the data quality for modeling. In the first step, the data was split into four quarters: May 2018 to June 2018, August 2018 to October 2018, May 2019 to June 2019 and August 2019 to October 2019. In the next step, a full no-rain week was manually selected from each period. It was assumed that no-rain week is a good representation of municipal wastewater production. Lastly, for each period, no-rain week was subtracted from the data.

3.5 Selection of data for modeling

After data pre-treatment and removal of seasonal trends, the rain periods were chosen manually. It was decided that only periods at least 2 hours long will be taken into account for further analysis.

3.6 System identification procedure

System identification toolbox was used to calculate the dynamic parameters of each drainage zone. The first order transfer function with delay was chosen (2). Parameters were calculated independently for each rain period. Initial result assessment shows that some of calculates parameters has non-physical values. Therefore, all the transfer functions with very large Kp or very large Tp were removed, as these are seen not sensible considering the geographical distances between the drainage zones and the joint urban water tunnel. Transfer functions with negative Kp were also removed as these are seen physically impossible.

3.7 Screening index and statistical analysis

The screening index was calculated based on the transfer function parameters Kp, Tp and Td for each of the rain periods in each of the drainage zones. The box plots were prepared for each drainage zone. The screening indices were then imported to SPSS, and the null hypothesis of equal means between the different drainage zones was tested with Student T-test.

3.8 Multivariate correlation analysis

Multivariate analysis was applied to find linear corrections between the transfer function model parameters (Kp, Tp and Td) and features extracted from the precipitation data (total accumulated precipitation during rain shower, maximum precipitation, and duration between rain showers). The Matlab Statistics and Machine Learning toolbox, Regression Learner App with different linear regression models, regression trees and support vector machines were used.

4 Results

This section shortly presents the results for data pre-processing and system identification, and the results for the proposed screening index.

4.1 Results for system identification

The characterization of the system dynamic model parameters Kp, Tp and Td for the different drainage zones are given in Table 2. The box plots are given in Figure 2 for the process gains, Kp, Figure 3 for the time constants Tp and Figure 4 for the time delays Td.

The results for process gain Kp between precipitation and tunnel inlet flow rate seem reasonable; Large drainage zones like Sandvika, Hamang, Stabekk “harvest” more rain and therefore they have larger process gains than small drainage zones like Bjørnegård and Evjebakken.

The results for time delay Tp between precipitation and tunnel inlet flow rate seem reasonable; rain seeps faster through drainage zones with lots of buildings, roads and infrastructure like Sandvika than drainage zones with lots of private houses, parks and forest like Hamang.

The results for time delay Td between precipitation and tunnel inlet flow rate seem reasonable; Drainage zones close to the joint urban water tunnel inlet like Sandvika and Stabekk have shorter time delay than drainage zones further away like Søraasen, Jar and Hamang.

The standard deviation for all the dynamic parameters is high, which can also be observed from the box plots. This indicates that water flow through the urban drainage zone is a very nonlinear phenomenon.

Two approaches to “linearize” the system were attempted. First, to preprocess the input data by taking an inverse of the precipitation data $p(t)^{-1}$ before system identification, and second, by taking a square root of the precipitation data $p(t)^{(1/2)}$ before system identification. Both of these preprocessing approaches resulted in similar variation in the dynamic process parameters Kp, Tp and Td.

Table 2. Number of rain periods included N, average value and standard deviation for dynamic model parameters Kp, Tp and Td for the drainage zones.

Drainage zone	N	Kp_ave	Kp_std	Tp_ave	Tp_std	Td_ave	Td_std
Bjørnegård	63	5,5	3,9	35	82	54	97
Søraasen	61	392	907	439	925	86	105
Evjebakken	71	127	159	172	439	25	61
Jar	52	684	1164	480	1340	40	52
Sandvika	52	225	188	82	171	24	37
Hamang	69	511	868	409	721	39	51
Stabekk	61	765	810	178	227	26	52

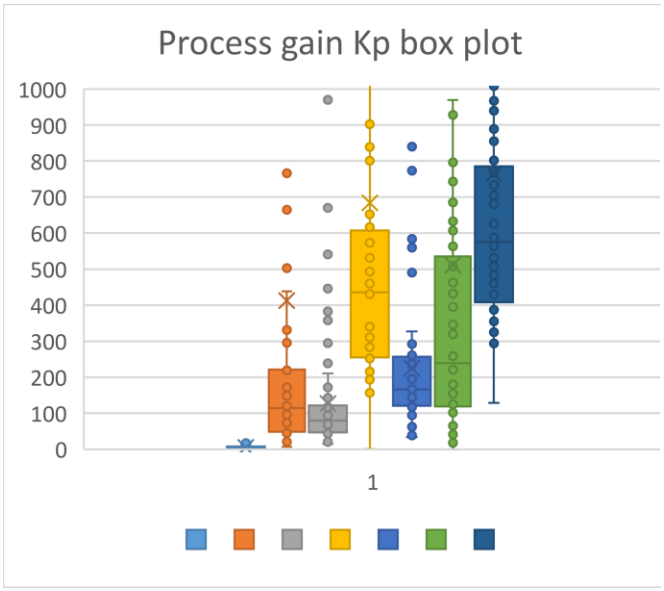

Figure 2. Box plots for identified process gain K_p in drainage zones Bjørnegård, Søraasen, Evjebakken, Jar, Sandvika, Hamang, Stabekk.

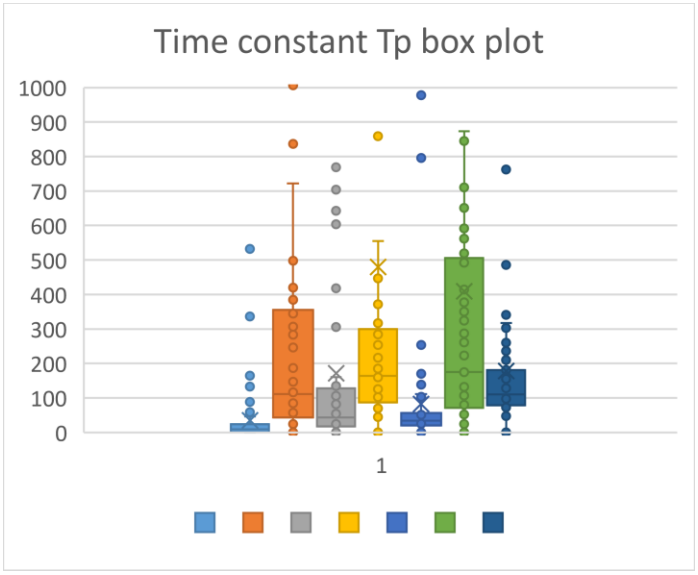

Figure 3. Box plots for identified time constants T_p in drainage zones Bjørnegård, Søraasen, Evjebakken, Jar, Sandvika, Hamang, Stabekk.

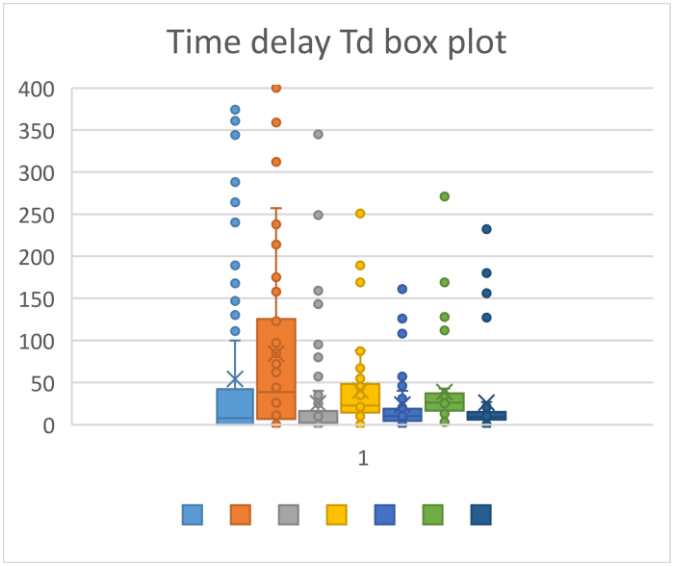

Figure 4. Box plots for identified time delays T_d in drainage zones Bjørnegård, Søraasen, Evjebakken, Jar, Sandvika, Hamang, Stabekk.

4.2 Results for multivariate analysis of the dynamic parameters

In order to explain the variation in the dynamic parameters Kp, Tp and Td, different explanatory variables were constructed from the available data, i.e. the precipitation measurements. To characterize the rain intensity, two indicators for each rain period j were constructed: Maximum precipitation during the rain period $P_{max,j}$, and total rain during the corresponding rain period $P_{tot,j}$. To characterize the water absorption capacity of the soil, one indicator was constructed, dry period before the rain period $T_{dry,j}$.

Linear regression models, regression trees and support vector machines in Matlab regression Learner app were applied to find linear correlations between dynamic parameters and constructed explanatory variables of the drainage zones, but no correlations with R^2 index over 0,3 were found. It is suggested to find other explanatory variables to characterize the water flow through the drainage zone and to use nonlinear multivariate methods such as neural networks to find the correlation.

4.3 Results for screening index

The screening index was constructed using the identified dynamic process parameters K_p, T_p and T_d for each drainage zone. The screening indices are presented in Figure 5 and the average values and standard deviations are given in Table 3. The standard deviation for the screening indices Si are much smaller than for the dynamic process parameters K_p, T_p and T_d. The results for screening index Si seem logical, small drainage zones like Bjørnebård and Søråsen and drainage zones further away from the joint urban water tunnel like Hamang have smaller S_i index, and therefore contribute less to the excess water in the joint urban water tunnel. Larger drainage zones close to the urban water tunnel like Sandvika and Stabekk have large Si index, and therefore contribute more to the excess water in the joint urban water tunnel. Based on the Screening index, we suggest that possibilities for blue-green infrastructure will further be investigated in these two drainage zones.

SPSS was used to run t-test on equality of means between two drainage zones. The null hypothesis states that the means of two drainage zones are equal. Equal variances are not assumed. The decision criteria are: For a two-tailed test with n-2 degrees of freedom, the level of significance is 0.05. The results of the independent samples t-test are given in Table 4. As the t-test values are much higher than 1.96 or much lower than -1.96, the null hypothesis is proven false. Thus, the mean values for screening indices between the Bærum drainage zones are statistically significantly different.

Table 3. Number of rain periods included N, average value and standard deviation screening index Si for the different drainage zones.

Drainage zone	N	Si_ave	Si_std
Bjørnegård	63	0,3	0,3
Søraasen	61	0,7	0,7
Evjebakken	71	1,3	0,9
Jar	52	2,2	1,7
Sandvika	52	3,0	1,6
Hamang	69	1,2	0,8
Stabekk	61	4,3	1,5

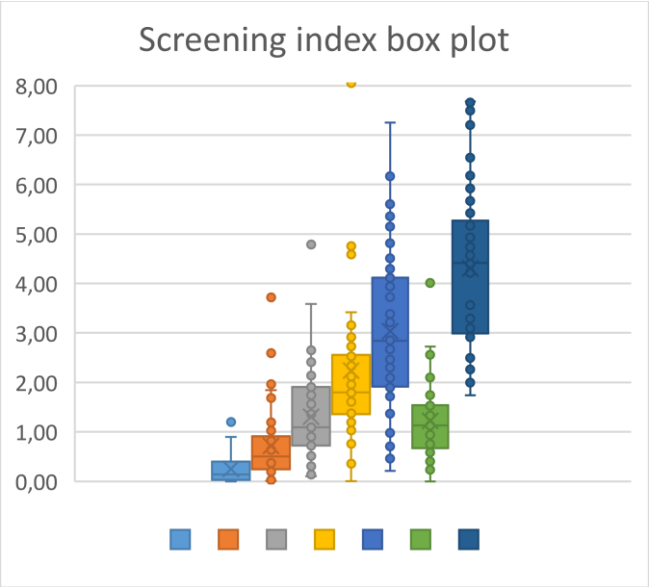

Figure 5. Box plot of the proposed screening index S_i for drainage zones Bjørnegård, Søraasen, Evjebakken, Jar, Sandvika, Hamang, Stabekk.

Table 4. T-test results for null hypothesis testing equality of means between drainage zones.

Drainage zone1	Drainage zone2	t	df	2-tail sig.	Mean diff	Std diff
Bjørne-gård	Søraasen	-5,1	78	0,000	-0,48	0,09
Søraasen	Evjebakken	-4,2	129	0,000	-0,58	0,13
Evjebakken	Jar	-3,7	71	0,000	-0,93	0,25
Jar	Sand-vika	-2,5	102	0,016	-0,79	0,32
Sandvika	Hamang	7,3	71	0,000	1,8	0,25
Hamang	Stabekk	-14	90	0,000	-3,1	0,22
Stabekk	Bjørne-gård	20	64	0,000	4,1	0,20
Stabekk	Sandvika	4,5	106	0,000	1,27	0,30

5 Discussion

This is study is first stage in modeling of nature-based solutions at urban drainage zones. To answer our first research question (RQ1), we applied system identification to the available, pre-processed and de-seasonalized data sets consisting of precipitation and drainage zone outlet flow rates. We conclude that it is possible to approximate the dynamic behavior of water flow through a drainage zone with first order plus time delay transfer function model. The model parameters highly nonlinear, and dependent on explanatory variables that were not included into the data collected.

To answer our second research question (RQ2), we introduced a screening index calculated with the dynamic parameters of transfer function model. The screening index was applied to all the rain periods at all of the drainage zones. The mean values of the screening index were statistically significantly different from each other. The classification of the drainage zones to high contributing and low contributing areas was based on the size of screening index. Small areas and areas far away got relatively small indices whereas large areas close to the water inlet point got relatively high indices. We conclude that the drainage zones can be classified using the proposed screening index. The drainage zones with high screening index should be considered for construction of blue-green infrastructure like NBS to avoid water spill to Oslo fjord.

6 Conclusions and further work

This study is a proof of concept that the available measurements, precipitation and drainage zone outlet flow rates, are enough to create a screening index that can separate the flow profiles of the different drainage zones according to their contribution to the excess water in the joint urban drainage tunnel. The simple dynamic modeling method with screening index is less accurate than traditional physically based and parameter based modeling methods, but a much faster and more cost-effective method to classify the drainage zones.

We suggest to continue the work by collecting data for the rest of the drainage zones in Bærum and the drainage zones in Oslo, and repeating the analysis for these drainage zones. As this is a data-driven approach, it is suggested that the method will be applied for large amounts of data, i.e. long time series of at least one year.

The next goal in the project is dynamic modeling of the different NBS approaches and testing of the effect of NBS for the Bærum and Oslo drainage zones. We are suggesting to create a simple NBS model that can evaluate the performance of the NBS for a certain size and type of drainage zones. Further we propose to apply multi-criteria analysis to consider the effect for excess water and the costs for building and maintaining the NBS at high risk drainage zones.

Acknowledgements

The authors greatly thank the VEAS senior manager Hilde Johansen for the project idea, contacts to the municipalities and active participation in the data collection. VEAS system engineer Jonas Pettersen and Bærum municipality engineer Anne Ellekjær Stavang are greatly tanked for collecting the data from their respective data systems and visualization of the measurement stations. This work has been also supported by EU Water JPI Project “Research-based Assessment of Integrated approaches to Nature-based SOLUTIONS (RainSolutions)” 2019-2021, Reference Number: WaterJPI-JC-2018_11. We would also like to thank Alida Alves Beloqui for insights in her modeling work at Wageningen university.

References

V. Barros, et all. Climate Change 2014: Impacts, adaptation, and vulnerability. Part B: Regional aspects. Contribution of working group II to the fifth assessment report of the Intergovernmental Panel on Climate Change. Cambridge University Press, Cambridge, United Kingdom and New York, NY, USA, pp. 1-32. 2014.

A. Beloqui. Combining Green-Blue-Grey Infrastructure for Flood Mitigation and Enhancement of Co-Benefits. CRC Press. 2020. doi.org/10.1201/9781003041818

G. Devia, B. Ganasri, G. Dwarakish. A review on hydrological models. Aquatic Procedia, 4: 1001-1007. 2015. doi.org/10.1016/j.aqpro.2015.02.126

N. Dolman. Nature-based solution in cities, In Proceedings - GPSC Resource Team Webinars. 2020. doi.org/10.13140/RG.2.2.20996.07049

B. Eisenberg, B. Polcher. Nature-based solutions – Technical Handbook. In UNaLab Project, Deliverable D, 5. 2020.

D. Haase. Reflections about blue ecosystem services in cities. Sustainability of Water Quality and Ecology 5: 77-83. 2015. doi:10.1016/j.swaqe.2015.02.003

W. Filho, et al. Assessing the impacts of climate change in cities and their adaptive capacity: Towards transformative approaches to climate change adaptation and poverty reduction in urban areas in a set of developing countries. Science of The Total Environment, 692: 1175-1190. 2019. doi.org/10.1016/j.scitotenv.2019.07.227

B. Kalsnes, V. Capobianco. Nature-based solutions. Landslides Safety Measures. SINTEF Community, Høgskoleringen 7 b, PO Box 4760 Sluppen, N-7465 Trondheim. 2019.

L. Ljung. System identification: theory for the user (2nd ed.). Prentice Hall PTR. 609 p. 1999.

L. Ma, Ch. He, H. Bian, L. Sheng. MIKE SHE modeling of ecohydrological processes: Merits, applications, and challenges. Ecological Engineering, 96: 137-149. 2016. doi.org/10.1016/j.ecoleng.2016.01.008

S. Marshal. Reference Module in Earth Systems and Environmental Sciences. Hydrology. 2013. doi.org/10.1016/B978-0-12-409548-9.05356-2

L. Rossman and W. Huber. Storm Water Management Model Reference Manual Volume I, Hydrology. U.S. EPA Office of Research and Development, Washington, DC, EPA/600/R-15/162A, 2015.

G. Somarakis, S. Stagakis, N. Chrysoulakis. Thinknature Nature-based solutions Handbook. 2019. DOI:10.26225/jerv-w202

X. Zhou, M. Helmers, Z. Qi. Evaluation of the MIKE SHE model for hydrologic modeling in a small agricultural watershed. Applied Engineering in Agriculture. 2013. DOI 10.13031/aea.29.9568

An Individual-based Model for Simulating Antibiotic Resistance Spread in Bacterial Flocs in Wastewater Treatment Plants

Svein H. Stokka[1], Roald Kommedal[2], Kristian Thorsen[1], Cansu Uluseker[2]

[1]Department of Elec. Eng. & Com. Sci., University of Stavanger, 4036 Stavanger, Norway

[2]Department of Chem. Biosci. & Env. Eng., University of Stavanger, 4036 Stavanger, Norway

cansu.uluseker@uis.no

Abstract

Wastewater treatment plants (WWTPs) receive wastewater that carries a variety of pollutants, including antibiotics and antibiotic-resistant bacteria. The potential for horizontal gene transfer of resistance through conjugation – direct cell-to-cell transfer of genes carried on a plasmid – is high in WWTPs because of high cell density and residence time in bacterial flocs. To better understand how resistance spreads by growth and conjugation in such flocs, we propose an individual-based model with a solver algorithm for dynamic simulation. Our model includes only the most relevant bacteria properties and functions such as movement, growth, division, gene transfer, and death. Simulation of our model suggests that resistance can increase by conjugation at the early growth stages of a floc and that the overall rate of gene transfer depends on floc size. Results indicate that our simple model can be a useful tool for examining how gene exchange and heterogeneity contribute to the spread of antibiotic resistance in bacterial flocs.

Keywords: antibiotic resistance, wastewater treatment, individual-based model, simulation

1 Introduction

Antibiotics are important pharmaceuticals for the treatment of infectious bacterial diseases (Hellweger *et al.*, 2011; Sabri *et al.*, 2020). Overuse and misuse of antibiotics have led to the increased development of antibiotic resistance (AR) (Duarte *et al.*, 2019). AR was estimated to be responsible for at least 700 thousand deaths in 2014 and is estimated to claim 10 million lives yearly by 2050, more than other major diseases such as diabetes and cancer (O'Neil, 2016).

Biological wastewater treatment plants (WWTPs) are environments with high potential importance for the spread of AR (Uluseker *et al.*, 2021). WWTPs contain rich microbial populations with very high cell densities (around 10^8 – 10^{10} cells per mL) supported by high nutrient availability (Jenkins and Wanner, 2014). Raw sewage originates from various sources and can contain large numbers of resistant bacteria (Hassoun-Kheir *et al.*, 2020). Studies have shown that resistance levels stay high throughout WWTPs (Amarasiri *et al.*, 2020; Gao *et al.*, 2012). Most resistant bacteria are fortunately removed together with other microorganisms during the final settling and sedimentation stages; the concentration of resistant bacteria in the sludge, however, can be as high as in the inlet raw sewage (Gao *et al.*, 2012). Resistant bacteria can proliferate in WWTPs, and they can spread their resistance genes to nonresistant bacteria through horizontal gene transfer (HGT). This is worrisome as resistance can spread from pathological bacteria that arrive with the wastewater to aquatic and soil bacteria that are well adapted to both the WWTP environment and to river and soil environments that receive WWTP effluents and biosolids.

Bacterial conjugation is a natural process of plasmid transfer between bacteria. A bacterium that contains a plasmid with one or several resistance genes can by conjugation transfer a copy of this plasmid to other bacteria, but only to bacteria that are compatible with the plasmid and the biological conjugation process (Koraimann *et al.*, 2004). Plasmids that can be shared through conjugation are called conjugative plasmids, and bacteria that can receive and transfer a conjugative plasmid are said to be competent. Such plasmids can carry antibiotic resistance genes (ARGs) and replicate in a wide range of host bacteria (Krone *et al.*, 2007).

In order to address the effect of bacterial growth and conjugation on the spread of AR in WWTP bacterial aggregates, we have designed an individual-based model (IbM) where each bacterium cell is a single and discrete entity that has its own internal state and that interacts only with its closest neighbours. Our model captures local heterogeneity and local interactions and can be used to simulate how resistance genes are transferred by conjugation within a bacterial floc. The IbM is constructed as a minimum model but includes key processes to capture the spread of ARGs.

2 Modelling

Individual bacteria are in the model placed in a *bacteria position grid* where each point in the grid corresponds to a position in the environment. There is also a substrate grid that is used to keep track of the concentration of the growth-limiting substrate, S, at each location and to model how substrate diffuses into the bacterial floc. Individual bacteria are described by their main processes: substrate uptake and cell growth,

reproduction, and cell death. Individual bacteria can interact with neighbours by conjugation of resistance plasmid and displacement (shoving), which happens as bacteria grows. The model is developed with a minimum of complexity to be suitable for simulating the spread of AR in a growing floc. It is implemented according to the Overview, Design and Details (ODD) standard protocol proposed by Grimm *et al.* (2006) and implemented in MATLAB.

Each bacterium has the following state variables: - position *P*, the bacterium's current position in the environment; - cell size *X*, the current dry mass of the bacterium; - resistance *R*, indicating whether the bacterium is resistant or not; - conjugation compatibility *C*, indicating whether the bacterium has the molecular machinery for horizontal gene exchange; - and remaining recovery time *T*, indicating the remaining recovery time after a conjugation event, i.e., the time before a donor or receiving bacterium again is capable of exchanging genetic material.

Our algorithm for simulation of bacterial growth and resistance gene transfer starts with individual bacteria being placed randomly in a defined region within the environment. This region represents the bacterial floc. A selected number of the cells are initialized, some with and some without resistance. Resistant bacteria are defined as carriers of a resistance plasmid. The substrate grid is also initialized. The algorithm then starts simulating the temporal evolution of the floc by an outer loop where shoving of overlapping bacteria and substrate diffusion occurs. For each temporal iteration, an inner loop tracks through all the individual cells. The algorithm is summarized in the flow chart in Figure 1 and model parameters are shown in Table 1.

The algorithm is explained in detail in the following:

Cell movement: Bacteria in the floc are considered non-motile, i.e., they do not move actively. Displacement of bacteria from shoving due to growth and division is implemented by a shoving mechanism based on Kreft *et al.* (2001). The bacteria are considered as hard spheres in a 2-dimensional plane. The radius of a bacterium is calculated as:

$$r = \sqrt[3]{\frac{3X}{4\pi\rho}} \tag{1}$$

where X is the cell size (in dry mass) and ρ is the density of the bacterium.

The overlap distances d_i^j from bacterium i to bacterium j *is* then calculated by using the formula:

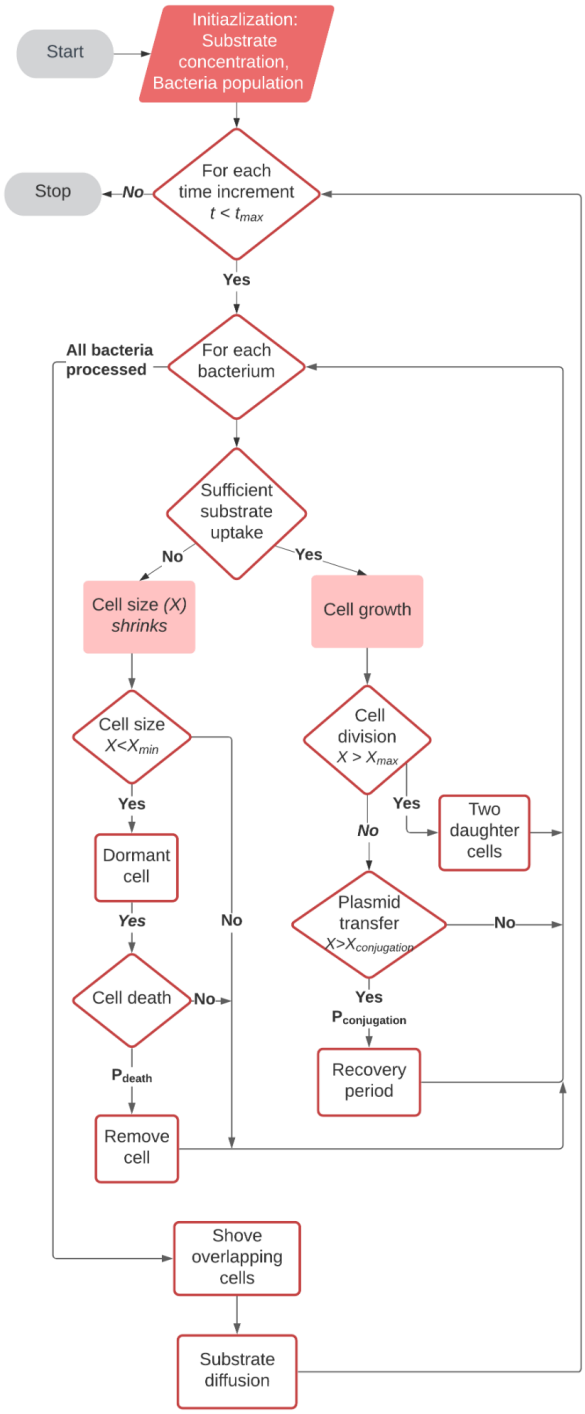

Figure 1. Flow chart of the simulation algorithm. Division, gene exchange, shoving and death are probabilistic events that depend on the properties of the individual cell and its neighbours. See the main text for a detailed explanation of the different steps.

$$d_i^j = kr_i + r_j - \left|\left|P_i - P_j\right|\right|_2 \tag{2}$$

where P_i and P_j are the position coordinates of bacterium i and j respectively, and k is a constant that accounts for maximal bacterial density or as Kreft *et al.*

(2001) states, the minimum spacing. The shove vector for bacterium i is then calculated as:

$$\Delta P_i = \sum_{j \in G_i} d_i^j \frac{P_i - P_j}{\left|\left|P_i - P_j\right|\right|_2} \quad (3)$$

where G_i is the set of bacteria that overlap with bacterium *i*, i.e., all bacterium *j* for which the overlap distance d_i^j is positive.

The maximum distance between bacteria that can have a positive overlap distance is $(k+1)r_{max}$. Since only positive overlap distance is needed in the shoving algorithm, all the potential members of G_i is found by only checking bacteria localized at grid points in the bacteria location grid that have a distance less than $\frac{(k+1)r_{max}}{2}$ away from the grid point containing bacterium *i*. The grid resolution is specified so that the 8 connected neighbourhood grid points contain all potential members of G_i.

Substrate diffusion: The substrate grid is initialized with a given substrate concentration at each point. The substrate is used during bacteria growth and a part of the bacteria dry mass is returned as a substrate when bacteria die. Therefore, the substrate concentration (in a location) is not constant, and the substrate will diffuse towards lower concentrations. A simple diffusion algorithm based on Kreft *et al.* (1998) is used where a 2-dimensional filter *DF* is used to calculate the transfer of the substrate from each point in the grid to the 8 adjacent points.

$$DF = \begin{bmatrix} 1 & 4 & 1 \\ 4 & -20 & 4 \\ 1 & 4 & 1 \end{bmatrix} \quad (4)$$

The concentration at the border of the grid is kept constant and the substrate grid is updated according to:

$$S_{grid,t+1} = S_{grid,t} + d_k(DF * S_{grid,t}) \quad (5)$$

where d_k is a diffusion constant that accounts for the diffusion coefficient and the length of each time step and $*$ is the convolution operator.

Bacteria functions and interactions: At every time step each cell performs the following:

1. *Substrate uptake:* The bacterium takes up nutrients from the substrate grid corresponding to the bacterium's current position. The concentration in the substrate grid is immediately updated. The substrate uptake rate is determined by a saturable function that depends on substrate concentration and cell size according to Monod kinetics:

$$v = V_{max} X \frac{S}{K_m + S} \quad (6)$$

where V_{max} is the maximum uptake rate per unit of dry mass and K_m is the half-saturation constant.

2. *Growth and maintenance:* Nutrients taken up from the environment are used for cell growth with efficiency according to a yield constant *Y*. The maintenance rate, i.e., how much substrate is used for non-growth metabolism, is modelled to be linearly dependent on cell size. The total growth rate is given by:

$$\Delta X = Yv - k_{maintenance} X \quad (7)$$

Resistant bacteria are modelled to have a 1% lower growth yield than non-resistant bacteria due to the metabolic burden of producing resistance enabling proteins (Gregory *et al.*, 2008). The effect of the metabolic burden is that it reduces the growth rate and increases the generation time. The cell shrinks if the available nutrients are insufficient for growth.

3. *Dormancy and Death:* If the cell size is below X_{min} the cell is starved and becomes dormant – a state where growth and maintenance stop. At each time step, a dormant bacterium may die with probability P_{death}, in the algorithm determined by the generation of a random number.

4. *Division:* If the cell size is above the normal size of a full-grown cell, X_{max}, the cell divides. A neighbourhood position is randomly selected and the cell divides by displacing occupants of the neighbouring position. The cell divides into two daughter cells where both cells get 40% of the size of the mother cell, and the remaining 20% of the mother cell is divided randomly between the two daughter cells. This unequal size helps to disrupt synchronous growth in the model. If the mother cell is resistant there is a probability P_{loss} that resistance is not transferred to the daughter. Resistant bacteria are competent for conjugation and there is a chance $P_{competent}$ that nonresistant bacteria become competent for conjugation during cell division or when they are added to the environment.

5. *Gene exchange:* If the cell size reaches $X_{conjugation}$, which is 80% of full-grown size X_{max}, and the cell is resistant it might spread its resistance to a competent nonresistant cell in its neighbourhood (Park *et al.*, 2018). Plasmid transfer has been estimated to happen on average at a rate of 10^{-3} per individual cell-to-cell interaction (Gregory *et al.*, 2008). Each time step, each potential donor cell checks whether neighbourhood cells are competent and nonresistant. If they are, conjugation occurs with probability $P_{conjugation}$. Plasmid transfer to the receiving nonresistant bacterium happens instantaneously. Under the condition that conjugation occurs, there is a recovery time (*T*) before the donor and

recipient cell can transfer a new plasmid (Gregory *et al.*, 2008).

Table 1. Simulation parameters. References: [a] (Kreft *et al.*, 1998), [b] (Kreft *et al.*, 2001), [c] (Gregory *et al.*, 2008), [d] (Park *et al.*, 2018). The values for unreferenced parameters are arbitrarily decided under the condition that they are plausible compared to the value of other parameters and that they give a reasonable system response. All parameters are given in arbitrary units.

Parameter description	***Parameter Value***
Grid size	500x500
X_{min}, minimum cell size[a]	0.1
X_{max}, maximum cell size[a]	0.5
k, minimum spacing[b]	1.3
K_m, half-saturation constant	0.01
$k_{maintenance}$, maintenance rate	0.002
Y, yield constant[a]	0.4
Cost of resistance on growth[c]	1%
Plasmid transfer rate[c]	10^{-3} per interaction
$X_{conjugation}$, cell size for conjugation[d]	80% of X_{max}

3 Results

We will here present some results from using our model to simulate how resistance spreads through conjugation and growth in a growing bacterial floc. Three different simulations have been implemented to illustrate how the two factors recovery time and probability for competence affect the spread of resistance.

The first simulation describes a small floc that starts with equal amounts of ten resistant and ten competent nonresistant bacteria with parameters from Table 1 and a modest recovery time of 200 time steps. The probability for nonresistant bacteria to be competent is set to 20%.

The second simulation is similar to the first one except for a longer recovery time of 300 time steps with a similar 20% probability for competence. This simulation is set up to illustrate the importance of recovery time on the spread of resistance in the floc.

A final simulation is made to understand the specific effect of the probability for competence. The probability for nonresistant bacteria to be competent is set to 10% while keeping the recovery time similar to simulation 1, as 200 time steps.

Note that the system parameters are set in arbitrary units. Our intention is to illustrate the function and qualitative behaviour of the model and not necessarily to show results that have a one-to-one relationship in specific biophysical units. Quantifying the model parameters with proper biophysical units would require experimental data and we will leave this for future development.

3.1 Gene exchange and resistance

For the first simulation, the floc is set up to initially contain ten resistant and ten nonresistant competent bacteria. The probability for a bacterium being competent, $P_{competent}$, is set to 0.2 and the recovery time, T, is set to 200 time steps, which is higher than the typical division time. Figure 2 provides snapshots of floc development for resistant (red) and nonresistant bacteria (blue) and transconjugant bacteria (green) during simulation. In the early stages of floc development, conjugation occurs in most of the floc. At t=500 most of the floc has become resistant as shown in the population plot in the bottom right of Figure 2. Transconjugants, bacteria that have received a plasmid are marked green to express the frequency of conjugation in the floc. At the later stages of floc development (t > 1000) conjugation is limited and happens mainly in the intersection of resistant and nonresistant bacteria at the edge of the floc. This is because most of the bacteria inside the floc are already resistant and because nutrient limitations, illustrated by the background colour that changes from white to grey and black as the substrate concentration reduces, cause bacteria in the deeper part of the floc to become dormant. At t=1000 regions of nonresistant bacteria surrounded by resistant bacteria have emerged, primarily due to shoving. Moreover, transconjugant bacteria occur on the border of the protrusions. The increase in resistance is after t=1000 mostly from growth. At t=4000, conjugation stops playing any significant part since resistant and nonresistant bacteria form and grow on different protrusions.

The population plot to the bottom right of Figure 2 summarises the resistant and nonresistant bacteria population during the simulation. It is apparent that since the very beginning of the simulation, resistant bacteria population in the floc is higher than nonresistant bacteria. In this case, it is seen that the population of resistant bacteria increase even though the resistant cells have a higher metabolic burden and a reduced growth rate compared to nonresistant cells.

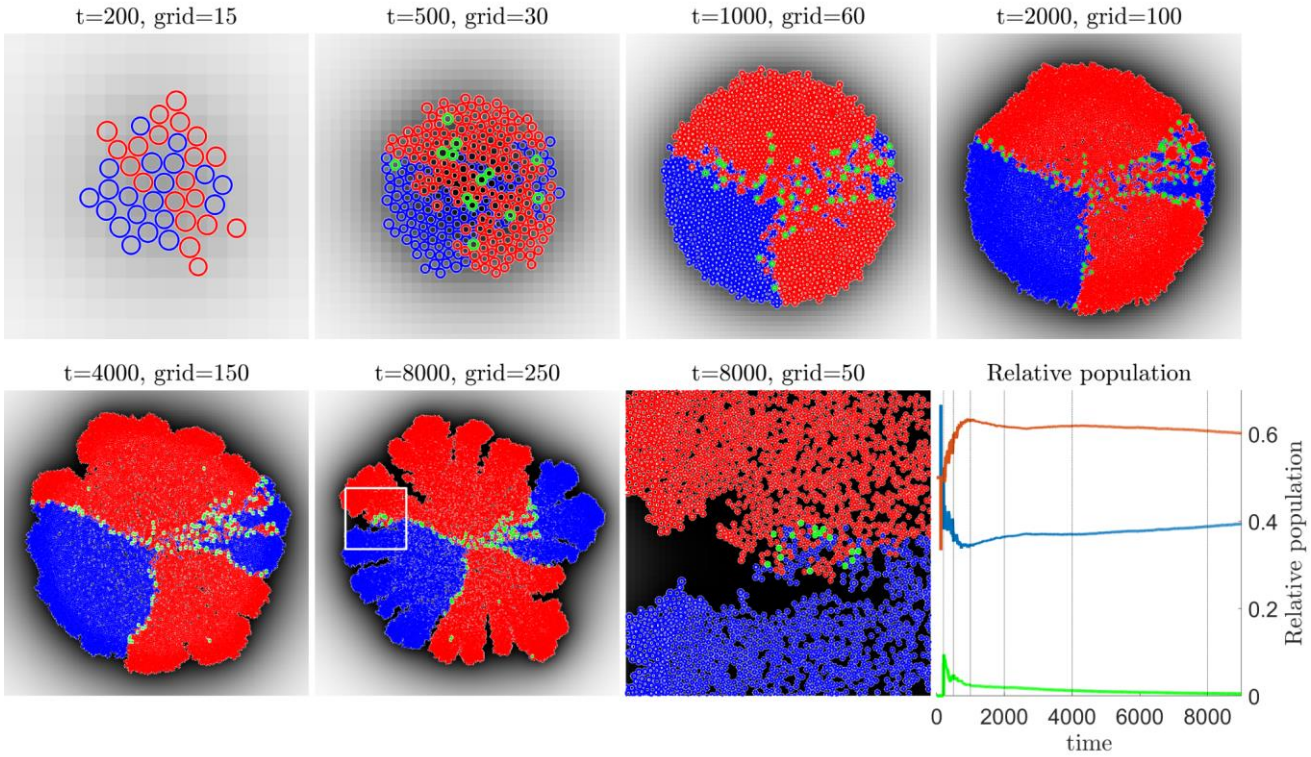

Figure 2. Population plot (lower right) and snapshots of floc development (other panels) from simulation 1. Timestep and size of the viewed grid are shown above the panels. Resistant (red), nonresistant bacteria (blue) and transconjugants (green). Substrate concentration is constant at the border of the nutrient grid and diffuses toward lower concentration, i.e., into the floc (grayscale, white is high concentration). Initially, at t=0 (not shown), ten resistant (red) and ten nonresistant bacteria are initialized in the middle of the environment. The probability of nonresistant bacteria being compatible is 20% while all resistant bacteria are competent. Conjugation recovery time is 200 time steps. At each time step, t, the simulation algorithm is run once. The rightmost snapshot of timestep 8000 (lower middle) shows a further zoomed in image of the floc shown in the snapshot to its left and illustrates how the resistant and nonresistant bacteria grow on separate protrusions.

3.2 Effect of longer recovery time

The second simulation is conducted to examine the effect of the recovery time on the spread of resistance. The recovery time, *T*, is increased to 300 time steps. Initial conditions and probability for competence are identical to the previous simulation, and ten resistant and ten nonresistant are placed in the middle of the environment at t=0. Figure 3 displays the snapshot results and the change in the bacteria population during the simulation. The results indicate that the relative bacteria populations are highly affected by the recovery time, *T*. As expected, increasing the recovery time decreases the resistant bacteria population in the floc.

The effect of conjugation is again larger in the early growth stages of the floc up till about time step t=2000. In the later growth stages, resistant and nonresistant populations grow in more distinct protrusions at the edge of the floc but a much larger proportion of bacteria are nonresistant in this simulation than in the previous.

The population plot in the bottom right of Figure 3 reveals that resistant bacteria have a minor advantage and that their population increases faster than nonresistant when the overall population is small. As the size of the floc increases, the intersection where conjugation can occur between resistant and nonresistant bacteria becomes smaller compared to the intersection between bacteria and substrate rich media where most of the growth occurs. The resistant population is noticeably higher than the nonresistant at t=2000, demonstrating the contributing effect of conjugation. As the floc grows, conjugation loses its effectiveness and the nonresistant bacteria population eventually overtakes the population of the resistant bacteria. Moreover, it is observed that a longer recovery time also affects the relative population of transconjugants. In simulation 2 there are fewer transconjugants than simulation 1.

3.3 Effect of lower probability for competence

The third simulation is performed to examine the effect of the probability for competence on the spread of resistance. The probability for a bacterium being competent, $P_{competent}$, is reduced to 0.1 and the recovery time, *T*, is kept 200 time steps as in simulation 1. Apart from this, simulation 3 uses the same initial

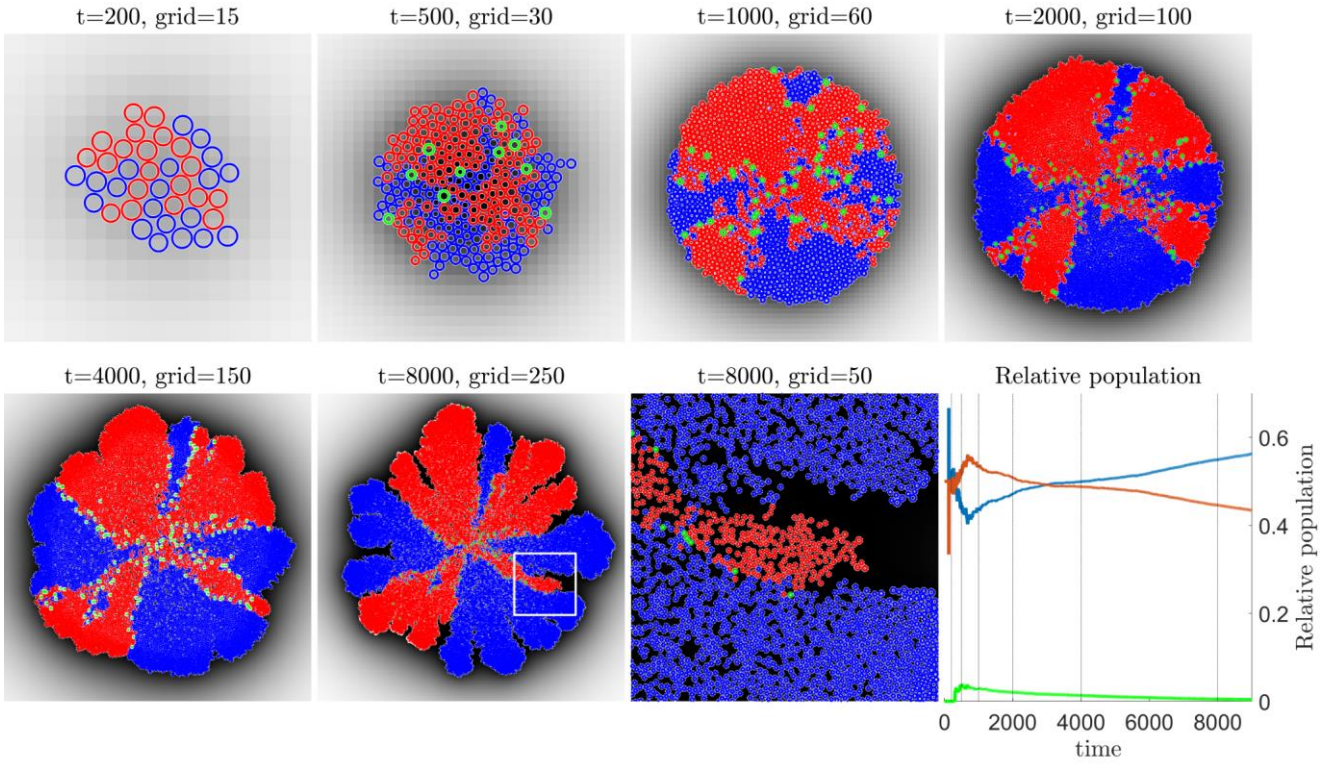

Figure 3. Population plot (lower right) and snapshots of floc development (other panels) from simulation 2. Timestep and size of the viewed grid are shown above the panels. Resistant (red), nonresistant bacteria (blue) and transconjugants (green). Substrate concentration is constant at the border of the nutrient grid and diffuses toward lower concentration, i.e., into the floc (grayscale, white is high concentration). Initially, at t=0 (not shown), ten resistant (red) and ten nonresistant bacteria are initialized in the middle of the environment. The probability of nonresistant bacteria being compatible is 20% while all resistant bacteria are competent. Conjugation recovery time is 300 time steps. At each time step, t, the simulation algorithm is run once.

conditions as in simulation 1, with ten resistant and ten nonresistant bacteria in the middle of the floc at t=0. The results of simulation 3 are shown in Figure 4, which shows the snapshot results and relative the population.

The overall growth and shape of the floc are similar to simulation 1, but the nonresistant bacteria population is higher. Initially, conjugation plays a significant role and transconjugants spread in the floc. However, in the later stage at t=2000, the floc starts to have a shape with clear distinct protrusions and the relative amount of transconjugants decrease.

The relative population plot in the bottom right of Figure 4 shows similarities with the results of simulation 1. It is observed that a lower value of the probability of competence has an impact on the relative population of resistant bacteria. It introduces a drop in the resistant bacteria population.

4 Discussion

The persistence of resistance and the interactions between bacteria with and without resistance are of utmost concern in a wastewater environment. In this work, relevant information about bacterial behaviour and interactions, especially on conjugation, are put together into an IbM. The model is a structurally realistic test environment for examining the effect of conjugation and nutrient limited growth on the spread of resistance in a bacterial floc. The model presented here is simplified but is still able to show that population size and substrate availability have notable effects in the floc.

A number of other mathematical models have been published to analyse bacterial interactions and improve our knowledge of the spread of antibiotic resistance (Birkegård *et al.*, 2018) and other biological phenomena. More specifically, IbMs have been used to shed light on interactions on the micro-level and to produce more mechanistically accurate representations of microbial systems (Kreft *et al.*, 2001; Hellweger et al., 2016). Moving aside from resistance spread, in particular, there have been attempts to make more general-purpose IbMs and solvers for bacterial systems, which in addition to basic functions like growth and substrate diffusion typically includes physical aspects like fluid flow, shear forces, and extracellular polymeric substance adhesion forces. Notable are iDynoMiCS (Lardon *et al.*, 2011) and NUFEB (Li *et al.*, 2019). Such IbMs may also include the possibility to have different

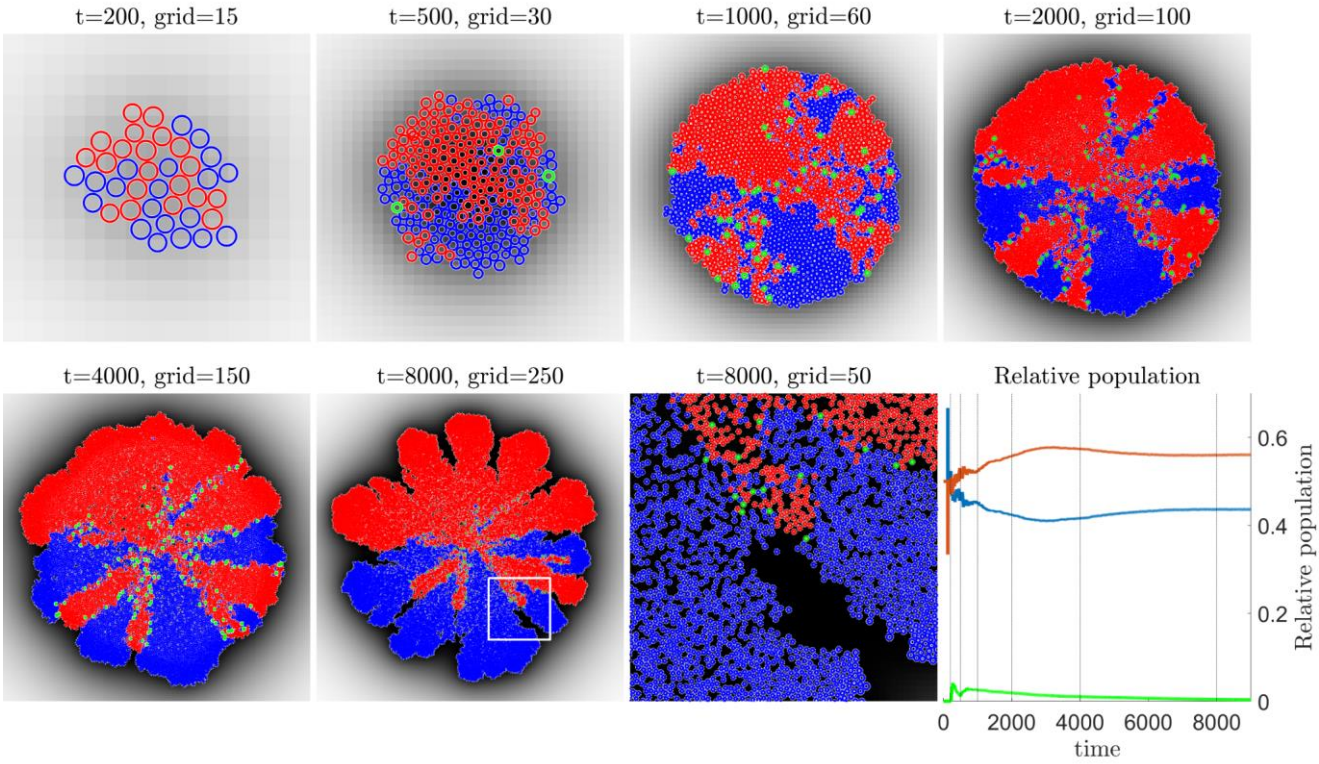

Figure 4. Population plot (lower right) and snapshots of floc development (other panels) from simulation 3. Timestep and size of the viewed grid are shown above the panels. Resistant (red), nonresistant bacteria (blue) and transconjugants (green). Substrate concentration is constant at the border of the nutrient grid and diffuses toward lower concentration, i.e., into the floc (grayscale, white is high concentration). Initially, at t=0 (not shown), ten resistant (red) and ten nonresistant bacteria are initialized in the middle of the environment. The probability of nonresistant bacteria being compatible is 10% while all resistant bacteria are competent. Conjugation recovery time is 200 time steps. At each time step, t, the simulation algorithm is run once.

species of bacteria in the system, e.g., species that are metabolically different like heterotrophic bacteria and autotrophic nitrifying bacteria. We will in the future examine the possibility to use such general-purpose bacterial IbMs for the task of modelling and simulating resistance spread, for example by including our model or parts of it into them, or by extending our model with functionality from them.

5 Conclusion and future development

In this paper, we have introduced an individual-based model for the spread of resistance in a bacterial floc through growth and horizontal gene transfer by conjugation. The attributes of each individual bacteria in the model includes metabolic processes such as substrate uptake and growth in addition to the processes of reproduction and conjugation. During the simulation, each bacterium in the model is updated according to an algorithm that considers the current state of the bacterium and its local neighbourhood. Simulations of the model show that the effect of conjugation varies as the floc grows. Conjugation can only occur between bacteria that are neighbours, and resistant and nonresistant bacteria seem to grow more and more on distinct protrusions as the floc and the overall population grows. Compared to population size, more conjugation occurs at the start of the simulation while it decreases in the later part of the simulation.

We plan to in the future work on finding ways to parameterize our current model with biological data from suitable experiments. And then to work on extending the model's functionality.

Acknowledgement

This work is supported by the European Union JPI-AMR grant Wastewater treatment plants as critical reservoirs for resistance genes (Gene-gas) through the Norwegian Research Council grant NFR 271177/H10.

References

M. Amarasiri, D. Sano, and S. Suzuki. Understanding human health risks caused by antibiotic resistant bacteria (ARB) and antibiotic resistance genes (ARG) in water environments: current knowledge and questions to be answered. *Crit. Rev. Environ. Sci. Technol*, 50(19), 2016–2059, 2020. doi:10.1080/10643389.2019.1692611

A. C. Birkegård, T. Halasa, N. Toft, A. Folkesson, and K. Græsbøll. Send more data: a systematic review of

mathematical models of antimicrobial resistance. *Antimicrobial Resistance and Infection Control*, 7:117, 2018. doi:10.1186/s13756-018-0406-1

D. J. Duarte, R. Oldenkamp, and A. M. J. Ragas. Modelling environmental antibiotic-resistance gene abundance: A meta-analysis. *Science of The Total Environment*, 659, 335-341, 2019. doi:10.1016/j.scitotenv.2018.12.233

P. Gao, M. Munir, and I. Xagoraraki. Correlation of *tetracycline* and *sulfonamide* antibiotics with corresponding resistance genes and resistant bacteria in a conventional municipal wastewater treatment plant. *Sci. Total Environ.*, 421–422, 173–183, 2012. doi:10.1016/j.scitotenv.2012.01.061

R. Gregory, J. R. Saunders, and V. A. Saunders. Rule-based modelling of conjugative plasmid transfer and incompatibility. *BioSystems*, 91, 201–215, 2008. doi:10.1016/j.biosystems.2007.09.003

N. Hassoun-Kheir, Y. Stabholz, J. U. Kreft, R. de la Cruz, J. L. Romalde, J. Nesme, S. J. Sørensen, B. F. Smeths, D. Graham, and M. Paul. Comparison of antibiotic-resistant bacteria and antibiotic resistance genes abundance in hospital and community wastewater: A systematic review. *Sci. Total Environ.*,743,140804, 2020. doi:10.1016/j.scitotenv.2020.140804

F. L. Hellweger, X. Ruan, and S. Sanchez. A Simple Model of *Tetracycline* antibiotic resistance in the aquatic environment (with application to the Poudre River). *Int. J. Environ. Res. Public Health*, 8, 480-497, 2011. doi:10.3390/ijerph8020480

F. L. Hellweger, R. J. Clegg, J. R. Clark, C. M. Plugge, and J. U. Kreft. Advancing microbial sciences by individual-based modelling. *Nat. Rev. Microbiol*, 14(7), 461–471, 2016. doi:10.1038/nrmicro.2016.62

D. Jenkins, and J. Wanner. Eds., Activated Sludge – 100 Years and Counting. London, UK: IWA Publishing, 2014.

G. Koraimann, and M. Wagner. Social behaviour and decision making in bacterial conjugation. *Front. Cell. and Infec. Microbiol*, 4, 763–783, 2004. doi:10.3389/fcimb.2014.00054

J. U. Kreft, G. Booth, and J. W. T. Wimpenny. BacSim, a simulator for individual-based modelling of bacterial colony growth. *Microbiology*, 144, 3275–3287, 1998. doi:10.1099/00221287-144-12-3275

J. U. Kreft, C. Picioreanu, J. W. T. Wimpenny, and M. C. M. van Loosdrecht. Individual-based modelling of biofilms. *Microbiology*, 147(11), 2897–2912, 2001. doi:10.1099/00221287-147-11-2897

S. M. Krone, R. Lu, R. Fox, H. Suzuki, E. M. Top. Modelling the spatial dynamics of plasmid transfer and persistence. *Microbiology*, 153(8), 2007. doi:10.1099/mic.0.2006/004531-0

L. A. Lardon, B. V. Merkey, S. Martins, A. Dötsch, C. Picioreanu, J.-U. Kreft, and B. F. Smets. iDynoMiCS: next-generation individual-based modelling of biofilms. *Environmental Microbiology*, 13(9), 2416-2434, 2011. doi:10.1111/j.1462-2920.2011.02414.x

B. Li, D. Taniguchi, J. P. Gedara, V. Gogulancea, R. Gonzalez-Cabaleiro, J. Chen, A. S. McGough, I. D. Ofiteru, T. P. Curtis, and P. Zuliani. NUFEB: A massively parallel simulator for individual-based modelling of microbial communities. *PLOS Computational Biology*, 15(12), e1007125, 2019. doi:10.1371/journal.pcbi.1007125

J. O'Neil. Tackling drug-resistant infections globally - AMR Review. *In: Ro A, ed. Resistance. London, United Kingdom*, 1, 84, 2016.

J. Park, M. Cho, and H. S. Son. Simulation model of bacterial resistance to antibiotics using individual-based modeling. *Journal of Computational Biology*, 25, 1–12, 2018. doi:10.1089/cmb.2018.0064

N. A. Sabri, H. Schmitt, Van der Zaan, H. W. Gerritsen, T. Zuidema, H. H. M. Rijnaarts, and A. A. M. .Langenhoff. Prevalence of antibiotics and antibiotic resistance genes in a wastewater effluent-receiving river in the Netherlands. *Journal of Environmental Chemical Engineering*, 8(1),102245, 2020. doi:10.1016/j.jece.2018.03.004

C. Uluseker, K. M. Kaster, K. Thorsen, D. Basiry, S. Shobana, M. Jain, G. Kumar, R. Kommedal, and I. Pala-Ozkok. A review on occurence and spread of antibiotic resistance in wastewaters and in wastewater treatment plants: mechanisms and perspectives. *Front. Microbiol.* 2021. doi:10.3389/fmicb.2021.717809

Methanol synthesis from syngas: a process simulation

Ramesh Timsina* Rajan k. Thapa Britt M.E. Moldestad Marianne S. Eikeland

Department of Process, Energy and Environmental Technology, University of South-Eastern Norway, Porsgrunn
{ramesh.timsina, rajan.k.thapa, britt.moldestad, marianne.eikeland}@usn.no
*Corresponding author: ramesh.timsina@usn.no

Abstract

Methanol is one of the major candidates to take over the petroleum based liquid transportation fuel. Methanol synthesis from syngas is proposed in this paper. The Aspen Plus simulation software was used to simulate the conversion process from syngas into methanol. A CSTR reactor with defined reaction kinetics was taken at 40 bar and 270°C to simulate the methanol synthesis. Hydrogen recycles gave an increase of 50.4% in the production of methanol as compared to the results without a H_2 recycle stream. The conversion of CO, CO_2 and H_2 are 50.4%, 99.8% and 100% respectively for the case with the H_2 recycle. Considering an operation of 8600 hr/year, the annual mass production of methanol is equal to 96492 tonnes for a feed rate of 154972 t/year. A distillation column is used to separate the methanol from water. Simulations were performed to calculate the minimum number of stages for the different recovery ratios of methanol in distillate and the required molar reflux ratio versus the purity of methanol in the distillate. The column temperature and the composition profile were analyzed for the column. The model provides the insights of the methanol synthesis plants for a specific quality and the quantity of methanol production.

Keywords: *methanol synthesis, Aspen Plus, process simulation, CO_2 mitigation, Distillation.*

Abbreviations: *CSTR - Continuous Stirred Tank Reactor, GHG - Green House Gas, STM - Syngas to Methanol, TPC - Thermo-Photo Catalyst,*

1 Introduction

The increasing environmental problems due to the excessive use of fossil fuels have led to implementing laws and agreements to limit global Green House Gas (GHG) emissions. Several countries agreed to the objective of the Paris Climate Change Conference (COP21), i.e. to limit the rise of global temperature less than 2°C by 2035 as compared to the preindustrial era (Dessens *et al.*, 2016). Thus, biomass is one of the promising alternatives for the replacement of fossil fuels based liquid transportation fuels in the near future. As compared to the other renewable energy sources, biomass can be converted into added-value products similar to that of fossil fuels and power (Puig-Gamero *et al.*, 2018).

Lignocellulosic biomass and biomass waste can be converted into value-added chemicals and biofuels via thermochemical or biochemical conversion. The biochemical route is complex and more expensive than thermochemical conversion (Sikarwar *et al.*, 2017). Among the different thermochemical conversion technologies, gasification is considered the cost-effective and efficient technology for lignocellulosic biomass (Sikarwar *et al.*, 2017). The lower emission of GHGs is due to the low-oxidation environment and lower amount of sulfur and nitrogen present in the biomass (Kumari & Mohanty, 2020; Pauls *et al.*, 2016). Gasification of biomass gives a product gas mainly consisting of syngas (CO, H_2). However, the gas also contains CH_4, CO_2, H_2O, N_2 and impurities such as tars, NH_3, H_2S.

After gas cleaning and conditioning, the syngas obtained from biomass gasification can be used to produce biofuels and chemicals such as methanol.

Methanol is one of the important industrial chemicals that can be used directly as a fuel or can be blended into conventional fuels. Methanol is an important ingredient for the production of formaldehyde, acetic acid, methyl tertiary butyl ether, and gasoline.

China is the leading producer of methanol, approximately 50% of the global production and a total of 43 million tons was produced in 2016 (Yang et al., 2018). However, methanol production is mainly based on natural gas and coal. Olah et al. (Olah, 2005) proposed a 'methanol economy' as a realistic technique compared to the widely mentioned 'hydrogen economy' due to the suitability of the existing liquid fuel

infrastructure (with a little modification) and higher safety compared to a hydrogen vehicle.

The current study gives insights into a methanol synthesis plant, its production scale. A study of the distillation column was done in greater detail. The column temperature and composition profile are presented. The relation between the minimum number of stages for the different recovery ratios of methanol in distillate and the required molar reflux ratio versus the purity of methanol in the distillate are presented in the paper.

2 Methanol synthesis from syngas and carbon dioxide

As the synthesis gas stream usually contains some amounts of CO_2, methanol can be produced via direct hydrogenation of CO and CO_2. Table 1 shows the reactions concerning the methanol synthesis and their reaction heats. Reaction (c) is the reverse water gas shift reaction which is mildly endothermic as opposed to reactions (a) and (b). Therefore, a significant amount of cooling duty is required for these types of reactors. The thermodynamics of the conversion limits the overall conversion and thus recycling of the unreacted gas is required to achieve higher conversion. Therefore, cooling duty and recycling capacity determines the successful operation of such reactors.

The mixture of CO and H_2 can also react to produce other hydrocarbons such as methane, ethanol, or higher hydrocarbons. Therefore, the selectivity and efficiency of the catalyst play an important role in the conversion efficiency of these types of reactors.

The methanol synthesis reactor requires a specific ratio of CO/CO_2:H_2, and it is hard to obtain the desired ratio directly from a gasifier. The ratio needs to be shifted to a higher hydrogen content and is usually done via a water gas shift reaction. Two moles of H_2 are needed to react with CO and three moles of H_2 are needed to react with CO_2 for methanol formation according to the reaction stoichiometric given in Table 1.

Table 1. Reaction formulas for methanol synthesis

Reactions	*Reaction heat (kJ/mol)*
(a) $CO + 2H_2 \rightleftharpoons CH_3OH$	-90.64
(b) $CO_2 + 3H_2 \rightleftharpoons CH_3OH + H_2O$	-49.67
(c) $CO_2 + H_2 \rightleftharpoons CO + H_2O$	+41

2.1 Previous works

Different literature studies on methanol production are based on different feedstock such as natural gas (Al-Sobhi & Elkamel, 2015; Kralj & Glavič, 2009), synthesis gas (Lange, 2001), CO_2 hydrogenation (Van-Dal & Bouallou, 2013) and coal (Li *et al.*, 2018).

Methanol synthesis has been a wide research topic over the years. Methanol synthesis from syngas was first suggested by Paul Sabatier in 1905 and the first industrial scale plant came into operation in 1923 by Badische Anilin-und-Soda-Fabrik (BASF). The technology has been studied extensively during the 1970's Arab Oil Embargo, as an alternative to fossil-based petroleum (Wu-Hsun 1994).

Inlet temperature, reactor pressure and temperature, reactor types, catalysts system and process configurations have been the most investigated parameters. Hoseiny et al. (Hoseiny *et al.*, 2016) and Manenti et al. (Manenti *et al.*, 2011) have investigated

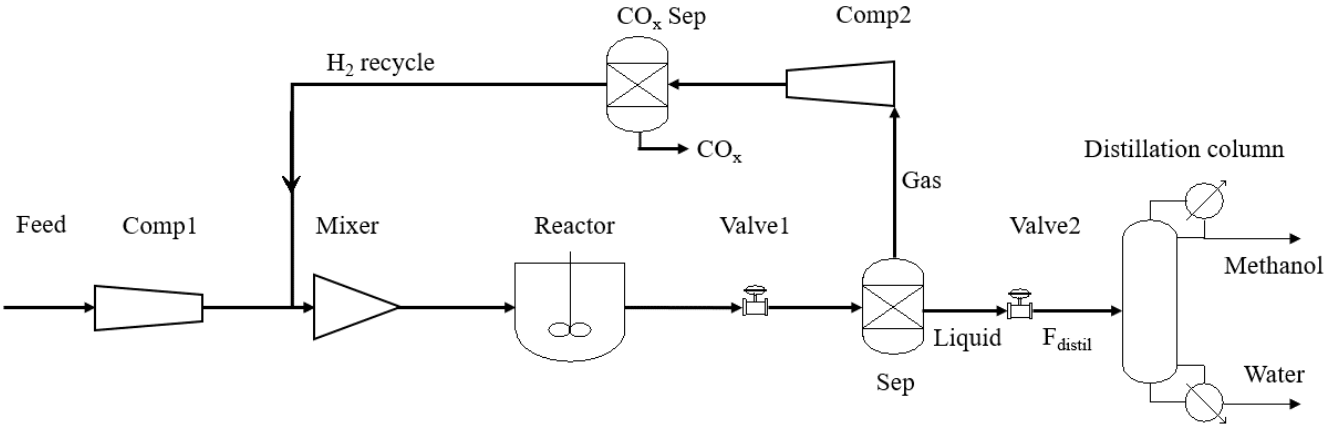

Figure 1. Schematic diagram for Aspen Plus model. Comp: Compressor, Sep: Separator, CO_x: Carbon oxides

the influence of feed temperature and reactor pressure in the methanol synthesis.

Cui and Kær (Cui & Kær, 2020) have studied the three different types of reactors i.e., adiabatic, water-cooled and gas-cooled reactor to investigate the traditional syngas to methanol (STM) process. The water-cooled reactor showed efficient heat removal, low hot-spot temperature and a relatively wide range of inlet temperature for control. The adiabatic reactor and the gas-cooled reactor demonstrated a relatively low and medium performance and low to medium capital costs (Cui & Kær, 2020).

Wu et al (Wu *et al.*, 2019) have developed a novel thermo-photo catalyst (TPC) for methanol production from syngas over Cu/Zn/Al catalyst. The authors demonstrated that the yield of methanol from TPC was 2.8 times higher than that from the thermal catalyst. TPC proved to be superior as compared to the thermal catalyst for the STM process.

Luyben (Luyben, 2010) has developed an economically feasible design for methanol production with three gas recycle streams to produce high quality methanol from syngas. Luyben showed a tradeoff between reactor pressure and feed compressor energy, reactor size and recycle flow rate, venting rate and reactant losses and flash pressure and flash compression energy (Luyben, 2010).

3 Materials and methods

Aspen Plus V11 was used to simulate the conversion of syngas into methanol. The process model developed in Aspen Plus is presented in Figure 1. The 'RK-Aspen' physical properties model was used for all the unit operations except the distillation column. Van Laar equations were used in the distillation column for the calculation of liquid activity coefficients. Different components as present in Table 4 were also defined in the physical property's environment. Table 4 also gives the mass flow rate for the different gases present in the feedstock and the molar ratio of CO:CO_2:H_2 is 1:3:10. A total of 11 moles is required to react completely with 1 mole of CO and 3 moles of CO_2, however, 10 moles of H_2 were taken due to the presence of the H_2 recycle path. The following assumptions were considered for the simulation process.

1. All gases were ideal.
2. Pressure and temperature were uniform inside the reactor.
3. The process was steady and isothermal.
4. The synthesis gas is pure and is supplied at a specified molar flow rate.

The standard operating condition for the methanol synthesis reactor are in pressure and temperature in the range of 50-100 atm and 220-280°C respectively (Ortiz *et al.*, 2013). The blocks used to simulate the methanol synthesis are summarized in Table 2.

Table 2. Block description used for methanol synthesis

Name	*Type, description*
Comp	Compressor: Both compressors compress the gases into 40 bars.
Reactor	RCSTR: Rigorous continuous stirred tank reactor with rate-controlled reactions based on known kinetics.
Sep	Separator: Separates liquids and gases.
CO_x Sep	Separator: Separates CO_x from H_2.
Distillation column	RadFrac: Rigorous 2 or 3- phase fractionation for single columns.

The pure syngas feed was compressed and heated up to the reactor operating pressure and temperature. Exothermic gas phase reactions were defined in the reactor for the synthesis of the methanol. The defined reactions in the reactor are presented in Table 1 and the reaction kinetics were taken from the study of Luyben (Luyben, 2010). The product from the reactor is depressurized to separate the non-converted gases from the liquid. The liquid enters into the distillation column to give methanol in the distillate and water in the bottom.

Table 3. The thermodynamic state of different units/flows

	Thermodynamic state	
	Temperature(°C)	Pressure (bar)
Feed	50	1
Comp1	-	40
Reactor	270	40
Valve1	-	10
Sep	60	10
Comp2	-	40
CO_x Sep	270	40
Valve2	-	1.5
F_{distil}	60	1.5

The conversion of hydrogen at this stage (without a recycle stream) is only about 50%, therefore a recycle stream is chosen to increase the hydrogen conversion. The separated gas is compressed to separate CO_x in another separator. H_2 separated from the CO_x separator enters the mixer before the reactor as a recycle feed. The

overview of the temperature and pressure in the different blocks and streams is presented in Table 3.

The methanol-water separation is fairly easy and is performed at 1.4 bar condenser pressure and 1.7 bar reboiler pressure. Txy diagram at 1.5 bar pressure is given in Figure 2. The plot gives the temperature range at which the distillation column should operate to give higher purity of methanol in the distillate. In the simulated case, the distillation column operates in the temperature range of 74.9 to 100.15°C.

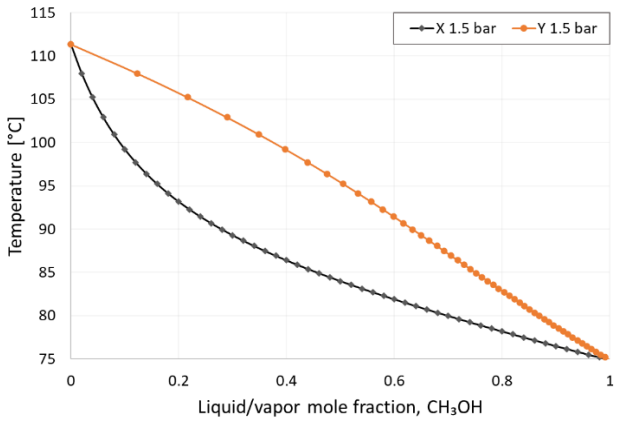

Figure 2. Txy diagram for methanol/water

A total condenser is selected for this simulation as sufficient cooling is available as the feed consists of 32.5 mass% of water at 60°C. This water is sufficient to condensate all the condensable vapor generated at the column overhead.

4 Results and discussion

Table 4 shows the mass balance for the simulated case. The table shows the yield of 2.33 tonnes of methanol per tonne of syngas (CO+H_2) supplied [calculated as methanol_out/(CO_in + H_2_in)]. Considering an operation of 8600 hr/year, the annual mass production of methanol is equal to 96492 tonnes. The conversion of CO, CO_2 and H_2 are 50.4%, 99.8% and 100% respectively and the results are similar to the study of Luyben (Luyben, 2010).

Table 4. Mass balance for the simulated case

Compound	In (t/hr)	Out (t/hr)
CO	2.8	1.39
CO_2	13.2	0.01
H_2	2.02	0
Methanol	0	11.22
H_2O	0	5.40

Several studies by different researchers show that methanol mainly originates from the CO_2 hydrogenation, and hardly from the CO hydrogenation (Kagan *et al.*, 1975; Nestler *et al.*, 2018). Therefore, CO conversion to methanol principally occurs via water gas shift reaction with subsequent CO_2 hydrogenation.

Simulations were performed to know the minimum number of stages for the desired recovery of methanol in distillate and the required molar reflux ratio for the desired purity of methanol in the distillate.

Figure 3 shows the minimum number of stages required to achieve the methanol recovery from 0.9 to 1. The number of minimum stages required increases linearly for up to around 98% methanol purity and increases exponentially after 98%. As most of the industrial scale, methanol synthesis plant operates at around 95% purity of methanol, which is relatively straightforward and doesn't overburden the column cost.

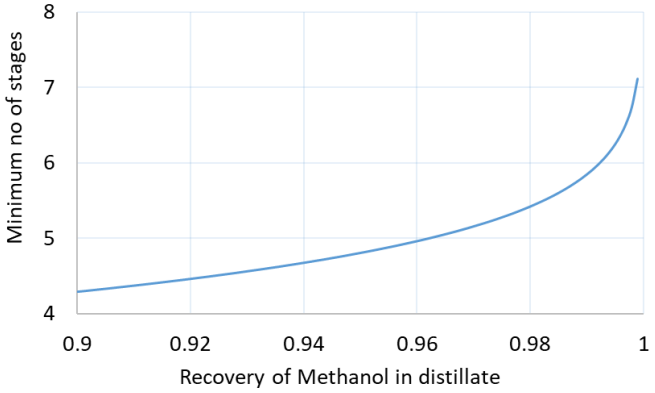

Figure 3. Minimum number of column stages required for corresponding methanol recovery

Figure 4 shows the purity of methanol for different molar reflux ratios. The purity of methanol increases with an increase in the molar reflux ratio, however the reboiler duty and cost increase linearly with an increase in reflux ratio. The purity of methanol synthesis increases steadily initially and exponentially for the higher methanol purity. Therefore, a tradeoff is required for the reflux ratio and the desired methanol purity in the column distillate.

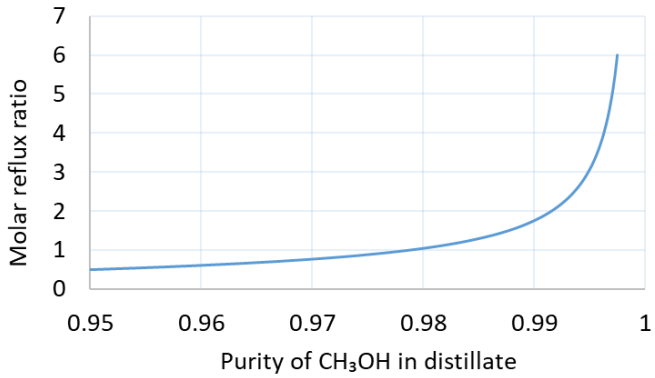

Figure 4. Molar reflux ratio vs methanol purity in distillate

As the total number of stages increases, energy costs and heat exchanger capital costs decrease, however, the total capital costs of the plant will increase. Therefore, a rigorous single distillation column with 7 stages was chosen to separate water from methanol. The selected number of stages gave the desired purity of methanol (95 mass percentage) in the distillate. The temperature profile across the stages is presented in Figure 5 and the liquid molar composition across the stages is presented in Figure 6. Stage 1 is the top of the column and stage 7 is the bottom of the distillation column.

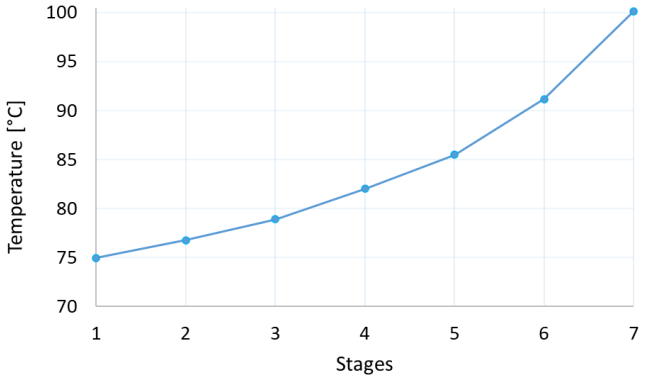

Figure 5. Column temperature profile

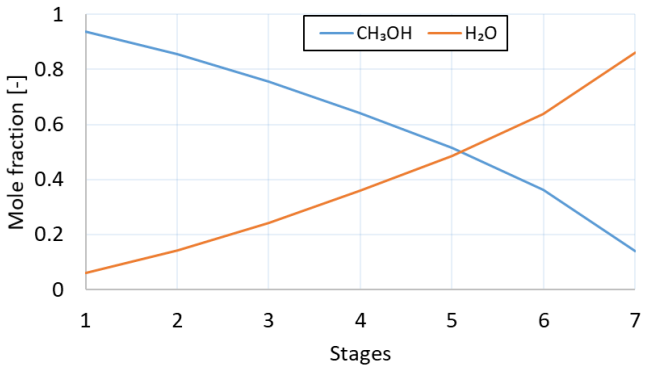

Figure 6. Column composition profile

The figure illustrates a gradual decrease in temperature from the bottom of the tower to the top of the distillation tower. The change of composition of methanol increases steadily from the bottom (stage 7) to the top (stage 1) and the mole fraction of water decreases steadily from the bottom to the top of the distillation tower.

The higher the system pressure, the smaller the reactor for a given recycle flow rate, which reduces the reactor and catalyst capital investment. However, for a given reactor size, the higher the pressure, the smaller the recycle flow rate, which reduces the recycle compressor capital investments and recycle compression energy.

Therefore, the design specification for a methanol synthesis plant depends upon the different parameters such as system pressure, temperature, reactor size, recycle flow rate, compressor energy, reflux ratio in the distillation column and the purity of methanol in the distillate.

Sensitivity analysis for the CSTR reactor showed relatively low sensitivity towards the change of temperature and pressure inside the reactor in the range of 220-280°C and 40-100 bar. The change in reactor pressure from 40 bar to 100 bar gave an increase of 1.7% in methanol production. Temperature variation from 220-280°C gave a 0.02% reduction in methanol synthesis.

5 Conclusion

A steady-state Aspen Plus™ model was developed to study the conversion of syngas into methanol. Simulations were performed to analyze the conversion process. The model was used to study the different integral parts of a methanol synthesis reactor such as compressor, heater, reactor, separator, and distillation column. The desired purity of methanol in the distillate was 95%. In order to achieve this for the given mass flow rate, a 7-stage rigorous two-phase single column was used.

The following results were obtained from the distillation column for the specified thermodynamic conditions.

- $\frac{CH_3OH \text{ in distillate}}{CH_3OH \text{ in feed}}$: 87.1%
- Distillate to feed ratio: 0.5
- Reflux ratio (molar): 1.2
- Purity of methanol in distillate: 96.4%
- Methanol production: 96492 tonnes/year

A cooling duty of 23.62 GJ/hr was required for the given flowrate specifications and a reactor size of 5 m³.

DOI: 10.3384/ecp21185444

The model can further be improved by adding a suitable catalyst in the reactor, selecting/optimizing the reaction kinetics as well as performing the sensitivity analysis for the synthesis reactor. The distillation column can be optimized further based on the required specification for the methanol plant.

Acknowledgments

The authors would like to thank the University of South-Eastern Norway (USN) for providing the necessary software for the simulation works. The authors would like to acknowledge the Bio4Fuels projects in Norway.

References

S. Al-Sobhi and A. Elkamel. Simulation and optimization of natural gas processing and production network consisting of LNG, GTL, and methanol facilities. *Journal of Natural Gas Science and Engineering 23*, 500-508, 2015. doi.org/10.1016/j.jngse.2015.02.023.

X. Cui and S. K. Kær. A comparative study on three reactor types for methanol synthesis from syngas and CO2. *Chemical Engineering Journal*, *393*, 124632, 2020. doi.org/10.1016/j.cej.2020.124632.

O. Dessens, G. Anandarajah and A. Gambhir. Limiting global warming to 2° C: What do the latest mitigation studies tell us about costs, technologies and other impacts? *Energy Strategy Reviews*, *13*, 67-76, 2016. doi.org/10.1016/j.esr.2016.08.004.

S. Hoseiny, Z. Zare, A. Mirvakili, P. Setoodeh and M. Rahimpour. Simulation–based optimization of operating parameters for methanol synthesis process: application of response surface methodology for statistical analysis. *Journal of Natural Gas Science and Engineering*, *34*, 439-448, 2016. doi.org/10.1016/j.jngse.2016.06.075.

Y. B. Kagan, L. Liberov, E. Slivinskii, S. Loktev, G. Lin, A. Y. Rozovskii, and A. Bashkirov. Mechanism of methanol synthesis from carbon dioxide and hydrogen.[Tracer study of conversion over Cu--Zn--aluminium oxide SNM-1 catalyst]. *Dokl. Chem.(Engl. Transl.);(United States), 221*. 1975

A. K. Kralj, and P. Glavič. Multi-criteria optimization in a methanol process. *Applied Thermal Engineering*, *29*(5-6), 1043-1049, 2009. doi.org/10.1016/j.applthermaleng.2008.05.015.

P. Kumari and B. Mohanty. Maximization of hydrogen production from pine needles steam gasification based on response surface methodology. *Biomass Conversion and Biorefinery*, 1-14, 2020. doi.org/10.1007/s13399-020-00761-7.

J.-P. Lange. Methanol synthesis: a short review of technology improvements. *Catalysis Today*, *64*(1-2), 3-8, 2001. doi.org/10.1016/S0920-5861(00)00503-4.

C. Li, H. Bai, Y. Lu, J. Bian, Y. Dong, and H. Xu. Life-cycle assessment for coal-based methanol production in China. *Journal of Cleaner Production, 188*, 1004-1017, 2018. doi.org/10.1016/j.jclepro.2018.04.051.

W. L. Luyben. Design and control of a methanol reactor/column process. *Industrial & Engineering Chemistry Research*, *49*(13), 6150-6163, 2010. doi.org/10.1021/ie100323d.

F. Manenti, S. Cieri, and M. Restelli. Considerations on the steady-state modeling of methanol synthesis fixed-bed reactor. *Chemical Engineering Science, 66*(2), 152-162, 2011. doi.org/10.1016/j.ces.2010.09.036.

F. Nestler, M. Krüger, J. Full, M. J. Hadrich, R. J. White, and A. Schaadt. Methanol synthesis–industrial challenges within a changing raw material landscape. *Chemie Ingenieur Technik*, *90*(10), 1409-1418, 2018. doi.org/10.1002/cite.201800026.

G. A. Olah. Beyond oil and gas: the methanol economy. *Angewandte Chemie International Edition, 44*(18), 2636-2639, 2005. doi.org/10.1002/anie.200462121.

F. G. Ortiz, A. Serrera, S. Galera, and P. Ollero. Methanol synthesis from syngas obtained by supercritical water reforming of glycerol. *Fuel, 105*, 739-751, 2013. doi.org/10.1016/j.fuel.2012.09.073.

J. H. Pauls, N. Mahinpey, and E. Mostafavi. Simulation of air-steam gasification of woody biomass in a bubbling fluidized bed using Aspen Plus: A comprehensive model including pyrolysis, hydrodynamics and tar production. *Biomass and bioenergy*, *95*, 157-166, 2016. doi.org/10.1016/j.biombioe.2016.10.002.

M. Puig-Gamero, J. Argudo-Santamaria, J. Valverde, P. Sánchez, and L. Sanchez-Silva. Three integrated process simulation using aspen plus®: Pine gasification, syngas cleaning and methanol synthesis. *Energy conversion and management*, *177*, 416-427, 2018. doi.org/10.1016/j.enconman.2018.09.088.

V. S. Sikarwar, M. Zhao, P. S. Fennell, N. Shah, and E. J. Anthony. Progress in biofuel production from gasification. *Progress in Energy and Combustion Science, 61*, 189-248, 2017. doi.org/10.1016/j.pecs.2017.04.001.

É. S. Van-Dal, and C. Bouallou. Design and simulation of a methanol production plant from CO2 hydrogenation. *Journal of Cleaner Production*, *57*, 38-45, 2013. doi.org/10.1016/j.jclepro.2013.06.008.

X. Wu, J. Lang, Y. Jiang, Y. Lin, and Y. H. Hu. Thermo–Photo Catalysis for Methanol Synthesis from Syngas. *ACS Sustainable Chemistry & Engineering*, *7*(23), 19277-19285, 2019. doi.org/10.1021/acssuschemeng.9b05657.

S. Yang, B. Li, J. Zheng, and R. K. Kankala. Biomass-to-Methanol by dual-stage entrained flow gasification: Design and techno-economic analysis based on system modeling. *Journal of Cleaner Production, 205*, 364-374, 2018. doi.org/10.1016/j.jclepro.2018.09.043.

C. Wu-Hsun. Methanol Production and Use. *Dekker*, 1994.

Modelling & simulation of an electrochemically mediated biofilm reactor for biogas upgrading

Marzieh Domirani Gamunu Samarakoon Carlos Dinamarca *

Department of Process, Energy and Environment, University of South-Eastern Norway, Norway,
{230749, gamunu.arachchige, carlos.dinamarca}@usn.no

Abstract

In this study, we develop a mechanistic model that contributes to the application of microbial electrochemical synthesis (MES) technology for biogas upgrading. The model considered two reactor compartments- a continuous-flow stirred-tank reactor (CSTR) and an MES biofilm reactor which are coupled through a recycle loop. The modelling of biogas production (i.e. anaerobic digestion (AD) process) in the CSTR follows the most used model for biogas process modelling, ADM-1. The MES biofilm model incorporates microbially active CO_2 reduction to CH_4. To formulate this reduction reaction rate, the Nernst expression was incorporated as a Monod-type kinetic expression. The simulations demonstrate the basic concepts of coupling MES reactor for biogas upgrade and its limitations. According to the simulation result, maximum CH_4 content of 87 % is achievable with recycling ratios of 0.4 and 0.6 when the biofilm volume-specific area is equal to 0.18 m^2/m^3, and 0.36 m^2/m^3 respectively. However, the conversion of CO_2 to CH_4 results in increased pH and consequently CH_4 production decreases by ~ 40 % compared to AD-CSTR without MES. Therefore, it is essential to maintain a proper pH to prevent the inhibition of AD. The rate of the CO_2 conversion to CH_4 can mainly be constrained by available substrate concentration (dissolved CO_2). The local potential of the cathode and the volume-specific area above 0.36 m^2/m^3 have minimum effects.

Keywords: MES, Biofilm, Anaerobic digestion, ADM-1, Bio-methane, Biogas, AQUASIM

1 Introduction

Anaerobic Digestion (AD) is a biological process that produces biogas from organic matter. Biogas contains 50-70 % methane (CH_4) and 30-50 % carbon dioxide (CO_2). The CH_4 content has a significant impact on biogas quality; thus, biogas should be purified before using as a transport fuel. Microbial Electrosynthesis (MES) is an effective technology to convert CO_2 to CH_4 with the help of electroactive microorganisms powered by electrical energy (Nelabhotla and Dinamarca, 2018). Thereby the CH_4 content of the biogas can be increased.

The MES cell consists of a cathode as the working electrode and an anode as the counter electrode. The possible chemical reactions of CO_2 conversion to CH_4 are presented (1-3) with standard potential in Volts (V) vs. Normal Hydrogen Electrode (NHE) (Geppert et al., 2016). The conversion of CO_2 to CH_4 occurs at the cathode through direct electron transfer (1) or indirectly via production of intermediates (2-3). The conversion of CO_2 to CH_4 with intermediate production of hydrogen (H_2) follows two steps: protons reduction to H_2 and then the produced H_2 is used as an electron donor for CO_2 reduction to CH_4.

$$CO_2 + 8H^+ + 8e^- \rightarrow CH_4 + 2H_2O \quad \text{-0.24 V} \quad (1)$$

$$8H^+ + 8e^- \rightarrow 4H_2 \quad \text{-0.41 V} \quad (2)$$

$$CO_2 + 4H_2 \rightarrow CH_4 + 2H_2O \quad (3)$$

Equation (1) is performed by electroactive microbes growing in the biofilm on the cathode (Siegert et al., 2015). These microorganisms use CO_2 as the only carbon source. Equation (2) can be biotic (Rozendal et al., 2008) or abiotic. The protons (H^+) and electrons (e^-) needed for the reduction reaction at the cathode are generated at the anode, by oxidizing water or easily degradable short-chain organics such as acetate. Another possible oxidation compound is ammonium (Sivalingam et al., 2020).

The surface area of the electrodes has a major impact on reactor efficiency. Increasing the cathode surface area can increase the number of catalyst bacteria available and enhance the MES system's efficiency by lowering the biocathode electrode's activation overpotential. Further, a lower potential for the transition of a certain quantity of electrons is more effective than a higher potential for the same amount of electrons (Mueller, 2012). Therefore, direct electron transfer (1) is more desirable than indirect reactions since it occurs at lower potentials.

Even though it is experimentally proved that integrating MES system in AD reactor system can increase the quality of biogas, the technology is still not mature for full-case implementations. The technology is still to be economically optimized. An MES unit (relatively smaller than a large-scale biogas reactor) can be integrated into an existing AD reactor before a full-scale implementation. Thereby, the technical and economic feasibility of the application can be evaluated. Further, in a unit as such, a pure electroactive methanogenic culture or an enriched methanogenic

consortium can be maintained at the cathode, while the biogas process happens in the main reactor.

This study focuses on a mechanistic modelling approach to study an MES reactor as an auxiliary unit to a main biogas reactor. The experimental work requires significant efforts to test a wide variety of operational conditions, while mathematical modelling can extrapolate such results and enhance our understanding of MES application in the biogas process.

2 Materials and methods

Figure 1 shows the reactor configuration of the model. An MES biofilm reactor compartment (MES-RBC) is coupled as an auxiliary unit to a main biogas reactor, which is a continuous-flow stirred-tank reactor (AD-CSTR). The MES-RBC is fed with the effluent from AD-CSTR. The effluent of the MES-RBC is recycled back to AD-CSTR. The reactors are operated under the mesophilic condition (35 °C). The model is formulated in the simulation tool, AQUASIM 2.1.

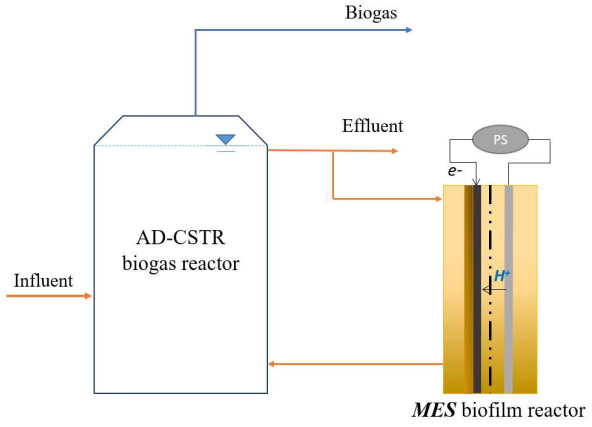

Figure 1. Schematic diagram representing MES biofilm reactor coupled with AD-CSTR reactor (for biogas production). CSTR – continuous-flow stirred-tank reactor, AD – Anaerobic digestion, MES - Microbial electrosynthesis, PS – power supply.

2.1 AD-CSTR reactor

The main biogas process occurs in AD-CSTR. The reactor has a volume of 28 m^3. The reactor is fed as described in the simulation outline (Section 2.4). The most common platform for biogas process modelling Anaerobic Digestion Model No.1 (ADM-1) (Batstone et al., 2002) was used to simulate the biogas process in AD-CSTR.

2.1.1 ADM-1 model

The ADM-1 is structured on anaerobic biochemical reactions catalysed by intra or extracellular enzymes and act on the pool of biologically available organic material (Figure 2).

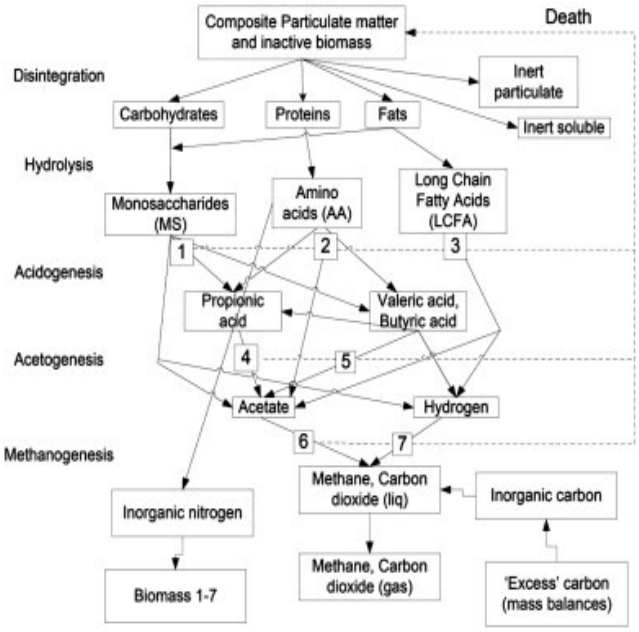

Figure 2. The reaction paths in ADM-1 (Batstone et al., 2002), with the following microbial groups: (1) sugar degraders, (2) amino acid degraders, (3) LCFA degraders, (4) propionic acid degraders, (5) butyric and valeric acid (VFA) degraders, (6) acetoclastic methanogens, and (7) hydrogenotrophic methanogens, taken from (Lauwers et al., 2013).

The anaerobic digestion (AD) process decomposes complex organic materials into the final product, biogas (CH_4 and CO_2) through several decomposition steps. The first step is the disintegration of complex organic material into particulate constituents (carbohydrates, proteins, and lipids). The next step is the hydrolysis of those particulate constituents into soluble sugars, amino acids and long-chain fatty acids (LCFAs). The hydrolysis products are then fermented into volatile fatty acids (acidogenesis step in Figure 2). These acids are broken down to acetate and hydrogen (acetogenesis). The final step is methanogenesis in which acetoclastic methanogens converts acetate to methane, and hydrogenotrophic methanogenesis converts carbon dioxide and hydrogen to CH_4.

The model incorporates these steps as rate equations. The kinetics of disintegration and hydrolysis steps are expressed as a first-order reaction rate. The substrate uptake rates are described using substrate-level Monod saturation kinetic equations (Monod, 1949). Biomass decay rates for each microorganism type is first order and is described with an independent set of expressions. The detailed description of the model can be found (Batstone et al., 2002).

2.2 MES-BRC

The volume of MES-BRC is 2.8 m^3 (10 % of AD-CSTR volume). The reactor is fed with effluent from AD-CSTR, and the flow rate is increased stepwise as a ratio of the effluent flowrate from AD-CSTR.

Table 1. Model parameters used for bioelectrochemical processes in MES-BRC according to [a] (Samarakoon et al., 2019); [b] (Processes, 2002); [c](Reichert, 1998); [d](Cunningham, 2001); m.d.-determined by the model. MES - Microbial electrosynthesis, RBC - biofilm reactor compartment.

Parameters	Description	Unit	Value
km_eet	maximum electrons uptake rate	Kmol-e Kg COD Xd^{-1}	4.5[a]
X_eet	concentration of electroactive biomass	Kg COD m^{-3}	m.d.
S_co2	concentration of dissolved CO_2	M	m.d.
Ks-co2	Half saturation constant for CO_2 reduction	M	0.06[a]
F	Faraday's constant	C $mol\text{-}e^{-1}$	96485
R	Ideal gas constant	J mol^{-1} K^{-1}	8.314
T	Temperature	K	308
η	Local potential	V	change
I_NH_limit	Microbial growth inhibition due to limitation of inorganic nitrogen	-	reported formula[b]
Y_eet	Yield of bio-electroactive biomass	Kg COD-X/Kmol-e	0.48[a]
D_X	Diffusivity of biomass	m^2d^{-1}	1×10^{-7} [c]
D_S_co2	Diffusivity of dissolved CO_2	m^2d^{-1}	0.00012171
rho	Biomass density	Kg COD m^{-3}	25[c]
LF	Biofilm thickness	m	m.d.
LL	Boundary layer thickness	m	0.0001[c]
uf	Growth velocity of biofilm	md^{-1}	m.d.
A	Cathode biofilm area	m^2	change
R'	Recycle ratio		change
Kdec_x_eet	first order decay rate of X_eet	d^{-1}	0.02[a]

To simplify the process modelling in MES-BRC, only the chemical reaction which is based on the direct electron transfer process (1), was considered. The electroactive microorganism performs the reaction as microbial growth on a substrate. The specific microbial community in this case is electroactive methanogens which grow on the cathode surface. These bacteria take electrons from the cathode and deliver them to CO_2 as the final acceptor, using CO_2 as a carbon source for biomass growth. As a result, the availability of both the electron donor and the electron acceptor will limit the reaction rate. The overall reaction rate can be defined as (4) detailed in (Samarakoon et al., 2019). The stoichiometric coefficient of this biotic process is the same as in hydrogenotrophic methanogenesis (i.e H_2 uptake) in ADM-1.

$$\rho_{eet} = k^0_{m-eet} X_{eet} \left(\frac{S_{CO}}{K_{S_{CO2}} + S_{CO2}}\right)\left(\frac{1}{1+\exp\left[-\frac{F}{RT}\eta\right]}\right) I_{ph} I\_NH\_limit \quad (4)$$

ρ_{eet}- kinetic rate. The last term in the parenthesis in (4) which is derived from the Monod equation is referred as the Nernst-Monod term. The main assumption for its use is that microbial kinetics control electron consumption. The Nernst-Monod term shows that the rate of substrate uptake increases as the local potential increases until a constant maximum level is reached. R is the ideal gas constant, T is absolute temperature, F is Faraday constant, η is local potential in reference to E_{KA}. E_{KA} is the potential in which the substrate consumption rate will reach half of the maximum substrate consumption. η is equal to $\eta = E_{KA} - E_{cathode}$. E_{KA} refers to the reference potential ($E \equiv 0$), thus $\eta = -E_{cathode}$ (Marcus et al., 2007). X_{eet} is the concentration of electrically active microorganisms, I_{ph} is an inhibitor that describes microbial growth due to extreme pH conditions, *I_NH_limit* is an inhibitor that describes microbial growth due to the limitation of soluble inorganic nitrogen. Other parameters: $k_{m\text{-}eet}{}^0$ - maximum uptake rate, S_{CO2} - dissolved CO_2 concentrations, K_{CO2} – half maximum rate concentrations for substrates S_{co2}. In addition to the bio-electrochemical process, decay of electrochemical active biomass X_{eet} is defined as a process in MES-BRC. The rate (dec_X_{eet}) is first-order (5) where $k_{dec\text{-}eet}$ is the first-order decay rate.

$$dec\_X_{eet} = X_{eet} k_{dec-eet} \quad (5)$$

The type of biofilm reactor (in AQUASIM tool) was set to be "confined". The biofilm matrix is a rigid structure with no suspended solid in pore volume. The pore volume consists of only a liquid phase and dissolved solids. The rate of porosity was considered zero. The surface detachment velocity of the biofilm is assumed to be global and set initially as 0.63 times the growth velocity of the biofilm as proposed by (Botheju and Bakke, 2008). More detail about the biofilm reactor compartment in AQUASIM tool can be found in (Wanner and Morgenroth, 2004). Other assumptions made for MES-BRC modelling:

1. The biofilm model is one-dimensional.
2. Biofilm surface area is constant at the given areas (A) for the simulation.
3. The electroactive methanogens catalyze CO_2 reduction to CH_4 (1). This microbial community can acquire electrons directly from the solid cathode.
4. Only the cathodic biofilm in MES-BRC is considered in the modelling (the reaction at the anode is not included).
5. Only electroactive methanogens are present in the biofilm on the cathode surface (any other parallel biochemical and bio-electrochemical reactions are neglected).
6. The inhibition that describes electroactive microbial growth due to extreme pH conditions (I_{ph}) is neglected.
7. The anode side (which is not included in the modelling) supplies an unrestricted proton flow and electron current flow (to the cathode side). The transport of H^+ in biofilm is comparatively faster.

2.3 Model parameters

The model parameters used for the processes in AD-CSTR are similar to the reported sludge digestion experiment with ADM-1 simulations (Siegrist et al., 2002) and are presented in Table .

2.4 Simulation outline

First, a simulation was run only with AD-CSTR without coupling MES-BRC i.e., there was no feed flow to MES-BRC and the processes (4 and 5) were deactivated. The reactor settings of AD-CSTR, and its feed composition were the same as in (Siegrist et al., 2002). The composition of the feed is given in Table 2. The reactor is fed with sludge from a wastewater treatment plant for 50 days (Figure 3). The feed flow increases at day 16 and day 37 (AD reactors are in general started with low organic loading and then gradually increased so that stable reactor operation is achieved).

Table 2. Influent feed composition to AD-CSTR.

Compounds	*Concentrations kg COD/m³*
Amino acids	4.2
Fatty acids	6.3
Monosaccharides	2.8
Complex particulates	10.0
Total	23.3

The bio-electrochemical process was activated at day 50 while maintaining a constant feed rate (5.31 m^3/d) to AD-CSTR. The influent flow to MES-BRC reactor was set as a fraction of effluent from AD-CSTR (i.e., Recycle ratio, R' × effluent flow). The recycle ratio (R') increase stepwise from 0.1 to 0.8 (0.1, 0.2, 0.4, 0.6 and 0.8). The corresponding hydraulic retention times (HRT) for each R' are 5.3, 2.6, 1.3, 0.9 and 0.7 days respectively. The local cathode potential (η) was increased from -0.200 to +0.200 V stepwise (step size =0.05) at every 10 days for each recycle ratio. This simulation procedure was followed for 3 different cathodic biofilm areas: 0.5 m^2, 1 m^2 and 1.5 m^2 which are equal to volume-specific areas of 0.18, 0.36 and 0.54 m^2/m^3, respectively.

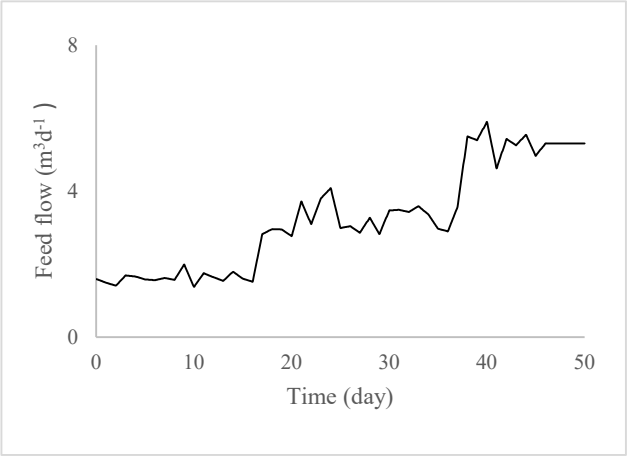

Figure 3. The sludge feed flow to AD-CSTR (Siegrist et al., 2002).

3 Results and Discussion

Figure 4 shows the biogas production rate and the composition of the biogas from AD-CSTR when it is not coupled with MES-RBC. As the feed rate is increased during the first 50 days, the biogas production rate increases. The reactor produces biogas ~ $45m^3/d$ at day 50 with ~ 65 % CH_4 content. This simulation reported (Siegrist et al., 2002) was done for baseline results and the microbial adaptation before any change was made to the conventional biogas process.

Figure 5 shows how the CH_4 content in the biogas from AD-CSTR changes at different recycle ratios (R') when it is coupled with MES-BRC and the local potential of the biocathode varies. CH_4 content increases with the recycle ratio (i.e. the feed flow to MES-BRC increases). The reason is that dissolved CO_2 coming with the recycle flow from the main reactor is converted to CH_4 in MES-BRC and more CH_4 is fed back to AD-CSTR. Increasing local potential (Ƞ) does not make a significant influence on CH_4 content under the condition of this study. This indicates that it is the electron acceptor; in this case, dissolved CO_2 that limits the rate of the conversation reaction (1).

Similarly, the cathodic biofilm area over 1 m^2 does not influence CH_4 content. However, when the area is chosen as 0.5 m^2 and R' is equal to 0.4, the CH_4 content is about 87 % (which is the same at R=0.6). On the other hand, when the area is equal to 1 m^2, at the same recycle ratio (R= 0.4) the CH_4 content is lower, about 72 %. This indicates that increasing the area from 0.5 to 1 m^2 has given a negative impact on the CO_2 reduction processes. It is in contradiction to the fact that the increased area

provides more biomass available for the conversion processes. A higher cathode area causes higher electron flow and sufficient area for biofilm to grow (Nelabhotla and Dinamarca, 2018; Sydow et al., 2014; Zhang et al., 2019). The reason for this negative influence observed in the current simulation might be due to the larger biofilm thickness at A=1 m^2 compared to A=0.5 m^2. Initially higher biomass concentration is available for A=1 m^2 compared to A=0.5 and it results in the thicker biofilm for A=1 m^2. Thicker biofilm makes resistance to substrate transfer within the biofilm. This finding suggests the importance of maintaining a proper biofilm thickness in the process. Further, it is also important to properly model the biofilm surface detachment velocity so that an applicable biofilm thickness is maintained.

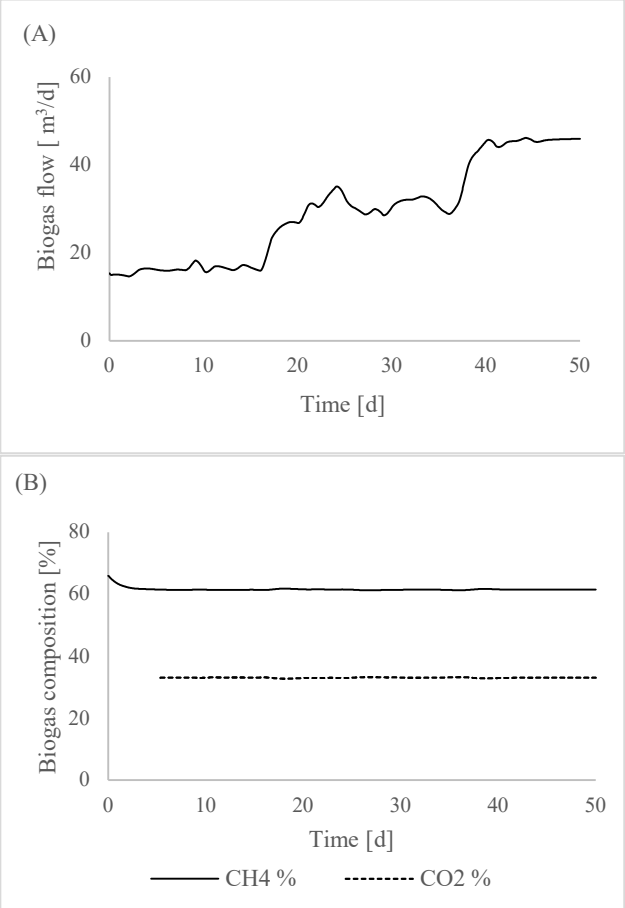

Figure 4. Biogas production rate (A) and its composition (B) from AD-CSTR (when it is not connected with MES-RBC). The feed rate changes at days 16 and 37.

Even though CH_4 content increases with the recycle ratio, the total biogas production decreases with the recycle ratio (Figure 6, the simulation results are the same for A=1 and 1.5, therefore the result corresponding to A=1 is only presented). In another word, biogas production decreases as CH_4 content increases. For the case corresponding to the highest CH_4 content (87 %), biogas production decreases by 55 % compared to AD-CSTR without MES.

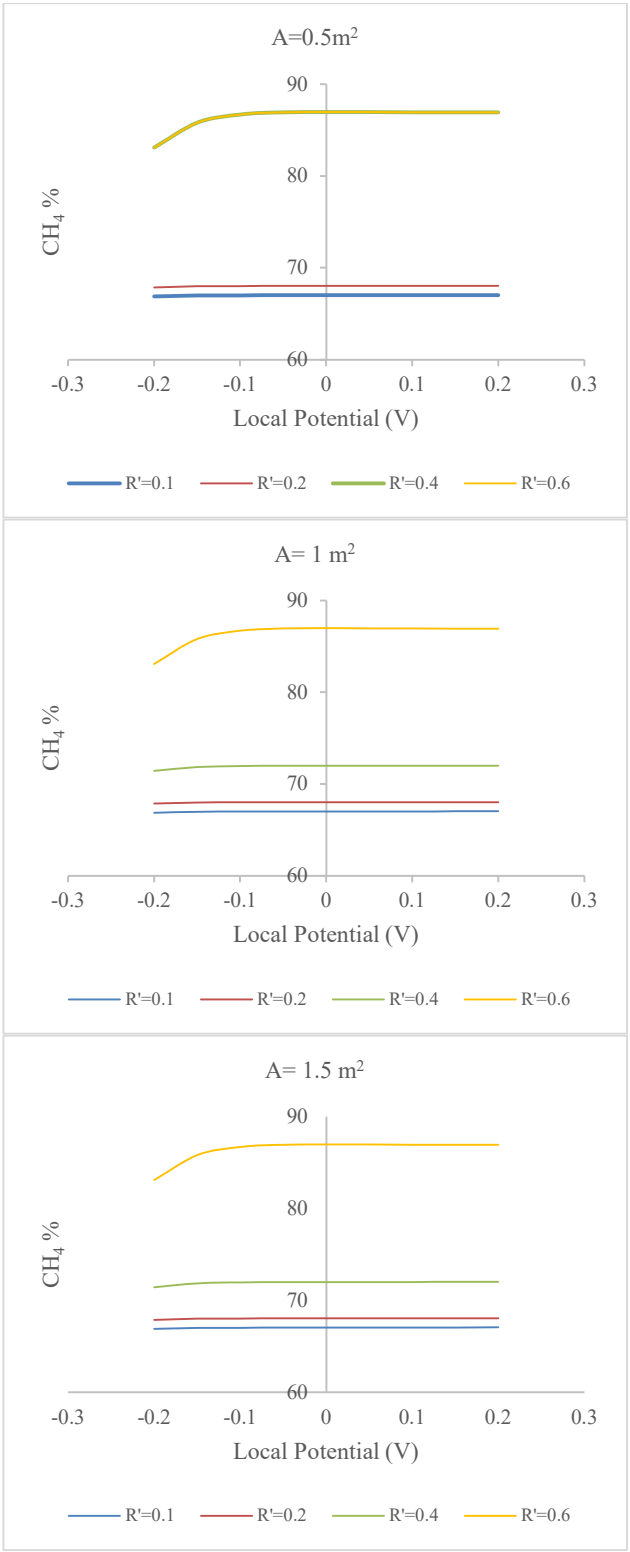

Figure 5. CH_4 content (%) in biogas from AD-CSTR (coupled with MES-BRC) vs. local potential (Π) from -0.2 to +0.2V (step size=0.05) at different recycle ratios (R') and area (A)=0.5,1.0 and 1.5m^2.

The increasing recycle ratio allows more CO_2 from the biogas rector (AD-CSTR) to convert to CH_4. Consequently, bicarbonate strength in the bulk liquid of the reactor (AD-CSTR) decreases and hence pH rises

(Figure 8). The elevated pH can lead to deprotonation of ammonium ions, releasing free ammonia. Free ammonia strictly inhibits acetoclastic methanogens, the bacterial group which is responsible for the decomposition of acetate into methane (Figure 2). In conventional AD, a major portion of biogas is produced via this acetate pathway. When recycle ratio is equal to 0.8, pH rises to 10 (the result is not presented) and acetoclasic methanogens' activity completely terminates. The result is the same for all three biofilm areas studied. However, in the real-case application of MES, the free ammonia can oxidize at the anode (Sivalingam et al., 2020), thereby its inhibition can be mitigated.

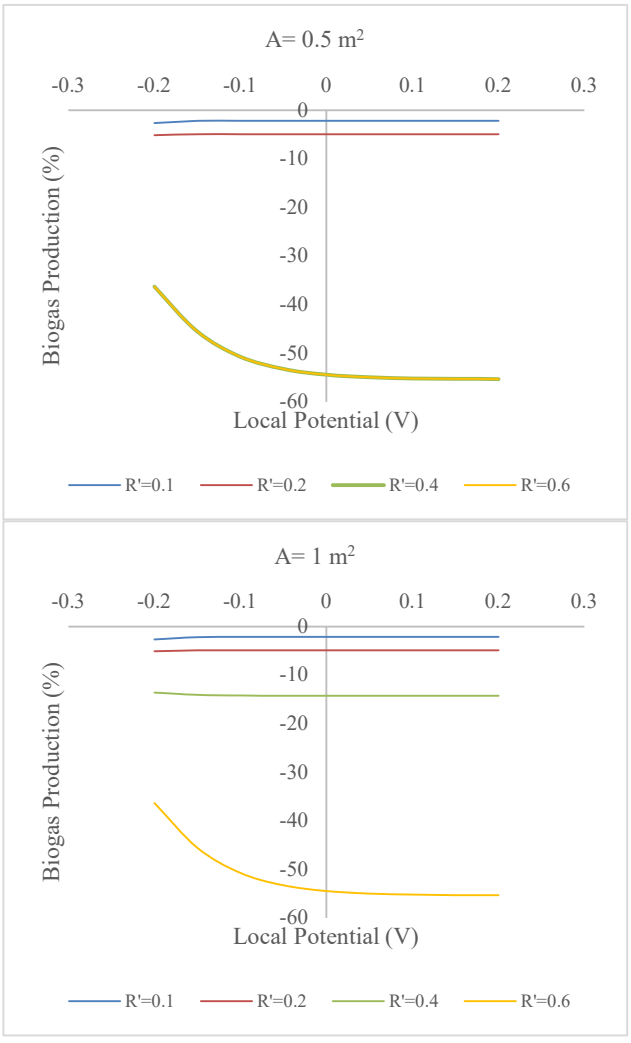

Figure 6. Biogas production in AD-CSTR reactor coupled with MES-BRC compared to AD-CSTR without MES when the local potential (Ƞ) increases from -0.2 to +0.2V (step size=0.05) for different recycle ratios (R') and A=0.5 and 1m^2.

Due to the reduction in total biogas production in AD-CSTR coupled with MES-BRC, the CH_4 production also decreases as CH_4 content increases or the recycle ratio increases (Figure 7, the simulation results are the same for A=1 and 1.5, therefore the result corresponding to A=1 is only presented). CH_4 production decreases by 40 % at the highest CH_4 content observed (87 %) at R= 0.4 and 0.6 when the biofilm area is equal to 0.5 m^2 and, at R=- 0.6 when the biofilm area is equal to 1 m^2. However, a previous experimental study reported that MES could increase CH_4 yield by 10-15 % compared to that produced in a reactor without MES operation (Nelabhotla and Dinamarca, 2019).

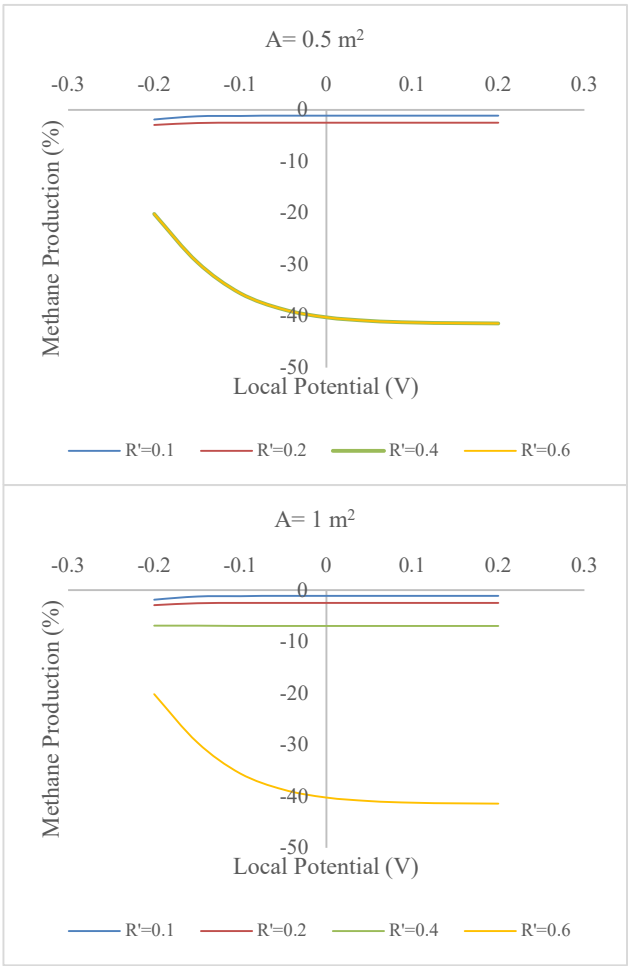

Figure 7. CH_4 production in AD-CSTR reactor coupled with MES-BRC compared to AD-CSTR without MES when the local potential (Ƞ) increases from -0.2 to +0.2V (step size=0.05) for different recycle ratios (R') and A=0.5 and 1m^2.

In the present modelling approach, the other processes (both microbial processes and Physico-chemical reactions) in AD were not considered in MES-BRC. If the processes as such were taken into account, the severe impact on biogas production due to pH rise might not be observed, since the AD processes itself can produce some alkalinity/buffer capacity. Further, such a pH rise can also be avoided if extra CO_2 is added from an external source as suggested by (Samarakoon et al., 2019).

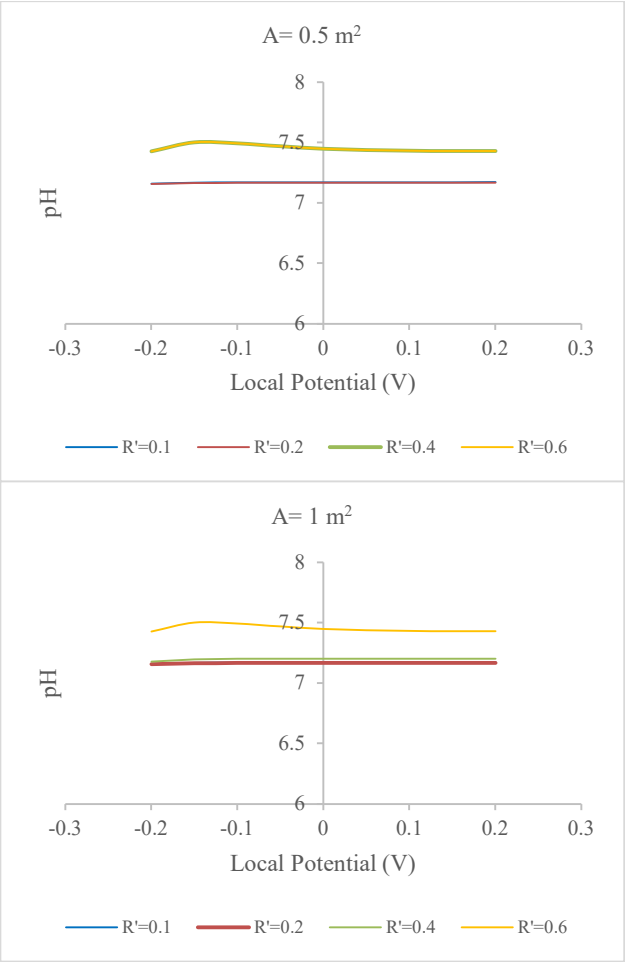

Figure 8. Response of pH in AD-CSTR coupled with MES-BRC when the local potential (Ƞ) increases from -0.2 to +0.2V (step size=0.05) for different recycle ratios (R') and A=0.5 and 1 m^2.

The diffusion coefficient can also have a significant impact on the CO_2 reduction rate. To understand the effect of diffusivity on CH_4 production, low and high values were chosen for the diffusivity coefficient of dissolved CO_2 for a single simulation case. This examination was done on the case where the local potential is equal to +0.2 V, A=1, and for all recycle ratios. The high and low diffusivity coefficient values were 0.002 m^2/d and 0.00002 m^2/d, respectively. Only a 0.11% increase in CH_4 production at the higher value (result not presented) was observed. However, it could be expected that at the lower local potential the diffusivity constant may influence the production.

3.1 Limitations of the model and suggestions for improvement.

In the present model, only the bioelectrochemical CO_2 reduction process and microbial decays are the activated processes in the biofilm reactor (MES-BRC). It means that the model modification assumes only one microorganism (X_{eet}) is growing in the cathodic biofilm, while in the real case, other microorganisms' growth or other microbial processes (Figure 2) also exist.

Both pH and IN have a greater impact on the biological processes. However, the acid-based equilibrium and charge balance (i.e. physicochemical processes) which are vital for pH and inorganic nitrogen (IN) concentration determinations were also not considered in the biofilm modelling (in MES-BRC). Hence, their influence on biofilm growth cannot be studied with the current model. Due to these limitations, the model prediction might be far-off from the real case scenarios even though the model can give a qualitative understanding of the new application.

As a suggestion to improve the model one step further, ADM-1 with the bioelectrochemical CO_2 reduction process can be implemented in MES-BRC. However, ADM-1 model with AQUASIM software uses a differential-algebraic system of equations (DAE) to model the AD process in CSTR. On the other hand, the solver for the biofilm reactor compartment (BRC) model in AQUASIM cannot numerically handle the DAE system. Therefore, implementing ADM-1 with BRC in AQUASIM is not straightforward. The acid-base equilibrium processes should be removed and redefined as dynamic processes as reported by (Botheju and Bakke, 2008). In Addition, how it will affect ADM-1 with CSTR should also be investigated since the reactor configuration (Figure 1) consists of both CSTR and BRC.

Furthermore, the present model requires proper parameter estimation and validation based on real case scenarios.

4 Conclusion

The proposed model can be used to illustrate the principle of MES coupled with AD for biogas upgrading by bio-electrochemically transforming CO_2 to CH_4. The model can be used to study some significant process parameters such as cathode local potential (η) recycle ratio, cathode area, and biofilm detachment velocity on the MES integrated with AD reactor.

The simulations show that coupling the MES biofilm reactor with a recycle loop increases CH_4 content in the biogas. The maximum CH_4 content achieved is 87 % with recycle ratios (R') of 0.4 (1.3 d HRT) and 0.6 (0.9 d HRT) when the biofilm volume-specific area is equal to 0.18 m^2/m^3 and 0.36 m^2/m^3 respectively (under the reactor condition studied). However, the conversion of CO_2 to CH_4 results in elevated pH in the main biogas reactor and consequently CH_4 production decreases by ~ 40 % compared to AD-CSTR without MES. Therefore, it is essential to maintain a proper pH to prevent the inhibition.

The rate of the CO_2 conversion to CH_4 can mainly be constrained by available substrate concentration (dissolved CO_2) and the cathode local potential and volume-specific area above 0.36 m^2/m^3 have minimum effects.

References

D. J. Batstone, J. Keller, I. Angelidaki, S. V. Kalyuzhnyi, S. G. Pavlostathis, A. Rozzi, W. T. M. Sanders, H. Siegrist, and V. A. Vavilin. The IWA Anaerobic Digestion Model No 1 (ADM1). *Water Science and Technology, 45*(10): 65-73, 2002. doi:10.2166/wst.2002.0292.

D. Botheju and R. Bakke. Implementation of ADM 1 model in AQUASIM biofilm reactor compartment, 2008. from www.scansims.org

A. B. A. Cunningham. The Hypertextbook, 2001. Retrieved from http://www.hypertextbookshop.com/ biofilmbook/v 005/r001/Contents/01_Topics/ 10_Chapter_10/02_S ection_2/02_Intermediate/ 01_Page_1.html

F. Geppert, D. Liu, M. van Eerten-Jansen, E. Weidner, C. Buisman, and A. ter Heijne. Bioelectrochemical Power-to-Gas: State of the Art and Future Perspectives. *Trends in Biotechnology, 34*(11): 879-894, 2016. doi:https://doi.org/10.1016/ j.tibtech.2016.08.010.

J. Lauwers, L. Appels, I. P. Thompson, J. Degrève, J. F. Van Impe, and R. Dewil. Mathematical modelling of anaerobic digestion of biomass and waste: Power and limitations. *Progress in Energy and Combustion Science, 39*(4): 383-402, 2013. doi:https://doi.org/10.1016/j.pecs.2013.03.003.

A. K. Marcus, C. I. Torres, and B. E. Rittmann. Conduction-based modeling of the biofilm anode of a microbial fuel cell. *Biotechnology and Bioengineering, 98*(6): 1171-1182, 2007. doi:10.1002/bit.21533.

J. Monod. The growth of bacterial cultures. *Annual Review of Microbiology, 3*(1): 371-394, 1949. doi:10.1146/annurev.mi.03.100149.002103.

J. Mueller. (2012). *PhD thesis*, *Microbial catalysis of methane from carbon dioxide The Future of Renewable Energy is Inside You.* The Ohio State University.

A. B. T. Nelabhotla and C. Dinamarca. Electrochemically mediated CO2 reduction for bio-methane production: a review. *Reviews in Environmental Science and Bio/Technology, 17*(3): 531-551, 2018. doi:10.1007/s11157-018-9470-5.

A. B. T. Nelabhotla and C. Dinamarca. Bioelectrochemical CO_2 Reduction to Methane: MES Integration in Biogas Production Processes. *Applied Sciences, 9*(6): 1056, 2019.

I. W. A. Task Group for Mathematical Modelling of Anaerobic Digestion Processes. *Anaerobic digestion model no.1 (ADM1)* (Vol. No.13). IWA Publishing. 2002.

P. Reichert. AQUASIM 2.0-Tutorial. *Swiss Federal Institute for Environmental Science and Technology (EAWAG): Dübendorf, Switzerland*, 1998.

R. A. Rozendal, A. W. Jeremiasse, H. V. M. Hamelers, and C. J. N. Buisman. Hydrogen Production with a Microbial Biocathode. *Environmental Science & Technology, 42*(2): 629-634, 2008. doi:10.1021/es071720+.

G. Samarakoon, C. Dinamarca, A. B. T. Nelabhotla, D. Winkler, and R. Bakke. Modelling Bio-Electrochemical CO_2 Reduction to Methane. *SINTEF Proceedings*: 55-61, 2019.

M. Siegert, M. D. Yates, A. M. Spormann, and B. E. Logan. Methanobacterium Dominates Biocathodic Archaeal Communities in Methanogenic Microbial Electrolysis Cells. *ACS Sustainable Chemistry & Engineering, 3*(7): 1668-1676, 2015. doi:10.1021/acssuschemeng.5b00367.

H. Siegrist, D. Vogt, J. L. Garcia-Heras, and W. Gujer. Mathematical Model for Meso- and Thermophilic Anaerobic Sewage Sludge Digestion. *Environmental Science & Technology, 36*(5): 1113-1123, 2002. doi:10.1021/es010139p.

V. Sivalingam, C. Dinamarca, G. Samarakoon, D. Winkler, and R. Bakke. Ammonium as a Carbon-Free Electron and Proton Source in Microbial Electrosynthesis Processes. *Sustainability, 12*(8): 3081, 2020. doi:doi:10.3390/su12083081.

A. Sydow, T. Krieg, F. Mayer, J. Schrader, and D. Holtmann. Electroactive bacteria--molecular mechanisms and genetic tools. *Appl Microbiol Biotechnol, 98*(20): 8481-8495, 2014. doi:https://doi.org/10.1007/s00253-014-6005-z.

O. Wanner and E. Morgenroth. Biofilm modeling with AQUASIM. *Water Science and Technology, 49*(11-12): 137-144, 2004. doi:10.2166/wst.2004.0824.

Z. Zhang, Y. Song, S. Zheng, G. Zhen, X. Lu, T. Kobayashi, K. Xu, and P. Bakonyi. Electro-conversion of carbon dioxide (CO2) to low-carbon methane by bioelectromethanogenesis process in microbial electrolysis cells: The current status and future perspective. *Bioresour Technol, 279*: 339-349, 2019. doi:https://doi.org/10.1016/j.biortech.2019.01.145.

Anaerobic Digestion of Aqueous Pyrolysis Liquid in ADM1

Dheeraj Raya[1] Nirmal Ghimire[1] Gudny Øyre Flatabø[1,2] Wenche Hennie Bergland[1]

[1]Department of Process, Energy and Environmental Technology, University of South-Eastern Norway
[2]Scanship AS, Nedre Langgate 19, 3126, Tønsberg, Norway
rayadheeraj@gmail.com, nirmal.ghimire@usn.no, gudny.flatabo@scanship.no, wenche.bergland@usn.no

Abstract

Aqueous pyrolysis liquid (APL) is formed from pyrolysis of lignocellulosic biomass and is considered as a possible feed for anaerobic digestion (AD). APL is known to contain many components that can have a negative impact on the AD process. In this study, APL is fed into experimental AD batch reactors and modelled as a substrate using the Anaerobic Digestion Model No. 1 (ADM1), extended by addition of the inhibitors phenol, furfural, and 5-hydroxymethylfurfural (HMF). Simulation performed with the extended ADM1 has a better ability to predict the behavior of APL than the standard ADM1. Reducing the inhibition constants and startup concentration of active biomass during simulation of APL at high organic load resulted in improved fit with experimental results, but these inhibitors alone cannot explain the reduced methane production rate at high organic load.

Keywords: Anaerobic Digestion, Lignocellulosic biomass, Aqueous Pyrolysis Liquid, phenol, furfural, HMF, inhibition, ADM1

1 Introduction

Dry lignocellulosic biomasses are abundant in nature and can be harvested sustainably (Feng and Lin, 2017). Using thermochemical and biochemical processes, we can convert such biomasses into energy, either for heat or electricity generation or even as a transport fuel such as biomethane (Pang, 2019). Pyrolysis, a thermochemical process used for dry biomasses, produces value added products such as biochar, syngas, bio-oil, and aqueous pyrolysis liquid (APL) (McNamara et al., 2016).

APL has a high organic content, showing potential for conversion to biogas through anaerobic digestion (AD) (Hübner and Mumme, 2015). However, APL is a complicated mixture – known to contain more than 400 chemical compounds – many of which can have a negative impact on the AD process (Seyedi et al., 2019). Compounds such as phenols, furfural, and 5-hydroxymethylfurfural (HMF) present in APL are known to be inhibitory to AD (Torri and Fabbri, 2014).

Anaerobic digestion, a biochemical process mostly used for treating wastewater, produces biogas that can be upgraded to biomethane. Methanogenesis is the final step that converts acetate (acetoclastic) and hydrogen (hydrogenotrophic) into methane and is also often a rate limiting step in the AD process. APL concentration of 2-4 g COD/L (COD: chemical oxygen demand) has been previously reported to completely inhibit the AD process (Seyedi et al., 2019). Constituents of APL such as phenol, furfural and HMF inhibits the methanogenesis process completely at concentration of 2.5 g/L (Olguin-Lora et al., 2003), 2 g/L (Ghasimi et al., 2016) and 2 g/L (Ghasimi et al., 2016) respectively.

However, microorganisms present in AD are known to thrive in the presence of inhibitory compounds, managing to degrade them during the AD process. Phenol, a weak acid, is broken down to the intermediate benzoate, before it is degraded completely to acetate and hydrogen (Fezzani and Ben Cheikh, 2009). Similarly, furfural and HMF also breaks down anaerobically producing acetate as the final product (Zhang et al., 2012).

The Anaerobic Digestion Model No.1 (ADM1) (Batstone et al., 2002), developed by the International Water Association (IWA), has been widely used by the scientific community for evaluating the performance of AD processes under different substrate and reactor configurations. However, the model has been limited to only major AD processes to make it simpler and easier for modification in the future as per need. Complex substrates such as APL are gaining interest and the constituent phenol is already implemented in ADM1 (Fezzani and Ben Cheikh, 2009), but modifications are needed to study the inhibition caused by the APL constituents furfural and HMF.

Through this study, we aim to better understand the effects of inhibitory compounds present in APL, represented by phenols, furfural and HMF, to predict and simulate the dynamic behavior of AD of APL using ADM1.

2 Materials and Methods

Batch anaerobic reactors, fed APL and run mesophilic, are compared with ADM1 extended with the inhibitor's phenol, furfural, and HMF, known to be present in APL.

2.1 Analytical methods

Total COD (tCOD), soluble COD (sCOD), volatile fatty acids (acetic acid, propionic acid, butyric acid, iso-butyric acid), pH, and ammonium content were analyzed as described in Bergland et al., (2015).

2.2 Material Characterization

2.2.1 APL

APL was obtained from pyrolysis of commercial softwood pellets (Norway spruce and Scots pine 60/40 per volume, Hallingdal Trepellets AS) at 600˚C, using the Biogreen® technology. The pyrolysis liquid was condensed from syngas cooled to 5-8 ˚C, and the APL provided was the top phase decanted after settling by gravity for two weeks in a cool environment.

APL had a tCOD and sCOD of 456 and 428 g/L and contained 75.83 and 5.33 g/L of acetic acid and propionic acid, respectively. APL had a low pH of 2.46.

2.2.2 Inoculum

Inoculum was obtained from Lindum AD plant in Drammen, Norway, a mesophilic process with an installed thermal hydrolysis step prior to AD. The plant treats sewage sludge from surrounding municipalities (about 90% of total volatile solids) and food waste from industry. The inoculum was collected from the effluent stream of the reactor and had a pH of 7.97, total solids (TS) of 16.78 g/L, volatile solids (VS) of 13.14 g/L, and total ammonium nitrogen (TAN) of 486 mg/L.

2.3 Batch Reactor Set up

Anaerobic biogas potential tests were performed in the Automatic Methane Potential Test System II (AMPTS II, Bioprocess Control® Sweden AD, Lund, Sweden 2017). It is used to determine the methane production from any biodegradable material. The experimental procedure can be found in Ghimire et al. (2020). Batch reactors of 500 mL were used with 300 mL of inoculum, and APL was added to have an organic load (OL) of 1.2 and 2.4 g COD APL per litre of inoculum. Additional blank reactors included only inoculum and was used to consider the background methane production. All the reactors were run at 35 ℃ for 54 days with 2 parallels for each test.

2.4 Modelling and Simulation

The original ADM1 was extended by the addition of phenol, furfural and HMF as inhibitory compounds (extended ADM1) (Figure 1). The inclusion of these inhibitory compounds requires the addition of 8 processes (Table 1).

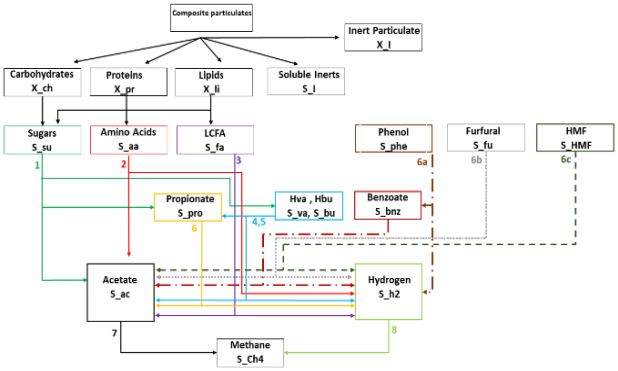

Figure 1. A brief schematic of the extended ADM1.

Table 1. Biochemical stochiometric coefficients and kinetic rate equations for compounds (only additional processes and compounds to standard ADM1 are shown).

	j	6a	6a-1	6b	6c	7	8	9	10	11	22a	22b	22c	22d	22	
	Component ->i	S_phe	S_bnz	S_fu	S_HMF	S_ac	S_h2	S_ch4	S_IC	S_IN	X_Phe	X_bnz	X_fu	X_HMF	X_ac	Rate [ρ_j, kgCOD/m^3*d]
	Process															
6a	Uptake of Phenol						f_h2_phe*(1-Y_phe)	-sum(C_i*vi_6a) i=1-9,11-24	-(Y_phe)* N_bac		Y_phe					km_phe*(S_phe/(Ks+S_phe))*X_phe*I_1
6a-1	Uptake of Benzoate		-1				f_h2_bnz*(1-Y_bnz)	sum(C_i*vi_6a-1) i=1-9,11-24	-(Y_bnz)* N_bac		Y_bnz					km_bnz*(S_bnz/(Ks+S_bnz))*X_bnz*I_1*I_h2_bnz
6b	Uptake of Furfural			-1			f_ac_fu*(1-Y_fu)	sum(C_i*vi_6b) i=1-9,11-24	-(Y_fu)* N_bac				Y_fu			km_fu*(S_fu/(Ks+S_fu))*X_fu*I_1
6c	Uptake of HMF				-1	f_ac_HMF*(1-Y_HMF)	f_ac_HMF*(1-Y_HMF)	sum(C_i*vi_6c) i=1-9,11-24	-(Y_HMF)* N_bac					Y_HMF		km_HMF*(S_HMF/(Ks+S_HMF))*X_HMF*I_1
7	Uptake of Acetate					-1	(1-Y_ac)	-sum(C_i*vi_7) i=1-9,11-24	-(Y_ac)* N_bac						Y_ac	km_ac*(S_ac/(Ks+S_ac))*X_ac*I_2
13a	Decay of X_phe										-1				kdec_X_phe*X_phe	
13a-1	Decay of X_bnz											-1			kdec_X_bnz*X_bnz	
13b	Decay of X_fu												-1		kdec_X_fu*X_fu	
13c	Decay of X_HMF													-1	kdec_X_HMF*X_HMF	
14	Decay of X_ac														-1 kdec_X_ac*X_ac	Inhibition: I_1=I_pH*I_NH_lim; I_2=I_pH*I_NH_lim*I_NH3_xac*I_phe_ac*I_fu_ac*I_HMF_ac

Each conversion process was implemented by several kinetic expressions that describe the conversion processes in terms of rate constants and substrate concentration. The conversion of inhibitory compounds to their respective products was described using Monod's growth kinetic equation. Endogenous decay of the biomass degrading the inhibitory compounds was modelled using first order kinetics, and dead biomass was maintained as composite particulates as in the original ADM1.

The detailed stoichiometry of all the processes and rate equations used are presented (Table 1) with their respective values (Table 2). The uptake of acetate in the extended ADM1 was modified by addition of inhibition from phenols, furfural and HMF as shown by process 7 in Table 1. Inhibition by phenol, furfural and HMF was modelled using a non-competitive inhibition function (1) (Batstone et al., 2002).

$$I = \frac{1}{1+\frac{S}{K_i}} \quad (1)$$

I = Inhibition, S = concentration of substrate in kg COD/m^3, and K_i = inhibition constant (concentration of substrate that inhibits the activity of the microorganisms by 50%).

Phenol is a weak acid and both phenol and benzoate contribute to pH changes. The charge balance equation used in the standard ADM1 (Batstone et al., 2002) was extended to include the contributions from phenol and benzoate (2).

$$S_{H^+} - S_{OH^-} = S_{HCO_3^-} + \frac{S_{ac^-}}{64} + \frac{S_{pro^-}}{112} + \frac{S_{bu^-}}{160} + \frac{S_{va^-}}{208} + \frac{S_{phe^-}}{224} + \frac{S_{bnz^-}}{240} + S_{An^+} - S_{cat^+} - S_{NH_4^+} \quad (2)$$

Where S_{phe^-} and S_{bnz^-} are phenol (3) and benzoate ion concentration (4), implemented in ADM1 as described by Batstone et al. (2002).

$$S_{phe^-} - \frac{K_{a,phe} \times S_{phe}}{K_{a,phe} + S_{H^+}} = 0 \quad (3)$$

Where $K_{a,phe}$ (phenolic acid dissociation constant) is 1×10^{-10}(Sharma and Kaminski, 2012).

$$S_{bnz^-} - \frac{K_{a,bnz} \times S_{bnz}}{K_{a,bnz} + S_{H^+}} = 0 \quad (4)$$

Where the $K_{a,bnz}$ (benzoic acid dissociation constant) is 6.3×10^{-5} (*Ionization Constants of Organic Acids*, n.d.)

Table 2. Kinetics parameters and their respective value used for degradation of phenol, furfural and HMF

Parameter	*Description*	*Unit*	*Phenol*	*Benzoate*	*Furfural*	*HMF*	*Value*
C	Carbon content in compound	KmoleC/kg COD	0.391[a]	0.0343[a]	5/160[e]	6/192[e]	-
Km	Maximum uptake rate	d-1	15[a]	8[a]	10[c]	10[c]	-
Ks	Half saturation constant for uptake	kg CODs/m3	30[a]	15.5[a]	10[c]	10[c]	-
Kdec	Decay rate for biomass	d-1	0.02	0.02	0.02[d]	0.01[c]	-
Y	Yield of biomass on uptake	kg CODx/kg CODs	0.01[a]	0.013[a]	0.08[d]	0.1[c]	-
Ki	Inhibition on methanogens from compound	kg CODs/m3	1.12[a]	-	2.105[e]	2.05[e]	-
Ki_bnz_h2	Inhibition on benzoate degraders by hydrogen	kg CODs/m3	-	9.50E-05[b]	-	-	-
X	Concentration of biomass	kg CODx/m3	0.21	0.24	0.12	0.18	-
f_bnz_phe	Yield of benzoate from phenol		-	-	-	-	0.87[a]
f_h2_phe	Yield of hydrogen from phenol		-	-	-	-	0.13[a]
f_ac_bnz	Yield of acetate from benzoate		-	-	-	-	0.51[a]
f_h2_bnz	Yield of hydrogen from benzoate		-	-	-	-	0.49[a]
f_ac_fu	Yield of acetate from furfural		-	-	-	-	0.8[d]
f_h2_fu	Yield of hydrogen from furfural		-	-	-	-	0.2[d]
f_ac_HMF	Yield of acetate from HMF		-	-	-	-	0.88[c]
f_h2_HMF	Yield of hydrogen from HMF		-	-	-	-	0.12[c]

[a] (Fezzani and Ben Cheikh 2009)
[b] (Elshahed et al. 2001)
[c] (Liu et al. 2017)
[d] (Brune, Schoberth, and Sahm 1983)
[e] calculated

2.4.1 APL characteristics

APL concentrations implemented in ADM1 (Table 3) were measured based on APL characteristics. Phenol, furfural and HMF concentrations are not known and were from reporting APL from birch bark (hardwood) pyrolysed at 600 °C.

Table 3. APL composition used for simulations.

Parameters	*Value*
Acetic acid (g/L)	75.832[f]
Propionic acid (g/L)	5.33 [f]
Phenol (g/L)	25[g]
Furfural (g/L)	10[h]
HMF (g/L)	7 [h]
Soluble Inorganic Nitrogen (kmole/m^3)	0.025[e]
X_C	Calculated

Around 50 % of the APL COD is unknown and was added as complex particulate (X_C) already present in the ADM1.

2.4.2 Determination of inhibition constant for furfural and HMF

Prior knowledge of the inhibition constant for furfural and HMF (1) required for modelling the inhibition effect is not found in the literature. Experimental results of specific methanogenic activity (SMA) from Ghasimi et al. (2016) is used to determine the IC_{50} value that can be used as inhibition constant K_i (1). Thus, inhibition constant values are calculated graphically to obtain the IC_{50} value, the concentration of substrate at which 50% inhibition occurs (Figure 2).

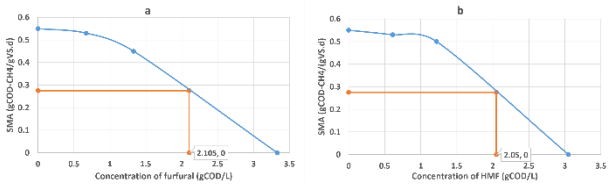

Figure 2. IC_{50} value determination using graphical method for a: furfural and b: HMF. Based on SMA activity from Ghasimi et al. (2016).

2.4.3 Simulation strategy

To evaluate the extended model, the simulation was performed based on three strategies:

1. Vary the concentration of inhibitory compounds to evaluate the effect (Table 4).
2. Vary the inhibition constant to evaluate the sensitivity in the model (Table 5).
3. Vary the startup active biomass concentration of inhibitory compounds degraders. Both sufficient and low startup concentration of biomass (X_low=X×0.1) were tested.

Table 4. Concentration of inhibitory compounds in APL used in simulations of AD of APL at OL of 1.2 and 2.4 g COD/L.

Inhibitory compounds	*Sim-base*	*Sim-inhib-low*	*Sim-inhib-avg*	*Sim-inhib-high*
Phenol (g/L)	25	5	25	40
Furfural (g/L)	10	5	25	40
HMF (g/L)	7	5	25	40

Table 5. Inhibition constant used in simulations of AD of APL at OL of 2.4 g COD/L.

Inhibition constant	*Sim-base*	*Sim-Ki_low_1*	*Sim-Ki_low_2*	*Sim-Ki_low_3*
KI_fu (kg COD/m^3)	2.10	0.84	0.21	0.11
KI_HMF (kg COD/m^3)	2.05	0.82	0.21	0.10
KI_phe (kg COD/m^3)	1.12	0.45	0.11	0.06

3 Results and Discussion

3.1 Experimental Results

The methane production rate (Figure 3) was low for APL with OL of 2.4 g COD/L (APL2.4) and was same as Blank (only inoculum) till day 2, whereas APL with OL of 1.2 g COD/L (APL1.2) had a gradual methane production until day 20 with no lag phase. Unpublished results during batch AD tests of the same APL gave increased lag phase when the organic load was higher than 2 g COD/L and total inhibition at OL of 3 g COD/L.

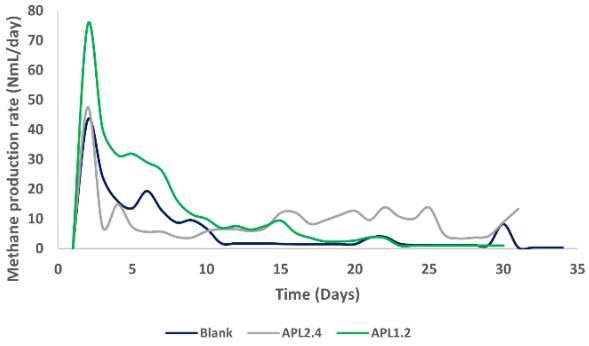

Figure 3. Methane production rate from batch test of APL at organic load of 1.2 and 2.4 g COD/L referred to as

[f] Measured
[g] (Yu et al. 2020)
[h] (Torri and Fabbri 2014)

APL1.2 and APL2.4, respectively, along with results from blank (only inoculum).

3.2 Simulation results

3.2.1 Simulation of APL

Simulation of APL1.2 (sim1.2) by standard ADM1 and extended ADM1 shows a good fit to the experimental results (Figure 4), however, both standard and extended ADM1 was not able to follow the trend of methane production rate at high OL (sim2.4).

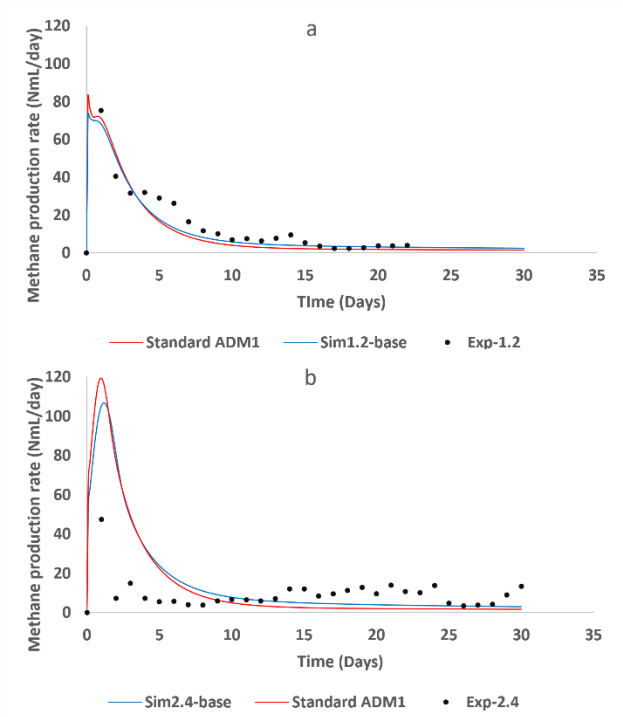

Figure 4. Simulated methane production rate using standard ADM1 (red line), extended ADM1 model (blue line) and experimental results (black dots) for APL a: at organic load of 1.2 g COD/L (Sim1.2-base) b: at organic load of 2.4 g COD/L (Sim2.4-base).

3.2.2 Simulation with varying inhibitory compound concentration

Simulations performed with varying concentrations of inhibitory compounds revealed only a small effect on the methane production rate for APL at low OL of 1.2 g COD/L (Figure 5). However, the effect from high inhibitor concentrations at OL of 2.4 g COD/L of APL was more pronounced. High OL and thereby high concentration of inhibitory compounds resulted in inhibition and a lower maximum methane production rate.

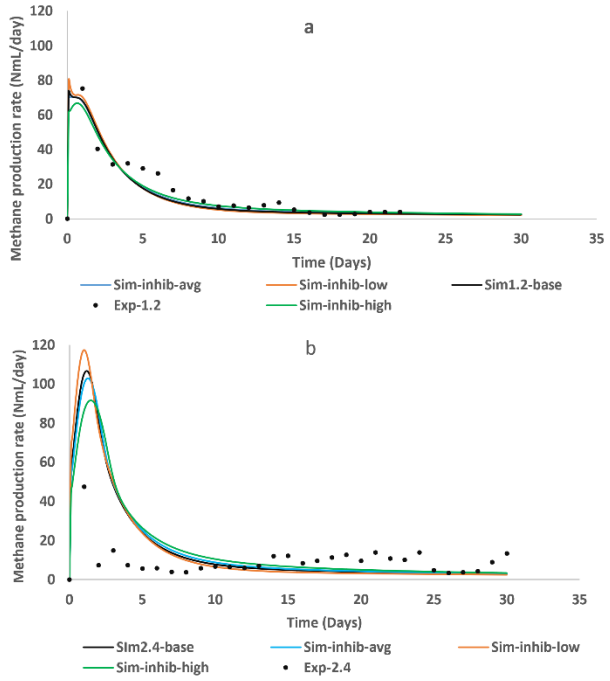

Figure 5. Simulation with varying concentration of inhibitory compounds (Table 5). a: simulated methane production rate for APL1.2 with experimental results (black dots) b: simulated methane production rate for APL2.4 with experimental results (black dots).

The inhibition by the individual inhibitory compounds increased with an increase in concentration (Figure 6). Phenol causes the highest inhibition effect on the methanogens. The total effect from the inhibitors can however not explain the low fit between the simulations and the experiment with OL of 2.4 g COD APL/L (Figure 5).

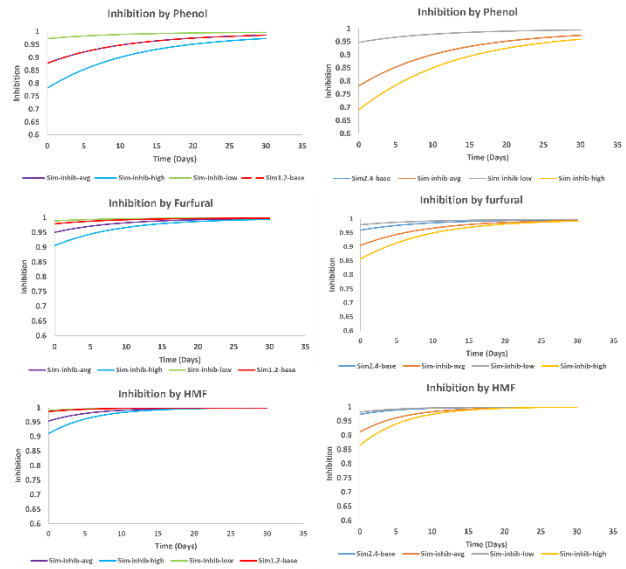

Figure 6. Inhibition by inhibitory compounds on methanogens. 1 is no inhibition at all and 0 is full inhibition. a: simulated inhibition for APL OL of 1.2 g COD/L b: simulated inhibition for APL OL of 2.4 g COD/L.

3.2.3 Simulation with varying inhibition constant and low biomass concentration of inhibitory compound degraders

Reducing the estimated inhibition constants (Table 5) resulted in a maximum methane production rate that decreased drastically (Figure 7). This is however not based on real inhibition constants but rather reveals the high degree of sensitivity towards a change in the inhibition constant. The concentration of active initial biomass degrading the individual inhibitory compounds is not known and reducing these concentrations (Figure 7) also reveals an effect further reducing the gap between experiment and simulated methane production rate at OL 2.4 g COD APL/L.

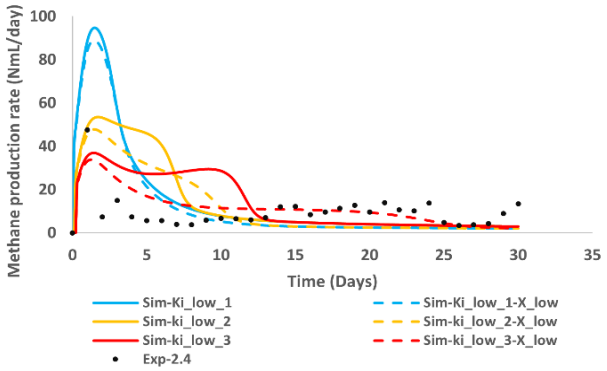

Figure 7. Simulated methane production rate with low initial startup concentration of inhibitory compounds degrading biomass (Sim-Ki_low_3-X_low, Sim-Ki_low_2-X_low, and Sim-Ki_low_1-X_low) represented by dashed lines and simulation with only change in inhibition constant for inhibitory compounds represented by lines. Experiment with OL 2.4 g COD APL/L (black dots).

Even though the inhibition constant used in Sim-Ki_low_3-X_low was low, it can be justified that there are a lot of unknown compounds in APL that have potential to inhibit the methanogenesis. Compounds such as chlorinated alkenes and alkanes, nitros and nitriles are known to severely inhibit the methanogenesis even at low concentrations (Blum and Speece, 1991). Thus, there is the possibility that the inhibition seen using the lowest inhibition constant (Sim-Ki_low_3 and Sim-Ki_low_3-X_low in Figure 7) could also be observed if further inhibitory compounds are added to the model, such as ketones, polyaromatic hydrocarbons and esters – which are also known to be present in APL and known to inhibit methanogenesis (Blum and Speece, 1991). Microorganism can however also be adapted to inhibitors (Badshah, 2012;Wen, 2020) suggesting lower inhibition over time in continuous AD reactors.

4 Conclusion

The effect of the inhibitors furfural, HMF, and phenols present in APL using ADM1 reveals a high sensitivity of the inhibition constant (made from 50% inhibition of the methanogens). When using realistic values for the inhibition constants and concentrations of inhibitory compounds, the reduced methane production rate at high organic load of APL cannot be explained by furfural, HMF, and phenols alone in batch AD. APL contains several known and unknown compounds and it is suggested to study more of these to find the combined inhibitory effect.

References

M. Badshah. Evaluation of process parameters and treatments of different raw materials for biogas production (PhD Thesis), Lund University, 2012. https://lup.lub.lu.se/record/3130472

D. J. Batstone, J. Keller, I. Angelidaki, S. V. Kalyuzhnyi, S. G. Pavlostathis, A. Rozzi, W. T. M. Sanders, H. Siegrist, and V. A. Vavilin. The IWA Anaerobic Digestion Model No 1 (ADM1). *Water Science and Technology*, *45*(10), 65–73, 2002. https://doi.org/10.2166/wst.2002.0292

W. H. Bergland, C. Dinamarca, M. Toradzadegan, A. S. R. Nordgård, I. Bakke, and R. Bakke. High rate manure supernatant digestion. *Water Research*, *76*, 1–9, 2015. https://doi.org/10.1016/j.watres.2015.02.051

D. J. Blum, and R. E. Speece. *A database of chemical toxicity to environmental bacteria and its use in interspecies comparisons and correlations*. *63*(3), 198–207, 1991.

G. Brune, S. M. Schoberth, and H. Sahm. Growth of a Strictly Anaerobic Bacterium on Furfural (2-Furaldehyde). *Applied and Environmental Microbiology*, *46*(5), 1187–1192, 1983. https://doi.org/10.1128/AEM.46.5.1187-1192.1983

M. S. Elshahed, V. K. Bhupathiraju, N. Q. Wofford, M. A. Nanny, and M. J. McInerney. Metabolism of Benzoate, Cyclohex-1-ene Carboxylate, and Cyclohexane Carboxylate by "Syntrophus aciditrophicus" Strain SB in Syntrophic Association with H2-Using Microorganisms. *Applied and Environmental Microbiology*, *67*(4), 1728–1738, 2001. https://doi.org/10.1128/AEM.67.4.1728-1738.2001

Q. Feng, and Y. Lin. Integrated processes of anaerobic digestion and pyrolysis for higher bioenergy recovery from lignocellulosic biomass: A brief review. *Renewable and Sustainable Energy Reviews*, *77*, 1272–1287, 2017. https://doi.org/10.1016/j.rser.2017.03.022

B. Fezzani, and R. Ben Cheikh. Extension of the anaerobic digestion model No. 1 (ADM1) to include phenol compounds biodegradation processes for simulating the anaerobic co-digestion of olive mill wastes at mesophilic temperature. *Journal of Hazardous Materials*, *172*(2–3), 1430–1438, 2009. https://doi.org/10.1016/j.jhazmat.2009.08.017

D. S. M. Ghasimi, K. Aboudi, M. de Kreuk, M. H. Zandvoort, and J. B. van Lier. Impact of lignocellulosic-waste intermediates on hydrolysis and methanogenesis under thermophilic and mesophilic conditions. *Chemical Engineering Journal*, *295*, 181–191, 2016. https://doi.org/10.1016/j.cej.2016.03.045

N. Ghimire, R. Bakke, and W. H. Bergland. Thermophilic Methane Production from Hydrothermally Pretreated

Norway Spruce (Picea abies). *Applied Sciences*, *10*(14), 4989, 2020. https://doi.org/10.3390/app10144989

T. Hübner, and J. Mumme. Integration of pyrolysis and anaerobic digestion – Use of aqueous liquor from digestate pyrolysis for biogas production. *Bioresource Technology*, *183*, 86–92, 2015. https://doi.org/10.1016/j.biortech.2015.02.037

Ionization Constants of Organic Acids. (n.d.). Retrieved April 21, 2021, from https://www2.chemistry.msu.edu/faculty/reusch/VirtTxtJml/acidity2.htm

B. Liu, V. A. Ngo, M. Terashima, and H. Yasui. Anaerobic treatment of hydrothermally solubilised sugarcane bagasse and its kinetic modelling. *Bioresource Technology*, *234*, 253–263, 2017. https://doi.org/10.1016/j.biortech.2017.03.024

P. J. McNamara, J. D. Koch, Z. Liu, and D. H. Zitomer. Pyrolysis of Dried Wastewater Biosolids Can Be Energy Positive. *Water Environment Research*, *88*(9), 804–810, 2016. https://doi.org/10.2175/106143016X14609975747441

P. Olguin-Lora, L. Puig-Grajales, and E. Razo-Flores. Inhibition of the acetoclastic methanogenic activity by phenol and *alkyl* phenols. *Environmental Technology*, *24*(8), 999–1006, 2003. https://doi.org/10.1080/09593330309385638

S. Pang. Advances in thermochemical conversion of woody biomass to energy, fuels and chemicals. *Biotechnology Advances*, *37*(4), 589–597, 2019. https://doi.org/10.1016/j.biotechadv.2018.11.004

S. Seyedi, K. Venkiteshwaran, and D. Zitomer. Toxicity of Various Pyrolysis Liquids From Biosolids on Methane Production Yield. *Frontiers in Energy Research*, *7*, 5, 2019. https://doi.org/10.3389/fenrg.2019.00005

I. Sharma and G. A. Kaminski. Calculating pKa values for substituted phenols and hydration energies for other compounds with the first-order Fuzzy-Border continuum solvation model. *Journal of Computational Chemistry*, *33*(30), 2388–2399. PubMed, 2012. https://doi.org/10.1002/jcc.23074

C. Torri, and D. Fabbri. Biochar enables anaerobic digestion of aqueous phase from intermediate pyrolysis of biomass. *Bioresource Technology*, *172*, 335–341, 2014. https://doi.org/10.1016/j.biortech.2014.09.021

C. Wen, C. M. Moreira, L. Rehmann, and F. Berruti. Feasibility of anaerobic digestion as a treatment for the aqueous pyrolysis condensate (APC) of birch bark. *Bioresource Technology*, *307*, 123199, 2020. https://doi.org/10.1016/j.biortech.2020.123199

X. Yu, C. Zhang, L. Qiu, Y. Yao, G. Sun, and X. Guo. Anaerobic digestion of swine manure using aqueous pyrolysis liquid as an additive. *Renewable Energy*, *147*, 2484–2493, 2020. https://doi.org/10.1016/j.renene.2019.10.096

Y. Zhang, B. Han, and T. C. Ezeji. Biotransformation of furfural and 5-hydroxymethyl furfural (HMF) by Clostridium acetobutylicum ATCC 824 during butanol fermentation. *New Biotechnology*, *29*(3), 345–351, 2012. https://doi.org/10.1016/j.nbt.2011.09.001

A Model of Aerobic and Anaerobic Metabolism in Cancer Cells – Parameter Estimation, Simulation, and Comparison with Experimental Results

Svein H. Stokka[1] Eivind S. Haus[1] Gunhild Fjeld[2] Tormod Drengstig[1] Kristian Thorsen[1]

[1]Department of Electrical Engineering and Computer Science, University of Stavanger, Norway,
{svein.h.stokka, eivind.haus, tormod.drengstig, kristian.thorsen}@uis.no
[2]Stavanger University Hospital, Stavanger, Norway, gunhild.fjeld@sus.no

Abstract

We present a mathematical model of metabolism in cancer cells that is capable of describing both aerobic oxidative metabolism and anaerobic fermentation metabolism, and how cancer cells shift between these metabolic states when exposed to different substrates and different enzymatic inhibitors. The model is designed to be used in combination with experimental data gathered with an Agilent Seahorse XF metabolic analyzer. The model is parameterized in a manual tuning procedure to fit experimental data, and validated against experimental data from another setup, to which the model shows good conformity. We also investigate the structural identifiability of the model. The results indicate that the model is structurally identifiable, and that it can thus be uniquely parameterized, using the following 5 measurements: extracellular concentrations of glucose, glutamine and lactate, proton production rate (a Seahorse XF analyzer measurement) and oxygen consumption rate.

Keywords: biological systems, cancer metabolism, simulation, parameter estimation, biotechnology

1 Introduction

Cancer is a group of diseases where cells grow and proliferate uncontrollably (Jones and Thompson, 2009). An emerging hallmark of cancer is reprogrammed energy metabolism (Hanahan and Weinberg, 2011). Metabolism is important in understanding how different cancer cells proliferate and develop into tumors and metastases, and for designing and testing therapeutic strategies.

Cancer cells differ from non-cancerous cells in that they typically have a high uptake of glucose and a shift from energetically efficient oxidative metabolism to less efficient anaerobic fermentation even in the presence of O_2. This phenomenon is the so-called Warburg effect (Liberti and Locasale, 2016; Warburg, 1956). Many cancer cells also have an increased metabolic reliance on glutamine (Wise and Thompson, 2010), which is the most abundant free amino acid in muscles and blood plasma.

In this paper we present a model of aerobic and anaerobic metabolism in cancer cells designed to be used in combination with experiments performed using an Agilent Seahorse XF analytic instrument, a commonly used tool for studying and metabolic phenotyping cancer cells. The Seahorse XF instrument measures oxygen consumption rate (OCR) and extracellular acidification rate (ECAR) in live cells under controlled conditions. The instrument features automatic injection and mixing of up to four substances and can run experiments that reveal how cells respond to addition of metabolic substrates and how they respond to forced blocking of certain metabolic pathways by the addition of enzymatic inhibitors (Agilent, 2019).

2 Modeling

Our model includes cellular uptake and metabolism of glucose and glutamine, and describes the most prominent metabolic processes by simplified kinetic expressions. The model deals with enzymatic reactions, i.e. fast changes in metabolic reaction rates, due to immediate additions of substrates and inhibitors. Since the timescale of experiments are in the order of minutes to a maximum of a few hours, significantly shorter than the doubling time for typical cell lines used in these experiments, cell growth is not considered in the model. The Caco2 cell line used in this work has a doubling time in the range of days (Hidalgo et al., 1989). Figure 1 shows a schematic overview of the model (see also Table 1 for a list of abbreviations). The model has the following 12 state variables: the internal concentrations of metabolites and metabolic intermediates (glucose, pyruvate, glutamine, α-ketoglutarate, and lactate), the internal concentration of ADP and ATP (for energy production and balance), the concentration of NAD^+ and NADH (the electron carrier in oxidative production of ATP), and the external concentrations of glucose, glutamine, and lactate. There are in total 11 metabolic reactions, or flow expressions, in the model. As indicated by the red and green symbols in Figure 1, the model also includes the effect of the following 5 inhibitors: 2-DG (2-deoxyglucose), rotenone, antimycin A, oligomycin and CCCP (Carbonyl cyanide m-chlorophenyl hydrazone). These inhibitors are often used in Seahorse experiments, such as glycolysis- and mitochondrial stress tests (Agilent, 2019).

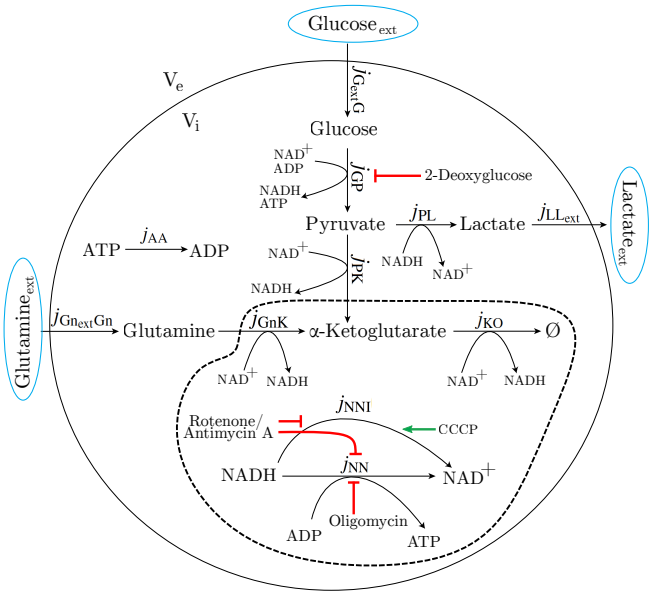

Figure 1. Overview of the model. The fully drawn circle is the cell membrane. Inside the dotted line is the mitochondria. The black arrows are metabolic reactions and the red and green lines show inhibitors/activators often used in Seahorse experiments.

Table 1. List of abbreviations.

G	glucose
P	pyruvate
Gn	glutamine
K	α-ketoglutarate
L	lactate
NAD^+	nicotinamide adenine dinucleotide (oxidized form)
NADH	nicotinamide adenine dinucleotide
ATP	adenosine triphosphate
ADP	adenosine diphosphate
G_{ext}	extracellular glucose
Gn_{ext}	extracellular glutamine
L_{ext}	extracellular lactate
OCR	oxygen consumption rate
ECAR	extracellular acidification rate
PPR	proton production rate
TCA cycle	tricarboxylic acid cycle
2-DG	2-deoxyglucose

Notation

The reactions in the model are simplified and each reaction actually covers multiple enzyme catalyzed reaction steps. Unless otherwise stated, we assume that the overall reactions are irreversible and we use the rate constants k to describe the maximum reaction- or transport rate. We use subscript to denote the reaction, e.g., the rate constant for glycolysis, j_{GP}, is k_{GP}. The effect of substrates in reactions are expressed by saturation ratios $r\,(0 \leq r \leq 1)$, where we use subscript to denote the reaction and superscript to denote the substrate. We use saturation ratios based on the Micahelis-Menten equation. As an example, the contribution of glucose G to the glycolysis rate j_{GP} is described in the saturation ratio given as $r^{G}_{GP} = \frac{G}{K^{G}_{GP}+G}$, where K^{G}_{GP} is the half-saturation constant.

The expressions for the different reactions in the model will be explained in the following.

Transport

With a few exceptions, such as O_2 and CO_2, most molecules cannot freely diffuse across the cell membrane, and thus, transport across the cell membrane is dependent on transport proteins. Glucose is transported across the cell membrane by glucose transporter proteins (SLC2A family) through facilitated diffusion – a passive process where the concentration gradient provides energy for protein mediated transport across the membrane. The so-called GLUT1 transporter protein (SLC2A1) is of special interest in studies of cancer metabolism, as it is abundant in many human tumor types (DeBerardinis et al., 2008; Hanahan and Weinberg, 2011).

Glutamine is transported across the cell membrane by several amino acid transporters, but most notably by SLC1A5 and SLC6A14 which are commonly upregulated in cancer cells (Scalise et al., 2017; Cha et al., 2018).

Lactate is transported out of the cell by monocarboxylate transporters (MCTs), a type of symporter that couple protons (H^+) and monocarboxylate transport, and hence, lactate excretion is coupled with extracellular acidification.

The expressions for transport of glucose, glutamine and lactate in Eqs.(1)-(3) respectively, are all modeled as facilitated diffusion through transporter proteins where we use the fixed site carrier model (Baker and Widdas, 1973) describing transport through a membrane pore with binding sites on both sides of the membrane.

$$j_{G_{ext}G} = k_{G_{ext}G} \frac{G_{ext} - G}{\left(K^{G_{ext}}_{G_{ext}G} + G_{ext}\right)\left(K^{G}_{G_{ext}G} + G\right)} \quad (1)$$

$$j_{Gn_{ext}Gn} = k_{Gn_{ext}Gn} \frac{Gn_{ext} - Gn}{\left(K^{Gn_{ext}}_{Gn_{ext}Gn} + Gn_{ext}\right)\left(K^{Gn}_{Gn_{ext}Gn} + Gn\right)} \quad (2)$$

$$j_{LL_{ext}} = k_{LL_{ext}} \frac{L - L_{ext}}{\left(K^{L}_{LL_{ext}} + L\right)\left(K^{L_{ext}}_{LL_{ext}} + L_{ext}\right)} \quad (3)$$

The transport of glucose ($j_{G_{ext}G}$) and glutamine ($j_{Gn_{ext}Gn}$) are defined positive into the cell, whereas the transport of lactate ($j_{LL_{ext}}$) is defined positive out of the cell.

Glycolysis and fermentation

Glucose is converted to pyruvate in a series of 10 enzyme catalyzed reactions in the glycolysis pathway. The net production for each glucose molecule through the glycolysis is 2 pyruvate-, 2 ATP- and 1 NADH molecules. The modeled expression for the glycolytic flux, j_{GP}, given as

$$j_{GP} = k_{GP}\, r^{G}_{GP}\, r^{ADP}_{GP}\, r^{NAD}_{GP} \quad (4)$$

depend on glucose, ADP and NAD^+.

Cells regenerate NAD^+ to sustain glycolysis, and if O_2 is available most cells prefer to oxidize NADH in the mitochondria to produce more ATP. In the absence of O_2, cells regenerate NAD^+ through fermentation by reducing pyruvate to lactate. Cancer cells, however, often show a preference for fermentation even in the presence of O_2, which refers to the so-called Warburg effect or aerobic glycolysis. The expression for fermentation, j_{PL}, is given as

$$j_{\mathrm{PL}} = k_{\mathrm{PL}}\, r_{\mathrm{PL}}^{\mathrm{P}}\, r_{\mathrm{PL}}^{\mathrm{NADH}} \tag{5}$$

Oxidative metabolism

In the mitochondria (the inside of the dashed line in Figure 1) organic material such as pyruvate can be further catabolized in the TCA cycle (tricarboxylic acid cycle) to produce large quantities of NADH, which is oxidized to NAD^+ by O_2 in the electron transport chain. The oxidation of NADH is coupled to ATP production by a proton gradient across the inner mitochondrial membrane, where the gradient is sustained by proton transport by the electron transport chain and used by ATP synthase to produce ATP. This process is called oxidative phosphorylation. To account for proton leak, we use the following two fluxes to describe oxidative phosphorylation.

$$j_{\mathrm{NN}} = k_{\mathrm{NN}}\, r_{\mathrm{NN}}^{\mathrm{NADH}}\, r_{\mathrm{NN}}^{\mathrm{ADP}} \tag{6}$$

$$j_{\mathrm{NNI}} = k_{\mathrm{NNI}}\, \mathrm{NADH} \tag{7}$$

where j_{NN} describe the regeneration of NAD^+ coupled to ATP production and j_{NNI} describe the regeneration of NAD^+ coupled to proton leak across the membrane.

Pyruvate is transported into the mitochondria where it is completely catabolized in the TCA cycle producing 4 NADH molecules for each pyruvate molecule. In the model we describe the catabolism of pyruvate in two steps: first conversion of pyruvate to TCA intermediate α-ketoglutarate, j_{PK} in equation (8), and second conversion of α-ketoglutarate to oxaloacetate, j_{KO} in equation (9).

In addition, glutamine enters the TCA cycle through glutaminolysis, j_{GnK} in equation (10), where glutamine is converted to α-ketoglutarate that also produce NAD(P)H. Oxaloacetate is in the model treated as a sink (symbol Ø in Figure 1) as we do not include further anabolic processes.

$$j_{\mathrm{PK}} = k_{\mathrm{PK}}\, r_{\mathrm{PK}}^{\mathrm{P}}\, r_{\mathrm{PK}}^{\mathrm{NAD}} \tag{8}$$

$$j_{\mathrm{KO}} = k_{\mathrm{KO}}\, r_{\mathrm{KO}}^{\mathrm{K}}\, r_{\mathrm{KO}}^{\mathrm{NAD}} \tag{9}$$

$$j_{\mathrm{GnK}} = k_{\mathrm{GnK}}\, r_{\mathrm{GnK}}^{\mathrm{Gn}}\, r_{\mathrm{GnK}}^{\mathrm{NAD}} \tag{10}$$

Energy consumption

We assume that the cellular energy consumption, j_{AA}, depends on ATP availability as follows:

$$j_{\mathrm{AA}} = k_{\mathrm{AA}}\, r_{\mathrm{AA}}^{\mathrm{ATP}} \tag{11}$$

State equations

Equations (1) - (11) represent the 11 reactions in our model, giving the following 12 state equations of our model:

$$\dot{\mathrm{G}} = j_{\mathrm{G_{ext}G}} - j_{\mathrm{GP}} \tag{12}$$

$$\dot{\mathrm{P}} = 2\, j_{\mathrm{GP}} - j_{\mathrm{PK}} - j_{\mathrm{PL}} \tag{13}$$

$$\dot{\mathrm{Gn}} = j_{\mathrm{Gn_{ext}Gn}} - j_{\mathrm{GnK}} \tag{14}$$

$$\dot{\mathrm{K}} = j_{\mathrm{PK}} + j_{\mathrm{GnK}} - j_{\mathrm{KO}} \tag{15}$$

$$\dot{\mathrm{L}} = j_{\mathrm{PL}} - j_{\mathrm{LL_{ext}}} \tag{16}$$

$$\dot{\mathrm{NAD}} = j_{\mathrm{PL}} + j_{\mathrm{NN}} + j_{\mathrm{NNI}} - j_{\mathrm{GnK}} - 2\, j_{\mathrm{GP}} - 2\, j_{\mathrm{PK}} - 2\, j_{\mathrm{KO}} \tag{17}$$

$$\dot{\mathrm{NADH}} = -\dot{\mathrm{NAD}} \tag{18}$$

$$\dot{\mathrm{ATP}} = 2\, j_{\mathrm{GP}} + 2.5\, j_{\mathrm{NN}} - j_{\mathrm{AA}} \tag{19}$$

$$\dot{\mathrm{ADP}} = -\dot{\mathrm{ATP}} \tag{20}$$

$$\dot{\mathrm{nG}}_{\mathrm{ext}} = -\,\mathrm{V_i}\, j_{\mathrm{G_{ext}G}} \tag{21}$$

$$\dot{\mathrm{nGn}}_{\mathrm{ext}} = -\,\mathrm{V_i}\, j_{\mathrm{Gn_{ext}Gn}} \tag{22}$$

$$\dot{\mathrm{nL}}_{\mathrm{ext}} = \mathrm{V_i}\, j_{\mathrm{LL_{ext}}} \tag{23}$$

where $\mathrm{V_i}$ is the total cellular volume. Note that the extracellular state variables are expressed in amount in moles instead of concentration because the extracellular volume may change. The extracellular concentration of glucose, glutamine and lactate are found by dividing their respective amount by the extracellular volume $\mathrm{V_e}$.

3 Seahorse XF

The Seahorse XFp Analyzer measures OCR and ECAR on live cells placed in a specialized well plate. The measurements are performed by sinking a sensor into the well creating a microchamber with a volume of $2\,\mu$l where changes in pH and O_2 concentration occur more rapidly due to the small volume.

ECAR measurements, which is the change of pH in the microchamber ($-\frac{d\mathrm{pH}}{dt}$), are converted to PPR (proton production rate), which is a measure of the number of protons (H^+) excreted from the cells. Excretion of lactate is the primary source of extracellular acidification and is related to PPR (mol/s) by

$$\mathrm{PPR} = \mathrm{V_i}\, j_{\mathrm{LL_{ext}}} \tag{24}$$

OCR is a measurement of cellular O_2 consumption, ($-\frac{d\mathrm{O_2}}{dt}$), where oxidation of NADH in oxidative phosphorylation is the primary consumer of O_2. Since 2 NADH molecules is oxidized for each O_2 molecule, OCR (mol/s) is related to oxidative phosphorylation by

$$\mathrm{OCR} = \frac{\mathrm{V_i}}{2}\,(j_{\mathrm{NN}} + j_{\mathrm{NNI}}) \tag{25}$$

Inhibitors

The model is designed to be used in combination with experimental results from so called glycolysis- and mitochondrial stress tests performed with the Seahorse XFp

Analyzer. In these experiments, inhibitors that block or disrupt certain metabolic pathways in the cells are injected into the wells. The following describe these inhibitors and how we implement their effect in the model.

2-Deoxyglucose (2-DG) is a glucose analogue that is transported through the cell membrane by GLUT1. Inside the cell 2-DG and its derivatives inhibit early steps in glycolysis, j_{GP}. We implement the injection of 2-DG as a 99% decrease in the rate constant for glycolysis, k_{GP}.

Oligomycin is an inhibitor of the enzyme complex ATP synthase, which phosphorylate ADP in oxidative phosphorylation, and we implement the injection of oligomycin as a decrease in the rate constant k_{NN} by 99%. Oxidation of NADH still occurs, but at a lower rate, primarily due to proton leak across the mitochondrial inner membrane, which is described by j_{NNI}.

CCCP is an inhibitor of oxidative phosphorylation, i.e. it uncouples the oxidation of NADH with ATP synthesis by destroying the proton gradient across the inner mitochondrial membrane and therefore acts as an activator of oxidative phosphorylation coupled to proton leak. We implement the injection of CCCP as an increase in the rate constant for the oxidation of NADH coupled to proton leak k_{NNI}. The factor of increase is a tuning parameter during parameter estimation, where we initially increase k_{NNI} by a factor of 100.

Rotenone and antimycin A inhibit oxidative phosphorylation by limiting the oxidation of NADH. We implement the effect of these inhibitors as a 99% decrease in the rate constants for oxidative phosphorylation k_{NN} and k_{NNI}

4 Parameter estimation

The model was fitted to experimental data from a glycolysis stress test, a method that measures key properties of the glycolytic pathway, in a manual parameter tuning procedure. We performed the experimental test on cancer cells from the cancer cell line Caco2 (Hidalgo et al., 1989). In the test the cells are initially starved for glucose, but glutamine is available in the media. The Seahorse XFp Analyzer then sequentially adds: (i) glucose, starting glycolytic activity, (ii) oligomycin, inhibiting mitochondrial ATP production in oxidative phosphorylation and thereby increasing glycolytic activity to maximal capacity, (iii) CCCP, further inhibiting oxidative phosphorylation, and (iv) 2-DG, inhibiting glycolysis. Initial media volume in the wells, the extracellular volume V_e, is 180 μl and for each injection the volume increase by 25 μl. The cell culture contained an estimate of 15000 cells, which based on average cell size for Caco2 cells (Hidalgo et al., 1989), correspond to a total cell volume $\mathrm{V_i}$ of 0.0204 μl.

The possible ranges of the reaction fluxes in the model were calculated from OCR and PPR measurements based on the stoichiometry. Prior to glucose injection, glucose uptake is restricted since glucose is not available in the media and therefore glucose uptake $j_{\mathrm{G_{ext}G}}$ is zero. By assuming that oligomycin and 2-DG completely inhibit ATP coupled oxidative phosphorylation and glycolysis respectively, further restrictions on fluxes were possible; j_{NN} was set to zero after oligomycin injection and j_{GP} was set to zero after 2-DG injection.

In order to identify a set of initial model parameters, we use the glucose phase which is after the addition of glucose but prior to the addition of inhibitors. Having both glucose and glutamine present in the growth media is common in experiments, and thus, it enables us to use available literature data, see Table 2. To obtain stationary conditions in the model, external concentrations of glucose, glutamine and lactate were considered constant and the differential equations were solved for the rate constants. Uptake of glucose $j_{\mathrm{G_{ext}G}}$ and glutamine $j_{\mathrm{Gn_{ext}Gn}}$, excretion of lactate $j_{\mathrm{LL_{ext}}}$ and ATP coupled oxidative phosphorylation j_{NN} were considered known in the calculation since they are the easiest fluxes to measure or estimate from OCR and PPR. We use $j_{\mathrm{G_{ext}G}} = 2.26\mathrm{mM/min}$, $j_{\mathrm{Gn_{ext}Gn}} = 3.47\mathrm{mM/min}$, $j_{\mathrm{LL_{ext}}} = 4.25\mathrm{mM/min}$ and $j_{\mathrm{NN}} = 10.4\mathrm{mM/min}$. As a starting point the saturation ratios r were set to $\frac{1}{2}$, which is equivalent to setting the half-saturation constants K equal to their respective substrate concentrations in Table 2.

Table 2. Assumed steady state concentration (SS [mM]) after glucose injection. These values are used in the manual tuning procedure. *Obtained from (Shestov et al., 2014). **Experimental setup.

G	5	K	1	NADH	0.1	$\mathrm{G_{ext}}$**	10.0
P*	0.5	L	0.5	ATP*	3.0	$\mathrm{Gn_{ext}}$**	0.2
Gn	0.1	NAD*	0.5	ADP	1	$\mathrm{L_{ext}}$	0.1

Manual tuning

With the initial parameter set (Table 3), we simulated the model and compared it to measurements of OCR and PPR, see Figure 2, panel A. We see that the model poorly captures the dynamics, especially PPR in phases 3-5.

As a measure to improve the model, we decreased $\mathrm{K_{GP}^{NAD}}$ and $\mathrm{K_{PL}^{NADH}}$ significantly; in such a way that glycolysis and fermentation became saturated with $\mathrm{NAD^+}$ and NADH, respectively, causing PPR to increase as response to oligomycin and CCCP injection, see phases 3 and 4 of panel B. The increased rate of glycolysis from saturated $\mathrm{NAD^+}$ was compensated for by reducing the rate constant for glycolysis k_{GP} by a factor of 2. It was not necessary to compensate the rate of fermentation, as it is limited by glycolysis, and most pyruvate is already fermented to lactate, i.e. the flux from pyruvate to α-ketoglutarate is small.

We observe that the model response in panel B is improved compared to panel A. In order to further improve the model response with respect to proton leak (OCR) before CCCP injection (phase 1-3), we adjusted the rate constant k_{NNI} until the model response fitted the experimental results in phase 3. This is a well suited tuning method as oxidative phosphorylation coupled to ATP production, j_{NN}, is inhibited in phase 3.

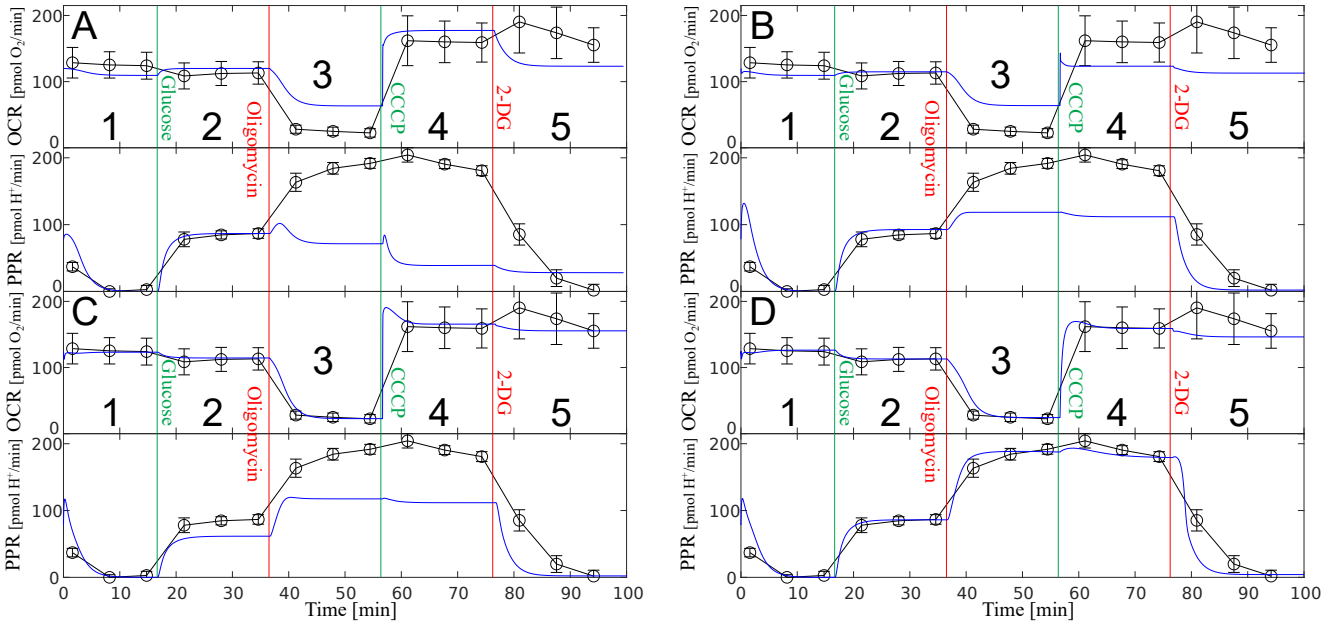

Figure 2. Simulation (blue) and experimental measurements (black) of oxygen consumption rate (OCR) and proton production rate (PPR calculated from ECAR) for the parameter estimation procedure. Injections of glucose and metabolic inhibitors shown on vertical lines. **A** Simulation based on the initial parameter set, see main text. **B** Glycolysis and fermentation were saturated with NAD^+ and NADH respectively to increase PPR as a response to oligomycin and CCCP injection. The increased glycolytic flux from this adjustments was compensated. **C** Oxidative phosphorylation coupled to proton leak prior to CCCP injection was adjusted so it described OCR after oligomycin injection. Glutaminolysis and the energy consumption rate was adjusted so that it better described the glucose injection. **D** Response after last adjustments. Glycolysis was increased until PPR coincided with experimental data after oligomycin injection. The increased glycolytic flux after glucose injection was compensated by reducing ADP availability through increasing oxidative phosphorylation coupled to ATP production. As a last step the effect of CCCP on oxidative phosphorylation coupled to proton leak was adjusted until OCR after CCCP injection coincided with experimental data.

We also observe that after glucose addition (panel B, phase 2), the model response of OCR is opposite of the experimental results. To improve this response, we increased the rate of glutaminolysis k_{GnK} and decreased the energy consumption rate k_{AA}, see panel C. This adjustment of the energy consumption rate was necessary both to decrease the rate of glutaminolysis and glycolysis, and to shift the glucose metabolism towards fermentation in phase 2.

The response in panel C shows a relative good fit to the experiment in OCR but a not so good fit in PPR. To improve the PPR response in phases 3 and 4, we increased the rate for glycolysis k_{GP} to ensure that glucose is fermented to lactate at maximal capacity after oligomycin injection (phase 3). As this adjustment also increase the rate of glycolysis during phase 2, were the PPR became too high, an increase in the rate of oxidative phosphorylation coupled to ATP production k_{NN} was necessary. Furthermore, to improve the OCR response in phase 4 after the addition of CCCP, we decreased k_{NNI} once again, this time however, we changed the value of k_{NNI} when it is affected by CCCP.

The resulting simulation after tuning, shown in panel D, shows a good fit with the experimental data, especially considering that only 8 parameters were adjusted during the manual tuning. Parameter values before and after tuning are listed in Table 3. However, in phase 3 after the addition of oligomycin, the response is too fast with respect to PPR, and too slow with respect to OCR. This is possibly a result of not including compartmentalization in the model, resulting in increased ADP availability in the mitochondria from inhibition of ATP synthase by oligomycin, immediately affecting the glycolysis in the model.

The rapid increase and peak in OCR after CCCP injection in phase 4 is in the model caused by rapid depletion of accumulated α-ketoglutarate after oligomycin injection, i.e. it signifies accumulation of TCA intermediates in the cells. Similarly, the small transient increase in PPR from CCCP injection is in the model a result of accumulation of lactate after the preceding oligomycin injection. This is due to saturation in lactate excretion where increased external volume from the injection of CCCP is associated with dilution of external lactate, which increases the concentration gradient and therefore allows a higher flux.

The experimental data show a transient increase in OCR after injection of 2-DG in phase 5, which is not captured by the model; it is not clear why this transient occurs.

Validation

To validate the model and parameters identified through the glycolysis stress test, we compared the model with experimental data from a so-called mitochondrial stress test which measures key properties for mitochondrial respiration. We used the same cell line Caco2 with the same

Table 3. Estimated parameter values. Rate constants k [mM/s] and half saturation constants (K) in [mM]. For parameters that were adjusted in the manual tuning both the initial- and final estimates are included. * k_{NNI} when CCCP is present.

Par	Value	Par	Value	Par	Value
$K^{\mathrm{G_{ext}}}_{\mathrm{G_{ext}G}}$	10	$K^{\mathrm{L_{ext}}}_{\mathrm{LL_{ext}}}$	0.1	$K^{\mathrm{Gn}}_{\mathrm{GnK}}$	0.1
$K^{\mathrm{G}}_{\mathrm{G_{ext}G}}$	5	$k_{\mathrm{L_{ext}L}}$	0.0354	$K^{\mathrm{NAD}}_{\mathrm{GnK}}$	0.5
$k_{\mathrm{G_{ext}G}}$	1.508	$K^{\mathrm{P}}_{\mathrm{PK}}$	0.5	$K^{\mathrm{K}}_{\mathrm{KO}}$	1
$K^{\mathrm{G}}_{\mathrm{GP}}$	5	$K^{\mathrm{NAD}}_{\mathrm{PK}}$	0.5	$K^{\mathrm{NAD}}_{\mathrm{KO}}$	0.5
$K^{\mathrm{ADP}}_{\mathrm{GP}}$	1	k_{PK}	0.018	k_{KO}	0.2493
$K^{\mathrm{P}}_{\mathrm{PL}}$	0.5	$K^{\mathrm{Gn_{ext}}}_{\mathrm{Gn_{ext}Gn}}$	0.2	$K^{\mathrm{NADH}}_{\mathrm{NN}}$	0.1
k_{PL}	0.2833	$K^{\mathrm{Gn}}_{\mathrm{Gn_{ext}Gn}}$	0.1	$K^{\mathrm{ADP}}_{\mathrm{NN}}$	1
$K^{\mathrm{L}}_{\mathrm{LL_{ext}}}$	0.5	$k_{\mathrm{Gn_{ext}Gn}}$	0.04624	$K^{\mathrm{ATP}}_{\mathrm{AA}}$	3

Par	Initial	Final	Par	Initial	Final
$K^{\mathrm{NAD}}_{\mathrm{GP}}$	0.5	0.001	$K^{\mathrm{NADH}}_{\mathrm{PL}}$	0.1	0.001
k_{GP}	0.3013	0.377	k_{GnK}	0.2313	0.37
k_{AA}	1.0173	0.865	k_{NN}	0.693	1.11
k_{NNI}	0.2267	0.057	$*k_{\mathrm{NNI}}$	22.67	1.995

number of cells as in the glycolysis stress test. The media in the mitochondrial stress test contain glutamine and glucose, but at a lower concentration (5mM) than after the glucose injection in the glycolysis stress test (10mM). The Seahorse XFp Analyzer sequentially adds (i) oligomycin, (ii) CCCP, (iii) Rotenone and (iv) antimycin A. The last two are new compared to the glycolysis stress test, and they both inhibit oxidative phosphorylation.

The simulation and the experimental data from the mitochondria stress test is shown in Figure 3 and shows a remarkable good fit. The relatively unaffected PPR response (both experimentally and simulated) is expected since all the injections inhibit oxidative phosphorylation and fermentation operate at maximal capacity to sustain glycolysis for energy production.

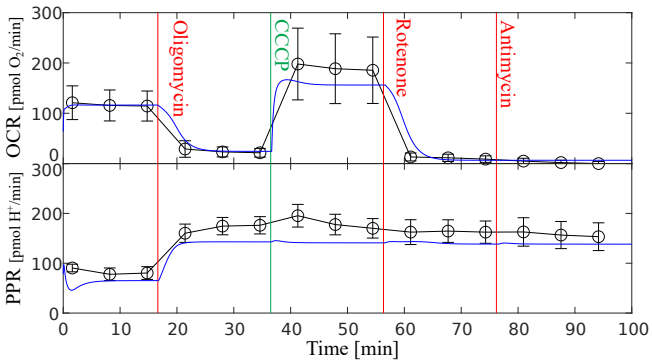

Figure 3. Simulation (blue) and experimental measurements (black) of oxygen consumption rate (OCR) and proton production rate (PPR calculated from ECAR) for a mitochondrial stress test. Injections of metabolic inhibitors shown on vertical lines.

5 Structural properties

Intrigued by the model's ability to fit the experimental results and to capture the main dynamics, we wanted to examine the structural properties of the model in more detail. We wanted to investigate the possibilities for using an automated method for parametrization. Thus we needed to see if the model could be uniquely parameterized from available data and chose to look at the *structural identifiability* of the model.

In this context, the number of measurements are of importance. Adding more measurements to the experimental setup, especially substances inside the cell, like internal concentrations of metabolites, will increase the experimental complexity and cost. We therefore wanted to explore whether the Seahorse measurements (PPR and OCR) together with the external concentrations of glucose, glutamine and lactate form a sufficient set of measured outputs for parameter identifiability.

Structural identifiability

We will first briefly explain the concept of structural identifiability. A model based on a general non-linear state space form: $\frac{dx(t)}{dt} = f(x(t),u(t),\theta)$ and $y(t) = h(x(t),u(t),\theta)$ is identifiable if all parameters θ can be uniquely determined from the system input $u(t)$ and the measured system output $y(t)$ (Miao et al., 2011). A generic form of identifiability is structural identifiability, where the term *structural* indicates that it depends solely on the model structure, i.e. structural identifiability is completely determined by the structure of the system equations and the output function (Villaverde, 2019). For a model to be structurally identifiable, all of its parameters must be structurally identifiable. If this is not the case, it is structurally unidentifiable. If a model is found to be structurally identifiable with a chosen set of measured outputs, it is theoretically possible to uniquely estimate the parameters of the model based on these measurements.

Method

Over time a variety of methods to investigate structural identifiability have been suggested. Some examples are analytic approaches using Taylor series or similarity transformation (Chis et al., 2011; Miao et al., 2011). One major weakness of these and other analytic methods are that the resulting set of non-linear equations can be computationally difficult to solve because of their complexity. Given the amount of parameters in our model, this would be the case for us. Therefore we chose a method suggested and used by Stigter et al. in (2015), (2017), (2018). This method is designed for use on models with many parameters and uses a hybrid numerical and symbolic approach.

With this method the model is simulated with parameter values randomly chosen within a constrained box of realistic parameter values. This is repeated 10 times to ensure robustness. A set of singular values and a set of correlated parameters θ_{corr} are calculated from these simu-

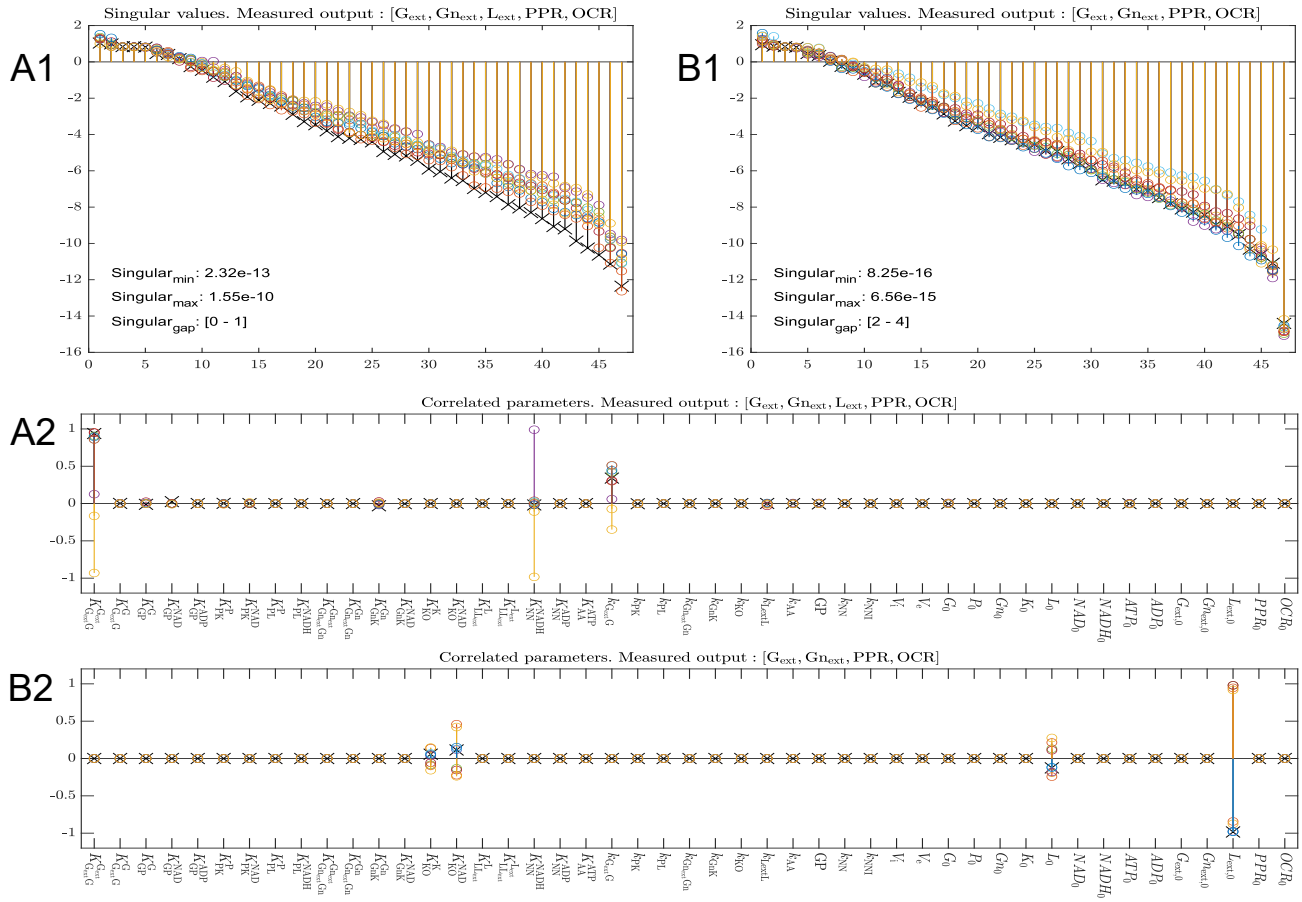

Figure 4. **A1** Log scale plot of singular values. No discernible gap between the smallest singular values indicates structural identifiability. **B1** Log scale plot of singular values without measurement of external lactate L_{ext}. Singular values 10^3 orders of magnitude smaller than panel A1 and a defined gap indicates structural unidentifiability. **A2** Plot of correlated parameters related to panel A1. This plot does not give any relevant information when the model is structurally identifiable. **B2** Plot of correlated parameters related to panel B1. From the plot we see that the parameters $[K^{L}_{LL_{ext}}, K^{L_{ext}}_{LL_{ext}}, L_0, L_{ext}]$ are correlated.

lations. The singular values, or more specifically a prominent jump in numerical value of the lowest singular values, will indicate whether the model is structurally unidentifiable, while the set of correlated parameters will indicate which parameters are causing this structural unidentifiability. A symbolic calculation with this reduced set of parameters θ_{corr} can then be performed to confirm the results indicated by the simulations. For a more in depth explanation of the method see (Stigter and Molenaar, 2015).

Experiments and results

In addition to the 12 states of the model, we add PPR and OCR as states to be used as measured outputs in the algorithm. The model has a total of 47 parameters, including 20 half saturation constants, 11 rate constants, internal and external volume, and the initial conditions of the 14 states.

A natural first choice of measurements are the PPR and OCR provided by the Seahorse XFp analyzer. However, they proved insufficient to obtain structural identifiability.

We included therefore the three external concentrations $[G_{ext}, Gn_{ext}, L_{ext}]$ in our measured output set as they are relatively easy to measure during an experiment. Running the algorithm with these 5 measured outputs gave the results shown in Figure 4, panels A1 and A2. Very small singular values and a clear gap, typically greater than 3 (Joubert et al., 2018), between the smallest singular values would indicate structural unidentifiability. In panel A1 we observe a gap of an order between 0 and 1, indicating structural identifiability. When a model is found to be structurally identifiable from the singular values plot, the plot of correlated parameters (such as in panel A2) does not contribute with any relevant information (even if it looks like two or more parameters are correlated). The symbolic verification supports the conclusion from the simulations.

Having a situation where measurements of OCR and PPR together with the 3 external concentrations are enough for the model to be structurally identifiable, we wanted to investigate whether we could remove one of the external concentration measurements and still obtain the same result. Thus, running the algorithm three times with one of the external measurements left out for each run resulted in all runs indicating a lack of structural identifiability. Panels B1 and B2 in Figure 4 show the results

with the measurement of external lactate L_{ext} left out. The plot of singular values in panel B1 shows that the smallest singular values are of order 10^{-15} to 10^{-16} and that there is a clear gap between the two smallest singular values. Panel B2 shows a plot of the correlated parameters for this case, i.e. $\theta_{\text{corr}} = [K^{L}_{LL_{ext}}, K^{L_{ext}}_{LL_{ext}}, L_0, L_{ext}]$. This is a reasonable result since all these parameters can be found in equation (3) describing the transport of lactate out of the cell. Performing the symbolic calculation with this reduced parameter set θ_{corr} also indicates structural unidentifiability, confirming the numerical results.

6 Conclusions

We constructed a dynamic model of aerobic and anaerobic metabolism in cancer cells designed to be used in combination with experiments performed using an Agilent Seahorse XF analytic instrument. The model consist of 12 state variables including the external concentration of glucose, glutamine and lactate and describes 2 common types of reprogrammed energy metabolism in cancer cells, i.e. aerobic glycolysis and glutamine addiction.

Parameter values were estimated based on experimental data from a glycolysis stress test on the Caco2 cell line in a manual tuning procedure. The model was then validated with experimental data from a mitochondrial stress test on the same cell line with promising results.

Our experiments indicate that the model is structurally identifiable with a set of 5 measured outputs $[G_{ext}, Gn_{ext}, L_{ext}, PPR, OCR]$. These are measurements that are simple to perform experimentally and that can be performed in vivo (without killing cells). However, we must keep in mind that this is a purely theoretical result and in practice it could still be difficult to uniquely parameterize the model based on only these 5 measured outputs.

For future work we will investigate an automatic method for parameterization as an alternative to manual parameter tuning. Our results from the structural identification analysis supports a possible unique parameterization with an automated algorithm.

References

Agilent. Brochure - Agilent seahorse XF live-cell metabolism solutions for cancer research, 2019. URL `https://www.agilent.com/en/solutions/cell-analysis/cell-metabolism/cancer-metabolism`.

G. F. Baker and W. F. Widdas. The asymmetry of the facilitated transfer system for hexoses in human red cells and the simple kinetics of a two component model. *The Journal of Physiology*, 231(1):143–165, 1973. doi:10.1113/jphysiol.1973.sp010225.

Y. J. Cha, E. S. Kim, and J. S. Koo. Amino acid transporters and glutamine metabolism in breast cancer. *International Journal of Molecular Sciences*, 19(3), 2018. doi:10.3390/ijms19030907.

O. T. Chis, J. R. Banga, and E. Balsa-Canto. Structural identifiability of systems biology models: A critical comparison of methods. *PLoS ONE*, 6(11), 2011. doi:10.1371/journal.pone.0027755.

R. J. DeBerardinis, J. J. Lum, G. Hatzivassiliou, and C. B. Thompson. The biology of cancer: Metabolic reprogramming fuels cell growth and proliferation. *Cell Metabolism*, 7 (1):11–20, 2008. doi:10.1016/j.cmet.2007.10.002.

D. Hanahan and R. A. Weinberg. Hallmarks of cancer: The next generation. *Cell*, 144(5):646–674, 2011. doi:10.1016/j.cell.2011.02.013.

I. J. Hidalgo, T. J. Raub, and R. T. Borchardt. Characterization of the human colon carcinoma cell line (Caco-2) as a model system for intestinal epithelial permeability. *Gastroenterology*, 96(3):736–749, 1989. doi:10.1016/0016-5085(89)90897-4.

R. G. Jones and C. B. Thompson. Tumor suppressors and cell metabolism: A recipe for cancer growth. *Genes and Development*, 23(5):537–548, 2009. doi:10.1101/gad.1756509.

D. Joubert, J. D. Stigter, and J. Molenaar. Determining minimal output sets that ensure structural identifiability. *PLoS ONE*, 13(11):1–19, 2018. doi:10.1371/journal.pone.0207334.

M. V. Liberti and J. W. Locasale. The Warburg effect: How does it benefit cancer cells? *Trends in Biochemical Sciences*, 41 (3):211–218, 2016. doi:10.1016/j.tibs.2015.12.001.

H. Miao, X. Xia, A. S. Perelson, and H. Wu. On identifiability of nonlinear ODE models and applications in viral dynamics. *SIAM Review*, 53(1):3–39, 2011. doi:10.1137/090757009.

M. Scalise, L. Pochini, M. Galluccio, L. Console, and C. Indiveri. Glutamine transport and mitochondrial metabolism in cancer cell growth. *Frontiers in Oncology*, 7:1–9, 2017. doi:10.3389/fonc.2017.00306.

A. A. Shestov, X. Liu, Z. Ser, A. A. Cluntun, Y. P. Hung, L. Huang, D. Kim, A. Le, G. Yellen, J. G. Albeck, and J. W. Locasale. Quantitative determinants of aerobic glycolysis identify flux through the enzyme GAPDH as a limiting step. *eLife*, 3:e03342, 2014. doi:10.7554/eLife.03342.

J. D. Stigter and J. Molenaar. A fast algorithm to assess local structural identifiability. *Automatica*, 58:118–124, 2015. doi:10.1016/j.automatica.2015.05.004.

J. D. Stigter, M. B. Beck, and J. Molenaar. Assessing local structural identifiability for environmental models. *Environmental Modelling and Software*, 93:398–408, 2017. doi:10.1016/j.envsoft.2017.03.006.

A. F. Villaverde. Observability and structural identifiability of nonlinear biological systems. *Complexity*, 2019, 2019. doi:10.1155/2019/8497093.

O. Warburg. On the origin of cancer cells. *Science*, 123(3191): 309–314, 1956. doi:10.1126/science.123.3191.309.

D. R. Wise and C. B. Thompson. Glutamine addiction: A new therapeutic target in cancer. *Trends in Biochemical Sciences*, 35(8):427–433, 2010. doi:10.1016/j.tibs.2010.05.003.

Simulation of condensation in biogas containing ammonia

Lars Erik Øi[1] Terje Bråthen[1] Jon Hovland[2]

[1]Department of and Process, Energy and Environmental Technology, University of South-Eastern Norway
[2]SINTEF Tel-Tek, SINTEF Industry, Porsgrunn, Norway

lars.oi@usn.no

Abstract

Condensation in raw biogas during compression is a problem because the CO_2 and water in the liquid phase is very corrosive. Raw biogas typically contains 60 mol-% methane, 40 mol-% CO_2, is saturated with water and may contain contaminants as ammonia (NH_3). In case of NH_3, it is of interest whether it has influence on the dew point (condensation) temperature. The aim of this work is to calculate the dew point under different conditions using different equilibrium models. Phase envelopes showing the two-phase area are also calculated. For dry mixtures of methane and CO_2 with up to 1 mol-% NH_3 (a high value for biogas), the different models gave similar results. When the NH_3 increased from 0 to 1 mol-%, the dew point temperature increased with approximately 3 K. When water was included, the amount of calculated NH_3 dissolved in water varied considerably with the model. The electrolyte based models Sour PR, Sour SRK and Electrolyte NRTL did not calculate reasonable dew point temperatures, but the dissolved amounts of NH_3 and CO_2 were more reasonable using the electrolyte models compared to using PR or SRK. For biogas simulation including NH_3, a simple equation of state as PR or SRK can be recommended to determine the dew point. If accurate composition of the condensed liquid is to be calculated, an electrolyte based model like Sour PR, Sour SRK or the Electrolyte NRTL is recommended.

Keywords: CO_2, methane, water, biogas, phase envelope, Aspen HYSYS, Aspen Plus

1 Introduction

Condensation in biogas containing water is a challenge because the CO_2 and water in the liquid phase is very corrosive. Raw biogas typically contains 60 mol-% methane, 40 mol-% CO_2, is saturated with water and may contain contaminants as H_2S and NH_3. Under compression up to 300 bar, it is a question whether condensation will occur. NH_3 is very soluble in water, and the solubility increases in the presence of CO_2 because the liquid becomes acidic. When the biogas contains NH_3, it is of interest whether it has influence on the dew point temperature. It is also of interest how much CO_2 and NH_3 will condense in the liquid phase.

This work is a continuation of the work from Øi and Hovland (2018), Bråthen et al. (2019) and Bråthen et al. (2020) which did not consider NH_3.

Traditionally, gas mixture properties of methane, CO_2 and water are calculated in a process simulation program with standard models like PR (Peng and Robinson, 1976) and SRK (Soave, 1972). There is traditionally only one constant binary parameter for each component pair, but in the process simulation tools Aspen HYSYS and Aspen Plus, the binary parameter for e.g. water/CO_2 can be made temperature dependent. Other models including electrolyte models are also available in Aspen HYSYS and Aspen Plus. Properties of mixtures of the biogas components have been studied extensively in natural gas processing where the methane concentration is very high (Kunz and Wagner, 2012). The same components have also been studied in the development of CO_2 injection into different hydrocarbon reservoirs (Ziabakhsh-Ganji and Kooi, 2012). There have been found few articles about process simulation of biogas (Tan et al., 2017; Pellegrini et al., 2015; Ahmad et al., 2018). The articles Nabgan et al. (2016) and Sotoft et al. (2015) are about simulation of ammonia stripping in biogas production reactors and processes.

When using fitted binary parameters (k_{ij} parameters) these models simulate the gas phase and the condensation point reasonably accurately (within a few degrees) at least below the critical point which is 46 bar for methane and 74 bar for CO_2 (Øi and Hovland 2018; Bråthen et al., 2019; Bråthen et al., 2020).

Studies of models for vapour/liquid equilibrium in the methane/CO_2/water-system have been performed by Jarne (2004), Austegard et al. (2006), Privat and Jaubert (2014), Al Ghafri et al. (2014), Legoix et al. (2017) and Bråthen et al. (2019). Austegard et al. (2006) concluded that a simple equation of state like SRK is satisfactory to describe the vapour phase, but more complex models are necessary to describe the liquid phase.

Several authors have studied models for the system CO_2/water (Spycher et al., 2003; Longhi, 2005; Aasen et al., 2017). Bråthen et al. (2019; 2020) concluded that

PR and SRK with a standard k_{ij} value were able to simulate this system satisfactory, at least for the vapour phase up to the critical point (40-70 bar).

There are much available literature on data, thermodynamics and simulation of mixtures of NH_3. Neumann et al. (2020) present an equation of state for many components. It is based on a Helmholz energy model similar to the Gerg-2008 model (Kuntz and Wagner, 2012) which is a standard model in natural gas simulation.

The NH_3/CO_2/water/system is extensively studied (Ayers, 1985; Kurz et al., 1995; Jilvero et al., 2015). Gudjonsdottir et al. (2016) discuss models also including solid formation of different salts from concentrated solutions of NH_3 and CO_2 in water. This is typical conditions for ammonia based processes for CO_2 capture.

In this work, the emphasis is on the standard PR and SRK methods available in the process simulation programs Aspen HYSYS and Aspen Plus. In the case of calculation of the liquid composition after condensation, the electrolyte based models Sour PR, Sour SRK and Electrolyte-NRTL are evaluated.

The aim of this work is to calculate the dew point or condensation of biogas containing NH_3 under different conditions with varied temperature, pressure and gas composition and using different equilibrium models.

2 Simulation Programs and Models

2.1 Available models in Aspen HYSYS and Aspen Plus

Øi and Hovland (2018) and Bråthen et al. (2019) simulated dry biogas (CH_4 and CO_2) and mixtures also containing water using the process simulation programs Aspen HYSYS and Aspen Plus. The equilibrium models SRK (Soave, 1972), PR (Peng and Robinson, 1976) and also other models were used.

The reason why the simple models PR and SRK are selected, is that the models and fitted binary parameters are usually available in different process simulation programs. Other commercial process simulation programs are ProMax, ChemCad and ProTreat.

In Aspen HYSYS and Aspen Plus the PR and SRK models have only one adjustable parameter for each binary component pair, but for some components, and especially water/CO_2 and water/H_2S, this parameter may be temperature dependent.

2.2 Description of the PR Equation of state

Equations for the SRK equation of state are shown in (1) to (8) from Aspen HYSYS Version 10. Aspen HYSYS and Aspen Plus Version 10 were used in the simulations. More details are discussed in Bråthen et al. (2019).

$$p = \frac{RT}{v-b} - \frac{a}{v(v+b)} \quad (1)$$

$$b = \sum_{i=1}^{N} x_i b_i \quad (2)$$

$$b_i = \frac{0{,}08664 R T_C}{p_c} \quad (3)$$

$$a = \sum_{i=1}^{N}\sum_{j=1}^{N} x_i x_j \left(a_i a_j\right)^{0,5}\left(1-k_{ij}\right) \quad (4)$$

$$a_i = a_{ci}\alpha_i \quad (5)$$

$$a_{ci} = \frac{0{,}42748 R^2 T_c^2}{p_c} \quad (6)$$

$$\alpha_i = \left[1 + m_i\left(1 - T_r^{1/2}\right)\right]^2 \quad (7)$$

$$m_i = 0{,}48 + 1{,}574\omega_i - 0{,}176{\omega_i}^2 \quad (8)$$

P, T, v and R are the pressure, temperature, molar volume and the universal gas constant. T_c is the critical temperature, ω is the acentric factor and T_r is the reduced temperature (the ratio between T and T_c). The binary interaction parameter k_{ij} (= k_{ji}) is a constant for a binary component pair and x_i is the mole fraction for component i. In the PR equation, equation 1, 3, 6 and 8 are replaced by equation 9, 10, 11 and 12.

$$p = \frac{RT}{v-b} - \frac{a}{v(v+b)+b(v-b)} \quad (9)$$

$$b_i = \frac{0{,}077796 R T_C}{p_c} \quad (10)$$

$$a_{ci} = \frac{0{,}457235 R^2 T_c^2}{p_c} \quad (11)$$

$$m_i = 0{,}37464 + 1{,}54226\omega_i - 0{,}26992{\omega_i}^2 \quad (12)$$

2.3 Recommended Binary Parameters

The binary parameter k_{ij} is normally a constant for each binary pair. When utilizing the default k_{ij} values in Aspen HYSYS and Aspen Plus, the k_{ij} values are constant for all component pairs except for water/CO_2 and water/H_2S where it is a temperature dependent function. Different optimized values for the k_{ij} values can be found because the parameters may be optimized for different conditions, e.g. for accurate prediction of either the gas phase or the condensate phase. For the calculation of dew points, it is reasonable to use binary interaction coefficients optimized for the gas phase (Bråthen et al., 2019).

The PR and SRK versions used in Aspen Plus are equal to the Aspen HYSYS versions shown in (1) to (12), except that some of the numerical values are slightly different. Especially the coefficients in the m_i expressions (8) and (12) are slightly different.

The parameters in (1) to (12) may be slightly different in different process simulation programs. The alfa (α_i) parameter in equation (7) is calculated

differently in the PR-Twu and SRK-Twu models (Twu et al., 1991).

A k_{ij} value for water/CO_2 close to 0.19 is suggested by Ziabakshsh-Ganji and Kooi (2012), Li et al. (2014) and Bråthen et al. (2019). Some recommends different k_{ij} values dependent on emphasis on the vapour or liquid phase (Austegard et al., 2006).

The standard k_{ij} value in Aspen HYSYS and Aspen Plus for water/NH_3 is -0.253 for PR and -0.273 for SRK. Skogestad (1980) states that the value -0.28 for SRK gives a good fit to experimental data.

2.4 Electrolyte models in Aspen HYSYS and Aspen Plus

Traditional equations of state are not taking ions in solution into account. Aspen HYSYS and Aspen Plus have two models Sour PR and Sour SRK which are based on electrolyte calculations. The Sour PR model is using PR for the gas phase and a Wilson equation (API, 1980) for the liquid phase. It is developed for stripping components like CO_2, H_2S and NH_3 from water in hydrocarbon processing. More complex models are also available. In Aspen Plus, the Electrolyte NRTL model is available. The standard Electrolyte NRTL in Aspen Plus use the Redlich Kwong equation of state for the vapour phase. Que and Chen (2011) have combined Electrolyte NRTL in Aspen Plus with the SAFT model for the vapour phase. Gudjonsdottir et al. (2016) compare different models including the extended UNIQUAC equation and is also including solid salt simulation and non-ideality in the liquid phase.

The most important equations in electrolytic calculations of the CO_2/carbonate and NH_3/ammonium systems are based on the solubility of the gases in water and on the ion equilibriums of the ionization step for NH_3 and two ionization steps for CO_2. The equations (15 to 24) are from Øi (2012) with equations for solubility and ionization of NH_3 included. These are similar to equations found in API (1980) and Gudjonsdottir et al. (2016). One challenge with these models in a process simulation tool is that the electrolyte models normally use concentrations in e.g. (mol/liter) while process simulation tools like Aspen HYSYS and Aspen Plus use calculations based on mole fractions.

Equation (13) and (14) shows solubility and ionization of NH_3. The "g" and "liq" in equation (13) and (15) indicate the gas and liquid phase. All the other equations are indicating concentrations in the liquid phase.

$$NH_3(g) \leftrightarrow NH_3\,(liq) \qquad (13)$$

$$NH_3 + H_2O \leftrightarrow NH_4^+ + OH^- \qquad (14)$$

$$CO_2(g) \leftrightarrow CO_2(liq) \qquad (15)$$

In the liquid phase, CO_2 reacts with hydroxide to bicarbonate according to Equation (16).

$$CO_2 + OH^- \leftrightarrow HCO_3^- \qquad (16)$$

The fast proton transfer reactions (17 and 18) also occur. Equation (17) is the water self-ionization reaction and (18) describes the deprotonation of the bicarbonate ion to carbonate ion:

$$H_2O \leftrightarrow H^+ + OH^- \qquad (17)$$

$$HCO_3^- \leftrightarrow CO_3^{2-} + H^+ \qquad (18)$$

The reactions in Equations (13 to 18) can be described with equilibrium constants. The equilibrium in Equations (13 and 15) is normally described by a temperature dependent Henry's constant which connects the partial pressure of the CO_2 in the gas with the concentration of CO_2 in the liquid.

$$p_{CO2} = He_{CO2} \cdot C_{CO2} \qquad (19)$$

$$p_{NH3} = He_{NH3} \cdot C_{NH3} \qquad (20)$$

Equations (21 to 24) represent the equilibrium constants for the reactions in Equations (14) and (16 to 18).

$$K_{14} = \frac{C_{NH_4^+} \cdot C_{H^+}}{C_{NH3} \cdot C_{H2O}} \qquad (21)$$

$$K_{16} = \frac{C_{HCO_3^-}}{C_{CO2} \cdot C_{OH^-}} \qquad (22)$$

$$K_{17} = \frac{C_{H^+} \cdot C_{OH^-}}{C_{H2O}} \qquad (23)$$

$$K_{18} = \frac{C_{CO3_3^{2-}} \cdot C_{H+}}{C_{HCO_3^-}} \qquad (24)$$

In addition an equation for the charge balance is needed, e.g. by setting the sum of concentrations for the negative ions equal to the sum of concentrations for positive ions. To solve this equation set, component material balances for the total of nitrogen containing components and for the total of carbon containing components can be included. This is traditional if only the liquid phase is simulated.

If the gas composition, pressure and the temperature dependent equilibrium constants are known, this equation set can be used to calculate the dew point temperature and all the liquid concentrations including the ion concentrations.

3 Process Description and Simulation Specifications

3.1 Process description of raw biogas compression

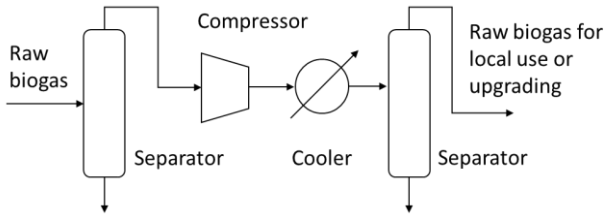

Figure 1. A raw biogas compression process

The principle for a traditional raw biogas compression process is shown in Figure 1. The compression can be up to 300 bar.

The actual process is discussed in more detail in Hovland (2017), Øi and Hovland (2018) and Bråthen et al. (2019). Bråthen et al. (2020) used the same approach for dew point calculations of biogas mixtures containing H_2S.

In Øi and Hovland (2018), Bråthen et al. (2019; 2020) it is stated that condensation during compression is a problem that should be avoided.

3.2 Simulation specifications

In earlier work, process simulations have been performed for different conditions relevant for biogas production as in Øi and Hovland (2018) and Bråthen et al. (2019; 2020). The models PR, SRK, PRSV (Stryjek-Vera, 1986), TST, PR-Twu and SRK-Twu were used. The default parameters (especially the k_{ij} for water/CO_2) were used. Phase envelopes showing the dew and bubble point curve for a temperature and pressure range have been calculated. In the dry gas cases, the HYSYS 2-phase option was selected for phase envelope calculations. In the cases including water and NH_3, the ComThermo 3-phase option was selected.

Calculations have been performed with both Aspen HYSYS and Aspen Plus. In Aspen Plus the Peng-Robinson and RKSoave models were selected. The B and D cases are referring to Øi and Hovland (2018) and simulated in Bråthen et al. (2019; 2020).

In earlier simulations (Case B) dry biogas with 40 mol-% methane and 60 mol-% CO_2 starts at 37 °C and 1 bar, is cooled to 10 °C and is compressed to 64 bar. In this work, 1 mol-% NH_3 is added, and the mol-% methane is reduced to 39.

In earlier simulations (Case D), 59.9 kmol/h methane, 40 kmol/h CO_2 and 0.1 kmol/h water is mixed at 37 ºC and 1 bar, cooled to 10 °C, and then compressed to 64 bar. In this work, 1 mol-% NH_3 is added, and the mol-% methane is reduced to 58.9.

4 Process Simulation, Results and Discussion

4.1 Simulation of dry methane/CO_2 mixture including H_2S/NH_3 (Case B)

An Aspen HYSYS flow-sheet model of the process for the base case simulation is presented in Figure 2.

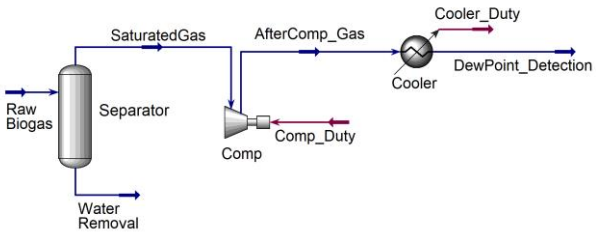

Figure 2. Aspen HYSYS flow-sheet for compression and cooling

In earlier calculations, Case B was of interest because a 40 % methane and 60 % CO_2 has a dew point close to 0 °C. Earlier evaluations from Øi and Hovland (2018) and Bråthen et al. (2019) have shown that below 60 mol-% CO_2, no condensation should appear if the temperature is kept above -3 °C.

Table 1. Dew point at 64 bar, cricondenterm and cricondenbar for a mixture of 39 mol-% methane, 60 mol-% CO_2 and 1 mol-% NH_3 (Case B)

Model	T_{DEW}	T_{CRIC} (ºC)	P_{CRIC} (bar)
PR Hysys	-2.8	1.0	91.0
SRK Hysys	-2.7	1.3	89.8
TST Hysys	1.6	2.0	83.9
PR-Twu Hysys	-3,7	0.1	91.6
SRK-Twu Hysys	-3.2	0.8	92.2
Sour PR Hysys	-2.8	1.0	91.0
Sour SRK Hysys	-2.7	1.4	90.0
PR Aspen Plus	-2.9	-0.9	90.0
SRK Aspen Plus	-1.2	-0.9	89.9

The results in Table 1 are similar to the results from Øi and Hovland (2018) and Bråthen et al. (2019), and also similar to the results with 1 % H_2S (Bråthen et al., 2020). The results in Aspen HYSYS and Aspen Plus are not identical due to slightly different model parameters. The dew points are typically 2-4 K less than the calculations for mixtures without NH_3. These deviations are in the same order of magnitude compared to the deviation in calculated dew point between different models used. The dew point change was slightly higher when adding NH_3 compared to the change when H_2S was added (Bråthen et al., 2020).

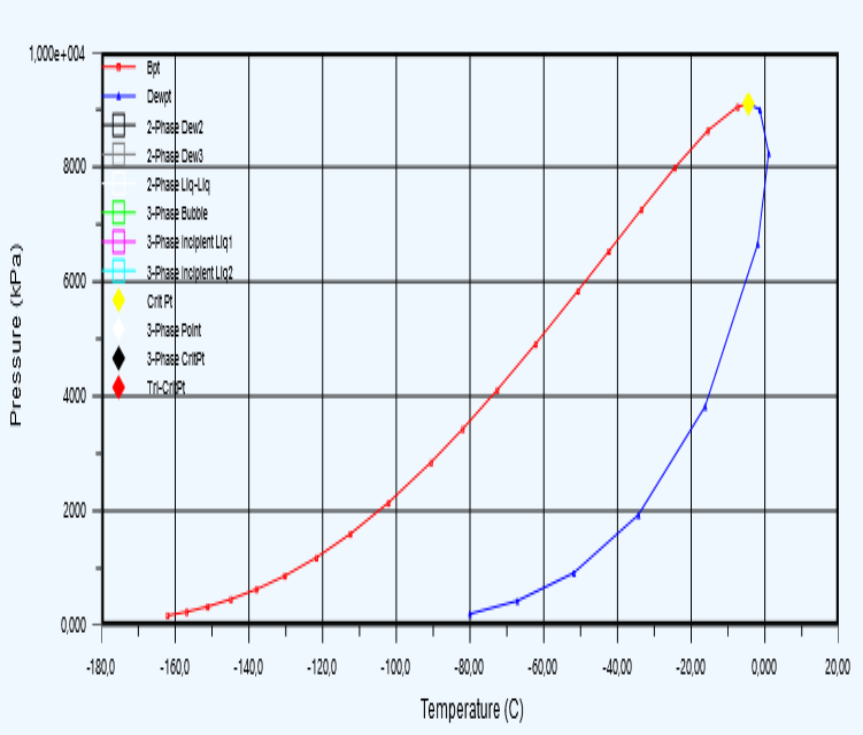

Figure 3. Phase envelope, Peng-Robinson, CH_4=0.39, CO_2=0.6, NH_3=0.01. PR with default k_{ij} values.

Also when NH_3 is included, the calculated cricondenterms with different models have a deviation of typically 2-4 K. It is concluded that the results can be expected to be fairly accurate for all the models evaluated. Even with 1 mol-% NH_3, very little condensation will appear above 0 °C in a dry biogas with more than 40 mole-% CH_4. This was also the conclusion without H_2S from Hovland (2017), Øi and Hovland (2018) and Bråthen et al. (2019; 2020).

The phase envelope from Aspen HYSYS is shown in Figure 3. The dew point curve is to the right. The point with the highest temperature is the cricondenterm. The point with the highest pressure is the cricondenbar. In the critical point for the mixture, the compositions in both phases are equal.

The phase envelope in Figure 3 is very close to the phase envelope in Bråthen et al. (2019) which was calculated without NH_3. But the cricondenterm is 3 K higher. This is the same comparison as the comparison in Table 1 which was also compared with simulations without NH_3. The deviation in temperature seems to be less than 4 K. According to Figure 3, there should not occur any condensation (two-phase) between 90 and 300 bar.

These simulations indicate that the calculated dew points and phase envelopes for dry biogas including up to 1 mol-% NH_3 are reasonably accurate for all the models tested.

4.2 Simulation of compression of a raw biogas including water and NH_3, CaseD

The process (Case D) was simulated with water and NH_3 included. The simulations are similar to the simulations in Bråthen et al. (2019; 2020) and in this work 1 mol-% NH_3 is added, and the mole fraction of methane is reduced correspondingly. The results are shown in Table 2.

Table 2. Dew point at 64 bar, cricondenterm and pressure at cricondenterm for 58.9 mol% CH_4, 40 mol% CO_2, 1 mol% NH_3, 0.1 mol% water, Case D

Model	T_{DEW} (°C)	T_{CRIC} (°C)	P_{CRIC} (bar)
PR	30.4	-18.6	86.3
SRK	31.1	-19.5	85.5
PRSV	30.9	-19.7	85.9
PRTwu	21.4	-22.1	86.1
SRKTwu	22.5	-18.9	86.8

Compared to the dew point temperatures without NH_3 (Bråthen et al., 2019), the dew point was 4-6 K higher. The deviation between the models were small. The TST model was also tried (as in earlier work), but the deviation in dew point temperature was considerable compared with the other models (about 10 K). The dew point temperatures in Table 2 were also calculated in Aspen Plus with PR and SRK and that gave as expected similar results.

The calculated cricondenterm values in Table 2 are very much lower than the values in Bråthen et al. (2019) but similar to the values calculated by Bråthen et al. (2020). The reason for the difference is probably because the values in Aspen HYSYS Version 10.0 and later are calculated without taking water into account. This is a problem also when calculating a phase envelope as in Figure 4. The phase envelope in the figure is without NH_3.

The dew point temperature was also calculated with the electrolyte models Sour PR and Sour SRK (in Aspen HYSYS) and with the Electrolyte NRTL model (Electr-NRTL in Aspen Plus). When using the Sour PR model, the dew point was calculated to 37.7 °C without NH_3, and it gave unreasonable values for gas streams with NH_3. When the Electrolyte NRTL model was used, the dew point temperature increased slightly from 51.4 °C without NH_3 to 53.0 °C with 1 mol-% NH_3. This indicates that the simple PR and SRK models give more accurate dew point temperatures than the electrolyte based models, at least for low NH_3 content.

The challenge with combining an electrolyte model with a gas phase model is well known. In the Aspen HYSYS user guide, it is stated that the flash calculation for Sour PR is much slower than the standard EOS because the method performs an ion balance for each calculation of the electrolyte model. Que and Chen (2011) have combined Electrolyte NRTL in Aspen Plus with the SAFT model for the vapour phase.

4.3. Calculation of dew point and liquid composition at different NH_3 levels in gas

In Table 3, the calculated liquid composition is shown for different NH_3 compositions for the traditional PR equation and for the electrolyte Sour PR model.

Table 3. Dew point at 64 bar and liquid composition for different NH_3 concentrations in gas and for the PR and Sour PR models of 59.9 mol% CH_4, 40 mol% CO_2, 0.1 mol% water, Case D

Model	$y_{NH3=0}$	**0.01%**	**0.1%**	**1%**
T_{DEW}(PR)	26.5	26.8	27.3	30.4
xCO_2(PR)	0.009	0.0085	0.0086	0.0092
xNH_3(PR)	0	0.0032	0.027	0.14
T_{DEW}(SOUR PR)	37.7	-3.51	-1.60	-19.5*
xCO_2(Sour PR)	0.009	0.108	0.266	0.7709*
xNH_3(Sour PR)	0	0.0848	0.263	0.0791*

As commented in the previous subsection, the Sour PR model calculates unreasonable dew points (which decrease with increasing NH_3 amount) for these conditions, even without NH_3. The PR model calculates a slight increase in dewpoint, which is reasonable.

The PR equation calculates too low solubilities of CO_2 and NH_3 in the liquid. This is expected because PR and SRK are not electrolyte based models. Non-electrolyte models calculate the dissolved NH_3 and CO_2 only based on equation (19 and 20).

Because NH_3 makes the water phase less acidic, the CO_2 concentration is expected to increase when the NH_3 concentration increases. This is the case for the electrolyte model Sour PR. It is also seen that the amount of CO_2 and NH_3 is about equal for the case of 0.01 % and 0.1 % NH_3. This is reasonable because that gives a close to neutral water solution. Equation (21) shows that the ratio between the NH_4^+ and NH_3 concentrations increases when the H^+ concentration (or pH) increases. Equation (22) shows that the ratio between the HCO_3^- and CO_2 concentrations increases when the OH^- concentration increases.

For the case of 1 % NH_3 in the gas, the concentrations of CO_2 and NH_3 become very large, and this is probably outside the reasonable range for the Sour PR model. Similar calculations have also been performed using the Electrolyte NRTL model. That gave more CO_2 and less NH_3 in the solution compared to the Sour PR model. For NH_3 values typically for biogas which are lower than 0.1 %, the calculated liquid compositions using the Sour PR model are reasonable.

4.4. Phase envelope calculations

The phase envelope for PR with k_{ij}=0.19 from Table 2 is shown in Figure 4. The phase envelope in Figure 4 is from Bråthen et al. (2019) without NH_3. Based on the results in Table 2, the dew point line to the right in the figure will deviate (increase) with order of magnitude 3 K. For reasonable NH_3 levels in biogas below 0.1 mol-%, the deviation compared to the phase envelope is expected to be less than 1 K. For pressures above the critical point (about 90 bar), the dewpoint is expected to decrease slightly according to Figure 4.

As stated in earlier work, it is expected that the uncertainty in dew point calculations increases when the pressure increases and the mixture is close to the critical point which is about 70 bar (Øi and Hovland, 2018; Bråthen et al., 2019).

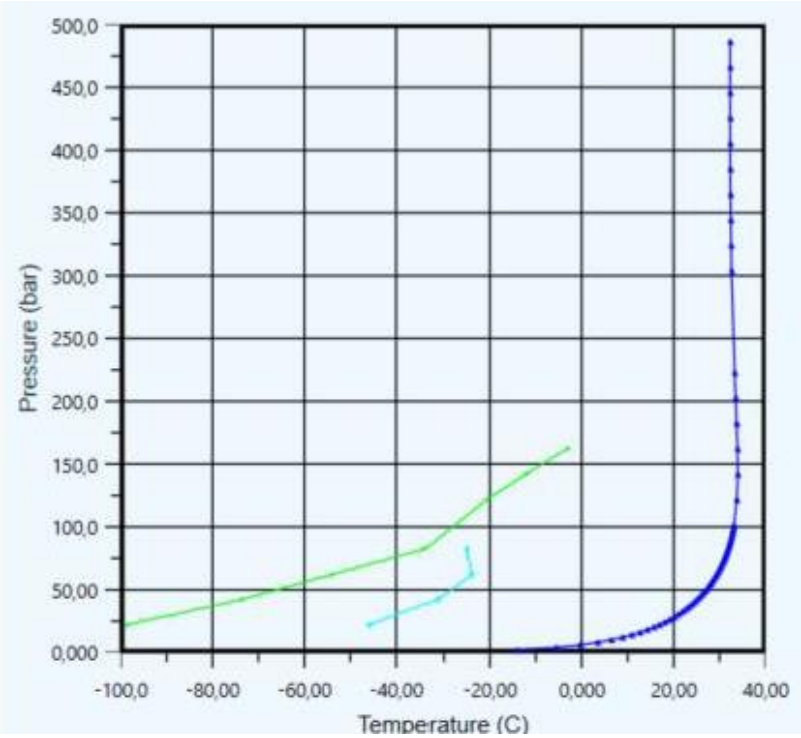

Figure 4. Phase envelope for PR model, 59,9 mol% CH_4, 40 mol% CO_2, 0.1 mol% water: k_{ij} =0.19 for water/CO_2 (Bråthen et al., 2019)

5 Conclusion

Specified mixtures of raw biogas with and without water have been simulated at different temperatures and pressures. The effect of adding up to 1 mol-% NH_3 to the mixtures have been evaluated. For some conditions, phase envelopes have been calculated and different models have been compared.

For mixtures of methane and CO_2 with up to 1 mol-% NH_3 (a high value for biogas), the different models gave similar results. Under normal ambient temperatures (above 0 °C), a mixture with more than 40 mol-% methane will not give any condensation. When the NH_3 increased from 0 to 1 mol-%, the dew point temperature increased with 3.0 K. A phase envelope for biogas with 1 mol-% NH_3 is only slightly different from an earlier calculated phase envelope for biogas without NH_3.

When raw biogas is cooled or compressed, water will condense first. NH_3 will dissolve in the water, and the amount of calculated NH_3 dissolved in water varied significantly with the model.

For biogas simulation including NH_3, a simple equation of state as PR or SRK can be recommended to determine the dew point. If accurate composition of the condensed liquid is to be calculated, an electrolyte based model like Sour PR or Electrolyte NRTL is recommended.

References

A. Aasen, M. Hammer, G. Skaugen, J. P. Jakobsen and Ø. Wilhelmsen. Thermodynamic models to accurately describe the PVTxy-behaviour of water/carbon dioxide mixtures, *Fluid Phase Equilibria*, 442:125-139, 2017.

N. E. Ahmad, M. Mel and N. Sinaga. Design of Liquefaction Process of Biogas using Aspen HYSYS Simulation. *Journal of Advanced Research in Biofuel and Bioenergy*, 2:10-15, 2018.

API (American Petroleum Institute). A New Correlation of NH_3, CO_2 and H_2S Volatility Data from Aqueous Sour Water Systems. EPA report 600/2-80-067, 1980.

S. Z. S. Al Ghafri, E. Forte, G. C. Maitland, J.J. Rodriguez-Henriquez and J. P. M. Trusler. Experimental and Modeling Study of the Phase Behaviour of (Methane + CO_2 + Water) Mixtures. *Journal of Physical Chemistry*, 118:14462-14478, 2014.

G. P. Ayers. Solubility of ammonia in water in the presence of atmospheric CO_2. *Tellus*, 37B:35-40, 1985.

A. Austegard, E. Solbraa, G. de Koeijer and M. J. Mølnvik. Thermodynamic models for calculating mutual solubilities in H_2O-CO_2-CH_4 mixtures. *Trans IChemE, Part A, Chem. Eng. Res. Des.*, 84(A9):781-7946, 2006.

T. Bråthen, L. E. Øi and J. Hovland. *Simulation of Dew Points in Raw Biogas Using PR and SRK Equations of State*. In Linköping Electronic Conference Proceedings SIMS 60, pp. 31-36, 2019. doi: 10.3384/ecp20170112.

T. Bråthen, L. E. Øi and J. Hovland. *Simulation of condensation in Raw Biogas containing H_2S*. In Linköping Electronic Conference Proceedings SIMS 61, pp. 300-305, 2020. doi.org/10.3384/ecp20176300.

V. Gudjonsdottir and C. I. Ferreira. Comparison of Models for Calculation of the Thermodynamic Properties of NH_3-CO_2-H_2O Mixture. *International Refrigeration and Air Conditioning Conference*. Paper 1641 (2016).

J. Hovland. *Compression of raw biogas – A feasibility study*. Tel-Tek report 2217020-1, 2017. Available on https://www.biogas2020.se/wp-content/uploads/2017/06/2217020-1compressionrawbiogas.pdf

C. Jarne, S. T. Blanco, M. A. Gallardo, E. Rauzi, S. Otin and I. Valesco. Dew Points of Ternary Methane (or Ethane) + Carbon Dioxide + Water Mixtures: Measurements and Correlation. *Energy & Fuels*, 18:396-404, 2004.

H. Jilvero, K. J. Jens, F. Normann, K. Andersson, M. Halstensen, D. Eimer and F. Johnsson. Equilibrium measurements of the NH_3-CO_2-H_2O system – measurements and evaluation of vapor-liquid equilibrium data at low temperatures. *Fluid Phase Equilibria*, 385:237-247, 2015.

O. Kunz and W. Wagner. The GERG-2008 Wide-Range Equation of State for Natural Gases and Other Mixtures: An Expansion of GERG-2004. *J. Chem. Eng. Data*, 57:3032-3091, 2012.

F. Kurz, B. Rumpf and G. Maurer. Vapor-liquid-solid equilibria in the system NH_3-CO_2-H_2O from around 310 to 470 K: New experimental data and modeling. *Fluid Phase Equilibria*, 104:261-275, 1995.

L. N. Legoix, L. Ruffine, J. P. Donval and M. Haeckel. Phase Equilibria of the CH_4-CO_2 Binary and the CH_4-CO_2-H_2O Ternary Mixtures in the Presence of a CO_2-Rich Liquid Phase. *Energies*, 10(2034):1-11, 2017. Doi:10.3390/en10122034.

J. Li, L. Wei and X. Li. Modeling of CO_2-CH_4-H_2S-brine based on cubic EOS and fugacity-activity approach and their comparisons. *Energy Procedia*, 63:3598-3607, 2014.

J. Longhi. Phase equilibria in the system CO_2-H_2O I: New equilibrium relations at low temperatures. *Geochimica et Cosmochimica Acta*, 69(3): 529-539, 2005.

B. Nabgan, T.A.T. Abdullah, W. Nabgan, A. Ahmad, I. Saeh and K. Moghadamian. Process Simulation for Removing Impurities From Wastewater Using Sour Water 2-Strippers system via Aspen Hysys. *Chem. Prod. Process Model*, 11(4):315-321, 2016.

T. Neumann, M. Tho, I. H. Bell, E. Lemmon and R. Span. Fundamental Thermodynamic Models for Mixtures Containing Ammonia. *Fluid Phase Equilibria*, 511:112496, 2020.

D. Peng and D. B. Robinson. A New Two-Constant Equation of State. *Industrial & Engineering Chemistry Fundamentals*, 15(1):59-646, 1976.

L. Pellegrini. Biogas to liquefied biomethane via cryogenic upgrading technologies. *Renewable Energy*, 124:75-83, 2018.

R. Privat and J. N. Jaubert, *Predicting the Phase Equilibria of Carbon Dioxide Containing Mixtures Involved in CCS Processes Using the PPR78 Model*. InTech, 2014. Available on http://dx.doi.org/10.5772/57058.

H. Que and C.C. Chen. Thermodynamic Modeling of the NH_3-CO_2-H_2O system with Electrolyte NRTL Model. *Ind. Eng. Chem. Res.*, 50(19):11406-11421, 2011.

S. Skogestad. Experience in Norsk Hydro with cubic equations of state. *Fluid Phase Equilibria*, 67:179-188 1983.

G. Soave. Equilibrium constants from a modified Redlich Kwong equation of state. *Chemical Engineering Science*, 27:1197-1203, 1972.

L F. Sotoft, M. B. Pryds, A. K. Nielsen and B. Norddahl. Process Simulation of Ammonia Recovery from Biogas Digestate by Air Stripping with Reduced Chemical Consumption, 37:2465-2470, 2015.

N. Spycher, K. Pruess and J. Ennis-King. CO_2-H_2O mixtures in the geological sequestration of CO_2. I. Assessment and calculation of mutual solubilities from 12 to 100 ºC and up to 600 bar. *Geochimica et Cosmochimica Acta*, 67 (16):3015-3031, 2003.

R. Stryjek and J. H. Vera. PRSV – An Improved Peng-Robinson Equation of State with New Mixing Rules for Strongly Nonideal Mixtures. *The Canadian Journal of Chemical Engineering*, 64:334-340, 1986.

Y. Tan, W. Nookuea, H. Li, E. Thorin and J. Yan. Cryogenic technology for biogas upgrading combined with carbon capture – a review of systems and property impacts. *Energy Procedia*, 142:3741-3746, 2017.

C. H. Twu, D. Bluck, J. R. Cunningham and J. E. Coon. A Cubic Equation of State with a New Alpha Function and a New Mixing Rule. *Fluid Phase Equilibria*, 69:33-50, 1991.

Z. Ziabakhsh-Ganji and H. Kooi. An Equation of State for thermodynamic equilibrium of gas mixtures and brines to allow simulation of the effects of impurities in subsurface CO_2 storage. *International Journal of Greenhouse Gas Control*, 11(Supplement):S21-S34, 2012.

L. E. Øi and J. Hovland. *Simulation of Condensation in Compressed Raw Biogas Using Aspen HYSYS*. In Linköping Electronic Conference Proceedings SIMS 59, pp. 31-36, 2018. doi: 10.3384/ecp1815331.

L. E. Øi. *Removal of CO_2 from exhaust gas*. PhD Thesis, Telemark University College, Porsgrunn. (TUC 3: 2012)

Epidemiological Models and Process Engineering

Bernt Lie

University of South-Eastern Norway, Porsgrunn, Norway, Bernt.Lie@usn.no

Abstract

The paper discusses the principles behind epidemiology models, with examples taken from the classic SIR (suspectible-infected-recovered) and SEIR (S-exposed-IR) models. Both continuous time deterministic and stochastic models are treated, where the stochastic models are based on Poisson-distributed events/reactions. These models use real approximations to the integers representing the number of people in each of the classes S, (E,) I, R. An alternative stochastic representation is the first reaction time description, where the variables are kept as integers, and where one instead computes the time between each event. The models are presented in a form compatible with standard chemical engineering models.

Based on the model description, the SIR and SEIR models are fitted to a measles case study using the Markov Chain Monte Carlo approach. For the given data, the SIR model appears to give much smaller uncertainty in predicitons. The continuous time stochastic description and the firt reaction time approaches give similar variation in the models.

An important measure of the state of epidemics is the *reproduction number*, R, which tells whether the infection is growing or decreasing from an initial infection. The development of an expression for R is indicated both from eigenvalues and from the Next-Generation Approach, and it is shown that the expression for R is identical for the SIR and the SEIR model.

The principles of epidemiology model development discussed in the paper are used in models ranging from HIV/AIDS to COVID-19.

Keywords: epidemiology, reaction engineering, deterministic models, stochastic models, model fitting, measles case study

1 Introduction

1.1 Background

The COVID-19[1] pandemic spreading in 2020 initially caused fear, irrational hoarding of consumer goods, uncertainty about future food supply, and economic depression. References to historic disasters such as the Black Death and the "Spanish Flu" were drawn. This period also spawned a renewed interest in epidemiology to understand how infections spread, and a massive effort in development of virus medicine and vaccines. Policy making and society saw challenges hardly faced before on how to adapt to the development in real time. The effort to develop vaccines has probably been the largest directed effort since space exploration, and similar to space technology, the medical developments will have wide ranging consequences. The sociological experiment faces serious questions regarding the limits of governing and personal freedom.

Although developed within life sciences, epidemiological models have much in common with chemical reaction engineering. A key difference is that while chemistry operates with particle numbers in the order of 10^{23}, epidemiological models operate with number of people in the range of 10^2– 10^9. Deterministic epidemics models are common, but the "law of large numbers" as used in chemical engineering does not really apply, and stochastic formulations are of interest.

Policy making and epidemics mitigation has much in common with feedback control under uncertainty. It is therefore of interest to relate epidemiological models to formulations and notation from chemical reaction engineering and process control.

1.2 Previous work

Pandemics such as COVID-19 are not new. The (bacterial) bubonic plague[2] that came to Europe ca. 1346-47 became known as the *Black Death* (1346–1353), and killed an estimated 60% of the population in Europe (50-80 million), and some 75–200 million worldwide. Poland closed its borders, and was more or less spared from the plague; Iceland was partially spared since sailors died before the ships arrived to Iceland. An artistic work from this period expressed an almost modern belief in science:

> "Elegant ladies, as I believe you know, the wisdom we mortals possess does not merely consist of remembering things past and apprehending the present, but on the basis of these two activities being able to predict the future, which is considered by serious men to be the highest form of human intelligence."
>
> Boccaccio, Giovanni (1349-1351/-52). *The Decameron*, p. 851. Translated by Wayne A. Rebhorn. W. W. Norton & Company. Kindle Edition.

[1] COVID-19 is the COrona VIrus Disease originating in 2019. The World Health Organization and Wikipedia.com both appear to write COVID-19 in all caps.

[2] https://en.wikipedia.org/wiki/Bubonic_plague

The "Spanish Flue"[3] or the *1918 influenza pandemic*, infected up to 500 million, with 17–100 million deaths. Classical epidemiology models were developed in the decade following the "Spanish Flu".

Historically, the population of N individuals was partitioned into a deterministic 3 compartmental model consisting of those who are susceptible to an infection (S), those who have been infected (I), and those who have recovered (R), (Kermack and McKendrick, 1927). Considering infections as *reactions*, and reaction events following a Poisson distribution, a determistic model can be converted to a stochastic model and solved using stochastic differential equation solvers. Alternatively, the model can be solved using Gillespie's algorithm, which is based on work in the statistics community ca. 1930–1950[4] and also assumes that reactions follow a Poisson distribution (Gillespie, 1976, 1977).

Approximately at the same time as the deterministic Kermack-McKendrick model, the stochastic *Reed-Frost* model was formulated which describes the same SIR types; this model was published much later, (Schwabe et al., 1977). This model is based on SIR compartmentalization, is discrete in time, and assumes a stochastic infection transmission with a fixed probability. To some degree, this model is related to *agent-based* models, where one could envision tracking of individuals within a compartment.

A good, general introduction to epidemiology models is (Keeling and Rohani, 2008). See also (Martcheva, 2015), who gives a more mathematically oriented overview with elements of stability results using Lyapunov theory. In (Brauer et al., 2019), various complex epidemiology models are discussed, with a number of case studies. An important concept related to infection spreading is the so-called *reproduction number*, R, which is related to initial stability of the infection model. An alternative to the above "balance" type models, is models whare "particles" move around in space, and are infected based on some stochastic model due to proximity to other infected "particles", e.g., (Britton and Pardoux, 2019).

Classical epidemiological models use a *spatial description* (Euler description) where the focus is on a number of compartments of fixed area/people with fixed attributes (age, immune level, etc.) where people move in and out of the various compartments/attributes. An alternative could be a *material description* (Lagrangian description) where one instead track the status of each individual or a group of individuals of similar attributes, and how these move about in the world, get into proximity with other people, and get infected with a certain probability. Such *material descriptions* are sometimes referred to as *agent-based* models.[5] Agent-based models are not discussed in this paper.

1.3 Scope

The focus in this work is to relate basic epidemiology models to process engineering concepts such as balance equations, "chemical" reactions, and mass action rates. A comparison between deterministic and various stochastic models is given. Some basic analysis is provided, together with methods for model solution and model fitting. As a simple case study, a model of a measles outbreak is used, and model fitting is developed. The paper is organized as follows: in Section 2, some details of the problem scope with materials and methods is given, in Section 3, the methods in Section 2 are applied to a case of measles infection. Section 4 provides basic analysis of models with reference to epidemics growth and reduction: development of expressions for the basic reproduction number. Section 5 provides some conclusions.

All computations in the paper are carried out using language Julia, which has an excellent package for solving both deterministic and stochastic differential equations (`DifferentialEquations.jl`; (Rackauckas and Nie, 2017a), (Rackauckas and Nie, 2017b), (Rackauckas and Nie, 2018)), as well as standard least squares model fitting (package `BlackBoxOptim.jl`) and Markov Chain Monte Carlo methods (`Turing.jl`). Plotting is done with package `Plots.jl`.

2 Materials and methods

2.1 Number balance

In epidemiology models, individuals are categorized into n_{X} types/classes X_j with $j \in \{1,\ldots,n_{\mathrm{X}}\}$. The number of individuals in *class/compartment* X_j is denoted $X_j \in \mathbb{N}_0$, and the total number of individuals in the *population* is $N = \sum_{j=1}^{n_{\mathrm{X}}} X_j$. For efficiency, we collect individuals X_j into vector $X \in \mathbb{N}_0^{n_{\mathrm{X}}}$.

A general (vector) number balance for the individuals in the compartments is

$$X(t+\Delta t) = X(t) + \int_t^{t+\Delta t} \left(\dot{X}_{\mathrm{i}}(\theta) - \dot{X}_{\mathrm{e}}(\theta) + \dot{X}_{\mathrm{g}}(\theta)\right) \mathrm{d}\theta. \tag{1}$$

Here, $\dot{X} \in \mathbb{Z}^{n_{\mathrm{X}}}$ denotes *flow rate*, with subscripts i: immigration, e: emigration, and g: generation, and $\dot{X}_{\mathrm{g}} = N \cdot r_{\mathrm{g}}$, where the per capita rate of generation vector r_{g} for the n_{X} *classes* is

$$r_{\mathrm{g}} = \nu^{\mathsf{T}} r \tag{2}$$

and $\nu \in \mathbb{Q}^{n_{\mathrm{r}} \times n_{\mathrm{X}}}$ is the *stoichiometric reaction matrix*, while r is the rate of reaction *per capita* for the n_{r} *reactions*.

If we make the assumption that the elements of X are "large" numbers so that $\left|\left(X(t+\Delta t) - X(t)\right)_j\right| \ll \left|X(t)_j\right|$,

[3] The disease apparently was first observed in Haskell County, Kansas, USA in January 1918, with first known case being an army cook at Camp Funston in Kansas, March 4, 1918.

[4] https://en.wikipedia.org/wiki/Gillespie_algorithm

[5] Some presentations of epidemiology refer to Lagrangian and Eulerian *movement* in an unconventional way, e.g., Martcheva (2015), pp. 389–392.

we make the approximation $X \in \mathbb{R}_0^{n_X}$. If we also assume that the integrand is a *continuous function of time*[6], the mean value theorem allows the result

$$\frac{\mathrm{d}X}{\mathrm{d}t} = \dot{X}_\mathrm{i} - \dot{X}_\mathrm{e} + N \cdot \left(\nu^\mathsf{T} r\right). \tag{3}$$

With similar assumptions, we can describe the total population as

$$\frac{\mathrm{d}N}{\mathrm{d}t} = \dot{N}_\mathrm{i} - \dot{N}_\mathrm{e} + \dot{N}_\mathrm{g}. \tag{4}$$

Introducing the per capita number $\check{X}$, $\check{X} \triangleq X/N$, and similarly $\dot{X}_\mathrm{i} \triangleq \dot{N}_\mathrm{i} \cdot \check{X}_\mathrm{i}$, $\dot{X}_\mathrm{e} \triangleq \dot{N}_\mathrm{e} \cdot \check{X}_\mathrm{e}$, the per capita model is

$$\frac{\mathrm{d}\check{X}}{\mathrm{d}t} = \frac{\dot{N}_\mathrm{i}}{N}\left(\check{X}_\mathrm{i} - \check{X}\right) + \nu^\mathsf{T} r - \frac{\dot{N}_\mathrm{g}}{N}\check{X}. \tag{5}$$

2.2 Assumptions on the total population

Simple epidemiology models consider a single compartment with constant population: either dead people are considered part of the population and births are neglected, or birth rate and death rate are assumed to be equal. If the spread of the infection is slow compared to the birth/death cycle, population growth must be included in the model.

If infection rate and level of illness depends on internal coordinates such as age, underlying illnesses, etc., it may be necessary to pose separate models for each age group, etc. In this case, "birth" and "death" into each age group or group of underlying conditions must be included.

If there is a geographical distribution in the number of infected per capita, some sort of distributed model should be used. Examples could be one compartment per country, per region, per municipality, per suburb, or other natural groupings. In this case, it may be necessary to include immigration and emigration for the individual compartments — this depends on the level of interaction vs. the rate of infection spread.

2.3 The classical continuous SIR description

In the classical (Kermack and McKendrick, 1927) model, the population of N individuals is divided into 3 groups: individuals of type S are *susceptible* for infection, individuals of type I are *infected*, while individuals of type R have *recovered* from the infection (or died), thus $X = (S, I, R)$. There is a chain of "reactions" $\mathrm{S} \to \mathrm{I} \to \mathrm{R}$, which can be broken down into two independent parallel events $\mathscr{E}_j$ — interaction with infection $\mathscr{E}_\mathrm{i}$ of rate r_i, and recovery $\mathscr{E}_\mathrm{r}$ of rate r_r:

$$\begin{aligned} \mathscr{E}_\mathrm{i} &: \mathrm{S} \overset{\mathrm{I}}{\to}{}^{k_\mathrm{i}} \mathrm{I}, \quad r_\mathrm{i} \\ \mathscr{E}_\mathrm{r} &: \mathrm{I} \to^{k_\mathrm{r}} \mathrm{R}, \quad r_\mathrm{r}. \end{aligned}$$

Here, $\mathrm{S} \overset{\mathrm{I}}{\to}{}^{k_\mathrm{i}} \mathrm{I}$ indicates that an infected individual *catalyses* the transformation of a susceptible S into a new infected individual I without "consuming" the original infecting individual, with a frequency factor k_i or with a mean interval $\tau_\mathrm{i} = 1/k_\mathrm{i}$.[7] The infection rate r_i per capita takes place with a certain probability when a susceptible individual is in proximity of an infected individual, thus the probability of infection depends on the relative concentration of the two types, in accordance with the *law of mass action* in chemical kinetics,

$$r_\mathrm{i} = \frac{1}{\tau_\mathrm{i}}\check{S}\check{I} = k_\mathrm{i}\check{S}\check{I}.$$

At the same time, $\mathrm{I} \to^{k_\mathrm{r}} \mathrm{R}$ indicates a simple recovery (i.e., no catalysis) from infected I to recovered R during a mean time of $\tau_\mathrm{r} = 1/k_\mathrm{r}$. The reaction r_r depends only on the concentration of the infected type, thus

$$r_\mathrm{r} = \frac{1}{\tau_\mathrm{r}}\check{I} = k_\mathrm{r}\check{I}.$$

The stoichiometric reaction is

$$\underbrace{\begin{pmatrix} -1 & 1 & 0 \\ 0 & -1 & 1 \end{pmatrix}}_{=\nu} \begin{pmatrix} \mathrm{S} \\ \mathrm{I} \\ \mathrm{R} \end{pmatrix} \leftarrow \begin{pmatrix} 0 \\ 0 \end{pmatrix}$$

where ν is the *stoichiometric matrix*. It follows that

$$\begin{pmatrix} r_{\mathrm{S,g}} \\ r_{\mathrm{I,g}} \\ r_{\mathrm{R,g}} \end{pmatrix} = \nu^T \begin{pmatrix} r_\mathrm{i} \\ r_\mathrm{r} \end{pmatrix} = \begin{pmatrix} -r_\mathrm{i} \\ r_\mathrm{i} - r_\mathrm{r} \\ r_\mathrm{r} \end{pmatrix}.$$

2.4 Extension: the SEIR description

In the SEIR description, individuals are classified as type S (*susceptible*), type E are *exposed* to infection, but the infection is latent, type I (*infected*), and type R (*recovered*). This gives $X = (S, E, I, R)$, and neglecting birth and death, $N = S + E + I + R$. The chain of events $\mathrm{S} \to \mathrm{E} \to \mathrm{I} \to \mathrm{R}$, can be broken down into the three parallel independent events $\mathscr{E}_\mathrm{i}$, $\mathscr{E}_\mathrm{e}$, and $\mathscr{E}_\mathrm{r}$ with rates r_i, r_e, and r_r, respectively:

$$\begin{aligned} \mathscr{E}_\mathrm{i} &: \mathrm{S} \overset{\mathrm{I}}{\to}{}^{k_\mathrm{i}} \mathrm{E}, \qquad r_\mathrm{i} = \frac{1}{\tau_\mathrm{i}}\check{I}\check{S} = k_\mathrm{i}\check{I}\check{S} \\ \mathscr{E}_\mathrm{e} &: \mathrm{E} \to^{k_\mathrm{e}} \mathrm{I}, \qquad r_\mathrm{e} = \frac{1}{\tau_\mathrm{e}}\check{E} = k_\mathrm{e}\check{E} \\ \mathscr{E}_\mathrm{r} &: \mathrm{I} \to^{k_\mathrm{r}} \mathrm{R}, \qquad r_\mathrm{r} = \frac{1}{\tau_\mathrm{r}}\check{I} = k_\mathrm{r}\check{I}. \end{aligned}$$

The stoichiometric reaction is

$$\underbrace{\begin{pmatrix} -1 & 1 & 0 & 0 \\ 0 & -1 & 1 & 0 \\ 0 & 0 & -1 & 1 \end{pmatrix}}_{=\nu} \begin{pmatrix} \mathrm{S} \\ \mathrm{E} \\ \mathrm{I} \\ \mathrm{R} \end{pmatrix} \leftarrow \begin{pmatrix} 0 \\ 0 \\ 0 \end{pmatrix}$$

[6] Invalid for stochastic processes!

[7] Note that $\tau_\mathrm{i} = 1/k_\mathrm{i}$ is *not* the length of time an infected person stays infected (which probably is more or less constant), but rather the mean interval between each time one infected individual causes a susceptible to become infected. In other words, if a freshly infected person is removed from society (e.g., locked up, or otherwise put away), then $\tau_\mathrm{i} \to \infty$, alternatively $k_\mathrm{i} \to 0$, but the same infected person will still recover (or die) in finite time.

where ν is the *stoichiometric matrix*. It follows that

$$\begin{pmatrix} r_{\mathrm{S,g}} \\ r_{\mathrm{E,g}} \\ r_{\mathrm{I,g}} \\ r_{\mathrm{R,g}} \end{pmatrix} = \nu^T \begin{pmatrix} r_{\mathrm{i}} \\ r_{\mathrm{e}} \\ r_{\mathrm{r}} \end{pmatrix} = \begin{pmatrix} -r_{\mathrm{i}} \\ r_{\mathrm{i}} - r_{\mathrm{e}} \\ r_{\mathrm{e}} - r_{\mathrm{r}} \\ r_{\mathrm{r}} \end{pmatrix}.$$

2.5 Poisson distribution in events

Let N_t be the (random) number of events that already have occurred at time t, and let $N_{t+\Delta t}$ denote the number of events that have occurred at time $t+\Delta t$. Introducing $\Delta N_t \triangleq N_{t+\Delta t} - N_{\mathrm{t}}$, it follows that in the interval $[t, t+\Delta t]$, we have $\Delta N_t \in \mathbb{N}_0$ new occurrences. When occurances appear with a constant mean rate λ, random variable ΔN_t is Poisson distributed, $\Delta N_t \sim \mathbf{Pois}(\lambda)$, with

$$\mathbb{E}(\Delta N_t) = \lambda$$
$$\mathbb{V}(\Delta N_t) = \lambda.$$

Next, consider the random *generation rate* $R = \frac{\Delta N_t}{\Delta t}$ in a relatively short time interval Δt, and an average rate of generation $\bar{r}$ so that $\lambda = \bar{r} \cdot \Delta t$. There is no guarantee that realization $r = \frac{\Delta n}{\Delta t}$ is an integer, but the random variable R is distributed according to a quasi continuous Poisson distribution, $R \sim \mathbf{cPois}(\bar{r})$, where for "large" $\bar{r}$,

$$\mathbb{E}(R) \approx \bar{r}$$
$$\mathbb{V}(R) \approx \bar{r}.$$

Furthermore, for realistic values of $\bar{r}$, the random rate R will approach a normal distribution $R \sim \mathbf{N}\left(\bar{r}, \sqrt{\bar{r}}\right)$.

2.5.1 Stochastic differential equation

When the reaction rate is random (r in Eq. 3 becomes R), the mean value theorem is invalid, and Eq. 3 must be rephrased as a stochastic differential equation (SDE)

$$\mathrm{d}X = \dot{X}_{\mathrm{i}}\mathrm{d}t - \dot{X}_{\mathrm{e}}\mathrm{d}t + N \cdot \left(\nu^{\mathsf{T}} R\right)\mathrm{d}t.$$

With $R \sim \mathbf{N}\left(\bar{r}, \sqrt{\bar{r}}\right)$ and introducing $Z \sim \mathbf{N}(0,1)$, this can be rephrased as

$$\mathrm{d}X = \left(\dot{X}_{\mathrm{i}} - \dot{X}_{\mathrm{e}} + N \cdot \left(\nu^{\mathsf{T}} \bar{r}\right)\right)\mathrm{d}t + N \cdot \left(\nu^{\mathsf{T}} \sqrt{\bar{r}}\right) Z \mathrm{d}t.$$

Using an SDE solver, a number of realizations are found. Then based on these realizations, statistics (mean, etc., including the distribution) can be computed for each time instance. Alternatively, an associated determistic Fokker-Planck equation can be posed, and solved to find the probability distribution directly.

When formulating the SDE, the approximation $X \in \mathbb{R}^{n_{\mathrm{X}}}$ is used.

2.5.2 First reaction time

Let N_t be the random number of arrivals accumulated at time t. Let ΔT_t be the random time it takes for the event of one additional arrival, assuming that someone arrived at time t.

By definition, the following two events are equivalent:

$$(\Delta T_t > \Delta t) \equiv (N_t = N_{t+\Delta t}).$$

With $\Delta N_t \sim \mathbf{Pois}(\lambda)$, it can be shown that ΔT is *Exponentially* distributed, $\Delta T \sim \mathbf{Exp}(\bar{r})$, or alternatively with U uniformly distributed $U \sim \mathbf{U}_{[0,1)}$ we can use

$$\Delta T = -\frac{1}{\bar{r}} \ln(U).$$

In the simplest version of Gillespie's algorithm, a three step procedure is used: (i) first, a uniform random number generator is used to find which event takes place (i.e., which of the reaction takes place), (ii) secondly, the time ΔT until next event is computed by drawing from an Exponential distribution. (iii) Then only the event found from (i) is carried out, and the time index is updated to $t_{i+1} = t_i + \Delta T$.

A number of realizations of the first reaction time model can be carried out, and it is possible to compute statistics for each time point.

Alternatively, similarly as for SDEs and the Fokker-Planck equation, a deterministic *master equation* can be posed to describe the probability distribution of the solution for the first reaction time model.

When using the first reaction time formulation, we maintain the fact that the number of people are integers, $X \in \mathbb{N}_0^{n_{\mathrm{X}}}$.

2.6 Reproduction number

The *reproduction* number of the disease is the average number of persons that an individual infects before recovering. The *basic reproduction* number R_0 is the reproduction number when (i) starting from a disease-free state, (ii) for the zeroth generation, i.e., the natural reproduction at initial time when everyone are susceptible, prior to invoking any mitigation policy.

For the SIR model, the initial time Jacobian $J_{\check{X}}$ of the model vector field is

$$J_{\check{X}} = \begin{pmatrix} -k_{\mathrm{i}}\check{I} & -k_{\mathrm{i}}\check{S} & 0 \\ k_{\mathrm{i}}\check{I} & k_{\mathrm{i}}\check{S} - k_{\mathrm{r}} & 0 \\ 0 & k_{\mathrm{r}} & 0 \end{pmatrix}.$$

Starting from a disease-free state, $\check{I}(0) \equiv 0$,

$$J_{\check{X}} = \begin{pmatrix} 0 & -k_{\mathrm{i}}\check{S}(0) & 0 \\ 0 & k_{\mathrm{i}}\check{S}(0) - k_{\mathrm{r}} & 0 \\ 0 & k_{\mathrm{r}} & 0 \end{pmatrix}.$$

$J_{\check{X}}$ has two eigenvalues in the origin, and one eigenvalue at

$$\lambda = k_{\mathrm{i}}\check{S}(0) - k_{\mathrm{r}}.$$

Table 1. Daily number of measles infected at boarding school with 763 boys in Northern England, January-February 1978. Taken from (Martcheva, 2015).

Day	# infected	Day	# infected
3	25	9	192
4	75	10	126
5	227	11	71
6	296	12	28
7	258	13	11
8	236	14	7

Stability requires $\lambda < 0$,

$$\frac{k_\mathrm{i}\check{S}(0)}{k_\mathrm{r}} < 1.$$

The infection rate constant k_i varies with mitigation policy, etc. Let k_i^0 denote the natural rate constant *without* mitigation. The *basic reproduction number* R_0 is assessed when $\check{S}(0) \equiv 1$ and without mitigation, hence

$$\mathsf{R}_0 = \frac{k_\mathrm{i}^0}{k_\mathrm{r}}.$$

With mitigation, we could define an *effective reproduction number* $\mathsf{R} \triangleq k_\mathrm{i}/k_\mathrm{r}$.[8]

2.7 Model fitting

In simple model fitting, model parameters and initial states are posed as unknowns in a loss function that measures the difference between experimental data and a shooting (ballistic) formulation of the model. More sophisticated methods for Bayes estimation are conveniently solved using Markov Chain Monte Carlo methods (MCMC), see, e.g., (Evensen, 2009) for a practical introduction with his Ensemble Kalman Filter approach. Other methods and tools exist.

2.8 Measles case study

At a boarding school in North England, January–February 1978, measles infection was observed among the 763 pupils, with 25 infections on assumed day 3 of the epidemic. The evolution of observed infections was as recorded in Table 1.

In (Martcheva, 2015), a SIR model is used to model the infection, assuming that $N = 763$ is constant, and that all pupils are locked up in the school. The basic reproduction number for measles is estimated to be in the range $\mathsf{R}_0 \in [16, 18]$, (Keeling and Rohani, 2008), which should be contrasted to the range $[3, 4]$ for seasonal flu.

[8] R_0 and R has nothing to do with the number R of recovered.

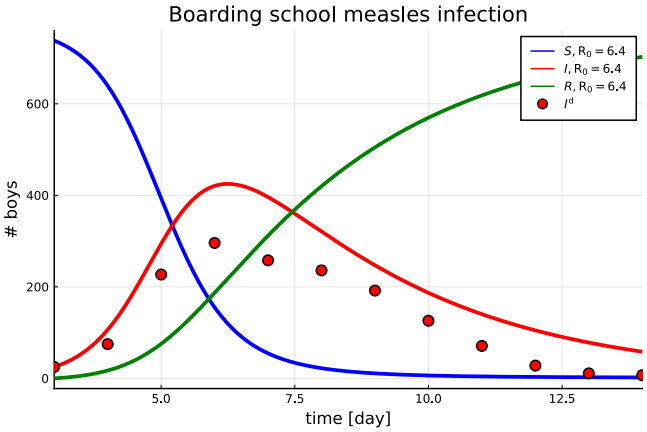

Figure 1. Comparing SIR model with original parameters vs. registered infection data for boarding school in North England, January–February 1978.

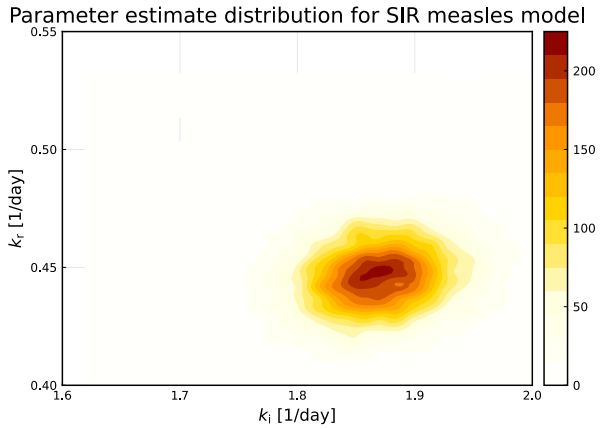

Figure 2. Distribution in Bayes estimates of parameters $\tau_\mathrm{r} = 1/k_\mathrm{i}$ and $\tau_\mathrm{i} = 1/k_\mathrm{r}$ in SIR model based on infection data for boarding school in North England, January–February 1978. Dr. Tamas Papp, TU Wien, provided the function of doing this plot.

3 Measles case study

3.1 SIR model

3.1.1 Deterministic model with model fitting

With the data in Table 1, and using parameters ((Martcheva, 2015), p. 127)

$$k_\mathrm{i} = \beta N = 0.0025 \cdot 763 = 1.9075$$
$$k_\mathrm{r} = \alpha = 0.3,$$

the deterministic model fits data reasonably well, Figure 1.

It is of interest to find better model parameters. Without going into details, the `Turing.jl` package for Julia supports Markov Chain Monte Carlo (MCMC) estimation of the model parameters, with parameter probability distribution as in Figure 2.

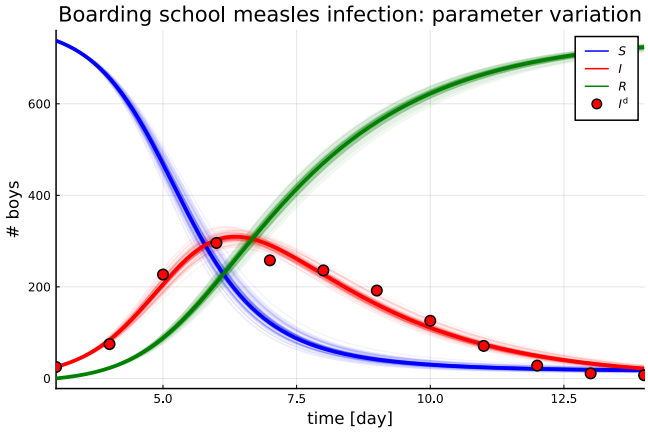

Figure 3. Comparing SIR model *data retrodiction* vs. registered infection data for boarding school in North England, January–February 1978. Dark/thick lines are based on the point estimates.

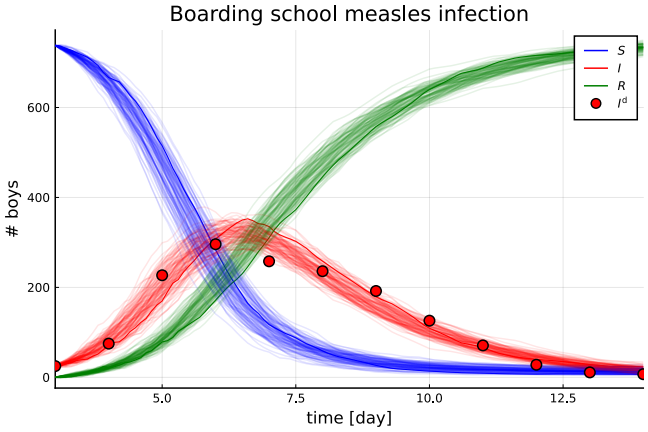

Figure 4. Stochastic realizations (trajectories) for an ensemble of 100 possible scenarios.

Point estimators (mean values) of the parameters are found to be:

$$k_{\mathrm{i}} \approx 1.817$$
$$k_{\mathrm{r}} \approx 0.4618,$$

which gives an *effective* reproduction number of $\mathrm{R} \approx 1.817/0.4618 \approx 3.9$. MCMC provides a number of possible parameter values, and this parameter uncertainty translates into prediction uncertainty, known as *data retrodiction*; results are given in Figure 3 in pale/thin lines, together with the simulation when using the point estimates in dark/thick lines.

From the data retrodiction, we see that there is relatively little uncertainty in the model even with varying parameters. This indicates that the model has quite good predictive properties.

3.1.2 SDE model

Using basic data from the deterministic simulation, we expand the model to a set of stochastic differential equations as described Section 2.5.1. The results are shown in Figure 4.

3.1.3 First reaction event model

Instead of formulating the model as Stochastic Differential Equations, we can write integer difference equations with first reaction event description for changes, see Section 2.5.2. The results are shown in Figure 5, and should be compared to the results in Figure 4.

3.2 SEIR model

It is of interest to consider the SEIR model for the measles case, where we assume that I_3 is known, that $R_3 = 0$, that N is known, but that S_3 or E_3 are unknown; we choose to estimate S_3. Reusing the model parameters for k_{i} and k_{r} from the SIR model, we initially assume that $k_{\mathrm{e}} = 2$; see Figure 6.

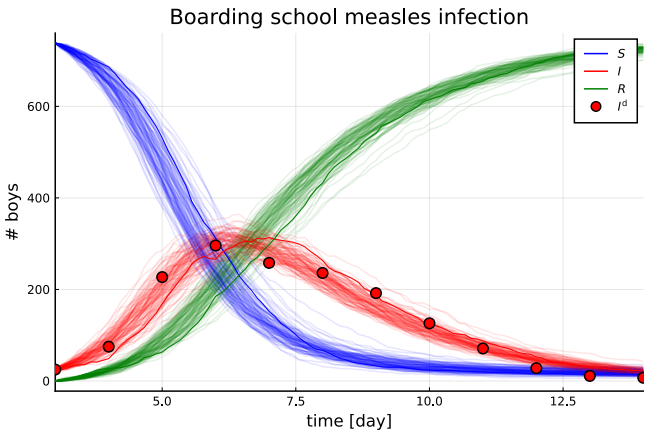

Figure 5. Stochastic realizations (trajectories) for an ensemble of 100 possible scenarios using Gillespie's First Reaction Method.

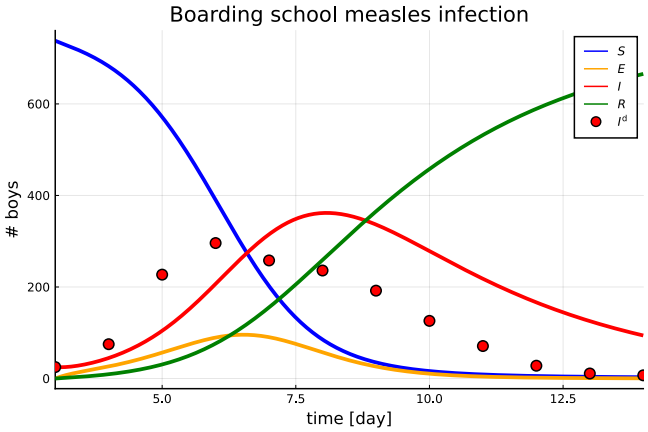

Figure 6. SEIR model with original parameters vs. registered infection data for boarding school in North England, January–February 1978.

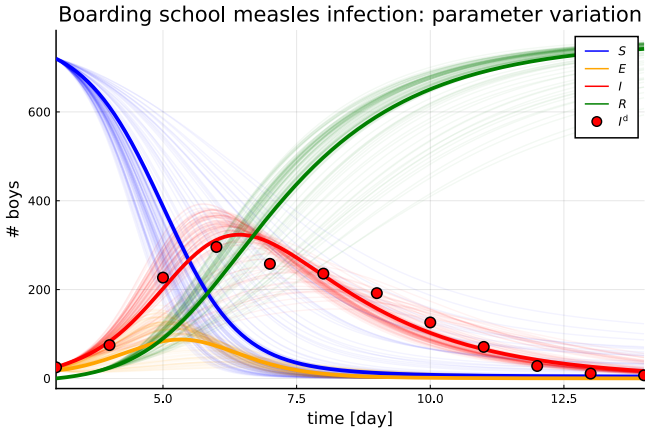

Figure 7. Comparing SEIR model data *retrodiction* vs. registered infection data for boarding school in North England in January–February 1978. Dark lines are based on the point estimates.

We can also fit the parameters of the SEIR model, including the initial value of S_3. The result are the following point estimates (mean value):

$$\begin{aligned} k_\mathrm{i} &\approx 2.50 \\ k_\mathrm{e} &\approx 2.826 \\ k_\mathrm{r} &\approx 0.477 \\ S_3 &\approx 720 \end{aligned}$$

If we draw estimates of these parameters and initial value and redo simulations, the data retrodiction is as in Figure 7. As we see, the uncertainties in the retrodiction of the SEIR model, Figure 7, are far larger than the uncertainties in the retrodiction of the SIR model, Figure 3. This may indicate that the measles infection is best modeled by a SIR model, but it must be remembered that we have few data points and the SEIR model has almost twice as many parameters as the SIR model[9].

4 Analysis of epidemiology models

4.1 Condition for infection growth

With model

$$\frac{\mathrm{d}\check{X}}{\mathrm{d}t} = F\left(\check{X}\right)$$

in per capita variables $\check{X}$, a standard procedure for finding conditions for infection growth is to analyze the Jacobian

$$J_{\check{X}_0} = \left.\frac{\partial F}{\partial \check{X}}\right|_{\check{X}_0},$$

where $\check{X}_0$ is the operating point. In general, the operating point will depend on the current states.

[9]Estimated parameters for the SIR model: k_i, k_r, and standard deviation in output error. Estimated parameters for the SEIR model: k_i, k_e, k_r, initial value for S_3, and standard deviation in output error.

In a standard way, stability can be assessed based on eigenvalues, or related Routh-Hurwitz criteria. However, eigenvalues are often difficult to compute for realistic models.

An alternative is the *Next-Generation Approach* (van den Driessche, 2017; Martcheva, 2015). With model

$$\frac{\mathrm{d}\check{X}}{\mathrm{d}t} = \nu^\mathsf{T} r$$

where $r = r\left(\check{X}\right)$, assume that $\check{X}$ has been sorted such that $\check{X} = (x,y)$ and x contains the *infected* compartments while y contains all other compartments. Thus, we have the differential equations

$$\begin{aligned} \frac{\mathrm{d}x}{\mathrm{d}t} &= f(x,y) \\ \frac{\mathrm{d}y}{\mathrm{d}t} &= g(x,y) \end{aligned}$$

where

$$\begin{pmatrix} f(x,y) \\ g(x,y) \end{pmatrix} = \nu^\mathsf{T} r(x,y).$$

We split $f(x,y)$ into two terms,

$$f(x,y) = \mathscr{F}(x,y) - \mathscr{V}(x,y)$$

where $\mathscr{F}_i(x,y)$ contains the rate of *appearance* of *new infections* in compartment i, while $\mathscr{V}_i(x,y)$ include all other terms: births, deaths, disease progression, recovery. Observe that $\mathscr{F}(x,y)$ and $\mathscr{V}(x,y)$ are not necessarily unique.

Let F and V be the Jacobians of $\mathscr{F}$ and $\mathscr{V}$ in the disease-free case given by x^0, y^0, where $x^0 = 0$ and $y^0 \geq 0$:

$$\begin{aligned} F &= \left.\frac{\partial \mathscr{F}(x,y)}{\partial x}\right|_0 \\ V &= \left.\frac{\partial \mathscr{V}(x,y)}{\partial x}\right|_0. \end{aligned}$$

Then $N = FV^{-1}$ is the *Next-Generation Matrix*. Let $\rho(N)$ denote the *spectral radius* of matrix N: with λ_i the eigenvalues of N, $\rho(N) = \max_i |\lambda_i|$. We can then define the reproduction number R as

$$\mathsf{R} \triangleq \rho^m\left(FV^{-1}\right)$$

where m is some integer to make $\mathsf{R} \propto k_\mathrm{i}$. The infection is under control/decreases if $\mathsf{R} < 1$, and is out of control/grows if $\mathsf{R} > 1$.

4.2 Stability from SEIR model

For the SEIR model with $\check{S}(0) = 1$, the disease-free Jacobian is

$$J_{\check{X}(0)} = \begin{pmatrix} 0 & 0 & -k_\mathrm{i} & 0 \\ 0 & -k_\mathrm{e} & k_\mathrm{i} & 0 \\ 0 & k_\mathrm{e} & -k_\mathrm{r} & 0 \\ 0 & 0 & k_\mathrm{r} & 0 \end{pmatrix},$$

and it is feasible to find R from eigenvalue analysis. However, for illustration, we consider the Next-Generation Approach.

Here, $x = (\check{E}, \check{I})$, and we need to extract elements $(2:3, 2:3)$, i.e.,

$$J_0 = \begin{pmatrix} -k_e & k_i \\ k_e & -k_r \end{pmatrix} = \underbrace{\begin{pmatrix} 0 & k_i \\ k_e & 0 \end{pmatrix}}_{=F} - \underbrace{\begin{pmatrix} k_e & 0 \\ 0 & k_r \end{pmatrix}}_{=V},$$

and the Next-Generation Matrix N is

$$N = FV^{-1} = \begin{pmatrix} 0 & k_i \\ k_e & 0 \end{pmatrix} \begin{pmatrix} k_e & 0 \\ 0 & k_r \end{pmatrix}^{-1} = \begin{pmatrix} 0 & \frac{k_i}{k_r} \\ 1 & 0 \end{pmatrix},$$

with eigenvalues

$$\det \begin{pmatrix} \lambda & -\frac{k_i}{k_r} \\ -1 & \lambda \end{pmatrix} = \lambda^2 - \frac{k_i}{k_r} = 0$$

and spectral radius

$$\mathsf{R} = \rho^m(N) = \sqrt[m]{\frac{k_i}{k_r}};$$

where we choose $m = 2$ so that $\mathsf{R} \propto k_i$; $\mathsf{R} = \frac{k_i}{k_r}$ — just as for the SIR model, see Section 2.6.

5 Conclusions

An overview of principles for formulating epidemiological models has been given. Here, models based on balance laws are treated; the principle is identical to what is used in chemical engineering and other process engineering fields. A deterministic model is the starting point, and it is discussed how the assumption of Poisson distribution in the reactions events leads to either a stochastic differential equation or the first reaction time model/Gillespie formulation. These ideas of Poisson distribution carries over to chemical reactions in general.

Based on the published measles infection data, a susceptible-infected-recovered (SIR) epidemiological model is fitted to data using a Markov Chain Monte Carlos approach (MCMC), and appears to be adequate. It is also possible to fit an extended model with an exposed class (SEIR) to the measles data, but this gives much wider uncertainty in model parameters, with resulting large uncertainty in model predictions.

In an analysis part, several ways of finding an expression for the reproduction number R are discussed; R is used to describe the stability of an infection. The Next-Generation Approach is probably the method that is simplest to use for complex models.

This paper lays out the fundamental ideas behind epidemiology models, as used, e.g., in COVID-19 studies.

References

Fred Brauer, Carlos Castillo-Chavez, and Zhilan Feng. *Mathematical Models in Epidemiology*. Number 69 in Texts in Applied Mathematics. Springer, New York, 2019. ISBN 978-1-4939-9826-5.

Tom Britton and Etienne Pardoux, editors. *Stochastic Epidemic Models with Inference*. Number 2255 in Lecture Notes in Mathematics. Springer, Springer Nature, Switzerland, 2019. ISBN 978-3030308995.

Geir Evensen. *Data Assimilation. The Ensemble Kalman Filter*. Springer, Berlin, 2nd edition, 2009. ISBN 978-3-642-03710-8.

Daniel T. Gillespie. A general method for numerically simulating the stochastic time evolution of coupled chemical reactions. *Journal of Computational Physics*, 22(4):403–434, 1976. doi:https://doi.org/10.1016/0021-9991(76)90041-3.

Daniel T. Gillespie. Exact stochastic simulation of coupled chemical reactions. *The Journal of Physical Chemistry*, 81 (25):2340–2361, 1977. doi:10.1021/j100540a008.

Matt J. Keeling and Pejman Rohani. *Modeling Infectious Diseases in Humans and Animals*. Princeton University Press, 41 William Street, Princeton, New Jersey 08540, 2008. ISBN 978-0-691-11617-4.

W.O. Kermack and A.G. McKendrick. A contribution to the mathematical theory of epidemics. *Proceedings of the Royal Society A.*, 115(772):700–721, 1927. doi:https://royalsocietypublishing.org/doi/10.1098/rspa.1927.0118.

Maia Martcheva. *An Introduction to Mathematical Epidemiology*, volume 61 of *Texts in Applied Mathematics*. Springer, New York, 2015. ISBN 978-1-4899-7611-6.

Christopher Rackauckas and Qing Nie. DifferentialEquations.jl — A Performant and Feature-Rich Ecosystem for Solving Differential Equations in Julia. *Journal of Open Research Software*, 5(15), 2017a. doi:10.5334/jors.151.

Christopher Rackauckas and Qing Nie. Adaptive methods for stochastic differential equations via natural embeddings and rejection sampling with memory. *Discrete and continuous dynamical systems. Series B*, 22(7):2731, 2017b.

Christopher Rackauckas and Qing Nie. Stability-Optimized High Order Methods and Stiffness Detection for Pathwise Stiff Stochastic Differential Equations. *arXiv:1804.04344 [math]*, 2018. URL `http://arxiv.org/abs/1804.04344`.

C.W. Schwabe, H.P. Riemann, and C.E. Franti. *Epidemiology in Veterinary Practice*. Lea & Febiger, 1977. pp. 258–260.

Pauline van den Driessche. Reproduction numbers of infectious disease models. *Infectious Disease Modelling*, 2(3):288–303, aug 2017. doi:10.1016/j.idm.2017.06.002.

COVID-19 Models and Model Fitting

Bernt Lie

University of South-Eastern Norway, Porsgrunn, Norway, Bernt.Lie@usn.no

Abstract

The paper discusses how to use cumulative confirmed infected numbers to find basic infection parameters. Next, an extension of the SEIR model, the SEICUR model from the literature (a renaming of the SEIRU model) is introduced, with details of how to compute the full set of model parameters, as well as the reproduction number R. A discussion is given of how the infection rate parameter relates to mitigation policy and various natural variations. Based on a simple mitigation model, an equivalent mitigation policy is found for Italy, Spain, and Norway. An indication of how to use feedback control theory to develop mitigation policy planning is given.
Keywords: COVID-19 models, deterministic models, model fitting, control relevance

1 Introduction

1.1 Background

The COVID-19[1] pandemic spread in 2020 initially caused fear, irrational hoarding of consumer goods, uncertainty about future food supply, and economic depression, but also spawned a renewed interest in epidemiology to understand how infections spread, and a massive effort in development of virus medicine and vaccines. Policy making and society saw challenges hardly faced before on how to adapt to the development in real time.

Data for the number of COVID-19 infected and deaths related to this, started to appear in January-February 2020. Initially, the number of infected and deaths were highly uncertain and underreported due to lack of reliable test procedures. Due to many asymptomatically infected, the true number of infected is still uncertain, while the number of deaths is more certain. Still, there is a discussion on whether people die *of* COVID-19 or *with* COVID-19. Relatively reliable sources suggest around 600 thousand deaths in USA as of this writing[2], while some report more than 900 thousand deaths in USA based on some estimate of underreporting[3].

A number of COVID-19 models have been developed since March 2020; many of them are vague on how to integrate data with the models, few discuss mitigation policy (hand cleaning, social distancing, etc.), how to design such policy under model uncertainty, and the effects of virus mutation and vaccination.

1.2 Previous work

Classical epidemiology models were developed in the decade following the "Spanish Flu". A renewed *public* interest in epidemic models started with the AIDS/HIV epidemic some decades ago; these models have been used to study other infectious diseases, e.g., (Brauer et al., 2019). (Lie, 2021) gives a brief overview of such general models from a process engineering point of view.

(Zlojutro et al., 2019) give a general framework, pre COVID-19, for border control to mitigate global outbreaks, and include stochastic models per country, with transport between countries by airlines. The *IHME COVID-19 Forecasting Team*[4] give a general overview of their model in (Reiner et al., 2021)[5]. An early study by Imperial College London[6] convinced the government in USA to take the epidemic more seriously. Many models have been provided on-line in web pages. A review of COVID-19 models is given by (Rahimi et al., 2021).

It is difficult to find models that are described completely, with model parameters. One such model is that of (López and Rodó, 2020), giving parameters for various regions in Spain. The SEIRU and SIRU models, (Liu et al., 2020b,a,c), are relatively; symbol R denotes *reported* cases instead of the conventional use of R as *recovered*. These SEIRU class models are macro models for each country, and have the *important advantage* over other models that the "reported" class equals the number of reported infected. Yet another model is that used by the Public Health Institute in Norway, (Øyvann, 2020), and probably several other centers for disease control (CDC) in Europe. In Norway, this model is posed for each municipality (possibly also for certain suburbs), and includes migration between each compartment — estimated from anonymized mobile phone locations.

A key parameter in all models is the infection rate. The infection rate is a problematic quantity which varies with natural phenomena and season, as well as mitigation pol-

[1] COVID-19 is the COrona VIrus Disease originating in 2019. The World Health Organization and Wikipedia.com both appear to write COVID-19 in all caps.

[2] https://www.worldometers.info/coronavirus/, https://coronavirus.jhu.edu/

[3] https://covid19.healthdata.org/united-states-of-america?view=cumulative-deaths&tab=trend

[4] The Institute for Health Metrics and Evaluation (IHME) is an independent global health research center at the University of Washington

[5] https://covid19.healthdata.org/united-states-of-america?view=cumulative-deaths&tab=trend

[6] https://www.imperial.ac.uk/mrc-global-infectious-disease-analysis/covid-19/covid-19-planning-tools/

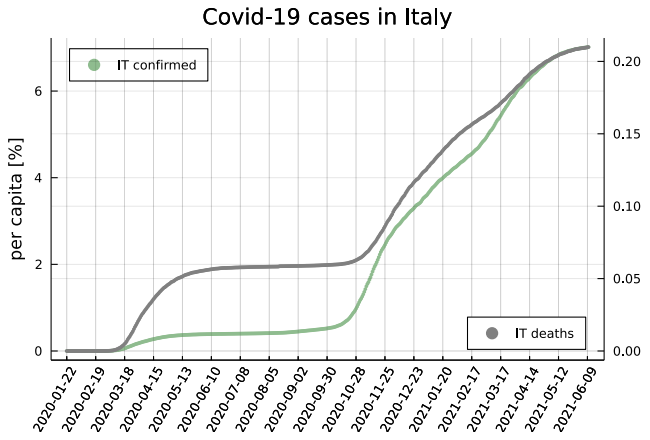

Figure 1. Cumulative number of confirmed infected in Italy vs. time (darkseagreen; left ordinate axis), and cumulative number of dead (grey; right ordinate axis).

icy and occurrence of mutations.

1.3 Scope

In Section 2, some available data are discussed, and basic model parameters are found. The SEICUR model is introduced (recasting of the SEIRU model), with procedures for finding model parameters. This model is constrasted to the Public Health Institute (PHI) of Norway. The infection rate parameter is related to mitigation policy, and expressions for reproduction number is given. In Section 3, the SEICUR model is fitted to data for Italy, Spain, and Norway. In Section 4, the results are discussed, and some conclusions are drawn.

All computations in the paper are carried out using language Julia, with packages `DifferentialEquations.jl`, (Rackauckas and Nie, 2017a), (Rackauckas and Nie, 2017b), (Rackauckas and Nie, 2018), `LsqFit.jl` for initial curve fitting, `BlackBoxOptim.jl` for equivalent mitigation policy fitting, and `Plots.jl` for plotting results.

2 Materials and Methods

2.1 COVID-19 data

Web page `https://github.com/octonion/COVID-19`, at folder `csse_covid_19_data`, subfolder `csse_covid_19_time_series`, file `time_series_covid19_confirmed_global.csv` provides daily updates of globally confirmed infected. Pre-treatment is required: some countries give regional data; others total data for the country. Here, we will focus on models for Norway, Italy, and Spain. Figure 1 shows cumulative number of infected and dead in Italy. Although it is possible to also model the rate of deaths, this is not done in this paper.

2.2 Initial evolution of $\mathfrak{C}$

Form of initial evolution Let $\mathfrak{C}$ denote the number of cumulative confirmed infected, which can be expressed as

$$\frac{\mathrm{d}\mathfrak{C}}{\mathrm{d}t} = \varphi \tag{1}$$

where φ is the rate at which people are confirmed infected. The actual expression for φ depends on the infection model. In the initial phase of an epidemic starting from the disease-free case, the rate at which people become confirmed infected increases exponentially

$$\varphi(t) = \varphi_0 \exp(\lambda \cdot (t - t_0)),$$

with $\lambda > 0$. Let $\Delta t \triangleq t - t_0$, $\Delta\mathfrak{C}(\Delta t) \triangleq \mathfrak{C}(t) - \mathfrak{C}(t_0)$, and $\chi_0 \triangleq \frac{\varphi_0}{\lambda}$, it follows that

$$\Delta\mathfrak{C}(\Delta t) = \chi_0 (\exp(\lambda \cdot \Delta t) - 1). \tag{2}$$

Parameters λ and φ_0 from time series of $\mathfrak{C}$ Assuming that time series data for $\Delta\mathfrak{C}(\Delta t)$ are known, we can tune χ_0 and λ to fit $\Delta\mathfrak{C}(\Delta t)$ to a function

$$\Delta\mathfrak{C}(\Delta t) = \chi_0 (\exp(\lambda \cdot \Delta t) - 1)$$

where we need to choose t_0, store the corresponding $\mathfrak{C}(t_0) = \mathfrak{C}_0$. Finally, we find φ_0 from $\varphi_0 = \lambda \cdot \chi_0$.

Parameters λ and φ_0 from $\mathfrak{C}$ in two data points If $\mathfrak{C}$ is known in two time instances t_0 and t_1, the slope of $\mathfrak{C}$ is known at t_0, $\Delta t = t_1 - t_0$, and the cumulative number of confirmed infected is *growing*,

$$\alpha \triangleq \frac{\Delta\mathfrak{C}/\Delta t}{\mathrm{d}\mathfrak{C}/\mathrm{d}t|_0} > 1,$$

it can be shown that λ is given by

$$\lambda = -\frac{\frac{1}{\alpha} + \mathscr{W}_{-1}\left(-\frac{1}{\alpha}\exp\left(-\frac{1}{\alpha}\right)\right)}{\Delta t}, \tag{3}$$

where $\mathscr{W}_{-1}(\cdot)$ is the lower branch of the Lambert W function.

With λ computed from Eq. 3, we find φ_0 as

$$\varphi_0 = \lambda \cdot \chi_0 = \left.\frac{\mathrm{d}\mathfrak{C}}{\mathrm{d}t}\right|_0. \tag{4}$$

The accuracy of this method of computing φ_0 and λ from two data points depends on how accurately $\frac{\mathrm{d}\mathfrak{C}}{\mathrm{d}t}|_0$ can be found.

Parameters and initial values for Italy Data for Italy for the 9 d period February 23 – March 3, 2020 indicates relatively exponential growth for φ, leading to a good fit for $\mathfrak{C}(t)$, Figure 2.

The following procedures are used to estimate λ and φ_0:

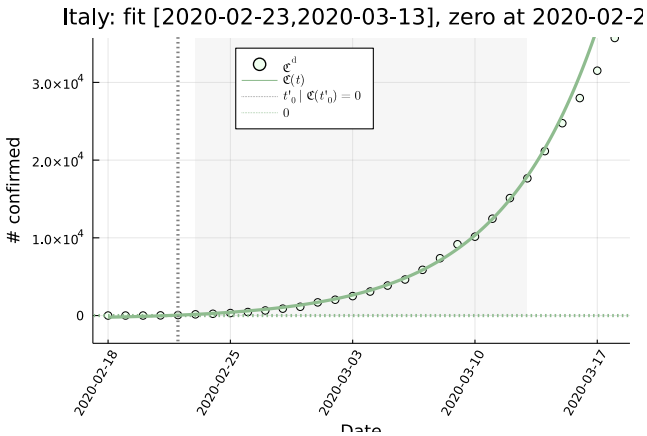

Figure 2. Fit of $\mathfrak{C}$ for Italy in the period February 23 – March 3, 2020.

Method 1 Fitting $\Delta\mathfrak{C}(\Delta t) = \chi_0(\exp(\lambda\cdot\Delta t)-1)$ to the data $\mathfrak{C}$. Computing φ_0 from $\varphi_0 = \lambda\cdot\chi_0$.

Method 2 Using the Lambert W approach, Eq. 3, to find λ, and next finding $\frac{\mathrm{d}\mathfrak{C}}{\mathrm{d}t}\big|_0$ found from fitting $\Delta\mathfrak{C}(\Delta t) = \chi_0(\exp(\lambda\cdot\Delta t)-1)$, and computing φ_0 according to Eq. 4 as $\varphi_0 = \frac{\mathrm{d}\mathfrak{C}}{\mathrm{d}t}\big|_0$.

Method 3 Using the Lambert W approach to find λ with $\frac{\mathrm{d}\mathfrak{C}}{\mathrm{d}t}\big|_0 \approx \frac{\mathfrak{C}(t_1)-\mathfrak{C}(t_0)}{t_1-t_0}$ where $t_1 = t_0+1$ and t_0 is February 23, 2020; $\varphi_0 = \frac{\mathrm{d}\mathfrak{C}}{\mathrm{d}t}\big|_0$.

Method 4 Using the Lambert W approach to find λ with $\frac{\mathrm{d}\mathfrak{C}}{\mathrm{d}t}\big|_0$ found by fitting a 3rd order polynomial to $\mathfrak{C}$ and computing the initial derivative of $\mathfrak{C}$; $\varphi_0 = \frac{\mathrm{d}\mathfrak{C}}{\mathrm{d}t}\big|_0$.

Method 5 Using the Lambert W approach to find λ with $\frac{\mathrm{d}\mathfrak{C}}{\mathrm{d}t}\big|_0$ found by fitting a 2nd order polynomial to $\log\mathfrak{C}$ and computing the initial derivative of $\mathfrak{C}$; $\varphi_0 = \frac{\mathrm{d}\mathfrak{C}}{\mathrm{d}t}\big|_0$.

The results show that Methods 1, 2, 3, and 5 give relatively similar results, while Method 4 gives a rather different result. The reason is that polynomial fit to $\mathfrak{C}$ gives a poor estimate of the initial derivative. Also for other countries, Method 1 appears to give the most reliable results, followed by Method 2. Here, we report the parameters from Method 1.

Summary parameters and initial values Table 1 gives a summary of fitted parameters t_0, t_1, $\mathfrak{C}_0$, φ_0, and λ for Italy, Spain, and Norway, based on Method 1.

2.3 SEICUR model

2.3.1 Reaction mechanism

An SEIR model with the infected I population extended to (I,C,U) was proposed for COVID-19 in (Liu et al., 2020b)[7], Figure 3.

The proposed mechanism implies that *susceptibles* S are infected by some "pre-infected" I and the non-quarantined *unconfirmed* U leading to the *exposed* phase E, which is infected but not yet infectious. These exposed E then are converted to the "pre-infected" I class, which then either become more serious cases and are *confirmed* infected C, or stay as *unconfirmed* U. Finally, the confirmed infected and the unconfirmed end up in the *recovered* population R (which includes those who die). We will refer to this model as the SEICUR model.

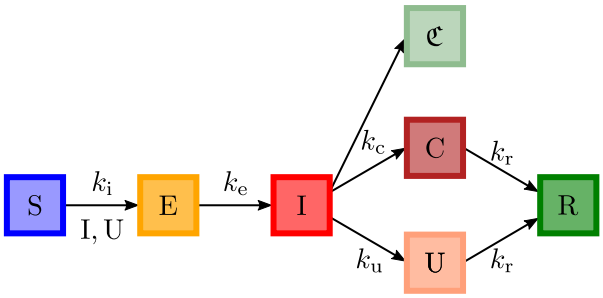

Figure 3. Flow of SEICUR reactions.

The following mechanism describes the reactions:

$$\begin{aligned}
\mathscr{E}_\mathrm{i}&:\mathrm{S}\overset{\mathrm{I+U}^{k_\mathrm{i}}}{\rightarrow}\mathrm{E}, & r_\mathrm{i} &= k_\mathrm{i}\left(\check{I}+\check{U}\right)\check{S}\\
\mathscr{E}_\mathrm{e}&:\mathrm{E}\rightarrow^{k_\mathrm{e}}\mathrm{I}, & r_\mathrm{e} &= k_\mathrm{e}\check{E}\\
\mathscr{E}_\mathrm{c}&:\mathrm{I}\rightarrow^{k_\mathrm{c}}\mathrm{C}, & r_\mathrm{c} &= k_\mathrm{c}\check{I}\\
\mathscr{E}_\mathrm{u}&:\mathrm{I}\rightarrow^{k_\mathrm{u}}\mathrm{U}, & r_\mathrm{u} &= k_\mathrm{u}\check{I}\\
\mathscr{E}_\mathrm{cr}&:\mathrm{C}\rightarrow^{k_\mathrm{r}}\mathrm{R}, & r_\mathrm{cr} &= k_\mathrm{r}\check{C}\\
\mathscr{E}_\mathrm{ur}&:\mathrm{U}\rightarrow^{k_\mathrm{r}}\mathrm{R}, & r_\mathrm{ur} &= k_\mathrm{r}\check{U}.
\end{aligned}$$

We introduce

$$\begin{aligned}
k_\mathrm{cu} &= k_\mathrm{c}+k_\mathrm{u}\\
k_\mathrm{c} &= \eta k_\mathrm{cu}.
\end{aligned}$$

Thus, specifying k_cu and η, we can find

$$\begin{aligned}
k_\mathrm{c} &= \eta k_\mathrm{cu}\\
k_\mathrm{u} &= (1-\eta)\,k_\mathrm{cu}.
\end{aligned}$$

The model assumes that the total population is fixed, and that a preliminary fitting to find ϕ_0 and λ has been carried out, Table 1. In the model fitting, the cumulative number of confirmed infected are used as observation y, i.e.,

$$y(t) = \mathfrak{C}(t)$$

where

$$\frac{\mathrm{d}\mathfrak{C}}{\mathrm{d}t} = k_\mathrm{c}I$$

with $\mathfrak{C}(t_0)$ assumed known. Thus, $\varphi = k_\mathrm{c}I$ in Eq. 1.

In the initial phase of infection spread before confirmed cases, it can be questioned whether members of the C class *quarantine*. Thus, one could consider that also members of compartment C participate in the infection. We will neglect this possibility here.

[7]The reference uses symbols (I,R,U); here, R ("registered") has been changed to C ("confirmed") to observe the classic meaning of R as "recovered")

Table 1. Values for t_0, t_1, $\mathfrak{C}_0$, φ_0 and λ for some countries. Parenthesis after dates t_0 and t_1 indicates the element number in the times series for the data. Population size N taken from `https://www.worldometers.info/coronavirus/` ca. April 2020.

Country	t_0	t_1	$\mathfrak{C}_0$	φ_0	λ	N
Italy	2020-02-23 (33)	2020-03-14 (52)	155	112	0.178	60443857
Spain	2020-02-24 (34)	2020-03-13 (51)	2	6.09	0.281	46758424
Norway	2020-02-27 (37)	2020-03-14 (52)	1	2.73	0.318	5429635

2.3.2 Approximate initial response

With the initial number of susceptibles $S(t_0)$ having a value close to the total population N, $S(t_0) \approx N$, and $S(t_0)$ being more or less constant in the first phase of the epidemic, the dynamic model can be approximated with a linear model with $X = (S,E,I,C,U,R)$ for "small" $(t-t_0)$,

$$\frac{\mathrm{d}X}{\mathrm{d}t} \approx MX.$$

Matrix M has two zero columns, thus has two eigenvalues in the origin; these reflect the approximate pure integrator of S and the true pure integrator for R. It thus suffices to consider subsystem $X' = (E,I,C,U)$ when considering infection growth:

$$\frac{\mathrm{d}X'}{\mathrm{d}t} = \underbrace{\begin{pmatrix} -k_\mathrm{e} & k_\mathrm{i} & 0 & k_\mathrm{i} \\ k_\mathrm{e} & -k_\mathrm{cu} & 0 & 0 \\ 0 & k_\mathrm{c} & -k_\mathrm{r} & 0 \\ 0 & k_\mathrm{u} & 0 & -k_\mathrm{r} \end{pmatrix}}_{M'} X'. \tag{5}$$

The structure of the system causes the single, positive eigenvalue λ of M' to dominate the dynamics during growth, with solutions $X'_i(t)$ for the elements of X':

$$X'_i(t) = \exp(\lambda(t-t_0)) X'_{i,0}. \tag{6}$$

2.3.3 Parameters and initial states

Parameters φ and λ are as found in Section 2.2, where $\varphi = k_\mathrm{c} I$ for the SEICUR model.

Assuming that k_cu, η, k_e, and k_r are *known*, and

$$k_\mathrm{c} = \eta k_\mathrm{cu} \tag{7}$$
$$k_\mathrm{u} = k_\mathrm{cu} - k_\mathrm{c}, \tag{8}$$

I_0 can be found from $k_\mathrm{c} I_0 = \varphi_0$ and known k_c,

$$I_0 = \frac{\varphi_0}{k_\mathrm{c}}. \tag{9}$$

Inserting the assumed solutions of Eq. 6 into the linearized differential equation Eq. 5 while cancelling the common term $\exp(\lambda(t-t_0))$, this leads to:

$$\lambda E_0 \approx k_\mathrm{i}(I_0 + U_0) - k_\mathrm{e} E_0 \tag{10}$$
$$\lambda I_0 \approx k_\mathrm{e} E_0 - k_\mathrm{cu} I_0 \tag{11}$$
$$\lambda C_0 \approx k_\mathrm{c} I_0 - k_\mathrm{r} C_0 \tag{12}$$
$$\lambda U_0 \approx k_\mathrm{u} I_0 - k_\mathrm{r} U_0. \tag{13}$$

The three last of these, Eqs. 11–13 can be solved wrt. E_0, C_0, and U_0 to give

$$E_0 = \frac{\lambda + k_\mathrm{cu}}{k_\mathrm{e}} I_0 \tag{14}$$
$$C_0 = \frac{k_\mathrm{c} I_0}{\lambda + k_\mathrm{r}} \tag{15}$$
$$U_0 = \frac{k_\mathrm{u} I_0}{\lambda + k_\mathrm{r}}. \tag{16}$$

The first one, Eq. 10, can be solved wrt. k_i to give

$$k_\mathrm{i} = \frac{(\lambda + k_\mathrm{e}) E_0}{I_0 + U_0}. \tag{17}$$

By assuming zero recovered, $R_0 = 0$, and known population N, we can compute the initial value of S:

$$S_0 = N - E_0 - I_0 - C_0 - U_0 - R_0. \tag{18}$$

2.3.4 Reproduction number

Using the *Next-Generation Approach*, (Lie, 2021), write $M' = F - V$. Making V lower triangular,

$$M' = \underbrace{\begin{pmatrix} 0 & k_\mathrm{i} & 0 & k_\mathrm{i} \\ 0 & 0 & 0 & 0 \\ 0 & 0 & 0 & 0 \\ 0 & 0 & 0 & 0 \end{pmatrix}}_{=F} - \underbrace{\begin{pmatrix} k_\mathrm{e} & 0 & 0 & 0 \\ -k_\mathrm{e} & k_\mathrm{cu} & 0 & 0 \\ 0 & -k_\mathrm{c} & k_\mathrm{r} & 0 \\ 0 & -k_\mathrm{u} & 0 & k_\mathrm{r} \end{pmatrix}}_{=V}, \tag{19}$$

this gives the simplest Next-Generation Matrix; here, both F and V^{-1} are *positive* matrices. The Next-Generation Matrix N is

$$N = FV^{-1}$$
$$\Downarrow$$
$$N = \begin{pmatrix} \frac{k_\mathrm{i}}{k_\mathrm{cu}}\left(1 + \frac{k_\mathrm{u}}{k_\mathrm{r}}\right) & \frac{k_\mathrm{i}}{k_\mathrm{cu}}\left(1 + \frac{k_\mathrm{u}}{k_\mathrm{r}}\right) & 0 & \frac{k_\mathrm{i}}{k_\mathrm{r}} \\ 0 & 0 & 0 & 0 \\ 0 & 0 & 0 & 0 \\ 0 & 0 & 0 & 0 \end{pmatrix}.$$

N has 3 eigenvalues in the origin, and one positive eigenvalue, which is the spectral radius:

$$\rho(N) = \frac{k_\mathrm{i}}{k_\mathrm{cu}}\left(1 + \frac{k_\mathrm{u}}{k_\mathrm{r}}\right) = \frac{k_\mathrm{i}}{k_\mathrm{r}}\left(1 - \eta + \frac{k_\mathrm{r}}{k_\mathrm{cu}}\right).$$

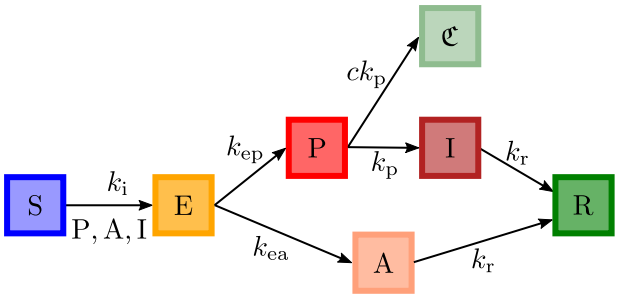

Figure 4. Flow of SEPIAR reactions.

We choose the following expression for R:

$$\mathsf{R} \triangleq \frac{k_i}{k_r}\left(1-\eta+\frac{k_r}{k_{cu}}\right), \tag{20}$$

which is the same as proposed in (Liu et al., 2020a).

(Sanche et al., 2020) cite initial estimates of R_0 for COVID-19 to be in the range $[2.2, 2.7]$.This number varies with location and time (mutations). The Delta mutant reportedly has R_0=6,[8] or perhaps even up to 8.

2.4 The Norwegian PHI model

The Publich Health Institute of Norway operates with what can be termed the SEPIAR model, Figure 4.

Here, P is a pre-symptomatic infectious stage, I is the symptomatic, infectious stage, and A is an asymptomatic yet slightly infectious stage. This is essentially a slightly extended SEIR model where I is (P, I, A). Numbers are provided for the various reaction constants.

The key difficulty with this model is that it does not directly correlate confirmed cases $\mathfrak{C}$ to the states; in Figure 4, it is indicated that $\frac{\mathrm{d}\mathfrak{C}}{\mathrm{d}t} = ck_pP$, but constant c is unknown.

2.5 Variation in infection rate

The infection rate k_i is uncertain, and will also vary due to:

1. Mitigation effects: (a) Hygiene, (b) Social distancing, (c) Use of face mask, (d) Quarantining, (e) Closing spaces with loud talk = reducing spreading by saliva/aerosols.

2. Meteorological effects: (a) Increased humidity causes aeorosols/saliva droplets to travel shorter, (b) Stronger solar irradiation/higher temperature kills virus faster; (Wu et al., 2020).

3. Health + sociology: (a) Age/co-morbidity: old people/with co-morbidity are more affected by COVID-19, (b) Genetic effects: blood type, etc. may influence infection rate, (c) Immune system status, (d) Life/behavioral patterns.

4. Mutations.

[8] Dr. Tim Spector: https://youtu.be/OHBua3aXQ7c

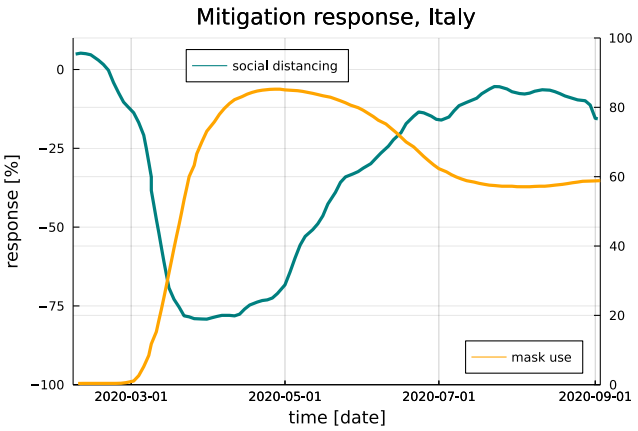

Figure 5. Social distancing (teal color, left ordinate) and mask (gold color, right ordinate) use in Italy, according to model of `https://covid19.healthdata.org/global?view=total-deaths&tab=trend`. Screen capture data converted to time series using WebPlotDigitizer, `https://automeris.io/WebPlotDigitizer/`.

Ideally, vaccination does not change the infection rate.[9] Instead, vaccination reduces the number of people susceptible to infection, see expression for infection rate r_i in Section 2.3.1.

2.6 Mitigation

Mitigation policies utilize effects that reduce infection rate. Typical examples are hygiene, social distancing, face mask use, quarantining, etc. The mitigation policy consists of recommendations or enforcing of law from the government, denoted $u(t)$, and this leads to a response from the public, denoted $x(t)$. For a better description, we might also include seasonal quantities (humidity, etc.), virus mutation, etc., as a *disturbance* $w(t)$ to a description.

Figure 5 proposes response in social diatancing and face mask use in Italy in the first 6 months of the COVID-19 pandemic. It is not clear whether these response data are based on actual observations, or based on some vague estimates.

A more formal description of how the mitigation policy u and disturbance variable w with response x transforms itself into an infection rate k_i, would be

$$\frac{\mathrm{d}x}{\mathrm{d}t} = f(x,u,w) \tag{21}$$

$$k_i = g(x,u)\,. \tag{22}$$

Here, x is some state which describes the dynamics of the change of k_i, and may include people's inertia towards taking measures into use, and the tendency that people get tired of the measures and want to get back to normal life. The model with $f(x,u,w)$ and $g(x,u)$ could be found through some system identification technique when u, to some degree w, and k_i are known.

[9] ...assuming that vaccinated are immune — experience has shown some cases of breahthrough infection of vaccinated.

In principle, we could add *outputs* in addition to k_i, such as social distancing and mask use as in Figure 5, or other quantities such as humidity, etc.: this would help to give a more accurate mitigation model.

As an *alternative* to using system identification to fit a model from known mitigation policy u and disturbance w to known outputs, we could find some *equivalent* mitigation policy u_fm by postulating a fixed model structure, e.g.,

$$\frac{\mathrm{d}x}{\mathrm{d}t} = \frac{1}{T_\mathrm{m}}(u_\mathrm{fm} - x) \tag{23}$$

$$k_\mathrm{i} = k_\mathrm{i}^0 x, \tag{24}$$

and compute which input sequence u_fm gives a good model fit to confirmed cases. Here, T_m is the *mitigation* time constant, typically chosen to be 7–10 d. It follows that such an *equivalent* mitigation policy u_fm will include seasonal variations in infection rate, as well as the effect of virus mutation, etc. In other words, by comparing an equivalent mitigation policy u_fm from two different time instances, or in two different countries, we can not directly related u_fm to a specific level of social distancing, mask use, etc.: a value of $u_\mathrm{fm} = 0.5$ in June 2020 could imply a different level of social activity than a level of $u_\mathrm{fm} = 0.5$ in February 2021.

In the normal, pre COVID-19 situation with $u_\mathrm{fm} = 1$, x will asymptotically approach $x = 1$, and $k_\mathrm{i} \to k_\mathrm{i}^0$. As u_fm becomes smaller and smaller due to a low social contact mitigation policy, x will asymptotically approach a smaller and smaller value until it reaches value $x = 0$ for zero social contact. For that case, $k_\mathrm{i} \to 0$, which means that the reaction rate $\propto k_\mathrm{i}$ approaches zero. In the work of (Liu et al., 2020c), etc., the assumption of $x \to 0$ is assumed, which is unrealistic. In a realistic mitigation effect, we need to take into account a time varying mitigation policy u_fm.

3 Model Fitting

3.1 Initial evolution

Simulation of the initial (unmitigated) case of Italy using the SEICUR model is depicted in Figure 6.

As Figure 6 shows, the initial model reponse in $\mathfrak{C}$ fits the data $\mathfrak{C}^\mathrm{d}$ quite well, which should be expected: the model parameters were found by fitting the model to the initial data.

Based on the initial fitting, this gives a basic reproduction number of $\mathsf{R}_0 = 3.2$ for Italy. Similar numbers for Spain and Norway are found to be $\mathsf{R}_0 = 4.7$ and $\mathsf{R}_0 = 5.4$, respectively.

3.2 Fitted mitigation policy

3.2.1 Case Norway

It is possible to propose a "fitted" mitigation policy u_fm such that good correspondence model and confirmed infection cases is achieved. The fitted policy is depicted in Figure 7.

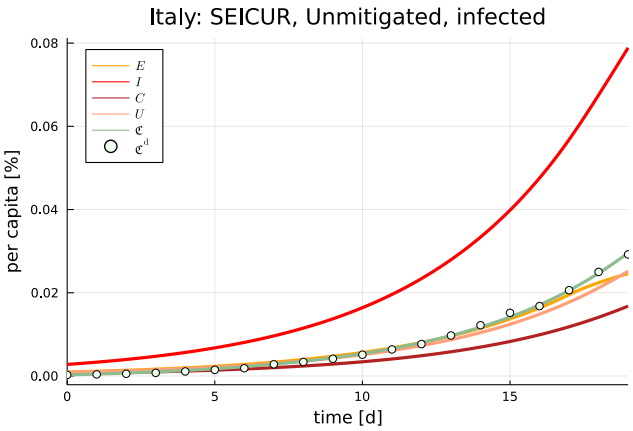

Figure 6. Initial (unmitigated) evolution according to the SEICUR model for Italy.

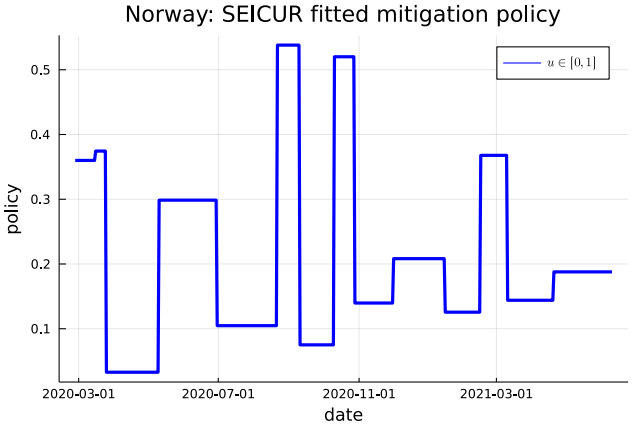

Figure 7. Fitted mitigation policy tuned to SEICUR model for Norway.

The resulting SEICUR model simulation with comparison to cumulative confirmed infections is shown in Figure 8. It may also be instructive to compare the smoothed 7-day avareage $\frac{\mathrm{d}\mathfrak{C}}{\mathrm{d}t}\big|_\mathrm{smooth}$ with $k_\mathrm{c} I$, Figure 9. As seen, this gives very good model fit in $\mathfrak{C}$, and decent fit in $\frac{\mathrm{d}\mathfrak{C}}{\mathrm{d}t}\big|_\mathrm{smooth}$.

An important comment is that vaccination started in Norway (and in Europe) in early 2021. In the above fitting, vaccination has not been taken into account, and thus the equivalent mitigation policy of Figure 7 and subsequent figures for Italy and Spain includes the effect of vaccination. If vaccination has had an important role for avoiding infection spread, including vaccination in the model should have lead to a more relaxed mitigation policy.

3.2.2 Case: Italy

The fitted policy is depicted in Figure 10.

The resulting SEICUR model simulation with comparison to cumulative confirmed infections is shown in Figure 11.

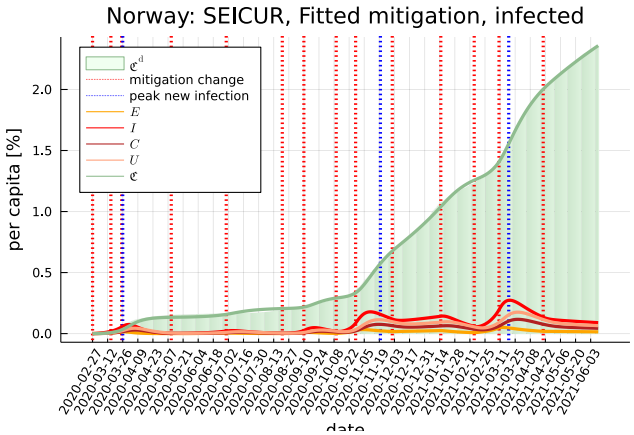

Figure 8. SEICUR model simulation with fitted mitigation policy as in Figure 7.

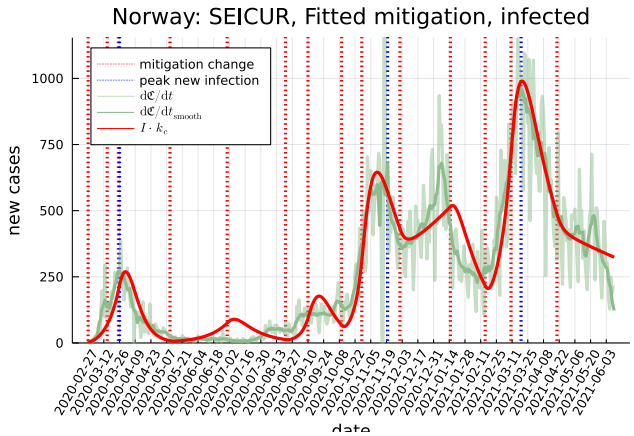

Figure 9. SEICUR model simulation with fitted mitigation policy as in Figure 7.

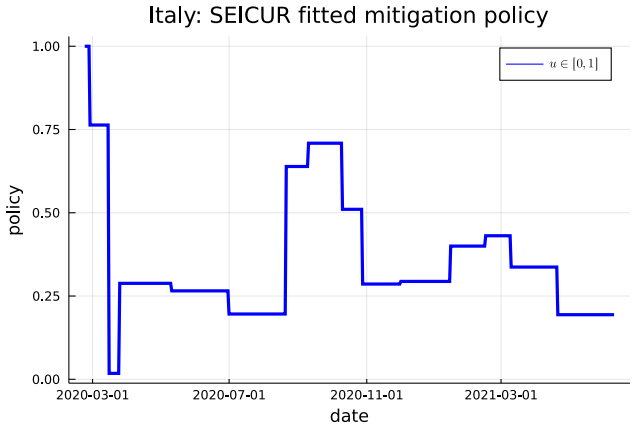

Figure 10. Fitted mitigation policy tuned to SEICUR model for Italy.

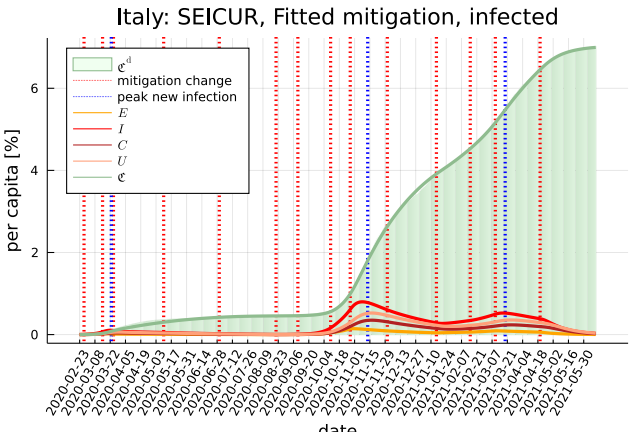

Figure 11. SEICUR model simulation with fitted mitigation policy as in Figure 10.

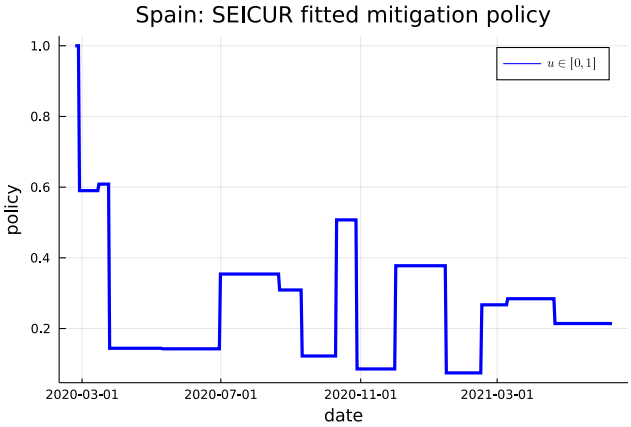

Figure 12. Fitted mitigation policy tuned to SEICUR model for Spain.

3.2.3 Case: Spain

The fitted policy is depicted in Figure 12.

The resulting SEICUR model simulation with comparison to cumulative confirmed infections is shown in Figure 13.

4 Discussion and conclusions

An overview has been given of a specific COVID-19 model of (Liu et al., 2020a), here denoted the SEICUR model. The minor advantage of this model over the Norwegian Public Health Institute model is related to the latter's lack of specifying how states related to confirmed cases. A number of methods to fit basic parameters φ_0 and λ to cumulative confirmed cases is given. Next, with a given model structure and some predetermined parameters from clinical data, a discussion on how to find the remaining model parameters is given, including k_i^0, from φ_0 and λ. Simulation of the model in an initial phase confirms that the model fit is adequate. An original contribution of the paper is the generalization of the initial model fit Eq. 2 to be independent of the model. Another contribution is the use of the Lambert W approach to estimate

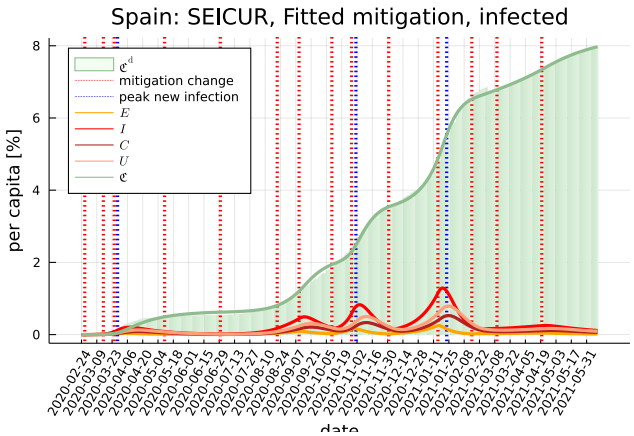

Figure 13. SEICUR model simulation with fitted mitigation policy as in Figure 12.

parameters λ and φ_0. These initial data have been fitted for Norway, and re-fitted for Italy and Spain. Also, the procedure of finding model-dependent parameters (k_i) and initial states (I_0, E_0, C_0, E_0) has been streamlined compared to the original papers. A detailed derivation of the reproduction model is given.

For extended periods of time after the initial phase, mitigation policy, seasonal changes, and virus mutation makes it necessary to add some modification to the infection rate constant k_i. Here, infection rate constant modification is done via an equivalent mitigation policy which is found by fitting the model to data for cumulative confirmed cases. The result is a very good fit. The results also indicate that the fit to the (averaged) daily new confirmed cases is less good, which should be expected: using cumulative data always smooths the information.

The formulation of the effect of a *fitted* mitigation policy on the infection rate constant is new, and the actual fitting of this policy for countries Norway, Italy, and Spain is new. The fitted mitigation policy at the current time could be used in conjunction with model prediction over a future horizon to design a feedback controller which could compute an advice on future mitigation policy, e.g., using Model Predictive Control. Because of the uncertainty in the computed equivalent mitigation policy u due to seasonal variations, etc., such a controller will be prone to a certain level of uncertainty.

References

Fred Brauer, Carlos Castillo-Chavez, and Zhilan Feng. *Mathematical Models in Epidemiology*. Number 69 in Texts in Applied Mathematics. Springer, New York, 2019. ISBN 978-1-4939-9826-5.

Bernt Lie. Epidemiological Models and Process Engineering. In *Proceedings, SIMS EUROSIM 2021, Oulu Finland, September 21–23*, 2021.

Z. Liu, P. Magal, O. Seydi, and G. Webb. A COVID-19 epidemic model with latency period. *Infectious Disease Modelling*, 5: 323–337, 2020a. doi:10.1016/j.idm.2020.03.003.

Zhihua Liu, Pierre Magal, Ousmane Seydi, and Glenn Webb. A model to predict covid-19 epidemics with applications to south korea, italy and spain. *SIAM News*, 2020b. https://sinews.siam.org/Details-Page/a-model-to-predict-covid-19-epidemics-with-applications-to-south-korea-italy-and-spain.

Zhihua Liu, Pierre Magal, and Glenn F Webb. Predicting the number of reported and unreported cases for the COVID-19 epidemics in china, south korea, italy, france, germany and united kingdom. apr 2020c. doi:10.1101/2020.04.09.20058974.

Leonardo López and Xavier Rodó. A modified SEIR model to predict the COVID-19 outbreak in Spain and Italy: simulating control scenarios and multi-scale epidemics. *Results in Physics*, 2020. doi:10.1016/j.rinp.2020.103746. URL `https://pubmed.ncbi.nlm.nih.gov/33391984/`.

Stig Øyvann. Jakten på en presis beskrivelse av epidemien. *Computerworld*, 38(6):26–30, December 2020.

Christopher Rackauckas and Qing Nie. DifferentialEquations.jl — A Performant and Feature-Rich Ecosystem for Solving Differential Equations in Julia. *Journal of Open Research Software*, 5(15), 2017a. doi:10.5334/jors.151.

Christopher Rackauckas and Qing Nie. Adaptive methods for stochastic differential equations via natural embeddings and rejection sampling with memory. *Discrete and continuous dynamical systems. Series B*, 22(7):2731, 2017b.

Christopher Rackauckas and Qing Nie. Stability-Optimized High Order Methods and Stiffness Detection for Pathwise Stiff Stochastic Differential Equations. *arXiv:1804.04344 [math]*, 2018. URL `http://arxiv.org/abs/1804.04344`.

Iman Rahimi, Fang Chen, and Amir H. Gandomi. A review on COVID-19 forecasting models. *Neural Computing and Applications*, 2021. doi:https://doi.org/10.1007/s00521-020-05626-8.

Jr. Reiner, Robert C., Ryan M. Barber, James K. Collins, and more. Modeling COVID-19 scenarios for the United States. *Nature Medicine*, 27:94–105, 2021. doi:https://doi.org/10.1038/s41591-020-1132-9.

Steven Sanche, Yen Ting Lin, Chonggang Xu, Ethan Romero-Severson, Nick Hengartner, and Ruian Ke. High Contagiousness and Rapid Spread of Severe Acute Respiratory Syndrome Coronavirus 2. *Emerging Infectious Diseases*, 26(7), July 2020. ISSN 1080-6059. URL `https://wwwnc.cdc.gov/eid/article/26/7/20-0282_article`.

Yu Wu, Wenzhan Jing, Jue Liu, Qiujue Ma, Jie Yuan, Yaping Wang, Min Du, and Min Liu. Effects of temperature and humidity on the daily new cases and new deaths of COVID-19 in 166 countries. *Science of the Total Environment*, 729(139051), August 2020. doi:https://doi.org/10.1016/j.scitotenv.2020.139051.

Aleksa Zlojutro, David Rey, and Lauren Gardner. A decision-support framework to optimize border control for global outbreak mitigation. *Scientific Reports*, (2216), 2019. doi:https://doi.org/10.1038/s41598-019-38665-w.

Extended COVID-19 Models

Bernt Lie

University of South-Eastern Norway, Porsgrunn, Norway, Bernt.Lie@usn.no

Abstract

The paper discusses how to extend the SEICUR model with a description of migration. Next, the SEICUR model is extended with a description of age distribution, for the case that infection and serious illness depends on age. Finally, the SEICUR model is extended with models of vaccination. Simulation of the SEICUR model for Italy and Spain indicated that the number of migrants per day between the two countries need to be relatively large before a significant change in infection is noticed. However, this was based on the assumption of average spreaders among the migrants. The age distribution model is mainly of use when considering serious illness and death, and was not pursued further. Vaccination data for Italy, Spain, and Norway, shows that for countries with a low fraction of infected (e.g., Norway), vaccination allows for a noticeable relaxation in mitigation, while for countries which already have a high fraction of infected (e.g., Spain), the effect of vaccination is relatively smaller due to the larger fraction of people already recovered. The extended models allow for a more realistic study of COVID-19 spread, and how to optimize mitigation policies vs. vaccination.

Keywords: COVID-19 models, deterministic models, complex models, vaccination policy

1 Introduction

1.1 Background

The COVID-19[1] pandemic spreading in 2020 initially caused fear, irrational hoarding of consumer goods, uncertainty about future food supply, and economic depression, but also spawned a renewed interest in epidemiology to understand how infections spread, and a massive effort in development of virus medicine and vaccines. Policy making and society saw challenges hardly faced before on how to adapt to the development in real time.

More than one year after the pandemic outbreak in February/March 2020, fitted epidemic macro models are becoming more reliable due to large amounts of data, and vaccination is well underway in some countries. Still, for accurate mitigation policy, the models have shortcomings. Current mitigation models have poor description of seasonal variations, genetic/health variations, cultural variations, and demographic variations. In addition, relations between infection, treatment, and death is lacking in understanding.

Spreading by migration is clearly important, with travel restrictions and lock-downs being key instruments in taming infection spread. Data from the past year has shown that age distribution is an important determining factor for serious illness/death. Data from Europe and USA indicate that a combination of genetics, nutrition, health care, culture, and living conditions put some groups more at risk. But seasonal variation in temperature, solar irradiation, humidity, etc. also plays an important role, whether this is directly by influencing infection rates, or indirectly by keeping people more outdoor and therefore reducing infection rates.

In Europe, the initial spread in the winter/spring of 2020 saw a dramatic reduction starting in late May/June 2020, and lasting until late September 2020. Most likely, this was a combination of improved hygiene and some social distancing. But it is almost certain that there also was a seasonal element in this reduction. The winter/spring of 2021 has been marked by vigorous vaccination in Europe and North America, and again: the number of infected is going down.

Both for COVID-19 and for future epidemics, it is of interest to study how extended infection models can be developed.

1.2 Previous work

Classical epidemiology models were developed in the decade following the "Spanish Flu". A renewed *public* interest in epidemic models started with the AIDS/HIV epidemic some decades ago; these models have been used to study other infectious diseases, e.g., (Brauer et al., 2019). (Lie, 2021a) gives a brief overview of such general models from a process engineering point of view.

Many COVID-19 models are available on the internet, e.g., from the *IHME COVID-19 Forecasting Team*[2], see (Reiner et al., 2021)[3]. (Zlojutro et al., 2019) give a general framework for reducing spread via migration. Early work at Imperial College London[4] was important in stressing the importance of mitigation policy. Some relatively complete *macro* models include that of (López and Rodó,

[1] COVID-19 is the COrona VIrus Disease originating in 2019. The World Health Organization and Wikipedia.com both appear to write COVID-19 in all caps.

[2] The Institute for Health Metrics and Evaluation (IHME) is an independent global health research center at the University of Washington

[3] https://covid19.healthdata.org/united-states-of-america?view=cumulative-deaths&tab=trend

[4] https://www.imperial.ac.uk/mrc-global-infectious-disease-analysis/covid-19/covid-19-planning-tools/

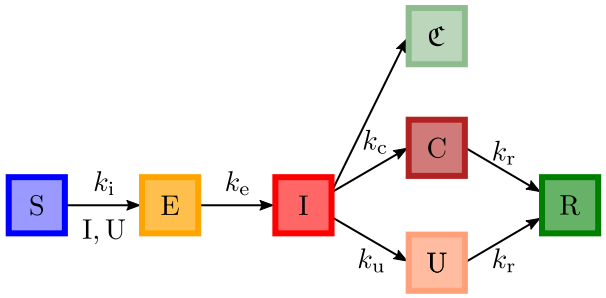

Figure 1. Flow of SEICUR reactions.

2020), (Liu et al., 2020b,a,c), (Øyvann, 2020), and others. (Lie, 2021b) gives an overview of how to fit the SEIRU (SEICUR) model to cumulative confirmed infected data, with applications to Italy, Spain, and Norway.

1.3 Scope

Here, the focus is on extending a model from (Lie, 2021b) to be (i) more general, and (ii) more useful. Extensions relate to network models/distributed models, and to age dependent models. Network models can also be used to study the effect of migration/tourism. A further extension is the effect of vaccination. By combining vaccination rates and mitigation policy, control engineering may suggest an "optimal" return to normalcy

In Section 2, the SEICUR model is extended with migration terms, and with age distribution. Some simple models of vaccination are proposed. In Section 3, the SEICUR model is studied with migration between some countries, and with vaccination. In Section 4, the results are discussed, and some conclusions are drawn.

All computations in the paper are carried out using language Julia, with packages `DifferentialEquations.jl` for solving models, (Rackauckas and Nie, 2017a), (Rackauckas and Nie, 2017b), (Rackauckas and Nie, 2018), `BlackBoxOptim.jl` for fitting mitigation policy, and `Plots.jl` for plotting results.

2 Materials and Methods

2.1 Reaction mechanism

A SEIR model with the I population extended to (I,C,U) was proposed for COVID-19 in (Liu et al., 2020b; Lie, 2021b) Figure 1.

The above, proposed mechanism implies that *susceptibles* S are infected by some "pre-infected" I and the non-quarantined *unconfirmed* U leading to the *exposed* phase E, which is infected but not yet infectious. These exposed E then are converted to the "pre-infected" I class, which then either become more serious cases and are *confirmed* infected C, or stay as *unconfirmed* U. Finally, the confirmed infected and the unconfirmed end up in the *recovered* population R (which includes those who die). We will refer to this model as the SEICUR model.

For class X, let X denote the number of people in that class, and $\check{X}$ the number of people per capita. The following mechanism describes the reactions; :

$$\begin{aligned}
\mathscr{E}_\mathrm{i} &: \mathrm{S} \overset{\mathrm{I+U}}{\to}{}^{k_\mathrm{i}} \mathrm{E}, & r_\mathrm{i} &= k_\mathrm{i}\left(\check{I}+\check{U}\right)\check{S} \\
\mathscr{E}_\mathrm{e} &: \mathrm{E} \to^{k_\mathrm{e}} \mathrm{I}, & r_\mathrm{e} &= k_\mathrm{e}\check{E} \\
\mathscr{E}_\mathrm{c} &: \mathrm{I} \to^{k_\mathrm{c}} \mathrm{C}, & r_\mathrm{c} &= k_\mathrm{c}\check{I} \\
\mathscr{E}_\mathrm{u} &: \mathrm{I} \to^{k_\mathrm{u}} \mathrm{U}, & r_\mathrm{u} &= k_\mathrm{u}\check{I} \\
\mathscr{E}_\mathrm{cr} &: \mathrm{C} \to^{k_\mathrm{r}} \mathrm{R}, & r_\mathrm{cr} &= k_\mathrm{r}\check{C} \\
\mathscr{E}_\mathrm{ur} &: \mathrm{U} \to^{k_\mathrm{r}} \mathrm{R}, & r_\mathrm{ur} &= k_\mathrm{r}\check{U}.
\end{aligned}$$

We introduce

$$\begin{aligned}
k_\mathrm{cu} &= k_\mathrm{c} + k_\mathrm{u} \\
k_\mathrm{c} &= \eta k_\mathrm{cu}.
\end{aligned}$$

Thus, specifying k_cu and η, we can find

$$\begin{aligned}
k_\mathrm{c} &= \eta k_\mathrm{cu} \\
k_\mathrm{u} &= (1-\eta)\, k_\mathrm{cu}.
\end{aligned}$$

(Lie, 2021b) details how to fit the model to cumulative confirmed infection cases, and how to find initial states.

2.2 Migration

We consider the response in infection when compartments open up for migration exchange at rate $\dot{N}$ people per day. With X_i denoting a general population state, $X_i \in (S,E,I,C,U,R)$, the emigration rate of class X_i is

$$\dot{X}_i^\mathrm{e} = \dot{N}\check{X}_i = \dot{N}\cdot X_i/N$$

where we have assumed homogeneous mixing of the population. The balance equation for class X_i with constant population N is then

$$\frac{\mathrm{d}X_i}{\mathrm{d}t} = \dot{X}_i^\mathrm{i} - \dot{X}_i^\mathrm{e} + N\left(\nu^\mathsf{T} r\right)_i$$

where ν is the *stoichiomatric matrix*, (Lie, 2021a), and r is the vector of rates of reaction for the events, (Lie, 2021a,b). For a constant population $N = \sum_i X_i$, it is required that $\sum_i \dot{X}_i^\mathrm{i} = \sum_i X_i^\mathrm{e}$.

Without loss of generality, consider two compartments, each with constant populations N_1 and N_2, which have open borders with migration rate $\dot{N}$ between each other and closed borders to every other compartment. Neglecting the possibility of people staying on the border, it follows that we must require

$$\dot{X}_{i,1}^\mathrm{i} = \dot{X}_{i,2}^\mathrm{e};$$

the number of people per day of class i *immigrating* to compartment 1 must equal the number of people per day of class i *emigrating* from compartment 2.

If we also include a model for equivalent mitigation policy as in (Lie, 2021b), the SEICUR model for compartment $j \in \{1,2\}$ is then

$$\frac{\mathrm{d}S_j}{\mathrm{d}t} = \dot{N}\left(\frac{S_{\bar{j}}}{N_{\bar{j}}} - \frac{S_j}{N_j}\right) - k_{\mathrm{i}}^{0,j} x_{\mathrm{fm}}^{j} (I_j + U_j) S_j / N_j$$

$$\frac{\mathrm{d}E_j}{\mathrm{d}t} = \dot{N}\left(\frac{E_{\bar{j}}}{N_{\bar{j}}} - \frac{E_j}{N_j}\right) + k_{\mathrm{i}}^{0,j} x_{\mathrm{fm}}^{j} (I_j + U_j) S_j / N_j - k_{\mathrm{e}} E_j$$

$$\frac{\mathrm{d}I_j}{\mathrm{d}t} = \dot{N}\left(\frac{I_{\bar{j}}}{N_{\bar{j}}} - \frac{I_j}{N_j}\right) + k_{\mathrm{e}} E_j - k_{\mathrm{cu}} I_j$$

$$\frac{\mathrm{d}C_j}{\mathrm{d}t} = k_{\mathrm{c}} I_j - k_{\mathrm{r}} C_j$$

$$\frac{\mathrm{d}U_j}{\mathrm{d}t} = \dot{N}\left(\frac{U_{\bar{j}}}{N_{\bar{j}}} - \frac{U_j}{N_j}\right) + k_{\mathrm{a}} I_j - k_{\mathrm{r}} U_j$$

$$\frac{\mathrm{d}R_j}{\mathrm{d}t} = \dot{N}\left(\frac{R_{\bar{j}}}{N_{\bar{j}}} - \frac{R_j}{N_j}\right) + k_{\mathrm{r}} (C_j + U_j)$$

$$\frac{\mathrm{d}x_{\mathrm{fm}}^{j}}{\mathrm{d}t} = \frac{1}{T_{\mathrm{fm}}^{j}} \left(u_{\mathrm{fm}}^{j} - x_{\mathrm{fm}}^{j}\right)$$

Here, $\bar{j}$ denotes the complement of j, i.e., if $j = 1$, then $\bar{j} = 2$, and vice versa. In the model above, it has been assumed that the confirmed infected are quarantined, and are not allowed to travel. Furthermore, it has been assumed that model parameters k_{e}, k_{cu}, k_{a}, and k_{r} are independent of the compartment.

2.3 Demographic distribution

Most likely, infection rates, severity of infection, and recovery time vary with demographic distribution of the population. Here, we focus on age distribution. Description of demographic distribution is mainly of interest when the model is extended with a distribution in the severity of infections, such as a separate class for the number of deaths.

Without loss of generality, suppose we divide the population into a young population of N_{y} people with SEICUR members S_{y}, E_{y}, I_{y}, C_{y}, U_{y}, and R_{y}, and an old population of $N_{\mathrm{o}} = N - N_{\mathrm{y}}$ people with members S_{o}, E_{o}, I_{o}, C_{o}, U_{o}, R_{o}. For simplicity, assume both N and $N_{\mathrm{y}} = \gamma N$ are constant, with γ being the fraction of young.

We assume that young people are infected at equal rate $k_{\mathrm{i}}^{\mathrm{y}}$ when meeting either young or old infected, and that old people are infected at equal rate $k_{\mathrm{i}}^{\mathrm{o}}$ when meeting either young or old infected. Similarly, we assume that young and old recover at rates $k_{\mathrm{r}}^{\mathrm{y}}$ and $k_{\mathrm{r}}^{\mathrm{o}}$, respectively. Furthermore, we assume that people become confirmed and unconfirmed infected at rates $k_{\mathrm{c}}^{\mathrm{y}}$, $k_{\mathrm{u}}^{\mathrm{y}}$ and $k_{\mathrm{c}}^{\mathrm{o}}$, $k_{\mathrm{u}}^{\mathrm{o}}$, respectively.

Relative to the rates in Section 2.1, for simplicity we assume that young infected I_{y}, U_{y} and old infected I_{o}, U_{o} infect the young susceptibles at equal rate. The same assumption is made for the old susceptibles, but the infection rate constants may differ. Thus, with $I = I_{\mathrm{y}} + I_{\mathrm{o}}$ and $U = U_{\mathrm{y}} + U_{\mathrm{o}}$, this implies that the infection rates are, $j \in \{\mathrm{y}, \mathrm{o}\}$:

$$r_{\mathrm{i}}^{j} = k_{\mathrm{i}}^{j} (I + U) S_j / N^2.$$

The other rates remain as in Section 2.1. In the rate expression $N \cdot r_{\mathrm{i}}^{j}$, we need to use the full population if we assume that the mixture of young and old population is perfectly homogeneous.

Finally, we need to take into account that people are born at a rate $\dot{N}_{\mathrm{b}}$ and die at a rate $\dot{N}_{\mathrm{d}}$; for a constant population, $\dot{N}_{\mathrm{d}} = \dot{N}_{\mathrm{b}}$. This means that people are transferred from young to old at a rate $\dot{N}_{\mathrm{b}}$. For young people ($j = \mathrm{y}$), we have

$$\dot{S}_{\mathrm{y}}^{\mathrm{b}} = \dot{N}_{\mathrm{b}};$$

people are born as young, and all are assumed to be susceptible at birth. Similarly, the susceptible "die", or rather *age* from young to old, as

$$\dot{S}_{\mathrm{y}}^{\mathrm{d}} = \dot{N}_{\mathrm{b}} \frac{S_{\mathrm{y}}}{N_{\mathrm{y}}}.$$

Note that we need to use the number of young susceptibles per young population here, i.e., the correct fraction is $\frac{S_{\mathrm{y}}}{N_{\mathrm{y}}}$. For all other classes in the SEICUR model, $\dot{X}_{\mathrm{y}}^{\mathrm{b}} \in \{\dot{E}_{\mathrm{y}}^{\mathrm{b}}, \dot{I}_{\mathrm{y}}^{\mathrm{b}}, \dot{C}_{\mathrm{y}}^{\mathrm{b}}, \dot{U}_{\mathrm{y}}^{\mathrm{b}}, \dot{R}_{\mathrm{y}}^{\mathrm{b}}\}$, it follows that

$$\dot{X}_{\mathrm{y}}^{\mathrm{b}} \equiv 0.$$

Ageing from "dying" young into "born" old implies

$$\dot{E}_{\mathrm{y}}^{\mathrm{d}} = \dot{N}_{\mathrm{b}} \frac{E_{\mathrm{y}}}{N_{\mathrm{y}}} = \dot{E}_{\mathrm{o}}^{\mathrm{b}}$$

$$\dot{I}_{\mathrm{y}}^{\mathrm{d}} = \dot{N}_{\mathrm{b}} \frac{I_{\mathrm{y}}}{N_{\mathrm{y}}} = \dot{I}_{\mathrm{o}}^{\mathrm{b}}$$

$$\dot{C}_{\mathrm{y}}^{\mathrm{d}} = \dot{N}_{\mathrm{b}} \frac{C_{\mathrm{y}}}{N_{\mathrm{y}}} = \dot{C}_{\mathrm{o}}^{\mathrm{b}}$$

$$\dot{U}_{\mathrm{y}}^{\mathrm{d}} = \dot{N}_{\mathrm{b}} \frac{U_{\mathrm{y}}}{N_{\mathrm{y}}} = \dot{U}_{\mathrm{o}}^{\mathrm{b}}$$

$$\dot{R}_{\mathrm{y}}^{\mathrm{d}} = \dot{N}_{\mathrm{b}} \frac{R_{\mathrm{y}}}{N_{\mathrm{y}}} = \dot{R}_{\mathrm{o}}^{\mathrm{b}}.$$

Old people die out of their classes at rates due to ageing:

$$\dot{S}_{\mathrm{o}}^{\mathrm{d}} = \dot{N}_{\mathrm{b}} \frac{S_{\mathrm{o}}}{N_{\mathrm{o}}}$$

$$\dot{E}_{\mathrm{o}}^{\mathrm{d}} = \dot{N}_{\mathrm{b}} \frac{E_{\mathrm{o}}}{N_{\mathrm{o}}},$$

$$\dot{I}_{\mathrm{o}}^{\mathrm{d}} = \dot{N}_{\mathrm{b}} \frac{I_{\mathrm{o}}}{N_{\mathrm{o}}}$$

$$\dot{C}_{\mathrm{o}}^{\mathrm{d}} = \dot{N}_{\mathrm{b}} \frac{C_{\mathrm{o}}}{N_{\mathrm{o}}}$$

$$\dot{U}_{\mathrm{o}}^{\mathrm{d}} = \dot{N}_{\mathrm{b}} \frac{U_{\mathrm{o}}}{N_{\mathrm{o}}}$$

$$\dot{R}_{\mathrm{o}}^{\mathrm{d}} = \dot{N}_{\mathrm{b}} \frac{R_{\mathrm{o}}}{N_{\mathrm{o}}}.$$

For $j \in \{\mathrm{y}, \mathrm{o}\}$, we thus have

$$
\begin{aligned}
\frac{\mathrm{d}S_j}{\mathrm{d}t} &= \dot{S}_j^{\mathrm{b}} - \dot{S}_j^{\mathrm{d}} - k_{\mathrm{i}}^j (I+U) S_j/N \\
\frac{\mathrm{d}E_j}{\mathrm{d}t} &= \dot{E}_j^{\mathrm{b}} - \dot{E}_j^{\mathrm{d}} + k_{\mathrm{i}}^j (I+U) S_j/N - k_{\mathrm{e}}^j E_j \\
\frac{\mathrm{d}I_j}{\mathrm{d}t} &= \dot{I}_j^{\mathrm{b}} - \dot{I}_j^{\mathrm{d}} + k_{\mathrm{e}}^j E_j - k_{\mathrm{cu}}^j I_j \\
\frac{\mathrm{d}C_j}{\mathrm{d}t} &= \dot{C}_j^{\mathrm{b}} - \dot{C}_j^{\mathrm{d}} + k_{\mathrm{c}}^j I_j - k_{\mathrm{r}}^j C_j \\
\frac{\mathrm{d}U_j}{\mathrm{d}t} &= \dot{U}_j^{\mathrm{b}} - \dot{U}_j^{\mathrm{d}} + k_{\mathrm{u}}^j I_j - k_{\mathrm{r}}^j U_j \\
\frac{\mathrm{d}R_j}{\mathrm{d}t} &= \dot{R}_j^{\mathrm{b}} - \dot{R}_j^{\mathrm{d}} + k_{\mathrm{r}}^j (C_j + U_j)
\end{aligned}
$$

where we have used that $N\left(r_{\mathrm{c}}^j + r_{\mathrm{u}}^j\right) = \left(k_{\mathrm{c}}^j + k_{\mathrm{u}}^j\right) I_j = k_{\mathrm{cu}}^j I_j$. Here, $N_{\mathrm{o}} = N - N_{\mathrm{y}} = (1-\gamma)N$.

To take advantage of this demographic extension of the SEICUR model, it is really necessary to extend the model and split the recovered class into those surviving, and those dying. This extension is relatively straightforward, but is not pursued here, since it requires fitting this extended model to additional data of cumulative deaths.

2.4 Extinction of COVID-19

2.4.1 Herd immunity

So-called *herd immunity* is reached when there are too few susceptible left to drive the infection growth. Just before herd immunity is reached, the infection rate increases dramatically, before dying out. When herd immunity is reached, a large fraction of the population will have become recovered; in the SEICUR model, the class of recovered includes those who die.

Some researchers and politicians have suggested that one should let COVID-19 go its natural course, and aim for herd immunity. The alternative is to impose mitigation policies to reduce the number of infected at any time, while waiting for vaccines.

Clearly, aiming for herd immunity with no mitigation would have put an end to COVID-19 relatively quickly. However, the number of seriously ill from the infection would have completely overwhelmed the hospital system, leading to a high fraction of deaths among the infected. Aiming for herd immunity has rarely been an explicit policy, but a few countries have at times lost control of the infection growth, with near collapse in the health system. The main idea behind a mitigation policy is to attempt to keep the number of seriously infected at any time within the capacity of the health system and thus minimize the number of deaths.

2.4.2 Vaccination

Let V denote the class of vaccinated, and let $\dot{V}$ denote the vaccination rate for a compartment. We will assume that only susceptible S are vaccinated.

Crude model In a *crude* vaccination model, we assume that vaccinated *immediately* become recovered, with efficacy η. For the SEICUR model, vaccination only changes the expressions for S and R, which become

$$
\begin{aligned}
\frac{\mathrm{d}S}{\mathrm{d}t} &= -\eta \dot{V} - k_{\mathrm{i}} (I+U) S/N \\
\frac{\mathrm{d}R}{\mathrm{d}t} &= \eta \dot{V} + k_{\mathrm{r}} (C+U).
\end{aligned}
$$

Semi-crude model A *slightly less crude* model could utilize that it takes a certain time interval τ_{v} before good vaccine protection is achieved, and then operate with a *filtered* vaccination rate

$$
\frac{\mathrm{d}\dot{V}_{\mathrm{f}}}{\mathrm{d}t} = \frac{1}{\tau_{\mathrm{v}}} \left(\dot{V} - \dot{V}_{\mathrm{f}}\right)
$$

with expressions for S and R now becoming

$$
\begin{aligned}
\frac{\mathrm{d}S}{\mathrm{d}t} &= -\eta \dot{V}_{\mathrm{f}} - k_{\mathrm{i}} (I+U) S/N \\
\frac{\mathrm{d}R}{\mathrm{d}t} &= \eta \dot{V}_{\mathrm{f}} + k_{\mathrm{r}} (C+U).
\end{aligned}
$$

Mechanistic model In a more *realistic* mechanistic vaccination model, vaccinated are still partially susceptible, and it takes a certain time τ_{v} before full vaccination is achieved. This transformation of vaccinated into recovered can be described by the reaction

$$
\mathscr{E}_{\mathrm{v}} : \mathrm{V} \rightarrow^{k_{\mathrm{v}}} \mathrm{R}, \qquad r_{\mathrm{v}} = k_{\mathrm{v}} \check{V}
$$

with $k_{\mathrm{v}} = 1/\tau_{\mathrm{v}}$. The number of recovered is then modified to

$$
\frac{\mathrm{d}R}{\mathrm{d}t} = k_{\mathrm{v}} V + k_{\mathrm{r}} (C+U).
$$

The vaccinated population V will still be susceptible, but with a relatively low average infection rate over the time constant τ_{v}. This implies that there will be an additional infection reaction

$$
\mathscr{E}_{\mathrm{i}}^{\mathrm{v}} : \mathrm{V} \overset{\mathrm{I+U}}{\rightarrow}^{k_{\mathrm{i}}^{\mathrm{v}}} \mathrm{E}, \qquad r_{\mathrm{i}}^{\mathrm{v}} = k_{\mathrm{i}}^{\mathrm{v}} \left(\check{I} + \check{U}\right) \check{V}
$$

where $k_{\mathrm{i}}^{\mathrm{v}}$ is considerably smaller than k_{i} for an efficient vaccine. The total expression for V is then

$$
\begin{aligned}
\frac{\mathrm{d}V}{\mathrm{d}t} &= \dot{V} - N \cdot r_{\mathrm{v}} - N \cdot r_{\mathrm{i}}^{\mathrm{v}} \\
&\Downarrow \\
\frac{\mathrm{d}V}{\mathrm{d}t} &= \dot{V} - k_{\mathrm{v}} V - k_{\mathrm{i}}^{\mathrm{v}} (I+U) V/N.
\end{aligned}
$$

The expressions for the number of exposed E becomes

$$
\frac{\mathrm{d}E}{\mathrm{d}t} = k_{\mathrm{i}} (I+U) S/N + k_{\mathrm{i}}^{\mathrm{v}} (I+U) V/N - k_{\mathrm{e}} E.
$$

The remainder of the model is as before.

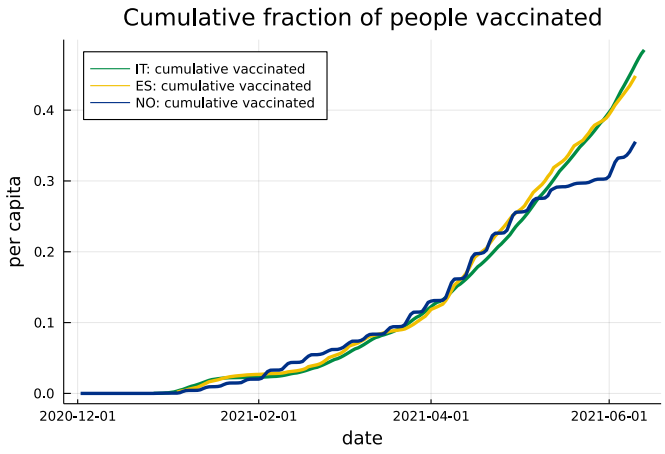

Figure 2. Cumulative fraction of people that have received at least one vaccine dose vs. time (IT = Italy, ES = Spain, NO = Norway; line color refers to a key color in national flags).

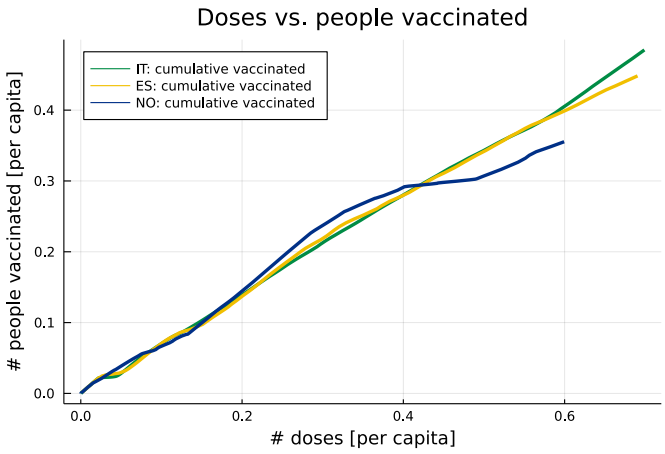

Figure 3. Cumulative fraction of doses vs. people that have received at least one vaccine dose (IT = Italy, ES = Spain, NO = Norway; line color refers to a key color in national flags).

The efficacy η is now determined indirectly by $k_{\mathrm{i}}^{\mathrm{v}}$. One possible definition of the efficacy is unity minus the fraction of the rate at which vaccinated get infected, and the rate at which susceptible get infected,

$$\eta = 1 - \frac{k_{\mathrm{i}}^{\mathrm{v}}\,(I+U)\,V/N}{k_{\mathrm{i}}\,(I+U)\,S/N} = 1 - \frac{k_{\mathrm{i}}^{\mathrm{v}} V}{k_{\mathrm{i}} S}.$$

We assume an efficient vaccine, so that in steady state, $\left|\dot{V} - k_{\mathrm{v}} V\right| \gg k_{\mathrm{i}}^{\mathrm{v}}\,(I+U)\,V/N$, thus $\mathrm{d}V/\mathrm{d}t \to 0$ leads to

$$V = \frac{1}{k_{\mathrm{v}}}\dot{V} = \tau_{\mathrm{v}}\dot{V}.$$

Then, approximately,

$$k_{\mathrm{i}}^{\mathrm{v}} = (1-\eta)\,k_{\mathrm{i}}\frac{S}{\tau_{\mathrm{v}}\dot{V}}.$$

This expression is not entirely satisfactory, as $k_{\mathrm{i}}^{\mathrm{v}}$ depends on the remaining number of susceptible S and the vaccination rate $\dot{V}$. A simpler expression is

$$k_{\mathrm{i}}^{\mathrm{v}} = (1-\eta)\,k_{\mathrm{i}}.$$

Vaccination rate Figure 2 shows the cumulative number of *people* having received at least one vaccine dose (per capita) in Italy, Spain, and Norway. The ripples in the data are due to slower vaccination in week-ends.

Figure 3 shows the *actual* cumulative fraction of administered *doses* vs. the cumulative fraction of *people* receiving at least one vaccine dose, for Italy, Spain, and Norway.

Efficacy varies with vaccine types, where mRNA based vaccines (e.g., those of Phizer and Moderna) seem to provide 95+% efficacy, while vector based vaccines (e.g., AstraZeneca, Sputnik, etc.) seem to provide in the range 50-85% efficacy. These numbers have been reduced with the emergence of more aggresive mutations such as the Delta variant.

Typically, full vaccination is assumed 1–3 weeks after the final dose; for most vaccines, two doses are required. In Norway, initially, two dose vaccines were given with 3 week intervals. Then this was changed to 4 weeks, then to 6 weeks, then to 12 weeks, then moved back to 9 weeks, etc. Thus, τ_{V} may vary with time to some degree.

2.4.3 Qualitative effect of mitigation + vaccination

Initial requirement for stability for the disease-free case is that the basic reproduction number is less than unity, $\mathsf{R}_0 < 1$, (Lie, 2021a,b). This requirement is based on the assumption that the entire population is susceptible, i.e., that $\check{S}(0) = S(0)/N = 1$. If the infection dies out, and then is in the process of re-starting, the requirement for stability is that $\check{S}(0)\,\mathsf{R} < 0$. Here, it should be noted that $\mathsf{R} \propto k_{\mathrm{i}}$, the infection rate constant, where $k_{\mathrm{i}} = k_{\mathrm{i}}^0 \cdot u_{\mathrm{fm}}$ in the steady state of the mitigation policy; k_{i}^0 is the infection rate constant *without* mitigation, and $u_{\mathrm{fm}} \in [0,1]$ is the equivalent mitigation policy which depends on seasonal variations, etc. Thus, $\mathsf{R} = \mathsf{R}_0 u_{\mathrm{fm}}$, and the infection is kept under control when

$$\check{S}(0)\,\mathsf{R}_0^0 u_{\mathrm{fm}} < 1.$$

It follows that with $\check{S}(0) = 1$, the equivalent mitigation policy u_{fm} must be chosen such that

$$u_{\mathrm{fm}} \leq 1/\mathsf{R}_0^0.$$

Some initial estimates of R_0^0 from March 2020 suggested that $\mathsf{R}_0^0 \in [2.2, 2.7]$ or so[5]. Some of the more recent virus mutations (British, South-African, Indian) are more infectious, with the Delta mutant having $\mathsf{R}_0 = 6$ or even higher. This could indicate that R_0^0 is as a minimum $\mathsf{R}_0^0 = 5$ at the moment, leading to the requirement that $u_{\mathrm{fm}} \leq 0.2$.

The effect of vaccination, on the other hand, is essentially to reduce $\check{S}(0)$. It follows that to go back to the normal, pre-COVID-19 situation with $u_{\mathrm{fm}} = 1$, we need to

[5]Early estimates from China indicated values up to 4 or 5.

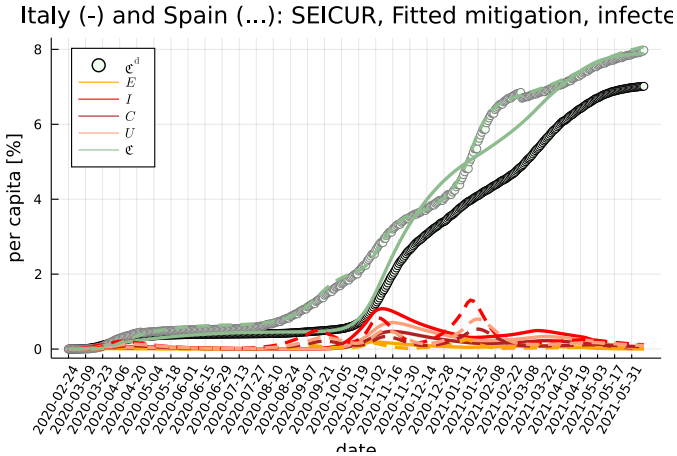

Figure 4. SEICUR models for Italy (solid) and Spain (dotted) with fitted mitigation, and with $\dot{N} = 10^4$ persons/day exchange rate.

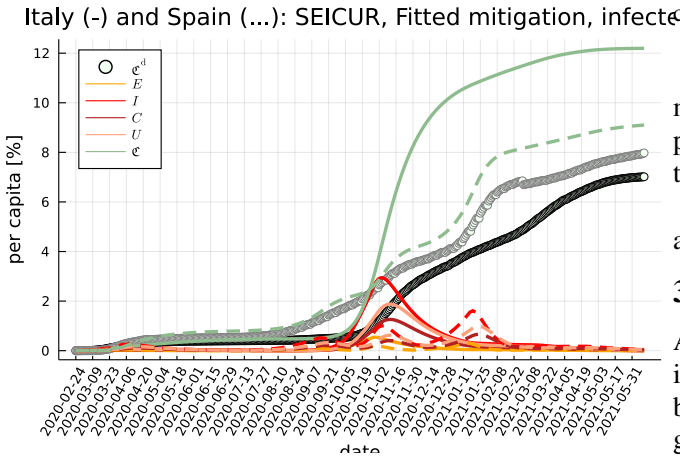

Figure 5. SEICUR models for Italy (solid) and Spain (dotted) with fitted mitigation, and with $\dot{N} = 10^5$ persons/day exchange rate.

reduce $\check{S}(0)$ to $\check{S}(0) \leq 0.2$, which implies that 80% of the population must be vaccinated.

Because the most vulnerable, those that have a high risk of dying, probably are vaccinated early, society may function more or less as normal with fewer than 80% vaccinated — but must then accept that there is a certain number of infected at any time.

3 Results

3.1 Migration

Figures 4 and 5 display resulting change in infections caused by migration between Italy and Spain when these countries are assumed closed for other countries, first with $\dot{N} = 10^4$ persons/day, Figure 4, and with $\dot{N} = 10^5$ persons/day, Figure 5.

The results in Figs. 4, 5 indicate that migration needs to be considerable to give an effect. The results should be used with caution, though: (i) data used in equivalent mitigation policy fitting already has some interaction with

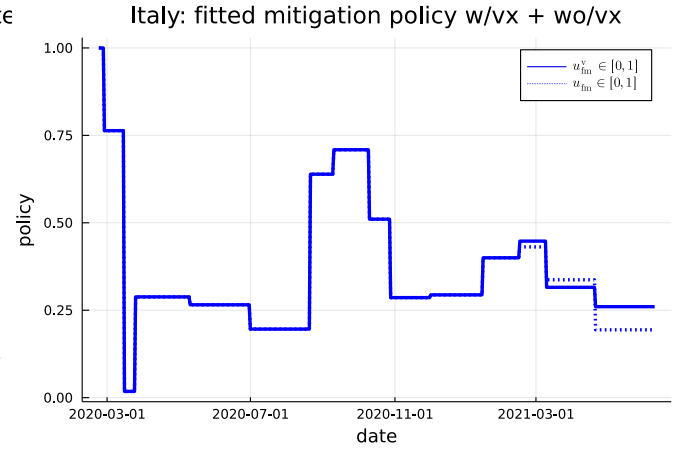

Figure 6. Fitted equivalent mitigation policy u_{fm}^{v} for Italy based on SEICUR model *extended* with *semi-crude* vaccination model, compared to fitted equivalent mitigation policy u_{fm} based on the pure SEICUR model ((Lie, 2021b). Vaccine is administered according to Figure 2.

multiple countries, and (ii) "super-spreaders" (in densely populated bars, discoteques, ...) are perhaps more likely to migrate than average spreaders.

The idea of interaction between countries as indicated above, is the basis for *network models*.

3.2 Herd immunity

Although not shown here, using the fitted mitigation policy for Italy for the period February 2020 – late October 2020, and making forecasts while keeping the mitigation policy at the level of late October 2020 into the future, those forecasts indicated that Italy would have reached herd immunity before Christmas 2020. The consequence would have been a health system with considerably higher strain than in April 2020. Italy introduced restrictions/lock-downs ca. October/November 2020 which reduced the infection spread sufficiently to avoid this situation, see (Lie, 2021b).

3.3 Vaccination

Here, we consider the simplified case of (i) use of the fitted mitigation policy, (ii) use of the "semi-crude" vaccination model with $\eta_{\text{v}} = 0.8$ and $\tau_{\text{v}} = 28\,\text{d}$, and (iii) actual vaccination rates.

The resulting equivalent mitigation policy for Italy *with* vaccination, u_{fm}^{v}, vs. *without* vaccination, u_{fm}, is displayed in Figure 6. u_{fm}^{v} is the *real* equivalent policy, while u_{fm} is a hypothetical policy when neglecting vaccination.

The resulting equivalent mitigation policy for Spain *with* vaccination, u_{fm}^{v}, vs. *without* vaccination, u_{fm}, is displayed in Figure 8.

The resulting equivalent mitigation policy for Norway *with* vaccination, u_{fm}^{v}, vs. *without* vaccination, u_{fm}, is displayed in Figure 9.

For all countries, the model fit to the cumulative number of confirmed cases (Lie, 2021b) is just as good whether

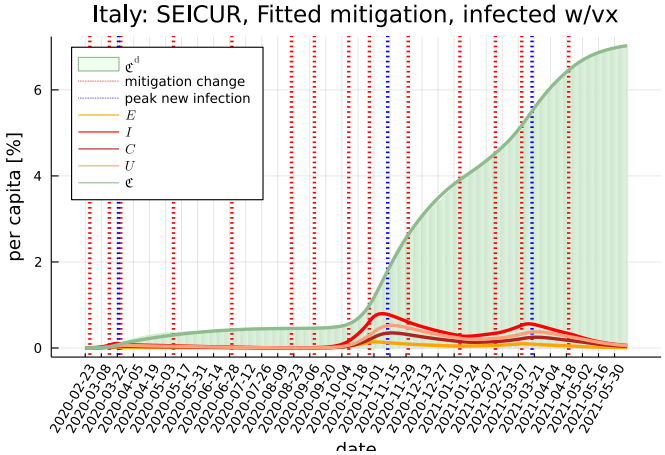

Figure 7. SEICUR model extended with vaccination model, simulation with fitted mitigation policy u_{fm}^{v} as in Figure 6. Vaccine is administered according to Figure 2.

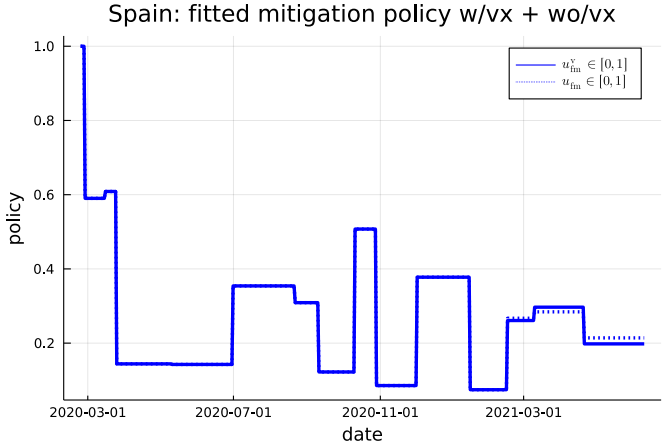

Figure 8. Fitted equivalent mitigation policy u_{fm}^{v} for Spain based on SEICUR model *extended* with *semi-crude* vaccination model, compared to fitted equivalent mitigation policy u_{fm} based on the pure SEICUR model ((Lie, 2021b). Vaccine is administered according to Figure 2.

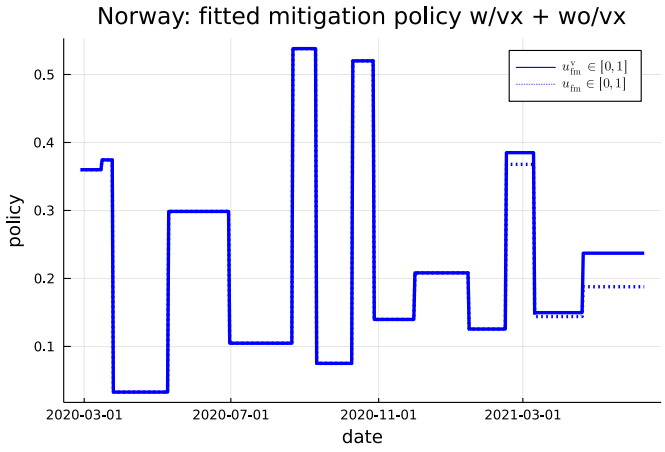

Figure 9. Fitted equivalent mitigation policy u_{fm}^{v} for Norway based on SEICUR model *extended* with *semi-crude* vaccination model, compared to fitted equivalent mitigation policy u_{fm} based on the pure SEICUR model ((Lie, 2021b). Vaccine is administered according to Figure 2.

the SEICUR model is extended with the vaccinatin model — leading to equivalent mitigation policy u_{fm}^{v}, or whether vaccination is baked into u_{fm}.

The number of certified infected per capita (and thus: recovered) is highest in Spain, a little lower in Italy, e.g., Figure 4, and quite low in Norway. It is not clear whether the various countries choose to vaccinate people who have *recovered*. As Figs. 6–9 illustrate, the mitigation policy *with* vaccination (u_{fm}^{v}) is less restrictive for Norway and (partially for) Italy compared to the case when there is no vaccination (u_{fm}). For Spain, the situation is less clear. In conclusion, vaccination allows for relaxing the mitigation policy.

3.4 Quenching COVID-19: the importance of vaccination

When a certain fraction of the population has either recovered from COVID-19, or has been vaccinated, herd immunity is reached and infection will die out. An interesting question is whether the current reduction in infection in North America, Europe, and a few other countries is due to rapid vaccination roll-out. This question is not trivial to assess: there was a similar reduction in infection in May–June 2020, so it is possible that the reduction in infection is (partially) due to a seasonal variation in infection rate constants.

It seems like vaccination has dramatically reduced the death rates from COVID-19; this will reduce the strain on the health care system. But it is still possible that there will be growths in infection during the fall of 2021, both due to seasonal variations and due to new mutations.

4 Conclusions

In this paper, the SEICUR model discussed in (Lie, 2021b) has been extended in several directions. First the model is extended with migration terms. Comparing the effect of migration solely between Italy and Spain, the model indicates that the number of people per day moving between the countries must be relatively high before a significant change in infection is observed. However, this is based on the assumption that the migrants are "average spreaders". Some tourists engaging in nightlife activities will most likely be "super spreaders", so to get a more accurate description, it would probably be necessary to distinguish between super spreaders and regular spreaders.

Second, the SEICUR model is extended to handle demographic variations due to age dependence in rate constants. This is particularly important when considering the risk of serious illness and death. Because this paper has not considered confirmed death rates, simulations have not been carried out and the presentation is mainly included for illustration/future studies.

Thirdly, the SEICUR model is extended with a description of vaccination, with 3 models of the effect of vaccination. The "semi-crude" model has been added to the SEICUR model, and an equivalent mitigation policy has

been fitted to the data when the vaccination model is included. The results indicate that vaccination has most effect on the equivalent mitigation policy in countries with a low level of confirmed infections (e.g., Norway), and less effect in countries with a higher number of confirmed infected (e.g., Spain). This may be due to vaccinating people who have already recovered, or to the relative reduction in the number of susceptibles due to vaccination.

Realistic COVID-19 models need to include migration/network description between the various compartments, and for the case that demographics influence the degree of illness, age distribution models and other types of models distributed in co-morbidity should be used. In the models studied here, an equivalent mitigation policy has been assumed. For more realistic models, it is recommended to improve the effect of genetics, seasonal variations, etc. in the infection rate expression.

The spreading of the Delta mutation in the second and third quarters of 2021 would probably have necessitated using different model parameters (frequency factors, etc.), and would have complicated the total model. Also, hesitance against vaccination in various populations would need to be taken into consideration.

The SEICUR model with the extension of the vaccination model holds the potential for computing some "optimal" transition between mitigation and vaccination using feedback control theory (e.g., Model Predictive Control). Essentially, the "fitted" mitigation policy u_{fm} is the control variable, and one could specify a cost function for future infection, and then compute how an "optimal" future mitigation policy should be in order to tackle the infection. Some important caveats are that (i) the current model does not describe seasonal variations in infection rate constant, thus relatively short future horizons should be used, (ii) the "fitted" mitigation policy is not directly related to concrete policies ("social distancing", "mask use"), etc. In summary, MPC is more useful if the mitigation model is extended to hold real mitigation policies u instead of "fitted" mitigation policy u_{fm} — it is non-trivial to figure out quantitative real policies from u_{fm} — beyond "we need a stricter policy" or "we can relax the policy".

References

Fred Brauer, Carlos Castillo-Chavez, and Zhilan Feng. *Mathematical Models in Epidemiology*. Number 69 in Texts in Applied Mathematics. Springer, New York, 2019. ISBN 978-1-4939-9826-5.

Bernt Lie. Epidemiological Models and Process Engineering. In *Proceedings, SIMS EUROSIM 2021, Oulo Finland, September 21–23.*, 2021a.

Bernt Lie. COVID-19 Models and Model Fitting. In *Proceedings, SIMS EUROSIM 2021, Oulo Finland, September 21–23.*, 2021b.

Z. Liu, P. Magal, O. Seydi, and G. Webb. A COVID-19 epidemic model with latency period. *Infectious Disease Modelling*, 5: 323–337, 2020a. doi:10.1016/j.idm.2020.03.003.

Zhihua Liu, Pierre Magal, Ousmane Seydi, and Glenn Webb. A model to predict covid-19 epidemics with applications to south korea, italy and spain. *SIAM News*, 2020b. https://sinews.siam.org/Details-Page/a-model-to-predict-covid-19-epidemics-with-applications-to-south-korea-italy-and-spain.

Zhihua Liu, Pierre Magal, and Glenn F Webb. Predicting the number of reported and unreported cases for the COVID-19 epidemics in china, south korea, italy, france, germany and united kingdom. apr 2020c. doi:10.1101/2020.04.09.20058974.

Leonardo López and Xavier Rodó. A modified SEIR model to predict the COVID-19 outbreak in Spain and Italy: simulating control scenarios and multi-scale epidemics. *Results in Physics*, 2020. doi:10.1016/j.rinp.2020.103746. URL `https://pubmed.ncbi.nlm.nih.gov/33391984/`.

Stig Øyvann. Jakten på en presis beskrivelse av epidemien. *Computerworld*, 38(6):26–30, December 2020.

Christopher Rackauckas and Qing Nie. DifferentialEquations.jl — A Performant and Feature-Rich Ecosystem for Solving Differential Equations in Julia. *Journal of Open Research Software*, 5(15), 2017a. doi:10.5334/jors.151.

Christopher Rackauckas and Qing Nie. Adaptive methods for stochastic differential equations via natural embeddings and rejection sampling with memory. *Discrete and continuous dynamical systems. Series B*, 22(7):2731, 2017b.

Christopher Rackauckas and Qing Nie. Stability-Optimized High Order Methods and Stiffness Detection for Pathwise Stiff Stochastic Differential Equations. *arXiv:1804.04344 [math]*, 2018. URL `http://arxiv.org/abs/1804.04344`.

Jr. Reiner, Robert C., Ryan M. Barber, James K. Collins, and more. Modeling COVID-19 scenarios for the United States. *Nature Medicine*, 27:94–105, 2021. doi:https://doi.org/10.1038/s41591-020-1132-9.

Aleksa Zlojutro, David Rey, and Lauren Gardner. A decision-support framework to optimize border control for global outbreak mitigation. *Scientific Reports*, (2216), 2019. doi:https://doi.org/10.1038/s41598-019-38665-w.

Intelligent epidemiological models for COVID-19

Esko K. Juuso

Control Engineering, Environmental and Chemical Engineering, Faculty of Technology,
University of Oulu, Finland
esko.juuso@oulu.fi

Abstract

The coronavirus COVID-19 is affecting around the world with strong differences between countries and regions. Extensive datasets are available for visual inspection and downloading. The material has limitations for phenomenological modelling but data-based methodologies can be used. This research focuses on intelligent modelling on the basis of these datasets. The methodology has been tested in the analysis of daily new confirmed COVID-19 cases and deaths in six countries. The datasets are studied per million people to get comparable indicators. Nonlinear scaling brings the data of different countries to the same scale and linear interactions represent the varying operating conditions well. The same approach operates for both the confirmed cases and deaths and can be used for any country or group of people. The effects of the vaccinations were clearly shown at the end of the analyzed period. During the pandemic, the scaling functions expanded for the confirmed cases but remained practically unchanged for the confirmed deaths which is consistent with increasing testing. Limitations are seen if there are too many interacting things, e.g. several infection transmission chains which are in different stages. The feasibility analysis needs to be extended to the modelling with inputs. The presented approach is promising for this wider analysis.

Keywords: intelligent methods, temporal analysis, dynamic modelling, digital twins, COVID-19

1 Introduction

The coronavirus COVID-19 is affecting around the world. There are strong differences between countries and regions. People of all ages can be infected but older people and people with pre-existing medical conditions are more vulnerable to becoming severely ill. The risk is presented with three parameters:

- Transmission rate evaluated by the number of newly infected people,
- Case fatality rate (CFR) based on the percent of cases that result in death,
- Vaccine performance as a prevention measure.

An online interactive dashboard is hosted by the Center for Systems Science and Engineering (CSSE) at Johns Hopkins University for visualising and tracking reported cases of *coronavirus disease 2019 (COVID-19)* in real time (CSSE, 2021; Dong et al., 2020). Transmission dynamics is difficult to explain since the characteristics of a novel disease include many uncertainties. The open evidence review (Jefferson et al., 2021) makes information about active research on modes of transmission available.

The effective reproduction number (R) of an infectious disease is used for modelling. The tracking of the parameter is done by assuming a model structure. An example of this approach is presented in (Arroyo-Marioli et al., 2021) where the Kalman filter and a SIR model has been used for tracking R for COVID-19.

The steady-state simulation models are linear *multiple input, multiple output (MIMO)* models $\vec{y} = F(\vec{x})$, where the output vector $\vec{y} = (y_1, y_2, \ldots, y_n)$ is calculated by a linear function F from the input vector $\vec{x} = (x_1, x_2, \ldots, x_m)$. Statistical modelling in its basic form uses linear regression for solving the model coefficients. Linear methodologies are suitable for large multivariable systems and can be extended with quadratic and interactive terms response surface methodologies (Box and Wilson, 1951). Principal components compress the data by reducing the number of dimensions with a minor loss of information (Jolliffe, 2002). Partial least squares regression (PLS) is an extension of these ideas (Gerlach et al., 1979). Known semi-physical models of inputs are important in linear modelling, see (Ljung, 1999). In linear parameter varying (LPV) models, an exogeneous variable measured during the operation, modifies the local linear models (Ljung, 2008).

Dynamic data-driven modelling with parametric models, also known as identification (Ljung, 1999), is the key methodology in the dynamic modelling. These models use the static mapping and NARX/Nonlinear AutoRegressive with eXogenous structures with a finite number of inputs and outputs. The dynamic structures are reduced in dynamic models based on fuzzy set systems or neural networks (Babuška and Verbruggen, 2003).

Generalized norms are used in data analysis to extract features from waveform signals collected from the statistical databases (Lahdelma and Juuso, 2011). The computation of the norms can be divided into the computation of equal sized sub-blocks, i.e. the norm for several samples can be obtained as the norm for the norms of individual samples. This means that norms can be recursively updated (Juuso, 2011). The same methodologies can be

used for analysing the data distributions in less frequent data, e.g. daily COVID-19 data. Distributions of the variables provide useful information about fluctuations, trends and models. This has been used in temporal analysis for all types of measurements, features and indices. Recursive updates of the parameters are needed in prognostics. (Juuso, 2020)

Dynamic LE models use the static mapping and NARX input models in the same way as fuzzy set systems and neural networks. The main difference is that the input and output variables are processed by a nonlinear scaling method, which originates from the membership functions used in fuzzy systems. (Juuso and Leiviskä, 1992; Juuso, 2004) Constraints handling (Juuso, 2009) and data-based analysis (Juuso and Lahdelma, 2010), improve possibilities to update the scaling functions recursively (Juuso, 2011). Different fuzzy approaches can be efficiently combined with LE models where the interactions between the scaled variables are linear (Juuso, 2014).

This research aims to develop unified intelligent models for analyzing the fluctuations, trends and severity of the corona situations. Parametric systems are used to adapt the solution for varying operating conditions caused by local areas and groups of people. Recursive updates are used in the parametric models.

2 COVID-19 data

This research uses the complete COVID-19 dataset maintained by Our World in Data. The collection of the COVID-19 data is updated daily and includes data on confirmed cases, deaths, hospitalizations, and testing. Raw data on confirmed cases and deaths for all countries is sourced from the COVID-19 Data Repository by the Center for Systems Science and Engineering (CSSE) at Johns Hopkins University. Data visualizations rely on work from many people and organizations (Ritchie et al., 2020).

The Our World in Data has created a new description of all our data sources available at the GitHub repository where all the data can be downloaded. These datasets were used as a data source in this research. The collection of data is presented as tabular data where every column of a table represents a particular variable, and each row corresponds to a given record of the data set for a specific country on a certain day. Each record consists of one or more fields, separated by commas. The data can be visualised in the COVID-19 DataExplorer for individual countries. Several countries can be compared by selecting them for the view. The maps available in DataExplorer help in focusing on the analysis.

The analysis uses confirmed COVID-19 cases whose number is lower than the number of actual cases. The main reason for that is limited testing which also varies between countries and time. Therefore, the analysis is done country-wise. The pandemic introduces an increasing number of new COVID-19 cases but countries also make progress in reducing the speed towards zero new cases (Figure 1). However, the increase can start again as can be seen in the data of different countries. The pandemic can restart if it is active somewhere. The difficult periods vary between countries.

A part of the pandemic cases leads to hospitalizations and deaths. Both increases and reductions can be seen in the daily new confirmed COVID-19 deaths (Figure 2. During the outbreak of the pandemic, the calculated case fatality rate (CFR) was a poor measure of the mortality risk since it depends on the number of tests and at that time there were few tests. The true number of cases was much higher. Later the number of tests has increased strongly, but not in all countries.

An increasing number of variants and mutations has effects on the number of cases. Vaccinations were just started during the studied period. All these have strong effect on the dynamics of the pandemic. The problems become more case specific but can in the same time activate in many locations.

The research focused on the temporal analysis is aimed on finding situations for more detailed modelling and action planning.

3 Methodologies

The modelling needs to be adapted in the appropriate situations. The unified analysis requires that all the features are in the same scale. In this research, this is done by combining the nonlinear scaling and the intelligent temporal analysis. This methodology allows recursive updates of the scaling functions.

3.1 Nonlinear scaling

The nonlinear scaling brings various measurements and features to the same scale by using monotonously increasing scaling functions $x_j = f(X_j)$ where x_j is the variable and X_j the corresponding scaled variable. The function $f()$ consist of two second order polynomials, one for the negative values of X_j and one for the positive values, respectively. The corresponding inverse functions $X_j = f^{-1}(x_j)$ based on square root functions are used for scaling to the range [-2, 2], denoted as linguistification. The monotonous functions allow scaling back to the real values by using the function $f()$. (Juuso, 2004)

The parameters of the functions are extracted from measurements by using generalized norms and moments. The support area is defined by the minimum and maximum values of the variable, i.e. a specific area for each variable $j, j = 1, \ldots, m$. The central tendency value, c_j, divides the support area into two parts, and the core area is defined by the central tendency values of the lower and the upper part, $(c_l)_j$ and $(c_h)_j$, correspondingly. This means that the core area of the variable j defined by $[(c_l)_j, (c_h)_j]$ is within the support area.

The corner points are defined by iterating the orders, p,

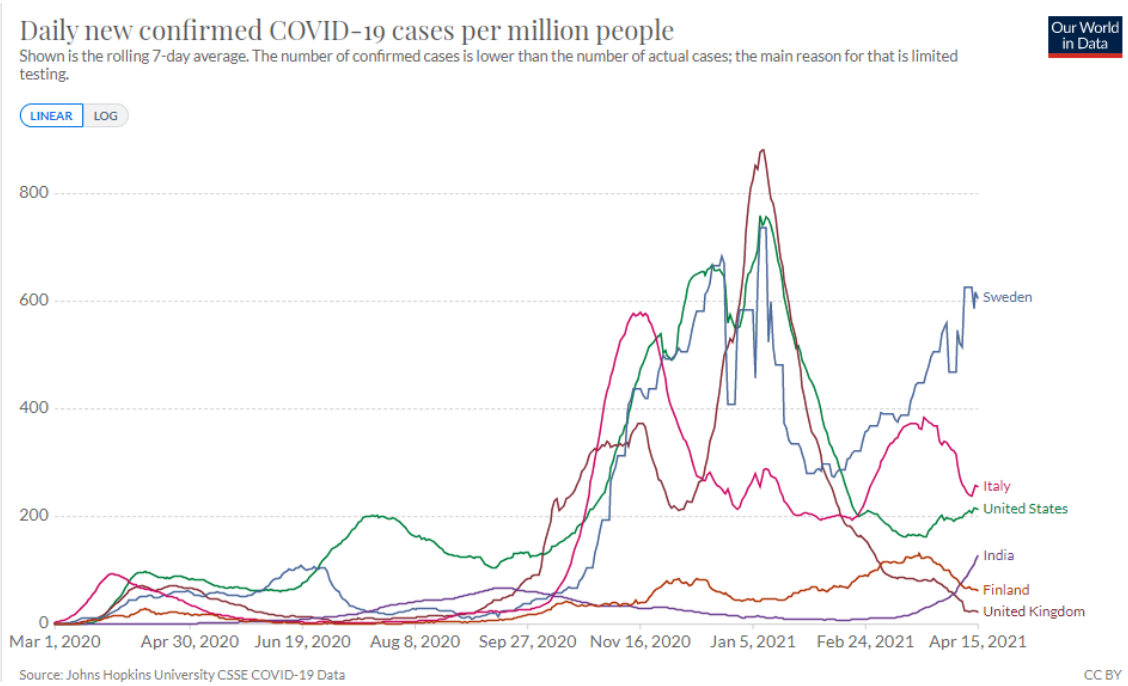

Figure 1. Daily new confirmed COVID-19 cases per million people, rolling 7-day averages collected from (Our, 2021) for selected countries.

of the corresponding generalised norms

$$||^{\tau}M_j^p||_p = (M_j^p)^{1/p} = [\frac{1}{N}\sum_{i=1}^{N}(x_j)_i^p]^{1/p}, \quad (1)$$

where $p \neq 0$, is calculated from N values of a sample, τ is the sample time. This provides possibilities to recursively update the scaling functions since the generalized norms can be recursively updated. The iteration is based on the generalized skewness (Juuso and Lahdelma, 2010).

The scaled values should preserve the directions of the temporal changes with time. To achieve this, the scaling functions should be monotonously increasing. This is achieved by limiting the ratios,

$$\begin{aligned} \alpha_j^- &= \frac{(c_l)_j - \min(x_j)}{c_j - (c_l)_j}, \\ \alpha_j^+ &= \frac{\max(x_j) - (c_h)_j}{(c_h)_j - c_j}, \end{aligned} \quad (2)$$

in the range $[\frac{1}{3}, 3]$. The corner points are adjusted if these limitations are not filled. There are several alternatives to select the points to tune. (Juuso, 2009)

The second order polynomials,

$$\begin{aligned} f_j^- &= a_j^- X_j^2 + b_j^- X_j + c_j, \quad X_j \in [-2, 0), \\ f_j^+ &= a_j^+ X_j^2 + b_j^+ X_j + c_j, \quad X_j \in [0, 2], \end{aligned} \quad (3)$$

are monotonously increasing if the coefficients are defined as follows:

$$\begin{aligned} a_j^- &= \tfrac{1}{2}(1 - \alpha_j^-)\,\Delta c_j^-, \\ b_j^- &= \tfrac{1}{2}(3 - \alpha_j^-)\,\Delta c_j^-, \\ a_j^+ &= \tfrac{1}{2}(\alpha_j^+ - 1)\,\Delta c_j^+, \\ b_j^+ &= \tfrac{1}{2}(3 - \alpha_j^+)\,\Delta c_j^+, \end{aligned} \quad (4)$$

where $\Delta c_j^- = c_j - (c_l)_j$ and $\Delta c_j^+ = (c_h)_j - c_j$.

3.2 Steady-state LE modelling

The nonlinear scaling transforms the nonlinear problem $\vec{y} = F(\vec{x})$ to a linguistic equation (LE) model represented by a compact equation

$$x_{out}(t) = f_{out}\left(-\frac{1}{A_{i\,out}}\sum_{j=1, j\neq out}^{m} A_{ij}\, f_j^{-1}(x_j(t - n_j))\right), \quad (5)$$

where the functions f_j and f_{out} are scaling functions. Each variable j has its own time delay n_j compared to the variable with latest time label. In the general case, the the weight factors

$$w_{ij} = -\frac{A_{ij}}{A_{i\,out}}. \quad (6)$$

The coefficients A_{ij} and $A_{i\,out}$ can be set to one or to a chosen value by modifying the scaling functions.

The directions of the interactions analyzed with these methodologies are aimed to be valid in a wider area than the scaling functions of the individual model variables. The quadratic effects are embedded in the scaling approach and the model can handle various kinds of interactions. Subsets of scaled variables can form linguistic principal components (LPCs) and PLS regression could be useful in modelling. The LPV modelling further extends the feasible areas of the model parameters.

3.3 Dynamic LE modelling

In NARX models, the input and output values are chosen according to appropriate system orders. In the regressor

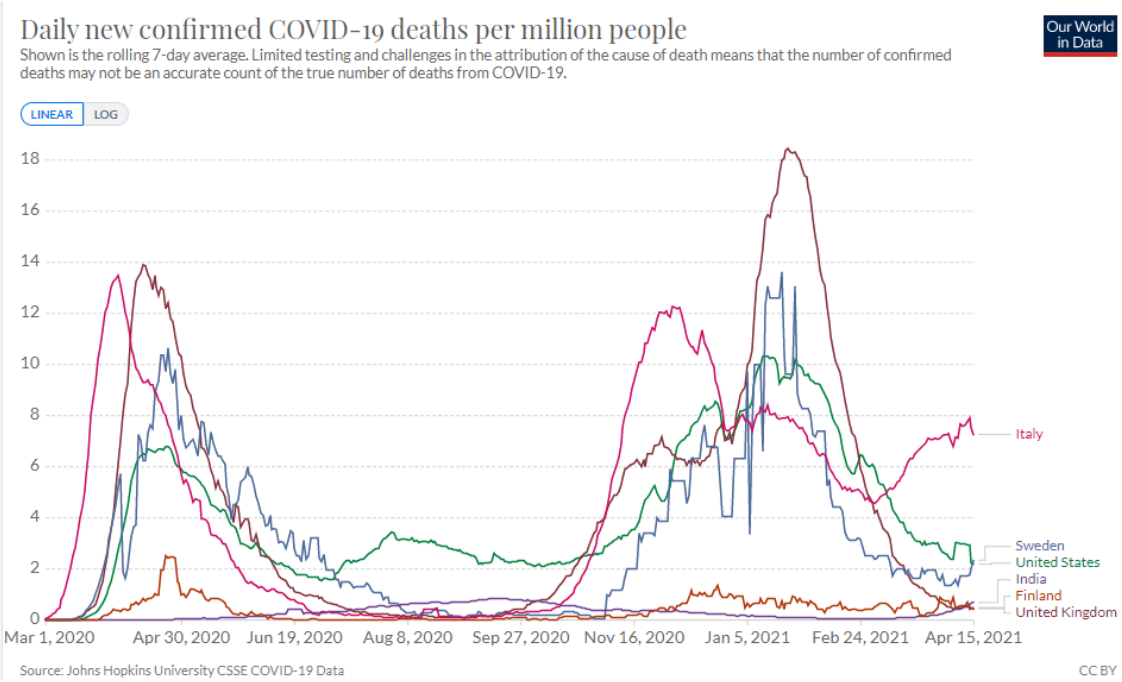

Figure 2. Daily new confirmed COVID-19 deaths per million people, rolling 7-day averages collected from (Our, 2021) for selected countries.

vector, the number of past inputs and outputs may become too high if nonlinear effects are needed. The nonlinear scaling reduces the number of input and output signals needed for the modelling of nonlinear systems. In the default dynamic LE model,

$$Y_{out}(k) + a_1 Y_{out}(k-1) = \sum_{j=1, j\neq out}^{m} b_j U_j(k-n_j) + e(t), \quad (7)$$

where $Y_{out}(k)$, $Y_{out}(k-1)$ and $U_j(k-n_j)$ are the scaled values of the variables and $e(t)$ is a noise term. The scaling function f_{out} is not changing between time steps $k-1$ and k. The delays n_j of the inputs can depend on the operating conditions and need to be calculated if variable step numerical integration is used.

A wide variety of situations can be represented with composite local models which are based on the same model equations (7) and case specific scaling functions f_j and f_{out}. Overlapping local models can be combined with fuzzy set systems by using case specific solutions which are first scaled back to the real values.

4 Epidemiological modelling

Data collection and working practices were under development during the first months of the COVID-19 pandemic. In this research, the modelling was started with the variable selection and analysis in the varying operating conditions.

4.1 Variable selection

New cases. The modelling uses daily new confirmed COVID-19 cases and deaths as output variables. The study was done for the same countries as in (Juuso, 2021). Six countries were Finland, India, Italy, Sweden, United Kingdom and United States.

The rolling 7-day averages were used for the research study since they operated smoothly for the confirmed deaths as well. The cases were analyzed per million people to improve the sensitivity of the analysis for small countries. Situations vary strongly between countries and periods of time.

Hospital patients, hospital admissions and intensive care patents could be analyzed with the same methodologies, but the datasets are much more limited.

The datasets include also test activities, vaccination and stringency information.

Operating conditions. The number of tests was everywhere very low in the beginning of the pandemic in the spring of 2020. The confirmed new cases remained low for the first 240 days (Juuso, 2021) for all the countries compared in this research (Figure 1). Since similar differences were not seen in new confirmed deaths (Figure 2), the severe cases were detected already in the beginning. A high number of undetected cases is in agreement with the high values of excess mortality.

COVID-19 was activated country by country. In this research, a high number of cases per million people appeared in the sequence Italy, the UK, Sweden and the USA. Finland had a low number of cases and India hardly

any. During the summer of 2020, both new cases and deaths went down, although the number of tests was increased. An exception was the USA where both remained high, which was true situation since the share of positive tests was high as well. India had all the time very few cases, but the test activity was very low and the share of positive tests was high meaning that the situation was similar with the spring of 2020 in other countries.

In the autumn of 2020, the number of cases and deaths started to rise again in the same sequence as previously. The number cases was rising fast and the number of deaths only slightly.

Vaccinations started in December 2020 and increased steadily, fastest in the UK and USA (Table 1) where the number of new cases dropped fast. The decrease continued although the number of tests was increased.

Table 1. Cumulative COVID-19 tests and vaccinations per 100 people by April 12, 2021 (Our, 2021).

	Tests	One dose	Two doses
Finland	76.1	20.93	1.79
India	18.5	6.82	0.97
Italy	88.2	15.6	6.65
Sweden	77.2	15.18	6.26
United Kingdom	189.0	47.28	11.22
United States	120.0	39.28	24.89

The society can take actions to prevent the pandemic to expand. The stringency index presented in (Hale et al., 2021) is a composite measure based on nine response indicators including school closures, workplace closures, and travel bans, rescaled to a value from 0 to 100 (100 = strictest). This index was highest in India and lowest in Finland.

The reproduction rate represented as the average number of new infections caused by a single infected individual. If the rate is greater than 1, the infection is able to spread in the population. If it is below 1, the number of cases occurring in the population will gradually decrease to zero. The estimate rates (Arroyo-Marioli et al., 2021) were very high in the spring of 2020 since the detected COVID-19 cases were almost all serious cases.

4.2 Data analysis

The nonlinear scaling approach aims to simplify the modelling work. The normalisation keeps the directions of the effects but would leave the analysis of nonlinear effects to the modelling. For all six countries, the data analysis was taken from the research on temporal analysis (Juuso, 2021). The country specific lines were extracted from the full dataset with all the countries by using the DataExplorer. Selected time periods were used in the analysis.

Within each country, the risk levels are represented by using nonlinear scaling. The scaling functions are defined by five corner points by generalized norms whose orders

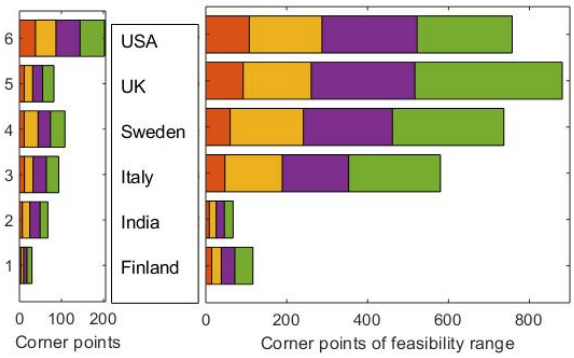

Figure 3. Parameters $\min(x_j)$, $(c_l)_j$. c_j, $(c_h)_j$ and $\max(x_j)$ for the daily new confirmed cases: first 240 days (left) and all data (right) , all based on 7-day rolling average of confirmed cases per million people (Juuso, 2021).

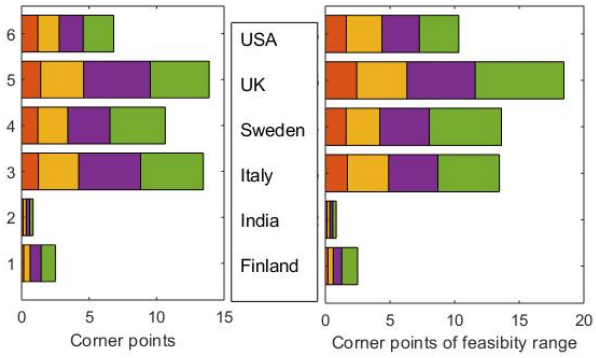

Figure 4. Parameters $\min(x_j)$, $(c_l)_j$. c_j, $(c_h)_j$ and $\max(x_j)$. for the daily new confirmed deaths: first 240 days (left) and all data (right), all based on 7-day rolling average of confirmed cases per million people (Juuso, 2021).

are obtained from the data. The parameters of the scaling functions are country and time period specific (Figures 3 and 4). The differences between the early and later stages of the pandemic are very clear. For the death cases, the differences are hardly visible.

The confirmed cases and deaths were analysed per million people but still the relative values are still much higher in the UK, the USA and Italy than in Finland.

4.3 Feasibility results

The default dynamic LE model (7) is studied for all the analyzed data. The cases were the same as in the temporal analysis presented in (Juuso, 2021). The first phase is the nonlinear scaling of the variables. In this research, the variables are the daily new confirmed COVID-19 cases (Figure 1) and deaths (Figure 2).

The input variables could be the vaccination level, stringency index and active level of infections. Vaccinations were just coming at the end of the studied period. The

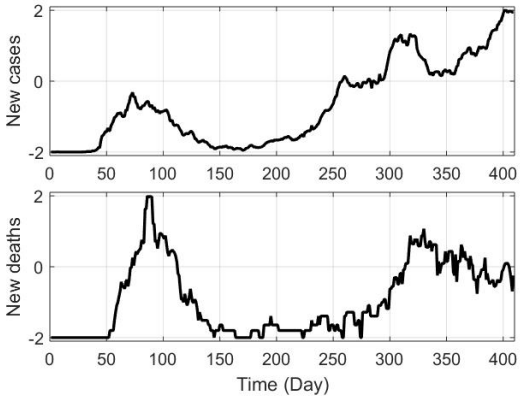

Figure 5. Scaled daily COVID-19 cases and deaths in Finland.

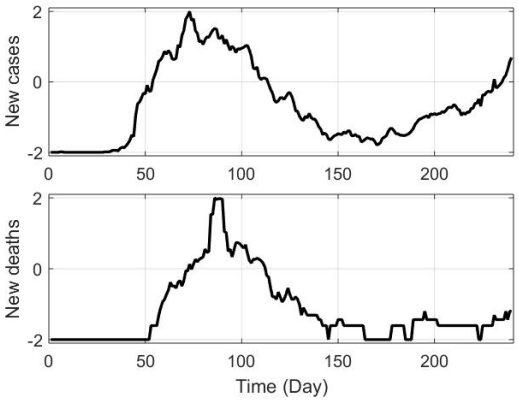

Figure 6. Scaled daily COVID-19 cases and deaths in Finland during the first 240 days.

stringency index was not yet on a practical level. There were not measurements for the active level of infections.

This section is a feasibility study of the linear interactions of the scaled data in different countries having different operating conditions.

Finland. During the first days of the pandemic, the levels of the daily new cases were much lower than in Autumn and Winter. In spite of that, the levels of deaths were already at the same level as later. For Finland, this is seen in Figure 5 and 6. The difference in operating conditions is clear in the parameters of the scaling functions (Figures 3 and 4).

Linear interactions operate well for the changes in the scaled values. The time delay from the changes of confirmed cases to the confirmed deaths is about two weeks. The steep slope at the beginning of the cases could be caused by the delayed detection of them. The analysis reveals details which are hardly visible in Figures 1 and 2, including a drastic change in deaths seen in Figures 5 and 6). On December 2020, there was a maximum area for both new cases and deaths. After that, the new infections were increasing but the new deaths went down (Figure 5).

Italy. Italy was first country in Europe to meet the pandemic which may have cased the very slope seen in the linear model (Figure 7). There was also a very short time delay between the detected cases and deaths. Later the time delay went to the same two weeks which was in Finland. For Italy, the scaling functions were much steeper than for Finland (Figures 3 and 4). There was a maximum area slightly earlier than in Finland and the infection levels remained constant. The new deaths went down.

Sweden. Sweden had considerably softer actions for controlling the pandemic. According to the conformed deaths, the first period of the pandemic lasted about 50 days longer than in Finland and Italy (Figure 8). There were also a high level of infections during the whole Summer. The scaling functions were comparable with the Italian ones. Time delays between confirmed cases and deaths

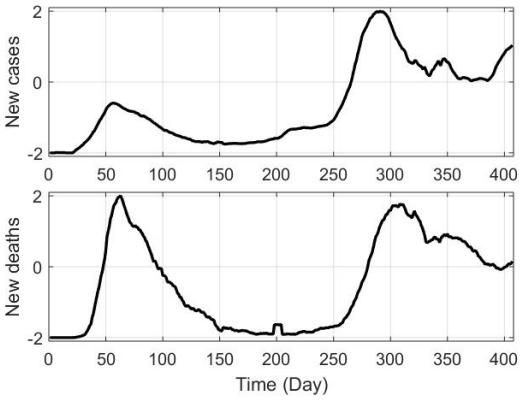

Figure 7. Scaled daily COVID-19 cases and deaths in Italy.

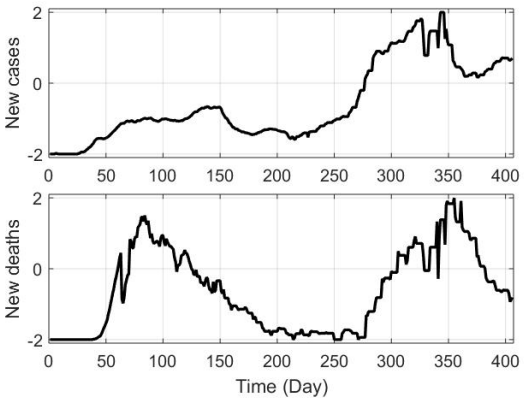

Figure 8. Scaled daily COVID-19 cases and deaths in Sweden.

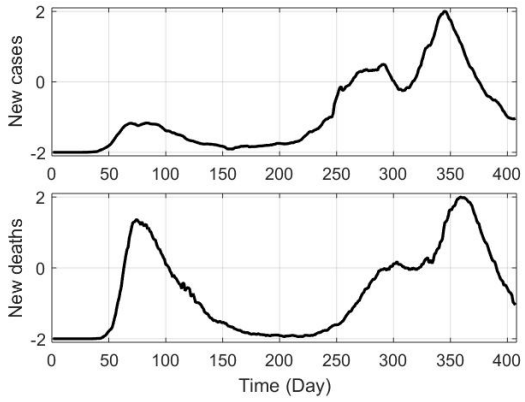

Figure 9. Scaled daily COVID-19 cases and deaths in the United Kingdom.

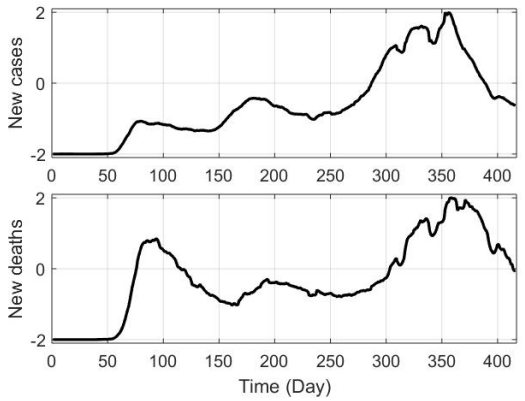

Figure 10. Scaled daily COVID-19 cases and deaths in the United States.

were not easy to find since the level of infections was high continuously.

United Kingdom. The scaling functions are the steepest for the United Kingdom (Figures 3 and 4). The first period of the pandemic went very closely in the same way as in Finland and Italy. In the autumn of 2020, a short maximum area was slightly before the similar period in Italy. This was followed by a short maximum period and a very steep decrease for both the new cases and deaths (Figure 9. The decrease is considerably faster than in the first pandemic period. This improvement is linked with the widening vaccination (Table 1).

USA. Scaling functions are quite steep already in the first period. The first period of the pandemic started in the same way as in Finland, Italy and the UK (Figure 10). Summer 2020 was different: the recovery was slow, even slower than in Sweden. The level of new infections and deaths were all the time higher than in other countries. Three peaks were detected in November-December 2020

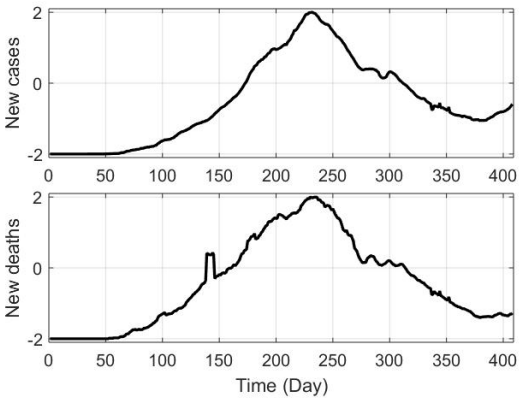

Figure 11. Scaled daily COVID-19 cases and deaths in India.

could be from different infection transmission chains. After them, the level of new infections go down almost as fast as in the UK. Also, here this improvement is linked with the widening vaccination (Table 1). The time difference between the last peaks of the infections and the deaths is again close to two weeks.

India. India was in the starting phase: the parameters of the scaling functions have very low values (Figures 3 and 4 and the time difference between the peaks of the infections and the deaths are small (Figure 11).

5 Discussions

The nonlinear phenomena are well presented with the combination of the nonlinear scaling and linear interactions for different countries in varying operating conditions. The same approach operates for both the confirmed cases and deaths. Different countries and specific periods, including periods where the data quality is not sufficient, are analyzed in the same scale $[-2,2]$.

The effects of the vaccinations at the end of the analyzed period are clear, especially the UK and the USA but also Finland, Italy and Sweden where the vaccinations were just started.

Limitations are seen if there are too many interacting things, e.g. several infection transmission chains which are in different stages. Situations of this kind of are active in the summer of 2020 in Sweden and the USA. Three infection chains in November-December 2020 are interacting. The actual inputs would be needed in those situations.

6 Conclusions and future studies

The combination of the nonlinear scaling and linear interactions operates well for different countries in varying operating conditions. This aggregated material was used for analyzing some countries. The analysis can be done with this approach for any country which has data in the overall dataset.

The analysis can be done in similarly for different subsets. Specific scaling functions can be used in local analysis and for groups of people to increase the sensitivity of the temporal analysis. The data material already includes hospital patients and patients in intensive care. The progress in people vaccinations provides more material for comparisons. Also, different variants can be taken in the analysis.

References

Our world in data. https://ourworldindata.org/, 2021. Accessed: 2021-07-10.

F. Arroyo-Marioli, F. Bullano, S. Kucinskas, and C. Rondón-Moreno. Tracking r of COVID-19: A new real-time estimation using the kalman filter. *PLoS ONE*, 16(1):1–16, 2021.

R. Babuška and H. Verbruggen. Neuro-fuzzy methods for nonlinear system identification. *Annual Reviews in Control*, 27 (1):73–85, 2003.

G. E. P. Box and K. B. Wilson. On the experimental attainment of optimum conditions. *Journal of the Royal Statistical Society. Series B*, 13(1):1–45, 1951.

CSSE. COVID-19 data repository by the center for systems science and engineering (CSSE) at Johns Hopkins University. https://github.com/CSSEGISandData/COVID-19, 2021. Accessed: 2021-07-10.

E. Dong, H. Du, and L. Gardner. An interactive web-based dashboard to track covid-19 in real time. *Lancet Inf Dis.*, 20(5): 533–534, 2020. doi:10.1016/S1473-3099(20)30120-1.

R. W. Gerlach, B. R. Kowalski, and H. O. A. Wold. Partial least squares modelling with latent variables. *Anal. Chim. Acta*, 112(4):417–421, 1979.

Thomas Hale, Noam Angrist, Rafael AU Goldszmidt, Beatriz Kira, Anna Petherick, Toby Phillips, Samuel Webster, Emily Cameron-Blake, Laura Hallas, Saptarshi Majumdar, and Helen Tatlow. A global panel database of pandemic policies (oxford covid-19 government response tracker. *Nature Human Behaviour*, 5:529–538, 2021. doi:10.1038/s41562-021-01079-8.

T. Jefferson, E. A. Spencer, A. Plüddemann, N. Roberts, and C. Heneghan. Transmission dynamics of COVID-19: An open evidence review. https://www.cebm.net/evidence-synthesis/transmission-dynamics-of-covid-19/, 2021. Accessed: 2021-07-10.

I. T. Jolliffe. *Principal Component Analysis*. Springer, New York, 2 edition, 2002. 487 pp.

E. Juuso and S. Lahdelma. Intelligent scaling of features in fault diagnosis. In *7th International Conference on Condition Monitoring and Machinery Failure Prevention Technologies, CM 2010 - MFPT 2010, 22-24 June 2010, Stratford-upon-Avon, UK*, volume 2, pages 1358–1372, 2010. URL www.scopus.com.

E. K. Juuso. Integration of intelligent systems in development of smart adaptive systems. *International Journal of Approximate Reasoning*, 35(3):307–337, 2004. doi:10.1016/j.ijar.2003.08.008.

E. K. Juuso. Tuning of large-scale linguistic equation (LE) models with genetic algorithms. In M. Kolehmainen, editor, *Revised selected papers of the International Conference on Adaptive and Natural Computing Algorithms - ICANNGA 2009, Kuopio, Finland, Lecture Notes in Computer Science*, volume LNCS 5495, pages 161–170. Springer-Verlag, Heidelberg, 2009. doi:10.1007/978-3-642-04921-7_17.

E. K. Juuso. Recursive tuning of intelligent controllers of solar collector fields in changing operating conditions. In S. Bittani, A. Cenedese, and S. Zampieri, editors, *Proceedings of the 18th World Congress The International Federation of Automatic Control, Milano (Italy) August 28 - September 2, 2011*, pages 12282–12288. IFAC, 2011. doi:10.3182/20110828-6-IT-1002.03621.

E. K. Juuso. Intelligent methods in modelling and simulation of complex systems. *Simulation Notes Europe SNE*, 24(1):1–10, 2014. doi:10.11128/sne.24.on.102221.

E. K. Juuso. Expertise and uncertainty processing with nonlinear scaling and fuzzy systems for automation. *Open Engineering*, 10(1):712–720, 2020. doi:10.1515/eng-2020-0080.

E. K. Juuso. Intelligent temporal analysis of coronavirus statistical data. *Open Engineering*, 2021. doi:10.1515/eng-2020-0285.

E. K. Juuso and K. Leiviskä. Adaptive expert systems for metallurgical processes. In S.-L. Jämsä-Jounela and A. J. Niemi, editors, *Expert Systems in Mineral and Metal Processing, IFAC Workshop, Espoo, Finland, August 26-28, 1991, IFAC Workshop Series, 1992, Number 2*, pages 119–124, Oxford, UK, 1992. Pergamon.

S. Lahdelma and E. Juuso. Signal processing and feature extraction by using real order derivatives and generalised norms. Part 1: Methodology. *International Journal of Condition Monitoring*, 1(2):46–53, 2011. doi:10.1784/204764211798303805.

L. Ljung. *System Identification - Theory for the User*. Prentice Hall, Upper Saddle River, N.J., 2nd edition, 1999.

L. Ljung. Perspectives on system identification. In M. J. Chung and P. Misra, editors, *Plenary papers, milestone reports & selected survey papers, 17th IFAC World Congress, Seoul, Korea, July 6-11, 2008*, pages 47–59. IFAC, 2008. http://www.ifac-papersonline.net/.

Hannah Ritchie, Esteban Ortiz-Ospina, Diana Beltekian, Edouard Mathieu, Joe Hasell, Bobbie Macdonald, Charlie Giattino, Cameron Appel, Lucas Rodés-Guirao, and Max Roser. Coronavirus pandemic (COVID-19). *Our World in Data*, 2020. https://ourworldindata.org/coronavirus.